Parallel Performance of the Multi-threaded ICCG Solver in Electromagnetic Finite Element Analyses on the Latest Processors

K. Semba[1, 2], **K. Tani**[1], **T. Yamada**[1], **T. Iwashita**[3], **Y. Takahashi**[4], **and H. Nakashima**[3]

[1]Engineering Division, JSOL Corporation, Tokyo, Japan
[2]Graduate School of Informatics, Kyoto University, Kyoto, Japan
[3]Academic Center for Computing and Media Studies, Kyoto University, Kyoto, Japan
[4]Department of Electrical Engineering, Doshisha University, Kyoto, Japan

Abstract— The performance of multithreaded incomplete Cholesky conjugate gradient solvers in finite element electromagnetic field analysis is analyzed. We compare the parallel performance of the additive Schwarztype incomplete Cholesky preconditioned conjugate gradient (AS-ICCG) solver and the parallelized incomplete Cholesky conjugate gradient solver using algebraic block multicolor ordering (ABMC-ICCG) on the latest processors. A numerical test of the interior-permanent-magnet motor model analysis shows that the ABMC-ICCG solver has faster computation speed than the AS-ICCG solver in 16-core executions on an Intel® Xeon® E5 processor, and attains a 7.6-fold speedup relative to the sequential solver. Moreover, we analyze performance on an Intel® Xeon Phi™coprocessor and attain a 35-fold speedup relative to the sequential solver on the same coprocessor using the ABMC-ICCG solver.

1. INTRODUCTION

In finite element electromagnetic field analysis (FEA), a linear sparse iterative solver typified by an incomplete Cholesky conjugate gradient (ICCG) method accounts for most of the computational time, and thus a speedup of the solver is desired. Accordingly, we have investigated the use of multithreaded parallel processing in FEA. While the multithreaded iterative solver is used in a shared memory parallel computational node such as a personal computer having multicore processors, it can also work as an internal solver in a distributed memory parallel solver employing domain decomposition for a cluster of computational nodes.

Earlier in our research, we developed a multithreaded ICCG solver using algebraic block multicolor (ABMC) ordering [1]. The ABMC ordering is a parallel ordering technique that has better solver performance than conventional multicolor ordering [2] in FEA for practical models such as interior-permanent-magnet (IPM) motors. However, it was found that the convergence of the solver was significantly degraded when the effect of the external circuit was taken into account. Consequently, we proposed a new parallelization technique in which the unknowns related to the external circuit are dealt with separately from the unknowns for the field variables during the reordering process [3]. The new parallel solver exhibits good convergence for the model with the external circuit.

In the present research, we examine the parallel multithreaded solver based on ABMC ordering in FEA conducted on the latest processors and compare its performance with the additive Schwarztype incomplete Cholesky preconditioned conjugate gradient method [4], which is one of the most popular parallelization techniques when employing the ICCG method. Numerical tests for performance evaluation were conducted on the latest multicore processor (Intel® Xeon® E5) and an Intel® Xeon Phi™coprocessor based on Intel® Many Integrated Core (MIC) architecture.

2. FINITE-ELEMENT ELECTROMAGNETIC-FIELD ANALYSIS

This paper considers FEA in the low frequency range for electric machines such as electric motors. The governing equation derived from the Maxwell equations is

$$\nabla \times \frac{1}{\mu} \nabla \times A + \sigma \frac{\partial A}{\partial t} = J_0, \tag{1}$$

where A is the magnetic vector potential, μ the magnetic permeability, σ the electrical conductivity, t time, and J_0 the forced current density [5]. The boundary conditions are given as

$$A \times n = 0 \quad \text{for the Dirichlet boundary,} \tag{2}$$

$$(\nabla \times A) \times n = 0 \quad \text{for the Neumann boundary,} \tag{3}$$

where n is an outward vector normal to analysis region.

In practical analyses, the effect of external circuits should be considered for the electromagnetic source. In this case, the Maxwell equations are simultaneously solved with the voltage equation

$$[V] - [R][I] - [v_{coil}] = 0. \tag{4}$$

Because the voltage equation holds for each closed-loop circuit, Equation (4) is written in matrix-vector form. Here, $[V]$ is the source voltage, $[R]$ the resistance, and $[I]$ the current passing through the resistance. The vector $[v_{coil}]$ is the induced voltage in the coil, which is calculated by FEA as

$$[v_{coil}]_i = \frac{\partial \Phi}{\partial t} = \int_{\Omega_c} \left\{ \frac{\partial A}{\partial t} \cdot (\nabla \times T^i) \right\} dv. \tag{5}$$

The suffix "i" is the ID of the coil, Φ the flux of the coil, T the current vector potential, and Ω_c the coil region, and $\int dv$ denotes volume integration.

Moreover, the nonlinearity of the magnetic permeability is generally considered in practical analyses. In the present research, the well-known Newton-Raphson (NR) method is used for nonlinear analysis. Consequently, the linear system to solve in each NR step, which is derived from Equations (1) and (4), is given by

$$[K][\delta x] = [f], \tag{6}$$

where $[K]$ is the coefficient matrix, $[\delta x]$ the unknowns corresponding to the correction for the magnetic vector potential A and the current I, and $[f]$ the right-hand-side vector based on the residual of Equations (1) and (4). In the analysis, the linear system (6) is solved by an ICCG solver.

3. PARALLELIZED ICCG SOLVERS

In this paper, we evaluate two parallelized (multithreaded) ICCG solvers.

3.1. Additive Schwarz-type IC Preconditioned CG Method

Additive Schwarz incomplete Cholesky preconditioning is that in which incomplete factorization is used for the subdomain solver [4]. A set of unknowns is divided into n_t subsets, where n_t is the number of threads. Each subdomain corresponds to a subset, and the (localized) incomplete Cholesky factorization yields a block diagonal structure of the preconditioner matrix. In other words, the off-diagonal elements of the coefficient matrix that relates to two different threads are ignored in the construction of the preconditioner. Consequently, each thread independently performs the forward and backward substitutions for the preconditioning step in iterations. Although no thread synchronization is required in the parallelized preconditioning step, the technique often suffers from degradation of the convergence rate when the number of threads is increased. It is noted that the parallelization method is introduced as the "block ICCG method" in [6] and is called the "localized ICCG method" in some of the literature.

3.2. Parallel ICCG Method Based on ABMC Ordering

The ABMC method is a parallel ordering technique that can be used for parallelization of the ICCG method [1]. Employing the technique, a set of unknowns V is divided into multiple blocks of size s (or adjusted to $s-1$ automatically in practice). A color is then assigned to each block satisfying the condition that two different blocks having an identical color have no data relationship in the coefficient matrix. Consequently, the reordered matrix has the form shown in Fig. 1 and the substitutions are parallelized blockwise in each color. Employing this technique, although the convergence rate depends on the number of colors and block size, the rate is unaffected by the number of threads. This property of the ABMC method is preferable for execution using many threads. Moreover, it has been shown that the ABMC method has the advantages of a high cache hit ratio and fast convergence over conventional multicolor ordering.

However, significant convergence degradation was observed when the ABMC method was applied to the linear system arising from FEA in which a practical model with external circuits is solved. Therefore, we introduced the partial reordering, where only the unknowns related to the potentials are reordered, in previous work [3], and use it in the present analysis.

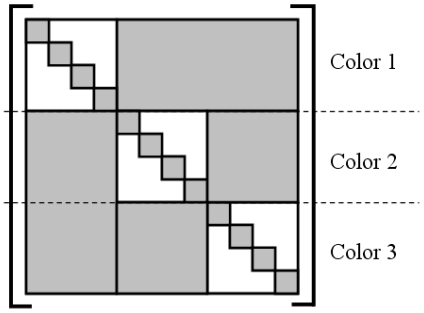

Figure 1: Example of a coefficient matrix obtained by ABMC ordering.

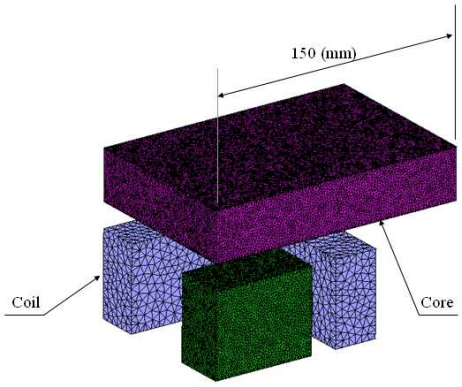

Figure 2: Electromagnet analysis model.

4. NUMERICAL RESULTS

4.1. Computers and Analysis Models

The main objective of the present research is to evaluate the performance of the multithreaded ICCG solver in the computational environment of the latest processor technology. We use two different computational platforms. One is a computational node composed of two Intel® Xeon® E5-2670 processors. The processor has eight cores based on Sandy Bridge microarchitecture. The other platform is the Intel® Xeon® Phi coprocessor based on Intel® MIC architecture. The coprocessor has 60 physical cores, on each of which up to four threads can run using hyper-threading technology. For multithreading, we use OpenMP on both computational platforms. Additionally, several directives are inserted into the program for the implementation on the Xeon® Phi coprocessor. One of the virtues of the coprocessor is that it is unnecessary to largely modify the original Open MP code oriented toward general multi-core processors.

We conducted numerical tests for two FEA models: models of an electromagnet and IPM motor. The solution time was recorded and evaluated for the first nonlinear iteration at the second time step. The convergence criterion is that the relative residual norm is less than 1.0×10^{-8}. Moreover, in the present analysis, to avoid breakdown of the incomplete factorization, shifted incomplete Cholesky factorization is used. The acceleration factor (shift parameter) is fixed at 1.2 in the numerical test.

4.2. Analysis of the Electromagnet Model

The mesh model is shown in Fig. 2. The model is discretized by 967,363 first-order tetrahedral elements. Eddy current is taken into account in the core. The number of total unknowns is 1,115,046. For the ABMCICCG solver, we fix the block size at 64 in the analysis.

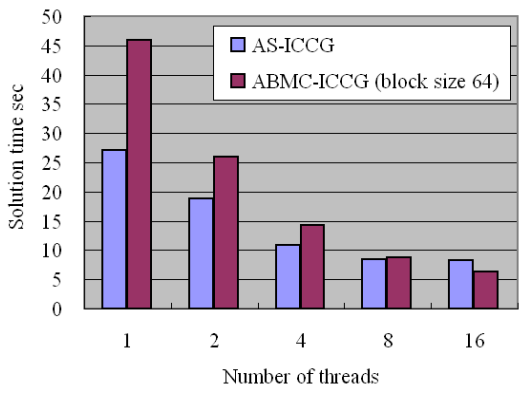

Figure 3: Solution time for the electromagnet model on an Intel Xeon E5 processor.

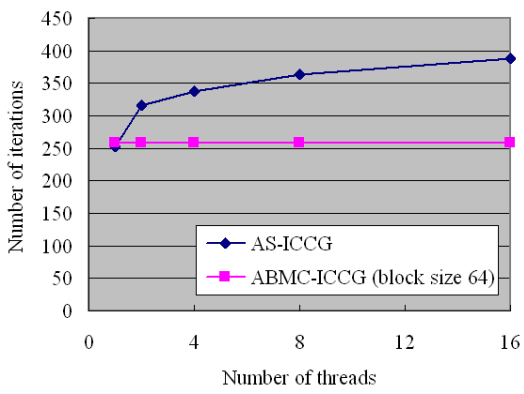

Figure 4: Solution time for the electromagnet model on an Intel Xeon E5 processor.

The solution time measured for the Xeon® E5 processor is shown in Fig. 3, where AS-ICCG refers to the additive Schwarztype incomplete Cholesky preconditioned conjugate gradient method. In the comparison of sequential computation, the AS-ICCG solver is faster than the ABMC-ICCG solver. However, the solution time for the ABMC-ICCG solver employing 16 threads is 6.4 (sec) (7.2-fold parallel speedup) and shorter than that for the AS-ICCG solver (8.2 (sec)). This is mainly because of the different convergence characteristics of the two solvers. Fig. 4 shows that the number of iterations increases from 252 (sequential solver) to 388 (16 threads) for the AS-ICCG solver, whereas the ABMC-ICCG solver maintains a constant convergence rate independent of the number of threads, which means that the ABMC-ICCG solver performs better than the AS-ICCG solver in a highly multithreaded environment.

4.3. Analysis of the IPM Motor

The IPM motor model includes an external circuit that feeds the current source which is shown in Fig. 5. The model is discretized by 360,152 first-order tetrahedral elements. Eddy current is considered in the regions of the permanent magnet and the stator core, which has a lamination factor of 99%. The number of unknowns is 384,965. The block size of the ABMC ordering is set to 512.

The solution time and number of iterations for processing on the Xeon® E5 are shown in Figs. 6 and 7 respectively. The numerical result is similar to that for the electromagnet model analysis. Although the AS-ICCG solver is faster than the ABMC-ICCG solver in sequential computation, and the latter solver has better performance in parallel computations using 16 threads. The ABMC-ICCG solver attains a 7.6-fold speedup on 16 cores. The parallel performance can be said to be relatively good considering that the performance of a parallel iterative solver is strongly affected by the memory bandwidth in general.

As mentioned above, the ABMC-ICCG solver has a suitable convergence property for execution using a large number of threads. We thus investigated the parallel performance of the ABMC-ICCG solver on the Xeon® Phi coprocessor. By setting the block size to 60, we attain an approximately 35-fold speedup using 240 threads compared with the sequential computation as shown in Fig. 8.

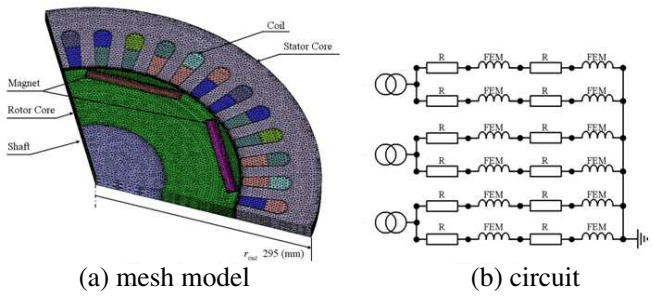

Figure 5: IPM motor model with external circuit.

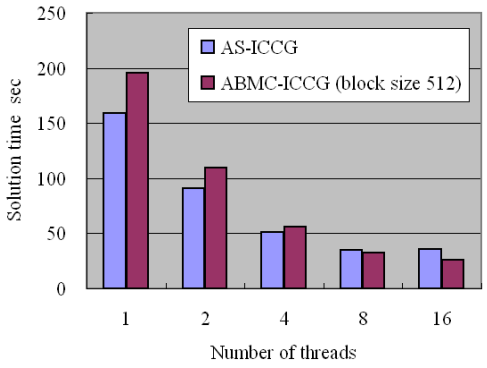

Figure 6: Solution time for the IPM motor model on an Intel Xeon E5 processor.

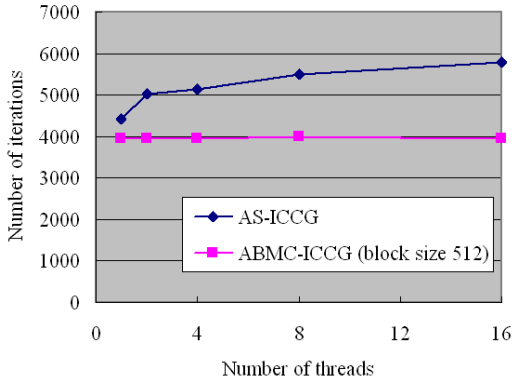

Figure 7: Number of iterations for the IPM motor model on an Intel Xeon E5 processor.

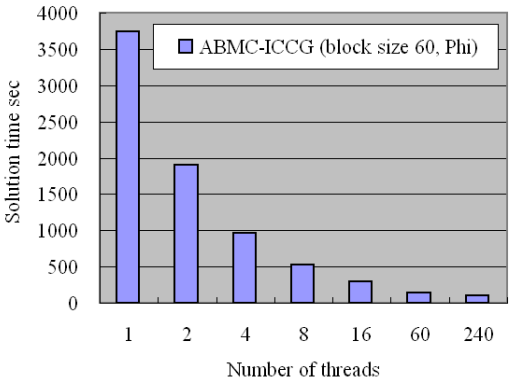

Figure 8: Solution time for an IPM motor model on an Intel Xeon Phi coprocessor.

5. CONCLUSIONS

We examined the parallel performance of the additive Schwarztype incomplete Cholesky preconditioned conjugate gradient (AS-ICCG) solver and parallelized ICCG solver based on ABMC ordering (ABMC-ICCG) in finite-element electromagnetic-field analysis carried out on an Intel® Xeon® E5 processor. The ABMC-ICCG solver achieves 7.2- and 7.6-fold speedups using 16 threads relative to the sequential solver in two numerical tests, and it is faster than the AS-ICCG solver in parallel computation. This is because the ABMC-ICCG solver maintains a constant convergence rate independent of the number of threads, whereas the AS-ICCG solver suffers convergence degradation as the number of threads increases. This result indicates that the ABMC-ICCG solver is more suitable than the AS-ICCG solver in a highly parallel computation environment. Next, we conducted a numerical test on the latest coprocessor, the Intel® Xeon® Phi based on MIC architecture, which allows us to use many more threads than a general multi-core processor. On the Xeon® Phi coprocessor, the ABMC-ICCG solver attains a 35-fold parallel speedup using 240 threads. In analysis of further speedup, we will tackle the development of the parallelized ICCG solver that more effectively uses the single instruction multiple data (SIMD) operation of Xeon® Phi as future work.

REFERENCES

1. Iwashita, T., H. Nakashima, and Y. Takahashi, "Algebraic block multi-color ordering method for parallel multi-threaded sparse triangular solver in ICCG method," *IEEE 26th International Parallel Distributed Processing Symposium*, 2012.
2. Saad, Y., *Iterative Methods for Sparse Linear Systems*, 2nd Edition, SIAM, Philadelphia, PA, 2003.
3. Semba, K., K. Tani, T. Yamada, T. Iwashita, Y. Takahashi, and H. Nakashima, "Parallel performance of multi-threaded ICCG Solver based on algebraic block multi-color ordering in finite element electromagnetic field analyses," *15th Biennial IEEE Conference on Electromagnetic Field Computation*, 2012.
4. Benzi, M., W. Joubert, and G. Mateescu, "Numerical experiments with parallel orderings for ILU preconditioners," *Electronic Transactions on Numerical Analysis*, Vol. 8, 88–114, 1999.
5. Silvester, P. P. and R. L. Ferrari, *Finite Elements for Electrical Engineers*, 3rd Edition, Cambridge University Press, 1983.
6. Vollaire, C. and L. Nicolas, "Preconditioning techniques for the conjugate gradient solver on a parallel distributed memory computer," *IEEE Trans. Magn.*, Vol. 34, 33473350, 1998.

Maxwell Equations of Electromagnetic and Gravitational Fields in the Curved Spaces

Zi-Hua Weng
School of Physics and Mechanical & Electrical Engineering
Xiamen University, Xiamen 361005, China

Abstract— The paper proposes three basic postulates, to introduce the octonion space into the field theory, and then to describe simultaneously the physical features of the electromagnetic field and of the gravitational field in the curved octonion space. From the conceptions of the orthogonality, connection, and parallel transport in the curved octonion space, it is able to yield the octonion metric coefficient, connection coefficient, and curvature. The decomposition of the gravitational source's definition deduces the gravitational field equations in the curved space, while the disassembling of the electromagnetic source's definition produces the electromagnetic field equations in the curved space. The result reveals that the connection coefficient and curvature in the curved octonion space will direct impact the electromagnetic field equations, gravitational field equations, and their physical features.

1. INTRODUCTION

J. C. Maxwell was the first to adopt the quaternion and the vector terminology to simultaneously describe the electromagnetic theory. The algebra of quaternions was invented by W. R. Hamilton in 1843. More than twenty years after that, the quaternion was taken apart into the scalar part and vector part. J. C. Maxwell began to study the electromagnetic field around 1850, and mixed naturally two methods to depict the physical features of electromagnetic fields [1]. Currently the electromagnetic theory described by the vector is quite mature, while the electromagnetic theory depicted by the quaternion is not so successful.

As the ordered couple of quaternions, the octonion was invented independently by J. T. Graves in 1843 and A. Cayley in 1845. Just like the complex number, the octonion also can be divided into two components, the quaternion and the S-quaternion, while the S-quaternion is the product of another quaternion and the 'fourth imaginary unit'. The 'fourth imaginary unit' is independent to the 'three imaginary unit' of the quaternion. The result reveals that the quaternion is suitable to describe the physical features of gravitational fields, while the S-quaternion is propitious to depict the physical features of electromagnetic fields. And may be that can partly explain why it is not completely successful before to describe the electromagnetic field theory directly by the quaternion (rather than the S-quaternion).

It is one new research technique to adopt the octonion method to simultaneously describe the electromagnetic and gravitational theories. In the research technique, it is necessary to introduce three basic postulates as follows [2]. From the three basic postulates, the algebra of octonions can be introduced into the field theory, and then to describe the physical features of the electromagnetic and gravitational fields.

The first postulate: individual space-time. The space-time extended from the electromagnetic field is different from the one extended from the gravitational field. The viewpoint of R. Descartes, M. Faraday, and A. Einstein etc. claims that, the field is an irreducible element of physical description, while the space-time is only the extension of the field and does not claim existence on its own. Further each field extends its individual space-time. That is, the space-time extended from the electromagnetic field is independent to that from the gravitational field. They are quite similar but independent to each other.

The second postulate: quaternion space. Each space-time extended respectively from the field, including the electromagnetic field and gravitational field, can be chosen as the quaternion space. According to the viewpoint of W. R. Hamilton and J. C. Maxwell etc., the space-time in the physics can be chosen as the quaternion space. These two space-times, extended respectively from the electromagnetic field and the gravitational field, both can be considered as the quaternion space, and are perpendicular to each other, so that they can combine together to become an octonion space. Therefore the octonion space can be used to describe the physical features of the electromagnetic field and the gravitational field.

The third postulate: dimensional homogeneity. It is necessary to introduce the coefficient to maintain the dimensional homogeneity for all of physical quantities in the same one formula. In

order to maintain the dimensional homogeneity, the physical quantity of the electromagnetic field should be multiplied by the undetermined coefficient, when the two kinds of physical quantities exist in the same one octonion formula. The undetermined coefficient can be determined by comparing with the classical theories of the electromagnetic field [3] and of the gravitational field.

According to the above three postulates, each space-time extended respectively from the electromagnetic field or the gravitational field can be chosen as the flat or curved quaternion space. Further the quaternion space for the electromagnetic field and that for the gravitational field can be combined together to become the octonion space, which may be flat or curved.

2. CURVED QUATERNION SPACE

In the curved quaternion space, from the definition of the quaternion orthogonality, it is able to define the quaternion parallel transport and connection, and then to define further the quaternion metric coefficient, connection coefficient, and curvature etc..

In the flat quaternion space, the quaternion product $\mathbb{G} \circ \mathbb{H}$ of two quaternions, $\mathbb{G}(g^0, g^1, g^2, g^3)$ and $\mathbb{H}(h^0, h^1, h^2, h^3)$, consists of the scalar part $\mathbb{G} \odot \mathbb{H}$ and the vector part $\mathbb{G} \otimes \mathbb{H}$. According to the definition of quaternion orthogonality, $\mathbb{G}$ and $\mathbb{H}$ are on an orthogonal state when $\mathbb{G} \odot \mathbb{H} = 0$. The definitions of the quaternion parallel transport and quaternion connection can be derived from the conception of quaternion orthogonality.

In the curved quaternion space, the quaternion radius vector is $\mathbb{R}_g(u^0, u^1, u^2, u^3)$, and the quaternion tangent frame is $\{\mathbf{e}_i\}$. The quaternion space-time interval is defined as

$$dR^2 = d\mathbb{R}_g \odot d\mathbb{R}_g = g_{ij} du^i du^j, \tag{1}$$

where the metric coefficient, $g_{ij} = \mathbf{e}_i \odot \mathbf{e}_j$. The quaternion tangent frame, $\mathbf{e}_i = \partial\mathbb{R}/\partial u^i$. $\mathbf{e}_0$ is the scalar. $\odot$ denotes the quaternion scalar product. $u^0 = ct$, c is the speed of light, and t is the time. $i, j, k, m = 0, 1, 2, 3$.

Just like the tensor theory, for the physical quantity $Y^i(\mathbb{P})$ of one point $\mathbb{P}$ in the curved quaternion space, the component of the quaternion covariant derivation with respect to the coordinate u^k is,

$$\nabla_k Y^i = \partial Y^i/\partial u^k + \Gamma^i_{jk} Y^j, \tag{2}$$

where Γ^i_{jk} is the connection coefficient.

3. GRAVITATIONAL FIELD EQUATIONS

In the curved quaternion space, the expansion of the gravitational source's definition is able to deduce the gravitational field equations of the curved space. The gravitational potential, $\mathbb{A}_g(a^0, a^1, a^2, a^3)$, is defined as,

$$\mathbb{A}_g = \Diamond \circ \mathbb{X}_g = \Diamond \odot \mathbb{X}_g + \Diamond \otimes \mathbb{X}_g, \tag{3}$$

where $\Diamond x^i = (\mathbf{e}^k \nabla_k) x^i$, $\mathbf{e}^i = g^{ij}\mathbf{e}_j$. The quaternion physical quantity, $\mathbb{X}_g = x^j \mathbf{e}_j$. The scalar part of $\mathbb{A}_g$ is, $\Diamond \odot \mathbb{X}_g = a$, with $a = a^0$. The vector part of $\mathbb{A}_g$ is, $\Diamond \otimes \mathbb{X}_g = \mathbf{a}$, with $\mathbf{a} = a^p \mathbf{e}_p$. And $\mathbb{A}_g$ contains the connection coefficient Γ^i_{jk}. $p, q = 1, 2, 3$.

From the gravitational potential, the gravitational strength, $\mathbb{B}_g(k^0, k^1, k^2, k^3)$, is defined as,

$$\mathbb{B}_g = \Diamond \circ \mathbb{A}_g = \Diamond \odot \mathbb{A}_g + \Diamond \otimes \mathbb{A}_g, \tag{4}$$

where the scalar part of $\mathbb{B}_g$ is, $\Diamond \odot \mathbb{A}_g = k^0 \mathbf{e}_0$. And the vector part of $\mathbb{B}_g$ is, $\Diamond \otimes \mathbb{A}_g = k^p \mathbf{e}_p$. The gauge condition is chosen as $k^0 = 0$. And $\mathbb{B}_g$ contains the curvature R^i_{jkm}. $\nabla a^i = (\mathbf{e}^q \nabla_q) a^i$.

The vector part of gravitational strength can be decomposed as, $k^p \mathbf{e}_p = \mathbf{g}/c + \mathbf{b}$, and

$$\mathbf{g}/c = \nabla_0 \circ \mathbf{a} + \nabla \circ a, \tag{5}$$

$$\mathbf{b} = \nabla \times \mathbf{a}, \tag{6}$$

where the strength component $\mathbf{g}$ is similar to the electric intensity, and is relevant to the linear acceleration. The strength component $\mathbf{b}$ is similar to the magnetic flux density, and is related with the angular velocity. $\nabla \circ a = (\mathbf{e}^q \nabla_q) \circ (a^0 \mathbf{e}_0)$. $\nabla \times \mathbf{a} = (\mathbf{e}^q \nabla_q) \times (a^p \mathbf{e}_p)$. $\nabla_0 \circ \mathbf{a} = (\mathbf{e}^0 \nabla_0) \circ (a^p \mathbf{e}_p)$.

From the gravitational strength, the gravitational source, $\mathbb{S}_g(s^0, s^1, s^2, s^3)$, is defined as,

$$-\mu\mathbb{S} = -(\mu_g\mathbb{S}_g - \mathbb{B}_g^* \circ \mathbb{B}_g/c) = (\Diamond + \mathbb{B}_g/c)^* \circ \mathbb{B}_g, \tag{7}$$

where the scalar part of $\mathbb{S}_g$ is, $-\Diamond^* \odot \mathbb{B}_g/\mu_g$, and the vector part of $\mathbb{S}_g$ is, $-\Diamond^* \otimes \mathbb{B}_g/\mu_g$. And $\mathbb{S}_g$ contains the partial derivative of the curvature R^i_{jkm}. μ and $\mu_g < 0$ are the coefficients. In the quaternion space, $-\mu_g\mathbb{S}_g = \Diamond^* \circ \mathbb{B}_g = \Diamond^* \odot \mathbb{B}_g + \Diamond^* \otimes \mathbb{B}_g$.

The scalar part of the gravitational source $\mathbb{S}_g(s^0, s^1, s^2, s^3)$ is, $-\Diamond^* \odot \mathbb{B}_g/\mu_g = s^0\mathbf{e}_0$, and can be rewritten as

$$\nabla^* \cdot (\mathbf{g}/c + \mathbf{b}) = -\mu_g s^0\mathbf{e}_0. \tag{8}$$

In the local range of the curved quaternion space, the 'Gauss's law' is derived from the definitions of the gravitational potential and the gravitational strength,

$$\nabla \cdot \mathbf{b} = 0, \tag{9}$$

and then the above two equations deduce the Newton's law of gravitation,

$$\nabla^* \cdot (\mathbf{g}/c) = -\mu_g s^0\mathbf{e}_0, \tag{10}$$

where $\nabla \cdot \mathbf{b} = (\mathbf{e}^q\nabla_q) \cdot (b^p\mathbf{e}_p)$. The above will be degenerated into the Newton's law of gravitation in the static gravitational field, when $\mathbf{a} = 0$ and $\mathbf{b} = 0$.

The vector part of the gravitational source $\mathbb{S}_g(s^0, s^1, s^2, s^3)$ is, $-\Diamond^* \otimes \mathbb{B}_g/\mu_g = s^p\mathbf{e}_p$, and can be rewritten as

$$\nabla_0 \circ (\mathbf{g}/c + \mathbf{b}) + \nabla^* \times (\mathbf{g}/c + \mathbf{b}) = -\mu_g s^p\mathbf{e}_p. \tag{11}$$

In the local range of the curved quaternion space, the definitions of the gravitational potential and the gravitational strength deduce the following equation,

$$\nabla_0 \circ \mathbf{b} + \nabla^* \times (\mathbf{g}/c) = 0, \tag{12}$$

and then the above two equations yield the 'Ampere's law' of gravitation,

$$\nabla_0 \circ (\mathbf{g}/c) + \nabla^* \times \mathbf{b} = -\mu_g s^p\mathbf{e}_p, \tag{13}$$

where the effect of the linear momentum $(s^p\mathbf{e}_p)$ is inconspicuous generally, because the μ_g of the gravitation field is so weak.

The definition of gravitational source can also be written as D'Alembert equation,

$$-\mu_g\mathbb{S}_g = \Diamond^* \circ (\Diamond \circ \mathbb{A}_g) = \Diamond^2\mathbb{A}_g, \tag{14}$$

where the term, $\Diamond^2 a^i = (\Diamond^* \circ \Diamond)a^i$, contains the partial derivative of the curvature R^i_{jkm}.

In the curved quaternion space, Equations (9), (10), (12), and (13) constitute the gravitational field equations. The gravitational field equations reveal that the mass and the linear momentum both will produce the gravitational field. The strength components $\mathbf{b}$ and $\mathbf{g}$ can be induced each other in the gravitational field. By means of the experiment measurement of the gravitational field equations in the curved quaternion space, one can appraise the departure degree of the curved quaternion space from the flat quaternion space. The research technique of the gravitational field equations in the curved quaternion space can be generalized into the analysis of the electromagnetic field equations in the octonion space.

4. CURVED OCTONION SPACE

In the curved octonion space, from the definition of the octonion orthogonality, it is able to define the octonion parallel transport and connection, and then to define the octonion metric coefficient, connection coefficient, and curvature etc..

The octonion space consists of the quaternion space and the S-quaternion space. In the quaternion space for the gravitational field, the quaternion radius vector is $\mathbb{R}_g(u^i)$, and the quaternion tangent frame is $\{\mathbf{e}_i\}$. In the S-quaternion space for the electromagnetic field, the S-quaternion radius vector is $\mathbb{R}_e(U^j)$, and the S-quaternion tangent frame is $\{\mathbf{E}_j\}$. In the curved octonion space, the octonion radius vector is $\mathbb{R}(u^i, U^j) = \mathbb{R}_g(u^i) + k_{eg}\mathbb{R}_e(U^j)$. The octonion radius vector can be written as $\mathbb{R} = u^s\mathbf{e}_s$, via the transforming $u^{j+4} = k_{eg}U^j$ and $\mathbf{e}_{j+4} = \mathbf{E}_j$. $r, s, t, u = 0, 1, 2, 3, 4, 5, 6, 7$.

In the octonion space, the octonion product $\mathbb{A} \circ \mathbb{B}$ of two octonions, $\mathbb{A}(a^r)$ and $\mathbb{B}(b^s)$, consists of the scalar part $\mathbb{A} \odot \mathbb{B}$ and the vector part $\mathbb{A} \otimes \mathbb{B}$. According to the definition of octonion orthogonality, the $\mathbb{A}$ and $\mathbb{B}$ are on an orthogonal state when $\mathbb{A} \odot \mathbb{B} = 0$. The conception of octonion orthogonality is able to deduce the definitions of the octonion parallel transport and connection.

The octonion space-time interval is defined as

$$dR^2 = d\mathbb{R} \odot d\mathbb{R} = g_{rs} du^r du^s, \tag{15}$$

where the metric coefficient, $g_{rs} = \mathbf{e}_r \odot \mathbf{e}_s$. The octonion tangent frame, $\mathbf{e}_r = \partial\mathbb{R}/\partial u^r$. $\mathbf{e}_0$ is the scalar. $\odot$ denotes the octonion scalar product. $u^0 = ct$, c is the speed of light, and t is the time.

Just like the tensor theory, for the physical quantity $Y^s(\mathbb{P})$ of one point $\mathbb{P}$ in the curved octonion space, the component of the octonion covariant derivation with respect to the coordinate u^t is,

$$\nabla_t Y^s = \partial Y^s/\partial u^t + \Gamma^s_{rt} Y^r, \tag{16}$$

where Γ^s_{rt} is the connection coefficient.

5. ELECTROMAGNETIC FIELD EQUATIONS

In the curved octonion space, the expansion of the electromagnetic source's definition deduces the electromagnetic field equations in the curved space. The octonion field potential, $\mathbb{A} = \mathbb{A}_g + k_{eg}\mathbb{A}_e$, can be defined as,

$$\mathbb{A} = \Diamond \circ \mathbb{X} = \Diamond \odot \mathbb{X} + \Diamond \otimes \mathbb{X}, \tag{17}$$

where the electromagnetic potential is $\mathbb{A}_e(A^0, A^1, A^2, A^3)$. $\Diamond A^p = (\mathbf{e}^k \nabla_k) A^p$. The octonion physical quantity, $\mathbb{X} = \mathbb{X}_g + k_{eg}\mathbb{X}_e$. The S-quaternion physical quantity, $\mathbb{X}_e = X^j \mathbf{E}_j$. The scalar part of $\mathbb{A}_e$ is, $\Diamond \odot \mathbb{X}_e = \mathbf{A}_q$, with $\mathbf{A}_q = A^0 \mathbf{E}_0$. The vector part of $\mathbb{A}_e$ is, $\Diamond \otimes \mathbb{X}_e = \mathbf{A}$, with $\mathbf{A} = A^p \mathbf{E}_p$. And $\mathbb{A}_e$ contains the connection coefficient Γ^s_{rt}.

From the above, the octonion field strength, $\mathbb{B} = \mathbb{B}_g + k_{eg}\mathbb{B}_e$, can be defined as

$$\mathbb{B} = \Diamond \circ \mathbb{A} = \Diamond \odot \mathbb{A} + \Diamond \otimes \mathbb{A}, \tag{18}$$

where the electromagnetic strength is $\mathbb{B}_e(K^0, K^1, K^2, K^3)$. The scalar part of $\mathbb{B}_e$ is, $\Diamond \odot \mathbb{A}_e = K^0 \mathbf{E}_0$, while the vector part of $\mathbb{B}_e$ is, $\Diamond \otimes \mathbb{A}_e = K^p \mathbf{E}_p$. The gauge condition of the electromagnetic potential is $K^0 = 0$. And $\mathbb{B}_e$ contains the curvature R^r_{stu}.

The vector part of the electromagnetic strength can be decomposed into, $K^p \mathbf{E}_p = \mathbf{E}/c + \mathbf{B}$,

$$\mathbf{E}/c = \nabla_0 \circ \mathbf{A} + \nabla \circ \mathbf{A}_q, \tag{19}$$

$$\mathbf{B} = \nabla \times \mathbf{A}, \tag{20}$$

where $\mathbf{E}$ is the electric intensity, and $\mathbf{B}$ is the magnetic flux density. $\nabla \circ \mathbf{A}_q = \nabla \circ (A^0 \mathbf{E}_0)$. $\nabla \times \mathbf{A} = \nabla \times (A^p \mathbf{E}_p)$. $\nabla_0 \circ \mathbf{A} = \nabla_0 \circ (A^p \mathbf{E}_p)$.

From the octonion field strength, the octonion field source $\mathbb{S}$ can be defined as

$$-\mu\mathbb{S} = -(\mu_g \mathbb{S}_g + k_{eg}\mu_e \mathbb{S}_e - \mathbb{B}^* \circ \mathbb{B}/c) = (\Diamond + \mathbb{B}/c)^* \circ \mathbb{B}, \tag{21}$$

where the electromagnetic source is $\mathbb{S}_e(S^0, S^1, S^2, S^3)$. The scalar part of $\mathbb{S}_e$ is, $-\Diamond^* \odot \mathbb{B}_e/\mu_e$, while the vector part of $\mathbb{S}_e$ is, $-\Diamond^* \otimes \mathbb{B}_e/\mu_e$. And $\mathbb{S}_e$ contains the partial derivative of curvature R^r_{stu}. μ and $\mu_e > 0$ are the coefficients. In the quaternion space, $-\mu_g \mathbb{S}_g = \Diamond^* \circ \mathbb{B}_g = \Diamond^* \odot \mathbb{B}_g + \Diamond^* \otimes \mathbb{B}_g$. In the S-quaternion space, $-\mu_e \mathbb{S}_e = \Diamond^* \circ \mathbb{B}_e = \Diamond^* \odot \mathbb{B}_e + \Diamond^* \otimes \mathbb{B}_e$.

The scalar part of $\mathbb{S}_e(S^0, S^1, S^2, S^3)$ is, $-\Diamond^* \odot \mathbb{B}_e/\mu_e = S^0 \mathbf{E}_0$, and can be written as,

$$\nabla^* \cdot (\mathbf{E}/c + \mathbf{B}) = -\mu_e S^0 \mathbf{E}_0. \tag{22}$$

In the local range of the curved octonion space, the Gauss's law of magnetism is derived from the definitions of the electromagnetic potential and the electromagnetic strength,

$$\nabla \cdot \mathbf{B} = 0, \tag{23}$$

and then the above two equations deduce the Gauss's law,

$$\nabla^* \cdot (\mathbf{E}/c) = -\mu_e S^0 \mathbf{E}_0. \tag{24}$$

The vector part of electromagnetic source $\mathbb{S}_e(S^0, S^1, S^2, S^3)$ is, $-\Diamond^* \otimes \mathbb{B}_e/\mu_e = S^p\mathbf{E}_p$, and can be rewritten as

$$\nabla_0 \circ (\mathbf{E}/c + \mathbf{B}) + \nabla^* \times (\mathbf{E}/c + \mathbf{B}) = -\mu_e S^p \mathbf{E}_p. \tag{25}$$

In the local range of the curved S-quaternion space, the definitions of the electromagnetic potential and the electromagnetic strength can deduce the Faraday's law,

$$\nabla_0 \circ \mathbf{B} + \nabla^* \times (\mathbf{E}/c) = 0, \tag{26}$$

and then the above two equations deduce the Ampere-Maxwell law of electromagnetism,

$$\nabla_0 \circ (\mathbf{E}/c) + \nabla^* \times \mathbf{B} = -\mu_e S^p \mathbf{E}_p. \tag{27}$$

The definition of electromagnetic source can also be written as D'Alembert equation,

$$-\mu_e \mathbb{S}_e = \Diamond^* \circ (\Diamond \circ \mathbb{A}_e) = \Diamond^2 \mathbb{A}_e, \tag{28}$$

where the term, $\Diamond^2 A^i = (\Diamond^* \circ \Diamond) A^i$, contains the partial derivative of the curvature R^r_{stu}.

In the curved S-quaternion space, Equations (23), (24), (26), and (27) constitute the electromagnetic field equations. The electromagnetic field equations reveal that the electric charge and the electric current both will yield the electromagnetic field. The strength components $\mathbf{E}$ and $\mathbf{B}$ can be induced each other in the electromagnetic field. By means of the experiment measurement of the electromagnetic field equations in the curved S-quaternion space, one can appraise the departure degree of the curved S-quaternion space from the flat S-quaternion space.

6. CONCLUSIONS

How to introduce the octonion into the field theory is one basic puzzle to bother the scholar for a long time. The three basic postulates in the paper may be one of approaches to solute the puzzle. From the three basic postulates, the paper introduces the octonion to describe simultaneously the physical features of the electromagnetic and gravitational fields. According to the basic postulates, the space-times, which extended from the electromagnetic field or the gravitational field, can be chosen as the quaternion spaces. Further they can constitute the flat or curved octonion space.

In the curved quaternion space, from the definitions of quaternion orthogonality and parallel transport, it is able to define the metric coefficient, connection coefficient, and curvature etc of the curved space. The decomposition of the gravitational source's definition deduces the gravitational field equations, including the 'Ampere's law' of gravitation, 'Gauss's law', and Newton's law of gravitation etc in the curved quaternion space. The connection coefficient and curvature will direct impact the gravitational field equations in the curved quaternion space. By means of the experiment measurement and comparison, one can appraise the departure degree of the curved quaternion space from the flat quaternion space.

In the curved octonion space, from the definitions of octonion orthogonality and parallel transport, it is able to define the metric coefficient, connection coefficient, and curvature etc of the curved space. The decomposition of the electromagnetic source's definition deduces the electromagnetic field equations, including the Gauss's law, Gauss's law of magnetism, Faraday's law, and Ampere-Maxwell law etc in the curved S-quaternion space. The connection coefficient and curvature will direct impact the electromagnetic field equations in the curved S-quaternion space. By means of the experiment measurement and comparison, one can appraise the departure degree of the curved S-quaternion space from the flat S-quaternion space.

ACKNOWLEDGMENT

This project was supported partially by the National Natural Science Foundation of China under grant number 60677039.

REFERENCES

1. Maxwell, J. C., *A Treatise on Electricity and Magnetism*, Dover Publications Inc., New York, 1954.
2. Weng, Z.-H., "Electromagnetic field equations described with the octonions," *Modern Physics*, Vol. 1, No. 1, 17–22, 2011 (in Chinese).
3. Tsagas, C. G., "Electromagnetic fields in curved spacetimes," *Classical and Quantum Gravity*, Vol. 22, No. 2, 393–407, 2005.

Adjoint Fields of Electromagnetic and Gravitational Fields in the Curved Spaces

Zi-Hua Weng
School of Physics and Mechanical & Electrical Engineering
Xiamen University, Xiamen 361005, China

Abstract— J. C. Maxwell introduced the quaternion to describe the feature of electromagnetic field. This method illumines other scholars to bring the quaternion space into the gravitational theory. Currently the octonion space is able to depict the characteristics of electromagnetic field and gravitational field simultaneously. Further the octonion space can escalate the physical content of these two fields. The character of octonion operator allows each field in the octonion space to possess adjunctively the adjoint field. In the octonion space, the electromagnetic field has one adjoint field. The adjoint field of electromagnetic field possesses some features of gravitational field, and may be one candidate of the dark matter field. Similarly the gravitational field has one adjoint field, which provides some features of electromagnetic field. The octonion space can be chosen as the flat space or curved space. In the curved octonion space, the connection coefficient and the curvature have the influences on the physical quantities about the electromagnetic field, the gravitational field, and their adjoint fields.

1. INTRODUCTION

The octonion space [1] can be separated into the quaternion space [2] and the S-quaternion space. The quaternion space is fit for depicting the feature of gravitational field, while the S-quaternion space is propitious to describe the character of electromagnetic field [3]. Further the octonion space can contain some extra physical contents, including the electromagnetic adjoint field and gravitational adjoint field [4].

As one octonion, the gravitational potential can generate adjunctively one adjoint field in the S-quaternion space. The adjoint field of gravitational field has some features of electromagnetic field, and can impact the movement of the electric charge and the electric current. Similarly the electromagnetic potential, as one octonion, can produce adjunctively one adjoint field in the quaternion space. The adjoint field of electromagnetic field has some features of gravitational field, and can affect the movement of the mass and the linear momentum. Obviously the adjoint field of electromagnetic field is one of candidates of dark matter field [5].

The octonion space may be the flat space, and even the curved space [6]. In the curved octonion space, from the conception of the octonion orthogonality and parallel, one can define the octonion parallel transport, and then the octonion connection coefficient and curvature. The result states that the octonion space bending can impact the physical quantity related with the electromagnetic field, gravitational field, and their adjoint fields [7].

2. CURVED OCTONION SPACE

In the flat quaternion space, the quaternion is $\mathbb{Q}_g(q^i)$, and the basis vector is $\{\mathbf{i}_i\}$. Meanwhile in the flat S-quaternion space, the S-quaternion is $\mathbb{Q}_e(Q^j)$, and the basis vector is $\{\mathbf{I}_j\}$. In the flat octonion space, the quaternion $\mathbb{Q}_g(q^i)$ and the S-quaternion $\mathbb{Q}_e(Q^j)$ can be combined together to become the octonion,

$$\mathbb{Q} = \mathbb{Q}_g + k_{eg}\mathbb{Q}_e = q^s\mathbf{i}_s, \tag{1}$$

where $q^{j+4} = k_{eg}Q^j$, and $\mathbf{i}_{j+4} = \mathbf{I}_j$. $r,\ s,\ t,\ u = 0,\ 1,\ 2,\ 3,\ 4,\ 5,\ 6,\ 7$. $i,\ j = 0,\ 1,\ 2,\ 3$. k_{eg} is a coefficient.

In the curved octonion space, the octonion radius vector is, $\mathbb{R}(u^i, U^j) = \mathbb{R}_g(u^i) + k_{eg}\mathbb{R}_e(U^j)$. In the quaternion space for the gravitational field, the quaternion radius vector is $\mathbb{R}_g(u^i)$, and the quaternion tangent frame is $\{\mathbf{e}_i\}$. In the S-quaternion space for the electromagnetic field, the S-quaternion radius vector is $\mathbb{R}_e(U^j)$, and the S-quaternion tangent frame is $\{\mathbf{E}_j\}$. By means of the transformation, $u^{j+4} = k_{eg}U^j$ and $\mathbf{e}_{j+4} = \mathbf{E}_j$, the octonion radius vector is written as, $\mathbb{R} = u^s\mathbf{e}_s$.

The octonion space-time interval is defined as

$$dR^2 = d\mathbb{R} \odot d\mathbb{R} = g_{rs}du^r du^s, \tag{2}$$

where the metric coefficient, $g_{rs} = \mathbf{e}_r \odot \mathbf{e}_s$. The octonion tangent frame, $\mathbf{e}_r = \partial\mathbb{R}/\partial u^r$. $\mathbf{e}_0$ is the scalar. $\odot$ denotes the octonion scalar product. $u^0 = v_0 t$, v_0 is the speed of light, and t is the time.

For the octonions, $\mathbb{A}(a^r)$ and $\mathbb{B}(b^s)$, the octonion product $\mathbb{A} \circ \mathbb{B}$ includes the scalar part $\mathbb{A} \odot \mathbb{B}$ and the vector part $\mathbb{A} \otimes \mathbb{B}$. When $\mathbb{A} \odot \mathbb{B} = 0$, $\mathbb{A}$ and $\mathbb{B}$ are orthogonal. And then the octonion parallel transport in the curved octonion space can be defined from the octonion orthogonality.

In the curved octonion space, the octonion quantity $\mathbb{A}_1$ in the tangent space $\mathbb{T}_1$ of one point $\mathbb{M}_1$ on the octonion manifold, can be decomposed in the tangent space $\mathbb{T}_2$ of the point $\mathbb{M}_2$ near $\mathbb{M}_1$. According to the definition of octonion orthogonality, the octonion quantity $\mathbb{A}_1$ can be decomposed as the projection part $\mathbb{A}_2$ in the tangent space $\mathbb{T}_2$, and the orthogonal part $\mathbb{N}_2$ being orthogonal to the tangent space $\mathbb{T}_2$. Then the octonion quantity $\mathbb{A}_2$ is parallel transported from the octonion quantity $\mathbb{A}_1$.

In curved octonion space, the method, which the covariant derivation is defined from the limit in the curved quaternion space, can be extended to the covariant derivation for the curved octonion space, when the quaternion parallel transport and the quaternion tangent frame are substituted respectively by the octonion parallel transport and the octonion tangent frame. Meanwhile the quaternion orthogonality is substituted by the octonion orthogonality.

Just like the tensor theory, in the curved octonion space, for the physical quantity $Y^s(\mathbb{P})$ of one point $\mathbb{P}$, the component of the octonion covariant derivation with respect to the coordinate u^t is,

$$\nabla_t Y^s = \partial Y^s/\partial u^t + \Gamma^s_{rt} Y^r, \tag{3}$$

where Γ^s_{rt} is the connection coefficient.

The connection coefficient can be expressed as,

$$\Gamma^s_{rt} = (1/2) g^{us} \left(\partial g_{ru}/\partial u^t + \partial g_{ut}/\partial u^r - \partial g_{tr}/\partial u^u \right), \tag{4}$$

where $g^{us} = (g_{us})^{-1}$.

3. GRAVITATIONAL ADJOINT FIELD

In the curved octonion space, if there is only the gravitational potential, $\mathbb{A}_g = A^i_g \mathbf{e}_i$, the octonion gravitational strength, $\mathbb{B}_g = \mathbb{B}_{gg} + \mathbb{B}_{ge}$, can be defined as,

$$\mathbb{B}_g = \Diamond \circ \mathbb{A}_g = \Diamond_g \odot \mathbb{A}_g + \Diamond_g \otimes \mathbb{A}_g + \Diamond_e \odot \mathbb{A}_g + \Diamond_e \otimes \mathbb{A}_g, \tag{5}$$

where the gravitational strength is, $\mathbb{B}_{gg} = \Diamond_g \odot \mathbb{A}_g + \Diamond_g \otimes \mathbb{A}_g$. The gravitational adjoint strength is, $\mathbb{B}_{ge} = \Diamond_e \odot \mathbb{A}_g + \Diamond_e \otimes \mathbb{A}_g$. $\Diamond = \Diamond_g + \Diamond_e$. $\Diamond_g = \mathbf{e}^i(\partial/\partial u^i)$, $\Diamond_e = \mathbf{E}^i \partial/\partial(k_{eg} U^i)$. $\mathbf{e}^i = g^{ij}\mathbf{e}_j$, $\mathbf{E}^i = g^{ij}\mathbf{E}_j$.

In the gravitational field, the scalar part of $\mathbb{B}_{gg}$ is, $\Diamond_g \odot \mathbb{A}_g = k^0_{gg}\mathbf{e}_0$, and the vector part of $\mathbb{B}_{gg}$ is, $\Diamond_g \otimes \mathbb{A}_g = k^p_{gg}\mathbf{e}_p$. The gauge condition is chosen as, $k^0_{gg} = 0$. The vector part of $\mathbb{B}_{gg}$ can be separated further, that is, $k^p_{gg}\mathbf{e}_p = \mathbf{g}_g/v_0 + \mathbf{b}_g$. The strength part, $\mathbf{g}_g/v_0 = \nabla_{g0} \circ \mathbf{A}_g + \nabla_g \circ A_g$, is related with the acceleration, with $\mathbf{g}_g$ being the gravitational acceleration. And the strength part, $\mathbf{b}_g = \nabla_g \times \mathbf{A}_g$, is related with the angular velocity. $\nabla_g \circ A_g = (\mathbf{e}^q \nabla_{gq}) \circ (A^0_g \mathbf{e}_0)$. $\nabla_g \times \mathbf{A}_g = (\mathbf{e}^q \nabla_{gq}) \times (A^p_g \mathbf{e}_p)$. $\nabla_{g0} \circ \mathbf{A}_g = (\mathbf{e}^0 \nabla_{g0}) \circ (A^p_g \mathbf{e}_p)$. $\Diamond_g A^i_g = \mathbf{e}^j \nabla_{gj} A^i_g$. $p,\ q = 1,\ 2,\ 3$.

In the adjoint field for gravitational field, the scalar-like part of adjoint strength $\mathbb{B}_{ge}$ is, $\Diamond_e \odot \mathbb{A}_g = K^0_{ge}\mathbf{E}_0$, and the vector part of adjoint strength $\mathbb{B}_{ge}$ is, $\Diamond_e \otimes \mathbb{A}_g = K^p_{ge}\mathbf{E}_p$. The gauge condition is chosen as, $K^0_{ge} = 0$. The vector part of $\mathbb{B}_{ge}$ can be separated further, that is, $K^p_{ge}\mathbf{E}_p = \mathbf{G}_g/v_0 + \mathbf{B}_g$. The strength component, $\mathbf{G}_g/v_0 = \nabla_{e0} \circ \mathbf{A}_g + \nabla_e \circ \mathbf{A}_g$, while the strength component, $\mathbf{B}_g = \nabla_e \times \mathbf{A}_g$. $\nabla_e \circ A_g = (\mathbf{E}^q \nabla_{eq}) \circ (A^0_g \mathbf{e}_0)$. $\nabla_e \times \mathbf{A}_g = (\mathbf{E}^q \nabla_{eq}) \times (A^p_g \mathbf{e}_p)$. $\nabla_{e0} \circ \mathbf{A}_g = (\mathbf{E}^0 \nabla_{e0}) \circ (A^p_g \mathbf{e}_p)$. $\Diamond_e A^i_g = \mathbf{E}^j \nabla_{ej} A^i_g$.

The octonion gravitational source, $\mu_g \mathbb{S}_g = \mu_{gg}\mathbb{S}_{gg} + \mu_{ge}\mathbb{S}_{ge}$, can be defined as,

$$-\mu\mathbb{S} = -\left(\mu_g \mathbb{S}_g - \mathbb{B}^*_g \circ \mathbb{B}_g/v_0\right) = (\Diamond + \mathbb{B}_g/v_0)^* \circ \mathbb{B}_g, \tag{6}$$

or

$$\begin{aligned} -\mu_g \mathbb{S}_g \ =\ & \Diamond^* \circ \mathbb{B}_g = \Diamond^*_g \odot \mathbb{B}_{gg} + \Diamond^*_g \otimes \mathbb{B}_{gg} + \Diamond^*_e \odot \mathbb{B}_{ge} + \Diamond^*_e \otimes \mathbb{B}_{ge} \\ & + \Diamond^*_g \odot \mathbb{B}_{ge} + \Diamond^*_g \otimes \mathbb{B}_{ge} + \Diamond^*_e \odot \mathbb{B}_{gg} + \Diamond^*_e \otimes \mathbb{B}_{gg}, \end{aligned} \tag{7}$$

where the gravitational source is, $\mathbb{S}_{gg} = -(\Diamond_g^* \odot \mathbb{B}_{gg} + \Diamond_g^* \otimes \mathbb{B}_{gg} + \Diamond_e^* \odot \mathbb{B}_{ge} + \Diamond_e^* \otimes \mathbb{B}_{ge})/\mu_{gg}$. The gravitational adjoint source is, $\mathbb{S}_{ge} = -(\Diamond_g^* \odot \mathbb{B}_{ge} + \Diamond_g^* \otimes \mathbb{B}_{ge} + \Diamond_e^* \odot \mathbb{B}_{gg} + \Diamond_e^* \otimes \mathbb{B}_{gg})/\mu_{ge}$. μ, μ_{gg}, and μ_{ge} are coefficients.

In the gravitational field, the scalar part of gravitational source $\mathbb{S}_{gg}$ is, $-(\Diamond_g^* \odot \mathbb{B}_{gg} + \Diamond_e^* \odot \mathbb{B}_{ge})/\mu_{gg} = s_{gg}^0 \mathbf{e}_0$, and $(s_{gg}^0 \mathbf{e}_0)$ is related with the mass density. While the vector part of $\mathbb{S}_{gg}$ is, $-(\Diamond_g^* \otimes \mathbb{B}_{gg} + \Diamond_e^* \otimes \mathbb{B}_{ge})/\mu_{gg} = s_{gg}^p \mathbf{e}_p$, and $(s_{gg}^p \mathbf{e}_p)$ is related with the density of linear momentum. In general, the gravitational effect of the source term $(\Diamond_e^* \odot \mathbb{B}_{ge} + \Diamond_e^* \otimes \mathbb{B}_{ge})$ can be neglected.

In the adjoint field for gravitational field, the scalar-like part of gravitational adjoint source $\mathbb{S}_{ge}$ is, $-(\Diamond_g^* \odot \mathbb{B}_{ge} + \Diamond_e^* \odot \mathbb{B}_{gg})/\mu_{ge} = S_{ge}^0 \mathbf{E}_0$, and the vector part of $\mathbb{S}_{ge}$ is, $-(\Diamond_g^* \otimes \mathbb{B}_{ge} + \Diamond_e^* \otimes \mathbb{B}_{gg})/\mu_{ge} = S_{ge}^p \mathbf{E}_p$. In general, the effect of the adjoint source term $(\Diamond_e^* \odot \mathbb{B}_{gg} + \Diamond_e^* \otimes \mathbb{B}_{gg})$ can be neglected.

4. ELECTROMAGNETIC ADJOINT FIELD

In the curved octonion space, if there is only the electromagnetic potential, $\mathbb{A}_e = A_e^i \mathbf{E}_i$, the octonion electromagnetic strength, $\mathbb{B}_e = \mathbb{B}_{eg} + \mathbb{B}_{ee}$, can be defined as,

$$\mathbb{B}_e = \Diamond \circ \mathbb{A}_e = \Diamond_g \odot \mathbb{A}_e + \Diamond_g \otimes \mathbb{A}_e + \Diamond_e \odot \mathbb{A}_e + \Diamond_e \otimes \mathbb{A}_e, \tag{8}$$

where the electromagnetic strength is, $\mathbb{B}_{eg} = \Diamond_g \odot \mathbb{A}_e + \Diamond_g \otimes \mathbb{A}_e$. The electromagnetic adjoint strength is, $\mathbb{B}_{ee} = \Diamond_e \odot \mathbb{A}_e + \Diamond_e \otimes \mathbb{A}_e$.

In the electromagnetic field, the scalar-like part of electromagnetic strength $\mathbb{B}_{eg}$ is, $\Diamond_g \odot \mathbb{A}_e = k_{eg}^0 \mathbf{E}_0$, and the vector part of electromagnetic strength $\mathbb{B}_{eg}$ is, $\Diamond_g \otimes \mathbb{A}_e = k_{eg}^p \mathbf{E}_p$. The gauge condition is chosen as, $k_{eg}^0 = 0$. The vector part of electromagnetic strength $\mathbb{B}_{eg}$ can be separated further, that is, $k_{eg}^p \mathbf{E}_p = \mathbf{g}_e/v_0 + \mathbf{b}_e$. The strength component, $\mathbf{g}_e/v_0 = \nabla_{g0} \circ \mathbf{A}_e + \nabla_g \circ A_e$, is related with the electric intensity $\mathbf{g}_e$. While the strength component, $\mathbf{b}_e = \nabla_g \times \mathbf{A}_e$, is the magnetic flux density. $\nabla_g \circ A_e = (\mathbf{e}^q \nabla_{gq}) \circ (A_e^0 \mathbf{E}_0)$. $\nabla_g \times \mathbf{A}_e = (\mathbf{e}^q \nabla_{gq}) \times (A_e^p \mathbf{E}_p)$. $\nabla_{g0} \circ \mathbf{A}_e = (\mathbf{e}^0 \nabla_{g0}) \circ (A_e^p \mathbf{E}_p)$. $\Diamond_g A_e^i = \mathbf{e}^j \nabla_{gj} A_e^i$.

In the adjoint field for electromagnetic field, the scalar part of adjoint strength $\mathbb{B}_{ee}$ is, $\Diamond_e \odot \mathbb{A}_e = K_{ee}^0 \mathbf{e}_0$, and the vector part of adjoint strength $\mathbb{B}_{ee}$ is, $\Diamond_e \otimes \mathbb{A}_e = K_{ee}^p \mathbf{e}_p$. The gauge condition is chosen as, $K_{ee}^0 = 0$. The vector part of $\mathbb{B}_{ee}$ can be separated further, that is, $K_{ee}^p \mathbf{e}_p = \mathbf{G}_e/v_0 + \mathbf{B}_e$. The strength component, $\mathbf{G}_e/v_0 = \nabla_{e0} \circ \mathbf{A}_e + \nabla_e \circ A_e$, while the strength component, $\mathbf{B}_e = \nabla_e \times \mathbf{A}_e$. $\nabla_e \circ A_e = (\mathbf{E}^q \nabla_{eq}) \circ (A_e^0 \mathbf{E}_0)$. $\nabla_e \times \mathbf{A}_e = (\mathbf{E}^q \nabla_{eq}) \times (A_e^p \mathbf{E}_p)$. $\nabla_{e0} \circ \mathbf{A}_e = (\mathbf{E}^0 \nabla_{e0}) \circ (A_e^p \mathbf{E}_p)$. $\Diamond_e A_e^i = \mathbf{E}^j \nabla_{ej} A_e^i$.

The octonion electromagnetic source, $\mu_e \mathbb{S}_e = \mu_{eg} \mathbb{S}_{eg} + \mu_{ee} \mathbb{S}_{ee}$, can be defined as,

$$-\mu \mathbb{S} = -(\mu_e \mathbb{S}_e - \mathbb{B}_e^* \circ \mathbb{B}_e/v_0) = (\Diamond + \mathbb{B}_e/v_0)^* \circ \mathbb{B}_e, \tag{9}$$

or

$$\begin{aligned} -\mu_e \mathbb{S}_e \;=\; & \Diamond^* \circ \mathbb{B}_e = \Diamond_g^* \odot \mathbb{B}_{eg} + \Diamond_g^* \otimes \mathbb{B}_{eg} + \Diamond_e^* \odot \mathbb{B}_{ee} + \Diamond_e^* \otimes \mathbb{B}_{ee} \\ & + \Diamond_g^* \odot \mathbb{B}_{ee} + \Diamond_g^* \otimes \mathbb{B}_{ee} + \Diamond_e^* \odot \mathbb{B}_{eg} + \Diamond_e^* \otimes \mathbb{B}_{eg}, \end{aligned} \tag{10}$$

where the electromagnetic source is, $\mathbb{S}_{eg} = -(\Diamond_g^* \odot \mathbb{B}_{eg} + \Diamond_g^* \otimes \mathbb{B}_{eg} + \Diamond_e^* \odot \mathbb{B}_{ee} + \Diamond_e^* \otimes \mathbb{B}_{ee})/\mu_{eg}$. The electromagnetic adjoint source is, $\mathbb{S}_{ee} = -(\Diamond_g^* \odot \mathbb{B}_{ee} + \Diamond_g^* \otimes \mathbb{B}_{ee} + \Diamond_e^* \odot \mathbb{B}_{eg} + \Diamond_e^* \otimes \mathbb{B}_{eg})/\mu_{ee}$. μ, μ_{gg}, and μ_{ge} are coefficients.

In the electromagnetic field, the scalar-like part of electromagnetic source $\mathbb{S}_{eg}$ is, $-(\Diamond_g^* \odot \mathbb{B}_{eg} + \Diamond_e^* \odot \mathbb{B}_{ee})/\mu_{eg} = s_{eg}^0 \mathbf{E}_0$, and $(s_{eg}^0 \mathbf{E}_0)$ is related with the density of electric charge. While the vector part of electromagnetic source $\mathbb{S}_{eg}$ is, $-(\Diamond_g^* \otimes \mathbb{B}_{eg} + \Diamond_e^* \otimes \mathbb{B}_{ee})/\mu_{eg} = s_{eg}^p \mathbf{E}_p$, and $(s_{eg}^p \mathbf{E}_p)$ is related with the density of electric current. In general, the electromagnetic effect of the source term $(\Diamond_e^* \odot \mathbb{B}_{ee} + \Diamond_e^* \otimes \mathbb{B}_{ee})$ can be neglected.

In the adjoint field for electromagnetic field, the scalar-like part of electromagnetic adjoint source $\mathbb{S}_{ee}$ is, $-(\Diamond_g^* \odot \mathbb{B}_{ee} + \Diamond_e^* \odot \mathbb{B}_{eg})/\mu_{ee} = S_{ee}^0 \mathbf{e}_0$, and the vector part of electromagnetic adjoint source $\mathbb{S}_{ee}$ is, $-(\Diamond_g^* \otimes \mathbb{B}_{ee} + \Diamond_e^* \otimes \mathbb{B}_{eg})/\mu_{ee} = S_{ee}^p \mathbf{e}_p$. In general, the effect of the adjoint source term $(\Diamond_e^* \odot \mathbb{B}_{eg} + \Diamond_e^* \otimes \mathbb{B}_{eg})$ can be neglected.

5. TWO ADJOINT FIELDS

In the curved octonion space, when there are simultaneously the electromagnetic potential, $\mathbb{A}_e$, and gravitational potential, $\mathbb{A}_g$, some physical definitions may be more complicated than that in the above cases, including the definitions of field potential, field strength, and field source etc..

The octonion field potential, $\mathbb{A} = \mathbb{A}_g + k_a\mathbb{A}_e$, is defined as

$$\mathbb{A} = \Diamond^* \circ \mathbb{X} = \Diamond_g^* \circ \mathbb{X}_g + \Diamond_e^* \circ (k_{eg}\mathbb{X}_e) + \Diamond_g^* \circ (k_{eg}\mathbb{X}_e) + \Diamond_e^* \circ \mathbb{X}_g, \tag{11}$$

where the octonion physical quantity, $\mathbb{X} = \mathbb{X}_g + k_{eg}\mathbb{X}_e$. The quaternion physical quantity, $\mathbb{X}_g = x_g^j\mathbf{e}_j$, while the S-quaternion physical quantity, $\mathbb{X}_e = X_e^j\mathbf{E}_j$. The gravitational potential is extended to, $\mathbb{A}_g = \Diamond_g^* \circ \mathbb{X}_g + \Diamond_e^* \circ (k_{eg}\mathbb{X}_e)$, with $\mathbb{A}_g = a_g^j\mathbf{e}_j$. The electromagnetic potential is extended to, $\mathbb{A}_e = \{\Diamond_e^* \circ \mathbb{X}_g + \Diamond_g^* \circ (k_{eg}\mathbb{X}_e)\}/k_a$, with $\mathbb{A}_e = A_e^j\mathbf{E}_j$. k_a is the coefficient.

The octonion field strength, $\mathbb{B} = \mathbb{B}_g + k_b\mathbb{B}_e$, is defined as

$$\mathbb{B} = \Diamond \circ \mathbb{A} = \Diamond_g \circ \mathbb{A}_g + \Diamond_e \circ (k_a\mathbb{A}_e) + \Diamond_g \circ (k_a\mathbb{A}_e) + \Diamond_e \circ \mathbb{A}_g, \tag{12}$$

where the gravitational strength is extended to, $\mathbb{B}_g = \Diamond_g \circ \mathbb{A}_g + \Diamond_e \circ (k_a\mathbb{A}_e)$, with $\mathbb{B}_g = k_g^j\mathbf{e}_j$. The electromagnetic strength is extended to, $\mathbb{B}_e = \{\Diamond_g \circ (k_a\mathbb{A}_e) + \Diamond_e \circ \mathbb{A}_g\}/k_b$, with $\mathbb{B}_e = K_e^j\mathbf{E}_j$. The gravitational gauge condition is chosen as, $k_g^0 = 0$, and the electromagnetic gauge condition is chosen as, $K_e^0 = 0$. The term, $\Diamond_e \circ (k_a\mathbb{A}_e)$, of the gravitational strength, $\mathbb{B}_g$, is contributed from the electromagnetic adjoint field. And the term, $\Diamond_e \circ \mathbb{A}_g$, of the electromagnetic strength, $\mathbb{B}_e$, is contributed from the gravitational adjoint field. k_b is one coefficient.

The octonion field source, $\mathbb{S}$, is defined as,

$$-\mu\mathbb{S} = -(\mu_g\mathbb{S}_g + k_s\mu_e\mathbb{S}_e - \mathbb{B}^* \circ \mathbb{B}/v_0) = (\Diamond + \mathbb{B}/v_0)^* \circ \mathbb{B}, \tag{13}$$

and that is separated into two parts in the quaternion and S-quaternion spaces respectively,

$$-(\mu_{gg}\mathbb{S}_{gg} + k_s\mu_{ee}\mathbb{S}_{ee}) = \Diamond_g^* \circ \mathbb{B}_g + \Diamond_e^* \circ (k_b\mathbb{B}_e), \tag{14}$$

$$-(k_s\mu_{eg}\mathbb{S}_{eg} + \mu_{ge}S_{ge}) = \Diamond_g^* \circ (k_b\mathbb{B}_e) + \Diamond_e^* \circ \mathbb{B}_g. \tag{15}$$

In the quaternion space for the gravitational field, the physical experiment may not distinguish the gravitational effect contributed from the terms, $\mathbb{S}_{gg}$ and $\mathbb{S}_{ee}$, to a certain extent. In some measurement ranges, the field source parts, $\mathbb{S}_{gg}$ and $\mathbb{S}_{ee}$, will mix together to present to the equation. The gravitational source is extended into, $\mathbb{S}_g = -\{\Diamond_g^* \circ \mathbb{B}_g + \Diamond_e^* \circ (k_b\mathbb{B}_e)\}/\mu_g$, with $\mathbb{S}_g = s_g^j\mathbf{e}_j$. And the term, $\Diamond_e^* \circ (k_b\mathbb{B}_e)/\mu_g$, of the gravitational strength, $\mathbb{S}_g$, is contributed from the electromagnetic adjoint field.

In the S-quaternion space for the electromagnetic field, the physical experiment may not distinguish the electromagnetic effect contributed from the terms, $\mathbb{S}_{eg}$ and $\mathbb{S}_{ge}$, to a certain extent. In some measurement ranges, the field source parts, $\mathbb{S}_{eg}$ and $\mathbb{S}_{ge}$, will mix together to present to the equation. The electromagnetic source is extended into, $\mathbb{S}_e = -\{\Diamond_g^* \circ (k_b\mathbb{B}_e) + \Diamond_e^* \circ \mathbb{B}_g\}/(\mu_e k_s)$, with $\mathbb{S}_e = S_e^j\mathbf{E}_j$. And the term, $\Diamond_e^* \circ \mathbb{B}_g/(\mu_e k_s)$, of the gravitational strength, $\mathbb{S}_e$, is contributed from the gravitational adjoint field. k_s is the coefficient.

In the electromagnetic field, gravitational field, and their adjoint fields, the octonion angular momentum, energy-torque, and power-force can be defined from the octonion linear momentum and the quaternion operator.

The octonion angular momentum $\mathbb{L}(l^i, L^j)$ is written as,

$$\mathbb{L} = \mathbb{R} \circ \mathbb{P} = \mathbb{R} \odot \mathbb{P} + \mathbb{R} \otimes \mathbb{P}, \tag{16}$$

where the scalar part of $\mathbb{L}$ is $\mathbb{R} \odot \mathbb{P} = l^0\mathbf{e}_0$, and the vector part is $\mathbb{R} \otimes \mathbb{P} = l^p\mathbf{e}_p + L^0\mathbf{E}_0 + L^p\mathbf{E}_p$. The linear momentum of octonion field source is $\mathbb{P} = \mu\mathbb{S}/\mu_{gg}$.

The octonion energy-torque $\mathbb{W}(w^i, W^j)$ is defined as,

$$\mathbb{W} = v_0(\Diamond + \mathbb{B}/v_0) \circ \mathbb{L} = v_0(\Diamond + \mathbb{B}/v_0) \odot \mathbb{L} + v_0(\Diamond + \mathbb{B}/v_0) \otimes \mathbb{L}, \tag{17}$$

where the scalar part of $\mathbb{W}$ is $v_0(\Diamond + \mathbb{B}/v_0) \odot \mathbb{L} = w^0\mathbf{e}_0$, and is relevant to the energy. Meanwhile the vector part of $\mathbb{W}$ is, $v_0(\Diamond + \mathbb{B}/v_0) \otimes \mathbb{L} = w^p\mathbf{e}_p + W^0\mathbf{E}_0 + W^p\mathbf{E}_p$. And the term $w^p\mathbf{e}_p$ is related with the torque.

The octonion power-force $\mathbb{N}(n^i, N^j)$ is,

$$\mathbb{N} = v_0(\Diamond + \mathbb{B}/v_0)^* \circ \mathbb{W} = v_0(\Diamond + \mathbb{B}/v_0)^* \odot \mathbb{W} + v_0(\Diamond + \mathbb{B}/v_0)^* \otimes \mathbb{W}, \tag{18}$$

where the scalar part of $\mathbb{N}$ is $v_0(\Diamond + \mathbb{B}/v_0)^* \odot \mathbb{W} = n^0\mathbf{e}_0$, and is relevant to the power. Meanwhile the vector part of $\mathbb{N}$ is $v_0(\Diamond + \mathbb{B}/v_0)^* \otimes \mathbb{W} = n^p\mathbf{e}_p + N^0\mathbf{E}_0 + N^p\mathbf{E}_p$, and is dealt with the force. The scalar term $n^0\mathbf{e}_0$ and scalar-like term $N^0\mathbf{E}_0$ are related with the mass continuity equation and the current continuity equation respectively.

In the curved octonion space, the connection coefficient and curvature have some influences on the field strength, field source, angular momentum, energy, torque, power, force, the mass continuity equation, and the current continuity equation etc about the electromagnetic field, gravitational field, and their adjoint fields.

6. CONCLUSIONS

After the quaternion was adopted to describe the physics feature of electromagnetic fields, the quaternion is used to depict the gravitational field currently. However the quaternion space for electromagnetic field is independent to that for gravitational field. These two quaternion spaces can be combined together to become the octonion space. The quaternion space may be either flat or curved. Correspondingly the octonion space, which consists of these two quaternion spaces, is either flat or curved.

In the curved quaternion space for gravitational field, there are the gravitational potential, $\mathbb{A}_g$, and the quaternion operator $\Diamond_g$. The operation of the quaternion operator $\Diamond_g$ on the gravitational potential, $\mathbb{A}_g$, will yield the gravitational strength and gravitational source in sequence. The definition of gravitational source will deduce the gravitational equations, including the Newton's law for gravitation. The operation of the quaternion operator $\Diamond_g$ on the electromagnetic potential, $\mathbb{A}_e$, will yield the electromagnetic strength and electromagnetic source in sequence. The definition of electromagnetic source will infer the electromagnetic equations, including Maxwell's equations.

In the curved S-quaternion space for electromagnetic field, there are the electromagnetic potential, $\mathbb{A}_e$, and the S-quaternion operator $\Diamond_e$. The operation of the S-quaternion operator $\Diamond_e$ on the gravitational potential, $\mathbb{A}_g$, will yield the gravitational adjoint strength and gravitational adjoint source in sequence. The gravitational adjoint field possesses some features of electromagnetic fields. The operation of the S-quaternion operator $\Diamond_e$ on the electromagnetic potential, $\mathbb{A}_e$, will yield the electromagnetic adjoint strength and electromagnetic adjoint source in sequence. The electromagnetic adjoint field possesses some features of gravitational fields.

The results reveal that the gravitational adjoint field will impact the movement of the electric charge and current, while the electromagnetic adjoint field will affect the movement of the mass and linear momentum. The connection coefficient and curvature of curved octonion space will impact directly on the physical features of electromagnetic field, gravitational field, gravitational adjoint field, and electromagnetic adjoint field etc..

ACKNOWLEDGMENT

This project was supported partially by the National Natural Science Foundation of China under grant number 60677039.

REFERENCES

1. Cayley, A., *The Collected Mathematical Papers of Arthur Cayley*, The Cambridge University Press, Cambridge, 1889.
2. Hamilton, W. R., *Elements of Quaternions*, Longmans, Green & Co., London, 1866.
3. Maxwell, J. C., *A Treatise on Electricity and Magnetism*, Dover Publications Inc., New York, 1954.
4. Weng, Z.-H., "Charge continuity equation in the adjoint fields," *PIERS Proceedings*, 63–67, Suzhou, China, Sep. 12–16, 2011.
5. Zwicky, F., "On the masses of nebulae and of clusters of nebulae," *Astrophysical Journal*, Vol. 86, No. 3, 217–246, 1937.
6. Tsagas, C. G., "Electromagnetic fields in curved spacetimes," *Classical and Quantum Gravity*, Vol. 22, No. 2, 393–407, 2005.
7. Weng, Z.-H., "Electromagnetic and gravitational fields in the curved octonion spaces," *PIERS Proceedings*, 1372–1376, Moscow, Russia, Aug. 19–23, 2012.

Dense Waves in Electromagnetic and Gravitational Fields

Zi-Hua Weng
School of Physics and Mechanical & Electrical Engineering
Xiamen University, Xiamen 361005, China

Abstract— The quaternion is able to describe the physical features of the electromagnetic field and gravitational field. In the quaternion space for the electromagnetic field, the quaternion radius vector combines with the integral of electromagnetic potential to become the compounding radius vector. From the quaternion operator and the compounding radius vector, it is able to deduce the compounding field strength, field source, and wave equation of the electromagnetic field. According to the compounding wave equation, the compounding field strength is one transverse wave, which transmission direction is perpendicular to the electric intensity and magnetic flux density, and is able to impact the movements of other trial charges, and then to form the electromagnetic dense waves. The quaternion space for the gravitational field is independent to that for the electromagnetic field. In the quaternion space for the gravitational field, the quaternion radius vector combines with the integral of gravitational potential to become the compounding radius vector. From the quaternion operator and the compounding radius vector, it is able to deduce the compounding field strength, field source, and wave equation of the gravitational field. According to the compounding wave equation, the compounding field strength is one transverse wave, which transmitted along the orbital tangent direction, and is able to influence the movements of other objects, and then to form the gravitational dense waves.

1. INTRODUCTION

J. C. Maxwell [1] was the first to apply the algebra of quaternions to describe the physical features of electromagnetic fields. Currently the quaternion space is able to depict the electromagnetic theory as well as the gravitational theory. The quaternion space for the gravitational field is independent to that for the electromagnetic field, but two quaternion spaces can combine together to become the octonion space. In the octonion space, it is able to describe simultaneously the physical features of electromagnetic field and gravitational field.

In the quaternion space for electromagnetic field, the quaternion radius vector and the integral of electromagnetic potential constitute the compounding radius vector in the quaternion compounding space. In the quaternion space for gravitational field, the quaternion radius vector and the integral of gravitational potential compose the compounding radius vector in the quaternion compounding space. The quaternion compounding space for the gravitational field is independent to that for the electromagnetic field, but two quaternion compounding spaces can combine together to become the octonion compounding space [2]. In the octonion compounding space, it is able to describe simultaneously the physical features of the movement deviated from the equilibrium state in the electromagnetic and gravitational fields.

In the octonion compounding space, from the quaternion operator and octonion compounding radius vector, it is able to define the octonion compounding field potential, field strength, and field source etc. Decomposing of the definition of octonion compounding field source produces the field equations and wave equation. The octonion compounding field equations predict the undulation feature of orbits when the object's movement is deviated from the equilibrium state. The wave equations in the octonion compounding space deduce the wave and transmission features of the compounding field strength when the object's movement is deviated from the equilibrium state.

In the quaternion compounding space for gravitational field, when the star moving around the galaxy center deviates from the movement equilibrium state, its orbit will occur the undulations along the radial and tangent directions as well as the direction perpendicular to the orbital plan. And the undulation will cause the fluctuation of star density, while it may be the original reason to cause the density wave of stars [3]. In the quaternion compounding space for electromagnetic field, when the negative trail charge, which moved round the positive charged particle with high quantity of electric charge, deviates from the movement equilibrium state, its 'orbit' will occur the undulations along the radial and tangent directions as well as the direction perpendicular to the 'orbital plan'. And the undulation will cause the density fluctuation of negative trial charges.

2. QUATERNION COMPOUNDING SPACE

Currently the quaternion space is able to depict the gravitational features. In the quaternion space, the quaternion radius vector combines with the integral of gravitational potential to become the compounding radius vector, which is considered as the radius vector in the quaternion compounding space (function space). Similarly the quaternion velocity and the gravitational potential constitute the compounding field potential of the gravitational field. And then the compounding field strength and field source can be deduced from the quaternion operator and the compounding field potential in the gravitational field.

In the quaternion space for gravitational field, the basis vectors of quaternion are, $\mathbf{i}_0$, $\mathbf{i}_1$, $\mathbf{i}_2$, and $\mathbf{i}_3$, with $\mathbf{i}_0 = 1$. The quaternion radius vector is $\mathbb{R}_g(r_0, r_1, r_2, r_3) = \Sigma(\mathbf{i}_i r_i)$, the quaternion velocity is $\mathbb{V}_g(v_0, v_1, v_2, v_3) = v_0 \lozenge \circ \mathbb{R}_g$, the quaternion angular velocity is $\mathbb{Y}_g(y_0, y_1, y_2, y_3) = \lozenge \circ \mathbb{V}_g$, the quaternion linear acceleration is $\mathbb{Z}_g(z_0, z_1, z_2, z_3) = -\lozenge^* \circ \mathbb{Y}_g$. Herein the quaternion operator is $\lozenge = \Sigma \mathbf{i}_i(\partial/\partial r_i)$, with $i = 0, 1, 2, 3$. v_0 is the speed of light. $*$ is the quaternion conjugation.

In the gravitational field, the quaternion physical quantity is $\mathbb{X}_g(x_0, x_1, x_2, x_3)$, which is the integral of the quaternion field potential $\mathbb{A}_g(a_0, a_1, a_2, a_3)$, that is, $\mathbb{A}_g = \lozenge \circ \mathbb{X}_g$. The quaternion field strength is $\mathbb{B}_g(h_0, h_1, h_2, h_3) = \lozenge \circ \mathbb{A}_g$. The quaternion field source is $\mathbb{S}_g(s_0, s_1, s_2, s_3)$, and its definition is $\mu_g \mathbb{S}_g = -\lozenge^* \circ \mathbb{B}_g$. Herein the gravitational constant $\mu_g < 0$. Comparing with the classical gravitational theory, it is found, $\mathbb{S}_g = m\mathbb{V}_g$, with m being the mass density.

In the quaternion space for gravitational field, the quaternion radius vector $\mathbb{R}_g$ combines with the quaternion physical quantity $\mathbb{X}_g$ to become the quaternion compounding radius vector, $\bar{\mathbb{R}}_g = \mathbb{R}_g + k_{rx}\mathbb{X}_g$, or the quaternion compounding physical quantity, $\bar{\mathbb{X}}_g = \mathbb{X}_g + K_{rx}\mathbb{R}_g$. The quaternion compounding radius vector $\bar{\mathbb{R}}_g$ is considered as the radius vector in the quaternion compounding space. In the quaternion compounding space, the quaternion compounding velocity is $\bar{\mathbb{V}}_g = v_0 \lozenge \circ \bar{\mathbb{R}}_g = \mathbb{V}_g + v_0 k_{rx}\mathbb{A}_g$, the quaternion compounding angular velocity is $\bar{\mathbb{Y}}_g = \lozenge \circ \bar{\mathbb{V}}_g$, and the quaternion compounding angular acceleration is $\bar{\mathbb{Z}}_g = -\lozenge^* \circ \bar{\mathbb{Y}}_g$. Similarly in the gravitational field, the quaternion compounding field potential is $\bar{\mathbb{A}}_g = \lozenge \circ \bar{\mathbb{X}}_g = \mathbb{A}_g + (K_{rx}/v_0)\mathbb{V}_g$, the quaternion compounding field strength is $\bar{\mathbb{B}}_g = \lozenge \circ \bar{\mathbb{A}}_g = \mathbb{B}_g + (K_{rx}/v_0)\mathbb{Y}_g$, and the quaternion compounding field source is $\mu_g \bar{\mathbb{S}}_g = -\lozenge^* \circ \mathbb{B}_g$. Herein $\bar{\mathbb{S}}_g = m\bar{\mathbb{V}}_g$. $\bar{\mathbb{S}}_g = \mathbb{S}_g + \mathbb{Z}_g/(\mu_g k_{rx})$. $\mathbb{Z}_g = (\mu_g k_{rx}^2 m v_0)\mathbb{A}_g$. k_{rx} and K_{rx} are the coefficients, with $K_{rx} = 1/k_{rx}$.

From the decomposing of the definition of compounding field source, it is able to deduce the gravitational field equations and wave equation in the quaternion compounding space.

3. GRAVITATIONAL DENSITY WAVE

In the quaternion compounding space for gravitational field, the decomposing of the definition of the compounding field source,

$$\mu_g \bar{\mathbb{S}}_g = -\lozenge^* \circ \bar{\mathbb{B}}_g, \tag{1}$$

can deduce the gravitational field equations,

$$\nabla \cdot \bar{\mathbf{b}} = 0, \quad \nabla^* \times \bar{\mathbf{g}}/v_0 + \partial_0 \bar{\mathbf{b}} = 0, \tag{2}$$

$$-\mu_g \bar{s}_0 = \nabla^* \cdot \bar{\mathbf{g}}/v_0, \quad -\mu_g \bar{\mathbf{s}} = \nabla^* \times \bar{\mathbf{b}} + \partial_0 \bar{\mathbf{g}}/v_0, \tag{3}$$

where $\bar{\mathbb{S}}_g = \bar{s}_0 + \bar{\mathbf{s}}$. $\bar{\mathbb{B}}_g = \bar{h}_0 + \bar{\mathbf{h}}$. $\bar{\mathbf{h}} = \bar{\mathbf{b}} + \bar{\mathbf{g}}/v_0$. The gauge condition is $\bar{h}_0 = 0$.

When $\bar{\mathbf{h}} \neq 0$, the star's movement in the gravitational field of the galaxy system will deviate from the weightlessness state, that is

$$\bar{\mathbf{g}} = \mathbf{g} + \mathbf{a} \neq 0, \quad \bar{\mathbf{b}} = \mathbf{b} + \mathbf{y} \neq 0, \tag{4}$$

where the linear acceleration is, $\mathbf{a} \approx d\mathbf{r}/dt$, in the quaternion space. $\mathbb{R}_g = r_0 + \mathbf{r}$. $\mathbf{r} = \Sigma(\mathbf{i}_j r_j)$. The rotational velocity is $\mathbf{y} \approx \nabla \times \mathbf{v}$. $\mathbb{V}_g = v_0 + \mathbf{v}$. $\mathbf{v} = \Sigma(\mathbf{i}_j v_j)$. $j = 1, 2, 3$.

In the quaternion compounding space, Eqs. (2) and (3) yield the gravitational wave,

$$\bar{\mathbf{g}}(\bar{r}) = \bar{\mathbf{g}}_0 \circ \exp(-i\mathbf{i}\alpha), \quad \bar{\mathbf{b}}(\bar{r}) = \bar{\mathbf{b}}_0 \circ \exp(-i\mathbf{i}\alpha),$$

where $\bar{\mathbf{g}}_0$ and $\bar{\mathbf{b}}_0$ are the constant vectors. $\exp\{\mathbf{i}(a + ib)\} = \cos(a + ib) + \mathbf{i}\sin(a + ib)$. a and b both are real. i is the imaginary unit, with $i^2 = -1$. $\mathbf{i}$ is the quaternion unit, with $\mathbf{i}^2 = -1$. The wave vector is $\mathbf{k} = \Sigma(\mathbf{i}_j k_j)$, the radius vector is $\bar{\mathbf{r}} = \Sigma(\mathbf{i}_i \bar{r}_i)$, with k_j being the coefficient. $\alpha = -\Sigma(k_j \bar{r}_j)$, and $(i\alpha)$ is imaginary angle.

The gravitational wave is the transverse wave, and that meets following equations,

$$\mathbf{k}\cdot\bar{\mathbf{g}}_0=0,\quad \mathbf{k}\cdot\bar{\mathbf{g}}_0'=0,\quad \mathbf{k}\cdot\bar{\mathbf{b}}_0=0,\quad \mathbf{k}\cdot\bar{\mathbf{b}}_0'=0, \tag{5}$$

$$\mathbf{k}\times\bar{\mathbf{g}}_0'+\omega\bar{\mathbf{b}}_0=0,\quad \mathbf{k}\times\bar{\mathbf{g}}_0-\omega\bar{\mathbf{b}}_0'=0, \tag{6}$$

$$\mathbf{k}\times\bar{\mathbf{b}}_0'+\omega\bar{\mathbf{g}}_0/v_0^2=0,\quad \mathbf{k}\times\bar{\mathbf{b}}_0-\omega\bar{\mathbf{g}}_0'/v_0^2=0, \tag{7}$$

where $\bar{\mathbf{g}}_0'=\bar{\mathbf{g}}_0\circ\mathbf{i}$ and $\bar{\mathbf{b}}_0'=\bar{\mathbf{b}}_0\circ\mathbf{i}$ are two new components of gravitational waves.

In the quaternion compounding space, within a certain period of time for some existing reasons, the star's orbital movement in the gravitational field of galaxy system may deviate from the equilibrium state. This will result in the undulation of compounding field strength of the gravitational field, that is, $\bar{\mathbf{h}}\neq 0$.

The undulation of compounding field strength of the gravitational field possesses some features of transverse wave. The direction of transverse wave is perpendicular to the rotational direction as well as the acceleration direction, and that is close to the direction of velocity. This induces the diversification of star's orbit along the radial and tangent directions.

According to the gravitational wave equation in the quaternion compounding space, the compounding field strength is the transverse wave. In the orbital movement model of the star moving around the galaxy center, the transmission direction of transverse wave is perpendicular to the gravitational acceleration and velocity curl. That is, the transverse wave transmits along the tangent direction of orbit. When the transverse wave transmits to another point, it appears the differentiation along the radial and tangent directions. These two components will impact the orbital movements of other stars, and then to form the relevant density wave.

In the gravitational field of galaxy system, within a certain period of time for some reasons, there is the gravitational wave in the point A_1 with the compounding field strength, $\bar{\mathbf{h}}_1=\bar{\mathbf{g}}_1/v_0$, and it arouses the radial fluctuation of star orbit. Subsequently the gravitational wave transmits along the tangent direction to reach the point A_2. There is the compounding field strength, $\bar{\mathbf{h}}_2=\bar{\mathbf{g}}_2'/v_0+\bar{\mathbf{g}}_2''/v_0$, in the point A_2, and its radial and tangent components are respectively, $\bar{\mathbf{g}}_2'/v_0$ and $\bar{\mathbf{g}}_2''/v_0$. According to Eq. (4), the gravitational wave component, $\bar{\mathbf{g}}_2'/v_0$, will force the star orbit to fluctuate along the radial direction, while the gravitational wave component, $\bar{\mathbf{g}}_2''/v_0$, will result in the orbit undulation along the tangent direction. Further the compounding field strength $\bar{\mathbf{h}}_2$ and compounding velocity $\bar{\mathbb{V}}_g$ will induce the undulation perpendicular to the orbital plane. As a whole the multidirectional undulations represent as the gather density fluctuation of abundant stars.

4. *S*-QUATERNION COMPOUNDING SPACE

The quaternion space was applied firstly by J. C. Maxwell to depict the physical features of electromagnetic field. However the quaternion space for the electromagnetic field is independent to that for the gravitational field. In the quaternion space for the electromagnetic field, the quaternion radius vector and the integral of electromagnetic potential constitute the compounding radius vector. The latter can be considered as the radius vector in the quaternion compounding space (function space) for the electromagnetic field. Similarly the quaternion velocity and the electromagnetic potential compose the compounding field potential of the electromagnetic field. And then the compounding field strength and field source can be deduced from the quaternion operator and the compounding field potential in the electromagnetic field.

The imaginary number can be dissembled into two components, the real part and the imaginary part. Similarly the octonion can be broken down into two components, the quaternion and the *S*-quaternion. The comparison of these two numbers reveals that the *S*-quaternion is similar to the imaginary part of the imaginary number. Therefore the method, which applying the quaternion to study the gravitational features, can be generalized to the electromagnetic theory, in which adopting the *S*-quaternion to analyze the electromagnetic features.

In the *S*-quaternion space for electromagnetic field, the basis vectors of *S*-quaternion are, $\mathbf{I}_0$, $\mathbf{I}_1$, $\mathbf{I}_2$, and $\mathbf{I}_3$. The *S*-quaternion radius vector is $\mathbb{R}_e(R_0,R_1,R_2,R_3)=\Sigma(\mathbf{I}_iR_i)$, the *S*-quaternion velocity is $\mathbb{V}_e(V_0,V_1,V_2,V_3)=v_0\Diamond\circ\mathbb{R}_e$, the *S*-quaternion angular velocity is $\mathbb{Y}_e(Y_0,Y_1,Y_2,Y_3)=\Diamond\circ\mathbb{V}_e$, and the *S*-quaternion linear acceleration is $\mathbb{Z}_e(Z_0,Z_1,Z_2,Z_3)=-\Diamond^*\circ\mathbb{Y}_e$. Herein $*$ is the octonion conjugation.

In the electromagnetic field, the *S*-quaternion physical quantity is $\mathbb{X}_e(X_0,X_1,X_2,X_3)$, which is the integral of the *S*-quaternion field potential $\mathbb{A}_e(A_0,A_1,A_2,A_3)$, that is, $\mathbb{A}_e=\Diamond\circ\mathbb{X}_e$. The physical quantity $\mathbb{X}_e$ is considered as the generalization of the Hertz vector. The *S*-quaternion field

strength is $\mathbb{B}_e(H_0, H_1, H_2, H_3) = \Diamond \circ \mathbb{A}_e$. The S-quaternion field source is $\mathbb{S}_e(S_0, S_1, S_2, S_3)$, and its definition is $\mu_e \mathbb{S}_e = -\Diamond^* \circ \mathbb{B}_e$. Herein the electromagnetic constant $\mu_e > 0$. Comparing with the classical electromagnetic theory, it is found, $\mathbb{S}_e = q\mathbb{V}_e$, with q being the density of electric charge.

In the S-quaternion space for electromagnetic field, the S-quaternion radius vector $\mathbb{R}_e$ combines with the S-quaternion physical quantity $\mathbb{X}_e$ to become the S-quaternion compounding radius vector, $\bar{\mathbb{R}}_e = \mathbb{R}_e + k_{rx}\mathbb{X}_e$, or the S-quaternion compounding physical quantity, $\bar{\mathbb{X}}_e = \mathbb{X}_e + K_{rx}\mathbb{R}_e$. The S-quaternion compounding radius vector $\bar{\mathbb{R}}_e$ is considered as the radius vector in the S-quaternion compounding space. In the S-quaternion compounding space, the S-quaternion compounding velocity is $\bar{\mathbb{V}}_e = v_0 \Diamond \circ \bar{\mathbb{R}}_e = \mathbb{V}_e + v_0 k_{rx}\mathbb{A}_e$, the S-quaternion compounding angular velocity is $\bar{\mathbb{Y}}_e = \Diamond \circ \bar{\mathbb{V}}_e$, and the S-quaternion compounding angular acceleration is $\bar{\mathbb{Z}}_e = -\Diamond^* \circ \bar{\mathbb{Y}}_e$. Similarly in the electromagnetic field, the S-quaternion compounding field potential is $\bar{\mathbb{A}}_e = \Diamond \circ \bar{\mathbb{X}}_e = \mathbb{A}_e + (K_{rx}/v_0)\mathbb{V}_e$, the S-quaternion compounding field strength is $\bar{\mathbb{B}}_e = \Diamond \circ \bar{\mathbb{A}}_e = \mathbb{B}_e + (K_{rx}/v_0)\mathbb{Y}_e$, and the S-quaternion compounding field source is $\mu_e \bar{\mathbb{S}}_e = -\Diamond^* \circ \bar{\mathbb{B}}_e$. Herein $\bar{\mathbb{S}}_e = q\bar{\mathbb{V}}_e$. $\bar{\mathbb{S}}_e = \mathbb{S}_e + \mathbb{Z}_e/(\mu_e k_{rx})$. $\mathbb{Z}_e = (\mu_e k_{rx}^2 q v_0)\mathbb{A}_e$.

From the decomposing of the definition of compounding field source, it is able to deduce the electromagnetic field equations and wave equation in the S-quaternion compounding space.

5. ELECTROMAGNETIC DENSITY WAVE

In the S-quaternion compounding space for the electromagnetic field, the decomposing of the definition of the compounding field source,

$$\mu_e \bar{\mathbb{S}}_e = -\Diamond^* \circ \bar{\mathbb{B}}_e, \tag{8}$$

can deduce the electromagnetic field equations,

$$\nabla \cdot \bar{\mathbf{B}} = 0, \quad \nabla^* \times \bar{\mathbf{E}}/v_0 + \partial_0 \bar{\mathbf{B}} = 0, \tag{9}$$

$$-\mu_e \bar{\mathbf{S}}_0 = \nabla^* \cdot \bar{\mathbf{E}}/v_0, \quad -\mu_e \bar{\mathbf{S}} = \nabla^* \times \bar{\mathbf{B}} + \partial_0 \bar{\mathbf{E}}/v_0, \tag{10}$$

where $\bar{\mathbb{S}}_e = \bar{\mathbf{S}}_0 + \bar{\mathbf{S}}$. $\bar{\mathbf{S}}_0 = \bar{S}_0 \mathbf{I}_0$. $\bar{\mathbf{H}}_0 = \bar{H}_0 \mathbf{I}_0$. $\bar{\mathbb{B}}_e = \bar{\mathbf{H}}_0 + \bar{\mathbf{H}}$. $\bar{\mathbf{H}} = \bar{\mathbf{B}} + \bar{\mathbf{E}}/v_0$. The gauge condition is $\bar{\mathbf{H}}_0 = 0$.

When $\bar{\mathbf{H}} \neq 0$, the movement of the trial charge in the electromagnetic field of the positive electric charge Q will deviate from the 'weightlessness' state, that is

$$\bar{\mathbf{E}} = \mathbf{E} + \mathbf{a}_e \neq 0, \quad \bar{\mathbf{B}} = \mathbf{B} + \mathbf{Y} \neq 0, \tag{11}$$

where the linear acceleration is, $\mathbf{a}_e \approx d\mathbf{R}/dt$, in the S-quaternion space. $\mathbb{R}_e = \mathbf{R}_0 + \mathbf{R}$. $\mathbf{R}_0 = R_0 \mathbf{I}_0$. $\mathbf{R} = \Sigma(\mathbf{I}_j R_j)$. The rotational velocity is $\mathbf{Y} \approx \nabla \times \mathbf{V}$. $\mathbb{V}_e = \mathbf{V}_0 + \mathbf{V}$. $\mathbf{V} = \Sigma(\mathbf{I}_j V_j)$. $\mathbf{V}_0 = V_0 \boldsymbol{I}_0$.

In the S-quaternion compounding space, the electromagnetic field equations yield the electromagnetic wave,

$$\bar{\mathbf{E}}(\bar{r}) = \bar{\mathbf{E}}_0 \circ \exp(-i\mathbf{I}\alpha), \quad \bar{\mathbf{B}}(\bar{r}) = \bar{\mathbf{B}}_0 \circ \exp(-i\mathbf{I}\alpha),$$

where $\bar{\mathbf{E}}_0$ and $\bar{\mathbf{B}}_0$ are the constant vectors. $\exp\{\mathbf{I}(a+ib)\} = \cos(a+ib) + \mathbf{I}\sin(a+ib)$. a and b are real. i is the imaginary unit, with $i^2 = -1$. $\mathbf{I}$ is the octonion unit, with $\mathbf{I}^2 = -1$. The wave vector is $\mathbf{K} = \Sigma(\mathbf{I}_j K_j)$, with K_j being the coefficient. $\alpha = -\Sigma(K_j \bar{r}_j)$, and $(i\alpha)$ is imaginary angle.

The electromagnetic wave is the transverse wave, and that meets following equations,

$$\mathbf{K} \cdot \bar{\mathbf{E}}_0 = 0, \quad \mathbf{K} \cdot \bar{\mathbf{E}}_0' = 0, \quad \mathbf{K} \cdot \bar{\mathbf{B}}_0 = 0, \quad \mathbf{K} \cdot \bar{\mathbf{B}}_0' = 0, \tag{12}$$

$$\mathbf{K} \times \bar{\mathbf{E}}_0' + \omega \bar{\mathbf{B}}_0 = 0, \quad \mathbf{K} \times \bar{\mathbf{E}}_0 - \omega \bar{\mathbf{B}}_0' = 0, \tag{13}$$

$$\mathbf{K} \times \bar{\mathbf{B}}_0' + \omega \bar{\mathbf{E}}_0/v_0^2 = 0, \quad \mathbf{K} \times \bar{\mathbf{B}}_0 - \omega \bar{\mathbf{E}}_0'/v_0^2 = 0, \tag{14}$$

where $\bar{\mathbf{E}}_0' = \bar{\mathbf{E}}_0 \circ \mathbf{I}$ and $\bar{\mathbf{B}}_0' = \bar{\mathbf{B}}_0 \circ \mathbf{I}$ are two new components of electromagnetic waves.

In the S-quaternion compounding space, within a certain period of time for some existing reasons, the orbital movement of negative trial charge in the electromagnetic field of positive electric charge may deviate from the equilibrium state. This will result in the undulation of compounding field strength of the electromagnetic field, that is, $\bar{\mathbf{H}} \neq 0$.

The undulation of compounding field strength of the electromagnetic field possesses some features of transverse wave. The direction of transverse wave is perpendicular to the electric intensity as well as the magnetic flux density, and that is close to the direction of velocity. This induces the diversification of the 'orbit' of negative trial charge in the radial and tangent directions.

According to the electromagnetic wave equation in the S-quaternion compounding space, the compounding field strength is the transverse wave. In the orbital movement model of the negative trial charge moving around the positive electric charge, the transmission direction of transverse wave is perpendicular to the electric intensity and magnetic flux density. That is, the transverse wave transmits along the tangent direction of orbit. When the transverse wave transmits to another point, it appears the differentiation along the radial and tangent directions. These two components will impact the 'orbit' movements of trial charge, and then to form the relevant density wave.

In the electromagnetic field of positive electric charge Q, within a certain period of time for some reasons, there is the electromagnetic wave in the point A_1 with the compounding field strength, $\bar{\mathbf{H}}_1 = \bar{\mathbf{E}}_1/v_0$, and it arouses the radial fluctuation of the 'orbit' of negative trial charge. Subsequently the electromagnetic wave transmits along the tangent direction to reach the point A_2. There is the compounding field strength, $\bar{\mathbf{H}}_2 = \bar{\mathbf{E}}_2'/v_0 + \bar{\mathbf{E}}_2''/v_0$, in the point A_2, and its radial and tangent components are respectively, $\bar{\mathbf{E}}_2'/v_0$ and $\bar{\mathbf{E}}_2''/v_0$. From Eq. (11), it is found that the electromagnetic wave component, $\bar{\mathbf{E}}_2'/v_0$, will force the trial charge's orbit to fluctuate along the radial direction, while the electromagnetic wave component, $\bar{\mathbf{E}}_2''/v_0$, will result in the 'orbit' undulation along the tangent direction. Further the compounding field strength $\bar{\mathbf{H}}_2$ and compounding velocity $\bar{\mathbb{V}}_e$ will induce the undulation perpendicular to the 'orbital plane'. As a whole the multidirectional undulations represent as the gather density fluctuation of abundant trial charges.

6. CONCLUSIONS

The quaternion space was adopted to describe the electromagnetic features. Currently the quaternion space is applied to describe the gravitational features. However the quaternion space for electromagnetic field is independent to that for gravitational field.

In the quaternion space for gravitational field, the quaternion operator and the compounding field potential of gravitational field are able to deduce the compounding field strength and field source. And the decomposing of the definition of compounding field source produces the field equations and wave equation of gravitational field in the quaternion compounding space.

In the quaternion compounding space, according to the gravitational wave equation, the compounding field strength is the transverse wave. In the orbital movement model of the star moving around the galaxy center, the transmission direction of transverse wave is perpendicular to the gravitational acceleration and velocity curl. That is, the transverse wave transmits along the tangent direction of orbit. When the transverse wave transmits to another point, it appears the differentiation along the radial and tangent directions. These two components will impact the orbital movements of other stars, and then to form the relevant density wave.

In the S-quaternion compounding space, according to the electromagnetic wave equation, the compounding field strength is the transverse wave. In the orbital movement model of the negative trial charge moving around the positive electric charge, the transmission direction of transverse wave is perpendicular to the electric intensity and magnetic flux density. That is, the transverse wave transmits along the tangent direction of orbit. When the transverse wave transmits to another point, it appears the differentiation along the radial and tangent directions. These two components will impact the 'orbit' movements of trial charge, and then to form the relevant density wave.

ACKNOWLEDGMENT

This project was supported partially by the National Natural Science Foundation of China under grant number 60677039.

REFERENCES

1. Maxwell, J. C., *A Treatise on Electricity and Magnetism*, Dover Publications Inc., New York, 1954.
2. Weng, Z.-H., "Near-weightlessness movements in electromagnetic fields," *PIERS Proceedings*, 1372–1376, Taibei, Taiwan, March 25–28, 2013.
3. Lin, C.-C. and F. H.-S. Shu, "On the spiral structure of disk galaxies," *Astrophysical Journal*, Vol. 140, No. 2, 646–655, 1964.

Numerical Modelling of Heat Flow Distribution Based on the Nodal Heating Method

Eva Kroutilova, **Pavel Fiala**, **Premysl Dohnal**, **and Radim Kadlec**
Department of Theoretical and Experimental Electrical Engineering
Brno University of Technology, Technicka 12, Brno 616 00, Czech Republic

Abstract— The paper presents a solution of the thermal problem based on the modified nodal heating method. This technique exploits the classic nodal voltage method, and thus the vector of unknown quantities contains mainly nodal heating oriented from the individual independent nodes to the reference node. The vector of unknown quantities is nevertheless extended to include certain nodal thermal fluxes, the heating of ideal sources in particular. Test examples of a switchgear are shown as an instance of the solution.

1. THE NODAL HEATING METHOD

The thermal problem is formulated using partial solutions of the partial differential equations

$$\frac{\partial^2\Theta}{\partial x^2}+\frac{\partial^2\Theta}{\partial y^2}+\frac{\partial^2\Theta}{\partial z^2}=-\frac{q}{\lambda}, \tag{1}$$

where λ [W · m^{-1} · K^{-1}] is the specific thermal conductivity of the environment and q [W · m^{-3}] are the specific losses. If the heat in the intended area heat does not rise, then $q = 0$, and Poisson's equation transforms into the Laplace equation

$$\frac{\partial^2\Theta}{\partial x^2}+\frac{\partial^2\Theta}{\partial y^2}+\frac{\partial^2\Theta}{\partial z^2}=0 \tag{2}$$

within reference [1]. With these equations, partial derivations are replaced by differences (FDM), and the sequentially homogeneous problem is substituted by a network with constant parameters. Thus, we obtain the problem with concentric parameters exhibiting strongly non-linear behaviour of functions. This nonlinearity is caused by the non-linear thermal dependence of portions of the problem; here, it is possible to use the relations in reference [1] as an example. A simple iteration method is selected for the solution of the non-linear problem [2]. In the iteration process, we observe the change of temperature rise in the selected node of the model network with respect to the previous iteration step. In this context, there holds the formula for the termination of the iteration process of step k

$$\left|\Theta_i^k-\Theta_i^{k+1}\right|\le\varepsilon_k, \tag{3}$$

where Θ_i^k is the temperature, Θ_i^{k+1} the temperature of the next step, E_k the selected sufficiently small number, i the node number of the FDM model network.

The solution of a linear circuit using the nodal heating method comprises three phases:

1) One of the circuit nodes is chosen as the so-called reference node; as a rule, the node is assigned the sequence number of 0. Its heating is considered to be equal to zero. The remaining — or independent — nodes are numbered, and their heating is marked positively with respect to the reference node (the so-called nodal heating) as Θ_{10}, Θ_{20}, …, $\Theta_{(n-1)0}$.

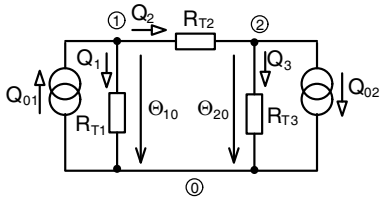

Figure 1: A scheme complementing the nodal heating method.

2) For the individual independent nodes, we formulate equations according to Kirchhoff's first law. Thermal fluxes from the node are denoted by the plus sign, while fluxes to the node have the minus sign. Then, by solving the system of equations, we obtain the size of the nodal temperature rise in the circuit.

3) The calculation of the thermal fluxes and temperature rise on individual elements of the circuit is performed.

The nodal temperature rise method requires the sources in the circuit (both independent and controlled) to be exclusively thermal flux sources. In this method, the sources will be replaced with equivalent thermal flux sources. Examples of the solution are shown in reference [1].

2. THE MODIFIED NODAL HEATING METHOD (MHNM)

The modified nodal heating method is based on the classic nodal voltage method, which means that the vector of unknown quantities contains mainly nodal heating oriented from the individual independent nodes to the reference node. The vector of unknown quantities is nevertheless extended to include certain nodal thermal fluxes, the heating of ideal sources in particular. The related details are described in [1].

3. EXAMPLES OF THE SOLUTION

Test examples of the switchgear will be shown as an instance of the solution. For the given configuration, these examples are realized in three variants. While the first variant is solved for a confined space (natural air circulation, radiation, convection), the second variant is a model having ventilation openings with natural air flow (turbulent circulation, radiation, convection), and the third option is characterised by forced air flow (turbulent circulation, radiation, convection). The model was designed in parts according to the physical processes (convection, conduction, radiation, ...); simultaneously, the concentric parameters were designed and the FDM model set up together with the iteration solver. On the screen, all the model network nodes (temperature rise) and the three observed points T_1, T_2 and T_3 are monitored (this is shown in Fig. 2). After termination of the iteration process, the nodal values were compared with the model described here as well as with the model solved by means of the FEM.

4. MODEL TEMPERATURE TASKS TO VALIDATE THE RESULTS

The model of the thermal problem for verifying the results of the ANSYS-based routine processing was assembled using the finite element method. The equations of the thermal model are based on the formulation of the first law of thermodynamics

$$q_A + \rho_A c_A v_A \cdot div\, T_A - div\,(k_A\, grad\, T_A) = \rho_A c_A \left(\frac{\partial T_A}{\partial t_A}\right), \tag{4}$$

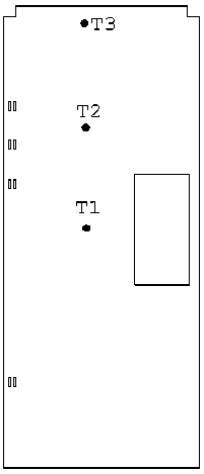

Figure 2: An example of the monitored distribution of temperatures: overall view.

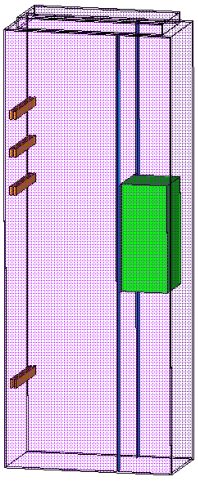

Figure 3: An example of the resulting tested network distribution in the switchgear.

where q_A is the specific heat, ρ_A the specific density, c_A the specific latent heat, T_A the temperature, t_A the time, k_A the coefficient of thermal conductivity, ν_A the medium flow velocity.

Respecting Snell's law, the model can be simplified to the form

$$q_A + \rho_A\, c_A v_A \cdot div\, T_A - div\,(k_A\, grad\, T_A) = \rho_A\, c_A \left(\frac{\partial T_A}{\partial t_A}\right). \tag{5}$$

A similar solution, together with the other results, is described in reference [1].

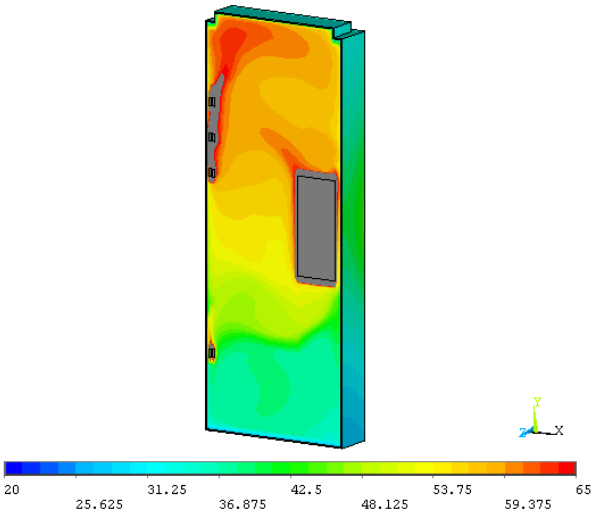

Figure 4: An example of the final temperature distribution of the switchgear case and apparatus (casual flow, without air holes).

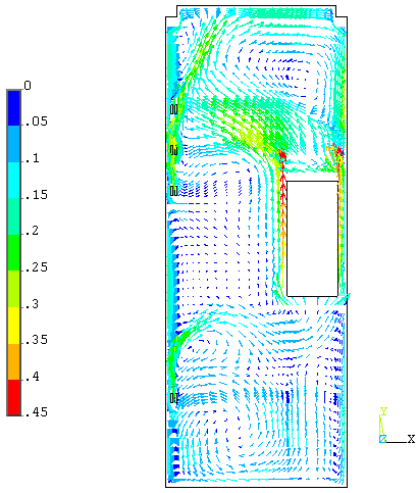

Figure 5: An example of velocity distribution [m/s], (casual flow, without air holes).

Table 1: Comparison of the results.

	Without air holes			Casual flow, with air holes			Air circulation, with air holes			
	FEM	standard	MNHM	FEM	standard	MNHM	FEM		MNHM	
T_1 [°C]	57	47	58	26	31	27	$36^{(1)}$	$23^{(2)}$	$34^{(1)}$	$21^{(2)}$
T_2 [°C]	62	53	64	31	36	29	$35^{(1)}$	$22^{(2)}$	$33^{(1)}$	$28^{(2)}$
T_3 [°C]	60	59	60	32	41	31	$34^{(1)}$	$21^{(2)}$	$33^{(1)}$	$26^{(2)}$
T_{vicinity} [°C]	20	20	20	20	20	20	20	20	20	20

5. CONCLUSION

Table 1 shows an example of the results for temperatures obtained via calculation according to the standard solution (with a common program), by means of the ANSYS-based FEM numerical analysis, and through the presented MHNM. The calculated air circulation values were $0.018277\,\text{kg/s}^{(1)}$ and $0.18277\,\text{kg/s}^{(2)}$. The result obtained using the modified nodal heating method corresponds to the values provided by the FEM and computed via standard programs. The deviation between the individual numerical solutions did not exceed 5%.

A significant advantage of modified nodal heating is the simplicity of the solution, which becomes evident when compared with the complexity and computational demands of the FEM model produced in the Ansys system.

ACKNOWLEDGMENT

This work was supported by Czech Science Foundation (13-09086S), a project of the BUT Grant Agency, No. FEKT-S-11-5/1012, and a project from the Education for Competitiveness Operative Programme, No. CZ.1.07.2.3.00.20.0175, (Electro-researcher).

REFERENCES

1. Kroutilová, E. and T. Bachorec, "Modeling temperature conditions in the switchgear," Research Report, UTEE, FEKT, VUT v Brne, 2007.
2. Rektorys, K., *Prehled Uzité MATEMATIKY*, SNTL, Praha, 1968
3. Cap, M., P. Marcon, K. Bartusek, et al., "Measuring of temperature fields using MR tomography," *PIERS Proceedings*, 1040–1042, Cambridge, USA, July 5–8, 2010.
4. Kadlecová, E., "Automated system of calculation of reflecting surface of light sources," Disertation Thesis, UTEE, FEKT, VUT v Brne, 2004.
5. Kadlec, R., E. Kroutilova, and P. Fiala, "Multiple reflection from layered heterogeneous medium," *PIERS Proceedings*, 87–90, Suzhou, China, September 12–16, 2011.
6. Mikulka, J., T. Kriz, E. Kroutilova, et al., "Numerical modeling of light sources with R-FEM method in CFX environment," *PIERS Proceedings*, 424–427, Xi'an, China, March 22–26, 2010.
7. Kadlecová, E. and P. Fiala, "New directions in modeling the lighting systems," *Radioengineering*, Vol. 13, No. 4, 75–80, 2004, ISSN: 1210-2512.
8. Kadlec, R., P. Fiala, and E. Kroutilová, "Numerical modeling by raytracing," *Proceedings of the International Workshop on Teleinformatics and Electromagnetic Field*, 14, Paris, UTEE, FEKT, VUT v Brne, 2008, ISBN: 9788021437180.
9. Kroutilová, E., "Hybridní numerické metody," Habilitation Thesies, UTEE, FEKT, VUT v Brne, May 2013.
10. Kadlec, R., P. Fiala, and D. Nespor, "Electromagnetic wave propagation in heterogeneous structures," *PIERS Proceedings*, 1031–1034, Cambridge USA, July 5–8, 2010.

Approaches to the Modelling of Multilayer Materials

Eva Kroutilova, **Pavel Fiala**, **Premysl Dohnal**, **and Radim Kadlec**
Department of Theoretical and Experimental Electrical Engineering
Brno University of Technology, Technicka 12, Brno 616 00, Czech Republic

Abstract— The authors evaluate the applicability of different numerical methods for the solution of practical problems related to material engineering. In this context, the paper presents various approaches to solving the transmission of electromagnetic waves through a multilayer material that consists of environments with different material properties. The proposed solutions can be used, for example, in the modelling of the propagation of electromagnetic waves in metamaterials and nanostructures.

1. MODELLING OF MULTILAYERED MATERIALS

Multilayered materials and systems based on, for example, metallic, intermetallic, polymeric, and ceramic constituents have become increasingly important in satisfying structural requirements of the current and future high-performance products. The materials are suitable for a wide variety of applications including thermal barrier coatings, aircraft structural components and wear-resistant coatings, processing techniques such as reactive sputter deposition, sedimentation processing, pressureless cosintering, and rapid prototyping via laminated object fabrication. Further investigation into the problem of multilayered material applications is required. Most hitherto presented papers focus on the mechanical behaviour and modelling of multilayered systems and reveal significant effects of layer thickness, spacing, and constituent properties of the fracture and fatigue behaviour of such systems. Multilayered materials have proved themselves to be of technological importance in a wide variety of industrial and medical applications, for example catalysis, molecular separation, and drug delivery in the human organism; however, they are also critical to a number of environmental issues such as the path of contaminants and groundwater quality [1–4].

A suitable example of solving the non-stationary problem of the transient state consists in the extended wave equation model for the electromagnetic wave passing through the multilayered material. The model is based on the complete wave equation

$$\nabla^2 u + g\frac{\partial^2 u}{\partial t^2} - f\left(x, y, z, t\right) = 0,\ \forall g\left(x, y, z\right) < 0, \tag{1}$$

where g, h, x, y, z are the general continuous or sequentially continuous (non-continuous, discrete) functions of the variable u. It is important to note that, even though we know the numerical result, the exact solution is very demanding in terms of the model formation and the solution time. However, we may conveniently use a solution approach which will utilize simplification to accelerate the entire analysis; also, the partial loss of accuracy that occurred in the full model will now be within acceptable tolerance. A large number of numerical methods and commercially distributed programs are available for the automatised calculation of physical problems.

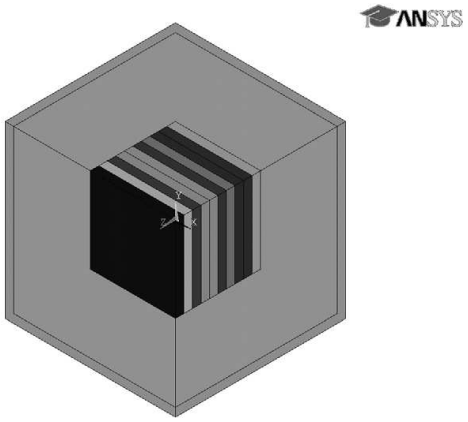

Figure 1: A geometrical representation of the task.

The group of frequently applied techniques includes, above all, the Ray-tracing method, the Radiosity method, and the Finite element method (FEM). The first of these approaches is based on solving the task as a 2D model by means of the Comsol Electromagnetic Waves analysis (the Finite element method is used). The second technique solves the task as a 3D model, using the Ansys Frequency Electromagnetic Field Simulation (the FEM is applied). Within the last technique, the task is solved as a 2D model via the Ray-tracing simulation. A geometrical representation of the task is provided in Fig. 1, where the surfaces of a heterogeneous material with several layers are shown. The layers consist of the following media: ***material 1*** (air): $e = 1$, $m = 1$, ***material 2*** (water): $e = 81$, $m = 0.999991$, ***material 3*** (salt): $e = 6$, $m = 0.9999841$.

2. 2D MODEL CREATED BY MEANS OF THE COMSOL MULTIPHYSICS ELECTROMAGNETIC WAVES ANALYSIS

COMSOL Multiphysics is a software for various applications in engineering and physics, which enables the solution of multiphysical tasks and coupled phenomena.

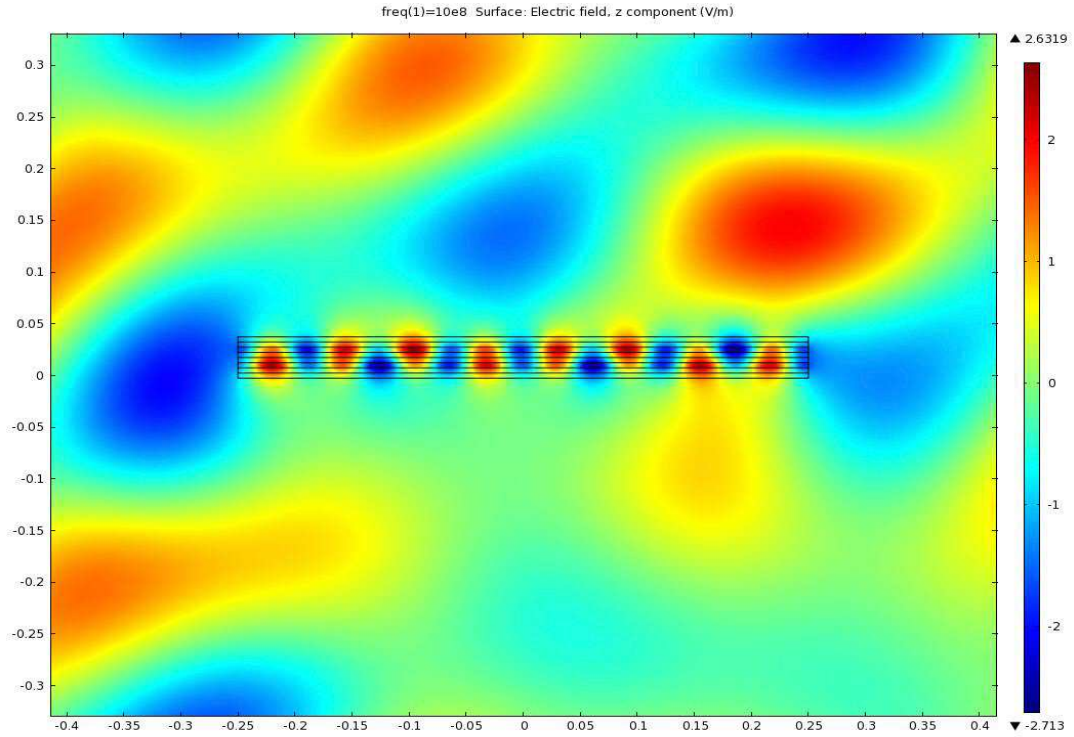

Figure 2: The results of the 2D model obtained via the comsol multiphysics electromagnetic waves analysis.

The software comprises a solver and simulation tools, and the simulation process is based on the finite element method. The results of the solution are indicated in Fig. 2; more details can be found in [5] and [6].

3. 3D MODEL PRODUCED BY THE ANSYS FREQUENCY ELECTROMAGNETIC FIELD SIMULATION

ANSYS enables us to perform various types of engineering simulation required by the concrete design process.

4. 2D MODEL OBTAINED VIA THE RAY-TRACING SIMULATION

Ray tracing is a versatile technique that uses the same model to integrate aspects of the light/object interaction which were previously handled by separate ad hoc algorithms. These aspects include reflection, hidden surface removal, and shadows. The idea of ray tracing consists in tracing the light for each pixel from the eye or viewpoint through the monitored element directly to the location. The principle of the ray tracing method is described in Fig. 4.

In the Matlab program, algorithms were created that simulate the reflection and refraction in the lossy environment on the boundary between dielectrics. The reflection and refraction are

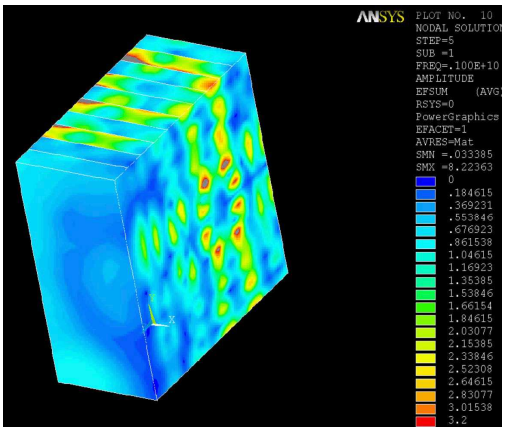

Figure 3: The results for the waves on the surface of a heterogeneous material: Ansys solution.

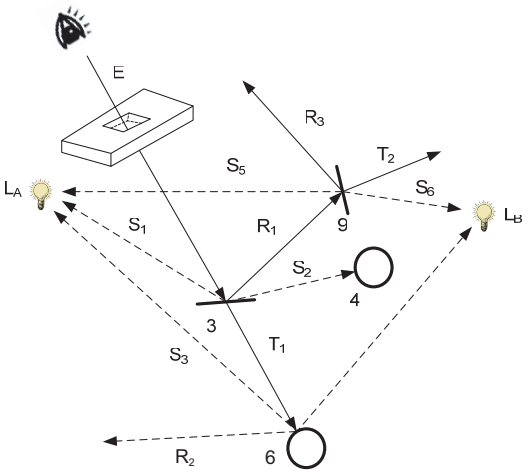

Figure 4: The principle of the ray tracing method.

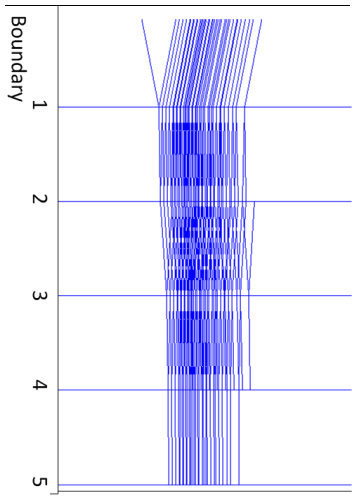

Figure 5: The reflection and refraction of the electromagnetic waves on a layered medium for the TE wave in Matlab (8000 cycles).

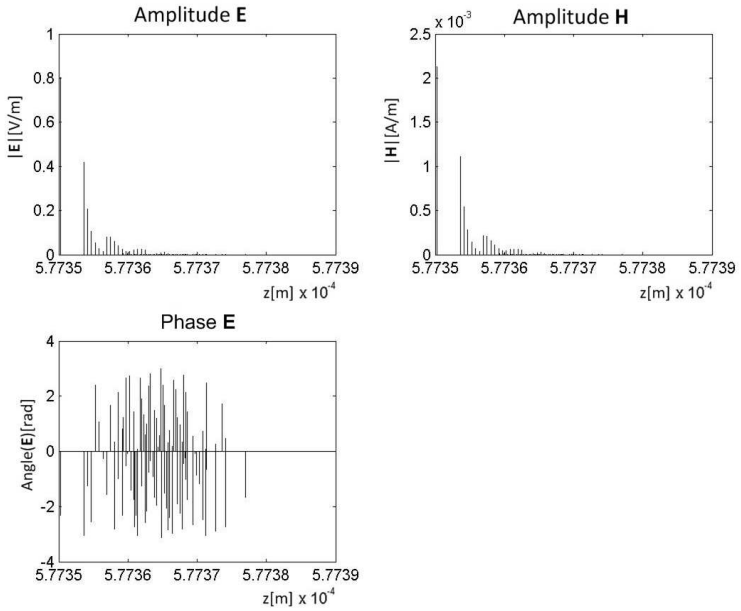

Figure 6: The intensity of the electric and magnetic components of the TE wave outside the layered medium; the space between the layers is $5 \cdot 10^{-9}$ mm.

consistent with Snell's law for electromagnetic waves. An electromagnetic wave is understood as the electric field strength and the magnetic field strength. For simplicity, we will analyse separately the **E** vector parallel to the boundary (also known as the TE wave) and the **H** vector parallel to the boundary (also known as the TM wave). Fig. 6 shows the intensity of the electric and magnetic components of the TE wave outside the layered medium; the indicated response of the environment is related to 5 layers of the same thickness, namely $5 \cdot 10^{-9}$ mm. More results can be found in [5–9].

5. CONCLUSION AND COMPARISON OF THE RESULTS

The paper describes three approaches to numerical models. For simple cases (such as a planar interface), the behaviour of an incident wave can be calculated analytically via Snell's law and the Fresnel equations, which are fundamental tools for analyzing the reflection and refraction of electromagnetic waves on the boundary between multilayered materials. Using the Matlab program for the analytical solution of the propagation, reflection, and refraction of wideband electromagnetic signals in the province of multilayered optical materials is a time-consuming approach. This method is suitable mainly for the specific purposes of a detailed analysis of particular problems. Therefore, numerical methods are applied to facilitate the calculation process, and a wide range of programs such as ANSYS, Comsol, or Matlab can be utilized to support the actual numerical modelling process. The solution performed in the Matlab environment is the simplest of the three proposed approaches, and this technique can be applied to verify the results provided by the other two programs based on the finite element method (Comsol and ANSYS). The results obtained by means of all the approaches correspond to theoretical expectations. In terms of the time intensity, the solution using the 2D Comsol Multiphysics is significantly less demanding than the analysis carried out via Ansys and 2D ray tracing. Moreover, because the Ansys-based solution has been designed as 3D, it is also computationally intensive and provides more accurate results.

The approaches described in this paper are suitable for the analysis of beam refraction to the other side from the perpendicular line during the passage of the wave through the interface. This phenomenon occurs in metamaterials.

ACKNOWLEDGMENT

This work was supported by Czech Science Foundation (13-09086S), a project of the BUT Grant Agency, No. FEKT-S-11-5/1012, and a project from the Education for Competitiveness Operative Programme, No. CZ.1.07.2.3.00.20.0175, (Electro-researcher).

REFERENCES

1. Cygan, R. T., J. A. Greathouse, H. Heinzb, and A. G. Kalinichev, "Molecular models and simulations of layered materials," *Journal of Materials Chemistry*, Vol. 19, No. 17, 2009, DOI: 10.1039/b819076c.
2. Kroutilová, E., "Hybridní numerické metody," Habilitation thesies, VUT v Brně, FEKT, UTEE, May 2013.
3. Kadlecová, E., "Automated system of calculation of reflecting surface of light sources," Disertation thesis, VUT v Brně, FEKT, Brno, 2004.
4. Kadlecová, E. and P. Fiala, "New directions in modeling the lighting systems," *Radioengineering*, roč, Vol. 13, č, No. 4, 75–80, 2004, ISSN: 1210-2512
5. Roubal, Z., R. Kadlec, E. Kroutilova, and P. Fiala, "Algorithms for electromagnetic waves on interface," *PIERS Proceedings*, 425–428, Kuala Lumpur, Malaysia, March 27–30, 2012.
6. Kadlec, R., P. Fiala, and D. Nespor, "Electromagnetic wave propagation in heterogeneous structures," *PIERS Online*, Vol. 6, No. 7, 613–616, 2010.
7. Kadlec, R., P. Marcoň, E. Kroutilova, and P. Fiala, "Response of multilayer materials to electromagnetic waves," *PIERS Proceedings*, 580–583, Taipei, Taiwan, March 25–28, 2013.
8. Kadlec, R., E. Kroutilová, and P. Fiala, "Multiple reflection from layered heterogeneous medium," *PIERS Online*, Vol. 7, No. 7, 633-636, 2011.
9. Kadlec, R., P. Fiala, and E. Kroutilová, "Numerical modeling by raytracing," *Proceedings of the International Workshop on Teleinformatics and Electromagnetic Field*, 14, UTEE, FEKT VUT v Brně, Paris, 2008, ISBN: 9788021437180.

Inhomogeneous Spatially Dispersive Electromagnetic Media

Jonathan Gratus[1, 2] **and Matthew McCormack**[1, 2]

[1]Physics Department, Lancaster University, LA1 4YB, UK
[2]The Cockcroft Institute, Sci-Tech Daresbury, Keckwick Lane
Daresbury, Warrington, WA4 4AD, UK

Abstract— Two key types of inhomogeneous spatially dispersive media are described, both based on a spatially dispersive generalisation of the single resonance model of permittivity. The boundary conditions for two such media with different properties are investigated using Lagrangian and distributional methods. Wave packet solutions to Maxwell's equations, where the permittivity varies and is periodic in the medium, are then found.

1. INTRODUCTION

All media are, at least to some extent, both temporally and spatially dispersive [1–5]. A temporally dispersive medium takes time to respond to an electromagnetic signal. A spatially dispersive medium responds not only to a signal at a particular point, but to signals in the neighbourhood of that point. Likewise all media are inhomogeneous, both on the macroscopic scale due to the finite nature of any sample of material, and on the microscopic scale.

Metamaterials [6–10] offer a way of constructing spatially dispersive media with desired electromagnetic properties. Compact, high gradient, accelerators have a wide range of applications in academia, industry, energy and health. A dielectric wakefield accelerator [6] uses electrons to create a field in a dielectric which in turn accelerates further electrons. Using a spatially dispersive dielectric with a periodic inhomogeneity, requires a knowledge about which electromagnetic fields propagate in such dielectric and how the fields pass through the vacuum-dielectric boundary.

For this article we will assume that there is a linear constitutive relationship between the polarization field $\mathbf{P}(t,\mathbf{x}) = \mathbf{D}(t,\mathbf{x}) - \mathbf{E}(t,\mathbf{x})$ and electric field $\mathbf{E}(t,\mathbf{x})$. All media respond linearly for sufficiently small electromagnetic fields and ultimately all media, including the vacuum, are non linear for sufficiently high fields. To simplify the analysis we make the following assumptions.

- There is no magnetization so that $\mathbf{H} = \mathbf{B}$.
- All fields are functions of time t and one spatial coordinate $x = x_1$, thus independent of x_2, x_3. In frequency domain, $k_2 = k_3 = 0$ and we set $k = k_1$.
- The electric and polarization fields are transverse so that $E_1(t,x) = 0$, $P_1(t,x) = 0$ and $B_1(t,x) = 0$. This assumption automatically satisfies the two non-dynamic source free Maxwell's equations.
- We choose a linearly polarized wave so that in the $(\mathbf{e}_1, \mathbf{e}_2, \mathbf{e}_3)$ frame $\mathbf{E}(t,x) = E(t,x)\mathbf{e}_2$, $\mathbf{P}(t,x) = P(t,x)\mathbf{e}_2$ and $\mathbf{B}(t,x) = B(t,x)\mathbf{e}_3$.

The relationship between $P(t,x)$ and $E(t,x)$ analysed here is a generalisation of the single resonance model of permittivity. The first generalisation is a simple extension to make the medium spatially dispersive, achieved by introducing a finite propagation speed β,

$$\tilde{P}(\omega,k) = \frac{\tilde{E}(\omega,k)}{\omega^2 - 2i\lambda\omega + (\alpha^2 - \lambda^2) - \beta^2|k|^2} \tag{1}$$

where $\tilde{P}(\omega,k) = \int_{-\infty}^{\infty}\int_{-\infty}^{\infty} e^{-2\pi i(\omega t + kx)} P(t,x)dtdx$ is the Fourier transform of $P(t,x)$. Media with such a constitutive relation can be constructed using a cross wire configuration [10].

The second generalisation is to allow the quantities λ, α and β to depend on position x. To do this we replace the frequency-wave number relation (1) with the PDE in space and time given by

$$-\frac{1}{(2\pi)^2}\frac{\partial^2 P}{\partial t^2} + \frac{2\lambda(x)}{2\pi}\frac{\partial P}{\partial t} + \big(\alpha(x)^2 - \lambda(x)^2\big)P + \frac{\partial}{\partial x}\Big(\frac{\beta(x)^2}{(2\pi)^2}\frac{\partial P}{\partial x}\Big) = E \tag{2}$$

It is easy to see that if λ, α and β are constants then the Fourier transform of (2) reproduces (1). We consider two types of inhomogeneity.

In Section 3 we consider a simple boundary between two homogeneous regions. For spatially dispersive media the standard boundary conditions for Maxwell's equations are insufficient to completely specify the solutions for outgoing waves in terms of the incoming waves. The additional equations are called "additional boundary conditions" (ABC) and have often drawn controversy [6–10, 12–14]. For the boundary between a spatially dispersive medium and the vacuum the standard ABC are given by Pekar [12]. In this article, we consider the boundary conditions between two spatially dispersive regions. We consider two methods for deriving the boundary conditions for Maxwell's equations for non-spatially dispersive media: One is the distributional or pill box method, the other is to use a Lagrangian method to derive natural boundary conditions. We show these give the same boundary conditions, which reduce to Pekar's boundary condition in the limit where $\beta \to 0$ in one of the regions.

In Section 4, we consider a periodic structure where α and λ are periodic with the same period. We assume that these quantities take the form of a constant term plus a small periodic inhomogeneity, e.g., $\alpha(x) = \alpha_0 + \alpha_1 \cos x$ where the α_1 is small. The goal in this section is to find solutions to the source free Maxwell equations, i.e., the dispersion relations. However since the medium is inhomogeneous it is not possible to find single mode solutions of the form $e^{2\pi i(\omega t + kx)}$ and is therefore necessary to look for packet solutions of the form $e^{2\pi i\omega t}\hat{P}(x)$. In the following we present an analytic form for an approximate solution for $\hat{P}(x)$. In addition we present a numerical method for finding the permitted frequencies and $\hat{P}(x)$.

In Section 5, we give a discussion of the implications of this research.

2. MAXWELL'S EQUATIONS AND STATIONARY MEDIA

From $\mathbf{E}(t,x) = E(t,x)\mathbf{e}_2$ etc., the source free dynamical Maxwell's equations become $E' = -\dot{B}$ and $B' = -(\dot{E} + \dot{P})$ which we can combine to give $E'' = \ddot{E} + \ddot{P}$. Taking the Fourier transform with respect to t gives

$$(2\pi)^{-2}\hat{E}'' = -\omega^2\left(\hat{E} + \hat{P}\right) \tag{3}$$

where $\hat{P}(\omega, x) = \int_{-\infty}^{\infty} e^{-2\pi i\omega t}P(t,x)dt$. In most cases, in the following, we will not explicitly write the ω argument in $\hat{E}$ and $\hat{P}$.

The Fourier transform of the constitutive relation (2) is

$$(2\pi)^{-2}\left(\beta^2(x)\hat{P}'\right)' + L(x)\hat{P} = \hat{E} \quad \text{where} \quad L(x) = (\omega + i\lambda(x))^2 + \alpha(x)^2 \tag{4}$$

3. ADDITIONAL BOUNDARY CONDITIONS FOR SPATIALLY DISPERSIVE MEDIA

In this section we set the media parameters $\alpha(x)$, $\beta(x)$, $\lambda(x)$ to be piecewise constant: $\alpha(x) = \theta(-x)\alpha_{\mathbf{L}} + \theta(x)\alpha_{\mathbf{R}}$ etc., so that $L(x) = \theta(-x)L_{\mathbf{L}} + \theta(x)L_{\mathbf{R}}$, for media constants $\alpha_{\boldsymbol{\mu}}, \beta_{\boldsymbol{\mu}}, \lambda_{\boldsymbol{\mu}} \geq 0$ with $\boldsymbol{\mu} = \mathbf{L}, \mathbf{R}$. Here $\theta(x)$ is the Heaviside step function $\theta(x) = 0$ for $x < 0$ and $\theta(x) = 1$ for $x > 0$.

Eliminating $\hat{E}$ from (3) and (4) we have a fourth order ODE for $\hat{P}(x)$. For each region this is solved by

$$\hat{E}(x) = A^+_{\boldsymbol{\mu}}e^{2\pi ik^+_{\mu}x} + A^-_{\boldsymbol{\mu}}e^{-2\pi ik^+_{\mu}x} + B^+_{\boldsymbol{\mu}}e^{2\pi ik^-_{\mu}x} + B^-_{\boldsymbol{\mu}}e^{-2\pi ik^-_{\mu}x} \tag{5}$$

where

$$k^{\pm}_{\boldsymbol{\mu}} = \frac{\sqrt{\beta^2_{\boldsymbol{\mu}}\omega^2 + L_{\boldsymbol{\mu}} \pm \sqrt{(\beta^2_{\boldsymbol{\mu}}\omega^2 - L_{\boldsymbol{\mu}})^2 + 4\beta^2_{\boldsymbol{\mu}}\omega^2}}}{\sqrt{2}\beta_{\boldsymbol{\mu}}} \tag{6}$$

Since $\lambda_{\boldsymbol{\mu}} > 0$ the waves are damped in the direction of motion, (see Figure 1). Maxwell's equations give us two boundary conditions

$$\left[\hat{E}\right] = 0 \quad \text{and} \quad \left[\hat{E}'\right] = 0 \tag{7}$$

where $[\hat{E}]$ is the discontinuity $[\hat{E}] = \lim_{x\to 0+}\hat{E}(x) - \lim_{x\to 0-}\hat{E}(x)$. However, we need two additional boundary conditions for $[\hat{P}]$ and $[\hat{P}']$. In the usual scattering problem we prescribe the incoming wave amplitudes $\{A^-_{\mathbf{L}}, B^-_{\mathbf{L}}, A^+_{\mathbf{R}}, B^+_{\mathbf{R}}\}$ and we calculate the outgoing wave amplitudes $\{A^+_{\mathbf{L}}, B^+_{\mathbf{L}}, A^-_{\mathbf{R}}, B^-_{\mathbf{R}}\}$.

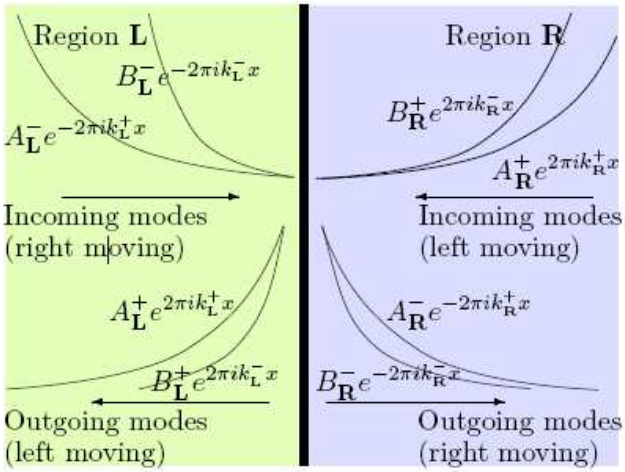

Figure 1: Incoming and outgoing modes, given in (5).

3.1. Lagrangian Formulation of Boundary Conditions

Due to the damping term, it is non trivial to formulate a Lagrangian which gives rise to both Maxwell's equations and the constitutive relation (2). However since we are interested in the boundary conditions, is it sufficient to use the Fourier transform Equations (3) and (4). These can be derived by varying the action

$$\mathcal{S}[\hat{E},\hat{P}] = \int \mathcal{L}\left(\hat{E},\hat{E}',\hat{P},\hat{P}',x\right)dx \tag{8}$$

where

$$\mathcal{L}\left(\hat{E},\hat{E}',\hat{P},\hat{P}',x\right) = \frac{1}{2}\left(\frac{(\hat{E}')^2}{(2\pi)^2\omega^2} - \hat{E}^2 + \frac{\beta(x)^2}{(2\pi)^2}(\hat{P}')^2 - L(x)\hat{P}^2\right) - \hat{E}\hat{P} \tag{9}$$

Varying (8) with respect to $\hat{E}$ and $\hat{P}$ away from the boundary yields (3) and (4) respectively. In order to obtain the boundary conditions we must consider variations with support which includes the boundary $x = 0$. It is necessary to assume $\hat{E}$ and $\hat{P}$ are continuous, i.e.,

$$\left[\hat{E}\right] = 0 \quad \text{and} \quad \left[\hat{P}\right] = 0 \tag{10}$$

Varying (8) with respect to $\hat{P}$ then gives

$$\begin{aligned}\delta_{\hat{P}}\mathcal{S} &= \int_{-\infty}^{\infty}\delta_{\hat{P}}\mathcal{L}dx = \int_{-\infty}^{\infty}\left(\frac{\beta(x)^2}{(2\pi)^2}\hat{P}'\delta\hat{P}' - L(x)\hat{P}\delta\hat{P} - \hat{E}\delta\hat{P}\right)dx \\ &= \int_{-\infty}^{0}\frac{d}{x}\left(\frac{\beta(x)^2}{(2\pi)^2}\hat{P}'\delta\hat{P}\right) + \int_{0}^{\infty}\frac{d}{x}\left(\frac{\beta(x)^2}{(2\pi)^2}\hat{P}'\delta\hat{P}\right) = -\left[\frac{\beta(x)^2}{(2\pi)^2}\hat{P}'\right]\delta\hat{P}\end{aligned}$$

Since this vanishes for all variations $\delta\hat{P}$, one has

$$\left[\beta(x)^2\hat{P}'\right] = 0 \tag{11}$$

Similarly varying (8) with respect to $\hat{E}$ gives

$$[\hat{E}'] = 0. \tag{12}$$

In the limiting case $\beta_{\mathbf{L}} \to 0$, the left hand region is only temporally dispersive. One must make a choice about the behaviour of $\{A_{\mathbf{L}}^{+}, A_{\mathbf{L}}^{-}, B_{\mathbf{L}}^{+}, B_{\mathbf{L}}^{-}\}$ in this limit. For a certain choice the boundary conditions (7), (10) and (11) reduce to Pekar's ABC

$$\left[\hat{E}\right] = 0, \quad \left[\hat{E}'\right] = 0 \quad \text{and} \quad \left[\hat{P}\right] = 0 \tag{13}$$

3.2. Distributional Method of Boundary Conditions

Given smooth functions $f_{\mathbf{L}}(x)$ and $f_{\mathbf{R}}(x)$ and setting $f(x) = \theta(-x)f_{\mathbf{L}}(x)+\theta(x)f_{\mathbf{R}}(x)$, then one has $f''(x) = \delta'(x)[f]+2\delta(x)[f']+\theta(-x)f''_{\mathbf{L}}(,x)+\theta(x)f''_{\mathbf{R}}(x)$. In order to avoid multiplying distributions we must assume P is continuous and set $P'(x) = \theta(-x)P'_{\mathbf{L}}(x) + \theta(x)P'_{\mathbf{R}}(x)$. Substituting this into (3) and (4) again implies (10), (11) and (12).

$$\left[\hat{E}\right] = 0, \quad \left[\hat{P}\right] = 0, \quad \left[\hat{E}'\right] = 0 \quad \text{and} \quad \left[\hat{P}'\right] = 0 \tag{14}$$

In the limit $\beta_{\mathbf{L}} \to 0$, for appropriate choices, these again reduce to Pekar's ABC (12).

4. PERIODIC MEDIA

In this section we investigate media where the constitutive quantity $L(x)$ in (4) is periodic $L(x+1) = L(x)$ and β is constant. We assume that the amplitude of the inhomogeneity is dominated by the first mode, that is

$$L(\omega, x) = L_0(\omega) + 2\Lambda(\omega)\cos(2\pi x) \tag{15}$$

Taking the Fourier transforms of (3) and (4) with respect to x we get $(\omega^2 - k^2)\tilde{E}(k) = -\omega^2\tilde{P}(k)$ and $-k^2\beta^2\tilde{P} + (\tilde{L} * \tilde{P})(k) = \tilde{E}(k)$. Combining these into a single equation gives

$$\left(\tilde{L} * \tilde{P}\right)(k) = \left(\beta^2k^2 - \frac{\omega^2}{\omega^2 - k^2}\right)\tilde{P}(k) \tag{16}$$

We look for periodic solutions of the form

$$\hat{P}(x) = \sum_{m=-\infty}^{\infty} P_m e^{2\pi imx} \tag{17}$$

whose Fourier transform $\tilde{P}(k)$ consists of a series of delta functions $\tilde{P}(k) = \sum_{m=-\infty}^{\infty} P_m\delta(k-m)$. Substituting (16) and (14) into (15) yields the difference equation

$$\Lambda P_{k-1} + f_kP_k + \Lambda P_{k+1} = 0 \quad \text{where} \quad f_k = \frac{\beta^2k^4 + \omega^2 + \left(\omega^2 - k^2\right)L_0(\omega) - \beta^2\omega^2k^2}{\omega^2 - k^2} \tag{18}$$

Observe that having higher order modes in $L(\omega, x)$ will result in more terms in (17). We can trivially solve (17) simply by arbitrarily fixing P_0 and P_1 and then using (17) to solve for all subsequent P_k. However, in general, this will lead to P_k's which diverge $|P_k| \to \infty$ as $k \to \pm\infty$. The Fourier transform of this would therefore be a non-smooth wave which may not even be continuous. Therefore for physical solutions, we demand that $|P_k| \to 0$ as $k \to \pm\infty$. As we see below we can obtain approximate analytic solutions for small Λ. In addition we also give a numerical method for finding arbitrary solutions.

4.1. Approximate Analytic Wave Packet Solutions

We have found two approximate analytic solutions in the case when $\Lambda \ll L_0$, an even solution $(\omega^{(e)}, P^{(e)})$ and an odd solution $(\omega^{(o)}, P^{(o)})$. Since these are approximate solutions, we set the left hand side of (17) to $\mathcal{Q}_k$, that is $\mathcal{Q}_k = \Lambda P_{k-1} + f_kP_k + \Lambda P_{k+1}$ so that $\mathcal{Q}_k = 0$ is an exact solution to (17). By contrast we solve $\mathcal{Q}_k = O(\Lambda^p)$ for some order p which depends on k.

The even solution $\omega = \omega^{(e)}$ is given by

$$\left(f_1 - \Lambda^2\left(\frac{1}{f_2} + \frac{2}{f_0}\right)\right)\Big|_{\omega=\omega^{(e)}} = 0 \tag{19}$$

$P^{(e)}$ is then given by

$$P^{(e)}_{-1} = 1, \quad P^{(e)}_0 = -\frac{2\Lambda}{f_0}, \quad P^{(e)}_1 = 1 \quad \text{and} \quad P^{(e)}_m = \frac{(-\Lambda)^{|m|-1}}{\prod_{k=2}^{|m|} f_k} + O\left(\Lambda^{|m|+1}\right) \tag{20}$$

By direct substitution into $\mathcal{Q}_m$ shows $\mathcal{Q}_0 = 0$, $\mathcal{Q}_{\pm1} = O(\Lambda^4)$ and $\mathcal{Q}_m = O(\Lambda^{|m|+1})$ for $|m| \geq 2$.

The odd solution $\omega = \omega^{(o)}$ is given by

$$\left(f_1 - \frac{\Lambda^2}{f_2}\right)\Big|_{\omega=\omega^{(o)}} = 0 \tag{21}$$

and $P_m^{(o)}$ by

$$P_{-1}^{(o)} = -1, \quad P_0^{(o)} = 0, \quad P_1^{(o)} = 1 \quad \text{and} \quad P_m^{(o)} = \text{sign}(m)\frac{(-\Lambda)^{|m|-1}}{\prod_{k=2}^{|m|} f_k} + O\left(\Lambda^{|m|+1}\right) \tag{22}$$

Again $\mathcal{Q}_0 = 0$, $\mathcal{Q}_{\pm 1} = O(\Lambda^4)$ and $\mathcal{Q}_m = O(\Lambda^{|m|+1})$ for $|m| \geq 2$.

Depending on how L_0 and Λ depend on ω these are often the lowest two modes. The shape of these modes is given in Figure 2, using the numerical approach below. In this case the even mode $(\omega^{(e)}, P^{(e)})$ cannot be supported by the medium and is damped.

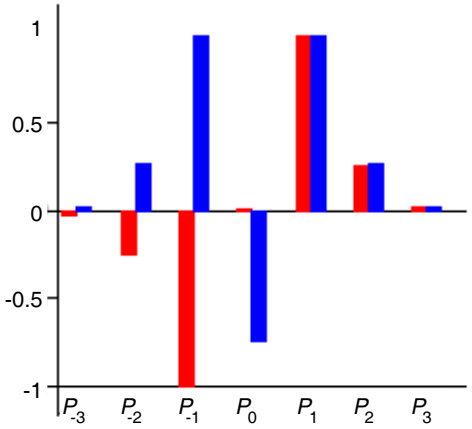

Figure 2: P_e (blue) and P_o (red) for $L_0 \equiv 1$, $\Lambda \equiv 0.75$. In this case $\omega^{(e)} = 0.753i$ and $\omega^{(o)} = 0.399$

4.2. Numerical Approaches

A numerical approximation scheme, which is valid if $\Lambda \not\ll L_0$ and gives packets in addition to (19)–(21), is as follows: Choose an integer $N \geq 2$. Then assume that $P_m \approx 0$ for $|m| > N$ thus truncating the infinite set of equation given by (17) to a set of $2N+1$ linear equations for $\{P_{-N}, \ldots, P_N\}$. Write this in matrix language $M\underline{b} = \underline{0}$ where M is a $(2N+1) \times (2N+1)$ matrix with $M_{k,k} = f_{k-N-1}$, $M_{k,k-1} = M_{k,k+1} = \Lambda$ and $\underline{b}_k = P_{k-N-1}$. Solve $\det(M) = 0$ to obtain values for ω. The corresponding null spaces give P_m.

5. CONCLUSION AND DISCUSSION

In this article we address two key problems: What wave packets can propagate though a spatially dispersive medium and how wave packets behave as they pass through a boundary between two media.

We have given two methods of deriving the boundary conditions for a junction between two spatially dispersive regions. These two methods give the same boundary conditions. These boundary conditions are tied to the choice of differential equation and ultimately depend on the microstructure of the materials.

We have given approximate solutions to Maxwell's equations for a periodic spatially dispersive medium. Since we have only given two modes, it is natural explore the behaviour of a general mode. From the numerical approach it appears that the higher frequency resemble the case for homogeneous media. This is currently being explored.

ACKNOWLEDGMENT

The authors are grateful for the support provided by STFC (the Cockcroft Institute ST/G008248/1), EPSRC (the Alpha-X project EP/J018171/1) and the Lancaster University Faculty of Science and Technology studentship program. In addition the authors would like to thank David Burton (Physics Department, Lancaster University) and Adam Noble (Physics Department, Strathclyde University) for help in preparing this article, and the referee for making useful suggestions.

REFERENCES

1. Agranovich, V. M. and V. L. Ginzburg, *Spatial Dispersion in Crystal Optics and the Theory of Excitons*, Wiley-Interscience, New York, 1967.
2. Agarwal, G. S., D. N. Pattanayak, and E. Wolf, "Electromagnetic fields in spatially dispersive media," *Phys. Rev. B*, Vol. 10, No. 4, 1447–1475, 1974.
3. Belov, P. A., R. Marques, S. I. Maslovski, I. S. Nefedov, M. Silveirinha, C. R. Simovski, and S. A. Tretyakov, "Strong spatial dispersion in wire media in the very large wavelength limit," *Phys. Rev. B*, Vol. 67, No. 11, 113103, 2003.
4. Gratus, J. and R. W. Tucker, "Covariant constitutive relations and relativistic inhomogeneous plasmas," *J. Math. Phys.*, Vol. 52, 042901, 2011.
5. Gratus, J. and R. W. Tucker, "Covariant constitutive relations, landau damping and non-stationary inhomogeneous plasmas," *Progress In Electromagnetics Research M*, Vol. 13, 145–156, 2010.
6. Maslovski, S. I., T. A. Morgado, M. G. Silveirinha, C. S. R. Kaipa, and A. B. Yakovlev, "Generalized additional boundary conditions for wire media," *New Journal of Physics*, Vol. 12, No. 11, 113047, 2010.
7. Silveirinha, M. G., "Additional boundary condition for the wire medium," *IEEE Transactions on Antennas and Propagation*, Vol. 54, No. 6, 1766–1780, 2006.
8. Silveirinha, M. G., C. A. Fernandes, and J. R. Costa, "Additional boundary condition for a wire medium connected to a metallic surface," *New Journal of Physics*, Vol. 10, No. 5, 053011, 2008.
9. Silveirinha, M. G., "Additional boundary conditions for nonconnected wire media," *New Journal of Physics*, Vol. 11, No. 11, 113016, 2009.
10. Costa, J. T. and M. G. Silveirinha, "Macroscopic electromagnetic response of arbitrarily shaped spatially dispersive bodies formed by metallic wires," *Physical Review B*, Vol. 86, No. 7, 075129, 2012.
11. Rosenzweig, J. B., G. Andonian, P. Muggli, P. Niknejadi, G. Travish, O. Williams, K. Xuan, and V. Yakimenko, "High frequency, high gradient dielectric wakefield acceleration experiments at SLAC and BNL," *AIP Conference Proceedings*, Vol. 1299, No. 1, 364–369, 2010.
12. Pekar, S. I., "The theory of electromagnetic waves in a crystal in which excitons are produced," *J. Explt. Theoet. Phys. (U.S.S.R)*, Vol. 6, No. 33, 785–200, 1958.
13. Zeyher, R., J. L. Birman, and W. Brenig, "Spatial dispersion effects in resonant polariton scattering. I. Additional boundary conditions for polarization fields," *Phys. Rev. B*, Vol. 6, 4613–4616, 1972.
14. Henneberger, K., "Additional boundary conditions: An historical mistake," *Phys. Rev. Lett.*, Vol. 80, No. 13, 2889–2892, 1998.

An Electromagnetic Meta-lens Based on a New SRR Type for Antenna Gain Enhancement

Akram Boubakri and Fethi Choubeni
INNOV'COM Lab, Higher School of Communications, Carthage University, Ariana, Tunisia

Abstract— In this paper, we propose an electromagnetic meta-lens based on a new SRR type called diamond SRR. This new SRR form show's an ameliorated relative band of about 88% at the x band. The lens is made by an array of diamond SRR and wire and show at 10 GHz a refraction index of about −2.67 and a gain rise of 2 dB when associated with a rectangular patch antenna operating at the same frequency.

1. INTRODUCTION

Perfect lenses introduced by J. Pendry [1] on 2000 are lenses based generally on metamaterials in order to go beyond the diffraction limit and ameliorate the resolution of the structure. As other examples we can mention the invisibility cloak when creating such a band gap around a structure and bend electromagnetic wave and also in the case of our application, there is the collimating lens for antenna directivity improvement. This last is known to promise subwavelength focusing through negative refraction index and even has the power to focus the evanescent mode waves and it can be realized in the microwave band with a negative index slab made with SRR and wire.

2. ELECTROMAGNETIC META LENS DESIGN

2.1. Diamond SRR

Many types of LHM such as ones consisting of a periodic arrangement of wire and the SRRs, the Ω-like structure, the double S-shaped resonators, and also transmission line are designed and fabricated to exhibit the LH property. Nevertheless the performance including the bandwidth, loss and the unit cell size of the LHM are still calling for improvement. In the literature the collimating lenses are built with an array of SRR and wire, exhibiting a negative refractive index and improving the resolution by focusing the evanescent mode waves. We introduce in this paper a new form of SRR which is the diamond SRR as it's shown in Figure 1.

Our unit cell is composed of a diamond SRR and wire in its opposite face and parallel to the gap. According to transmission line theory, LHM can exist as long as there are the distributed shunt inductance and series capacitance simultaneously; and the performance of LHM will be good if the frequency response of the shunt inductance and series capacitance is stable. In our structure the capacitive behavior is assured by the gap g and it has an influence on the resonance frequency. The unit cell is simulated with HFSS and it presents at 10 GHz, −15 dB as return loss. We conclude also from the Figure 1 above that our metamaterials (diamond SRR with wire) has a relative bandwidth of about 88.37%, this value remain the highest value as it displayed in the table below where we compared it with other types of resonator.

Table 1: Comparison of the relative bandwidths for different metamaterials structure.

Structures	CLS/SRR [2]	SRR/Rod [3]	Double S [4]	SSRR [5]	D/SRR
Relative bandwidth	3.2%	12.2%	46%	56.4%	88.37%

In addition, we use the simulation result's to extract the effective parameters of the unit cell with the smith method which is an external approach where we compute, ε_{eff}, μ_{eff} and n using S parameters, results are displayed on Figure 2.

Our unit cell has at 10 GHz a LH behavior with a negative refractive real part of −2.76. This negative value is shown for a large bandwidth since our unit cell has also a broad band behavior.

2.2. Metalens to Ameliorate Antenna Gain

We use in this study a rectangular patch antenna designed on a dielectric board with a permittivity of 2.25 and a permeability of 1. The antenna dimensions are $w = 9$ mm and $L = 15$ mm to operate at 10 GHz. The antenna is simulated with HFSS and it has a gain of 8 dB and a return loss of about −25 dB.

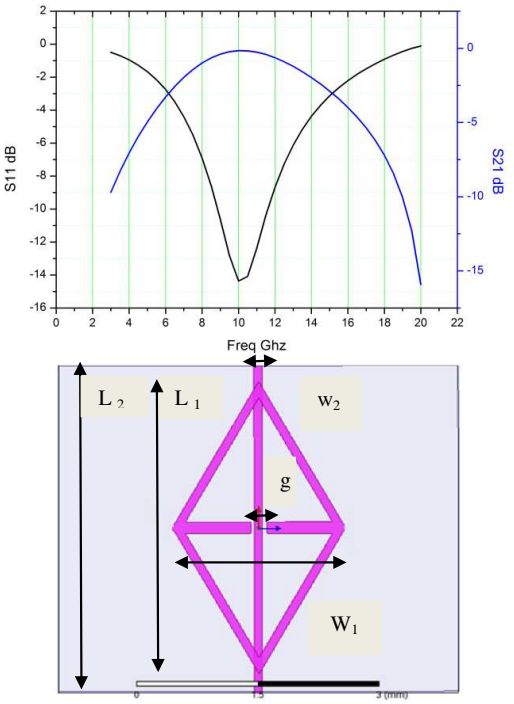

Figure 1: Diamond SRR unit cell and its S parameters $W_1 = 2.17\,\text{mm}$; $g = 0.2\,\text{mm}$; $w_2 = 0.1\,\text{mm}$; $L_2 = 4.2\,\text{mm}$; $L_1 = 3.75\,\text{mm}$.

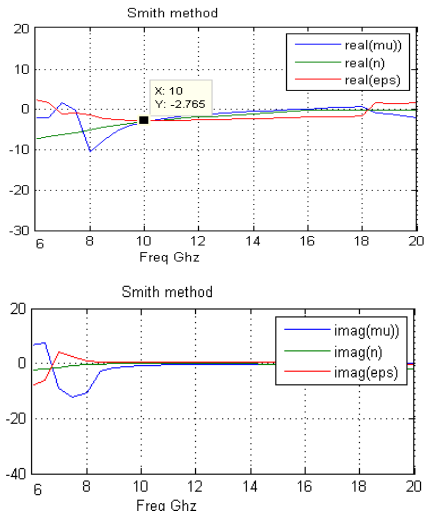

Figure 2: Extraction of unit cell effective parameters.

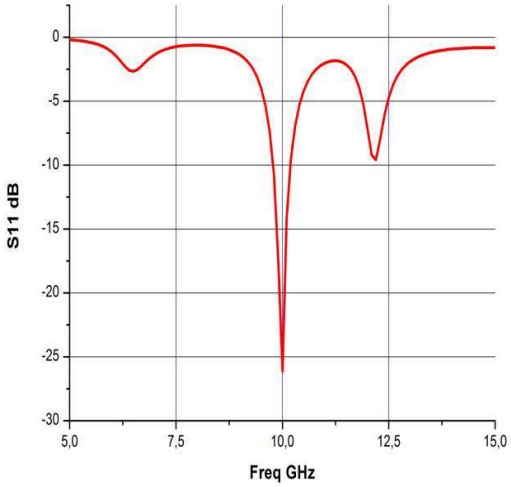

Figure 3: S_{11} parameters of the rectangular patch antenna.

Also, our metalens is made with a periodic array of the unit cell with an optimal value of periodicity of 4 mm in x and y directions.

The antenna and metalens above with a distance of 1 mm ($\lambda/28$) are simulated also with HFSS and the results are displayed on Figures 4(a) and (b) below.

The antenna gain was ameliorated of 25% (2 dB) to reach 10 dB and this, as we say before, is due to the amplification of the evanescent mode wave.

The Figure 4 shows that the use of the meta-lens was decreased the backward radiation in E and H plan. In addition *since* the amelioration is more clear in H plane, we have an improvement in gain and directivity with an angular width at $-3\,\text{dB}$ of 20° less than the antenna without meta-lens.

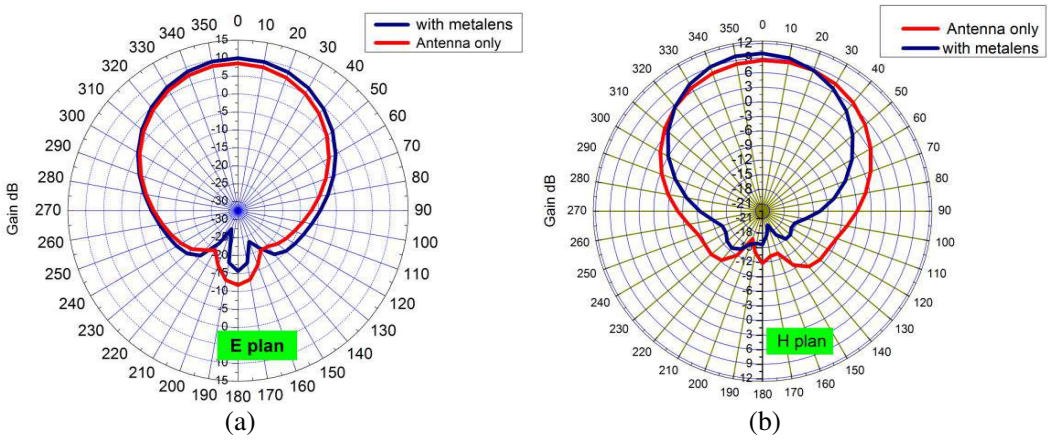

Figure 4: Gain and directivity enhancement in (a) E plane and (b) H plane.

3. CONCLUSION

In this study, we present a meta-lens based on Diamond SRR, this last has the highest relative bandwidth and when associated with wire it exhibits a negative refraction index for wide band. Our meta-lens let us to improve the antenna parameters such 25% rise in gain and directivity and a lessening of the angular width at -3 dB of 20° in H plan.

REFERENCES

1. Pendry, J. B., "Negative refraction makes a perfect lens," *Physical Review Letters*, Vol. 85, No. 18, 3966–3969, Oct. 2000.
2. Ziolkowski, R. W., "Design, fabrication, and testing of double negative metamaterials," *IEEE Transactions on Antennas and Propagation*, Vol. 51, 1516–1529, 2003.
3. Smith, D. R. and N. Kroll, "Negative refractive index in left-handed materials," *Physical Review Letters*, Vol. 85, 2933–2936, 2000.
4. Huangfu, J., L. Ran, H. Chen, X.-M. Zhang, K. Chen, T. M. Grzegorczyk, and J. A. Kong, "Experimental confirmation of negative refractive index of a metamaterial composed of Omega-like metallic patterns," *Applied Physics Letters*, Vol. 84, 1537–1539, 2004.
5. Wu, R. Q., Y.-M. Fan, M.-F. Wu, J. Wu, and L.-W. Li, "Design of planar LHM with broad bandwidth and miniaturized cell," *IEEE Antennas and Propagation Society International Symposium*, 487–490, 2006.

Multifunctionalized Self-supported (Nano) Membranes as Integrated Platform for Plasmonic Metamaterials

Zoran Jakšić[1], **Filip Radovanović**[1], **Aleksandra Nastasović**[2], **and Jovan Matovic**[3]

[1]Centre of Microelectronic Technologies and Single Crystals
Institute of Chemistry, Technology and Metallyrgy, University of Belgrade
Njegoševa 12, Belgrade 11000, Serbia
[2]Centre for Chemistry, Institute of Chemistry, Technology and Metallyrgy
University of Belgrade, Njegoševa 12, Belgrade 11000, Serbia
[3]Institute for Sensor and Actuator Systems, Technical University Vienna
Gusshausstrasse 27-29/366-MST, Vienna A-1040, Austria

Abstract— We considered the possibility to fabricate multifunctional nanocomposite membranes as a platform for plasmonic metamaterials, simultaneously incorporating pores, built-in functional groups and active nanoparticles. To this purpose we combined lamination and inclusion of nanofillers into the membrane host. For the basic material we chose macroporous crosslinked copolymers based on glycidyl methacrylate (GMA). The epoxy group present in GMA molecule is readily transformed into various functional groups that further serve as affinity enhancers, ensuring the usability of the membranes as pre-concentrators of selected agents in plasmonic sensors. To form GMA-based membranes we used a recently proposed method combining the traditional immersion precipitation with photopolymerization and crosslinking of functional monomers. Further functionalization is obtained by in-situ formation of noble metal nanoparticles directly within the GMA host. In this way membranes with simultaneous plasmonic, adsorbent and catalytic functionality are obtained. We considered the use of the our structures for plasmonic chemical sensors where separator, pre-concentrator and binding agent are integrated with the plasmonic crystal, as well as for plasmonic enhancement of photocatalytic reactions in microreactors. Our approach gives a highly tailorable element compatible with microelectromechanical systems (MEMS) technologies and readily transferable across platforms.

1. INTRODUCTION

Plasmonics is a burgeoning field of electromagnetics that ensures electromagnetic fields confinement and manipulation at nanoscale through the use of metal-dielectric nanostructures [1]. Some of its applications are enhanced light trapping in photodetectors or solar cells, photo-assisted catalysis and ultra-sensitive chemical and/or biological sensors.

In plasmonics an electromagnetic field with a wavevector exceeding that in free space is bound to an interface between materials with positive and with negative relative dielectric permittivity and is evanescent in both directions perpendicular to that interface. The planar distribution of the field maximum coincides with the form of ultrathin membranes. Such overlap makes membranes a platform of interest for plasmonics. Through a proper control of membrane properties one is in principle able to tailor the response of the whole plasmonic system. Among notable examples are freestanding (self-supported) nanomembranes, structures with a thickness below 100 nm and extremely large aspect ratios, often in excess of 1,000,000 [2, 3]. They are electromagnetically symmetrical, proven to support propagation of long-range surface plasmons polaritons [4] and can be used to enhance the design freedom in all of the quoted application fields.

In their basic form membranes are simple and thus allow for a relatively limited applicability, but their fields of use and tailorability can be vastly expanded through nanocompositing [5]. This is not unlike to the case of living organisms, the most complex and sophisticate natural form, where membranes are the most widespread building block, and where the difference between the living and inanimate is achieved through functionalization of very simple lipid bilayer structures [6].

There are a number of methods to perform multifunctionalization of artificial membranes. The most noted nanocompositing approaches are lamination (multilayering), inclusion of nanoparticle fillers, patterning, surface activation and surface sculpting [5, 7].

Membranes are a new building block in plasmonics. Thus publications dealing with this issue are relatively rare, but their number is rapidly increasing. Although multifunctionalization is the key to a successful application of membranes in plasmonics, currently only a small fraction of publications is dedicated to this field [8].

One of the materials convenient for membranes in plasmonics is glycidyl methacrylate (GMA). The epoxide group present in GMA molecules is readily transformed into various functional groups including amino, thiol, azole and pyrazole, pyridine and other groups [9] that further serve as affinity enhancers. Some examples of such functionalizations include heavy metals adsorption [10] and enzyme immobilization [11].

In this paper, we consider the applicability of GMA-based membranes as a platform for plasmonic metamaterials. After outlining our concept of multifunctionalization for plasmonics, we present some experimental results dedicated to simultaneous formation of pores within GMA-based membranes, functionalization of their epoxy groups and introduction of metal nanoparticles. We give some characterization results and outline some possible future directions.

2. CONCEPT

Figure 1 shows the basic concept of our approach. A membrane made of dielectric material (in our case copolymerized GMA) is in contact with the plasmonic part (material with free electron gas, typically noble metal) — Fig. 1(a). Membrane is functionalized to ensure enhanced active area for adsorption (through inclusion of pores), has target-specific binding agents (functional groups that bind to targeted analyte) and possibly nanoparticles of plasmonic material or catalyst. The membrane overlaps with the region of evanescent surface plasmon polariton (SPP) field. Thus conventional dielectric is replaced by a multifunctionalized one.

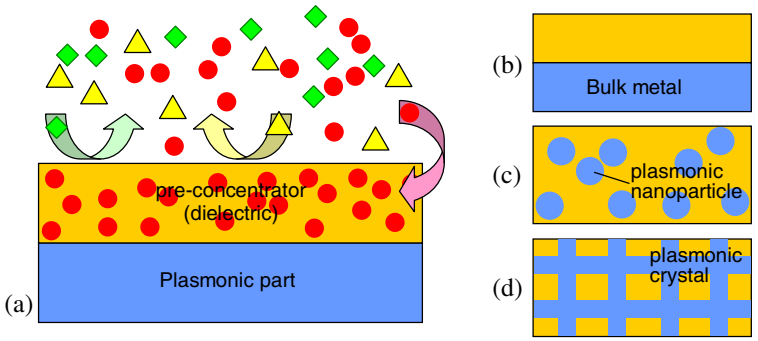

Figure 1: Use of multifunctionalized membrane for enhancement of plasmonic devices. (a) Dielectric membrane as pre-concentrator; (b) application of porous membrane to conventional surface plasmon resonance structure using bulk metal; (c) nanoparticle-based structure; membrane is dielectric host; (d) plasmonic metamaterial case; membrane is the dielectric part of plasmonic crystal.

This approach can be applied to all three main groups of plasmonic devices. The first one is represented by the conventional surface plasmon resonance structure where the plasmonic part is bulk noble metal, usually gold or silver (Fig. 1(b)); the membrane is simply placed or deposited on the metal surface. The second one is a membrane with incorporated plasmonic nanoparticle fillers, which ensures localized plasmon functionality (Fig. 1(c)). Finally, in the most general case, membrane may form a plasmonic metamaterial structure through combination with plasmonic material in an ordered fashion. In these metamaterials the membrane forms the dielectric part of a plasmonic crystal used for dispersion tailoring and having a desired group velocity that may be superluminal ("fast light"), subluminal ("slow light") or negative ("left-handed light") [12]. Such a plasmonic crystal may have a simple 1D form where thin sheets of metal and multifunctionalized membrane alternate, 2D form (functional surface) where a pattern of metal structures is defined on a dielectric membrane or even a full 3D structure.

Figure 2(a) shows the function of the multifunctionalized membrane as a pre-concentrator of a targeted agent. The inclusion of functional groups (shown as red "Y" forms at the interior surfaces of the pores) ensures the possibility that the membrane binds a targeted species or a range of species only. The inclusion of pores increases the effective surface for adsorption. Thus a larger quantity of the targeted species is captured within the membrane, exactly in the position of the SPP field maximum. The additional functionalization is done through inclusion of nanoparticles.

Nanoparticles are introduced throughout the membrane volume, and a proportional amount of these nanoparticles will be localized at the interior surfaces of the pores and thus exposed to external species. If these particles are plasmonic, then the freestanding membrane itself is a convenient medium for localized plasmon function. They can also be catalyst nanoparticles

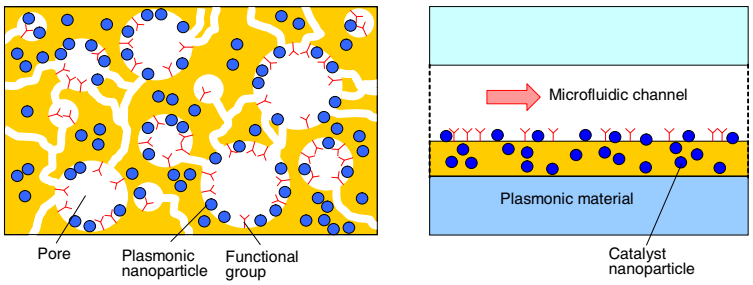

Figure 2: Schematic of membrane multifunctionalization principle (pores, functional groups and embedded nanoparticles). (a) Use as pre-concentrator for a plasmonic sensor; (b) plasmonic enhancement of photocatalytic processes in microfluidic channel of a microreactor.

(Fig. 2(b)), ensuring the applicability in photo-enhanced catalysis. Here the SPP field serves as photo-enhancer, since its intensity can be several orders of magnitude higher than that of a wave propagating in the free space. Such electromagnetic field is obviously evanescent and bound to the surface, but a microfluidic channel shape can be tailored to coincide with the SPP wave. It should be mentioned that instead of pore formation the equivalent functionality can be enabled by the use of the solution-diffusion mechanism in non-porous membranes.

3. EXPERIMENTAL

In order to obtain porosity in GMA-based membranes, we started from polyethersulfone (PES) matrix [13]. GMA was incorporated into PES polymer solution, combined with trimethylolpropane trimethacrylate (TMPTMA) crosslinker. The prepared solutions were cast on a glass plate and placed in an experimental enclosure blanketed with nitrogen gas. Photoinduced copolymerization was done by UV radiation for 10 minutes before the immersion precipitation and final solidification. The exposure doze, mainly in the UVA region, was $4.5\,\mathrm{J/cm^2}$, measured by YK-35UV radiometer.

Thus processed, the GMA-based membrane develops an asymmetric structure, with smallest pores near the top and gradually spreading to reach the largest dimensions at the bottom of the structure.

In order to obtain targeted functional groups in GMA, the epoxide groups were treated with diethylene triamine under alkaline conditions, thus opening their rings and transforming them into amine functionality. SEM analysis of the structures was performed using a JEOL JSM-6610 L instrument. Fig. 3(a) shows SEM micrographs of the bottom of the GMA-based membrane, while its cross-section is presented in Figs. 3(b)–(d). The asymmetry across the membrane thickness is clearly visible. One can also notice a fine structure of pores beyond the macroscopic level; the GMA-based functionalized membranes retain a "foamy" structure.

Our further experiments dealt with the introduction of silver nanoparticle fillers into GMA-based membranes. We started from a polished Si wafer functionalized with (3-aminopropyl) trimethoxysilane. A thin layer containing GMA, 2-hydroxyethyl methacrylate (HEMA) or polyvinylpyrrolidone (PVP), and trimethylolpropane trimethacrylate (TMPTMA) and 2% $AgNO_3$ solution in *N*-methyl pyrrolidone (NMP) was deposited over it. UV radiation was used to generate silver nanoparticles and simultaneously perform polymerization forming a GMA-containing hydrogel nanocomposite membrane. The final samples were $7\,\mu\mathrm{m}$ thick, as measured by Talystep profilometer.

Figure 4 shows the measured absorbance spectra of glycidyl methacrylate hydrogel with Ag nanoparticle fillers. UV-vis spectra were made by a Thermo Scientific Evolution 60 spectrometer, while FTIR-ATR spectra were recorded by Nicolet 6700 spectrometer equipped with a Smart ATR Diamond accessory. Fig. 4(a) shows spectra with added HEMA (top two curves) or PVP (bottom curve). Absorbance maximum is approximately at 415 nm, which corresponds to a mean diameter of spherical silver nanoparticles of about 30 nm. Fig. 4(b) shows FTIR absorbance spectra of a GMA-HEMA-TMPTMA sample in (5–16.6) μm, i.e., (2000–600) $\mathrm{cm^{-1}}$ range. The spectrum shows peaks corresponding to carbonyl groups at $1720\,\mathrm{cm^{-1}}$ and the epoxy group at $906\,\mathrm{cm^{-1}}$, which is related with GMA.

The experiments showed that GMA can be readily functionalized by three different properties of interest for plasmonics. Each of them can be separately optimized — i.e., the pore size and distribution can be tailored, epoxy groups can be functionalized toward one or more different

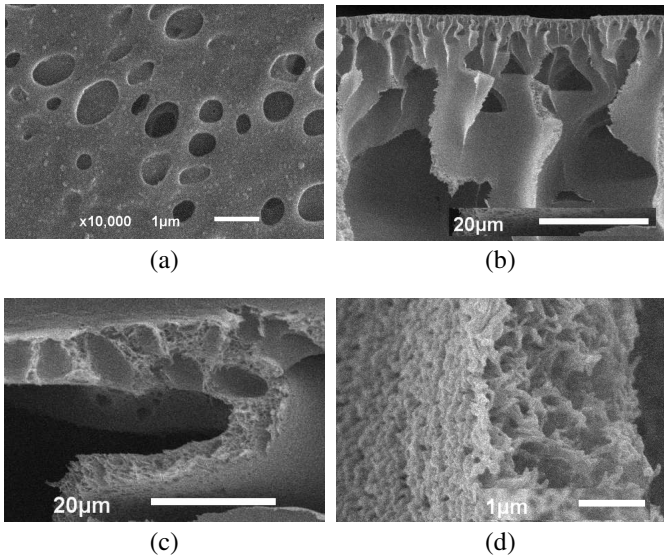

Figure 3: SEM images of precursor asymmetric PES membranes with adsorbent particles of crosslinked glycidyl methacrylate copolymer. (a) Bottom view of the membrane; (b) membrane cross-section neat the top; (c) membrane cross-section neat the bottom; (d) enlarged cross-section neat the bottom.

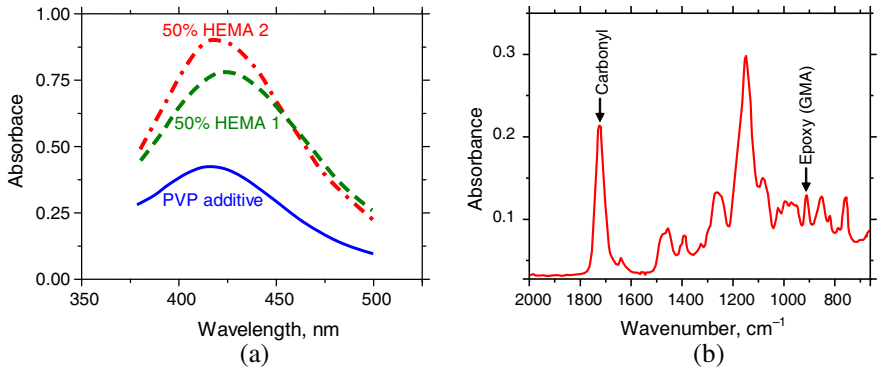

Figure 4: Absorbance spectra of glycidyl methacrylate copolymer hydrogel nanocomposite membrane incorporating silver nanoparticle fillers. (a) UV-vis absorbance; (b) IR absorbance.

analytes, and nanoparticle inclusions themselves can have different functionalities and even several different kinds of nanoparticles can be introduced simultaneously.

4. CONCLUSION

We presented a concept for multifunctionalization of membranes for the use in plasmonic sensors and plasmon-enhanced photocatalysis. The obtained platform can be implemented in the conventional SPR structures, nanoparticle-based devices and metamaterial structures based on plasmonic crystals. In our experiments we simultaneously imparted three different properties of interest to membranes based on glycidyl methacrylate: porosity giving an increase of effective surface for adsorption, target-selective functional groups and incorporated spherical plasmonic nanoparticles (silver with a 30 nm mean diameter). Our further plans include development of different functional groups to serve as pre-concentrators of targeted analytes, which includes oxides of sulfur and nitrogen and heavy metals pollutants. Multifunctionalized membranes are compatible with microelectromechanical systems (MEMS) technologies and are readily transferable across platforms by simple mechanical means. Details on the technological procedure for membrane multifunctionalization are out of the scope of this conference and will be published elsewhere.

ACKNOWLEDGMENT

This work has been partially funded by Serbian Ministry of Education, Science and Technological Development within the framework of the projects TR 32008 and III 43009.

REFERENCES

1. Barnes, W. L., A. Dereux, and T. W. Ebbesen, "Surface plasmon subwavelength optics," *Nature*, Vol. 424, No. 6950, 824–830, 2003.
2. Jiang, C., S. Markutsya, Y. Pikus, and V. V. Tsukruk, "Freely suspended nanocomposite membranes as highly sensitive sensors," *Nature Mater.*, Vol. 3, No. 10, 721–728, 2004.
3. Jakšić, Z., S. M. Vuković, J. Buha, and J. Matovic, "Nanomembrane-based plasmonics," *J. Nanophotonics*, Vol. 5, 051818.1–20, 2011.
4. Berini, P. "Long-range surface plasmon polaritons," *Adv. Opt. Photon.*, Vol. 1, 484–588, 2009.
5. Jakšić, Z. and J. Matovic, "Functionalization of artificial freestanding composite nanomembranes," *Materials*, Vol. 3, 165–200, 2010.
6. Matović, J. and Z. Jakšić, *Bionic (Nano) Membranes*; *Biomimetics — Materials, Structures and Processes. Examples, Ideas and Case Studies*, P. Gruber, D. Bruckner, C. Hellmich, H.-B. Schmiedmayer, H. Stachelberger, I. C. Gebeshuber, Eds., 9–24, Springer, Berlin, 2011.
7. Jakšić, Z., S. M. Vuković, J. Buha, and J. Matovic, "Nanomembrane-based plasmonics," *J. Nanophotonics*, Vol. 5, 051818.1–20, 2011.
8. Matović, J. and Z. Jakšić, *Nanomembrane: A New MEMS/NEMS Building Block*, in *Micro Electronic and Mechanical Systems*, K. Takahata, Ed., 61–84, In-Tech, Rijeka, 2010.
9. Kalal, J., F. Švec, and V. Maroušek, "Reactions of epoxide groups of glycidyl methacrylate copolymers," *J. Polym. Sci. Part C, Polym. Sym.*, Vol. 47, 155–166, 1974.
10. Nastasović, A., Z. Sandić, L. Suručić, D. Maksin, D. Jakovljević, and A. Onjia, "Kinetics of hexavalent chromium sorption on amino-functionalized macroporous glycidyl methacrylate copolymer," *J. Hazard. Mater.*, Vol. 171, 153–159, 2009.
11. Miletić, N., R. Rohandi, Z. Vuković, A. Nastasović, and K. Loos, "Surface modification of macroporous poly (glycidyl methacrylate-co-ethylene glycol dimethacrylate) resins for improved Candida antarctica lipase B immobilization," *React. Funct. Polymers*, Vol. 69, 68–75, 2009.
12. Milonni, P. W., *Fast Light, Slow Light and Left-handed Light*, Taylor & Francis, Abingdon, Oxford, 2004.
13. Guillen, G. R., Y. Pan, M. Li, and E. M. V. Hoek, "Preparation and characterization of membranes formed by nonsolvent induced phase separation: A review," *Ind. Eng. Chem. Res.*, Vol. 50, 3798–3817, 2011.

Automatic Tracking of Bandpass Sampling OFDM Signal in Mobile Environment

Xin Wang and Heung-Gyoon Ryu
Department of Electronic Engineering, Chungbuk National University, Cheongju 361-763, Korea

Abstract— In this paper, a combined OFDM system and bandpass sampling method using Multiple Signal Classification (MUSIC) algorithm for automatic (angle of arrival) AOA tracking is discussed. And we propose a new method that adding (time division multiplexing) TDM with bandpass sampling in the same time to avoid interference due to RF filter characteristics. Also, we consider Doppler effect for the targets' movement in mobile environment and after compensating the Doppler effect with a valid range, the system performances well. Computer simulation results show that the performances of MUSIC spectrum for AOA due to various conditions and demonstrates the accuracy of AOA estimations.

1. INTRODUCTION

Smart antenna is one of the possible solutions to increase the channel capacity due to an increase in the number of mobile units and the need for high-speed digital communication in mobile communication. Smart antenna utilizes the beamforming technique to spatially direct the electromagnetic power to an intended mobile unit while spatially null the signal power along other mobile units. The system needs the process of angle of arrival estimation to locate the mobile unites before beamforming can be performanced. Angle of arrival estimation technology play an important role in enhancing the performance of adaptive arrays for mobile wireless communications [1]. A number of angle of arrival estimation algorithms have been developed. For the most recent ones being MUSIC [2] and ESPRIT [3] algorithms, who both utilizing subspace-based on exploiting the eigen structure of the input covariance matrix and thus requires a higher computation effort. Although ESPRIT needs less computation, the MUSIC algorithm is found to be more stable and accurate [4]. In this paper, we use the MUSIC algorithm combine the OFDM bandpass sampling signal model to perform the antennas sensing to allow accurate azimuth. The accuracy of the estimation in azimuth increases proportional to the number of antenna elements utilized.

Bandpass sampling can be used for direct down conversion without analog mixers. In practice, the required sampling rate for ADC can be too high to be achieved if the Nyquist sampling theorem is to be satisfied [5]. So we use bandpass sampling which is a technique that samples high data rate signals with smaller sampling rate than Nyquist sampling rate to relax the demand for ADCs. After down-sampling about over two band signals using bandpass sampling, the signals are digitized and then two band signals can be received [6].

In this paper, we propose a bandpass sampling technique with time division multiplexing (TDM). In previous system, although over two signals can be down-sampling without interference between signals, it is possible to generate interference due to RF filter characteristics. RF filter cannot cut adjacent band signals so the remaining adjacent band signals (undesired signals) can affect desired signals. So we propose bandpass sampling with TDM that can avoid previous problems to separate over two signals timely.

2. SYSTEM MODEL

2.1. OFDM Signal and Multi-antenna Receiver

In this paper we consider two signals that have different center frequency. Transmitted signals are based on OFDM. Eq. (1) is the signals in time domain.Assume that there are two received bands. $X^A_{k,m}$ and $X^B_{k,m}$ are transmitted signals respectively. As Eq. (1), the signals is represented after IFFT in time domain.

$$x(t) = \begin{cases} \frac{1}{\sqrt{N}} \sum_{k=0}^{N-1} X^A_{k,m} e^{j(\frac{2\pi k}{N} + f_A)t}, x_A(t) \\ \frac{1}{\sqrt{N}} \sum_{k=0}^{N-1} X^B_{k,m} e^{j(\frac{2\pi k}{N} + f_B)t}, x_B(t) \end{cases} \quad (1)$$

The receiver is equipped with an uniform linear array (ULA) of M sensors located along a straight line. The system can be viewed as the multiplication of each received ray by a steering

vector considering the direction of arrival of each multipath. Assume that there are $P\,(P < M)$ uncorrelated narrowband signals $x_p(t)$ received by ULA from different direction θ_p, corrupted by AWGN, where $p = 1, 2, P$. The observation is given as

$$X(t) = \sum_{p=1}^{P} a(\theta_p) * x_p(t) + n(t) \tag{2}$$

where $a(\theta)$ is the array steering vector given by

$$a(\theta) = \begin{bmatrix} 1 & \mathrm{e}^{-j2\pi d \sin\theta/\lambda} & \dots & \mathrm{e}^{-j2\pi d \sin\theta(M-1)/\lambda} \end{bmatrix}^T \tag{3}$$

where d is the inter element spacing, λ is the signal wavelength. When we take snapshot at time $k = 1, 2, \dots, K$, we can get

$$X(k) = \sum_{p=1}^{P} a(\theta_p) * x_p(k) + n(k) \tag{4}$$

where noise $n(k)$ is assumed to be both temporally and spatially white, and uncorrelated with signal $s_p(k)$.

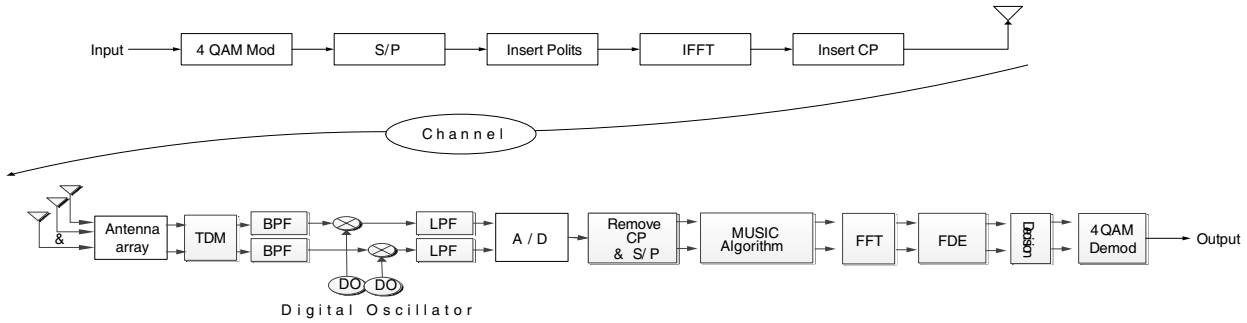

Figure 1: System mode.

2.2. Angle of Arrival Detection using MUSIC

MUSIC stands for MUltiple SIgnal Classification. The covariance matrix, R, is the collected data for each of the array receivers in the time domain. The correlation matrix is given as [7]

$$R = E\left[XX^H\right] = AR_sA^H + \sigma^2 I \tag{5}$$

where R_s is the $P \times P$ signal correlation matrix. σ^2 is the white noise power. The noise subspace E_N used in MUSIC can be obtained from eigenvalue decomposition of R, and the spatial spectrum of MUSIC is given by

$$P(\theta) = \frac{1}{a(\theta)^H E_N E_N^H a(\theta)} \tag{6}$$

3. DOPPLER EFFECT AND COMPENSATION

The orthogonally among subcarriers is often destroyed by the CFOs due to oscillator mismatches. So Doppler effect was generated and degrades performance. Doppler effects cause shifting in frequency domain and phase rotation in time domain.

Signal $x(t)$ is like (7) due to Doppler effect.

$$y_n = \sum_{k=0}^{N-1} H_k \cdot X_k \cdot e^{i2\pi \frac{k+\varepsilon}{N}} + z_n \tag{7}$$

Signal $x(t)$ is like (8) due to Doppler effect in time domain.

Channel H is represented as product of X. Doppler effect is represented phase rotation in frequency domain. k, n, ε are sub-carrier, symbol, normalized Doppler frequency respectively in (7).

$$\begin{aligned} Y_p &= \sum_{m=0}^{N-1}\sum_{k=0}^{N-1} H_{k,m}\cdot X_{k,m}\cdot e^{i2\pi\frac{(k+\varepsilon)}{N}}\cdot e^{-i2\pi\frac{m}{N}} + Z_p \\ &= H_p\cdot X_p e^{i2\pi\varepsilon p} + \sum_{\substack{m=0\\ m\neq k}}^{N-1}\sum_{k=0}^{N-1} H_{k,m}\cdot X_{k,m}\cdot e^{i2\pi\frac{(k-m)}{N}}\cdot e^{i2\pi\frac{\varepsilon}{N}} + Z_p \end{aligned} \tag{8}$$

In (8), first stage is phase rotation and second stage is ICI. Where p is symbol in frequency domain and k, m are sub-carrier before IFFT in transmitter and sample before FFT in receiver. Phase rotation of Doppler is different per symbol andICI is generated when one sub-carrier affects other sub-carriers.

Normalized offset value is divided by carrier spacing. We consider direction of receiver is heading toward to transmitter.

$$\varepsilon = \frac{f_d}{carrierspacing}, \quad f_d = \frac{v\cdot f_c}{c} \tag{9}$$

In this system, we compensate those problems with synchronization signal and block type pilot and assume that the receiver speed is constant. f_d, c, v are Doppler frequency, the velocity of light, the speed of receiver respectively.

The problem of Doppler effect is compensated with block type pilot. The phase rotation is estimated by doing interpolation between pilots, because the receiver speed is not dramatically changed.

$$Y_p = H_p\cdot X_p e^{i2\pi\varepsilon p} + Z_p \tag{10}$$

Phase rotation is estimated using received pilot signals.

$$P(i) = \sum_{i=1}^{N} mean\left\{\sum_{n=1}^{64} Block\_Pilot(i+n-1)\right\} \tag{11}$$

$$\frac{angle\{P(i)\} - angle\{P(i+1)\}}{pilot\_interval}\cdot([1:pilot\_interval-1]) \tag{12}$$

$$i = 1,\ 2,\ \ldots$$

P is average of block type pilot. Eq. (12) represents linear interpolation using P, so the symbols that have not pilots is estimated. But if there is too long pilot interval or Doppler frequency, it is difficult to compensate the effect.

4. PROPOSED BANDPASS SAMPLING METHOD

4.1. Existing Structure

Existing multi-band system with bandpass sampling finds sampling frequency that doesn't overlap signals between multi-band signals according to (7). But to select multi-band signals respectively, RF filter is used. Although RF filter has good Q value, the RF filter can't remove all adjacent signals. So the remaining adjacent signal is able to be overlap when multi-band signals are converted at low frequency band.

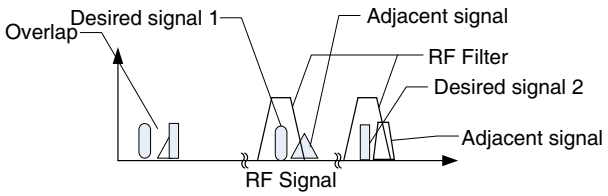

Figure 2: The problem when signals are to be sub-sampling from RF band.

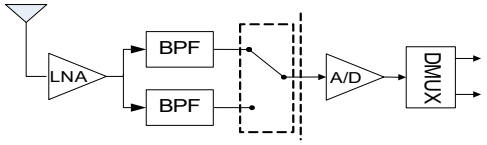

Figure 3: A multi-band receiver structure that joint bandpass sampling and TDM method.

Bandpass sampling about multi-band of over 2 bands meet condition like (13) [7]. To convert the two signals in low frequency band without interference between signals, F_{IF}, A and F_{IF}, B have to meet (13).

$$\begin{aligned} &0 < F_{IF,A} - BW_A/2, \quad F_S > F_{IF,A} - BW_A/2 \\ &0 < F_{IF,B} - BW_B/2, \quad F_S > F_{IF,B} - BW_B/2 \\ &\text{if } F_{IF,B} > F_{IF,A} \quad F_{IF,B} - BW_B/2 > F_{IF,A} + BW_A/2 \\ &\text{if } F_{IF,A} > F_{IF,B} \quad F_{IF,A} - BW_A/2 > F_{IF,B} + BW_B/2 \end{aligned} \tag{13}$$

First, the signals that are converted in low frequency band are large than 0 and smaller than $Fs/2$ respectively. Second, the low frequency part of F_{IF}, A is larger than the high frequency part of F_{IF}, B (F_{IF}, $B < F_{IF}$, A)or, the low frequency part of F_{IF}, B (F_{IF}, $A > F_{IF}$, A) is larger than the high frequency part of F_{IF}, A (F_{IF}, $B > F_{IF}$, A).

4.2. Proposed Structure

We propose a method that adds TDM method in bandpass sampling method.

The proposed structure is like Figure 4.

$$\begin{aligned} &0 < F_{IF,A} - BW_A/2, \quad F_S > F_{IF,A} - BW_A/2 \\ &0 < F_{IF,B} - BW_B/2, \quad F_S > F_{IF,B} - BW_B/2 \end{aligned} \tag{14}$$

Multi-band signals are received with antennas and the signals pass through LNA. Afterward, the multi-band signals are divided into two signals by filter. And each signal is sampled as two times faster than the existing bandpass sampling frequency. At Sampling & Holder and ADC, TDM and bandpass sampling are performed at the same time. The signals that are received with TDM has no interference between receiving singles because the signals is divided in time. Therefore, the converted signals just satisfy (14) instead of (13). So it is possible to give an low sampling frequency.

5. SIMULATION AND DISCUSSION

Table 1: Simulation parameters.

OFDM system	
The number of Subcarriers	64
Bandwidth	20 MHz
Symbol Period	4 µs
Subcarrier Spacing	312.5 kHz
CP Length	0.8 µs
Modulation	4-QAM
Channel	AWGN
Target A azimuth	10°
Target B azimuth	50°

Figure 4 indicates BER performance when Doppler effect occurs. We can see the performance according to Doppler scale. The two bands have no difference according to Doppler scale. The two bands have no difference due to TDM. In the case of Doppler effect $\varepsilon = 0.01$, for that both A band and B band without compensating,we can't communicate because of the phase rotation. And after compensating phase rotation, there is small performance degradation comparing to the theory curve because of existing ICI. And when the Doppler effect is give $\varepsilon = 0.05$, we can't communicate as we use block type pilot and do linear interpolation which is difficult to estimate fast phase rotation.

Figure 5 shows spatial spectrum of MUSIC with 4 receiver antenna arrays due to different SNRs. We can see that both target A and target B are tracked with accurate angle whose are 10° and 50°. And we can also see that more higher the SNR is, the shaper the spectrum pointing the angle performances.

Figures 6 and 7 show that MUSIC spectrum performance due to different array antenna numbers under the same SNR environment. And we can see that the more array antenna number is, the more accurately the system can separate the signals which performances as a sharper spectrum.

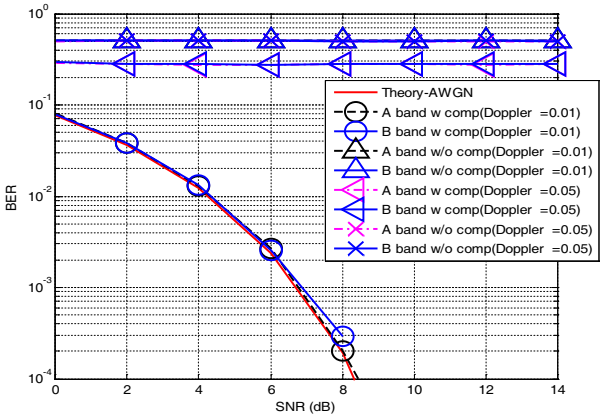

Figure 4: BER performance with Doppler.

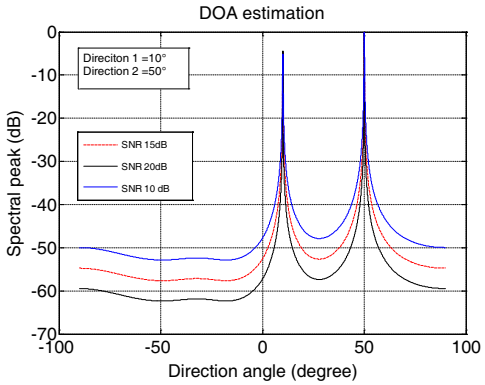

Figure 5: AOA estimation due to SNR change.

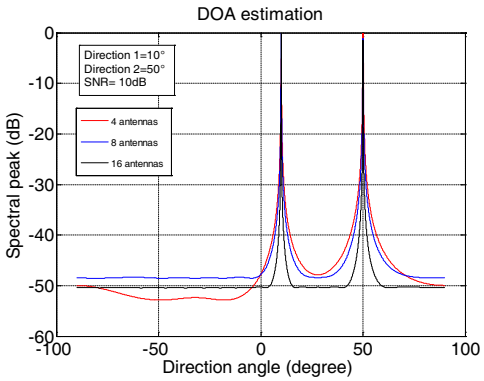

Figure 6: AOA estimation due to array antenna numbers with SNR = 10 dB.

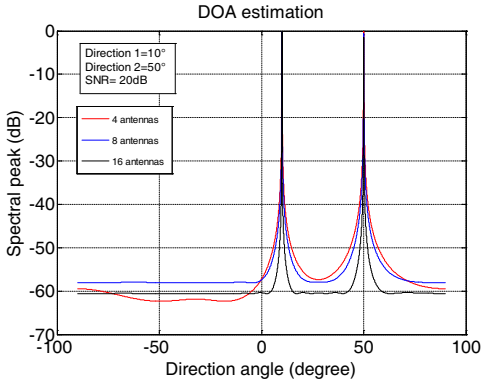

Figure 7: AOA estimation due to array antenna numbers with SNR = 20 dB.

6. CONCLUSIONS

In this paper, we discussed and performance a automatic AOA tracking method using MUSIC algorithm by bandpass sampling method. And we also proposed a adding TDM with bandpass sampling method which can avoid interference. By considering the Doppler effect and compensating the effect, system using proposed method performances well. And simulation shows using MUSIC algorithm to estimate the AOA under different conditions.

ACKNOWLEDGMENT

This research was supported by Basic Science Research Program through the National Research Foundation of Korea (NRF) funded by the Ministry of Education, Science and Technology (No. 201-2017339)

REFERENCES

1. Schmidt, R., "Multiple emitter location and signal parameter estimation," *IEEE Transactions on Antennas and Propagation*, Vol. 34, No. 3, 276–280, Mar. 1986.
2. Paulraj, A., R. Roy, and T. Kailath, "A subspace rotation approach tosignal parameter estimation," *Proceedings of the IEEE*, Vol. 74, No. 7, 1044–1046, Jul. 1986.
3. Lavate, T., V. Kokate, and A. Sapkal, "Performance analysis of MUSIC and ESPRIT DoA estimation algorithms for adaptive array smart antennain mobile communication," *International Journal of Computer Networks (IJCN)*, Vol. 2, No. 3, 152–172, Jul. 2010.
4. Walden, R. H., "Performance trends for analog-to-digital converters," *IEEE Commun. Mag.*, Vol. 37, No. 2, 96–101, Feb. 1999.
5. Akos, D. M., M. Stockmaster, J. B. Y. Tsui, and J. Caschera, "Directbandpass sampling of multiple distinct RF signals," *IEEE Trans. Commun.*, Vol. 47, No. 7, 983–988, Jul. 1999.
6. Wang, J., Y. J. Zhao, and Z. G. Wang. "A MUSIC like DOA estimation method for signals with low SNR," *GSSM 2008*, 321–324, Apr. 2008.
7. Tseng, C.-H. and S.-C. Chou, "Direct downcon version of multiband RF signals using bandpass sampling," *IEEE Trans. Commun.*, Vol. 5, No. 1, 72–76, Jan. 2006.

A Reconfigurable Miniaturized Spiral Monopole Antenna for TV White Spaces

M. Y. Abou Shahine[1], **M. Al-Husseini**[2], **Y. Nasser**[1], **K. Y. Kabalan**[1], **and A. El-Hajj**[1]

[1]American University of Beirut, Beirut 1107 2020, Lebanon
[2]Lebanese Center for Studies and Research, Beirut 2030 8303, Lebanon

Abstract— This paper presents a novel design of a reconfigurable miniaturized planar spiral monopole antenna suitable for TVWS applications. The proposed antenna is designed on a FR4 epoxy substrate fed by a microstrip line over a partial ground plane. This antenna, designed for the high frequency of the UHF band (600–800 MHz), operates with 1 dB transmission gain. By inserting a tunable inductor on the spiral monople and modifying its inductance, frequency reconfigurability is attained, and the antenna can operate at different bands in the 600–800 MHz range. These bands range between 15 to 20 MHz which is suitable for TVWS applications.

1. INTRODUCTION

TV white spaces (TVWS) refer to the unused portions of the spectrum in the TV band, freed up by the transition from analogue to digital TV broadcasting, which can be used for new services and applications [1]. TVWS have very interesting benefits where radio signals in the 470–790 MHz spectral bandwidth, have a very long range. This implies a lower cost for networks deployment since fewer base stations are needed to provide the same coverage with excellent building penetration properties. Another benefit in this un-used frequency range resides in its spectrum organization: huge, free, unlicensed and globally harmonized [2]. In 2008, the Federal Communications Commission FCC has adopted rules to allow unlicensed use of TV white space. This leads to important innovation in the UHF band and provides long distance broadband access to rural areas with limited coverage [3].

Due to the increasing interest in the TVWS applications, several antennas have been recently designed to operate in the UHF band, including ones with broadband operation, i.e., designed to operate in the entire UHF band [4–7], and other designs with narrowband but reconfigurable operation [8–10]. The compact broadband monopole slot antenna reported in [4] exhibits a wide bandwidth (460–1000 MHz) to be used in digital TV applications by using a feed-in space and a straight gap. A pair of slot lines is adopted in order to minimize the antenna size, and this can accomplish good impedance matching at the UHF band. In [5], a broadband miniaturized antenna providing a wide operating bandwidth for Digital TV (DTV) signal reception in the UHF band in mobile handheld devices is designed using eight quarter-wavelength slots with a compact size. The asymmetric fork-like monopole antenna for digital video broadcasting-terrestrial (DVB-T) signal reception for application in the UHF band is presented in [6]. The proposed antenna consists of two two-branch strip monopoles on a rectangular ground plane with a concave which results in a wide bandwidth of 461 MHz (451–912 MHz). In [7], an internal antenna for Digital Video Broadcasting-Handheld (DVB-H) service is designed having a size suitable for a mobile handset and having enough bandwidth to cover the whole DVB-H (470 MHz–702 MHz) band. However, and to reduce bandwidth, researchers moved to design reconfigurable narrowband inverted F-Antennas to operate in the whole UHF band. This meander antenna dedicated to the mobile TV in [8] uses PIN diodes inserted in different points of the radiating element to dynamically cover the frequency UHF band. In [9], a compact low cost inverted F antenna dedicated to the DVB-H (470–862 MHz) is designed. This antenna is suitable to small mobile devices and the operating frequency is tuned with a varactor diode component. A frequency-tunable Inverted F-Antenna (IFA) for DVB-H suitable for small mobile devices is reported in [10]. The operating frequency of the antenna is tuned with a varactor component which loads the IFA element and thus enables it to resonate at different frequencies. This kind of tunable narrowband antenna is suitable for DVB-H reception, since one channel in a bandwidth of 8 MHz is received at a time.

In this paper, a miniaturized planar spiral monopole antenna is introduced to attain frequency reconfigurability in the UHF band. The designed antenna operates in the higher part of the UHF band (600–800 MHz) and is suitable for TVWS applications. In this antenna, frequency reconfigurability is obtained by inserting a tunable inductor on the spiral monople. The geometry and

the design guidelines of the proposed antenna structures are presented in Section 2. Experimental results are presented in Section 3. In Section 4 a brief conclusion is given.

2. ANTENNA STRUCTURE AND DESIGN

The configuration of the proposed antenna is shown in Fig. 1. It is based on the design presented in [11]. A square spiral monopole antenna is designed on a 105 mm × 40 mm FR4 epoxy substrate of thickness $h = 0.8$ mm and fed by a 2vmm width microstrip line over a partial ground plane. The size of the spiral structure is 50 mm × 30 mm with a width of 1 mm and a gap of 5 mm between the spirals as shown in Fig. 1.

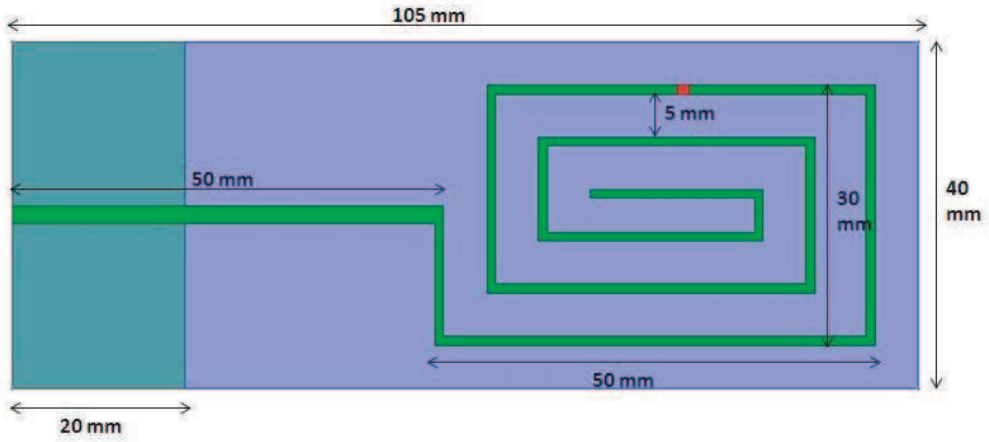

Figure 1: Configuration and dimensions of the proposed antenna.

The spiral wire is used as a radiating element of the monopole antenna to minimize the size of antenna. As a miniaturized radiating element, the meander line is widely employed. However, the radiation power is reduced since the direction of the current on the meander line is opposite for neighboring wire, therefore the antenna gain will be very low. In our design, the current in the spiral structure is in the same direction for neighboring wire, thus the radiation efficiency is enhanced and the gain is improved [11].

Frequency reconfigurability is obtained by inserting a tunable inductor (Chip Inductor-0603CT) on the spiral monople as shown in Fig. 1 (red color) and modifying its inductance. This idea of reconfigurability was used in [12]. The size of the tunable inductor is compatible with the size of the spiral and its inductance ranges between 1 and 56 nH. The antenna is designed and simulated using Ansoft HFSS.

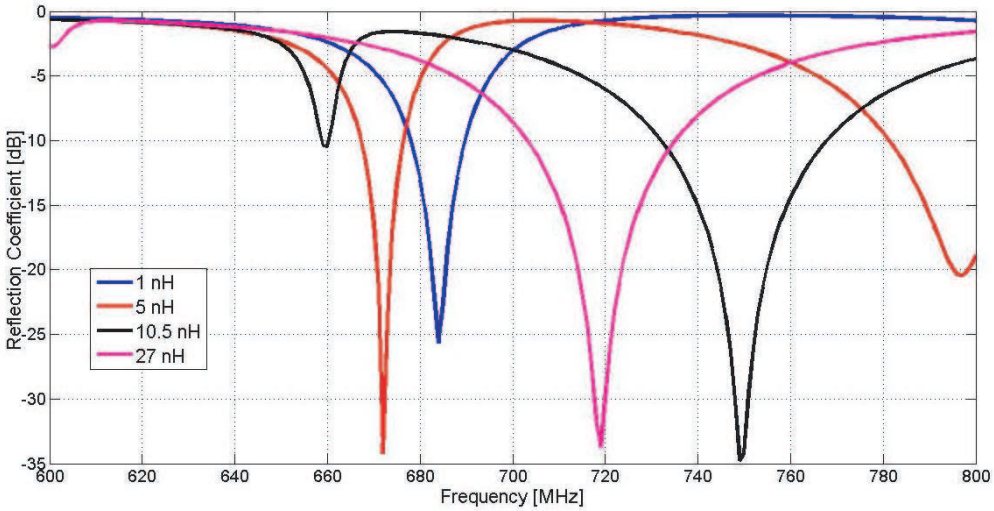

Figure 2: Reflection coefficient of the antenna for different inductance values.

3. RESULTS AND DISCUSSION

The simulated reflection coefficient plots of the reconfigurable antenna are given in Fig. 2 for the indicated inductance values. It is clear that frequency reconfigurability has been achieved. Considering four different values for the inductor, i.e., $L = 1$, 5, 10.5 and, 27 nH, frequency reconfigurability is attained in the higher part of the UHF band (600–800 MHz) and the antenna can operate at different bands in this 600–800 MHz range. These bands range between 15 to 20 MHz which is suitable for TVWS applications.

The gain of the proposed antenna is given in Fig. 3. It is about 1 dB: a good gain given the small size of this antenna. The radiation patterns of this antenna are omni-directional over its bands of operation, as shown in Fig. 4, with almost equal radiation in the H-plane, and radiation with the shape of digit 8 in the E-plane.

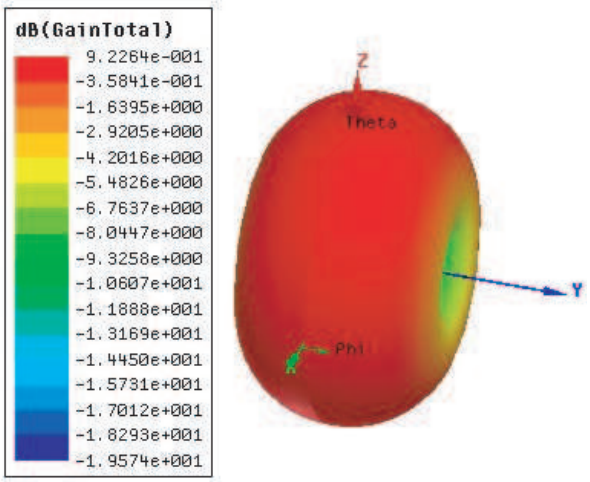

Figure 3: Simulated gain of the proposed antenna.

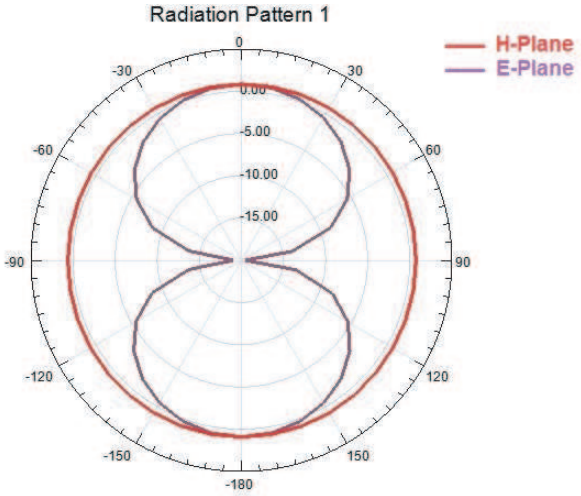

Figure 4: Simulated radiation patterns of the proposed antenna.

4. CONCLUSION

A reconfigurable miniaturized planar spiral monopole antenna suitable for TVWS applications is proposed in this paper. Frequency reconfigurability is attained through inserting a tunable inductor on the spiral monople and changing its inductance. This antenna can operate at different bands which range between 15 to 20 MHz, in the 600–800 MHz band, with omni-directional patterns and an acceptable gain of 1 dB given the small size of the antenna. This bandwidth, the small and the compact size of this antenna, and the frequency reconfigurability make this antenna a practical one that can be used for TVWS applications.

ACKNOWLEDGMENT

The authors would like to thank the Lebanese National Council for Scientific Research for supporting this research work.

REFERENCES

1. Nekovee, M., "A survey of cognitive radio access to TV white spaces," *International Journal of Digital Multimedia Broadcasting*, Vol. 2010, Article ID 236568, 11 pages, April 2010.
2. Dicks, D., "TV white spaces: A spectrum opportunity starts to open up," *Innovation Observatory*, August 12, 2011.
3. Fitch, M., M. Nekovee, S. Kawade, K. Briggs, and R. Mackenzie, "Wireless service provision in TV white space with cognitive radio technology: A telecom operator's perspective and experience," *IEEE Communication Magazine*, Vol. 49, No. 3, 64–73, 2011.
4. Tsai, C.-Y. and O. T.-C. Chen, "Compact broadband monopole slot antenna for digital TV applications," *IEEE Asia-Pacific Conference on Antennas and Propagation (APCAP)*, 61–62, Singapore, August 27–29, 2012.

5. Chou, J.-H., H.-J. Li, D.-B. Lin, and W.-C. Shih, "Miniaturized DTV broadband slot antenna for handheld devices," *IEEE AP-S International Symposium on Antennas and Propagation 2012*, 1–2, Chicago, July 8–14, 2012.
6. Huang, C.-Y., B.-M. Jeng, and C.-F. Yang, "Wideband monopole antenna for DVB-T applications," *Electronic Letters*, Vol. 44, No. 25, 1448–1450, 2008.
7. Yu, Y., U. Kim, Y. Jang, and J. Choi, "Design of an internal antenna for DVB-H mobile application," *IEEE Asia Pacific Microwave Conference (APMC)*, 1–4, Macau, December 16–20, 2008.
8. Canneva, F., J. Ribero, and R. Staraj, "Reconfigurable meander antenna for DVB-H band," *2010 Interantional Workshop on Antenna Technology (iWAT)*, 1–4, Lisbon, March 1–3, 2010.
9. Huitema, L., T. Reveyrand, E. Arnaud, C. Decroze, and T. Monediere, "A compact and reconfigurable DVB-H antenna for mobile handheld devices," *Proceedings of the 5th European Conference on Antennas and Propagation (EUCAP)*, 1314–1317, Rome, April 11–15, 2011.
10. Berg, M., M. Komulainen, V. Palukuru, H. Jantunen, and E. Salonen, "Frequency-tunable DVB-H antenna for mobile terminals," *IEEE AP-S International Symposium on Antennas and Propagation 2007*, 1072–1075, Honolulu, June 9–15, 2007.
11. Lee, H.-K., T.-K. Lee, W.-H. Jang, and J.-W. Lee, "Miniaturization of planar spiral monopole antennas with parasitic elements for terrestrial DMB applications," *Proceedings of International Society for Asphalt Pavements (ISAP) 2005*, 573–576, Seoul, 2005.
12. Abdulhadi, A. E. and R. Abhari, "Tunable compact printed monopole antenna for passive UHF RFID tags," *IEEE AP-S International Symposium on Antennas and Propagation 2012*, 1–2, Chicago, July 8–14, 2012.

Dual Polarized High Front-to-back Ratio Microstrip Slot Antenna

Mohamed S. El-Gendy, **Haythem H. Abdullah**, **and Esmat A. Abdallah**
Electronics Research Institute, Dokki, Giza, Egypt

Abstract— A novel dual-band dual-polarized microstrip slot antenna used in mobile base stations is proposed. The antenna supports the operating bands of GSM900 (0.88–0.96) GHz, DCS1800 (1.71–1.88) GHz, PCS1900 (1.85–1.99) GHz, and UMTS2100 (1.92–2.17) GHz. The antenna is fabricated using low cost FR4 dielectric substrates. The antenna is based on two orthogonal rectangle slots centered by a square slot etched on the ground plane and incorporates two orthogonal microstrip feeding lines placed underneath the FR4 substrate on the opposite side of the ground plane to achieve dual polarization. The simulated isolation between the two ports is better than −45 dB overall the operating bands. The measured isolation for the proposed antenna between the two ports does not exceed −30 dB within the operating bands. The average front-to-back ratio is 17.15 dB at GSM900, 29.12 dB at DCS1800, 18.47 dB at PCS1900 and 16.03 dB at UMTS2100. Average antenna gains about 7.7 dBi and 6.6 dBi have been obtained for the lower and the upper bands, respectively. The design is dedicated to the single antenna array element that could be incorporated in an array in order to construct the base station antenna.

1. INTRODUCTION

The rapid development of mobile communication systems needs broadband and low cost antennas for base stations. The second generation (2G) for mobile systems, such as GSM1800 and GSM1900, requires frequency bands 1710–1880 MHz and 1850–1990 MHz. The third generation (3G) for mobile systems, such as CDMA-2000, WCDMA, and TD-SCDMA, requires frequency band 1920–2170 MHz. Therefore, a bandwidth of 23.71% (i.e., 1.71–2.17 GHz) is required for 2G/3G base station antennas in order to overcome the capacity problems in the conventional base station (i.e., GSM900).

In recent years, a lot of broadband antennas have been developed for base stations [1]. The commonly used antennas for base stations include adjacent patch antennas/radiators operated at different frequencies [2], aperture stacked patchs antenna (ASPs) [3] Quasi Yagi-Uda printed antennas [4], reactive loading [5] and others have been reported in the last few years to obtain much larger bandwidth or dual band behavior.

Several designs which support dual-band dual-polarized operations have been reported for application in mobile communication systems. The element design in [6] based on reactive loading technique [5]. The antenna is a dual-band dual polarized patch antenna with double-sided notch. It covers two operating bands, the lower band that support GSM900 and the upper band that support DCS1800, PCS1900 and UMTS2100. The antenna provides two orthogonal linear polarizations with isolation of 30 dB between the ports for each of these bands. The antenna dimension is about $290 \times 220 \times 21.8\,\text{mm}^3$. The peak gain of this antenna is about 11.8 dBi and 7 dBi for lower and upper bands, respectively. The main defect of this antenna is its relatively high back radiation that is observed at the upper band.

In this paper, a dual-band dual-polarized microstrip slot antenna for mobile base stations is proposed in order to operate in both 2G and 3G frequency bands of mobile phone communications. The two orthogonal slot antennas are used for transmitting and receiving operations. The simulated isolation between the two ports is better than −45 dB overall operating bands. The measured isolation characteristic does not exceed −30 dB. The average front-to-back ratio is 17.15 dB at GSM900, 29.12 dB at DCS1800, 18.47 dB at PCS1900 and 16.03 dB at UMTS2100. The proposed antenna has a low cost due to the use of FR4 substrate layers. Another advantage of the proposed antenna is the use of only two orthogonal ports for transmitting and receiving (dual polarization feed) at all the operating frequency bands (GSM900/DCS1800/PCS1900/UMTS2100). The paper is organized as follows; Section 2 introduces the antenna design while Section 3 presents the simulated and measured results. Conclusion is given in Section 4.

2. ANTENNA DESIGN AND CONFIGURATION

The geometry of the proposed microstrip slot antenna with detailed components and design parameters is shown in Figure 1. The proposed antenna is composed of multi layers of FR4 and air/foam substrates. The main reason for using FR4 material is for reducing the overall cost of the antenna

fabrication and to make it more rigid in construction. The overall antenna dimensions are about $300 \times 300 \times 73.175\,\text{mm}^3$. The dimensions of the ground plane with the rectangular and square cross are $140 \times 140\,\text{mm}^2$. Three layers of FR4 dielectric material with dielectric constant of $\varepsilon_r = 4.5$ with loss tangent equals 0.025 and substrate height of 1.5 mm and two air/foam layers ($\varepsilon_r = 1$). The two foam layers are placed one between the transmitting feed layer and the FR4 dielectric substrate layer of the first reflector and the second foam layer is placed between the first reflector and the second reflector. Four foam spacers at the edges are used in order to fix the five layers of the antenna. The dual polarized operation is achieved, utilizing two orthogonal rectangular slots with square slot etched on the ground plane. The excitation of the slot radiator is done via a two orthogonal U-shaped microstrip feed lines. One feeding network is placed in a separate substrate beneath the slot antenna substrate while the other one is placed above it. The feeding network is matched to $50\,\Omega$ impedance. The excitation of the two orthogonal slots is done symmetrically. It is worth noting that no air bridges are needed for the two feed networks since they are placed on

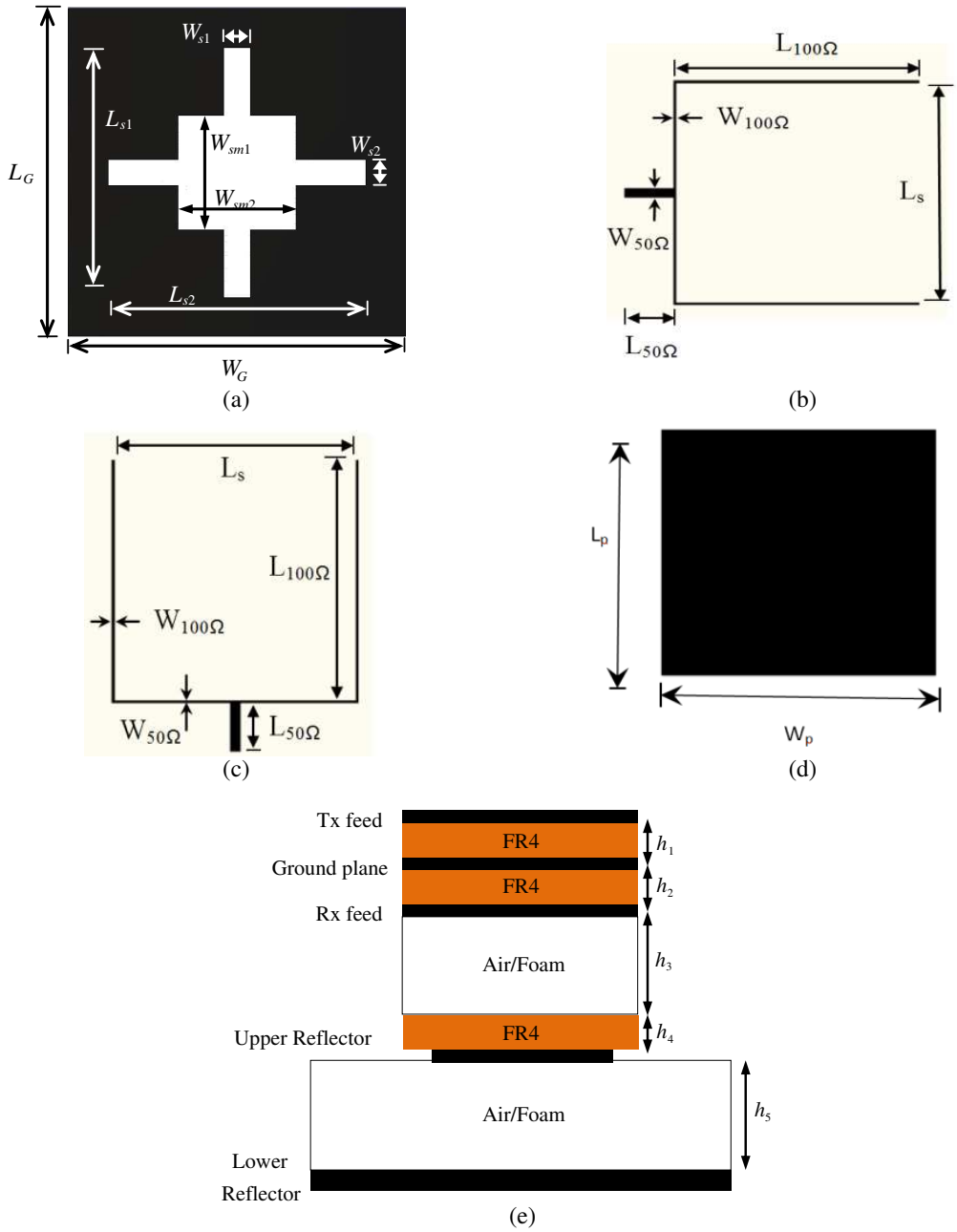

Figure 1: Antenna layers and its side view. (a) Slotted ground plane, (b) Tx feeding layer, (c) Rx feeding layer, (d) first reflector, (e) side view.

different substrates. The choice of the step rectangular shape slot is to match the required bands used in mobile base station. The ordinary rectangular slot etched on the ground plane doesn't give the performance of the dual band operation used in mobile communication. A high front-to-back ratio is obtained at both operating bands utilizing two reflectors underneath the radiating slot. The length of the first square reflector is 0.3 of the wavelength at the lower frequency band 915 MHz, and is placed at quarter wavelength of the upper frequency bands apart from the radiating slot at 1940 MHz, which acts at the same time as a radiator at the lower band (915 MHz). The second square reflector is placed at quarter wavelength of the frequency band apart from the radiating slot at 915 MHz.

The antenna dimensions shown in Figure 1 are: $W_{50\,\Omega} = 2.82\,\text{mm}$, $W_{100\,\Omega} = 0.64\,\text{mm}$, $L_{S1} = L_{S2} = 107\,\text{mm}$, $W_{S1} = W_{S2} = 11\,\text{mm}$, $L_G = W_G = 140\,\text{mm}$, $W_{Sw1} = W_{Sw2} = 49\,\text{mm}$, $L_s = 75.54\,\text{mm}$, $L_{5\,\Omega} = 14.36\,\text{mm}$ $W_{50\,\Omega} = 2.82\,\text{mm}$, $L_p = W_p = 99\,\text{mm}$, $h_1 = h_2 = h_4 = 1.5\,\text{mm}$, $\varepsilon_{r1} = \varepsilon_{r2} = \varepsilon_{r4} = 4.5$, $h_3 = 35\,\text{mm}$, $h_5 = 32\,\text{mm}$, $\varepsilon_{r3} = \varepsilon_{r5} = 1$.

3. RESULTS AND DISCUSSIONS

A single element antenna with optimized dimensions has been simulated using CST STUDIO SUITE ver. 2011. Figure 2 depicts the simulated return loss and isolation between ports of the transmitting and the receiving sides. The simulated results are compared to the measured ones where good agreement is observed.

As shown in Figure 2, the simulated results of the proposed antenna cover the, GSM 900, DCS 1800, PCS 1900, and UMTS 2100 bands at both ports. The antenna is measured using vector network analyzer Agilent: 8719ES. The measured results in Figure 2 show a $-10\,\text{dB}$ impedance bandwidth 122.4 MHz at the lower band while it shows 550 MHz at the upper bands. The measured isolation between the two ports is better than $-30\,\text{dB}$ at lower band (GSM900) and the upper bands (DCS1800, PCS1900 and the UMTS2100). The Front-to-back ratio (FBR) is an important parameter for the antennas used in mobile base stations. The FBR at the lower band (GSM900) is about 17.15 dB. The simulated radiation pattern shown in Figure 3 depicts that HPBW is 60.8° and 74.1° for the horizontal and vertical planes, respectively at the lower frequency and it is 50° and 127° for the horizontal and vertical planes, respectively at the upper frequency.

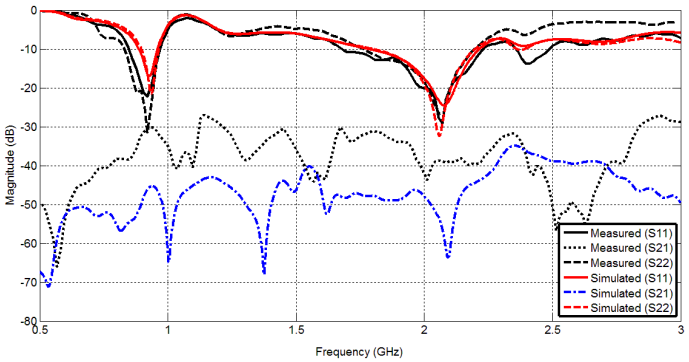

Figure 2: Measured and simulated results of return loss and insertion loss for the two ports.

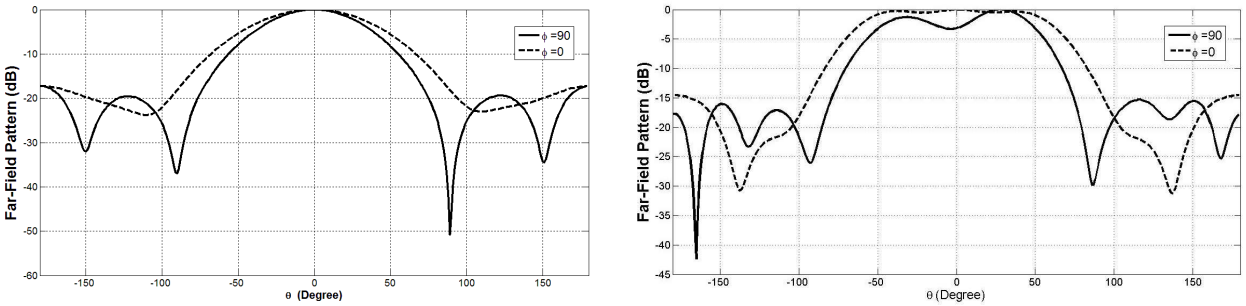

Figure 3: Simulated radiation pattern at: (a) 915 MHz, (b) 1940 MHz.

4. CONCLUSIONS

A dual-band dual-polarized microstrip slot radiating antenna with optimized parameters has been simulated using CST STUDIO SUITE ver. 2011 and fabricated using photolithographic process. The proposed antenna has a low cost due to the use of only three FR4 substrate layers. The antenna is suitable for the transmission and reception in the assigned bands of the (GSM900/DCS1800/PCS1900/UMTS2100) applications. The simulated bandwidth and isolation between the two ports are compared to the measured results where good agreement is observed. The measured isolation between ports does not exceed -30 dB at both the lower and the upper bands. The average FBR is 17.15 dB at GSM900, 29.12 dB at DCS1800, 18.47 dB at PCS1900 and 16.03 dB at UMTS2100. The overall antenna dimensions are about $300 \times 300 \times 73.175\,\text{mm}^3$ which suits the mobile base station application.

ACKNOWLEDGMENT

This work is done under the contract between the National Telecom Regulatory Authority (NTRA), Ministry of Communications and Information Technology (MCIT), Egypt and the Electronics Research Institute (ERI), Ministry of Scientific Research, Egypt.

REFERENCES

1. Fujimoto, K., *Antennas for Base Stations in Mobile Antenna Systems Handbook*, 3rd Edition, 141–211, Artech House, Inc., Boston, 2008.
2. Amiri, N. and K. Forooraghi, "Dual-band and dual-polarized microstrip array antenna for GSM900/DCS1800 MHz base stations," *IEEE International Symposium on Antennas and Propagation Society*, 4439–4442, 2006.
3. Targonski, S. D., R. B. Waterhouse, and D. M. Pozar, "Design of wideband aperture-stacked patch microstrip antennas," *IEEE Trans. Antennas Propag.*, Vol. 46, No. 9, 1245–1251, Sep. 1998.
4. Kaneda, N., W. R. Deal, Y. Qian, R. Waterhouse, and T. Itoh, "A broadband planar quasiyagi antenna," *IEEE Trans. Antennas Propag.*, Vol. 50, 1158–1160, Aug. 2002.
5. Nakano, H. and K. Vichien, "Dual-frequency square patch antenna with a rectangular notch," *Electron. Lett.*, Vol. 25, No. 16, 106–1068, 1989.
6. Moradi, K. and S. Nikmehr, "A dual-band dual-polarized microstrip array antenna for base stations," *Progress In Electromagnetics Research*, Vol. 123, 527–541, 2012.

A Proximity-fed Elliptical-shaped Aperture UWB Antenna with Triple Band-rejection Property

Mohamed Mamdouh M. Ali[1], **Ayman Ayd R. Saad**[2], **and Elsayed Esam M. Khaled**[1]

[1]Electrical Engineering Department, Assiut University, Assiut, Egypt
[2]Kosseir Radio, Telecom Egypt, Kosseir 84712, Egypt

Abstract— In this paper, an elliptical-shaped aperture UWB antenna with triple frequency band-rejection characteristics is proposed. The antenna has a compact volume of $22.5 \times 24 \times 1.5\,\text{mm}^3$. Matching between a sector-disk shaped radiating patch and the 50 Ohm microstrip line is manipulated through a proximity-feed technique. Double shunt stubs are used to enhance the impedance bandwidth of the antenna. The band notches at WiMAX of 3.3–3.9 GHz, lower WLAN of 5.15–5.35 GHz and upper WLAN of 5.725–5.825 GHz are realized by embedding three resonating elements; a reversed F-shaped slot etched in the patch, a reversed U-shaped slot etched in the feed line, and a parasitic flipped C-shaped strip around the patch, respectively. The antenna is fabricated and an electrical equivalent lumped-circuit is obtained. The experimental data show good agreement with the simulation results along with the equivalent circuit results which obtained using Vector Fitting (VF) technique. The antenna provides almost omnidirectional patterns, relatively flat gain and high radiation efficiency over the entire UWB frequency band excluding the rejected ones.

1. INTRODUCTION

The ultra-wideband (UWB) communications have drawn much attention since the U.S. Federal Communication Commission authorized, in 2002, the unlicensed use of the UWB with a frequency range of 3.1–10.6 GHz for commercial purposes [1]. The UWB antenna has been rapidly developed as one of the essential components in UWB communication systems. However, the existences of other wireless narrowband standards that already occupy frequencies in the UWB band, such as WLAN (5.15–5.35 GHz, 5.725–5.825 GHz) and WiMAX (3.3–3.9 GHz), require rejection of these frequencies from the UWB antenna response. Various solutions have been studied in literature to generate single, dual or more frequency band notches, based on embedding resonators into the main body of the UWB antenna [2–7].

In this paper, a proximity-fed UWB elliptical-shaped aperture antenna with triple band-notched characteristics is proposed. The proposed antenna achieves a measured bandwidth ranging from 3.2 to 11.6 GHz. Triple band notches are obtained by embedding a reversed F-shaped slot into the radiating patch, a reversed U-shaped slot into the feeding line as well as adding a parasitic flipped C-shaped strip around the patch. These three structures are corresponding to the WiMAX (3.20–4.19 GHz), the lower WLAN (5.02–5.32 GHz) and the upper WLAN (5.51–6.10 GHz) frequency bands, respectively. An electrical lumped elements equivalent circuit of the proposed antenna is illustrated. Also the antenna is fabricated. Details of the antenna design with simulation results and experimental data are presented and discussed.

2. ANTENNA DESIGN

Based on several parametric studies, the geometry of the proposed triple band-notched UWB antenna is illustrated in Fig. 1. The prototype antenna is fabricated on a $22.5\,(L) \times 24\,(W)\,\text{mm}^2$ FR4 substrate with relative permittivity 4.7, a loss tangent $\tan\delta = 0.025$, and a thickness $h = 1.5\,\text{mm}$. A sector-disk shaped radiating patch of radius $R_p = 5.0\,\text{mm}$ is placed non-concentrically inside a ground plane aperture (GPA) represented by an elliptical slot of $r_x = 11\,\text{mm}$ and $r_y = 9.9\,\text{mm}$ etched off the ground plane. The center of the elliptical GPA is on the same vertical symmetric line of the substrate. The distance between the lower edge of the patch and the lower edge of the elliptical slot is 1.9 mm. The patch is excited using a $50\,\Omega$ proximity-feed microstrip line placed on the other side of the substrate with width $W_f = 2.76\,\text{mm}$ and length, $L_f = 9.6\,\text{mm}$. The microstrip line is put symmetrically with the vertical symmetric line of the substrate and started with the lower edge of the ground plane. To improve the impedance matching, double stubs are connected in shunt to the feed line with uniform width 0.3 mm and lengths $L_{S1} = 2.62\,\text{mm}$ and $L_{S2} = 3.62\,\text{mm}$ at distances $P_{S1} = 7\,\text{mm}$ and $P_{S2} = 3.2\,\text{mm}$ from the end of the line as shown in Fig. 1.

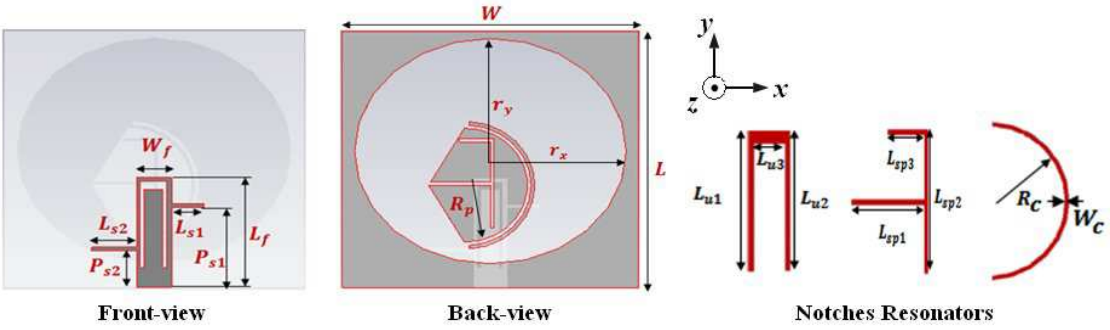

Figure 1: Geometric description of the proposed antenna and the notches resonators.

To create triple notched bands separately, three different resonators are added to the prototype antenna design as shown in Fig. 1. For the WiMAX frequency notch, a reversed F-shaped slot is etched off the radiating patch with uniform width 0.3 mm and lengths $L_{sp1} = 5$ mm, $L_{sp2} = 7.8$ mm, and $L_{sp3} = 2.5$ mm, which is corresponds to a quarter wavelength resonator. To generate a notched band for the lower WLAN band, a reversed U-shaped slot etched off the feed line with width 0.3 mm for the lengths $L_{u1} = L_{u2} = 7.55$ mm and width 0.7 mm for the length $L_{u3} = 1.5$ mm, which is corresponds to a half wavelength resonator. Allocating a parasitic flipped C-shaped strip around the patch with radius $R_c = 5.3$ mm, thickness $W_c = 0.3$ mm, and a uniform separation of 0.3 mm between the patch and the parasitic strip provides a band notch corresponding to the upper WLAN band. This specified parasitic strip corresponds to a half wavelength resonator. The dimensions of these resonators are optimized using parametric analysis. The band notches characteristics of the proposed antenna can be controlled by properly adjusting the parameters of these resonant elements.

3. RESULTS AND DISCUSSION

3.1. Antenna Equivalent Circuit Modeling

In order to consider the effect of integrating the proposed antenna in the communication system with the whole system simulation, the equivalent circuit of the proposed antenna is obtained based on the VF technique. The method is described as follows: First, the response of the input admittance of the proposed antenna obtained by simulation is calculated in the frequency range of interest. Second, the simulated response of the input admittance is fitted by means of the VF technique to obtain the rational function. Finally, the rational function is converted into a SPICE-compatible lumped-element equivalent circuit and the synthesized components values are obtained.

The rational approximation of a certain frequency domain response can be expressed as [8]:

$$F(s) = \sum_{k=1}^{N} \frac{res_k}{s - p_k} + d + se \tag{1}$$

where res_k and p_k denote the kth residues and poles, respectively, which are either real quantities or complex conjugate pairs of N identical set of poles (order of approximation), $s = j\omega$ represents the complex frequency, d is a real constant term and e is a real proportional term. The terms d and e are optional.

The details of this procedure to obtain the equivalent circuit of UWB antenna can be found in [3, 4]. Here $F(s)$ is applied to the simulated admittance-type function, $Y(s)$, for the proposed antenna. The set of the initial poles is found to be 12 complex pairs ($N = 24$) linearly spaced over the frequency range of interest (2 to 12 GHz) with 3 iterations to refine the fitting to a very accurate approximation. The fitting procedure provides 12 complex conjugate pairs. Table 1 shows the component values for the equivalent circuit of the proposed antenna corresponding to the rational approximation. Consequently, the equivalent circuit model for the input admittance of the proposed antenna for $N = 24$ and $d = e = 0$ is synthesized as shown in Fig. 2.

A major limitation of this equivalent circuit is the presence of negative resistors which makes the circuit non-physical. However, VF technique guaranteed the enforcement of passivity for admittance function approximated by rational functions [9], as the whole equivalent circuit will always consumes power, whatever we connect to it.

Table 1: Equivalent circuit Parameters of the proposed antenna for $N = 24$ and $d = e = 0$.

Type and No. of poles	$\boldsymbol{L}$ (H)	$\boldsymbol{R}$ (Ω)	$\boldsymbol{C}$ (F)	$\boldsymbol{R'}$ (Ω)
Complex 1	4.76E–10	13.69236	2.16E–13	−712.187
Complex 2	7.06E–08	6934.243	1.01E–15	−10254.2
Complex 3	2.86E–08	679.4053	7.68E–15	−7384.15
Complex 4	5.12E–09	137.4618	5.06E–14	−1173.44
Complex 5	7.27E–09	−293.328	2.89E–14	739.3407
Complex 6	5.05E–08	645.2759	8.95E–15	−9626.1
Complex 7	6.33E–09	−208.199	4.96E–14	443.1597
Complex 8	1.48E–08	95.31957	1.92E–13	−1068.03
Complex 9	−4.57E–08	1149.346	−1.87E–14	−1975.03
Complex 10	5.45E–09	62.94981	2.47E–13	−2706.91
Complex 11	−2.05E–06	6009431	−5.68E–20	−6010377
Complex 12	3.82E–08	−769.349	1.77E–14	2743.409

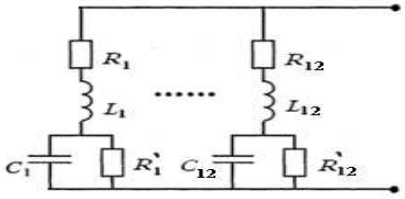

Figure 2: Equivalent circuit of the proposed antenna.

3.2. Antenna Performance

The performance of the proposed antenna has been analyzed and optimized using full-wave electromagnetic simulator CST Microwave Studio. The antenna is fabricated and the photograph of the implemented antenna with the notched structures is shown in Fig. 3(a). The antenna performance was measured by Agilent HP8719ES vector network analyzer. The measured and simulated VSWR of the proposed triple band notches antenna along with the equivalent circuit results are shown in Fig. 3(b). It can be observed that the calculated results agree very well with the measured data. The designed antenna has a measured bandwidth covering the entire UWB frequency band from 3.2 to 11.6 GHz for VSWR ≤ 2, with triple notched bands at 3.20–4.19, 5.02–5.32, and 5.51–6.10 GHz for VSWR > 2. As compared with the reported antennas in literature [6, 7], the proposed antenna provides good performance in a similar working frequency band including the specified notched bands but with less complexity and smaller size.

The radiation patterns of the fabricated antenna were measured using compact multi probe antenna test station model STARLAB-18, STAR-007-A-0019, equipped with VNA model Agilent

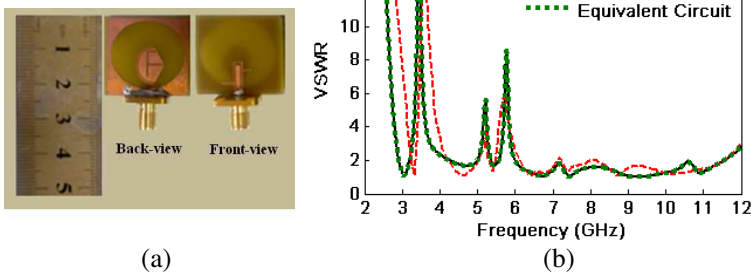

(a) (b)

Figure 3: (a) Photograph of the fabricated antenna. (b) VSWR characteristics of the proposed antenna.

PNA E8363B. The measured and simulated far-field radiation patterns of E_θ and E_φ in two principle planes, yz and xz planes of the antenna at frequencies of 3.1, and 7 GHz are illustrated in Fig. 4. The figure demonstrates that the prototype antenna is characterized by omnidirectional patterns in the yz plane (E-plane), while it is a quasi-omnidirectional pattern in the xz plane (H-plane).

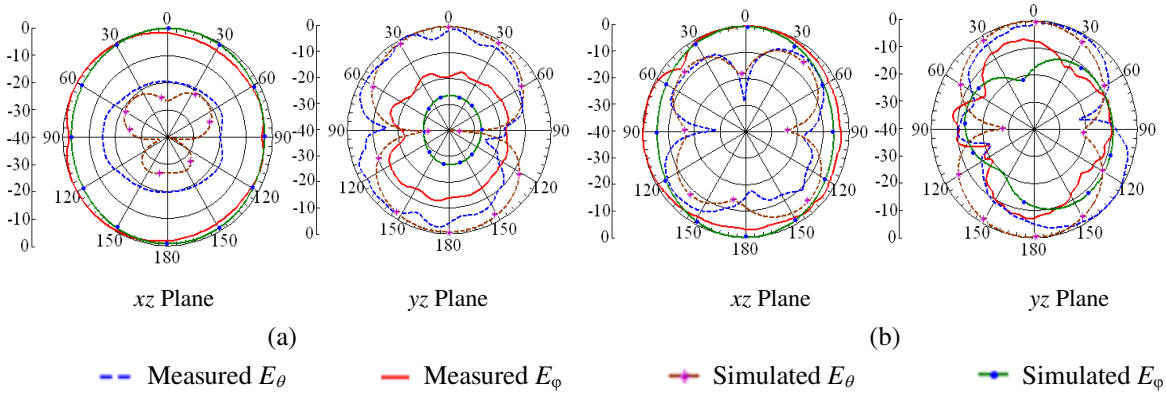

Figure 4: Radiation patterns of the proposed antenna for frequencies, (a) 3.1 GHz, and (b) 7 GHz.

Figure 5 illustrates the measured and simulated gain of the proposed antenna with and without the notched structures. It is seen that the average peak gain of the antenna is around 3 dBi all over operating band, except that at the notched bands significant sharply reductions in the gain are observed.

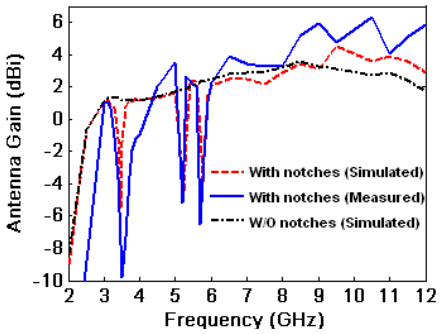

Figure 5: Gain of the proposed antenna with and without notched structures.

4. CONCLUSION

A Novel planar aperture antenna with triple band notches characteristics for UWB applications is proposed and discussed in this paper. To achieve triple notches bands, three resonating elements are introduced. The three notches are at the WiMAX, lower WLAN and upper WLAN applications. An electrical lumped-element equivalent circuit is obtained for the proposed antenna. The proposed antenna is fabricated. The measured data show a good agreement with the simulated results along with the equivalent circuit results which obtained using a rational function approximation based on VF technique. The measured VSWR $\leq$ 2 completely covers the UWB range of 3.2–11.6 GHz with triple notches band at 3.20–4.19, 5.02–5.32, and 5.51–6.10 GHz. The measured VSWR, band-notched characteristics, radiation patterns, and peak gains of the proposed antenna are presented and studied which validate the using of the proposed antenna for UWB applications.

REFERENCES

1. Federal Communications Commission, "First report and order," Revision of Part 15 of the Commission's Rule Regarding Ultra-wideband Transmission Systems, Feb. 2002.
2. Khaled, E. E. M., A. A. R. Saad, and D. A. Salem, "A proximity-fed annular slot antenna with different a band-notched manipulations for ultra-wideband applications," *Progress Electromagnetics Research B*, Vol. 37, 289–306, 2012.

3. Saad, A. A. R., D. A. Salem, and E. E. M. Khaled, "Design and circuit-modeling of a novel printed split-ring resonator antenna with 5.5 GHz band-notched characteristics," *30th National Radio Science Conference (NRSC 2013)*, 100–108, NTI, Cairo, Egypt, Apr. 2013.
4. Saad, A. A. R., E. E. M. Khaled, and D. A. Salem, "A novel proximity-fed UWB printed slot antenna with 3.6/5.5 GHz dual band-notched characteristics: design and circuit-modeling," *30th National Radio Science Conference (NRSC 2013)*, 90–99, NTI, Cairo, Egypt, Apr. 2013.
5. Zhang, J., S. W. Cheung, and T. I. Yuk, "CPW-coupled-fed elliptical monopole UWB antenna with dual-band notched characteristic," *PIERS Proceedings*, 823–827, Kuala Lumpur, Malaysia, Mar. 27-30, 2012.
6. Liao, X.-J., H.-C. Yang, N. Han, and Y. Li, "Aperture UWB antenna with triple band-notched characteristics," *Electronics Letters*, Vol. 47, No. 2, 77–79, Jan. 2011.
7. Zhu, F., S. Gao, T. S. H. Anthony, T. Brown, J. Li, G. Wei, and J. Xu, "Asymmetric UWB aperture antenna with triple band-notched function," *Proceedings of the Loughborough Antennas & Propagation Conference*, 1–4, Loughborough, UK, Nov. 2012.
8. Gustavsen, B. and A. Semlyen, "Rational approximation of frequency domain responses by vector fitting," *IEEE Transaction on Power Delivery*, Vol. 14, 1052–1061, Jul. 1999.
9. Gustavsen, B. and A. Semlyen, "Enforcing passivity for admittance matrices approximated by rational functions," *IEEE Transactions on Power System*, Vol. 16, 97–104, Feb. 2001.

Design and Development of Reconfigurable Microstrip Patch Antenna Using MEMS Switch for Ku-band Application

Prafulla Chandra Prasad and Neela Chattoraj
Department of Electronics and Communication Engineering
Birla Institute of Technology, Mesra, Ranchi, Jharkhand, India

Abstract— Reconfigurable multi-band antennas are attractive for many satellite applications where it is required to have a single common antenna that can be dynamically reconfigured to transmit (or receive) on multiple frequency bands. The design of printed microstrip antenna is reported in Ku-Band for wireless applications in this paper. The planar, very small, thin antenna with coaxial probe feed of 50 Ω is first realized at 15 GHz on a PTFE substrate having a dielectric constant of 2.5 and a substrate thickness of 1.6 mm. Simulations have been carried out with the Ansoft HFSS 13. On moving towards reconfigurability, the structure under investigation the schematic structure consist of two patches, one is driving patch of dimension $5 * 5.7\,\text{mm}^2$ and another defined as wing patch of dimension $5 * 1\,\text{mm}^2$ separated by 1 mm distance. MEMS (Micro electro Mechanical System) switch is applied between driven patch and wing patch. The gap between the two is varied by using MEMS switch. The switch may be closed or open and it changes the antenna operational frequency. When the switch closes, the wing patch is coupled with main patch by an inductance. When the switch opens, the wing patch is coupled with main patch by a capacitance. The simulation results show that the antenna can change the work frequency from 15 GHz to 15.65 GHz in Ku band with RFMEMS switch.

1. INTRODUCTION

Microelectromechanical systems (MEMS) and the application of this technology to RF systems enable production of tunable components with low power consumption, high linearity and high performance. The tunable characteristics of RF MEMS are employed in the integration of these components with antennas providing numerous advantages such as reconfigurability in the polarization, frequency, and radiation pattern.

It is a potential trend to make use of MEMS technology to manufacture the microstrip antenna. As Silicon has good mechanical property, and silicon micromachining technology is compatible of the manufacture of semiconductor. Silicon is used as material of antenna substrate. Antenna with MEMS technology and precision machining technology has a lot of advantages in terms of dimension, capability, cost and so on. This shrinks the volume of the communication system very much, improving reliability, increasing life-span, enhancing efficiency, and reducing power loss. For the long run of point to point communication, power, gain and efficiency become to be the key factors that restrict antenna. Microstrip antenna has so many excellences such as low profile, small volume and light weight that it is suitable for communication in the air. Inaddition, microstrip antenna is easier to realize circular polarization, convenient for arraying and capable to enhance output gain. So the MEMS-based Silicon Microstrip antennas have been extensively studied and applied [1–4].

In this paper, frequency reconfigurability of the antenna is achieved by connecting the driving patch to the wing patch by a RF MEMS switch. When the switch closes (ON condition) the wing patch get inductively coupled with main patch and when switch opens (OFF condition) the wing patch get capacitive coupled with main patch which led to change in operating frequency of antenna from 15 GHz to 15.65 GHz in Ku-Band. The proposed frequency of 15 GHz and 15.65 GHz belong to 14.4 to 15.35 GHz and 15.63 to 15.7 GHz band respectively with application in Fixed Satellite Service (FSS), Mobile Satellite Communication (Up-Link), Space research and Aeronautical Navigation. They find applications in space based radar, communication satellites, electronic intelligence, and aircraft navigations besides many other communications and sensing applications [9].

Parametric study have also been performed which is discussed in later section.

2. ANTENNA AND RF MEMS SWITCH DESIGN CONFIGURATION

The structure shown in Figs. 1(a) and (b) are basic antenna nearly square shaped microstrip patch antenna. The 50 Ω coaxial probe feed is located at (1.2, 2.2) from left bottom corner of patch. The antenna is simulated on a PTFE dielectric substrate ($\varepsilon_r = 2.5$) with height 1.56 mm. The length

and width of the ground plane and the substrate is $30 \times 30\,\text{mm}^2$ and length and width of the patch is $5 \times 5.7\,\text{mm}^2$. A wing patch of 5.7 mm to 1 mm is introduced with the main patch to change the operating frequency when connected to a RF MEMS switch and the patch antenna design is supported with a model design using Ansoft HFSS software [8] based on finite elements modeling (FEM) infinite ground plane has been taken for simulation of microstrip patch antenna. For switch its beam is of 500 µm in length and 60 µm in width all made of gold material. On simulating in Comsol the pull down voltage is coming to be around 10 volts and its substrate is silicon nitride.

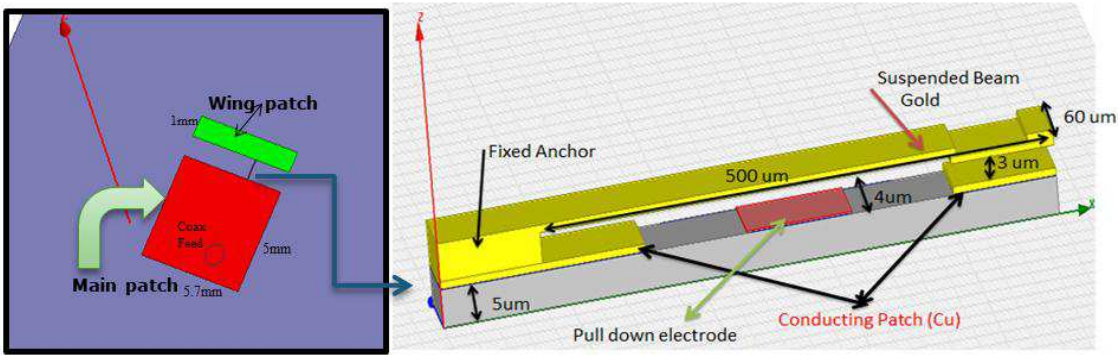

(a) (b)

Figure 1: (a) Antenna design and position of switch. (b) Detail dimension of RF switch.

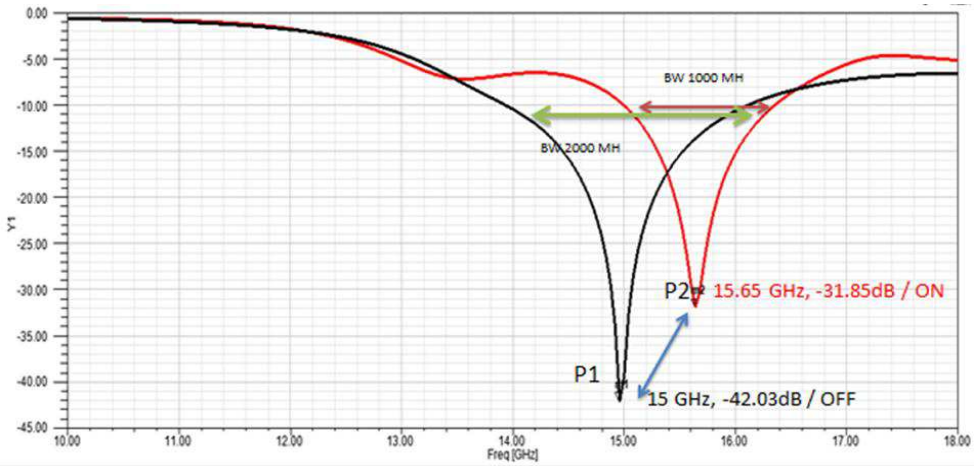

Figure 2: Return loss at both switching condition of RF MEMS switch.

3. RESULTS AND DISCUSSION

The reconfigurable antenna performance depends on the switching condition of MEMS switch either in "ON" and "OFF" states. Simulation has been performed by using HFSS simulator. The up and down state of both MEMSswitches are defined as OFF and ON state. From Fig. 2 shows the shift in frequency from 15 GHz to 15.65 GHz during the switching conditions. When switch beam is in upstate (OFF condition) the return loss is coming to be −42 dB at 15 GHz and under ON condition there is shift of frequency to 15.65 GHz with return loss of −31.85 dB with wide bandwidth.

Figures 3(a) and (b) indicate the simulated VSWR which is coming to be less than 2 and radiation patter at two frequency when phi = 0 and phi = 90.

For high frequency communication the gain of the antenna is one of the important factor for consideration and from Fig. 4(a) indicates the simulated gain of antenna at 15 GHz which is coming to be 6.3 dB at different values of the theta. In Fig. 4(b) shows the 3D radiation pattern of the antenna in z-direction. In this paper the mechanical deflection of beam is performed in the Comsol 4.2 software and voltage required to deflect the beam through simulation is about 10 volts. This graph of deflection is shown in the Fig. 5(a).

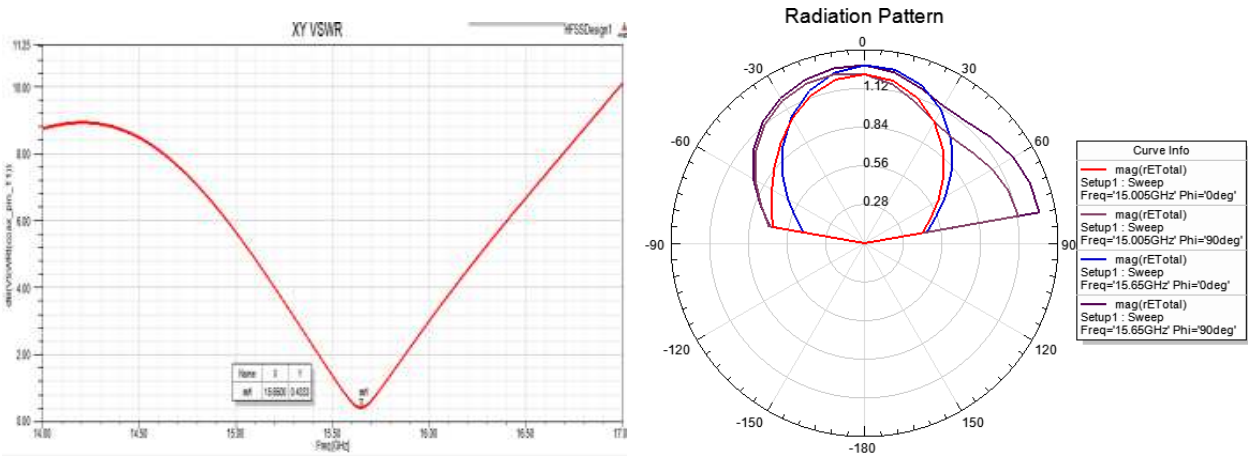

(a) (b)

Figure 3: (a) Simulated VSWR. (b) 2D radiation pattern at phi = 0 and phi = 90.

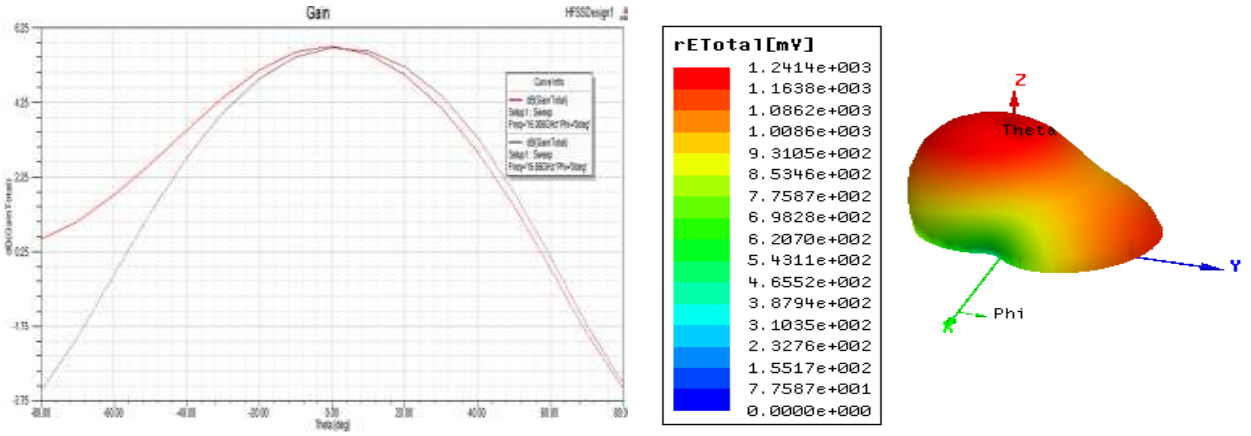

(a) (b)

Figure 4: (a) Gain of antenna. (b) 3D radiation pattern at 15 GHz.

4. PARAMETRIC STUDY

The systematic parametric study was performed in order to understand the frequency variation mechanism and to identify the influence of some physical parameters on the antenna. On varying the gap between the driving patch and wing patch from 0.2 mm to 5 mm, with designed at 1 mm gap from Fig. 5(b) concludes that on decreasing and increasing the gap there is slight variation in frequency due to capacitive coupling between them.

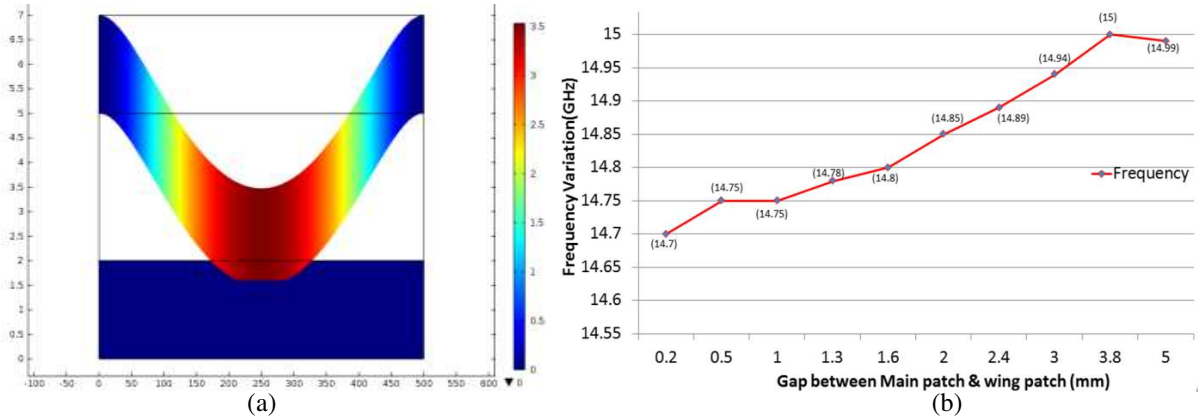

(a) (b)

Figure 5: (a) Mechanical deflection of beam. (b) Frequency variation with varying between main patch and wing patch.

From Fig. 6(a) and Fig. 6(b) shows the graph of frequency variation with the substrate thickness and different values of the permittivity of material and clearly indicates decrease in resonant frequency with increase in substrate height due to loss in it and similarly frequency decreases with increasing the value of the permittivity of material as due to increase in loss for higher values of permittivity.

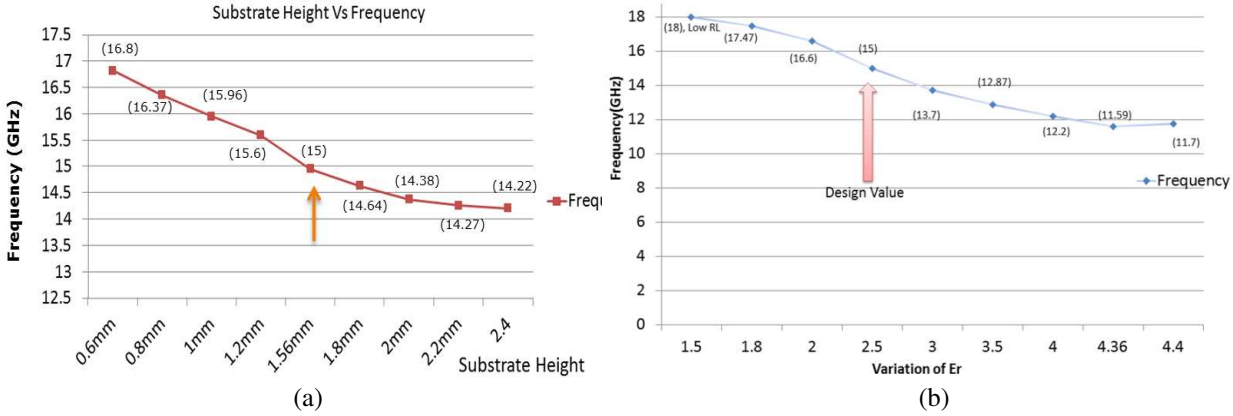

Figure 6: (a) Frequency variation with substrate thickness. (b) Effect of permittivity variation on frequency.

5. CONCLUSIONS

A novel Reconfigurable Microstrip Patch Antenna using MEMS Switch for Ku-Band Application has been designed in this paper which can shift the frequency from 15 GHz to 15.65 GHz by using MEMS switch. The future work left with us to fabricate the antenna and to perform experimental verification on Vector Network Analyzer. Proposed antenna shows reconfigurability behavior in Ku-Band with high gain (Average gain more than 6 dB) and wide bandwidth is simulated with HFSS version 13 a 3D electromagnetic simulation tool. The design frequency was chosen 15 GHZ. Generally microstrip gives narrow band and low gain. Here it is observed that gain is nearly about 6 dB and bandwidth is more than 900 MHz, return loss is around 42 dB and also dimension 5.7 mm × 5 mm with nearly good matching which is novelty of this design [5–7].

REFERENCES

1. Rebeiz, G. M., *RF MEMS Theory, Design, and Technology*, Wiley, Hoboken, NJ, 2003.
2. Feldner, L. M., C. D. Nordquist, and C. G. Christodoulous, "RF-MEMS reconfigurable patch antenna," *Antenna and Propagation Society International Symposium*, Vol. 2A, 338–391, 2005.
3. Pozar, D. M., "Microstrip antenna," *Proceeding of IEEE*, Vol. 80, No. 1, January 1992.
4. Wang, X., H. Zhao, Y. Niu, and Y. Zhang, "MEMS dual-band frequency and polarization reconfigurable microstrip antenna," *2nd IITA International Conference on Geoscience and Remote Sensing*, 51–53, 2010, ISBN No. 978-1-4244-8515-4/10.
5. Balanies, C. A., *Antenna Theory: Analysis & Design*, 2nd Edition, John Wiley & Sons, Inc., 1997.
6. Prasad, P. C., A. Sen, and N. Chattoraj, "Design and development of a single feed reconfigurable dual frequency microstrip antenna," *2nd IEEE International Conference on Communication and Signal Processing (ICCSP'13)*, 182–186, 2013, ISBN No. 978-1-4673-1620-0.
7. Ansoft High Frequency Structural Simulator (HFSS) Version 13.
8. Action by the Commission, *Federal Report and Order/Further Notice of Proposed Rulemaking*, (FCC 00-418), Chairman Kennard, Commissioners Ness, Powell and Tristani with Commissioner Fuchtgott-Roth, November 29, 2000.

Wideband Patch Antenna for X-band Applications

A. Harrabi[1], **T. Razban**[2], **Y. Mahe**[3], **L. Osman**[4], **and A. Gharsallah**[1]

[1]Faculty of Sciences of Tunis, Tunisia
[2]LUNAM, IETR UMR 6164, France
[3]Polytech'Nantes, Nantes, France
[4]Higher School of Communication of Tunis, Tunisia

Abstract— This paper presents the process of the designing of a broadband X-band antenna. A relative bandwidth of 20% was obtained for a footprint of less than $0.7\lambda_0 \times 0.7\lambda_0$. The gain of the antenna in the upper half-plane is about 5.1 dBi. A comparative study is also presented showing the advantages of the new antenna compared to a simple rectangular patch antenna.

1. INTRODUCTION

The design of a wideband antenna is an important issue of the current researches. Many contributions have technical solutions based on multi resonators. A first possibility consists of arranging the resonators one next to the other. By controlling the coupling level between the resonators, it becomes possible to form the bandwidth of the antenna. However, this solution has the disadvantage of a relatively large footprint that does not, in most cases, consider the networking. An alternative is to use extra layers based on multilayer technology [1, 2]. Technological sensitivity on the frequency response of the antenna, especially masks alignment, is then important as long as the center frequency of operation is high. We propose in this paper, a process leading to the design of a broadband X-band antenna whose dimensions are still less than $0.7\lambda_0$.

2. ANTENNA DESIGN

In a given planar technology, the bandwidth is determined by the thickness, the nature of the dielectric substrate and the geometry of the antenna. In order to expose the issue of bandwidth in simple planar structures and to set a benchmark in terms of space and bandwidth, a rectangular patch has first been sized (Figure 1). Whit given technological parameters, the bandwidth is maximized by increasing the width and decreasing the permittivity of the substrate. The dimensions of the antenna can then be deduced from the analytical expressions [3, 4]. The result, according to the simulation in CST Microwave Studio of the antenna in terms of the reflection coefficient is shown in Figure 1. A relative bandwidth of the order of 10% is obtained.

We can hardly get more bandwidth with this simple pattern. We propose then to modify the geometry of the radiating element to remove the lock.

The approach is to favor a polygonal geometry [5, 6] in order not to increase the size of the patch. This change aims to modify the distribution of surface current density which may generate multiple resonances. These are intrinsically linked to the dimensions $L1$ and $L2$ of the polygon (Figure 2).

The simulation result of the polygonal antenna reflection coefficient is shown in Figure 3. This figure shows that it appears a second resonance frequency. This frequency is related to the dimension

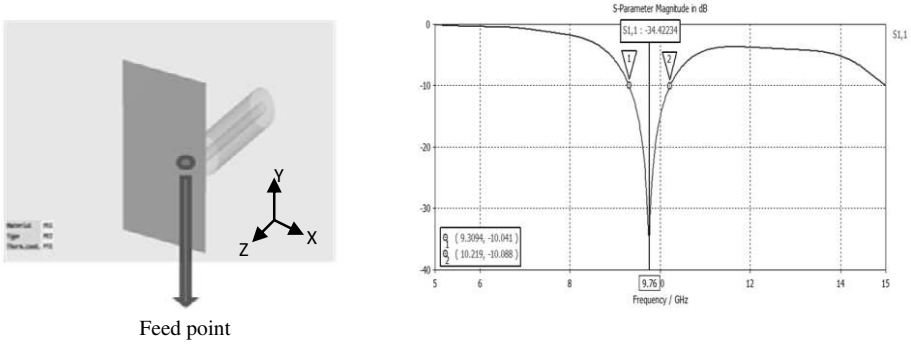

(a) (b)

Figure 1: (a) Rectangular patch antenna, (b) the reflection coefficient S_{11} simulation of the rectangular antenna.

$L2$ of the antenna. The fundamental frequency is influenced by $L1$. These dimensions are linked by the fact that the single excitation point must have matched impedance (50 Ω) with the two resonant frequencies. Table 1 gives the dimensions of this polygonal antenna.

For high bandwidth, we need to bring closer these two resonant frequencies. A possible way is to insert a circular slot in the middle of the polygon. This slot has a radius of 4.51 mm and a width of 310 µm (Figure 4). In this configuration, we also add as protective Radom, a Teflon layer with the thickness of $h = 1.58$ mm.

After optimization, we obtain the dimensions shown in Table 2 and the simulation results of reflection are given in Figure 5.

A bandwidth of 2 GHz is obtained but a shift towards higher frequencies has been observed. To lower the center frequency of the antenna, four elements of a length very much less than the wavelength are disposed around the polygonal antenna (Figure 6). The gap between the polygonal element and vertical parasitic elements is 330 µm and 230 µm for the side elements.

We observe a bandwidth greater than 20% for a center frequency of 9.75 GHz (Figure 6). The bandwidth is doubled compared to the reference antenna (the rectangular patch). In size, an antenna with dimensions of about $0.7\lambda_0 \times 0.7\lambda_0$ (Table 2) was obtained.

As for the radiation pattern, the proposed antenna keeps the radiation characteristics of a rectangular patch antenna. The radiation pattern obtained by simulation is then given in Figure 7.

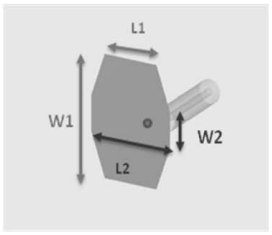

Figure 2: The polygonal antenna form.

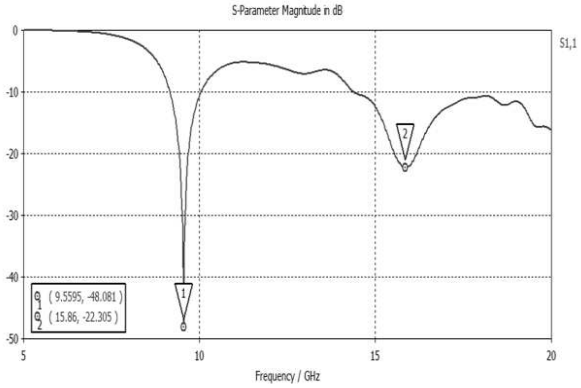

Figure 3: Simulated S_{11} parameter of the polygonal antenna.

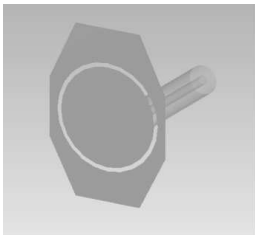

Figure 4: Polygonal antenna with the circular slot.

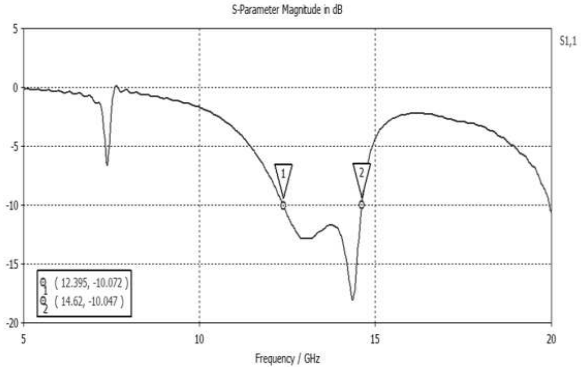

Figure 5: S_{11} simulation result of the antenna patch with circular slot.

Parameter	Value
$W1$	10 mm
$L1$	5.9 mm
$W2$	4 mm
$L2$	8 mm

Table 1: The polygonal antenna dimensions.

Parametre	Value (mm)
$W1$	10 mm
$L1$	5.9 mm
$W2$	4 mm
$L2$	8 mm

Table 2: The polygonal patch with the circular slot dimensions.

Table 3: The final antenna dimensions.

Parameter	Value
W	17.56 mm
L	18.04 mm

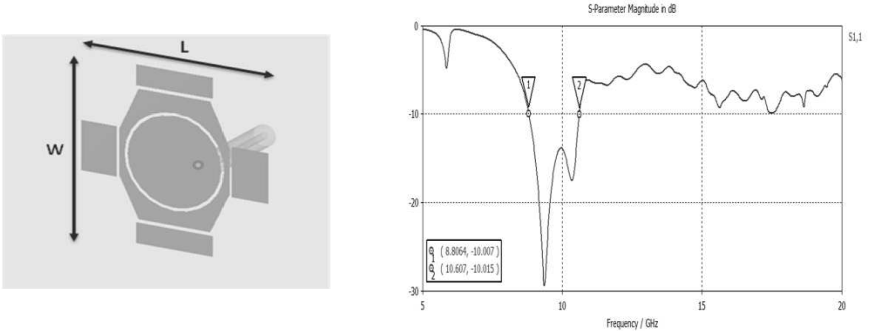

Figure 6: Proposed antenna shape and S_{11} parameter simulation result of the proposed antenna.

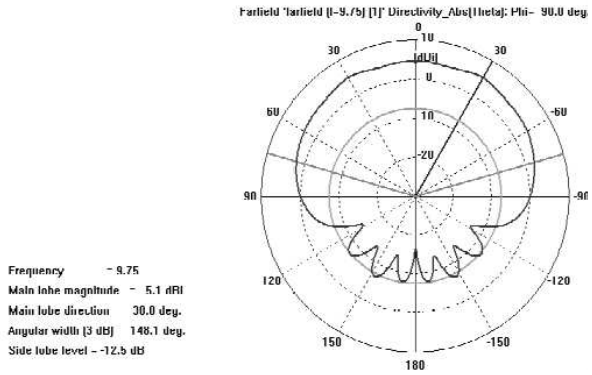

Figure 7: Radiation pattern of the proposed antenna, Phi = 90°.

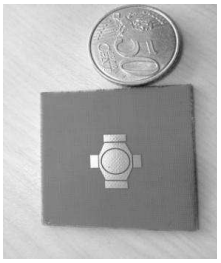

Figure 8: Photo of the prototype.

It has a directivity of 5.1 dBi.

3. PROTOTYPE AND MEASUREMENTS

A prototype of this antenna was made and measured. The antenna technology is based on a Teflon-glass substrate of a thickness of 1.58 mm, a relative permittivity of 2.55 and $\tan\delta = 0.007$. A Radom is added consisting of a first Epoxy-glass superstrat thickness of 1.58 mm, a relative permittivity of 4 and $\tan\delta = 0.02$ and a second Teflon-glass whose properties are similar to the chosen substrate.

The choice of these materials comes from the desire to develop a low cost solution and have a protected aerial assaults related to the environment. The introduction of the Radom was taken into account in the simulation of the antenna in its final form. A photo of the proposed antenna is given in Figure 8.

The frequency response of the reflection coefficient S_{11} obtained by simulation and measurement is given in Figure 9. The latter shows that the measure is consistent with the simulation. The two curves have in fact the same bandwidth of 2 GHz. The final size of the antenna is near $0.7\lambda_0 \times 0.7\lambda_0$ and so is compatible with the establishment of an antenna array.

From the radiation point of view, measurement shows good agreement with the simulation (Figure 10). A hemispherical radiation pattern is observed with a maximum gain in the normal axis of 5.1 dBi.

The following table provides a comparison between the rectangular patch antenna (Figure 1) and the proposed antenna (Figure 8).

The proposed antenna has a bandwidth greater than 20% which is the double of the conventional patch antenna bandwidth. Although the dimensions of the new antenna are higher than those of a patch antenna, but were lower than the wavelength, therefore it is still convenient for an antenna

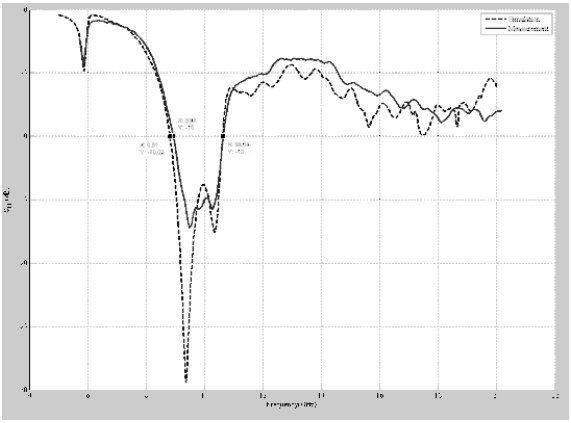

Figure 9: The reflection coefficient S_{11} results of the antenna: simulation and measurements.

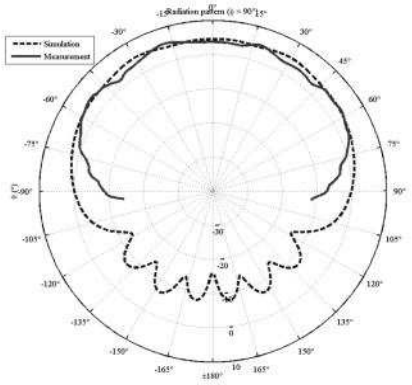

Figure 10: Simulation and measurement result of the antenna directivity at a frequency $f = 9.75\,\text{GHz}$.

Table 4: Comparison of the two models.

Parameter	Rectangular patch antenna	Proposed antenna
W	10.52 mm	17.56 mm
L	7.5 mm	18.04 mm
Bandwidth	$<$ **10%**	$>$ **20%**

array.

4. CONCLUSION

In this article, we presented the design and implementation of a broadband antenna (above 20%) operating in X-band. It has a footprint of around $0.7\lambda_0 \times 0.7\lambda_0$ compatible with the establishment of an antenna array. Its structure is simple and consists of a single radiating metal plane. Its implementation does not require precise alignment that is highly required for multi resonator antennas on several layers, generally available to achieve this range of bandwidth. This antenna radiates in the upper level with a maximum directivity of 5.1 dBi.

REFERENCES

1. Sentucq, B., "Design and realization of a broadband antenna network," Master Report, Supervisors: T. Razban, Y. Mahe, LUNAM University, University of Nantes, IETR, 2010–2011.
2. Dubrovka, F. F. and S. Y. Martynyuk, "Wideband dual polarized planar antenna arrays," *International Conference on Antenna Theory and Techniques*, Department of Theoretical Fundamentals Radio Engineering, Kiev Polytechnic Institute, National Technical University of Ukraine, Sevastopol, Ukraine, 91–96, September 9–12, 2003.
3. Balanis, C. A., *Antenna Theory Analysis and Design*, JohnWiley & Sons, New York, 1997.
4. Garg, R., P. Bhartia, I. Bahl, and A. Ittipiboon, *Microstrip Antenna Design Handbook*, Artech House Publishers, 2001.
5. Manzani, M., A. Alù, F. Bilotti, and L. Vegni, "Polygonal patch antenna for wireless communication," *IEEE Transanctions on Vehicular Technology*, Vol. 53, No. 5, Septempber 2004.
6. Manzani, M., A. Alù, F. Bilotti, and L. Vegni, "Design of polygonal antennas with a broad-band behavior via a proper perturbation of conventional rectangular radiators," *IEEE Antennas and Propagation Society International Symposium*, 0-7803-7846-/03/$17.00 ©IEEE, 2003.

A Fractal-based Printed Slot Antenna for Multi-band Wireless Applications

Seevan F. Abdulkareem, **Ali J. Salim**, **Ali I. Hammoodi**, **and Jawad K. Ali**
Microwave Research Group, Department of Electrical Engineering
University of Technology, Iraq

Abstract— Fractal geometries have shown to be attractive for antenna designers because of the unique features they offer. In this paper, a printed fractal based slot antenna has been introduced to be used in multi-band wireless applications. The slot structure of the proposed antenna is of an octagonal shape with a Koch fractal curve of the second iteration is applied on each of its sides. The slot structure has been etched on the ground plane of a substrate with relative permittivity of 4.4 and 1.6 mm thickness. On the reverse side of the substrate, a 50 ohm microstrip line feed has been etched. To enhance the coupling with the slot, the feed line has been loaded with a circular stub with embedded complementary circular split ring resonator. Based on the lowest resonant frequency, it has been found that the largest dimension of the proposed antenna slot structure is less than half the guided wavelength. Parametric study shows that the resulting antenna offers a multi-band behavior with enhanced gain and fractional bandwidths, besides the reasonable radiation characteristics throughout the resonating bands. With appropriate dimension scaling, the proposed antenna could be a suitable candidate for use in a wide variety of multi functions wireless applications.

1. INTRODUCTION

Various fractal geometries have become attractive for antenna designers to produce compact and multi-band antennas benefiting from their unique properties; space filling and self similarity respectively. Conventional fractal geometries such as Koch, Cantor, Hilbert, Sierpinski and other fractal curves have been successfully used to produce dual-band and multi-band printed slot antennas for various wireless applications.

In this context, the use of fractal geometries in the design of printed slot antennas can be classified into two categories. In the first category, direct application of fractal geometries has been adopted [1–5]. In this case, the fractal geometries constitute the whole antenna slot structures. However, dual-band and multi-band printed slot antennas with fractal slot structures based on circular shapes are reported in the literature [6–8]. In the second category, where indirect application of fractal geometries is suggested, the antenna slot structure is composed of a combination of Euclidian structures, such as triangle, square, rectangle and other polygons, and fractal geometries superimposed on these structures, where each line segment is replaced by fractal curve with certain iteration level [9–14].

It is worth to note that in the majority of the research work regarding the antenna design according to the second category, the feed lines are loaded with some type of stubs to enhance the coupling of the different resonant bands. Furthermore, antennas with stub loaded feed lines are characterized by relatively high gain as compared with those without stubs. Stubs have been found with different sizes and shapes. It has been reported with a square ring shape [12], a widened rectangular shape [13], a rectangular shape with embedded slot [14], etc..

In this paper, a microstrip line fed printed fractal slot antenna has been presented as a candidate for use in multi-band wireless applications. The slot structure of the proposed antenna is composed of an octagonal shape with each of its line segments being replaced by a 2nd iteration Koch fractal geometry. The antenna has been fed with a 50 Ω microstrip line etched on the reverse side of the substrate. To enhance the coupling of the various resonant bands, the feed line has been loaded with a circular stub. For additional coupling of the resonant bands, a complementary circular split ring resonator, CCSR, has been embedded in the circular stub. However, this CCSR offers a simple tuning means of the antenna resonant bands without changing the antenna dimensions.

2. THE ANTENNA STRUCTURE AND DESIGN

The slot structure of the proposed antenna is essentially based on the conventional octagonal shape. Each side of the octagon has been modified to be in the form of a 2nd iteration Koch fractal geometry. The slot structure has been etched on the top side of the substrate with feed

line has been printed on the reverse side, Figure 2. Modelling and performance evaluation of the proposed antenna has been carried out using commercially available EM simulator HFSS from Ansoft Corporation [15]. An initial design, has been carried out with a slot radius of 22.5 mm being etched on a ground plane dimensions of $75 \times 75\,\text{mm}^2$ and with 3.05 mm width microstrip feed line printed on the reverse side of an FR-4 substrate with relative permittivity of 4.4 and 1.6 mm thickness. With these parameters and feed line length, L_f, of 33 mm, the antenna offes a return loss response with a lowest resonant frequency, f_1, of about 2.43 GHz. However, there is another resonance occur at 1.3 GHz but it is not highly coupled.

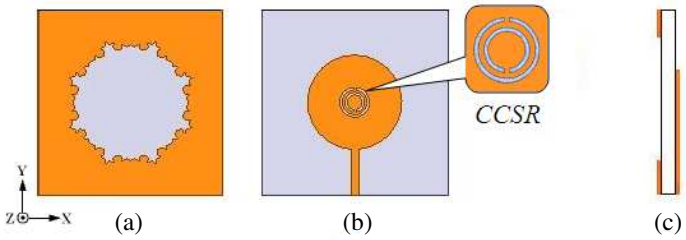

Figure 1: The structure of the proposed antenna with respect to the coordinate system. (a) The front view. (b) The bottom view with an enlarged section showing the CCSR, and (c) the side view.

To enhance the coupling of the resonant bands, the feed line has been loaded with a circular stub cocentred with and beneath the slot structure as shown in Figure 1(b). Starting with a stub radius, R_S, of 18 mm, the antenna offers a return loss response with four resonant bands centered at about 1.41, 2.35, 3.76, and 5.05 GHz respectively. As a means of further coupling and tuning of the resulting resonances, a complementary circular split ring resonator, CCSR, with a width and inter-ring spacing of 1 mm each, has been embeded at the center of the stub. With a stub radius, R_S, of 18 mm and a CCSR with inner radius, R_{CCSR}, of 6 mm, the antenna offers a return loss response with four resonant bands centered at about 1.10, 2.45, 3.96, and 5.25 GHz respectively. In this case, the lowest resonant frequency can be expressed in terms of the antenna slot perimeter, P_{SLOT}, and the substrate effective permittivity, ε_{eff}, as:

$$f_1 = \frac{2c}{P_{\text{SLOT}}\sqrt{\varepsilon_{eff}}} \tag{1}$$

where c is the speed of light in the free space. To save space, the derivation of Equation (1) will not be mentioned here. The combination of the feed line stub and the CCSR makes the proposed antenna possesses a wide variety of resonating bands covering almost all the recently available wirelss services within the adopted frequency range.

3. PERFORMANCE EVALUATION

A parametric study has been conducted to demonstrate the effects of many antenna parameters on its performance. Figure 2(a) demonstrates the effect of the feed line length variation on the return loss response of the antenna without loaded stub. Simulated return loss responses depicted in Figure 2(a) reveal that the antenna possesses a single resonant band within the swept frequency range 1–6 GHz. However, there is another resonant band out of this range positioned at about 8 GHz which is out of our attention. The effect of the variation of the feed line length is to change the position of the resonant band. The feed line length, L_f, has been increased from 33 to 37 mm in steps of 2 mm. As L_f increaes, the the resonant frequency has shifted higher to the right with correspondingly enhanced coupling.

The second parameter that has been adopted in the parametric study is the feed line loading stub size. Figure 2(b) demonstrates the antenna return loss responses corresponding to circular stub radii ranging from 18 to 20 mm in steps of 1 mm. It is implied that, the appearance of four resonant bands within the same swept frequency range is attributed to the feed line loading with the circular stub. In addition, the variation of the stub radius, R_S, has almost no effect on the lowest frequency band. However, different degrees of coupling have been achieved with the various values of R_S. Smaller stubs tend to lower the other resonant bands but with more enhanced coupling. On the other hand, with the use of stubs radii greater than 20 mm, the coupling becomes weaker and the higher resonant bands start to disappear.

The last step of the parametric study is to evaluate the effects of the embedded CCSR in the feed line stub on the resulting antenna performance. Observing the antenna return loss responses depicted in Figure 2(c), it is clear that the variation of the CCSR inner radius predominantly affects the first and the fourth resonant bands. The effect on the first resonant band is to shift its position permitting a considerable range of tunability, while the effect on the fourth band is to support the coupling leading to enhanced bandwidth. The far field radiation patterns for the E and H planes, at the centers of the four frequency bands, are shown in Figure 3. The results show a monopole like radiation characteristics with almost omnidirectional radiation. Furthermore, the corresponding gain at the four frequencies are of about 6.0, 2.3, 4.0, and 4.0 dB respctively. Figure 4 displays the surface current distribution on the modelled antenna with a circular stub of 17 mm radius and embedded CCSR with inner radius of 5 mm, at the four resonant bands. The effect of the CCSR on the antenna performance is clearly shown at f_1 and f_4. This confirms the results depicted in Figure 3(c), where the introduction of the CCSR predominantly affects the first and the fourth resonant bands. Observing the return loss responses depicted in Figures 1(b) and (c), it is clear that the proposed antenna could be presented as a candidate to cover different wireless applications such as Bluetooth, WLAN, SDAR-S, ISM, GPS, RFID, WiMAX.

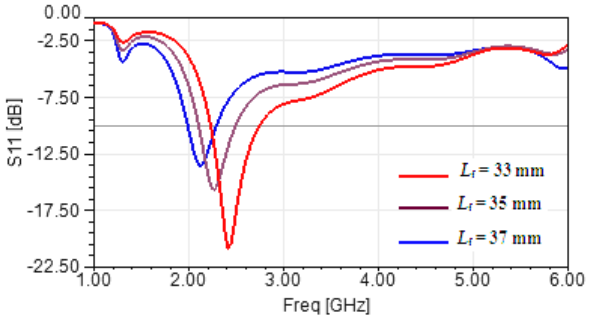

(a)

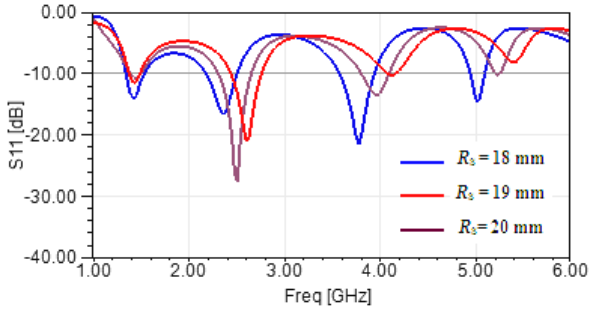

(b)

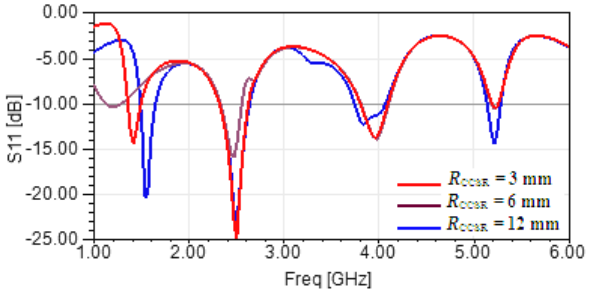

(c)

Figure 2: The simulated antenna return loss responses for (a) the antenna without loaded stub and the feed line as a parameter, (b) the antenna with loaded stub with stub radius as a parameter, and (c) the antenna with loaded stub and CCSR with CCSR radius as a parameter.

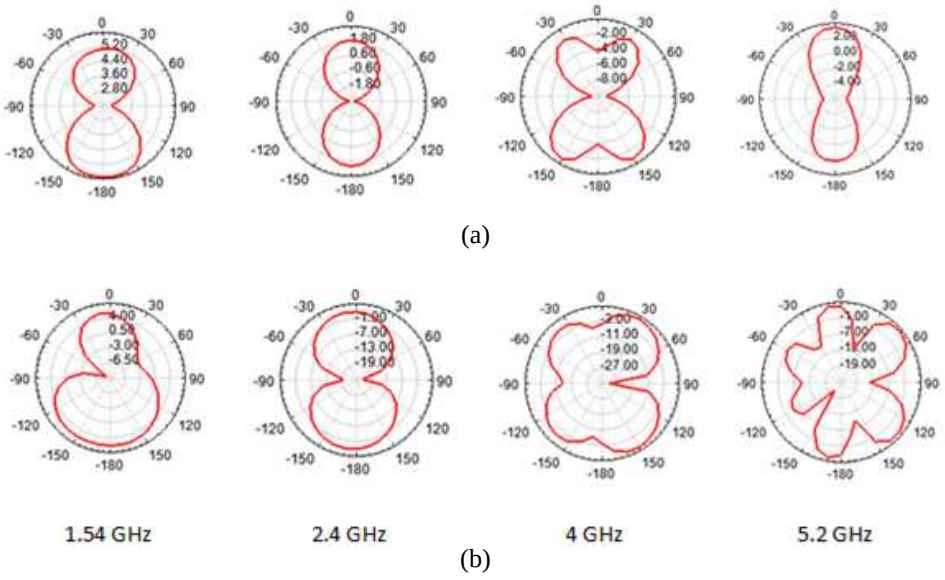

Figure 3: The simulated far field radiation patterns of the modelled antenna with circular stub of 17 mm radius and embedded CCSR with inner radius of 5 mm at the four resonant bands. (a) The E-plane, and (b) the H-plane.

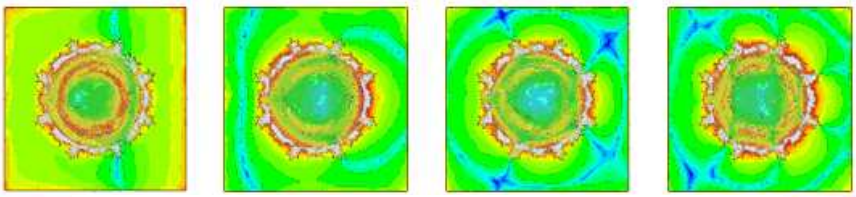

Figure 4: The simulated surface current distribution on the modelled antenna with circular stub of 17 mm radius and embedded CCSR with inner radius of 5 mm at: (a) f_1=1.54 GHz, (b) f_2=2.40 GHz, (c) f_3=4.00 GHz, and (d) f_4=5.20 GHz.

4. CONCLUSIONS

In this paper, a fractal based slot printed antenna with stub loaded microstrip feed line has been presented. The proposed antenna has shown to possess a multi-band behavior covering most of the commercial wireless services. It has been shown that the existence of the feed line stub enhances the coupling of the resonating bands. On the other hand, the introduction of the embedded CCSR in the circular stub structure provides an additional means of slight tuning of the resonant bands with further coupling. Furthermore, the proposed antenna offers good radiation characteristics and considerable gains throughout the resonant bands. This makes the proposed antenna a suitable candidate for use in a wide variety of multi function wireless applications. It is hopeful that the proposed antenna be attractive for antenna designers for the high degree of freedom it provides.

REFERENCES

1. Sayem, A. and M. Ali, "Characteristics of a microstrip-fed miniature printed Hilbert slot antenna," *Progress In Electromagnetics Research*, Vol. 56, 1–18, 2006.
2. Krishna, D. D., A. R., Chandran, and C. K., Aanandan, "A compact dual frequency antenna with Sierpinski gasket based slots," *Proceedings of the European Conference on Wireless Technologies*, 320–322, 2007.
3. Ali, J. K., "A new microstrip-fed printed slot antenna based on Moore space-filling geometry," *Proceedings of IEEE Loughborough Antennas & Propagation Conference*, UK, 2009.
4. Ali, J. K. and E. S. Ahmed, "A new fractal based printed slot antenna for dual band wireless communication applications," *PIERS Proceedings*, 1518–1521, Kuala Lumpur, Malaysia, March 27–30, 2012.

5. Kim, H. B. and K. C. Hwang, "Dual-port spidron fractal slot antenna for multiband gap-filler applications," *IEEE Transactions on Antennas and Propagation*, Vol. 60, 4940 –4943, 2012.
6. Chang, D. C., B. H. Zeng, and J. C. Liu, "CPW-fed circular fractal slot antenna design for dual-band applications," *IEEE Transactions on Antennas and Propagation*, Vol. 56, 3630–3636, 2008.
7. Mahatthanajatuphat, C., P. Akkaraekthalin, S. Saleekaw, and M. Krairiksh, "A bidirectional multiband antenna with modified fractal slot fed by CPW," *Progress In Electromagnetics Research*, Vol. 95, 59–72, 2009.
8. Choukiker, Y. K., S. Rai, and S. K. Behera, "Modified half-circle fractal antenna using DC theorem for 2.4/5.2 GHz WLAN application," *Proceedings of IEEE National Conference on Communications, (NCC)*, 2011.
9. Bisht, N. and P. Kumar, "A dual band fractal circular microstrip patch antenna for C-band applications," *PIERS Proceedings*, 852–855, Suzhou, China, September 12–16, 2011.
10. Ali, J. K., M. T. Yassen, M. R. Hussan, and A. J. Salim, "A printed fractal based slot antenna for multi-band wireless communication applications," *PIERS Proceedings*, 618–622, Moscow, Russia, August 19–23, 2012.
11. Choukiker, Y. K. and S. K. Behera, "ACS-fed Koch fractal antenna for wide–band applications," *International Journal of Signal and Imaging Systems Engineering*, Vol. 6, 9–15, 2013.
12. Mahatthanajatuphat, C. and P. Akkaraekthalin, "A multiband double square slot antenna with fractal geometry," *Proceedings of International Symposium on Antennas and Propagation*, 2006.
13. Zhang, H., H. Y. Xu, B. Tian, and X. F. Zeng, "CPW-fed fractal slot antenna for UWB application," *International Journal of Antennas and Propagation*, Vol. 2012, Article ID 129852, 1–4, 2012.
14. Krishna, D. D., M. Gopikrishna, C. K. Anandan, P. Mohanan, and K. Vasudevan, "CPW-fed Koch fractal slot antenna for WLAN/WiMAX applications," *IEEE Antennas and Wireless Propagation Letters*, Vol. 7, 389–392, 2008.
15. *Ansoft High Frequency Structure Simulator (HFSS)*, ver. 10.1, Ansof Corp., 2006.

Effects of the Length Variations of LYSO and Plastic Optical Fiber on the Energy Spectrum Responses of a Fiber-optic Radiation Sensor

W. J. Yoo[1], K. W. Jang[1], S. H. Shin[1], D. Jeon[1], B. G. Park[2], S. Kim[3], J. H. Moon[4], S. Cho[5], and B. Lee[1]

[1]School of Biomedical Engineering, Research Institute of Biomedical Engineering
Konkuk University, Chungju 380-701, Korea
[2]Department of Energy & Environmental Engineering, College of Engineering
Soonchunhyang University, Asan 336-745, Korea
[3]Department of Nuclear & Energy Engineering, Institute for Nuclear Science & Technology
Jeju National University, Jeju 690-756, Korea
[4]Department of Nuclear & Energy Engineering, College of Energy & Environment
Dongguk University, Gyeongju 780-714, Korea
[5]Department Organic Materials & Fiber Engineering
College of Engineering, Soongsil University, Seoul 156-743, Korea

Abstract— A scintillating fiber-optic radiation sensor (SFORS) having the flexible and insertable characteristics was developed for remote gamma-ray energy spectroscopy in narrow places. As a small sensing element, a cerium-doped lutetium yttrium orthosilicate (LYSO) crystal was used considering the many advantages of the LYSO such as high density, high effective Z-number, high light output, and good energy resolution. Using the fabricated SFORS, we measured the inherent gamma-ray energy spectrum of a Co-60 and then analyzed the effects of the length variations of a LYSO crystal and a plastic optical fiber (POF) on the energy spectrum responses of the SFORS.

1. INTRODUCTION

In general, optical fiber-based radiation sensors have many desirable qualities over conventional radiation sensors, such as their small sensing volume, substantial flexbility, remote sensing and real-time monitoring, and immunity to electromagnetic interference (EMI) [1, 2]. Paradoxically, however, the scintillating fiber-optic radiation sensors (SFORSs) have thus far not been deployed on a commercial scale for gamma-ray energy spectroscopy due to the physical and optical properties of both a sensing element and an optical fiber. The physical properties of sensing element are very important in the scintillation detector and it should be specially considered for SFORS because its sensing size is normally small and thus it cannot completely absorb the energy of charged particles. Generally, the energy spectroscopy outcome corresponding to various interactions between the gamma-ray and the scintillation material depends on the physical and optical properties of the scintillator including size, density, effective Z-number, peak emission, transparency, and scintillating light conversion efficiency [3]. In order to transmit scintillating light having energy spectrum information without signal loss, the length and diameter of an optical fiber should be also considered.

In this study, a small-sized SFORS having the flexible and insertable characteristics was developed for remote gamma-ray spectroscopy in narrow places including pipes and holes. Using a spectroscopic technique, we obtained the inherent gamma-ray energy spectrum of radioactive isotope and evaluated the effects of the length variations of scintillator and optical fiber on the energy spectrum responses.

2. MATERIALS AND METHODS

In developing the SFORS system for gamma-ray energy spectroscopy, the sensing probe of SFORS was fabricated using an inorganic scintillator and a plastic optical fiber (POF). As an inorganic scintillator, a cerium-doped lutetium yttrium orthosilicate (LYSO) crystal (Advanced Microwave Technologies Solution) was used to produce scintillating light owing to gamma-rays and it has a non-hygroscopic characteristic, a low radiation damage, and a high sensitivity against gamma-rays [4]. The decay time and the peak emission of the LYSO crystal are 40 ns and 402 nm, respectively. In order to guide scintillating light from a LYSO crystal to a light-measuring device, we used a

commercial grade POF (CK-120, Mitsubishi Rayon) having step-index and multimode characteristics. Core and cladding materials of this fiber are polymethylmethacrylate (PMMA) resin and fluorinated polymer, respectively, and the jacket is made of black polyethylene (PE). The refractive index of the core is 1.49 and the numerical aperture (NA) is about 0.5.

Figure 1 shows the structure of a sensing probe and the experimental setup for measuring gamma-ray energy spectrum using a SFORS. The outer surface of the LYSO crystal was coated with a Teflon-based reflector tape (BC-642, Saint-Gobain Ceramic & Plastics) to increase the collection efficiency of the scintillating light. The LYSO crystal was then covered with an aluminum foil and a black shielding tape to prevent ambient light. Finally, the LYSO crystal was coupled with a black PMMA holder to the distal end of a POF. As a gamma-ray emitter, a solid disc-type cobalt-60 (Co-60) was used and this radioactive isotope produces two distinct gammas, 1.17 and 1.33 MeV. When gamma-rays were irradiated on the sensing probe, the scintillating light was produced in the LYSO crystal and transmitted to the photomultiplier tube (PMT) module (H9305-03, Hamamatsu Photonics) through the POF. The current signals from the PMT were converted to voltage signals and amplified by the amplifier (C7319, Hamamatsu Photonics). Finally, the amplified voltage signals were measured by using a multichannel analyzer (MCA) system (EASY-MCA-8k, ORTEC).

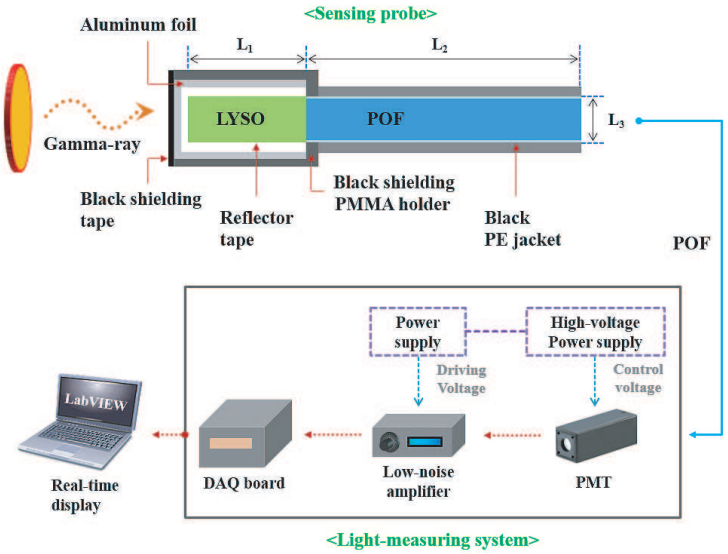

Figure 1: Experimental setup for measuring gamma-ray energy spectrum using a SFORS.

3. EXPERIMENTAL RESULTS

Since the size of the scintillator used in a SFORS is in a few mm, the sensing volume should be specially considered to measure inherent photopeaks (i.e., full-energy peak) in the energy spectrum of a radioactive isotope. Therefore, we carried out the experiment using three LYSO crystals with area of $3 \times 3\,\mathrm{mm}^2$ and length of 5, 10, and 15 mm to determine the adequate length of the LYSO crystal that can accurately measure gamma-ray energy spectrum with photopeaks. In this test, each LYSO crystal was directly connected to the faceplate window of the PMT using a black PMMA adapter without the POF. Fig. 2 shows the gamma-ray energy spectra for Co-60 according to the length (L_1) of the LYSO crystal. As increasing the length of the LYSO crystal from 5 to 15 mm, higher control voltages were required to supply on the PMT as shown in Fig. 2 and they were adequate voltages to obtain inherent photopeaks of Co-60 at the gamma-ray energy spectra. Because the absorption of primary gamma-ray and secondary charged particle energies increased as the length of LYSO crystal becomes longer from 5 to 15 mm, the counts of the scintillating light generated in LYSO crystal were also increased and thus more light signals having energy spectrum information were transmitted to the PMT through the transparent LYSO crystal. In addition, the full width at half maximum (FWHM) of the measured photopeak was decreased as the length of LYSO crystal became longer. As a result, the two photopeaks corresponding to photoelectrons were matched well with inherent photopeaks of the Co-60 when the length of LYSO crystal was 15 mm. It was accordingly assumed that the optimum length of LYSO crystal was about 15 mm

in our experimental setup for the gamma-ray energy spectroscopy considering the absorption of charged particle energy.

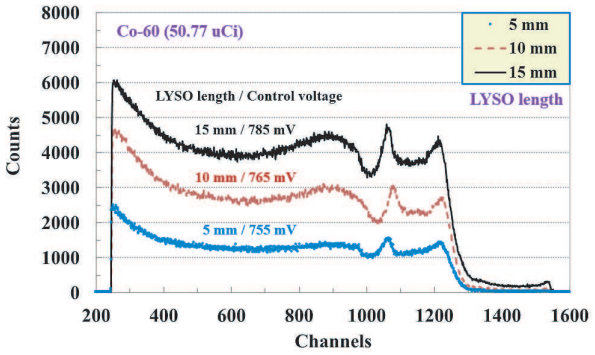

Figure 2: Measured gamma-ray energy spectra according to the length of LYSO.

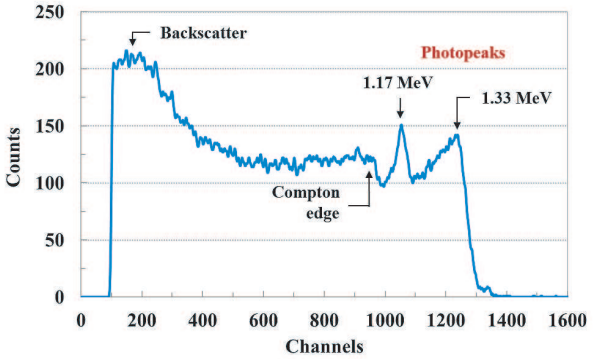

Figure 3: Gamma-ray energy spectrum for Co-60 measured by using the SFORS.

Figure 3 shows the gamma-ray energy spectrum for Co-60 measured by using the reference sensing probe of SFORS. Here, the reference sensing probe was composed of the square-shaped LYSO crystal with dimensions of $3 \times 3 \times 15\,\mathrm{mm}^3$ and the POF with a length of 1 m and a diameter of 3 mm. After a collection time of 180 seconds, the gamma-ray energy spectrum was graphed using the collected data of MCA. As shown in Fig. 3, we obtained the backscatter peak, the Compton edge and continuum, and photopeaks of Co-60 using energy spectroscopy and the measured two photopeaks well matched with the inherent photopeaks of Co-60.

Figure 4 shows the variation of energy spectrum for Co-60 according to the length (L_2) and diameter (L_3) of the POF which was performed as a light-guide to connect between the sensing probe and the PMT. In this test, the control voltage of the PMT power-supply was fixed at 915 mV and it was optimum voltage to obtain typical Co-60 spectroscopy for the POF with a length of 1 m and a diameter of 3 mm. As increasing the length of the POF from 0.1 to 3 m, the original wavelength of the scintillating light might be transmitted differently according to the optical properties of the step-index multi-mode POF, such as a spectral transmissivity and a material absorption. Furthermore, the FWHM of the photopeak increased as increasing the length of the POF because of a modal dispersion as shown in Fig. 4(a). As increasing the diameter of POF from 1 to 3 mm, more propagation modes were permitted in the POF and more light signals having energy spectrum information were transmitted to the PMT via the POF; these were to enable the formation of the photopeaks in spite of the pulse broadening due to the increment of the modal dispersion as shown in Fig. 4(b). Meanwhile, these distortions due to the length and diameter of the POF could be corrected to some extent by changing the control voltage of the PMT power-supply in a permitted range.

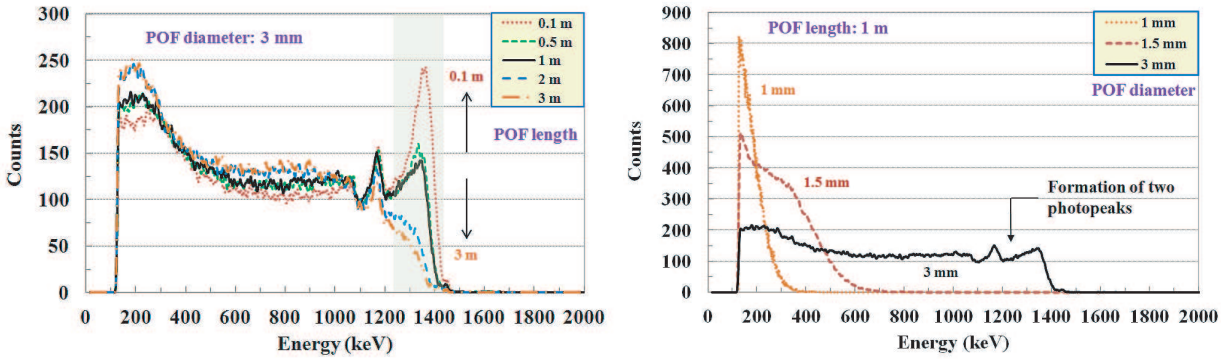

(a) (b)

Figure 4: Variations of gamma-ray energy spectrum according to (a) the length and (b) the diameter of the POF.

4. CONCLUSIONS

In this study, we analyzed the effects of the length variations of LYSO crystal on the energy spectrum and determined the length of the LYSO crystal to obtain the gamma-ray energy spectrum of radioactive isotope considering the absorption efficiency. Additionally, the performance of the fabricated SFORS was evaluated as functions of the length and diameter of the POF which was used to guide scintillating light. In conclusion, we demonstrated that the proposed SFORS could be used for remote gamma-ray energy spectroscopy. It is expected that a novel SFORS which has capabilities in real-time and remote measurements can be developed to obtain accurate gamma-ray energy spectra. Further studies will be carried out to fabricate a SFORS with various kinds of scintillators and metal-coated optical fibers for high temperature applications.

ACKNOWLEDGMENT

This work was supported by the National Research Foundation of Korea (NRF) grant funded by the Korea government (MEST) (No. 2013004348, No. 2012045539, and No. 2012037783).

REFERENCES

1. Huston, A. L., B. L. Justus, P. L. Falkenstein, R. W. Miller, H. Ning, and R. Altemus, "Remote optical fiber dosimetry," *Nucl. Instrum. Methods Phys. Res. Sect. B*, Vol. 184, 55–67, 2001.
2. Yoo, W. J., D. Jeon, J. K. Seo, S. H. Shin, K.-T. Han, W. S. Youn, S. Cho, and B. Lee, "Development of a scintillating fiber-optic dosimeter for measuring the entrance surface dose in diagnostic radiology," *Radiat. Meas.*, Vol. 48, 29–34, 2013.
3. Knoll, G. F., *Radiation Detection and Measurement*, 3rd Edition, 307–352, John Wiley & Sons, New York, 1999.
4. Chen, J., R. Mao, L. Zhang, and R.-Y. Zhu, "Gamma-ray induced radiation damage in large size LSO and LYSO crystal samples," *IEEE Trans. Nucl. Sci.*, Vol. 54, 1319–1326, 2007.

A Novel Multipath Limiting Quadrifilar Helix Antenna for Local Area Augmentation System

James A. Quinlan and Daniel N. Aloi
Department of Electrical and Computer Engineering, Oakland University, Rochester, MI, USA

Abstract— This paper describes the design of a Multipath Limiting Antenna (MLA) for use on Global Positioning Systems (GPS) Local Area Augmentation System (LAAS). This new antenna performs well on both L1 and L2, with independent feeds and element arrays that share the same phase center. This independence allows accurate independent tuning of the GPS bands. It uses single arrays to achieve its pattern, eliminating extra tuning and bifurcation of the phase center. It uses a Quadrifilar Helix Antenna (QHA) as its radiating element. QHA is known for being highly circularly polarized with excellent cross-polarization rejection. The QHA designed in this paper has been modified for wide-beam operation, and for close proximity to ground plane objects. This allows the design and placement of a feed disk underneath each QHA element, and a vertical support to house cabling, simplifying the overall feed system.

1. INTRODUCTION

There is a large interest in automated landing of aircraft, and in development of a Global Positioning Systems (GPS) Local Area Augmentation System (LAAS) as a navigational instrument precise enough to guide automated landing. GPS is a Global Navigation Satellite System (GNSS) operated by the United States Government. GPS satellites broadcast their time and position on Bands L1 (1575.42 MHz) and L2 (1227.6 MHz); receivers use this information to calculate their position. Well designed GPS receivers can achieve horizontal and vertical accuracy of 3 meters and 5 meters, respectively, 95% of the time.

LAAS is an aircraft landing system using Differential GPS (DGPS), in which a reference station broadcasts the difference between the measured satellite pseudoranges and the known fixed position of the receiver antenna. The still-in-design LAAS CAT III requirements feature greater positional accuracy — and, critically, much less time out-of-tolerance. An LAAS reference station must use a stationary ground Multipath Limiting Antenna (MLA) to meet these accuracy requirements.

2. ANALYSIS OF A WIDE BEAM CIRCULARLY POLARIZED MLA ELEMENT

Multipath error is the greatest cause of error in DGPS. An excellent explanation of multipath error can be found in [1]. A good set of requirements for an LAAS MLA can be found in [2]: a pattern requirement of 174° 6-dB beamwidth and all levels below −5° at least 30 dB below peak, for both L1 and L2. Several previous MLAs are Integrated MLA (IMLA), integrating an MLA for low zenith angles with a separate High Zenith Antenna (HZA). This leads to increased error, such as the bifurcation of the phase center at the handoff angle.

To assist in meeting these requirements, we use a vertical array with 21 elements, similar to that featured in [3]. This reduces our design task to finding a wide beamwidth element that can be assembled into a vertical array, and preferably is Right Hand Circularly Polarized (RHCP) for further multipath mitigation. The vertical array is 21 elements (11 active, 10 passive), ideally spaced half wavelength apart. A support structure is required for this; we chose a 2.2 in. OD metal conduit to provide a center support and house cabling to the elements. Note that 2.2 in. is 0.29λ at L1 and 0.23λ at L2, with λ representing free-space wavelength.

The electric field vector of an RHCP wave, as viewed from the source, can be represented by

$$(E_x, E_{yY}, E_{Zz}) \propto \left(\cos\frac{2\pi}{\lambda}(ct-z), \sin\frac{2\pi}{\lambda}(ct-z), 0\right) \tag{1}$$

This is assuming the wave points in the positive Z direction. A fixed, single-point receiving antenna would see this wave as:

$$(E_x, E_y, E_z) \propto (\cos\rho, \sin\rho, 0); \quad \rho = \frac{2\pi ct}{\lambda} \tag{2}$$

If the wave deviates from this direction, the receiver wave appearance becomes:

$$(E_x, E_y, E_z) \propto (\cos\rho(1-\sin\theta\cos\phi), \sin\rho(1-\sin\theta\sin\phi), \cos\rho\sin\theta\cos\phi + \sin\rho\sin\theta\sin\phi) \quad \rho = \frac{2\pi ct}{\lambda} \tag{3}$$

A quadrature feed is a well established method of providing circular polarization, with 4 elements progressively phased 90° apart. This establishes a 90° phase delay on E_x with respect to E_y. The design of these elements becomes difficult with a center supported vertical array, as these 4 elements are spaced apart at least as far as the center support. In practice, they are spaced even further to reduce near-field effects of a metallic support. This spacing causes the equidistant assumption to break apart as we move away from $\theta = 0°$.

Consider the case of 4 infinitesimal monopoles in the XY plane. Elements 1 and 3 are located along X, separated by distance D. Elements 2 and 4 are located along Y, separated by distance D. Each element experiences time displacement of the signal, creating:

$$\begin{aligned} \rho_1 &= \frac{2\pi c\,(t - D\sin\theta\cos\phi)}{\lambda} \\ \rho_2 &= \frac{2\pi c\,(t - D\sin\theta\sin\phi)}{\lambda} \\ \rho_3 &= \frac{2\pi c\,(t + D\sin\theta\cos\phi)}{\lambda} \\ \rho_4 &= \frac{2\pi c\,(t + D\sin\theta\sin\phi)}{\lambda} \end{aligned} \tag{4}$$

When D is non-trivial compared to the wavelength, extra phase delays are introduced that can be comparable to the 90° phase delay between E_x and E_y. Since real-world elements are not infinitesimal, D also varies along the length of the antenna element making time-displacement analysis is more difficult. Furthermore, the center support as a ground plane, reflector, and refractor. These phenomena can cause undesired nodes in the gain pattern of a wide beam quadrature fed antenna.

3. CONSTRUCTION OF WIDE BEAM MLA ELEMENT

One method of making it easier to predict and mitigate nodes is to use a quadrifilar helix antenna (QHA). Helices travel in a radial direction, keeping D constant among the elements. In [4] there is a good explanation about printed QHA (PQHA), in which the 4 elements are printed on a thin dielectric substrate and wrapped around a cylinder. This construction lowers weight and cost.

Helical antennas traditionally consist of multiple turns, and are excited well above their primary resonance, yielding a narrow-beam pattern. To meet to our need for a very wide beam-width, we designed in Ansoft HFSS a PQHA with turn number less than 1/10, and use a large helix diameter of 5 inches. We created one set of quadrature elements for L1, and another set offset by 45° for L2. We placed a ground plane underneath that is slightly smaller in same diameter. And to help feed impedance and the pattern, we raised the helix slightly, placed a ground rim underneath (printed

Figure 1: Ultra wide quadrifilar helix antenna for L1 and L2.

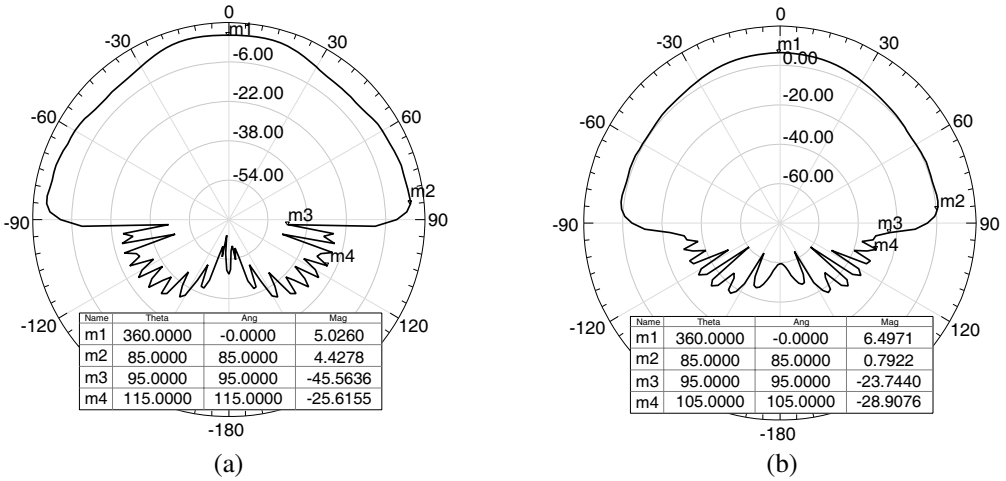

Figure 2: Radiation pattern for (a) L1 and (b) L2 for 21 element array.

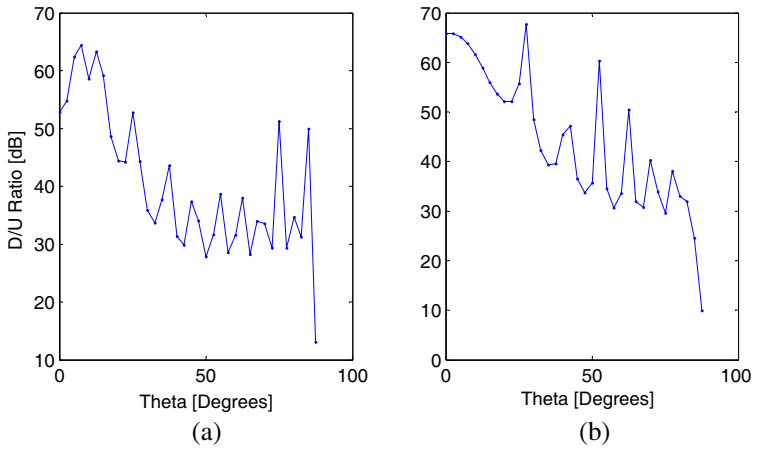

Figure 3: U/D gain ratio for (a) L1 and (b) L2 for 21 element array.

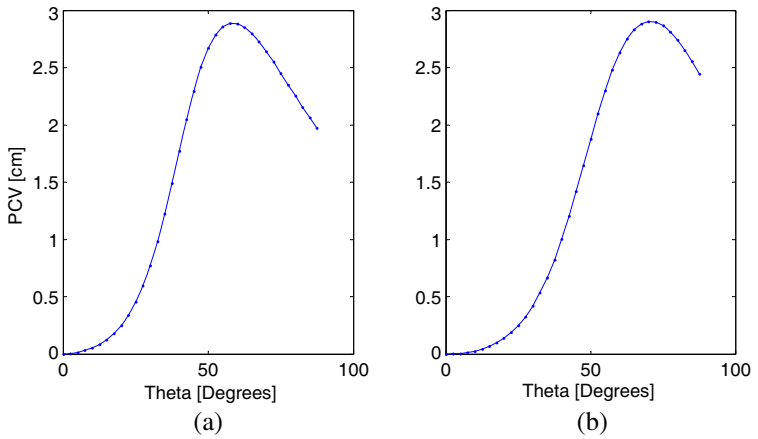

Figure 4: Phase center variance for (a) L1 and (b) L2.

on the same wrapped film as the helix elements), and added feed tabs to the ground plane. The ground plane houses a stripline feed system to provide the two quadrature feed systems. We call the structure an Ultra Wide Quadrifilar Helix Antenna (UWQHA). Figure 1 shows construction details.

Array theory requires array spacing less than half-wavelength to avoid nulls. We spaced our UWQHA 9 cm apart in the vertical direction, corresponding to 0.47λ at L1 and 0.37λ at L2. An

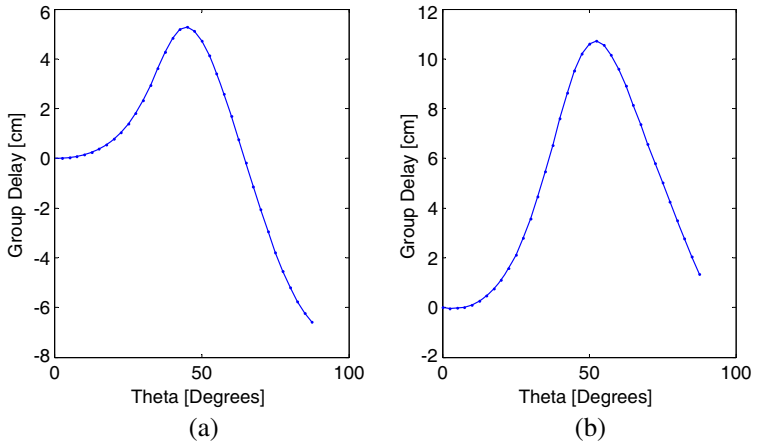

Figure 5: Group delay for (a) L1 and (b) L2.

HFSS simulation was run with one active UWQHA between two passive UWQHA (simulating array performance). The −10 dB Bandwidth is greater than 300 MHz for L1 and 200 MHz for L2; the latter suggesting that L5 (at 1176 MHz) could also be received with this antenna. Figure 2 shows the Radiation Pattern for a 21 element array, showing performance target being met for L1 and L2. Figure 3 shows the Desired/Undesired (Up/Down Right Hand Circularly Polarized) Gain Ratio, showing at least 30 dB difference throughout most of the range of operation. Figure 4 shows the Phase Center Variance (compared to $\theta = 0°$) at less than 3 cm difference for $\theta < 90°$. Figure 5 shows Group Delay (compared to $\theta = 0°$) at less than 7 cm for L1 and 12 cm for L2, for $\theta < 90°$.

4. CONCLUSION

This paper presented an Ultra Wide QHA and its use as a MLA. The UWQHA is a good candidate for wide beam vertical arrays, with a gain pattern and construction that array well. The application of a vertical array to the UWQHA radiation pattern allows operation as an LAAS reference antenna.

REFERENCES

1. Counselman, III, C. C., "Multipath-rejecting GPS antennas," *Proceedings of the IEEE*, Vol. 87, No. 1, 86–91, 1999.
2. Lopez, A. R., "GPS landing system reference antenna," *IEEE Antennas and Propagation Magazine*, Vol. 52, No. 1, 104–113, 2010.
3. Lopez, A. R., "GPS ground station antenna for local area augmentation system, LAAS," *Proceedings of the 2000 National Technical Meeting of The Institute of Navigation*, Anaheim, U.S., 2000.
4. Fu, S.-Q., S.-J. Fang, K. Lu, and Z.-B. Wang, "Printed quadrifilar helix antenna with integrated feed network," *IEEE International Symposium on Microwave, Antenna, Propagation and EMC Technologies for Wireless Communications*, 67–69, Beijing, China, 2009.
5. Rao, B. R., W. Kunysz, R. Fante, and K. McDonald, *GPS/GNSS Antennas*, Artech House, Boston, 2013.

Short-temporal Magnetosphere-ionosphere Predictors of Catastrophic Earthquakes

N. P. Sergeenko and A. L. Kharitonov
Pushkov Institute of Terrestrial Magnetizm, Ionosphere and Radiowave Propagation of the Russian Academy of Sciences, Moscow, Russia

Abstract— The analysis of ionosphere-geomagnetic predictors of catastrophic earthquakes is carried out. Formation of traveling large-scale irregularities of the electronic concentration of the positive sign in the main peak of the ionosphere and increase of the local magnetic field near epicenter of earthquakes are illustrated. For the first time splashes AE-index characterizing amplitude of the auroral electrojet 15–17 hours prior to the moment of the main push are found out. Existence of this effect on examples of nuclear explosions on various latitudes zones is confirmed. The possible physical mechanisms of occurrence of the apparent effects with use of literary data on satellite observations in the magnetosphere and radiating belts are discussed.

1. INTRODUCTION

There was the considerable quantity of the researches devoted to search of predictors of earthquakes in the ionosphere and the geomagnetic field last years. Possible physical mechanisms of observable effects were discussed. Works can be divided conditionally into two approaches: one approach is connected with studying of effects of the internal source located in Earth's crust [1], other approach is directed on research of the external reasons of the earthquakes, assuming that non-stationary geoeffective processes on the Sun and influence of fluctuations of the interplanetary environment on the change of seismic activity [2].

Geophysical predictors are expedient for dividing into three groups: the precursors predicting earthquakes in the very long-temporal future, long-temporal predictors of earthquakes and short-temporal predictors of earthquakes. This work concerns studying short-temporal magnetosphere-ionosphere predictors of earthquakes with advance time approximately 10–15 hours.

2. THE ANALYSIS OF IONOSPHERE-GEOMAGNETIC PREDICTORS OF EARTHQUAKES

In [3, 4] it is established that traveling large-scale irregularities of electronic concentration of the positive sign are formed in the main peak of the ionosphere 10–15 hours prior to the moments of catastrophic earthquakes with magnitude $M \geq 5$ and localization of ~ 1 thousand km to earthquake epicenter. Irregularities are characterized by contrast of 15–50% against the background electronic concentration, the horizontal sizes are 1–3 thousand km, speed of horizontal moving is the order of sound speed. They are the closed objects and can move on the distances exceeding radius of the Earth, up to round-the-world movements.

The main source of the information about ionosphere irregularities are files of critical frequencies of the ionosphere F2 layer on the world network of ionosphere stations of vertical sounding. At the analysis the relative variations δf_0F2 are calculated, that excludes regular seasonal and daily variations. For the description of geomagnetic conditions Dst, and AE-indexes were used. Dst — the index characterizes occurrence and development of the large-scale planetary geomagnetic storm. For identification of effects of substorms in the ionosphere we used the AE-indexes. We were considered the periods of disturbance at $AE > 100\,\mathrm{nT}$ [5].

$\delta f_0F2(t)$ variations during 10–12.08.1985 on of Japan, Irkutsk, Tomsk, Sverdlovsk, Moscow ionosphere stations are resulted on Fig. 1. This is the example when irregularities $\delta f_0F2(t) > 0$ appeared before catastrophic earthquakes were considered as predictors of the earthquakes. At this time there were three earthquakes with magnitudes $M \geq 6$ in of Pacific ocean, moments of their beginning are noted by vertical straight lines. In Fig. 1 three groups of impulses near to dotted straight lines are allocated. In all three cases some hours prior to earthquakes there were positive indignations with amplitude $15 \div 20\%$, traveling with the speed to 1000 km/hour on distances of 7–8 thousand km. This result corresponds to that rare situation when movement of the irregularities appeared before earthquakes, coincides with chains of stations of the vertical sounding of ionosphere located along the sublatitude arch of the big circle. This figure illustrates character of alternation of impulses from three various sources. Except described seismic - ionosphere effects,

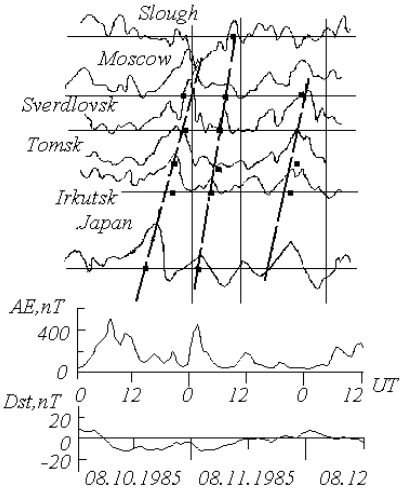

Figure 1: Ionosphere-geomagnetic conditions during earthquakes 08.10–12.1985.

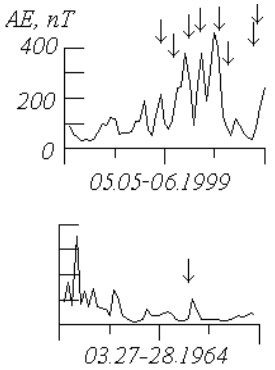

Figure 2: Geomagnetic conditions during earthquakes 05.06.1999 (see the table) and 03.27–28.1964.

on practically quiet geomagnetic background ($Dst \leq 10$ nT) 10.08 and 11.08 there were two geomagnetic substorms with amplitudes $AE \sim 500$ and 400 nT, and both substorms have occurred 17 and 13 hours accordingly prior earthquakes.

AE-indexes during time of "parade of earthquakes" 05.05–06.1999 are showed on Fig. 2. Characteristic of these earthquakes are resulted in the table. The moments of the beginning of earthquakes are noted in the Fig. 2 by arrows. It is visible, that AE has increased to ~ 130 nT ~ 15 hours prior to first jolt, further AE-splashes before all earthquakes also are observed. On the right on Fig. 2 geomagnetic characteristics during Alaska earthquake with magnitude $M = 8.5$ which was the subject of attention of many researchers (for example, [6]) are resulted. It is visible, that before this earthquake AE splash also is observed.

The beginning, geographical coordinates, the depth and magnitudes of 9 earthquakes on 05.06.1999.

No.	**beginning, UT**	**φ, degrees**	**λ, degrees**	***d*, km**	***M***
1	040123.88	19.25	145.53	164	5.00
2	041926.72	56.48	−152.86	24	5.10
3	065446.12	−11.22	66.08	10	5.30
4	090508.29	−32.79	−179.37	109	5.20
5	111530.98	−5.32	141.76	40	5.20
6	132132.30	−34.02	−178.97	33	5.50
7	135635.70	−5.25	141.71	33	5.10
8	230053.12	29.50	51.88	33	6.30
9	231324.85	29.40	51.90	33	5.30

3. THE ANALYSIS OF GEOMAGNETIC EFFECTS OF NUCLEAR DETONATIONS

For comparison we will consider behaviour of magnetosphere AE-index at artificial created situations with emitting of high energy particles in the ionosphere at experimental nuclear detonations.

Let's address to the analysis of geomagnetic conditions during nuclear detonations on high-latitude Novaya Zemlya nuclear experimental range. On Fig. 3(a) AE-indexes variations during 2 explosions are resulted. Both explosions of the megaton class, explosion 10.23.1961 have been made in air, explosion 10.27.73 — in the drill. By arrows in Fig. 3 the moments of explosions are shown. It is visible, that explosion in air was accompanied by AE splash to ~ 100 nT, explosion in the drill — to $AE \sim 600$ nT.

On Fig. 3(b), AE-indexes during nuclear explosions on Semipalatinsk and Nevada experimental ranges are resulted. From drawing obviously, that at middle latitudes nuclear explosions are

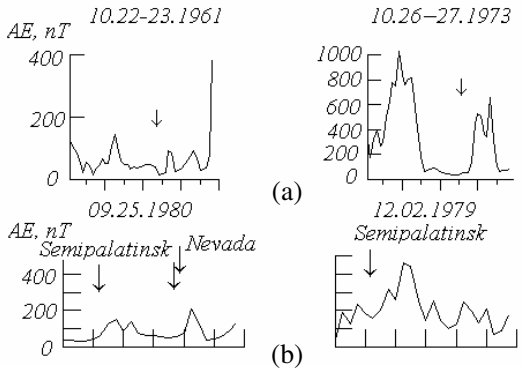

Figure 3: (a) Behaviour of the AE-index during nuclear explosions on Novaya Zemlya experimental range; (b) near Semipalatinsk and Nevada experimental ranges.

accompanied by effects in behaviour of the AE-index.

4. DISCUSSION

All observable splashes in the AE-index in preparation of earthquakes and during nuclear explosions can testify about seismic-magnetosphere communications.

Let's consider research experiments with nuclear explosions which were spent for studying of capture of energetic particles [7] by the magnetic field of the Earth such as it occurs at strong earthquakes. These particles appeared at 200–600 km altitudes over sea level. As the result of such explosions artificial radiating belts were created which, as well as natural radiating belts, represent the zone of huge concentration of the charged particles round the Earth, basically energetic electrons and protons.

At the first moment the particles formed at nuclear explosion in the ionosphere, are emitted in some certain point of Space. In some seconds they usually spread along the power line of the geomagnetic field corresponding to position of nuclear explosion. And in some hours at the expense of drift round the Earth they extend on all longitudes and form the "coverlet" shrouding the Earth. At the same time, the measurements made on "Ariel" satellite, have shown, that electrons of high energy arising after nuclear explosion, very quickly appeared at high latitudes [8]. And in that case the AE-index should increase at nuclear explosions.

Formation of the charged particles does not stop and after the completion of reaction of division. Division splinters contain superfluous quantity of neutrons and consequently break up with electrons emission. Thus, after nuclear explosion electrons are formed within several minutes and even hours. Formation such electrons is the most important source of artificial radiating belts.

By preparation of strong earthquake in the ionosphere and magnetosphere, apparently, there are processes similar to the above described processes at emitting of particles from nuclear explosions, that is the fault tectonic zone of Earth's crust is formed at the expense of micro cracks and energy are given off more big than energy of nuclear explosion to atmosphere. It is known, that porous pressure of fluids essential influence on occurrence of earthquakes. Therefore by earthquake preparation some hours prior to the basic push often there is the emission of radon and some other gases containing in the structure elements of radiating disintegration from the depth of the tectonosphere in the atmosphere [9]. When there is the emanation of such gases on the eve of earthquake, particles of elements of radiating disintegration, also as well as after nuclear explosions, start to move in space and time. Thus process of preparation of earthquake is often accompanied by electromagnetic radiation which also actively promotes penetration of the charged particles into the ionosphere. It is possible to consider movement of these charged particles as superposition of almost circular rotation round the power line of the magnetic field, rectilinear movement along the power line of the field and drift across power lines.

Thus, radioactive particles, after their emission in atmosphere as the result of nuclear explosion or emanations of radon and other gases with presence in their structure of radioactive elements test on themselves influence of several forces. Drift of particles along power lines of the magnetic field including in auroral areas where the AE-index is fixed, leads to its increase. Satellites measurements have shown, what even during the quiet period, the high-latitude border grasped electrons

corresponds approximately $\varphi \sim 75 \pm 2$ degrees northern and the southern latitude but should not settle down above 77 degrees of latitude.

It is known, that at longitudinal drift negative and positive charges drift in opposite directions. Therefore there is the division of charges and there is the azimuthal electric field. As the result there is the component of drift speed directed on radius from the centre of the Earth, that also promotes penetration of the charged particles from near surface of the Earth before earthquake in the ionosphere. Under some conditions in exosphere such drift can arise with the speed (V) from formula:

$$V = c(\mathbf{E} \times \mathbf{B})/B^2 \tag{1}$$

where $(\mathbf{E} \times \mathbf{B})$ — the multiplication of vectors of the electric and the geomagnetic field; c — the speed of the light. Drift of the charged particles under the influence of electric field is, as the rule, the prevailing kind of drift.

Formation positive irregularities of electronic concentration in the ionosphere in earthquake preparation period can be caused as emitting particles, and the processes similar to ionosphere effects from magnetosphere substorms (with growth AE). Electric fields of magnetosphere origins on ionosphere altitudes amplify in high latitudes to values of 200 mV/m, come on middle and even on equatorial latitudes, reaching there values of 10–15 mV/m at middle latitudes and 2–5 mV/m into the low latitudes. The amplitude of electric fields in 2–3 times more low in time of the typical not indignant conditions in the magnetosphere. Direct effects of strengthening of electric fields consist in redistribution of ionosphere plasmas by means of horizontal (in high latitudes) and vertical (in middle and low latitudes) carrying over, and also in Dgoul's heating of the neutral and ionic component owing to the ion-neutral friction. Increase of electronic concentration can be observed at the meridian electric field causing zone drift of plasma, and also to be the consequence of distribution of internal gravitational waves (in the afternoon at middle latitudes).

5. CONCLUSION

The analysis of ionosphere and geomagnetic data has shown, that the geophysical chain of the connected short-temporal, semidiurnal, magnetosphere, geomagnetic, ionosphere precursors of catastrophic earthquakes is observed. Tectonic preparation of earthquake can lead to generation magnetosphere substorms (AE-splashes) and to formation of large-scale traveling irregularities of electronic concentration in the main peak of the ionosphere. In the combination to other already studied precursors results of this work can be used in algorithms of the geophysical forecast of time of beginning and the place of the future earthquake.

REFERENCES

1. Rikitaki, T., *Earthquake Forecasting*, 388, 1982.
2. Sutinsky, A. D. and D. A. Oborin, "Influence of indignations of the interplanetary environment on seismicity and atmosphere of the Earth," *Geomagnetism and Aeronomy*, Vol. 37, 138, 1997.
3. Kalinin, U. K., A. A. Romanchuk, N. P. Sergeenko, and V. N. Shubin, "The large-scale isolated disturbances dynamics in the main peak of electronic concentration of ionosphere," *Journal of Atmospheric and Solar-terrestrial Physics*, Vol. 65, Nos. 11–13, 1175–1177, Jul.–Sep. 2003.
4. Danilkin, N. P., U. K. Kalinin, N. P. Kotonaeva, and I. L. Larichev, and N. P. Sergeenko, "Macroscale ionospheric irregularities registered by the MIR onboard ionosound," *International Journal of Geomagnetism and Aeronomy*, Vol. 4, No. 3, 2004.
5. Nishida, A., *Geomagnetic Diagnosis of the Magnetosphere*, 298, Springer-Velag, 1978.
6. Leonard, R. S. and R. A. Barnes, "Observation in ionospheric disturbances following the Alaska earthquake," *J. Geophys. Res.*, Vol. 70, No. 5, 1250–1253, 1965.
7. Hess, U. N., *Operation of "Sea Star"*, 8, Atomizdat, Moscow, 1964.
8. Durney, A. C., H. Elliott, R. J. Hynds, and J. J. Quently, "Sattellite observation of the energetic particle flux produced by the high-altitude nuclear explosion of July 9, 1962," *Nature*, Vol. 195, 1245, 1962.
9. Wakita, H., Y. Nakamura, K. Notsu, M. Noguchi, and T. Asada, "Radon anomaly: A possible precursor of the 1978 Izu-Oshima-Kinkai earthquake," *Science*, Vol. 207, 882–883, 1980.

Compact Low Phase Noise Oscillator Using Symmetrical Square Open-loop with Loaded T-stubs Resonator

S. J. Cho and N. Y. Kim
RFIC Center, Kwangwoon University, 447-1 Wolgye-dong, Nowon-ku, Seoul 139-701, Korea

Abstract— The design of a miniaturized microstrip stubs-loaded square open-loop with asymmetrical feeder lines resonator and its implementation to a microwave oscillator is studied in this paper. The adopted resonator is based on a combination of electric and magnetic couplings in the central open-gaps of the square loop resonators. Moreover, the combined couplings generate an electromagnetic (EM) flux between the two square open-loop resonators. The maximum coupling can be obtained by adjusting the open-loop gap, mounting the two open-loop resonators spacing, and the orientation of loaded-T-stubs inside the loop resonators. The asymmetrical port terminals also help to couple EM energy by maintaining 50 Ω impedance matching with input/output devices. The improved high Q factor characteristics and the higher transmission zero can be obtained high oscillator power and low phase noise characteristics. The resonator performance shows a return loss of −24.8 dB and an insertion loss of −1.6 dB at 5.9 GHz. In addition, according to design and performance of the resonator, this structure resulted in an optimized oscillator. The oscillator with this proposed resonator shows a good phase noise performance of −104.62 dBc/Hz at a 100 kHz offset from the carrier frequency of 6.2 GHz with an output power of 14.21 dBm.

1. INTRODUCTION

In case of microwave oscillator, due to excellent frequency conversion, stabilized carrier generation and low phase noise, microwave resonators are essential passive components. A good resonator needs to have an excellent Quality Factor (Q-factor) because Q-factor is deeply critical to the low phase noise of microwave oscillator. Resonators have seen significant development in these many different types such as the hairpin [1], ring [2], spiral [3] and dielectric resonators [4]. In the case of the conventional hairpin structure, its design has an inherently low Q-factor. Moreover, it needs large dimension because of the necessary additionally external resonator components. Dielectric substrates have a high Q-factor and are more stable at high temperatures, but they are costly. Therefore, it is a significant factor in resonator design to achieve a high Q-factor, low cost, reduced size. In order to achieve these three factors, we designed a resonator using square open-loop inside with the loaded shunt open T-stub techniques and a teflon substrate which provides a low cost, a good performance, and stability at high temperatures [5]. The resonator is miniaturized because square open-loop structures with small gaps and thin shunt T-stubs-loaded inside the loops that can concentrate both electric and magnetic couplings because of capacitive and inductive properties. Therefore, the high Q-factor of resonator is proved by its low phase noise parameter in the oscillator.

2. EXPERIMENTAL PROCEDURE

2.1. Design of High Q-factor Square Open-loop with T-stub Loaded Resonator

Figure 1 shows a schematic design layout of the proposed resonator with necessary dimensions and showing electric and magnetic coupling schemes. The square open-loop resonators tided up together for 5.9 GHz resonance frequency. The internally loaded T-stubs inside the wall enhance to combine magnetic coupling [6] and open-gap of the square loops placing in parallel with gap, g make to develop strong capacitive effects, hence electric coupling is possible [7]. The structure of combining two such open-loop resonators gives a strong inductive-coupling and effective capacitive-coupling. Moreover, the asymmetrical port terminals also help to couple EM energy easily by maintaining 50 Ω impedance matching with input/output devices. Many researchers have studied different stubs-loaded planar loop filters with various bandwidths for different applications. The proposed open-loop filter is able to be optimized Q-factor compared with the previous design works [8]. This loaded T-stub help magnetic field coupling for high Q-factor designed in Teflon substrate using wet etching techniques in the printed circuit technology. In the schematic, it can be clearly seen that the major filter dimensions and coupling behaviors. The gap distance, g and s between the two loops plays a vital role for designing the filter with desired resonant frequency and bandwidth. The Q-factor can be found by using the 3 dB bandwidth from the resonant frequency.

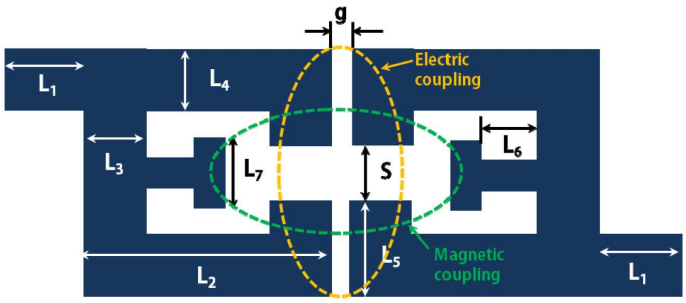

Figure 1: Layout of the proposed resonator.

The Q-factor is critical relation with phase noise performance of the oscillator and it can be estimated as shown in equation:

$$L(\Delta\omega) = 10\log\left[\frac{2FKT}{P_s}\left\{1+\left(\frac{\omega_0}{2Q\Delta\omega}\right)^2\right\}\left(1+\frac{\omega_1/f^3}{\Delta\omega_1}\right)\right] \quad (1)$$

2.2. Design of Oscillator Using Novel Resonator

The square open-loop inside with the loaded shunt open T-stub resonator is used in the oscillator in order to achieve an excellent output power and a low phase noise. The microwave oscillator consists of active devices and a frequency determining system, i.e., the resonator. The whole microwave oscillator circuits with resonator are shown in Fig. 2. Whole design is used the ADS tool; it utilizes an ATF13876 GaAs FET transistor. In this measurement, the FET is biased with 3.5 V of input drain voltage and has a 48 mA drain current at a −0.35 V gate voltage. The oscillator's gate biasing adopts a self-biasing network design by using $\lambda/4$ microstrip lines. The resonator is located in a series connection with the gate of the transistor. The transistor and spiral spurline resonator have a feedback loop gain greater than one. In order to provide DC bias blocking, we designed a stepped filter at the output port. Radial open stubs are used as an RF choke in both the drain and source in order to enhance the negative resistance. Therefore, the matching stub needs to be optimized in order to generate oscillation and control the output power. The oscillator is made with an optimized resonator in order to get an excellent output power and low phase noise characteristics.

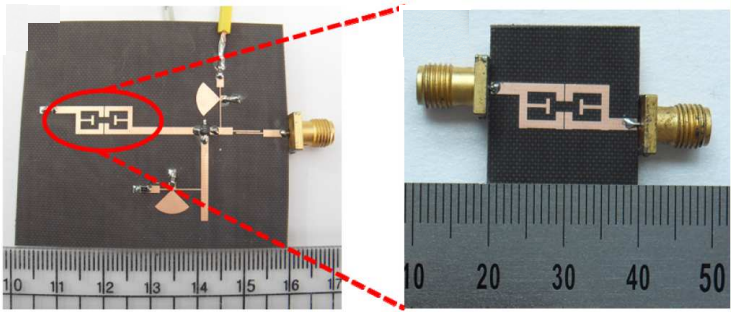

(a) (b)

Figure 2: (a) Photograph of the final fabricated oscillator, (b) enlarged the square open loop with loaded Tstubs resonator.

3. RESULTS AND DISCUSSIONS

A Teflon substrate with a relative dielectric constant of 2.54, a height of 0.54 mm, and a thickness of 0.18 mm was used for the fabrication. The simulation and measured results of the resonator agreed well; the results are shown in Fig. 3. The fabricated resonator was measured using an Agilent 8510C Vector Network Analyzer resonating at 5.9 GHz. The resonators' performances show a return loss of −24.8 dB, an insertion loss of −1.6 dB, and a quality factor of 150 at 5.9 GHz. The oscillator power and phase noise characteristics measured with an Agilent E4440A spectrum analyzer. Figure!4 show an output power of 15.44 dBm and a second harmonic suppression of −48.30 dBc, a phase noise characteristic of −104.62 dBc/Hz at a 100 kHz offset at a frequency of 6.2 GHz.

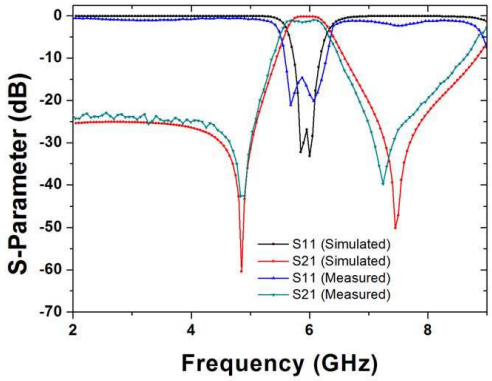

Figure 3: Simulated and measured S-parameter responses of the proposed resonator.

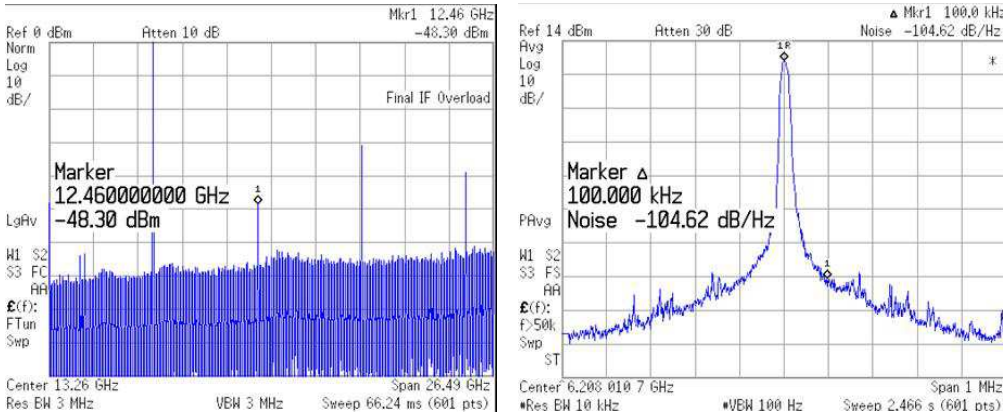

(a) (b)

Figure 4: (a) Measured output spectrum with the harmonic characteristics of the oscillator, (b) measured phase noise characteristics of the oscillator.

4. CONCLUSION

Low phase noise microwave oscillators using a symmetrical T-stubs square open-loop resonator are investigated, which are applied to C-band down or up-converter in a radar system. This proposed resonator has not only a high Q-factor but also an enhanced high oscillator performance compared to other square open-loop types under the same conditions. As a result, this microwave oscillator has a good output power and a low phase noise. Additionally, the micro strip structure application will be extended in MMIC process to obtain low cost and enable a sub miniaturization.

ACKNOWLEDGMENT

This research was supported by the National Research Foundation of Korea (NRF) grant funded by the Korea government (MEST) (No. 2012-0009224) and (No. 2012R1 A1A2004366). This work was also supported by a Research Grant from Kwangwoon University in 2013.

REFERENCES

1. Hong, J. S. and M. J. Lancaster, "Cross-coupled microstrip hairpin resonator filters," *IEEE Trans. Microw. Theory Tech.*, Vol. 46, No. 1, 118–122, 1998.
2. Kanadea, S. A. and V. Puri, "Study of thick film $Ni(_{1-x})Co_xMn_2O_4$, ($0 <= x <= 1$) using overlay technique on thick film microstrip ring resonator," *Microelectron. J.*, Vol. 37 No. 1, 1302–1305, 2006.
3. Cho, S. J. and N. Y. Kim, "A novel spiral meander spurline resonator and its implementation to a low-phase noise oscillator," *Microw. Opt. Tech. Lett.*, Vol. 53, No. 10, 2258–2262, Oct. 2011.
4. Panaitov, G. I., R. Ott, and N. Klein, "Dielectric resonator with discrete electromechanical frequency tuning," *IEEE Tran. Microw. Theory. Tech.*, Vol. 53, No. 11, 3371–3377, 2005.

5. Li, L., H. Liu, B. Teng, Z. Shi, W. Li, X. Li, and S. Wang, "Novel microstrip lowpass filter using stepped impedance resonator and spurline resonator," *Microw. Opt. Tech. Lett.*, Vol. 51, No. 1, 196–197, 2009.
6. Maharjan, R. K., B. Shrestha, and N. Y. Kim, "Compact microstrip square openloop bandpass filter using open stubs," *Electron Lett.*, Vol. 48, No. 3, 333–334, 2012.
7. Maharjan, R. K. and N. Y. Kim, "Miniature stubs-loaded square open-loop bandpass filter with asymmetrical feeders," *Microw.Opt. Tech. Lett.*, Vol. 55, No.2, 329–332, 2012.
8. Mondal, P. and M. K. Mandal, "Design of dual-band bandpass filters using stubloaded open-loop resonators," *IEEE Tran. Microw. Theory. Tech.*, Vol. 56, 150–155, 2008.

Open Stub Band-pass Filter Using Stepped Impedance Resonator for Size Reduction

K. C. Yoon[1], H. Lee[2], J. G. Lee[2], J. G. Park[2], T. Y. Kim[2], T. S. Jung[2], and J. C. Lee[2]

[1]RFIC Research Center, Kwangwoon University, 447-1 Wolgye-Dong, Nowon-ku, Seoul 139-701, Korea
[2]Department of Radio Science & Engineering, Kwangwoon University
447-1 Wolgye-Dong, Nowon-ku, Seoul 139-701, Korea

Abstract— This paper shows an open-stub narrow band-pass filter using a stepped-impedance-resonator (SIR). A SIR is adopted instead of transmission line to reduce the size of the BPF on the low dielectric substrate. The size of the conventional narrow BPF is reduced by more than 50% of its length of the transmission line within the inverter. The experimental results show that the insertion loss is 0.85 dB, return loss is 20.8 dB, and the fractional bandwidth is 10% at the center frequency of 5.8 GHz. The size of the filter is $12.7 \times 18.56\,\mathrm{mm}^2$.

1. INTRODUCTION

In wireless communication systems, band pass filter (BPF) is an essential component, which is usually used in both receivers and transmitters. The important factors for designing the band-pass filters are the characteristic of response, size reduction, and low cost [1]. To reduce the size of a band-pass filter (BPF), high (ε_r) substrate can be used while the cost is high. To get a compact size [1] and lower cost, several types of resonators such as U-shape resonator, SIR (Stepped Impedance Resonator) [2], and stubs components, have been proposed to design different kinds of BPFs [3].

Among these popular filters, a BPF with half-wavelength open-stubs shows very wide bandwidth [4]. If a stub BPF is designed to get narrow bandwidth ($< 10\%$) characteristic, the impedances of the stubs would be too low and the stubs can hardly be realized. The BPF with half-wavelength open-stubs in which narrow bandwidth can be obtained, has been suggested by adjusting the position of stubs using the external quality factor, Q_e without changing the impedance of the stubs [5]. In this paper, a narrow BPF with half-wavelength open-stubs is suggested to further reduce the horizontal-transmission line. In this case, the SIR can be used instead of transmission line to reduce the size of the BPF on the low dielectric substrate. From the experiment results, the new narrow BPF has been reduced in size by half-length as compared with the conventional narrow BPF in the transmission line.

2. BASIC STRUCTURE OF SIR

A half-wavelength SIR is composed of two sections of low impedance at both sides and high impedance in the middle as shown in Figure 1 [6].

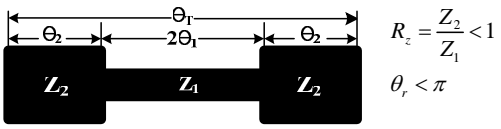

Figure 1: Structure of the stepped impedance resonator.

The input admittance Y_{in} seen from an open-end is given as [6],

$$Y_i = jY_2 \frac{2(R_z \tan\theta_1 + \tan\theta_2)(R_z - \tan\theta_1 \tan\theta_2)}{R_z(1-\tan^2\theta_1)(1-\tan^2\theta_2) - 2(1-R_z^2)\tan\theta_1 \tan\theta_2} \tag{1}$$

the resonant conditions are $Y_i = 0$ and $R_z = Z_2/Z_1 = \tan\theta_1\theta_1$, where the $\theta = \theta_1 = \theta_2$. Equation (1) is simplified as

$$Y_i = jY_2 \frac{2(1+R_z)(R_z - \tan^2\theta)\tan\theta}{R_z - 2(1+R_z+R_z^2)\tan\theta}. \tag{2}$$

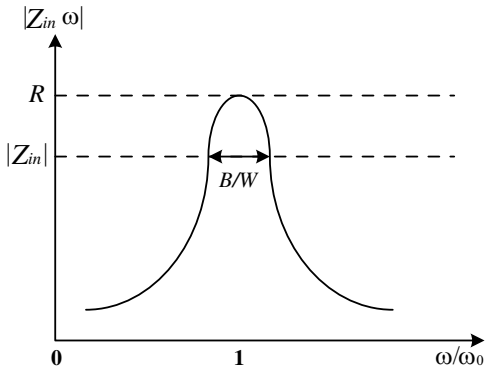

Figure 2: Input impedance magnitude $|Z_{in}|$ of the half-wavelength open-end circuited SIR vs. Frequency.

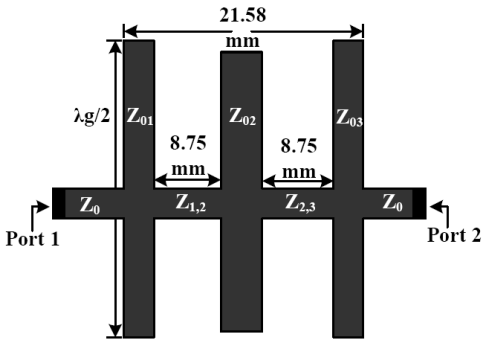

Figure 3: Structure of the BPF with half-wavelength open stubs for narrow bandwidth.

The resonant condition is written as

$$\theta = \theta_0 = \tan^{-1}\sqrt{R_z}. \tag{3}$$

The open-circuited half-wavelength SIR is expected to behave as a parallel resonant circuit in terms of magnitude of its input impedance $|Z_{in}|$ [6] and to be of the form as shown in Figure 2.

3. A NARROW BANDWIDTH BAND-PASS FILTER WITH HALF-WAVE LENGTH OPEN STUBS

A bandpass filter consists of series quarter wavelength transmission lines and shunt half-wavelength open stubs [6]. In general, if a BPF with stubs is designed to get narrow bandwidth ($< 10\%$) characteristic, the impedances of the stubs would be too low and the stubs can hardly be realized [6]. Therefore, this type of BPF can be a candidate for wide-band BPF application [6]. The BPF suggested in this paper, however, has flexibility in bandwidth by adjusting the position of stubs using the external quality factor, Q_e without changing the impedance of the stubs as shown in Figure 3.

The filters such as interdigital, combline, and hairpin filters are generally designed with tapped type, in which the position of tapping, l_t is the important factor to determine the bandwidth of filters [7]. The external quality factor, Q_e can be obtained by phase response of the stubs ($\omega_o/\Delta\omega_{\pm 90}$) with variation of the position (l_t) of the open stubs [6, 7]. The external quality factor, Q_e is determined by the EM simulation with the physical dimensions and the locations of open stubs. The external quality factor Q_e can be redefined as a function of location of stubs, l_t which is defined as the fractional bandwidth [7].

Figure 4 shows the simulation and measurement results for the flexible narrow bandwidth BPF with half-wave length open stubs. From the figure, the insertion losses of less than 0.6 dB and

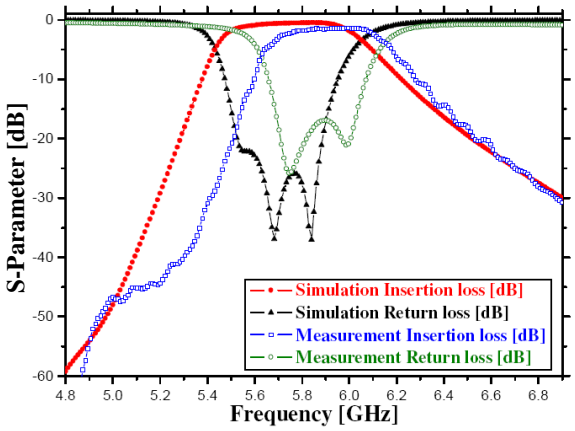

Figure 4: Experiment results for the narrow BPF with half-wavelength open stubs and FBW = 10%.

1.5 dB and the return losses of better than 18.5 dB and 17.5 dB with 10% bandwidth at the center frequency of 5.8 GHz are obtained, respectively.

4. NEW OPEN STUB BPF WITH SIR

The proposed narrow bandwidth BPF with half-wavelength open stubs has been reduced in size by half (1/2) compared with the conventional narrow bandwidth BPF in the horizontal-axis as shown in Figure 5. Table 1 shows the horizontal size of the conventional and proposed narrow BPF, respectively.

Figure 6 shows the simulation and measurement results of the proposed BPF with SIR, and these results are listed in Table 2.

There are some differences in simulation and measurement results due to dielectric loss, the effect of load resistance, and cable loss included from the measurement system. Figure 6 shows a photograph of the propose BPF with SIR. IE3D simulator is used for EM simulation and the filter is fabricated on the Teflon substrate with the height of 0.54 mm, conductor thickness of 0.018 mm, and relative dielectric constant of 2.54. The Agilent 8510 C vector network analyser is used for the measurement of the filter. The entire size of the proposed BPF is $12.7 \times 18.56\,\text{mm}^2$.

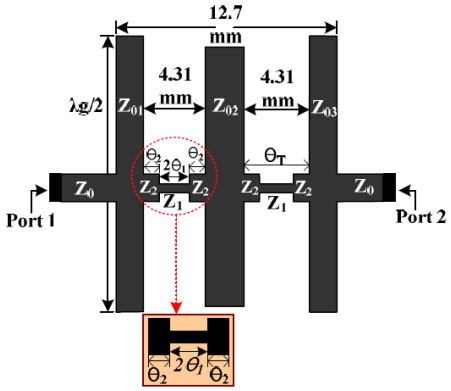

Figure 5: Proposed narrow compact-size BPF with half-wavelength open stubs using SIR.

Table 1: The size comparison of a narrow BPF with half-wavelength open stubs.

Kind of filters	Length of T.L [mm]	Whole size of filters Horizontal length [mm]
Conventional	8.75	21.58
New type	4.31	12.7

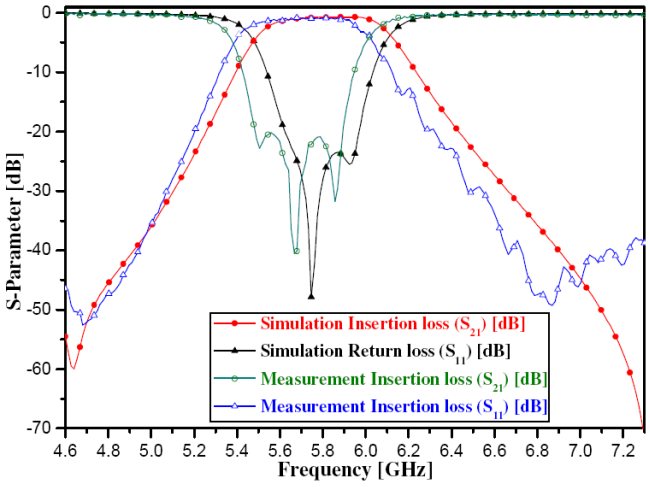

Figure 6: Simulation and measurement results of a proposed BPF sith SIR.

Table 2: Simulation and measurement results of a proposed BPF with SIR.

f_0 [GHz]	FBW [10%]	Simulation Results [dB]		Measurement Results [dB]	
		Insertion loss S_{21}	Return loss S_{11}	Insertion loss S_{21}	Return loss S_{11}
5.8	10	0.71	23.5	0.85	20.8

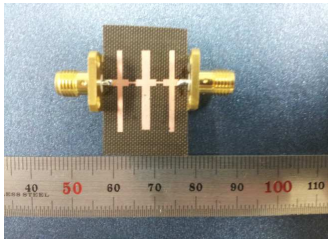

Figure 7: The proposed BPF with SIR.

5. CONCLUSION

In this paper, an open stub BPF with SIR has been suggested. The SIR can be used instead of transmission line which acts as an inverter in a conventional open stub BPF to reduce the size of the BPF on the low dielectric substrate. The proposed BPF's inverter has half-length compared with one of the conventional narrow BPF. The experimental results show the insertion loss of 0.85 dB and return loss of 20.8 dB with bandwidth of 10% at the center frequency of 5.8 GHz. This filter can be fabricated with IPD (Integrated Passive Device) and MEMS (Micro-electronics Mechanical System) because of its entirely planar structure and reduced size.

ACKNOWLEDGMENT

This work was supported by the National Research Foundation of Korea (NRF) grant funded by Korea government (MEST) (No. 2011-0029625).

REFERENCES

1. Krauss, H. L., C. W. Bostian, and F. H. Raab, *Solid State Radio Engineering*, John Wiley & Sons, 1980.
2. Mahyuddin, N. M., M. F. Ain, S. I. Hassan, and M. Singh, "A 10 GHz PHEMT dielectric resonator oscillator," *Proc. IEEE, Int. RF and Microwave Conf.*, 26–30, Sep. 2006.
3. Cassivi, Y. and K. Wu, "Low cost microwave oscillator using substrate integrated waveguide cavity," *IEEE Microwave Wireless Comp. Lett.*, Vol. 13, 48–50, Feb. 2003.
4. Lee, Y. T., J. S. Lim, C. S. Kim, D. Ahn, and S. W. Nam, "A compact-size microstrip spiral resonator and its applications to microwave oscillator," *IEEE Microwave and Wireless Comp. Lett.*, Vol. 12, No. 10, 375–377, Oct. 2002.
5. Zhang, H. and K. J. Chen, "Miniaturized coplanar waveguide bandpass filters using multi-section stepped-impedance resonator," *IEEE Trans. Microwave Theory Tech.*, Vol. 54, No. 3, 1090–1095, Mar. 2006.
6. Makimoto, M. and S. Yamashita, *Microwave Resonators and Filters for Wireless Communication Theory, Design and Application*, Springer, 2001.
7. Khanna, A. P. S. and Y. Garault, "Determination of loaded, unloaded, and external quality factors of a dielectric resonator coupled to a microstrip line," *IEEE Trans. Microwave Theory Tech.*, Vol. 31, 261–264, Mar. 1983.

Compact Reconfigurable Dual Mode Resonator with Switchable Band Using RF PIN Diodes

Hesham A. Mohamed[1], **Heba B. El-Shaarawy**[2], **Esmat A. Abdallah**[1], **and Hadia El-Hennawy**[3]

[1]Electronics Research Institute, Giza, Egypt
[2]Electronics and Communications Engineering Department, Faculty of Engineering
Cairo University, Giza, Egypt
[3]Electronics and Communications Engineering Department, Faculty of Engineering
Ain Shams University, Cairo, Egypt

Abstract— In this paper, a new miniaturized reconfigurable dual-mode stub-loaded resonator, which consists of a microstrip resonator with internal coupled lines and an open-circuited stub is presented. Based on the odd and even-mode equivalent circuits, the resonant characteristics of the proposed microstrip resonator are investigated. RF PIN diodes are used to switch the passband between GSM (1.83 GHz) and LTE-7 (2.6 GHz), and when changing the location of diode, filter could switch its passband from GSM (1.83 GHz) to UMTS (2.1 GHz) with asymmetric responses. The measured results for asymmetric frequency response has attenuation slope of 46.84 dB/GHz in the lower and 97.14 dB/GHz in the upper transition bands. Measured results show a very good agreement with the simulations where a 1.83 GHz center frequency with a 280 MHz bandwidth is obtained for the GSM state, and a 2.72 GHz, center frequency with a 144 MHz bandwidth is obtained for the LTE-7 filter state. The proposed bandpass filter has one transmission zero and its bandwidth is limited to 18%, is only suitable for narrow-band applications.

1. INTRODUCTION

Recent wireless communication systems require cost-effective, high quality and miniaturized devices with improved characteristics. Dual-mode microstrip filters are attractive due to their high selectivity characteristics. The first planar dual-mode resonator has been proposed by [1]. Dual-mode filters have wide applications in satellite communication, mobile communication, microwave, and millimeter-wave communication systems [2]. To date, switchable filters are key components in compact frequency agile communication systems; they allow selecting different bands of operation using a single filter with embedded tuning elements [3, 4]. Other advantages of tunable filters can be found at the subsystem level by reducing the total volume and velocity specifications of the analog to digital converters. Recent trends in reconfigurable filters include designs that can independently reconfigure its parameters to precisely cover bands of interests, these devices tune: both center frequency and bandwidth [3] or selectivity [5]. Important issues to consider when deciding a specific technology to reconfigure microwave filters are: frequency of operation, tuning speed, power consumption and size.

In this paper, a dual-mode resonator with reconfigurable frequency bands and UWB filter with DGS is proposed. The designed and fabricated filter is done on Rogers substrate (RO3010) with thickness of 0.635 mm, relative dielectric constant of 10.2, loss tangent= 0.0023 and the metallization thickness is 0.017 mm.

2. STRUCTURE OF THE DUAL MODE RESONATOR

The structure of the proposed dual-mode resonator was initially exhibited in [6], which consists of a microstrip resonator with internal coupled lines and quarter-wavelength open-circuited stub, as displayed in Fig. 1(a), where Y_1, θ_1, Y_3 and θ_3 denote the characteristic admittances and electric lengths of the microstrip line and open stub, respectively. Y_{odd}, Y_{even} and θ_2 indicate the odd- and even-mode characteristic admittances and electrical length of the coupled lines as shown in Fig. 1(b) and Fig. 1(c), respectively. Since the resonator is symmetrical in structure, the resonant condition can be analyzed by the classical method of even-and odd-mode excitation as listed in Table 1. For odd-mode excitation, there is a voltage null along the symmetrical plane A-A'. The equivalent circuit is shown in Fig. 1. Taking $\theta_1 = \theta_2 = \theta_3 = \theta$ for convenience, we can derive the input impedance (admittance) [6].

Where C is the speed of light in free space, L_1 is the length of the microstrip line, and ε_{eff} denotes the effective dielectric constant of the substrate.

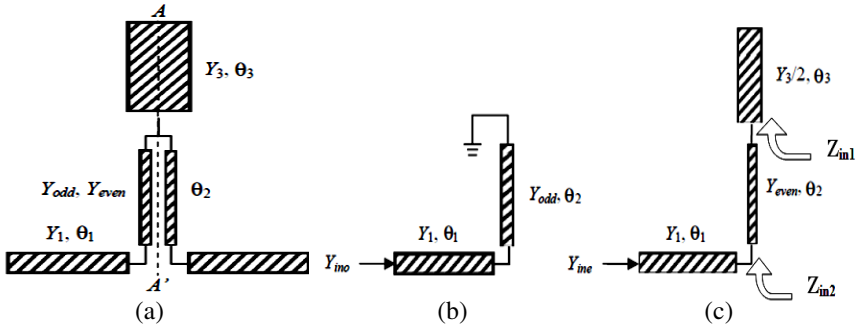

Figure 1: (a) Structure of the proposed dual-mode stub-loaded resonator, (b) odd-mode equivalent circuit, and (c) even-mode equivalent circuit.

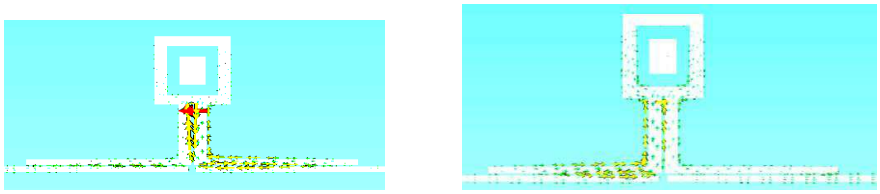

Figure 2: Simulated current distributions for the two modes of the proposed resonator, (a) odd mode, (b) even mode.

Table 1: Resonant conditions of the even-and odd-mode excitation [6].

Odd mode	$Y_{ino} = jY_1 \frac{Y_1(\tan(\theta))^2 - Y_o}{\tan(\theta)(Y_o + Y_1)}$	$\tan^2\theta = K_1 = \frac{Y_{odd}}{Y_1}$	$f_{odd} = \frac{C\tan^{-1}(\sqrt{K_1})}{2\pi L_1\sqrt{\varepsilon_{eff}}}$
Even mode	$Y_{ine} = jY_1 \frac{\tan\theta[Y_3 Y_{even} + Y_{even}^2 + Y_1 Y_{even}] - Y_1 Y_3 \tan^3\theta}{Y_1 Y_{even} - \tan^2\theta[Y_1 Y_3 + Y_3 Y_{even} + Y_{even}^2]}$	$\tan^2\theta = K_2 = \frac{Y_{even}}{Y_1} + \frac{Y_{even}^2}{Y_1 Y_3} + \frac{Y_{even}}{Y_3}$	$f_{even} = \frac{C\tan^{-1}(\sqrt{K_2})}{2\pi L_1\sqrt{\varepsilon_{eff}}}$

If $K_1 = K_2$, both fundamental resonant frequencies are exactly the same. If $K_1 < K_2$, then the resonator can generate a higher f_{even} than f_{odd}, and if $K_1 > K_2$, the resonator will make f_{even} lower than f_{odd}. In this investigation, only the value of Y_3 is changed, while keeping all other parameters constant. As a result, the fundamental even-mode resonant frequency of the proposed resonator can be flexibly controlled while the fundamental odd-mode resonant frequency is unaffected. Slow-wave structure can be implemented with simple modification by etched rectangular slot as shown in Fig. 2 incorporated in the open stubs, thereby this aperture tend to decrease the quality factor of filter, thus increasing the bandwidth [7, 8]. Coupling coefficient of resonator plays a key role in determining the bandwidth of a filter [9].

A full-wave EM eigenmode simulator CST 2011 [10] was used to characterize the current patterns for the resonator. Figs. 2(a) and (b) show the current patterns of the resulting two fundamental eigenmodes. At the fundamental odd-mode resonant frequency, there is no current flowing on the open-circuited stub, and the open-circuited stub does not perturb the fundamental resonant current distribution in Fig. 2(a). On the other hand, at the fundamental even-mode resonant frequency, there is current flowing on the open-circuited stub, which changes the current distribution path, thus changing the resonant frequency in Fig. 2(b).

3. DESIGN OF RECONFIGURABLE BANDPASS FILTER USING SYMMETRICAL STEP-IMPEDANCE RESONATORS

This section proposes the design and implementation of reconfigurable dual mode BPF using RF PIN diode switches. The reconfigurable filters is based on distributed current, which is able to demonstrate the location of RF PIN diode, to produce reconfigurable discrete states on a filter response, and are very attractive for low cost implementations. The systematic design procedure of the dual-passband filter can be mainly divided into three steps. First, the structural parameters of the constitutive SIRs including a resonator of Y_3 to control the transmission zeros must be determined. Then, the coupling scheme stage of Y_2, the fractional bandwidth design graph consid-

ering controlling the center of passband must be found [9]. Lastly, the coupled-line input/output impedance should be decided with tight coupling. The coupling structure makes it possible for the filter to generate one finite transmission zeros at the lower or upper stopbands, leading to the normalized element values of the Chebyshev low-pass filter prototype with 0.01 dB ripple can be obtained from [9] as, $g_0 = 1$, $g_1 = 0.4488$, $g_2 = 0.4077$, $g_3 = 1.1007$ that improves the passband and out-off-band performances [6].

According to the above studies, the two fundamental resonance frequencies can be controlled effectively, and obtained from equations in Table 1. The initial dimensions can be chosen using the above design procedure and then the CST 2011 is used to optimize the dimensions for 1.83 GHz GSM applications.

3.1. GSM-LTE Switchable Bandpass Filter Using Two RF PIN Diodes Switches

New miniaturized reconfigurable and switchable filter operating in the GSM (1.8 GHz) to LTE band 7 (2.6 GHz) bands by using RF PIN diodes, Fig. 3(a) illustrates the configuration of the two-pole filter, it consists of a resonator and two stepped-impedance feed lines which feed the proposed resonator with tight coupling with $K_1 < K_2$. The dimensions of this filter are listed in Table 2.

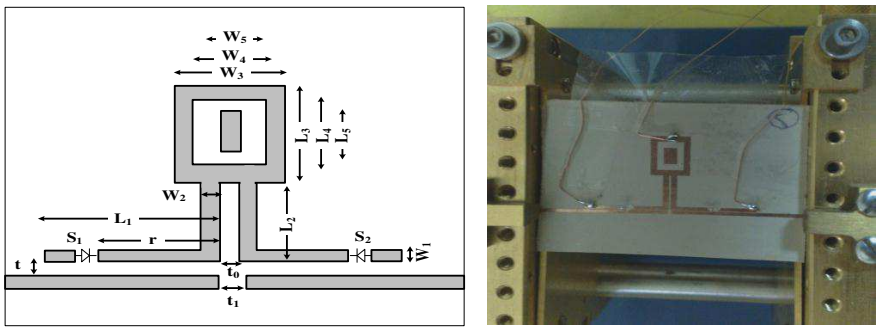

(a) (b)

Figure 3: (a) Configuration of the dual mode resonator with two RF PIN diode switches, and (b) photograph of the switchable bandpass filter.

Table 2: Dimensions of the dual mode filter after optimization. (All dimension in mm).

Top side	W_o	W_1	W_2	W_3	W_4	W_5	L_0	L_1	L_2	L_3	L_4	L_5	t	t_o	t_1
	0.6	0.6	0.95	6	4	2	10	11	6	7.4	5.4	3.2	0.15	0.25	0.63
Bottom side	d	d_1		d_2			S			S_1				S_2	
	0.7	26		11.4			3			2.3				3.2	

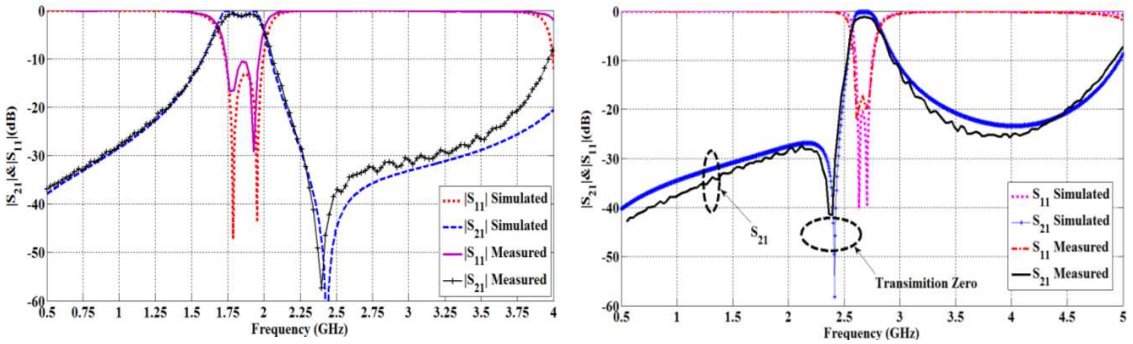

(a) (b)

Figure 4: GSM-LTE band7 Switchable Bandpass Filter using two RF PIN diodes. (a) Simulated and measured GSM (state ON). (b) Simulated and measured LTE band7 (state OFF).

The reconfigurable filter can be realized by using RF PIN diode HBND 4005 with resistor element in forward bias is equivalent to 4.7 Ω while the main capacitor element is 0.017 pF in the

reverse bias state [11], at certain position of $r = 6.2\,\text{mm}$ of coupled line as shown in Fig. 3(a). The diodes perturb the electric field and magnetic field, and increase the resonance frequency from 1.83 GHz to 2.6 GHz. The filter performance is presented in Fig. 4. Center frequency tuning has been achieved on a two poles filter configuration and the location of the transmission zero changes from higher frequency to lower frequency as RF PIN diode switched from ON state to OFF state. We investigated the effect of L_1 on both center frequency and location of transmission zeros. For $L_1 = 11\,\text{mm}$ the center frequency is 1.83 GHz as in Fig. 4(a) and when $L_1 = 5\,\text{mm}$ gives the center frequency is located at 2.6 GHz as in Fig. 4(b). The fabricated using photolithographic technique, a photo of the filter is shown in Fig. 3(b).

3.2. GSM-UMTS Switchable Bandpass Filter

Dual mode resonator filter is presented in the previous section, this filter has an asymmetrical frequency response, and we could tune its center frequency, and transmission zero position by varying the value of open stub Y_3.

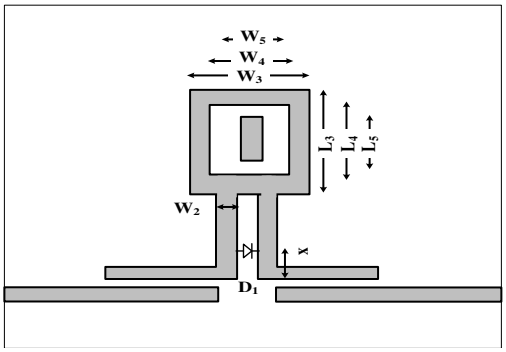

Figure 5: The reconfigurable dual mode BPF using RF PIN diode switch at $X = 0.85\,\text{mm}$ to switchable bandpass filter for GSM and UMTS.

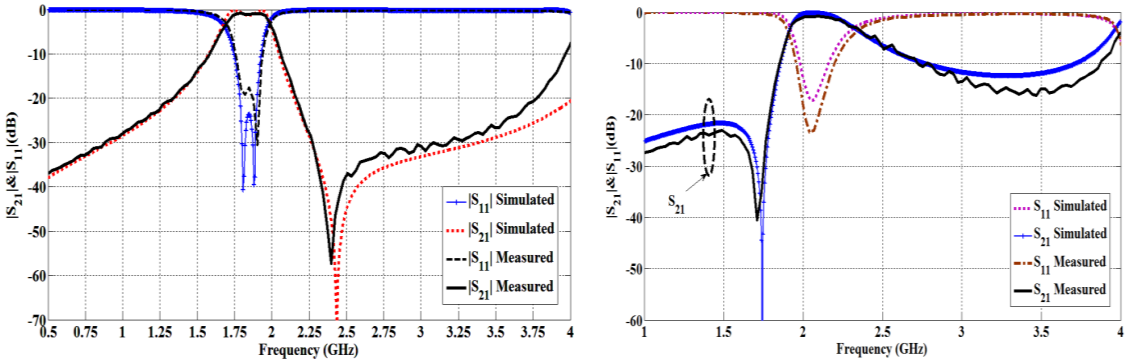

Figure 6: GSM-UMTS switchable bandpass filter using RF PIN diodes. (a) Simulated and measured GSM (state OFF). (b) Simulated and measured UMTS (state ON).

A reconfigurable center frequency, and transmission zero position using a dual mode resonator can be found by inserting the RF PIN Diode at $X = 0.85\,\text{mm}$ as shown in Fig. 5 without any change in the dimension of open stub W_3. Fig. 6 shows that the filter has an asymmetrical frequency response with two transmission poles in the passband and a one transmission zero in the stopband. The simulation of the insertion loss of the filter in the OFF state is 0.17 dB at 1.83 GHz, while the insertion loss of the filter in the ON state is 0.35 dB, at 2.1 GHz. The response exhibits a transmission zero located at 2.25 GHz and a bandwidth of 450 MHz (14.5%). The wideband state produced a bandwidth of 860 MHz (18%).

4. FUTURE WORK

The future work that we intend to do with respect to the presented dual mode resonator BPF is to implement a novel Defected Ground Structure to produce better performance and integration

capabilities, like increasing the characteristic impedance by additional effective inductance, which plays a great role in raising the phase constant and slow-wave effects to obtained UWB transmission systems which are characterized by an instantaneous fractional bandwidth of more than 60%, generate two transmission zeros and great sharpness (the transition band between stop-band/pass-band and pass-band/stop-band). The overall filter dimension is 26 mm × 15 mm, that provides size reduction over that of other publications, normally about 78% better that [7].

5. CONCLUSIONS

In this work, a novel switchable bandpass filter with two state discrete frequency bands has been demonstrated. This filter has the merit of compact size, and low insertion loss. Switchable filters can reduce the complexity of a system by allowing filter reconfigurability instead of having switched filter banks. In the first state, the filter has been designed to be able to switch between GSM (1.83 GHz) and LTE-band7 (2.6 GHz) bands and the second state when changing the location of diode filter could switch its passband from GSM (1.83 GHz) to UMTS (2.1 GHz). On inspection of the literature, it is clear that most of the reported methods of bandwidth tunability are for narrowband applications. Practically, some special applications of bandpass filters may require high selectivity on only one side of the pass band, but less or none on the other side in front end communication systems and mixtures. However, there is an increasing demand for reconfigurable wideband filters with high selectivity for wideband communications, radar and electronic warfare (EW) systems for processing signals involving large information with high data rate.

REFERENCES

1. Hong, J.-S. and M. J. Lancaster, "Bandpass characteristics of new dual-mode microstrip square loop resonators," *Electronics Lett.*, Vol. 30, No. 11, 891–892, 1995.
2. Liu C., P. Lu, and H. Shie, "Dual-mode double-ring resonators for microstrip band-pass-filter applications," *IEE Proc. — Microw. Antennas, Propag.*, Vol. 151, No. 5, October 2004.
3. Birto, Z., I. Limas, and S. Colpo, "Precise frequency and bandwidth control of switchable microstrip bandpass filters using diode and microelectro-mechanical system technologies," *IET Microw. Antennas Propag.*, Vol. 9, No. 4, 713–717, 2012.
4. Zhang, H. and K. J. Chen, "A microstrip bandpass filter with an electronically reconfigurable transmission zero," *European Microwave Conference*, 653–656, Sept. 9–12, 2006.
5. Tiwary, K. and N. Gupta, "Design of compact coupled microstrip line band pass filter with improved stopband characteristics," *Progress In Electromagnetics Research C*, Vol. 24, 97–109, 2011.
6. Hua, C., C. Chen, and C. Miao, "Microstrip bandpass filters using dual-mode resonators with internal coupled lines," *Progress In Electromagnetics Research*, Vol. 21, 99–111, 2011.
7. Apisak, W., S. Kunthphong, and S. Wanlop, "Stepped-impedance coupled resonators for implementation of parallel coupled microstrip filters with spurious band suppression," *IEEE Trans. Microw. Theory Tech.*, Vol. 60, No. 6, 1540–1548, June 2012.
8. Karshenas, F., A. R. Mallahzadeh, and J. Rashed-Mohassel, "Size reduction and harmonic suppression of parallel coupled-line bandpass filters using defected ground structure," *13th International Symposium on Antenna Technology and Applied Electromagnetics and the Canadian Radio Sciences Meeting*, 2009.
9. Matsuo, M., H. Yabuki, and M. Makimoto, "Dual-mode stepped-impedance ring resonator for bandpass filter applications," *IEEE Trans. Microw. Theory Tech.*, Vol. 49, No. 7, 1235–1240, 2001.
10. CST Microwave Studio Electromagnetic Field Simulation Software, Computer Simulation Technology, Darmstadt, Germany.
11. HPND 4005, Avago Technologies, United States.

Electromagnetic Field as Human Health Risk Factor: EMF Safety Ensuring by Hygienic Standardization

I. V. Bukhtiyarov, **N. B. Rubtsova**, **Yu. P. Paltsev**, **L. V. Pokhodzey**, **and S. Yu. Perov**
Federal State Budgetary Institution 'Research Institute of Occupational Health' under the Russian Academy of Medical Sciences, Moscow, Russian Federation

Abstract— Human health electromagnetic safety is one of electromagnetic compatibility problem. Electromagnetic fields (EMF) different frequency ranges are human health risk factor: cardio-vascular diseases, cancer, congenital malformations, neurodegenerative diseses. The main principle of electromagnetic safety is hygienic regulation. EMF hygienic standardization in Russia is based on the results of hygienic, clinical-physiological, epidemiological and experimental studies. Hygienic norms are developed for discrete frequency ranges. The main discrepancy of Russian and international EMF hydienic standardization approaches is in concepts of "cumulative" or "acute" factor effects, correspondingly. Hence EMF hygienic norms in RF are time dependent, comprising a principle "protection by time". The progress in EMF hygienic safety problem solving is time dependent norms for frequencies from 3 Hz up to 10 kHz development, as well as attempt of near zone EMF adequate evaluation (for $>$ 300 MHz frequency range) principles.

The problem of occupational and general public electromagnetic safety is increasing urgency in connection with increasing environment electromagnetic pollution and therefore increase health risks. Traditionally, electromagnetic field (EMF) main sources are the equipment of power- and radio transmission objects, radar and navigation systems. Last years the essential contribution into electromagnetic environment is brought by personal computers and mass medium, mobile telecommunication systems. Environmental EMF exposure in private life may be commensurable with occupational today. The most actual are the questions of EMF effects combined with another environmental factors exposure.

EMF occupational exposure may be risk factor of possible long-term effects like early atherosclerosis, coronary heart disease, essential hypertention, cancer (leukemia, brain tumors), congenital malformations, neurodegenerative diseses (Alzheimer's dementia, Parkinson's disease, ALS).

Critical organs and systems of radio-frequency range EMF exposure have been determined: nervous, cardiovascular, blood system, reproductive function; nervous-endocrine systems interrelation was determined (as hypothalamus-hypophysis-adrenal glands bark axis), first criteria of immune system changes are revealed; etc.

The WHO/International Agency for Research on Cancer (IARC) has classified extremely low frequency magnetic field as possibly carcinogenic to humans (Group 2B) (childhood leukemia) [1], radiofrequency electromagnetic fields as possibly carcinogenic to humans (Group 2B), based on an increased risk for glioma, a malignant type of brain cancer, associated with wireless phone use [2]. In 2013 March report of possible association of mobile phone EMF and possible thyriod gland cancer risk elevation has been published.

The hygienic regulation main principle for occupational and general public EMF exposure is health of present and subsequent generations' preservation. Occupational and environmental electromagnetic safety ensures by international (ICNIRP, CENELEC, EU) and national electromagnetic safety guidelines (that have significant differences often).

Hygienic EMF standards in former USSR and Russian Federation now are developed, as a rule, on the basis of hygienic, clinical and physiological, experimental, and last years epidemiological studies as well as scientific publications in peer reviewed journals. Hygienic researches are carried out on purpose definite the time-level EMF exposure parameters in real conditions; clinical and physiological — are directed to reveal health state and physiological functions unfavorable changes; epidemiological — to analyze the remote consequences of factor exposure; experimental — to study the features and character of EMF biological effects. The main bases of EMF norms setting are the experimental data of EMF exposure hazard effects threshold determination. Experimental studies play the leading role in hygienic norms substantiation, taking into account the results of experiment, from animals to human transfer criterion and hygienic safety factor (different for different frequency ranges and emission modes).

The principle of EMF chronic exposure adverse effect threshold definition is basis for hygienic norms in the Russian Federation. Hence, Russian EMF hygienic ocupational norms are time dependent, comprising a principle "protection by time". According to it, hygienic norms are developed for discrete frequency ranges and conditions. In Russia there are hygienic norms of occupational exposure for hypo-geomagnetic conditions, static electric and magnetic fields, 50 Hz EMF and radiofrequency EMF (from 10 kHz to 300 GHz), and for special EMF case (ultra broadband pulses) [3–6].

Table 1: EMF occupational exposure hygienic norms: Russian Federation and International [3, 10].

Frequency range	Russian Federation, permissible levels				ICNIRP; Directive 2004/40/EC, reference levels		
	Electric field strength	Magnetic field strength; magnetic flux density	Equivalent plane wave power density, seq.	Power exposition	Electric field strength	Magnetic field strength; magnetic flux density	Equivalent plane wave power density, seq.
Static field	20–60 kV/m 9.0–1.0 h per work shift	10–30 mT (local to limb exp. 15–50 mT) depending on time	-	-	-	2 T (8 T– exp. of lims)	-
50 Hz	5–25 kV/m depending on time	0.1–2.0 mT (local to limb exp. 0.8–6.4 mT) depending on time	-	-	10 kV/m	0.5 mT	-
≥ 10 –30 kHz	500 V/m (max. 1000 V/m) depending on time	50.0 (max. 100 A/m) depending on time	-	-	610 V/m	24.4 A/m	-
≥ 0.03 –3.0 MHz	50.0 V/m (max. 500 V/m) depending on time	5.0 A/m (max. 50 A/m) depending on time	-	20000 $(\text{V/m})^2 \cdot \text{h}$; 200 $(\text{A/m})^2 \cdot \text{h}$	610–203 V/m depending on frequency	24.4–0.53 A/m depending on frequency	-
≥ 3 –30 MHz	29.6 V/m (max. 300 V/m) depending on time	-	-	7000 $(\text{V/m})^2 \cdot \text{h}$	203–61 V/m depending on frequency	0.53–0.16 A/m depending on frequency	-
≥ 30 –50 MHz	10.0 V/m (max. 80 V/m) depending on time	0.3 A/M (max. 3.0 A/M depending on time	-	800 $(\text{V/m})^2 \cdot \text{h}$; 0.72 $(\text{A/m})^2 \cdot \text{h}$	61 V/m	0.16 A/m	10 W/m^2 (1 mW/m^2)
≥ 50 –300 MHz	10.0 V/m (max. 80 V/m) depending on time	-	-	800 $(\text{V/m})^2 \cdot \text{h}$	61 V/m	0.16 A/m	10 W/m^2 (1 mW/m^2)
$\geq$ 300 MHz –300 GHz	-	-	25.0 $\mu\text{W/cm}^2$ (max. 1000 $\mu\text{W/cm}^2$)	200 (μW $/\text{cm}^2) \cdot \text{h}$	61–137 B/M depending on frequency	0.16–0.36 A/M depending on frequency	10–50 W/m^2 (1–5 mW/m^2) depending on frequency

General public hygienic standards are developed for hypo-geomagnetic conditions, static electric field, power frequency (50 Hz) electric and magnetic fields and radiofrequency EMF (from 30 kHz to 300 GHz) [4, 7, 8] and for special case: mobile communication systems [9].

International EMF safety standards are based on peer reviewed scientific publications data. EMF exposure limits are termed "basic restrictions" and based directly on established health effects and biological considerations (current density or specific absorption rate (SAR) in different frequency ranges). Basic restrictions are often specified as quantities that may be impractical to measure. Other quantities are introduced for practical exposure assessment purposes to determine whether the basic restrictions are likely to be exceeded. These reference levels (ICNIRP) or maximum permissible exposure levels (IEEE) correspond to basic restrictions under worst case exposure conditions for one or more of the following physical quantities: electric field strength (E), magnetic field strength (H), magnetic flux density (B), power density (S), limb current (I), contact current (I) and, for pulsed fields, specific energy absorption (SA).

As a whole, principles and criteria of EMF health risk assessment and management in Russian Federation and International are similar. EMF control principles and methods on workplaces and in places of general public residing, basically, also sufficiently correspond. There are significant differences between permissible levels because of different approaches to EMF hygienic rating. The main difference is EMF cumulative effects concept (in Russia) and acute effects concept (in international). EMF occupational and general public exposure comparisons of hygienic norms are shown in Tables 1, 2.

Table 2: EMF general public exposure hygienic norms: Russian Federation and International [4, 7, 8, 11].

Frequency range	Russian Federation, permissible levels			ICNIRP, reference levels (WHO recommendation)		
	Electric field strength	Magnetic field strength; magnetic flux density	Equivalent plane wave power density, seq.	Electric field strength	Magnetic field strength; magnetic flux density	Equivalent plane wave power density, seq.
Static field	15 kV/m	-	-	-	400 mT	-
50 Hz	005 kV/m (max. 20 kV/m)	5 μT (max. 100 μT)	-	5 kV/m (max. 20 kV/m)	0.5 mT (max. 5.0 mT) Precautionary principles	-
20–22 kHz	500 V/m	4 A/m	-	87 V/m	5 A/m	
30–300 kHz	25 V/m	-	-	87 V/m	$5–0.73/f$ A/m	
0.3–3.0 MHz	15 V/m	-	-	$87–87/f$ V/m	$0.73/f$ A/m	-
3–30 MHz	10 V/m	-	-	$87/f–28$ V/m	$0.73/f–0.0037$	-
30–300 MHz	3 V/m*	-	-	28	0.0037 A/m	20 W/m^2 (0.2 mW/m^2)
0.3–300 GHz	-	-	10 μW/cm^2 25 μW/cm^{2**}	$1.375f–61$ V/m	$0.0037f–0.16$ A/m	$f/200–1.0$ mW/m^2

* Except for means broadcasting and TV (frequency ranges 48.5–108; 174–230 MHz);
** For cases of rotating or scanning modes of antenna functioning.

Therefore the Russian hygienic norms of EMF frequency ranges are more strict, than "reference levels" under the International guidelines, exception of EMF frequency range from ≥ 30 up to 50 MHz occupational exposure where MF referenced levels practically in 2 times strict than Russian permissible level. This value extends down to 300 MHz magnetic field (MF) (frequency range with MF hygienic norms absence). At the same time in all frequency ranges Russian maximal permissible levels for short-term exposure are higher than "reference levels" according to International guidelines.

The Russian general public permissible levels are stricter than International, except for special norms for inductive oven EMF emission (see Table 2).

The main differences between occupational and general public EMF exposure hygienic norms

together with norms of mobile phone EMF between the Russian Federation and the western countries are connected with basic differences in approaches to standardization: application of various criteria of effects evaluation (acute exposure effects as main criteria, "continuous" standardization, "basic restriction", "reference levels", SAR from one side and chronic exposure effects as main criteria, cumulative effects, power density, power exposure from another).

One of the main problems today is the EMF threshold permissible values international harmonization. The main complexity is represented with distinction in approaches to hygienic standardization. Possible way of occupational and general public EMF exposure hygienic norms harmonization can be preservation of hygienic norms which used in the Russian Federation already (for discrete frequency ranges and modes of EMF generation). For frequency ranges (or EMF components), and also modes of generation in which are absent in the Russian hygienic norms, as temporary the recommendations offered as international can be accepted. Russian EMF occupational exposure new hygienic norms for $>$ 3–10 kHz frequency range are developed (see Tables 3, 4) but not official published yet.

Table 3: Electric field 3 Hz–$<$ 30 kHz occupational exposure hygienic standards (draft).

Frequency f, Hz	Maximal permissible value E, kV/m		
	Exp. more than 2 h	Exp. up to 2 h	Exp. up to 0.2 h
3–$<$ 30	8.3	16.6	40
30–$<$ 300*	$250/f^*$	$500/f^*$	$1250/f^*$
300–$<$ 3000	0.8	1.6	4
3000–$<$ 30000	0.5	1.0	1.5

Table 4: Magnetic field 3 Hz–$<$ 30 kHz occupational exposure hygienic standards (draft).

Frequency f, Hz	Exposure characteristics	Maximal permissible value H, A/m		
		Exp. more than 2 h	Exp. up to 2 h	Exp. up to 0.2 h
3–$<$ 30	Total	$600/f^{1/2}$	$1200/f^{1/2}$	$2400/f^{1/2}$
	Local to limb	$1500/f^{1/2}$	$2800/f^{1/2}$	$6000/f^{1/2}$
30–$<$ 300*	Total	$4000/f^*$	$8000/f^*$	$80000/f^*$
	Local to limb	$20000/f^*$	$40000/f^*$	$160000/f^*$
300–$<$ 3000	Total	15	30	270
	Local to limb	70	140	500
3000–$<$ 30000	Total	10	20	100
	Local to limb	40	80	300

* 50 Hz MF is eliminated. 50 Hz MF hygienic standardization is according with Table 1.

Strong restriction in EMF hygienic norms improvement taking into account Russian and International criteria is EMF dose concept. Russian approach based in EMF cumulative effects including does not take into account the correction factors that are depend on radiation level. This parameter named "power exposition" is not completely adequate to "dose" definition, but takes into account possible effects of radiofrequency EMF energy storage. More close to dose concept may be approach that include specific absorption rate (SAR) for radiation levels evaluation in the near field. Russian approach is based in radiofrequency EMF physical characteristics, and SAR approach bases on the electric field strength and dielectric characteristics of human body [12].

Consequently the electromagnetic safety problem has some different aspects. One of them is continuation of medical and biological studies of EMF different frequency ranges and emission modes human health risks assessment, magnetic field component and new technical devices especially. The another future prospect of electromagnetic safety insurance (in Russian Federation especially) is dosimetry development in account the international experience, as well as dose and threshold permissible values interrelationships search, that must be substantiated by medical and biological

studies data. New complex methods of electric and magnetic EMF components as well as SAR levels measurement and evaluation must be developed.

REFERENCES

1. IARC Monographs on the Evaluation of Carcinogenic Risks to Humans. v. 80, "Non-ionizing radiation, Part 1: Static and extremely low-frequency (ELF) electric and magnetic fields," 426, WHO, 2002.
2. IARC Monographs on the Evaluation of Carcinogenic Risks to Humans. v.102, "Non-ionizing radiation, Part 2: Radiofrequency electromagnetic fields," 462, WHO, 2013.
3. SanPiN 2.2.4.1191-03, "Electromagnetic fields in occupational environments," Moscow, 2003 (in Russian).
4. SanPiN 2.1.8/2.2.4-1383, "Hygienic requirements to transmitting radio engineering objects placement and maintenance," Moscow, 2003 (in Russian).
5. SanPiN 2.1.8/2.2.4.2489-09, "Hypogeomagnetic fields in industrial, residential and public buildings and constructions," Moscow, 2009 (in Russian).
6. SanPiN 2.2.4.1329-03, "Requirements to staff safety under pulsed electromagnetic field exposer," Moscow, 2003 (in Russian).
7. SanPiN 2.1.2.2801-10, "Changes and addendums No. 1 to SanPiN 2.1.2.2645-10 'Sanitary-and-Epidemiological requirements to residential construction and living quarter residence conditions'," Moscow, 2010 (in Russian).
8. HN 2.1.8/2.2.4.2262-07, "Threshold permissible values of 50 Hz magnetic fields in residential construction, living quarter and residential area," Moscow, 2007 (in Russian).
9. SanPiN 2.1.8/2.2.4.1190-03, "Hygienic requirements to land mobile transmitting systems placement and maintenance," Moscow, 2003 (in Russian).
10. "Directive 2004/40/EC on the minimum health and safety requirements regarding the exposure of workers to the risks arising from physical agents (electromagnetic fields)," *Official Journal of the European Union*, L 159, Apr. 30, 2004.
11. "Council Recommendation 1999/519/EC on the limitation of exposure of the general public to electromagnetic fields (0 Hz to 300 GHz)," *Official Journal of the European Union*, L 199/59, Jul. 30, 1999.
12. Perov, S., Q. Balzano, and N. Kuster, "A scientific approach to RF safety harmonization," *Joint Meeting of The Bioelectromagnetics Society and the European Bioelectromagnetics Association*, 5–18, Davos, Switzerland, Jun. 14–19, 2009.

Design of an Optimal Multi-layered Electromagnetic Absorber through the Central Force Optimization Algorithm

J. E. González, I. Amaya, and R. Correa
Escuela de Ingenierías Eléctrica, Electrónica y de Telecomunicaciones
Universidad Industrial de Santander, Bucaramanga, Santander, Colombia

Abstract— Electromagnetic absorbers are elements designed to avoid (or at least reduce) reflection of electromagnetic energy in a given frequency band, which could otherwise be harmful to living beings, or simply cause interference with other electronic equipment. Thus, this article presents the results achieved by using a metaheuristic for optimizing their design in the frequency range of wireless communications, i.e., between 0.8 and 1.9 GHz. In this case, the algorithm proposed by Formato in 2007, i.e., Central Force Optimization (CFO), was used. Moreover, the approach laid out by Qubati and Dib in 2010, i.e., acceleration clipping, was also implemented. Results are compared between these two variants, and using different initial distributions (i.e., uniform, mixed, and random). Furthermore, a two-stage process was executed, striving to reduce the number of dimensions of the problem, thus allowing for further optimization. In the first stage of this procedure, all unknowns were considered (i.e., two variables for each layer, each one representing a given material and its thickness), and the algorithm was run 10 times. During the second stage, the materials of the best run were fixed, and the algorithm was also executed 10 times, just that in this case it only had to operate on half of the dimensions (i.e., one for each layer, which represents the fixed material thickness). It was found that, for a three layered electromagnetic absorber, better results than previously reported ones for Particle Swarm Optimization (PSO) and for interval analysis, were possible, though only for the modified CFO algorithm.

1. INTRODUCTION

During the last few decades new devices have been created, which can help prevent the adverse effects derived from an excessive exposure to electromagnetic radiation, or which can help reduce interference between devices They are known as electromagnetic absorbers, since their function is to, ideally, absorb all the incident energy in a given frequency spectrum, and dissipate it as heat. Because of this, they have become really important in applications such as the construction of anechoic cameras or in the cloaking at some frequencies. Their design, however, requires a balance between materials and geometries, since everything plays a major role in the total absorption capacity. There are multiple designs, but one of the most common is the planar Multilayered Electromagnetic Absorber (MEA), where energy is assumed to arrive perpendicular to the first layer and where the last layer is in contact with a perfect conductor.

CFO, on the other hand, stands for Central Force Optimization, and it is an algorithm that has been around since 2007, when Formato reported, for the first time, that it was possible to optimize an objective function by mimicking the effect of gravitational kinematics [1]. After that, it has been used in different fields and new modifications have been reported. This article shows the results achieved after optimizing the design of a MEA using CFO and considering its variant known as Acceleration Clipping (AC) [2]. Furthermore, it compares the data delivered when a second optimization stage is implemented, with a reduced number of dimensions.

2. THE OPTIMIZATION PROBLEM

A MEA is said to have N layers, where the last one is in direct contact with a perfect conductor (as was mentioned above). A travelling electromagnetic wave makes contact with the MEA with a normal incidence, and it should be completely absorbed (ideally). However, since a real-life situation is different from ideal, a portion of the energy will reflect back to the medium. Nonetheless, this information can be used to establish a performance index on the MEA, since the less it reflects, the better it will be. Thus, the reflection coefficient is given by Equation (1), where $Z_1(f)$ is the impedance of the first layer (the one in direct contact with the medium), which depends on the next layer (and this one in turn depends on the following one, and so on), as shown by Equation (2), where η_k is the impedance of the k-th layer, z_k is the z-coordinate of the k-th layer and $\mathcal{E}_{r_k}$, ε_{r_k}

are the relative permeability and permittivity (respectively) of the k-th layer.

$$R(f) = \frac{Z_1(f) - \eta_0}{Z_1(f) + \eta_0} \tag{1}$$

$$Z_k = \begin{cases} \eta_k \frac{Z_{k+1} + j\eta_k \tan\left(\omega z_k \sqrt{\mu_{r_k} \mathcal{E}_{r_k}}\right)}{\eta_k + jZ_{k+1} \tan\left(\omega z_k \sqrt{\mu_{r_k} \mathcal{E}_{r_k}}\right)} & k < N \\ j\eta_N \tan\left(\omega z_N \sqrt{\mu_{r_N} \mathcal{E}_{r_N}}\right) & k = N \end{cases} \tag{2}$$

Since the absorber is designed to operate over a frequency band, and not at just one frequency, the objective function given in Equation (3) is chosen, where B represents the desired frequency band, that corresponds to 0.8–1.9 GHz for the current research. It is important to remark that each layer requires a material and a thickness, so for every layer the optimization problem increases by two dimensions.

$$F_{obj} = 20 \log \left(\max |R(f)|, \ f \in B \right) \tag{3}$$

3. CFO WITH ACCELERATION CLIPPING (AC)

Since there are enough documents that explain the original CFO algorithm, and considering space restrictions, details are not given about it, but the interested reader is welcome to review [1, 3, 4]. In a similar fashion, it will only be discussed that AC is an improvement that was proposed by Qubati and Dib in 2010 [2]. As the name suggests, the modification consists on limiting the acceleration vector, so that probes will remain more time inside the search domain. The way of achieving this is to compare the acceleration vector with a scaled value of the diagonal value of the search domain. In case the former is higher, it will be clipped by the same scale factor of the latter ($A_{\max}$), thus slowing down the probes. According to the creators, a default value of 0.01 can be used, although good results can be achieved inside the range [0.001, 5]. It is important to remark here that $A_{\max} = 1$ generates the original CFO algorithm, since no scaling is carried out.

4. NUMERICAL RESULTS

In order to establish some common ground for the testing scenarios, the database shown in Table 1 was used, which has been previously reported in literature and which contains different kinds of materials [5] Moreover, results are compared with those obtained by [6], who used a Particle Swarm Optimization algorithm (PSO) and Interval Analysis (IA) to optimize this kind of device. Regarding restrictions, the design was limited to the mobile communications frequency band (i.e., 0.8–1.9 GHz) and each layer was defined to have a maximum thickness of 2 mm.

Table 1: Materials database [5].

<table>
<tr><td colspan="5">Lossless dielectric materials ($\mu_r = 1$)</td><td colspan="3" rowspan="2">Relaxed magnetic materials ($\varepsilon_r = 15$)
$\mu_r = \mu' - j\mu'' \quad \mu'(f) = \frac{\mu_m f_m^2}{f^2 + f_m^2} \quad \mu''(f) = \frac{\mu_m f_m f}{f^2 + f_m^2}$</td></tr>
<tr><td>Id</td><td colspan="4">ε_r</td></tr>
<tr><td>1</td><td colspan="4">10</td><td>Id</td><td>μ_m</td><td>f_m</td></tr>
<tr><td>2</td><td colspan="4">50</td><td>9</td><td>35</td><td>0.8</td></tr>
<tr><td colspan="5" rowspan="2">Lossy magnetic materials ($\varepsilon_r = 15$)
$\mu_r = \mu' - j\mu'' \quad \mu'(f) = \frac{\mu'}{f^a} \quad \mu''(f) = \frac{\mu''}{f^b}$</td><td>10</td><td>35</td><td>0.5</td></tr>
<tr><td>11</td><td>30</td><td>1.0</td></tr>
<tr><td>Id</td><td>μ'</td><td>a</td><td>μ''</td><td>b</td><td>12</td><td>18</td><td>0.5</td></tr>
<tr><td>3</td><td>5</td><td>0974</td><td>10</td><td>0961</td><td>13</td><td>20</td><td>1.5</td></tr>
<tr><td>4</td><td>3</td><td>1.000</td><td>15</td><td>0957</td><td>14</td><td>30</td><td>2.5</td></tr>
<tr><td>5</td><td>7</td><td>1.000</td><td>12</td><td>1.000</td><td>15</td><td>30</td><td>2.0</td></tr>
<tr><td colspan="5" rowspan="2">Lossy dielectric materials ($\mu_r = 1$)
$\varepsilon_r = \varepsilon' - j\varepsilon'' \quad \varepsilon'(f) = \frac{\varepsilon'}{f^a} \quad \varepsilon''(f) = \frac{\varepsilon''}{f^b}$</td><td>16</td><td>25</td><td>3.5</td></tr>
<tr><td colspan="3" rowspan="5">—</td></tr>
<tr><td>Id</td><td>ε'</td><td>a</td><td>ε''</td><td>b</td></tr>
<tr><td>6</td><td>5</td><td>0861</td><td>8</td><td>0569</td></tr>
<tr><td>7</td><td>8</td><td>0778</td><td>10</td><td>0682</td></tr>
<tr><td>8</td><td>10</td><td>0778</td><td>6</td><td>0861</td></tr>
</table>

4.1. One-stage Process

As a first approach, it was desired to observe the behavior of the original CFO algorithm while using three different initial distributions. In this case, they were defined as a completely random distribution, as a completely uniform distribution and as a mixed distribution, where the materials were uniformly distributed while the thickness was randomly initialized. Considering space restrictions, results are shown in [7], and it will only be said here that the best result was achieved using a mixed initial distribution, since it delivers the best reflection coefficient (−20.95 dB) while also providing the thinnest absorber (2.8674 mm).

Afterwards, acceleration clipping was implemented (using $A_{\max} = 0.49e^{-0.003t} + 0.01$), and the results shown in Table 2 were achieved. In this case, the best results were accomplished by using a completely random initial distribution, as opposed to the previous case. However, and even though the absorber configuration returned by this set of tests is thicker, it performs better, posing an improvement of a little bit more than 6 dB when compared to the previous design.

Table 2: Results achieved with CFO (considering AC) and three different initial distributions. Based on [7].

Algorithm		**First Layer**	**Second Layer**	**Third Layer**	**Total Thickness [mm]**	**Max Γ [dB]**
First Design (Random)	Material	16	4	4	3.8994	−27.11
	Thickness [mm]	0.8527	1.7466	1.3001		
Second Design (Uniform)	Material	4	5	1	4.4585	−21.75
	Thickness [mm]	1.5331	1.3398	1.5856		
Third Design (Mixed)	Material	4	5	8	4.4589	−22.00
	Thickness [mm]	1.7607	1.0227	1.6755		

4.2. Two-stage Process

In order to try and improve the previously shown results, and considering that the material of each layer is a discrete variable, it was decided to implement a two-stage process for both, the original and modified CFO algorithms, in the following way. During the first pass, the algorithm considers all six variables, and optimizes them. After that, the algorithm is run again, but this time the materials are set to the best ones found in the previous step, so it only has to optimize half the variables (i.e., the thickness of each layer) After applying this procedure with the original CFO, it was found that it was still better to use a mixed distribution, and the results were improved to a maximum reflection coefficient of −21.28 dB for an absorber 2.96 mm thick, even though they did not get near the ones reached by CFO with AC.

In the second case, i.e., for CFO and AC, results are shown in Table 3. As it is easily seen, results are further improved, even though the total thickness increased a bit. According to this data, it seems that whenever the original CFO is being used, a mixed distribution tends to provide better results, whereas a totally random initial distribution should be considered when using CFO with AC.

4.3. Results Evaluation

Striving to provide a general panorama of the results, it was decided to create Figure 1, which summarizes the best results of the previous tests, and which also shows the data reported by [6] when using PSO and IA. After a comparison with the aforementioned data, it was found that by using CFO with AC it was possible to improve the reflection coefficient by almost 5 dB, while reducing the total thickness about 0.3 mm (i.e., a MEA with a total thickness of 3.9 mm and a maximum reflection coefficient of −27.11 dB). Moreover, by implementing the dual-stage process the improvement on the reflection coefficient can go up to almost 6 dB, while the total thickness is reduced by 0.5 mm.

There are some things worth mentioning from Figure 1. For starters, it is evident that even though both designs which considered AC yielded similar maximum reflection coefficients, the dual stage allows for further improvements at different frequencies (up to around 5 dB), which becomes

Table 3: Results of the 2-stage process when using CFO and AC for 3 different initial distributions. Based on [7].

Algorithm		**First Layer**	**Second Layer**	**Third Layer**	**Total Thickness [mm]**	**Max Γ [dB]**
First Design (Random)	Material	16	4	4	3.7375	−28.76
	Thickness [mm]	0.7559	1.5191	1.4625		
Second Design (Uniform)	Material	4	5	1	4.3561	−21.94
	Thickness [mm]	1.6515	1.1722	1.5324		
Third Design (Mixed)	Material	4	5	8	4.3620	−22.01
	Thickness [mm]	1.7888	0.9823	1.5909		

even more important for the original version of CFO (up to more than 10 dB). Thus, the benefit of implementing the dual-stage process when optimizing a MEA is evident. As a second element of interest is the fact that AC allowed for more stable results over the frequency band. Nonetheless, results such as the ones yielded by PSO or IA manifest a higher absorption for frequencies below 1.2 GHz, so the decision of which design provides the best results will ultimately depend on the importance of each frequency in the spectrum of interest (e.g., for some applications frequencies around 1 GHz could be more important than those around 1.7 GHz). This, however, could be considered in the algorithm by including some weights for each frequency.

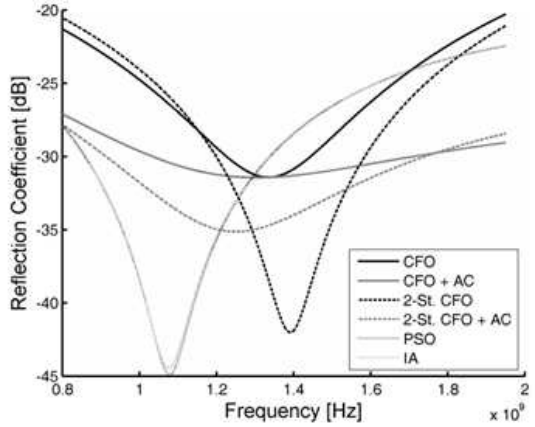

Figure 1: Frequency response of the best results found during this research and of those reported by [6].

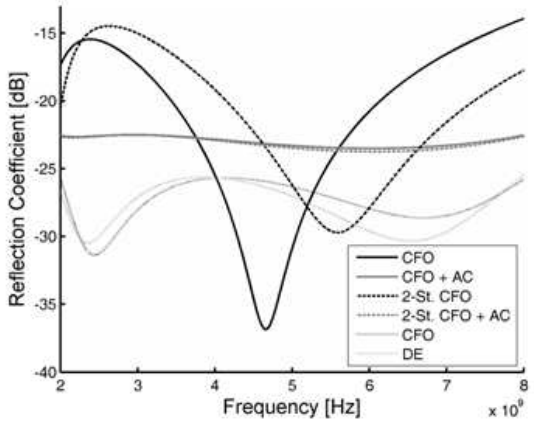

Figure 2: Frequency response of the best results found during this research and of the best two reported by [8].

4.4. Further Testing

Striving to increase the scope of the research a bit, it was decided to run the algorithm for the frequency range of 2.0–8.0 GHz, and to compare the results with those achieved by [8]. Since it was an exploratory test, the designs were restricted to three layers, though. Figure 2 shows the frequency response of the designs (including the best two found by [8]), and it can be seen that, once more, AC allows for more stable results. Moreover, it is important to remark that the dual stage improved the results (once again), and that even though the reflection coefficients are not as good as those previously reported, they are close by in spite of having two less layers, and they require a thinner absorber (i.e., the total thickness is of 4.26 mm as opposed to the 4.74 previously reported).

5. CONCLUSIONS

Based on the results achieved by this research, it can be concluded that by using CFO with AC, it is possible to obtain better results (in terms of maximum reflection coefficient) than those delivered by PSO or by IA, for a three layered MEA. Moreover, a two-stage process was implemented, which strived to reduce the problem's dimensions by half, finding that it was possible to improve the results further, even getting closer to those achieved with other metaheuristics for a five layers design. When using different initial distributions, it was observed that a totally random distribution seems to perform better with CFO and AC, while a mixed distribution yields better results for the original CFO algorithm. It is important to remember that, depending on each particular application, there could be one, or several, frequencies that are more important than others (e.g., because of interference with sensitive equipment), so it is recommended (as a next stage) to implement some kind of weighting function so the algorithm is able to consider this parameter.

REFERENCES

1. Formato, R. A., "Central force optimization: A new metaheuristic with applications in applied electromagnetics," *Progress In Electromagnetics Research*, Vol. 77, 425–491, 2007.
2. Qubati, G. M. and N. I. Dib, "Microstrip patch antenna optimization using modified central force optimization," *Progress In Electromagnetics Research B*, Vol. 21, 281–298, 2010.
3. Formato, R. A., "Central force optimization: A new deterministic gradient-like optimization metaheuristic," *OPSEARCH*, Vol. 46, No. 1, 25–51, Jun. 2009.
4. Green, R. C., L. Wang, M. Alam, and R. A. Formato, "Central force optimization on a GPU: A case study in high performance metaheuristics using multiple topologies," *2011 IEEE Congress on Evolutionary Computation (CEC)*, No. 2, 550–557, 2011.
5. Liu, H., L. Zhang, Y. Gao, Y. Shen, and D. Shi, "Electromagnetic wave absorber optimal design based on improved particle swarm optimization," *EMC 2009, IEICE*, 797–800, 2009.
6. Salazar, E. and J. Mora, "Diseño de absorbedores electromagnéticos óptimos utilizando optimización por enjambre de partículas y análisis de intervalos," B.Sc. Thesis, Universidad Industrial de Santander, 2011.
7. González, J. and C. Bayona, "Aplicación del método de optimización por fuerza central (CFO), al diseño de un absorbedor electromagnético óptimo," B.Sc. Thesis, Universidad Industrial de Santander, 2013.
8. Asi, M. and N. I. Dib, "Design of multilayer microwave broadband absorbers using central force optimization," *Progress In Electromagnetics Research B*, Vol. 26, 101–113, 2010.

Narrow Bipolar Pulses and Associated Microwave Radiation

M. R. Ahmad[1, 3], **M. R. Mohd Esa**[2, 3], **and V. Cooray**[3]

[1]FKEKK, Universiti Teknikal Malaysia Melaka, Malaysia
[2]FKE, Universiti Teknologi Malaysia, Malaysia
[3]Department of Engineering Science, Uppsala University, Sweden

Abstract— Narrow Bipolar Pulses (NBPs) is a special type of intra-cloud lightning discharge activities and was observed with both polarities: negative (NNBP) and positive (NPBP). It is known with other names also such as Narrow Bipolar Events (NBEs), energetic intracloud events, and Compact Intracloud Discharges (CIDs). NBP signatures have been measured by using various methods such as electric field change recording systems, HF-VHF direct measurement systems (filter-detector receiver), and satellite-based systems. To the best of our knowledge, there are no attempts have been made to measure NBP signatures at microwave region so far. In this paper, observations of microwave radiation from thunderstorms have been made during the northeastern monsoon season of 2012 in Malaysia. Fast electric field change recording and broadband microwave receiver systems have captured simultaneous records of NBPs electric field change and microwave radiation, respectively. Strong noise-like burst of microwave radiation pulses associated with NBP events were detected. The total duration of the microwave bursts of the pulses is in the range between 2 and 8 μs for both NNBPs and NPBPs. More than 70% of the recorded radiation bursts arrived a few microseconds before the onset of the corresponding NBPs. The analyzed temporal characteristics of the microwave radiation bursts for both NNBPs and NPBPs are similar and indistinctive. In contrast, the analyzed NNBPs and NPBPs temporal characteristics are distinctive to some extent.

1. INTRODUCTION

Previous studies on narrow bipolar pulses (NBPs) have been concentrated on the associated HF and VHF radiations only. Le Vine [2] reported observations of narrow positive bipolar pulses (NPBPs) at 3 MHz, 139 MHz, and 295 MHz using vertically polarized antennas. They observed that NPBP produced the strongest RF radiation and even larger than RF radiation of return strokes at these HF and VHF frequencies. Rison, et al. [3] reported observations of narrow negative bipolar pulses (NNBPs) at 63 MHz. They observed that the peak VHF radiation of NNBP was 30 dB greater than IC and CG events. Smith, et al. [5] reported observations of NPBPs recorded by broadband HF systems between 3 to 30 MHz using discone antennas. The broadband noise-like HF radiation bursts associated with NPBPs has a mean duration of 2.8 μs and amplitudes ten times larger than radiation from IC and CG discharges at HF frequencies. Sharma, et al. [4] reported observations of NPBPs at 5 and 10 MHz using parallel flat plate antennas. They observed that these HF radiations start with the onset of the NPBP event. Ahmad, et al. [1] reported observations of both NPBPs and NNBPs at 3 MHz and 30 MHz using parallel flat plate antennas. They found that nano-scale fine and sharp pulses embedded on the micro-scale NBP pulses. The overall duration of a nano-scale pulse is in the range between a few nanoseconds and 20 nanoseconds. These nano-scale pulses always trigger the 3 and 30 MHz narrowband receivers. These nano-scale pulses could be associated with the observed microwave radiation pulses presented in this paper.

In this paper, observations of microwave radiation bursts of pulses emitted during NBP event are reported for the first time. Both types of NBPs (NPBP and NNBP) are accompanied by the microwave radiation bursts and detail analysis of the time behavior between them is provided. The initial polarity of NBP is defined according to the atmospheric sign convention throughout the paper.

2. EXPERIMENTATION

The measurements were conducted between November and December 2012 during the northeast monsoon period at Observatory Station in Universiti Teknologi Malaysia (UTM), Johor, Malaysia, located at southern part of peninsular Malaysia (1°N, 103°E). The measuring system was situated on a top of a hill that is 132 meters above sea level and about 30 km away from Tebrau strait.

A diagram of the complete measurement instruments is shown in Fig. 1. The measurement instruments consist three main systems namely electric field change recording system, broadband microwave receiver system, and GPS-based time synchronization system. The electric field change

recording system was used to record fast variation of the vertical electric field change while the broadband microwave receiver system was used to capture microwave radiations associated with the recorded fast electric field change waveforms. A GPS timing server was used to maintain accurate clock synchronization of the digital storage oscilloscopes (DSOs) between the two systems. The broadband microwave receiver system consisted a Low Noise Amplifier (LNA) connected to a Band Pass Filter (BPF) with operating frequencies between 1.5 and 3 GHz. Electrical signals induced by the incident electric fields on a whip antenna with omni directional pattern (E-plane half power beam width 19 degrees and 9 dBi gain) were directed towards the LNA by using a 5 meters 50 Ω RG58 coaxial cable. The output electrical signals of the BPF were digitized directly by a DSO at a rate of 2.5 Giga Samples/second. A DSO at a rate of 25 Mega Samples/second digitized the output of electrical signals from the fast electric field change recording system.

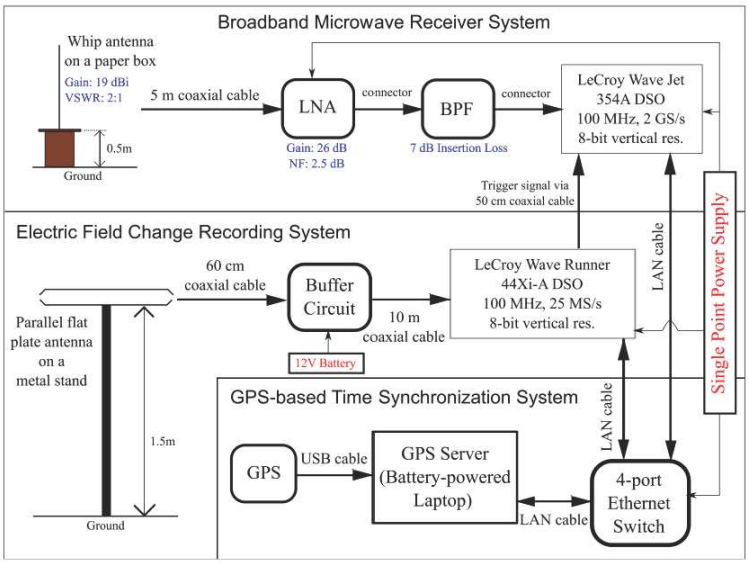

Figure 1: Diagram of the observational instruments consisting three systems to measure NBPs and its associated microwave radiations.

3. RESULTS AND DISCUSSION

A total number of 64 NBPs was analyzed where 58.7% of them were NNBPs and the others were NPBPs, which in good agreement with Ahmad, et al. [1] observation. Examples of NNBP and NPBP and their associated microwave radiation noise-like bursts are shown in Fig. 2 and Fig. 3, respectively. More than 70% of the observed microwave radiation bursts were recorded before the onset of their corresponding NBPs.

The pulse duration of NNBPs is varied between 9.5 and 90.46 µs with the mean value of 25.3 ±

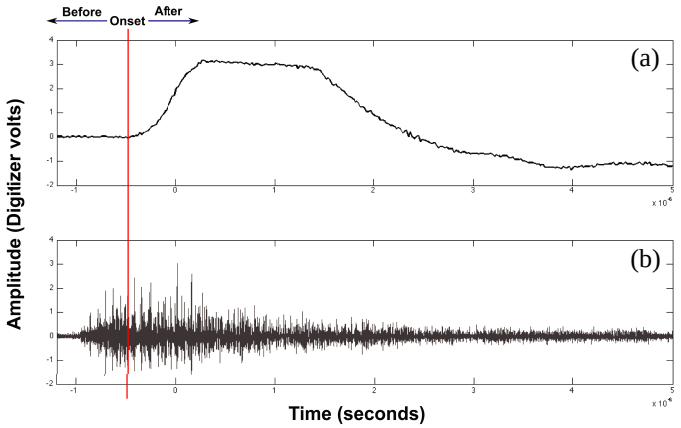

Figure 2: (a) A record of NNBP and (b) its associated noise-like microwave radiation burst.

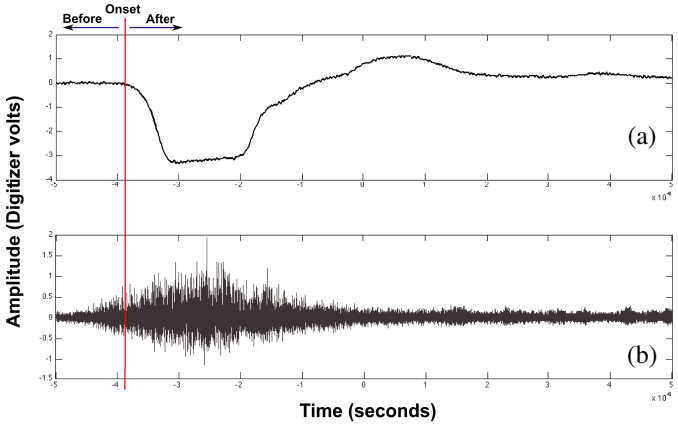

Figure 3: (a) A record of NPBP and (b) its associated noise-like microwave radiation burst.

19.8, which in good agreement to the duration obtained by Ahmad, et al. [1]. On the other hand, the pulse duration of NPBPs has shorter range and smaller mean values, varied between 5.6 and 25.5 µs with the mean value of 13.4 ± 7.5, which in good agreement with the recorded mean value by Le Vine [2], and Sharma, et al. [4]. The statistical distribution of zero crossing time (ZCT), rise time,

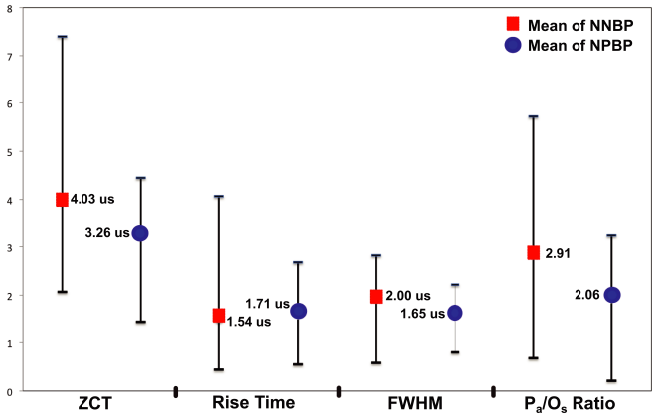

Figure 4: Statistical distribution of temporal characteristics for both NNBP and NPBP recorded from the fast electric field change recording system.

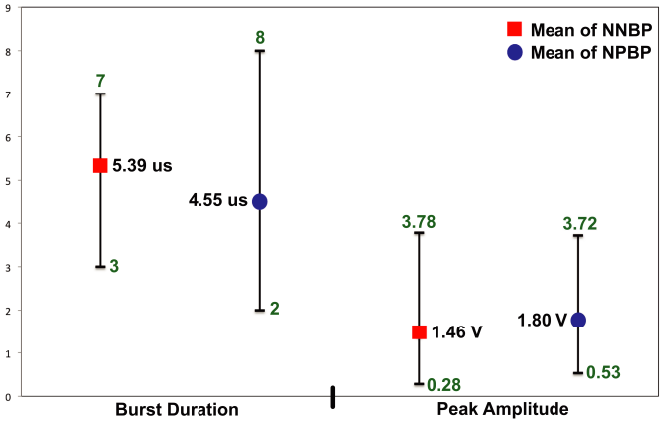

Figure 5: Statistical distribution of temporal characteristics for both NNBP and NPBP noise-like bursts recorded from the broadband microwave receiver system.

full width at half maximum (FWHM), and the ratio of initial peak to the overshoot peak (P_a/O_s) is plotted in Fig. 4 and comparable to the statistical distribution obtained by Sharma, et al. [4] and Ahmad, et al. [1]. The statistical distribution of the microwave radiation burst duration and peak amplitude is plotted in Fig. 5. The values of the burst duration for both NNBP and NPBP are almost 2 times higher than the value recorded by Smith, et al. [5] from broadband HF system.

4. CONCLUSIONS

Microwave radiation in the form of noise-like bursts was detected with more than 70% of the recorded radiation bursts has arrived a few microseconds before the onset of the corresponding NBPs. The analyzed temporal characteristics of the microwave radiation bursts for both NNBPs and NPBPs are similar and indistinctive. In contrast, the analyzed NNBPs and NPBPs temporal characteristics are distinctive to some extent.

ACKNOWLEDGMENT

The authors would like to thank IVAT lightning research team for their support in conducting the experimental work in UTM, Malaysia.

REFERENCES

1. Ahmad, H. and Z. A. Malek, "Characteristics of narrow bipolar pulses observed in Malaysia," *Journal of Atmospheric and Solar-terrestrial Physics*, Vol. 72, 534–540, 2010.
2. Le Vine, D. M., "Sources of the strongest lightning radiation from lightning," *Journal of Geophysical Research*, Vol. 85, No. C7, 4091–4095, 1987.
3. Rison, W., R. J. Thomas, P. R. Krehbiel, T. Hamlin, and J. Harlin, "A GPS-based three dimensional lightning mapping system: Initial observations in central new Mexico," *Geophysical Research Letter*, Vol. 26, No. 23, 3573–3576, 1999.
4. Sharma, S. R., M. Fernando, and V. Cooray, "Narrow positive bipolar radiation from lightning observed in SRI Lanka," *Journal of Atmospheric and Solar-terrestrial Physics*, Vol. 70, 1251–1260, 2008.
5. Smith, D. A., X. M. Shao, D. N. Holden, C. T. Rhodes, M. Brook, P. R. Krehbiel, M. Stanley, W. Rison, and R. J. Thomas, "A distinct class of isolated intracloud lightning discharges and their associated radio emissions," *Journal of Geophysical Research*, Vol. 104, No. D4, 4189–4212, 1999.

Coaxial Reflection Probe for Measurements of Temperature and Frequency Dependent Dielectric-properties of Low-loss Liquids

J. Vrba
Faculty of Biomedical Engineering, Czech Technical University in Prague, Czech Republic

Abstract— An existing measurement coaxial reflection probe suitable for measurements of frequency dependent dielectric properties of low-loss liquids was adapted here. A number of modifications made here led to an improved measurement performance in terms of significantly easier evaluation of LUT dielectric properties as well as easier probe handling. Furthermore, the probe was equipped here with a heat exchanger. Therefore, it is possible to measure dielectric properties of LUT at different temperatures. Measurements of different liquids with known dielectric properties, so called standard liquids were performed as well. A comparison of the here evaluated values of dielectric properties of the standard liquids with data published in professional literature verified here presented probe geometry and measurement procedure.

1. INTRODUCTION

Results of laboratory and field tests have shown that the high-power MW-field-induced separation of Oil and Water (O-W) emulsions has a potential to become a chemical-free alternative to conventional separation processes [1]. The separation mechanism of this process has not been fully understood yet and there is a need for further research. In the separation mechanism temperature and frequency dependent dielectric properties of the two main emulsion components, of water and oil, play an important role. While the temperature and frequency dependent model of dielectric properties of water already exists [2], a lack of in professional literature published dielectric properties of oils was found out.

An existing measurement coaxial reflection probe [3] suitable for measurements of frequency dependent dielectric properties of low-loss liquids was adapted here. It consists mainly of a coaxial transmission-line section filled with the measured liquid and short circuited at one end. Instead of the evaluation of dielectric properties of the Liquid Under Test (LUT) for every frequency point, the general model of dielectric properties of liquids, the Cole-Cole model [4] consisting of four real parameters, was used and these parameters were extracted directly.

A number of modifications made here led to an improved measurement performance in terms of significantly easier evaluation of LUT dielectric properties as well as easier probe handling. Furthermore, the probe was equipped here with a heat exchanger and therefore, it is possible to measure dielectric properties of LUT at different temperatures. Subsequently, it is possible to create temperature and frequency dependent models of the LUT's dielectric properties.

2. MEASUREMENT PROBE AND PROCEDURE

Compared with [3], the main differences in geometry, equivalent circuit and the measurement method used in this project are:

1. The cross-section dimensions of the probe used here are given by the 7/16 coaxial standard instead of SMA. Here, the inner and the outer radii of the measurement coaxial probe are 3.5 and 8 mm, respectively. This simplifies filling and emptying of the probe with high viscosity liquids and it also makes removal of possible air bubbles in the liquid before measurement easier.
2. Between the measurement reference plane and the probe input (the interface of the LUT region and PTFE), there are two different adapters (SMA to N, N to 7/16) and a 7/16 connector. The two adapters and the connector were measured and characterized separately using the necessary auxiliary structures and the influence of the two adapters and the connector located between the measurement/calibration reference plane and the input of the probe (the interface of the connector and the LUT) has been removed from measurements using a standard de-embedding procedure. The mathematical model of the measurement probe used here thus does not have to describe the effects of the adapters and consists of less parameters that need to be determined by fitting.

3. The equivalent circuit model of the probe consists of the transmission line model and an equivalent model of the short-circuit (see Fig. 2). In [3], additional circuit elements are used at the input of the probe. The reflection coefficient of the probe equivalent circuit model is denoted here as $\underline{S}_{11,\mathrm{mod}}$.
4. The reflection coefficient was measured directly using NVA instead of TDR measurements and conversions to S-parameter using FFT.
5. The probe presented here was equipped with a heat exchanger, which allowed the measurement of dielectric parameters at precisely set temperatures.
6. Poor contact of the inner and outer conductor, especially along the junction between the short-circuit metal plane and the outer conductor, could possibly lead to the excitation of higher order modes in the measurement probe. Special care was paid here to this problem and the design of the short-circuit geometry ensures that the above mentioned contact is good (see Fig. 1).

The probe was manufactured and the type A evaluations of the uncertainties were performed. Measurements of different liquids with known dielectric properties, so called standard liquids were performed as well. A comparison of the here evaluated values of dielectric properties of the standard liquids with data published in professional literature verified here presented probe geometry and measurement procedure (see Table 1).

With this measurement probe is possible to measure dielectric properties of LUT at different temperatures. This feature was tested and verified for temperatures in the temperature range from 10 to 70°C. Dielectric properties of sunflower and olive oil as well as of two commercial emulsion concentrates were measured in temperature and frequency range from 10 to 70°C and from 1 MHz to 3 GHz, respectively and corresponding empirical temperature and frequency models were created. These models will be presented elsewhere.

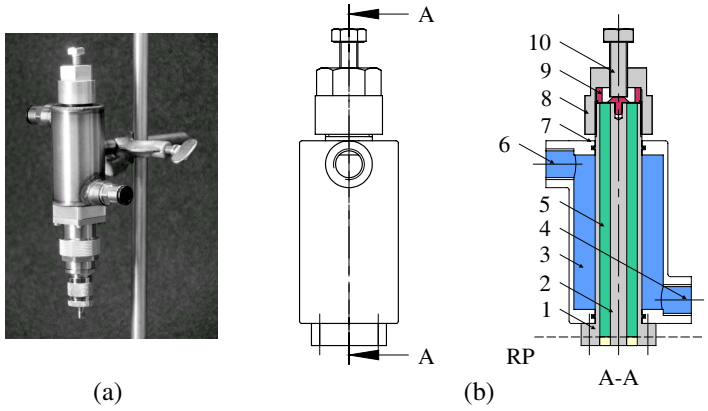

Figure 1: Picture of the probe with the heat exchanger. (a) During the measurement, the probe was equipped with a thermal insulation, which is omitted here in order to show the probe's geometry. A simplified technical drawing and a section of the measurement probe with the heat exchanger. (b) (1) and (2) are the outer and the inner conductor of the coaxial probe, respectively, (3) water, (4) water inlet, (5) LUT, (6) water outlet, (7) heat exchanger, (8) nut, (9) short-circuit, (10) bolt. Thermal insulation is omitted here in order to simplify the picture.

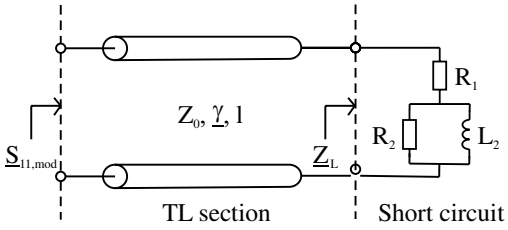

Figure 2: The equivalent-circuit model of the measurement probe, where ℓ, Z_0, $\underline{\gamma}$ is the physical length, complex characteristic impedance and the complex propagation constant of the transmission line, respectively.

Table 1: Comparison between the Cole-Cole parameters of ethanol and 2-propanol at 20°C evaluated here and published in [5, 6]. The values of the short-circuit equivalent-circuit elements are $R_1 = 1.17 \cdot 10^{-5}\,\Omega$, $R_2 = 4.84\,\Omega$ and $L = 0.084\,\text{nH}$.

Ethanol			
Parameter	Reference values [5]	[6]	Here measured values
ε_s [−]	25.16 ± 0.04	25.07	25.103 ± 0.014
ε_∞ [−]	4.486 ± 0.025	4.2	3.709 ± 0.089
f_r [MHz]	834 ± 0.004	1110	873.0 ± 10.0
β [−]	not available	0	0.0240 ± 0.0045
2-propanol			
Parameter	Reference values [5]	[6]	Here measured values
ε_s [−]	20.26 ± 0.06	19.0	20.487 ± 0.089
ε_∞ [−]	3.447 ± 0.016	3.2	3.321 ± 0.030
f_r [MHz]	358 ± 2	545	354.9 ± 5.2
β [−]	not available	0	0.0385 ± 0.0025

3. MEASUREMENTS AT DIFFERENT TEMPERATURES

At the very beginning of the evaluation of the Cole-Cole parameters of the LUT with the new probe, the control and adjustment of the LUT temperature was not used. The temperature of the measurement laboratory was considered to be exactly 20°C. A noticeable mismatch was shown between the computed and the measured reflection coefficient and this mismatch could not be compensated by the modification of the values of R_1, R_2 and L only. The mismatch disappeared with the addition of a fourth fitting parameter T (temperature). It turned out that the value of T, obtained by fitting, was slightly higher, about 0.6°C, than the considered laboratory temperature. After ensuring that the temperature of the LUT was constant, using the heat exchanger, the evaluated values of Cole-Cole parameters of the standard liquids agreed well with the values listed in [5, 6], see Table 1.

The LUT temperature control proved to be very important. For the measurement of dielectric properties of the LUT at a certain temperature, the following approach was used: The probe filled with the LUT was heated/cooled to the desired temperature; the standard liquids were measured at the same temperature prior to the measurement of the liquids of unknown dielectric properties. The measurements of the reflection coefficient of the probe filled with the standard liquid were used for the determination of R_1, R_2, L and the actual temperature T of the LUT. The evaluated Cole-Cole parameters of 2-propanol were compared with the values from [5, 6] and if the values matched, the Cole-Cole parameters of the liquids of unknown dielectric properties were evaluated as well.

4. CONCLUSIONS

In this article, an existing measurement coaxial reflection probe suitable for measurements of frequency dependent dielectric properties of low-loss liquids was adapted and additionally equipped with a heat exchanger. The probe was manufactured and measurements of different liquids with known dielectric properties, so called standard liquids were performed. A comparison of the here evaluated values of dielectric properties of the standard liquids with data published in professional literature verified here presented probe geometry and measurement procedure. With this measurement probe is possible to measure dielectric properties of LUT at different temperatures. This feature was tested and verified for temperatures in the temperature range from 10 to 70°C. Dielectric properties of sunflower and olive oil as well as of two commercial emulsion concentrates were measured in temperature and frequency range from 10 to 70°C and from 1 MHz to 3 GHz,

respectively and corresponding empirical temperature and frequency models were created. These models will be presented elsewhere.

REFERENCES

1. Hubrich, M., B. Schmidt, M. Kozariszczuk, A. John, R. H. Jansen, J. Vrba, and J. Wellenbuescher, "Ecologically friendly microwave treatment of oil emulsions as contribution to conserving resources by effluent free manufacture in industry," Project No. 01RI0616B, Tech. Rep. No. 4.61.163, VDEh-Betriebsforschungsinstitut GmbH (BFI), VDEh-Betriebsforschungsinstitut, Sohnstr. 65, 40237 Duesseldorf, June 2010.
2. Ellison, W. J., "Permittivity of pure water, at standard atmospheric pressure, over the frequency range 0–25 THz and the temperature range 0–100 C," *Journal of Physical and Chemical Reference Data*, Vol. 36, No. 1, 1–18, 2007.
3. Cataldo, A., E. Piuzzi, G. Cannazza, and E. De Benedetto, "Dielectric spectroscopy of liquids through a combined approach: Evaluation of the metrological performance and feasibility study on vegetable oils," *IEEE Sensors Journal*, Vol. 9, No. 10, 1226–1233, 2009.
4. Cole, K. S. and R. H. Cole, "Dispersion and absorption in dielectrics i. Alternating current characteristics," *The Journal of Chemical Physics*, Vol. 9, No. 4, 341, 1941.
5. Gregory, A. P. and R. N. Clarke, "Tables of complex permittivity of dielectric reference liquids at frequencies up to 5 GHz," *NPL Rep. CETM*, Vol. 33, 2001.
6. Buckley, F. and A. A. Maryott, "Tables of dielectric dispersion data for pure liquids and dilute solutions," *National Bureau of Standards Circular*, Vol. 589, U.S. Dept. of Commerce, National Bureau of Standards, 1958.

Design of Stripline Kicker for Tune Measurements in the MAX IV 3 GeV Ring

D. Olsson
MAX IV Laboratory, Lund University, Sweden

Abstract— During commissioning and routine operation of the MAX IV 3 GeV storage ring, the ability to measure the betatron tunes is important. For these measurements a shaker such as a stripline kicker is needed to excite coherent transverse oscillations of the beam within a narrow range of frequencies. In this paper, the design of this stripline kicker is described. Besides from operating as an active device during tune measurements, the stripline will also work as a BPM pick-up during normal operation.

1. INTRODUCTION

MAX IV will be Sweden's next-generation synchrotron radiation light source, and will consist of two storage rings and a full energy injector LINAC. The larger 3 GeV ring will have a circumference of 528 m, and the smaller 1.5 GeV ring a circumference of 96 m. In the 3 GeV ring, a stripline kicker will be used as a shaker during tune measurements. The beam oscillation is then monitored by a standard button BPM. However, the stripline kicker should also be used as a passive BPM pick-up during normal operation. The relevant parameters of the 3 GeV ring are given in Table 1 [1].

Beam energy	3.0 GeV
Maximum beam current	500 mA
RMS bunch length	5.6 cm
Main radio frequency	99.931 MHz
Harmonic number	176
Ring circumference	528 m
Betatron tune (horizontal/vertical)	42.20/14.28
Excitation frequency for tune measurements	500 MHz
BPM pick-up frequency	500 MHz

Table 1: Parameters of the MAX IV 3 GeV storage ring.

2. STRIPLINE DESIGN

We need four stripline electrodes since we like to shake the beam independently in the vertical and horizontal direction. Often the beam should be shaken in a direction tilted 45 degrees from the horizontal direction. For this reason, the strips are oriented accordingly at 45, 135, 225, and 315 degrees, as seen in Figure 1. The radius of curvature, R, is the same as the radius of the beam pipe, i.e., 13.5 mm. This value minimizes the unwanted effect of the beam impedance. Each strip has an angular extension of $\varphi_s = 45$ degrees and a thickness of 1 mm. The optimum stripline length L when considering kicker performance is $\lambda/4$, where λ is the RF excitation wavelength. Therefore, a length of $L = 15$ cm is chosen. Between each strip there is a region of extended (raised) ground. The angular gap φ_g between a strip and the extended ground region is 8.6 degrees. All the stripline components are made of Stainless Steel 316 L.

For the beam excitation described above, we need to operate the stripline kicker in the three different modes that are described in Table 2. Here, U_x is the applied RF amplitude of the corresponding strip (see Figure 1), where a negative amplitude is due to a phase shift of 180 degrees compared to the strip with positive potential. The sum mode is not actually a mode for beam excitation, but describes the potential distribution from the excitation of the beam itself assuming the beam is centered on the pipe. The characteristic impedance, Z_L, of each mode is obtained from electrostatic simulations in COMSOL Multiphysics and the results are seen in Table 2. It is possible to achieve an impedance closer to 50 Ω near the coaxial feedthroughs by using tapered strips, but since the purpose of the stripline is beam excitation and beam monitoring in a narrow

frequency range, there are no requirements for bandwidth. Therefore, the coaxial feedthroughs are just welded to the strips as shown in Figure 3.

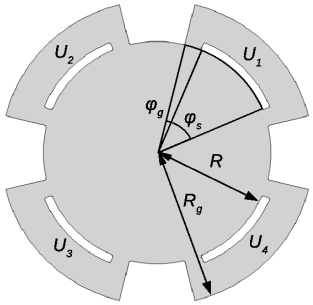

Figure 1: The 2D geometry of the stripline kicker.

Mode of operation	U_1	U_2	U_3	U_4	$Z_L\,[\Omega]$
Diagonal (d)	V_0	0	$-V_0$	0	50.0
Horizontal (h)	V_0	$-V_0$	$-V_0$	V_0	50.0
Vertical (v)	V_0	V_0	$-V_0$	$-V_0$	50.0
Sum (Σ)	V_0	V_0	V_0	V_0	53.4

Table 2: The modes of operation.

We can analytically obtain the electric scalar potential, $\Phi(\rho,\varphi)$, of the (first) propagating TEM modes along the stripline by solving Laplace equation in two dimensions. This is in the region where $0 \le \rho \le R$ and requires that we evaluate the striplines far away from their end-gaps. Here, we make an approximation by assuming that the azimuthal electric field in the gaps between the strips and the extended ground at $\rho = R$ is constant and that the radial component is zero, i.e., $\mathbf{E}(R,\varphi) = \pm\frac{V_0}{R\varphi_g}\hat{\varphi}$. By applying the conditions of full azimuthal periodicity, finite $\Phi(\rho = 0)$, and the potential at $\rho = R$ described above and in Table 2, we get $\Phi(\rho,\varphi)$ as the following Fourier series, cf. [2].

$$\Phi(\rho,\varphi)=\sum_{m=1}^{4}\frac{U_m}{\pi}\left(\frac{\varphi_s+\varphi_g}{2}+\frac{4}{\varphi_g}\sum_{n=1}^{\infty}\left(\frac{\rho}{R}\right)^n\frac{\sin\left(n\frac{\varphi_g}{2}\right)\sin\left(n\frac{\varphi_s+\varphi_g}{2}\right)}{n^2}\cos\left(n\left(\varphi-\frac{m\pi}{2}+\frac{\pi}{4}\right)\right)\right) \quad (1)$$

Figure 2 shows $\Phi(\rho,\varphi)$ in the diagonal, vertical, and sum mode obtained from (1) (upper figure) together with electrostatic simulations of the same modes in COMSOL (lower figure). The stripline geometry factor g described in [3] can be obtained from (1), and is shown in (2)–(4) for diagonal, horizontal/vertical, and sum mode. The transverse geometry factor is defined as $g_\perp = |\mathbf{E}(\rho = 0)|R$, and the longitudinal as $g_\parallel = \Phi(\rho = 0)$. Here, the excitation voltage V_0 is held at unit potential. In this case, $g_{\perp,d} = 0.57$ and $g_{\parallel,\Sigma} = 0.59$.

$$g_{\perp,d} = \frac{8}{\varphi_g\pi}\sin\left(\frac{\varphi_g}{2}\right)\sin\left(\frac{\varphi_s+\varphi_g}{2}\right) \quad (2)$$

$$g_{\perp,h/v} = \sqrt{2}g_{\perp,d} \quad (3)$$

$$g_{\parallel,\Sigma} = 2\frac{\varphi_s+\varphi_g}{\pi} \quad (4)$$

The cut-off frequency for the beam pipe is 6.5 GHz for the TE_{11} mode and 8.5 GHz for the TM_{01} mode. The 3D structure is simulated using the eigenmode solver in COMSOL. There are TE modes with frequencies below 6.5 GHz, but these can be neglected since they have a longitudinal shunt impedance close to zero and hence they do not affect the beam.

3. KICKER STRENGTH

The transverse shunt impedance Z_{sh} is the ratio of the square of the change in transverse beam voltage to the input power. When operating the striplines in diagonal mode, Z_{sh} is obtained from (5) [3], where c_0 is the speed of light and ω the angular frequency. Here, we assume that the line impedance and the termination impedance are the same as the stripline characteristic impedance, Z_L. Note that Z_{sh} is the same in horizontal/vertical mode as in (5) since the shunt impedance is inversely proportional to the input power, which has to be twice as high according to Table 2, and since $g_{\perp,h/v} = \sqrt{2}g_{\perp,d}$. At the excitation frequency of 500 MHz, the transverse shunt impedance is 1.6 kΩ.

$$Z_{sh} = 2Z_L\left(\frac{g_{\perp,d}c_0}{\omega R}\right)^2\sin^2\left(\frac{\omega L}{c_0}\right) \quad (5)$$

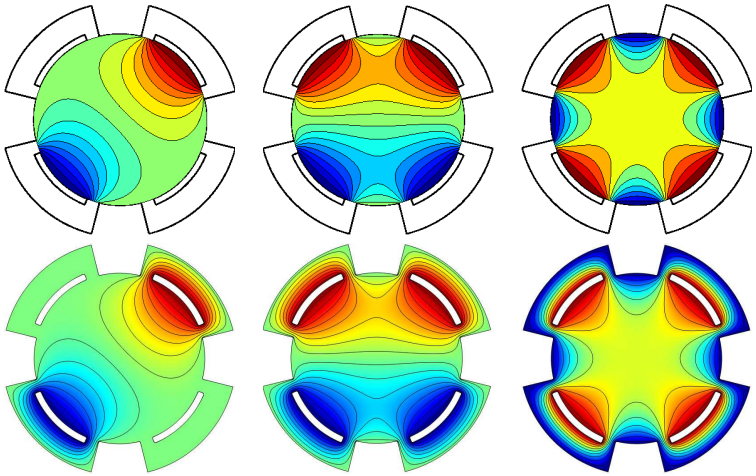

Figure 2: $\Phi(\rho, \varphi)$ obtained from (1) (upper) and from COMSOL simulations (lower). Here, (from the left) the diagonal, vertical, and sum mode are shown.

The maximum kick in radians, $\Delta\alpha$, for one passage is given by (6), where e is the elementary charge, P the applied RMS power, and E the beam energy.

$$\Delta\alpha = \frac{e\sqrt{2Z_{sh}P}}{E} \tag{6}$$

4. BEAM COUPLING AND PICK-UP CHARACTERISTICS

The longitudinal beam impedance $Z_{\|}$ is defined as the Fourier transform of the wake potential. For a stripline kicker, $Z_{\|}$ is given by (7) [3, 4]. This formula is only a valid approximation at lower frequencies where the RF mismatch at the stripline ends is negligible, and the wakes caused by the discontinuity of the surrounding structure are minor. In order to get a more accurate estimation of $Z_{\|}$, the whole geometry was simulated in CST Particle Studio using the wakefield solver. Here, all the coaxial feedthroughs are terminated with ports, and all metal surfaces have the same parameters as Stainless Steel 316 L ($\sigma = 1.32\,\mathrm{MSm}^{-1}$). Figure 3 shows the stripline in the CST Particle Studio environment, and Figure 4 shows $\mathrm{Re}(Z_{\|})$ obtained from the simulation and from (7).

$$Z_{\|} = \frac{Z_L}{8} g_{\|,\Sigma}^2 \left(2\sin^2\left(\frac{\omega L}{c_0}\right) + j\sin\left(\frac{2\omega L}{c_0}\right)\right) \tag{7}$$

The longitudinal beam impedance behaves like the circuit impedance when considering the dissipated power, P_{loss}, in the structure. P_{loss} is given by (8), where $\lambda(t)$ is the normalized charge distribution, I_0 the average beam current, and f_b the bunch repetition frequency. Since no resonance modes with considerable longitudinal shunt impedance exist below the cut-off frequency of the pipe, these mode currents have not been included in the calculations of P_{loss}. The storage ring will have third harmonic (Landau) cavities for bunch stretching, so the bunch distribution will be non-Gaussian. Therefore, a bunch shape described in [5] is used with values from Table 1.

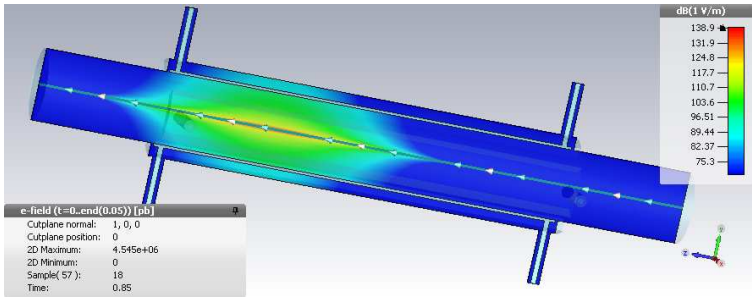

Figure 3: The electric field of a Gaussian bunch in CST particle studio.

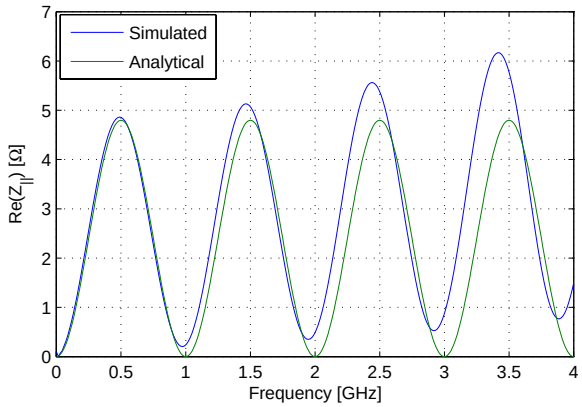

Figure 4: $\mathrm{Re}(Z_{\|})$ obtained from CST Particle studio, and from (7).

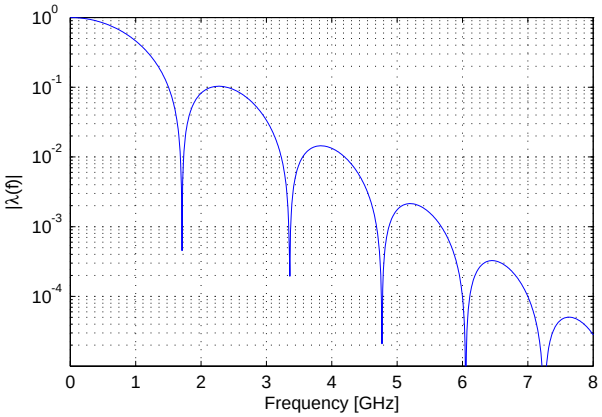

Figure 5: The charge distribution of the bunch in the frequency domain.

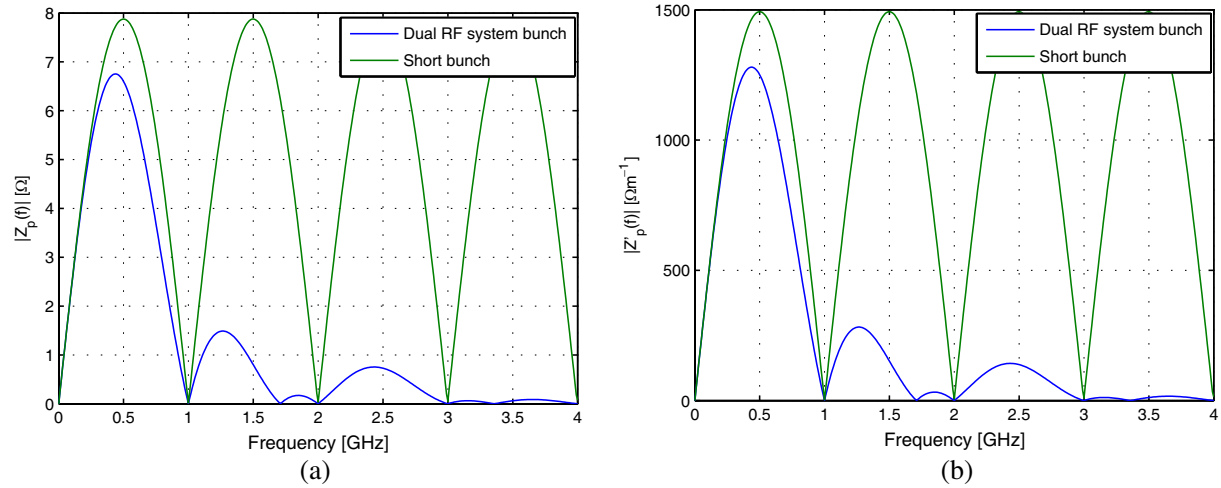

Figure 6: (a) $|Z_p|$ and (b) $|Z'_p|$ for the MAX IV bunch and for a much shorter bunch.

Figure 5 shows the normalized bunch, $\lambda(f)$, in the frequency domain. With uniform filling and at the maximum beam current (500 mA), the dissipated power is 8.9 W. Here, $Z_{\|}$ obtained from CST is used. However, most of the power will dissipate in the stripline terminations, so only a fraction will be transformed into heat inside the stripline.

$$P_{loss} = \frac{I_0^2}{\pi f_b} \int_0^{\infty} \mathrm{Re}(Z_{\|}(\omega))\lambda^2(\omega)d\omega \tag{8}$$

The longitudinal and transverse transfer impedances, Z_p and Z'_p, are important parameters when evaluating the performance of the stripline as a BPM. Z_p is defined as the ratio of the output port voltage to the beam current. If we only consider the ratio of the induced voltage at one port to the total beam current, we get Z_p given by (9). Z'_p is defined as the ratio of the output port voltage to the dipole moment of the beam. If we take the difference of the induced port voltage of two opposite located strips, and if the transverse beam deviation is diagonal, then Z'_p given by (10) and has the dimension $\Omega\mathrm{m}^{-1}$. Note that Z_p and Z'_p are often defined without the $\lambda(\omega)$ term in the literature.

$$Z_p = \frac{Z_L g_{\|,\Sigma}}{4}\lambda(\omega)e^{j(\pi/2-\omega L/c_0)}\sin\left(\frac{\omega L}{c_0}\right) \tag{9}$$

$$Z'_p = \frac{Z_L g_{\perp,d}}{R\sqrt{2}}\lambda(\omega)e^{j(\pi/2-\omega L/c_0)}\sin\left(\frac{\omega L}{c_0}\right) \tag{10}$$

We see from (9) and (10) that $\lambda(\omega)$ makes the transfer impedance decay faster for longer bunches. This is due to destructive interference between the two traveling pulses that are induced at the

stripline ends (the pulses have different signs). Figure 6 shows $|Z_p|$ and $|Z_p'|$ for the MAX IV bunch shown in Figure 5 and for a much shorter bunch. At 500 MHz, Z_p is 6.6 Ω, and Z_p' is 1.25 kΩm^{-1}.

5. CONCLUSION

The stripline kicker design for the MAX IV 3 GeV ring described in this paper has sufficient performance in terms of line matching, kick efficiency, beam impedance, and power dissipation. It will also work as a pick-up, and will be a good complement to the standard button BPMs in the ring during normal operation. There is also a good agreement between simulation results from COMSOL and CST and results obtained analytically.

REFERENCES

1. Leemann, S. C., Å. Andersson, M. Eriksson, L.-J. Lindgren, E. Walléen, J. Bengtsson, and A. Streun, "Beam dynamics and expected performance of Sweden's new storage-ring light source: MAX IV," *Physical Review Special Topics — Accelerators and Beams*, Vol. 12, 120701, 1–15, 2009.
2. Jackson, J. D., *Classical Electrodynamics*, 3rd Edition, Chapters 2–3, John Wiley & Sons, 1998.
3. Goldberg, D. A. and G. R. Lambertson, "Dynamic devices a primer on pickups and kickers," *AIP Conference Proceedings Series —Physics of Particle Accelerators*, 1992.
4. Chao, A. W. and M. Tigner, *Handbook of Accelerator Physics and Engineering*, 3rd Printing, Chapter 3.2, World Scientific, 2009.
5. Hofmann, A. and S. Myers, "Beam dynamics in a double RF system," *XIth International Conference on High Energy Accelerators CERN*, Genevea, 1980.

Compact Microstrip Patch Antenna for Ultra-wideband Applications

W. Mazhar[1, 2], **M. A. Tarar**[2], **F. A. Tahir**[2], **Shan Ullah**[2], **and F. A. Bhatti**[1]

[1]Military College of Signals (MCS)-Rawalpindi
National University of Sciences and Technology (NUST), Islamabad, Pakistan
[2]School of Electrical Engineering and Computer Science (SEECS)
National University of Sciences and Technology (NUST), Islamabad, Pakistan

Abstract— In this paper a novel design of compact microstrip UWB antenna with step impedance microstrip line is proposed.The antenna consists of a rectangular patch with slits on the top face and a partial ground with slots at the rear end. The antenna with dimension of 34 mm × 36 mm ($L \times W$) is fabricated on FR-4 epoxy dielectric with relative permittivity of 4.4. The designed antenna has the capability of operating between 3 GHz to 10.26 GHz with a 7.26 GHz bandwidth (f_h-f_l). The proposed antenna has Omni-directional radiation pattern on most of the operating band. Radiation pattern is measured in antenna anechoic chamber. Feed line used has characteristic impedance of 50 Ω. The proposed antenna is anaylzed in both frequency and time domain to check its appropriateness for UWB applications. SMA female connector is used for feeding. Antenna parameters such as return loss and radiation pattern show reasonable agreement with the simulated results.

1. INTRODUCTION

Antennas have fundamental importance in the field of wireless communication. With the rapid development and advancement of wireless broadband technologies we require light weight, low cost, and small size antennas.In recent years, a lot of research has been carried out to develop ultra wideband (UWB) antennas [1–3] due to their low cost, simple structure and wide impedance and pattern bandwidth. As the federal communication commission (FCC) prescribed the frequency range of 3.1 to10.6 GHz for commercial ultra-wideband (UWB) communication systems [2, 4], many researchers are paying much attention on UWB antennas since FCC has released commercial use of UWB for indoor communication systems [5]. However, there are existing wireless local area network (WLAN) bands [2, 6] and some satellite services at 8 GHz and 11 GHz that may create intrusion with a wideband communication structures operating at 2.9 to 12 GHz. With rapid development of broad operating frequency, one serious challenge is the miniaturization of antennas with broad impedance bandwidth and higher radiation efficiency [7]. In general UWB application antenna requires convenient impedance matching over broad frequency of operation. In recent past, the planar monopole antenna is most widely used for UWB application due to its wide impedance bandwidth, low cost and simple structure [8]. It has become one of the most prominent considerations for UWB applications. Several designs of monopole planar UWB antenna have been proposed. However some of these antennas involve complex parametric calculations and sophisticated fabrication process [9].

At this stage it is utmost necessary to present a relatively more simple but robust design of UWB antenna. In this research paper a simple design is proposed, this design is based on a microstrip rectangular patch. Design parameters like shape of radiator, ground plane as well as feeding structure are optimized to obtain the broadband impedance bandwidth [10, 11]. Microstrip antennas are mainly used in aircraft, spacecraft, satellite and missile applications where small size, low cost, high performance and ease of installation are major constraints.

Printed rectangular patch with partial ground technique is presented in this paper. Extensive parametric study of slits in patch and slots in the ground has also been carried out. Increase in overall bandwidth has been observed for effective position of these slits and slots. Details of antenna design, software simulation and measured results are also discussed.

2. DESIGN, ANALYSIS AND OPTIMIZATION

Optimized geometry of the proposed antenna is depicted in Figure 1 as under.

In Figure 1, the geometry of the proposed antenna is shown. Dimensions of the microstrip patch, transmission line, and slits in the patch are presented in Table 1. Usually we can adjust the operating frequency of our antenna by selecting the length of the patch; smaller dimension of the

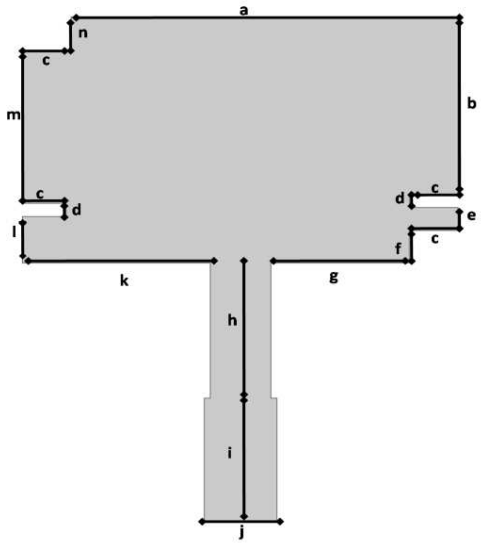

Figure 1: Geometry of proposedantenna.

Table 1: Table for dimensions.

a	16.0 mm	**g**	5.7 mm	**m**	6.8 mm
b	7.9 mm	**h**	6.0 mm	**n**	1.5 mm
c	2.0 mm	**i**	5.2 mm	**p**	10.0 mm
d	0.8 mm	**j**	3.0 mm	**w**	34.0 mm
e	1.0 mm	**k**	7.7 mm	**L**	36.0 mm
f	2.0 mm	**l**	2.2 mm		

patch results in higher resonating frequency and vice versa. Patch antenna is usually known for small bandwidth but different techniques like partial ground, addition of suitable slots in the ground and patch have been developed and studied, resulting in ultra wide bandwidth of antenna. However such UWB antenna often suffers for additional impedance matching network or large ground plane system. Printed UWB design is essentially an unbalanced design in which electric current is distributed on both radiator and ground plane. Therefore performance of UWB design is greatly affected by the shape of ground plane in terms of radiation pattern [12, 13], impedance bandwidth and resonating frequency of antenna. Such ground planes cause numerous design problems and complexities.

However various studies have been made by engineers to reduce this groundplane effect. One of them is the truncation of ground plane to reduce the effect of ground plane on overall performance of antenna [12]. Antenna efficiency in terms of return loss depends upon the impedance matching between patch and transmission feed line. We get more efficient results when both transmission feed and patch have perfect impedance matching. On the other hand substrate material and its height are also very important for radiation pattern, high gain and bandwidth of antenna. The quality factor of the small radiating structures increases due to proximity of grounding surface and high current density hence reduces antenna's impedance bandwidth. Meanwhile high current density results in increase of impedance and joule losses therefore decreasing the antenna gain [13, 14].

Dielectric material with higher permittivity is responsible for degradation of electrical field properties of the antenna as the surface waves produce a part of the total power available for direct propagation on the dielectric surface [1]. In the proposed design these parameters were optimized to get the broadband with high radiation efficiency.

The proposed antenna was designed and optimized by an FEM based antenna analysis software. Simulated geometry of antenna patch and ground plane is given in Figure 2.

For bandwidth enhancement, a number of techniques such as corner truncation, embedding of the slits in the main microstrip rectangular patch and using of partial ground with slits have been used. The positions of the slits and slots in the patch and ground plane at a suitable place have been

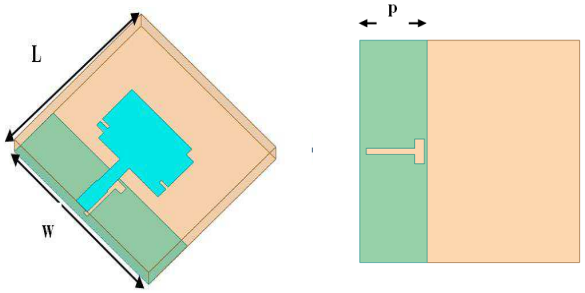

Figure 2: Patch and ground plane.

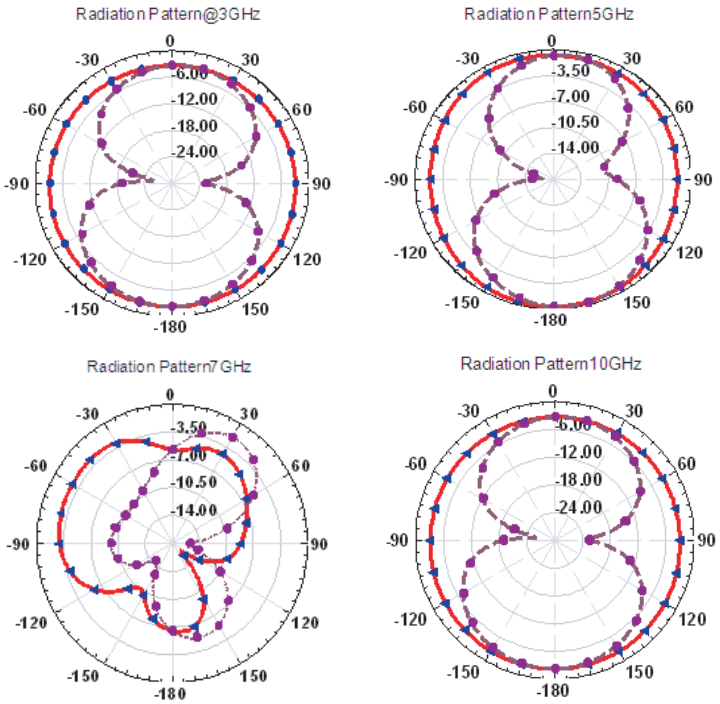

Figure 3: Simulated 2D Radiation Pattern at 3, 5, 8, 10 GHz. Red curve is for yz plane vertical cut and purple curve is for xy plane horizontal cut w.r.t patch lies in xy plane.

optimized for maximum bandwidth. The antenna is fabricated on FR-4 epoxy substrate having permittivity constant $\varepsilon_r = 4.4$, loss tangent $(\tan\delta) = 0.019$ and height $= 1.6$ mm, it is shown in Figure 5.

3. MEASURED RESULTS AND DISCUSION

The optimized antenna is fabricated and return loss is measured by using Agilent E8362C PNA Network Analyzer is shown in Figure 4 representing the characteristic bandwidth of 7.26 GHz from 3 GHz to 10.26 GHz. The measured results are in good agreement with the simulated results.

The 2D simulated radiation pattern of antenna on different operating frequencies are shown in Figure 3. It has been observed that on most of frequency range the antenna radiation pattern is Omni directional due to leakage of radiation by using of partial ground technique. The radiation pattern of the antenna is controlled by the current distribution on the patch and ground for UWB antennas. The Omni directional radiation pattern provides freedom in transmitter and receiver location.The performance of linearly polarized antennas is often described in terms of E & H plane. The measured antenna radiation pattern in xy plane at different frequencies are shown in Figure 6 is found to be in good agreement with the simulated results.

4. TIME DOMAIN ANALYSIS

Group delay is one the important parameter while discussing the UWB antennas. It represents the phase information with operating frequencies. Plot regarding the group delay measured through

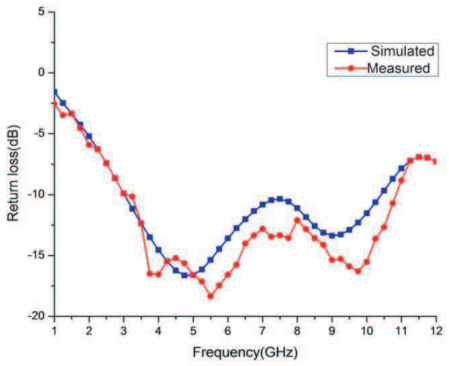

Figure 4: Return loss of antenna, blue curve for simulated results and red curve for measured results.

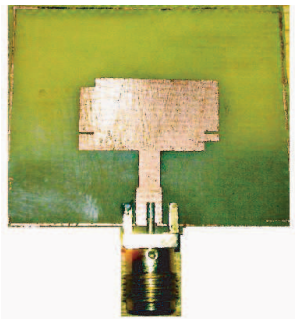

Figure 5: Fabricated antenna.

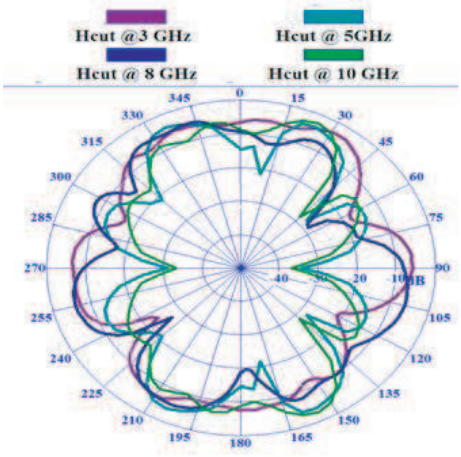

Figure 6: Measured 2D Radiation pattern in xy plane at 3, 5, 8 & 10 GHz.

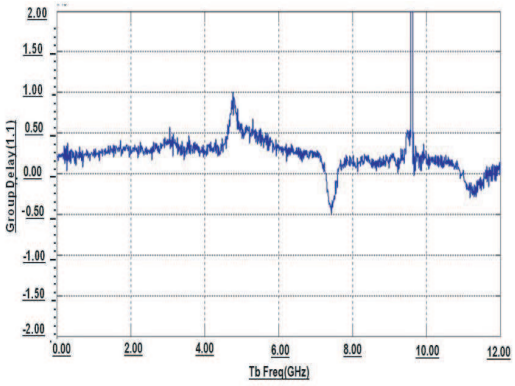

Figure 7: Measured Group Delay (ns) of antenna.

network analyzer is also shown in Figure 7.

Group delay is useful measure of time distortion which is usually calculated by differentiating phase with respect to frequency. It evaluates non dispersive behaviour of antenna as a derivative of far field response with respect to frequency [15]. If group delay variation exceeds more than 1 ns, phases are no more linear in far field and phase distortion occurs which can cause a serious problem for UWB applications.The group delay results in Figure 7 show that over the whole band, except at 9.5 GHz, is 0.25 within ± 0.75 which is in acceptable limits.

5. CONCLUSION

In this paper we have presented UWB antenna which is capable of supporting large bandwidth. Excitation of antenna is made through the wave port. By adding suitable slits and slots in the patch and ground, improvement in the bandwidth is achieved. By variation of the ground plane and patch size, a significant impedance bandwidth has been realized. So it can be considered as a key parameter for return loss and bandwidth enhancement.

REFERENCES

1. Lin, C.-C. and H.-R. C. Lin, "A 3–12 GHz UWB planartriangular monopole antenna with ridged ground-plane," *Progress In Electromagnetics Research*, Vol. 83, 307–321, 2008.
2. Li, X., L. Yang, S.-X. Gong, and Y.-J. Yang, "Ultra-wideband monopole antenna with four-band-notched characteristics," *Progress In Electromagnetics Research Letters*, Vol. 6, 27–34, 2009.
3. Khan, S. N., J. Hu, J. Xiong, and S. He, "Circular fractal monopole antenna for low VSWR UWB applications," *Progress In Electromagnetics Research Letters*, Vol. 1, 19–25, 2008.

4. "FCC, FCC first report and order on the ultra-wideband technology," 2002.
5. "New public safety applications and broadband internet access among uses envisioned by fcc authorization of ultra-wideband technology-FCC news release," 2002.
6. Schantz, H. G. and G. P. Wolenec, "Ultra wideband antenna having frequency selectivity," U.S. Patent No. 6774859B2, August 10, 2004.
7. Chen, Z. N., X. H. Wu, H. F. Li, N. Yang, and M. Y. W. Chia, "Considerations for source pulses and antennas in UWB radio systems," *IEEE Trans. Antennas Propag.*, Vol. 52, 1739–1748, Jul. 2004.
8. Nagalingam, M., "Circular patch UWB antenna with time domain analysis," *IEEE Region 8 SIBIRCON-2010*, 251–255, Irkutsk Listvyanka, Russia, July 11–15, 2010.
9. Lim, K.-S., M. Nagalingam, and C.-P. Tan, "Design and construction of microstrip uwb antenna with time domain analysis," *Progress In Electromagnetics Research M*, Vol. 3, 153–164, 2008.
10. Yang, T. and W. A. Davis, "Planar half-disk antenna structures for ultrawideband communications," *Proc. IEEE Int. Symp Antennas Propagation*, Vol. 3, 2508–2511, June 2004.
11. Chung, K., H. Park, and J. Choi, "Wideband microstrip-fed monopole antenna with a narrow slit," *Microw. Opt. Technol. Lett.*, Vol. 47, No. 4, 400–402, November 20, 2005.
12. Chen, Z. N., T. S. P. See, and X. Qing, "Small printed ultrawideband antenna with reduced ground plane effect," *IEEE Transactions on Antennas and Propagation*, Vol. 55, 383–388, 2007.
13. Simons, R. N., *Coplanar Waveguide Circuits, Components and Systems*, John Wiley & Sons Inc., Somerset, NJ, 2001.
14. Yang, S.-L. S., K.-F. Lee, A. A. Kishk, and K. M. Luk, "Design and study of wideband single feed circularly polarized microstrip antennas," *Progress In Electromagnetics Research*, Vol. 80, 45–61, 2008.
15. Thiripurasundari, D. and D. S. Emmanuel, "Compact dualband-reject UWB antenna with sharpband-edge frequency," *Progress In Electromagnetics Research Letters*, Vol. 36, 41–55, 2013.

A Theoretical Investigation of the Influence of Underground Power Cable Parameters on Magnetic Field Levels

Ivan Rostovskiy[1], **Oleksandr Okun**[1], **Sergii Shevchenko**[1], **and Leena Korpinen**[2]

[1]Department of Electrical Energy, National Technical University "Kharkiv Polytechnic Institute" Kharkiv, Ukraine

[2]Department of Electronics and Communications Engineering, Tampere University of Technology Tampere, Finland

Abstract— The aim of this paper is to investigate the influence of construction-based and grounding system parameters of underground power cables 6–10 kV on magnetic flux density levels. It is shown that grounding a system at its start or end point without grounding it at the ends is the worst in terms of the magnetic field levels due to the absence of induced current in a shield. Therefore, it is possible to decrease magnetic field levels above cables by increasing the currents in a shield by grounding cables at the ends and by varying the cable parameters, such as the distance between phases and a cross-section of the shield.

1. INTRODUCTION

High voltage power objects, such as substations, cables, and overhead transmission lines, are sources of low frequency magnetic fields. They cover major populated areas. In recent years, revised regulations limiting magnetic field levels in Ukraine have been introduced. Therefore, our group has previously considered magnetic field levels generated by high voltage power substations and power lines [1, 2].

The main task to be solved by the shield from copper conductors is the alignment of the electric field acting on the main cable insulation (core insulation), i.e., to perform their functions, the shield should be connected to the ground at least at one point. However, in practice, other types of grounding methods are utilized, such as grounding at the start or the end point and without grounding at the ends of cables.

According to research [3], currents in shields do not depend on resistance (cross-section) and the length of the cable's core, but they are determined by resistance and the cross-section of a shield as well as the distance between cable phases. Therefore, the aim of this study is to investigate the influence of construction-based and grounding system parameters of underground three-phase power cables on magnetic flux density levels above the surface of the ground.

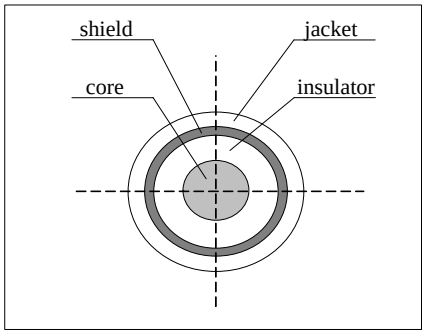

Figure 1: Cross-section of high voltage cable.

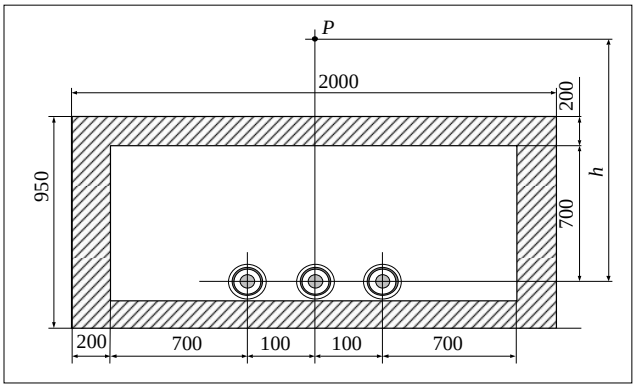

Figure 2: Scheme of three-phase power cable locations in a concrete pipe under the ground (Dimensions are in mm; h is the distance from the centre of the middle cables to the observation point P).

2. MATERIALS AND METHODS

Theoretical studies of magnetic fields were performed for common types of 6–10 kV power cables. Construction of these cables is presented in Figures 1 and 2. The cables consist of a mutually isolated core and shield, as well as external insulation of the shield. The 35 mm^2 cross-section core is made of copper conductors, and the 25 mm^2 cross-section shield with 2.8 mm thickness is made of aluminium. The material of the insulator (thickness of 4 mm) between the shield and core is composed of cross-linked polyethylene, and the outer jacket (5 mm) is made from plastic. The amplitude value of the adopted current was 200 A. Therefore, the currents in the cable core were shifted 120 degrees from one another.

To calculate the magnetic field produced by the high voltage power cable an approach was used based on the application of the numerical finite element method (FEM) by ANSYS, Inc. in two-dimensional form. The calculation results obtained using the finite element methodology were compared with the results obtained using a simple analytical formula based on the Biot-Savart law and neglecting currents in the cable shields. Table 1 presents the results of numerical and analytical comparisons.

Table 1: Comparison of magnetic field calculation results.

Calculation method	Maximum magnetic flux density B, μT at height h above middle phase cable				
	1 m	1.2 m	1.4 m	1.6 m	1.8 m
Analytical calculation	6.8	4.8	3.5	2,7	2.1
FEM modeling	6.5	4.7	3.5	2.7	2.0

3. RESULTS

Table 2 shows the results of calculation of magnetic fields produced by a power cable, given in Figure 1, under the different grounding method of cable shield.

Table 2: Results of magnetic field calculation under the different grounding method of cable shield.

Grounding method	Maximum magnetic flux density B, μT at height h above middle phase cable				
	1 m	1.2 m	1.4 m	1.6 m	1.8 m
grounding at the start and the end point of cables	4.1	3.0	2.4	2.0	1.7
grounding at the start or the end point (no currents in the shield), and without grounding at the ends	6.5	4.7	3.5	2.7	2.0

Table 3 shows the calculation results of magnetic fields produced by a power cable, given in Figure 1, under different cable shield cross-section (thickness).

Table 3: Results of magnetic field calculation under different cable shield cross-sections.

Shield cross-section, mm^2	Maximum magnetic flux density B, μT at height h above middle phase cable					Current density in shield, A/mm^2
	1 m	1.2 m	1.4 m	1.6 m	1.8 m	
25	4.1	3.0	2.4	2.0	1.7	1.2
35	3.6	2.8	2.3	1.9	1.6	1.0
50	3.3	2.6	2.2	1.8	1.5	0.9
100	2.8	2.3	1.9	1.7	1.5	0.6
150	2.5	2.1	1.8	1.6	1.4	0.5

Table 4 shows the results of calculation of magnetic fields produced by a power cable, given in Figure 1, under the different phase-to-phase distance between cables.

Table 4: Results of magnetic field calculation under the different distance between phases.

Distance between phases of cable	Maximum magnetic flux density B, μT at height h above middle phase cable					Current density in shield, A/mm^2
	1 m	1.2 m	1.4 m	1.6 m	1.8 m	
0.05	2.4	1.8	1.4	1.2	1.1	1.2
0.1	4.1	3.0	2.4	2.0	1.7	1.2
0.2	7.1	5.5	4.5	3.8	3.1	1.3
0.5	14.7	12.6	10.7	9.1	7.6	1.3

Table 5 shows the results of calculation of magnetic fields produced by a power cable, given in Figure 1, under the different conductivity of cable shield.

Table 5: Results of magnetic field calculation under the different conductivity of the cable shield.

Conductivity, S/m	Maximum magnetic flux density B, μT at height h above middle phase cable					Current density in shield, A/mm^2
	1 m	1.2 m	1.4 m	1.6 m	1.8 m	
$10 \cdot 10^6$	6.3	4.4	3.3	2.6	2.1	0.4
$40 \cdot 10^6$	4.7	3.5	2.7	2.2	1.8	1.1
$58 \cdot 10^6$	4.1	3.0	2.4	2.0	1.7	1.2
$100 \cdot 10^6$	3.1	2.5	2.0	1.8	1.5	1.4
$250 \cdot 10^6$	2.2	1.9	1.7	1.5	1.4	1.4

4. DISCUSSION AND CONCLUSION

From Table 2, it can be noted that the different grounding system of the shield leads to the different mechanisms of current appearance, and accordingly, to the different magnetic field values. Thus, under the scheme without grounding at the ends of cables, there is no loop current flow; therefore, induced currents in the cable shield equals zero.

Grounding at one point leads to a current flow between the core and shield the value, which is limited by capacitance of the insulator between the shield and core. This current creates additional active power losses in shields and flows down from the shield to its grounding device, which yields a value proportional to the length of the cable. However, these values are in amperes even for long cables. Therefore, magnetic field levels in this case are the same as in the previous grounding method, i.e., without grounding.

Under the last grounding method (at the start and the end point of cables) mechanism of appearance, the current in the shield is related to the presence of the mutual inductance between the core and the shield. The value of this current can be comparable with the current flowing in the core, i.e., it can be tens or hundreds of amperes. Thus, the magnetic field levels under this grounding method are lower than the previous two methods.

From Tables 3–5, it is clearly seen that for all three single-phase cables, regardless of their voltage class, when the cross-section and conductivity of the shield as well as the distance between the adjacent phases significantly increase, the currents in the cable's shield also increases, and values of these currents can be compared with the currents in the cable's core. This eventually leads to a decrease of the magnetic field levels produced.

However, it is worth mentioning that the currents in the shield lead to losses of energy and reduce cable lifetime. Consequently, methods to augment currents in the shield can be used only at places where magnetic fields of power cables reach the regulation limits and are located in proximity to populated objects and areas.

REFERENCES

1. Okun, O., S. Shevchenko, and L. Korpinen, "A comparison of magnetic fields inside and outside high voltage urban 110 kV power substations with the exposure recommendations of the Ukrainian regulatory authorities," *Radiation Protection Dosimetry*, Vol. 154, No. 4, 417–429, 2013.
2. Okun, A. and L. Korpinen, "Examples to reduce the EMF generated by HV power transmission lines of different design," *7th International Workshop on Biological Effects of EMF*, Malta, October 8–12, 2012.
3. Dmitriev, M. V., *Grounding of Single-phase 6–500 kV Power Cable's Shields,* Publishing House of Polytechnical University, Saint Petersburg, 2010 (in Russian).

Possible Methods for Limiting Magnetic Fields outside a High Voltage Power Substation by Changing the Phase Sequence of Busbar Wires

Oleksandr Okun[1], **Sergii Shevchenko**[1], **and Leena Korpinen**[2]

[1]Department of Electrical Energy, National Technical University "Kharkiv Polytechnic Institute" Kharkiv, Ukraine

[2]Department of Electronics and Communications Engineering, Tampere University of Technology Tampere, Finland

Abstract— The aim of our study is to examine the changing phase sequence method for limiting magnetic fields outside high voltage power substations. We consider the phase alternation of high and low voltage busbar wires on an example of a typical Ukrainian 110 kV power substation in two- and three-dimensional forms. It is finally shown that implementation of the proposed strategies significantly reduces magnetic flux density values outside of the territory of substations located in populated areas.

1. INTRODUCTION

High voltage (HV) power substations located in populated areas is one of the sources of low frequency magnetic fields. In recent years in Ukraine, active work has been carried out on the revision of the existing magnetic field limits, as specified by Ukrainian regulations. The newly proposed limit will be 0.5 μT [1], and as such, some power objects may not comply with this limit value.

It is known that magnetic field limiting methods related to constructive changes are usually quite expensive. Therefore, of special importance for this purpose, in our opinion, is the changing phase sequence method [2]. The aim of our study is to examine the method for limiting magnetic fields outside high voltage power substations.

2. MATERIALS AND METHODS

In general, high voltage power substations are characterized by horizontal multilevel performance of busbar wires with the same phasing ("C-B-A" — "C-B-A") in the cells. It is the worst variant in terms of the level of magnetic fields generated outside a power substation. But at the same time, this configuration makes it possible to change the phase sequence ("C-B-A" — "A-B-C") of the busbars of neighboring layers and neighboring cells (low and high voltage side of power transformer), which ultimately facilitates a reduction in magnetic field levels.

It is suggested to consider, in the first stage, the given phase-sequence methods on typical examples of a Ukrainian 110/10 kV power substation made according to the 'two blocks of line-transformer' scheme (Figure 1) in two-dimensional form, taking into account busbar design and mode characteristics. Then, in the final stage, consider the three-dimensional form based on a simulation model with finite element methodology previously used in studying magnetic field distribution at two typical power substations in the Ukraine [3].

The power substation under study has only horizontal varying single-level performance of HV busbar in two cells. The main dimensions of the substation's busbar adopted are as follows:

The distance between cells of the HV switchgear is 18 m;

The distance between the wires of the HV busbars is 2.5 m;

The average suspension height H of the HV busbars is 3.6 m (lower layer) and 11.2 m (upper layer);

The distance between the wires of the low voltage (LV) busbars is m;

The distance between cells of the LV busbars is 9 m; and

The average suspension height H of the LV busbars is 3 m.

Currents in the busbar wires are specified in accordance with [3]. The height h of the observation points is 2 m. A busbar wire is considered as a system of parallel linear currents over a flat earth. Each phase is calculated separately, and finally, the total field B is summed as a square root of the sum of the horizontal and vertical components squared.

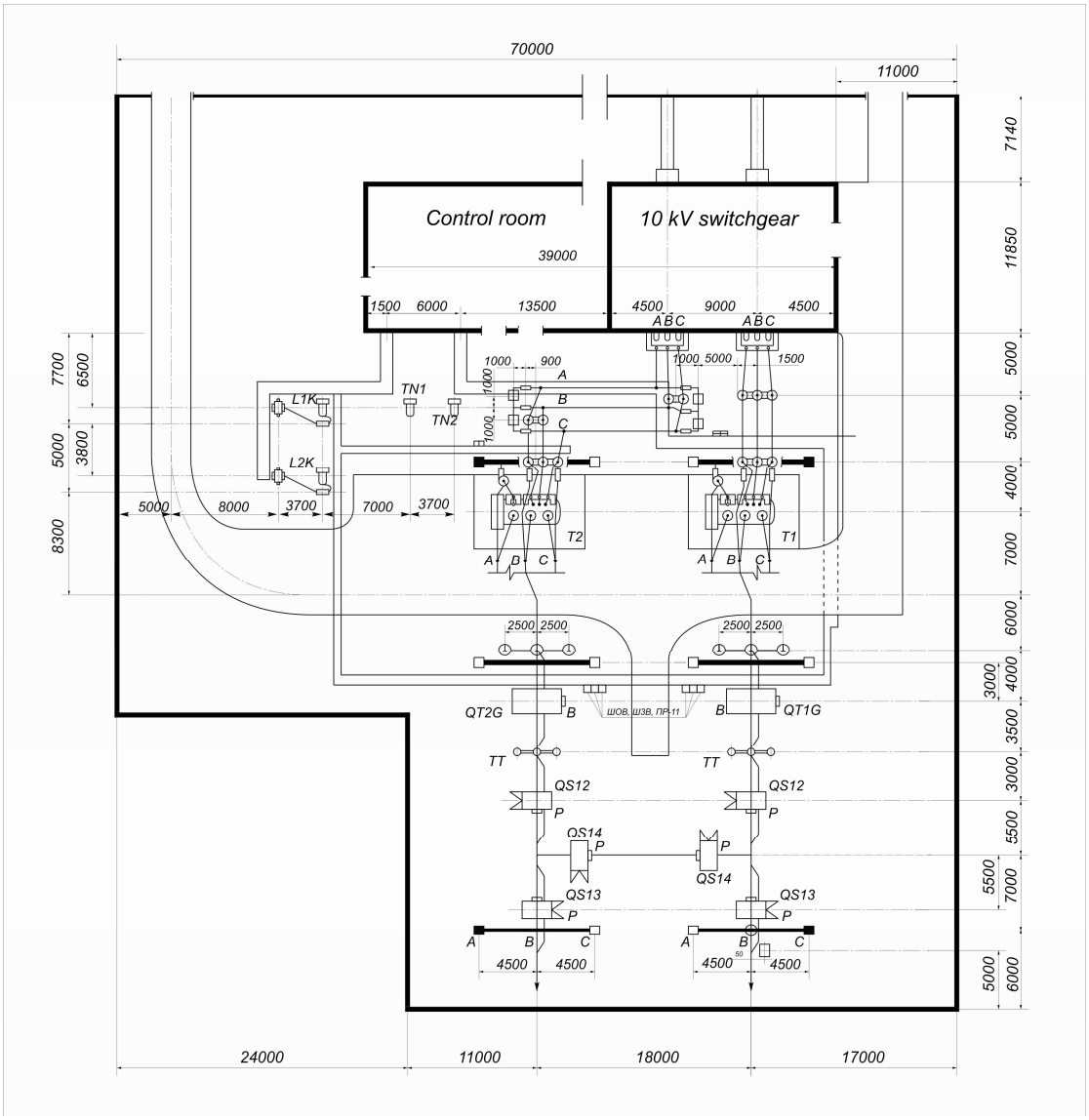

Figure 1: Plan of the 110 kV substations made according to the 'two blocks of line-transformer' scheme.

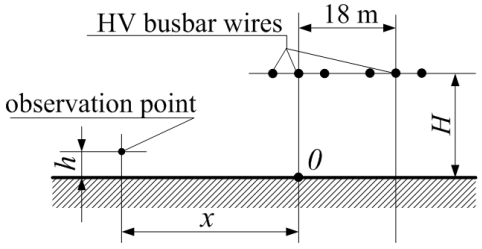

Figure 2: Cross-section of HV busbar wires of two neighboring cells. (H is the height of the HV busbars; 18 m is the distance between neighboring cells; h is the height, and x is the distance from the point of observation).

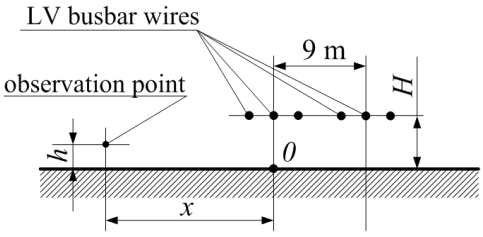

Figure 3: Cross-section of two neighboring LV busbar wires. (H is the suspension height of the LV busbars; 9 m is the distance between neighboring cells; h is the height, and x is the distance from the point of observation).

3. RESULTS

Table 1 shows the results of magnetic field calculations produced by HV busbar wire configurations of two cells given in Figure 2, under the different phase sequences.

Table 2 presents the results of magnetic field calculations produced by LV busbar wire configurations of two cells given in Figure 3, under the alternate phase sequence.

Table 1: Comparison of variants of reducing magnetic fields by alternating HV busbar wire phase of two cells (under phase current $I = 210\,\mathrm{A}$).

Phase sequence in busbar wires (Figure 2)	B, μT at distance x from projection of middle phase wire ("B"), m			
	0	20	40	60
$H = 11.2\,\mathrm{m}$ C B A C B A	1.52	0.44	0.14	0.07
$H = 3.6\,\mathrm{m}$ C B A C B A	19.67	0.52	0.15	0.07
$H = 11.2\,\mathrm{m}$ C B A A B C	2.00	0.25	0.05	0.02
$H = 3.6\,\mathrm{m}$ C B A A B C	20.60	0.31	0.05	0.02

Table 2: Comparison of variants of reducing magnetic fields by alternating LV busbar wire phase (under phase current $I = 2300\,\mathrm{A}$).

Phase sequence in busbar wires (Figure 3)	B, μT at distance x from projection of middle phase wire ("B"), m			
	0	20	40	60
$H = 3\,\mathrm{m}$ C B A C B A	354.87	2.58	0.72	0.34
$H = 3\,\mathrm{m}$ C B A A B C	371.82	0.94	0.15	0.05

The results of applying methods to reduce the magnetic field at a 110/10 kV power substation in the three-dimensional form based on a simulation model with finite element methodology are summarized in Table 3.

Table 3: Maximum magnetic flux density values under different methods applied to the 'two blocks of line-transformer' substation of 110/10 kV.

Method	B, μT (at 20 m distance from the substation's fence)	B, μT (at 30 m distance from the substation's fence)
without applying any measures (standard phasing)	0.20	0.15
phase alternation of HV busbar wires	0.16	0.11
phase alternation of LV busbar wires	0.11	0.08
phase alternation of HV and LV busbar wires together	0.07	0.03

4. DISCUSSION AND CONCLUSION

It is clearly seen from Tables 2 and 3 that that when we have the same direction of currents in neighboring cells (standard phasing), the magnetic field produced by a single cell is strengthened due to an additional field produced by currents with the same direction in busbar conductors of neighboring cells that are located at a distance of 9 or 18 m. When we have the opposite direction,

the effect of reducing the resulting magnetic field is achieved through partial compensation of the field produced by a single cell, using the field produced by the currents flowing in opposite directions in the phase conductors of neighboring cells.

Thus, in changing the current phase values of the neighboring cells at the edges of the next cell, i.e., at the limit distance from each other ("C-B-A" — "A-B-C"), it is possible to obtain a significant (3–6 times) magnetic field reduction at the distances of 40–60 m from the projection of the wire of the middle phase of the first cell in comparison with the standard phasing.

As it can be seen from Table 3, implementation of the proposed measures allows us to significantly reduce values of magnetic flux density outside the territory of power substations located in populated areas (for example, field value at the distance of 30 m from the substation's fence was 4.4 times lower under the phase alternation of the HV and LV busbar wires together) in comparison with standard phasing adopted in normal operation mode.

REFERENCES

1. Varshamova, I. S., O. A. Geljarovskaja, N. V. Krjukova, V. S. Lupikov, Ju. D. Rudas, and K. A. Savshenko, "Prospects of automatic systems application in power substation for their magnetic field compensation," *Visnyk NTU "KhPI" (Bulletin of NTU "KhPI')*, No. 60, 3–9, 2011 (in Russian).
2. Okun, A. and L. Korpinen, "Examples to reduce the EMF generated by HV power transmission lines of different design," *7th International Workshop on Biological Effects of EMF*, Malta, October 8–12, 2012.
3. Okun, O., S. Shevchenko, and L. Korpinen, "A comparison of magnetic fields inside and outside high voltage urban 110 kV power substations with the exposure recommendations of the Ukrainian Regulatory Authorities," *Radiation Protection Dosimetry*, Advance Access published October 15, 2012, doi:10.1093/rpd/ncs268.

An Improvement Method of Diversity Effect for the Linear Polarization Diversity by Decreasing the XPD Value

Deock-Ho Ha
Department of Information and Communications Engineering
Pukyong National University, Busan, Korea

Abstract— In this paper, in order to evaluate the diversity effect more accurately, we calculated correlation coefficient considering the XPD value obtained from the measurement data of both linear polarized waves and circular polarized waves. From the measurement analysis using the theoretical formula, it can be also seen that the linear polarization diversity reception scheme to create extremely less XPD value improve the diversity effect as well as circular polarization diversity.

1. INTRODUCTION

Generally, it is well known that circular polarization diversity is more effective than that of linear polarization diversity in short range wireless environment [1–3]. This is because the cross correlation coefficient of circular polarized waves shows extremely small value in short range wireless environment. To evaluate the diversity effect, the cross correlation coefficient between the two received branch signals has usually been employed. In this paper, in order to predict the diversity effect more accurately, we analyzed the correlation coefficient characteristic due to the XPD (Cross Polarization Discrimination) value between the two polarized waves received by polarization diversity model. Especially, we calculated correlation coefficient considering the XPD value obtained from the measurement data of 5.9 GHz frequency band based on Wireless Access in Vehicular Environments (WAVE).

2. THEORY OF POLARIZATION DIVERSITY RECEPTION

Figure 1 is a model of circular polarization diversity [4]. As shown in Fig. 1, a transmitting antenna emits a circularly polarized signal while the receiving end uses a two-branch polarized diversity antenna. In this model, a transmitting antenna emitted a circularly polarized signal while the receiving end used a two-branch polarized diversity antenna. In [4], the correlation coefficient ρ for the circular polarization reception model is analyzed as Equation (1).

$$\rho = \frac{\left(a^2+b^2\right)\left(a^2+c^2\right)\left(1+\Gamma^2\right)+2\Gamma\left(a^2-b^2\right)\left(a^2-c^2\right)-8\Gamma a^2bc}{\left[\left(a^2+b^2\right)\left(a^2+c^2\right)\left(1+\Gamma\right)^4\right]^{1/2}} \tag{1}$$

where, $XPD=\Gamma$, $a=\sin\lambda\cos\phi$, $b=\cos\nu\cos\lambda-\sin\nu\sin\phi\sin\lambda$, $c=\cos\nu\cos\lambda+\sin\nu\sin\phi\sin\lambda$.

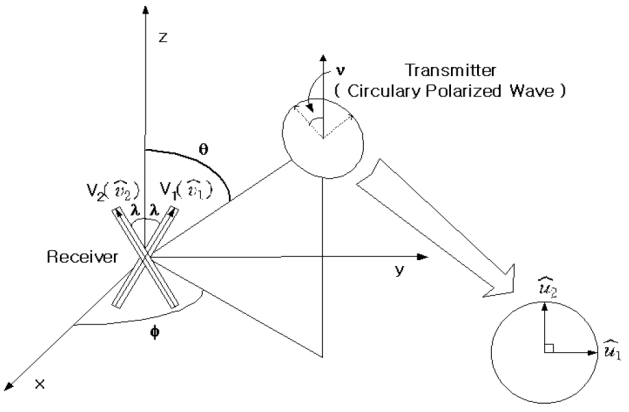

Figure 1: Reception model of circular polarization diversity.

And also, the correlation coefficient ρ for the linear polarization reception model is analyzed as Equation (2) in the literature [5].

$$\rho = \frac{\left(a^2 - bb'\Gamma\right)^2}{\left[a^8 + 2\Gamma a^6\left(b'^2 + b^2\right) + \Gamma^2 a^4\left(4b^2b'^2 + b'^4 + b^4\right) + 2\Gamma^3 a^2\left(b^4b'^2 + b^2b'4\right) + \Gamma^4 b^4 b'^4\right]^{\frac{1}{2}}} \tag{2}$$

where, $XPD = \Gamma$, $a = \sin\lambda\cos\phi$, $b = \cos\nu\cos\lambda - \sin\nu\sin\phi\sin\lambda$, $b' = \cos\nu\cos\lambda + \sin\nu\sin\phi\sin\lambda$.

3. MEASUREMENT AND ANALYSIS RESULTS

To estimate the performance of the polarization diversity effect, we conducted moving measurements in a short range LOS (Line-of Sight) propagation environment. In this measurement, spectrum analyzer received the signal strength of radio signal which transmitted the center frequency 5.9 GHz from the signal generator with the transmitting power 0 dBm. We fabricated a circular polarization micro-strip antenna which can receive each polarized waves, even vertical and horizontal waves. And then, we analyzed the XPD value for the measured circular and linear polarized signals. In Table 1, the character CX indicates that the transmitting antenna used a circular polarization antenna and the receiving antenna used a cross-handed circular polarization antenna. The character VH means a vertical and horizontal antenna combination. The XPD mean value for the case of using the circular polarized waves was 7 dB or less than that of using the vertically polarized wave. That is because the antenna combination for the case of CX can markedly remove the reflected waves which are reflected by an odd time [2, 3]. Generally, the circular polarization has a characteristic

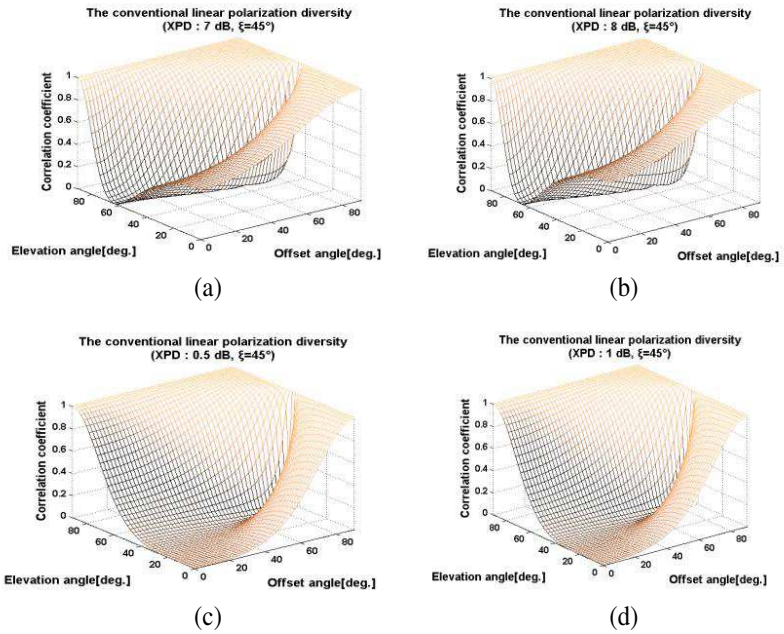

Figure 2: Correlation coefficients for the linear polarization diversity. (a) Measured XPD real value (7.0 dB), (b) measured XPD real value (8.0 dB), (c) supposed XPD value (0.5 dB), (d) supposed XPD value (1.0 dB).

Table 1: Mean and standard deviation for XPD for short range propagation environments (an example of 5.9 GHz frequency band signal).

		XPD (dB)	
		Mean	Standard deviation
Path 1	CX	1.38	7.14
	VH	8.21	7.28
Path 2	CX	1.41	8.13
	VH	8.72	8.07

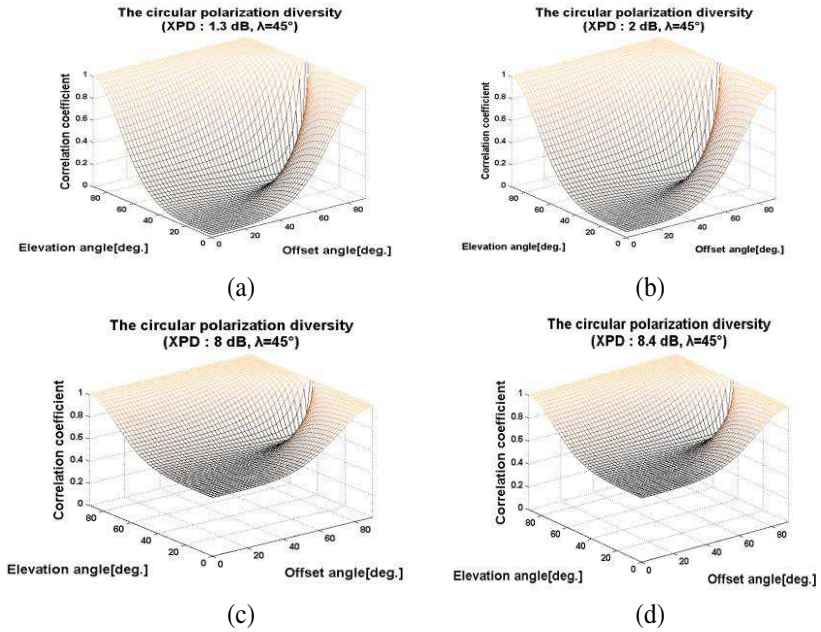

Figure 3: Correlation coefficients for the circular polarization diversity. (a) Measured XPD real value (1.3 dB), (b) measured XPD real value (2.0 dB), (c) supposed XPD value (8.0 dB), (d) supposed XPD value (8.4 dB).

that it can effectively remove the reflected waves which are reflected by odd time. By reducing the influences of reflected wave, the circular polarization can reduce the time delay spread and inter-channel interference [4, 6]. With this measurement result, we investigated the effect of the XPD factor for the correlation coefficients using Equations (1) and (2). Fig. 2 and Fig. 3 show the comparisons of two polarization diversity schemes. The correlation coefficient values of the circular polarization diversity as shown in the Figs. 2(a), (b), is much lower than that of linear polarization diversity of the Figs. 2(a), (b). Meanwhile, we can see another conditions in the Figs. 2(c), (d) and Figs. 3(c), (d). In these cases, we considered a supposed XPD value which could not be expected the actual XPD value in each real measurement conditions. Namely, it could not be expected a low XPD value of 0.5 and 1.0 dB for the case of the linear polarization diversity reception of the Figs. 2(c), (d) as well as high XPD value of 8.0 and 8.4 dB in circular polarization diversity reception of the Figs. 3(c), (d). As shown Figs. 2(c), (d) for the case of linear polarization diversity, it was also foreseen that an optimum reception scheme to create extremely low XPD value can improve the diversity effect. This will be the further research subject which will be composed diversity branches.

4. CONCLUDING REMARKS

We found that the correlation coefficient value of the circular polarization diversity system showed about 1.3 dB in a short range wireless propagation environment. This value shows 7.0 dB lower than that of conventional linear polarization diversity. From the measurement data analysis, in the case where the circular polarized wave was applied in wireless antenna system, the XPD value shows much lower than that of the linear polarized wave. So it can be predicted that circular polarization diversity is a more effective diversity technique to reduce the multi-path fading in short range radio propagation environments. And also it can be foreseen that an optimum reception scheme of the conventional linear polarization diversity to create extremely less XPD value can improve the diversity effect. Consequently, it was concluded that the XPD characteristic should be considered to estimate the diversity effect more accurately.

ACKNOWLEDGMENT

Following are results of a study on the "Leaders INdustry-university Cooperation" Project, supported by the Ministry of Education, Science & Technology (MEST).

REFERENCES

1. Rappaport, T. S. and D. A. Hawbaker, "Effects of circular and linear polarized antenna on wideband propagation parameters in indoor radio channels," *Proceedings of the GLOBECOM'91*, 1287–1291, 1991.
2. Kajawara, A., "On a circular polarization wave transmission in LOS indoor radio channels," *PIMRC A2.6*, 156–159, 1994.
3. Jung, H. C., J. D. Mock, and D. H. Ha, "Analysis of wideband propagation characteristics for the high transmission rate in indoor radio channels," *Proceedings of IEEE VTC'98*, Vol. 1, 298–302, Ottawa, Canada, May 1998.
4. Ahn, J. S., D. H. Ha, and P. D. Cho, "The circular polarization diversity effect considering XPD factor in an indoor radio propagation environment," *Journal of The Korea Electromagnetic Engineering Society*, Vol. 6, No. 1, 24–30, Jun. 2006.
5. Shin, E. and S. Safavi-Nacini, "A simple theoretical model for polarization diversity reception in wireless mobile environments," *IEEE International Symposium on Antenna and Propagation*, Vol. 2, 1332–1335, Aug. 1999.
6. Ha, D. H., Y. H. Ko, J. S. Ahn, and T. H. Kim, "Circular polarization diversity indoor wireless mobile environments," *Journal of The Korea Electromagnetic Engineering Society*, Vol. 4, No. 3, 128–136, Sep. 2004.

Numerical Study of Dual-frequency Stacked Annular-ring Microstrip Antenna

A. R. Messai[1], **A. Bourayou**[2], **S. Aris**[1], **and T. Fortaki**[2]

[1]Department of Electronics, Faculty of Sciences Technology
Constantine 1 University, Constantine 25000, Algeria
[2]Electronics Department, Faculty of Technology, Batna University, Batna 05000, Algeria

Abstract— The dual-frequency operation of a microstrip antenna consisting of two annular-rings in a stacked configuration is investigated. A rigorous analysis is performed using a dyadic Green's function formulation where the mixed boundary value problem is reduced to a set of coupled vector integral equations using the vector Hankel transform. The accuracy of the analysis has been confirmed by experimental measurements. It has been found that the two constitutive resonators of the stacked structure, which determine the dual-frequency behavior of the antenna, depend on the relative sizes of the circular-disks.

1. INTRODUCTION

Conventional microstrip antennas, consisting of a single conducting patch on a grounded dielectric substrate, have received much attention in recent years due to their many advantages, including low profile, light weight and easy integration with printed circuits [1]. However, due to their resonant behavior, they radiate efficiently only over a narrow band of frequencies, with bandwidths typically only a few percent. Dual-frequency structures are useful in situations where the antenna is required to operate efficiently at two distinct frequencies. Conventional microstrip antennas do not guarantee this type of operation. A more complex configuration, consisting of two microstrip patches in a stacked configuration, offers performance features that are not usually obtainable from the single-patch single-dielectric configuration. These features include higher gain, wider bandwidth and dual-frequency characteristics [2]. In the current paper, we investigate the dual-frequency behavior of stacked annular-ring microstrip patches fabricated on a two-layered substrate using a full-wave spectral domain technique in the vector Hankel transform domain. As in [2, 3], we consider both the case where the size of the top annular-ring is larger than the one of the bottom annular-ring and the opposite case.

2. THEORETICAL FORMULATION

Figure 1 shows the geometry of two stacked annular-rings placed above a ground plane. The bottom patch has an outer radius b_1 and an inner radius a_1 while the top one has an outer radius b_2 and an inner radius a_2. The substrate is assumed to be made of two layers of the same material and identical thickness. The material of the two-layered substrate is an isotropic dielectric with permeability μ_0 and permittivity $\varepsilon_0\varepsilon_r$. All fields and currents are time harmonic with the $e^{i\omega t}$ time dependence suppressed. Let $\mathbf{J}^i(\rho,\phi)$ (where T implies transpose and $i = 1, 2$) be the surface current density on the patch of outer radius b_i. Also, let $\mathbf{E}^i(\rho,\, \phi,\, z_i)$ be the value of the transverse electric field at the plane of the patch of outer radius b_i. Owing to the revolution symmetry of the multilayered medium of Figure 1 around the z-axis, the dependence of E_z and H_z on the ϕ coordinate is of type $e^{ik\phi}$ (where k is an integer). Following a mathematical reasoning similar to that explained in [2, 3], we can obtain a relation among $\mathbf{J}^1(\rho,\phi)$, $\mathbf{J}^2(\rho,\phi)$, $\mathbf{E}^1(\rho,\phi,z_1)$ and $\mathbf{E}^2(\rho,\phi,z_2)$ in the spectral domain given by:

$$\mathbf{e}_k^1(k_\rho, z_1) = \bar{\mathbf{G}}^{11}(k_\rho)\cdot\mathbf{j}_k^1(k_\rho) + \bar{\mathbf{G}}^{12}(k_\rho)\cdot\mathbf{j}_k^2(k_\rho) \quad (1)$$

$$\mathbf{e}_k^2(k_\rho, z_2) = \bar{\mathbf{G}}^{21}(k_\rho)\cdot\mathbf{j}_k^1(k_\rho) + \bar{\mathbf{G}}^{22}(k_\rho)\cdot\mathbf{j}_k^2(k_\rho) \quad (2)$$

where $\mathbf{j}_k^i(k_\rho)$ and $\mathbf{e}_k^i(k_\rho, z_i)$ are, respectively the vector Hankel transforms of $\mathbf{J}_k^i(\rho)$ and $\mathbf{E}_k^i(\rho\,, z_i)$ and $\bar{\mathbf{G}}^{11}$, $\bar{\mathbf{G}}^{12}$, $\bar{\mathbf{G}}^{21}$ and $\bar{\mathbf{G}}^{22}$ are the dyadic Green's functions of the stacked configuration. Now that we have the necessary Green's functions, the well-known Galerkin's procedure of the moment method can be easily applied to Equations (1) and (2) to obtain the complex resonant frequencies of the resonant modes of the stacked structure shown in Figure 1.

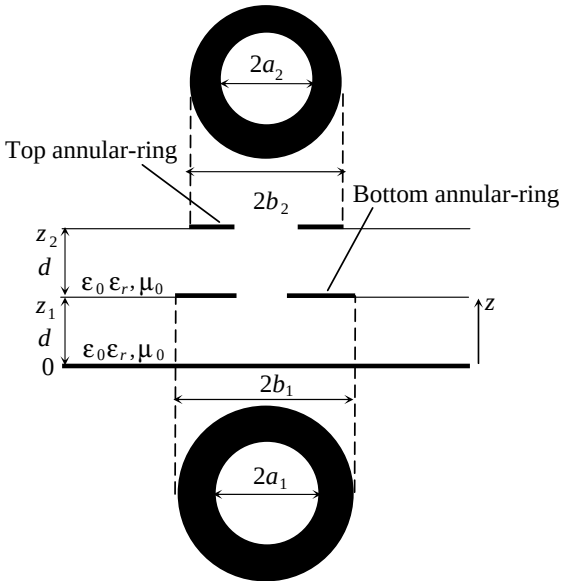

Figure 1: Structure of two stacked annular-ring microstriop antenna.

3. NUMERICAL RESULTS

The space-domain basis functions are chosen to be the TM current modes of the two magnetic-wall annular ring cavities with outer radii b_1, b_2 and inner radii a_1 and a_2. In order to validate the proposed approach, numerical results are obtained for the parameters used in the experiment of Dahele et al. [4], i.e., $b_1 = b_2 = 5\,\text{cm}$, $a_1 = a_2 = 2.5\,\text{cm}$, $d = 0.159\,\text{cm}$ and $\varepsilon_r = 2.32$. Due to the presence of the top annular-ring in the stacked configuration, two resonances are obtained. The lower resonant frequency is noted f_l while the upper resonant frequency is noted f_u. From the results of Table 1, it is clear that our results are in good agreement with the experimental values. This validates the proposed theory. Finally, it is important to note that from the different executions of the developed program, we have concluded that the two constitutive resonators of the stacked structure, which determine the dual-frequency behavior of the antenna, depend on the relative sizes of the annular-rings. This result is in accordance with that discovered theoretically for stacked rectangular patches [2].

Table 1: Comparison between our calculated lower and upper resonant frequencies with those of Dahele et al. [4] for the first three modes of the dual-frequency stacked annular ring microstrip antenna; $b_1 = b_2 = 5\,\text{cm}$, $a_1 = a_2 = 2.5\,\text{cm}$, $d = 0.159\,\text{cm}$ and $\varepsilon_r = 2.32$.

Mode	Lower and upper resonances (MHz)			
	Measured [4]		Our results	
	f_l	f_u	f_l	f_u
(1, 1)	864.5	919	859.1	921
(2, 1)	1704	1858.5	1701	1864
(3, 1)	2489	2722	2485	27.31

4. CONCLUSIONS

A theoretical analysis of resonant frequencies of the dual-frequency stacked annular-ring microstrip antenna has been proposed. Numerical results obtained are found to be in excellent agreement with measurements. It has been also found that the two constitutive resonators of the stacked structure, which determine the dual-frequency behavior of the antenna, depend on the relative sizes of the annular-rings. This result is in accordance with that discovered theoretically for stacked rectangular patches [2].

REFERENCES

1. Fortaki, T., L. Djouane, F. Chebbara, and A. Benghalia, "Radiation of rectangular microstrip patch antenna covered with a dielectric layer," *International Journal of Electronics*, Vol. 95, No. 9, 989–998, 2008.
2. Fortaki, T., L. Djouane, F. Chebbara, and A. Benghalia, "On the dual-frequency behavior of stacked microstrip patches," *IEEE Antennas and Wireless Propagation Letters*, Vol. 7, 310–313, 2008.
3. Benkouda, S., M. Amir, T. Fortaki, and A. Benghalia, "Dual-frequency behaviour of stacked high T_c superconducting microstrip patches," *Journal of Infrared, Millimeter, and Terahertz Waves*, Vol. 32, 1350–1366, 2011.
4. Dahele, J. S., K. F. Lee, and D. P. Wong, "Dual-frequency stacked annular-ring microstrip antenna," *IEEE Transactions on Antennas and Propagation*, Vol. 35, No. 11, 1281–1285, 1987.

Analysis of Multisection Rectangular Waveguide Impedance Transformers

Debendra Kumar Panda[1], **Sanjay Chouhan**[1], **and Ajay Chakraborty**[2]

[1]Jawaharlal Institute of Technology
Borawan, Kasrawad, Khargone, Madhya Pradesh 451228, India
[2]BIT Mesra, India

Abstract— A method of moment based analysis of multisection waveguide impedance transformer has been presented using multiple cavity modeling technique (MCMT). Every discontinuity is modeled with a cavity. Several cavities are formed to describe the whole structure. The analyzed waveguide structure has good agreement with the multiple cavity modeling technique (MCMT) and CST microwave studio simulated data.

1. INTRODUCTION

Waveguide based circuits are used dates back before World War II. Lewin [1] and Harrington [2] gave comprehensive study on the waveguides. The waveguide step junction is a basic building block of many waveguide based circuits and has been analyzed by a large number of researchers in last few decades. Arndt, Tucholke and Wriedt [3] gave data for multi-section double plane step transformers between X, Ku, K and Ka band waveguides. Multiple Cavity Modeling Technique (MCMT) has been used to analyze different waveguide structures [5–11]. In this paper, MCMT is used to analyze multisection waveguide impedance transformer. The technique involves in replacing all the apertures and discontinuities of the waveguide structures, with equivalent magnetic current densities so that the given structure can be analyzed using only magnetic field integral equation which has been discussed by this author [6]. A two section waveguide impedance transformer has been discussed by this author [11]. In this paper, this methodology has been used to examine the result of three and four section impedance transformers which increases the no of junctions from 3 to 4 and 5. Mat lab codes are written to analyze these structures.

2. FRMULATION OF THEORY

Theory for these multisection structures is same as described in [7]. Three dimensional view of three and four section waveguide impedance transformer is shown in Figure 1. The details of the regions and magnetic currents at the apertures are shown in Figure 2. The electric field at the ith aperture is assumed to be

$$\vec{E} = \hat{x} \sum_{p=1}^{M} E_p^{i,x} e_p^{i,x} + \hat{y} \sum_{p=1}^{M} E_p^{i,y} e_p^{i,y} \tag{1}$$

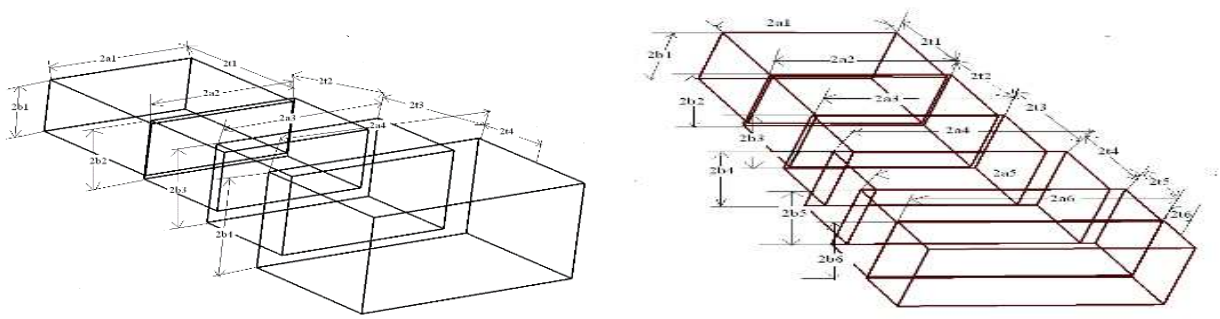

Figure 1: Three dimensional view of a three and four section waveguide impedance transformer.

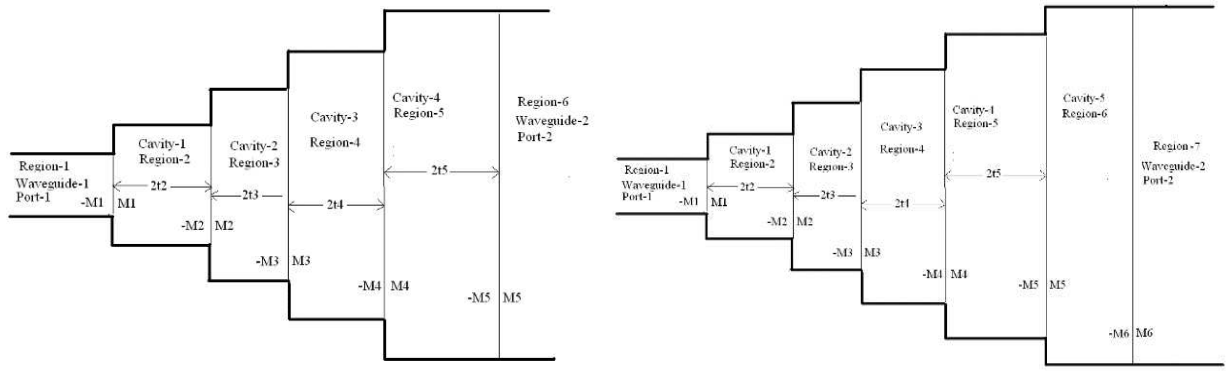

Figure 2: Details of regions and magnetic currents at the aperture of a three and four section waveguide impedance transformer.

Table 1: Dimensions of three and four section transformers between rectangular waveguides for Ku to X, K to Ku, Ka to K band and vice versa.

Waveguide Bands	**Number of Transformers**	**Transformer Dimensions in mm**								
		$\mathbf{2a}_1$	$\mathbf{2b}_1$	$\mathbf{2t}_1$	$\mathbf{2a}_2$	$\mathbf{2b}_2$	$\mathbf{2t}_2$	$\mathbf{2a}_3$	$\mathbf{2b}_3$	$\mathbf{2t}_3$
Ku-X and X-Ku	3	15.8	7.9	5	16.24	8.53	9.12	17.38	9.39	9.56
	4	15.8	7.9	5	16.44	8.68	9.48	17.73	9.33	8.84
Ku-K and K-Ku	3	10.67	4.32	5	10.99	5.05	6.54	12.24	6.52	6.81
	4	10.67	4.32	5	11.07	5.13	6.99	12.44	6.64	6.34
K-Ka and Ka-K	3	7.11	3.56	3	7.31	3.57	4.3	7.39	3.58	4.62
	4	7.11	3.56	3	7.37	3.9	4.62	7.79	4.08	4.08
Waveguide Bands	**Number of Transformers**	**Transformer Dimensions in mm**								
		$\mathbf{2a}_4$	$\mathbf{2b}_4$	$\mathbf{2t}_4$	$\mathbf{2a}_5$	$\mathbf{2b}_5$	$\mathbf{2t}_5$	$\mathbf{2a}_6$	$\mathbf{2b}_6$	$\mathbf{2t}_6$
Ku-X and X-Ku	3	20.81	10.15	9.16	22.86	10.16	5	–	–	–
	4	20.67	9.65	8.99	21.72	9.67	7.94	22.86	10.16	5
Ku-K and K-Ku	3	14.54	7.49	6.97	15.8	7.9	5	–	–	–
	4	14.06	6.8	6.39	14.24	6.97	5.34	15.8	7.9	5
K-Ka and Ka-K	3	9.16	4.23	5.01	10.67	4.32	5	–	–	–
	4	9.41	4.12	4.16	10.65	4.13	3.5	10.67	4.32	5

where the basis function e_p^i $(p = 1, 2, 3, \ldots, M)$ are defined by

$$e_p^{i,y} = \begin{cases} \sin\left\{\frac{p\pi}{2L}\left(x - x_w + L\right)\right\} & \text{for } \begin{matrix} x_w - L \le x \le x_w + L \\ y_w - W \le y \le y_w + W \end{matrix} \\ 0 & \text{elsewhere} \end{cases} \tag{2a}$$

$$e_p^{i,x} = \begin{cases} \sin\left\{\frac{p\pi}{2W}\left(y - y_w + W\right)\right\} & \text{for } \begin{matrix} x_w - L \le x \le x_w + L \\ y_w - W \le y \le y_w + W \end{matrix} \\ 0 & \text{elsewhere} \end{cases} \tag{2b}$$

The X-component of incident magnetic field at the aperture for the transmitting mode is a dominant TE_{10} mode and is given by

$$H_x^{inc} = -Y_0 \cos\left(\frac{\pi x}{2a_i}\right) e^{-j\beta z} \tag{3}$$

where $2a_i$ is the length of the exciting waveguide. The dimensions of the three and four section is given in Table 1. The internally scattered field is obtained by using the modal expansion approach. The modal voltages are given by the integrals (considering only e_p part of the aperture electric field).

The internally scattered field is obtained by using the modal expansion approach [2]. Once the electric field is obtained, the corresponding magnetic fields can be derived. The x-component of internally scattered magnetic field can be obtained as given in [6], with the cavity Green's function of electric vector potential "F" being determined, the next step is to find the scattered magnetic field inside the cavity region due to the magnetic currents. Towards this, the first step is to express the scattered magnetic field in terms of the electric vector potential and is given as follows:

$$\vec{H} = \frac{j}{\omega\mu}\left[\vec{\nabla}\times\vec{E}+\vec{M}\right] = \frac{j}{\omega\mu}\left[\vec{\nabla}\times\vec{\nabla}\times\vec{F}+\vec{M}\right] \tag{4}$$

At the region of the window, the tangential component of the magnetic field in the aperture should be identical and applying the proper boundary conditions at the aperture the electric fields can be evaluated. Applying the continuity condition of the magnetic field across the interfacing apertures, magnetic field integral equations with unknown magnetic currents are obtained, corresponds to the coupled magnetic field integral equations due to the magnetic currents M_1^x, M_1^y, M_2^x, M_2^y, M_3^x, M_3^y, M_4^x, M_4^y, M_5^x and M_5^y which are the unknown factors for a three section waveguide impedance transformer and M_1^x, M_1^y, M_2^x, M_2^y, M_3^x, M_3^y, M_4^x, M_4^y, M_5^x, M_5^y, M_6^x and M_6^y which are the unknown factors for a four section waveguide impedance transformer.

3. REFLECTION COEFFICIENT AND TRANSMISSION COEFFICIENT

To determine the reflection coefficient, we decouple the sources, one at $-\infty$ in the feed waveguide and the other at the window. The incident electric field due to the TE_{10} excitation at the $z = 0$ plane is:

$$E_y^{inc} = \cos\left(\frac{\pi x}{2a_i}\right) \tag{5}$$

When the window aperture is shorted, the electric field is the field reflected by the electric short circuit and is given by,

$$E_y^1 = -\cos\left(\frac{\pi x}{2a_i}\right) \tag{6}$$

When the generator in the feed waveguide is removed and replaced by a perfect match, the electric field for the dominant TE_{10} mode scattered by the window into the waveguide is derived and so also the reflection coefficient [11].

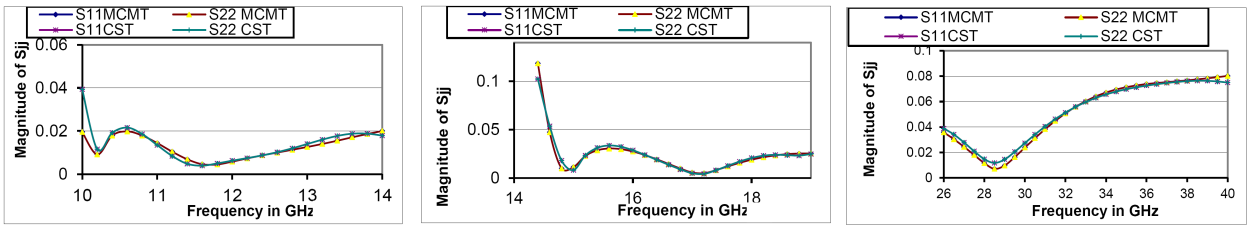

(a)

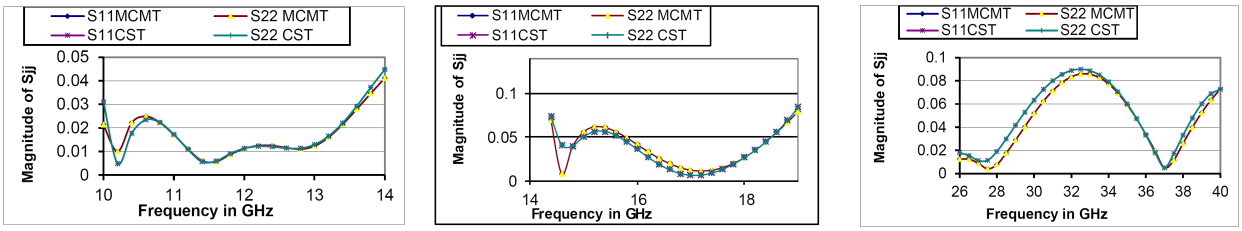

(b)

Figure 3: Comparison of MCMT and CST Microwave Studio simulated data of Magnitude of input reflection coefficient S_{jj} as a function of frequency if a TE_{10} — wave is incident at port $j = 1$ and $j = 2$ for three and four section waveguide impedance transformers in different bands, (a) and (b) respectively.

4. NUMERICAL RESULTS AND DISCUSSION

MCMT data obtained for the magnitude of reflection coefficient is compared with CST Microwave Studio simulated data for a three and four section waveguide impedance transformer from Ku to X, K to Ku and Ka to K band.

The magnitude of reflection coefficient of three and four section waveguide impedance transformers of different band are been shown in Figure 3, which shows a good agreement between CST Microwave studio data and MCMT data.

ACKNOWLEDGMENT

The support provided by Kalpana Chawla Space Technology Cell, IIT Kharagpur is gratefully acknowledged.

REFERENCES

1. Lewin, L., *Advanced Theory of Waveguide*, Iliffe, 1951.
2. Harrington, R. F., *Time-harmonic Electromagnetic Fields*, McGraw-Hill Book Company, New York, 1961.
3. Arndt. F., U. Tucholke, and T. Wriedt, "Computer-optimized multi-section transformers between rectangular waveguides of adjacent frequency bands," *IEEE Transactions on Microwave Theory and Techniques*, Vol. 32, No. 11, 1479–1484, Nov. 1984.
4. Bornemann, J. and R. Vahldieck, " Characterization of a class of waveguide discontinuities using a modified TE^x_{mn} mode approach," *IEEE Transactions on Microwave Theory and Techniques*, Vol. 38, No. 12, 1816–1821, Dec. 1990.
5. Panda, D. K. and A. Chakraborty, "Analysis of an 1 : 2 rectangular waveguide power divider for phased array application using multiple cavity modeling technique," *PIERS Proceedings*, 361–368, Cambridge, USA, Jul. 2–6, 2008.
6. Panda, D. K. and A. Chakraborty, "Multiple cavity modeling of a feed network for two dimensional phased array application," *Progress In Electromagnetic Research Letters*, Vol. 2, 135–140, 2008.
7. Panda, D. K., A. Chakraborty, and S. R. Choudhury, "Analysis of co-channel interference at waveguide joints using multiple cavity modeling technique," *Progress In Electromagnetic Research Letters*, Vol. 4, 91–98, 2008.
8. Panda D. K. and A. Chakraborty, "Analysis of a longitudinal rectangular waveguide power divider/combiner using multiple cavity modeling technique," *Proceedings of International Conferences on Industrial and Information System (ICIIS-2008)*, IEEE, IIT Kharagpur, Dec. 8–10, 2008.
9. Panda, D. K. and A. Chakraborty, "An efficient numerical technique to solve waveguide discontinuity problems," *Proceeding of International Conference on Global Computing and Communications*, 144–149, Hindustan University, India, Dec. 9–11, 2009.
10. Panda, D. K. and A. Chakraborty, "Analysis of single section impedance transformer using multiple cavity modeling technique," *International Conference on Communication, Computers and Devices*, Kharagpur, India, Dec. 10–12, 2010.
11. Panda, D. K. and A. Chakraborty, "Analysis of two section impedance transformer using multiple cavity modeling technique," *International Journal of Engineering and Innovative Technology (IJEIT)*, Vol. 2, No. 5, 107–112, Nov. 2012.

A Compact Elliptic Bandpass Filter Using Cross-coupled Miniaturised Hairpin Resonators Packaged by COB Method

C. Wang, Y. Li, and N. Y. Kim
RFIC Center, Kwangwoon University
447-1 Wolgye-dong, Nowon-ku, Seoul 139-701, Korea

Abstract— In this paper, a compact four-pole elliptic bandpass filter using cross-coupled miniaturized hairpin resonators is presented for X-band radar applications, which is packaged by chip-on-board method. The design methodology for the proposed bandpass filter, the corresponding semiconductor fabrication process, and the packaging method are described. The proposed bandpass filter is fabricated on a conventional 6-inch GaAs substrate using a standard semiconductor fabrication process; and it is then packaged by employing the chip-on-board method. The bare-chip measurements reveal an insertion loss of less than 1.3 dB in the 10.2 to 12.2 GHz passband; the return loss is better than 20.9 dB. The measured insertion loss for the packaged BPF is less than 2.1 dB; the passband return loss is better than −15.47 dB. The total size of the packaged bandpass filter is 6.76 mm × 5.85 mm × 2.5 mm.

1. INTRODUCTION

In modern communication systems, high-performance and compact microwave bandpass filters (BPFs) are important components for suppressing stop-band interference and improving the sensitivity of microwave wireless receivers. BPFs often have been designed using coupled half-wavelength resonators as building blocks. Obviously, a planar BPF with parallel-coupled $\lambda/2$ microstrips is too large to be used in modern systems. Therefore, size reduction has been an important issue in developing new microwave filters. To overcome this problem, various studies have investigated open-loop resonators [1], slow-wave resonators [2], spiral resonators [3], and hairpin resonators [4] as methods of reducing the circuit size. On the other hand, packaging determines the reliability and long-term stability of a microwave BPF; therefore, good packaging is essential for its commercial success [5]. We demonstrate the chip-on-board (COB) attachment of our proposed BPF to a standard printed circuit board (PCB), which is an alternative to undergoing a traditional packaging process as an individual IC.The COB assembly technology can simplify the overall process of designing and manufacturing a BPF, resulting in improved performance as a result of the shorter interconnection paths and the elimination of the device packaging.

In this paper, we present a design of a four-pole elliptic function X-band BPF using compact miniaturized hairpin resonators with a cross-coupled structure; it is fabricated using a semiconductor process and packaged by the COB method. Each resonator uses approximately 75% of the area of a square open-loop resonator, and the COB packaging method is applied to the fabricated BPF to increase performance and to reduce the cost and the space requirements.

2. EXPERIMENTAL PROCEDURE

2.1. Design of Four-pole Elliptic X-band Bandpass Filter Using Miniaturized Hairpin Resonator

The miniaturized cross-coupled hairpin resonators are based on sections of $\lambda/2$ open microstrips, so the fundamental resonance of each resonator occurs in the odd mode. Thus, during resonance, the electric field distribution at the central valley of the folded microstrip is at a maximum, and the electric field distributions at both ends of the coupled lines have minimum values with opposite signs. The conditions for this fundamental resonance can be derived from the stepped-impedance resonator. To design the four-pole elliptic function X-band BPF, cross-coupled structures were applied to generate finite transmission zeros, greatly improving the selectivity of the proposed BPF. According to the specification of the elliptic response, with $F_c = 11.25$ GHz and 3 dB−FBW = 20%, the coefficients and input/output (I/O) external quality factors can be calculated. The external

quality factors and the coupling coefficient matrixes are as follows:

$$Q_{er} = Q_{el} = 4.862$$

$$M = \begin{bmatrix} 0 & -0.0108 & 0.1614 & 0 \\ -0.0108 & 0 & 0 & 0.1614 \\ 0.1614 & 0 & 0 & 0.1285 \\ 0 & 0.1614 & 0.1285 & 0 \end{bmatrix}$$

The extraction process was accomplished by the full-wave simulator Advanced Design System (ADS) Momentum. Once the physical dimensions of each resonator are determined, the dimensions associated with the tap position of the I/O resonators and the gaps between adjacent resonators can be obtained by using the design curves.

The coupling spacing d_1 and d_2 for the required $M_{1,2}$ and $M_{3,4}$ can be determined from Figure 1(a) for the electric coupling and Figure 1(b) for the magnetic coupling, respectively. The mixed coupling spacing d_3 for $M_{1,3}$ can be found from Figure 1(c). The tapped line position for the required Q is determined from Figure 1(d).

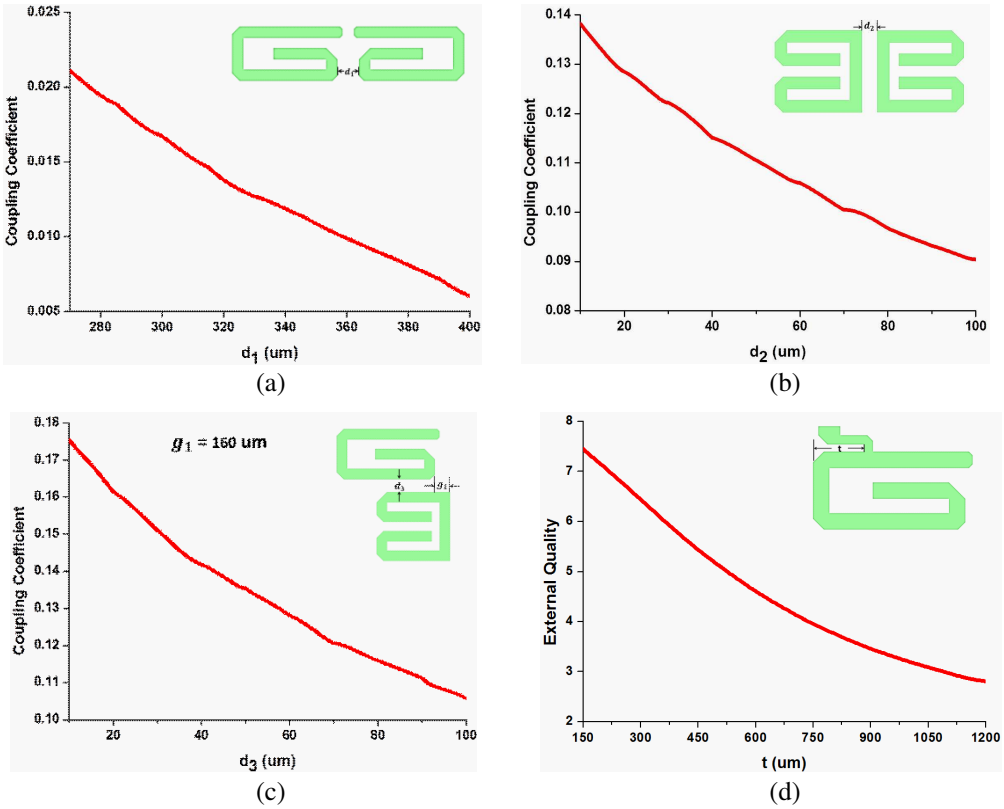

Figure 1: Simulated coupling coefficients versus the gaps between adjacent resonators: (a) electric coupling, (b) magnetic coupling, (c) mixed coupling, and (d) the simulated external quality factor against the tap position.

2.2. Analysis of Fabrication Processing and Chip-on-board Packaging Method

The fabrication process starts with a first passivation layer composed of SiN_x deposited by plasma-enhanced chemical-vapor deposition to a thickness of 2,000Å. Next, a 200/800Å-thick Ti/Au seed metal layer is deposited by sputtering to improve the substrate adhesion to the subsequent plated metal. The wafer is then masked to define the metal layer structures and electroplated conventionally using Cu/Au (9.5/0.5 µm)The fabricated miniaturized cross-coupled BPFis shown in Figure 2.

The package includes a 0.5-mm-thick Teflon PCB ($Er = 3.5$) on which there is a GaAs-based die with a thickness of 0.4 mm, as shown in Figures 3(a) and 3(b). There is an air cavity under the metal-based cover that is used in the circuit assembly. When designing the PCB, the effect of the pad and the loss of transmission line were considered; the designed PCB has good characteristics

as a transmission line, and no other external influences are introduced, which is demonstrated in Figure 3(c). After making the PCB, the COB process consists of three other major steps: 1) die attaching, 2) wire-bonding, and 3) encapsulation of the die and the wires. The die attach consists of applying a 0.025 mm die attach adhesive to the substrate and mounting the chip over the attaching material. The die placement must be accurate enough to ensure a proper orientation and a good die planarity. The wire-bonding process is similar to that used in traditional semiconductor assembly. The upper face of the plate holds a ground layer, which is connected by a via array to another ground layer set on the lower face of the plate. The spacing between the vias has to be as small as possible to prevent a mode excitation between the two layers. Finally, the die and bond wires are encapsulated to protect them from mechanical and chemical damage.

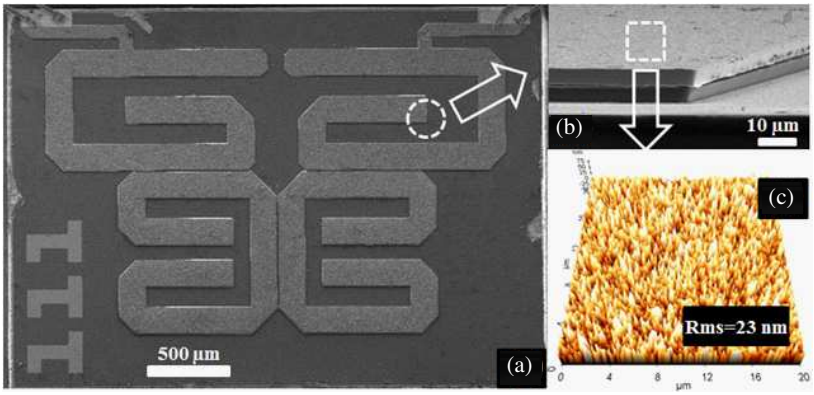

Figure 2: (a) The scanning electron microscope (SEM)-observed full view, (b) cross-section view, and (c) the surface morphology measured by atomic force microscope (AFM).

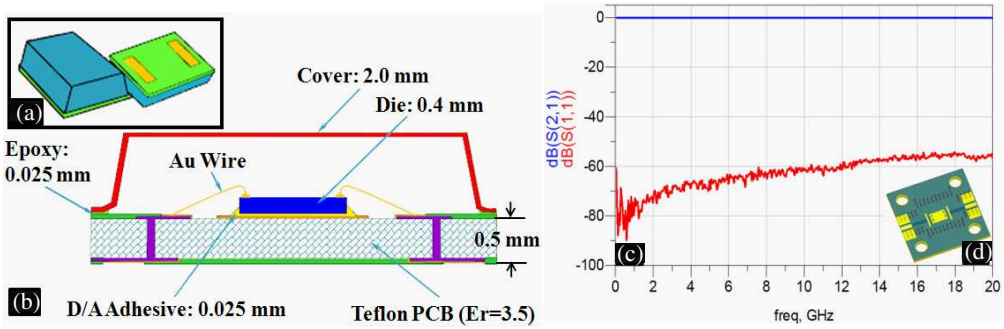

Figure 3: (a) The full view, (b) the cross-sectional view of the proposed COB packaging structure, (c) the measured frequency responses of the designed bare PCB and (d) the full view of the proposed PCB.

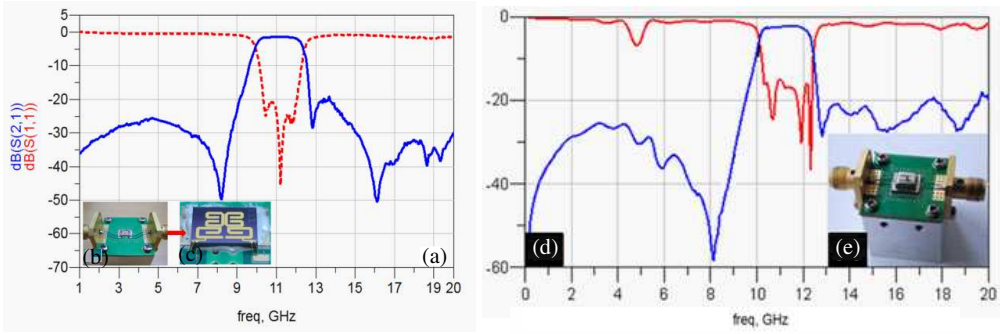

Figure 4: (a) The measured results of fabricated BPF, (b) the full view, (c) the enlarged photograph of the fabricated BPF sample with a die size is $3.86 \times 2.5 \times 0.4$ mm, (d) the measured S-parameters of the COB-packaged BPF and (e) the photograph of the COB packaged BPF attached to the sub-board PCB.

3. RESULTS AND DISCUSSIONS

The proposed cross-coupled BPF was designed, fabricated, packaged, and measured. Figure 4(a) shows the measured frequency response and fabricated photograph after die-attaching and wire-bonding. The X-band BPF has a die size of 3860 µm × 2500 µm, with an insertion loss of less than 1.3 dB and a return loss of higher than 20.9 dB. Two transmission zeros are located near the edge of the passband, with a high attenuation levels. Figure 4(b) presents the final measured results and a photograph of the packaged BPF. The insertion loss of the packaged BPF was typically less than 2.1 dB from 10.4 to 12.0 GHz, and the return loss was higher than 15.47 dB. Two transmission zeros were located at 8.2 and 12.6 GHz, with attenuation levels of 58.6 and 28.4 dB, respectively. The two transmission zeros were positioned near the edge of the passband to achieve sharp passband skirt performance. Compared to the conventional BPF prepared using other processes, the proposed filters are much more compact, covering an area of only 6.76 mm × 5.85 mm × 2.50 mm after packaging, and could be used directly in a module without any additional structure.

4. CONCLUSION

In this paper, a miniaturized cross-coupled hairpin X-band BPF, the corresponding semiconductor fabrication process, and the COB packaging method are presented for the size reduction and performance improvement of the BPF. There was good agreement between the experiments and simulation, demonstrating the validity of the circuit and packaging design strategies. The measured responses show that this BPF successfully covered the X-band frequency with a good insertion loss and a return loss across the passband. The size of the packaged BPF was only 6.76 mm × 5.85 mm × 2.50 mm. To the best of our knowledge, the presented BPF is the smallest of its kind and has better performance than those with similar functionality for X-band applications.

ACKNOWLEDGMENT

This research was supported by the National Research Foundation of Korea (NRF) grant funded by the Korea government (MEST) (No. 2012-0009224) and (No. 2012R1A1A2004366). This work was also supported by a Research Grant from Kwangwoon University in 2013.

REFERENCES

1. Li, X. and H. Wang, "An approach for multi-band bandpass filter design based on asymmetric half-wavelength resonators," *Progress In Electromagnetics Research*, Vol. 140, 31–42, 2013.
2. Zhang, J., J.-Z. Gu, B. Cui, and X.-W. Sun, "Compact and harmonic suppression open-loop resonator bandpass filter with tri-section SIR," *Progress In Electromagnetics Research*, Vol. 69, 93–100, 2007.
3. Dai, G. and M. Xia, "Novel miniaturized bandpass filters using spiral-shaped resonators and window feed structures," *Progress In Electromagnetics Research*, Vol. 100, 235–243, 2010.
4. Yang, M., J. Xu, Q. Zhao, L. Peng, and G. Li, "Compact, broad-stopband lowpass filters using SIRs-loaded circular Hairpin resonators," *Progress In Electromagnetics Research*, Vol. 102, 95–106, 2010.
5. Wang, C., W. S. Lee, F. Zhang, and N. Y. Kim, "Si-based packaging platform for LED module using electroplating method," *Electron. Lett.*, Vol. 46, No. 17, 1220–1221, 2010.

Directivity Enhancement of an X-band Horn Antenna Loaded by a Wire Medium

A. Tomaz[1], **Joaquim J. Barroso**[2], **Ugur C. Hasar**[3], **and Alberto J. Faro Orlando**[1]

[1]Technological Institute of Aeronautics (ITA), São José dos Campos, SP, Brazil
[2]National Institute for Space Research (INPE), São José dos Campos, SP, Brazil
[3]University of Gaziantep, Gaziantep, Turkey

Abstract— On the basis of full-wave electromagnetic simulation, the present work reports on a comparative study of the enhanced radiation properties of a standard X-band horn antenna loaded by a wire medium. Acting as an artificial dielectric the wire medium consists of an array of parallel metallic wires installed into the antenna with the wires oriented in the direction of the electric field. Performance of the original empty horn antenna is then compared with the same antenna when loaded by the periodic structure.

1. INTRODUCTION

Recent studies have shown that wire medium structures can provide an interesting approach to improve the radiation performance of microwave antennas. Under proper design, metallic wires periodically arranged in a regular pattern, and embedded in lightweight host material, behave as a homogenized artificial dielectric having a relative permittivity less than unity. Since the index of refraction relates to the permittivity via $n \sim \varepsilon^{1/2}$ such structure exhibits near-zero refractive index, which enables the realization of highly directive beams [1–9]. The present work presents the conceptual study of a wire metamaterial designed to enhance the radiation characteristics of a standard x-band antenna. A performance comparison at 8.87 GHz of the wire-loaded and antenna with its empty counterpart is discussed, highlighting the improvement in beam directivity of the loaded antenna.

2. WIRE MEDIUM STRUCTURE

A metamaterial wire medium can be designed by analytical models supported by full-wave electromagnetic simulations to meet specific requirements. In our study, the wire medium consists of thin metallic wires of diameter d and arranged on a square lattice of a periodic spacing a as shown in Fig. 1(a). If the wire radius and the periodic distance are very small in comparison with the wavelength inside the structure and for the case of plane-wave incidence with the electric field parallel to the wires, the wire medium can be described as an artificial dielectric with permittivity (relative to vacuum) given by

$$\varepsilon = \varepsilon_h \left(1 - \frac{f_c^2}{\varepsilon_h f^2}\right) \tag{1}$$

where ε_h is the permittivity of the host medium, f the frequency of the incident wave, and f_c the equivalent cutoff frequency determined as [8]

$$f_c = c\left[a\sqrt{2\pi\left(\ell n\frac{a}{\pi d} + 0.5275\right)}\right]^{-1} \tag{2}$$

The wire medium is envisaged to operate in the x-band (8.2–12.4 GHz), and for achieving optimum frequency response the geometrical parameters should be properly chosen by taking into account commercially available diameters for the metallic wire. The lattice constant and the wire diameter were chosen as $a = 10.0\,\text{mm}$ $d = 0.5\,\text{mm}$, yielding from (2) a cutoff frequency of 7.7 GHz. In this way, the effective index of refraction for the wire medium so designed by considering air as the host medium is shown in Fig. 1(b), where the resulting refractive index has an average value of 0.5 over the 8–13 GHz range.

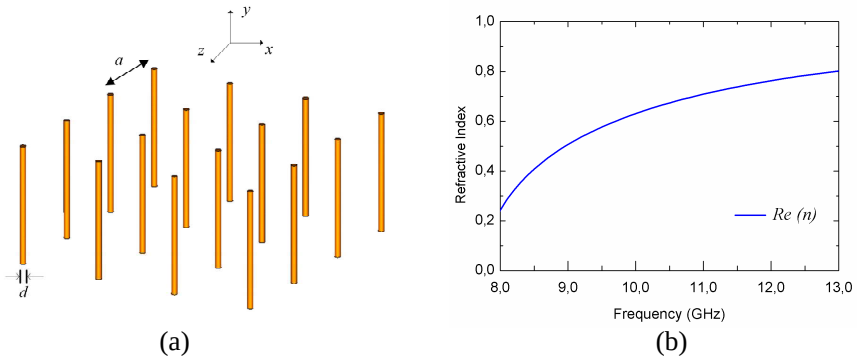

Figure 1: (a) Wire medium structure and (b) the corresponding refractive index calculated from (1).

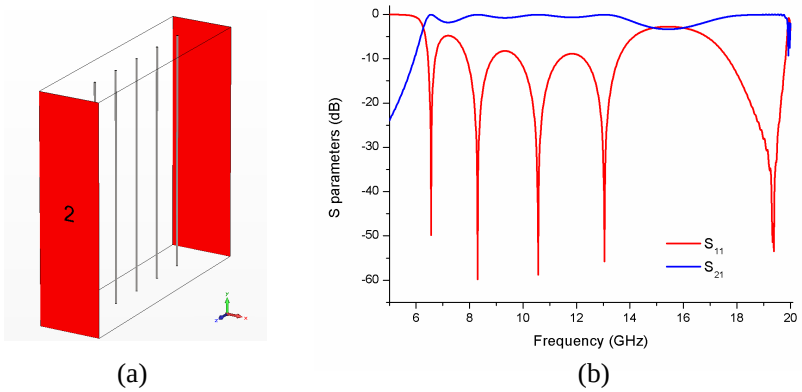

Figure 2: (a) Simulation setup of the periodic array of wires and (b) simulated S-parameters.

3. WIRE MEDIUM SIMULATION

The analytical model was verified through electromagnetic full-wave simulations by using the CST MWS software [10] to ascertain the behavior of the artificial dielectric formed by a periodic array of metallic wires. As displayed in Fig. 2(a), the simulated structure is composed of five 0.5-mm-diameter wires evenly spaced at 10.0 mm.

In the simulations, electric and magnetic boundary conditions were applied on the walls perpendicular and parallel to the wires, respectively, and two open ports were used to simulate the S-parameter response to a normally incident plane wave with the electric field polarized along the wires. Fig. 2(b) shows the simulated scattering parameters S_{11} and S_{21} of the periodic structure. In addition to a transmission band starting at about 7.0 GHz and extending up to 14.0 GHz, four resonance dips are noticed. Such resonances are due to the inductive coupling of the wires in the periodic of the structure, whereby N elements give rise to $N-1$ coupled resonances. Beyond the pass band, it appears the Bragg band gap identified by the frequency whose wavelength is twice the periodic distance, such that f_B (GHz) $= 15/a$ (cm). Increasing the number of wires, e.g., to twenty, would make the gap transition much sharper and just starting at 15.0 GHz, which is f_B for the design $a = 1.0$ cm.

4. ELECTROMAGNETIC SIMULATION OF THE WIRE-MEDIUM LOADED ANTENNA

A simulation setup (Fig. 3) was realistically implemented in the CST Microwave Studio [10]. The horn antenna is a replica of a standard commercial antenna fabricated by ATM Microwave [11]. Five rows of the wire medium previously discussed are loaded in the antenna. The arrays of metallic wires are accommodated and fixed in a Styrofoam plate 10.0 mm thick; this host material has a relative permittivity of 1.03 and loss tangent of 0.1×10^{-3} [12].

The simulated return loss of the wire-medium antenna is demonstrated in Fig. 4. Associated with the five loaded layers, four resonance dips are identified at 8.87, 10.08, 10.93, and 11.86 GHz. The leftmost dip at 8.65 GHz is a trapped-mode resonance likely to be ascribed to a mode trapped in the throat of the feedhorn.

Such peculiarities in the S_{11} spectrum result in a change of the radiation characteristics the

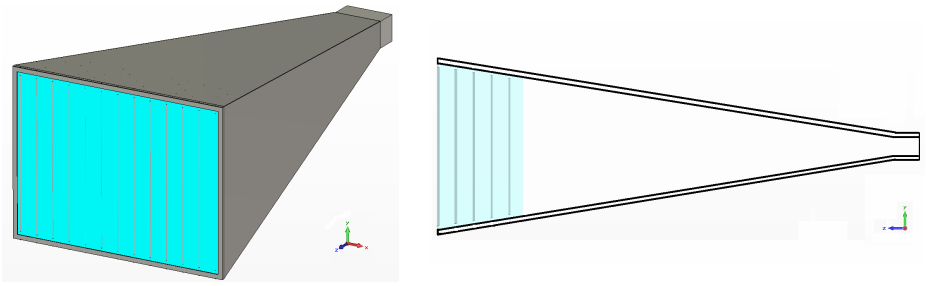

Figure 3: Horn antenna loaded with the wire medium: (a) perspective view and (b) cut-away view.

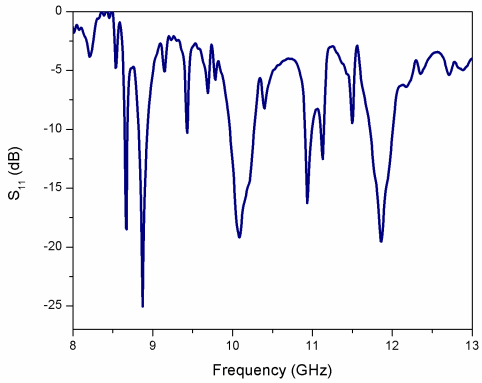

Figure 4: Simulated S_{11}-parameter for the loaded antenna.

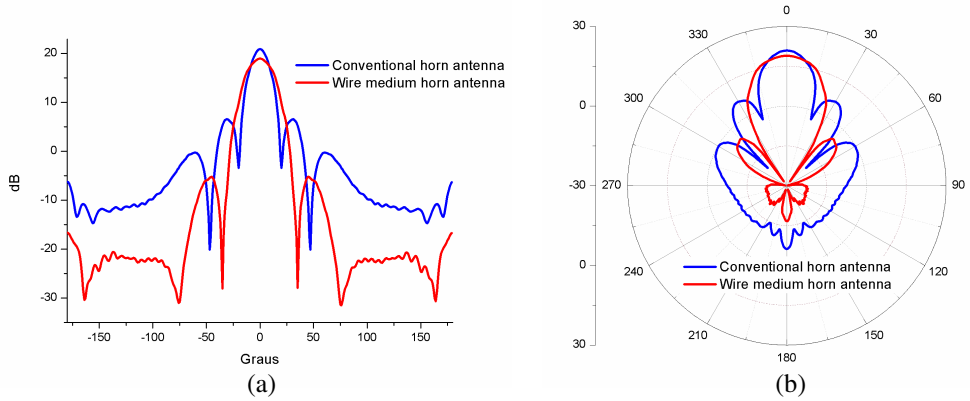

Figure 5: E-plane radiation patterns in (a) rectangular and (b) polar coordinates at 8.87 GHz.

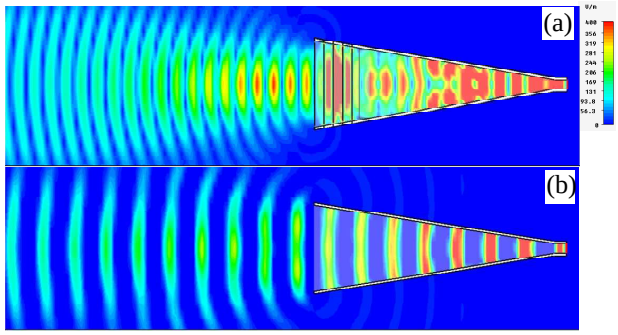

Figure 6: Electric field intensities radiated by (a) the wire-medium antenna and (b) the standard antenna at 8.87 GHz.

original antenna. This is demonstrated in Fig. 5 which compares the performance the loaded and empty antennas at 8.87 GHz. It is clearly apparent that the E-plane radiation pattern for the loaded antenna yields significantly reduced side lobes, at a level lower than -20 dB. Accordingly, we see in Fig. 6 that the intensity of the radiated electric field is far more concentrated along the axis of the wire-medium antenna.

5. CONCLUSION

Through electromagnetic simulations, this report has demonstrated how a properly designed wire-medium can enhance the radiation characteristics of a commercial standard X-band horn antenna. Such an enhancement is due to a refractive index near-zero effect providing a stronger concentration of energy in the central region of the loaded antenna's radiation pattern. The wiremedium antenna exhibits a high directivity and reduced side lobe level, in this case 10 dB below that of the conventional antenna. Wire media with different configurations and arrangements provide similar performance enhancement in other frequency ranges.

REFERENCES

1. Simovski, C. R., P. A. Belov, A. V. Atrashchenko, and Y. S. Kivshar, "Wire metamaterials: Physics and applications," *Adv. Mater.*, Vol. 24, 4229–4248, Aug. 2012.
2. Eleftheriades, G. V. and N. Enghetta, "Metamaterials: Fundamentals and applications in the microwave and optical regimes," *Proc. IEEE*, Vol. 99, No. 10, 1618–1621, Oct. 2011.
3. Ramaccia, D., F. Scattone, F. Bilotti, and A. Toscano, "Broadband compact horn antennas by using EPS-ENZ metamaterial lens," *IEEE Trans. on Antennas and Propag.*, Vol. 61, No. 6, 2929–2937, Jun. 2013.
4. Chen, H., B.-I. Wu, and J. A. Kong, "Review of electromagnetic theory in left-handed materials," *Journal of Electromagnetic Waves and Applications*, Vol. 20, No. 15, 2137–2151, 2006.
5. Wu, Q., P. Pan, F.-Y. Meng, L.-W. Li, and J. Wu, "A novel flat lens horn antenna designed based on zero refraction principle of metamaterials," *Appl. Phys. A*, Vol. 87, 151–156, 2007.
6. Enoch, S., G. Tayeb, P. Sabouroux, N. Guérin, and P. Vicent, "A metamaterial for directive emission," *Phys. Rev. Lett.*, Vol. 89, No. 21, Art. ID 213902, 2002.
7. Tomaz, A. and J. J. Barroso, "Refractive properties of artificial dielectrics consisting of a periodic wire medium," *IEEE International Symposium Antennas and Propagation and National Radio Science Meeting*, Orlando, 2013.
8. Kock, W. E, "Metal-lens antennas," *Proceedings of the IRE*, Vol. 34, No. 11, 828–836, Nov. 1946.
9. Hrabar, S., D. Bonefačić, and D. Muha, "Numerical and experimental investigation of basic properties of wire medium-based shortned horn antenna," *Microw. Opt. Techn. Lett.*, Vol. 51, No. 11, 2748–2753, Nov. 2009.
10. CST Microwave Studio, Version 2005, CST GmbH, Darmstadt, Germany.
11. Datasheet Advacend Technical Materials, Inc., "Horn antennas — Standard gain horn," 2012.
12. Barker-Jarvis, J., et al., "Dielectric and conductor-loss characterization and measurements on electronic packaging materials," *Nat. Inst. Standards Technol.*, Tech. Rep. 1520, Gaithersburg, MD, Jul. 2001.

Electric Field Tunable Domain Ferromagnetic Resonances in (111) Yttrium-iron Garnet Films

M. A. Popov[1], **I. V. Zavislyak**[1], **and G. Srinivasan**[2]

[1]Radiophysics Department, Taras Shevchenko National University of Kyiv, Kyiv 01033, Ukraine
[2]Physics Department, Oakland University, Rochester, MI 48309, USA

Abstract— The results of experimental investigation of electric field tuning of magnetic resonances in composite ferrite/piezoelectric YIG/PZT structure with YIG epitaxial film being in multiple-domain or saturated states are presented. Two separate groups of domain modes have been observed, at high and low frequency regions, when YIG domain structure has the form of stripe domains directed along bias in-plane magnetic field. Electric field tuning of resonance frequency being attributed to the appearance of stress induced first-order uniaxial magnetocrystalline anisotropy. Electric field (instead of magnetic field) control of microwave properties enables construction of simpler, more compact, planar ferrite UHF-band devices.

1. INTRODUCTION

In recent years, a numerous research have been devoted to the creation and investigation of new composite materials based on planar ferrite/piezoelectric structures that admit dual tuning-by both magnetic and electric fields [1]. Electric field control of microwave properties enables construction of simpler, more compact, planar magnetic devices [2]. Ferrite counterparts of such metamaterials could be yttrium-iron garnet (YIG) [1], barium hexaferrite [3], nickel ferrite [4], etc.. As it was experimentally and theoretically proven [5], dominant mechanism of the resonant frequency shift is the stress induced first-order uniaxial magneto crystalline anisotropy. However, all above mentioned investigations were concentrated on ferromagnetic resonances in saturated state, while domain resonances remain unexplored. Meanwhile domain resonances, due to their very nature, always exist in lower magnetic field, than classical ferromagnetic resonance. As far as providing substantial bias magnetic field is usually the biggest challenge during ferrite devices construction, investigation of magnetic excitation in ferrites in low field presents certain practical interest. The goal of this paper is to investigate the ferrite/piezoelectric structure with ferrite in unsaturated state, determine the influence of E-field induced mechanical stress on domain structure and domain resonances frequencies, and compare the frequency tuning result with those of saturated ferrite.

2. EXPERIMENTAL RESULTS

In this work, we investigated 10 µm thick epitaxial (single-crystal) film of YIG, grown on (111) plane of gadolinium gallium garnet $Gd_3Ga_5O_{12}$ (GGG) substrate using liquid phase epitaxy. Experimental measuring cell is shown on Fig. 1. YIG film on substrate was glued using epoxy to 0.2 mm thick disk-shaped lead titanate-zirconite (PZT) with metallized surfaces and contact pads for electric connection; the round hole, approximately 2 mm in diameter, was drilled in the PZT and used for domain observation via magneto optical Faraday effect. Sample was situated on shorted section of microstrip line, directly atop of the current-carrying stripe. External magnetic field was created using solenoid coil and applied as shown on the Fig. 1.

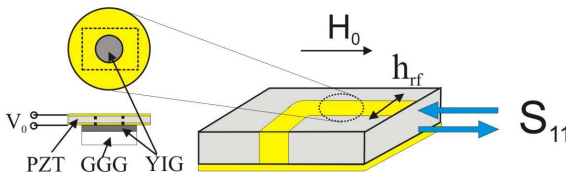

Figure 1: Experimental measuring cell.

Ferrite film was oriented in such way, that bias magnetic field was directed along ⟨110⟩ crystal axis. As the first step, we observed static domain structure using standard magnetooptic technique [6]. In zero bias field we got labyrinth domain structure with the domain walls lying along three equivalent ⟨110⟩ directions in the film plane. When in-plane magnetic field of several Oe was

applied, the periodic stripe domain structure with domains of equal width was formed, aligned along external magnetic field direction. Further increase in H_0 led to increase in width of energetically favorable domains and, finally, for large H_0, the film reached magnetically saturated state with uniform magnetization. During microwave measurements we primarily concentrated our attention on the bias field range of $H_{L-S} \leq H_0 \leq H_c$, where $H_{L-S} \approx 3$–4 Oe marks transition from labyrinth to stripe domain structure, and H_c is critical field for the transition from the saturated to multiple-domain state. We recorded the reflection coefficient S_{11} of measuring cell with ferrite-piezoelectric structure as a function of frequency for different bias fields in 0.01–1.5 GHz frequency range using a ROHDE&SCHWARZ R&S®ZVA8 vector network analyzer and extracted the frequency vs. field dependence for main magnetic resonance in both saturated and unsaturated states. The results for three different values of applied to piezoelectric static voltage, are presented on Fig. 2(a). Typical "butterfly" curve was observed in all cases, with minimum frequency point marking transition from saturated to multiple-domain state and determines critical field H_c. The drastic influence of E-field induced uniaxial anisotropy field on ferrite in unsaturated state is clearly visible. Also, the change of H_c with voltage, applied to PZT, was measured and depicted on Fig. 2(b).

From Fig. 2(a), one can notice two key features: 1) E-field tuning of magnetic resonance frequency in unsaturated ferrite is considerably greater, than tuning in saturated state, under otherwise equal conditions; 2) the sigh of frequency change is opposite, i.e., while applied -100 V voltage increases resonance frequency in saturated state, it shifts domain resonance frequency downward. The results of detailed frequency vs. piezovoltage dependency investigation is shown at Fig. 3 where bias field value was $H_{01} = 34$ Oe. We measured respectable 117 MHz frequency shift for domain resonance (for comparison, resonance in saturated state shown meager 18 MHz).

Note, that as we have previously shown [5], in ferrite films, largest frequency tuning take place for perpendicular bias and comprises approximately 140 MHz, while for in-plane bias tuning is at least 3 times smaller. However, perpendicular configuration also requires formidable bias field, in order to

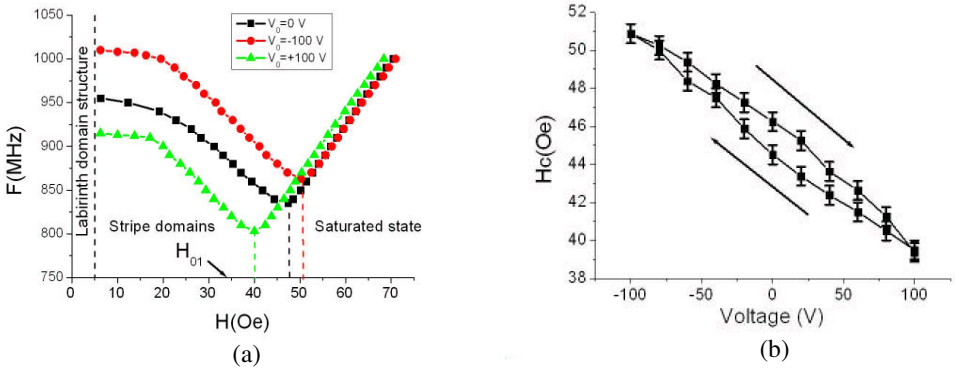

Figure 2: (a) Frequency vs. field dependence for magnetic resonances in ferrite-PZT structure at different voltage, applied to piezoelectric; (b) critical field as a function of voltage.

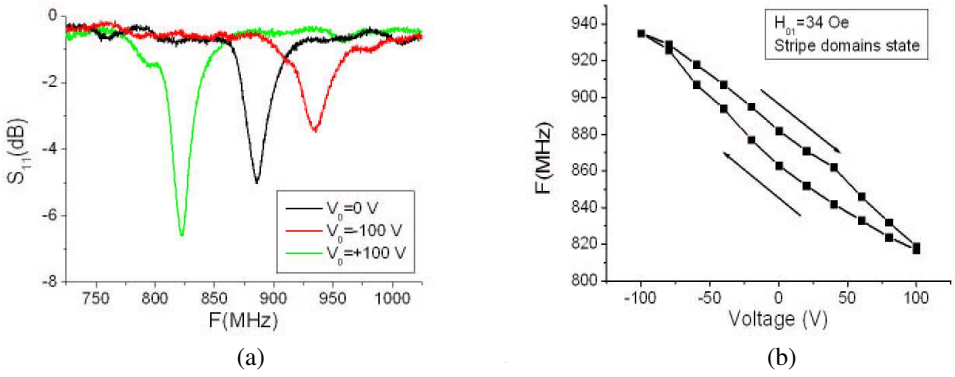

Figure 3: Tuning of resonant frequency of the YIG/PZT composite resonator with applied voltage for ferrite film in unsaturated state: (a) reflection characteristics; (b) F vs. V_0 curve.

overcome the shape demagnetizing field $4\pi M$, which in YIG case amounts approximately 1.8 kOe. Yet, here we have quite another situation: noticeable frequency tuning, in order of magnitude comparable with perpendicular-bias-tuning in saturated YIG, is achieved for in-plane bias mode, and, what is important, at very small magnetic field. Besides high-frequency domain resonance, that smoothly transformed into magnetostatic mode, during transition form multiple-domain to saturated state, we have registered few lower frequency domain resonances, having frequency in 200–500 MHz range. Such situation when two groups of domain modes with very different frequencies are observed is quite usual for measurements on ferrite sample with stripe domains [7, 8]. We have to note, that on the contrary to [7, 9] where low frequency resonances are predicted to appear for microwave excitation parallel to H field, in our case both resonances were excited simultaneously and for microwave excitation perpendicular to H field (as it is shown on Fig. 1). Altering excitation mode from perpendicular to parallel, by slowly moving sample toward the shorted end, make high- and low-frequency resonances disappear. Frequencies vs. field dependencies of three distinct low-frequency modes (labeled 1–3) are shown on Fig. 4(a). These modes, like their high frequency counterparts, appear at $H_0 = 2$–3 Oe, but, unlike them, their frequency increase with magnetic field. For bias field close to critical, these resonances become weak and undistinguished and gradually disappear.

Low-frequency domain modes are as well E-field tunable. Frequency tuning for main mode with applied piezovoltage is shown on Fig. 4(b). The voltage induced frequency changes are rather weak (14 MHz at ± 100 V), but easily traceable. From these results we can conclude, that low-frequency resonance behave differently from higher-frequency one: it has upward frequency vs. field slope and much weaker E-field tuning.

One more interesting feature of these low-frequency resonances is that in some range of bias

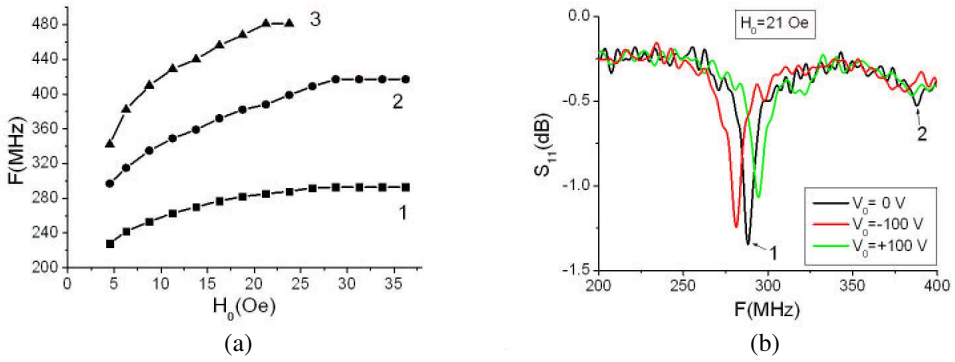

Figure 4: (a) Frequency vs. field dependence for low-frequency domain resonances at zero voltage; (b) voltage tuning of lowest frequency resonance.

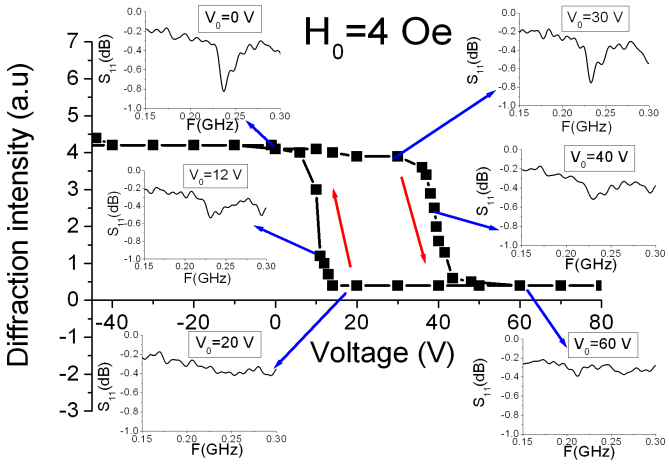

Figure 5: Correspondence between low-frequency domain resonance appearance and first diffraction maximum intensity.

magnetic fields they can exist only for some specific interval of static voltage. This point is illustrated on Fig. 5, where central graph shows the intensity of the first diffraction maximum of laser beam, diffracted on periodic stripe domain structure; while insets display respective reflection characteristic of YIG/PZT structure. Clear correspondence between low-frequency domain resonance and first diffraction maximum intensity is readily visible, proving, that those resonances own their existence to periodic stripe domain structure with equal-volume domains.

3. DISCUSSION

Theory gives the following expression, determining critical field H_c [10]:

$$H_c\left(H_c - H_{u1} - H_{cub}\right) - 2H_{cub}^2 = 0 \tag{1}$$

Here H_{cub} is cubic anisotropy field ($H_{cub} = -43\,\mathrm{Oe}$ [11] for pure YIG), and H_{u1} is the first order uniaxial anisotropy field, comprising of two parts: growth induced (permanent) anisotropy H_{U1}^G and additional stress (E-field)-induced term $H_{U1}^E(V_0)$. In turn, $H_{U1}^E(V_0)$ for (111) films can be expressed as

$$H_{U1}^E(V_0) = -\frac{3E}{1-\nu}\frac{\lambda_{111}}{M_S}\frac{d_{31}}{S}V_0 \tag{2}$$

where $\lambda_{111} = -2.8 \cdot 10^{-6}$ [11] is the YIG magnetostriction constant, E is Young's modulus ($E = 2$, $1 \cdot 10^{11}$ Pa for YIG), ν — Poisson's ratio ($\nu = 0.29$), $d_{31} = -2.7 \cdot 10^{-10}\,\mathrm{m/V}$ — PZT piezoelectric coefficient, V_0/S — is electric field strength, V_0 — applied voltage, S – piezoelectric thickness. Voltage-induced mechanical stress in YIG could be expressed as $\sigma = E/(1-\nu)(V_0/S)d_{31}$.

The Fig. 2(b), together with expression (1) allowed us to calculate H_{u1} as a function of V_0 and extract voltage induced part. It appears, that $\pm 100\,\mathrm{V}$ voltage, creates uniaxial anisotropy field of $\mp 17\,\mathrm{Oe}$. Meanwhile, substituting all the YIG and PZT material parameters in (2), we get $H_{U1}^E[Oe] = -0.23 \cdot V_0[V]$, that gives $\left|\Delta H_{U1}^E\right|(V_0 = 100\ V) = 23\,\mathrm{Oe}$, that is slightly more then experimentally obtained value, indicating non-perfectly rigid bonding between ferrite and PZT.

In saturated state main mode resonant frequency of in-plane biased anisotropic ferrite film is defined as [10]: $F = \sqrt{\left(\omega_H - \omega_M N_{||}\right)\left(\omega_H - \omega_M N_{||} + \omega_M - \gamma H_{cub} - \gamma H_{u1}\right) - 2\left(\gamma H_{cub}\right)^2}$, where $\omega_H = \gamma H_0$, $\omega_M = \gamma 4\pi M$, $4\pi M = 1800\,\mathrm{G}$ — saturation magnetization, γ gyromagnetic ratio, $N_{||} \approx 0$ — in-plane demagnetizing factor. Substituting here obtained H_{u1} values, we get peak-to-peak frequency change of 10 MHz, which is somewhat below experimental results.

Though there are number of fundamental theoretic works concerning domain resonances [7, 9, 12], all of them consider domain structure with equal-volume domains perpendicular to the direction of bias field. Theory for domain resonances in in-plane magnetized anisotropic ferrite with non-equal stripe domain structure parallel to H_0, to the best of our knowledge, has not been developed yet, so comparison is not possible as for now.

4. CONCLUSION

In summary, we have experimentally investigated electric field influence on domain structure and tuning of magnetic resonances in YIG epitaxial film in multiple-domain state. E field changes in domain structure, namely the transition from to saturated point was qualitatively and quantitatively explained by voltage-induced first-order uniaxial anisotropy change.

Two separate groups of domain modes with different frequency were excited with microwave field perpendicular to the in-plane bias H_0. Main mode of the lower-frequency group is situated at frequencies 200–300 MHz, with its frequency increasing with applied voltage and tuning range amounts less then 15 MHz. On the other hand, main high-frequency mode exists in 800–1000 MHz range and shows noticeable tuning of 120 MHz. This value is close to the best obtained results for ferrite film/PZT heterostructures with perpendicularly bias [5], despite that here magnetic field is actually laying in-plane.

That result opens up possibilities for practical applications of E-field tunable domain resonances. Indeed, we have 14% central frequency tuning, which, on the contrary to perpendicular magnetization case, takes place in extremely low bias magnetic field (few tens of Oe), which can be easily provided by small, planar permanent magnet. Moreover, natural domain resonance frequency in pure YIG appears to lie very close to GSM-900 working frequencies, that means, by proper choosing the bias field magnitude (see. Fig. 2(a)) one can provide electric field frequency scan that covers all GSM-900 uplink and downlink channels.

REFERENCES

1. Nan, C.-W., M. I. Bichurin, D. Viehland, et al., "Multiferroic magnetoelectric composites: Historical perspective, status, and future directions," *J. Appl. Phys.*, Vol. 103, No. 3, 031101, 2008.
2. Yang, G.-M., J. Lou, J. Wu, et al., "Dual H- and E-field tunable multiferroic bandpass filters with yttrium iron garnet film," *IEEE International Microwave Symposium Digest*, 2011, DOI: 10.119/MWSYM.2011.5972897.
3. Srinivasan, G., I. V. Zavislyak, and A. S. Tatarenko, "Millimeter-wave magnetoelectric effects in bilayers of barium hexaferrite and lead zirconate titanate," *Appl. Phys. Lett.*, Vol. 89, No. 15, 152508, 2006.
4. Li, N., M. Liu, Z. Zhou, et al., "Electrostatic tuning of ferromagnetic resonance and magnetoelectric interactions in ferrite-piezoelectric heterostructures grown by chemical vapor deposition," *Appl. Phys. Lett.*, Vol. 99, No. 19, 192502, 2011.
5. Popov, M. A. and I. V. Zavislyak, "Mechanism of electric frequency tuning in composite resonators based on epitaxial ferrite films," *Technical Physics Letters*, Vol. 38, No. 9, 865–868, 2012.
6. Zavislyak, I. V., V. P. Sohatsky, M. A. Popov, and G. Srinivasan, "Electric-field-induced reorientation and flip in domain magnetization and light diffraction in an yttrium-iron-garnet/lead-zirconate-titanate bilayer," *Phys. Rev B*, Vol. 87, No. 13, 134417, 2013.
7. Artman, J. O., "Microwave resonance relations in anisotropic single-crystal ferrites," *Phys. Rev.*, Vol. 105, No. 1, 62–73, 1957.
8. Vashkovskii, A. V., É. G. Lokk, and V. I. Shcheglov, "Propagation of zero-exchange spin waves in ferrite films with domain structure," *Journal of Experimental and Theoretical Physics Letters*, Vol. 63, 572–577, 1996.
9. Kirov, S. A., A. I. Pilshchikov, and N. E. Syryev, "Magnetostatic oscillations in sample with domain structure," *Fiz. Tverd. Tela (Leningrad)*, Vol. 16, No. 10, 3051–3056, 1974.
10. Zavislyak, I. V. and M. A. Popov, *Yttrium: Compounds, Production and Applications*, B. D. Volkerts, Editor, Nova Science Publishers Inc., New York, 2011.
11. Hansen, P., "Anisotropy and magnetostriction of gallium substituted yttrium iron garnet," *J. Appl. Phys.*, Vol. 45, No. 8, 3638–3642, 1974.
12. Vyzulin, S. A., S. A. Kirov, and N. E. Syryev, "Influence of the domain structure on the spectrum of magnetostatic oscillations in ferrite platelet," *Vestnik MGU, Ser. 3, Fiz. Astron.*, Vol. 24, No. 1, 92–94, 1983.

Electromagnetic Interactions between Interconnected Patch-ring (IPR) Structures and Planes in Electronic Packages and PCBs

Ivan Ndip[1, 2], **Micha Bierwirth**[2], **Stephan Guttowski**[1], **Herbert Reichl**[1, 2], **and Klaus-Dieter Lang**[1, 2]

[1]Fraunhofer IZM, Gustav-Meyer-Allee 25, Berlin 13355, Germany
[2]Technische Universität Berlin, Straße des 17, Juni 135, Berlin 10623, Germany

Abstract— In this contribution, an interconnected patch ring (IPR) structure for noise suppression in the cavity of power-ground plane pairs is designed, fabricated and measured. The impact of electromagnetic interactions between an integrated/embedded IPR and power/ground planes in electronic packages and printed circuit boards is extensively studied. Our results reveal that the presence of a metal layer (i.e., a power/ground plane) above an IPR causes the excitation of parallel-plate modes and undesired coupling, which leads to the disappearance of the stopband of the IPR. Design methods to prevent this disappearance are investigated.

1. INTRODUCTION

The continuous demand for portable and multifunctional wireless electronic products has fueled the need for the integration of RF/analogue, digital, MEMS and a myriad of other mixed-signal components/subsystems on a single chip or electronic package. For further miniaturization, these components must be integrated in very close proximity to each other. However, compact integration of mixed-signal components can only be achieved if efficient noise suppression/isolation methods are used, especially when the components share the same power distribution network (PDN). This is because noise, e.g., simultaneous switching noise (SSN), generated from digital components may propagate through the cavity of power-ground planes and couple to sensitive components, thereby causing either detuning of RF/analogue circuits, false switching of digital circuits or even malfunctioning of the entire system [1].

Amongst the numerous noise suppression/isolation methods studied so far, electromagnetic band gap (EBG) structures, based on Svienpipper's work on high impedance surfaces [2], have received most of the attention because of their efficiency in suppressing noise propagation in a wide range of frequencies. Consequently, many EBG configurations have been developed within the last decade. Examples include planar EBGs [3, 4], mushroom-type EBGs [5, 6] and hybrid EBGs [7, 8]. However, EBGs have some disadvantages which limit their application in system design. For example, since they are periodic structures, at least one of their metal layers is always segmented into many periodic unit cells. Each cell consists of a patch and inductive metal strips/branches. In some cases, surface mount capacitors and inductors are used to increase the design freedom. These surface-mount components and the periodic patches as well as the metal branches take-up much of the package/board space and leave little space for placement and routing of the "actual" components needed for system functionality [1]. Furthermore, the branch inductances of EBG cells greatly obstruct charge delivery from bypass capacitors to switching devices [9]. Lastly, due to the periodicity of the patches, transmission lines routed above the patterned layers of EBGs suffer from return-path discontinuity (RPD) problems, which severely degrade their electrical performance [10, 11].

To overcome these limitations, a new noise suppression/isolation structure, the interconnected patch-ring (IPR) structure, was proposed in [1, 12, 13]. The IPR is just as effective as EBGs in suppressing noise propagation but has many advantages over EBGs. For example, only a small portion of one of its metal layer is patterned along its periphery and no surface mount components are needed. Hence, when IPRs are used, a higher integration density in electronic packages and boards is achieved, no obstruction of charge delivery occurs and transmission lines have less RPD problems than when routed over EBGs.

However, when IPRs are integrated/embedded in electronic packages and printed circuit boards (PCBs) they may suffer from de-tuning effects and perhaps, may lose their stopband characteristics, because of the electromagnetic interactions between the IPRs and metal layers routed above them. To prevent this, the impact of these metal layers must be extensively investigated at the beginning of the design cycle. In [1, 12], this impact was not studied. Therefore, the goal of this paper is to systematically study the impact of the electromagnetic (EM) interactions between IPRs and metal

layers, and investigate design measures/rules which prevent the disappearance of the stopband of IPRs when they are integrated/embedded in electronic packages and PCBs.

The remaining part of this paper is structured as follows: In Section 2, a brief discussion on the structure, design and measurement of IPRs is given. The impact of the EM interactions between IPRs and metal layers is presented in section three, and in section four, design measures to minimize this impact are investigated.

2. STRUCTURE, DESIGN AND MEASUREMENT OF IPRS

Figure 1 shows the top and cross-sectional views of an IPR on Rogers 4305B substrate ($\varepsilon_r = 3.75$, $\tan(\delta) = 0.006$). Unlike EBGs which are made up of numerous patches in the form of an array, the IPR studied in this work consists only of two large patches, each having a length and width of L_p and W_p, respectively, as shown in Fig. 1. These patches contribute the majority of capacitance needed to achieve the desired stopband characteristics. Each patch is surrounded by a metal strip ring. Since the magnetic flux and hence, inductance of this metal strip is inversely proportional to its width, a thin strip is required to achieve large inductances. Therefore, the rings consume a very small area of the patches, and much space is left for the placement/routing of components needed for system functionality. Each ring is connected to its patch by a metal strip of length L_{bpr} and width W_{bpr}. Both rings are then interconnected as shown in Fig. 1(b).

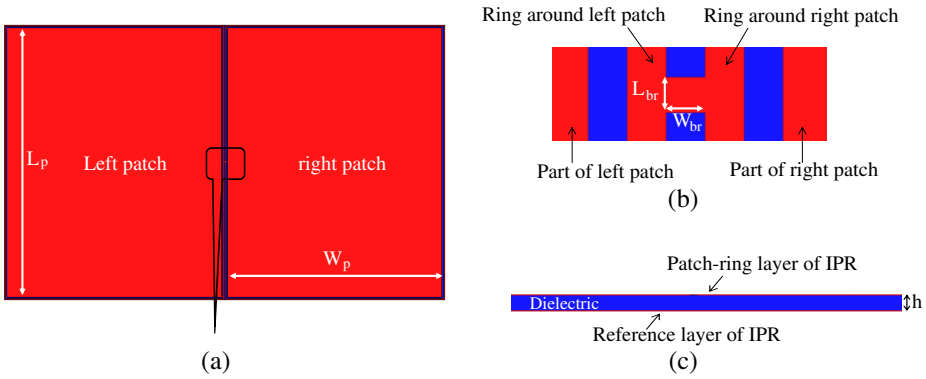

Figure 1: Top and cross-sectional views of an IPR structure.

The IPR was designed using Ansys HFSS (a finite-element–method (FEM) based electromagnetic field solver which solves Maxwell's equation in the frequency domain). To prevent noise propagation from 600 MHz to 2.7 GHz, the following dimensions of the IPR were used: $L_p = 49.25$ mm, $W_p = 42.9$ mm, $L_{bpr} = W_{bpr} = L_{brr} = W_{brr} = 0.2$ mm, $h = 0.508$ mm and a copper thickness of 30 µm. This frequency range was chosen, because it covers the operating bands of RF chips used for most wireless communication applications (e.g., GSM 800/900/1800/1900, UMTS, Bluetooth, 2.4 GHz WLAN and GPS). Therefore, any SSN generated by the digital components, e.g., processors, cannot couple to and detune the RF chips.

For experimental verification of the design, an IPR and a reference power-ground plane pair were fabricated on Rogers 4305B substrate. They were measured using a vector network analyzer (VNA) — HP 8510 C. The top views of the fabricated structures are shown in Fig. 2.

A comparison between measurement and simulation results of the IPR and reference power-ground plane pair having the same dimensions as the IPR is shown in Fig. 3. As can be seen in

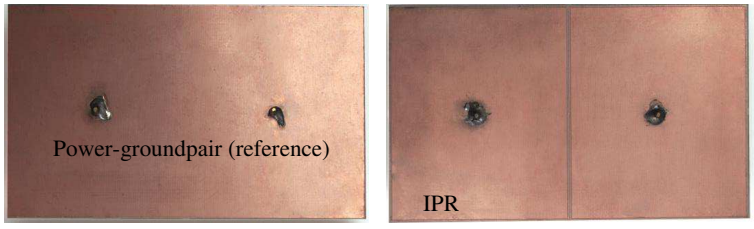

Figure 2: Photograph (top views) of fabricated reference power-ground plane pair and an IPR on Rogers 4305B.

this figure, the isolation between port 1 and 2 is better than −40 dB within the desired frequency range, when the IPR is considered. This implies that if, for example, a digital processor is placed in port 2 and any sensitive RF chip is placed in port 1, then less than 0.01% of the power (or noise) generated from the digital processor will reach the sensitive chip. It can also be seen from Fig. 3 that there is a very good correlation between measurement and simulation. This validates the simulation approach to design IPRs. In this work, the stopband suppression bandwidth is defined at −40 dB.

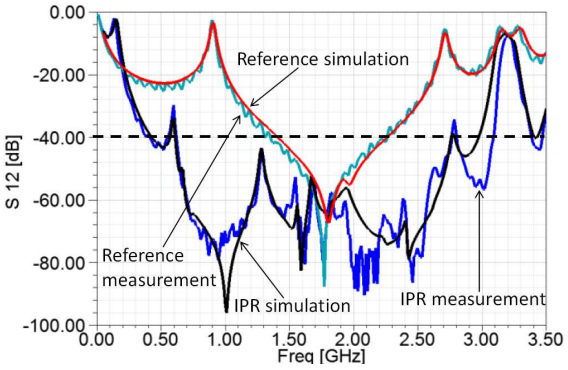

Figure 3: Comparison between measurement and simulation of IPR and reference power-ground plane pair.

3. IMPACT OF EM INTERACTIONS BETWEEN AN IPR AND A METAL LAYER ABOVE THE PATCH-RING LAYER OF THE IPR

When an IPR is not embedded/integrated in a package or PCB (i.e., in the absence of a metal layer above its patch-ring layer), all the return-current of the patch-ring layer flows on the reference layer of the IPR. In this case, the dimensions of the patches and rings are designed such that no noise/wave can propagate between the ports in the desired frequency range. However, when the IPR is embedded/integrated, part of the return-current of the patch-ring layer flows on the metal layer above the IPR and part flows on the IPR reference layer (see Fig. 4). Consequently, parallel-plate modes between the metal layer and the patch-ring layer are excited, leading to the propagation of noise. Furthermore, undesired coupling occurs between the metal layer and the IPR reference layer through the slots on the patch-ring layer. This coupling, together with the excited modes leads to the disappearance of the stopband of the embedded IPR, as shown in Fig. 5. For example at about 900 MHz, the presence of the metal layer at a distance (h_1) of 100 µm or 200 µm above the patch-ring layer of the IPR causes approximately 25% of power (noise) generated in port 2 to be coupled to port 1, as compared to approximately 0.01% noise coupling, when the IPR is not embedded/integrated.

4. INVESTIGATING METHODS TO PREVENT THE DISAPPEARANCE OF THE STOPBAND OF AN INTEGRATED IPR

To prevent the disappearance of the stopband of an embedded/integrated IPR, the coupling between the metal layer and IPR reference layer as well as the excitation of the additional parallel-plate

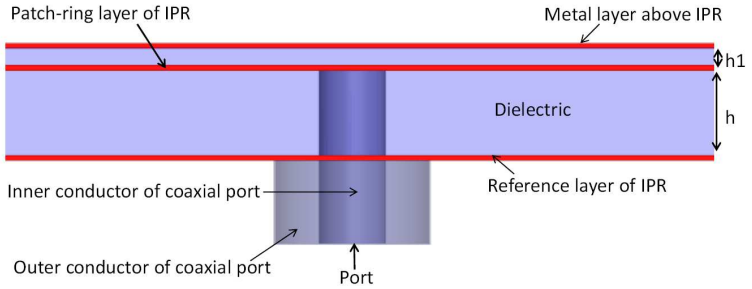

Figure 4: Cross-sectional view of an IPR patch showing the metal layer above the patch-ring layer of the IPR and the port (The dielectric is made transparent and the patch is zoomed for clarity).

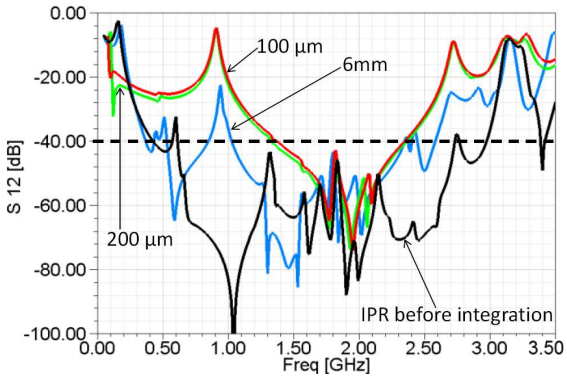

Figure 5: Impact of interactions between an integrated IPR and a metal layer above its patch-ring layer. In this example, the distances of separation (h_1) between the layers are 100 µm, 200 µm and 600 µm.

modes must be eliminated or minimized within the desired frequency range. This may be achieved either by increasing the distance of separation between the IPR and the metal layer above it and/or by interconnecting the metal layer with the reference layer or the patch-ring layer of the IPR using vias.

4.1. Increasing the Distance of Separation (h_1) between the Metal Layer and the IPR

When the distance of separation between the metal layer and patch-ring layer of the IPR is large, the impedance of the capacitive path of the return-current to the metal layer also becomes large. Consequently, most of the return-current of the patch-ring layer flows on the IPR reference layer and the coupling between the metal layer and the IPR reference layer is reduced. To verify the efficiency of this method, the structure was simulated with varying distances of separation between the metal layer and the patch-ring layer of the IPR. The simulation results are also plotted in Fig. 5. However, as can be seen in this figure, the distance of separation must be very large for this technique to be effective. Even at a distance of approximately 6 mm, the original stopband is not restored.

4.2. Interconnecting the Metal Layer and the Patch-ring Layer of the IPR

Figure 6 shows an enlarged cross-sectional view of one of the patches of the IPR, illustrating the position of the vias used for interconnecting both layers. These vias ensure that the return-current of the patch-ring layer flows to the metal layer predominantly as conduction current. Consequently, the excitation of the modes by the displacement current is minimized.

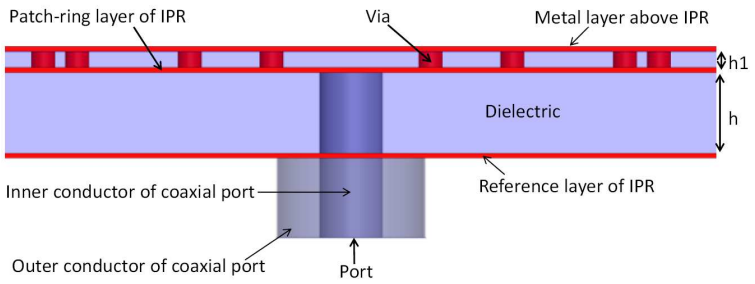

Figure 6: Cross-sectional view of an IPR patch showing the vias used for interconnecting the patch-ring layer of the IPR layer and a metal layer above it (The dielectric is made transparent and the patch is zoomed for clarity).

To investigate the efficiency of this method, the structure was simulated, considering 110 vias interconnecting the patch-ring layer and the metal layer. The results obtained are presented in Fig. 7. This figure shows that although the vias may help to minimize the excitation of modes between the metal layer and the patch-ring layer of the IPR, the coupling between the metal layer and the reference layer of the IPR is not suppressed. Since the ports of the IPR are connected between the patch-ring layer and its reference layer, minimizing the excitation of modes between the metal layer and the patch-ring layer is not enough to restore the stopband of the IPR.

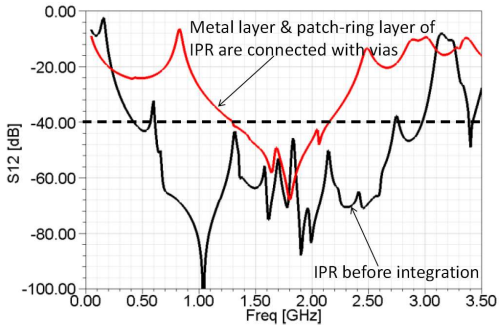

Figure 7: Impact of interconnecting the patch-ring layer and the metal layer above it.

4.3. Interconnecting the Metal Layer and the Reference Layer of the IPR

Coupling between the metal layer and the reference layer of the IPR is greatly minimized if they are interconnected with vias and brought to the same potential. Fig. 8 shows a cross-sectional view of the structure and the position of the vias. Although the vias pass through the patch-ring layer of the IPR, there is no galvanic contact between this layer and the vias. These vias ensure that although the parallel-plate modes between the patch-ring layer and the metal layer are not suppressed, the potential of the IPR reference layer around the ports is restored to its original state, prior to integration. As shown in Fig. 9, the number of vias around each port and and their distance of separation from the port have a huge impact on the restoration of the stopband. By using 4 vias around each of the ports of the IPR, placed at a distance of 125 µm from the port, the −40 dB stopband is restored.

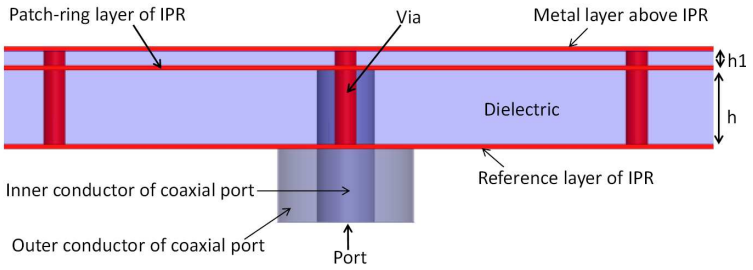

Figure 8: An enlarged view of an IPR patch showing the position of the vias interconnecting the reference layer of the IPR layer and the metal layer.

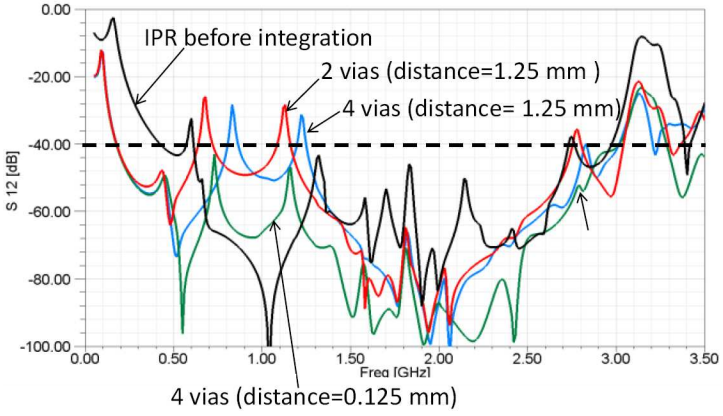

Figure 9: Impact of the number of vias interconnecting the reference layer of the IPR and the metal layer.

5. CONCLUSION AND SUMMARY

In this work, the impact of integrating/embedding IPRs in electronic packages and boards is studied. Electromagnetic interactions between the IPR and a metal layer above it cause the disappearance

of the stopband of the IPR. By interconnecting the metal layer and the reference layer of the IPR using vias around the port where the signals are excited, the stop band of the IPR is restored. It is therefore recommended that if an IPR is to be integrated/embedded in electronic packages and PCBs (i.e., if it is not to be placed on the first layer), then the IPR should be initially designed with consideration of the impact of interactions with a metal layer, so as to prevent the disappearance of the stopband, once it is integrated/embedded.

REFERENCES

1. Ndip, I., S. Guttowski, and H. Reichl, "A novel interconnected patch-ring (IPR) structure for noise isolation," *Proc. IEEE International Symposium on Electromagnetic Compatibility*, 328–333, Austin, TX, USA, Aug. 17–21, 2009.
2. Sievenpiper, D., "High-impedance electromagnetic surfaces," Ph.D. Dissertation, Department of Electrical Engineering, University of California at Los Angeles, Los Angeles, CA, 1999.
3. Joo, S.-H., D.-Y. Kim, and H.-Y. Lee, "A S-bridged inductive electromagnetic bandgap power plane for suppression of ground bounce noise," *IEEE Microwave and Wireless Components Letters*, Vol. 17, No. 10, 709–711, Oct. 2007.
4. Choi, J., V. Govind, and M. Swaminathan, "A novel electromagnetic bandgap (EBG) structure for mixed-signal system applications," *2004 IEEE Conf. on Radio and Wireless*, 243–246, Sep. 19–22, 2004.
5. Shahparnia, S. and O. M. Ramahi, "Miniaturized electromagnetic bandgap structures for ultra-wide band switching noise mitigation in high-speed printed circuit boards and packages," *IEEE 13th Topical Meeting on Elect. Performance of Electronic Packaging*, 211–214, 2004.
6. Rajo-Iglesias, E., L. Inclan-Sanchez, J.-L. Vazquez-Roy, and E. Garcia-Muoz, "Size reduction of mushroom-type EBG surfaces by using edge-located vias," *IEEE Microwave and Wireless Components Letters*, Vol. 17, No. 9, 670–672, Sep. 2007.
7. Kim, K. H. and J. E. Schutt-Aine, "Design of EBG power distribution networks with VHF-band cutoff frequency and small unit cell size for mixed-signal systems," *IEEE Microwave and Wireless Components Letters*, Vol. 17, No. 7, 489–491, Jul. 2007.
8. McKinzie, W. E., "A hybrid electromagnetic bandgap (EBG) power plane with discrete inductors for broadband noise suppression," *IEEE Electrical Performance of Electronic Packaging*, 91–94, Oct. 29–31, 2007.
9. Farzan, S. M. D. and Ramahi, "Effects of discrete bypass capacitors in power/ground planes with EBG structures," *IEEE International Symposium on Electromagnetic Compatibility*, 1–6, Aug. 18–22, 2008.
10. Scogna, A. C., A. Orlandi, and V. Ricchiuti, "Signal and power integrity analysis of differential lines in multilayer printed circuit boards with embedded electromagnetic bandgap structures," *IEEE Transactions on Electromagnetic Compatibility*, Vol. 52, No. 2, 357–364, May 2010.
11. Wu, T.-L., Y.-H. Lin, T.-K. Wang, C.-C. Wang, and S.-T. Chen, "Electromagnetic bandgap power/ground planes for wideband suppression of ground bounce noise and radiated emission in high-speed circuits," *IEEE Transactions on Microwave Theory and Techniques*, Vol. 53, No. 9, 2935–2942, Sep. 2005.
12. Ndip, I., S. Guttowski, and H. Reichl, "Modeling and analysis of a new packaging structure for noise isolation in mixed-signal systems," *42nd International Symposium on Microelectronics (IMAPS 2009)*, San Jose, CA, USA, Nov. 1–5, 2009.

Low Electrical Crosstalk Design Results of Monolithic Integraed Bi-directional Optoelectronic Transceiver and Its Package

Sungil Kim
Future Technology Research Department, Creative Future Research Laboratory
Electronics and Telecommunications Research Institute
138 Gajeong-ro, Yuseong-gu, Daejeon 305700, Korea

Abstract— We analyzed and measured electrical crosstalk phenomena for a 1.25 Gbps monolithic integrated bi-directional op-toelectronic transceiver (M-BiDi), which is a key component to constitute gigabit passive optical networks (PONs) for a fiber-to-the-home (FTTH). A package design result for the 1.25 Gbps M-BiDi based on a transistor outline (TO)-CAN style also presented. These results on this paper can be used for a design and fabrication of the 1.25 Gbps M-BiDi, and expended to a mixed-mode SoC (System-on-a Chip) field.

1. INTRODUCTION

To satisfy demands of high-speed internet services and high-density multimedia services, a fiber-to-the-home (FTTH) technology based on passive optical networks (PONs) has emerged as attractive solutions [1]. The PONs is expected to be economical way for the high-speed internet and high-density multimedia services. Therefore, a standardization sector in the Institute of Electrical and Electronics Engineers (IEEE) and in the International Telecommunication Union-Telecommunication standardization (ITU-T) has presented the standards for 1.25 Gbps PONs [2].

Generally, a hybrid integrated bi-directional optoelectronic transceiver (H-BiDi) for an optical network unit (ONU) of the PONs consists of electrical peripherals and an optical sub-assembly (OSA), which is composed of a laser diode (LD) as a transmitter, a digital photodiode (DPD) as a receiver, and a wavelength division multiplexer (WDM) filter as an optical isolator [3]. To develop a low cost and high performance transceiver, a monolithic integrated bi-directional opto-electronic transceiver (M-BiDi) on an InP substrate have to be needed because of a high productivity by reducing processing steps. According to [4–6], there were many research activities for a 155 Mbps M-BiDi. However, at present, there has been no report on the 1.25 Gbps M-BiDi.

For a design and a fabrication of the 1.25 Gbps M-BiDi, an electrical crosstalk should be considered because the operating frequency goes to gigahertz frequency bands. This is because the LD and the DPD are integrated on the same InP substrate. Since a signal line density of a package for the 1.25 Gbps M-BiDi have be increased, a package should be carefully designed to achieve the low electrical crosstalk levels. Accordingly, we have presented the low electrical crosstalk scheme for the 1.25 Gbps M-BiDi with the InP substrate and its package in this paper.

2. EXPERIMENTAL RESULTS

Figures 1(a) and (b) show a cross-sectional view of an in-line type 1.25 Gbps M-BiDi structure and a plain view of an experimental structure to characterize the electrical crosstalk. The 1.25 Gbps M-BiDi structure consists of the LD with 1.3 μm wavelength, a monitor PD (MPD) as an absorber for a reduction of an optical crosstalk, and the DPD with 1.49 μm wavelength on the same axis. These

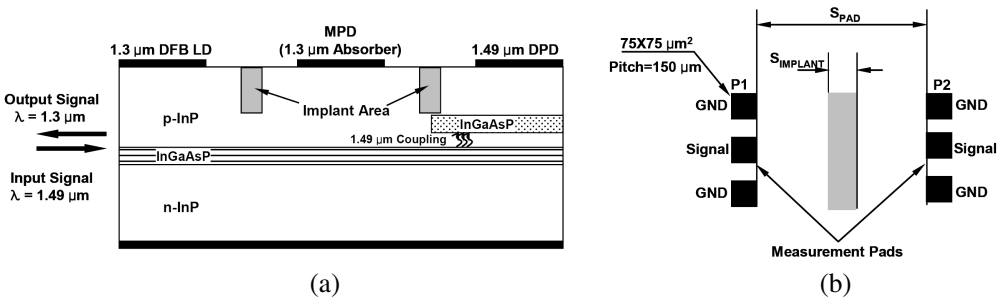

Figure 1: (a) A cross-sectional view of an in-line type 1.25 Gbps M-BiDi structure and (b) a plain view of an experimental structure to characterize electrical crosstalk phenomena.

elements were fabricated on the p-InP/InGaAsP/n-InP substrate. There are several techniques such as a trench, a dielectric filling and an ion-implantation to control the electrical crosstalk on a semiconductor. Due to an advantage of maintaining surface planarity, the latter is chosen for better metal, material step coverage and heat dispersion. We have implanted in fixed area ($S_{IMPLANT}$) between measurement pads (P_1 & P_2) to control the electrical crosstalk. An implant energy, a dose quantity, and an implant area ($S_{IMPLANT}$) have fixed 1.1 MeV, $5 \times 10^{13}\,cm^{-2}$, and 20 μm, respectively. To characterize the implant structure, we have varied a distance of measurement pads (S_{PAD}) from 20 μm to 600 μm, and a DC bias condition from −3 V to 3 V. In order to derive an equivalent circuit of the implant structure, we have measured the electrical crosstalk characteristics using network analyzer (HP8510C) and probe station (Cascade) in frequency rang from 1 GHz to 10 GHz.

Implant characteristics and equivalent circuits with $S_{PAD} = S_{IMPLANT} = 20\,\mu m$ under DC bias

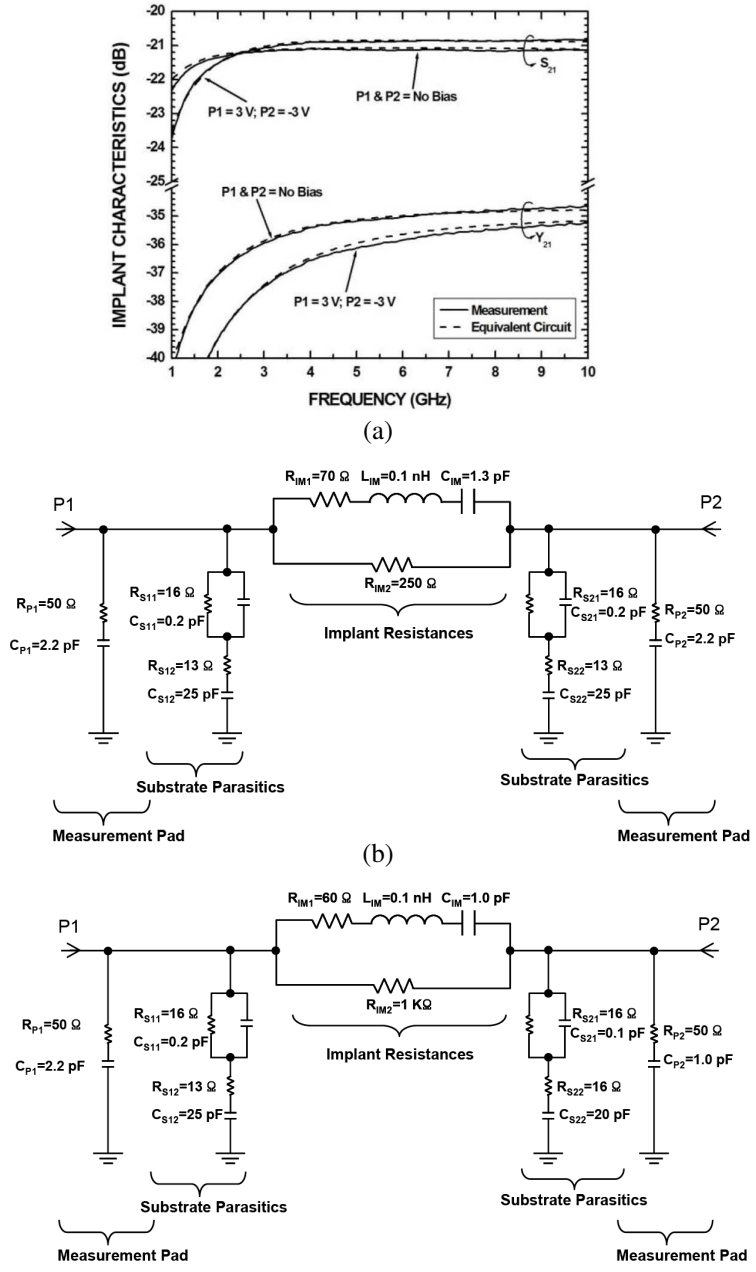

Figure 2: In the case of $S_{PAD} = S_{IMPLANT} = 20\,\mu m$. (a) Implant isolation characteristics, (b) an equivalent circuit with an equi-potential bias condition, and (c) an equivalent circuit with a forward-reverse bias condition.

conditions from −3 V to 3 V are shown in Fig. 2 to characterize the electrical crosstalk phenomena. Y_{21} and S_{21} are a direct and a substrate coupling characteristic of electromagnetics between pads. P_1 & P_2 = No Bias; $P_1 = 3$ V & P_2 = No Bias, and $P_1 = 3$ V & $P_2 = -3$ V are an equi-potential, a forward-suspended, and a forward-reverse operation condition, respectively. The equivalent circuit is composed of implant resistances, a measurement pad, and a substrate parasitic on the InP substrate. The measured data agree with fitted data by the equivalent circuit. The Y_{21} corresponding to P_1 & P_2 = No Bias is worse than the Y_{21} corresponding to $P_1 = 3$ V & $P_2 = -3$ V because of a variation of implant resistances. The S_{21} of $P_1 = 3$ V & $P_2 = -3$ V is worse than that of P_1 & P_2 = No Bias in a frequency range of over 1 GHz because of a variation of a capacitance.

When an implant structure with $S_{PAD} = S_{IMPLANT} = 20\,\mu m$ and $S_{PAD} = 200\,\mu m$ & $S_{IMPLANT} = 20\,\mu m$ applied to the 1.25 Gbps M-BiDi, the electrical crosstalk characteristics is shown by Fig. 3. Since the electrical crosstalk between the LD and the DPD has been less than −86 dB in the case of $S_{PAD} = 200\,\mu m$ & $S_{IMPLANT} = 20\,\mu m$, this implant isolation technique can be used for the 1.25 Gbps M-BiDi [2].

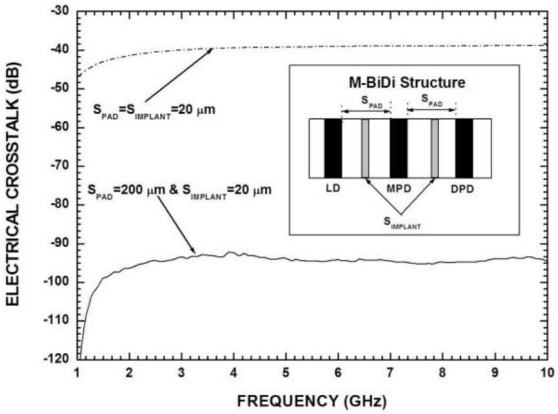

Figure 3: The electrical crosstalk characteristics of the in-line type 1.25 Gbps M-BiDi.

Figure 4 shows the electrical crosstalk calculation and simulation results of a transistor outline (TO)-CAN package for the 1.25 Gbps M-BiDi. Generally, the DPD output of the 1.25 Gbps M-BiDi goes to a transimpedance amplifier (TIA) with differential ouputs. Accordingly, the electrical crosstalk between TIA pins and a LD pin of the TO-CAN package is calculated. Based on our calculated results shown in Fig. 4(a), the electrical crosstalk between the LD pin and the TIA pins of the TO-CAN should be less than −67 dB with a design margin of 10 dB. Using high frequency structure simulator (HFSS) as the finite element method (FEM), the TO-CAN package with 11 pin is simulated and designed as shown in Fig. 4(b). The TO-CAN package size is $4 \times 5\,mm^2$. 'Cx_TOCAN_LD Signal-TOCAN TIA Signal' is the electrical crosstalk between between the LD pin and the TIA pins; 'Cx_TOCAN_LD Signal-PD Signal' is the electrical crosstalk between the LD pin and the DPD pad of the 1.25 Gbps M-BiDi; 'Cx_LD Signal-PD Signal' is the electrical crosstalk

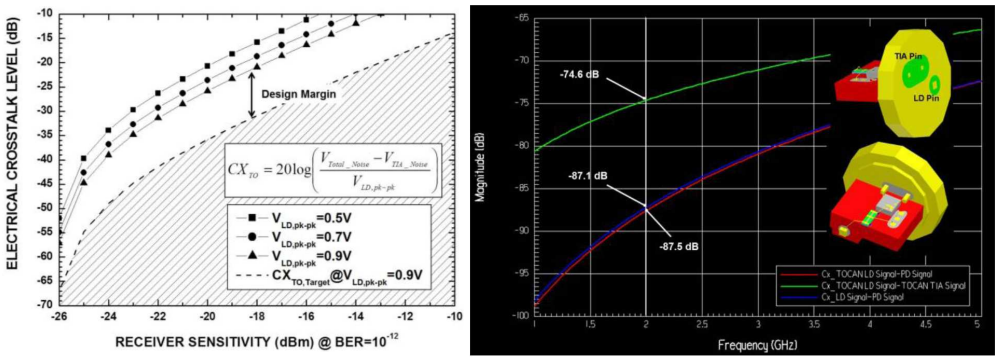

(a) (b)

Figure 4: The electrical crosstalk (a) calculation results and (b) simulation results of the TO-CAN package for the 1.25 Gbps M-BiDi.

between the LD pad and the DPD pad on the 1.25 Gbps M-BiDi. From the simulation results, we have found that the electrical crosstalk characteristics of the TO-CAN package and the 1.25 Gbps M-BiDi OSA is suitable to operate up to 1.25 Gbps.

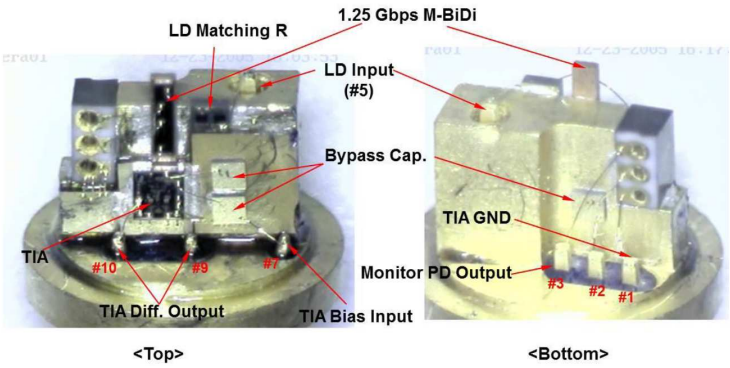

Figure 5: A photograph of the TO-CAN packaged 1.25 Gbps M-BiDi module.

A photograph of the TO-CAN packaged 1.25 Gbps M-BiDi module is shown in Fig. 5. It consists of the 1.25 Gbps M-BiDi, the TIA as a preamplifier, and some passive components such as an impedance matching resistor for the LD on the 1.25 Gbps M-BiDi and bypass capacitors for the TIA. In this figure, #1, #3, #5, #7, #9 and #10 are a TIA ground pin, a monitor PD output pin, a LD input pin to modulate the optical output of the LD using a LD driver, which is installed outside of the TO-CAN, a bias pin for the TIA, and differential pair output pin of the TIA. Pins such as #4, #6, #8, and #11 are used to supply electrical references (ground potential) for increasing operation stability of the TO-CAN packaged 1.25 Gbps M-BiDi.

3. CONCLUSION

In this paper, using an InP substrate, we have studied the implant characteristics to reduce the electrical crosstalk of a in-line type 1.25 Gbps monolithic integrated bi-directional optoelectronic transceiver (M-BiDi). Also, we have found out the equivalent circuits of an implant structure for a design and a fabrication of the 1.25 Gbps M-BiDi. From the measured results, the electrical crosstalk of the 1.25 Gbps M-BiDi is less than −86 dB when an implant structure is installed between a laser diode, a monitor photodiode, and a digital photodiode. Electrical design results of a transistor outline (TO)-CAN type package was presented and a assemble result was also presented. From the calculation and design results of the TO-CAN package, the electrical crosstalk of the TO-CAN package is less than −67 dB. Accodingly, a TO-CAN packaged 1.25 Gbps M-BiDi can be operate up to 1.25 Gbps. Consequently, the electrical crosstalk reduction scheme and design results in this paper can be helpful for a mixed-mode system-on-a chip (SoC), which integrates together with an optical chip and an analog/digital operated electrical chip.

REFERENCES

1. Miki, T., "Fiber-optic subscriber networks and system development," *IEICE Trans.,* Vol. E74, No. 1, 93–100, Jan. 1991.
2. Kim, S.-I., et al., "A low-crosstalk design of 1.25 Gbps optical triplexer module for FTTH systems," *ETRI Journal,* Vol. 28, No. 1, 9–16, Feb. 2006.
3. kurosaki, T., et al., "1.3/1.55 µm full-duplex WDM optical transceiver modules for ATM-PON (PDS) systems using PLC-hybrid-integration and CMOS-IC technologies," *IEICE Trans. Electron.,* Vol. E-82-C, No. 8, 1465–1474, Aug. 1999.
4. Nakajima, H., et al., "1.3 µm/1.55 µm in-line transceiver assembly with −27 dBm full-duplex sensitivity," *Electronics Letters*, Vol. 34, No. 3, 303–304, Feb. 1998.
5. Mallecot, F., et al., "−29.5 dBm sensitivity value, in full-duplex operation at 155 Mbit/s, of an in-line transmit-receive-device," *ECOC'98*, 375–376, Mardrid, Spain, Sep. 1998.
6. Hamacher, M., et al., "Monolithic integrated of lasers, photodiodes, waveguides and spot size converters on GaInAsP/InP for photonic ICs applications," *Conference on Indium Phosphide and Related Materials*, 21–24, 2000.

Recent Advances in 3D-IC EMC Measurement Methods

J. Wu[1], **E. Sicard**[2], **and J. Li**[1]

[1]College of Electronic Science and Engineering
National University of Defense Technology, Changsha, Hunan 410073, China
[2]National Institute of Applied Sciences, Toulouse 31077, France

Abstract— For 3D-ICs, the multiple active dies are stacked on top of each other which bring more EMC problems like vertical die to die EMI coupling, crosstalk in bonding or TSVs, increasing amount of radiation, worse thermal ageing effects and so on. To characterize the 3D-IC EMC issues, the EMC test is a big challenge as some 2D-IC measurement methods may no longer suitable for 3D-ICs.

1. INTRODUCTION

The main challenges of EMC tests can be classified as pertaining to (1) test flows, (2) test contents, and (3) test access. The conventional single-die chip test flow includes a wafer test and a final package test. And the EMC test can be implemented after fabrication. But for 3D-IC EMC test flow, it is necessary to test IC EMC pre-bonding especially for aggressive and sensitive circuits. The proposed test flow for 3D-IC EMC issues is illustrated in Fig. 1 where the EMC test is emerged in pre-bond tests and post-bond tests [1].

Due to the 3D-IC defects and the defects-induced circuit failures, people are concerning a lot on TSV defects test [2]. In literature [3], Chen tested the TSV defects like break (capacitance reduced) or impurity (resistive short) using sense amplification. In Hung's study of blind TSV [4], he found the short circuit by leakage current test and defined the thickness of the isolation layer with impedance simulation and measurement. To avoid the mixture of the IC defects and EMC issues, the primary test content of interconnect and then EM radiation and immunity measurements.

There are external and internal accesses for 3D-IC EMC test. The external access can use probes [5], nano contactor [6] or non-contact testing [7]. The internal access is design-for-test (DfT) whose architecture [8] is based on IEEE Std 1500 [9] or IEEE Std 1149.1 [10].

The International Electro-technical Commission (IEC) has released two major standards for IC EMC measurements, one for IC radiated and conducted emissions (IEC 61967) [11] and another for IC susceptibility (IEC 62132) [12]. One new project concerning measurement methods to characterize IC transient susceptibility (IEC 62215) [13] is also conducted. The IEC IC EMC measurement methods reference lists and status in 2012 is presented in [14]. For the standard EMC test board, 2D/3D IC does not make difference. Then, the present international standard methods are discussed for testing 3D-IC EMC issues. Finally, some non-standard methods are proposed according to the IC vertical stacked structural features.

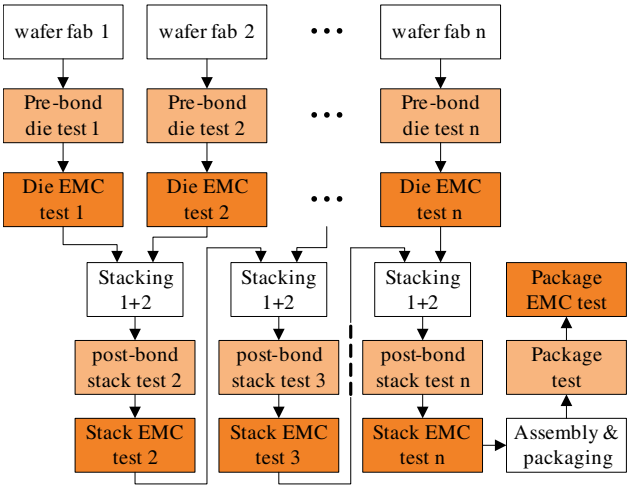

Figure 1: Potential test moments for a 3D-IC combined with EMC.

2. IC EMC TEST STANDARD METHODS

2.1. EMC Test Board — 2D/3D Does Not Make Difference

The test PCB board to be used depends on the specific measurement method. The test PCB should be designed in accordance with these general specifications and the additional specifications as required for the individual measurement methods. Such a board is necessary to compare the EMC performance of various ICs from different manufacturers. Constraints are given for those parameters influencing the EMC aspects [11–13]. For 2D or 3D ICs, there is no difference in the test board. So we can follow the same design guidelines as defined in the "General Conditions and Definitions" of IEC 61967, IEC 62132 and IEC 62215.

2.2. Standard IC Emission Measurement Methods — IEC 61967

IEC 61967 is a series of sustaining developing standards or proposals methods for IC emission measurement as listed in Table 1. With the development of ICs and electromagnetic environment, the methods have extended from 1 GHz to 18 GHz (Mode Stirred Chamber and GTEM methods). But for 3D-IC, some methods may not effective compared with 2D-IC: one reason is 3D-IC sub-circuits work in high frequency which exceeds the defined frequency range; another reason is not accessible or correct locating the noise source after the dies stacking in vertical.

For TEM/GTEM cell and IC-Stripline, the upper IC may play the role of shielding and is closer to septum (45 mm for TEM and 6.7 mm for Stripline). In IEC 61967-3/6 standards, combining laser and high-precision NFS may lead to precise 3D investigations. But lower die stack is shielded by upper dies [15]. To apply 1/150 Ω method in 3D-IC EMC test, each die would have a built-in 1 Ω probing for IC emission characterization.

Table 1: IEC measurement methods for IC emission.

Reference	Description	Status
IEC 61967-1	General Conditions and Definitions	Standard
IEC 61967-2	TEM cell and wideband TEM (GTEM)	Standard
IEC 61967-3	Surface scan	Standard
IEC 61967-4	1 Ω/150 Ω direct coupling	Standard
IEC 61967-5	Workbench Faraday Cage method (WBFC)	Standard
IEC 61967-6	Magnetic probe	Standard
IEC 61967-7	Mode Stirred Chamber	Proposal
IEC 61967-8	IC Stripline	Proposal

2.3. Standards IC Susceptibility Measurements Methods — IEC 62132

IEC 62132 is also a series of developing standards or proposals methods for IC susceptibility measurement as listed in Table 2. The TEM/GTEM Cell, WBFC, Mode Stirred Chamber and IC Stripline methods are proposed for both emission and susceptibility characterization. The most mature susceptibility measurement methods are the WBFC and DPI approaches. But for 3D-IC, the limitations mentioned above are also existed.

We can update some methods for 3D-IC tests. Take DPI method as example, each die would have built-in injection probes for IC immunity characterization.

2.4. Standards IC Immunity to Transients Measurements — IEC 62215

Electrical fast transients (EFTs) have become a very common type of interference generated in modern electronic applications [16]. The purpose of the new standard and proposal IEC 62215 [13] is to specify methods for characterizing the impulse immunity of ICs. The methods intend to cover transient immunity to impulses, electrostatic discharge (ESD), EFTs, and electrical overstress (EOS). This standard reuses some test methods defined in the standards IEC 61000-4-4 [17] and ISO 7637-2 [18].

3. IC EMC NON-STANDARD METHODS

While applying in 3D-IC EMC tests, the existing or publishing methods for IC tests have some challenge as below:

Table 2: IEC Measurement methods for IC susceptibility.

Reference	Description	Status
IEC 62132-1	General Conditions and Definitions	Standard
IEC 62132-2	TEM cell and wideband TEM (GTEM)	Standard
IEC 62132-3	Bulk Current Injection (BCI)	Standard
IEC 62132-4	Direct RF Power Injection (DPI)	Standard
IEC 62132-5	Workbench Faraday Cage method (WBFC)	Standard
IEC 62132-6	Local Injection Horn Antenna (LIHA)	Proposal
IEC 62132-7	Mode Stirred Chamber	Proposal
IEC 62132-8	IC Stripline	Standard
IEC 62132-9	Near Field scan immunity (NFSI)	Proposal

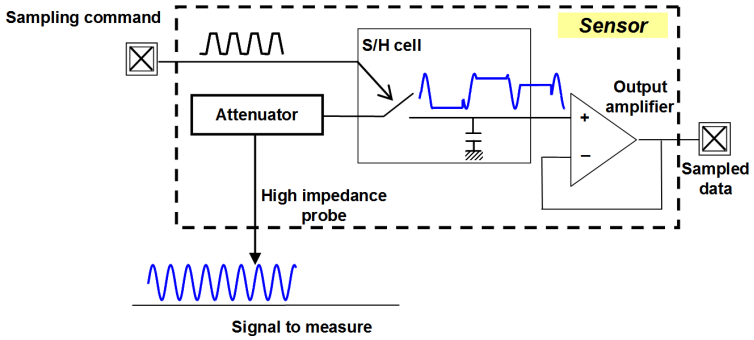

Figure 2: Architecture of the on-chip sensor.

- Micro-bumps are typically too small ($\leq$ 25 µm diameter), too dense ($\leq$ 40 µm pitch), too numerous, and too fragile to be probed with conventional probe technology [19]. Cantilever probes go down to 20 µm pitch, but do not support arbitrary array configurations. The minimum pitch of conventional vertical probes is 50 µm, insufficient for fine-pitch micro-bumps.
- The DfT architecture [20] for 3D die stacks is able to perform interconnects testing of micro-bumps and interposer connections. But its low bandwidth restricts the application on EMC tests.

So some non-standard methods should be proposed for 3D-IC EMC testing. The methods such as on-chip sampling test, contactless probing test, skate probe, combined IC EMC standard methods are discussed below.

3.1. On-chip Sampling Test

The acquisition is based on an on-chip sample and hold circuit that directly probes the voltage within IC interconnects. An associated post-processing ensures a reconstruction of the timing waveform. The detailed principle of this on-chip sensor is given in [21]. Sensor measurements ensure a better characterization of actual coupling of interferences within the circuit and a diagnosis of failure origins. With the on-chip sensor, we can use the advantage of inner sampling and enhance to reveal the actual susceptibility level in the chip level [22].

The main advantages of this sensor are its small surface, its large bandwidth (up to 2 GHz), its high linearity, and robustness to electrical stress, at the price of a simple design [23].

3.2. Contactless Probing Test

In direct testing, the requirements of a socket solution for TSV testing are: durability, scalability, minimum damage, path resistance, low capacitance and inductance. TSV tips are too fragile to be probed and conventional probe cards do not support variable contact-point locations [6]. The probe industry is working to make a significant improvement in scaling down the probe pitch and reducing the probe mark damage.

Wireless testing aims to replace probe needles with contactless circuits that link the wafer and ATE. Efforts are also spent on contact-less testing [24, 25], which by definition does not cause

any probe damage. The potential technologies for wireless testing include radio-frequency (RF), near-field, and optical communication.

3.3. Skate Probe Testing

In 3D-ICs, there are serious vertical noise coupling between logic ICs and RF/analog ICs [26, 27]. We can develop some skate probes as shown in Fig. 3 to locate and simulate the coupling noise.

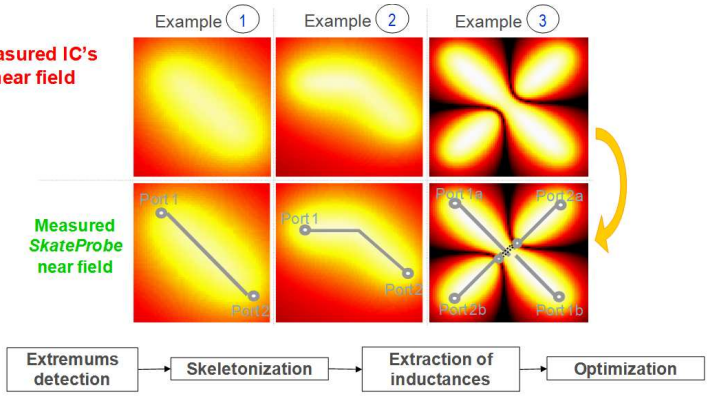

Figure 3: Stripline extraction examples and comparison between measured and emulated near-field scan [29].

In literature [28], the paper details two approaches for the evaluation of the near field radiated coupling between two nearby ICs and their EMC. The first method is based on an empirical comparison between the radiated emission level of the aggressor and the radiated susceptibility level of the victim. The second approach is a predictive method which mixes electrical and 3D electromagnetic simulations.

3.4. Combined Standard Methods

As listed in Tables 1–3, there are a lot of measurement methods for IC emission, susceptibility and immunity to transients. But the separated methods have limitations when applying in 3D-IC EMC test. One solution is developing new methods for 3D-ICs. Another more convenient solution is combining the existing standard methods, such as: DPI with GTEM, BCI with IC Stripline [29], LIHA with $1\,\Omega/150\,\Omega$ and so on.

Table 3: IEC measurement methods for IC immunity to transients.

Reference	Description	Status
IEC 62215-1	General Conditions and Definitions	Proposal
IEC 62215-2	SynchronousTransient Injection	Standard
IEC 62215-3	Non-SynchronousTransient Injection	Project
IEC 62215-4	Surge	Project
IEC 62215-5	Supply dips	Project
IEC 62215-6	Near Field scan immunity method	Project

In paper [30], two combined EMC standard measurement methods (direct power injection and near-field scan) were used to characterize the propagation of internal and external noise and disturbances inside an integrated circuit. It reported results based on both measurement methods, deals with some comparisons between magnetic fields scans at different frequencies with and without power injection to analyze the protection strategies integrated in the different cores.

4. CONCLUSIONS

This paper has presented a review on recent advances in 3D-IC EMC measurement methods. Some of the current IEC EMC test standards on IC emission, susceptibility and immunity to transients can be updated for 3D-ICs such as each die would have a built-in $1\,\Omega$ probing for IC emission characterization and have built-in injection probes for IC immunity characterization. But not all of the standard methods are compatible for 3D-ICs. Some non-standard methods are proposed for

3D-IC EMC testing. The methods such as on-chip sampling test, contactless probing test, skate probe, combined IC EMC standard methods are discussed. The on-chip sensor techniques enhance the extraction of die voltage especially in high frequency. Contactless probing test breaks through the existing probes limitation for 3D-ICs. Skate probe testing evaluates the interference in 3D-ICs complex multi-die design. Combined standard methods propose the extending of mature EMC test methods for 3D-ICs applications. The future study will focus on the implement of the above methods and developing new techniques for 3D-ICs EMC measurement.

REFERENCES

1. Marinissen, E. J., "Challenges and emerging solutions in testing TSV-based 2 1 over 2D- and 3D-stacked ICs," *Design, Automation & Test in Europe Conference & Exhibition (DATE)*, 1277–1282, Mar. 12–16, 2012.
2. Chakrabarty, K., S. Deutsch, H. Thapliyal, and F. Ye, "TSV defects and TSV-induced circuit failures: The third dimension in test and design-for-test," *2012 IEEE International Reliability Physics Symposium (IRPS)*, 5F.1.1–5F.1.12, Apr. 15–19, 2012.
3. Chen, P.-Y., C.-W. Wu, and D.-M. Kwai, "On-chip TSV testing for 3D IC before bonding using sense amplification," *Asian Test Symposium, ATS'09*, 450–455, Nov. 23–26, 2009.
4. Hung, J.-F., J. H. Lau, P.-S. Chen, S.-H. Wu, S.-J. Lai, M.-L. Li, S.-S. Sheu, P.-J. Tzeng, Z.-H. Lin, T.-K. Ku, W.-C. Lo, and M.-J. Kao, "Electrical testing of blind through-silicon via (TSV) for 3D IC integration," *2012 IEEE 62nd Electronic Components and Technology Conference (ECTC)*, 564–570, May 29, 2012–Jun. 1, 2012.
5. Thärigen, T., et al., "Wafer probing on fine-pitch micro-bumps for 2.5D- and 3DSICs," *Semicon European Manufacturing Test Conference (EMTC)*, Oct. 2011.
6. Yaglioglu, O. and B. Eldridge, "Direct connection and testing of TSV and microbump devices using NanoPierce^{TM} contactor for 3D-IC integration," *2012 IEEE 30th VLSI Test Symposium (VTS)*, 96–101, Apr. 23–25, 2012.
7. Scandiuzzo, M., S. Cani, L. Perugini, S. Spolzino, R. Canegallo, L. Perilli, R. Cardu, E. Franchi, C. Gozzi, and F. Maggioni, "Input/output pad for direct contact and contactless testing," *16th IEEE European Test Symposium (ETS)*, 135–140, May 23–27, 2011.
8. Jan Marinissen, E., et al., "A DfT architecture for 3D-SICs based on a standardizable die wrapper," *Journal of Electronic Testing: Theory and Applications*, Vol. 28, No. 1, Feb. 2012.
9. JTAG-1149.4 Explorer Mixed-signal Boundary-scan Evaluation System, www.jtag.com.
10. IEEE P1500 Web Site, http://grouper.ieee.org/groups/1500.
11. "Integrated circuits, measurement of electromagnetic emission, 150 kHz–1 GHz: General conditions and definitions — Part 1, international electrotechnical commission standard IEC61967-1," Mar. 2002.
12. "Integrated circuits, measurement of electromagnetic immunity, 150 kHz–1 GHz: General conditions and definitions — Part 1, international electrotechnical commission standard IEC62132-1," 2007.
13. "Integrated circuits — Measurement of impulse immunity — Part 2: Synchronous transient injection method, international electrotechnical commission standard IEC/TS 62215-2," Ed. 1.0, Sep. 2007.
14. Marot, C. and E. Sicard, "EMC standards at IC level — Status of IEC and technical goals of the SEISME project," *2012 Asia-Pacific Symposium on Electromagnetic Compatibility (APEMC)*, 9–12, May 21–24, 2012.
15. Baudry, D., Ph. D. Report, ESIGELEC, University Rouen, 2005.
16. Ramdani, M., E. Sicard, A. Boyer, S. Ben Dhia, J. J. Whalen, T. H. Hubing, M. Coenen, and O. Wada, "The electromagnetic compatibility of integrated circuits — Past, present, and future," *IEEE Transactions on Electromagnetic Compatibility*, Vol. 51, No. 1 78–100, Feb. 2009.
17. "Electromagnetic compatibility (EMC) — Part 4-4: Testing and measurement techniques — Electrical fast transient/burst immunity test, international electrotechnical commission standard IEC 61000-4-4," Jul. 2004.
18. "Road Vehicle — Electrical disturbances from conduction and coupling — Part 2: Electrical transient conduction along supply lines only, international organisation for standardization ISO 7637-2," 2004.
19. Mann, W. R., et al., "The leading edge of production wafer probe test technology," *Proceedings IEEE International Test Conference (ITC)*, 1168–1195, Oct. 2004.

20. Noia, B., "Testing and design-for-testability techniques for 3D integrated circuits," *20th Asian Test Symposium (ATS)*, 2011.
21. Vrignon, B. and S. Ben Dhia, "On-chip sampling sensors for high frequency signals measurement: Evolution and improvements," *Proceedings of the Fifth IEEE International Caracas Conference on Devices, Circuits and Systems*, Vol. 1, 270–275, Nov. 3–5, 2004.
22. Wu, J. F., E. Sicard, A. Boyer, S. Ben Dhia, J. C. Li, and R. J. Shen, "Enhancing accuracy of low-dropout regulator susceptibility extraction with on-chip sensors," *Electronics Letters*, Vol. 48, No. 11, 649–650, May 24, 2012.
23. Dhia, S., A. Boyer, B. Vrignon, M. Deobarro, and T. V. Dinh, "On-chip noise sensor for integrated circuit susceptibility investigations," *IEEE Transactions on Instrumentation and Measurement*, Vol. 61, No. 3, 696–707, Mar. 2012.
24. Moore, B., et al., "High throughput non-contact SIP testing," *Proceedings IEEE International Test Conference (ITC)*, Paper 12.3, Oct. 2007.
25. Jan Marinissen, E., et al. "Contactless testing: Possibility or pipe-dream?" *Proceedings Design, Automation, and Test in Europe (DATE)*, 676–671, Apr. 2009.
26. Koo, K., S. Lee, and J. Kim, "Vertical noise coupling on wideband low noise amplifier from on-chip switching-mode DC-DC converter in 3D-IC," *2011 8th Workshop on Electromagnetic Compatibility of Integrated Circuits (EMC Compo)*, 35–40, Nov. 6–9, 2011.
27. Lee, S., K. Koo, and J. Kim, "Analysis of die-to-die vertical crosstalk between clock-tree and voltage controlled oscillator in 3-D IC," *2011 IEEE International Symposium on Electromagnetic Compatibility (EMC)*, 28–32, Aug. 14–19, 2011.
28. Akue Boulingui, S., C. Dupoux, S. Baffreau, E. Sicard, N. Bouvier, and B. Vrignon, "An innovative methodology for evaluating multi-chip EMC in advanced 3G mobile platforms," *IEEE International Symposium on Electromagnetic Compatibility, EMC 2009*, 145–150, Aug. 17–21, 2009.
29. Klotz, F., "IC-Stripline, new method for emission and immunity," *EMC Compo.*, 2009.
30. Alaeldine, A., L. Bouchelouk, R. Perdriau, and M. Ramdani, "Analysis of the propagation of electromagnetic disturbances inside integrated circuits using direct power injection and near-field scanning," *IEEE International Symposium on Electromagnetic Compatibility, EMC 2009*, 151–155, Aug. 17–21, 2009.

All Optical Frequency Conversion Utilizing Nonlinear Dynamics of Semiconductor Lasers Subject to Optical Square Wave Injection

Shao-Wei Peng and Yu-Shan Juan
Department and Institute of Photonics Engineering
Yuan Ze University, 135 Yuan-Tung Road, Taoyuan County 32003, Taiwan

Abstract— Recently, nonlinear dynamics of the optically dynamical injection systems are of interested. Potential applications in microwave photonics such as broadband microwave frequency comb generation are demonstrated through an optically pulse-injected semiconductor laser. To the best of our knowledge, most studies focused on the nonlinear dynamics of the traditional continuous wave injection and dynamical pulse and sine wave injection. Nonlinear characteristics of the semiconductor laser subject to optical square wave injection are investigated the first time. In this work, nonlinear dynamics and characteristics of a semiconductor laser subject to optical square wave injection are investigated numerically. The periodic optical square waveforms for injection are generated from a laser (master laser) by using an external EO modulator on a laser (master laser). Under proper operational conditions, namely the repetition frequency and injection strength of the injected light, harmonic and sub-harmonic frequency-locked states with different locking ratios are observed at the output of the injected laser (slave laser). By examination of the electrical power spectra and time series generated from both the injection waveform and injected laser output, all optical frequency conversion are observed. The peaks of the injected laser output are induced by the injected square wave with repetition frequency of 1 GHz. The existence and enhancement of high-order harmonics lays on the foundation of frequency conversion. When applying a stronger injection level to the semiconductor laser, the conversion ratio can be continuously tuned to a higher value. As the result, the conversion ratio of 23 times is achieved due to the effect of bandwidth broadening in optical injection system. The proposed scheme possesses the advantages of low cost, compact, less system complexity, and more flexibility in frequency tuning which also shows the potential of high frequency microwave signal generation.

1. INTRODUCTION

Nonlinear dynamics of semiconductor lasers and its applications have been attracted much attention in the past decade. Various dynamical behaviors of semiconductor lasers subjected to optical injection [1], optical feedback [2], and optoelectronic feedback [3] have been observed and discovered. Different dynamical states found have gained considerable theoretical and practical attention because of their fundamental physics [4] and potential applications such as chaotic radar[5], chaotic lidar [6, 7], and chaotic comunications [8]. For optically dynamical injection, such as pulse or sine wave injection, potential applications in microwave photonics such as broadband microwave frequency comb generation are demonstrated through an optically pulse-injected semiconductor laser [9, 10]. To the best of our knowledge, most studies focused on the nonlinear dynamics of the traditional continuous wave injection and dynamical pulse and sine wave injection. Nonlinear characteristics of the semiconductor laser subject to optical square wave injection are investigated the first time. In this work, nonlinear dynamics and characteristics of a semiconductor laser subject to optical square wave injection are investigated numerically. The periodic optical square waveforms for injection are generated from a laser (master laser) by using an external EO modulator on a laser (master laser). Under proper operational conditions, namely the repetition frequency and injection strength of the injected light, harmonic and sub-harmonic frequency-locked states with different locking ratios are observed at the output of the injected laser. By examination of the electrical power spectra and time series generated from both the injection waveform and injected laser output, all optical frequency conversion are observed. Moreover, the numerical calculated mapping of the dynamical states of semiconductor laser subject to the square wave injection are discovered.

2. SCHEMATIC SETUP

The periodic optical square waveforms for injection are generated from the master laser by using an external EO modulator on it. The schematic setup of the semiconductor laser under repetitive optical square wave injection is shown in Fig. 1. The nonlinear behavior of the semiconductor

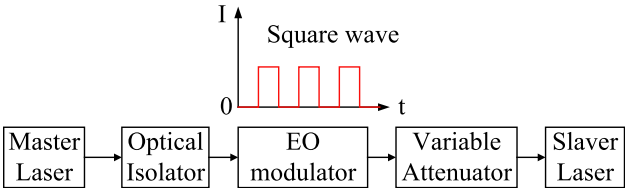

Figure 1: Schematic setup of a semiconductor laser under repetitive optical square wave injection.

laser with repetitive optical square wave injection can be derived by normalizing three coupled rate equations [11]:

$$\frac{da}{dt} = \frac{1}{2}\left[\frac{\gamma_c\gamma_n}{\gamma_s\tilde{J}}\tilde{n} - \gamma_p(2a+a^2)\right](1+a) + \xi_i(t)\gamma_c\cos(\Omega t+\phi) \tag{1}$$

$$\frac{d\phi}{dt} = -\frac{b}{2}\left[\frac{\gamma_c\gamma_n}{\gamma_s\tilde{J}}\tilde{n} - \gamma_p(2a+a^2)\right] - \frac{\xi_i(t)\gamma c}{1+a}\sin(\Omega t+\phi) \tag{2}$$

$$\frac{d\tilde{n}}{dt} = -\gamma_s\tilde{n} - \gamma_n(1+a)^2\tilde{n} - \gamma_s\tilde{J}(2a+a^2) + \frac{\gamma_s\gamma_p}{\gamma c}\tilde{J}(2a+a^2)(1+a)^2 \tag{3}$$

where a is the normalized optical field, ϕ is the optical phase difference, and $\tilde{n}$ is the normalized carrier density. $\tilde{J}$ is the normalized dimensionless injection current parameter, Ω is the detuning frequency, γ_c is the cavity decay rate, γ_n is the differential carrier relaxation rate, γ_p is the nonlinear carrier relaxation rate, b is the linewidth enhancement factor, γ_s is the spontaneous carrier relaxation rate, and n is the effective refractive index. The dimensionless injection parameter $\xi_i(t)$ is the normalized strength of the injection field received by the injected laser. The injection profile of each Square wave is described as:

$$\xi_i(t) = \begin{cases} \xi_{sq}, & \text{if} t \le \tau \\ 0, & \text{otherwise} \end{cases}$$

Here ξ_{sq} is the normalized injection strength of the square wave. τ is the duration that the function are active, and T is the period of function. The relaxation resonance frequency of the laser used in this simulation is $f_r = 10.25\,\text{GHz}$. Under proper operational conditions, including the normalized injection strength of square wave ξ_{sq}, repetition frequency f_{rep} of the repetitive square waves, and the detuning frequency Ω between the master laser and the slaver laser, various dynamical states including periodic oscillation, frequency-locked pulsation, and chaotic oscillation states can be found.

3. RESULTS

Figure 2(a) shows the time series of the injecting square wave (red curve) and the injected laser output (black curve), respectively. The corresponding power spectra are observed as shown in Fig. 2(b). A can be seen in Fig. 2(b), the frequency locked state generated by optically square wave injection with locking ratio of 18 is obtained. The peaks of the injected laser output are induced by the injected square wave with repetition frequency $f_{rep} = 1.0\,\text{GHz}$. The existence and enhancement of high-order harmonics lays the fundation of frequency conversion. As results, the frequency multiplication of 18 times is obtained by comparing in both time and frequency domains when operating the operational parameters of the detuning frequency $f_d = 1.5\,\text{GHz}$, the repetition rate $f_{rep} = 1.0\,\text{GHz}$, and the injection strength $\xi_{sq} = 0.112$. The phenomenon of frequency multiplication cause by the existence of P1 state when applying the same operational parameter in cw optical injection system, which induced the oscillation frequency increase with the higher injected source level in time series. Therefore, when applying a stronger injection level to the semiconductor laser, the conversion ratio can be continuously tuned to a higher value.

On the other hand, based on the observation of period-doubling behavior [11] typically seen in a cw optical injection case, the similar characteristics are also observed in dynamical square wave injection case. When applying the injecting square wave under $\xi_{sq} = 0.067$ and $f_d = 2.3\,\text{GHz}$, frequency division of 250 MHz is observed as the result of comparison in both time and frequency domains. As shown in Fig. 3(a), the main peak exists in every 4 period of square wave input, and

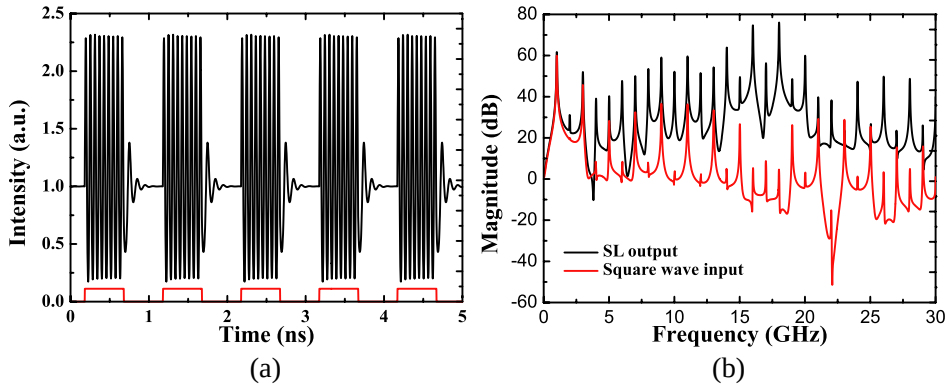

Figure 2: The time series and power spectra with injection strength of square wave $\xi_{sq} = 0.112$. The frequency multiplication of 18 times is observed.

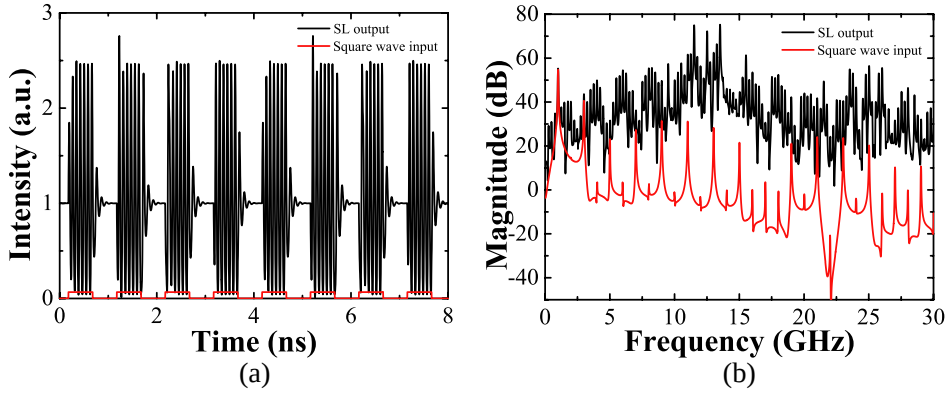

Figure 3: With injection level $\xi_{sq} = 0.067$, the frequency division of 250 MHz is discovered. (a) the time series and (b) the corresponding power spectrum are shown.

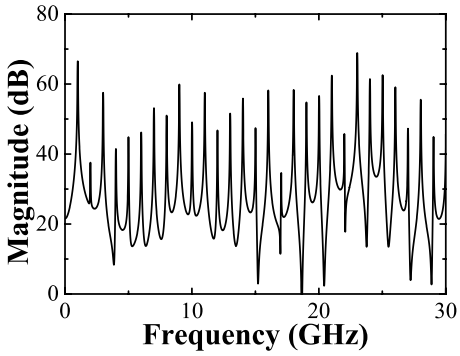

Figure 4: The bandwidth is further enhanced to 23 times under the conditions of injection strength $\xi_{sq} = 0.2$ and detuning frequency $f_d = 1.5$ GHz.

the corresponding power spectra are shown in Fig. 3(b). By comparing the input of square wave and the output of the injected laser, the phenomenon of frequency division of 4 times is obtained.

The interference of optical frequency at free running state and the shifted frequency results in the expansion of the bandwidth. In high optical injected level, the increase carrier density in the slave laser induce the shift of oscillation frequency [12]. Fig. 4 shows the power spectrum of injected laser output when applying the injection strength $\xi_{sq} = 0.2$. The conversion ratio is further increased to 23 times due to the effect of bandwidth broadening through optical injection with stronger injection strength.

To investigate the dynamics of the square wave injection system, it is important to know how the state of the laser transfer with the operational parameter, namely the injection strength and the detuning frequency. In order to understanding the change of the state preliminary, the repetition

rate is fixed at 1 GHz in this work. In Fig. 5, a numerically calculated mapping of the dynamical state of semiconductor laser with square wave injection is shown. As can be seen, we can easily operate the laser in the desired region by controlling the parameter. In this system, the complexity of the system increasing with the detuning frequency generally. The photonic microwave generation can be achieved by varying the injection strength and detuning frequency as in P1 state [13] with out high frequency feedback electronics. The chaotic state with broad bandwidths can also be generated for potential applications in secured communications.

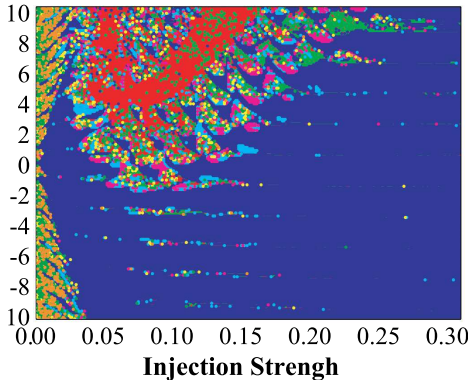

Figure 5: Mapping of numerically obtained dynamical region in the semiconductor laser subject to square wave injection system. The color of blue, green, yellow, and red represent P1, P2, P4, and chaotic states, respectively.

4. CONCLUSION

Characteristics of square wave injected semiconductor lasers are investigated numerically. In this work, frequency multiplication of 18 GHz and division of 250 MHz can be simultaneously demonstrated under proper operational condition and using a simple square wave injection system. Moreover, the bandwidth enhancement is further increased to 23 times due to the effect of bandwidth broadening in the optical injection system. The transformation of the state of square wave injection has been shown, and the complexity of the system increasing with the detuning frequency is observed in the numerical calculated mapping. The proposed scheme possesses the advantages of low cost, compact, less system complexity, and more flexibility in frequency tuning which also shows the potential of high frequency microwave signal generation.

ACKNOWLEDGMENT

The work described in this Letter was fully supported by a grant from the National Science Council of Taiwan under contract NSC 102-2218-E-155-003-MY3.

REFERENCES

1. Meng, X. J., T. Chau, and M. C. Wu, "Experimental demonstration of modulation bandwidth enhancement in distributed feedback lasers with external light injection," *Electron. Lett.*, Vol. 34, 2031–2032, 1998.
2. Mork, J., B. Tromborg, and J. Mark, "Chaos in semiconductor lasers with optical feedback: Theory and experiment," *IEEE J. Quantum Electron.*, Vol. 28, 93–108, 1992.
3. Tang, S. and J. M. Liu, "Chaotic pulsing and quasi-periodic route to chaos in a semiconductor laser with delayed opto-electronic feedback," *IEEE J. of Quantum Electron.*, Vol. 37, 329–336, 2001.
4. Eriksson, S. and A. M. Lindberg, "Observations on the dynamics of semiconductor lasers subjected to external optical injection," *J. Opt. B — Quantum and Semiclassical Opt.*, Vol. 4, 149–154, 2002.
5. Lin, F. Y. and J. M. Liu, "Chaotic radar using nonlinear laser dynamics," *IEEE J. Quantum Electron.* Vol. 40, 815–820, 2004.
6. Lin, F. Y. and J. M. Liu, "Chaotic lidar," *IEEE J. Select. Topics Quantum Electron.*, Vol. 10, 991–997, 2004.

7. Diaz, R., S. C. Chan, and J. M. Liu, "Lidar detection using a dual-frequency source," *Opt. Lett.*, Vol. 24, 3600–3602, 2006.
8. Lin, F. Y. and M. C. Tsai, "Chaotic communication in radio-over-fiber transmission based on optoelectronic feedback semiconductor lasers," *Opt. Express*, Vol. 15, 302–311, 2007.
9. Juan, Y. S. and F. Y. Lin, "Microwave frequency comb generation utilizing a semiconductor laser subject to optical pulse injection from an optoelectronic feedback laser," *Opt. Lett.*, Vol. 34, 1636–1638, 2009.
10. Juan, Y. S. and F. Y. Lin, "Ultra broadband microwave frequency combs generated by an optical pulse-injected semiconductor laser," *Opt. Express*, Vol. 17, 18596–18605, 2009.
11. Simpson, T. B., J. M. Liu, A. Gavrielides, V. Kovanis, and P. M. Alsing, "Period-doubling cascades and chaos in a semiconductor laser with optical injection," *Phys. Rev. A*, Vol. 173, 4181–4185, 1995.
12. Murakami, A., K. Kawashima, and K. Atsuki, "Cavity resonance shift and bandwidth enhancement in semiconductor lasers with strong light injection," *IEEE J. of Quantum Electron.*, Vol. 39, 1196–1194, 2003.
13. Juan, Y. S. and F. Y. Lin, "Photonic generation of broadly tunable microwave signals utilizing a dual-beam optically injected semiconductor laser," *IEEE Photon. J.*, Vol. 3, 644–650, 2011.

Multiband-OFDM Ultra Wideband Wireless Signals over Fiber Transmission

Xiupu Zhang[1, 2], **Bouchaib Hraimel**[2], **Dongya Shen**[1], **and Taijun Liu**[3]

[1]School of Information Science & Engineering, Yunnan University, Kunming, China
[2]Advanced Photonic Systems Lab, Concordia University, Montreal, Canada
[3]College of Information Science & Engineering, Ningbo University, Ningbo, Zhejiang, China

Abstract— Multiband-OFDM ultra wideband signals-over-fiber transmission is reviewed considering the impact of modulator nonlinearity, fiber dispersion, optical receiver response, out-of-band interferers due to subcarrier multiplexing and optical adjacent channel crosstalk due to WDM. Enabling techniques of reducing out-of-band interferers, improving modulation efficiency and photonic techniques for simultaneous millimeter-wave up/down conversion and optical subcarrier modulation are discussed.

1. INTRODUCTION

Orthogonal frequency division multiplexing (OFDM) ultra-wideband (UWB) wireless signal has attracted many applications. Due to OFDM characteristics, OFDM-UWB over fiber has been considered as a promising technique for distribution of OFDM-UWB wireless signals. OFDM does not require complicated chromatic dispersion management for transmission and also makes spectrum resources utilized efficiently. Despite its advantages, OFDM is very susceptible to nonlinearities from optical and wireless transmission, such as nonlinearities from optical transmitter and receiver etc.. The effect of fiber dispersion and nonlinearities of optical transmitter and receiver's response on OFDM subcarriers for multi-band (MB)-OFDM UWB over fiber links may degrade the transmission. Then, the impact of some key parameters of optical transmitter and receiver is required to be understood, such as laser phase noise, and receiver response, and how to design optical transmitters and receivers is one of the key technical issues.

An optical carrier carrying more optical subcarriers or multi-band RF signals is desired. Unfortunately, the optical subcarriers will interact with each other through nonlinearities from optical transmitters and use of direct photo-detection, thus generating distortion components, called out-of-band interferers, which may fall in another channels and degrading their signal to noise ratios. The impact of and how to suppress out-of-band interference is required to figure out.

When WDM technique is introduced to MB-OFDM UWB over fiber systems, adjacent channel crosstalk may destroy OFDM signal's orthogonality and thus limit transmission. Therefore, the impact of adjacent channel crosstalk on MB-OFDM UWB over fiber WDM system is necessary to know.

Higher modulation efficiency is preferred. To improve the modulation efficiency, new modulation techniques were introduced: optical double-sideband (ODSB) subcarrier modulation immune to fiber chromatic-dispersion-induced RF power fading, and optical single sideband (OSSB) modulation with tunable optical carrier to sideband ratio.

For millimeter-wave over fiber systems, simultaneous photonic frequency up/down-conversion and optical subcarrier modulation of millimeter-wave MB-OFDM UWB are preferred. Using an MZM or EAM for millimeter-wave up- or down-conversion was introduced.

In this paper, we review related achievements and accomplishments in microwave and millimeter-wave MB-OFDM UWB over fiber transmission.

2. IMPACT OF FIBER DISPERSION AND NONLINEARITIES OF OPTICAL TRANSMITTER AND RECEIVER RESPONSE

We first consider that an MZM is used for optical subcarrier modulation. The combined effect of fiber chromatic dispersion and MZM response nonlinearities on OSSB modulation of OFDM UWB signals was investigated [1] and it was found that all the OFDM subcarriers have identical relative amplitudes that increase almost linearly with the RF modulation index of up to 4% as shown in Figure 1. However, if modulation index is more than 4%, the subcarriers suffer from the amplitude distortion after fiber transmission, as shown in Figure 1, which shows the relative amplitudes of subcarriers at 1, 32, 64, 96 and 128 of 2nd band of UWB signals, thus optimum modulation index

is 4%. These amplitude mismatches between subcarriers will distort the received constellation and degrade the link performance. On the other hand, the subcarrier phase will depend on the fiber length and modulation index because fiber dispersion will induce different phase shifts for different subcarriers. It was found that different OFDM subcarriers have different phase shifts as shown in Figure 2, which shows relative phases of subcarriers corresponding to Figure 1. This relative phase shift between OFDM subcarriers will induce inter-carrier interference (ICI) and result in loss of orthogonality. For the optimum modulation index of 4%, the amplitude mismatch between OFDM subcarriers is negligible as shown in Figure 1; however the phase mismatch between subcarriers due to fiber dispersion is inevitable as shown in Figure 2 and will degrade the performance of the link. Due to phase distortion introduced by any phase noise and fiber dispersion, the error vector magnitude (EVM) of the link can be evaluated by

$$\left\langle \mathrm{EVM}_0^2 \right\rangle = 2 \left[\begin{array}{l} 1 - \exp\left(-0.5\sigma_\varphi^2\right) \cos\left(0.25\left(N_{ST}+2\right)\beta_2 L\omega_c \Delta\omega\right) \\ \times \mathrm{sinc}\left(0.25 N_{ST}\beta_2 L\omega_c \Delta\omega\right) / \mathrm{sinc}\left(0.5\beta_2 L\omega_c \Delta\omega\right) \end{array} \right],$$

where σ_φ^2 is the variance of RF carrier phase noise, N_{ST} is the total number of subcarriers of an OFDM signal, $\Delta\omega$ is the angular subcarrier spectral spacing, L is fiber length and β_2 is the group velocity dispersion (GVD) of the fiber, and ω_c is the RF carrier frequency. Accounting for other sources of noise such as thermal and relative intensity noise etc., the total EVM can be given by $\mathrm{EVM}^2 = \langle \mathrm{EVM}_0^2 \rangle + 1/\mathrm{SNR}$, where SNR is the received signal to noise ratio.

Since OFDM signals are very sensitive to amplitude and phase distortion, it is desired that the optical receiver does not introduce the amplitude and phase distortion. It was found that 5th order Chebyshev-II filter response of two times the bandwidth of the UWB signal is the optimum receiver for better EVM performance with reduced complexity and better rejection of adjacent interferers, as shown in Figure 3. This is because such filter has a flat magnitude response, better group delay response in the pass-band and reduced overshoot in the stop-band.

Similarly when an EAM integrated laser (EML) is used for optical transmitter, the EAM non-

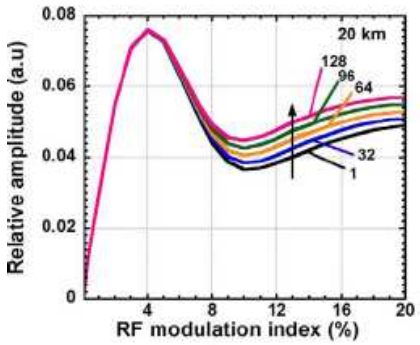

Figure 1: Calculated relative amplitude of subcarriers at 1, 32, 64, 96, and 128 for UWB over 20 km fiber.

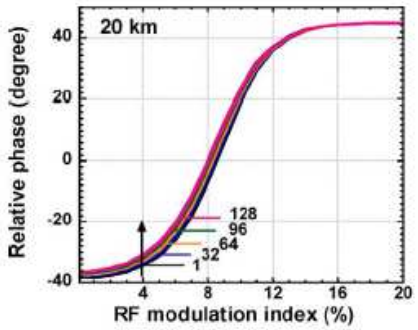

Figure 2: Calculated relative phase of sub-carriers. The others are the same as in Figure 1.

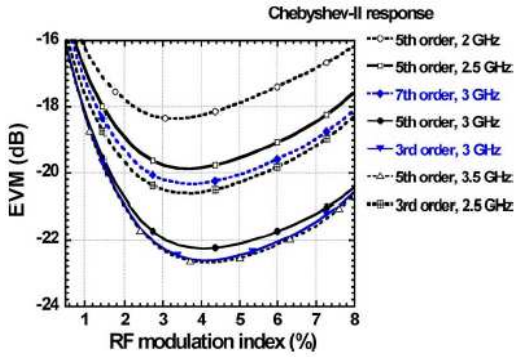

Figure 3: Impact of optical receiver response. The others are the same as in Figure 1.

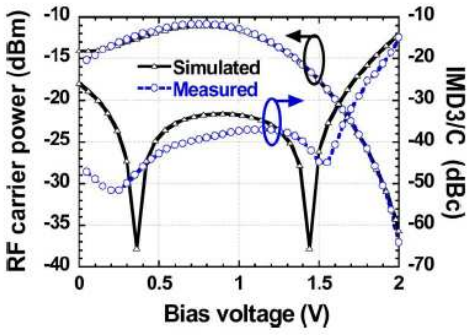

Figure 4: Impact of EAM bias after 20 km fiber.

linearities introduce amplitude and phase distortion as well as power fading for OFDM signals, thus limiting the link performance [2]. RF carrier phase noise will introduce phase noise in the OFDM subcarriers, and fiber chromatic dispersion will introduce amplitude distortion in the OFDM subcarriers and power fading in UWB signal. For high-frequency bands, the power fading can be the main limiting factor for an EML to be used in MB-OFDM UWB over fiber systems due to optical double sideband modulation and chromatic dispersion. The EVM expression for this case is slightly different from the above expression [2]. For an EML used for UWB over fiber, it is important to optimize the bias of the EAM, as shown in Figure 4. By optimizing the bias, RF carrier can be maximized and the ratio of 3rd order inter-modulation distortion (IMD3) to RF carrier can be minimized.

3. IMPACT OF LASER RELATIVE INTENSITY NOISE

The relative intensity noise (RIN) spectral density is small at the low frequencies and peaks at the relaxation resonance frequency and then gradually falls to the shot noise level. Therefore, the low-cost diode lasers' relaxation frequency may coincide with the RF signal frequency. When the transmitted RF signal has a wide bandwidth, the total RIN noise over the signal bandwidth is large.

We have shown experimentally in [3] that by increasing the laser output power the RIN peak can be shifted to higher frequency with a reduced magnitude. Figure 5 shows the impact of laser output power on MB-OFDM UWB over fiber. It is seen that the laser output power of more than 2 dBm will suppress RIN degradation.

On the other hand, fiber chromatic dispersion can convert the laser phase noise into RIN that could become the dominant noise source in broadband radio over fiber systems, such as MB-OFDM UWB over fiber. The converted RIN can be calculated by [3]

$$\mathrm{RIN}(L) = \mathrm{RIN}(0) + \frac{1}{\Omega_u - \Omega_l} \int_{\Omega_l}^{\Omega_u} \frac{16\pi\Delta\nu}{\Omega^2} \sin\left(\frac{1}{2}\beta_2 L\Omega^2\right) d\Omega,$$

where RIN(0) is the laser intrinsic RIN, $\Delta\nu$ is the laser linewidth, $\Omega_u - \Omega_l$ is the RF signal occupied bandwidth, β_2 is the fiber GVD, and L denotes the fiber length. The impact of converted RIN is illustrated in Figure 6, where RF carrier is 3.96 GHz, and the UWB signal has bandwidth of 528 MHz. The impact of converted RIN is also dependent on RF carrier frequency. Figure 7 shows the EVM of MB-OFDM UWB over fiber for RF carrier frequency from 3.9 to 10.6 GHz. Therefore, to reduce the impact of RIN on the broadband RF signal over fiber system, lasers with linewidth of less than 1 MHz should be used especially at high frequency.

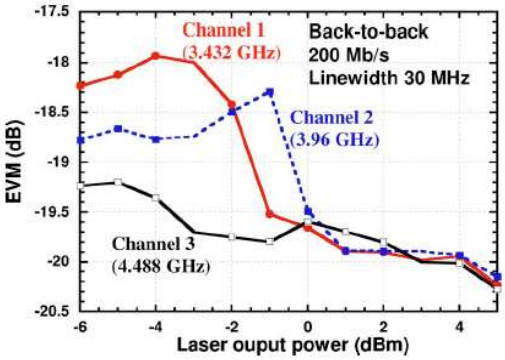

Figure 5: Measured EVM with laser output power.

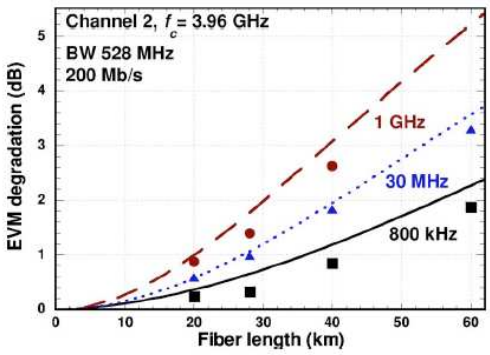

Figure 6: Calculated (line) and measured (points) EVM with respect to back-to-back.

4. IMPACT OF INTERFERENCE ON MB-OFDM UWB

In subcarrier multiplexed UWB over fiber systems, due to nonlinearities the interaction between subcarriers will introduce out-of-band interference, degrading the performance. It was found that the interference can be suppressed by using mixed polarization. For two bands UWB over fiber using a MZM, mixed polarization can reduce 2nd order nonlinearity induced interference significantly [4].

When WDM technique is used in MB-OFDM UWB over fiber, adjacent channel crosstalk in WDM systems may destroy OFDM signal's orthogonality and thus limit the transmission. It was

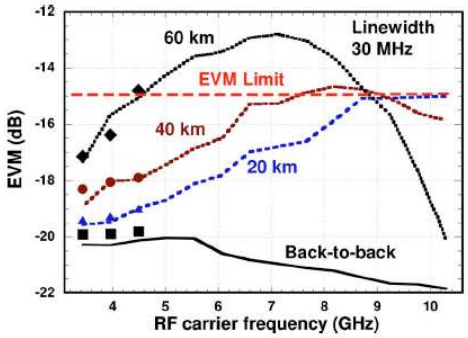

Figure 7: Calculated (line) and measured (points) EVM vs RF signal frequency.

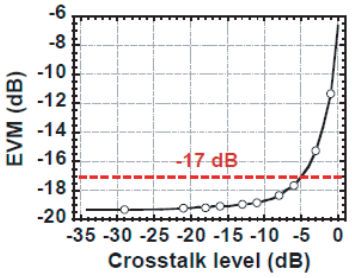

Figure 8: Measured EVM of channel 1 after 20 km fiber.

found that MB-OFDM UWB over fiber WDM system is robust to linear adjacent channel crosstalk not exceeding −5 dB as illustrated in Figure 8 [5]. Therefore linear crosstalk has less impact on OFDM signal.

5. IMPROVEMENT OF MODULATION EFFICIENCY

To reduce nonlinear distortion, OFDM UWB over fiber is operated at a low RF modulation index and thus MB-OFDM UWB has a low power spectral density. It was found that required optical power at optical receiver in OFDM UWB over fiber is reasonably higher than that in non-OFDM radio over fiber [1]. To improve the power efficiency and overcome the power fading due to chromatic dispersion, a tandem single sideband (TSSB) modulation with electrical phase shift (EPS) was demonstrated as shown in Figure 9 [6]. The dispersion-induced phase difference between upper and lower sidebands is compensated by splitting the RF signal into two phase shifted RF signals. The resulting RF signals will drive a dual electrode MZM (DE-MZM) in a TSSB modulation, i.e., each signal will generate different optical single sideband. It was shown that the TSSB-EPS outperforms OSSB by 3-dB improvement in power efficiency and mitigates power fading due to chromatic dispersion experienced in conventional ODSB. This is an important feature for millimeter-wave (mm-wave) over fiber systems.

To improve the modulation efficiency of OSSB modulation, an OSSB modulation with tunable optical carrier to sideband ratio (OCSR) was proposed [7]. In this technique an optical modulator that consists of an integrated dual parallel MZM (dMZM) is used for obtaining not only OSSB modulation but also tunability of OCSR simultaneously, as shown in Figure 10. Such a modulator will be vital for optimizing the performance by improving modulation efficiency and receiver sensitivity and by removing fiber chromatic dispersion induced RF power fading. A wide range of OCSR tunability can be obtained by altering bias voltage of dMZM. For an optical carrier carrying one subcarrier (one RF signal), RF power is maximized at OCSR = 0 dB. Similarly when an optical carrier carries two RF signals, the OCSR of 3-dB should be the optimum. For MB-OFDM UWB signal, after 20 km fiber transmission an EVM of −21.8-dB was obtained experimentally for an op-

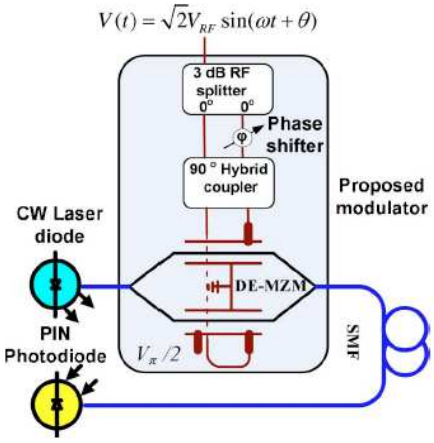

Figure 9: TSSB-EPS setup.

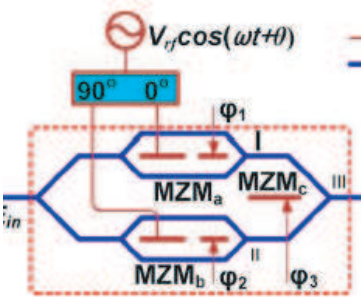

Figure 10: OSSB modulator with OCSR tunability.

tical carrier carrying one RF signal at an OCSR of 5.4 dB rather than 0 dB as shown in Figure 11. This is due to avoidance of clipping induced nonlinear distortion.

6. PHOTONIC FREQUENCY UP/DOWN-CONVERSION

Photonic up/down conversion of millimeter-waves is a cost-effective solution compared with direct electrical counterparts. Using frequency quadrupling with an MZM, a millimeter wave carrying multi-band frequency hopping OFDM UWB signals was optically upconverted to $\sim$ 30 GHz as shown in Figure 12 [8]. It was found that RF carrier power, which is generated by beating two 2nd order subcarriers, is maximized and the distortion, which is generated mainly by two 1st order subcarriers, is minimized when phase shift between the two MZMs is 180°, as shown in Figure 13 [8].

It was found that an EAM can be used for simultaneous frequency down-conversion and optical subcarrier modulation [9, 10], resulting in a low-cost base station. The principle is shown in Figure 14, two wavelength lights emitting from a central station, by four-wave mixing in an EAM uplink millimeter-wave converted to a low RF with optical subcarrier modulation. The frequency down-conversion from $\sim$ 30 GHz to $\sim$ 4 GHz and optical subcarrier modulation using an EAM were validated using MB-OFDM UWB over 20 km of single-mode fiber, and EVM of less than −21 dB was obtained. The theory of four-wave mixing and frequency down-conversion were given in [10] and it was found that four-wave mixing efficiency can be optimized. FWM generation is not only dependent on dc-bias voltage but also on RF modulation voltage of EAM. The converted optical subcarriers can have a tunable OCSR.

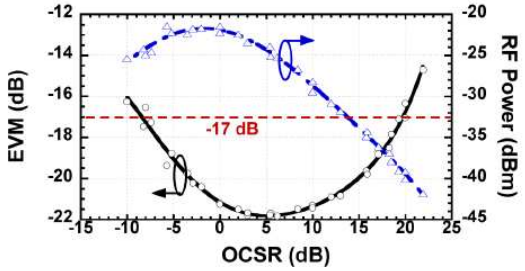

Figure 11: VM and RF power vs OCSR.

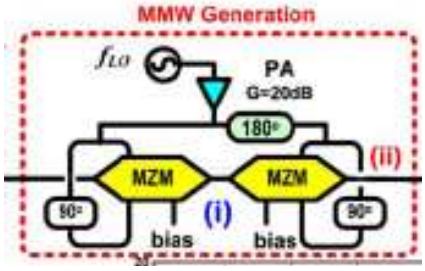

Figure 12: Frequency quadrupling using two MZMs.

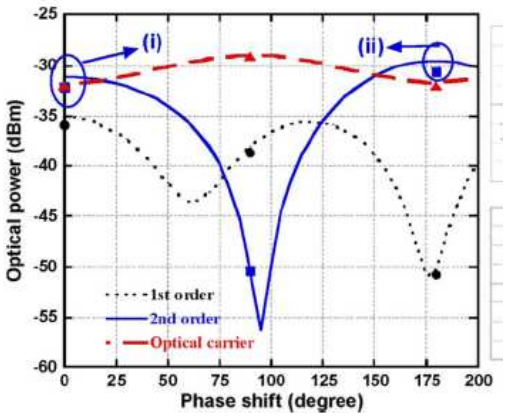

Figure 13: 1st and 2nd optical subcarrier power with phase shift between two MZMs.

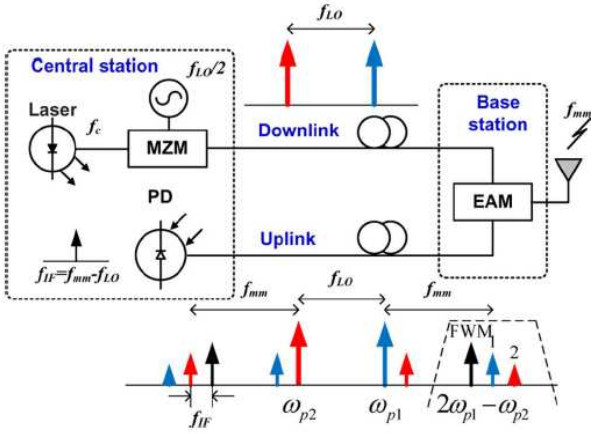

Figure 14: Frequency down-conversion using EAM.

7. CONCLUSION

We have reviewed the impact of modulator nonlinearity, fiber dispersion, optical receiver response, and out-of-band interference due to subcarrier multiplexing, and optical adjacent channel crosstalk due to WDM on the transmission performance of MB-OFDM UWB signals-over-fiber. It has been found that the nonlinearities due to optical subcarrier modulation combined with fiber dispersion

distort OFDM signals due to 3rd nonlinearity, and also introduce out-of-band interference for neighbour channels due to 2nd order nonlinearity. Linear crosstalk has little impact on OFDM signals. Optical receivers should have fifth-order Chebyshev-II filter response and two times bandwidth of OFDM RF signal to minimize the degradation of optical receiver's response on the link performance. Novel optical subcarrier modulations of TSSB and OSSB with OCSR tunability have been discussed. Photonic techniques for simultaneous millimeter-wave up/down conversion and optical subcarrier modulation for a down link using an MZM and an uplink using an EAM have been also demonstrated.

ACKNOWLEDGMENT

This work was supported in part by the Yunnan High-Tech Talents Recruitment Project 2012HA005, and also Ningbo University Sir Yue-Kong Pao's Chaired professorship and China "111" plan for Ningbo University.

REFERENCES

1. Sakib, M., B. Hraimel, X. Zhang, M. Mohamed, W. Jiang, K. Wu, and D. Shen, "Impact of optical transmission on multiband OFDM ultra-wideband wireless system with fiber distribution," *IEEE/OSA Journal of Lightwave Technology*, Vol. 27, 4112–4123, 2009.
2. Sui, C., B. Hraimel, X. Zhang, L. Wu, Y. Shen, K. Wu, T. Liu, T. Xu, and Q. Nie, "Impact of electro-absorption modulator integrated laser on MB-OFDM ultra-wideband signals over fiber systems," *IEEE/OSA Journal of Lightwave Technology*, Vol. 28, No. 24, 3548–3555, 2010.
3. Sakib, M., B. Hraimel, X. Zhang, K. Wu, T. Liu, T. Xu, and Q. Nie, "Impact of laser relative intensity noise on multiband OFDM ultra wideband wireless signal over fiber system," *OSA/IEEE Journal of Optical Communications and Networking*, Vol. 2, No. 10, 841–847, 2010.
4. Hraimel, B. and X. Zhang, "Impact of out-of-band interferers on MB-OFDM UWB transmission in radio over fiber systems," *Conference on Optical Fiber Communications, OFC*, Paper JW2A.85, LA, USA, 2012.
5. Hraimel, B. and X. Zhang, "Impact of crosstalk on MB-OFDM UWB transmission in radio over fiber WDM system," *Conference on Optical Fiber Communications, OFC*, paper OTuF4, LA, USA, 2011.
6. Hraimel, B., X. Zhang, M. Mohamed, and K. Wu, "Precompensated optical double-sideband subcarrier modulation immune to fiber chromatic dispersion induced RF power fading," *OSA/IEEE Journal of Optical Communications and Networking*, Vol. 1, No. 4, 331–342, 2009.
7. Hraimel, B., X. Zhang, Y. Pei, K. Wu, T. Liu, T. Xu, and Q. Nie, "Optical single-sideband modulation with tunable optical carrier to sideband ratio in radio over fiber systems," *IEEE/OSA Journal of Lightwave Technology*, Vol. 29, No. 5, 775–781, 2011.
8. Mohamed, M., B. Hraimel, X. Zhang, and K. Wu, "Optical generation of millimeter wave multiband OFDM UWB wireless signal and distribution over fiber," *IEEE Photonics Technology Letters*, Vol. 22, No. 15, 1180–1182, 2010.
9. Hraimel, B., X. Zhang, and K. Wu, "Photonic down-conversion of millimeter wave multiband orthogonal frequency division multiplexing ultra-wideband using four wave mixing in an electro-absorption modulator," *IEEE Journal of Lightwave Technology*, Vol. 28, No. 13, 1987–1993, 2010.
10. Zhu, R., B. Hraimel, and X. Zhang, "Analysis of simultaneous photonic frequency down-conversion and optical subcarrier modulation in an electro-absorption modulator," *IEEE/OSA Journal of Lightwave Technology*, Vol. 30, No. 3, 344–354, 2012.

An Efficient and Flexible Satellite Repeater Based on Optical Frequency Combs Technology

Xinwu Yang[1], **Kun Xu**[1], **Jie Yin**[2], **Yitang Dai**[1], **Feifei Yin**[1], **Jianqiang Li**[1], **Hua Lu**[2], **Tao Liu**[2], **and Yuefeng Ji**[1]

[1]State Key Laboratory of Information Photonics and Optical Communications
Beijing University of Posts and Telecommunications, Beijing 100876, China
[2]Beijing Institute of Satellite Information Engineering, Beijing 100086, China

Abstract— We propose a high efficient and flexible satellite repeater structure based on optical frequency combs technology with the ability of converting frequencies between C, Ku, K and Ka bands arbitrarily. A proof of concept experiment is demonstrated in which an input C band frequency of 6.1 GHz is successfully converted to 4.1 GHz, 3.9 GHz, 11.9 GHz, 19.9 GHz, etc. in separated channels. Performance is evaluated by multiplexing a 10 Mbps QPSK signal on the input RF carrier and about 9.3% EVM degradation in each channel is observed at 0 dBm input RF power compared with back to back condition.

1. INTRODUCTION

As the problems of frequency spectrum congestion and orbital resource depletion driving today's telecom satellite to operate at C, Ku, Ka, V and even higher bands, multi-band and multi-channel signals handlings, such as multiple local oscillators (LOs) distribution, band to band conversion, beam to beam cross connection, have become extremely inefficient, inflexible, costly and complex.

Recently, microwave photonics, with its unique characteristics of parallel signal processing over an extremely wide bandwidth, has been implemented to handle multi-band RF signals in several practical applications such as the European Space Agency's SAT'N LIGHT project [1] and the Atacama Large Millimeter Array (ALMA) [2], where the corresponding functions can hardly be realized by their electrical counterparts.

In this work, we propose a high efficient and flexible satellite repeater with parallel processing ability based on optical frequency combs technology. The proposed scheme consists of three sections, a multi-band local oscillator generation section, an inter- & intra-band frequency conversion section and a channel switching section. It is worth noting that only three frequency-fixed microwave sources are needed for the whole system and theoretically more than 7 bands (L to Ka) of microwave generation and frequency conversion can be supported. In the first section, dual coherent optical frequency combs with different center wavelength and frequency spacing are generated through electro-optic modulation technique. By heterodyning the generated dual-combs, multiple photonic microwave LOs within different frequency bands (e.g., C, Ku, K, Ka etc.) are achieved. Then, simultaneous inter- and intra-band microwave frequency conversion are implemented by adding a signal replication module to the first section. Input signal are optically mixed with one of the combs and replicated over each comb lines. After heterodyne with the other comb and optical periodical filtering process, the converted frequencies within different frequency bands are obtained in separated channels. In the channel switching section, an optical 4×4 MEMS switch routes the channelized signal within different bands to different output ports.

In a word, the first section provides multi-band LOs, the second and third section complete band to band conversion and beam to beam cross-connection respectively. We carry out a proof of concept experiment, in which an input C band frequency of 6.1 GHz is successfully converted to 4.1 GHz, 3.9 GHz, 11.9 GHz, 19.9 GHz, etc. in each channel. System impairments are assessed by modulating the input frequency with a 10 Mbps QPSK signal and about 9.3% EVM degradation compared with back to back condition is observed at 0 dBm input power. However, all the measured results are far below the maximum EVM limit of 31.6% for QPSK signal in a very wide power range.

2. PRINCIPLE

The principle of multi-band LOs generation and band to band frequency conversion can be explained in optical frequency domain as illustrated in Figs. 1(a) and (b) respectively. In reference to Fig. 1(a), one of the dual optical frequency combs, say Comb A, have a repetition rate f_{rA} which is slightly different with that of the other comb (say Comb B) f_{rB} and there also exists a small detuning

f_s between the two closest comblines. This alignment lead to a spacing increment between the comblines with same indices along high frequency direction. The frequency of each combline in Comb A can be expressed as

$$f_{CombA}(i) = f_0 + (i-1) \cdot f_{rA} \tag{1}$$

where the index i ($0 \leq i \leq n$) denotes the index of the combline relative to the first carrier f_0, n is the maximum index of the available combline. Similarly, the frequencies of Comb B is given as

$$f_{combB}(i) = f_0 + f_s + (i-1) \cdot f_{rB} \tag{2}$$

The values of f_{rA}, f_{rB} and f_s are carefully assigned that each combline of Comb A and that of Comb B with the same index fall in each passband of a periodic optical filter such like wavelength division multiplexer (WDM). Therefore, multiple microwave LOs with a serials of frequencies can be achieved by heterodyning each pair of these comblines,

$$f_{LO}(i) = f_s + (i-1) \cdot |f_{rA} - f_{rB}| \tag{3}$$

To avoid crosstalk between channels, the values of f_{rA}, f_{rB}, f_s and the maximum number of comblines n should satisfy the following limits,

$$n \leq 1 + \frac{BW - f_s}{f_{r,\max} - f_{r,\min}} \tag{4}$$

where $f_{r,\max} = \max\{f_{rA}, f_{rB}\}$, $f_{r,\min} = \min\{f_{rA}, f_{rB}\}$, BW denotes the passband width of the WDM filter. According to Eq. (4), more LOs can be achieved with less difference between f_{rA} and f_{rB}, and higher LOs can be obtained with much wider BW. Combs with more than 7 lines in good flatness and 40 GHz line to line spacing have already been generated in Ref. [3] that can potentially support more than 7 LOs generation from L to Ka band.

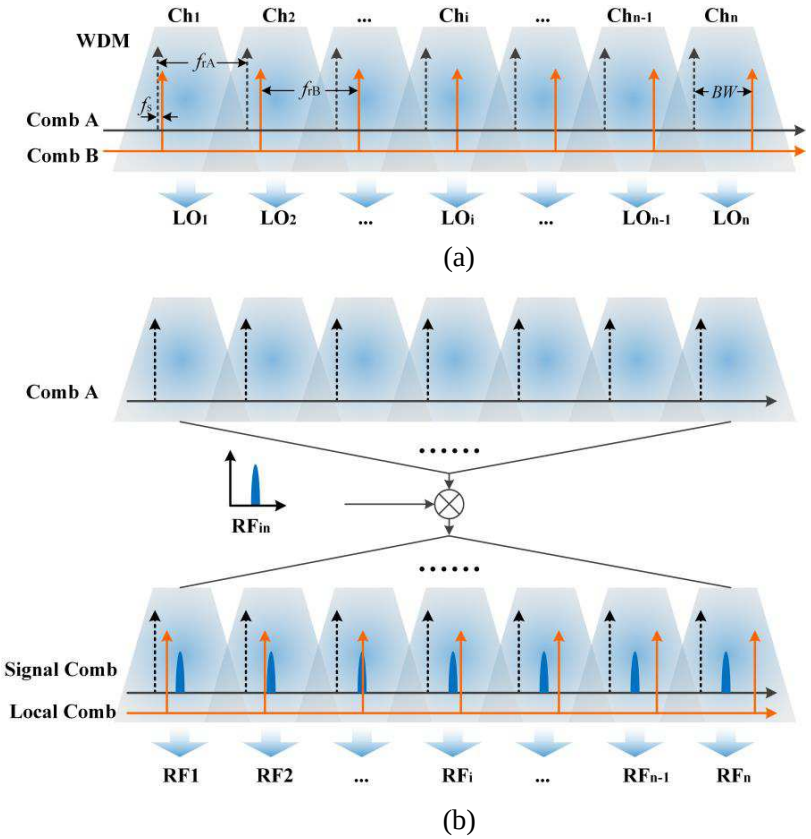

Figure 1: Optical frequency domain illustration of (a) multi-band LOs generation and (b) band to band frequency conversion based on dual coherent optical frequency combs.

Based on the LOs generated above, band to band frequency conversion can be readily implemented by modulating a RF signal on one of the combs. As shown in Fig. 1(b), the RF signal

within a supported bandwidth is spectrally replicated at each combline of one of the dual combs through electro-optical mixing way. Referring to the electrical heterodyne, we call this new comb a signal comb and correspondingly the other comb a local comb. Here, as shown in Fig. 1(b), single sideband (SSB) modulation is adopted for the mixing to efficiently make full use of the available bandwidth and avoid residual sideband crosstalk. Carriers can be further removed by aligning their frequencies to the gaps between the WDM passbands. Through channelization and heterodyne process, the converted signals within different bands are obtained,

$$f_{out}(i) = |f_{LO}(i) - f_{in}| \tag{5}$$

3. PROOF-OF-CONCEPT DEMONSTRATION

According to the principles, the proposed satellite repeater structure is shown in Fig. 2 which consists of multiple paths to support repeating incoming signals from C to Ka band. Note that all the paths share a common LOs generation module and an optical switch matrix which dramatically save LOs and space on satellite. The whole system can be divided into three sections, the Multi-band LOs generation section, the optical band to band conversion (including mixing and channelizing) section and the optical cross-connect section.

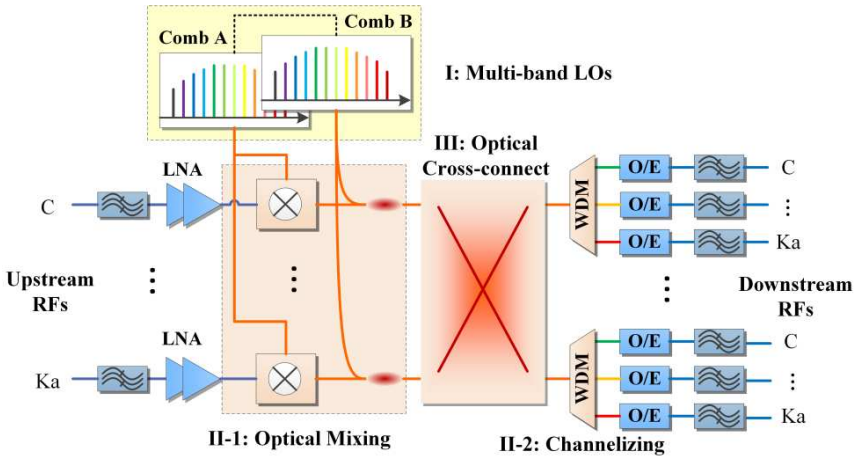

Figure 2: Conceptual architecture of multi-band satellite repeater based on optical frequency combs. LNA: low noise amplifier, WDM: Wavelength Division Multiplexing, O/E: optoelectronic conversion.

1) In the first section, dual coherent optical frequency combs with different center wavelength and frequency spacing are generated, by heterodyning which, multiple photonic microwave LOs within different frequency bands (e.g., C, Ku, K, Ka, etc.) can be achieved.

2) In the second section, the incoming RF signals are optically mixed with one of the combs through optical modulators to multicast the signal over each comblines. Then the new signal comb is combined with the local comb and channelized by the WDMs. After O/E conversion, the converted frequencies within different frequency bands are obtained in separated channels.

3) In the last section, an optical 4×4 MEMS switch is inserted between the mixing stage and channelizing stage to route the upstream signal within different bands (e.g., C, Ku, K and Ka) to their desired output ports.

In general, with the three sections, not only can the system convert one band of RF signal to any other band, it can also route the signals to any output port.

A proof of concept experiment was demonstrated to validate this proposal. In the multi-band LOs generation section, a simple optical frequency comb generation method [4] which only need one optical modulator and one frequency-fixed microwave source for each comb was chosen to generate dual combs with 5 flat comblines in each. It should be noted that the coherence is assured by feeding the two comb generators a common CW laser. Shift of center wavelength of one comb is through the method of selecting one sideband of DSB modulated lightwave, where a third frequency-fixed microwave source is required. In experiment, the generated dual coherent combs with 38 GHz and 30 GHz line to line spacing, respectively, and 18 GHz center wavelength shift were shown in Fig. 3(a). It can be seen that the overall flatness of both combs are kept below 0.9 dB and there is a 14.7 dB side mode suppression ratio. These dual coherent combs can provide photonic microwave LOs with

frequencies of 2 GHz, 10 GHz, 18 GHz, 26 GHz and 34 GHz. According to Eq. (5), these LOs can support arbitrary frequency conversion between C, Ku, K and Ka band, e.g., 6/4 GHz, 14/12 GHz, 30/20 GHz or 6/12 GHz, 30/4 GHz, etc. with format of upstream/downstream frequency bands that repeated on current telecomm satellites.

In the optical mixing stage of Section 2, an optical I/Q modulator was employed and works in carrier-suppressed single sideband modulation (CS-SSB) manner to mix a input 6.1 GHz RF signal with the 38 GHz spaced comb. Since the original carriers were eliminated, both the problems of residual frequency components and crosstalk are greatly mitigated in the channelizing stage. As shown in Fig. 3(b), the signal is replicated at right side of each original comblines which are suppressed more than 21.4 dB. It can be clearly seen that the converted frequencies will occur at 4.1 GHz, 3.9 GHz, 11.9 GHz, 19.9 GHz and 27.9 GHz in each channel.

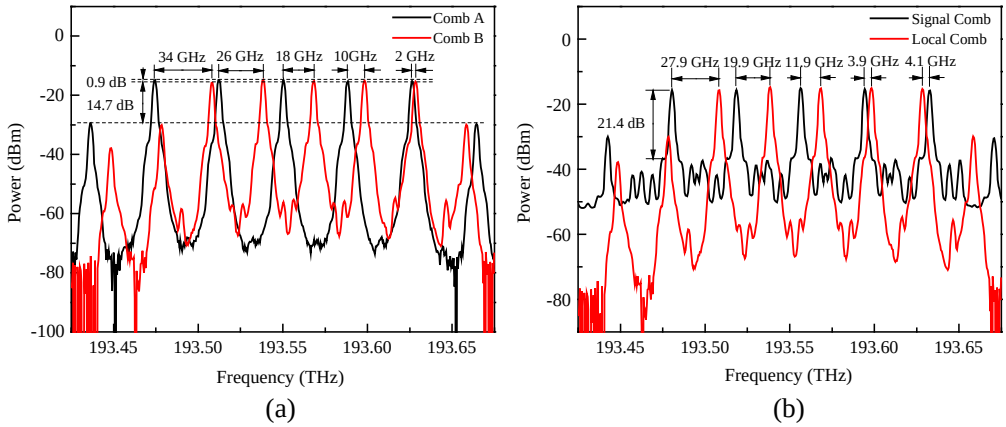

Figure 3: Optical spectra of the dual optical frequency combs with one of which (a) before and (b) after optical mixing with a C band RF signal under CS-SSB modulation condition.

In the channelizing stage of Section 2, We used a WaveShaper (Finisar 4000s) to emulate a WDM (according to Eq. (4)) with 38 GHz FSR and approximately 30 GHz passband width. Limited by the instruments and devices in laboratory and the too close channel spacing, (the latter will be mitigated by increasing the line to line spacing of each combs since the fact of poor resolution of current optical filtering technologies.) only the first three channels were photodected and measured as shown in Figs. 4(a), (b) and (c). The spurious products suppression ratio in 2 GHz bandwidth are between 30 dB and 46.7 dB under 20 kHz RBW measurement condition. Note that the spurious frequency components in Figs. 6(b), (c) can be attributed to the non-ideal CS-SSB modulation.

The performance of the proposed repeater system is also investigated. We multiplexed a 10 Mbps QPSK signal on the 6.1 GHz input RF carriers under test and measured the EVM in each output channel at different input RF powers. The results are shown in Fig. 5. As a reference, back to back measurement results are also plotted. As expected, all channels experience an EVM improvement

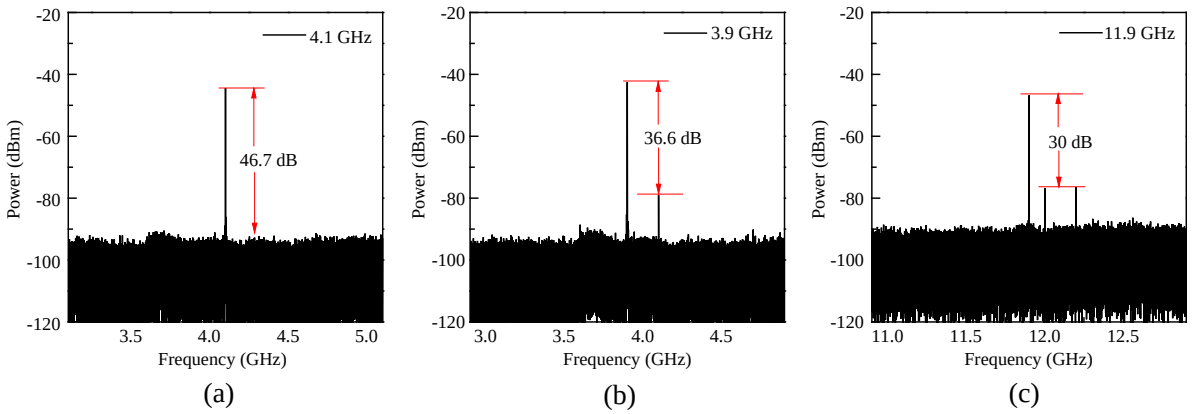

Figure 4: Electrical spectra of the converted signals from first three channels at (a) 4.1 GHz, (b) 3.9 GHz, and (c) 11.9 GHz.

as the input power increases. We can also find that the three channels performed almost the same in the interval of −4 dBm to 0 dBm and all have an approximate 9.3% EVM degradation compared with the back to back condition in this interval. Hence, it can be deduced that the unmeasured high frequency channels will behave similarly. It also should be noted that all these results are far below the EVM limit of 31.6% for QPSK format in a very wide power range.

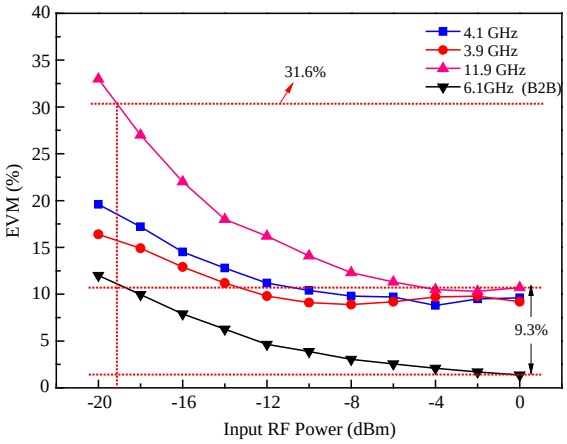

Figure 5: EVM versus input RF power at different channels compared with back to back measurement result.

4. CONCLUSION

In conclusion, by employing optical frequency combs technology in the application of satellite repeater, we proposed a high efficient and flexible frequency repeat structure with the ability of converting frequencies between C, Ku, K and Ka bands arbitrarily. Most importantly, the whole system only need three frequency-fixed microwave source. A proof of concept experiment was demonstrated in which a C band 6.1 GHz signal was successfully converted to 4.1 GHz, 3.9 GHz, 11.9 GHz, etc. with quite acceptable EVM performance. The proposed repeater structure may have better performance if the optical frequency combs are generated with wider line to line spacing so that comblines can be easily separated, since the optical discrimination of a few gigahertz is still a challenge to the conventional optical filtering technologies.

ACKNOWLEDGMENT

This work was supported in part by 863 Program (2011AA010306), National 973 Program (2012CB-315705), NSFC Program (61271042, 61107058 and 61120106001), and the Fundamental Research Funds for the Central Universities.

REFERENCES

1. Sotom, M., B. Benazet, A. Le Kernec, and M. Maignan, "Microwave photonic technologies for flexible satellite telecom payloads," *35th European Conference on Optical Communication, ECOC' 09*, 1–4, Vienna, Austria, 2009.
2. Cliche, J. F. and B. Shillue, "Precision timing control for radioastronomy — Maintaining femtosecond synchronization in the atacama large millimeter array," *IEEE Control Systems Magazine*, Vol. 26, 19–26, Feb. 2006.
3. Xie, X., R. Wang, Y. Dai, K. Xu, J. Wu, Y. Li, et al., "Coherent photonic RF channelizer by optical frequency combs and I/Q demodulation," *Optical Fiber Communication Conference and Exposition (OFC/NFOEC), 2012 and the National Fiber Optic Engineers Conference*, 1–3, 2012.
4. He, C., S. L. Pan, R. H. Guo, Y. J. Zhao, and M. H. Pan, "Ultraflat optical frequency comb generated based on cascaded polarization modulators," *Optics Letters*, Vol. 37, 3834–3836, Sep. 15, 2012.

Microwave Frequency Multiplication Based on Double-pass Modulation and Fiber Ring Microwave Photonic Filters

Zuowei Xu[1], **Hongyan Fu**[1,*], **Zhiping Cai**[1], **and Zhangwei Yu**[2]

[1]Department of Electronic Engineering, School of Information Science and Engineering
Xiamen University, Xiamen 361005, China
[2]Department of Applied Physics, Royal Institute of Technology (KTH)
Roslagstullsbacken 21, Stockholm 10691, Sweden

Abstract— In this article, a novel approach to generate high frequency multiplication microwave signal with double-pass modulation and fiber ring based microwave photonic filters (FRMPFs) is proposed and experimentally demonstrated. The results show that it's an effective way to generate high frequency signals with good tunability.

1. INTRODUCTION

Photonic generation of high frequency microwave signal has been intensively studied in the last few years, due to its advantages such as the capability of generating high quality microwave signal with high frequency and wideband tunability, etc. [1, 2]. There are many techniques to generate microwave signal in optical domain, and the external modulation method is one of the important techniques that enjoys the advantages such as, high signal stability, good tunability and system simplicity [3]. To generate high order harmonics, normally two or several modulators are used, and also a well-designed optical filter is needed to select the desirable harmonics, which both will increase the complexity and cost of the generation system [4, 5]. In this article, we use a double-pass modulation to generate high order harmonics and cascaded fiber ring based tunable microwave photonic filters are used to select the desirable harmonics. The fourth order harmonics with more than 10 dB signal to noise ratio have been achieved in the experiment.

2. EXPERIMENTAL SETUP AND OPERATION PRINCIPLE

The experiment setup is shown as Figure 1. The light from the broadband optical source is modulated by a commercial Mach-Zehnder modulator (MZM), which is driven by a large signal with a power of 25 dBm, and after that a remodulation is realized by using a fiber loop mirror which is formed by connecting an EDFA between two output ports of a 50 : 50 fiber coupler The modulated optical light from the MZM can be amplified and reflected back to the MZM again and re-modulated by the microwave signal via the same MZM. High order harmonic signals are generated and enhanced based on the nonlinear modulation characteristics of the large signal and the dual-pass modulation process, and this has been proved to be an effective way to generate high order harmonics [6]. By beating these harmonics on the photodiode (PD), high frequency microwave

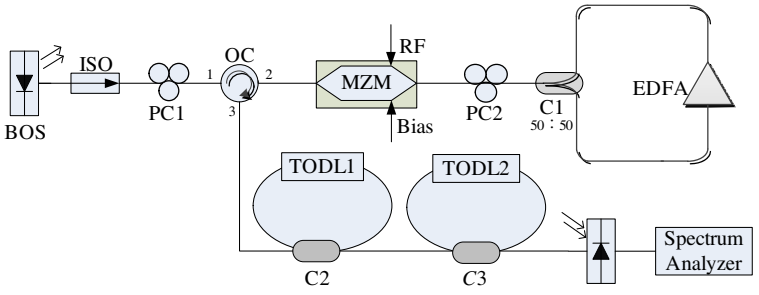

Figure 1: Experimental setup of the proposed microwave signal multiplication (BOS: broadband optical source, ISO: optical isolator, PC: polarization controller, MZM: Mach-Zehnder modulator, OC: optical circulator, C1 $\sim$ 3: optical coupler 1 $\sim$ 3, EDFA: erbium doped fiber amplifier, PD: photodiode.)

signals which are integral multiple of the low frequency drive signal can be generated. With a

*Corresponding author: Hongyan Fu (fuhongyan@xmu.edu.cn).

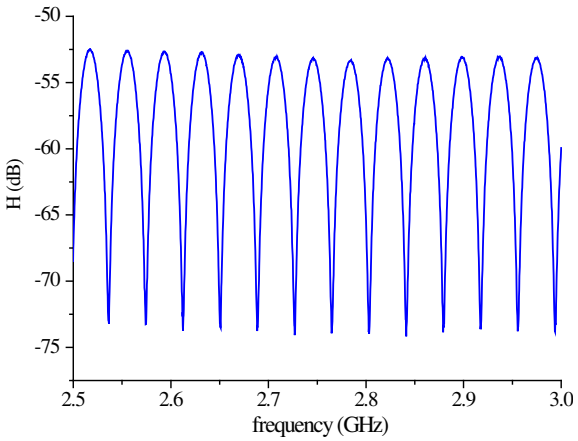

Figure 2: The frequency response of the FRMPF.

proper adjustment of the bias of the MZM, we could get high order multiplication signals with proper power.

In order to filter out the low frequency signal, a tunable FRMPF was used. The FRMPF is easy to be implemented by connecting a 2×2 coupler's input port with an output port. The frequency response function of the FRMPF could be expressed as:

$$H(f) = \frac{1 - k + (2k - 1)e^{-j2\pi fnL/c}}{1 - ke^{-j2\pi fnL/c}} \tag{1}$$

where f denotes the frequency of the microwave; k is the coupler coefficient of the coupler; c is the velocity of the light in vacuum; n and L stands for the refractice index and length of the fiber respectively. Figure 2 shows the measured frequency response of the FRMPF.

In order to get high suppression ratio we use a fiber coupler with a coupling coefficient of 0.7 ($k = 0.7$) and the length of the fiber ring is about 5.4 m. The frequency response of the FRMPF shows a periodic frequency response and it's free space range (FSR) could be expressed as

$$\text{FSR} = c/nL \tag{2}$$

With a TODL connected in the fiber ring, the FSR of the FRMPF can be tuned continuously. An arbitrary driving microwave signal with frequency of f can meet the notch points of the filter or the maximum points of the filter by carefully adjusting the length of the TODL in the fiber ring. With a periodic characteristics of the filter, we can deduce that if generated odd harmonics are in the notch points of the microwave photonic filter ($(n + 0.5)$FSR, $n = 1, 2, 3 \ldots$), the even harmonics are in the maximum points ($(2n + 1)$FSR, $n = 1, 2, 3 \ldots$) of the filter. So in this way, by using cascaded FRMPFs, the odd harmonics could be filtered out and the even harmonics remain, so that the even harmonic with desirable frequency can be obtained

3. EXPERIMENTAL RESULTS AND DISCUSSIONS

Figures 3(a) and (b) show the spectra of the generated harmonics before filtering and after one tunable FRMPF, respectively. Driving signal with frequency of 2.8 GHz, 2.9 GHz and 3.0 GHz have been used and harmonics with integral multiple of the driving frequency has been generated with the double-pass modulation, shown in Figure 3(a). By using one tunable FRMPF, and adjusting the length of fiber ring carefully to make the odd harmonics located in the notch of the filter and even harmonics located in the peak of the filter, the first and third order harmonics have been filtered out and the second and fourth order harmonics remained, as shown in Figure 3(b). The results also shows good signal generation tunability as the FRMPF is a tunable filter.

Based on the analysis above, we can filter out the second harmonic and select the fourth harmonic by using a second FRMPF with the notch located at the frequency of the second harmonic and the peak located at the fourth harmonic The experimental results are shown as Figure 4. Driving microwave signal with frequency of 2.4032 GHz is utilized. One can see that after the first FRMPF, the second and fourth order harmonics remain as shown in Figure 4(a), and by using the second FRMPF with proper length, the second order harmonic is filtered out while the fourth order

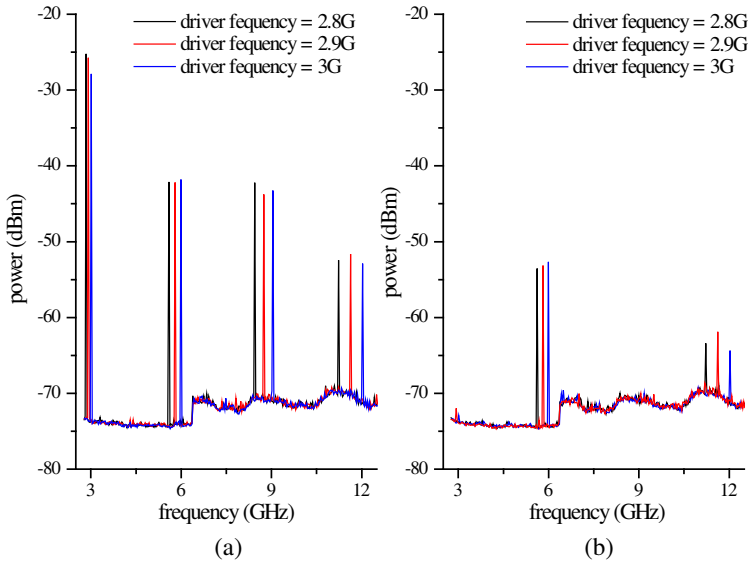

Figure 3: The spectrum of harmonics (a) without FPMPF and (b) with one FRMPF.

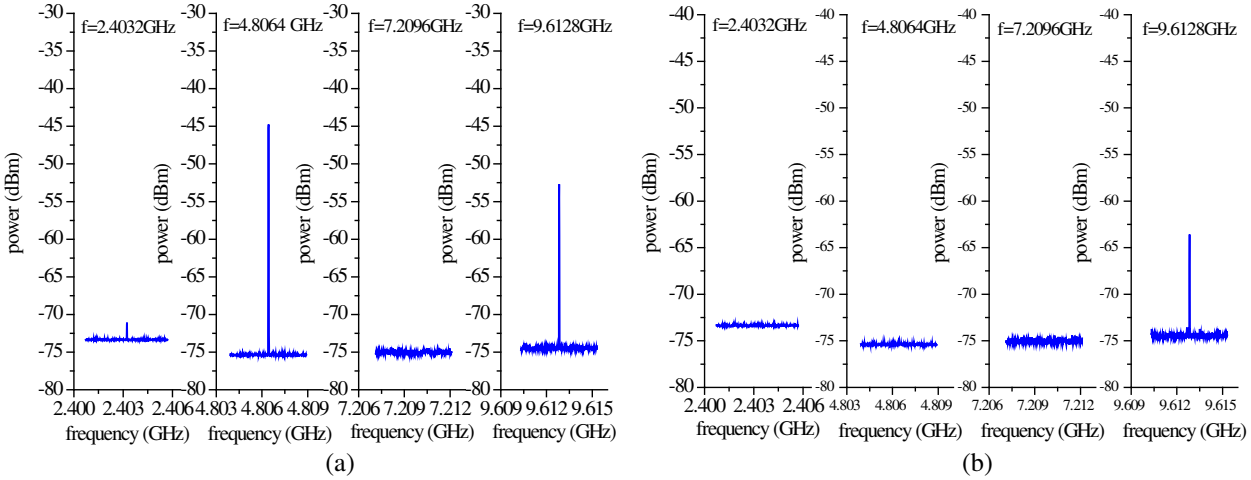

Figure 4: The detailed spectrum of harmonics (a) with one FRMPF and (b) with two cascaded FRMPFs.

harmonics of 9.6128 GHz remains, as shown in Figure 4(b). The signal to noise ratio of more than 10 dB is obtained in the experiment.

4. CONCLUSIONS

In this article, we proposed a new approach of microwave frequency multiplication with double-pass modulation and cascaded FRMPFs. By using cascaded FRMPFs with proper length, desirable high frequency even order harmonics can be selected, and fourth order harmonics with more than 10 dB signal to noise ratio have been achieved in the experiment. Microwave multiplication with higher order, better signal to noise ratio can be obtained by using more FRMPFs and optimizing the device parameters in this system, such as bias voltage of the MZM and the power of driving signal and so on. The proposed microwave frequency multiplication technique is an effective way to generate high frequency microwave with good tunability, and shows widely application potential in the fiber wireless communication systems.

ACKNOWLEDGMENT

This work is supported by National Natural Science Foundation of China (No. 61205059), Fundamental Research Funds for the Central Universities of Xiamen University (Grant No. 2010121059), and Ph.D. Programs Foundation of Ministry of Education of China (No. 20120121120037).

REFERENCES

1. Capmany, J. and D. Novak, "Microwave photonics combines two worlds," *Nature Photonics*, Vol. 1, No. 6, 319–330, 2007.
2. Yao, J., "Microwave photonics," *Journal of Lightwave Technology*, Vol. 27, No. 3, 314–335, 2009.
3. Li, W. and J. Yao, "Investigation of photonically assisted microwave frequency multiplication based on external modulation," *IEEE Transactions on Microwave Theory and Techniques*, Vol. 58, No. 11, 3259–3268, 2010.
4. Zhao, Y., X. Zheng, H. Wen, and H. Zhang, "Simplified optical millimeter-wave generation configuration by frequency quadrupling using two cascaded Mach–Zehnder modulators," *Optics Letters*, Vol. 34, No. 21, 3250–3252, 2009.
5. Qi, G., J. Yao, J. Seregelyi, S. Paquet, and C. Belisle, "Generation and distribution of a wide-band continuously tunable millimeter-wave signal with an optical external modulation technique," *IEEE Transactions on Microwave Theory and Techniques*, Vol. 53, No. 10, 3090–3097, 2005.
6. Ou, H., K. Zhu, C. Ye, and Y. Hu, "All-optical transversal filter with tap increasing and negative coefficients based on double-pass modulation," *IEEE Photonics Technology Letters*, Vol. 23, No. 14, 938–940, 2011.

Compact Quad-band PIFA Antenna for LTE Handsets with MIMO and Low Mutual Coupling

Khaled A. Abdelwahab[1], **Esmat A. Abdallah**[2], **and Mohamed Aboul-Dahab**[1]

[1]The Arab Academy for Science and Technology, Cairo, Egypt
[2]Electronics Research Institute, Dokki, Giza, Egypt

Abstract— In this paper Electromagnetic Band Gap (EBG) and Defected Ground Structure (DGS) have been proposed and applied to Planar Inverted-F Antenna (PIFA) with 2×2 MIMO. A 2D-EBG structure was designed and applied to the antenna ground plane for surface wave suppression and improved isolation between antenna elements. Two PIFA antennas with multi-band operation in the LTE frequency bands (Band 13 "US 700 Upper C" 746–787 MHz, Band 2 "PCS 1900" 1850–1990 MHz, Band-1 "IMT 2100" 1920–2170 MHz) and the Wi-Fi (IEEE 802.11y.2008) frequency band (3600–3700 MHz) are presented and analyzed. The fabricated prototype shows agreement with the simulated one.

1. INTRODUCTION

The digital era we live in has sparked numerous innovations in the smart phone market especially during the past decade. Market requirements for more compact and high capacity handsets are becoming more challenging by the day. Compact diversity antennas in the handset are needed more than ever now, at a time where Long Term Evolution (LTE) networks are being deployed in several countries. Multiple Input Multiple Output (MIMO) antennas have been shown to increase the overall capacity by being able to deliver simultaneous speed by utilizing multi-path signals [1]. Closely spaced antennas in the mobile handset have become an ever increasing challenge due to mutual coupling between antenna elements [2].

Planar Inverted F-Shaped Antennas (PIFA) have been widely recognized in mobile handsets due to their compact size and multi-band capabilities. They are also known to have simple designs, thus enabling them to be commercially available. By using shorting mechanisms, PIFA antennas can resonate at quarter-wavelengths thus reducing the conventional half-wavelength patch antenna size by 50%. Having low Specific absorption rate (SAR) values due to their reduced backward radiation makes PIFA antennas of considerable value. Narrow bandwidth has been known to be one of the limitations of PIFA antennas. The shorting via is one of the reasons for this limitation. To achieve wide bandwidth we may vary the ground size, include defected ground structures (DGS), and/or electromagnetic band-gap (EBG) structures [3] and [4].

The proposed structure consists of two PIFA antennas with meandered lines as well as a parasitic patch, all of which are shorted to the ground by using a shorting strip at an appropriate location. Multi-band operation in the LTE frequency bands (Band 13 "US 700 Upper C" 746–787 MHz, Band 2 "PCS 1900" 1850–1990 MHz, Band-1 "IMT 2100" 1920–2170 MHz) and the Wi-Fi (IEEE 802.11y.2008) frequency band (3600–3700 MHz) is achieved by cutting three slots into the PIFA antenna and including interdigitated capacitive strips. A folded patch at the back side of the dielectric substrate has been connected to the meandered line to increase the electrical length of the antenna thus achieving a low first resonant frequency [5].

In this paper, a DGS/EBG structure is proposed, different shapes are investigated namely the Star-shape and the I-shape [6]. Mutual coupling between the two antenna elements is decreased by more than 65 dB. Envelope correlation coefficient (ECC) is studied to evaluate the operation of the MIMO antenna. A prototype of the antenna is fabricated and the simulated results are compared with the experimental results.

2. ANTENNA DESIGN

Figure 1 shows the antenna structure, two PIFA antenna elements are suspended on both edges of an FR4 substrate with relative permittivity of 4.4. To operate at the lower LTE frequencies and maintain a compact size, the electrical length of the antenna has been increased by using a meandering line, a parasitic patch, and a folded patch on the back side of the antenna. The total antenna electrical length is approximately a quarter-wave length of the lowest operating LTE frequency. The size of each element is $12 \times 20 \times 0.8\,\text{mm}^3$. Dimensions for the PIFA antennas are stated in [5].

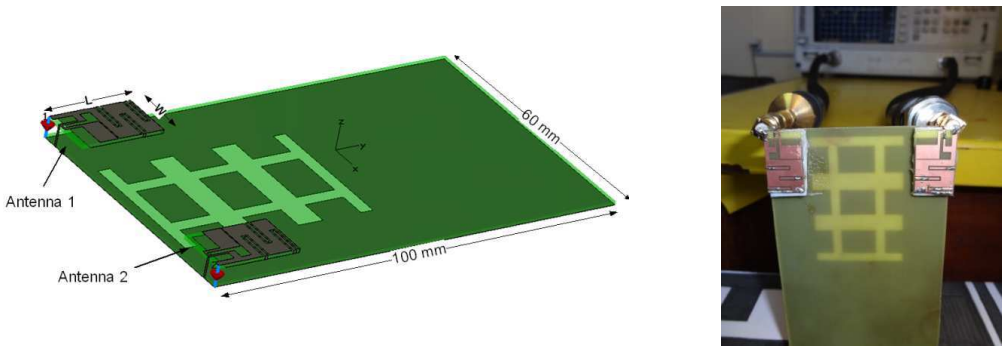

Figure 1: Proposed antenna design on CST and the fabricated prototype.

Figures 2(a) and (b) show the front and back of the antenna views, respectively. The DGS shape was etched on the ground between both antenna elements and is offset from the edge by 3 mm. Figure 2(c) shows how the DGS shape has evolved from an EBG structure with periodic I-shapes and gap g. The EBG structure in Figure 2(b) is the result of making the gap equal to zero. A Star-shape EBG has been design and is shown in Figure 2(d).

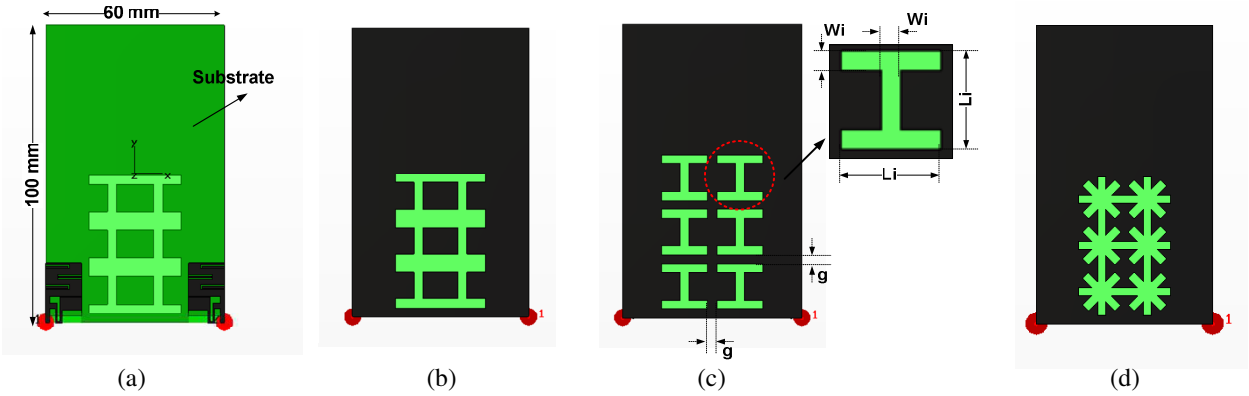

Figure 2: Antenna structure showing the antenna, (a) front view, (b) back view when $g = 0$, (c) back view when $g = 3$, and (d) back view of the proposed star-shape EBG.

The S-parameters for the proposed antenna were simulated using CST MWS and Ansoft's HFSS commercial software as shown in Figure 3. The results were compared with measurements and show good agreement.

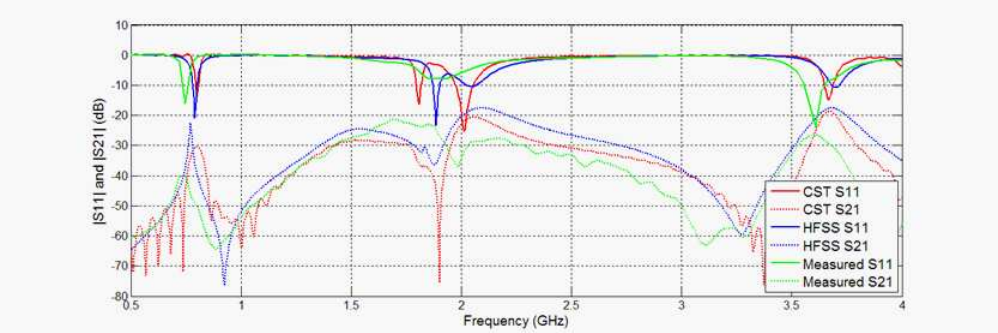

Figure 3: S-parameter simulations using CST MWS and Ansoft's HFSS, and the comparison with measurements.

3. ANTENNA ANALYSIS

PIFA antenna dimensions and parametric analysis was done exhaustively in [5], accordingly the discussions here will be focused on the proposed EBG shapes. To decrease mutual coupling between

the two antenna elements a 2D-EBG has been inserted at the center of the ground plane and offset 3 mm from the edge as seen in Figure 2(b). Several methods to decrease mutual coupling, such as substrate removal, cavity backed antennas, or the use of EBG structures, have been reported [7]. Comparisons between these methods have shown the unique capability of EBG structures in providing good isolation. The proposed I-shape and Star-shape were shown to have transmission coefficients of −75 dB and −66 dB, respectively. Figure 4 shows a decrease in mutual coupling of 65 dB at the higher LTE frequency bands as compared to the case where no DGS/EBG is employed.

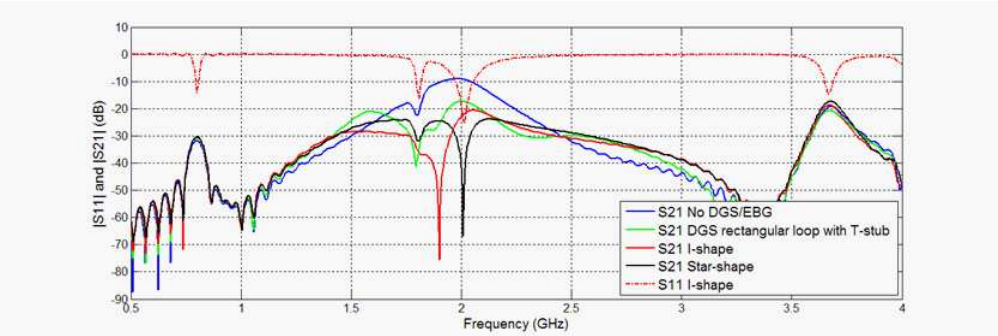

Figure 4: Simulated S-parameters on CST for (a) solid ground plane with no DGS/EBG, (b) rectangular loop DGS with T-stub [5], (c) proposed I-shape, and (d) star-shape.

Surface current distribution was simulated using CST, as shown in Figure 5 the entire PIFA structure contributes in radiation at the lower LTE frequency. Slots 2 and 3 are responsible for the majority of radiation in the higher LTE frequency, while slots 1 and 3 are responsible for radiation in the Wi-Fi frequency band.

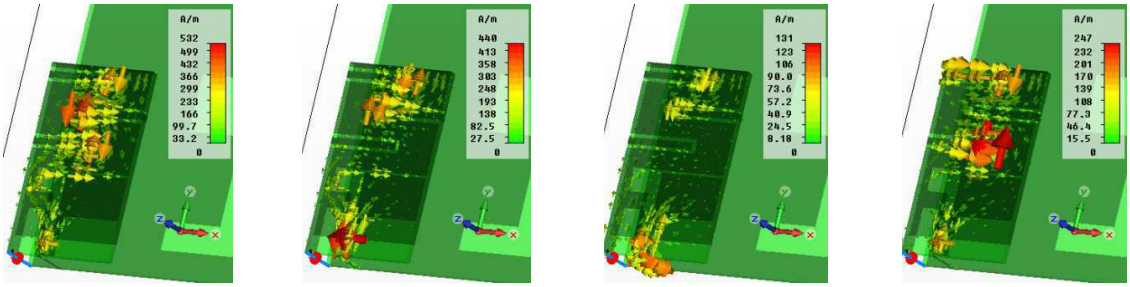

(a) (b) (c) (d)

Figure 5: Surface currents at frequencies of (a) 0.8 GHz, (b) 1.8 GHz, (c) 2 GHz, and (d) 3.6 GHz.

Figure 6 shows the simulated ECC that is calculated based on the S-parameters. The ECC for all bands is between 0.0001 and 0.01 which is well below the diversity criteria that requires ECC to be less than 0.5 [5], thus confirming the satisfactory operation of the MIMO antenna.

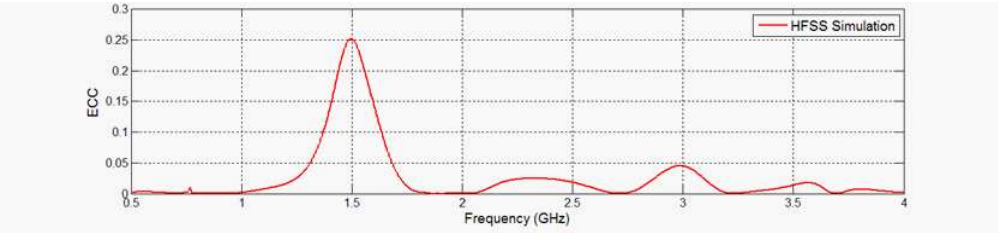

Figure 6: Envelope correlation coefficient against frequency.

Figure 7 illustrates the radiation pattern simulations on CST for all the frequency bands when exciting antenna 1 only.

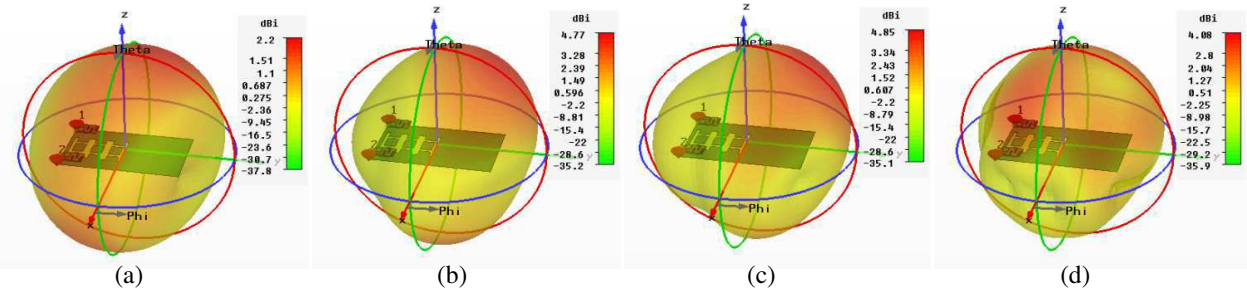

Figure 7: Radiation patterns at frequencies of (a) 0.8 GHz, (b) 1.8 GHz, (c) 2 GHz, and (d) 3.6 GHz.

4. PARAMETRIC ANALYSIS

This section presents the study performed on the effect of parameters such as Wi and Li on the S-parameters of the antenna. The DGS presented in [5] has only shown S_{21} of around -40 dB at the higher LTE frequency bands. Parametric analysis for the proposed EBG shapes in this paper show optimizations when varying the I-shape EBG width Wi and length Li. Figure 8(a) highlights the impact of varying Wi from 2.5 mm to 3.5 mm. The results show that the width can be adjusted according to the required band of operation, for the case at hand $Wi = 3$ mm has been chosen. Optimal EBG length Li has been found to be 15.5 mm in order to cover the higher LTE frequency band and at the same time achieve minimum S_{21} as seen in Figure 8(b).

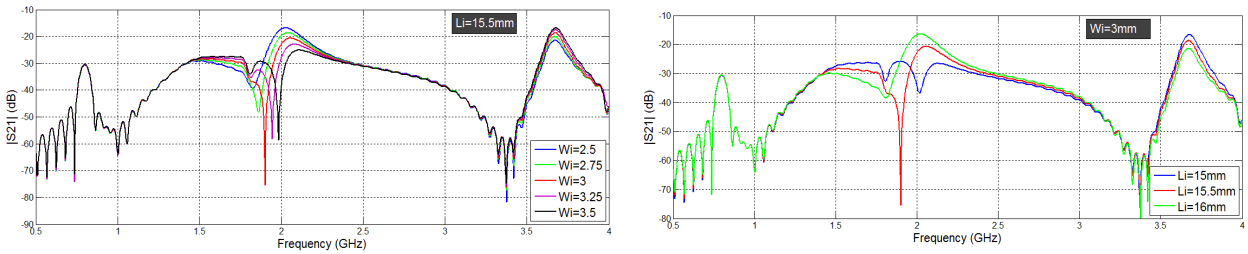

Figure 8: CST simulations showing the effect of changing the EBG dimensions (a) Wi and (b) Li on S-parameters.

5. CONCLUSION

A quad-band PIFA antenna for LTE applications was proposed in this paper. I-shape and Star-shape EBG structures have been proposed for mutual coupling reduction between MIMO antenna elements. They showed significant improvement in isolation especially in the higher LTE frequency bands. The effect of different EBG dimensions on the S-parameters was demonstrated and tuned for optimum performance. ECC was calculated and confirms the satisfactory performance of the MIMO antenna in LTE frequency bands. The proposed antenna was fabricated and measured, showing good correlation with the simulated results.

ACKNOWLEDGMENT

Khaled A. Abdelwahab would like to thank the Wireless Transmission BU, Alcatel-Lucent for their support.

REFERENCES

1. Konanur, A. S., K. Gosalia, S. H. Krishnamurthy, B. Hughes, and G. Lazzi, "Increasing wireless channel capacity through MIMO systems employing co-located antennas," *IEEE Trans. Microw. Theory Tech.*, Vol. 53, No. 6, 1837–1844, June 2005.
2. Rao, Q. and D. Wang, "A compact dual-port diversity antenna for long-term evolution handheld devices," *IEEE Trans. Veh. Technol.*, Vol. 59, No. 3, 1319–1329, March 2010.
3. Dou, W. P. and Y. W. M. Chia, "Novel meandered planar inverted-F antenna for triple-frequency operation," *Microwave Optical and Tech. Lett.*, Vol. 27, 58–60, April 2000.

4. Chen, H., K. Wong, and T. Chiou, "PIFA with a meandered and folded patch for the dual-band mobile phone application," *IEEE Trans. Antennas Propag.*, Vol. 51, No. 9, 2468–2471, September 2003.
5. Meshram, M. K., R. K. Animeh, A. T. Pimpale, and N. K. Nikolova, "A novel quad-band diversity antenna for LTE and Wi-Fi applications with high isolation," *IEEE Trans. Antennas Propag.*, Vol. 60, No. 9, 4360–4371, September 2012.
6. Nashaat, D., "Electromagnetic band-gap (EBG) structure for microstrip antenna systems (analysis and design)," Ph.D. Thesis, Faculty of Engineering, Ain Shams University, Cairo, Egypt, 2010.
7. Yang, F. and Y. Rahmat-Samii, "Microstrip antennas integrated with electromagnetic band-gap (EBG) structures: A low mutual coupling design for array applications," *IEEE Trans. Antennas Propag.*, Vol. 51, No. 10, 2936–2946, October 2003.

Reliable and Energy Efficient Communications for Wireless Biomedical Implant Systems

G. D. Ntouni, A. S. Lioumpas, and K. S. Nikita
School of Electrical and Computer Engineering, National Technical University of Athens, Greece

Abstract— During the last years, the implant devices tend to comprise a complete wireless transceiver, enabling the remote control of the monitoring. In contrast to conventional wireless communication systems, medical implants are characterized by much stricter limitations on size, reliability and power consumption, with the latter being of critical importance, since the replacement of the implants usually requires an invasive procedure.

In this paper, taking into account a realistic wireless propagation environment based on the IEEE P802.15 channel model, we investigate the system's performance in terms of the Bit error Probability under various scenarios. The results of this work indicate that the placement of the wearable relays on the human body (e.g., hip, wrist, ankle) plays an important role for both the total power consumption and the wireless link quality. Several scenarios are investigated, which give insight into the system requirements and its behavior under realistic wireless environments and power considerations.

1. INTRODUCTION

Wireless body area networks (WBANs) comprise low-power devices in, on or around the human body and are used in order to monitor physiological signals for healthcare applications [1]. More recently implant devices are used in many biomedical and clinical applications where the continuous wireless monitoring of a human body biological parameter is crucial. Ubiquity, reduced risk of infection and early diagnosis of a health risk are among the advantages of the WBANs with implant devices. Nevertheless, they usually involve an invasive procedure and therefore their reliability, low-power consumption and long-lifetime are vital characteristics that they should be provided.

In healthcare applications reliable communication implies that the communication link does not suffer from outages and that the quality of service (QoS) will be preserved within a desirable range, while maintaining the maximum transmission power below a required level. Low power transmissions are important because the radio frequency (RF) emissions may be harmful for the patients and also battery lifetime should not be reduced. The specific absorption rate (SAR), defined as the rate at which the human body absorbs RF energy, should comply with the Federal Communications Commission (FCC) regulations [2], laying out its expectations for the development and approval of new Medical Body Area Networks (MBANs), i.e., short-range, low-energy wireless networks capable of connecting medical devices together. Thus, the trade-off between transmission power and QoS is a substantial research topic of critical importance especially for WBANs.

Towards these goals, the concept of cooperative communications [3, 4] has been applied to WBANs in order to address the challenges related to energy efficiency and QoS requirements [1, 5]. In this paper, following the same concept, we consider using implantable devices employed with biosensors that transmit their measurements to an off-body access point (AP) through wearable devices which act as relays. The assessment of the performance of these systems over realistic wireless propagation channel models, especially developed for WBANs [6–9] constitutes our major motivation. Moreover, our work is also motivated by the crucial trade-off between the transmission power and the QoS requirements for medical applications involving implants. We evaluate the performance of cooperative WBANs over realistic wireless propagation channels under several scenarios with respect to the placement of the on-body wearable devices (e.g., wrist, chest). In this way, the complexity and power consumption are transferred from the implant device to the on-body relay, which is an efficient approach since they can be easily replaced, in contrast to the in-body implants.

2. SYSTEM MODEL

We consider a system model where an implant device S (source) communicates with an off-body access point D (destination), via a number of on-body devices R_i (relays), which decode-and-forward the signal they receive from the implant providing multiple copies of the transmitted signal at the destination. Specifically, we define these devices as follows: 1) Implant device: A device that

is implanted 50 mm to 90 mm under the skin. 2) Off-body device: An access point at a distance between 10 cm and 5 m away from the human body. 3) On-body or wearable device: A device on the surface of the human skin or at most 20 mm away from it.

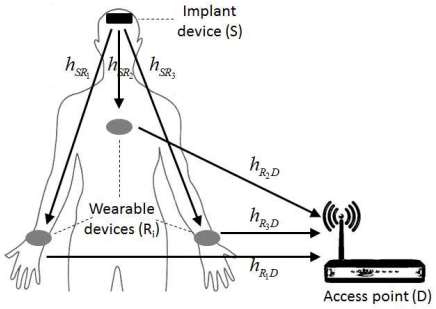

Figure 1: System model overview.

Denoting P_s and P_r as the transmitted power by the source and relay respectively, h_{SR} and h_{RD} as the channel coefficients between source-relay (S-R link) and relay-destination (R-D link) and N_0 as the power spectral density of the zero mean complex additive white gaussian noise introduced by the receiving device,

$$\gamma_{SR_i} = \frac{P_s \cdot |h_{SR_i}|^2}{N_0} \quad \text{and} \quad \gamma_{R_iD} = \frac{P_r \cdot |h_{R_iD}|^2}{N_0} \tag{1}$$

denote the instantaneous signal-to-noise ratio (SNR) of S-R_i and R_i-D links respectively.

3. CHANNEL MODEL

The IEEE P802.15.6 is working on understanding the RF signal propagation inside and around the human body and has already created realistic channel models for different scenarios and frequency bands which are used in biomedical applications [7]. In this paper, the communication channel from the implant to the off-body device (S-D link) is divided into two subchannels, the first one from the implant to the on-body device S-R_i and the second one from the on-body to the off-body device R_i-D, each of the which was modeled according to the IEEE P802.15.6 working group recommendations.

In order to serve biomedical applications the Federal Communication Commission (FCC) has adopted rules regarding the frequency bands and power limitations to support the development and use of medical Body Area Network devices [2]. The frequency bands used for communication in implant technology are the Medical Implant Communication Service (MICS) standing for the frequency band 402–405 MHz and the Industrial, Scientific and Medical (ISM) radio band between 2360 and 2400 MHz. Besides that, the MICS standard, established by FCC, recommends that the transmission power should be 25 µW in order to avoid the danger of EM emmisions for the human health [10], while the total noise power is −110.92 dBm at MICS and −117.73 dBm at ISM [10].

3.1. The S-R Communication Link

The statistical path loss model describing the power loss of the S-R link in MICS frequency band at a distance d between them, is expressed in dB as

$$P_L(d) = P_L(d_0) + 10n \log_{10} \frac{d}{d_0} + S \tag{2}$$

where $P_L(d_0)$ is the path loss in dB at a reference distance $d_0 = 50$ mm, n is the path loss exponent and $S \sim \mathcal{N}(0, \sigma^2)$ is a random variable that is normally distributed, the exact values of these parameters can be found in [6].

The squared absolute value of the channel gain h is connected with the path loss in dB as follows

$$|h_{SR}|^2 = 10^{-\frac{P_L(d)[\text{dB}]}{10}} \tag{3}$$

and using (2) and (3) it can be easily observed that

$$|h_{SR}|^2 = 10^{-\frac{P_L(d_0)+10n\log_{10}\frac{d}{d_0}}{10}} 10^{-\frac{S}{10}} = a10^{-\frac{S}{10}}, \tag{4}$$

It should be noted that the channel is not normalized, which means that when calculating the *SNR* of the channel, the path loss and shadowing effects are taken into account. This may make our comparisons a little bit more difficult, but offers accuracy as it deters the introduction of inconsistencies while comparing performances of systems in different environments.

When S is a normally distributed random variable with mean 0 and standard deviation σ, $Z = 10^{-\frac{S}{10}}$ has Log-normal distribution with $\mu_{\log} = 0$ and $\sigma_{\log} = \frac{\sigma \ln(10)}{10}$ [11, Ch. 5]. Thus, the *SNR* of the S-R link given by (1) can be expressed as

$$\gamma_{SR} = \frac{aP_s}{N_0} 10^{-\frac{S}{10}} \tag{5}$$

and has Log-normal distribution with $\mu_{\gamma_{SR}} = \ln(a\frac{P_s}{N_0})$ and $\sigma_{\gamma_{SR}} = \frac{\sigma \ln(10)}{10}$.

3.2. The R-D Communication Link

The path loss of the R-D link $P_{L_{RD}}$ at ISM frequency band depends on the distance and the orientation between the two devices, the wearable device location on body and the human subject motion. Thus, the best fitting distribution for these scenarios may be Log-normal, Gamma or Nakagami-m with appropriate parameters [6].

Taking into account that $|h_{RD}|^2 = P_{L_{RD}}$ and defining the signal-to-noise ratio (*SNR*) of the R-D link as

$$\gamma_{RD} = \frac{P_r |h_{RD}|^2}{N_0}, \tag{6}$$

the distribution that the *SNR* of this link has can be specified for each of the possible scenarios.

3.2.1. The Gamma Model

The path loss of the link $P_{L_{RD}}$ may also have Gamma distribution with shape parameter k and scale parameter θ. This implies that γ_{RD} (6) has Gamma distribution with $k_{\gamma_{RD}} = k$, scale parameter $\theta_{\gamma_{RD}} = \frac{P_r}{N_0}\theta$.

3.2.2. The Log-normal Model

For the case that the path loss $P_{L_{RD}}$ is log-normally distributed with location parameter μ and scale parameter σ, it can be inferred that γ_{RD} (6) has Log-normal distribution with $\mu_{\gamma_{RD}} = \mu + \ln(\frac{P_r}{N_0})$ and $\sigma_{\gamma_{RD}} = \sigma$ [11].

3.2.3. The Nakagami-m Model

For the case that the path loss of the R-D link has Nakagami-m distribution with parameters m and Ω, it can be inferred that γ_{RD} has also Nakagami-m distribution with parameters $m_{\gamma_{RD}} = m$ and $\Omega_{\gamma_{RD}} = \frac{P_r}{N_0}\Omega$.

4. PERFORMANCE ANALYSIS AND NUMERICAL RESULTS

4.1. Simulations

In the following we examine and compare the performance of the presented scheme in terms of the BER and the power transmission. The in-body device is implanted below the head skin at a depth of 60 mm monitoring brain edema for example, while the average horizontal distance between the walking human subject and the off-body access point is 2 m, with an orientation of 0 rads. Moreover, the relays may be placed either on the chest at a distance of about 30 cm from the implant or on the right wrist at a distance of about 50 cm away from the implant. We examine four different scenarios, depending on the position and the number of utilized relays: i) One relay on the chest ii) One relay on the wrist iii) One relay on the chest and one relay on the wrist iv) Two relays on the wrist.

The frequency of 402 MHz is employed for the transmission from the implant to the relays (S-R) and the frequency of 2.36 GHz from the relays to the off-body access point (R-D). The transmission power allocated to the relays may differ from that allocated to the implant device (P_{t_i}) as it can be easily observed by the values of the *SNR* in the boxes of all the following figures, where indices *i-c* and *i-w* stand for the implant to chest or wrist relay (S-R) link respectively and *c-o* and *w-o* for the chest or wrist relay to access point (R-D) link respectively. At this point, it should be noted that there is a constant difference between the average *SNR* of the implant-to-chest relay channel and the implant-to-wrist relay channel, i.e., $\overline{SNR}_{i\text{-}w} = \overline{SNR}_{i\text{-}c} - 9.36\,\text{dB}$.

4.2. Results

Figures 2(a) and 2(b) illustrate the BER of the communication link between an implant and an off-body device through a relay placed on the chest and the wrist respectively. The first observation that can be made concerns the impact of the relay transmission power. It can be easily observed that increasing the relay power improves the system performance until the BER reaches a ceiling. This occurs because the BER of the overall S-D communication link is determined by the worst link (S-R or R-D). This fact indicates the criticality of the communication link between the implant and the wearable device. Moreover, the importance of the relay position on the human body becomes evident by comparing the performance when either the chest or the wrist relay is employed. More specifically, placing the relay on the chest provides a better performance than placing it on the wrist.

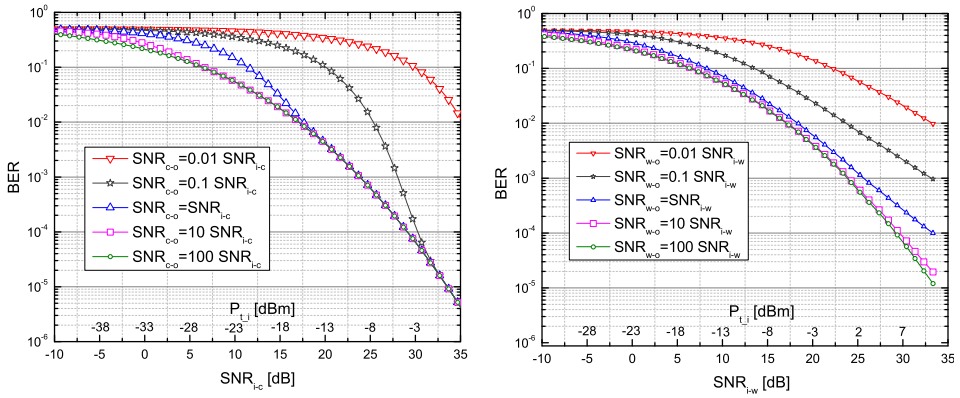

Figure 2: BER of the communication link between an implant and an off-body device through a relay placed (a) on the chest or (b) on the wrist.

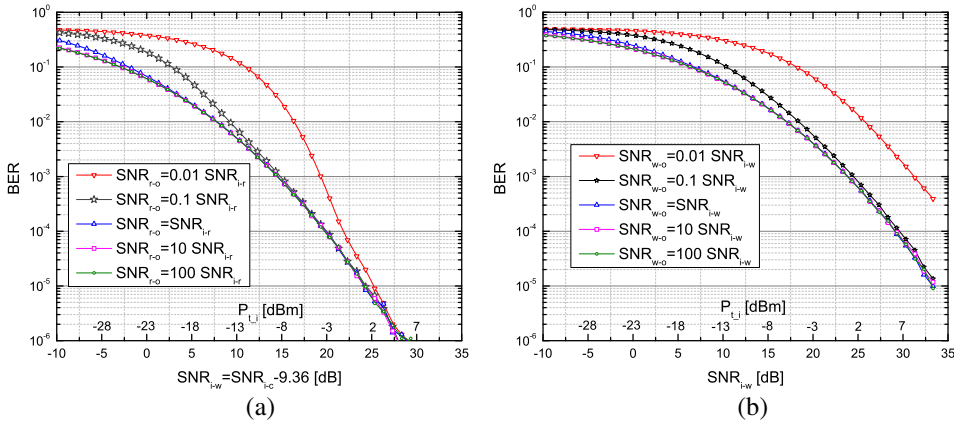

Figure 3: BER of the communication link between an implant and an off-body device through two relays placed (a) on the chest and the right wrist or (b) two relays both placed on the right wrist.

The performance of the system when two relays are employed simultaneously is illustrated in Fig. 3(a), where $\frac{SNR_{r\text{-}o}}{SNR_{i\text{-}r}} = \frac{SNR_{c\text{-}o}}{SNR_{i\text{-}c}} = \frac{SNR_{w\text{-}o}}{SNR_{i\text{-}w}}$. As depicted, depending on the channel conditions, employing two relays may not always result in sufficiently improved performance compared with the single relay case. For example, it can be seen that the performance gain that stems from adding a wrist relay is negligible, when a chest relay is already in use.

On the other hand, when the two relays that we used simultaneously are placed in the same part of the body, the system performance improves. This can be observed in Fig. 3(b) where two relays placed on the right wrist are used simultaneously. It is obvious that the system performance improves until it becomes replete and its performance is determined only by the S-R link efficiency from then on. Concerning the amount of power required, it was observed that the device consuming the greater amount of power is the implant placed inside the human body. Besides that, the performance of the S-R link is much worse than that of the R-D link, although it requires more power. For instance, the amount of power transmitted by the right wrist relay should be 10^5 times

lower than that of the implant in order for the mean *SNR* of the two links to be equal.

In conclusion, taking into account that the transmission power of the implant device should be 25 μW (−16 dBm) in order to avoid dangers of EM emissions for the human health, it can be inferred by the figures that increasing the transmission power of the relay is vital for our achieving a satisfactory error probability.

5. CONCLUSION

In this paper, we have evaluated the performance of the communication links between an implant and an off-body access point which communicate through relays. It was shown that the communication link that consumes the greatest amount of power and in most cases determines the performance of the whole system is the S-R link from the implant to the relay. This comes from the fact that the link influencing the total BER is that with the worst performance. Placing relays at the human body improves the system's reliability and proves to be energy efficient. However, there is a threshold in the amount of the relay transmission power above which the system becomes replete and then its performance is totally determined by the S-R link. Moreover, the part of the human body where the relay will be placed is an important parameter and the most advantageous location among those examined was proved to be the chest. Finally, using multiple relays is not always considered to be efficient, as the location where they will be placed and the way they will be combined strongly influences their performance.

ACKNOWLEDGMENT

The project is co-financed by the European Union (European Social Fund — ESF) and Greek national funds through the Operational Program "Education and Lifelong Learning" of the National Strategic Reference Framework (NSRF) — Research Funding Program: ARISTEIA, project 68/1142 DEMII-MED, Implantable and Ingestible MEdical Devices (IIMDs): Optimal-Performance-Oriented Design and Evaluation Methodology.

REFERENCES

1. Arrobo, G. E. and R. D. Gitlin, "Improving the reliability of wireless body area networks," *Proceedings of the Annual International Conference of the IEEE Engineering in Medicine and Biology Society, EMBC, 2011*, 2192–2195, Boston, USA, Aug. 2011.
2. Federal Communications Commission, "Rules and regulations: Medical area body network," *Federal Register*, Vol. 77, No. 176, 55715–55735, Sep. 2009.
3. Hong, Y.-W., W.-J. Huang, F.-H. Chiu, and C.-C. J. Kuo, "Cooperative communications resource constrained wireless networks," *IEEE Signal Process. Mag.*, Vol. 24, No. 3, 47–57, May 2007.
4. Michalopoulos, D. S., A. S. Lioumpas, G. K. Karagiannidis, and R. Schober, "Selective cooperative relaying over time-varying channels," *IEEE Transactions on Communications*, Vol. 58, No. 8, 2402–2412, 2010.
5. Smith, D. B. and D. Miniutti, "Cooperative body-area-communications: First and second-order statistics with decode-and-forward," *Proceedings of the IEEE Wireless Communications and Networking Conference (WCNC)*, 689–693, Paris, Apr. 2012.
6. Yazdandoost, K. Y. and K. Sayrafian-Pour, "Channel model for body area network (BAN)," *IEEE802.15.6 Technical Contribution*, Document ID: 15-08-0780-09-0006, 41–56, 2009.
7. Miniutti, D., L. Hanlen, D. Smith, A. Zhang, D. Lewis, D. Rodda, and B. Gilbert, "Narrowband on-body to off-body channel characterization for body area networks," *IEEE802.15.6 Technical Contribution*, Document ID: 15-08-0780-09-0006, Aug. 2008.
8. Oh, J. Y., J. H. Kim, H. S. Lee, and J. Y. Kim, "PSSK modulation scheme for high-data rate implantable medical devices," *IEEE Transactions on Information Technology in Biomedicine*, Vol. 14, No. 3, 634-640, May 2010.
9. Kim, M. and J. I. Takada, "Characterization of wireless on-body channel under specific action scenarios at sub-GHz bands," *IEEE Transactions on Antennas and Propagation*, Vol. 60, No. 11, 5364–5372, Nov. 2012.
10. Abouei, J., J. D. Brown, K. N. Plataniotis, and S. Pasupathy, "Energy efficiency and reliability in wireless biomedical implant systems," *IEEE Transactions on Information Technology in Biomedicine*, Vol. 15, No. 3, 456–466, May 2011.
11. Papoulis, A., *Probability, Random Variables and Stochastic Processes*, 3rd Edition, McGraw-Hill Kogakusha, 1991.

Numerical Investigation of Body-worn Ultra Wideband Antenna Localisation Techniques for Motion Capture Applications

Richa Bharadwaj, **Akram Alomainy**, **and Clive Parini**
School of Electronic Engineering and Computer Science, Queen Mary University of London
Mile End Road, London E1 4NS, United Kingdom

Abstract— This paper presents study of accurate body worn antennas localisation using Ultra Wideband time of arrival techniques. The localisation results obtained in presence of no obstacle are compared with those obtained in the presence of obstacles (e.g. wood and glass objects) near the base stations. Results show that accuracy in estimation of location of the sensor depends on position where it is placed on the human body as the presence of body would cause interference. It is observed that different base stations give different received signal output depending on line of sight (LOS) or non line of sight (NLOS). As expected there is more error obtained in estimation of sensor positions located on the human model due to presence of obstacles. The average accuracy in 3D localisation is around 2.5 to 4.5 cm when no obstacle is present. Presence of obstacle leads to reduction in accuracy of results (2 to 3 cm reduction) with glass showing higher (4 to 6 cm) average error in comparison to wood (3 to 4.5 cm).

1. INTRODUCTION

Localisation and motion tracking using body-worn sensors is emerging as an important research area based on Ultra Wideband (UWB) technology. Motion tracking itself is motivated by a variety of applications such as training of athletes, patient monitoring in medicine, localisation of people in home or office environment. The choice of sensors such as compact, efficient and low cost UWB antenna makes human localisation and activity monitoring a promising new application made possible by advances in UWB technology. Impulse Radio UBW technology offers various advantages such as high accuracy, robustness, low cost, high data rate, robustness towards multipath, ease of implementation and low energy consumption making it suitable for short range human localisation [1].

There are various wireless technologies available for human tracking and localisation such as infrared, ultrasound and Radio Frequency (RF) based technologies. Infrared signals are low power, and inexpensive but they cannot penetrate through obstructions, e.g. opaque objects require line of sight between transmitter and receiver and they are also susceptible against sunlight [2–4]. Ultrasound signals provide high accuracies in the short range. The systems based on ultrasound technology are relatively cheap but the precision is lower in comparison with IR-based systems. Radio frequency is used most commonly for localization purpose because these signals can penetrate through obstacles and can propagate to long distances. The RF signals are classified into narrow band (Radio Frequency Identification (RFID) and Wireless Local Area Network (WLAN)) and Ultra Wideband technology [4]. In the literature amongst these technologies, the ultra short pulse UWB based systems give high accuracy and due to its low power can carry signals through many obstacles that usually reflect signals at more limited bandwidths and at higher power [2–6]. An accuracy of 10 to 15 cm is achieved in commercial localisation systems with operating range of 50 cm [7] and also sub-millimetre range accuracy is possible using carrier based UWB systems as proposed in literature [6]. Thus UWB localisation has a widespread usage including localization of body worn sensors.

In this paper UWB 3D human body localisation is studied using 14 different sensors on the body using CST simulations in presence of different obstacles and the accuracy is compared with situation when no obstacle is present. The objective of the work is to achieve accurate localisation of the human body using data fusion time of arrival and peak detection techniques.

2. HUMAN BODY MODEL AND FULL WAVE METHOD SIMULATIONS

The frequency range used in the simulation is from 3 to 4 GHz and sine modulated Gaussian pulse is used for signal transmission. Single layer human body model consisting of muscle tissue having dielectric permittivity at 3.5 GHz (centre frequency) with 14 sensors is simulated using CST Microwave Studio [8]. The height of the human body is 1.72 m and has average built. The Tapered Slot UWB antennas [9] (Fig. 1) are used as sensors and base stations (BS), which are

positioned near the vertices of a cuboid (Fig. 2) which has dimensions of $2 \times 2 \times 1.8\,\mathrm{m}^3$. The TSA antenna is compact, cost effective and omni directional [10]. The TSA antenna has excellent impedance matching with return loss below $-10\,\mathrm{dB}$ and radiation performance in the UWB range with relatively constant gain across the whole frequency band. The total antenna size is $27\,\mathrm{mm} \times 16\,\mathrm{mm}$.

The position of the BS antennas is chosen in such a way that localisation information can be obtained accurately in 3 dimensional (3D) with respect to BS1 [10]. Block of glass ($150 \times 150 \times 5$) cm^3 and wood ($100 \times 100 \times 20$) cm^3 have been considered as objects that act like obstacles during the localisation simulation. The sensors are placed around 5 to 10 mm away from the human body surface mostly at the joints and the torso totalling to 14 on body sensors.

(a) (b)

Figure 1: Tapered slot UWB antenna (a) CST model and (b) fabricated antenna.

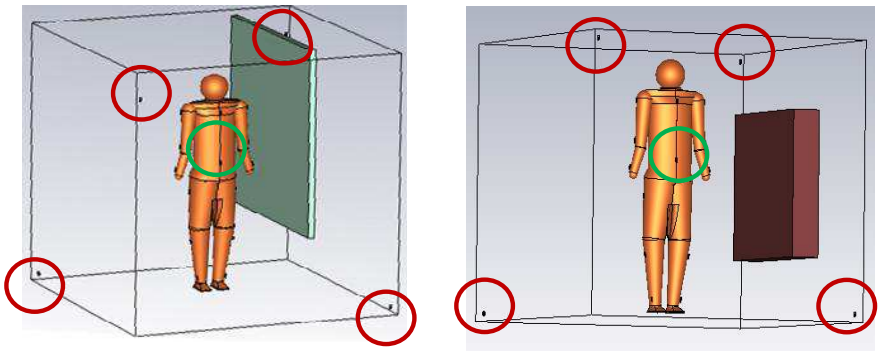

(a) (b)

Figure 2: Human body model with body worn sensors (green circle) that are localised using cuboid shape base station configuration (Base Station: red circle) with (a) glass and (b) wood as obstacle.

3. TIME OF ARRIVAL LOCALISATION TECHNIQUES

The Time of Arrival (TOA) based positioning outperforms other techniques such as Received Signal Strength (RSS) based, Angle of Arrival (AOA) based positioning due to fine time resolution of the UWB signal.The time of arrival between the mobile and base stations is estimated by considering the signal transmission in CST [9]. The first peak above 10% threshold of the normalized UWB pulse is considered for finding the time difference between the received and transmitted pulse. The time difference obtained is the TOA from the transmitted pulse from the target antenna to the receiver antenna which is one of the base stations.

The time of arrival data fusion method [1, 12] is used to find the unknown coordinates of the mobile station (MS) which is based on combining estimates of the TOA of the MS signal that arrives at four different BSs. Since the wireless signal travels at the speed of light ($c = 3 \times 10^8\,\mathrm{m/s}$), the distance between the MS and BSi is given by

$$r_i = (t_i - t_0)\, c \tag{1}$$

where t_0 is the time instant at which the MS begins transmission and t_i is the TOA of the MS signal at BSi. Let r_1, r_2, r_3 and r_4 represent the range measurements obtained from TOA measurements. The following four equations are solved jointly in order to estimate the position of the target (x_m,

$y_m,\ z_m$) via trilateration:

$$r_i^2 = (x_i - x_m)^2 + (y_i - y_m)^2 + (z_i - z_m)^2 \quad i = 1, 2, 3, 4 \tag{2}$$

4. RESULTS AND DISCUSSION

Figure 3(a) shows the estimated and actual sensor positions; good localisation accuracy is achieved with an average error of 2.5 to 4.5 cm for the situation of no obstacle. It is observed that the overall error in estimation of position reduces from sensor near the shoulder towards the sensor near the wrist. A similar trend of decrease in error is observed for the sensors placed near the thigh to the ankle. The average decrease in error is from 1–3 cm for arms and 2–4 cm for legs. The reason for the variation in error is that the sensor is near the torso for the case of shoulder and thighs which causes interference. The error obtained for the x, y and z coordinates show different range of localisation error (Fig. 3(b)) which can be related to the antenna radiation pattern, orientation of the antenna, presence of obstacles and base station configuration. 55% of the estimated values have localisation error of less than 3 cm. The average localisation accuracy for directional azimuth and elevation angles estimation is approx. 1 to 2 degrees.

Table 1: Cartesian coordinates: average error.

Case	**Average Estimated Error (cm)**		
	***X* axis**	***Y* axis**	***Z* axis**
None	2.77	2.578	4.48
Woo	3.95	4.04	4.79
Glas	4.50	6.5	6.7

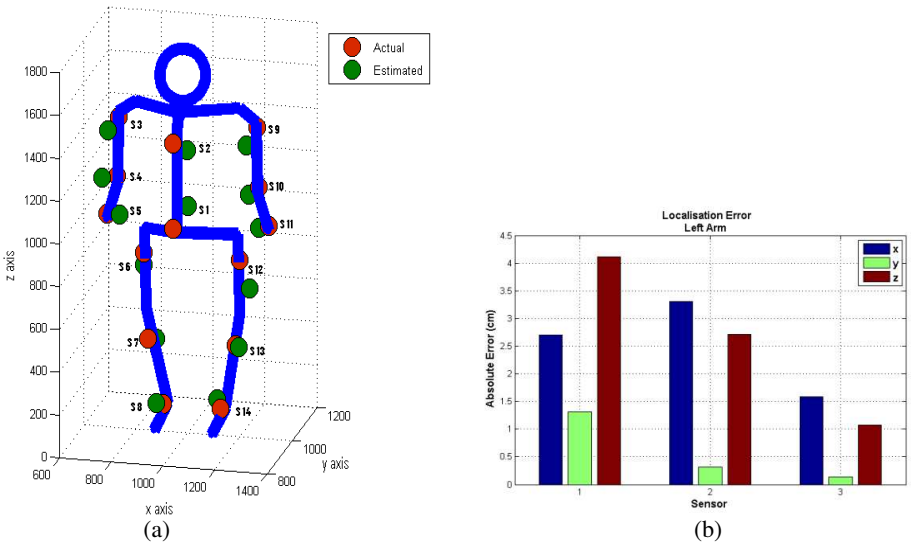

(a) (b)

Figure 3: Sensor locations (a) on the body comparing actual positions and estimated positions for TOA when no obstacle is present. (b) Example of localisation obtained for the left arm through TOA method. It is observed that the overall error reduces from sensor 1 (near the shoulder) towards the sensor 3 (near the wrist). Also the error obtained for the x, y and z coordinates are showing different range of error obtained.

Block of glass and wood are considered as objects that act like obstacles during the localisation simulation. The position of the sensors and base station antennas are kept same as that of the case with no obstacle present. It is observed that there is distortion in received pulse leading to variation in range value between base station and sensor on the body. More variation, delay and distortion of received signal is observed for glass object as it has higher permittivity of 4.28 in comparison to wood which has a permittivity of 1.4 and also has larger dimensions than that of wooden block. It is observed that different base stations give different received signal output depending on line of sight (LOS) or non line of sight situation (NLOS) [13]. Considering an example of senor 5 which is placed near the arm, the BS 2 is in NLOS situation with respect to the sensor which gives rise to

more reflections and wave distortions (Fig. 4(b)). BS 3 is in (line of Sight) LOS range of the sensor 5. Hence, similar waveforms are obtained for the three different cases studied for BS 3 (Fig. 4(a)). As expected there is more error obtained in estimation of sensor positions located on the human model due to presence of obstacles. Table 1. summarises the error obtained for the three different cases: no object present, wood and glass. The overall average accuracy in 3D localisation is around 2.5 to 4.5 cm using time of arrival data fusion method. Presence of obstacle leads to reduction in accuracy of results (2 to 3 cm reduction) with glass showing higher decrease (4 to 6 cm) of average error in comparison to wood (3 to 4.5 cm).

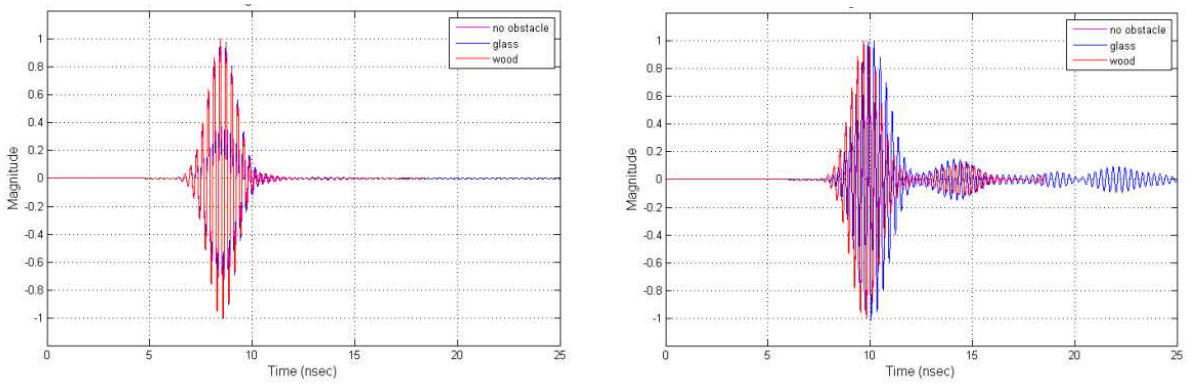

Figure 4: (a) Received signal between BS 3 and sensor 5 (LOS), (b) BS 2 is in NLOS range of sensor 5 for the three different cases.

5. CONCLUSION

Accurate human body localisation has been achieved using compact body worn sensors placed at different locations on the body using Ultra wideband technology. Presence of different obstacles and effect of human body on localisation accuracy has been analysed through simulations. The overall average accuracy in 3D localisation is around 2.5 to 4.5 cm using time of arrival data fusion method. Presence of obstacle leads to reduction in accuracy of results (2 to 3 cm reduction) with glass showing higher (4 to 6 cm) average error in comparison to wood (3 to 4.5 cm). Future work will be to consider realistic indoor experiment scenarios and perform body worn sensor localisation using compact and efficient UWB localisation system.

REFERENCES

1. Sahinoglu, Z., S. Gezici, and I. Guvenc, *Ultra-Wideband Positioning Systems: Theoretical Limits, Ranging Algorithms, and Protocols*, Cambridge University Press, Cambridge, U.K., 2008.
2. Gezici, S. and H. V. Poor, "Position estimation via ultra-wide-band signals," *Proceedings of the IEEE*, Vol. 97, No. 2, 386–403, Feb. 2009
3. Mekonnen, W., E. Slottke, H. Luecken, C. Steiner, and A. Wittneben, "Constrained maximum likelihood positioning for UWB based human motion tracking," *International Conference on Indoor Positioning and Indoor Navigation, IPIN 2010*, 1–10, Zurich, Switzerland, Sept. 2010
4. Zhang, D., F. Xia, Z. Yang, L. Yao, and W. Zhao, "Localization technologies for indoor human tracking," *Proceedings of the IEEE International Conference on Future Information Technology (FutureTech'10)*, Pusan, Korea, May 2010.
5. Clarke, A. P., "Active-RFID system accuracy and its implications for clinical applications," *IEEE Symp. Computer-Based Med. Sys.*, 21–22, Salt Lake City, USA, 2006.
6. Mahfouz, M. R., A. E. Fathy, M. J. Kuhn, and Y. Wang, "Recent trends and advances in UWB positioning," *IEEE MTT-S International Microwave Workshop on Wireless Sensing, Local Positioning, and RFID, IMWS 2009*, 1–4, Sept. 24–25, 2009.
7. Mitilineos, S. A., D. M. Kyriazanos, O. E. Segou, J. N. Goufas, and S. C. A. Thomopoulos, "Indoor localisation with wireless sensor networks," *Progress In Electromagnetics Research*, Vol. 109, 441–474, 2010.

8. Ur Rehman, M., Y. Gao, X. Chen, and C. G. Parini, "Effects of human body interference on the performance of a GPS antenna," *European Conference on Antennas and Propagation (EuCap)*, Edinborough, UK, November 2007.
9. Alomainy, A., A. Sani, A. Rahman, J. G. Santas, and H. Yang, "Transient characteristics of wearable antennas and radio propagation channels for ultrawideband body-centric wireless communications," *IEEE Transactions on Antennas and Propagation*, Vol. 57, No. 4, 875–884, April 2009.
10. Bharadwaj, R., A. Alomainy, and C. Parini, "Study of ultra wideband localisation techniques using various monitoring configurations," *2012 6th European Conference on Antennas and Propagation (EUCAP)*, 2035–2038, March 26–30, 2012.
11. Cheung, K. W., H. C. So, W. K. Ma, and Y. T. Chan, "Least squares algorithms for time-of-arrival-basedmobile location," *IEEE Transactions on Signal Processing*, Vol. 52, No. 4, 1121–1128, 2004.
12. Sayed, A. H., A. Tarighat, and N. Khajehnouri, "Network-based wireless location: challenges faced in developing techniques for accurate wireless location information," *IEEE Signal Processing Magazine*, Vol. 22, No. 4, 24–40, July 2005.
13. Seow, C. K. and S. Y. Tan, "Localization of omni-directional mobile device in multipath environments," *Progress In Electromagnetics Research*, Vol. 85, 323–348, 2008.

Characterization of Electro-textiles Using Wireless Reflectometry for Optimization of Wearable UHF RFID Tags

K. Koski[1], **E. Moradi**[1], **A. Vena**[1], **T. Björninen**[1], **L. Sydänheimo**[1], **L. Ukkonen**[1], **and Y. Rahmat-Samii**[2]

[1]Tampere University of Technology, Tampere, Finland
[2]University of California, Los Angeles, CA, USA

Abstract— Flexible and maintenance-free wearable ultra-high frequency (UHF) radio frequency identification (RFID) tag antennas are desired in wireless sensor systems in security, healthcare, and biomedical applications. Optimization of wearable antennas demands comprehensive knowledge of the electrical properties of the conductive electro-textiles used in the antenna structure. In this paper, we first propose a wireless reflectometry technique to accurately extract the sheet resistance of various electro-textiles. The technique relies on the measurement of the resonant peak of a scatterer. Its bandwidth and magnitude are strongly correlated with the conductive losses of the strips so that a relationship can be extracted. We then demonstrate that the electro-textiles, including conductive fabrics and embroidery textiles, can be accurately modeled using the sheet resistance as the only conductive material parameter for wearable antenna design.

1. INTRODUCTION

Wearable body-centric radio frequency identification (RFID) supports the wellness of people and play a key role in the development toward independent living. Wireless monitoring of people by means of low power and low cost technology is nowadays considered as one of the most promising features of wearable body-centric RFID systems [1, 2]. These systems include electronic devices, and sensing and signal processing abilities to enable functions such as monitoring of human vital signs [3], human movement and tracking [4], and detection of parameters of the environment, e.g., temperature or toxic gases. Wearable antennas play a key role in establishing a reliable and an efficient wireless communication link between body-worn electronics and the surrounding environment. These inexpensive antennas should be comfortable to wear and totally maintenance-free. Typically the wearable antenna is using conductive flexible materials that are easy to integrate with clothing [2]. These conductive materials are known as electro-textiles and include embroidery structures created from conductive threads and commercially available conductive fabrics Wearable passive UHF (860–960 MHz) RFID tag antennas are of great interest thanks to their low cost, easy integrability, and large communication ranges. They contribute toward an intelligent environment, where tag antennas will be seamlessly integrated with daily garments to enable wireless body-centric communication everywhere and at anytime [5].

As new unconventional materials for wearable antennas are emerging, it is of paramount importance to characterize their applicability in body-centric systems. Compared to conductive fabrics, embroidered structures are inhomogeneous. The conductivity is dependent on the direction of the current flow in the structure and the structure stitching density [2]. The thickness of the structure is not unambiguously defined. This creates challenges in modeling the embroidered structures for wearable antenna design.

In this paper we eliminate the uncertainty related to the embroidered structure thickness by using the sheet resistance as the modeling parameter. First, we apply wireless reflectometry to characterize the sheet resistance for two different embroidered patterns and for three different conductive fabrics. We then design and simulate dipole tag antennas using the measured sheet resistance as the only electro-textile modeling parameter. Finally, to verify the validity of the electro-textile model, we fabricate and measure dipole tag antennas in terms of their theoretical read ranges and we compare the measured read ranges with corresponding simulated values.

2. WIRELESS REFLECTOMETRY MEASUREMENTS

2.1. Radar Cross Section Measurements

We determine the sheet resistance for three different conductive fabrics from LessEMF; pure copper taffeta fabric (35% copper); ripstop silver fabric (pure silver coated onto nylon); and stretch fabric (silver plated 76% nylon 24% elastic fiber). Additionally, we characterize two different embroidered

structures. The wireless reflectometry measurement technique relies on the measurement of the resonant peak of a scatterer. The bandwidth and magnitude of the scatterer resonance peak is strongly correlated with the conductive losses of the scatterer strips so that a relationship can be extracted. We fabricate a scatterer of each electro-textile, in total five scatterers (Figure 1). We implement the scatterers on 100 µm-thick Kapton substrate ($\varepsilon_r = 3.5$ and $\tan\delta = 0.0027$). This substrate is thin and low-loss so it does not contribute substantially to the overall losses of the scatterer. The scatterer overall losses are mainly determined by the conductor to be characterized. The scatterers reflect a given electromagnetic response when illuminated by a plane wave. A resonant mode can be observed at a specific frequency, which is determined by the physical size of the scatterer. The scatterer dimensions are set by simulating a bulk copper reference scatterer in CST Microwave studio.

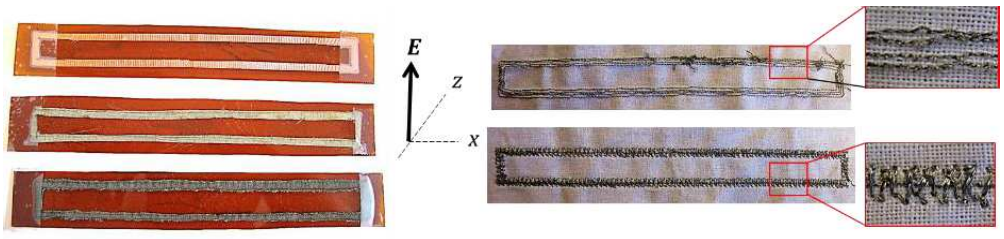

(a) (b)

Figure 1: Scatterers for wireless reflectometry measurements fabricated using different electro-textiles; (a) up to down: copper fabric; ripstop fabric; and stretch fabric; (b) up to down: embroidery 1 with threads aligned along the current flow; and embroidery 2 with threads aligned perpendicular to the current flow. The scatterer length, width and strip width are 158 mm, 16 mm, and 3 mm, respectively.

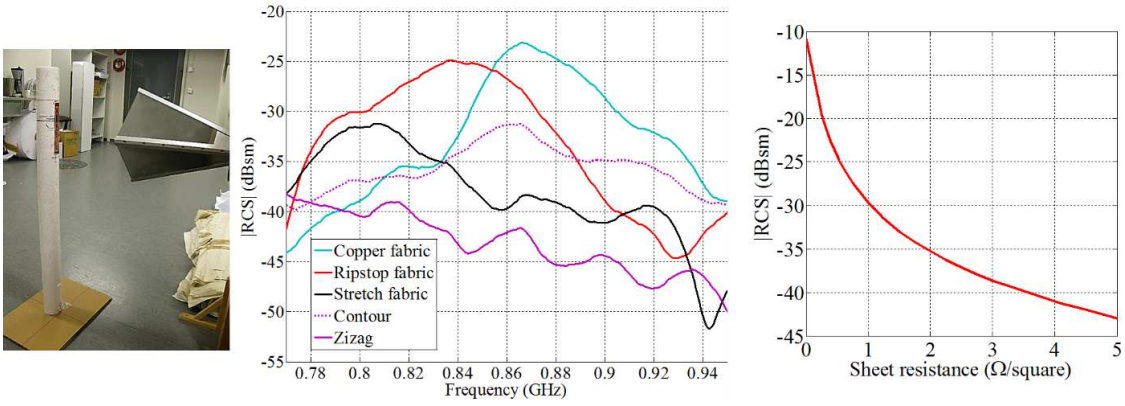

(a) (b) (c)

Figure 2: (a) Measurement set-up in mono-static configuration for monitoring of the RCS in horizontal polarization; (b) |RCS| measurement results for the fabricated scatterers in horizontal polarization; (c) correlation between electro-textile sheet resistance and measured peak RCS magnitude value.

We use a frequency-domain measurement set-up described in [6] to monitor the monostatic radar cross section (RCS) of the fabricated scatterers in horizontal polarization. The measurement set-up is shown in Figure 2(a). A two-port vector network analyzer (VNA) Agilent PNA E8358A is connected to a dual-polarized antenna ETS Lindgren 3164-04.

Using this configuration, the S_{11}^{scat} parameter is measured. The measured scattering parameter comprises the electromagnetic response from the scatterer and the background in horizontal polarization. Using a calibration technique explained in [6] and [7] we are able to separate the scatterer response from the background response. For this purpose, we first conduct an isolation (S_{11}^{iso}) measurement with no scatterer to exclude all static noise from the environment. Then, a measurement with a metallic rectangular plate (S_{11}^{ref}) having a known RCS (σ^{ref}) based on an analytical formula is conducted. The technique allows receiving the scatterer response in a real environment outside

an anechoic chamber. The scatterer RCS is attained using (1)

$$\sigma^{scat} = \left[\frac{S_{11}^{scat} - S_{11}^{iso}}{S_{11}^{ref} - S_{11}^{iso}}\right]^2 \sigma^{ref}. \tag{1}$$

The measured RCS magnitudes for the fabricated scatterers are shown in Figure 2(b). It can clearly be observed that the copper and ripstop fabrics are better conductors compared to the stretch fabric. The RCS magnitude values for embroidery 1 are greater than for embroidery 2, which supports the results in [2]. Next, the results presented in Figure 2(b) are used for sheet resistance extraction.

2.2. Sheet Resistance Extraction

We are able to accurately extract the sheet resistance values for the electro-textiles by comparing the height of the resonant peak in the measured and simulated scatterer monostatic RCS. Using CST Microwave studio we model the scatterer as an infinitely thin conductor having the sheet resistance as the only material parameter. Simulating the RCS with plane wave excitation for different sheet resistance values, we can find a correlation between the measured peak RCS magnitude and the sheet resistance value as shown in Figure 2(c).

From Figure 2(c), we attain a sheet resistance value of $0.40\,\Omega/\square$ for the copper fabric, $0.55\,\Omega/\square$ for the ripstop fabric, $1.25\,\Omega/\square$ for the stretch fabric and embroidery 1, and $4.5\,\Omega/\square$ for the embroidery 2. The sheet resistance accuracy is related to the measured RCS. Figure 2(c) shows that the slope of the curve is higher for lowsheet resistance values. Hence, low sheet resistance values are more accurate, as a large RCS change will give a small sheet resistance change.

3. ELECTRO-TEXTILE RFID TAG ANTENNA

3.1. RFID Tag Antennas Using Conductive Fabric

The achieved sheet resistance value of each electro-textile is further validated by designing, fabricating and measuring T-matched dipole tags made of the conductive fabrics. First, a 50 µm-thick copper tag operating in the UHF RFID frequencies is designed using ANSYS HFSS v.15 and the NXP UCODE G2iL SL3S1203AC0 chip model [8]. We then simulate the two-dimensional footprint of the designed copper tag with the sheet resistance value of each electro-textile separately. In simulations, the antenna is modeled as a sheet with zero thickness. A maximum mesh length of 1 mm is used on the antenna structure to increase the accuracy. Two prototypes from each electro-textile are fabricated to estimate the performance difference between two identical dipoles. We evaluate the tags in terms of their theoretical read range in an anechoic chamber (Figure 3(a)). The used RFID measurement system enables monitoring the tag reply as a function of transmitted power and transmission frequency. A calibration tag in the system hardware allows us to measure the wireless channel path loss L_{fwd} in the chamber, which is defined from the transmitter's output port to the input port of a hypothetic polarization-matched isotropic antenna aligned at the measurement plane. After channel characterization, we record the threshold power P_{th} from each tag. This is the minimum output power required to read the information stored in the IC of the tag. The measured theoretical read range is computed as

$$d_m = \frac{\lambda}{4\pi}\sqrt{\frac{\text{EIRP}}{L_{fwd}P_{th}}}, \tag{2}$$

where EIRP is the maximum equivalent isotropically radiated power allowed by local regulations (3.28 W in Europe). Simulation based read range is computed using equation

$$d_s = \frac{\lambda}{4\pi}\sqrt{\frac{\tau G_{\text{tag}}\text{EIRP}}{P_{\text{IC, sens}}}}, \quad \tau = \frac{4R_A R_{\text{IC}}}{|Z_A + Z_{\text{IC}}|^2} \tag{3}$$

where λ is the wavelength, τ is the tag antenna to IC power transfer coefficient, Z_A and Z_{IC} are the tag antenna and IC impedances, respectively, G_{tag} is the tag antenna gain, and $P_{\text{IC, sens}}$ is the sensitivity of the IC. As Figure 3(b) shows, there is up to 0.8 m read range difference between the measurement results of two identical dipoles. Considering this difference, we can claim that the simulation results match well with the measurement results. This proves the validity of the measured sheet resistance of the electro-textiles.

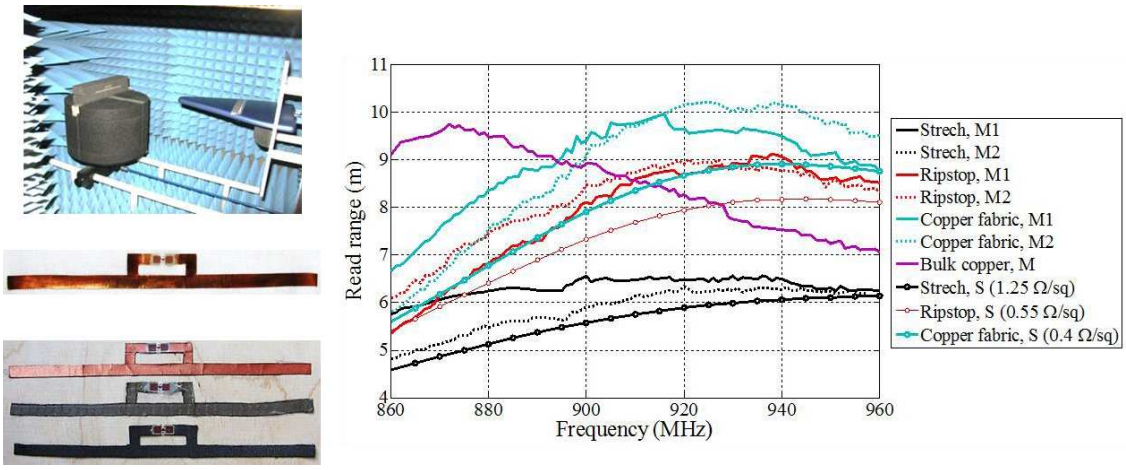

Figure 3: (a) Up to down: measurement setup; bulk copper dipole; copper fabric dipole; ripstop fabric dipole; and stretch dipole; (b) simulation and measurement results of the fabricated dipoles. In the legend, 'S' and 'M' correspond to simulation and measurement results, respectively.

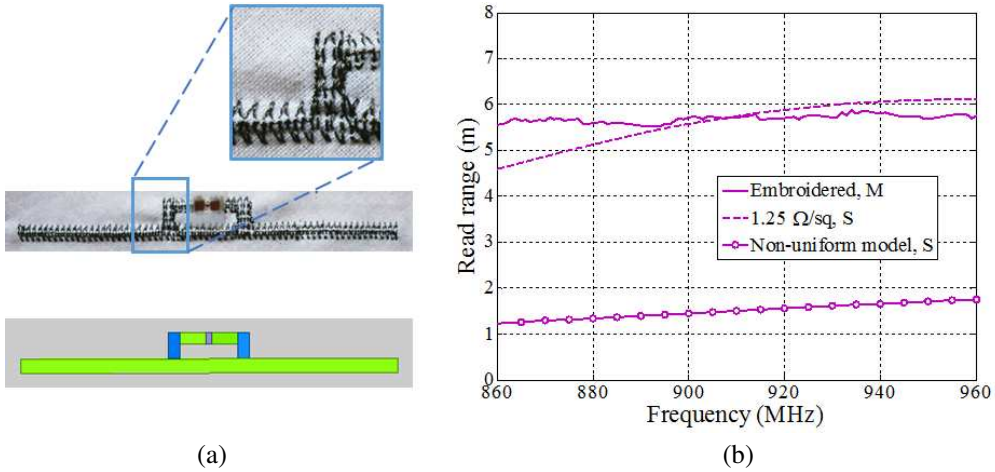

Figure 4: (a) Embroidered dipole and the non-uniform simulation model; (b) measurement results of the embroidered dipole, simulation results of a flat uniform simulation model with a sheet resistance of 1.25 Ω/□, and simulation results of the non-uniform structure.

3.2. Embroidered RFID Tag Antenna

Previously, embroidered dipoles have been modeled as uniform structures with distinct thickness and conductivity. In this paper, we have characterized an embroidered dipole as a two-dimensional object with a distinct sheet resistance. The dipole is embroidered on cotton using Shieldex 110f34 dtex 2-ply HC conductive thread.

As Figure 4(a) shows, the embroidered T-matched dipole consists of two regions (embroidery 1 and embroidery 2). The vertical sections of the T-matching network are made of the embroidery 1 structure, while the horizontal sections of the T-matching network and the dipole part are made of the embroidery 2 structure. In simulations, we model the embroidered dipole using two distinct regions (Figure 4(a)). The blue areas are assigned with a sheet resistance corresponding to that of the embroidery 1 structure (1.25 Ω/□). The green areas are assigned with a sheet resistance value corresponding to that of the embroidery 2 structure (4.5 Ω/□). This non-uniform model achieves read ranges 4 m less than the measured read range values. However, measured read ranges of the embroidered dipole match with the simulated read ranges of a uniform dipole with a sheet resistance of 1.25 Ω/□. Thus, we cannot model the embroidered dipole as a structure composed of distinct regions. Instead, it is better approximated as a continuous uniform structure. The simulated gains for the uniform and non-uniform models are similar. However, the simulated power transfer coefficient τ for the non-uniform model is significantly poorer compared to the uniform model. This

implies that the input impedance of the model is drastically changed when a non-uniform model is used. According to (3) a poorer impedance matching with all other parameters almost the same results in a shorter read range, as seen in Figure 4(b).

4. CONCLUSION

Characterization of electro-textile materials is necessary for wearable antenna design and optimization. We presented a wireless reflectometry technique to determine the sheet resistance for various electro-textiles. The measured sheet resistance values were used in the modeling of electro-textile dipole-type RFID tags. Our measurement results of fabricated electro-textile wearable RFID tags verified that our simulation model provides good agreement with the measured values. Future work includes design and optimization of electro-textile RFID tag antennas using the electro-textiles and the embroidery strip patterns studied in this paper. For this purpose sheet resistance values will be used as they make a useful and reliable parameter for future designs.

ACKNOWLEDGMENT

This work was supported by the Academy of Finland, Centennial Foundation of Finnish Technology Industries, the TUT Foundation, and the Finnish Funding Agency for Technology and Innovation (TEKES).

REFERENCES

1. Occhiuzzi, C., S. Cippitelli, and G. Marrocco, "Modeling, design and experimental of wearable RFID sensor tag," *IEEE Trans. Antennas Propag.*, Vol. 58, No. 8, 2490–2498, Aug. 2010.
2. Moradi, E., K. Koski, L. Ukkonen, Y. Rahmat-Samii, T. Björninen, and L. Sydänheimo, "Embroidered RFID tags in body-centric communication," *Proc. 2013 iWAT Conf.*, 362–365, Karlsruhe, Germany, Mar. 4–6, 2013.
3. Marrocco, G., "RFID for the remote monitoring of human subjects," *IEEE Trans. Antennas Propag.*, Vol. 55, No. 6, 1862–1870, Jun. 2007.
4. Rajagopalan, H. and Y. Rahmat-Samii, "Conformal RFID antenna design suitable for human monitoring and metallic platforms," *Proc. EuCAP Conf.*, 5 pages, Barcelona, Spain, Apr. 12–16, 2010.
5. Manzari, S., S. Pettinari, and G. Marrocco, "Miniaturized and tunable wearable RFID tag for body-centric applications," *Proc. RFID-TA Conf.*, 239–243, Nice, France, Nov. 5–7, 2012.
6. Vena, A., E. Perret, and S. Tedjini, "Chipless RFID tag using hybrid coding technique," *IEEE Trans. Microw. Theory Techn.*, Vol. 59, No. 12, 3356–3364, Dec. 2011.
7. Wiesbeck, W. and D. Kähny, "Single reference, three target calibration and error correction for monostatic, polarimetric free space measurements," *Proc. IEEE*, Vol. 79, No. 10, 1551–1558, Oct. 1991.
8. Björninen, T., L. Sydänheimo, and L. Ukkonen, "Development and validation of an equivalent circuit model for UHF RFIC IC based on wireless tag measurements," *Proc. AMTA Symp.*, 6 pages, Bellevue, WA, USA, Oct. 21–26, 2012.

Magnetic Field Expulsion in Perfect Conductors — The Magnetic Equivalent of Thomson's Theorem

Miguel C. N. Fiolhais[1] and Hanno Essén[2]

[1]LIP, Department of Physics, University of Coimbra, Coimbra 3004-516, Portugal
[2]Department of Mechanics, KTH, Stockholm 10044, Sweden

Abstract— Thomson's theorem states that electric charge density on metal conductors, at static equilibrium, is distributed on the surface of the conductors in such a way that the interior electric field is zero, and the electric field on the surface must be perpendicular to the surface. In this paper, we present a theorem for static magnetic fields, analogous of the Thomson's theorem of electrostatics. We prove, by making use of a variational principle, that the minimization of the magnetic field energy corresponds to the magnetic field expulsion of perfect conductive systems through surface currents. As a result, the current density distributes itself on the surface of the ideal conductor so that the interior magnetic field becomes zero, and all current flows on its surface.

This result is put into the context of superconductivity, and leads us to conclude the Meissner effect is not a pure quantum effect, restricted to superconductors, but rather a magnetostatic equilibrium state as a consequence of zero resistivity. In addition, the London equations are derived following an approach by Pierre-Gilles de Gennes where *"the superconductor finds an equilibrium state where the sum of the kinetic and magnetic energies is minimum, and this state, for macroscopic samples, corresponds to the expulsion of magnetic flux"*. For further confirmation, the same result is also derived in the classical limit of the Coleman-Weinberg model, the most successful quantum macroscopic theory of superconductivity.

A specific example is presented to corroborate the result of our theorem. In particular, an explicit solution for a minimal energy magnetic field configuration is analyzed, and found to be in agreement with our statement.

1. INTRODUCTION

The Thomson's theorem of electrostatics, first presented by Lord Kelvin in 1848, states that the total electric energy on a set of fixed conductors reaches its minimal value when the electric charge is distributed on the surface of the conductors, so that the interior electric field is zero and the surface electric field is normal to the surface. In other words, the expulsion of the external static electric fields from normal conductors can be seen as the most favorable energetic configuration, i.e., the equilibrium state of the system. This conclusion is well established and has been independently proven several times in the scientific literature [1–8].

In this paper, an equivalent theorem is presented for the magnetic field in the presence of perfect conductors. In this case, the minimal energy configuration of the magnetic field corresponds to the expulsion of the magnetic field from the interior of the perfect conductors through surface currents. This leads us to believe that the magnetic field expulsion from superconductors, first observed in 1933 by Walther Meissner and Robert Ochsenfeld [9], corresponds to a magnetostatic equilibrium state, as a direct consequence of zero resistivity.

This conclusion is not new though, in the sense that it has been independently presented in the scientific literature throughout the past decades [10–18]. However, it is often left aside in most textbooks on the subject, which attribute the phenomenon to quantum effects. This does not imply in any way that superconductivity itself is not a quantum effect, the authors do not support such idea. Instead, the magnetic field expulsion is not restricted to superconductors, appearing as a general property of any hypothetical perfect conductive system.

2. MAGNETIC ENERGY THEOREM

In a system of fixed perfect conductors in the presence of a magnetic field, the total energy of the system corresponds to the integration of the magnetic energy density over the full space. Since the magnetic field can be written as $\mathbf{B} = \nabla \times \mathbf{A}$, and $(\nabla \times \mathbf{A})^2 = \nabla \cdot [\mathbf{A} \times (\nabla \times \mathbf{A})] + \mathbf{A} \cdot [\nabla \times (\nabla \times \mathbf{A})]$,

the total magnetic energy can be expressed as,

$$\begin{aligned} E_{\mathrm{B}} &= \frac{1}{8\pi}\int \mathbf{B}^2 \mathrm{d}V \\ &= \frac{1}{8\pi}\int \mathbf{B}^2 \mathrm{d}V_{\mathrm{int}} + \frac{1}{8\pi}\int \mathbf{B}^2 \mathrm{d}V_{\mathrm{out}} \\ &= \frac{1}{8\pi}\int (\nabla\times\mathbf{A})^2\,\mathrm{d}V_{\mathrm{int}} + \frac{1}{8\pi}\int (\nabla\times\mathbf{A})^2\,\mathrm{d}V_{\mathrm{out}} \\ &= \frac{1}{8\pi}\int \nabla\cdot[\mathbf{A}\times(\nabla\times\mathbf{A})] + \mathbf{A}\cdot[\nabla\times(\nabla\times\mathbf{A})]\,\mathrm{d}V_{\mathrm{int}} \\ &\quad + \frac{1}{8\pi}\int \nabla\cdot[\mathbf{A}\times(\nabla\times\mathbf{A})] + \mathbf{A}\cdot[\nabla\times(\nabla\times\mathbf{A})]\,\mathrm{d}V_{\mathrm{out}}\,, \end{aligned} \tag{1}$$

where "int" stands for the perfect conductive regions, and "out" for the outer region. By making use of Gauss's theorem, and the Maxwell's equation, $\nabla\times\mathbf{B} = 4\pi\mathbf{j}/c$, the previous equation can be rewritten as,

$$E_{\mathrm{B}} = \frac{1}{2c}\int \mathbf{j}\cdot\mathbf{A}\,\mathrm{d}V_{\mathrm{int}} + \frac{1}{2c}\int \mathbf{k}\cdot\mathbf{A}\,\mathrm{d}S + \frac{1}{2c}\int \mathbf{j}_{\mathrm{src}}\cdot\mathbf{A}\,\mathrm{d}V_{\mathrm{src}} \tag{2}$$

where S corresponds to the surface of the perfect conductive region, while the last term corresponds to the external source of the magnetic field in the outer region. Note that in this last term, the electric current, $\mathbf{j}_{\mathrm{src}}$, is set by the external source.

For the electric current density in the interior volume, one can write the following relation:

$$\nabla\cdot(\lambda\mathbf{j}) = \lambda\nabla\cdot\mathbf{j} + \nabla\lambda\cdot\mathbf{j}\,, \tag{3}$$

where λ is a scalar function in space, and will work as a Lagrange multiplier. Using the continuity equation and Gauss's theorem, Eq. (3) becomes,

$$\int \nabla\lambda\cdot\mathbf{j}\,\mathrm{d}V_{\mathrm{int}} = \int \nabla\cdot(\lambda\mathbf{j})\;\mathrm{d}V_{\mathrm{int}} = \int \lambda\mathbf{j}\cdot\mathrm{d}\mathbf{S} = 0, \tag{4}$$

since the current density cannot point outwards at the surface. In a similar fashion, using the continuity equation for the surface current and Green's theorem, the following relation,

$$\nabla_{\mathrm{S}}\cdot(\lambda\mathbf{k}) = \lambda\nabla_{\mathrm{S}}\cdot\mathbf{k} + \nabla_{\mathrm{S}}\lambda\cdot\mathbf{k}\,, \tag{5}$$

turns into,

$$\int \nabla_{\mathrm{S}}\lambda\cdot\mathbf{k}\,\mathrm{d}S = \int \nabla_{\mathrm{S}}\cdot(\lambda\mathbf{k})\,\mathrm{d}S = \oint \lambda\mathbf{k}\cdot\hat{\mathbf{n}}\,\mathrm{d}l = 0\,, \tag{6}$$

where $\hat{\mathbf{n}}$ is the outward-pointing unit normal vector on the boundary. After implementing these Lagrange multipliers terms, the magnetic energy becomes,

$$E_{\mathrm{B}} = \frac{1}{2c}\int \mathbf{j}\cdot(\mathbf{A}-\nabla\lambda)\,\mathrm{d}V_{\mathrm{int}} + \frac{1}{2c}\int \mathbf{k}\cdot(\mathbf{A}-\nabla_{\mathrm{S}}\lambda)\,\mathrm{d}S + \frac{1}{2c}\int \mathbf{j}_{\mathrm{src}}\cdot\mathbf{A}\,\mathrm{d}V_{\mathrm{src}} \tag{7}$$

By minimizing this total energy as a function of the volume and surface currents, the result is,

$$\delta E_{\mathrm{B}} = \frac{1}{2c}\int \delta\mathbf{j}\cdot(\mathbf{A}-\nabla\lambda)\,\mathrm{d}V_{\mathrm{int}} + \frac{1}{2c}\int \delta\mathbf{k}\cdot(\mathbf{A}-\nabla_{\mathrm{S}}\lambda)\,\mathrm{d}S\,. \tag{8}$$

Since the current in the source region of the magnetic field is set by the external conditions, and can be seen as a boundary condition, it is not subject to variations. As a result, in the interior perfectly conducting region, the magnetic vector potential becomes $\mathbf{A} = \nabla\lambda$, which implies that the magnetic field and the volume current are zero in this region. The magnetic vector potential also becomes tangent to the surface at the boundary, $\mathbf{A} = \nabla_{\mathrm{S}}\lambda$. In conclusion, *the magnetic energy is minimized by surface current distributions such that the magnetic field is zero in the interior of the perfectly conducting region, while the surface magnetic vector potential is tangent to the surface* [8].

3. MEISSNER EFFECT IN SUPERCONDUCTORS

The Meissner effect is often deceptively used to distinguish perfect conductors from superconductors. In fact, Meissner himself claimed there was no classical explanation for the flux expulsion, upon the discovery of the effect, because the Ohm's law infinite conductivity implies there can be no change in the magnetic field, since this would give rise to an infinite current density. This reasoning is however flawed: Ohm's law is not applicable in the zero resistance limit, as inertia prevents infinite currents [18].

Of course, a superconductor is not just a simple perfect conductor, as it comprises a much richer phenomenology [19–23], and the very nature of zero resistivity can only be explained with quantum mechanics [24–26]. In particular, the presence of a quartic interaction at the macroscopic level gives rise to first- and second-order phase transitions between the ohmic and superconductive states, according to the Ginzburg-Landau theory [27]. Nonetheless, it is clear the magnetic field expulsion appears as a direct consequence of zero resistivity, corresponding to a magnetostatic equilibrium state, and not a genuine quantum effect [18].

These conclusions have been independently derived several times in the scientific literature. In particular, Pierre-Gilles de Gennes presented a more general derivation of the flux expulsion in his textbook *Superconductivity of Metals and Alloys* using a minimum energy principle [11]. In this derivation, at absolute zero the internal energy density of a superconductor is written as the sum of the electromagnetic field energy density $\mathcal{U}_{EM}$, the kinetic energy density of the moving superconducting charge carriers $\mathcal{U}_K$, and the condensation energy $\mathcal{U}_S$:

$$\mathcal{U} = \mathcal{U}_S + \mathcal{U}_{EM} + \mathcal{U}_K = \mathcal{U}_S + \frac{1}{8\pi}\mathbf{B}^2 + \frac{1}{2}nm\mathbf{v}^2, \tag{9}$$

where n is the density of charge carriers of mass m and charge e. In this low temperature limit, the drift velocity of the free electrons is approximately equal to their total velocity. Using Maxwell's equation and $\mathbf{j} = en\mathbf{v}$, the total energy of the system becomes:

$$E_{\mathrm{B}} = \int \mathcal{U}_S + \mathcal{U}_{EM} + \mathcal{U}_K \,\mathrm{d}V = \int \mathcal{U}_S \,\mathrm{d}V + \frac{1}{8\pi}\int \mathbf{B}^2 + \lambda_L^2 \left(\nabla \times \mathbf{B}\right)^2 \,\mathrm{d}V, \tag{10}$$

where n is assumed to be constant in the region where there is current, and the London penetration depth is,

$$\lambda_L = \sqrt{\frac{mc^2}{4\pi n e^2}}\,. \tag{11}$$

Assuming the condensation energy is constant while the remaining two terms vary in response to external field variations, the energy minimum corresponds precisely to the London equation [28] for the magnetic flux expulsion,

$$\mathbf{B} - \lambda_L^2 \nabla^2 \mathbf{B} = 0. \tag{12}$$

This conclusion is presented in de Gennes book as: *"The superconductor finds an equilibrium state where the sum of the kinetic and magnetic energies is minimum, and this state, for macroscopic samples, corresponds to the expulsion of magnetic flux"*. Moreover, as shown in [29], the London equations can also be derived using the classical limit of the Coleman-Weinberg model [30], the most successful quantum macroscopic theory of superconductivity. The London equation for the flux appears naturally as the the time-independent variational equation derived from classical Lagrangian of the Coleman-Weinberg model, i.e., without applying any quantum corrections.

4. EXAMPLE

In this paper, we will stick to a very simple example which explicitly shows the decrease of the magnetic energy in the presence of a superconductor. Let's consider two infinite cylindrical surfaces (depicted in Figure 1) along the z-axis with an inner radius R_2 and an outer radius R_1. Assuming an uniform current I flows in the inner cylindrical surface in the z-axis direction, and the same current value flows in the opposite direction in the outer cylindrical surface, the magnetic field all over space is given by,

$$\mathbf{B} = \begin{cases} 0\,, & \text{if } \rho < R_2 \\ (2/c)(I/\rho)\,\hat{\phi}\,, & \text{if } R_2 \le \rho \le R_1 \\ 0\,, & \text{if } \rho > R_1 \end{cases} \tag{13}$$

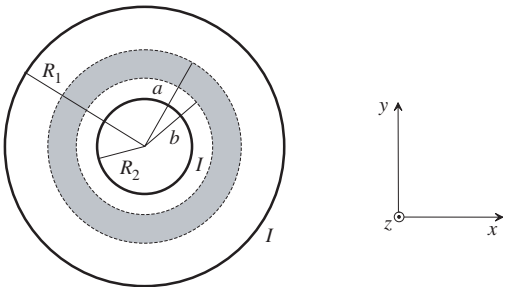

Figure 1: Transverse view of the cylinders system in the xy plane.

which leads to a total energy per segment L of the cylinder,

$$\mathcal{U}/L = \frac{1}{8\pi}\int \mathbf{B}^2 \mathrm{d}V = \frac{I^2}{c^2}\log\frac{R_1}{R_2}\,. \tag{14}$$

Now let's consider there is a hollow superconductor in between the two surfaces, with inner radius b and outer radius a. In order to ensure a zero magnetic field inside the superconducting region, the current in the inner superconducting surface must flow uniformly with the same magnitude but in the opposite direction of the current at $\rho = R_2$. Of course the current in the superconductor must be conserved, so there must also exist an uniform current in the outer superconducting surface with the same magnitude but in the opposite direction to compensate the one at $\rho = b$. As a result, the magnetic field is now,

$$\mathbf{B} = \begin{cases} 0\,, & \text{if } \rho < R_2 \\ (2/c)(I/\rho)\,\hat{\phi}\,, & \text{if } R_2 \le \rho \le b \\ 0\,, & \text{if } b \le \rho \le a \\ (2/c)(I/\rho)\,\hat{\phi}\,, & \text{if } a \le \rho \le R_1 \\ 0\,, & \text{if } \rho > R_1 \end{cases} \tag{15}$$

and the magnetic energy becomes,

$$E_{\mathrm{B}}/L = \frac{1}{8\pi}\int \mathbf{B}^2 \mathrm{d}V = \frac{I^2}{c^2}\log\frac{R_1}{R_2} - \frac{I^2}{c^2}\log\frac{a}{b}\,. \tag{16}$$

It is thus obvious the magnetic energy decreases when the region between $b \le \rho \le a$ becomes superconducting, with a magnetic field energy variation of $\Delta E_{\mathrm{B}}/L = -(I^2/c^2)\log(a/b)$. Several other explicit solutions of minimum magnetic energy can be found in [8].

5. CONCLUSIONS

A theorem on the magnetic energy minimum in a system of perfect, or ideal, conductors was presented. This result was derived using the variational principle, analogously to Thomson's theorem on the equilibrium electric field and charge distribution in a system of normal conductors. The magnetic energy is minimized when the current distribution is a surface current density with zero interior magnetic field, or in other words, perfect conductors are perfectly diamagnetic in the magnetostatic equilibrium. This agrees with the magnetic field expulsion in superconductors, and implies that Meissner effect is a direct result of zero resistivity. A specific example presented in this paper shows explicitly the decrease of the magnetic field energy in the presence of a superconductor.

REFERENCES

1. Jackson, J. D., *Classical Electrodynamics*, 3rd Edition, John Wiley & Sons, New York, 1999.
2. Coulson, C. A., *Electricity, Oliver and Boyd*, 3rd Edition, Edinburgh, 1953.
3. Panofsky, W. K. H. and M. Phillips, *Classical Electricity and Magnetism*, 2nd Edition, Dover, New York, 2005.
4. Landau, L. D. and E. M. Lifshitz, *Electrodynamics of Continuous Media*, 2nd Edition, Butterworth-Heinemann, Oxford, 1984.
5. Bakhoum, E. G., *J. Electrostatics*, Vol. 66, 561, 2008.
6. Kovetz, A., *Electromagnetic Theory*, Oxford University Press, Oxford, 2000.

7. Sancho, M., J. L. Sebastián, and V. Giner, *Eng. Sci. Educ. J.*, Vol. 10, 26, 2001.
8. Fiolhais, M. C. N., H. Essén, C. Providencia, and A. B. Nordmark, "Magnetic field and current are zero inside ideal conductors," *Progress In Electromagnetics Research B*, Vol. 27, 187–212, 2011.
9. Meissner, W. and R. Ochsenfeld, *Naturwiss*, Vol. 21, 787, 1933.
10. Cullwick, E. G., *Proc. IEE, Part C, Monographs*, Vol. 103, 441, 1956.
11. De Gennes, P. G., *Superconductivity of Metals and Alloys*, Perseus books, Reading, 1999.
12. Pfleiderer, J., *Nature*, Vol. 210, 614, 1966.
13. Karlsson, P. W., *Arch. f. Elektrotech*, Vol. 67, 29, 1984.
14. Badía-Majós, A., *Am. J. Phys.*, Vol. 74, 1136, 2006.
15. Kudinov, E. K., *Phys. Solid State*, Vol. 48, 1147, 2006.
16. Mahajan, S. M., *Phys. Rev. Lett.*, Vol. 100, 075001, 2008.
17. Essén H., *Europhys. Lett.*, Vol. 94, 47003, 2009.
18. Essén, H. and M. C. N. Fiolhais, *Am. J. Phys.*, Vol. 80, 164, 2012.
19. Abrikosov, A. A., *Zh. Eksp. Teor. Fiz.*, Vol. 32, 1442, 1957.
20. Halperin, B. I., T. C. Lubensky, and S. Ma, *Phys. Rev. Lett.*, Vol. 32, 292, 1972.
21. Kleinert, H., *Lett. Nuovo Cimento*, Vol. 35, 405, 1982.
22. Kleinert, H., *Europhys. Lett.*, Vol. 74, 889, 2006.
23. Kleinert, H., *Gauge Fields in Condensed Matter*, Vol. I, World Scientific, Singapore, 1989.
24. Cooper, L. N., *Phys. Rev.*, Vol. 104, 1189, 1956.
25. Bardeen, J., L. N. Cooper, and J. R. Schrieffer, *Phys. Rev.*, Vol. 106, 162, 1957.
26. Bardeen, J., L. N. Cooper, and J. R. Schrieffer, *Phys. Rev.*, Vol. 108, 1175, 1957.
27. Ginzburg, V. L. and L. D. Landau, *Zh. Eksp. Teor. Fiz.*, Vol. 20, 1064, 1950.
28. London, F. and H. London, *Proc. Roy. Soc. A*, Vol. 149, No. 866, 71, 1935.
29. Fiolhais, M. C. N. and H. Essén, *Int. J. Theor. Phys.*, Vol. 52, 1701, 2013.
30. Coleman, S. and E. Weinberg, *Physical Review D*, Vol. 7, 1888, 1973.

The Darwin-Breit Magnetic Interaction and Superconductivity

H. Essén[1] **and M. C. N. Fiolhais**[2]

[1]KTH, Sweden
[2]University of Coimbra, Portugal

Abstract— A number of facts indicating the relevance of the Darwin magnetic interaction energy in the superconducting phase are pointed out. The magnetic interaction term derived by Darwin is the same as the, so called, Breit term in relativistic quantum mechanics. While this term always is a small perturbation in few body systems it can be shown to be potentially dominating in systems of large numbers of electrons. It is therefore a natural candidate in the explanation of emergent phenomena — phenomena that only occur in sufficiently large systems. The dimensionless parameter that indicates the importance of the magnetic energy is the number of electrons times the classical electron radius divided by the size of the system. The number of electrons involved are only the electrons at the Fermi surface; electrons with lower energy cannot contribute to current density and thus not to the magnetic field.

The conventional understanding of superconductivity has always been problematic and no really reductionistic derivation exists. The idea that the inductive inertia, due to magnetism, is important in the explanation of superconductivity was first advanced by Frenkel and later brought up by Welker before it was prematurely discarded. So were theories involving Wigner crystallization. We speculate that the answer requires the combination of a Wigner lattice and the Darwin interaction. We point out that the Darwin interaction can be shown to have the right order of magnitude to explain the energy scales involved in normal superconductors. The London magnetic moment of rotating superconductors and the Meissner effect and their connection are discussed next. The London moment is shown to indicate that the number of electrons involved in the superconducting condensate is such that the Darwin interaction cannot be neglected.

1. INTRODUCTION

The standard understanding of superconductivity, at least of the original low temperature type, is, since the Bardeen-Cooper-Schrieffer (BCS) publication in 1957 [1, 2], that it is due to phonons. These are assumed to produce an attractive interaction in a way analogous to the photon mediated electromagnetic interaction in vacuum. While this theory is microscopic in the sense that results are derived from the interaction between electrons it can not be considered as a fundamental theory since electrons do only have weak and electromagnetic interactions. There is no fundamental coupling constant for electron-phonon interactions, nor is the analogy between phonons and photons convincing for several reasons. The typical speed of phonons is the speed of sound and this speed is much lower that the typical speed of conduction electrons which is the Fermi velocity. Phonons are by definition acoustic and represent changes in mass density or velocity. Hence there is no electromagnetic effect associated with them, except possibly as some higher order effect. In fact most evidence on phonon coupling to the superconducting electrons can be interpreted as the destruction of the condensate by lattice oscillations. Consequently many theoretical physicists of accomplishment and integrity are still trying to understand the superconducting phase-transition from a more fundamental point of view (Hirsch [3, 4], Vasiliev [5]). We will also do this here. In particular we will point out that the magnetic interaction energy cannot be neglected.

We first point out how the magnetic interaction between electrons is very accurately described by the Darwin Lagrangian. To get some information on the quantum mechanics and statistical mechanics of the electrons one must proceed to the corresponding Hamiltonian — a non-trivial step. The various approximations to the Darwin Hamiltonian are then reviewed. After that we present some results that arise directly from electrodynamics for perfect conductors: The Meissner effect [6–8] and the London moment [9]. Finally there is a short account of how the magnetic interaction might work on electrons at the Fermi surface of metals.

2. THE DARWIN APPROXIMATION TO ELECTROMAGNETISM

In modern theoretical physics the Lagrangian formalism is considered the most basic. In 1920 Charles Galton Darwin published [10] an approximation to the electromagnetic Lagrangian that removed the field degrees of freedom. It resulted from an expansion of the retarded potentials in

v/c to second order and contains only the positions and velocities of the charged particles of the system. In this approximation all electric and magnetic effects, except radiation, are well described. This Lagrangian is,

$$L = T + \sum_a \frac{e_a}{2}\left[\frac{\mathbf{v}_a}{c}\cdot\mathbf{A}(\mathbf{r}_a) - \phi(\mathbf{r}_a)\right], \tag{1}$$

where T is the kinetic energy and ϕ is the Coulomb potential,

$$\phi(\mathbf{r}_a) = \sum_{b(\neq a)} \frac{e_b}{|\mathbf{r}_a - \mathbf{r}_b|} = \sum_{b(\neq a)} \frac{e_b}{r_{ba}}, \tag{2}$$

and (hats are used for unit vectors, gaussian units are employed),

$$\mathbf{A}(\mathbf{r}_a) = \sum_{b(\neq a)} \frac{e_b[\mathbf{v}_b + (\mathbf{v}_b\cdot\hat{\mathbf{r}}_{ba})\hat{\mathbf{r}}_{ba}]}{2cr_{ba}}, \tag{3}$$

is the form of the vector potential derived by Darwin. The form guarantees that the potential is divergence free.

To get the corresponding Hamiltonian one must perform the usual Legendre transform. This means that one must solve the equations

$$\mathbf{p}_a = \frac{\partial L}{\partial \mathbf{v}_a}, \tag{4}$$

defining the generalized momenta in terms of the velocities, to get the velocities in terms of the momenta, and then insert the result in,

$$H = \sum_a \mathbf{v}_a\cdot\frac{\partial L}{\partial \mathbf{v}_a} - L. \tag{5}$$

Even if only the non-relativistic kinetic energy, $T = \sum_a m_a\mathbf{v}_a^2/2$, is used the solution of the Equation (4) involve the inversion of a large matrix. However, again using expansion in the parameter v/c one obtains the Darwin Hamiltonian,

$$H = \sum_{a=1}^{N}\left[\frac{\mathbf{p}_a^2}{2m_a} + \frac{e_a}{2}\phi_a(\mathbf{r}_a) - \frac{e_a}{2m_ac}\mathbf{p}_a\cdot\mathbf{A}_a^p(\mathbf{r}_a)\right], \tag{6}$$

where,

$$\mathbf{A}_a^p(\mathbf{r}) = \sum_{b(\neq a)}^{N} \frac{e_b[\mathbf{p}_b + (\mathbf{p}_b\cdot\hat{\mathbf{r}}_b)\hat{\mathbf{r}}_b]}{2m_bc|\mathbf{r} - \mathbf{r}_b|}. \tag{7}$$

This, original, Darwin Hamiltonian is correct if small v/c really makes the Legendre inversion accurate. This is, however not necessarily the case for systems with large numbers of particles, and consequently this Hamiltonian may not be correct for superconductors and plasmas, or other macroscopic systems. It is possible to derive a second order correction, considered as a correction to the approximation in the Legendre transform [11, 12].

By going to a continuum point of view and assuming a constant density of charged particles one can discover that the vector potential actually must be exponentially damped, like a Yukawa potential. This was discovered by Bethe and Fröhlich [13] in 1933, independently of Darwin's work. Later this has been studied more carefully [14, 15] by starting from the Darwin formalism and also by demanding that the vector potential remains divergence free, even when there is exponential damping. The length scale of the damping,

$$\lambda = \frac{1}{\sqrt{4\pi r_e n}}, \tag{8}$$

is given by the same formula as that for the penetration depth in superconductors. Here $r_e = e^2/mc^2$ is the classical electron radius and n the number density of electrons.

Bethe and Fröhlich [13] noted that if n is the density of all electrons in some material one gets the surprising conclusion that magnetic field cannot penetrate into any material. I one instead interprets n as the number density of the conduction electrons one still gets the strange conclusion that all metals would be perfectly diamagnetic. In superconductors n is the density of electrons in the superconducting condensate and this is a much smaller number. So what determines the number density to be used in (8)? A clue comes from the fact that magnetism is intrinsically a retardation effect, and depends on the finite speed of light and the position and velocity of the charge. Thus it seems as if the only electrons that should be counted in n are the electrons that have simultaneously defined position and velocity. This, of course, requires that they behave like semiclassical wave packets, instead of being in pure delocalized momentum states.

Consider Eqs. (1) or (6). We wish to estimate when the magnetic contributions to the Lagrangian or Hamiltonian no longer is a perturbation. If one simply assumes that the velocities or momenta are parallel it is easy to see that these terms become comparable to the kinetic energy term when

$$\nu = \frac{Nr_e}{R} \tag{9}$$

where N is the number of electrons with correlated velocities (momenta), r_e is the classical electron radius and R is the typical distance between electrons (size of the system). When this dimensionless number ν no longer is small the magnetic term cannot be neglected. In the next section we'll see that for superconductors this number is 3.

3. ELECTRODYNAMICS AND THE LONDON MOMENT

London [16] showed (see also [17–19]), using his phenomenological theory of superconductivity, that a superconducting sphere that rotates with angular velocity $\mathbf{\Omega}$ will have an induced magnetic field (Gaussian units)

$$\mathbf{B} = \frac{2mc}{|e|}\mathbf{\Omega} \tag{10}$$

in its interior. Here m and e are the mass and charge of the electron. This prediction has been experimentally verified with considerable accuracy and is equally true for high temperature and heavy fermion superconductors [20, 21]. With minor modifications it is also valid for other axially symmetric shapes of the body, for example cylinders or rings.

The most direct way of understanding formula (10) is, in fact, quite simple. The superconducting electrons, which are always found just inside the surface [16], are not dragged by the positive ion lattice so when it starts to rotate the superconducting electrons ignore this and remain in whatever motion they prefer. This, however, means that there will be an uncompensated motion of positive charge density on the surface of the body. This surface charge density, σ, will, of course, be the same as the density of superconducting electrons, but of opposite sign, and will produce the magnetic field. Using this we can calculate the number, N, of superconducting electrons.

It is well known that a rotating uniform surface charge density will produce a uniform interior magnetic field in a sphere. If this rotating surface charge density is σ, then the total charge Q is given by

$$Q = N|e| = 4\pi R^2\sigma, \tag{11}$$

and the resulting magnetic field in the interior is

$$\mathbf{B} = \frac{2}{3}\frac{Q}{cR}\mathbf{\Omega} = \frac{8\pi}{3}\frac{\sigma R}{c}\mathbf{\Omega}, \tag{12}$$

where R is the radius of the sphere (relevant formulas for the calculation can be found in Essén [22]). Putting $Q = N|e|$ and comparing this equation with (10) one finds that the number N must be given by $N = 3Rmc^2/e^2 = 3R/r_e$. We thus find that the number defined in Eq. (9) has the value

$$\nu = \frac{Nr_e}{R} = 3, \tag{13}$$

where r_e is the classical electron radius, and N the number of electrons contributing to the supercurrent. Note that here R is the radius of the superconducting sphere, while in (9) R is the harmonic mean of all inter-particle distances, but the order of magnitude of ν is significant.

Note that the fundamental results above are universally true for all superconductors. How can this be if superconductivity is caused by some effective interaction with the lattice? A study of the connection between the London moment and the exclusion of a magnetic field from the interior in terms of the Darwin formalism can be found in [9]. The reason that the current is only on the surface is that this minimizes the magnetic energy as shown in Fiolhais et al. [6].

4. MAGNETIC ENERGY OF ELECTRONS ON THE FERMI SURFACE

Speculations of a magnetic origin of superconductivity originate quite early. Frenkel [23] advanced the idea that inductive inertia causes the phenomenon. It was this idea that Bethe and Fröhlich [13] tried to disprove when they, to their consternation, discovered that all metals are perfectly diamagnetic, not just superconductors. Later the German physicist Welker [24, 25] advanced similar ideas. Since Welker was not aware of the exponential damping effect he discovered that the magnetic interaction term in fact tends to diverge in large system.

Essén [26] studied the energy lowering effect of the original Darwin Hamiltonian (6) if one assumes that only electrons on the Fermi surface, i.e., electrons that can behave semiclassically since many quantum states are available to them, contribute. One idea is that at low density of states (low density of semiclassical electrons) a Wigner [27] lattice forms and that the electrons in this lattice then move with correlated momenta.

Since the Fermi surface is two-dimensional one does not get the divergence that a three-dimensional distribution would give. Assuming that the electrons on the Fermi surface are distributed anisotropically in an optimal way one can the show that the Darwin approximation reduces the energy per electron at the Fermi surface by an amount,

$$\Delta_D \approx 1.43 \cdot r_e \, k_F \, \mathcal{E}_F, \tag{14}$$

where k_F is the Fermi wave number and $\mathcal{E}_F$ is the Fermi energy [26]. In a typical metal this gives an energy lowering $\Delta_D \approx 10^{-4}\mathcal{E}_F$ which is in reasonable agreement with the smaller experimental energy gaps. This shows, if nothing else, that the Darwin magnetic energy ought to be a relevant quantity in superconductors.

5. CONCLUSION

We have reminded the reader of the fact that electrons interact also via magnetic fields. Macroscopically this corresponds to such phenomena as the attraction of parallel currents and the pinch effect in plasma physics, microscopically to the Breit [28] interaction. The Darwin approximation and formalism may seem unfamiliar and exotic but it is in fact completely equivalent to ordinary electromagnetism when radiation can be neglected. Since several fundamental and universal facts of superconductivity, such as the London moment and the Meissner effect, are easily understood in terms of electrodynamics and magnetic energy, one is tempted to conjecture that this interaction energy also should be important in the microscopic realm. The order of magnitude estimate in the last section reinforces this impression.

REFERENCES

1. Bardeen, J., L. N. Cooper, and J. R. Schrieffer, "Theory of superconductivity," *Phys. Rev.*, Vol. 108, 1175–1204, 1957.
2. Gabovich, A. M. and V. I. Kuznetsov, "What do we mean when using the acronym BCS? The Bardeen-Cooper-Schrieffer theory of superconductivity," *Eur. J. Phys.*, Vol. 34, 371–382, 1913.
3. Hirsch, J. E., "BCS theory of superconductivity: It is time to question its validity," *Phys. Scr.*, Vol. 80, 035702(11), 2009.
4. Hirsch, J. E., "Superconductors as giant atoms predicted by the theory of hole superconductivity," *Phys. Lett. A*, Vol. 309, 457–464, 2003.
5. Vasiliev, B. V., "Superconductivity as a consequence of an ordering of the electron gas zero-point oscillations," *Physica C*, Vol. 471, 277–284, 2011.
6. Fiolhais, M. C. N., H. Essén, C. Providentia, and A. B. Nordmark, "Magnetic field and current are zero inside ideal conductors," *Progress In Electromagnetics Research B*, Vol. 27, 187–212, USA, 2011.
7. Essén, H. and M. C. N. Fiolhais, "Meissner effect, diamagnetism, and classical physics — A review," *Am. J. Phys.*, Vol. 80, 164–169, 2012.

8. Fiolhais, M. C. N. and H. Essén, "Electrodynamics of perfect conductors," *Int. J. Theor. Phys.*, Vol. 52, 2013, DOI 10.1007/s10773-013-1491-9.
9. Essén, H., "Electrodynamic model connecting superconductor response to magnetic field and to rotation," *Eur. J. Phys.*, Vol. 26, 279–285, 2005.
10. Darwin, C. G., "The dynamical motions of charged particles," *Phil. Mag.*, Ser. 6., Vol. 39, 537–551, 1920.
11. Essén, H., "Darwin magnetic interaction energy and its macroscopic consequences," *Phys. Rev. E*, Vol. 53, 5228–5239, 1996.
12. Essén, H., "Phase-space energy of charged particles with negligible radiation: Proof of spontaneous formation of magnetic structures and new effective forces," *Phys. Rev. E*, Vol. 56, 5858–5865, 1997.
13. Bethe, H. and H. Fröhlich, "Magnetische Wechselwirkung der Metallelektronen. Zur Kritik der Theorie der Supraleitung von Frenkel," *Z. Physik*, Vol. 85, 389–395, 1933.
14. Essén, H., "Magnetism of matter and phase-space energy of charged particle systems," *J. Phys. A: Math. Gen.*, Vol. 32, 2297–2314, 1999.
15. Essén, H. and A. B. Nordmark, "Hamiltonian of a homogeneous two-component plasma," *Phys. Rev. E*, Vol. 69, 036404-1–9, 2004.
16. London, F., *Superfluids, Volume 1, Macroscopic Theory of Superconductivity*, 2nd Edition, Dover, New York, 1961.
17. Brady, R. M., "Correction to the formula for the london moment of a rotating superconductor," *Journal of Low Temperature Physics*, Vol. 49, 1–17, 1982.
18. Cabrera, B. and M. E. Peskin, "Cooper-pair mass," *Phys. Rev. B*, Vol. 39, 6425–6430, 1989.
19. Liu, M., "Rotating superconductors and the frame-independent london equation," *Phys. Rev. Lett.*, Vol. 81, 3223–3226, 1998.
20. Tate, J., B. Cabrera, S. Felch, and J. T. Anderson, "Precise determination of the cooper-pair mass," *Phys. Rev. Lett.*, Vol. 62, 845–848, 1989.
21. Sanzari, M. A., H. L. Cui, and F. Karwacki, "London moment for heavy-fermion superconductors," *Appl. Phys. Lett.*, Vol. 68, 3802–3804, 1996.
22. Essén, H., "Magnetic fields, rotating atoms, and the origin of diamagnetism," *Phys. Scr.*, Vol. 40, 761–767, 1989.
23. Frenkel, J., "On a possible explanation of superconductivity," *Phys. Rev.*, Vol. 43, 907–912, 1933.
24. Welker, H., "Über ein elektronenteoretisches Modell des Supraleiters," *Phys. Z.*, Vol. 39, 920–925, 1938.
25. Welker, H., "Supraleitung und magnetische Austauschwechselwirkung," *Z. Physik*, Vol. 114, 525–551, 1939.
26. Essén, H., "A study of lattice and magnetic interactions of conduction electrons," *Phys. Scr.*, Vol. 52, 388–394, 1995.
27. Wigner, E., "On the interaction of electrons in metals," *Phys. Rev.*, Vol. 46, 1002–1011, 1934.
28. Breit, G., "The effect of retardation on the interaction of two electrons," *Phys. Rev.*, Vol. 34, 553–573, 1929.

The Magnetic Force as a Kinematical Consequence of the Thomas Precession

David C. Lush
2462 63rd Ave SE, Mercer Island, Washington 98040, United States

Abstract— An examination of the electromagnetic interaction of two classical charged particles from the point of view of relativistic kinematics provides insight into the nature of the magnetic force, and reveals the necessity of other forces that may correspond to the strong and weak fundamental forces. The magnetic force is viewed as arising as a consequence of the Thomas precession, as seen by an observer co-moving with a charged test particle accelerating under the influence of the Coulomb field of another, non-accelerating, field-creating charge. The accelerated observer with a component of motion non-radial to the field-source particle sees the rest frame of the field-source particle as Thomas precessing, but no Coriolis force exists in the source particle rest frame, as it is an inertial frame owing to the field-source particle lack of acceleration. The observer moving with the test particle thus sees an anti-Coriolis force acting in the inertial field-source particle rest frame. The accelerated observer also sees coordinate axes that are fixed in an inertial laboratory frame where the field-source particle is uniformly translating, and so causing a magnetic field, as Thomas precessing, but with a different angular velocity than that of the Thomas precession observed of the inertial reference frame where the source particle is stationary. Therefore a Coriolis effect must also exist in the description of the test particle motion between the field-source rest frame and the laboratory frame. Given that the only electromagnetic force acting in the field-source particle rest frame is the purely radial Coulomb force, a resulting non-Coulomb force on the test particle is seen to exist in the laboratory frame by the observer co-moving with the test particle, that is a residual of the anti-Coriolis force. This residual non-Coulomb force can be equated to the magnetic force on the test particle in the laboratory frame.

The accelerating observer also sees a similar lack of centrifugal and Euler pseudoforces in the field-source particle rest frame as requiring other tangible forces. In particular, he predicts an anticentrifugal force that is always attractive and may plausibly overcome Coulomb repulsion in the highly relativistic limit and at nucleonic scale, similarly to the strong fundamental force. The magnetic interaction between two highly-accelerating relativistic charges is then examined and shown to be similar to the expected anticentrifugal force in the case of bound circular motion.

1. INTRODUCTION

The rest frames of charged particles interacting electromagnetically are known to rotate relative to the laboratory inertial reference frame due to the Thomas precession [1]. Typically, when a coordinate system or reference frame rotates relative to an inertial reference frame, kinematics requires that rotational pseudoforces must be present in the rotating frame. However, it is clear that Thomas precession cannot cause rotational pseudoforces in general, because it depends only on the relative motion between two reference frames, and the Thomas-precessing coordinate frame may be an inertial frame if it is the observer of the Thomas precfession that is accelerating. Thus, for example, since there can be no Coriolis force in the rest frame of a field-source charged particle that is translating with constant velocity, an observer co-moving with a charged test particle that is translating relative to the field-source particle, and cross-accelerating relative to the translation, must infer the presence of forces in the field-source particle rest frame that compensate for the lack of Coriolis force the observer expects due to the observed Thomas precession.

The necessity of an observer moving non-inertially to infer pseudoforce-compensating forces implies even in inertial frames the existence of related forces, the most obvious of which can be recognized as the magnetic part of the Lorentz force. The formal similarity of the magnetic force to a Coriolis force can be viewed as a direct consequence of it arising from Coriolis effects. Similar reasoning when extended to centrifugal and Euler pseudoforces implies the existence of other tangible forces. These may provide non-quantum-mechanical bases for the strong and weak fundamental forces. It is shown further that under highly relativistic and short range conditions, the force on a charged particle due to the magnetic acceleration, or radiative, field can behave similarly to a predicted anticentrifugal force caused by Thomas precession. That is, in the highly relativistic limit, the magnetic field of an accelerating charge can cause a force between two charges that is attractive independent of the relative polarity of the charges, and is predicted to overcome Coulomb repulsion at approximately nucleonic scale.

That the magnetic force can be directly related to the effect of Thomas precession has been previously noted by Bergström [2]. The present analysis however differs from that of [2] in at least one important respect. The present argument invokes the Thomas precession observed from the point of view of an observer moving and accelerating along with a particle being acted on by a magnetic force, rather than a Thomas precession of the rest frame of the accelerating particle itself, and centered around the particle, as seen from an inertial reference frame. No centrifugal or Euler forces can exist in the Thomas-precessing test particle rest frame because such forces, unlike the Coriolis force, vanish at the center of rotation. Thus, while the Bergström argument precludes an associated centrifugal force due to Thomas precession, the present analysis would seem to require a centrifugal-like force of the Thomas precession, as well as an Euler-like force when the two-particle motion is non-circular so that the angular velocity of the relative Thomas precession is time varying.

2. ELECTROMAGNETIC INTERACTION OF TWO CHARGED PARTICLES, WHERE ONE PARTICLE IS NON-ACCELERATING

The relativistic law of inertia for a particle of momentum $\mathbf{P}$ and rest mass m, acted on by a force $\mathbf{F}$ is

$$\mathbf{F} = \frac{d\mathbf{P}}{dt} = \frac{d}{dt}\left[\gamma m \mathbf{v}\right] = \dot{\gamma} m \mathbf{v} + \gamma m \mathbf{a}, \tag{1}$$

where $\mathbf{v}$ is the particle velocity and $\mathbf{a} \equiv d\mathbf{v}/dt \equiv \dot{\mathbf{v}}$ its acceleration, and $\gamma \equiv 1/\sqrt{(1-(v/c)^2}$ with $v \equiv |\mathbf{v}|$ and c the speed of light. The acceleration due to $\mathbf{F}$ is thus

$$\mathbf{a} = \left[\frac{1}{\gamma m}\right]\left[\mathbf{F} - \dot{\gamma} m \mathbf{v}\right] = \left[\frac{1}{\gamma m}\right]\left[\mathbf{F} - \gamma^3 (\boldsymbol{\beta}\cdot\dot{\boldsymbol{\beta}}) m \mathbf{v}\right], \tag{2}$$

where $\boldsymbol{\beta} \equiv \mathbf{v}/c$ (and using the well-known identity that $\dot{\gamma} = \gamma^3(\boldsymbol{\beta}\cdot\dot{\boldsymbol{\beta}})$). The force of interest is the Lorentz force on a moving charged particle in the electromagnetic field caused by another point-like moving charged particle. In this case the electromagnetic field is exactly described by the Liénard-Wiechert field expressions [3]. The Liénard-Wiechert field expressions for the electric field $\mathbf{E}$ and magnetic field $\mathbf{B}$, in three-vector notation, are

$$\mathbf{E}(\mathbf{r},t) = q\left[\frac{\mathbf{n}-\boldsymbol{\beta}}{\gamma^2\left(1-\boldsymbol{\beta}\cdot\mathbf{n}\right)^3 R^2}\right]_{\mathrm{ret}} + \frac{q}{c}\left[\frac{\mathbf{n}\times\left((\mathbf{n}-\boldsymbol{\beta})\times\dot{\boldsymbol{\beta}}\right)}{\left(1-\boldsymbol{\beta}\cdot\mathbf{n}\right)^3 R}\right]_{\mathrm{ret}} \tag{3}$$

and

$$\mathbf{B}(\mathbf{r},t) = \left[\mathbf{n}\times\mathbf{E}\right]_{\mathrm{ret}}, \tag{4}$$

where $\mathbf{r}$ is the displacement from a field-source charged particle at the retarded time $t' \equiv t - R/c$ to a field point at time t, $R \equiv |\mathbf{r}|$, and $\mathbf{n} = \mathbf{r}/R$. Also $\boldsymbol{\beta} \equiv \mathbf{v}/c$, where $\mathbf{v}$ is the field-source particle velocity, and q is the electric charge. The subscript "ret" refers to that the quantity in the brackets is evaluated at the retarded time.

The first term on the right hand side of Eq. (3) is called the velocity, or non-radiative, electric field. The second is called the acceleration or radiative electric field. In the case of the electromagnetic field caused by a non-accelerating charge, the acceleration fields vanish identically. It can also be seen by inspection that the magnitude of the electric field difference from the Coulomb field of the charge (that is, the electric field in the rest frame of the field-source charge) due to motion is small when $\beta \ll 1$. Since the magnetic force strength due to a non-accelerating charge is generally of order $(v/c)^2$ compared to the Coulomb force, it will be sufficient to represent all forces and fields only to this order, until the expectation of an anti-centrifugal force is considered in Section 4.

From (3) and with the field source particle non-accelerating, the electric field is exactly

$$\mathbf{E}(\mathbf{r},t) = q_s\left[\frac{\mathbf{n}-\boldsymbol{\beta}_s}{{\gamma_s}^2\left(1-\boldsymbol{\beta}_s\cdot\mathbf{n}\right)^3 R^2}\right]_{\mathrm{ret}}, \tag{5}$$

and the magnetic field is exactly

$$\mathbf{B}(\mathbf{r},t) = q_s\left[\frac{\boldsymbol{\beta}_s\times\mathbf{n}}{{\gamma_s}^2\left(1-\boldsymbol{\beta}_s\cdot\mathbf{n}\right)^3 R^2}\right]_{\mathrm{ret}}. \tag{6}$$

Let $\mathbf{r}_s$ and $\mathbf{r}_t$ represent position vectors to an electromagnetic field source charged particle of mass m_s, and a test particle of mass m_t, in an inertial reference frame (IRF) that will be referred to as the laboratory frame, and $R \equiv |\mathbf{r}| \equiv |\mathbf{r}_t - \mathbf{r}_s|$. The velocities of both the source and test particles are assumed nonvanishing in the laboratory frame. It is also assumed that the particles have no intrinsic magnetic moments. The test particle cannot influence the motion of the field-source particle because the field-source particle is considered to be arbitrarily massive, or to be constrained from accelerating by being part of an ensemble of current carriers in a fixed neutral wire. The Lorentz force on the test particle in the laboratory frame due to the magnetic and electric fields is then (in Gaussian units)

$$\mathbf{F} = \frac{q_t \mathbf{v}_t}{c} \times \mathbf{B} + q_t \mathbf{E}, \tag{7}$$

or, substituting for $\mathbf{E}$ and $\mathbf{B}$ using Eqs. (5) and (6),

$$\mathbf{F} = q_t q_s \boldsymbol{\beta}_t \times \left[\frac{\boldsymbol{\beta}_s \times \mathbf{n}}{{\gamma_s}^2 \left(1 - \boldsymbol{\beta}_s \cdot \mathbf{n}\right)^3 R^2} \right]_{\text{ret}} + \left[\frac{q_t q_s \left(\mathbf{n} - \boldsymbol{\beta}_s\right)}{{\gamma_s}^2 \left(1 - \boldsymbol{\beta}_s \cdot \mathbf{n}\right)^3 R^2} \right]_{\text{ret}}. \tag{8}$$

For the uniformly translating field source particle, it is straightforward to evaluate the retardation effects explicitly and rewrite Eq. (8) in terms of non-retarded quantites. The result accurate to order $(v/c)^2$ is

$$\mathbf{F} \approx \frac{q_s q_t}{R^2} \left[\boldsymbol{\beta}_t \times \left[\boldsymbol{\beta}_s \times \mathbf{n}\right]\right] + \frac{q_s q_t \mathbf{n}}{\left(1 + 9(\boldsymbol{\beta}_s \cdot \mathbf{n})^2/2 - {\beta_s}^2/2\right) R^2}. \tag{9}$$

If the force of Eq. (9) is considered as consisting of electric and magnetic parts so that $\mathbf{F} \equiv \mathbf{F}_{\text{electric}} + \mathbf{F}_{\text{magnetic}}$, it will be useful to further consider the electric part of the force as consisting of a Coulomb force plus additional terms that are at order β and higher powers of β, where the Coulomb part of the electric force is

$$\mathbf{F}_{\text{Coul}} \equiv \frac{q_t q_s}{R^3}(\mathbf{r}_t - \mathbf{r}_s) = \frac{q_t q_s \mathbf{r}}{R^3}. \tag{10}$$

The acceleration of the test particle due to the Coulomb force, using Eq. (2), is

$$\mathbf{a}_{\text{Coul}} = \left[\frac{1}{\gamma_t m_t}\right] \left[\mathbf{F}_{\text{Coul}} - {\gamma_t}^3 (\boldsymbol{\beta}_t \cdot \dot{\boldsymbol{\beta}}_t) m_t \mathbf{v}_t\right], \tag{11}$$

which to order $(v/c)^2$ is

$$\mathbf{a}_{\text{Coul}} \approx \frac{\mathbf{F}_{\text{Coul}}}{\gamma_t m_t} - (\boldsymbol{\beta}_t \cdot \dot{\boldsymbol{\beta}}_t)\mathbf{v}_t, \tag{12}$$

The acceleration of the test particle due to the Coulomb force, neglecting the relativistic terms from Eq. (2) that are of order β^2 and higher, is then

$$\mathbf{a}_{\text{Coul}} \approx \frac{q_t q_s \mathbf{r}}{m_t R^3}. \tag{13}$$

If we let $\mathbf{F} \equiv \mathbf{F}_{\text{electric}} + \mathbf{F}_{\text{magnetic}}$ with $\mathbf{F}_{\text{magnetic}} = q_t \boldsymbol{\beta}_t \times \mathbf{B}$, then the magnetic force can be rewritten using Eq. (6) as

$$\mathbf{F}_{\text{magnetic}} \approx \left[\frac{q_t q_s}{R^2}\right] \left[\boldsymbol{\beta}_t \times (\boldsymbol{\beta}_s \times \mathbf{n})\right] = 2 m_t \boldsymbol{\omega} \times \mathbf{v}_t, \tag{14}$$

with

$$\boldsymbol{\omega} = -\left[\frac{q_t q_s}{2 c m_t R^2}\right] \left[\boldsymbol{\beta}_s \times \mathbf{n}\right] = -\left[\frac{1}{2c^2}\right] \left[\mathbf{v}_s \times \mathbf{a}_{\text{Coul}}\right]. \tag{15}$$

Now, Eq. (14) shows that the magnetic force on the test particle is formally identical to a Coriolis force that would be present if the reference frame of the description was rotating with angular velocity magnitude as given by Eq. (15). The sign choice made here on the right hand side of the equality of (14) is opposite to that of a Coriolis force, however, anticipating that the magnetic

force is not actually a Coriolis force, but rather is a kinematical consequence of the *absence* of a Coriolis force in the laboratory frame, in spite the perception by the observer co-moving with test particle that the laboratory frame is gyrating. Furthermore, the angular velocity expression of Eq. (15) is similar to the expression for the Thomas precession [3] in the limit of small v/c, of the rest frame of a particle with velocity $\mathbf{v}$ and acceleration $\mathbf{a}$ relative to the observer seeing the Thomas precession. That is,

$$\boldsymbol{\omega}_{\mathrm{T}} \approx \frac{1}{2}\frac{\mathbf{a}\times\mathbf{v}}{c^2}. \tag{16}$$

The laboratory frame acceleration relative to the observer co-moving with the test particle is simply the opposite of the test particle acceleration, since the laboratory frame is non-accelerating. The labortory frame relative velocity similarly is the opposite of the test particle velocity as observed from the laboratory frame. Substituting these values in Eq. (16) results in

$$\boldsymbol{\omega}_{\mathrm{T}} \approx \frac{1}{2}\frac{(-\mathbf{a}_t)\times(-\mathbf{v}_t)}{c^2} = \frac{1}{2}\frac{\mathbf{a}_t\times\mathbf{v}_t}{c^2}, \tag{17}$$

which however is not identical to the angular velocity of Eq. (15) above. In order to successfully derive the magnetic force from the Thomas precession seen from the test particle accelerating rest frame, it is necessary to consider not just the Thomas precession of the laboratory frame, but also that of the field source particle rest frame, in both cases as seen by the test particle co-moving observer.

3. THE MAGNETIC FORCE AS A CORIOLIS EFFECT OF THE THOMAS PRECESSION

From the point of view of the test particle co-moving observer, the angular velocity of Thomas precession, based on Eq. (16), of a coordinate axis centered on the field-source particle and moving with it so the field source particle remains at the origin is

$$\boldsymbol{\omega}_s \approx \frac{1}{2}\frac{(-\mathbf{a}_t)\times(-\mathbf{v})}{c^2} = -\frac{1}{2}\frac{\mathbf{a}_t\times\mathbf{v}_s}{c^2} + \frac{1}{2}\frac{\mathbf{a}_t\times\mathbf{v}_t}{c^2}, \tag{18}$$

with $\mathbf{v}$ here and henceforth defined as $\mathbf{v} \equiv \dot{\mathbf{r}} \equiv \dot{\mathbf{r}}_t - \dot{\mathbf{r}}_s \equiv \mathbf{v}_t - \mathbf{v}_s$. The same observer also sees a Thomas precession around an arbitrary point in the laboratory frame with angular velocity (as noted previously as Eq. (17)

$$\boldsymbol{\omega}_l \approx \frac{1}{2}\frac{(-\mathbf{a}_t)\times(-\mathbf{v}_t)}{c^2} = \frac{1}{2}\frac{\mathbf{a}_t\times\mathbf{v}_t}{c^2}. \tag{19}$$

The relative angular velocity of the laboratory frame compared to the source particle rest frame is then

$$\boldsymbol{\omega}_r \equiv \boldsymbol{\omega}_l - \boldsymbol{\omega}_s \approx \frac{1}{2}\frac{\mathbf{a}_t\times\mathbf{v}_s}{c^2}. \tag{20}$$

The observer co-moving with the test particle thus sees the laboratory frame as rotating with angular velocity $\boldsymbol{\omega}_r$ with respect to the field source particle rest frame. Although the test particle co-moving observer sees both frames as rotating, it is the relative rotation that determines the kinematical relationship between the two frames. If the law of motion is known in either of the two frames, it can be determined in the other using standard kinematical techniques. If the source rest frame is taken as the non-rotating frame, then the test particle co-moving observer predicts that the lab frame equation of motion must be the source frame equation plus the Coriolis, Euler, and centrifugal rotational pseudoforces. These can be viewed as antipseudoforces since the source particle rest frame is rotating with a larger-magnitude angular velocity than the laboratory frame, from the point of view of the test particle rest frame observer, yet the electromagnetic interaction in the source particle rest frame is perfectly radial and so lacking in any rotational pseudoforces from the point of view of an observer co-moving with the field source particle. (This is only to be expected, since an observer co-moving with the uniformly-translating field source particle is moving inertially.) The distinction between ordinary and anti-pseudoforces becomes critical to the argument of Section 4 below that the strong fundamental force is similar in a certain sense to a centrifugal force, because since a centrifugal force is always outward from a center of rotation, the anti-centrifugal force must be always attractive.

The expected anti-Coriolis force in the laboratory frame relative to the source particle rest frame, as observed from the test particle rest frame is

$$\mathbf{F}_{\text{anti-Coriolis}} = 2m_t\boldsymbol{\omega}_r \times \mathbf{v}_t, \tag{21}$$

or, with the relative angular velocity of the Thomas precession between the source and laboratory frames given by Eq. (20),

$$\mathbf{F}_{\text{anti-Coriolis}} = \frac{m_t}{c^2}\left[\mathbf{a}_t \times \mathbf{v}_s\right] \times \mathbf{v}_t. \tag{22}$$

Approximating the test particle acceleration as that due to the Coulomb force of the electric field of the source particle as given by Eq. (13) obtains, with some rearrangement,

$$\mathbf{F}_{\text{anti-Coriolis}} = \frac{q_t q_s}{c^2 R^2}\left[\mathbf{v}_t \times \left[\mathbf{v}_s \times \mathbf{n}\right]\right]. \tag{23}$$

Comparing with Eq. (14), it is apparent that

$$\mathbf{F}_{\text{anti-Coriolis}} = \frac{q_t q_s}{R^2}\left[\boldsymbol{\beta}_t \times \left[\boldsymbol{\beta}_s \times \mathbf{n}\right]\right] = \mathbf{F}_{\text{magnetic}}. \tag{24}$$

The magnetic force on the test particle is thus interpretable as an anti-Coriolis force caused by Thomas precession.

It seems worth remarking that although the Coriolis and other inertial pseudoforces generally are directly proportional to the mass of the object on which they appear to act, the anti-Coriolis force manifesting here (and also the Coriolis-magnetic force found by Bergström in [2]) does not depend on the test particle mass. The amount of Thomas precession seen by the test particle rest frame observer is inversely proportional to the test particle mass, which has directly canceled the mass factor that would be otherwise present. Such cancelation of the mass factor is of course essential to admitting the possibility that the magnetic force is a Coriolis-like force. However, the argument presented here seems to also be applicable to other situations where such cancelation cannot occur. Specifically, had the field-source particle been allowed to freely accelerate in the Coulomb field of the test particle, then this acceleration would have contributed to the Thomas precession of the source particle rest frame seen by the observer in the test particle rest frame, with the amount of additional Thomas precession depending inversely on the mass of field-source particle. Thus, an additional anti-Coriolis force component would be present that would be proportional to the ratio of the test particle to source particle masses. In the case of interactions between equal-mass particles where the field-source particle is not constrained from accelerating, as in a neutral wire, this would seem to result in a doubling of the strength of the magnetic interaction. This doubling would be expected to manifest, for example, in the spin-orbit interaction strength of positronium.

4. STRENGTH OF THE ANTI-CENTRIFUGAL FORCE OF THE THOMAS PRECESSION COMPARED TO COULOMB REPULSION

The same arguments that lead to expectation of an anti-Coriolis force of the Thomas precession lead also to expectation of a anticentrifugal force due to the Thomas precession, that can be given notionally as

$$\mathbf{F}_{\text{anticentrifugal}} \equiv \mathbf{F}_{\text{a.c.}} \equiv \gamma m\boldsymbol{\omega}_{\text{T}} \times \left(\boldsymbol{\omega}_{\text{T}} \times \mathbf{r}\right), \tag{25}$$

with (using again the formula for the angular velocity of the Thomas precession given in [3], but here without specialization to small v/c),

$$\boldsymbol{\omega}_{\text{T}} = -\left(\gamma - 1\right)\frac{\left[\mathbf{v} \times \mathbf{a}\right]}{v^2} \approx -\gamma\frac{\left[\mathbf{v} \times \mathbf{a}\right]}{v^2} = -\gamma\frac{\left[\boldsymbol{\beta} \times \mathbf{a}\right]}{c\beta^2} \tag{26}$$

for β approaching unity. (The relativistic version of the centrifugal force on which Eq. (25) is based, that includes the leading Lorentz factor, γ, is derived in [4].) Thus,

$$\mathbf{F}_{\text{a.c.}} = \frac{\gamma_t m_t}{c^2 {\beta_s}^4}{\gamma_s}^2\left[\boldsymbol{\beta}_s \times \mathbf{a}_s\right] \times \left(\left[\boldsymbol{\beta}_s \times \mathbf{a}_s\right] \times \mathbf{r}\right). \tag{27}$$

For Coulomb attraction or repulsion in the case of mutual circular motion of the two charged particles and neglecting effects of retardation, Eq. (2) gives the acceleration of one of the particles in the laboratory frame due to the velocity electric field of the other as

$$\mathbf{a}_1 = \left[\frac{1}{\gamma_1 m_1}\right] \frac{q_1 q_2 \mathbf{r}_{12}}{{\gamma_2}^2 R^3}, \tag{28}$$

where $\mathbf{r}_{12} \equiv \mathbf{r}_1 - \mathbf{r}_2$, and where the two particles are now distinguished by the subscripts 1 and 2, since the field-source particle is no longer constrained to be non-accelerating, and in fact is accelerating under the influence of the Coulomb field of particle 2. Therefore the notion of a test particle that doesn't influence the field-source particle motion must be abandoned, and the subscripts s and t have been replaced by 1 and 2. In the approximation valid in the highly relativistic case that β_1 and β_2 approaching unity and for circular motion neglecting retardation, and assuming the acceleration of particle 1 is Coulombic, the expected magnitude of the anticentrifugal force acting on particle 2 is thus

$$\left|\mathbf{F}_{\text{a.c.}}\right| \approx \frac{\gamma_2 m_2}{c^2}\left|\mathbf{a}_1\right|^2 R \approx \frac{\gamma_2 m_2}{c^2} \frac{{q_1}^2 {q_2}^2 {\gamma_1}^2}{{\gamma_1}^2 {m_1}^2 {\gamma_2}^4 R^3} = \frac{m_2}{c^2} \frac{{q_1}^2 {q_2}^2}{{m_1}^2 {\gamma_2}^3 R^3}. \tag{29}$$

If it is assumed the two particles are of like charge polarity with charge magnitude of the order of the elementary charge, and repulsed by Coulomb repulsion, yet circularly orbiting each other with laboratory-frame velocities near the speed of light, then it will be a simple matter to calculate approximately (i.e., neglecting retardation) at what orbital radius the anticentrifugal force will overcome Coulomb repulsion. This orbital radius can then be compared with the measured size of a nucleon such as the proton.

Equating the anticentrifugal force of Eq. (29) and the magnitude of the electric force part of Eq. (7) neglecting retardation obtains, for equal mass particles and asumming $|q_1| = |q_2| = e$ (with e the fundamental charge magnitude) and $\gamma_1 = \gamma_2 \equiv \gamma$, and using the proton mass for γm,

$$R \approx \frac{e^2}{\gamma m c^2} \approx 10^{-15}\,\text{cm}. \tag{30}$$

This orbital radius or (strictly) inter-particle separation is about two orders of magnitude less than the estimated size of the proton [5]. Thus the present analysis would seem to indicate that the expected centrifugal force of the Thomas precession is too weak to potentially account for the fundamental strong force that binds quarks into nucleons. However, the present contribution should be considered only an initial progress report for an ongoing effort that has yet to take into account important effects such as retardation, that may substantially change the present result.

5. THE STRONG FORCE OF MAXWELL-LORENTZ ELECTRODYNAMICS

It is worth noting that a force similar to the expected anticentrifugal force of the Thomas precession can be found in relativistic electrodynamics. Based on the Liénard-Wiechert field expressions provided above as Eqs. (3) and (4), the magnetic force on particle 2 due to the acceleration field of particle 1 is generally

$$\mathbf{F}_{\text{magnetic}} = \frac{q_2 \mathbf{v}_2}{c} \times \mathbf{B} = q_2 \boldsymbol{\beta}_2 \times \left[\mathbf{n} \times \left[\frac{q_1}{c}\left[\frac{\mathbf{n} \times \left((\mathbf{n} - \boldsymbol{\beta}_1) \times \dot{\boldsymbol{\beta}}_1\right)}{\left(1 - \boldsymbol{\beta}_1 \cdot \mathbf{n}\right)^3 R}\right]\right]\right]_{\text{ret}}, \tag{31}$$

where here $\mathbf{n} \equiv \mathbf{r}_{21}/R \equiv (\mathbf{r}_2 - \mathbf{r}_1)/R$ with $R \equiv |\mathbf{r}_2 - \mathbf{r}_1|$. The acceleration of particle 1 in the electric velocity field of particle 2 is found from Eqs. (2) and (3), neglecting retardation and assuming mutually circular orbital motion of particle 1 around particle 2, as

$$\mathbf{a}_1 \approx \frac{q_2 q_1}{\gamma_1 m_1 {\gamma_2}^2 R^3}\left[\mathbf{r}_{12}\right] \equiv -\frac{q_2 q_1}{\gamma_1 m_1 {\gamma_2}^2 R^2}\left[\mathbf{n}\right], \tag{32}$$

or, if $\dot{\boldsymbol{\beta}}_1 = \mathbf{a}_1/c \approx -a_1 \mathbf{n}/c$ with $a_1 \equiv |\mathbf{a}_1|$, and still neglecting retardation,

$$\mathbf{F}_{\text{magnetic}} \approx \boldsymbol{\beta}_2 \times \left[\mathbf{n} \times \left[\mathbf{n} \times (\boldsymbol{\beta}_1 \times \mathbf{n})\right]\right] \frac{q_2 q_1}{c^2 R} \frac{q_2 q_1}{\gamma_1 m_1 {\gamma_2}^2 R^2}. \tag{33}$$

Now assume mutual circular motion and let $\hat{\mathbf{x}}$, $\hat{\mathbf{y}}$, $\hat{\mathbf{z}}$ represent orthogonal unit vectors in a right-handed coordinate system, and align $\hat{\mathbf{x}}$ with $\mathbf{n}$ and $\hat{\mathbf{y}}$ with $\mathbf{v}_1$. Then for circular motion with $\boldsymbol{\beta}_2 = -\boldsymbol{\beta}_1$ and $|\boldsymbol{\beta}_2| = |\boldsymbol{\beta}_1| \approx 1$, and neglecting retardation, Eq. (33) for the magnetic force on particle 2 due to its motion in the magnetic acceleration field of particle 1 becomes

$$\mathbf{F}_{\text{magnetic}} \approx (-\mathbf{n}) \frac{{q_2}^2 {q_1}^2}{\gamma_1 m_1 c^2 {\gamma_2}^2 R^3}. \tag{34}$$

Recalling that $\mathbf{n}$ is directed towards particle 2 from particle 1, it is apparent that this force is attractive for like charges, as well as for opposite. Also, comparing Eq. (34) with Eq. (29), it is apparent that, for mutual circular motion and neglecting retardation,

$$\mathbf{F}_{\text{magnetic}} \approx \frac{\gamma_2 m_1}{\gamma_1 m_2} \mathbf{F}_{\text{anticentrifugal}}. \tag{35}$$

In the case of equal mass particles with $\gamma_1 = \gamma_2$ so that $\mathbf{F}_m \approx \mathbf{F}_{\text{anticentrifugal}}$, it is apparent that the "strong" magnetic force is approximately equal to the predicted anticentrifugal force of the Thomas precession.

6. CONCLUDING REMARKS

It has been proposed that relativistic kinematical considerations necessitate that the Thomas precession gives rise to certain forces that resemble the rotational pseudoforces known as the Coriolis, Euler, and centrifugal forces. It has been shown that the predicted anti-Coriolis force of the Thomas precession accounts to order v^2/c^2 for the existence of the magnetic force. The possible correspondence of the strong fundamental force to an anticentrifugal force of the Thomas procession was also investigated. Further effort is needed to ascertain the correspondence, if any, of the strong force to a predicted anticentrifugal force of the Thomas precession.

REFERENCES

1. Thomas, L. H., "The kinematics of an electron with an axis," *Philos. Mag.*, Vol. 3, 1–22, 1927.
2. Bergström, A., "On the origin of the magnetic field," *Il Nuovo Cimento*, Vol. 14B, No. 2, 235–242, 1973.
3. Jackson, J. D., *Classical Electrodynamics*, 3rd Edition, Wiley, New York, 1998.
4. Arendt, Jr., P. N., "Electromagnetic forces and fields in a rotating reference frame," (preprint) arXiv:astro-ph/9801194v1, Jan. 1998.
5. Mohr, P. J., B. N. Taylor, and D. B. Newell, "The 2010 CODATA recommended values of the fundamental physical constants," MD 20899, National Institute of Standards and Technology, Gaithersburg, 2011.

Development of Graphical User Interface for Modern FDTD Simulation Tool

S. Orłowski and T. P. Stefański
Department of Microwave and Antenna Engineering
Gdansk University of Technology, Narutowicza 11/12, Gdansk 80-233, Poland

Abstract— In this contribution, the development of a graphical user interface (GUI) for the in-house written FDTD solver is presented. GUI facilitates the edition of simulation parameters, drawing 3-D objects, generation of material matrices, human body modeling and visualization of simulation results. In the developed code, the OpenGL library was employed to visualize the FDTD computational domain, place 3-D objects and assign material parameters to each object. Moreover, the GPU-accelerated method for the material matrix generation was implemented inside the developed GUI. The code was developed using modern software technologies and up-to-date design patterns. Due to layered structure of the software architecture and strongly object-oriented design pattern, the code can be easily tested and extended in the future.

1. INTRODUCTION

The finite-difference time-domain (FDTD) method has been applied to a variety of problems in microwave and antenna engineering, electromagnetic compatibility and photonics [1]. Although the FDTD algorithm is relatively easy to implement in software, simulations with the use of this method also require execution of pre- and post-processing tasks. Moreover, a fully functional and easy to use graphical user interface (GUI) is highly desired. Currently, several simulation tools based on the FDTD method are available on the market, e.g., CST Microwave Studio [2] or SEMCAD X [3]. Unfortunately, software techniques and technologies used for the development of these tools have not been widely identified and described in the literature. Moreover, GUIs of commercial tools have been under development for several years, hence their development processes are not flexible and open for introduction of novel software technologies.

From the software engineering point of view, development of a standalone software package for the FDTD method is a challenge due to its complexity. This process requires the development of computational engine, GUI, as well as pre- and post-processing modules. C and/or C++ are languages of choice in the case of computational engine and some pre-processing modules while other modern and high-level languages are a natural choice for GUI and post-processing modules. To accelerate computations, the parallel processing on a multicore central processing unit and a graphics processing unit is widely employed. Graphics libraries are necessary to visualize the computational domain and simulation output consisting of 1-D, 2-D and 3-D data. To sum up, the development of any simulation tool involves various computer architectures, languages, technologies and supporting libraries.

In this contribution, we describe the development of GUI for the in-house written FDTD solver. The developed FDTD solver is facilitated by computational techniques based on the discrete Green's function. It is the novelty which differs the developed tool from any commercially available FDTD solver. However, in this paper, we focus on the software architecture issues that were previously reported in the literature [4, 5] but still require discussion due to the fast progress of software engineering. Therefore, we describe the development of our simulation tool that is based on modern software technologies and up-to-date design patterns. Due to layered structure of the software architecture and strongly object-oriented design pattern, the whole solution can be easily tested and extended in the future. Hopefully, the presented implementation of the simulation package will be useful for other researchers developing scientific codes.

2. SOFTWARE ARCHITECTURE

C# was chosen as a programming language for the GUI development within Microsoft .NET framework [6]. This is a managed language and its compilation produces a managed code executable by the common language runtime virtual machine. On the other hand, the FDTD computational engine is an unmanaged code which directly runs under the control of operating system. To deal with both managed and unmanaged environments, C++/CLI has been introduced [7]. C++/CLI code can utilize the FDTD engine with pre-processed data as well as it exposes this functionality to

GUI. Due to unmanaged nature of OpenGL, a managed wrapper over native OpenGL functionalities was introduced. The layered software architecture was implemented with the following layers: (i) unmanaged FDTD engine, (ii) wrapper for unmanaged code (C++/CLI) and (iii) managed GUI (C#). Main advantage of this layered architecture stems from isolation of components of the software package which simplifies design, development and testing processes [4]. For the GUI development, the model-view-presenter (MVP) design pattern was employed. It produces streamlined and reusable code that is easy to test.

The developed software package consists of the following two main modules (see Fig. 1):

(i) GUI with all dependencies (projects, static libraries, dynamic linked libraries and other resources),
(ii) the solver executing the FDTD computations.

Although these two modules are standalone applications (executable binaries), the GUI module is able to run the solver. Such an architecture allows running these modules independently when it is necessary. For instance, a user can separately run the solver on high performance computers. During execution of the solver, its process communicates with GUI process using standard out (stdout) and standard error (stderr) channels. From the architecture point of view, this solution separates presentation and post-processing layers from the computational engine. During computations, the solver writes results on a hard disc that can be loaded and visualized by GUI.

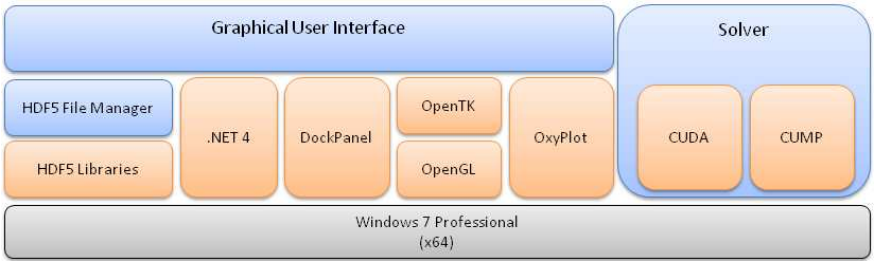

Figure 1: Architecture of the software package. Blue parts were developed by the authors.

GUI employs .NET framework along with the WindowsForms controls. This is a very powerful runtime environment with extensive collection of base class libraries that supports object-oriented and up-to date programming techniques with modern design patterns. This approach enhances security of the code by using automatic memory management (called garbage collector), separate application domains as well as it also increases the level of abstraction. Therefore, smaller models can be used in the application architecture by developers. Drawbacks include slower startup speed, slower memory management and increased usage of system resources. To avoid these potential gaps, managed wrappers were introduced over native (unmanaged) code. Managed wrapper acts as a mediator design pattern which provides communication between managed and unmanaged parts of the system. In our architecture, all parts that need maximum performance are executed in an unmanaged context, or as an unmanaged process. Simulation results are wrapped and transferred to a managed context by mediators. The OpenGL library is used for presentation of the simulation domain along with the OpenTK managed wrapper. The OxyPlot library is used for data plotting. The input and output files are managed by a file manager using the HDF5 library [8].

3. MODEL OF DATA REPRESENTATION

The GUI layer allows to edit input data for the solver as well as to present simulation output. In the developed tool, the dock-style GUI model with MDI panels was implemented using the DockPanel library. The GUI form was divided into the following parts:

(i) main form that represents main menu (a parent for all MDI child panels),
(ii) simulation properties dock panel that presents input simulation properties,
(iii) 3-D object properties dock panel that shows 3-D object properties,
(iv) 3-D view panel that is a view port of the OpenGL graphical engine,
(v) output dock panel for logging purpose,
(vi) result form for presentation of results.

A user can easily arrange these panels according to his own needs, see Fig. 2. The main form is a master project which manages all forms defined in the solution. GUI utilizes MVP design pattern to control the presentation of data. In this pattern, the model is an interface defining data displayed by GUI. The view displays data provided by the model as well as it routes events (user commands) to the presenter. The view interacts with model for data binding, therefore it acts as a supervising controller. Presenters manage data received from repositories, format it (with the model) and deliver it to the view. Automated unit tests can cover presenter methods. For the MVP pattern, *IBaseView* and *IBaseRepository* interfaces were introduced. Based on these interfaces abstract and generic class *BasePresenter* was defined. This class is a base class for all presenters that combines the *IBaseView* and *IBaseRepository* objects into a single object. The UML diagram of the *BasePresenter* class is shown in Fig. 3. All views, e.g., simulation properties, implement own version of the view interface based on *IBaseView*, the repository based on *IBaseRepository* and the presenter derived from the *BasePresenter* class. The UML diagram of simulation properties is shown in Fig. 4.

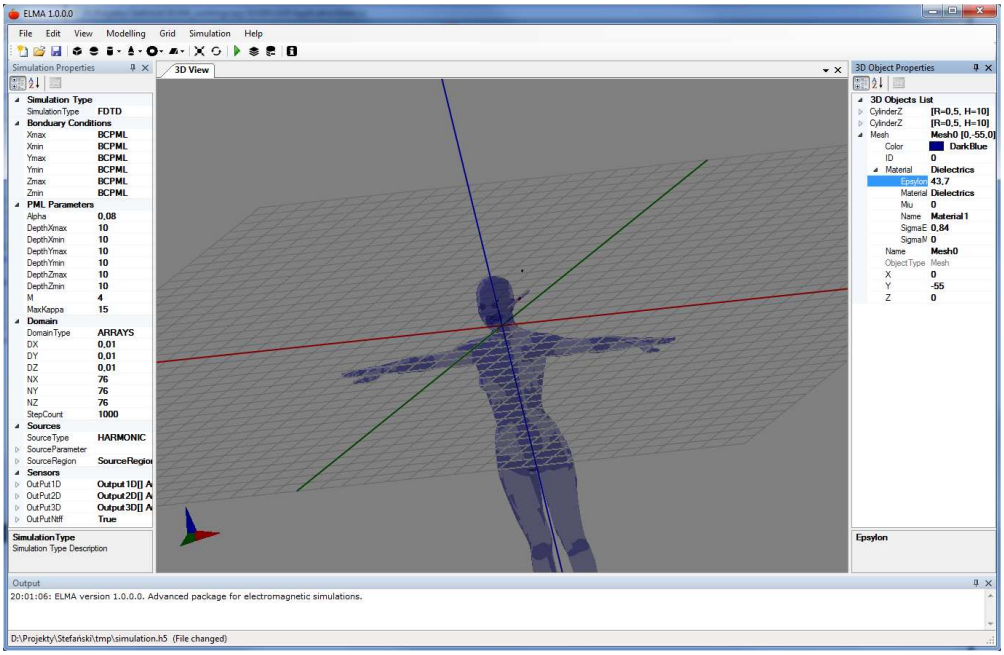

Figure 2: GUI standard view. Human CAD model was imported.

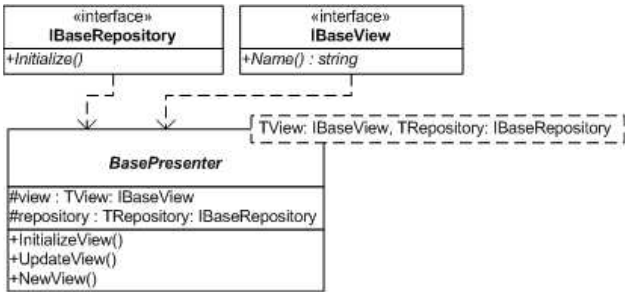

Figure 3: Class diagram for BasePresenter.

In general, similar models are adapted to all view forms in the project. Therefore, all presentation forms have the same interface but they are specialized to present different information. It facilitates not only the development process but also it will help to develop new functionalities in the future.

The simulation input parameters and results can be efficiently exposed into .NET managed classes using properties concept. A property is accessed syntactically as a field of a class. In the source code, the property is connected with a private data member exhibited by an accessor function. Moreover, the .NET framework provides data binding mechanism based on properties that

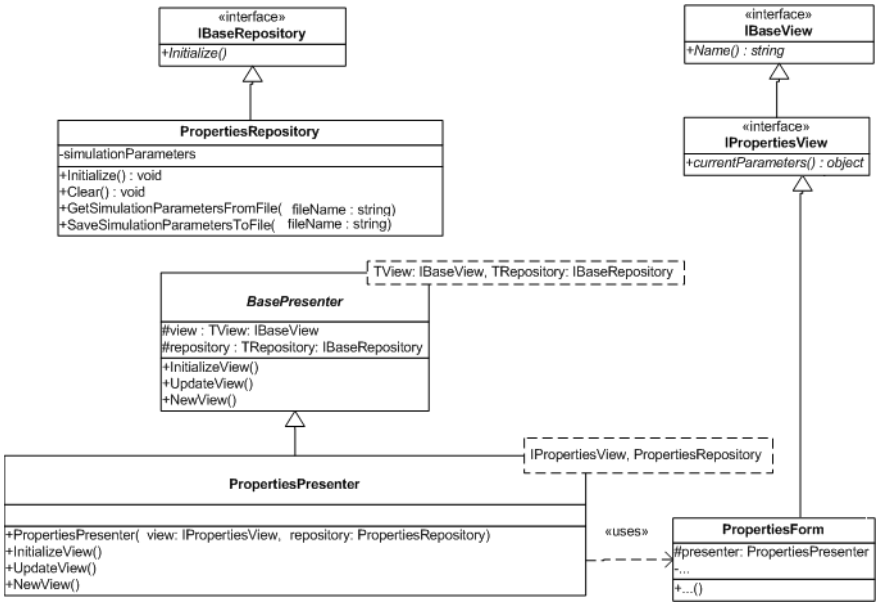

Figure 4: UML diagram of the MVP design pattern implemented in the developed software package. PropertiesForm is the view class for current presenter (contains more members which are not presented in this figure). This class derives from the Forms class being the part of the WindowsForms library. Presenter designated for PropertiesView is a member of the view class.

were used to bind and synchronize the presenter with view as a data repository. The *PropertyGrid* control is useful for this purpose. All data types that are defined in MVP models are completed with *TypeConverterAttribute* descriptors for all members. This mechanism allows developer to define its own way of presenting the data member. Therefore, all parameters of the simulation can be presented in clear and unified way for a user.

4. VISUALISATION OF RESULTS

Simulation results returned by the solver module can be split into four categories: (i) 1-D data, (ii) 2-D planes for 2-D data representation, (iii) 2-D planes for 3-D data representation and (iv) 3-D surfaces representing output of the near-to-far-field transformation. Each type of results can be associated with appropriate presenters in the OpenGL engine. Additional dock panel was introduced for this purpose, see Fig. 5. This mechanism ensures that any type of results provided

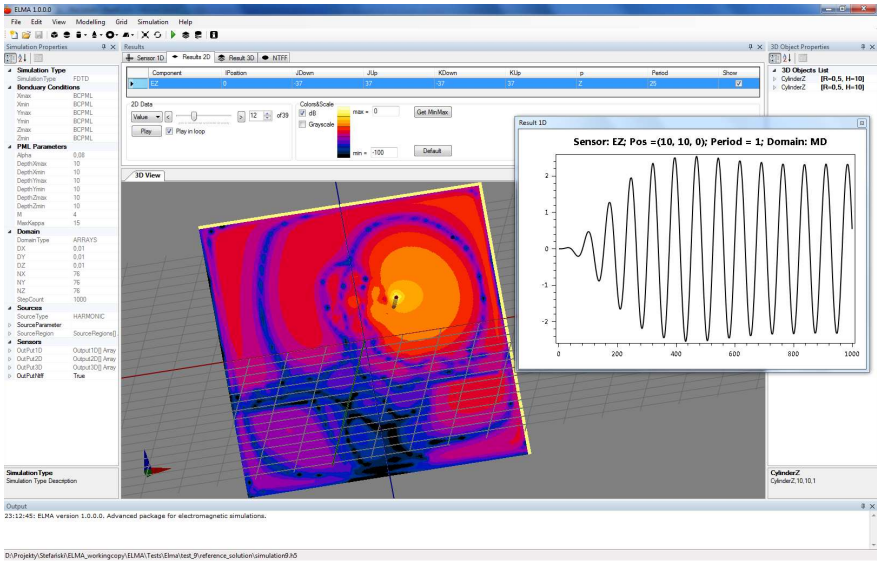

Figure 5: Results of a simulation — human model exposed to the radiation.

by the solver module can be presented by the results visualization engine.

5. SOFTWARE PACKAGE FOR ELECTROMAGNETIC SIMULATIONS

The presented above software architecture and data model were employed for development of the software package for electromagnetic simulations. It supports three main functions: (i) edition of input parameters for simulations, (ii) running simulations and (iii) presentation of results. The package was expanded with functionalities related to integrated development environments, e.g., data validation, error and warring messages, etc.. The OpenGL graphical engine supports drawing of geometrical objects as well as importing CAD objects. It implements the standard arc-ball procedure for rotation of the 3-D scene. The picking of 3-D objects was developed to allow a user selecting objects by mouse click.

6. CONCLUSIONS

We have presented the layered software architecture for computational electromagnetics codes. This architecture simplifies the development of new features of the software package by using well defined design patterns along with own engine for data management. This approach also facilitates automated tests. The object-oriented architecture utilized in this project and the extensive .NET base class library simplify the application model and relationship between types. The separation of code into the GUI and solver executable modules allows to run simulations on systems without graphical interface as well as it enables the visualization of results on systems not supporting the solver module.

ACKNOWLEDGMENT

This work was realized within the HOMING PLUS Program of the Foundation for Polish Science, co-financed from the European Union Regional Development Fund.

REFERENCES

1. Taflove, A. and S. C. Hangess, *Computational Electrodynamics: The Finite-difference Time-domain Method*, 3rd Edition, Artech House, Boston, MA, 2005.
2. Computer Simulation Technology, available online: http://www.cst.com.
3. SEMCAD X, available online: http://www.speag.com/products/semcad/overview/.
4. Fernandes, L. C. and A. J. M. Soares, "Software architecture for the design of electromagnetic simulators," *IEEE Antennas Propag. Magazine*, Vol. 55, No. 1, 155–168, 2013.
5. Yu, W. and R. Mittra, "Development of a graphical user interface for the conformal finite-difference/time-domain (CFDTD) software package," *IEEE Antennas Propag. Magazine*, Vol. 45, No. 1, 58–74, 2003.
6. The C# Language Specification, ver. 4.0 ECMA Library, electronic file available at: http://www.ecma-international.org/publications/files/ECMA-ST/Ecma-334.pdf, 2006.
7. The C++/CLI Language Specification, ver. 1.0, ECMA Library, electronic file available at: http://www.ecma-international.org/publications/files/ECMA-ST/ECMA-372.pdf, 2005.
8. The HDF5 Software Documentation, electronic file available at: http://www.hdfgroup.org/HDF5/doc/index.html, 2013.

Examination of Discrete Green's Function Approach to Absorbing Boundary Condition in FDTD Method

M. Wiktor[1] and T. P. Stefanski[2]

[1]Gdansk Medical University, M. Skodowskiej-Curie 3a, Gdansk 80-210, Poland
[2]Gdansk University of Technology, Narutowicza 11/12, Gdansk 80-233, Poland

Abstract— The paper presents an implementation of absorbing boundary condition (ABC) utilizing the discrete Green's function (DGF) for termination of the finite-difference time-domain (FDTD) grid. Although a simplified one dimensional FDTD grid was considered in our investigations, almost all numerical issues can be demonstrated in this way. A convolution of DGF with equivalent current sources measured over two displaced Huygens surfaces next to the boundary provides almost exact boundary value with the reflection error of ABC comparable to the numerical noise level. Strategies for truncation of DGF waveforms in the developed ABC implementation are discussed. Obtained results demonstrate that at a reasonable computational cost, the error level can be kept below $-100\,\mathrm{dB}$ using the windowing technique.

1. INTRODUCTION

Consistent coupling of integral operators with the finite-difference time-domain (FDTD) method requires discrete formulation of the fundamental electromagnetic theorems and a discrete equivalent of the Green's function, known as the FDTD-compatible Green's function or the discrete Green's function (DGF) [1–3]. Computing a convolution of current sources with dyadic DGF allows one to obtain the FDTD solution without execution of the time-marching procedure. Implementation of the absorbing boundary condition (ABC) in the FDTD method is one of the key DGF applications. Consistency with the electromagnetic theory on a grid guarantees the highest accuracy of the DGF-based ABC.

Since the impulse response of the FDTD grid can be calculated in advance for each iteration (time step) and any cell position, boundary values can be found yielding absorption of outgoing waves. Several ABC implementations employing DGF have been presented in the literature [4, 5]. In [5], the electric field at the domain boundary was calculated as the convolution of DGF with the magnetic field measured next to the boundary. Due to calculation of the boundary value as the convolution of DGF with the field measured on a single Huygens surface, the reflection error was obtained at the level of $-50\,\mathrm{dB}$.

In this paper, the improvement of the previously proposed DGF-based ABC [5] is presented. Finally, an amplitude of a wave reflected from the domain boundary was minimized to the numerical noise level ($-300\,\mathrm{dB}$). Similarly to [4, 5], we consider a simplified one-dimensional (1-D) grid which, despite its simplicity, allows to demonstrate properties of the proposed DGF-based ABC implementation. Since global ABC algorithms can be computationally expensive, a tradeoff between accuracy of computations and their runtime is also discussed in this contribution.

2. DGF-BASED ABC

Let us consider the 1-D FDTD grid ($\Delta x, E\,|_i^n, H\,|_i^n$) terminated by ABC at the cell I. FDTD cells are numbered as shown in Figure 1.

Figure 1: 1-D FDTD grid.

The Huygens box is placed in close proximity to the boundary and comprises of two surfaces separated by a half-cell distance. This implementation of the Huygens box is consistent with the equivalence theorem in the discrete domain [6, 7]. The equivalent electric and magnetic currents

can be found using the magnetic and electric fields measured over the Huygens surfaces:

$$J_{eq}\,|_{I-1}^{n} = -\frac{H\,|_{I-1}^{n}}{\Delta x} \tag{1}$$

$$M_{eq}\,|_{I-1}^{n} = \frac{E\,|_{I-1}^{n}}{\Delta x} \tag{2}$$

The electromagnetic field at the grid boundary is computed as the convolution of the equivalent current sources and the $G_{ee}\,|_{1}^{n}, G_{eh}\,|_{1}^{n}$ components of dyadic DGF:

$$E\,|_{I}^{n} = \sum_{n'} \left[G_{ee}\,|_{1}^{n-n'} \quad G_{eh}\,|_{1}^{n-n'} \right] \begin{bmatrix} J_{eq}\,|_{I-1}^{n'} \\ M_{eq}\,|_{I-1}^{n'} \end{bmatrix} \tag{3}$$

Dyadic DGF can be found directly [8], or can be computed by running auxiliary simulations with the Kronecker delta excitations. In the reported investigations, the latter approach was employed. Assuming infinite numerical precision of computations, these two methods of the DGF generation are equivalent.

3. ABC IMPLEMENTED WITH THE USE OF TRUNCATED DGF

In order to evaluate the accuracy of DGF-based ABC, electric field waveforms sampled at distance equal to 15 cells from the grid boundary ($E\,|^{n}$) were compared with the reference solution ($E_{ref}\,|^{n}$). The relative error has been calculated as:

$$\text{Error}\,|^{n} = 20\log_{10}\frac{\left|E\,|^{n} - E_{ref}\,|^{n}\right|}{\max\left|E_{ref}\,|^{n}\right|} \tag{4}$$

The modulated Gaussian pulse excitation (center frequency corresponding to the wavelength $\lambda = 10\Delta x$) was employed in the reported test results. The procedure described in the previous section results in the reflection error comparable to the numerical noise level. For double precision computations, it is around -300 dB. However, such an accuracy can be obtained only if the convolution (3) extends for all previous values of the equivalent currents $J_{eq}\,|_{I-1}^{n}, M_{eq}\,|_{I-1}^{n}$. It means, that all current samples starting from the beginning of a simulation have to be stored in data buffers. For longer simulations, it will lead to performance and memory issues.

A straightforward solution is to limit the convolution summation (3) by truncation of the DGF waveform to K samples. However, the abrupt truncation of DGF may result in a significant error of the DGF-FDTD method [3]. Looking at 1-D G_{ee} DGF plotted in Figure 2, one can notice that the pulse response of the grid is decaying very slowly. This means that distant time samples may also contribute to the boundary value in this ABC implementation.

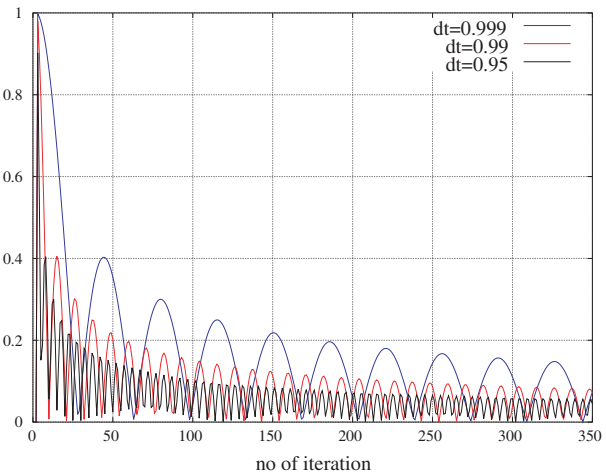

Figure 2: Absolute value of G_{ee} DGF for varying time-step size Δt (Δt is normalized to its maximal value $\Delta t_{\max}$ guaranteeing stable simulation).

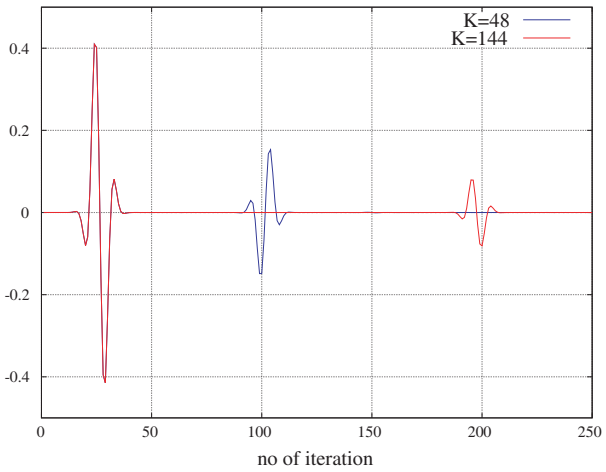

Figure 3: Electric field waveform measured 15 cells from ABC implemented with the use of truncated DGF. The reflected pulse is visible for 100/200 iteration.

The abrupt truncation of the convolution summation (3) results in a propagation of reflected wave for $n > K$, see Figure 3. The first pulse represents the wave impinging at ABC whilst the second pulse represents the wave reflected from ABC. In the case of imperfect PML or Mur ABC [9], the reflected wave should be observed after approximately 30–40 iterations. However, the returning wave is observed much later for DGF-based ABC. Depending on the DGF length (K parameter), the reflected wave is delayed by approximately K samples. This behavior is typical for DGF-based ABC since inaccuracy caused by this type of ABC has different origin compared to PML or Mur ABC.

4. ABC IMPLEMENTED WITH THE USE OF WINDOWED DGF

In order to avoid discontinuity caused by the abrupt truncation of DGF and minimize amplitude of the reflected wave, a windowing of DGF was employed to make its decay more smooth [3]. In our investigations, we tested the Hann window function:

$$\text{Hann}\,|^n = \begin{cases} 1 & n \le \frac{2K}{3} \\ \frac{1+\cos\left(\pi \frac{n-2K/3}{K/3}\right)}{2} & n > \frac{2K}{3} \end{cases} \tag{5}$$

The reflection error waveform for different window lengths is presented in Figure 4. The reflection error of DGF-based ABC is caused not by inaccurate ABC matching to the FDTD grid, but by

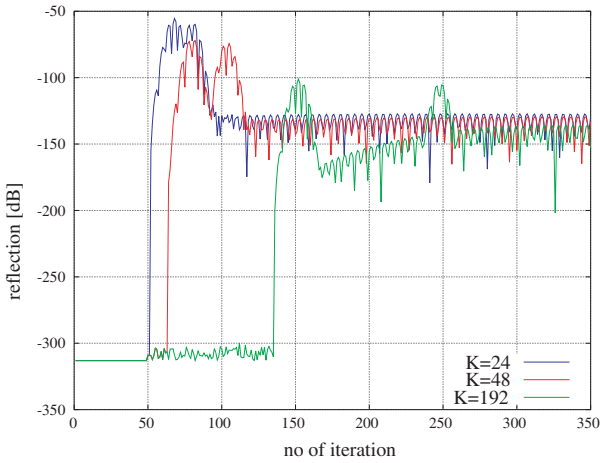

Figure 4: Reflection error waveforms for varying length of the Hann window applied to DGF ($\Delta t = 0.95$).

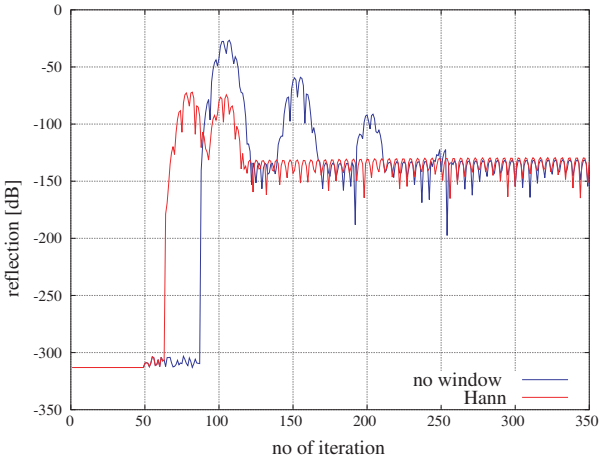

Figure 5: Reflection error waveforms for abrupt truncation of DGF (no window) and the Hann window applied to DGF ($K = 48$, $\Delta t = 0.95$).

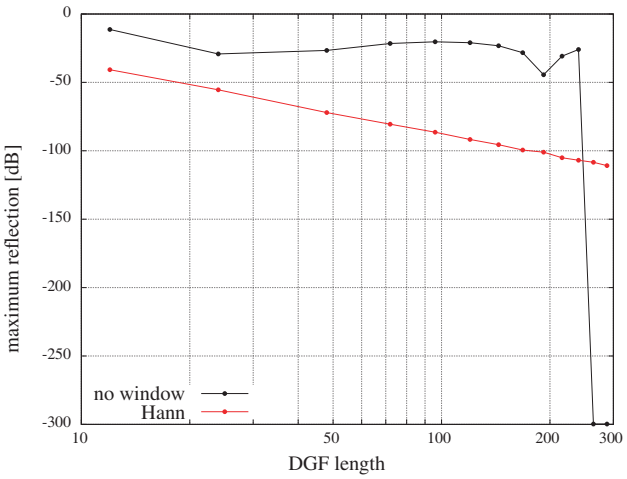

Figure 6: Maximum reflection error vs. DGF length for abrupt truncation of DGF (no window) and the Hann window applied to DGF ($\Delta t = 0.95$).

the spurious pulse discussed in the previous section. As seen, the delay of the spurious pulse is approximately equal to the DGF length. However, by tuning parameters of the window function, it is possible to delay and attenuate the reflected pulse, as presented in Figure 5.

The maximum reflection error vs. the DGF length is presented in Figure 6. As seen, application of the windowing technique, instead of the abrupt DGF truncation, significantly improves the ABC accuracy. In order to keep the error at the level of −50 dB as in [5], the Hann window should be longer than 24 samples. Doubling the DGF length results in the error level comparable to the well tuned PMLs (−70 dB). The DGF length equal to 200 samples provides the ABC error at the level of −100 dB. In the case of the abrupt truncation of DGF, the reflection error is significant as long as the DGF length is smaller than the number of iterations in the simulation. For the DGF length approaching to the number of iterations in the simulation, the reflection error achieves the numerical noise level.

5. SUMMARY

In this paper, the performance of DGF-based ABC has been demonstrated. Although a simplified 1-D FDTD grid was considered in our investigations, almost all numerical issues have been demonstrated in this way. Obtained results demonstrate that at a reasonable computational cost, the error level can be kept below −100 dB using the windowing technique.

6. ACKNOWLEDGMENT

This work was supported by the National Science Centre under contract DEC-2012/05/D/ST7/00141.

REFERENCES

1. Vazquez, J. and C. Parini, "Discrete Green's function formulation of FDTD method for electromagnetic modelling," *Electron. Lett.*, Vol. 35, No. 7, 554–555, Apr. 1999.
2. Holtzman, R. and R. Kastner, "The time-domain discrete Green's function method (GFM) characterizing the FDTD grid boundary," *IEEE Trans. Antennas Propag.*, Vol. 49, No. 7, 1079–1093, Jul. 2001.
3. Stefanski, T. P., "Accuracy of the discrete Green's function formulation of the FDTD method," *IEEE Trans. Antennas Propag.*, Vol. 61, No. 2, 829–835, Feb. 2013.
4. Holtzman, R., R. Kastner, E. Heyman, and R. Ziolkowski, "Stability analysis of the Green's function method (GFM) used as an ABC for arbitrarily shaped boundaries," *IEEE Trans. Antennas Propag.*, Vol. 50, No. 7, 1017–1029, Jul. 2002.
5. Ma, W., "Discrete Green's function formulation of the FDTD method and its application," Ph.D. Dissertation, Queen Mary University of London, 2004.
6. Merewether, D. E., R. Fisher, and F. W. Smith, "On implementing a numeric Huygen's source scheme in a finite difference program to illuminate scattering bodies," *IEEE Trans. Nucl. Sci.*, Vol. 27, No. 6, 1829–1833, 1980.
7. Martin, T., "An improved near- to far-zone transformation for the finite-difference time-domain method," *IEEE Trans. Antennas Propag.*, Vol. 46, No. 9, 1263–1271, 1998.
8. Kastner, R., "A multidimensional Z-transform evaluation of the discrete finite difference time domain Green's function," *IEEE Trans. Antennas Propag.*, Vol. 54, No. 4, 1215–1222, Apr. 2006.
9. Taflove, A. and S. C. Hagness, *Computational Electrodynamics: The Finite-difference Time-domain Method*, 3rd Edition, Artech House, Boston, 2005.

Driven Eigenproblem Computation for 2D Periodic Structures

Huanlei Chen[1], **Thomas F. Eibert**[1], **and Wenquan Che**[2]

[1]Lehrstuhl für Hochfrequenztechnik, Technische Universität München, Germany
[2]Department of Communication Engineering, Nanjing University of Science and Technology, China

Abstract— The driven eigenproblem computation analyzes the dispersion and attenuation behavior of periodic structures by solving the corresponding excitation problem in the eigenvalue domain. The unit cell of periodic structures is analogized to a resonator and stimulated with appropriately arranged excitation. By monitoring the field quantities, pairs of (resonance frequency, wavevector) as eigenvalues can be obtained. The driven method has been implemented in a hybrid finite element boundary integral (FEBI) solver for 2D periodic structures, where complex wavevectors for propagating modes with attenuations or leaky and evanescent modes are supported. The driven method was proved to be efficient and accurate in one dimensional periodic structures, like corrugated dielectric slab and composite right-/left-handed (CRLH) leaky wave antenna based on SIW. In this work, the driven method is employed for two dimensional metamaterials. A mushroom structure is analyzed to demonstrate the versatility of the driven method.

1. INTRODUCTION

With increasing operating frequency, periodic structures based on substrate integrated waveguides (SIWs) and metamaterials are attracting more and more research interests with the advantages of low loss and high quality factor for microwave, millimeter wave or even terahertz frequencies. The study about dispersion and attenuation behaviors helps to better understand and design periodic structures. However, due to large model size, fine details and often open configurations, the modeling of the electromagnetic fields inside and outside the periodic structures is often a complicated complex eigenproblem with a very large number of unknowns. The full-wave modeling methods based on classical numerical methods [1, 2] often face the difficulty of slow convergence and low accuracy, especially for large-size numerical systems which are induced by periodic structures with very fine details. Compared to the pure mathematical approach of common eigenproblem solvers, the driven eigenproblem computation method solves eigenproblems by solving the corresponding excitation problems in the domain of the eigenvalue [3]. According to Floquet's theorem, the driven method analogizes the unit cell of periodic structures to a resonator model and simplifies the eigenvalue determination for large numerical systems by monitoring the resonance behavior. Comparing with time-domain excitation techniques, the driven method works directly in the eigenvalue domain and is able to concentrate the entire excitation energy in one isolated eigenmode. With appropriately arranged excitation, e.g., port excitation or distributed current densities excitation, one or more particular modes can be stimulated in the unit cell of periodic structures. By searching the extremum for the field quantities, the corresponding pairs of (resonance frequency, wavevector) as eigenvalues can be obtained. This converts the eigenvalue searching into a maximization approach. The driven method was proved to be efficient and accurate in one dimensional periodic structures, like corrugated dielectric slab and composite right-/left-handed (CRLH) leaky wave antenna based on SIW [3–5]. As a continuation, the driven method is employed for two dimensional metamaterials in this work. A mushroom structure [6] is analyzed to demonstrate the versatility of the driven method.

2. DRIVEN EIGENPROBLEM FORMULATION

2.1. Eigenproblem-Resonator Analogy Formulation

According to Floquet's theorem, the eigenproblem of a periodic structure can be solved in form of a unit cell with periodic boundary condition. Consider a periodic eigenproblem of the unit cell according to

$$L(\omega, \mathbf{k}_0)x = 0, \tag{1}$$

with suppressed time dependence $e^{j\omega t}$. $\mathbf{k}_0$ is the three-dimensional wavevector, which defines the non-periodic functional dependence in space. L represents some form of Maxwell's equations with appropriate boundary conditions and material relations. x is the vector solution of the operator

equation. In discretized version, for example the numerical solutions by finite element or by the method of moments, the operator equation is typically discretized and leads to a linear homogenous equation system

$$[A_{mn}(\omega, \mathbf{k}_0)]x_n = 0. \tag{2}$$

A_{mn} are the matrix entries as a function of $(\omega, \mathbf{k}_0)$ and x_n are the unknown expansion coefficients of the field solution. The eigenvalues here are pairs of $(\omega, \mathbf{k}_0)$, which make the system singular and indicate one or more propagating modes.

In electric circuits, a shunt resonator consisting of a capacitor C and an inductor L with a loss conductance G_L can also be expressed as

$$Y(\omega_{\text{res}})U = \left[j(\omega C - \frac{1}{\omega L}) + G_L \right] U = 0. \tag{3}$$

For a series resonator, with a loss resistor R_L instead of G_L, it can be expressed as

$$Z(\omega_{\text{res}})I = \left[j(\omega L - \frac{1}{\omega C}) + R_L \right] I = 0. \tag{4}$$

The eigenvalues in (3) and (4) are ω_{res}, which make the equation singular. In a lossy system, ω_{res} is a complex quantity. The analogy between the eigenproblem in (2) and the resonance condition in (3) and (4) opens up an opportunity to convert the eigenproblem into a resonator problem where the eigenvalue is the resonance frequency. Consequently, the eigenvalue determination is equivalent to searching for the resonance frequency ω_{res} when the resonator is excited. In other words, the eigenproblem of the periodic structure can be solved in the domain of eigenvalue by solving the corresponding excitation problem.

2.2. 2D Periodic Eigenproblem Formulation

Considered a 2D infinite periodic configuration as illustrated in Fig. 1. The geometry or the material distribution is periodic along the x- and y-axis with lattice vector $\boldsymbol{\rho}_a$ and $\boldsymbol{\rho}_b$, respectively. In direction of the z-axis the configuration is divided into several layers. The possibly inhomogeneous parts are included in one layer, which can be represented in a unit cell and discretized with a tetrahedral mesh. According to Floquet's theorem, the fields in the structure can be expressed as

$$\mathbf{E}(\mathbf{r} + m\boldsymbol{\rho}_a + n\boldsymbol{\rho}_b) = \mathbf{E}(\mathbf{r})e^{-j\mathbf{k}_{t00}\cdot(m\boldsymbol{\rho}_a + n\boldsymbol{\rho}_b)}, \tag{5}$$

$$\mathbf{H}(\mathbf{r} + m\boldsymbol{\rho}_a + n\boldsymbol{\rho}_b) = \mathbf{H}(\mathbf{r})e^{-j\mathbf{k}_{t00}\cdot(m\boldsymbol{\rho}_a + n\boldsymbol{\rho}_b)}, \tag{6}$$

with

$$\mathbf{k}_{t00} = k_{x00}\hat{x} + k_{y00}\hat{y}. \tag{7}$$

$\mathbf{k}_{t00}$ is the wavevector parallel to the xy-plane and corresponding to the (00)th Floquet mode. The pairs of $(\mathbf{k}_{t00}, \omega_{\text{res}})$ are the eigenvalues of the eigenproblem of periodic structure. In the driven resonator model, the resonance frequency can be easily located by monitoring the electromagnetic field, for example the electric field or another observable, which will reach an extremum at the resonance frequency. There are many ways to provide excitation to the analysis model. One is port excitation which employs the electric circuits and network theory. By monitoring the S-parameters between the input and output ports, the resonance frequency can be found. Meanwhile the perturbation method is applied to calculate the attenuation of the transmitted wave. The port excitation is conveniently realized with some commercial numerical solvers, e.g., CST Microwave Studio [7] however with its application restricted to small attenuation scenarios due to the limitation in the flexibility of the periodic boundary conditions [4]. The other way is distributed current densities excitation, which is realized with a hybrid finite element boundary integral (FEBI) solver [8] in this work and has the advantages of all-mode stimulation and mode selection. With full support of complex wavevectors for the periodic boundary condition, the direct analysis of the evanescent and leaky modes is possible [3, 5]. Solving the eigenproblem of periodic structures by solving the corresponding excitation problem makes the eigenvalue $(\mathbf{k}_{t00}, \omega_{\text{res}})$ searching process a maximization. With some initial estimations based on the previous solutions, the driven method repeats the iterations of the solution of the excitation problem with slightly varying parameters. This can be performed by sweeping the frequency with a fixed wavevector as well as scanning the complex plane of the wavevector at a fixed frequency. Some methods like Brent's and Powell's methods are introduced to accelerate the speed of convergence of the searching iterations [5].

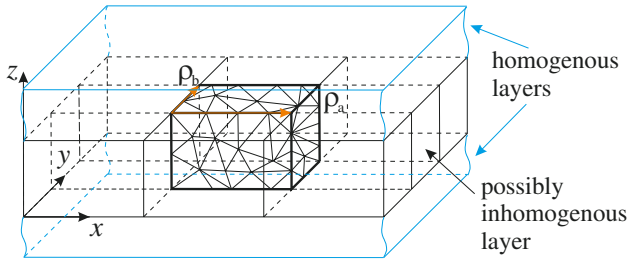

Figure 1: 2D infinite periodic configuration.

3. NUMERICAL RESULTS

The driven method has been successfully applied to 1D periodic structures, e.g., corrugated dielectric slab and composite right-/left-handed (CRLH) leaky wave antenna based on SIW [4, 5]. In this work, the driven method is applied to 2D periodic structures. As shown in Fig. 2, a mushroom structure is periodic in x- and y-direction with the unit cell dimension of 5.0 mm × 5.0 mm. The mushroom structure consists of a layer of top patches and the ground plane. The top patches are connected to the ground plane by vias of 0.2 mm diameter. Between the top and the ground metal layers, a dielectric substrate with $\varepsilon_r = 2.2$ is sandwiched. Under the top patches inside the substrate there is a cap layer to introduce an extra series capacitor. The thickness of the upper and lower substrates are $h_1 = 0.127$ mm and $h_2 = 1.697$ mm.

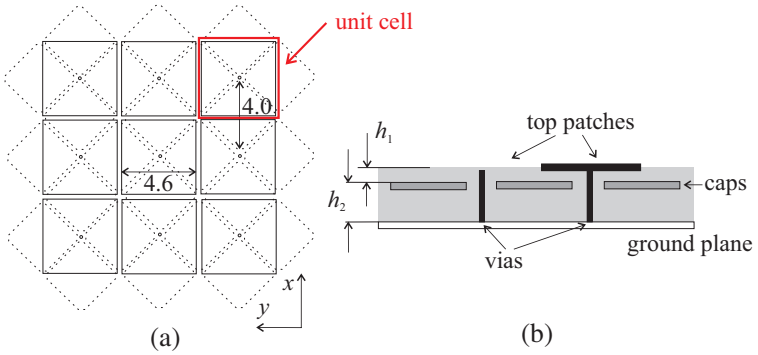

Figure 2: The mushroom structure [6] and its unit cell. The period of the unit cell is 5.0 mm × 5.0 mm. The mushroom structure consists of the top patches and a ground plane which are connected by vias. Between the top layer and the ground plane, there is a dielectric substrate with $\varepsilon_r = 2.2$ and a cap layer is under the top patches. (a) Dimensions of the configuration in mm. (b) The side view of the mushroom structure. The distance between the top patches and the caps is $h_1 = 0.127$ mm and the one between the caps and the ground plane is $h_2 = 1.697$ mm.

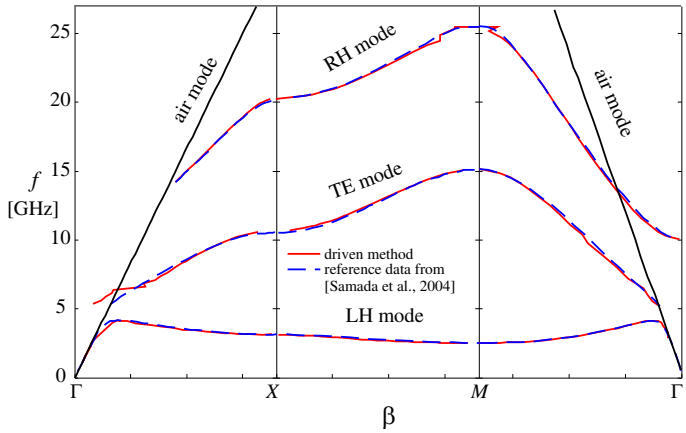

Figure 3: Dispersion diagrams of the mushroom structure in Fig. 2 compared to the reference data from [6].

As a 2D periodic configuration along both the x- and y-direction, the dispersion diagram of the mushroom structure is a 2D function $f_n(k_x, k_y)$, where n labels the number of the mode. Therefore, the *irreducible Brillouin zone* was introduced to demonstrate the dispersion curve for it [6]. The unit cell of the mushroom structure was first discretized with a triangular mesh on the surface and a first order tetrahedral mesh in the substrate. In total, 31193 tetrahedral mesh cells were generated. Then it was analyzed with the driven method as implemented in FEBI and excited with distributed current densities. The average computation time for one frequency with the driven method is 1165.5 s. Compared to the results obtained by full wave (FEM) analysis with periodic boundary conditions applied at the edges of the unit cell in [6], the driven method achieves a perfect

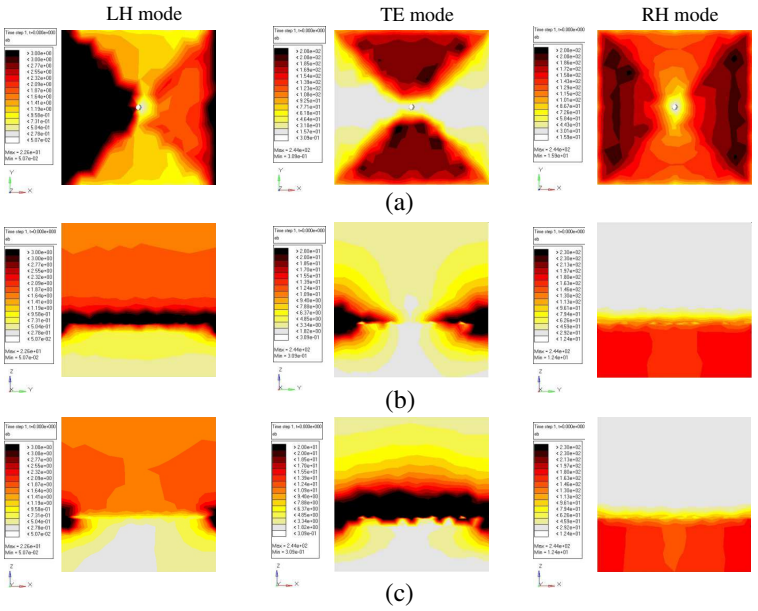

Figure 4: Modal field distribution of the three modes of the mushroom structure in Fig. 2 in the Γ-X segment of the irreducible Brillouin zone. The first column is the LH mode, the second column is the TE mode, the third column is the RH mode. (a), (b), and (c) stand for the cross section of the xy-, yz-, and zx-plane, respectively.

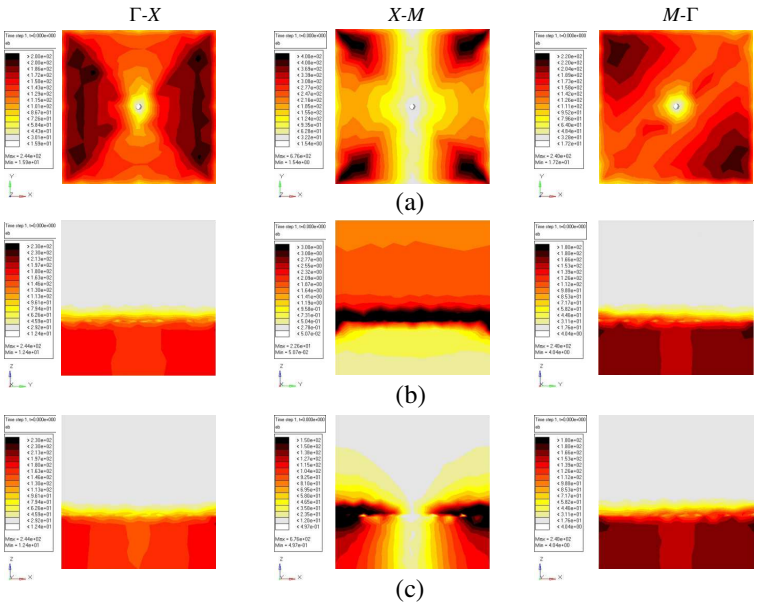

Figure 5: Modal field distribution of the RH modes of the mushroom structure in Fig. 2 in the irreducible Brillouin zone. The first column is in the segment Γ-X, the second column is in the segment X-M, the third column is in the segment M-Γ. (a), (b), and (c) stand for the cross section of xy-, yz-, and zx-plane, respectively.

match, as depicted in Fig. 3.

Figures 4 and 5 give some examples of modal field distributions of the mushroom structure. Fig. 4 demonstrates the E-field distributions of the three modes in the Γ-X segment of the irreducible Brillouin zone. The E-field distributions in different cross sections which belong to one mode are displayed in one column. The left-hand (LH) mode at 2.62 GHz is in the first column, the TE mode at 9.11 GHz is in the second column, and in the third column is the right-hand (RH) mode at 14.23 GHz. The first row shows the field distributions in the xy-plane, the second row in the yz-plane, and the third row in the zx-plane. The E-field distributions for RH mode in different segments of irreducible Brillouin zone are depicted in Fig. 5. The E-field distributions at 14.23 GHz in segment Γ-X are in the first column, the ones at 23.68 GHz in X-M are in the second column, and the ones at 13.93 GHz in M-Γ are in the third column.

4. CONCLUSION

Driven eigenproblem simulations open up a possibility to solve eigenproblems as excitation problems in the eigenvalue domain. The driven method can efficiently deliver the dispersion and attenuation analysis of periodic structures by analogizing the unit cell of periodic structure with periodic boundary to a resonator, which can be stimulated by either port or distributed current densities. Consequently, the eigenvalue searching procedure is converted to a maximization of the function of (frequency, wavevector). The application of 2D mushroom structure demonstrates the capability of the driven method in complicated configuration and multi-mode operation.

ACKNOWLEDGMENT

Supported by Deutsche Forschungsgemeinschaft (DFG) through the TUM International Graduate School of Science and Engineering (IGSSE) and under grant EI 352/11 − 1.

REFERENCES

1. Xu, F., K. Wu, and W. Hong, "Finite-difference time-domain modeling of periodic guided-wave structures and its application to the analysis of substrate integrated nonradiative dielectric waveguide," *IEEE Trans. Microw. Theory Tech.*, Vol. 55, No. 12, 2502–2511, 2007.
2. Deslandes, D. and K. Wu, "Accurate modeling, wave mechanisms, and design considerations of a substrate integrated waveguide," *IEEE Trans. Microw. Theory Tech.*, Vol. 54, No. 6, 2516–2526, 2006.
3. Eibert, T. F., Y. Weitsch, H. Chen, and M. E. Gruber, "Solving periodic eigenproblems by solving corresponding excitation problems in the domain of the eigenvalue," *Progress In Electromagnetics Research*, Vol. 126, 65–84, 2012.
4. Eibert, T. F. and J. L. Volakis, D. R. Wilton, and D. R. Jackson, "Hybrid FE/BI modeling of 3D doubly periodic structures utilizing triangular prismatic elements and a MPIE formulation accelerated by the Ewald transformation," *IEEE Trans. Antennas and Propagation*, Vol. 47, No. 5, 843–850, May 1999.
5. Chen, H., T. F. Eibert, and W. Che, "The eigenproblem computation with the brent's method acceleration," *European Conference on Antennas and Propagation (EuCAP)*, Prague, Czech, March 2012.
6. Sanada, A., C. Caloz, and T. Itoh, "Planar distributed structures with negative refractive index," *IEEE Trans. Microw. Theory Tech.*, Vol. 52, No. 4, 1252–1263, 2004.
7. 3D EM Field Simulation — CST Computer Simulation Technology, http://www.cst.com.
8. Eibert, T. F., J. L., Volakis, D. R. Wilton, and D. R. Jackson, "Hybrid FE/BI modeling of 3D doubly periodic structures utilizing triangular prismatic elements and a MPIE formulation accelerated by the Ewald transformation," *IEEE Trans. Antennas Propagat.*, Vol. 47, No. 5, 843–850, May 1999.

Hight Order FD Computation of TE and TM Modes in Single Grid

A. Fanti, **M. Simone**, **and G. Mazzarella**
University of Cagliari, Italy

Abstract— We describe here a High Finite Difference Frequency Domain approach to the mode computation in rectangular and circular waveguide with use of a single grid for both TE and TM modes.

1. INTRODUCTION

In FDTD analysis of waveguide components, the knowledge of the modal expansion can reduce significantly the computation time, by modeling each homogeneous waveguide trunk as a (small) set of FDTD problems [1]. This approach, however, requires the knowledge of the waveguide mode functions, either analytically, or numerically, on a grid matched to the 3D FDTD grid used in the inhomogeneous regions. The same knowledge of mode function as useful in the analysis of waveguide junction using mode matching [2], solution of waveguide problems with sources [3], and the method of moments (MOM) analysis of thick-walled waveguide apertures [4]. Apart from same simple geometries, mode computation cannot be done in closed forms, so that suitable numerical techniques must be used. Among them, finite difference techniques [5], despite of their long history, are still yery popular both for their simplicity and computational effectiveness. One of their main drawback, however, is the requirement of two different grids, namely one for TE modes and the other for TM modes due to the different boundary condition This requirement is present, to the best of our knowledge, in virtually every paper on the subject. This can be a problem when different grids must be matched at a plane interface, such as in mode matching or FDTD solution of discontinuities. Aim of the communication is to explore, and assess, the feasibility of use of a single grid for both TE and TM modes. In order to get a modal expansion to be used in FDTD [1] we select the TM grid, which can be naturally matched to the FDTD one. We first consider a rectangular waveguide, to detail our approach in the simplest case, and then extend it to polare case [6].

2. DESCRIPTION OF THE TECHNIQUE

Let use consider a rectangular waveguide. Both TE and TM modes can be found [3] from a suitable scalar eigenfunction, solution of the Helmothz equation:

$$\nabla_t^2\phi + k_t^2\phi = 0 \tag{1}$$

with the boundary condition (BC):

$$\frac{\partial\phi}{\partial n} = 0TE \quad \phi = 0TM \tag{2}$$

at the boundary of the rectangular waveguide. Numerical solution of this eigenvalue problem using the FD approach requires that both the Equation (1) and the BC (2) can be replaced by a discretizead version, i.e, replacing derivatives with finite approximations. This transform (1) in to a matrix eigenvalue problem, whose eigenvectors contains the samples of ϕ at the discretization nodes. The resulting matrix is sparse so a very effective computation is possible. Assuming a regular Cartesian grid with spacing $\Delta x,\ \Delta y$ and letting $\phi_{ij} = \phi(i\Delta x, j\Delta y)$ as sample values, we need a discretized version of (1) on each sampling point. For a point P see Fig. 1(a) we can use a fourth-order Taylor expression as:

$$\begin{aligned}
\phi_D &= \phi_P + \left.\frac{\partial\phi}{\partial y}\right|_P \cdot (+2\Delta y) + \frac{1}{2}\left.\frac{\partial^2\phi}{\partial y^2}\right|_P \cdot (+2\Delta y)^2 + \frac{1}{6}\left.\frac{\partial^3\phi}{\partial y^3}\right|_P \cdot (+2\Delta y)^3 + \frac{1}{24}\left.\frac{\partial^4\phi}{\partial y^4}\right|_P \cdot (+2\Delta y)^4 \\
\phi_N &= \phi_P + \left.\frac{\partial\phi}{\partial y}\right|_P \cdot (+\Delta y) + \frac{1}{2}\left.\frac{\partial^2\phi}{\partial y^2}\right|_P \cdot (+\Delta y)^2 + \frac{1}{6}\left.\frac{\partial^3\phi}{\partial y^3}\right|_P \cdot (+\Delta y)^3 + \frac{1}{24}\left.\frac{\partial^4\phi}{\partial y^4}\right|_P \cdot (+\Delta y)^4 \\
\phi_M &= \phi_P + \left.\frac{\partial\phi}{\partial y}\right|_P \cdot (-\Delta y) + \frac{1}{2}\left.\frac{\partial^2\phi}{\partial y^2}\right|_P \cdot (-\Delta y)^2 + \frac{1}{6}\left.\frac{\partial^3\phi}{\partial y^3}\right|_P \cdot (-\Delta y)^3 + \frac{1}{24}\left.\frac{\partial^4\phi}{\partial y^4}\right|_P \cdot (-\Delta y)^4 \\
\phi_B &= \phi_P + \left.\frac{\partial\phi}{\partial y}\right|_P \cdot (-2\Delta y) + \frac{1}{2}\left.\frac{\partial^2\phi}{\partial y^2}\right|_P \cdot (-2\Delta y)^2 + \frac{1}{6}\left.\frac{\partial^3\phi}{\partial y^3}\right|_P \cdot (-2\Delta y)^3 + \frac{1}{24}\left.\frac{\partial^4\phi}{\partial y^4}\right|_P \cdot (-2\Delta y)^4
\end{aligned} \tag{3}$$

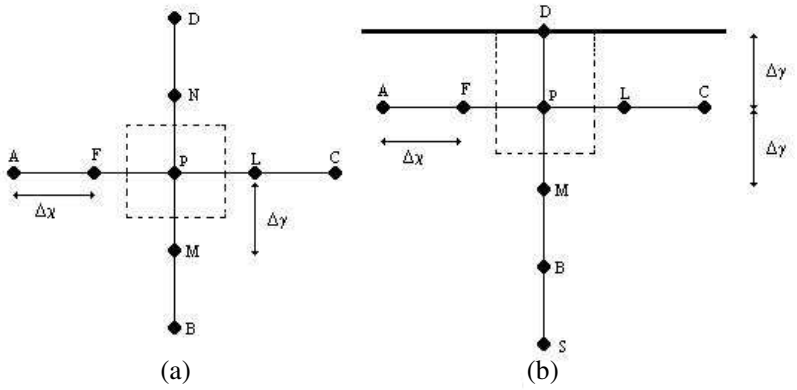

Figure 1: (a) Internal point of grid TE and TM. (b) Boundary point for TM case.

Adding the linear combination of last equations we find:

$$\left.\frac{\partial^2\phi}{\partial y^2}\right|_P = -\frac{1}{14Dy^2}\phi_D - \frac{1}{14Dy^2}\phi_B + \frac{16}{14Dy^2}\phi_N + \frac{16}{14Dy^2}\phi_M - \frac{30}{14Dy^2}\phi_P \tag{4}$$

Likely in x direction:

$$\left.\frac{\partial^2\phi}{\partial x^2}\right|_P = -\frac{1}{14Dx^2}\phi_C - \frac{1}{14Dx^2}\phi_A + \frac{16}{14Dx^2}\phi_L + \frac{16}{14Dx^2}\phi_F - \frac{30}{14Dx^2}\phi_P \tag{5}$$

Therefore,

$$\nabla_t^2\phi_p = \frac{1}{14}\left(-\frac{\phi_D}{Dy^2} - \frac{\phi_B}{Dy^2} + \frac{16\phi_N}{Dy^2} + \frac{16\phi_M}{Dy^2} - \frac{\phi_C}{Dx^2} - \frac{\phi_A}{Dx^2} + \frac{16\phi_L}{Dx^2} + \frac{16\phi_F}{Dx^2}\right) + -\frac{2}{14}\left(\frac{15}{Dy^2} + \frac{15}{Dx^2}\right)\phi_P \tag{6}$$

This equation can be used for all internal points to get the discretized form of (1):

$$\frac{1}{14}\left(-\frac{\phi_{i+2,j}}{Dy^2} - \frac{\phi_{i-2,j}}{Dy^2} + \frac{16\phi_{i+1,j}}{Dy^2} + \frac{16\phi_{i-1,j}}{Dy^2} - \frac{\phi_{i,j+2}}{Dx^2} - \frac{\phi_{i,j-2}}{Dx^2} + \frac{16\phi_{i,j+1}}{Dx^2} + \frac{16\phi_{i,j-1}}{Dx^2}\right) + -\frac{2}{14}\left(\frac{15}{Dy^2} + \frac{15}{Dx^2}\right)\phi_{i,j} = -k_t^2\phi_{i,j} \tag{7}$$

Equation (7) cannot be used for boundary points, where BC (2) must be enforced. The standard solution is to use different grids for TE and TM, as in Fig. 2. In this case, however, we use the TM grid for both type of modes (and BC). Let us consider an edge point P, and consider the nearby points M, B, and S ad shown in Fig. 1(b). For a TM mode, $\phi_D = 0$ and since D is a sampling point, we can solve the linear system of taylor expansions and replacement (4):

$$\left.\frac{\partial^2\phi}{\partial y^2}\right|_P = \frac{6}{12Dy^2}\phi_B + \frac{4}{12Dy^2}\phi_N - \frac{1}{12Dy^2}\phi_S - \frac{20}{12Dy^2}\phi_P \tag{8}$$

For a TE mode, instead, we consider a y axis normal to the boundary, and with P as origin, and express the potential in D, P, M, B, and S through a fourth order polynomial approximation:

$$\phi = \frac{1}{12}ay^4 + \frac{1}{6}by^3 + \frac{1}{2}cy^2 + dy + e \tag{9}$$

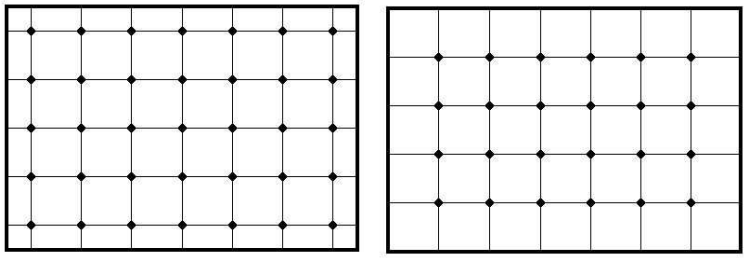

Figure 2: Standard TE and TM gri.

Forcing both the BC in D and the potential sample values:

$$\begin{aligned}
\left.\frac{\partial\phi}{\partial y}\right|_D &= \frac{4}{12}a\Delta y^3+\frac{3}{6}b\Delta y^2+cy+d=0\\
\phi_P &= e\\
\phi_M &= \frac{1}{12}a\Delta y^4-\frac{1}{6}b\Delta y^3+\frac{1}{2}c\Delta y^2-d\Delta y+\phi_P\\
\phi_B &= \frac{16}{12}a\Delta y^4-\frac{8}{6}b\Delta y^3+\frac{4}{2}c\Delta y^2-2d\Delta y+\phi_P\\
\phi_S &= \frac{81}{12}a\Delta y^4-\frac{27}{6}b\Delta y^3+\frac{9}{2}c\Delta y^2-3d\Delta y+\phi_P
\end{aligned} \tag{10}$$

system (10) can be easy solved obtaining:

$$\left.\frac{\partial^2\phi}{\partial y^2}\right|_P = 2ay^2+by+c=c=\frac{1}{150\Delta y^2}\cdot(138\phi_B-123\phi_M-29\phi_S+14\phi_P) \tag{11}$$

(11), togheter with (6) gives the discretized form of the laplacian in P

$$\frac{1}{14Dx^2}(-\phi_C-\phi_A+16\phi_L+16\phi_F)+\frac{1}{150\Delta y^2}\cdot(138\phi_B-123\phi_M-29\phi_S)-\left(\frac{30}{14Dx^2}-\frac{14}{150\Delta y^2}\right)\phi_P \tag{12}$$

Which is the replacement of (7) for external points in TE modes.

The same approach can be extended also to polar grid for circular waveguides [7].

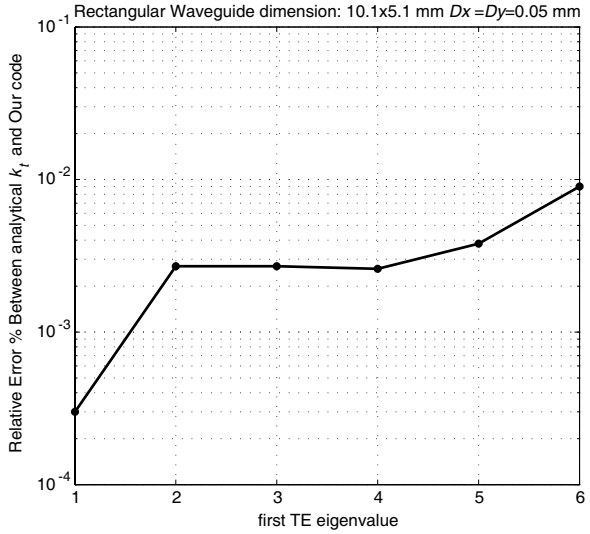

Figure 3: Comparison between our hight FDFD code and analytic results for TE modes in rectangular waveguide.

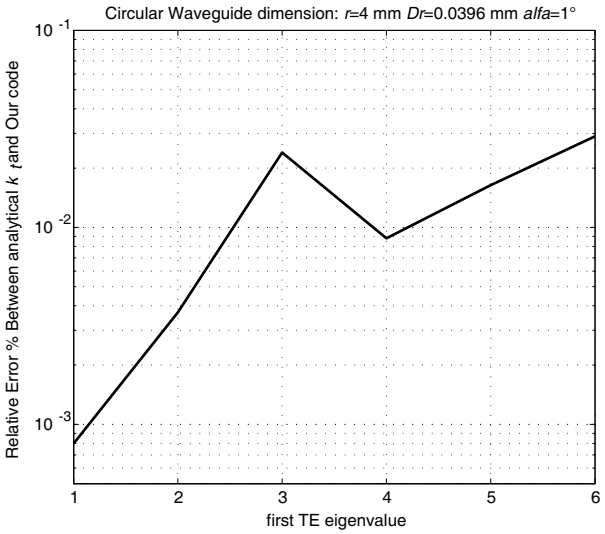

Figure 4: Comparison between our hight FDFD code and analytic results for TE modes in circular waveguide.

3. NUMERICAL RESULTS

It is easy to see that k_t^2 is the eigenvalue of an highly sparse matrix, since, for each row of it, no more than 9 elements can be different from zero. Therefore, very effective routines can be used to compute the smallest eigenvalues (the only ones of interest) and the corresponding eigenvectors, i.e., the field distribution of the modes inside the waveguide. To verify the validity of our High FDFD technique using single grid, we have analyzed rectangular and circular waveguide, and compared the eigenvalues of the first few TE modes with their exact values (shown Fig. 3 and Fig. 4).

4. CONCLUSION

A High Order FDFD approach in the single grid to the computation of the all modes of the waveguide has been described. The typical sparse matrix obtained by the FDFD allows an effective computation of the eigenvalues, with a very good accuracy, as shown by our tests.

ACKNOWLEDGMENT

Alessandro Fanti, Gratefully acknowledges Sardinia Regional Government for the financial support (P.O.R. Sardegna F.S.E. Operational Programme of the Autonomous Region of Sardinia, European Social Fund 2007–2013 — Axis IV Human Resources, Objective l.3, Line of Activity l.3.1 Avviso di chiamata per il finanziamento di Assegni di Ricerca.

Marco Simone, Gratefully acknowledges Sardinia Regional Government for the financial support of his PhD scholarship (P.O.R. Sardegna F.S.E. Operational Programme of the Autonomous Region of Sardinia, European Social Fund 2007–2013 — Axis IV Human Resources, Objective l.3, Line of Activity l.3.1.).

REFERENCES

1. Alimenti, F., P. Mezzanotte, L. Roselli, and R. Sorrentino, "Efficient analysis of waveguide components by FDTD combined with time domain modal expansion," *MGWL*, Vol. 5, 351–353, Oct. 1995.
2. Wexler, A., "Solution of waveguide discontinuities by modal analysis," *IEEE Trans. Microwave Theory and Techniques*, Vol. 15, 508–517, Sep. 1967.
3. Collin, R. E., *Field Theory of Guided Waves*, 2nd Edition, IEEE Press, New York, 1991.
4. Mazzarella, G. and G. Montisci, "A rigorous analysis of dielectric-covered narrow longitudinal shunt slots with finite wall thickness," *Electromagnetics*, Vol. 19, 407–418, Oct. 1999.
5. Morton, K. W. and D. F. Mayers, *Numerical Solution of Partial Differential Equations, An Introduction*, Cambridge University Press, 2005.
6. Fanti, A. and G. Mazzarella, "A finite difference polar-cartesian grid approach for mode computation in rounded-end waveguides," *Aces Journal*, Vol. 26, No. 9, Sep. 2011, ISSN: 1054-4887.
7. Fanti, A. and G. Mazzarella, "Curvilinear finite difference approach to the computation of modes of circular and elliptic waveguides," *Proc. Int. Conf. on Applied Electromagnetics and Communications, (ICECom 2010)*, Dubrovnik, Croazia, Sep. 20–23, 2010.

3D Conductivity Image Reconstruction Based on Electrical Impedance Tomography

T. Kříž and J. Dědková
Department of Theoretical and Experimental Electrical Engineering
Brno University of Technology, Kolejní 4, Brno 612 00, Czech Republic

Abstract— The authors present the application of deterministic methods for the calculation of conductivity images in electrical impedance tomography. Reconstruction based on electrical impedance tomography is predominantly characterized as the solution of a 2D problem; however, this paper contains a description of the conductivity reconstruction procedure utilizing three-dimensional models. Within electrical impedance tomography, the calculation of conductivity is realized using measured voltages on the electrodes placed at the edge of the examined object. In the course of the calculation process, an electric current source is connected to the sample. A direct current source enables us to obtain electrical conductivity distribution in the investigated object; with an alternating current source, we acquire the values of both the amplitude and the phase of the measured voltage and are thus able to obtain impedivity distribution. As a nonlinear inverse problem, the calculation of conductivity based on the measured voltage values is highly ill-posed. The reconstruction process is described as the minimization of a suitably selected function. In order to ensure stability of the solution, the Tikhonov regularization method or Total variation method is used, the regularization term complements the objective function. The paper describes a mathematical model of the solved 3D conductivity reconstruction problem.

1. INTRODUCTION

The electrical impedance tomography (EIT) is a widely investigated problem with many applications in physical and biological sciences. Geophysical imaging is used for searching underground conducting fluid plumes near the surface and obtaining information about rock porosity or fracture formation. Another application of EIT is for example in non-destructive testing and identification of material defects like cracks or identification of corrosion in production materials. Medical imaging can be used primarily for the detection of pulmonary emboli, non-invasive monitoring of heart function and for breast cancer detection. The theoretical background of EIT is given in [1, 2]. The principle of EIT is based on the back image reconstruction, which is highly ill-posed inverse problem. The aim is to reconstruct, as accurately and fast as possible, the internal conductivity or permittivity distributions in two or three dimensional models.

EIT can be divided into three groups according to the characteristics of the object during one measurement cycle:

- Absolute — the characteristics of the object does not change, the result is a static image of conductivity.
- Differential — object properties changes slowly, for the reconstruction of the use of two sets of measurements (observations of lung function).
- Dynamic — change properties of an object changes significantly.

Using of the EIT has a number of advantages. The biggest advantage is the use of passive electrical properties of the reconstructed objects without its affecting. There isn't need to take samples or placing the probe into the investigated object. The EIT is a very quick method can obtain up to 200 images per second. Compared this method with other tomographic methods is relatively cheap.

The main disadvantage is the low spatial resolution. Reconstruction of the internal impedance is nonlinear ill-posed inverse problem. Therefore, the need sophisticated software for obtaining internal distribution conductivity.

Usually, a set of voltage measurements is acquired from the boundaries of an investigated volume, whilst this is subjected to a sequence of low-frequency current patterns. In principle, measuring both the amplitude and the phase angle of the voltage can result in images of the electric conductivity and permittivity in the interior of a body.

To obtain data is used measuring system for the EIT which is consist of a set of measuring electrodes (usually 16 or 32 in the layer). These voltage electrodes are located on the edge of the

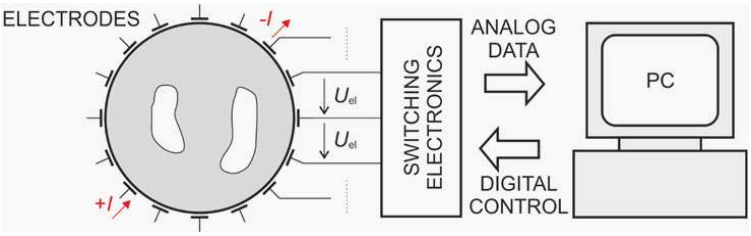

Figure 1: Measuring system for EIT.

object together with current electrodes and the measured voltage to them. To eliminate undesirable galvanic phenomena and electrolysis, we supply alternating current at lower frequencies of up to tenths of units of Hz to kHz and, less intensely, tens of mA. Because the EIT is non-linear and ill-posed task and thus is very sensitive to noise and contact impedance. The complete electrodes model was created. This model includes all these effects [2–4].

The field can be considered a steady current field, which is governed by the Laplace equation. Further we will consider only the conductivity σ for simplicity. The scalar potential U can be therefore introduced, and so the resulting field is conservative and the continuity equation for the current density can be expressed by the potential U

$$\operatorname{div}(\sigma \operatorname{grad} U) = 0. \tag{1}$$

Equation (1) together with the modified complete electrode model equations are discretized by the finite element method (FEM) in the usual way. Using the FEM we calculate approximate values of electrode voltages for the approximate element conductivity vector $\sigma(NE \times 1)$, NE is the number of finite elements. Furthermore, we assume the constant approximation of the conductivity σ on each of all elements. The forward EIT calculation yields an estimation of the electric potential field in the interior of the volume under certain Neumann and Dirichlet boundary conditions.

To solve the forward task we can use the finite element method. Mathematical procedures of the spatial conductivity reconstruction is follows. The geometrical model is discretized by finite element grid normal procedure. We suppose the area with the grid which is consist of NE elements and NU nodes. The electrical potential is expressed with using nodal values and the approximation function W_j

$$U = \sum\nolimits_{NU} U_j W_j(x, y, z). \tag{2}$$

Application of the Galerkin method to (1.1) and integrating integration by parts we get

$$\int_{\Omega} \sigma \operatorname{grad} W_i \cdot \operatorname{grad} U d\Omega = 0, \tag{3}$$

where U is nodal electrical potential and σ is a volume conductivity.

The forward solution is described by system of NU equations for the nodal potentials.

$$GU = F, \tag{4}$$

where G is the system matrix with coefficients g_{ik} which are given as sum of contributions from all elements (e) with common node i

$$\Delta g_{ij}^{(e)} = \int_{\Omega} \sigma^{(e)} \operatorname{grad} W_i^{(e)} \cdot \operatorname{grad} W_j^{(e)} d\Omega. \tag{5}$$

There are used deterministic and stochastic for EIT reconstruction to solving an inverse problem. Deterministic approach for minimizing suitable objective function use Newton iteration method, leas square method, steepest descent method and conjugate gradient method. Stochastic approaches use probability theory, heuristic methods or genetic algorithms. Both approaches have advantages and disadvantages. Deterministic methods are use in this work. There is minimizing suitable objective function by least square method. There is add regularization term to objective function to obtain stable solution. Tikhonov regularization method (TR) and Total variation method (TV) are most widely used in EIT image reconstruction.

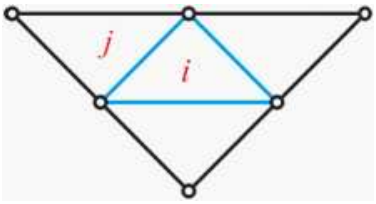

Figure 2: Assembly of the regularization matrix for TRM.

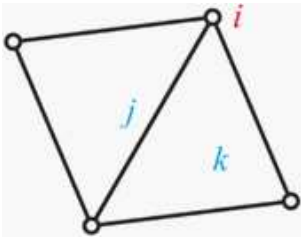

Figure 3: Assembly of the regularization matrix for TVM.

2. TIKHONOVA REGULARIZATION METHOD

If the Tikhonov regularization method used for reconstruction by the EIT, objective function has the shape

$$\Psi(\sigma) = \frac{1}{2}\sum \|U_M - U_{\mathrm{FEM}}\|^2 + \alpha \|\mathbf{R}\sigma\|^2, \tag{6}$$

where σ is the vector of unknown conductivity, U_M is the vector of voltage on the electrodes placed on the edge of the object, $U_{\mathrm{FEM}}(\sigma)$ is a vector calculated voltages at the edge of an object using FEM, α is a regularization parameter and $\mathbf{R}$ is the regularization matrix representative of the link adjacent elements in the FEM grid.

Regularization matrix is a square matrix expressing the relationship between the distribution of σ to elements grid. Regularization matrix structure can be described such that the i-th row and j-th column is -1 with respect to the adjacent elements and the main diagonal is the sum of the adjacent elements.

Gauss-Newton recursion is then

$$\sigma_{i+1} = \sigma_i + \left(\mathbf{J}_i^T\mathbf{J}_i + \alpha\mathbf{R}^T\mathbf{R}\right)^{-1}\left(\mathbf{J}_i^T\left(U_M - U_{\mathrm{FEM}}\left(\sigma_i\right)\right) - \boldsymbol{\alpha}\mathbf{R}^T\mathbf{R}\sigma_i\right). \tag{7}$$

Jacobian expresses the sensitivity of the electrode potential to change the conductivity of the element

$$\mathbf{J} = \frac{\partial U_i}{\partial \sigma}\begin{pmatrix} \frac{\partial U_{1i}}{\partial \sigma_1} & \cdots & \frac{\partial U_{1i}}{\partial \sigma_{NE}} \\ \vdots & \ddots & \vdots \\ \frac{\partial U_{Li}}{\partial \sigma_1} & \cdots & \frac{\partial U_{Li}}{\partial \sigma_{NE}} \end{pmatrix}. \tag{8}$$

The Tikhonov regularization method disadvantage is that the stability and accuracy of the solution is very sensitive to the size of the regularization parameter α and the initial set of value of conductivity σ. It happens that the results of Tikhonov regularization method oscillates in areas with a step changes σ. A more detailed description in [1–4].

3. TOTAL VARIATION METHOD

Another regularization technique often used to solve inverse problems is the method of total variation. This method successfully eliminates problems with oscillations.

When the Total variation method used for conductivity reconstruction by EIT there is added regularization term to objective function. The objective function for Total variation method is

$$\Psi(\sigma) = \frac{1}{2}\sum \left(U_M - U_{\mathrm{FEM}}(\sigma)\right)^2 + \alpha \mathrm{TV}_\beta, \tag{9}$$

where σ is the vector of unknown conductivity in the model, U_M is the vector of the voltage on the electrodes placed on the edge of the object, $U_{\mathrm{FEM}}(\sigma)$ is a vector calculated voltages at the edge of an object using FEM, α is a regularization parameter and and TV is a regularization term

$$\mathrm{TV}_\beta = \sum_{NE}\int |\mathrm{grad}\,\sigma|\, d\Omega = \sum \sqrt{\|\mathbf{R}\sigma\| + \beta}, \tag{10}$$

where $\mathbf{R}$ is a suitable regularization matrix describing the connection of adjacent elements, and β is a small positive parameter represents of the effect on the smoothness during $\Psi(\sigma)$.

It was created several variations of this method. One of them is the PD-IPM (Interior Primal-Dual-Point-Method). For this variant of the regularization matrix size (number of edges x number of grid elements). Regularization matrix structure can be described by non-zero elements of the i-th line (edge) having a value of 1 (or -1) in columns j (or k), which represent the indices of elements with a common edge.

PD-IPM algorithm is based on interpolation between the lagged diffusivity method and Newton's method. From the beginning, the algorithm behaves like a lagged diffusivity method that is stable and around minima behaves like Newton's method, which converges quickly.

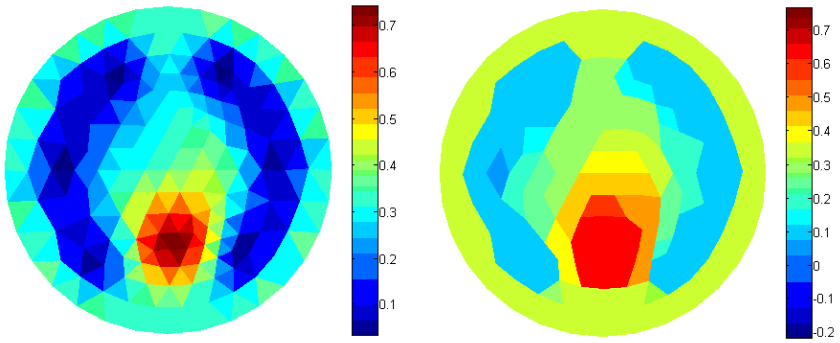

Figure 4: Results obtained by Tikhonov regularization method and total variation method.

4. CONCLUSIONS

Electrical impedance tomography is a method to diagnose defect locations, especially in the human body. The existence of a number of factors that can strongly influence the result (noise, measurement accuracy). It is difficult to precisely describe the properties of the environment in which it is searched defect. Reconstruction of correct images, especially in 3D dimension of the voltage on the contact electrodes, it is therefore very difficult. So far was the development of computational methods for EIT created a number of scientific papers, but you can't say that you will always receive a satisfactory result. This is because there are a number of ambiguities, which can not affect the calculations.

ACKNOWLEDGMENT

The research described in the paper was financially supported by project of the BUT Grant Agency FEKT-S-11-5/1012 and projekt CZ.1.07.2.3.00.20.0175, Elektro-vyzkumnik.

REFERENCES

1. Cheney, M., D. Isaacson, and J. C. Newell, "Electrical impedance tomography," *SIAM Rev.*, Vol. 41, No. 1, 85–101, 1999.
2. Borsic, A., "Regularization methods for imaging from electrical measurement," Ph.D. Thesis, Oxford Brookes University, 2002.
3. Paulson, K., W. Lionheart, and M. Pidcock, "Optimal experiments in electrical impedance tomography," *IEEE Trans. Med. Imaging*, 681–686, 1993.
4. Rigaud, B., Y. Shi, N. Chauveau, and J. P. Morucci, "Experimental acquisition system for impedance tomography with active electrodes approach," *Med. Biol. Eng. Comput.*, 593–599, 1993.

An Electrical Explanation of the Electrical Behavior of Metals

S. L. Vesely[1] **and A. A. Vesely**[2]

[1]I.T.B. — C.N.R., Italy
[2]Via L. Anelli 13, Milano, Italy

Abstract— We interpret the Wiedemann-Franz (W-F) law as well as the metallic reflection behavior in Rubens and Hagen (R-H) experiments in terms of electrical signals.

1. INTRODUCTION

Since their formulation, Maxwell equations posed the problem of understanding the meaning of electromagnetic variables. Physical understanding is related to experiments. However, until the variables are tied to 1800's concepts, it is difficult to explain by means of electromagnetism the more sophisticated electrical measurements that became possible at later times. It is highly desirable to approach electromagnetism so as to cover the usual aspects of telecommunications and also seamlessly account for those *unencoded* (raw) electrical responses that the electromagnetic theory originated from. However, discrete formal systems, such as those deployed in telecommunications, do not fully cover the continuum spanned by classical electromagnetic variables, and the viewpoint has to be changed toward different frameworks.

For this paper, we restrict to metallic matter, and revisit the link among three different effects of its; that is, electrical conduction, thermal conduction, and metallic reflection. That's interesting not only for the relationships between raw and encoded received signals, but also because condensed matter physics is an offspring of Sommerfeld's update of Drude's model.

2. ON THE ELECTRICAL AND OPTICAL ASPECTS OF METALS

Some properties have been associated to metals since ancient times, they are expressed by adjectives such as malleable, ductile, shiny, magnetic, and thermal conductor. Other ones, such as electrical and electrolytic behavior, were recognized in relatively recent times. Specifically, though, it can be seen that the circa 40 types of commercially relevant metals and alloys don't behave uniformly, and differences among them are often material. While electromagnetism covers the three phenomenologies of electricity, magnetism, and optics, for material-specific properties it limits itself to the recording of empirical evidence such as the dispersive behavior of reflectivity and conductivity[1]. By contrast, electrodynamics acknowledges an issue about a logically coherent interpretation of all electromagnetic phenomena, but then it carries out the task of associating the matter to its radiation properties by reducing to mechanical concepts so as to resort to analytical mechanics. A consequence of that reinterpretation is that the compatibility with the units of measurements used in mechanics becomes a burden encompassing all areas of physics, and is never questioned, not even when comparing entirely electromagnetic behaviors[2]. In some cases, for example comparing the electrical response of a material with that of an equivalent circuit, that compatibility is not needed, and it might be restrictive to be constrained to it.

Now let's briefly rehash the laws associated with the Wiedemann-Franz (W-F) and Rubens-Hagen (R-H) experiments. W-F law says good electrical conductors conduct heat better than bad ones. The experiments carried out about 1850 established a procedure to compare thermal conductivity κ with electrical conductivity σ, for metals. It consists in measuring both conductivities separately and computing the ratio $L \equiv \frac{\kappa}{\sigma T}$, where T is the absolute temperature common to both measurements. The procedure takes into account that rods of different diameter are needed to readily measure each quantity, and principally that the value of electrical conductivity varies with temperature markedly. Likewise, electric current through conductors gives raise to Joule and

[1]In classical optics metals are regarded as mirrors, while dielectric prisms are given a dispersion curve. The latter is the relationship between the wave propagation velocity, or, better, its angular frequency ω, and the corresponding wave number k. In electrical engineering, *dispersion curve* refers to the variation of any electrical parameter as a function of frequency. As electrical parameters usually depend on other characteristics too, its shape can be considered qualitatively, or referring to specific conditions.

[2]When it is not required to compare a measurement with dynamical quantities, it suffices to express the values of electrical measurements as cross-ratio logarithms (dB). That eases the comparison of electric measurements over extended frequency ranges. See also note 14 below.

Thomson thermoelectric effects[3], thereby producing heat that would affect the measurement of thermal conductivity. Because of that mutual influence, a method to attain a proportionality law must provide for avoiding their simultaneous occurrence. It is a delicate subject to interpret temperature differences. W-F detected them along a rod heated to 100°C by direct contact with a brass cylinder at one end, and interpreted them as due to heat flow along the rod. Today, the radiated heat is identified with infrared radiation (IR). Thus, heat conduction on objects similar to monopole antennas can be compared with ground waves transmission[4] [1].

R-H law, which says that mirrors made of good conductors reflect well, is conceived as an extension of the chromatic dispersion law for dielectrics to the dispersive behavior of metals at the IR frequencies [2]. Indeed, before reaching the optical range, the quantity $k = \frac{2\pi}{\lambda} = \frac{2\pi}{\lambda_0} n = \frac{2\pi}{\lambda_0}\frac{c}{v} = \frac{\omega}{v}$, where λ_0 stands for t he vacuum wavelength, can take complex values, whereby the interpretation of metallic behavior becomes controversial. Thus, the statement of the law calls *reflection* an optical phenomenon extended to IR. Its mathematical form, which can be derived from both Drude theory and Maxwell equations, is like $1 - R \equiv A \propto 1/\sqrt{\sigma}$, where $R \approx 1$ is the reflective power, A the absorptive power[5], and σ the conductivity. When $\omega \to 0$, the Joule effect is proportional to the resistivity and allows to identify absorptivity with heat dissipation. However, conductivity losses are higher at high frequency (HF) than DC, and metals don't conduct electricity at IR frequencies. Hence, the R-H relation cannot be considered an equation that holds as frequency varies. Conductivity is meant at DC, reflectivity at IR. For an alternative interpretation of A, consider the propagation of radiation in the experiments on frustrated total internal reflection in dielectrics; for example, inserting a glass slab after a glass-air interface. By analogy, it would make sense to consider evanescent waves also in metals. As for $R \approx 1$, which holds in the optical range, we may assume that Faraday cages reflect at DC, but even then we cannot say whether conductors can work as mirrors in the IR. Loosely, Kirchoff law says that, since hot metal filaments of incandescent light bulbs emit, cold ones can absorb at the same frequencies, thereby conflating the reflectivity R into the emissive power P[6]. Historically, R-H carried out their experiments to verify Drude's theory without making further theoretical assumptions: They measured reflection, and the intensity of light transmitted through chemically deposited metal films of thickness ranging [0.04–0.1] μm. It was during those experiments, while trying to extend measurements toward microwaves (MW), that Rubens discovered residual rays (Reststrahlen) in dielectrics, that is selective amplification of radiation. The task of exploring the behavior of metals from DC to the ultraviolet (UV) range and beyond was completed by resorting to new suitable sources and sensors, after WWII. Times are mature for theoretical attempts to bring frequency ranges together in a unitary way.

3. EXPLANATIONS BASED ON THE STATISTICAL DYNAMICS OF ELECTRONS

The W-F and R-H experiments require electrical explanations to be coherent with thermodynamical ones. They support several theories of the microscopic functioning. Firstly, the classical Drude-Lorentz theory identifies the electric current with a stream of free electrons. The analogy between that and the heat flow is used to transfer the statistical formulation from thermodynamics to electrodynamics. That analogy is of circumscribed applicability, because the free electrons assumed to explain electrical conduction cannot be considered in the computation of the molecular specific heat[7] $C_p = T\frac{\partial S}{\partial T}$. Secondly, the quantum approach, leading to quantum electrodynamics (QED), remedies that incongruity by applying fermion statistics, a new statistics, to the degenerate

[3]Among thermoelectric effects, the most renowned are those of Seebeck and Peltier occurring at the junction between different metals. Joule and Thomson effects occur even in homogeneous metals. By definition, the Joule effect is the irreversible conversion to heat of the work done by a charge q flowing between two points having potential difference ΔV. In 1948, H. Callen considered all thermoelectric effects as due to mutual interference between heat flow and electric current, and applied Onsager's reciprocal relations. According to his interpretation, the Joule contribution extracts the entropy produced by the flow of current, and the Thomson contribution injects entropy to supply the flow of entropy per particle.

[4]Antenna engineers call *radiation resistance* of the equivalent circuit of an antenna the part of resistance at the feed-point which is converted into far field radiation. However note two points: (1) The electron interpretation of current flow in open circuits was expedient to the mechanical understanding; (2) As pointed out by Jackson, the behavior of antennas in the linear range should be addressed as a boundary value problem. In addition, for transmitter antennas, the electrically stressed metallic structure emits, among others, also radiations which are not launched. Possibly, ground waves are an example of those emissions: Albeit they propagate over considerable distances, they are guided by the conducting floor.

[5]By definition $A = \frac{1}{d}\log_{10}\frac{I_0}{I}$, where d is the path length through the material, I_0 and I the intensity of the incident and transmitted radiation respectively. In R-H's work of 1902 on the absorption of thin films, reflected radiation is excluded from I_0, and I is measured using a linear thermopile.

[6]Kirchhoff defines the absorptive power $A = 1 - R$ such that $\frac{P_s}{A_s} = P_s = \frac{e}{1-R}$, where the index s refers to black body.

[7]Generally, $C_P > C_V$. The Dulong-Petit law, $C_V M = 3R$, where M is the molar mass and R the gas constant, holds for non-conductors too, but fails at low temperatures.

electron gas. In addition, the new statistics lowers the value of C_p at very low temperatures, in agreement with experiments. However, it requires quantization of the electromagnetic field too, besides considering discrete matter. Thirdly, disregarding both electron-electron interactions and collective plasma modes, a semi-classical theory was developed by F. Bloch[8]: By applying Fermi's statistics to the single particle solution at given temperatures, he showed that only a fraction of the electrons bear so much energy as to contribute to electrical and thermal conduction. According to his model, which is justified by the theory of chemical valence[9], the electrostatic potential due to the metal ion cores of the lattice creates an energy gap between a lower energy band, called the valence band, and a higher energy band, which accounts for conduction. The mathematical aspect is often presented stemming from Kronig and Penney, who assume that the ion cores form a 1-dimension, infinitely extended arrangement of barriers of potential strength $V_0 a'$[10], separated by wells with pitch $a = a_0 + a'$. Thus, the free electron satisfies the time independent Schrödinger wave equation in a rectangular potential well, $\frac{d^2\psi}{dx^2} + \frac{2m}{\hbar^2}E\psi = 0$, and the lattice periodicity allows to attribute periodical coefficients $A = A(x) = A(x + na)$ for $n = \pm 1, \pm 2, \ldots$, to its probability amplitude ψ. At each a'-wide barrier, the Schrödinger equation becomes $-\frac{d^2\psi}{dx^2} + \frac{2m}{\hbar^2}V_0\psi \approx 0$. The additional condition that both $\psi(x) = A(x)e^{ikx}$ and its derivative connect smoothly across the barriers determines the appearance of energy gaps[11]. For k values far from the energy gaps, the probability $\psi(x)\psi^*(x)$ of finding the electron at x is not appreciably different from that of the free electron. At the gaps, where $k \to \pm\frac{n\pi}{a}$, the distribution tends to the discrete energy eigenvalues E_n of the bound electron. For the physical aspect, quantal theories provide no direct interpretation. As crystal lattices are studied by x-rays scattering, the phenomenological Bragg reflection condition[12] $2a\sin(\theta) = n\lambda$ is often called also to explain the behavior of conduction electrons. Substituting for λ in the above expression, one gets $k = \frac{n\pi}{a}\frac{1}{\sin(\theta)}$, which becomes $\frac{n\pi}{a}$ for normal incidence angles. However, it is not legitimate to derive that the electron is somehow scattered by lattice ion cores, since E_n are the energy eigenvalues of the bound states.

L. Brillouin proposed an alternative interpretation by analogy with the analytical dynamics of vibrating mechanical systems of points, and applying a *principle of permanence* to oscillations. He realized that the energy eigenvalues can be determined by restricting the dispersion curve to the interval $|k| < \left|\frac{\pi}{a}\right|$ (first Brillouin zone), or even to the reduced zone $(0, \frac{\pi}{a})$, and therefore related the electron propagation in metals with the dispersion of lumped-element low pass filters. Network synthesis results differ from Brillouin's: (1) There is no obvious relationship between the steady state distribution of the electron at the barrier and the characteristic frequency $\omega = \frac{1}{\sqrt{LC}}$ of a constant k lumped low pass filter section; (2) the comparison involves an infinitely extended lattice on the one hand and on the other a ladder network, which necessarily consists of a low number of cascade connected sections; and (3) Bloch obtained the dispersion relation $k + n\frac{2\pi}{a} = \frac{1}{\hbar}\sqrt{2mE}$ $n = 0, \pm 1, \pm 2, \ldots$ under the hypothesis of a periodic lattice, while Brillouin comparison refers to the reduced zone only.

4. EXPLANATIONS HINTING AT INFORMATION THEORIES

Brillouin's analogy between energy gaps in metal conduction and the Bode cutoff frequency of low pass filters stands upon the statistical thermodynamic interpretation of the electrical current and Bloch's model of metals. If the outcome of that analogy is to avail of an equivalent circuit

[8]The semi-classical theory is applied especially in molecular modeling of conformational changes associated with protein ligand binding. Electronic correlation is taken into account by means of electronic density functionals. The density functional theory, which relies on machine numerical processing, originates from the Hartree-Fock method. In that form, Bloch's theory can be applied to surface plasmon polaritons and artificial crystals.

[9]According to the theory of chemical valencies, only the electrons of incomplete outer shells contribute to chemical bonds. Bonds can be ionic, covalent, and apparently metallic.

[10]To leave the tunnel effect out, it is assumed that $V_0 \to \infty$, but $V_0 a' < \infty$. That entails $E \ll V_0$.

[11]A free electron can have any amount of energy $E = \frac{1}{2}mv^2$, which is not quantized. Letting $p = mv = \hbar k$, one has $k \equiv \frac{2\pi}{\lambda} = \frac{p}{\hbar} = \frac{1}{\hbar}\sqrt{2mE}$, and the dispersion curve is given by the parabola $\omega = \frac{\hbar}{2m}k^2$. By subdividing the path into infinitely many intervals of pitch a, energy doesn't get quantized, but the dispersion curve becomes a family of parabolas with vertexes $\pm\frac{2\pi}{a}n$. However, a free electron constrained within a single well of pitch a_0 is subject to the boundary conditions of the eigenfunctions, with corresponding quantized eigenvalues $E_n = \frac{\hbar^2}{2m}(\frac{\pi}{a_0}n)^2$, where $k_n = \pm(\frac{\pi}{a_0})n$. If the wells are interleaved with barriers, Bloch's periodic solution attains an energy gap for $k_n = \pm(\frac{\pi}{a})n$, because the solutions defined on the intervals of length a_0 are joined with those of energy $E - V_0$ at the barriers a'.

[12]Bragg's condition is for the maximally exposed spots of the film, where it assumes constructive interference of scattered x-rays.

of metallic matter, then Thévenin's and Norton's theorems are conceptually simpler. Otherwise, if Brillouin's approach is to be a hint on how to treat the electrical response of materials in a telecommunications framework, then we have to consider it along the lines of developments such as those due to Shannon, Wiener, and Kolmogorov [3]. We distinguish two parts for the latter case: 1) the conceptual contributions of communication and information theories to electromagnetism, and 2) the aim and the meaning of interpreting the electrical response of materials as signals.

For part (1) we just note that Shannon's approach to information theory hinges on Boolean logic and Venn's diagrams, and prefigures that information theory can be built upon logic without referring to statistical mechanics[13] [4, 5].

Part (2) concerns signals interpretation. It depends on part (1) in the following sense: Assuming there is a physical world, some of its properties can be ascertained by probing it with radiation, which we perceive, either directly or after detection. Signals — encoded as well as unencoded — are different from carrier-frequencies. Availing of the hindsight brought about by experience with electrical devices, as well as of the ability to view the whole electromagnetic spectrum and bring together measures obtained at different ranges, the response of a material at given conditions can be compared with the electrical functioning of known linear (passive) devices, rather than pairing DC current and electron flow, IR radiation and heat, UV radiation and chemical rays, and so forth[14]. It might also be possible to distinguish whether the response to a given electromagnetic input is approximately linear or not, and in the latter case look for an additional phenomenology possibly associated with such response. That response-oriented kind of revision of the phenomenology associated with W-F and R-H could bring out insights, which could then be applied to new electrical devices.

For metals, it makes sense to subdivide the whole spectrum roughly into three ranges. We are interested in the *conduction band*, with $\omega \approx 0\,\mathrm{Hz}$ center-band and cutoff frequency toward HF. We don't mean an energy range here, just the spectral range associated with electrical conduction. In order to handle signals uniformly, we regard it as similar to higher frequency bands, albeit irradiation hardly occurs at low frequencies. Next, for W-F experiments, according to Wien's displacement law a black body at thermal equilibrium at 100°C has a peak emission in the IR around $\lambda_{\max} = \frac{2898}{T} = 7.765\,\mu\mathrm{m}$. The spectral shape attributed to the thermal radiation is unique. However, when excited otherwise, metals give off radiation with different spectral distributions. For example, the operating frequency of a correctly grounded and driven rod monopole antenna about 75 cm long is in the VHF range. Peak frequency, radiation pattern, and merit factor (Q) of W-F conductor rods could have been different than those of a resonant antenna, because they were fed by direct contact with a heated brass sleeve, and top loaded with another brass sleeve. W-F found that a good conductor rod exhibits a linear temperature gradient, while thermal drop is much stronger and non-linear for a similar rod of iron, in a still air environment. We would infer that iron has much broader channels than copper in the MW-to-IR region, based on the experience of adding Yttrium Iron Garnet (YIG) or ferrite inserts into cavities of the copper anode block of magnetrons, in an attempt to stabilize their output power frequency, which we suppose would happen by lowering the cavity's loaded Q [6]. Finally, for R-H experiments, we have to also consider the UV zone of metal response. When excited in the UV, metals exhibit both plasma oscillations and photoelectric effect. For silver films in the near UV, R-H report a *peak of transparency*[15], which we would call *fluorescence*. However one interprets it, the radiation scattered back from the film

[13] The amount of information transmitted per symbol by a source with N possible outcomes, and expressed in bits, is $H(X) \equiv -k_S \sum_{m=1}^{N} p_m(X) \log_2[p_m(X)]$, where k_S is a constant, X is a random variable with values in the set of available symbols $\{x_1, \ldots, x_N\}$, and $(p_1, \ldots, p_N)$ is their probability distribution, $p_m = P(X = x_m)$. Usually, H is related to the distribution W of dynamical microstates for each thermodynamical macrostate in Boltzmann's entropy $S = k_B \log_e W$, by generalizing Shannon entropy without stressing the change in the logarithm basis too much $H = -\int_{-\infty}^{\infty} p(x) \log_e[p(x)]\,dx$, where $p(x)$ becomes a density. E. T. Jaynes made a new start by observing that Shannon's information theory is built on probability theory, which grounds on logical rules. According to him the logical approach to probability theory goes back to Laplace. Even geometrical approaches are alternative to statistical mechanics.

[14] Let's recall that the inner working of signal detectors varies depending on the frequency range, among other factors. While signals and modulations can be compared to one another independently of the carrier frequency, the spectral range is relevant only for interpretations which include transduction mechanisms among their considerations. See also note 2 above.

[15] We recall that R-H measured the transmitted *intensity* at various frequencies. If a quadrature detector is used, both amplitude and phase can be obtained. For the time function: $h(t) = Ae^{-bt},\ t > 0$ and $h(t) = 0,\ t < 0$, the Fourier transform is $H(\omega) = A\int_0^{+\infty} e^{-(b+j\omega)t}\,dt = \frac{A}{b+j\omega}$. In rectangular coordinates that means $H(\omega) = \Re[H] + j\Im[H]$, where $\Re[H] = A\frac{b}{b^2+\omega^2}$ is the Lorentzian absorption shape centered about $\omega_0 = 0$, and $\Im[H] = -A\frac{\omega}{b^2+\omega^2}$ is the dispersion curve associated with it. Using the polar form, it is $H(\omega) = |H|\,e^{j\theta(\omega)} = \frac{A}{\sqrt{b^2+\omega^2}} \exp[j\tan^{-1}(-\frac{\omega}{b})]$. The intensity would then be the squared amplitude value, which enters in the autocorrelation: $H(\omega) * H(\omega) = \int H(\omega)H(\omega_0 - \omega)d\omega = \int H(\omega)H(-\omega)d\omega = \int |H(\omega)|^2\,d\omega$.

surface towards the source at the UV peak is distinct from the mirror reflection of silver in the optical range, as the former is accompanied by transparency.

5. TENTATIVE INTERPRETATION BASED ON RECEIVED SIGNALS

5.1. Crosstalk, Coupling, and Resonance Bands

Consider the phenomenon which, borrowing the term from broadcasting, we may call *crosstalk*. It is the interference received while tuned to a channel at a given carrier frequency, from a source transmitting at a different frequency. At normal temperatures, the conduction band with nominal carrier frequency 0 Hz, as well as higher bands up to IR are excited in metals, and there are intermodulation products. Crosstalk from higher frequencies shows up as thermal noise at the conduction band [7]. Crosstalk from conduction band interferes at IR frequencies, and reaches the nearby optical range so that the metal-specific luster becomes visible looking at the metallic surface. The crosstalk is a purely electrical distortion, not amenable to mechanical explanations, and is not a coupling. However, when feeding DC, the metallic structure allows coupling between the DC channel and MW and IR modes, resulting in various levels of thermoelectric transduction[16] [8], such as light emission, Joule effect, and possibly radiation of conducted/guided signals. The stronger the coupling, the more involved the material structure, the more side effects, and the more intricate the phenomenological descriptions. If we attribute transduction to an electric resonance coupling, conduction is a non-fluorescing resonance, while resonances in the IR and UV can fluoresce. In the optical range, only colored metals show fluorescing bands[17].

5.2. Mirrors

Metallic reflection is a phenomenon associated with bands in DC, IR, and UV, but not related to fluorescence. Two distinct facts contribute to our tentative explanation of mirror functioning, firstly the luster, secondly the high standing wave ratio (SWR) at the metallic surface, that is the refractoriness to light transmission/absorption. We already explained the luster as a consequence of the IR bands interfering with the light rectified by metallic reflection. We explain refractoriness by analogy with electric attenuation by quartz tuned circuits in VHF. A simple crystal filter in series with the source and load resistances shows a fundamental peak and some odd overtones in its frequency response. At the fundamental mode, the reactance characteristic of its series RC_SL[18] shunted by a 100-fold capacitance C_P has two frequencies of zero phase, referred to as series ($\omega_S = \frac{1}{\sqrt{LC_S}}$) and parallel ($\omega_P = \omega_S\sqrt{1+\frac{C_S}{C_P}}$) resonance frequencies, in increasing frequency order. The frequency separation between them, which usually amounts to a few kHz, is called the bandwidth of the filter. The narrower it is, the higher the loaded Q of the filter. Beyond the parallel resonance a quartz becomes non-responsive. In the visible *octave* between IR and UV, the attenuation of metallic thin films is very strong, because the visible range is crammed between two peaks of very high Q. The higher the IR peak's Q, the better the reflective power at its toe. R-H law good conductors are good mirrors could then be a consequence of the marked narrowness of good conductors' IR bands.

6. EPILOGUE

We have briefly explored the viability of a signal-oriented interpretation of the W-F and R-H experiments. Our explanation of those experiments and of the physical laws thereby derived attributes the electrical coupling between fed DC band and IR bands to the metallic structure. Even if we believe intermodulation arises due to the involvement of the matter, we don't think that an analysis of such unencoded modulations would lead to a general linear model of the matter itself. Rather, some of the properties of the matter can be ascertained by probing it with radiation. Within that

[16]The number of radiating IR bands grows as the DC power fed to the sample grows. When the power is so much that IR bands saturate, the excitation becomes visible. That may suggest that type I superconductivity corresponds to DC excitation with no coupling to any channel between MW and IR, and is thus the simplest phenomenon of these. On establishing any coupling, the resistivity undergoes an abrupt increase, which indicates that some IR mode is starting to radiate, and the superconducting state consequently decays. Rosenberg's work shows the slope changes of thermal conductivity and resistivity, which in our opinion are associated with the onset of IR excitation and with saturation.

[17]Thin gold foils reflect in the red and transmit in the green (circa 486 nm) because the fluorescence extends throughout the whole depth of the foil. Colloidal gold fluoresces in various colors depending on its concentration, in a way similar to cavity pulling.

[18]Quartz is piezoelectric. The resistance belongs to the equivalent circuit in the vicinity of the operating frequency, and doesn't imply that electric power gets dissipated.

task, each electromagnetic response can be considered a signal from the sample, rather than the average measures of the dynamical system's state variables.

REFERENCES

1. Jackson, J. D., "How an antenna launches its input power into radiation: The pattern of the Poynting vector at and near an antenna," arXiv:physics/0506053v1, 2005.
2. Goldhammer, D. A., "Bemerkungen zur Abhandlung des Hrn. E. Cohn 'zur Elektrodynamik der Leiter'," *Ann. Phys. Chem.*, Vol. 46, 99–104, 1892.
3. Kolmogorov, A. N., "Logical basis for information theory and probability theory," *IEE T. Inform. Theory*, Vol. 14, No. 5, 662–664, 1968.
4. Jaynes, E. T., *Probability Theory: The Logic of Science*, Copyright by Edwin T. Jaynes, St. Louis, MO, 2002.
5. Veblen, O., "The modern approach to elementary geometry," *Rice Inst. Pamphlet*, Vol. 21, No. 4, 209–222, 1934.
6. Neubauer, N., R. Sah, A. Dudas, R. Johnson, M. Popovic, and A. Moretti, "Phase and frequency locked magnetrons for SRF sources," *Proceedings, 24th Conference, Pac'11*, 4005–4007, New York, USA, March 2011.
7. Johnson, J. B., "Thermal agitation of electricity in conductors," *Phys. Rev.*, Vol. 32, 97–109, 1928.
8. Rosenberg, H. M., "The thermal conductivity of metals at low temperatures," *Phil. Trans. R. Soc. Lond. A*, Vol. 247, 441–497, 1955.

A Methodology for Short Basis Velocity Measurement in Moving Objects

P. Fiala, M. Friedl, M. Kovac, V. Benes, R. Koci, and I. Behunek
Department of Theoretical and Experimental Electrical Engineering
Brno University of Technology, Technická 3082/12, Brno 616 00, Czech Republic

Abstract— The velocity of various objects is currently measured within a large number of disciplines and activities. This paper presents velocity measurement in single-shot nonlinear processes, which occur only once and are thus characterized by zero repeatability. The measurement methods must therefore enable the recording, saving, and retroactive evaluation of the processes at a pre-defined accuracy; all these operations are performed to facilitate comparison of the recorded event and other similar processes. The methods commonly applied in the measurement of object velocity are based on optical and electromagnetic effects. In this context, the main disadvantage of optoelectronic methods consists in that the detector cannot be placed immediately behind the plasma source (or, generally, objects other than the projectile). Further problematic aspects can be identified in the emitted raw powder particles, muzzle flash, and shock wave, namely spurious effects leaving a track where the information from the launched projectile could be lost. However, the electromagnetic method described in the paper does not possess the disadvantages of the optical methods. We therefore present a design of an induction sensor fitted with an electronic signal processing system; this design is based on numerical evaluation of the relativistic effect occurring in the application of the electromagnetic principle of position sensing/object velocity [1]. The final part of the paper contains a discussion of the measured results.

1. INTRODUCTION

In fast-moving objects, velocity is determined by measuring the position and time. Thus, in most measurement procedures, it is important to detect the position of the object at the start and end points of the measured path and to determine the length of the time during which the monitored body travels the given distance. Projectile detection is conducted using two parallel structures (ports) located from each other at an exactly defined distance, which is referred to as the basis. As the projectile must pass through both these ports, the structures have to be placed in a perfectly parallel manner. The block diagram of this type of measurement system is shown in Fig. 1. The individual ports indicate the passage of the projectile and generate the START-STOP pulses; the function of the pulses is to activate and deactivate the fast counter (a microcontroller unit) used to measure the time at which the projectile passes through the ports. Based on the known dimension of the basis and the passage time of the projectile, it is then easy to acquire the average speed value of the projectile flight at the distance given by the basis of the sensor. However, we also need to consider possible measurement errors [1].

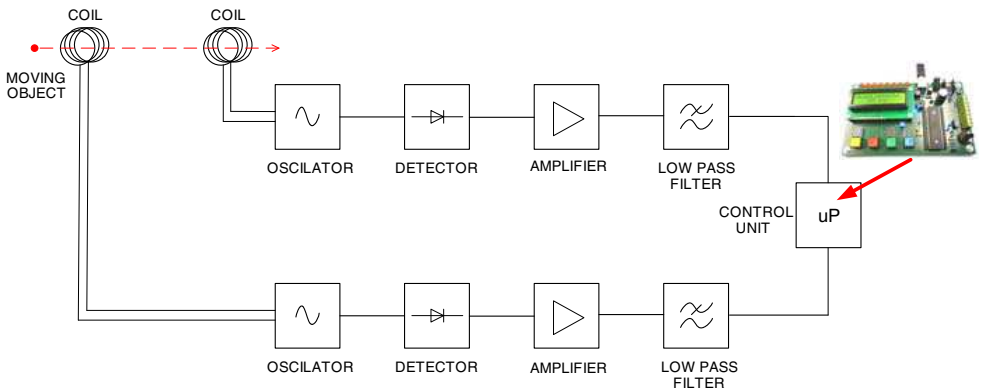

Figure 1: Block diagram of the system for the measurement of fast-moving objects.

2. METHODOLOGY FOR THE MEASUREMENT OF VELOCITY

The ports measuring the velocity of a fast-moving object are based on either the optical or the electromagnetic principles, and each of these two approaches has been used to produce several types of ports [2–4].

(a) (b) (c) (d)

Figure 2: Different port types: (a) diode, (b) laser, (c) sky-screen, (d) electromagnetic.

Optical methods are applied to evaluate the shadow cast by the flying object; this shadow enables us to determine the position of the object, namely the moments of its passage through the port. Thanks to their independence of the material and size of the measured object, these methods are of universal character. A general drawback of optical methods consists in the parasitic sources of light that affect the shadow cast by the projectile. As shown in the image above, the individual optical port types include diode structures, in which the source of light is an array of LEDs whose light is sensed by several fast PIN diodes; laser structures, whose design is identical with that of the diode ports; and sky-screen structures, which are suitable predominantly for outdoor use because they utilize daylight as the source of light. The basic components of a port are optical lenses, a filtering aperture, photodetecting elements, and evaluating circuits Using the optical lenses, we can acquire the information on the flying object even at large distances from the projectile, which is a key aspect in this type of port. Magnetoelectric methods utilize mainly coils, whose properties are influenced by the passage of the projectile; alternatively voltage can be induced in these coils. One of the variants of the magnetoelectric methods is the technique which uses magnetic flux density to generate a pulse during the passage of the projectile through the coil. The magnetized projectile is surrounded by a static magnetic field; during the passage of the projectile through the measuring coil, this field will be changing proportionally to the speed of the projectile and depending on the relative motion of the object and the port [7].

The complete Maxwell equations in Heaviside's notation are covariant in all the systems; therefore, it is not important to specify the system within which the observer moves, because the described relations always hold true. After deriving the four-vector, and respecting the Lorentz transformation for the moving electric charge with density ρ from the perspective of two individual systems A and A' relatively moving at velocity $\mathbf{v}$, the source current density is written in the form

$$\mathbf{J}_s = \rho \frac{\partial \mathbf{s}}{\partial t} + jc\rho\mathbf{u}_t, \tag{1}$$

where $\mathbf{s}$ is the position vector of a material point in the coordinate system. Then, the interface between the dielectric with electric permittivity ε and the conductive material having conductivity γ is

$$\mathrm{rot}\mathbf{E} = -\frac{\partial \mathbf{B}}{\partial t} + \mathrm{rot}\left(\mathbf{v}\times\mathbf{B}\right) - \frac{1}{\gamma}\mathrm{rot}\left(\rho\mathbf{v} + jc\rho\mathbf{u}_t\right). \ \mathrm{rot}\mathbf{H} = \rho\mathbf{v} + \gamma\left(\mathbf{v}\times\mathbf{B}\right) + jc\rho\mathbf{u}_t + \frac{\partial \mathbf{D}}{\partial t} + \mathrm{rot}\left(\mathbf{v}\times\mathbf{D}\right), \tag{2}$$

where $\mathbf{H}$, $\mathbf{J}$, $\mathbf{E}$, $\mathbf{D}$, $\mathbf{B}$ are the vectors of magnetic field intensity, current density, electric field intensity, electric flux density, magnetic flux density, respectively, and ρ is the specific of electric charge density.

Applying Maxwell's equation (Heaviside notation) for the presence of the electric charge in the modelled area, Fig. 3, the expression for the current density $\mathbf{J}$ can be written in the form for the interface between the dielectric and the conductive layer. Then for the unabbreviated expression, respecting the motion at velocity $\mathbf{v}$ in all directions, the current density in relation to the moving systems A-A' can be written as

$$\mathbf{J}_\square = \frac{J'_x - v_x \mathrm{div}\left(\frac{\varepsilon'}{\gamma'}\mathbf{J}'_\Delta\right)}{\sqrt{1-\left(\frac{\|\mathbf{v}\|}{c}\right)^2}}\mathbf{u}_x + \frac{J'_y - v_y \mathrm{div}\left(\frac{\varepsilon'}{\gamma'}\mathbf{J}'_\Delta\right)}{\sqrt{1-\left(\frac{\|\mathbf{v}\|}{c}\right)^2}}\mathbf{u}_y + \frac{J'_z - v_z \mathrm{div}\left(\frac{\varepsilon'}{\gamma'}\mathbf{J}'_\Delta\right)}{\sqrt{1-\left(\frac{\|\mathbf{v}\|}{c}\right)^2}}\mathbf{u}_z + j\frac{c\,\mathrm{div}\left(\frac{\varepsilon'}{\gamma'}\mathbf{J}'_\Delta\right) - \frac{v_x}{c}J'_x - \frac{v_y}{c}J'_y - \frac{v_z}{c}J'_z}{\sqrt{1-\left(\frac{\|\mathbf{v}\|}{c}\right)^2}}\mathbf{u}_t. \tag{3}$$

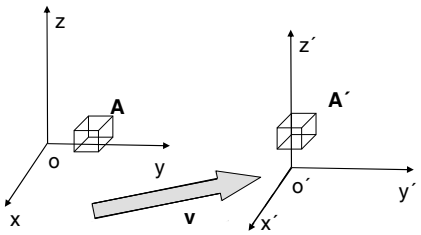

Figure 3: Relation of two moving systems with the objects A and A', moving mutually at velocity $\mathbf{v}$.

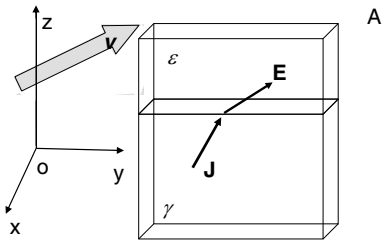

Figure 4: Approximation of the conditions on the dielectric/metal interface in the model.

The expression for current density in the area of conductive material with conductivity γ can be written from relations (1), (2) in the form assuming zero value of electric charge ρ in the electrically conductive material (metal)

$$\mathbf{J}_{\square} = \frac{\mathbf{J}'_{\Delta} + j\mathbf{v}\rho'}{\sqrt{1 - \left(\frac{\|\mathbf{v}\|}{c}\right)^2}}\rho = \frac{\rho' - \frac{v}{c^2}\mathbf{J}'_{\Delta}}{\sqrt{1 - \left(\frac{\|\mathbf{v}\|}{c}\right)^2}} \tag{4}$$

Another magnetoelectric technique utilizes two measuring coils; compared to the previously mentioned approach, this method is characterized by a different evaluation procedure.

3. SENSORS FOR VELOCITY MEASUREMENT

With respect to the fact that the measurement of instantaneous velocity $\mathbf{v}$ of moving objects is converted to the measurement of position, the design of the port was realized utilizing the principle of eddy currents known from inductance sensors of position. The principle of inductance sensors with a suppressed magnetic field consists in suppressing the magnetic field of the sensor by the magnetic field of the eddy currents [5, 6]. An electrically conductive and magnetically non-conductive (diamagnetic) material is inserted in the alternating field of the sensor with magnetic field intensity $\mathbf{H}$. In this material, the action of the sensor's field induces eddy currents, which, in their environment, create a magnetic field having its own intensity; according to Lenz's law, this field then acts against the field that induced it.

The actual port contains a coil wound around a small plastic tube through which the projectile passes. The coil is supplied with an alternating current signal that facilitates the generation of an alternating magnetic field in the environment of the port. While the metal projectile moves through the port, this field will enable the creation of eddy currents inside the projectile. The eddy currents induced in the projectile will excite a magnetic field in its vicinity; this field will act against the field that induced it. The interaction between the primary and the induced fields will then produce a change of the actual induction of the port coil.

To determine the dimensions of the coil, we utilized models based on the finite element method applied within a FEM program. Using the models, we also monitored the change of the actual inductance of the coil in relation to the position of the object and diameter of the coil. The resulting behaviour of the relations determined for the model of the coil are shown in Fig. 6. The parameters of the coil are defined as follows: 500 turns, diameter of 10 mm and winding length of 10 mm.

Figure 5: Detail of the fabricated coil.

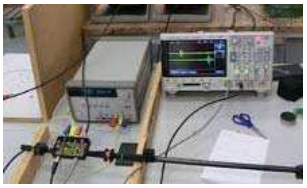

Figure 6: Measurement system with two ports and electronics.

4. RESULTS OF THE EXPERIMENTAL MEASUREMENT

Using the fabricated prototype, we completed the research by performing a large number of test measurements, which were conducted both in the laboratories of the DTEEE, FEEC BUT and in the facilities managed the PROTOTYPA company. The obtained signals are presented in Figs. 5 (one sensor) and 6 (two sensors).

The measured data were digitized and processed using the MATLAB program, in which we peformed the numerical postprocessing and evaluated the envelopes of the signals from the individual sensors.

5. CONCLUSION

This paper presents the basic methods for the measurement of instantaneous velocity **v** in fast-moving objects. The described techniques are markedly based on the principles of the electromagnetic field. In the process of conducting the research, we respected the relative motion of the systems and its influence on the data measured by the sensors. An effective measurement system with the basis of 10 cm was set up.

The theoretical models were numerically processed and evaluated by means of partial experiments conducted using the finite element method. Connection (and effects too) was proved to exist between the inductance L of the sensor coil and the position of the moving metal object. Based on the performed analyses, we designed and fabricated a functional sample of the induction sensor.

The resulting sensor system comprises two measuring coils and the related electronics. Using the fabricated prototype, we completed our activities by conducting experimental measurements at the specialized facilities of the PROTOTYPA company where the realized device was compared with a commercial alternative.

ACKNOWLEDGMENT

The research described in the paper was financially supported by a grant of the Czech Ministry of industry and Trade, no. FR-TI1/001, and a project of the BUT Grant Agency, id. code FEKT-S-11-5/1012.

REFERENCES

1. Li, B., X. Wang, H. Pan, and K. Luo, "Study on error analysis of measuring projectile's speed using induction-type coil target," *International Conference on Electrical and Control Engineering (ICECE)*, [cit. 4.11.2011], ISBN 978-1-4244-6880-5, Wuhan, 2010.
2. Yu, J., X. Wang, and Y. Li, "Velocity and position measurement for projectile using double optical detectors and reflectors," *Symposium on Photonics and Optoelectronics, SOPO*, [cit. 4.11.2011], ISBN 978-1-4244-4412-0, Wuhan, 2009, DOI: 10.1109/SOPO.2009.5230204, Dostupné z: http://ieeexplore.ieee.org/xpl/articleDetails.jsp?tp=&arnumber=5230204.
3. Liu, J. and L. Yu, "Laser-based apparatus for measuring projectile velocity," *9th International Konference on Electronic Measurement & Instruments, ICEMI'09*, [cit. 9.12.2011], ISBN 978-1-4244-3864-8, Peking, 2009, DOI: 10.1109/ICEMI.2009.5274503, Dostupné z: http://ieeexplore.ieee.org/xpl/articleDetails.jsp?tp=&arnumber=5274503.
4. PROTOTYPA, 2007, [cit. 9.12.2011], Dostupné z: http://www.prototypa.cz/me-nu1.html.
5. Xiong, X. F., D. R. Kong, and X. F. Ruan, "Mechanism analysis of induction-type coil target for velocity measurement," *Advanced Materials Research*, [cit. 18.12.2011], 2011, DOI: 10.4028/www.scientific.net/AMR.301-303.666, Dostupné z: http://www.scientific.net/AMR.301-303.666.
6. Spohn, D., "Inductive sensing for velocity measurement at a U.S. air force laboratory," *Sensor*, [cit. 18.12.2011], Jan. 9, 1998, Dostupné z: http://www.sensorsmag.com/sensors/motion-velocity-displacement/inductive-sensingvelocity- measurement-a-us-air-force-labora-854.
7. Fiala, P., Z. Szabo, and M. Friedl, "EMHD models respecting relativistic processes of trivial geometries," *PIERS Proceedings*, 95–98, Suzhou, China, Sep. 12–16, 2011.

Harmonic and Intermodulation Performance of Contact-type MEM Microswitches

Muhammad Taher Abuelma'atti
King Fahd University of Petroleum and Minerals, Box 203, Dhahran 31261, Saudi Arabi

Abstract— This paper presents a new technique for predicting the harmonic and intermodulation performance of the contact-type MEMS microswitch under multi-sinusoidal excitation. The special cases of the contact-type MEMS microswitch excited by two and sixteen equally-spaced equal-amplitude sinusoids are considered in detail and the feasibility of obtaining closed-form mathematical expressions for the even- and odd-order harmonics and intermodulation products, of any order, is studied. The results show that the relative third-order intermodulation rapidly deteriorates when the number of sinusoids applied to the contact-type MEMS microswitch is increased. The results obtained are in excellent agreement with the previously reported measurements and simulation results.

1. INTRODUCTION

Microwave microelectromechanical systems (MEMS) microswitches are widely used in a wide range of RF communication systems. This is attributed to their low cost, small size and weight, and reconfigurability. Unfortunately, MEMS microswitches are nonlinear and, therefore, would generate harmonics and intermodulation products when excited by a multisinusoidal signal. Prediction of the amplitudes of these harmonics and intermodulation products is, therefore, a prerequisite to estimate the effect of MEMS microswitches nonlinearities on the performance of RF systems. In the literature this problem was approached using different assumptions [1–3]. Inspection of these approaches shows that they suffer from one or more of the following disadvantages:

1. Use of Volterra series analysis, thus restricting the analysis to weak nonlinearities.
2. Assuming that the input is formed of a two sinusoids signal; thus restricting the analysis to signals with two-tones only which is not the case for real signals.
3. Recourse to computer aided design (CAD) models.
4. Recourse to numerical techniques for fast prediction of two-tone intermodulation.
5. Use of numerical techniques based on the harmonic balance formulation, thus facing the convergence problems.

The major intention of this paper is, therefore, to present an alternative analytical technique for predicting the harmonic and intermodulation performance of MEMS contact-type microswitches. The proposed technique do not use numerical analysis or CAD models, avoid the use of Volterra series and the harmonic balance techniques and assumes that the input is formed of a multisinusoidal signal as is usually the case.

2. ANALYSIS

Figure 1 shows the schematic of a MEMS microswitch [2, 3]. When a voltage is applied between the gate electrode and the source the cantilever beam anchored to the source in pulled down. This causes a contact between the contact bumps on the underside of the beam and the drain. In [2] it was shown that the switch resistance can be expressed as

$$R_s = R_0(1 + \varepsilon \sin(2\omega t - \phi)) \tag{1}$$

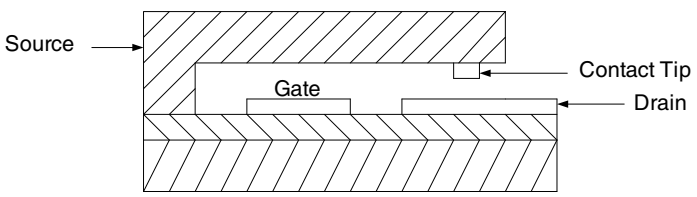

Figure 1: Schematic of a MEMS microswitch [2, 3].

where R_0 is the average switch resistance at the frequency ω, ε is a dimensionless parameter, and ϕ is the phase shift. Equation (1) implies that the input signal to the switch is formed of one sinusoid. Assuming that the input signal is formed of two sinusoids with frequencies that are close together, Equation (1) was used in [2, 3] to predict the intermodulation performance of the MEMS microswitch excited by a two-sinusoid signal. In this case the average resistance R_0 is replaced by a time-dependent resistance varying at the difference frequency between the two input sinusoids; see Equation (6) of [2] and Equation (2) of [3]. No attempt has been reported for predicting the harmonic and intermodulation performance of a MEMS microswitch excited by an equally-spaced multisinusoidal signal.

A multisinusoidal signal comprising $M = 2^N$, $N = 1, 2, 3, 4, \ldots$ equal-amplitude equally-spaced sinusoids can be expressed as

$$V_{in}(t) = X \sum_{m=1}^{M} \sin(\omega_1 + (m-1)\Delta)t \tag{2}$$

In Equation (2), X is the amplitude of the input sinusoid and Δ is the frequency separation between two consecutive frequencies. By successive use of the trigonometric identity of Equation (3)

$$\sin\theta + \sin\psi = 2\cos\left(\frac{\theta-\psi}{2}\right)\sin\left(\frac{\theta+\psi}{2}\right) \tag{3}$$

Equation (2) can be rewritten as

$$V_{in}(t) = 2^N X \left(\prod_{n=1,2,3,\ldots}^{N} \cos\left(2^{n-2}\Delta t\right)\right)\left(\sin\left(\omega_1 + \frac{2^N-1}{2}\Delta\right)t\right) \tag{4}$$

Thus, for the case of two equally-spaced input sinusoids, that is $N = 1$, Equation (4) reduces to

$$V_{in}(t) = 2X\cos\left(\frac{\Delta}{2}t\right)\left(\sin\left(\omega_1 + \frac{1}{2}\Delta\right)t\right) \tag{5}$$

and for the case of 16 equally-spaced input sinusoids, that is $N = 4$, Equation (4) reduces to

$$V_{in}(t) = 16X\cos\left(\frac{\Delta}{2}t\right)\cos\left(\Delta t\right)\cos\left(2\Delta t\right)\cos(4\Delta t)\left(\sin\left(\omega_1 + \frac{15}{2}\Delta\right)t\right) \tag{6}$$

Equation (5) is the same as [Equation (5) of [2] and Equation (1) of [3]]. Equation (4) is new and can be used for studying the intermodulation performance of contact-type MEMS microswitches when the source voltage comprises 2^N equal-amplitude equally-spaced sinusoids. Following the findings and assumptions reported in [2, 3], the variation of the resistance of the contact-type microswitch with the input signal of Equation (4) can be expressed as

$$R_s(t) = R_0\left(1 + \beta\prod_{n=1,2,3,\ldots}^{N}\cos\left(2^{n-1}\Delta t\right)\right)\left(1 + \varepsilon\sin\left(2\omega_1 + \left(2^N-1\right)\Delta\right)t\right) \tag{7}$$

In Equation (7), the parameters β and ε are dependent on both power and frequency. In deriving Equation (7) it is assumed that the resistance varies not at the input frequency but at twice the input frequency [2, 3]. In Equation (7) it is assumed, without loss of generality, that the potential phase shifts between the signal and the thermal response of the device are zeros. Following the assumptions made in [2, 3] and since β and ε are usually small quantities much less than unity, then the term in Equation (7) containing the product of β and ε can be ignored, and Equation (7) can be approximated as

$$R_s(t) = R_0\left(1 + \beta\prod_{n=1,2,3,\ldots}^{N}\cos\left(2^{n-1}\Delta t\right) + \varepsilon\sin\left(2\omega_1 + \left(2^N-1\right)\Delta\right)t\right) \tag{8}$$

As was done in [2, 3] by connecting the microswitch in a circuit comprising the series connection of a source of the multisinusoidal signal of Equation (2) with internal resistance R and an equal load resistance R, as shown in Fig. 2, the voltage across the load resistance can be expressed as

$$V_L(t) = \frac{X \sum_{m=1}^{M} \sin(\omega_1 + (m-1)\Delta)t}{2 + \frac{R_0}{R}\left(1 + \beta \prod_{n=1,2,3,\ldots}^{N} \cos\left(2^{n-1}\Delta t\right)\right) + \varepsilon \sin\left(2\omega_1 + \left(2^N - 1\right)\Delta\right)t\Bigg)} \tag{9}$$

Using the approximation $1/(1+x) \approx 1 - x$ for $x \ll 1$, and since $\beta R_0/(2R + R_0) \ll 1$ and $\varepsilon R_0/(2R + R_0) \ll 1$, then Equation (9) can be approximated as

$$\begin{aligned} V_L(t) \;=\; & \frac{XR}{2R + R_0} \sum_{m=1}^{M} \sin(\omega_1 + (m-1)\Delta)t \\ & \left(1 - \frac{\beta R_0}{2R + R_0} \prod_{n=1,2,3,\ldots}^{N} \cos\left(2^{n-1}\Delta t\right) - \frac{\varepsilon R_0}{2R + R_0} \sin\left(2\omega_1 + \left(2^N - 1\right)\Delta\right)t\right) \end{aligned} \tag{10}$$

Equation (10) contains a large number of terms including intermodulation products and components with frequencies equal to the source frequencies. Equation (10) can, therefore, be used for calculating the amplitudes of the load voltage components corresponding to the input frequencies as well as the intermodulation frequencies for any scenario of the input with a number of sinusoids $= 2^N$, $N = 1, 2, 3, 4, \ldots$.

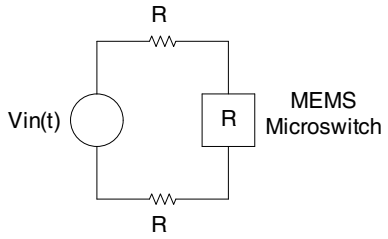

Figure 2: Circuit diagram of a microswitch excited by a voltage source with equal source and load resistances.

3. HARMONICS AND INTERMODULATION PRODUCTS

Equation (10) represents the load voltage in a circuit comprising a MEMS contact-type microswitch, a load resistance and excited by a multisinusoidal source with source resistance equal to the load resistance. Using Equation (10), and simple trigonometric manipulations, the load voltage component of frequency ω_1 can be expressed as

$$V_{1,0}(t) = \frac{XR}{2R + R_0}\left(1 - \frac{2^N - 1}{2}\frac{\beta R_0}{2R + R_0}\right)\sin\omega_1 t - \frac{XR}{2R + R_0}\left(\frac{1}{2}\frac{\varepsilon R_0}{2R + R_0}\right)\cos\omega_1 t \tag{11}$$

Similar expressions can be obtained for the load voltage component at frequency $\omega_1 + \Delta$, $\omega_1 + 2\Delta$, $\ldots$, $\omega_1 + (2^N - 1)\Delta$. The load voltage intermodulation component of frequency $\omega_1 \pm \Delta$ can be expressed as

$$V_{2,1}(t) = \frac{2^N - 1}{2}\frac{XR}{2R + R_0}\frac{\beta R_0}{2R + R_0}\sin(\omega_1 - \Delta)t \tag{12}$$

Similar expressions can be obtained for the load voltage intermodulation component at frequency $\omega_1 \pm 2\Delta$, $\omega_1 \pm 3\Delta, \ldots, \omega_1 \pm (2^N - 1)\Delta$. It is worth noting here that some of the intermodulation components may share the same spectral lines with the original source frequencies. If $\varepsilon \ll \beta$ as is usually the case, Equation (11) reduces to

$$V_{1,0}(t) = \frac{XR}{2R + R_0}\left(1 - \frac{2^N - 1}{2}\frac{\beta R_0}{2R + R_0}\right)\sin\omega_1 t \tag{13}$$

Inspection of Equation (13) reveals that even if $\beta \ll 1$, as is usually the case, the quantity $\frac{2^N-1}{2}\frac{\beta R_0}{2R+R_0}$ may not be $\ll 1$. Thus, it appears that as the number of sinusoids, comprising the source voltage, increases the output amplitude of the components corresponding to the source frequencies will be reduced. Moreover, some of the intermodulation components may share the same spectral lines with the source frequencies. This means that the temperature dependence of the MEMS microswitch resistance will result in severe degradation of the load voltage when the number of the sinusoids in the source is relatively large. Equations (12) and (13) are general and can be used for studying the effect of the temperature dependence of the resistance of contact-type MEMS microswitches on the intermodulation performance of circuits involving them when the source comprises $2^N, N = 1, 2, 3, 4, \ldots$. sinusoids.

4. CONCLUSION

In this paper, an improved theoretical analysis for the intermodulation performance of contact-type MEMS microswitch has been presented. A source voltage comprising 2^N equal-amplitude equally-spaced sinusoids is assumed. First a closed form expression is obtained for the source voltage. This expression is a function of the frequency separation between two consecutive sinusoids (Δ), the number of sinusoids (N) and the frequency of the first sinusoid (ω_1). Using this expression, a closed-form expression has been obtained for the relative third-order intermodulation performance of the contact-type MEMS microswitch. This expression is general and is valid for any value of N. Using this expression the third-order intermodulation of the contact-type MEMS microswitch when the source comprises two equal-amplitude sinusoids, that is $N = 2$, can be obtained as a special case. The analysis presented here clearly shows that the third-order intermodulation performance rapidly deteriorates with the increase in the number of sinusoids comprising the source.

REFERENCES

1. Dussport, L. and G. M. Rebeiz, "Intermodulation distortion and power handling in RF MEMS switches, varactors, and tunable filters," *IEEE Transactions on Microwave Theory and Techniques*, Vol. 51, 1247–1256, 2003.
2. Johnson, J., G. G. Adams, and N. E. McGruer, "Determination of intermodulation distortion in a MEMS microswitch," *IEEE International Microwave Symposium Digest*, 2135–2138, 2005.
3. Johnson, J., G. G. Adams, and N. E. McGruer, "Determination of intermodulation distortion in a contact-type MEMS microswitch," *IEEE Transactions on Microwave Theory and Techniques*, Vol. 53, 3615–3620, 2005.

Giant Magnetoimpedance Effect in Nanocrystalline Microwires

A. Talaat[1], **V. Zhukova**[1], **M. Ipatov**[1], **J. M. Blanco**[2], **M. Churyukanova**[3], **S. Kaloshkin**[3], **E. Kostitcyna**[3], **E. Shuvaeva**[3], **V. Sudarchikova**[3], **L. Gonzalez-Legarreta**[4], **B. Hernando**[4], **and A. Zhukov**[1, 5]

[1]Dpto. Fisica de Materiales, UPV/EHU, San Sebastian 20018, Spain
[2]Dpto. de Física Aplicada, EUPDS, UPV/EHU, San Sebastian 20018, Spain
[3]National University of Science and Technology "MISIS", Moscow 119049, Russia
[4]Dpto. de Física, Universidad de Oviedo, Calvo Sotelo s/n, Oviedo 33007, Spain
[5]IKERBASQUE, Basque Foundation for Science, Bilbao 48011, Spain

Abstract— We studied GMI effect and magnetic properties of Finemet-type FeCuNbSiB microwires. We observed that GMI magnetic field and frequency dependences and magnetic softness of composite microwires produced by the Taylor-Ulitovski technique can be tailored either controlling magnetoelastic anisotropy of as-prepared FeCuNbSiB microwires or controlling their structure by heat treatment or changing the fabrication conditions. GMI effect has been observed in as-prepared Fe-rich microwires with nanocrystalline structure.

1. INTRODUCTION

Studies of glass coated ferromagnetic microwires (typically of 5–30 μm in diameter) have attracted growing attention in the last few years owing to their outstanding soft magnetic properties (magnetic bistability, enhanced magnetic softness, GMI effect, fast domain wall propagation) and possibility to obtain glass-coated microwires with different structure (amorphous, nanocrystalline, granular) [1, 2]. Particularly, recent studies have demonstrated that optimization of soft magnetic properties and GMI effect of amorphous glass coated microwires is possible choosing the appropriate chemical composition of metallic nucleus and adequate annealing conditions [1].

In some cases, nanocrystallization allows achieving good magnetic softness and enhanced GMI effect in ferromagnetic microwires. Such soft magnetic character is usually attributed to vanishing magnetocrystalline anisotropy and the very small magnetostriction value when the grain size approaches 10 nm [3, 4]. Like for conventional nanocrystalline materials, average anisotropy for randomly oriented α-Fe(Si) grains is negligibly small when the average grain is about 10–20 nm. Consequently, low values of coercivity in the nanocrystalline microwires were ascribed to small effective magnetic anisotropy. In addition to the suppressed magnetocrystalline anisotropy, low magnetostriction values provide the basis for the superior soft magnetic properties observed in particular compositions [3, 4]. Low values of the magnetostriction are essential to avoid magnetoelastic anisotropies arising from internal or external mechanical stresses.

Generally magnetic properties and overall shape of hysteresis loops of amorphous ferromagnetic microwires depend on the composition of the metallic nucleus as well as on the composition and thickness of the glass coating. As discovered before, shape of hysteresis loops changes from rectangular, typical for amorphous Fe-rich compositions, to inclined, typical for Co-rich compositions [5]. Amorphous microwires with vanishing magnetostriction exhibit quite soft magnetic properties.

Such strong dependence of the hysteresis loops on these parameters should be attributed to the magnetoelastic energy given by:

$$K_{me} \approx 3/2\lambda_s\sigma_i, \tag{1}$$

where λ_s is the saturation magnetostriction and σ_i is the internal stress. The magnetostriction constant depends mostly on the chemical composition and is vanishing in amorphous Fe-Co based alloys with Co/Fe $\approx$ 70/5 [5–7]. One of the peculiarities of the fabrication technique of glass-coated microwires is that it involves the simultaneous solidification of composite microwire consisting of ferromagnetic nucleus surrounded by glass coating. Quite different thermal expansion coefficients of the glass and the metallic alloys introduce considerable internal stresses inside the ferromagnetic nucleus during simultaneous fast solidification of the composite microwire [1, 6, 8, 9]. The estimated values of the internal stresses in these glass coated microwires arising from the difference in the thermal expansion coefficients of metallic nucleus and glass coating are of the order of 100–1000 MPa, depending strongly on the ratio between the glass coating thickness and metallic core diameter [8–11], increasing with the glass coating thickness. Such large internal stresses give rise to a drastic

change of the magnetoelastic energy, K_{me}, even for small changes of the glass-coating thickness at fixed metallic core diameter. Additionally, such a change of the ρ-ratio should be related to the change of the magnetostriction constant with applied stress [6, 12]:

$$\lambda_s = (\mu_o M_s/3)(dH_k/d\sigma), \tag{2}$$

where $\mu_o M_s$ is the saturation magnetization.

It is worth mentioning, that residual stresses of glass-coated microwires arising during simultaneous solidification of metallic nucleus and glass coating, mostly have been estimated from the simulations of the process of simultaneous solidification of metallic nucleus inside the glass tube [6–8] and experimental determination of such residual stresses is rather complex. One of the experimental evidence of existence of such stresses is the dependence of hysteresis loops and particularly magnetic properties (coercivity, remanent magnetization) on ρ-ratio [6, 8].

Consequently, tailoring of the magnetoelastic energy, K_{me}, is essentially important for optimization of magnetic properties of glass-coated microwires [1, 6, 8].

Accordingly, any method allowing estimation of internal stresses in glass-coated microwires is quite suitable for soft magnetic properties optimization.

In the case of glass-coated microwires, existence of the outer glass-coating with physical properties completely different from metallic nucleus alloys (different thermal conductivity, thermal expansion coefficients ...) in some cases drastically affects structure and magnetic properties of glass-coated microwires [1]. Thus, crystalline structure, crystallization temperature and magnetic properties of nanocrystalline microwires are rather different from nanocrystalline ribbons of the same composition [1–3].

In this paper, we studied the effect of the nanocrystallization on magnetic properties, structure and GMI of Finemet-type amorphous and nanocrystalline microwires.

2. EXPERIMENTAL

We studied Finemet-type $Fe_{70.8}Cu_1Nb_{3.1}Si_{14.5}B_{10.6}$, $Fe_{71.8}Cu_1Nb_{3.1}Si_{15}B_{9.1}$, $Fe_{73.8}Cu_1Nb_{3.1}Si_{13}B_{9.1}$ and $Fe_{70.8}Cu_1Nb_{3.1}Si_{16}B_{9.1}$ glass-coated microwires with different metallic nucleus diameter, d, and total microwire diameter, D, were produced by modified Taylor-Ulitovsky method [1–3]. It is worth mentioning, that the strength of internal stresses is determined by ratio ρ [6, 9]. Therefore, controllable change of the ρ-ratio allowed us to control the residual stresses.

Hysteresis loops have been determined by flux-metric method, as described elsewhere [1, 2]. We measured magnetic field dependences of impedance, Z, and GMI ratio, $\Delta Z/Z$, for as-prepared samples and after heat treatments. We used specially designed micro-strip sample holder. The sample holder was placed inside a sufficiently long solenoid that creates a homogeneous magnetic field, H. The sample impedance Z was measured using vector network analyzer from reflection coefficient S_{11}. The DC bias current I_B was applied to the sample through a bias-tee element. All experimental graphs show both ascending and descending branches of the field dependencies of the real part of impedance Z so that the magnetic hysteresis can be evaluated. More details on experimental technique can be found in Ref. [1].

Structure and phase composition have been checked using a BRUKER (D8 Advance) X-ray diffractometer with Cu K_α ($\lambda = 1.54$ Å) radiation.

3. RESULTS AND DISCUSSION

All as-prepared and even annealed Finemet-type microwires at annealing temperature, T_{ann}, below first crystallization process, present squared hysteresis loops similar to Fe-rich amorphous microwires (Fig. 1).

As expected from previous studies of Fe-rich amorphous microwires [1], coercivity, H_C, of as-prepared Finemet-type microwires depends on ratio $\rho = d/D$ (Fig. 2). Annealing temperature dependence of coercivity of $Fe_{71.8}Cu_1Nb_{3.1}Si_{15}B_{9.1}$ microwires shown in Fig. 3 present considerable magnetic softening at annealing temperatures, T_{ann}, between 800 and 900 K as previously observed in other Finemet-type materials and Finemet-type microwires [1, 13]. Consequently, although GMI effect in as-prepared Fe-rich microwires is rather small, after annealing we observed increasing of the GMI effect (Figs. 4(a) and 4(b)). Enhancement of the $\Delta Z/Z$ ratio is related with magnetic softening of studied microwires after annealing and internal stress relaxation. Indeed applied and internal stresses considerably affect GMI effect [12]. Generally, measurements of the GMI effect in nanocrystalline microwires involve preparation of the electrical connections of rather brittle nanocrystalline samples.

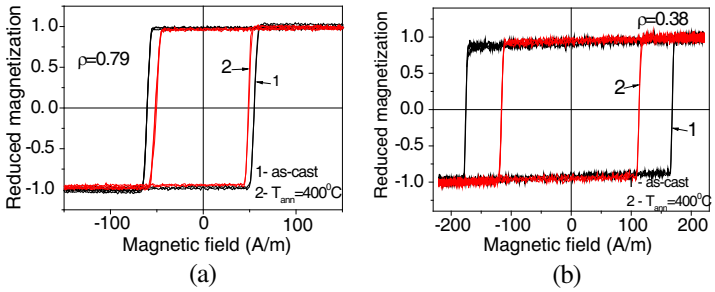

Figure 1: Hysteresis loops of as-prepared and after the heat treatment $Fe_{70.8}Cu_1Nb_{3.1}Si_{14.5}B_{10.6}$ microwires with different $\rho = d/D$ ratios: (a) $\rho = 0.79$, (b) $\rho = 0.38$.

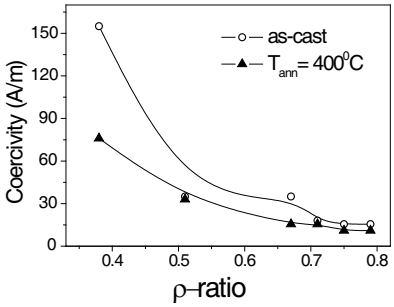

Figure 2: Coercivity dependence on ρ-ratio for as-prepared $Fe_{70.8}Cu_1Nb_{3.1}Si_{14.5}B_{10.6}$ microwires.

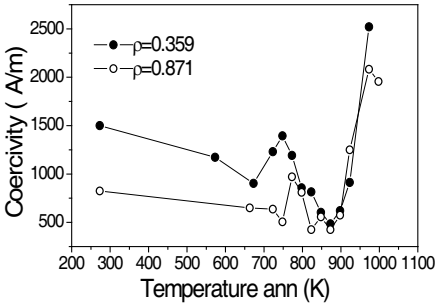

Figure 3: Annealing temperature dependence of coercivity of $Fe_{71.8}Cu_1Nb_{3.1}Si_{15}B_{9.1}$ microwires with different ρ-ratios.

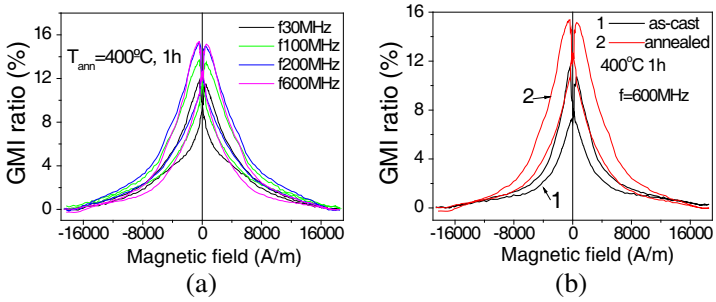

Figure 4: (a) $\Delta Z/Z(H)$ dependences of $Fe_{73.8}Cu_1Nb_{3.1}Si_{13}B_{9.1}$ amorphous microwires annealed at 400°C measured at different frequencies and (b) $\Delta Z/Z(H)$ dependences of $Fe_{73.8}Cu_1Nb_{3.1}Si_{13}B_{9.1}$ amorphous microwires measured in as-prepared and annealed at 400C samples at 600 MHz.

X-ray studies show, that as-prepared $Fe_{73.8}Cu_1Nb_{3.1}Si_{13}B_{9.1}$ microwire exhibit nanocrystalline structure. The structure consists of of α-Fe nanocrystallites with average grain size about 12 nm and amorphous matrix (Fig. 5(a)). The grain size has been estimated the average grain size can be estimated from the width of the crystalline peak using the Debye-Scherrer equation. For comparison X-ray diffraction pattern of completely amorphous as-prepared $Fe_{70.8}Cu_1Nb_{3.1}Si_{14.5}B_{10.6}$ microwire is shown in Fgi. 5(b). In as-prepared $Fe_{73.8}Cu_1Nb_{3.1}Si_{13}B_{9.1}$ microwires we observed considerable GMI effect (up to $\Delta Z/Z \approx 30\%$ at $f = 100$ MHz, see Fig. 5(c)). Observed considerable GMI effect in as-prepared $Fe_{73.8}Cu_1Nb_{3.1}Si_{13}B_{9.1}$ microwires is much higher that of $Fe_{70.8}Cu_1Nb_{3.1}Si_{14.5}B_{10.6}$. This difference must be attributed to amorphous structure of $Fe_{70.8}Cu_1Nb_{3.1}Si_{14.5}B_{10.6}$ and nanocrystalline structure of $Fe_{73.8}Cu_1Nb_{3.1}Si_{13}B_{9.1}$ microwires.

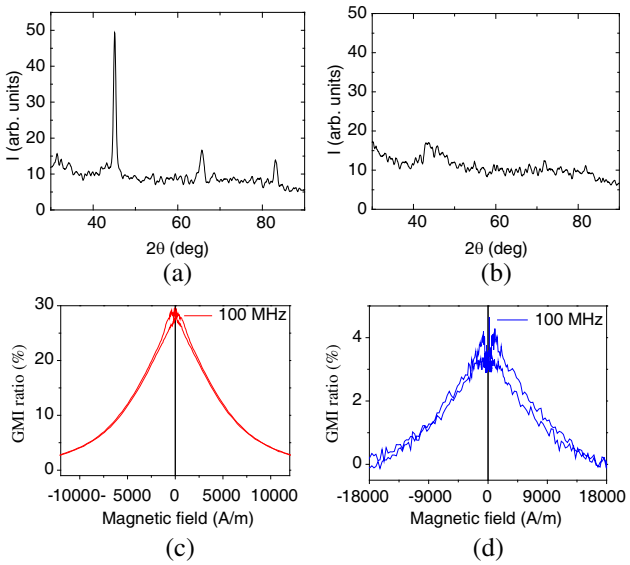

Figure 5: (a) X-ray diffraction patterns of as-prepared $Fe_{73.8}Cu_1Nb_{3.1}Si_{13}B_{9.1}$ ($\rho = 0.6$) and (b) $Fe_{70.8}Cu_1Nb_{3.1}Si_{14.5}B_{10.6}$ ($\rho = 0,87$) microwires and (c), (d) GMI effect in the same samples.

4. CONCLUSIONS

The study of magnetic and thermal properties of nano-scaled Finemet-type FeCuNbSiB and Co-Cu glass-coated microwires reveals that increase of stresses in the amorphous metallic nucleus considerably affect magnetic properties of these materials. In Finemet-type FeCuNbSiB the reduction of the ρ-ratio, results in the rise of coercivity. We observed magnetic softening and considerable GMI effect in Finemet-type FeCuNbSiB with nanocrystalline structure. Magnetoelastic anisotropy affects soft magnetic properties and GMI effect of FeCuNbSiB micrfowires.

ACKNOWLEDGMENT

This work was supported by EU ERA-NET programme under project "SoMaMicSens" (MANUN ET-2010-Basque-3), by EU under FP7 "EM-safety" project, by Spanish Ministry of Science and Innovation, MICINN under Project MAT2010-18914, by the Basque Government under Saiotek 11 MICMAGN project (S-PE11UN087) and by federal target program "Scientific and scientific-pedagogical personnel of innovative Russia", state contract No. 14.18.21.0783.

REFERENCES

1. Zhukova, V., M. Ipatov, and A. Zhukov, *Sensors*, Vol. 9, 9216–9240, 2009.
2. Jiles, D. C., *Acta Materialia*, Vol. 51, 5907–5939, 2003.
3. Arcas, J., C. Gómez-Polo, A. Zhukov, M. Vázquez, V. Larin, and A. Hernando, *Nanostructured Materials*, Vol. 7, No. 8, 823–834, 1996.
4. Dudek, C., A. L. Adenot-Engelvin, F. Bertin, and O. Acher, *J. Non-Cryst. Solids*, Vol. 353, 925–927, 2007.
5. Zhukov, A. and V. Zhukova, "Magnetic properties and applications of ferromagnetic microwires with amorphous and nanocrystalline structure," 162, Nova Science Publishers, Inc. 400 Oser Avenue, Suite 1600 Hauppauge, NY 11788, 2009.
6. Zhukov, A., V. Zhukova, J. M. Blanco, A. F. Cobeño, M. Vazquez, and J. Gonzalez, *J. Magn. Magn. Mater.*, Vols. 258–259, 151–157, 2003.
7. Konno, Y. and K. Mohri, *IEEE Trans. Magn.*, Vol. 25, No. 5, 3623–3625, 1989.
8. Chiriac, H., T.-A. Ovari, and A. Zhukov, *J. Magn. Magn. Mater.*, Vols. 254–255, 469–471, 2003.
9. Velázquez, J., M. Vazquez, and A. Zhukov, *J. Mater. Res.*, Vol. 11, 2499–2505, 1996.
10. Chiriac, H., T.-A. Ovari, and G. Pop, *Phys. Rev. B*, Vol. 52, 10104–10113, 1995.
11. Antonov, A. S., V. T. Borisov, O. V. Borisov, A. F. Prokoshin, and N. A. Usov, *J Phys D: Appl. Phys.*, Vol. 33, 1161–1168, 2000.
12. Blanco, J. M., A. Zhukov, and J. Gonzalez, *J. Appl. Phys.*, Vol. 87, No. 9, 4813–4815, 2000.
13. Herzer, G., *J. Magn. Magn. Mat.*, Vol. 294, 99–106, 2005.

Astronaut Monitoring for Bow Shock Front of Petergius Nebular

Shigehisa Nakamura
Kyoto University, Japan

Abstract— This work concerns to an astronaut monitoring for a bow shock front of the Petergius Nebular. This is a case of the applications of the electromagnetic waves in the infrared band which is introduced for this purpose of monitoring. The author had ever in the field of satellite monitoring of the earth surface, though in this work, a passive sensor of infrared signals is reversed to direct to the space outside of the planet earth. A brief note is given on what found at a monitoring under a mission operated as ASTRO-F conducted by JAXA after launched in 2006.

1. INTRODUCTION

The author introduces a note to a finding in the mission ASTRO-F operated by JAXA after launching an astronaut with a polar orbital motion around the planet earth.

First, a brief note to the mission is introduced. The author had ever his chance to work for a satellite monitoring of the earth surface so that the sensor for the infrared beam had been used in order to detect for the electromagnetic waves out of the earth into the space.

In this work, the sensor is used for detecting electromagnetic waves form the space to the earth surface ill order to see what is an astronomical signal.

In the mission named as ASTRO-F, a successive operation is continuing for finding any astronomical event, for example, a birth of a new nebular or a structure of the space in the scope of astronomy.

One of the finding during the mission by this time must be an interesting case of a bow shock front pattern detected by the infrared beam sensor mounted on the astronaut.

This mission is continuing to monitor all of the events in a form of infrared signals so that it could be expected the other signals for finding some new processes s in the astronomical space.

2. A BRIEF REVIEW NOTE

In the early age, it had been only used some kinds of astronomical telescope using a set of several lenses fixed inside a hand-made tube. Kepler must had found the planets motions by using one of the optical telescope for astronomical use. This type of the telescope is called by name of the Newton type.

In order to see a more detailed pattern of the planets in the solar system, an improved telescope has been designed. First step was to get a more precise curvature of the lense.

The other techniques were to use a mirror-lenses system in order to finer figure of the planet surface patterns.

Astronomers had tried to obtain a large concave mirror with an appropriate focus.

In order to have a more clear image of the planets, the astronomers had been worked as if they were the technological specialists fo making a excellent mirror for obtaion any clear image.

As an advance of the researches in astronomy, optical observations of the planets has been continued though a passive infrared beam sensor is introduced to get an advanced information on the planets.

After an artificial satellite was launched, the planets' pattern has made clear even without any correction of the atmospheric contaminations.

An introduction of spacecraft is a more excellent technique for obtaining various kinds of the information.

Now, at present, there are many kinds of astronomical missions.

The mission named as ASTRO-F is one of them, launched on 22 February 2006 and in service successively.

3. SOURCE OF INFRARED BEAM

In the case of an infrared beam monitoring in the astronomical space, it is necessary to be aware of the background field.

The beam as the background is taken to be uniform consisted by the Far infrared beams.

Adding to the above, a Far-infrared beam must be radiated out of the intersteller dusts in a form of a thermal radiation just near surface of the nebulars.

4. STAR FORMATION ON ZONE IN THE SPACE

In the space, there is a star formation zone. For example, a covering area of the constellation of Orion is now a star formation zone. In this area, several spiral pattern of the nebular.

New birth of a star is found in some spiral branch of the nebular. It is expected a new birth of a star that is bright in the spiral of the interested nebular.

5. BOW SHOCK FRONT OF PETERGIUS NEBULAR

The scientists in JAXA have informed us that the mission is on the way to expected works, so as that the monitoring is informing that a bow shock front is exist in the front of the Petergius tracking axis.

It has been confirmed that the Petergius nebular is in motion in a 32 km/sec. Then, this bow shock front pattern in the monitoring imagery should be quite similar to the case that the planet earth in the solar system.

An attention should be this bow shock front possibly taken to be equivalent to the plasma sheath of the planet earth in the solar system.

6. SPACE FIELD AROUND PETERGRUS NEBULAR

With the author's understand of what result of the monitoring is obtained, there is a similar space pattern in the typical nebular space comparing to the plasma sheath of the planet earth in the solar system.

The information in the monitoring the bow shock front of Petergius nebular should be taken to be a sidereal wind just like that of the solar wind for the planet earth.

7. EFFECT OF SIDEREAL FLOW

In order to realize the monitored result about Petergius nebular, it is necessary to an existence of the strong sidereal wind affecting to determine the specific pattern of the bow shock front around Petergius nebular.

Even after following the scientists for the mission of ASTRO-F, the author has to assume an uniform sidereal flow.

8. GREAT MAGELLAN NEBULAR

Now, it should be considered that the sidereal flow radiated out of the Great Magellan nebular is contributive to form the bow shock front around Petergius nebular.

9. DRIFTING OF PETERGIUS NEBULAR

Looking at again, the information in the monitored Petergius nebular, then, it can be seen that the bow shock front around Petergius nebular is oblique a little relative to the sidereal flow out of Great Magellan nebular.

Now, it should be considered that the distance between Peterguis nebular and Great Magellan nebular is about 1000 years in the optical path time.

At this time, the author is hard to evaluate any quantitative energetics about Petergius nebular.

Simply, it is possible to assume another strong cosmic flow in order to realize though there is no reference data available for understanding the monitoring result here.

In addition, the author has no key now to discuss three dimensional process of what noted above.

10. DISCUSSIONS AND CONCLUSIONS

As stated above, in order to see the details, it should be promoted more advanced research in next step. The mission of ASTRO-F is now on running.

The author wishes that this work could be helpful for realizing Petergius nebular even under the author has only limited references at present (for example, [1–4]).

By this time, a linear system has been taken as a reference at realizing the observed result though some additional view must be given after considering nonlinear processes.

The author is aware of that the present works in space science are promoted only in a scale of the planet earth in the solar system yet.

REFERENCES

1. Chapman, S. and J. Bartels, *Geomagnetism*, 1049, Oxford University Press, London, 1940.
2. Chapman, S., *Solar Prasma, Geomagnetism, and Aurora*, 141, Gordon and Breach, NY, 1964.
3. Berchem, J. and C. T. Russel, "The thicknes of the magnetopause current layer," *Journal of Geopgysical Research*, Vol. 87, 2108–2114, 1982.
4. Miura, A. and P. L. Pritchett, "Nonlocal stability analysis of the MHD Kelvin-Helmholtz instability in a compressible plasma," *Journal of Geophysical Research*, Vol. 87, 7431–7444, 1982, doi:10.1029/JA087iA09p07431.

Spacecraft Monitoring for Magnetic Field of Planet Mercury

Shigehisa Nakamura
Kyoto University, Japan

Abstract— A brief note is introduced about spacecraft monitoring for magnetic field of the planet Mercury. A review of the related researches is introduced first for a convenience to clarify what is the main purpose of this work. Recent spacecraft monitoring of the magnetic fields around the planet Mercury is interesting at comparing to what have been studied about the magneticfield around the planet earth. What is the observed result in the MESSENGER project for a spacecraft monitoring of Mercury's environment, is introduced for demonstrating that what have been observed on and around the earth. This could be taken to be similar to the cases of the pattern found around Mercury in a linealized theoretical model. The findings at spacecraft monitoring cover the instability in Mercury's magnetic field. This finding could be a trigger of the advanced research for magnetic disturbance evolution as a physical process around the planet earth. Some part of this work might be looked as if it was quite similar to what found during satellite thermal monitoring of an ocean front evolution on the earth.

1. INTRODUCTION

This is for introducing about on magnetic field on a solar quiet day of the planets Mercury in the solar system. By this time, the author has introduced about satellite monitoring of the earth surface though it is intended to see what pattern is found in the other planets of the solar system. For example, the earth's magnetic field has been updated now, and there are many running project for detecting the planets in the solar system by using spacecraft monitoring. In the recent years, the spacecraft monitoring of the planets has been developed to give us some interesting observed data. The author here would like to introduce results observations for the magnetic field for the planet Mercury.

Referring to the observations introduced in this work, it could be possible to know about what pattern of environment could be found around the interested planets. The planet Mercury in this case, is some of the specific cases in the MESSENGER project for detecting Mercury's environment for understanding what could be found as the processes around the Mercury's magnetopause, which might be taken to be a quite similar case of the processes found during the satellite thermal monitoring of the ocean front evolution on the earth.

What is introduced in this work could be a key for us to obtain a more advanced understanding of the magnetic fields of the planets in the solar system in relation to that of the planet earth.

2. REVIEW NOTE

The author has been noted about satellite monitoring of the earth surface for these years which could be helpful for understanding of the dynamical processes appearing on the earth surface. On the other hand, the author has to note that spacecraft monitoring has been developed on the bases of the knowledge and technique for satellite monitoring. The spacecraft monitoring has been applied for monitoring or detecting the planets except the earth in the solar system.

The solar system is, at present (in 2010), is classified after the definition by IAU (International Astronomical Union) as that the inner planets (Mercury and Venus), the earth as reference, and the outer planets (Mars, Jupiter, Saturn, Uranus and Neptune).

The inner planets are between the sun and he earth. The existing astronomical catalogue tells us that the inclination of the interested planet relative to the solar equatorial plane. For example, the inclinations of the Venus and Mercury are as follows.

(1) That is to say, the inclination of Mercury is nearly equal to zero.
(2) As for the case, the inclination of Venus is 177.4 degree.
(3) As for the case, the inclination of the earth is 23.44 degree.

Referring to the above data about the inclinations, it can be seen that the environments of the three planets are essentially different from each other though it is quite similar when some conditions fit to a specific state under the astronomical parameters, with

(A) Mercury rotating in 25.38 days circulates in ca 0.24 years on the orbit around the sun,

(B) Venus rotating in 58.65 days circulates in ca 0.61 years on the orbit around the sun,
(C) Earth rotating in one day circulates in one year on the orbit around the sun.

With what introduced the astronomical factors for the Mercury, Venus and the earth, it can be seen that each rotating axis of the interested planets is different from each other and the time lengths of one day on the planet Mercury and Venus are about 25.38 and 58.65 days respectively.

When the author concentrate his interest in the magnetic main field of the above three planets, it is strongly interesting to see what is an effect of each planet rotation to the corresponding planet's daily magnetic variation.

In the following sections, the author introduces what pattern of a daily magnetic variation around the planet Mercury in comparison to the earth's daily magnetic variation as shown"S_q" for a case of solar quiet day on the earth.

As for the case of the earth, the earth's magnetic field has been surveyed and observed for more than 100 years. In 1940, Chapman and Bartels [1] introduced "Geomagnetism" as a part of Geophysics and updated [2]. The author had ever found an indoor model experiment of Terrella for reproducing aurora oval by Birkeland in Norway in Chapman's publication [1]. Birkeland had learned Maxwell's electromagnetics under Henri Poincare in Paris, and then, he had learned electromagnetic waves under Herz, and, he had his expeditions for finding an electron flow from the sun in relation to the magnetic variations on the earth surface.

There have been many reports and researches concerning the newly found results on the bases of the data sets obtained by the spacecraft monitoring. The author would not here introduce all of what are taken to be the contribution reduced from the data obtained by the spacecraft.

3. MONITORING MAGNETIC FIELD PATTERN

As for the magnetic field around the earth, the author had introduced after his digests of references [l, 2]. The magnetopause and magnetosphere of the earth under the influence of the solar wind was theoretically clarified to give an illustration to relate where a couple of the possible aurora ovals can be formed. The University of Alaska has continuing observation of the aurora boreares at Fairbanks and sub-bases for those observations and monitoring. The scientists have utilized the base fixed on land surface, aircrafts, artificial satellites mounted sensors for monitoring.

Scientific aspect of the aurora australis has been recorded for more than fifty years since the International Antarctic Survey Project was composed and started. The early Antarctic expeditions had get an advanced survey by the glacier ships, the aircraft and the polar orbital satellites prepared in a form of artificial product.

Berchem and Russel [3] studied on the thickness of the magnetopause current layer around the earth in 1982.

Miura and Pritchett [4] presented their work on nonlocal stability analysis of the MHD Kelvin-Helmholtz instability in a compressible plasma. Since then, the team in Japan has promoted to solve Kelvin-Helmholtz instability at the earth's magnetopause.

4. MAGNETIC FIELD OF MERCURY

Anderson in Johns Hopkins University and his group in 2007 (including Slavin) had presented their contribution for problem on the magnetometer instrument in relation to the project of MESSENGER [5].

After Anderson [5], Slavin [6] in NASA and his group presented their contribution, for example, Mercury (in 2008), observations of Mercucy's magnetosphere (in 2009), and observation of extreme loading and unloading of Mercury's magnetic tail (in 2010).

After Slavin group's contribution, Boardsen [7] in NASA presented a report on observation of Kelvin-Helmholtz waves along the dusk-side boundary of Mercury's magnetosphere during MESSENGER's third flyby (in 2010).

Boardsen et al. [7] has given a notice as that Kelvin-Helmholtz waves (K-H waves) driven by solar wind flow around planetary magnetospheres have been reported at the planet earth and Saturn, most convincingly by the identification of vortices at both bodies referring to the references. He noted that Mercury's close proximity to the Sun offers the opportunity to observe these waves under much higher solar wind pressure, higher interplanetary magnetic field (IMF) intensities, and lower Alfvenic Mach numbers than those typically observed at one AU (Astronomical Unit) or in the outer solar system. Further, the small size of this magnetosphere relative to the Larmor radii of shocked solar wind and planetary ions is important. Typically at earth the thickness

of the magnetopause current layer is many ($\sim$ 10) times the magnetosheath ion Larmor radii, so the effects of finite Larmor radius are difficult to observe. Boardsen [7] reviews that kinetic simulations show that, as the velocity-shear layer thickness approaches the ion Larmor diameter, strong dawn/dask asymmetries arlse. Because Mercury's magnetosphere is ~ 8 times smaller than earth's magnetosphere, finite ion Larmor-radius effects at Mercury should be more readily observed. Moreover, because Mercury does not have an ionosphere, there is no ionospheric dissipation of these waves as they propagate down the magnetospheric flanks, in contrast to the situation at the earth where such dissipation is strong.

Slavin et al. (for example, [7]) reported the observation of three azimuthal rotations in the magnetic filed direction near Mercury's magnetpause during the first flyby by the spacecraft for the project of MESSENGER (Mercury Surface, Space Envlrollment, Geochemistry, and Ranging) on 14 Januaw 2008. The IMF direction was northward and was therefore favorable to the development of K-H waves in the magnetosphere. From a detailed analysis of this event, it is concluded that the wave signature was not that of a nonlinear K-H wave and that the magnetopause showed no signs of any perturvations. The period of these rotations was $\sim$ 70 sec, and the wave length was estimated to be in the range of 4 to 10 times of R_M, where R_M is Mercury's radius. Determination of magetic field orientations near the magnetopause is important because magnetic tension forces in the flow direction tend to stabilize this boundary. During the first flyby, the tailward component of the magnetic field was small on the magnetosheath side and was dominant on the magnetospheric side of the magnetopause.

No evidence of K-H waves was detected during the second MESSENGER flyby on 6 October 2008, during which the IMF component normal to Mercury'8 orbital plane was strongly southward. During this second flyby, the magnetic tension arising from the large tailward magnetic field component ($\sim 30\,\mathrm{nT}$) observed on both sides of the magnetopause acted to suppress the K-H instability.

During MESSENGER's third flyby on 29 September 2009, multiple magnetopause crossings were observed by the MESSENGER magnetometer along the (inbound) dusk-side leg of trajectory, and, Slavin suggested that the multiple crossings could be due to the K-H instability. Then, Boardsen et al. [7] presented an analysis of these boundary encounters, and they compared the results with the predictions of theory. Their findings indicated that the MESSENGER might have observed highly steepened, possibly turbulent, K-H boundary waves during its third flyby crossing of the dusk-side boundary of Mercury's magnetosphere.

The MESSENGER project introduced above was undertaken after the support by the NASA Discovery Program under contract to the Johns Hopkins University and to the Carnegie Institution of Washington.

There might be a more advanced research on the related problems after the successive observations and researches in the next ages.

5. CONCLUSIONS

The author introduced a note on spacecraft monitoring of the planet Mercury in brief though this is a tiny part of the big project conducted by NASA. A review note is in the next section to the introduction. Background of the planet earth problem is noted in short, which might help those to understand what a kind of findings on the geomagnetic filed is shown. An updated notice about spacecraft monitoring of the planet Mercury is given on the bases of the observed data. A part of the data obtained by observations might be suggesting Kelvin-Helmholtz instability around the magnetopause of the planet Mercury. Nevertheless, the details could be seen after the successive spacecraft monitoring for obtaning new findings to see what is specific around the planet Mercury. It is strongly required to have a more advanced research by the spacecraft monitoring.

The author has to note that this work could be helpful for realizing the spacecraft monitoring of the planets as an extensive work of the satellite monitoring of the earth surface to find various dynamical and physical processes.

REFERENCES

1. Chapman, S. and J. Bartels, *Geomagnetism*, 1049, Oxford University Press, London, 1940.
2. Chapman, S., *Solar Prasma, Geomagnetism, and Aurora*, 141, Gordon and Breach, NY, 1964.
3. Berchelll, J. and C. T. Russel, "The thickness of the magnetopause current layer," *Journal of Geopgysical Research*, Vol. 87, 2108–2114, 1982.

4. Miura, A. and P. L. Pritchett, "Nonlocal stability analisis of the MHD Kelvin-Helmholtz instabittty in a compressible plasma," *Journal of Geophysical Research*, Vol. 87, 7431–7444, 1982, doi:10.1029/JA087iA09p07431.
5. Anderson, B. J., M. H. Acuna, D. A. Lohr, J. Scheifele, A. Raval, H. Korth, and J. A. Slavin, "The magnetometer instrument on MESSENGER," *Space Science Review*, Vol. 131, 417–450, 2007, doi:10.1007/sl1214-007-9246-7.
6. Slavin, J. A., "Mercury's magnetosphere after MESSENGER's first flyby," *Science*, Vol. 321, 85–89, 2008, doi:10.1126/science.1159040.
7. Boardsen, S. A., T. Sundberg, J. A. Slavin, B. J. Anderson, H. Korth, S. C. Solomon, and L. G. Blomberg, "Observations of Kelvin-Helmholtz waves along the dusk-side boundary of Mercury's magnetosphere during MESSENGER's third flyby," *Geophysical Research Letters*, Vol. 37, L12101, 2010, doi:10.1029/2010GL0.

Monitoring for Sea Caldera Formed at Tsunami Earthquake

Shigehisa Nakamura
Kyoto University, Japan

Abstract— The author introduces a key to forming process of sea caldera at tsunami earthquake. Special reference after satellite monitoring shows a specific pattern of the earth surface displacements around the seismic, epicenter of the tsunami earthquake. The available satellite data is in the area on land around 500 km square. The other geological survey in the coastal zone seems to support the process of the sea caldera formation. The author notes a brief note to the sea caldera especially in relation to the 2011 tsunami earthquake in the northwestern Pacific.

1. INTRODUCTION

In this work, the author introduces a key to forming process of sea caldera at a tsunami earthquake. Special reference is the data of the earth surface displacement pattern at one of one of the tsunami earthquakes. This data was distributed by Geographic Survey Institute after the systematic processing of the signals in relation to the earth surface displacement pattern in an area about 500 km square covering the seismic epicenter of the 201l tsunami earthquake in the northwest Pacific.

There had a severe damage on the coastal zones facing to the seismic epicenter as the seismic waves propagated in the solid crust and on the sea floor.

In the coastal zones, several drums containing fuels tossed up at the acceleration effect of the sudden seismic waves on the coastal flat area. At the forcing of the seismic waves, there had seen plenty ruins of the structures and lifelines. Therefore, any tele-communication systems of the local official functions destructed to be isolated so that the public and citizen activities were lost severely.

Shortly after that seismic waves, abnormally hazardous tsunamis hit the coastal zones to wash up the flat fields for plantations and the height of the tsunamis were beyond the design height of tsunmi-protection works. Storage of the fuels just located on the coastal zone crushed or floated and fired up.

No protection work were in malfunction, as some of the office was overturned just on site of the location facing the sea even in a harbor or inside of any protection works.

Then, this happening was noticed "a Far-East Crisys" which were informed everyone in the world. The victims and suffered people had left isolated in the suffered area.

The scientists had started later after the seismic shoks and the violent tsunamis. Nevertheless, it was hard to see how the seismic event was severe.

In this work, the author notes about a possible process to be formed a sea caldera as a result of the action of the unexpectedly severe seismic motion accompanied by the tsunamis.

2. SATELLITE MONITORING

In order to demonstrate what process must had been seen, the author take a special reference, that is the case of the 2011 tsunami earth quake in the northwest Pacific.

There must be many surveys and reports though it is fact that the scientists in the protection works at natural hazards.

The scientists had felt a pre-seismic signal before the main shock with the hazardous seismic and tsunami actions.

The author would not here write about all of the things and materials but what were monitored and surveyed for suggesting a sea caldera formation process shortly.

The satellite monitoring of the earth surface displacement pattern around the seismic shock event is effective to see what scale was for the displacement pattern on the earth surface.

The monitoring informed us the 3D-process of the earth surface displacement.

This pattern was quite similar to that of the viscous water flow around the weir which had been applied for measuring gauge in the field of hydraulics, especially, of open-channel hydraulics. Nevertheless, there should be considered similitude in the properties of the materials, i.e., a water mass in viscous phase and the earth surface material as a part of the earth crust covering the spherical earth.

As for the energy transfer process of this tsunami earthquake, the energy source must be taken as on the mid-Atlantic ridge where, the magma upwells to contact with the ocean water on the sea floor to forln a couple of stripe on both side of the ridge.

The magma stripes are cooling down during their contact to the ocean water in a certain time to be an additional part of the spreading crusts.

Nevertheless, it is hard to monitor the crust spreading process by a simple satellite monitoring. It is convenient for the scientists to take on-land process as a reference to see the extensive trend undersea.

3. GEOPHYSICAL SURVEY

One of the survey teams found a normal fault in a form of a fresh geological exposure at a gap formed by the main shock a normal fault. It is assured by the research group of Kyoto University. The group leader had noticed about the specific pattern on-site after the survey's result briefing with his digestive comments in these coastal zone in 2011.

The scientists of Tohoku University have their knowledge as their belief about the specific locality of the frequent formations of the seismic normal fault patterns.

In fact, every one of the past seismic shocks had formed ever a reverse fault respectively in these one hundred years.

Nevertheless, the case of the 2011 earthquake, the normal faults were found in the coastal zone.

Adding to the above, in a part of the flat field on the coastal area, ground level became lower than that before the seismic main shock. This pattern is consistent to the monitored result of the vertical displacement in the corresponding flat field though this vertical change was reduced after the satellite monitoring.

4. OFFSHORE SEA FLOOR SOUNDING

One of the ocean research functions, JAMSTEC, had released a vertical section of the two crust meeting zone where layered sediments are found.

Looking at this vertical section, an intrusion of a sharp wedge from the Eurasian plate through the North American crust can be seen meeting off the seismic epicenter.

A part of the tip of the wedge must be moved creeping under the resistive action of the lower part of the sedimentation block.

The author is considering that this one section obtained as a remanent static pattern by sounding along a line settled for the survey. The pattern in the vertical section could be analyzed in a scope of dynamics though some of the scientists in the field of geology, especially, of sedimentology, might be tend to consider this pattern in a scope of a static sedimentary process.

5. INTRUDING WEDGE FROM EURASIAN PLATE

In this cross section, the author has an understanding of a dynamic process for the intruding wedge. There is left some ambiguity though two or three minor fault must be formed in relation to the intruding wedge.

Then, the author feels it necessary to have his attention to the shortening materials can be seen below the horizontal path of the intruding wedge. The tip of the wedge looks to be in a state of a cantilever.

The wedge surely be originated by the materials in relation of that monitored by the satellite monitoring on-land just around the seismic epicenter.

Then, the interface under the tip wedge must be crossed at the point of the seismic epicenter to get to the final stage as seen the vertical section obtained at the operation of sounding during the survey ship moving along the scheduled log line.

A fault line in this vertical section should be passed the seismic epicenter to extent the fault up to the part of the Pacific plate.

Adding to the above, a vent formation by the intruding materials can be seen. This vent must be helpful for upheaval of the horizontal layer upward after the magma's activated motion intruding into the vent formed by the shortening material from the Eurasian plate.

6. NORMAL FAULTS IN PACIFIC

Several cracks as the normal faults should be formed after the wedge tip intrusion.

In a case of a cantilever, forcing downward at the free end should be ted to fall down after making several cracks in the upper part of the wedge tip. Each one of the cracks should be in a kind of "normal fault".

These normal faults help to make ease the magma's vertical motion in the vent.

There is no data about the magma's motion in the area of the two plates meeting though there is left that a higher possibility of the magma's vertical action in the vent surely be effective to toss up the sea floor.

This is a most possible case for the 2011 tsunami earthquake, with the author's concept for the 2011 tsunami earthquake, all of the observed data in geology, geodesy, upper atmosphere, and, tsunamis with sea level raise.

7. SEA CALDERA

The consistency of the all of the available data obtained by satellite monitoring, land surface survey, ocean floor sounding, and some applications of several other scientific fields.

Then, the author has to introduce a high possibility is that a caldera in a similar earthquake. There might be a flat formed by the materials from the inside the sea caldera.

The ash must be consisted by the materials from the Eurasian plate and some shortening boundary materials filled in the crack or in the normal faults, the magma which must be the most contributive materials at sea caldera formation as well as the effective to the 2011 tsunami earthquake.

8. SEISMIC VACANT ZONE

The scientists, especially, scientists in the field of seismology have been aware of a seismic vacant zone, where no seismic activity has been detected and monitored.

The location of the seismic vacant zone is just located the sea caldera noted above. As for the seismic vacant zone, the seismologists have taken it as a strange zone.

Then, the author reminds that the seismic waves propagate under some effects of diffraction and reflection inside the earth surface. This fact was found by the seismologists in early age more than 100 years ago. The internal structures inside of the earth were studied by the seismologists ever. Reminding this experience of the seismologists, it can be understood that a specific property of the seismic vacant zone.

The materials in the seismic vacant zone should be different from the materials outside of the seismic vacant zone.

It is sure that the seismic vacant zone is surrounded by the stratified rocky layers in a solid phase.

Inside of the seismic vacant zone, it must be formed by materials in a little other phase of the solid rocks different from the materials in the surrounding solid rocks stratification.

Inside of the seismic vacant zone, it must be filled by a shortening boundary materials, some of lava as porous state of the magma, or crushed segments of the stratified rock materials nevertheless it is hard to assure what kinds of materials are exist there.

Then, the author feels it easy that the sea caldera could be formed at the location of the seismic vacant zone.

9. DISCUSSIONS AND CONCLUSIONS

The author noted in order to help to find a key for understanding some specific part of tsunami earthquakes in a scientific scope. A sea caldera and a seismic vacant zone might be found and be well understood by an advanced research after satellite monitoring of the earth surface, the monitoring the earth surface displacement could be effective to see mechanism of tsunami earthquakes. For this purpose, a special reference is taken account of the author's illustration for his convenience. The author has introduced the eruptions of volcanoes under glacier in Iceland in these ten years to relate the 2011 tsunami earthquake in the Pacific. The author feels it necessary to make some upheaval and subsidence of the stratified rock layer in solid phase, if it is in need of an application of visco-elastic or elasto-plastic process for the dynamical process with a consideration of the energy transfer mechanisms.

Lastly, the author has to notices to the scientists that an advanced research in a scope of geophysics in a global scale or geological scale should be promoted in a scope of a visco-elastic or elasto-plastic process successively.

Essentially, the earthquakes are caused by breaking process of the earth crust even though assumed to be elastic in the early stage of the seismology.

A Two Order Bandpass Filter Designed with Lowpass Filter Sections

Xing J. Zhong, Jun D. Ye, De X. Qu, and Rong Huang
College of Communication Engineering, PLA University of Science & Technology, Nanjing 210007, China

Abstract— A two order bandpass filter designed with lowpass filter sections was presented in this paper. The lowpass filter section were derived from stepped impedance lowpass filter. An equivalent capacitor composed of slot was inserted in series in the lowpass filter. This filter section suppressed the signals in a wide band, thus made the bandpass filter contained them have a wide stopband. Measured results accord well with the simulated results, showing good performance of the filter.

1. INTRODUCTION

In modern wireless communication system, high performance bandpass filters with small size, low insertion loss, high selectivity, wide stopband are usually demanded. Many efforts have been made to find the structures which could compose filters with high performance [1–8]. Many efforts have also been made to design filters with wide stopband, such as using stepped impedance resonators, defected ground structures, lowpass filters, etc. [9–15]. A direct method of producing wide stoband is using a lowpass filter before or after the bandpass filter. To make the whole structure have a wide stopband, the lowpass filter need to have a wide stopband. In this paper, the lowpass filter sections were introduced in the banpass filter itself, thus not only made a wide stopband, but also had a compact size. And unlike the traditional lowpass filters, the lowpass filter sections did not need to keep a low insertion loss in the passband, because it is only part of the resonators.

2. FILTER DESIGN

2.1. Framework of the Filter

Figure 1 shows the framework of the bandpass filter with lowpass filter sections. Where part A and part B compose one resonator of the filter, part $A1$ and part $B1$ compose the other resonator. For the design simplicity, the two resonators have identical structure. Two equivalent capacitor model the couple effects at two ends between the two resonators are also given in the figure, and $P1$ and $P2$ are respectively the input port and output port.

There are two lowpass filter sections in Fig. 1, one is composed by A, Cc and $B1$, the other is composed by B, Cc and $A1$. For example, the $P1$, B, Cc, $A1$ and $P2$ compose a lowpass filter $F1$. Different from the traditional lowpass filter, the lowpass filter $F1$ doesn't need to keep a low insertion loss in the passband, but need to suppress the signal in a wide band, thus could lead the bandpass filter have a wide stopband.

2.2. Resonator Design

Usually used lowpass filter is stepped impedance lowpass filter, for example, Fig. 2 shows one.

In Fig. 2, $P1$ and $P2$ are the input port and output port transmission lines with characteristic impedance of 50 Ohm, section $S1$ and $S3$ are the high impedance transmission lines, $S2$ is the low impedance transmission line. This kind of lowpass filter could not be used directly in the bandpass filter showing in Fig. 1 as there is a series capacitor in the signal paths of the bandpass filter. Breaking section $S2$ symmetrically into two part could resolve the problem. Letting the resulted

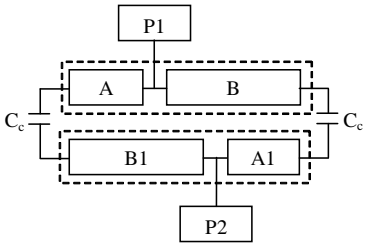

Figure 1: Framework of the two order bandpass filter with lowpass filter sections.

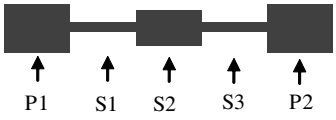

Figure 2: A stepped impedance lowpass filter of order three.

two parts couple to each other could form a series capacitor in the signal path, as showing in Fig. 3, the equivalent circuit is also shown in Fig. 4, in which Cc models the coupling effects between part $S21$ and part $S22$.

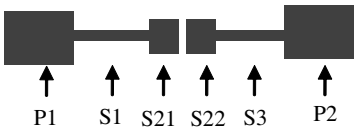

Figure 3: A stepped impedance lowpass filter of order three.

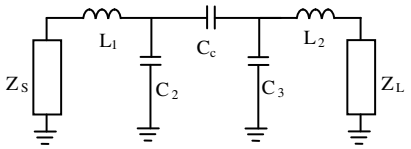

Figure 4: Equivalent circuit of Fig. 3.

Having lowpass filter sections, the next step is to construct resonators based on these sections. Letting B in Fig. 1 represent $S1$ and $S21$ in Fig. 3, it is needed to add additional sections (represented by A in Fig. 1) connecting with $S1$ (not considering the port $P1$), thus certain resonating frequency could be obtained through adjusting these additional sections.

Using dielectric substrate with relative permittivity of 2.2 and thickness of 0.93 mm, the lowpass filter sections were constructed as shown in Fig. 5(a) with the capacitor Cc realized by the slot of 0.3 mm, frequency response of them was shown in Fig. 6.

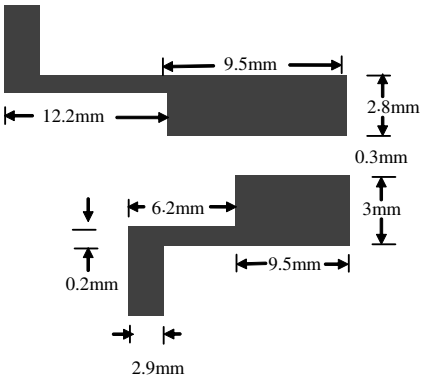

(a)

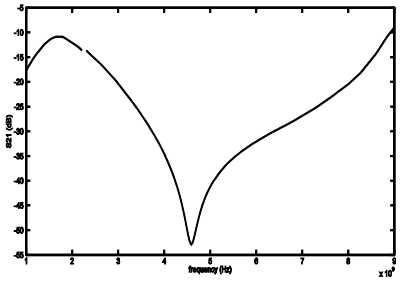

(b)

Figure 5: (a) Lowpass filter sections in the bandpass filter. (b) Simulated frequency response of the lowpass filter sections.

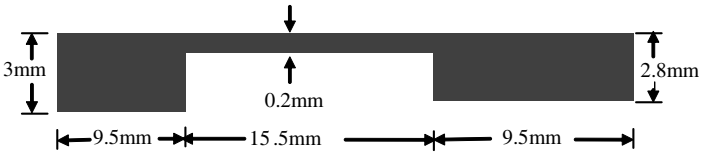

(a)

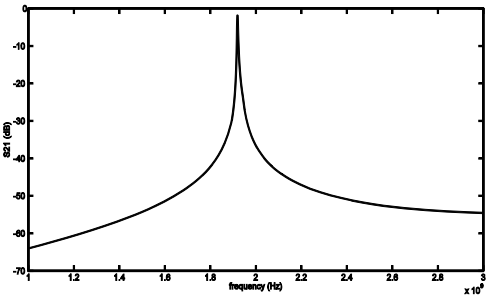

(b)

Figure 6: (a) Dimensions of the constructed resonator. (b) Simulated frequency response of the resonator.

It is clear in Fig. 5(b) that the lowpass filter sections suppress signals well till 8 GHz, but the pass band has a large insertion loss. This doesn't matter in the bandpass filter design. Let B and A represent the upper part and lower part respectively, connect A and B to form the resonator as show in Fig. 6(a), the frequency response of the resonator is shown in Fig. 6(b).

Figure 6(b) shows that this resonator resonating at frequency 1.92 GHz. And through adjusting part A and part B of the resonator, another certain frequency could also be obtained.

2.3. Filter Design

Using the resonator above, a two order bandpass filter with center frequency at 1.92 GHz is designed. To obtain enough coupling, the two resonators couple to each other at two ends as showing in Fig. 7(a). There are two lowpass filter sections seen form input and output, one is at the left, the other is at the right. Wide stopband is obtained due to the lowpass filter sections, the simulated frequency response is shown in Fig. 7(b).

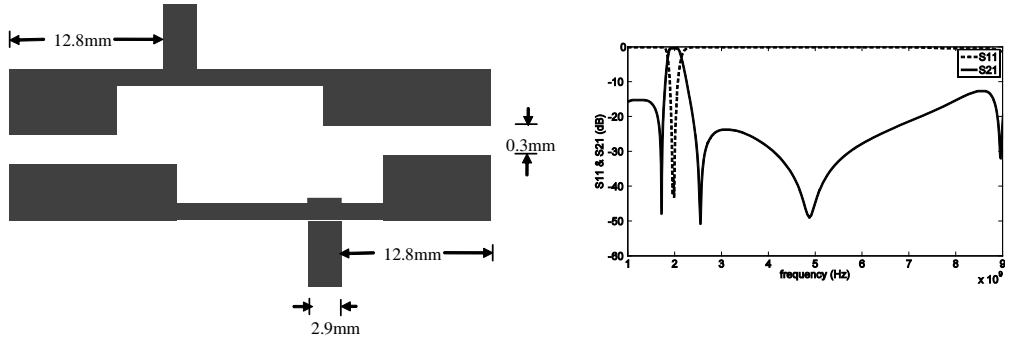

(a) (b)

Figure 7: (a) Bandpass filter with lowpass filter sections. (b) Simulated frequency response of the two order bandpass filter.

3. FABRICATION AND EXPERIMENT

Using material above, the designed filter was fabricated under standard PCB process. Then the Agilent PNA 5230C is used to measure the filter performance. The simulated and measured results were shown in Fig. 8.

Figure 8 shows that though the lowpass filter sections has a large insertion loss in the passband of the bandpass filter, the bandpass filter contains these sections has a low insertion loss in the passband with max insertion loss less than 0.4 dB. But due to the lowpass filter sections, this filter has a so wide stopband that the signal suppression is larger than 15 dB from 2.5 GHz to 7 GHz. The difference among simulated and measured results is a little larger, the reason may be that the fabrication precision is not precise enough and there is transmission lines with width only of 0.2 mm, slots with width of 0.3 mm. Fig. 8 also shows that two transmission zeros occurred in lower stopband and upper stopband of the filter. These two transmission zeros are caused by the tapping positions of the input and output transmission lines. Fig. 9 shows photograph of the proposed filter.

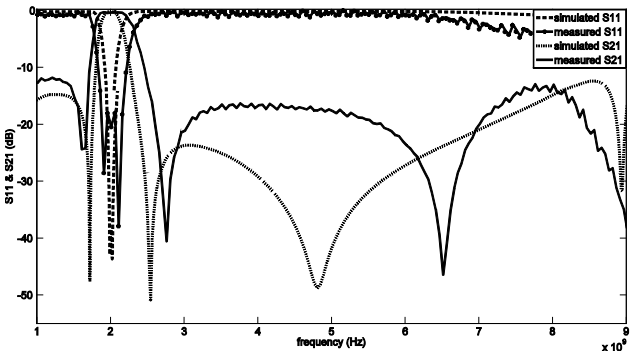

Figure 8: Simulated and measured results of the filter.

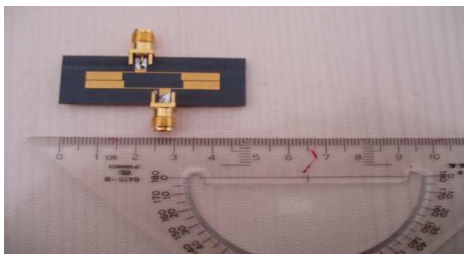

Figure 9: Photo of the filter.

4. CONCLUSION

This work present a two order bandpass filter with lowpass filter sections. The lowpass filter section suppresses signals in a wide band, letting the bandpass filter have a wide stopband. Measured results accord well with the simulated results, showing good performance of the filter.

ACKNOWLEDGMENT

This work was supported in part by the National Natural Science Foundation of China (NSFC) under Grant 61271105 and in part by the Chinese NSFC under Grant 61271103.

REFERENCES

1. Ma, K. X., J. G. Ma, K. S. Yeo, and M. A. Do, "A compact size coupling controllable filter with separate electric and magnetic coupling paths," *IEEE Trans. Microw. Theory Tech.*, Vol. 54, 1113–1119, Mar. 2006.
2. Lee, S. Y. and C. M. Tsai, "New cross-coupled filter design using improved Hairpin resonators," *IEEE Trans. Microw. Theory Tech.*, Vol. 48, 2482–2490, Dec. 2000.
3. Hong, J. S. and M. J. Lancaster, "Microstrip cross-coupled trisection bandpass filters with asymmetric frequency characteristics," *IEEE Trans. Microw. Theory Tech.*, Vol. 46, 84–90, Feb. 1999.
4. Chang, C. Y. and C. C. Chen, "A novel coupling structure suitable for cross-coupled filters with folded quarter-wave resonators," *IEEE Microwave and Wireless Components Letters*, Vol. 13, 517–519, Dec. 2003.
5. Liao, C. K., P. L. Chi, and C. Y. Chang, "Microstrip realization of generalized Chebyshev filters with box-like coupling schemes," *IEEE Trans. Microw. Theory Tech.*, Vol. 55, 147–153, Jan. 2007.
6. Chu, Q.-X. and H. Wang, "A compact open-loop filter with mixed electric and magnetic coupling," *IEEE Trans. Microw. Theory Tech.*, Vol. 56, 431–439, Feb. 2008.
7. Rosenberg, U. and S. Amari, "Novel coupling schemes for microwave resonator filters," *IEEE Trans. Microw. Theory Tech.*, Vol. 50, 2896–2902, Apr. 2002.
8. Hong, J. S. and M. J. Lancaster, "Coupling of microstrip square open-loop resonators for cross-coupled planar microwave filters," *IEEE Trans. Microw. Theory Tech.*, Vol. 44, 2099–2109, Dec. 1996.
9. Kuo, J. T. and E. Shih, "Microstrip stepped-impedance resonator bandpass filter with an extended optimal rejection bandwidth," *IEEE Trans. Microw. Theory Tech.*, Vol. 51, 1554–1559, 2003.
10. Fok, S. W., P. Cheong, K. W. Tam, and R. P. Martins, "A novel microstrip square-loop dual-mode bandpass filter with simultaneous size reduction and spurious response suppression," *IEEE Trans. Microw. Theory Tech.*, Vol. 55, 2033–2041, 2006.
11. Wand, C. H., P. H. Deng, and C. H. Chen, "Coplanar-waveguide-fed microstrip bandpass filters with capacitively broadside-coupled structures for multiple spurious suppression," *IEEE Trans. Microw. Theory Tech.*, Vol. 51, 1554–1559, 2003.
12. Cheong, P., S. W. Fok, and K. W. Tam, "Miniaturized parallel coupled-line bandpass filter with spuious-response suppression," *IEEE Trans. Microw. Theory Tech.*, Vol. 53, 1810–1816, 2005.
13. Chin, K. S. and D. J. Chen, "Harmonic-suppressing bandpass filter based on coupled triangular open-loop stepped-impedance resonators," *Microwave and Optical Technology Lett.*, Vol. 52, No. 1, 187–191, Jan. 2010.
14. Li, R., D. I. Kim, and C. M. Choi, "Compact structure with three attenuation poles for improving stopband characteristics," *IEEE Microwave and Wireless Components Letters*, Vol. 16, No. 12, 663–665, 2006.
15. Tu, H. W. and K. Chang, "Compact second harmonic-suppressed bandstop and bandpass filters using open stubs," *IEEE Trans. Microw. Theory Tech.*, Vol. 54, No. 6, 2497–2502, 2006.

70 GHz Tx and Rx LCP SoP Module for Point-to-point Millimetre Wave Applications

Young Chul Lee
Department of Electronics Engineering, Mokpo National Maritime University (MMU), Korea

Abstract— In this paper, a 70 GHz Amplitude-Shift-Keying (ASK) transmitter and receiver system-on-package (SoP) module based on a liquid-crystal polymer (LCP) substrate has been presented for point-to-point millimeter-wave communication applications. Two frequency multipliers (MTLs), a driver amplifier (DA), high-gain LNA block, ASK modulator and de-modulator are integrated in each metal-backed LCP substrate. The size of the fabricated transmitter (Tx) and receicer (Rx) SoP module are $30.11 \times 22.54 \times 2.15\,\mathrm{mm}^3$ and $22.95 \times 22.54 \times 2.15\,\mathrm{mm}^3$, respectively. For operation test, using an intermediate frequency (IF) of 20 MHz with ±25 mV and −0.7 V for off-set, frequency spectrum of the Tx and Rx were measured. The output power of the Tx is −10.17 and −11.91 dBm at 72.1 and 74.9 GHz, respectively, by forcing the local oscillation (LO) frequency of 12.017 and 12.48 GHz with 5.0 dBm power. By interconnecting a Tx with Rx module, de-modulated signal pattern is obtained using a oscilloscope.

1. INTRODUCTION

Lately, the demands for higher-capacity and -speed Ethernet networks have rapidly increased. By using a millimeter wave (mm-wave) [1], free space optical (FOS) [2], and fiber-optic network, various systems have been developed. In the case of FOS and fiber-optic communications, there are some limitations due to the natural environment such as fog and rain and expensive cost of the installation. The wireless communication systems using mm-waves are a competitive alternative in respects of install time, cost, and natural environments, compared to the FOS, fiber-optic communications, and short-range wireless communication applications. Wireless point-to-point (PtP) communication systems using a V (60 GHz) — and E ($70 \sim 80$ GHz) — band have been developed for high-capacity and -speed Ethernet applications. However, 60 GHz has one drawback of the additional propagation loss due to oxygen absorption [3], so, 60 GHz PtP links are in general limited to the indoor applications. On the other hand, E-band systems using 70 and 80 GHz can provides longer link range and higher speed because of no oxygen absorption and more available bandwidth, respectively, can be offered [4].

In order to commercially realize these E-band link applications, a cost effective radio module is required. The system-on-package (SoP) approach [5] using a low-temperature co-fired ceramic (LTCC) and liquid-crystal polymer (LCP) technology has been demonstrated to be suitable technology integrating active and passive circuits into a compact single substrate.

Although the LTCC technology has provided very dense multilayer integration and good electrical performance, the design at mm-wave bands has become challenging due to limitation of design rules [6]. Also, the LCP's low loss ($\tan\delta = 0.002 \sim 0.004$), low cost, low water absorption (0.04%) and low permittivity ($\varepsilon_r = 2.9 \sim 3.0$) make very attractive for RF and mm-wave SoP applications.

In this work, a 70 GHz Amplitude-Shift-Keying (ASK) transmitter (Tx) and receiver (Rx) system-on-package (SoP) module based on a liquid-crystal polymer (LCP) substrate has been presented for point-to-point millimeter-wave communication applications.

2. DESIGN AND FABRICATION OF THE ASK TRANSMITTER AND RECEIVER LCP MODULE

The radio systems with an ASK modulation technique have been widely used for mm-wave applications [7] because of its simplicity and power efficiency. In the case of an ASK non-coherent de-modulation technique by using a simple envelope detector, there are no needs of a coherent LO signal. Especially, the ASK modulation has been investigated and utilized for gigabit transmitting systems using millimeter-wave bands whose analog-digital converter (ADC) is hard to be implemented.

A block diagram of a 7 GHz ASK Tx and Rx is shown in Fig. 1. Its carrier center frequency is 72.1 and 74.9 GHz for up- and down-link applications and also its bandwidth is 2.2 GHz. The Tx part consists of an up-converting mixer as a ASK modulator, LO, and amplifier block. Six commercially available GaAs MMICs such as two frequency multipliers (MTLs, 2X and 3X), two

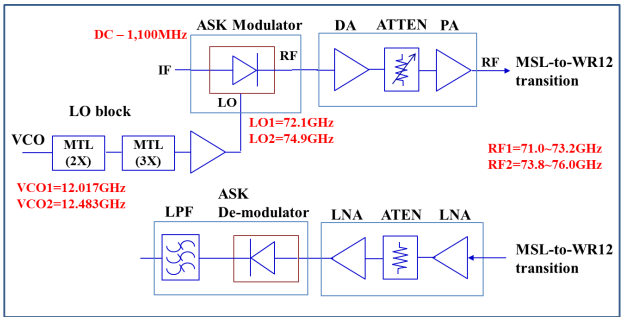

Figure 1: Block diagram of a 70 GHz ASK transmitter and receiver module for point-to-point wireless communication systems.

driving amplifiers (DAs), an attenuator (ATTEN), and a power amplifier (PA). The external local oscillation (LO) signal of 12.017 and 12.483 GHz for the Tx is multiplied by 6 times and amplified in order to drive the modulator. The Rx part is composed of four GaAs MMICs: two LNAs and a ATTEN for a gain block and a mixer for a de-modulator. A LPF is inserted to the IF path. RF ports of the Tx and Rx are rectangular waveguides (WR12). A microstrip line-to-WR12 transitions are integrated into the RF paths.

In order to integrate the designed 70 GHz ASK Tx and Rx into each LCP SoP module, the metal-backed LCP substrate incorporating a WR12 waveguide is used. The probe-type WR12-to-microstrip transition is designed on the LCP substrate. The cavities to mount MMICs were formed in the LCP substrate. The metal lines on the LCP were gold-plated. In order to compensate parasitics due to wire-bonding between the MMIC and LCP board, microstrip-type matching circuits were designed on the LCP substrate. Fig. 2(a) shows the vertical structure of the 70 GHz Tx and Rx LCP SoP module. The designed 70 GHz ASK Tx and Rx module was fabricated in the commercial foundry. The size of the fabricated Tx and Rx SoP module is $30.11 \times 22.54 \times 2.15\,\text{mm}^3$ and $22.95 \times 22.54 \times 2.15\,\text{mm}^3$, respectively. The fabricated Tx and Rx module is integrated into each metal case for the test. Figs. 2(b) and (c) show the fabricated Tx and Rx module in the metal case.

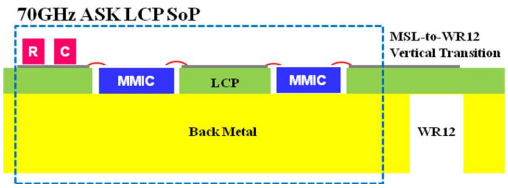

(a) Vertical structure

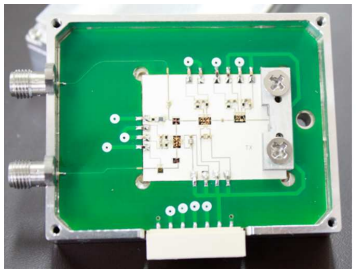

(b) ASK Tx module

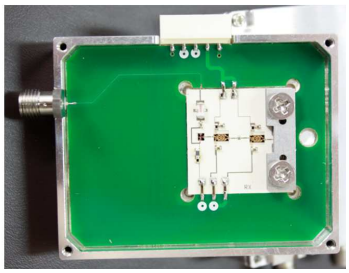

(c) ASK Rx module

Figure 2: LCP SoP modules using the metal backed LCP substrate.

3. MEASURED RESULTS

Figure 3 shows the measured RF spectrums of the fabricated ASK Tx LCP SoP module. For ASK modulation, the IF signal generated by a pulse pattern generator (Agilent Tech. 81110A) was used to the IF port of the ASK Tx module and also an off-set voltage of −0.7 V was forced to it. At the LO frequency of 72.102 and 74.9 GHz with the power of 5 dBm and IF of 20 MHz with ±50 mV the output power (P_{out}) of 10.17 and 11.91 dBm is achieved at 72.1 and 74.9 GHz, respectively, considering cable losses and attenuation in the RF path.

For de-modulation test of the Rx module, the Tx and Rx module are connected using a WR12 waveguide. By using a oscilloscope, IF signals in the Tx and Rx module were measured and are shown in Fig. 4.

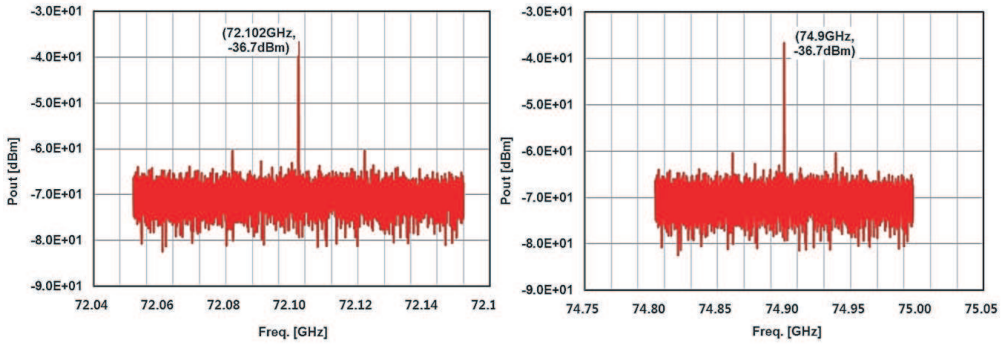

Figure 3: Measured frequency spectrum characteristics of the fabricated ASK Tx LCP SoP module.

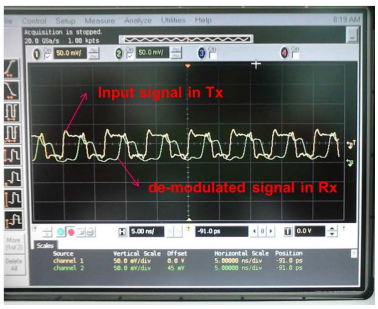

Figure 4: Measured IF signals in the Tx and Rx module.

4. CONCLUSIONS

In this paper, a 70 GHz ASK Tx and Rx SoP module based on a metal-backed LCP substrate has been presented for point-to-point wireless communication applications. Two frequency multipliers (MTLs), a driver amplifier (DA), high-gain LNA block, ASK modulator and de-modulator are integrated in each LCP module. The size of the fabricated transmitter (Tx) and receicer (Rx) SoP module are $30.11 \times 22.54 \times 2.15\,\mathrm{mm}^3$ and $22.95 \times 22.54 \times 2.15\,\mathrm{mm}^3$, respectively. The output power of the Tx module is -10.17 and -11.91 dBm at 72.1 and 74.9 GHz, respectively. By interconnecting a Tx with Rx module, de-modulated signal pattern is measured using a oscilloscope.

REFERENCES

1. Smulders, P., "Exploiting the 60 GHz band for local wireless multimedia access: Prospects and future directions," *IEEE Commun. Magzine*, 140–147, 2002.
2. Kamalakis, T.. et al., "Hybrid free space optical/millimeter wave outdoor links for broad-band wireless access networks," *18th Annual IEEE Symposium on PIMRC*, 2007.
3. Marcus, M. and B. Pattan, "Millimeter-wave propagation: Spectrum management implications," *IEEE Microwave Magazine*, 54–62, 2005.
4. Sevimli, O., V. Dyadyuk, D. Abbott, J. Bunton, R. Kendall, L. Stokes, M. Shen, and S. Smith, "Multi-Gigabit wireless link development," *2006 Auswireless Conference*, 2006.
5. Lee, Y. C., T.-W. Kim, A. B. Ariffin, and N.-G. Myoung, "60-GHz amplitude shift-keying receiver LTCC system-on-package module," *Microwave and Optical Technology Letters*, Vol. 53, No. 4, 758–761, 2011.
6. Pinel, S., S. Sarkar, R. Bairavasubramanian, J.-H. Lee, M. Tentzeris, J. Papapolymerou, and J. Laskar, "Highly integrated LTCC and LCP millimeter wave functions for 3D-SOP high data rate wireless systems," *Electronic Components and Technology Conference*, 764–768, 2005.
7. Tarusawa, Y., H. Ogawa, and T. Hirota, "A new constant resistance ask modulator using double-sided MIC," *IEEE Transaction on Microwave Theory and Techniques*, Vol. 35, No. 9, 819–822, 1987.

The Design and Implementation of an EMC Pre-compliance Board

F. R. L. Silva[1], **L. R. Ribeiro**[1], **L. P. Dias**[1], **W. J. Santos**[1], **C. E. Capovilla**[2], **and H. X. Araujo**[1]

[1]Universidade Federal de São João Del Rei — UFSJ, Ouro Branco, Brazil
[2]Universidade Federal do ABC — UFABC, Santo André, Brazil

Abstract— In this work, the EMC — Electromagnetic Compatibility of Integrated Circuits, electronic boards and home appliances is deal with the use of a conducted emission technique. In general, as the IC the major responsible of unintentional emissions and coupling, some specific pre-compliance setup tests are employed to analyze these detrimental effects to the system as a whole. Therefore, an EMC Pre-Compliance Board — EPCB was designed and built to operate from 150 KHz to 30 MHz. Additional techniques were used to improve the EPCB in terms of frequency range and performance. Simulated and experimental results are compared to validate the EPCB test setup.

1. INTRODUCTION

The necessity to control the electromagnetic emissions and interference between circuits and electronic devices becomes a crucial point to assure its correct operation inside an electromagnetic environment. Some approaches were designed to support the pre-compliance tests (EMC/EMI/EMS) setups, which are not designed to replace the well-known compliance equipments (anechoic chamber, stirring chamber, blue test chamber, etc.) but, it gives a previously information about the device behavior [1]. All of them have consolidated standards and regulations.

The electrical circuit of any electronic device produces some kind of noise, which can reach levels of power that interfere in undesired ways on the operation of the equipment around and the environment as a whole. Each device generates a characteristic noise, due to its electrical circuit [2]. Depending on the electromagnetic emission of these noises, other electronic devices can then receive the interference by a path of radiation or, much less frequently a direct electrical connection.

The analysis of conducted emission aims to measure how much electromagnetic radiation (noise) is conducted in an electronic equipment to the grid by the power cord. Such issuance may not exceed the established standards [3], so that the overcoming of the imposed limit causes interference in the operation of other devices that are connected on the same network.

In this context, the EPCB test setup will be used between the power cord of the device under test and the power outlet, to verify if the DUT meets the standards of conducted emission. The frequency range of the implemented board starts from 150 KHz to 30 MHz. Simulated and experimental results are compared to validate the EPCB test setup.

2. EMC CONDUCTED METHOD

Since the mid-90s every electronic device must be submitted to stricter EMC measurement, and their entries in the market are directly related to it responses on these test. Although problems related to interference during the Second War, only in the late 70s that the problems related to EMC became of public knowledge in general due to the problems presented by television, communication equipment, audio and video displays, among many other applications [4].

By definition, electromagnetic interference — EMI is the process in which electromagnetic energy is transmitted from one electronic device to another via radiated or conducted emission or both. On the other hand, the electromagnetic susceptibility — EMS deals with devices sensitive to interference from other devices. Thus, the EMC tests usually comprise both EMI and EMS measurement of the same electronic device. In Fig. 1 is shown the coverage of the electromagnetic compatibility.

Therefore, several EMC tests platforms were designed to evaluate the performance of electronic circuits and devices aimed at preventing problems related to interference or immunity within an electromagnetic environment. Among the most common and robust EMC platform, is the Anechoic Chamber [5], which for several years has been the main method of evaluating the electromagnetic behavior of antennas, electronic devices, vehicles and even airplanes. However, the high value required for their construction and maintenance, and the complexity of its operating system, makes infeasible its acquisition for the analysis of small electronic devices. Therefore, other methods [5, 6]

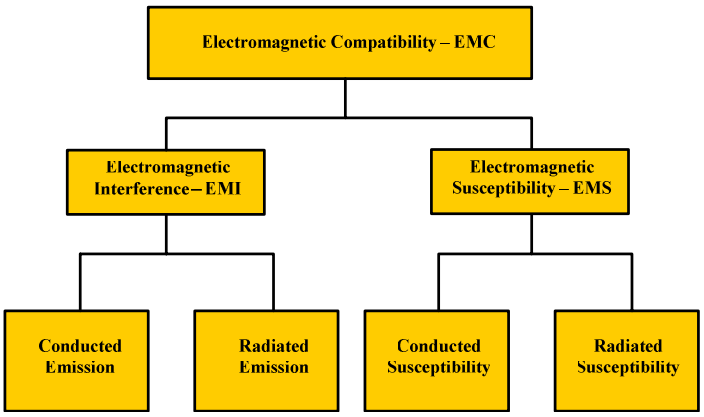

Figure 1: Electromagnetic compatibility subdivided into EMI and EMS measurements [2].

less complex and costly show good results related to the interference and immunity analysis known as pre-compliance test.

Different approaches assist the pre-compliance test, which are governed by their own standards and rules [7]. These setups include the TEM/GTEM cells, magnetic loop, magnetic probe, Workbench Faraday Cage, OATS — Open Area Test Site, 1/150 Ω conducted, LISN — Line Impedance Stabilization Network, among others.

The pre-compliance setup tests, at the level of electronic systems are defined by the standards CISPR 25/2002 (special international committee on radio interference) for spurious emissions, and the ISO-11452 for interference susceptibility measurements. Thus, two major standards have been defined, with a first one for radiated and conducted emission and the second one for immunity RF test.

By definition, the conducted interference is that in which occurs undesirable transfer of electromagnetic energy along a conductor through disturbances between the phase line and the ground power supply, and is governed by the standard IEC 61967-4. There are several tools and methodologies to perform conducted tests, and the frequency range normally used is 150 KHz–30 MHz, except in military applications that eventually require the extension band.

The most common method used for this type of analysis is the LISN, also known by AMN — Artificial Mains Network, which works through the AC power supply of the device to be analyzed. In spite of the minimum frequency of the conducted emission tests is normally around 150 KHz, by the power switching held by the LISN is possible to achieve a minimum frequencies around 9 kHz. The advantages of using the LISN in conducted tests are mainly related to the fact that it provides electromagnetic insulation against the external environment and characterize the impedance of the DUT — device under test. However, its cost may be a limiting factor.

Other method widely used in performing conducted interferences measurements is the 1/150 Ω, where is possible to measure the noise current in each driven pin of the DUT. The basic model consists of the presence of a low value resistance in series with the output pin of the DUT. Therefore, it is possible to measure the voltage across the known resistor and then determine the noise current. Based on the fact that most IC emission problems arise through the noise that is carried out by the pins of the IC, this method presents itself as a good indicator. However, for each DUT and application the equivalent circuit must be adapted and adjusted.

3. EMC PRE-COMPLIANCE BOARD — EPCB

To evaluate the conducted emission provided by a laptop, an electromagnetic compatibility pre-compliance board using resistors, capacitors and inductors was designed and built. The schematic of the designed circuit is shown in Fig. 2. The series inductance avoids that the noise coming from the device under test becomes into the grid, being directed to the 1 KΩ resistor on which the measurement is made using the spectrum analyzer. Any present noises on the line are misappropriated by the 1 µF capacitor placed in parallel with the network, thereby not affecting the measurement.

To perform the simulations, the Multisim Software was employed. The board was designed to operate at 127 V and 60 Hz, the classical Brazilian standard. To obtain the impedance variation of the circuit as a function of the frequency, the AC analyses and the equivalent impedance were needed. In Fig. 3, is shown the EPCB unconnected and connected to a DUT and its impedance

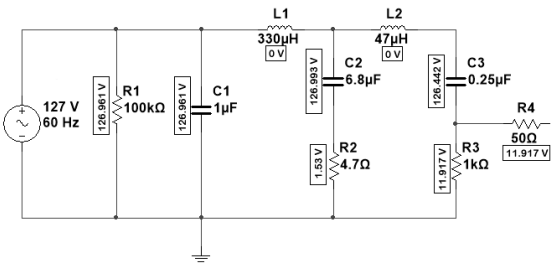

Figure 2: EPCB schematic.

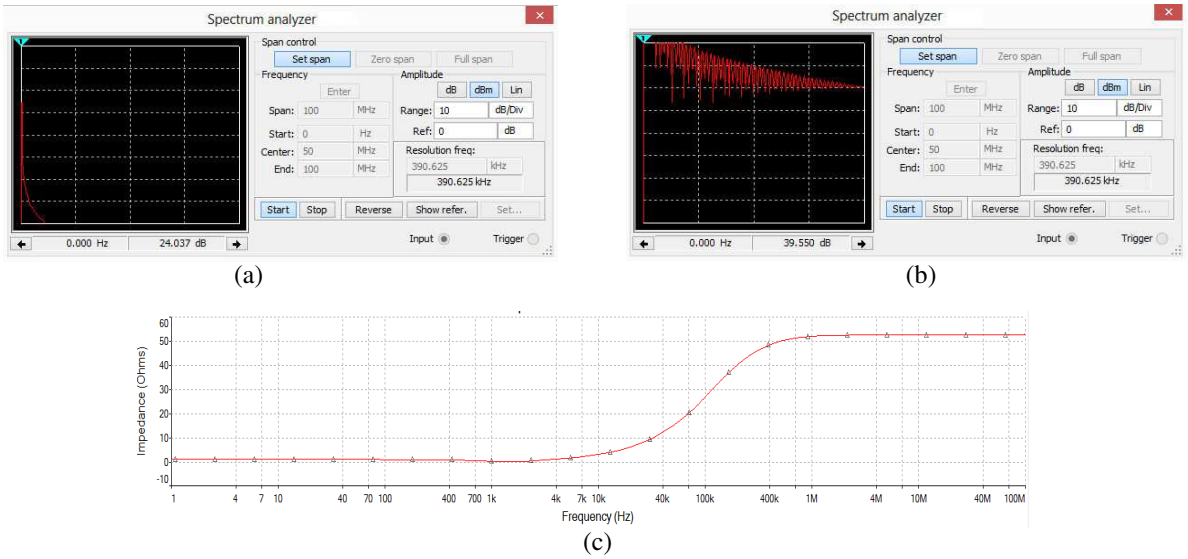

Figure 3: (a) Unconnected to the DUT; (b) connected to the DUT; (c) characteristic impedance of the EPCB.

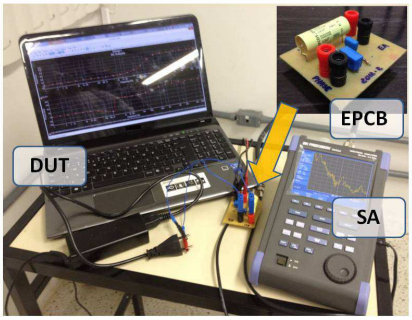

Figure 4: Conducted emission test setup using an EPCB.

variation as a function of the frequency which tends to 50 Ω.

The test setup, as shown in Fig. 4, was performed in accordance to CISPR and FCC — Federal Communications Commission, agency in charge of standardization of radio communications and cable in the U.S. The test equipment used was a BK Precision Series 2650A spectrum analyzer, a certified FCC class B laptop, which served as the DUT and the EPCB. In Fig. 5, is shown the conducted emission scan of the fully configured, certified, class B laptop. To compare the response provided by the EPCB, a measurement with a commercial LISN was also done. Both results are compared to the CISPR and FCC standards. From the obtained results, is possible to observe the good agreement of this low cost pre-compliance test. As the laptop is certified, it was expected that the radiated emission levels must satisfied the standards. However, there are resonances around 30 MHz, which can be caused by disturbances, provided by battery charger, connections between the motherboard and peripherals devices or even due to the heating. Meanwhile, is important to

emphasize that these resonances levels are minimal, and could also be inserted by the test platform.

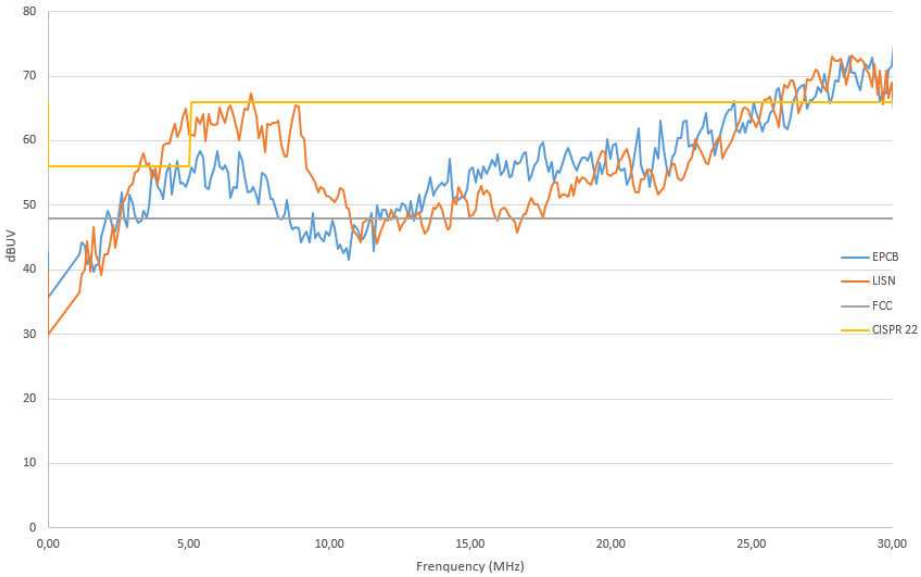

Figure 5: Measurement results of a conducted emission for a certified Class B laptop.

4. CONCLUSIONS

The voltage and current in distribution lines are often corrupted by transient, distortions and other disorders, that come from natural sources such as lightning and also by the operation of electrical and electronic devices. These interferences are conducted over long distances and then coupled to other equipments connected to the grid.

Therefore, in this work, an EMC Pre-Compliance Board — EPCB was designed and built to operate from 150 KHz to 30 MHz. It was shown the development of the proposed device since the design, simulations and experimental measurements. To validate the constructed board, it was used a commercial LISN, working at the same frequency range. The analysis of a certified class B laptop was also done performed in accordance to CISPR and FCC standards. Thereby, from the obtained results the EPCB test setup was clearly validate.

REFERENCES

1. Montrose, M. I. and E. M. Nakauchi, *Testing for EMC Compliance*, Wiley Interscience, New York, 2004.
2. Dhia, S. B., M. Ramdani, and E. Sicard, *Electromagnetic Compatibility of Integrated Circuits: Techniques for Low Emission and Susceptibility*, Springer, New York, 2006.
3. Paul, C. R., *Introduction to Electromagnetic Compatibility*, Wiley Series in Microwave and Optical Engineering, 1992.
4. "Electromagnetic compatibility (EMC) — Part 4: Testing and measurement techniques — Section 3: Radiated, radio-frequency, electromagnetic field immunity test," International Standard CEI/IEC 1000-4-3, Geneva, February 1995.
5. Clay, S., "Improving the correlation between OATS, RF Anechoic room and GTEM radiated emissions measurements for directional radiators at frequencies between approximately 150 MHz and 10 GHz," *IEEE International Symposium on Electromagnetic Compatibility*, Vol. 2, 1119–1124, Denver, USA, August 24–28, 1998.
6. De Araujo, H. X. and L. C. Kretly, "EMC pre-compliance test of RFIC and RF systems using a laboratory GTEM chamber," *PIERS Proceedings*, 896–900, Moscow, Russia, August 19–23, 2012.
7. Hamid, R., M. Cetintas, and E. H. Karacadag, "EMC Test Facilities at UME," *IEEE International Symposium on Electromagnetic Compatibility, EMC'03*, 2003.

Magnetoelectric Transducers

R. V. Petrov, A. N. Soloviev, K. V. Lavrentyeva, I. N. Solovyev, V. M. Petrov, and M. I. Bichurin
Novgorod State University, Russia Federation

Abstract— In the article, the theoretical and experimental modeling of the magnetoelectric (ME) transducers is described. In this work, two types of the ME transducers are considered. The first one is the piezoelectric transformer with magnetic component (PTM). The exciter is fabricated as a multilayer structure with layers of different lengths. The second type of the transducers is ME variable inductor. Correctness of the method is confirmed by obtained frequency dependence of the voltage step-up and thickness dependence of inductance tunability.

1. INTRODUCTION

ME effects have deserved careful study during the last decade due to energy transfer from magnetic (electric) field to electric (magnetic) one [1]. ME materials have a wide range of potential applications. There are many types of the ME transducers. In this work, two types of the ME transducers are considered. The first one is the piezoelectric transformer with magnetic component (PTM). PTM relates to the new branch of electronics called magnetoelectric electronics. PTM is a main component of a secondary power supply. The magnetoelectric transducers consists of amorphous magnetic material (Metglas) and piezoelectric lead zirconate titanate (PZT) layer that is poled along its thickness direction. PTM uses the direct ME effect, which consists of inducing the electrical voltage in applied magnetic field [1].

The second device is variable inductor with magnetoelectric composite core. It includes a core based on magnetostrictive-piezoelectric layered structure and working coil. The core material shows converse magnetoelectric effect, which consists of inducing the magnetization in applied electric field. Thus application of voltage across the piezoelectric layer gives rise to a change in inductance. Layers are bonded together with epoxy adhesive. Control voltage is applied to metal electrodes of PZT layer. As a rule, these devices find application in voltage regulation, power harmonic filters, voltage-controlled oscillators, filters, and matching networks in wireless systems [2].

The main objectives of this work are the modeling of system operation, equivalent circuits method, and analysis of amplitude-frequency characteristics.

2. THEORETICAL MODELING

The magnetoelectric transducers are based on the ME and the piezoelectric effects [1].

The change in the inductance of the ME inductor is closely related to the strain mediated ME coupling within the ME core material, which leads to electric field induced changes of magnetization. For ferromagnets, especially those with high permeability, the permeability is very sensitive to an applied magnetic field or a stress.

The strain of magnetostrictive and piezoelectric phase are respectively

$$\begin{cases} {}^{p}S_1 = {}^{p}s_{11}{}^{p}T_1 + d_{31}E_3 \\ {}^{m}S_1 = {}^{m}s_{11}{}^{m}T_1 + q_{11}H_1 \end{cases}, \tag{1}$$

where ${}^{p}T_1$ is the stress and ${}^{p}s_{11}$ is the compliance of the piezoelectric phase, ${}^{m}T_1$ is the stress and ${}^{m}s_{11}$ is the compliance of the magnetostrictive phase, d_{31} is the piezoelectric coefficient of piezoelectrics, q_{11} is the piezomagnetic coefficient of ferromagnetic, E_3 and H_1 are external electric and magnetic fields.

The magnetic induction ${}^{m}B_1$ of magnetostrictive phase is governed by

$${}^{m}B_1 = \mu_{11}H_1 + q_{11}{}^{m}T_1, \tag{2}$$

where μ_{11} — permeability of ferromagnetic.

For finding the solution of media motion equation, the following boundary conditions are used at $x = 0$ and $x = L$ [1]

$${}^{p}S_1 = {}^{m}S_1, \quad {}^{p}T_1 \cdot {}^{p}t + {}^{m}T_1 \cdot {}^{m}t = 0. \tag{3}$$

Assuming a long cylindrical coil with a circular cross section, the following expression for inductance was obtained

$$L = \frac{\mu_0 \left(t_m d(\mu_{eff} - 1) + \pi R^2\right) N^2}{2l}, \tag{4}$$

where μ_{eff} is effective magnetic permeability of the sample, d is width of the core, R is radius of the cross section of the coil, l is core length, N is the number of coil turns.

The effective magnetic permeability was found to be equal to

$$\mu_{eff} = \frac{\mu_0 M_s^2}{\frac{3\lambda_s t_p (d_{31} E_3 - q_{11} H_1)}{t_m {}^p s_{11} + t_p {}^m s_{11}} + \frac{\mu_0 M_s I N}{l}} + 1, \tag{5}$$

where M_s is saturation magnetization of metglass, λ_s is saturation magnetostriction, I is current in the winding coils.

The metglass thickness ($^m t$) dependence of inductance tunability ($\Delta L/L_{\max,}$) is shown in Figure 1 for different PZT thicknesses.

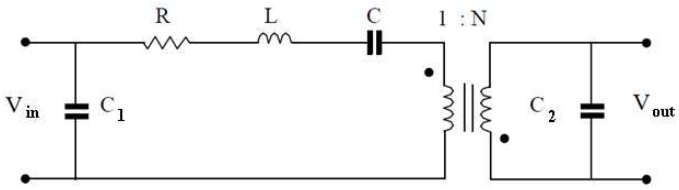

Figure 1: Simplified electrical equivalent circuit of PT.

It is notable that inductance strongly depends on the thickness of magnetostrictive and piezoelectric phases. The maximum change of inductance is 70% for PZT thickness $^p t = 0.1$ mm, metglass thickness $^m t = 120\,\mu$m and operation frequency of 100 kHz.

The PT electrical equivalent circuit was composed by electro-associations method. After analyzing the circuit the calculated expressions of the equivalent circuit parameters were obtained [3].

The input (C_1) and output (C_2) capacitance are given by:

$$C_1 = \frac{\varepsilon_{33}^T \cdot \left(1 - k_{31}^2\right) \cdot b \cdot l_1}{a}; \quad C_2 = \frac{\varepsilon_{33}^T \cdot \left(1 - k_{33}^2\right) \cdot b \cdot a}{l_2}; \tag{6}$$

where b and a are the transformer width and the transformer thickness, l_1 and l_2 are the first resonator and the second resonator lengths, respectively, ε_{33}^T is the dielectric permittivity of the material, k_{33} is the electromechanical coupling coefficient of longitudinal modes, k_{31} is the electromechanical coupling coefficient of transverse modes.

The mechanical part inductance (L), the transfer ratio (N), the wave impedance (z_0) and the mechanical resistance (R) have the form:

$$L = 4 \cdot a \cdot b \cdot l_1 \cdot \rho; \quad N = 2b \cdot d_{31} \cdot Y_1^E; \quad z_0 = a \cdot b \cdot \sqrt{\rho \cdot Y_1^E}; \quad R = \frac{2\pi \cdot z_0}{Q_M}; \tag{7}$$

where ρ is the material density, d_{31} is the piezoelectric coefficient, Y_1^E is the elastic constant.

The operating frequencies range of the longitudinal modes is expressed by the equation [1]:

$$\Delta f = \frac{4}{\pi^2} \cdot \frac{k_{31}^2}{1 - k_{31}^2} \cdot f_p; \tag{8}$$

The voltage step-up ratio (K_T) is calculated by the expressions:

$$K_T = \frac{\sqrt{m} 4 \cdot Q_M \cdot k_{33}^2 \cdot d_{31} \cdot l_1}{\pi^2 \cdot \left(1 - k_{33}^2\right) \cdot d_{33} \cdot a}; \tag{9}$$

where Q_M is the mechanical quality factor.

3. EXPERIMENTAL RESULTS

In the experiment, we demonstrate a PTM by bonding a ME plate and a piezoelectric transformer (PT) polarized along thickness direction. The PT was prepared using $Pb(Zr,Ti)O_3$ plate which is 12 mm long, 10 mm wide and 0.2 mm thick [3]. The PT step-up transformer was divided into two parts marked input one with 5 mm in length and output one with 7 mm in length, as shown in Figure 2(a). The ME composite was prepared using $Pb(Zr,Ti)O_3$/Metglas with 26 mm in length, 10 mm in width and 0.3 mm in thickness. PTM was prepared by bounding the ME composite and PT together with glue as shown in Figure 2(b), and curing at 150°C under 5 MPa for 30 min to get good mechanical coupling.

The voltage step-up ratio of PTM (V_{out}/V_{in}) was measured as output voltage (V_{out}) in response to the input voltage (V_{in}). A sine voltage V_{in1} was applied on the input port of the transformer with a signal generator and a sine voltage V_{in2} was applied on the coil with another signal generator. The output voltage V_{out} was measured with an osclilloscope under 1 MΩ resistance load [4]. Resonance occurs when the driving frequency is near the natural frequency of PTM. In this case a stronger voltage step-up ratio is achieved. Generally, we used a voltage near the resonance frequency. Thus the PTM properties were studied near the resonance frequency. The voltage step-up ratios of pure PT are 2 and 5 at a half-wavelength vibration frequency (41.9 kHz) and full-wavelength vibration frequency (89.7 kHz), correspondingly, under a 1 MΩ resistance load. Then PTM was placed in a magnetic field. The voltage step-up ratio was measured under various magnetic fields applied along the length of the composite.

The ME voltage coefficient (α_V) was measured using a dynamic method with a small ac magnetic sine signal δH_{ac} superimposed on a dc magnetic field H_{bias}, both of which were along the length of PTM. The sine magnetic field was applied with a solenoid powered by an generator of the sine signal. The solenoid has 200-turn Cu wire with 26 mm in length wrapped around the ME composite and connected to a oscilloscope. Then the uniform elastic strain was excited in the Metglas layers via magnetostrictivity due to the converse piezomagnetic effect. Correspondingly, PT was driven

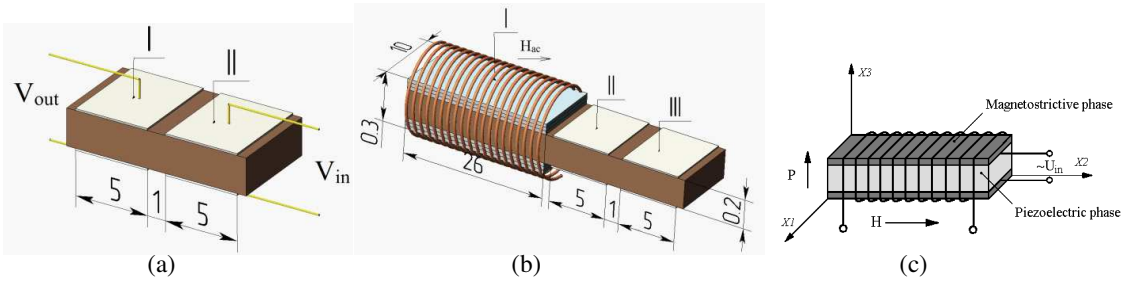

Figure 2: Schematic illustration of (a) design of PT with connection diagram of the circuit (I — the output port of PT, II — the input port of PT), (b) design of PTM (I — the ME composite with coil, II — the output port of PT, III — the input port of PT), (c) design of the variable ME inductor.

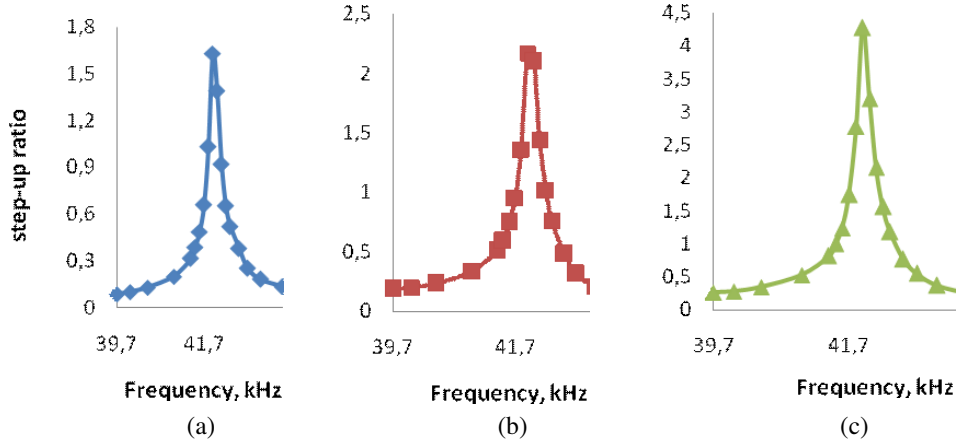

Figure 3: Schematic illustration of the frequency dependence of the voltage step-up ratio of (a) the ME composite, (b) the pure PT, (c) PTM.

into as strain through the mediated stress. Then the voltages were induced in the input port of PT and the input port of the ME composite due to the piezoelectricity relative to the transverse piezoelectric coefficient (d_{31}), which were collected with an oscilloscope. The ME voltage coefficient was estimated as $\alpha_V = dV_{\rm ac}/dH_{\rm ac}$. Figures 3(a), (b) show the voltage step-up coefficient of PT and the ME composite, respectively. This dependence They share the same behaviours as in the individual devices. Figure 3(c) shows the voltage step-up coefficient of PTM. In this device, PT and the ME composites function together.

Figure 4 shows the metglass thickness experimental dependence of inductance tunability $\Delta L/L_{\rm max}$ for different thicknesses of PZT for applied voltage of 500 V. When increasing metglass thickness, the value of inductance tunability increases up to a maximum (approximately 120 μm) and then one decreases sharply. In addition, the maximum of inductance is higher when the thickness of the PZT is thinner. When PZT thickness are 0.1 mm, 0.5 mm, 1 mm the maximum value of inductance tunability are 21%, 18 % and 13%, respectively.

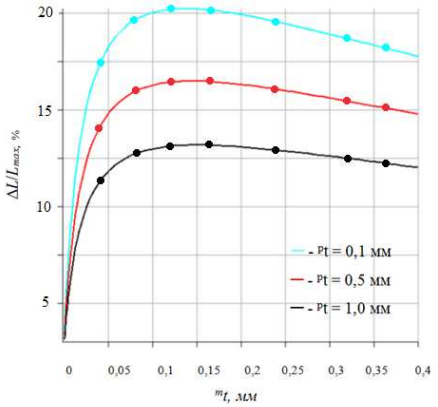

Figure 4: Schematic illustration of the metglass thickness dependence of inductance tunability $\Delta L/L_{\rm max}$ for different thicknesses of PZT.

4. CONCLUSIONS

We proposed a dual excitation of piezoelectric transformer. Figure 3 shows the voltage step-up ration of PTM under various inclusions. One sharp voltage step-up peak were observed near 41.9 kHz, corresponding to the half-wavelength vibration mode. The half-wavelength resonance frequency decrease with maxima magnetic field around 15 Oe. The corresponding voltage step-up ratio is 2.1 without magnetic field and 4.3 with maxima magnetic field.

Also ME composites are ideal for variable inductor application, because they enable one to control magnetic permeability by electric field with minimum power consumption. The magneto-electric variable inductor have large tenability range, high quality factors, diminutiveness, and low energy consumption.

The theoretical research is found to be in qualitative agreement with recent experimental results.

ACKNOWLEDGMENT

The reported study was partially supported the grant of the Federal Target Program "Scientific and pedagogical staff of innovative Russia" on 2009-2013 and by RFBR research project #13-02-98801.

REFERENCES

1. *Magnetoelectricity in Composites*, Eds., M. I. Bichurin and Dwight Viehland, 273, Pan Stanford Publishing, Singapore, 2012.
2. Bichurin, M. I., V. M. Petrov, and R. V. Petrov, "Direct and inverse magnetoelectric effect in layered composites in electromechanical resonance range: A review," *Journal of Magnetism and Magnetic Materials*, Vol. 324, No. 21, 3548–3550, 2012.
3. Soloviev, A. N., M. I. Bichurin, and D. V. Kovalenko, "Piezoelectric multilayer transformer," *PIERS Proceedings*, 893–895, Moscow, Russia, August 19–23, 2012.
4. Zhou, J.-P., P. Wang, J. Yang, P. Liu, and H.-W. Zhang, "Large converse magnetoelectric response in Rosen-type transformer and Terfenol-D laminated composite," *J. Appl. Phys.*, Vol. 111, 2012.

Shielding Effectiveness of Plasma Coated Multi-layered Shields

P. D. Tosun[1], **S. Ozen**[2, 3], **and S. Helhel**[2, 3]

[1]Faculty of Engineering and Physical Sciences, University of Surrey, UK
[2]Electrical and Electronics Engineering, Akdeniz University, Turkey
[3]Industrial and Medical Applications of Microwaves Research and Application Centre
Akdeniz University, Turkey

Abstract— Shielding effectiveness (SE) of multi-layered shield models of two and three layered structures are investigated. For high frequency analysis, SE declines are noted.

1. INTRODUCTION

Electromagnetic compatibility (EMC) is a term which is related to electromagnetic interference. It is basically defined as a system's full functioning without any disturbances of electromagnetic noise of near systems as well as its minimum emission of electromagnetic interference (EMI) of any kind towards other systems [1]. Within the environment, electric field (EF) and magnetic field (MF) sources are considered as potential EMI sources. Since most of the devices are powered by electricity, EMC and EMI are two mainly studied subjects. One of the most effective ways to prevent EMI other than minimizing EF and MF emissions in the first place by using better circuit components and etc., is shielding of the EMI source.

Shielding is a method of blocking EMI. There are various applications of shielding which are simply to keep the interference within the borders of the shields [2]. Material properties of the shielding substance are very essential at the effectiveness of interference prevention. It affects the total loss of electromagnetic waves. Conductivity properties and skin depth (thickness) of the shielding material influence reflection and absorption losses of the shield which result in a decline at the overall total loss. In addition to that apertures on the shield surface affect the shielding performance as well. With that in mind, plasma polymerization technique is used as a tool to overcome this problem.

Plasma polymerization technique is a surface modification method which uses a high energy source to produce plasma of desired polymer. High energy source defines the method. It is applicable to various surfaces and provides a wide range of material modification [3–5]. Besides various applications, it is reported that the technique provide with the most stabile coatings [6, 7]. Stability and the homogeneity of the coating ensure better SE values due to less apertures on the shielding surface.

2. THEORY OF TWO AND THREE LEVEL MULTI-LAYERED SHIELDS

2.1. Shielding Theory

The effectiveness of the shielding is related to materials' properties, is mentioned before. The effectiveness is basically measured as the difference between the incident and transmitted waves. In a screen or shield model, this difference is caused by three things. A part of the wave is reflected which creates reflection loss (R), some of wave's energy is absorbed which is accepted as absorption loss (A) and multi reflection which causes multi reflection loss (MR), is the reflection of some of the absorbed wave. Total loss (TOT) of the screen which determines the effectiveness of the shield is the accumulation of these losses (1).

$$TOT_{\mathrm{dB}} = R_{\mathrm{dB}} + A_{\mathrm{dB}} + MR_{\mathrm{dB}} \tag{1}$$

2.2. Two and Three Layered Shields

In a screen model seen at Figure 1, $\boldsymbol{\eta}$ surface impedance and $\mathbf{d}$ surface depth values represent different type of materials and skin depth values of the different parts of the model.

Theoretical calculations of R, A and M for the two layered shield model are given below (2)–(5). Since there are two layers, MR is calculated for two layers separately and overall MR value is assumed to be the summation of these two MR values.

$$R_{\mathrm{dB}} = 20\log\left(\frac{1}{2} + \left|1 + \frac{\eta_1}{\eta_0}\right|\right) + 20\log\left(\frac{1}{2} + \left|1 + \frac{\eta_2}{\eta_1}\right|\right) + 20\log\left(\frac{1}{2} + \left|1 + \frac{\eta_0}{\eta_2}\right|\right) \tag{2}$$

$$A_{\mathrm{dB}} = 20\log\left(e^{\frac{d}{\delta}}\right) = 8.69\cdot\left(\frac{d_1}{\delta_1}+\frac{d_2}{\delta_2}\right) \tag{3}$$

$$MR_{\mathrm{dB}} = 20\log\left|1-\left(\frac{(\eta_1-\eta_0)\cdot(\eta_2-\eta_{in2})}{(\eta_1+\eta_0)\cdot(\eta_1+\eta_{in2})}\right)\cdot e^{-2\left(\frac{1}{\delta_1}+\frac{1}{j\delta_1}\right)\cdot d_1}\right| + 20\log\left|1-\left(\frac{(\eta_2-\eta_1)\cdot(\eta_2-\eta_0)}{(\eta_2+\eta_1)\cdot(\eta_2+\eta_0)}\right)\cdot e^{-2\left(\frac{1}{\delta_2}+\frac{1}{j\delta_2}\right)\cdot d_2}\right| \tag{4}$$

$$\eta_{in2} = \eta_2\cdot\frac{\eta_0\cosh\left(\frac{1}{\delta_2}+\frac{1}{j\delta_2}d_2\right)+n_2\sinh\left(\frac{1}{\delta_2}+\frac{1}{j\delta_2}d_2\right)}{n_2\cosh\left(\frac{1}{\delta_2}+\frac{1}{j\delta_2}d_2\right)+n_0\sinh\left(\frac{1}{\delta_2}+\frac{1}{j\delta_2}d_2\right)} \tag{5}$$

$\boldsymbol{\eta}_{in2}$ is calculated using transmission line model. In this way, input impedance of the second medium is calculated depending on the first and last medium impedances in terms of skin depths of these media. Similar calculations for three layered model can be carried out using above equations. MR value is calculated for three different media in that model.

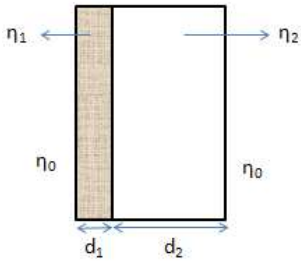

Figure 1: Two layered shield combined from two different materials (modified from [2]).

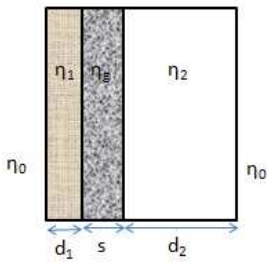

Figure 2: Three layered shield combined of three different materials (modified from [2]).

Table 1: Conductivity and magnetic permeability constants for different materials.

Material	σ_r **[S/m]**	μ_r **[H/m]**
Silver	1.05	1
Copper	1	1
Gold	0.7	1
Stainless Steel (430)	0.02	500
Steel (SAE 1045)	0.1	1000

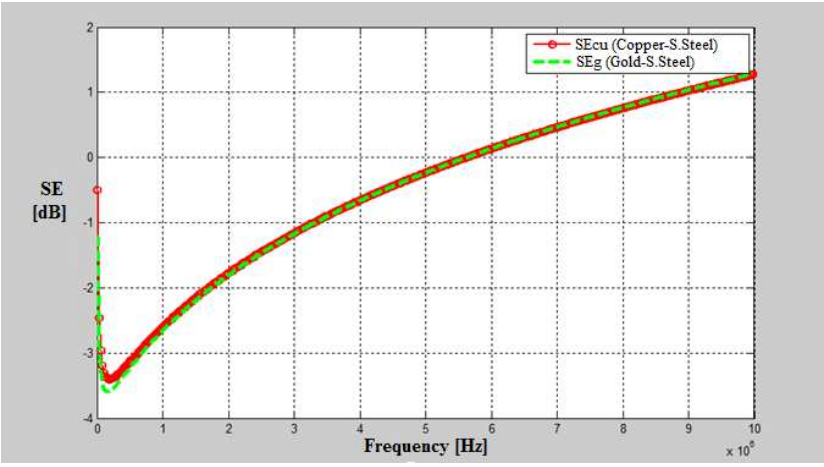

Figure 3: SE graphs of copper and gold on stainless steel.

2.3. Two and Three Layered Shield Models

2.4. Copper-stainless Steel and Gold-stainless Steel Model

In these models, stainless steel is chosen as a substrate material and copper and gold are chosen as coating materials due to their high conductivity properties. This high conductivity provides a high value of R and depending on the skin depth of the second medium which is stainless steel part in this case, A values may vary but the TOT is expected to be high as well. Therefore, effects of different materials on the SE are investigated. In Figure 3 shielding effectiveness of two layered copper-stainless steel and gold-stainless steel models are given. In the making of the models, magnetic permeability and conductivity constants of various materials are used as seen in Table 1.

2.5. Aluminium-Nickel on Glass Model

In this model glass is used as substrate and aluminium and nickel are coated on each other over glass base. Both glass thickness and coating thickness are compared as seen at Figure 4. Coating materials' sequence had no effect on the SE.

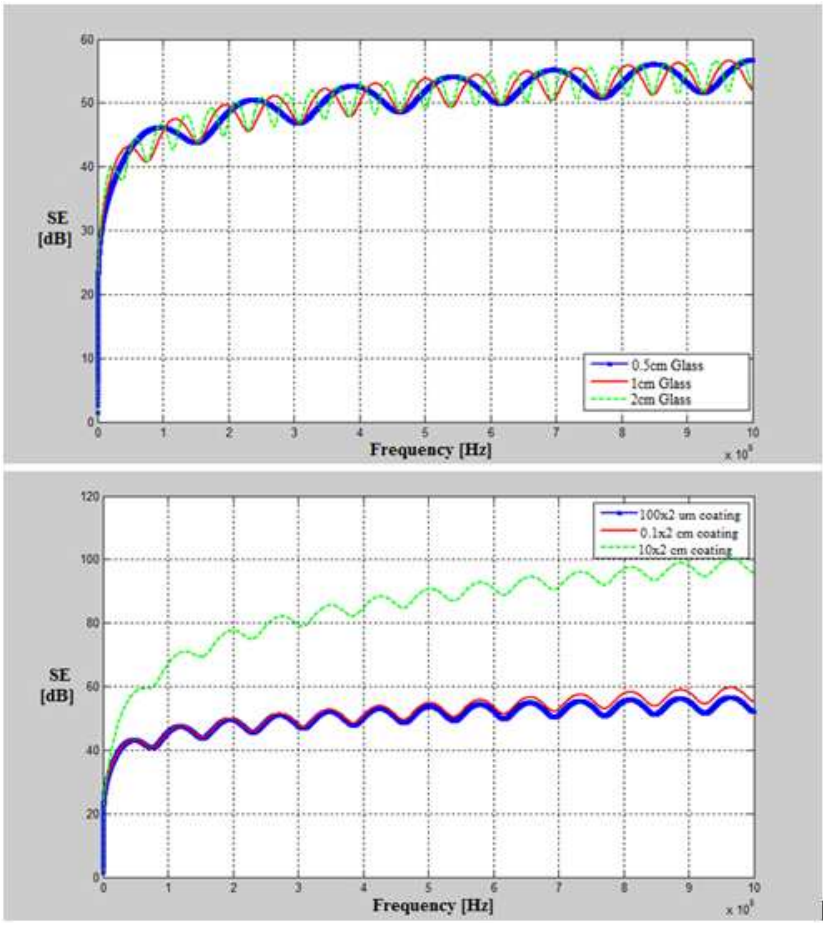

Figure 4: SE of different glass thicknesses and various coating sizes.

3. CONCLUSIONS

In all two layered shielding models, SE drop of 2.5 dB is observed at around 0.25 Hz resonance frequency. Conductivity increased reflection loss as expected therefore gold on stainless steel screen model showed better SE values since it has a higher conductivity constant than copper. High frequency analyses were conducted for three layered structures with coating thicknesses 100 µm, 0.1 cm and 10 cm. SE values declined due to the drop of R of the shield. In addition to that, overall surface thicknesses (as seen on Figure 4) increased SE as the thickness increased due to high absorption loss values.

These models presented some of the expected results but they cannot explain every possibility since properties of shielding material change with size. For coatings which are in micro and nano

scale material properties show unfamiliar patterns [7]. Therefore more experiments and theoretical calculations must be conducted to get healthier results for these structures.

ACKNOWLEDGMENT

This study was supported by Akdeniz University, Scientific Research Projects Supporting Unit (BAPYB).

REFERENCES

1. Ari, N. and S. Ozen, *Electromagnetic Compatibility*, Palme Yayincilik, Ankara, 2008.
2. Kaiser, K., *EMI Sources and Shielding: Electromagnetic Compatibility Handbook*, CRC Press, New York, 2005.
3. Ratner, D. M., A. S. Hoffman, and F. J. Schoen, *Biofilms, Biomaterials and Device Related Infections: An Introduction to Materials in Medicine*, Elsevier Academic Press, 2004.
4. Hseuh, H., M. Blaskiewicz, P. He, Y. Lee, C. Pai, R. Todd, L. Wang, J. Wei, D. Weiss, and S. Ornl, "Physical and electromagnetic properties of customized coatings for SNS injection ceramic chambers and extraction ferrite kickers," *Proceedings of 2005 Particle Accelerator Conference*, 3028–3030, Knoxville, Tenesse, USA, May 2005.
5. Kostyuk, G. I. and E. A. Voliak, "Design features of parts and high performance cutting tool with multi-layer plasma ion coatings," *XXth International Symposium on Discharges and Electrical Insulation in Vacuum*, 257–260, Tours, France, July 2002.
6. Kir, E., L. Oksuz, and S. Helhel, "Preparation of poly(2-chloroaniline) membrane and plasma surface modification," Applied Surface Science, Vol. 10, 2574–2579, 2006.
7. Cokeliler, D., H. Goktas, P. D. Tosun, and S. Mutlu, "Infection free titanium allos by stabile thiol based nanocoatings," *Journal of Nanoscience and Nanotechnology*, Vol. 10, 2583–2589, 2010.

Metamaterial Inspired Microstrip Patch

Surabhi Dwivedi[1], **Vivekanand Mishra**[1], **and Yogesh P. Kosta**[2]

[1]ECED, S.V.N.I.T., Surat, India
[2]Marwadi Education Foundation's Group of Institutions, Rajkot, India

Abstract— An introduction is presented on radome structure. And radome structure (patch cover) modeling and design concepts are studied and comparisons are made with the MTM included patch. Various advantages are evaluated over the existing technology.

Over the past decade, the need for small, compact and low cost antennas has increased tremendously for applications such as wireless communications and radar. Microstrip patch antennas, though popular for these applications, are difficult to miniaturize, since their resonant frequency is determined by the dominant (TMZ110) mode of the patch cavity (the region immediately beneath the patch). Nevertheless, numerous miniaturization techniques using shorting posts, active loading or high permittivity dielectrics have been conceived to lower the resonant frequency of patch antennas without increasing their size. Unfortunately, as the demand for ever smaller patch antennas increases, these techniques fail to produce the required size reductions.

1. INTRODUCTION

Two ways to simulate a patch antenna has been demonstrated. The return loss is obtained for slotted patch and compared with the metamaterial included slotted patch response. The deviation in solution time and the results are the important factors that are considered. Miniaturization of the patch antenna is to the core of our effort and the enhancement of bandwidth is obtained by slotting of the patch. Microstrip antennas are a relatively new generation of antennas and are preferable for many applications over the broad frequency range from 500 MHz to 50 GHz also called "patch antennas" or "printed antennas" or "planar antennas".

Contrary to a conventional DPS-DPS cavity resonator, here, as d_{DPS} is reduced, the value of d_{DNG} can also become smaller in order to satisfy the dispersion relation, and the layers can conceptually be as thin or as thick as otherwise needed as long as relation is satisfied. The total thickness of such a thin cavity $d_{\mathrm{DPS}}+d_{\mathrm{DNG}}$ may turn out to be much smaller than the standard $\lambda/2$ which, for low-frequency applications, may provide significant miniaturization in cavity resonator designs. The cavity mode can exist in this structure even when the total thickness may be less than the conventional $\lambda/2$.

Pairing these two reactive "impedances" with opposite signs may produce the conditions for a resonance. Furthermore, reducing the thicknesses of both layers can affect the values of these equivalent impedances, but their signs stay opposite. As a result, the DPS-DNG pair can still remain resonant, as we reduce their thickness while maintaining a certain ratio of thicknesses (although the bandwidth of this resonance is affected as the size is reduced). This feature is not present for a pair of conventional DPS-DPS thin layers, and it is due to juxtaposing DPS and DNG layers (and, similarly, also for ENG and MNG layers). Such pairing of complementary materials can provide us with the possibility of having sub-wavelength "compact resonant structures" in the form of sub-wavelength cavities, waveguides, and scatterers.

2. MATHEMATICAL RELATIONS

Extraction of negative parameters (permittivity and permeability)

$$\varepsilon_i(\omega) = 1 - \frac{\omega_e^2}{\omega^2}, \quad \mu_i(\omega) = 1 - \frac{\omega_m^2}{\omega^2}$$
$$\omega_0 = 2\pi f_0, \quad \omega_e = 2.34\omega_0, \quad \omega_m = 1.98\omega_0$$

For $f_0 = 2.5\,\mathrm{GHz}$, $\omega_0 = 15.7\,\mathrm{GHz}$, $\omega_e = 36.7566\,\mathrm{GHz}$, $\omega_m = 15.7\,\mathrm{GHz}$

3. KEY CONCEPTS PROPOSED BY RESEARCHERS

Negative refraction in DNG Media: Ziolkowski and Heyman's mathematical derivation.

When ε <0 and μ <0 in lossless DNG medium

$$\sqrt{\varepsilon} = \sqrt{-|\varepsilon|} = -j\sqrt{|\varepsilon|} \qquad \sqrt{\mu} = \sqrt{-|\mu|} = -j\sqrt{|\varepsilon|}$$

Frequency (GHz)	ε	μ
1	−33.2225	−23.5025
1.5	−14.21	−9.89
2	−7.55563	−5.125625
2.5	−4.4756	−2.9204
3	−2.8025	−1.7225
3.5	−1.79367	−1.000204082
4	−1.13891	−0.53140625

4. MATHEMATICS OF MTM

For a microstrip transmission line of width u and a conventional dielectric substrate height h.

The effective relative permittivity of the air-substrate-microstrip system is described below:

$$\mu_{MTM}(f) = \frac{1}{\sqrt{\varepsilon_{eff}(f)}} - 1 \quad \varepsilon_{MTM}(f) = \varepsilon_{eff}(f)\mu_{MTM}(f)$$

where,

$$\varepsilon_{eff}(f) = \varepsilon_r - \frac{\varepsilon_r - \varepsilon_{es}}{1 + G\left(\frac{f}{f_d}\right)^2} \quad \varepsilon_{es} \cong \left(\frac{\varepsilon_r + 1}{2}\right) + \left(\frac{\varepsilon_r - 1}{2}\right)\left[1 + 10\left(\frac{h}{u}\right)\right]^{-ab}$$

$$a = 1 + \left(\frac{1}{49}\right)\log\left[\left(\frac{u}{h}\right)^4 + \frac{\left(\frac{u}{52h}\right)^2}{\left(\frac{u}{h}\right)^4} + 0.432\right] + \frac{1}{18.7}\log\left[1 + \left(\frac{1}{18.1} * \frac{u}{h}\right)^3\right]$$

$$b = 0.564\left(\frac{\varepsilon_r - 0.9}{\varepsilon_r + 3.0}\right)^{0.053} \qquad G = 0.6 + 0.0009 Z_C$$

$$Z_C \cong \frac{1}{2\pi}\sqrt{\frac{\mu_0}{\varepsilon_{es}\varepsilon_0}}\log\left[F_1\left(\frac{h}{u}\right) + \sqrt{1 + \left(2\left(\frac{h}{u}\right)\right)^2}\right]$$

$$F_1 = 6 + (2\pi - 6)\exp[-(30.666h/u)^{0.7528} \quad f_d = \left(\frac{Z_C}{2\mu_0 h}\right)$$

The goal is to design an MTM that can be included with the microstrip line in some manner to make it dispersionless, i.e., we want to produce a dispersion-compensated segment of trans-mission line. This means we want to introduce an MTM with relative permittivity and permeability so that the overall relative permittivity and permeability of the system is

$$\varepsilon(f)/\varepsilon_0 = \varepsilon_{eff}(f) + \varepsilon_{MTM}(f) \quad \mu(f)/\mu_0 = 1 + \mu_{MTM}(f)$$

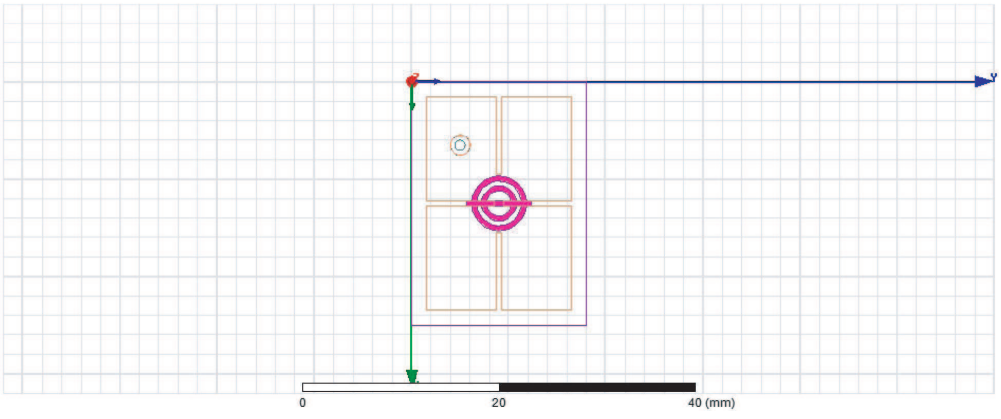

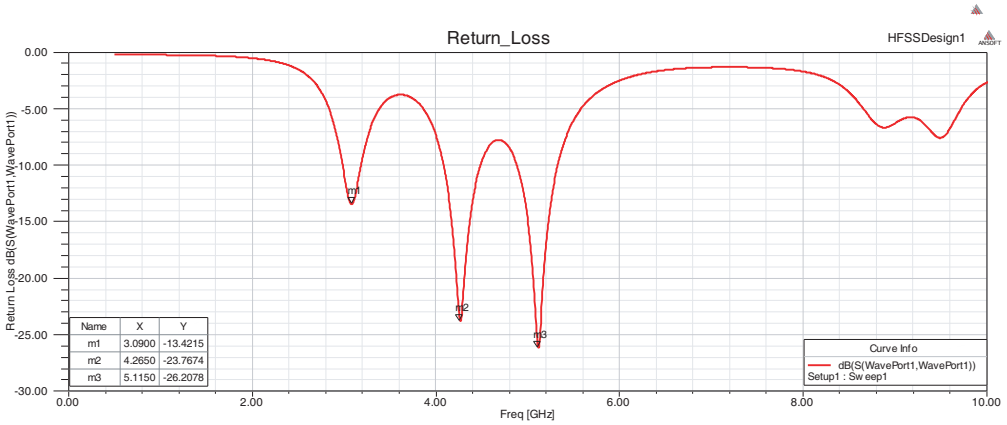

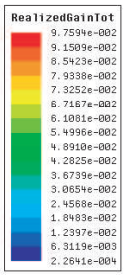

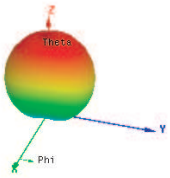

5. SIMULATED RESULTS

see figures above.

6. BW CALCULATIONS

Table 1: Comparative study of bandwidth improvement.

BW(%) (MTM)	First Band	Second Band	Third Band
	4.1525	4.5346	3.7267
BW(%) (Simple Patch)	5.128	4.4247	3.5714
BW Improvement	19.02%	2.42%	4.16%

7. CONCLUSION

Triband Operation of slotted patch antenna for 1 to 4 GHz of frequency band is obtained with optimized results in terms of return loss. It can be concluded that after appropriate slotting the patch the triband is shifted more towards left of the frequency axis, i.e., upto 1.4200 GHz. Moreover all the three bands are obtained between 1.4450–2.4100 GHz. With increase in width of the patch from 25 mm to 30 mm 8.71% increase in bandwidth is observed. It is also concluded that the model with an infinite substrate required less triangles to mesh the model and simulated faster than the model with a specified substrate size. The difference in the resonance frequency is approximately 2.5% and would become greater if substrate dimensions are decreased further. The difference between the two models will decrease as the specified size of the substrate increases and thus can more accurately be represented by an infinite substrate. After inclusions of the metamatrial the bandwidth increment is 11.13% as compared to the substrate with Teflon as the dielectic and volume remains almost constant as some of the dielectric from substrate is removed for inserting the unit cell. Moreover, dead weight of the structure is ignored.

Experimental Graduate Projects on Electromagnetism in Physics Courses

J. Íñiguez[1], V. Raposo[1], A. G. Flores[1], M. Zazo[1], and P. Hernández-Gómez[2]

[1]Departamento de Física Aplicada, Universidad de Salamanca, Salamanca E-37071, Spain
[2]Departamento de Electricidad y Electrónica, Universidad de Valladolid, Valladolid E-47071, Spain

Abstract— In recent years an increasing relevance of the graduate works in physics at our universities is being recognized. Unfortunately it is not easy to provide enough interesting ideas on experimental assignments to our students in order to satisfactorily develop these projects and often we resort to theoretical, bibliographic or computational works. Efforts should be made to increase the experimental project ratio including subjects that can be completed with an additional theoretical task or some numerical simulation.

Here we propose a set of selected ideas that we have developed or are currently in progress in our laboratory of electromagnetism. There are basically studies on electromagnetic induction in conductive materials and electro-dynamic systems in which the presence of magnetic forces are relevant. A few examples are discussed here.

The first one corresponds to the study of the damped fall of a magnet through a hollow conducting tube, in which, after a simple calculation of the induced current, we can calculate the conductivity of the tube according to its radius and wall thickness.

The second is a proposal concerning with the measurement of electrical conductivity in metallic tubes based on the screening of the magnetic field inside it at low frequencies.

Another is related to a study on magnetic levitation by induced ac currents in non-magnetic conductors at low frequencies allowing us to distinguish the two components of the current responsible for levitation and heating respectively.

One more is related to a simple and precise method to measure the electrical conductivity in nonferromagnetic tubes, rods and slabs without electric contacts. The results are readily obtained by analyzing the eddy currents in the sample when it is subjected to an harmonic magnetic field and can be obtained from a measurement of the phase of the induced voltage in a short probe coil located inside the tube or around the rod or slab when the sample is axially excited by a long primary coil.

Another interesting idea corresponds to the analysis of the behavior of a small-scale model of a magnetic levitation system based on the Inductrack concept. Drag and lift forces acting on our prototype moving above a continuous copper track are studied analytically following a simple low-speed approach.

And finally we present a study on magnetic actuators based on rare-earth permanent magnets concerning the correct choice of the aspect ratio and volume.

1. ESTIMATION OF THE ELECTRIC CONDUCTIVITY OF A METALLIC NONFERROMAGNETIC TUBE BY STUDYING THE DAMPED FALL OF A MAGNET INSIDE IT

The damped fall of a magnet inside a conductive tube is usually done as a qualitative demonstration related to electromagnetic induction or Faraday's law. A quantitative study of the induced currents in the tube responsible for the damping of the fall, allows relate the parameters involved in the problem to the geometry and electromagnetic characteristics. Obviously, the induced currents above and below the falling magnet attract/repel respectively, thereby yielding the damping effect, the equation of motion being

$$M\frac{dv}{dt} = Mg - kv \tag{1}$$

where k represents the damping coefficient associated with the induced currents and M the mass of the magnet. If we integrate Eq. (1), we obtain

$$v(t) = \frac{Mg}{k}\left(1 - e^{-\frac{k}{M}t}\right) \tag{2}$$

Experimentally we observe that the asymptotic speed (Mg/k) is reached almost instantaneously ($\tau = M/k \ll 1\,\mathrm{s}$), and we concluded that, for a tube length l of several decimeters, the speed can be considered practically uniform. For example, for a copper tube with dimensions $l = 1\,\mathrm{m}$, inner radius $b = 6.5\,\mathrm{mm}$, outer radius $c = 7.5\,\mathrm{mm}$ and a SmCo-magnet of mass $M = 9.3\,\mathrm{g}$, height $h = 10\,\mathrm{mm}$ and radius $a = 6\,\mathrm{mm}$, a falling time of 12.3 s is obtained.

To relate the falling time to the geometry and electromagnetic parameters of the tube-magnet system we will work only considering the dipolar contribution. This can be a reasonable approximation in agreement with the usual dimensions of tubes and magnets. According to Fig. 1, the magnitude of the induced azimuthal electric field, E, in a loop of radius radius ρ ($b \leq \rho \leq c$) at a distance z from the magnet (represented by its magnetic moment $\mathbf{m}$), in terms of the magnetic vector potential, $\mathbf{A}$, is

$$\begin{aligned} E(\rho,z) &= \left|\frac{\partial \mathbf{A}\,(\rho,z,t)}{\partial t}\right| = v\left|\frac{\partial \mathbf{A}}{\partial z}\right| = v\left|\frac{\partial}{\partial z}\left(\frac{\mu_0}{4\pi}\frac{\mathbf{m}\times\mathbf{r}}{r^3}\right)\right| \\ &= v\frac{\partial}{\partial z}\left[\frac{\mu_0 m\rho}{4\pi\left(\rho^2+z^2\right)^{2/3}}\right] = v\frac{3\mu_0 m}{4\pi}\frac{\rho z}{\left(\rho^2+z^2\right)^{5/2}} \end{aligned} \tag{3}$$

while the power dissipated in the tube will be

$$P_{dip} = \int\limits_{tube} \sigma E^2 dv = \sigma v^2 \frac{9\mu_0^2 m^2}{16\pi^2}\int_{-q}^{p}\int_{b}^{c}\frac{\rho^2 z^2}{\left(\rho^2+z^2\right)^5}2\pi\rho d\rho dz \tag{4}$$

Having in mind that b and c are much smaller than p and q (the distances to the tube ends), we can integrate Eq. (4) and obtain

$$P_{dip} \approx \sigma\, v^2 \frac{15\mu_0^2 m^2}{1024}\left(\frac{1}{b^3}-\frac{1}{c^3}\right) \tag{5}$$

Consequently, the energy balance, $P_{dip} = Mgv$, allows us to write

$$\sigma = \frac{1024}{15}\frac{Mg}{\mu_0^2 m^2}\frac{c^3 b^3}{c^3-b^3}\frac{1}{v} \tag{6}$$

The accuracy of this result was checked after determining the magnetic moment of the SmCo-magnet experimentally [1]. To do so, we suspended it from a very thin cotton thread and measured its oscillating period in the presence of the Earth's magnetic field. Substituting this magnetic moment in Eq. (6) and measuring falling speeds, the conductivity is found to be $24\times10^6\,\Omega^{-1}\mathrm{m}^{-1}$, which corresponds to approximately 41% of the published value [2], illustrating the need to include higher-order multipolar contributions or a more precise approach [1].

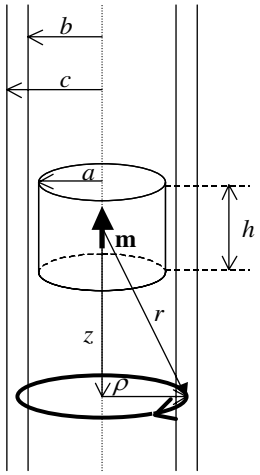

Figure 1: Notation used in the calculations.

2. SCREENING OF THE MAGNETIC FIELD IN METALLIC TUBES VERSUS ELECTRICAL CONDUCTIVITY

Studying on ac magnetic screening in the low frequency approximation leads to expressions that relate the screening coefficient to the geometry and conductivity of the metallic non-magnetic tubes. The set-up is shown in Fig. 2. It consists of a long solenoid ($b \ll l$) with N turns which carry an alternating current of variable frequency, a non-magnetic conductive tube with mean radius a and very thin wall ($t \ll a$) located coaxially inside the solenoid, and a small magnetic field probe in the axis of the tube. In the quasi-static limit and in the absence of the conductive tube, the magnetic induction in the axis of the solenoid is uniform and is given by

$$B(t) = B_0 \cos(\omega\, t) = \frac{\mu_0 N}{l} I_0 \cos(\omega\, t) \tag{7}$$

where I_0 is the amplitude of the alternating current in the solenoid and ω is its angular frequency. The magnetic induction can be easily measured with the help of a small air coil and a voltmeter. When the conductive tube is introduced into the solenoid, an azimuthal induced current appears in it, and the magnetic field in its interior is reduced. At low frequencies the skin effect can be ignored, and the current distribution may be considered almost uniform in the $l \times t$ section of the tube (see the shaded area in Fig. 2). For non-magnetic metallic tubes with a wall thickness up to 1 mm, it is possible to neglect the skin effect for frequencies up to several kHz [3]. Resistance and self-induction exhibited by a thin-walled non-magnetic conductive tube with azimuthal currents can be expressed in the approximate form as

$$R = \frac{1}{\sigma}\frac{2\pi a}{lt} \qquad L = \mu_0 \frac{\pi a^2}{l} \tag{8}$$

while the mutual inductance coefficient between the solenoid and the tube is

$$M = \mu_0 N \frac{\pi a^2}{l} = NL \tag{9}$$

In phasorial representation, the induced electromotive force in the conductive tube is

$$\bar{\varepsilon} = -i\omega M \bar{I} \tag{10}$$

where for convenience we use complex notation ($i = \sqrt{-1}$). Thus, the current in the tube is

$$\bar{I}_t = -\frac{i\omega\, M}{R + i\omega L}\bar{I} \tag{11}$$

Equation (11) allows us to write the magnetic field corresponding to this current in the form

$$\bar{B}_t = \mu_0 \frac{\bar{I}_t}{l} = -\frac{\mu_0}{l}\left(\frac{i\omega\, M}{R + i\omega L}\right)\bar{I} \tag{12}$$

which shows how for $R \ll \omega L$, the inductive component gives a counter-phase contribution with respect to $\bar{B}$ and the resistive component, for $R \gg \omega L$ has a phase delay of $\pi/2$. Finally, the total magnetic induction inside the tube is

$$\bar{B} + \bar{B}_t = \frac{\mu_0}{l}\left[N - \frac{\omega\, M\,(\omega L + iR)}{R^2 + \omega^2 L^2}\right]\bar{I} \tag{13}$$

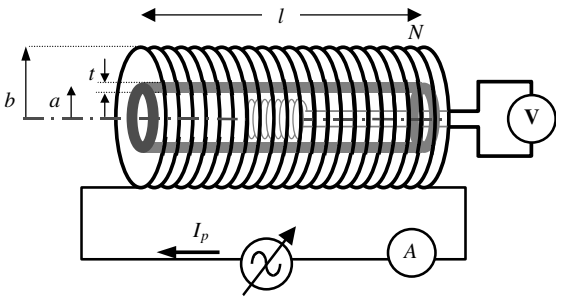

Figure 2: Experimental setup consisting of a solenoid and a conducting tube.

and the magnetic screening coefficient η, defined as the relative variation with respect to $|\bar{B}|$,

$$\eta = \frac{\left|\bar{B}\right| - \left|\bar{B} + \bar{B}_t\right|}{\left|\bar{B}\right|} = 1 - \frac{R}{\sqrt{R^2 + \omega^2 L^2}} = 1 - \frac{1}{\sqrt{1 + k^2\, f^2}} \tag{14}$$

with $k = \mu_0 \pi \sigma a t$.

Our experimental measurements show a very high accuracy with respect to the published data. For example, in copper tubes with 21 mm diameter and 1 mm wall thickness working up to 4 kHz we found a conductivity of $59.6 \times 10^6\, \Omega^{-1}\mathrm{m}^{-1}$, only an error of 0.7% [2].

3. MAGNETIC LEVITATION BY INDUCED AC CURRENTS

Over the last fifty years much attention has been focused on magnetic levitation by induced currents for its potential applications in the area of magnetic launchers and train transportation. Besides, inductive heating in ac currents is also a noteworthy research objective. Here we report a method for obtaining simple and precise expressions that allow calculation of the forces and heating power undergone by a nonmagnetic conductive loop or disk when submitted to an alternating magnetic field.

Let us consider a quasi-filamentary ring of radius ρ formed by a nonmagnetic conductive wire of conductivity σ and radius $a \ll \rho$. A coil wound around a ferrite core is placed a distance z below the ring, and coaxially with it, as shown in Fig. 3. The coil carries an alternating current of variable amplitude and frequency. The alternating magnetic flux encircled by the ring induces azimuthal eddy currents on it, which are responsible for its magnetic levitation (Ampère's law) and heating (Joule's law). For small coil sizes with respect to ρ and z, we can consider our ring as being submitted to the magnetic induction $\mathbf{B}(t)$ of an alternating point dipole with magnetic moment $\mathbf{m}(t)$. To simplify the calculations, we assume a working frequency at which the penetration depth due to the skin effect will be greater than the wire radius a. Therefore, the currents in the ring are readily calculated by evaluating the induced azimuthal electric field, $\mathbf{E}$, with the help of the magnetic vector potential $\mathbf{A}$ [4]

$$\mathbf{E} = -\frac{\partial \mathbf{A}}{\partial t} = -\frac{\partial}{\partial t}\left(\frac{\mu_0}{4\pi}\frac{\mathbf{m}(t) \times \mathbf{r}}{r^3}\right) = -\frac{\mu_0}{4\pi}\frac{\dot{m}(t)\rho}{\left(\rho^2 + z^2\right)^{3/2}}\,\mathbf{u}_\varphi \tag{15}$$

where $\dot{m}(t)$ is the time derivative of the magnetic dipole moment. And the induced electromotive force is

$$\varepsilon = \oint \mathbf{E} \cdot d\mathbf{l} = 2\pi\rho E_\varphi = -\frac{\mu_0}{2}\frac{\dot{m}\rho^2}{\left(\rho^2 + z^2\right)^{3/2}} \tag{16}$$

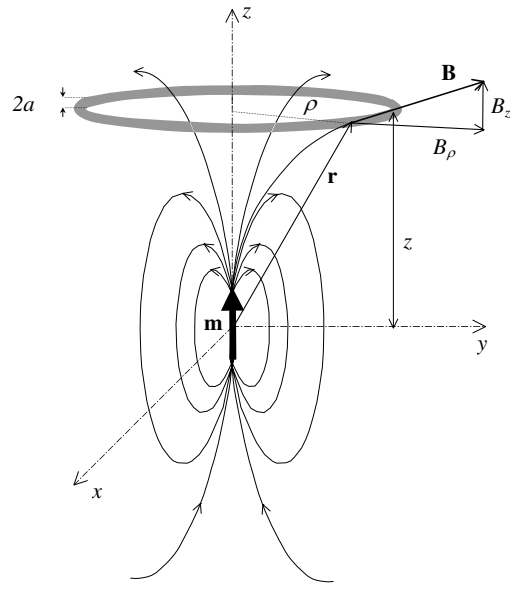

Figure 3: Simplified diagram of the experimental setup consisting of an alternating magnetic dipole and a conductive nonmagnetic ring suspended from a balance.

The current cannot be calculated simply as $I = \varepsilon/R$, R being the ring resistance. Were this done, we would have I and $\mathbf{B}$ out of phase by $\pi/2$, and hence the average value of the Ampère's force, $\mathbf{F} = I \oint dl \times \mathbf{B}$, would be null. Is also necessary including the self-inductance of the ring. The expression for resistance is easy but calculation of its self-inductance is very complicated but the literature offers simple approximations for a single circular loop [5].

$$R = \frac{2\rho}{\sigma\, a^2} \qquad L \approx \mu_0\, \rho \left(\ln \frac{8\rho}{a} - \frac{7}{4} \right) \tag{17}$$

and the induced current can be written as

$$\bar{I} = \frac{\bar{\varepsilon}}{R + i\omega L} \tag{18}$$

ω being the angular frequency. It explains how for $\omega \ll R/L$ the current is essentially resistive, giving a contribution delayed by $\pi/2$ with respect to $\bar{B}$, only being responsible for the ring heating. For $\omega \gg R/L$, the inductive component increases and provides a contribution delayed by π with respect to $\bar{B}$, which is associated with the magnetic levitation.

After integrating the Ampère's law around the ring, we obtain the value of the vertical force. Therefore, the phasorial form of the magnetic levitation force experienced by the ring will be

$$\bar{F} = -2\pi\rho \bar{I} \bar{B}_\rho \tag{19}$$

$\bar{B}_\rho$ representing the radial component (see Fig. 3) of the magnetic field of the point dipole

$$\bar{B}_\rho = \frac{3\mu_0}{4\pi} \frac{\bar{m} z \rho}{\left(\rho^2 + z^2\right)^{5/2}} \tag{20}$$

We can find the mean value of the levitating force by averaging the expression in Eq. (19)

$$\mathbf{F}_m = \frac{3\mu_0^2}{4} \frac{z \rho^4 m_{rms}^2 \omega^2 L}{\left(\rho^2 + z^2\right)^4 \left(R^2 + \omega^2 L^2\right)} \mathbf{u}_z \tag{21}$$

where m_{rms} represents the root-mean-square value of the magnetic dipole moment. And in a similar way we can find the energy dissipated in the ring

$$P_m = \frac{\mu_0^2}{4} \frac{\rho^4\, m_{rms}^2\, \omega^2\, R}{\left(\rho^2 + z^2\right)^3 \left(R^2 + \omega^2 L^2\right)} \tag{22}$$

Experimental results show the dependence of the magnetic levitation force versus the magnetic moment and frequency, clearly illustrating the accuracy of our calculations. With the help of the usual curve-fitting techniques we obtained a value for the electrical conductivity of our copper ring of $58 \times 10^6\, \Omega^{-1}\mathrm{m}^{-1}$, which only deviates slightly from its published value.

4. MEASUREMENT OF THE ELECTRICAL CONDUCTIVITY IN TUBES, RODS AND SLABS WITHOUT ELECTRIC CONTACTS

The analysis of the induced current distribution in conducting wires subjected to harmonic excitations is important on designing many electrical devices such as transformers and transmission lines. Induction phenomena in conducting samples subjected to a harmonic longitudinal magnetic field are responsible for the eddy currents which flow perpendicularly to the axis of the conductor. We study the electromagnetic field in conductive slabs, rods, and tubes in a harmonic longitudinal magnetic field. As is usual for good conductors, the calculations are made neglecting Maxwell's displacement current, in such a way that the validity of the calculations typically reaches frequencies up to several GHz [6–8]. We propose a method for the electromagnetic characterization of a sample, so that it suffices to measure the phase angle between the current in a primary coil, the source of the external magnetic field, and the induced voltage in a secondary coil encircling the sample or inside the tube. It is to be remarked that longitudinal defects are usually present in many conducting alloys as a consequence of the extrusion procedure with which they are manufactured. In particular, the azimuthal induced currents are markedly reduced by the presence of longitudinal faults in extruded samples, and the effective electrical conductivity is much smaller than the

expected in samples without defects. By making measurements in an appropriate frequency range, it is possible to locate the defects as well as to make a reasonable estimation of their size [8–13].

In the case of tubes, see Fig. 4, the voltage induced on a coil of radius $a \leq R_{in}$ is [12]

$$V_{tube\text{-}in} = -\frac{d\Phi}{dt} = -i\omega\mu\pi a^2 H_{in} e^{i\omega t} = -i\omega\mu\pi a^2 \frac{\mathrm{Q J_0}\left(kR_{in}\right) - \mathrm{P Y_0}\left(kR_{in}\right)}{\mathrm{Q J_0}\left(kR_{ext}\right) - \mathrm{P Y_0}\left(kR_{ext}\right)} H_s e^{i\omega t} \tag{23}$$

$\mathrm{J_0}$ and $\mathrm{Y_0}$ represent Bessel functions of the first and second kind, $k^2 = -i\omega\mu\sigma$ and P and Q are complex quantities depending on the frequency and tube characteristics defined as

$$\mathrm{P} = \mathrm{J_1}\left(kR_{in}\right) - \frac{kR_{in}}{2}\mathrm{J_0}\left(kR_{in}\right) \qquad \mathrm{Q} = \mathrm{Y_1}\left(kR_{in}\right) - \frac{kR_{in}}{2}\mathrm{Y_0}\left(kR_{in}\right) \tag{24}$$

Figure 5 shows the polar graph for our copper tube up to frequencies of 20 kHz. The magnitude of the phasor initially increases with the applied frequency, but at greater frequencies the phasor diminishes while it rotates clockwise around the origin. A complete information can be gained from this type of graphical representation, not only concerning the phase angle but also the values of the real and imaginary parts of the induced voltage, and the increasing magnetic screening that the hollow tube undergoes at increasing frequencies.

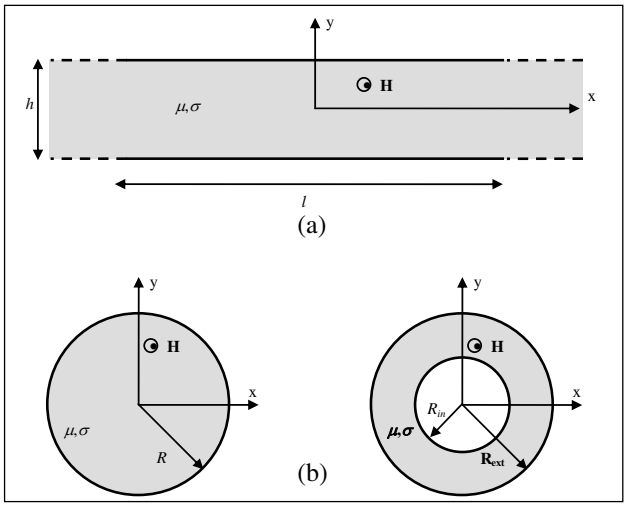

Figure 4: (a) A metal slab of conductivity σ and permeability μ placed in a magnetic field $\mathbf{H} = H_s e^{i\omega t}\mathbf{u_z}$ parallel to its axis. (b) Transversal views of a long metal rod, or (c) a tube placed in an axial magnetic field $\mathbf{H} = H_s e^{i\omega t}\mathbf{u_z}$.

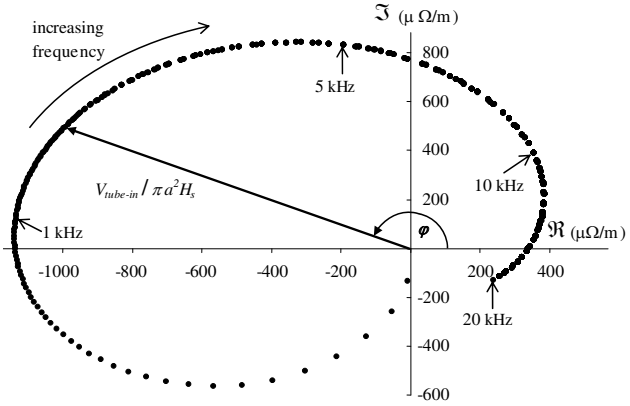

Figure 5: Polar plot of the induced voltage versus frequency measured in a probe coil inside a copper tube showing its real and imaginary parts. For clarity, instead of $V_{\text{tube-in}}$ we show the induced voltage per unit area and H_s, measured in units of $\mu\Omega/\mathrm{m}$, which depends only on the tube radii and conductivity, independent of the primary and secondary coils.

5. MAGNETIC LEVITATION SYSTEM BASED ON THE INDUCTRACK CONCEPT

The existence of a braking force when a non-ferromagnetic conductor moves in a magnetic field is well known. It is explained on the basis of Faraday's induction law and gives rise to power dissipation in the conductive material. Conversely, the presence of a repulsive force is less well known. This lift force is also a simple consequence of the induction law, and it tends to impel the conductor towards regions with a weaker magnetic field, giving rise to a diamagnetic behavior. This force begins to become significant when the relative speed between the conductor and the sources of the magnetic field increases. As well, this lift force can also become quite important when the experiment is done by exciting the non-ferromagnetic conductor with harmonic magnetic induction at increasing frequencies. Analysis of the levitation force requires precise examination of the map of magnetic induction lines in the conductive material, in a similar way to the study of the equations of magnetohydrodynamics. This force grows markedly with the delay of the induced currents in the conductive materials for increasing speed, as a consequence of the diffusion of the magnetic field lines. From the viewpoint of the circuitry, it should be noted that the lift force reveals its importance when the inductive behavior of the moving conductor begins to become important with respect to its resistive character; i.e., when its inductive reactance is comparable or greater than its resistance, $L\omega \geq R$, ω being the characteristic angular frequency of the problem. In sum, the induced electromotive force in a loop of the conductive material, ε, supplies a current $I = \varepsilon/Z$, Z being the impedance of the loop. The in-phase component of this induced current with respect to the electromotive force interacts with the magnetic induction and is responsible for the drag force and the corresponding power dissipation in the conductor. In contrast, the component in quadrature of that current provides the magnetic levitation force, perpendicular to the movement.

Recently, the opportunity of making use of strong magnets based on rare earths with NdFeB compositions has encouraged interest in developing transportation systems supported on this kind of electrodynamic suspension technology (EDS), because it is inherently stable even without active control. Thus, conventional techniques of electromagnetic suspension (EMS), in which the levitation of the system is achieved by means of the magnetostatic interaction between magnets and coils (including superconductive magnets), have perhaps aroused less interest because they are intrinsically unstable as a consequence of Earnshaw's theorem, and because they use huge amounts of power. Currently, several projects are focusing on the development of transportation systems and electromagnetic launchers based on EDS technology by magnetic levitation combined with linear synchronous motor (LSM) propulsion systems. Among the different EDS technologies, the so-called Inductrack is promising. This proposal employs an interesting configuration of permanent magnets calledHalbach array, arranged in the bottom of the car body, at a short distance from the conductive track.

The simple scheme of this arrangement we used (Figs. 6 and 7) shows how the rotating magnetization of the successive parts of the Halbach array causes a strong asymmetry in the magnetic induction lines of force above and below the magnets. This array uses five magnets, four blocks per period λ (the Halbach *wavelength*) with the magnetization axis rotating by 90 degrees in each section. The magnetic induction lines are concentrated in the conductive track, which when it moves undergoes an alternating magnetic flux that is responsible for the induced currents and consequently of the magnetic drag and levitation forces. We report the analysis of a small prototype of a low-speed magnetic levitation system using a Halbach-type magnet array. To accomplish this, we placed a copper rim over a carbon fiber wheel driven by an electric motor, in such a way that it would enable the experiment to be performed very easily [14, 15]. The analysis of the system is based on a 2D-approach (see Fig. 6).

According to Maxwell equations in source-free regions, $\nabla \cdot \mathbf{B} = 0$ and $\nabla \times \mathbf{B} = 0$ we obtain

$$B_x \approx B_0 e^{\frac{2\pi}{\lambda} y} \sin \frac{2\pi}{\lambda} x \qquad B_y \approx -B_0 e^{\frac{2\pi}{\lambda} y} \cos \frac{2\pi}{\lambda} x \tag{25}$$

and the approximate values for drag and lift forces per unit area at low speed v

$$\begin{aligned} \frac{\mathbf{F_D}}{\mathrm{s}}(\mathrm{v}) &= \mathbf{v} \frac{\sigma B_0^2}{4k} \left(e^{2ky_1} - e^{2ky_2} \right) \cos\left[\operatorname{atan}\left(k\tau\,\mathrm{v}\right)\right] \\ \frac{\mathbf{F_L}}{\mathrm{s}}(\mathrm{v}) &= \mathbf{u}_y \frac{\mathrm{v}\sigma B_0^2}{4k} \left(e^{2ky_1} - e^{2ky_2} \right) \sin\left[\operatorname{atan}\left(k\tau\,\mathrm{v}\right)\right] \end{aligned} \tag{26}$$

in terms of the track conductivity σ, the quantity $k = 2\pi/\lambda$, the maximum value of magnetic field B_0 and τ which represents the characteristic relaxation time of the L-R equivalent circuit.

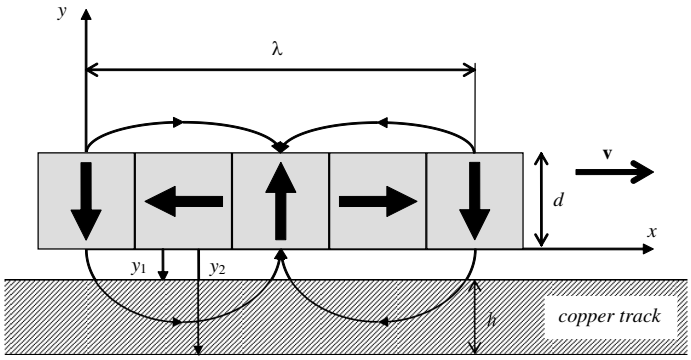

Figure 6: Simple scheme of a 1.25λ-Halbach array; arrows indicate the direction of the magnetization in the magnets. The co-ordinate system and the conductive track are also shown.

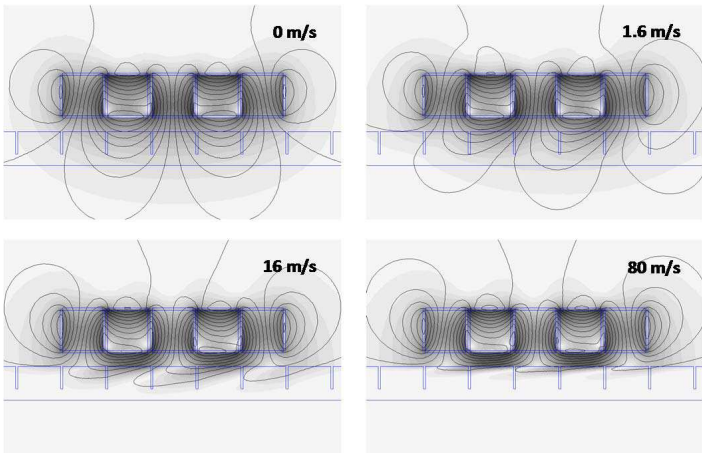

Figure 7: Numerical simulations of the field pattern in the conductive track at several speeds. The Halbach period is 80 mm and therefore the frequency is $f = v/\lambda = 12.5v$, v measured in m/s.

Figure 8 represents a set of experimental measurements. Our set up is conformed by a Halbach arrangement of 100 mm length (1.25 times the space period), 20 mm height and 25 mm width of NdFeB magnets with a mass of 0.59 kg including its holder. The copper rim is 40 mm in width and 15 mm in height, and is located at a short distance (from 2 to 30 mm) below the magnets. To protect the system from excessive vibrations the speed limit of the track is about 8 to 10 m/s. Experimental values are smaller than those expected by about 20 or 30%, which is a good result according with our approach and the limitations concerning a simple 2D model.

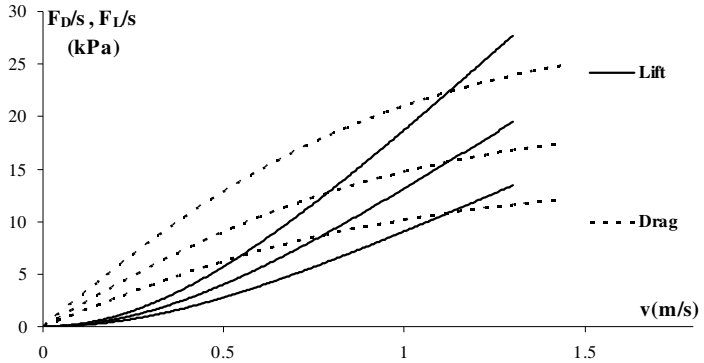

Figure 8: Experimental results obtained for the lift and drag forces per unit area versus speed at three different distances (6, 8 and 10 mm) between the magnet array and the copper track.

6. CHOICE OF THE BEST ASPECT RATIO IN MAGNETS TO IMPROVE FORCES IN MAGNETIC ACTUATORS

Magnetic springs are frequently used to provide either a constant assisting or resisting force. Its design previously requires the technique to maximizethe forces between the magnets forming the system. Here is a study on the forces between magnets, attending to their aspect ratio, separation and volume, with the aim of optimizing the spring magnet behavior. A set of experimental measurements confirm our calculations. Forces between cuboid-shaped magnets can be easily calculated for uniform magnetized samples via the magnetic energy gradientor using the interaction between magnetization currents (k_m) or magnetic charges (σ_m)

$$\vec{F}_{12} = \frac{\mu_0}{4\pi} \int_{S_2} \sigma_{m2} \int_{S_1} \frac{\sigma_{m1}}{R_{12}^3} \vec{R}_{12} ds_1 ds_2 \tag{27}$$

while for more complicated geometries the use of numerical solutions will be needed.

The main results are summarized as follows. For a particular value of the distance between magnets and a constant volume of the magnetic material, there is an optimum aspect ratio that maximizes the repulsive or attractive force between them. This can be explained qualitatively by taking into account the interactions of the magnetic surface charges at the end of the magnets. For very long cylinders, the amount of charge is very small and hence the resulting force is weak. In contrast, for very flat magnets (slab-like) the positive and negative magnetic charges are very close, and although the total magnetic charge is increased strongly, the magnetic field, and also the force, are reduced significantly. In fact, for an infinite magnetic slab, the magnetic field outside is null. Finally, for an adequate aspect ratio the amount of magnetic charge and its separation is optimum and the force will be maximized. Changing the distance that separates the magnets requires a different aspect ratio to maximize the forces, as can be understood again from the balance of the separation of the magnetic charges at both bases and the distance between the magnets. Finally, for a fixed aspect ratio the force evidently increases with the magnet volume, but it is possible to obtain a compromise by calculating the force versus volume relationship, which again presents an optimum value [16]. In Fig. 9, a comprehensive summary is presented.

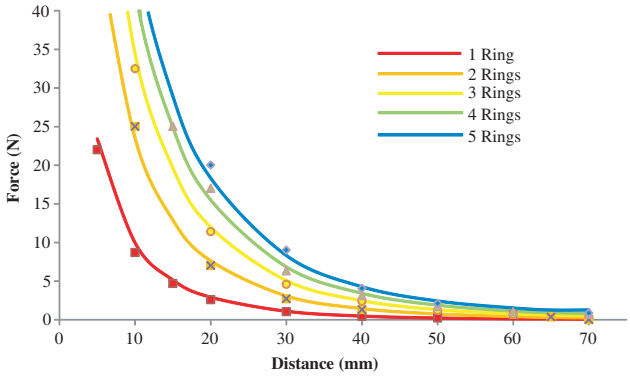

Figure 9: Experimental results for five different pairs of ring-shaped magnets. Plots correspond to theoretical aspect ratio values of 0.286 (for a volume of 2302 mm^3) (red), 0.572 (for a volume of 4604 mm^3) (orange), 0.858 (for a volume of 6906 mm^3) (yellow), 1.144 (for a volume of 9208 mm^3) (green) and 1.43 (11510 mm^3) (blue).

REFERENCES

1. Íñiguez, J., V. Raposo, A. Hernández-López, A. G. Flores, and M. Zazo, "Study of the conductivity of a metallic tube by analyzing the damped fall of a magnet," *Eur. J. Phys.*, Vol. 25, 593–604, 2004.
2. Goodfellow, Metals and Materials for Research and Industry, http://www.goodfellow.com/.
3. Íñiguez, J., V. Raposo, A. G. Flores, M. Zazo, and A. Hernández-López, "Measurement of the electrical conductivity of metallic tubes by studying magnetic screening at low frequency," *Am. J. Phys.*, Vol. 73, 206–210, 2005.
4. Popovic, B. D., *Introductory Engineering Electromagnetic*, Addison-Wesley, Reading, MA, 1971.

5. Íñiguez, J., V. Raposo, A. G. Flores, M. Zazo, and A. Hernández-López, "Magnetic levitation by induced eddy currents in nonmagnetic conductors and conductivity measurements," *Eur. J. Phys.*, Vol. 26, 951–957, 2005.
6. Jackson, J. D., *Classical Electrodynamics*, 3rd Edition, Wiley, New York, 1998.
7. Íñiguez, J., V. Raposo, and P. Hernández, "Contactless technique for low frequency measurement of resistivity in non-magnetic conductive tubes," *IEEE Trans. on Magn.*, Vol. 56, No. 2, 418–421, 2007.
8. Materials Evaluation, The American Society for Nondestructive Testing. Available: http://www.asnt.org/publications/materialseval/materialseval.htm.
9. Íñiguez, J. and V. Raposo, "Measurement of conductivity in metals: A simple laboratory experiment on induced currents," *Eur. J. Phys.*, Vol. 28, 1125–1129, 2007.
10. Íñiguez, J., V. Raposo, and P. Hernández, "Study of inhomogeneities in non-magnetic tubes by means of a contactless inductive technique," *Materials Science Forum*, Vols. 587–588, 258–262, Trans. Tech. Publications Inc., 2008.
11. Íñiguez, J., V. Raposo, and M. Zazo, "Measurement of electrical conductivity in nonferromagnetic tubes and rods at low frequencies," *Am. J. Phys.*, Vol. 77, 949–953, 2009.
12. Íñiguez, J., V. Raposo, M. Zazo, A. García-Flores, and P. Hernández-Gómez, "The electromagnetic field in conductive slabs and cylinders submitted to a harmonic longitudinal magnetic field," *Am. J. Phys.*, Vol. 77, 1074–1081, 2009.
13. Íñiguez, J., V. Raposo, and M. Zazo, "Non-contact conductivity measurements in nonferromagnetic pipes and rods: The choice of working frequency," *Sensor Letters*, Vol. 7, No. 3, 387–389, 2009.
14. Íñiguez, J. and V. Raposo, "Laboratory scale prototype of a low speed electrodynamic levitation system based on a Halbach magnet array," *Eur. J. Phys.*, Vol. 30, 367–379, 2009.
15. Íñiguez, J. and V. Raposo, "Numerical simulation of a simple low-speed model for an electrodynamic levitation system based on a Halbach magnet array," *J. Magn. Mat. Magn.*, Vol. 322, 1673–1676, 2010.
16. Iñiguez, J., V. Raposo, A. G. Flores, and M. Zazo, "Choice of the best aspect ratio in magnets for force improvement," *Key Engineering Materials*, Vol. 543, 101–104, Materials Science Forum, Trans. Tech. Publications Inc., 2013.

RF Heating of Conducting Film/Silicon Substrate Structure: The Heat Explosion Theory Approach

M. Sinder[1], **J. Pelleg**[1], **V. Meerovich**[2], **and V. Sokolovsky**[2]

[1]Department of Materials Engineering, Ben Gurion University, Beer Sheva 84105, Israel
[2]Physics Department, Ben Gurion University, Beer Sheva 84105, Israel

Abstract— Heating by a radio-frequency (RF) magnetic field can be successfully applied in technological processes of fabrication of films and layers of metal, silicide, boride or nitride on silicon substrates. In the present work the heating kinetics is analyzed as a function of film thicknesses, sheet resistances of the conducting layers, specimen dimensions, their thermal parameters, as well as the amplitude and frequency of applied RF magnetic field. It was shown that, depending on the relation between the structure parameters and applied field, two regimes of the heating can be realized. The first one is characterized by heating of the structure up to a finite temperature determined by equilibrium between dissipated power loss due to eddy-currents and heat transfer to environment. The second regime corresponds to fast unlimited temperature increase (heat explosion). The criterion of realization of one of regimes is obtained in analytical form. Growth of a new phase (silicide) is analyzed and it is shown that new phase formation in metal film-silicon structures occurs during heat explosion.

1. INTRODUCTION

Radio-frequency (RF) heating is one of the rapid thermal processing methods used to obtain fast reaction rates at fabrication of thin film structures in the semiconductor industry [1]. To apply RF heating, a thin film deposited on a substrate, e.g., silicon, must be a conductor with metal-like character (metals, some silicides, borides or nitrides). To achieve the properties of conducting film/silicon substrate structures required for their application in microelectronics, these structures have to be heated up to $\sim 1000°$C. Such high temperature heating is accompanied by a sharp increase in the conductivity of the silicon substrate with temperature, which can lead to a fast, non-stationary, self-accelerated and like-explosive heating. The explosive temperature increase under the RF heating has been observed in experiments [1]. The mathematic description of the process should be based on the consideration of the eddy-current losses and non-stationary thermal processes in the metal-silicon structure with nonlinear thermal dependence of the structure characteristics. This approach was applied in [2, 3] for the qualitative theoretical analysis, and the obtained results were compared with the experimental data for the RF heating of Ta-Ti film on Si substrate.

In the present paper, using the analytical and numerical calculations, the criterion of the realization of the explosive regime is obtained.

2. THEORETICAL MODEL

We consider an infinity long conducting film-silicon structure in the RF magnetic field perpendicular to the structure surface. It is assumed that the structure thickness and width are comparatively small so that the magnetic field is uniform inside the structure and equals to the external field. The period of the RF field is much less than the characteristic time of the heating and, hence, the eddy current losses can be determined from the quasi-stationary Maxwell equations [1]. The loss power W per unit of surface area of the structure, averaged through the area, may be presented by

$$W = K\left(\mu_0 H \omega L\right)^2 \left(d_S/\rho_S + d_C/\rho_C\right) \tag{1}$$

where K is the specimen shape coefficient which equals 1/24 for a long strip; μ_0 is the vacuum magnetic permeability; H and ω are the amplitude and angular frequency of the external magnetic field, respectively; L is the characteristic size of specimen (strip width), d_s, d_c and ρ_s, ρ_c are the thicknesses and resistivities of the silicon substrate and conductor film, respectively.

Since the specimen is placed in a vacuum chamber, the heat transfer from the structure surface is taken according to the Stefan-Boltzmann law

$$Q = \sigma_{SB}\left(T^4 - T_{room}^4\right), \tag{2}$$

where σ_{SB} is the Stefan-Boltzmann constant.

Assuming that the temperatures of the substrate and conducting film are equal, the non-stationary thermal equation can be presented in the following form

$$CdT/dt = W - Q \tag{3}$$

where T is the averaged temperature of the structure, $C \equiv d_S c_{pS} \nu_S + d_C c_{pC} \nu_C$, c_{pS} and c_{pC} are the heat capacities of the substrate and conductor film, respectively, ν_S and ν_C are the densities of the substrate and conductor film, respectively. The temperature dependencies of the resistivities are taken in the form [1–3]:

$$\rho_C = \rho_{C0}\,(T/T_0)\,, \tag{4}$$

$$\rho_S = \rho_{S0} \exp\left(+E_a/k_B T\right), \tag{5}$$

where ρ_{C0}, ρ_{S0}, T_0, and E_a are the fitting independent constants, k_B is the Boltzmann constant.

Qualitative analysis of the model [2, 3] showed possibility of two heating regimes: a) achieving an equilibrium state with a constant temperature and b) a non-stationary unlimited heating. The first regime is realized when the equation

$$W = Q \tag{6}$$

has two real positive solutions for temperature. The smaller temperature corresponds to the stable thermal equilibrium state. If the equation has no real roots, it corresponds to the second heating regime. The boundary between these two regimes determines the so-called critical state when Eq. (6) has only one real root. The resistivity of the substrate exponentially increases with temperature while the power of heat transfer from the structure surface increases proportional to T^4. The non-stationary unlimited heating under these conditions corresponds to the heat explosion theory [4].

3. CRITICAL STATE

Let us analyze the critical state using a dimensionless equation, which can be deduced from Eqs. (l)–(5):

$$\frac{d\theta}{d\tau} = \alpha e^{\frac{\theta}{1+\theta/\beta_1}} + \frac{1}{\beta_1+\theta} - \gamma\left[(\beta_1+\theta)^4 - \beta_0^4\right] \tag{7}$$

where $\theta = \frac{T-T_1}{\Theta}$, $\tau = t/t^*$, $\Theta = \frac{k_B T_1}{E_a} T_1$, $\alpha = \frac{d_S \rho_{C0}}{d_C \rho_{S0}} \frac{\Theta}{T_{C0}} e^{-E_a/k_B T_1}$, $\beta_0 = \frac{T_{room}}{\Theta}$, $\beta_1 = \frac{T_1}{\Theta} = \frac{E_a}{k_B T_1}$, $t^* = \frac{C\Theta}{K(\mu_0 H \omega L)^2} \frac{\rho_{C0}}{d_C} \frac{\Theta}{T_{C0}}$,

$$\gamma = \frac{\sigma_{SB}\Theta^4}{K\left(\mu_0 H \omega L\right)^2} \frac{\rho_{C0}}{d_C} \frac{\Theta}{T_{C0}}. \tag{8}$$

At low temperatures, in the initial stage of heating, the total losses in the structure are mainly determined by the losses in the film while at higher temperatures achieved in the heat explosion the main contribution is the losses in the substrate. We determine the characteristic temperature T_1 as a temperature at which the losses in the film and the substrate are equaled $d_S/\rho_S(T_1) = d_C/\rho_C(T_1)$.

For real structures the estimation gives that $\theta \ll \beta_1$ at $T \approx T_1$, and taking into account the definition of T_1 we obtain $\alpha = 1/\beta_1$. Then Eq. (7) can be rewritten as

$$\frac{d\theta}{d\tau} = \frac{1}{\beta_1} e^{\theta} + \frac{1}{\beta_1} - \frac{\theta}{\beta_1^2} - \gamma\left[\beta_1^4 + 4\beta_1^3\theta - \beta_0^4\right]. \tag{9}$$

The initial condition for Eq. (3) $T = T_{room}$ at $t = 0$ in the dimensionless form: $\theta(\tau = 0) = \beta_0 - \beta_1$.

Equation (6) has a single real positive solution if the right-hand side of (9) and its derivative equal zero [4]. In the approximation of $\theta \ll \beta_1$ the solution of the equation system is $\theta_{cr} = \ln(1/\beta_1 + 4\gamma_{cr}\beta_1^4)$ at $\gamma_{cr} = (\beta_1+1)/[\beta_1^2(\beta_1^4 - 4\beta_1^3 - \beta_0^4)]$. If $\gamma > \gamma_{cr}$ the stable equilibrium thermal regime is realized, at $\gamma < \gamma_{cr}$ the temperature increases with no limit. For the typical values of $T_1 = 825\,\mathrm{K}$, $E_a = 0.6\,\mathrm{eV}$, β_0 and β_1 are estimated as 3.1 and 8.4, respectively, and $\gamma_{cr} = 4.85 \cdot 10^{-5}$, $\theta_{cr} = -0.96$.

Using usually measured value of the sheet resistance of a conducting film, $R_\square = \rho_{C0}/d_C$, the condition for existence of a single solution of (6) can be represented in the form:

$$R_\square/(H\omega)^2 = A = \mu_0 \gamma_{cr} L^2 K \beta_0 / \left(\sigma_{SB}\Theta^4\right). \tag{10}$$

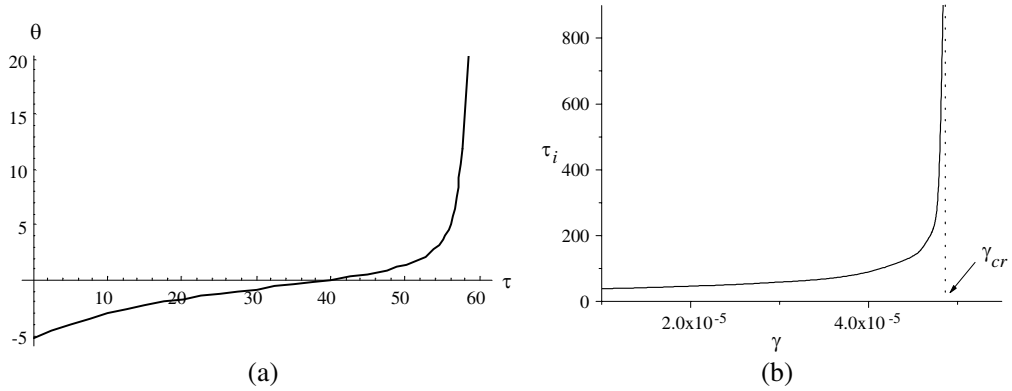

Figure 1: Numerical simulation of heating: (a) simulation of the heat explosion at $\gamma = 3 \cdot 10^{-5}$, (b) the duration of the inductive period as a function of the parameter γ at $\beta_0 = 3.1$ and $\beta_1 = 8.4$.

The stable equilibrium state is achieved at $R_\square > AH^2\omega^2$ while the heat explosion is observed at $R_\square < AH^2\omega^2$. These results were confirmed experimentally [2, 3].

4. INDUCTIVE PERIOD OF HEAT EXPLOSION

The heat explosion process can be separated into two stages: during the first stage, the inductive period, the temperature smoothly increases with time. The second stage is associated with very fast temperature growth [1–4]. Fig. 1(a) presents the numerical solution of Eq. (7). One can clearly see these two stages. For practice, it is very important to estimate the duration of the first stage. The duration τ_i of the inductive period can be estimated by integration of Eq. (7)

$$\tau_i = \int\limits_{-\beta_1+\beta_0}^{+\infty} \left(\frac{1}{\beta_1} e^{\frac{\theta}{1+\theta/\beta_1}} + \frac{1}{\beta_1+\theta} - \gamma \left[(\beta_1+\theta)^4 - \beta_0^4 \right] \right)^{-1} d\theta \tag{11}$$

The dependence of the inductive period duration on the parameter γ obtained by numerical integration is presented in Fig. 1(b). The integration gives $\gamma_{cr} = 4.85 \cdot 10^{-5}$. The obtained above analytical approximation for γ_{cr} well agrees with this value.

5. SILICIDE LAYER GROWTH

In the semiconductor industry the heating of the conducting film-silicon structure is applied to obtain silicides (silicon-metal compounds) [5, 6]. According to the diffusion limited growth model, the thickness x of the silicide layer is given by a solution of the following equation [6]:

$$dx^2/dt = D_0 e^{-E_{sil}/k_B T} \tag{12}$$

where E_{sil} and D_0 are the activation energy and pre-exponential coefficient, respectively.

At $\gamma > \gamma_{cr}$ when temperature increases up to a limit, the main growth of silicide layer occurs under the thermal equilibrium and the layer thickness increases proportionally to $t^{1/2}$.

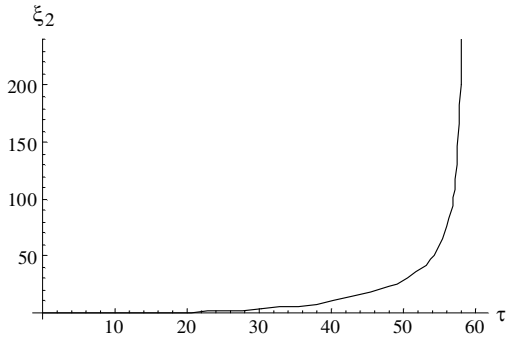

Figure 2: Dependence of ξ^2 on time at $\gamma = 3 \cdot 10^{-5}$, $\beta_0 = 3.1$, $\beta_1 = 8.4$, and $\delta = 1$.

At $\gamma < \gamma_{cr}$, under the heat explosion, the layer thickness slowly grows with time during the inductive period and increases very fast during the second stage of the heating (Fig. 3). The metal film is completely consumed in a short time range near the end of the inductive period (Fig. 2). Fig. 2 presents numerical solution of Eq. (12) rewritten in the following dimensionless form:

$$\frac{d\xi^2}{d\tau} = e^{\frac{\delta\theta}{1+\theta/\beta_1}}$$

where $\delta = E_{sil}/E_a$, $\xi = x/x^*$, $x^* = \sqrt{D_0 t^* e^{-E_{sil}/k_B T_1}}$.

6. CONCLUSION

Analysis of heating caused by RF magnetic field showed that character of the process is determined by a dimensionless parameter γ. At $\gamma > \gamma_{cr}$ the structure is heated up to a finite temperature determined by equilibrium between dissipated power loss due to eddy-currents and heat transfer to environment. At $\gamma > \gamma_{cr}$ the regime corresponds to fast unlimited temperature increase (heat explosion). The obtained analytical approximation for γ_{cr} is in well agreement with the numerical result $\gamma_{cr} = 4.85 \cdot 10^{-5}$.

It is shown that the new phase formation in metal film-silicon structures occurs during the heat explosion and the metal film is completely consumed in a short time range near the end of the inductive period.

REFERENCES

1. Sinder, M., J. Pelleg, V. Meerovich, and V. Sokolovsky, "RF heating of the conductor film on silicon substrate for thin film formation," *Mat. Sci. and Eng. A*, Vol. 302, No. 1, 31–36, 2001.
2. Pelleg, J., S. Rosenberg, and M. Sinder, "Silicide film formation in the Ta/Ti/Si system by RF induction heating," *Mat. Res. Soc. Symp. Proc.*, Vol. 1230, MM06-01, 2010.
3. Pelleg, J., S. Rosenberg, and M. Sinder, "Heat explosion approach to radiofrequency heating of a conductor film on silicon substrate: Application for silicide film formation," *Acta Mater.*, Vol. 59, 4283–4290, 2011.
4. Zeldovich, Y. B., G. I. Barenblatt, V. B. Librovich, and G. M. Makhviladze, *Mathematical Theory of Combustion and Explosion*, Plenum, New York, 1985.
5. Maex, K. and M. van Rossum, Editors, *Properties of Metal Silicides*, INSPEC, London, 1995.
6. Murarka, S. P., *Silicides for VLSI Applications*, 104–105, Academic Press, New York, 1983.

Size-effects on Optical Properties of Asymmetric Plasmonic Nanodisk Trimer

Masoud Ahmadsimab and Tavakol Pakizeh
Faculty of Electrical and Computer Engineering, K. N. Toosi University of Technology, Tehran 16314, Iran

Abstract— We present the size and configuration effects on optical properties of an asymmetric nanodisk (Ag) trimer based on dipole interaction model and numerical calculations. The structure made of three Ag nanodisks of the diameter $D = 100\,\text{nm}$ and thickness $T = 25\,\text{nm}$. Opposite to the symmetric structure composed of such nanodisks the asymmetric structure has a new mode in its optical extinction spectrum occurring between the two modes described for the symmetric structure. The properties of this new mode remarkably affects by the size and also by the asymmetric configuration of the structure. We apply theoretical analysis of coupled dipole approximation (CDA) to compare the symmetric and asymmetric optical properties of such structure. The results of theoretical method compared with the numerical simulations.

1. INTRODUCTION

Optical properties of nanostructures composed of interacting nanoparticle clusters such as trimers and quadrumers are of great interest to design plasmonic systems [1]. The capability of plasmonic nanoparticles resulted from supporting localized oscillations of surface plasmons known as LSPR [2] caused various optical properties of nanostructures (e.g., applications such as plasmonic sensing) [3–5]. The resonance frequencies of the LSPRs strongly depend on the size, shape and the surrounding dielectrics [6, 11, 12]. More over the interactions between the modes of the plasmonic systems is highly affected by the configurations of the nanostructures. Such interactions also leads to a large field enhancement. Symmetry breaking through the structures can cause to excite a new interacting mode in the systems [3, 4]. In previous studies [8, 9] on plasmonic trimers and quadrumers the group theory used as a powerful tool to describe and investigate the plamonic properties of the symmetric structures. In this paper we use couple dipole approximation [10] as a theoretical method to investigate the properties of the new interacting mode in the asymmetric configurations of the silver nanodisk trimer. Thus we assume that each nanodisk as an oblate spheroid which is described with the electrostatic polarizability [11]. The numerical simulations utilize to compare with the theoretical calculations. The asymmetry make such that $r_1 = r_2 = D + 10\,\text{nm}$ and the size of the disks increased with the aspect ratio keep constant ($D/T = 4$). The configuration of the nanostructure schematically shown in Fig. 1 below.

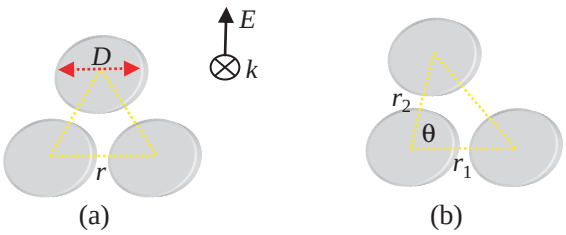

Figure 1: (a) Schematic of symmetric trimer composed of three nanodisk placed on the vertexes of an equilateral triangle. The diameter of the disks is $D = 100\,\text{nm}$ and thickness $T = 25\,\text{nm}$. (b) The asymmetric trimer which made through structure such that the distances $r_1 = r_2 = D + 10\,\text{nm}$ and the angle $\theta = 70°$. The incident field illuminated aligned along the base of trimers and polarization of the field is along the major principal axis of the nanodisks.

2. THEORY AND ANALYSIS

The coupled dipole approximation approach consider a nanoparticle placed in a medium which there exist an electric field E as a polarizable dipole. Each nanoparticle would be assumed as a dipole moment in response to the local electric field. Therefore each nanodisk illuminated by the electric field E could be replaced with an interacting dipole with the polarizability P. It has demonstrated

that the polarizability of an spheroid with the polarization of the applied field parallel to one of its principal axis is [11]

$$\alpha(\omega) = 4\pi abc \frac{\varepsilon(\omega) - \varepsilon_m}{3\varepsilon(\omega) + 3L(\varepsilon(\omega) - \varepsilon_m)} \tag{1}$$

which a, b and c are the principal axis of the spheroid and $\varepsilon(\omega)$, ε_m are the permittivities of the nanoparticles and the local host of the medium, respectively. The geometrical factor L is related to the axis of the spheroid and can be calculated due to the aspect ratio of the nanoparticle. In order to obtain more accurate results in this method specially in the case of some larger particles it is necessary to apply some modifications on the polarizability known as modified long wavelength approximation (MLWA) [6]. In this treatment the radiation damping of the induced dipole of larger particles that effects on the spectrum linewidth and resonance wavelength will be considered. The spontaneous emission of the induced dipole of larger particles leads to broaden the linewidth of the spectrum. The depolarization factor made through changing the aspect ratio of the particles by increasing the size, cause to LSPR resonances shifts to longer wavelengths. Each induced dipole moment caused by the interaction between nanoparticle with the incident field E would be:

$$P_i = \alpha_i \cdot E_i(r_i) \tag{2}$$

the incident field for a single particle considered as sum of the incident field and the scattered field of interacting other dipoles. Thus the major pure incident field of the nanoparticles is

$$E_i(r_i) = E_0 \exp(ik \cdot r) - \sum_{i \neq j} A_{ij} P_j \tag{3}$$

the E_0 and k are the amplitude and wave vector of the incident field and the interaction terms are of form:

$$A_{ij}P_{ji} = \frac{\exp(ikr_{ij})}{r_{ij}^3} \times \left\{ k^2 r_{ij} \times (r_{ij} \times P_j) + \frac{(1 - ikr_{ij})}{r_{ij}^2} \left(r_{ij}^2 P_j - 3r_{ij}(r_{ij} \cdot P_j) \right) \right\} \tag{4}$$

The extinction cross section of the particle can be calculated from:

$$C_{ext} = k\mathrm{Im}\{\alpha\} \tag{5}$$

where the $k = 2\pi/\lambda$ is the wave number. In order to develop calculation results in good agreement with the exact solution the MLWA approximation used by considering the expression [6]:

$$F = \left(1 - \frac{2}{3} ik^3 \alpha - \frac{k^2}{b} \alpha \right)^{-1} \tag{6}$$

3. RESULTS AND DISCUSSIONS

In this paper, we apply the CDA method to calculate the extinction spectrum for the single nanodisk, symmetric and the asymmetric trimer composed of nanodisks with the diameter $D = 40\,\mathrm{nm}$ and thickness $T = 20\,\mathrm{nm}$. The dielectric function of the nanodisks used in the theoretical and numerical calculations obtained from the curved fitted of the experimental data [7]. The nanodisks are small in corresponding to quasi-static consideration, thus the calculations based on the theoretical results are compatible with the numerical calculations as it is shown in Fig. 2. Fig. 2(a) demonstrates that the theoretical calculation correspond to symmetric, the blue curve, exhibits two hybridized mode to the red and the blue of the single resonance [8]. The black curve in Fig. 2(b) shows another mode which is resulted from breaking the symmetry of the structure.

Figure 3 demonstrate that by increasing the size of the nanoparticles this active new mode separate and occur in between the two mode of the symmetric case. The asymmetry made through the structure in a way that the two distances r_1 and r_2 are equal and the aspect ratio keep constant ($D/T = 4$). Fig. 3(b) shows the numerical simulation of the asymmetric structure of the increasing diameter from $D = 60\,\mathrm{nm}$ to $120\,\mathrm{nm}$. By increasing the size of the disks the interactions becomes stronger and thus the peaks are shifting to a longer wavelength in theoretical and numerical calculation of Figs. 3(a) and (b). The MLWA modification considered in the theoretical calculation results in a better agreement between the CDA method and the numerical simulation.

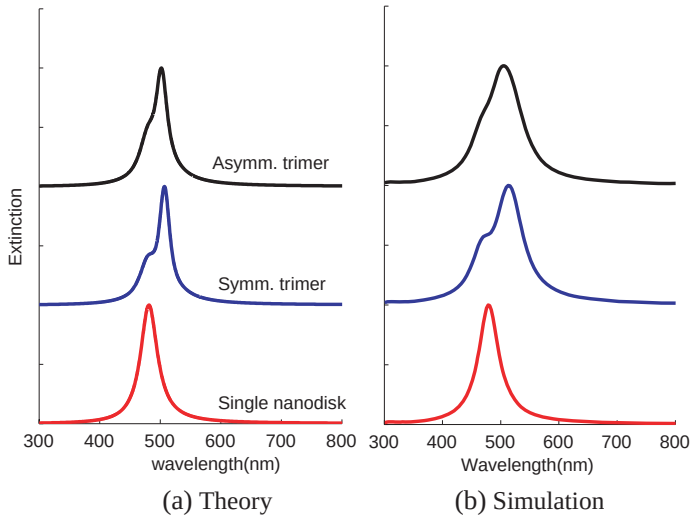

Figure 2: (a) Theoretical calculation based on CDA method obtaine for a single Ag nanodisk and symmetric equilateral trimer and an asymmetric trimer for small nanodisks of diameter $D = 40\,\text{nm}$ and thickness $T = 20\,\text{nm}$. (b) The numerical simulation results.

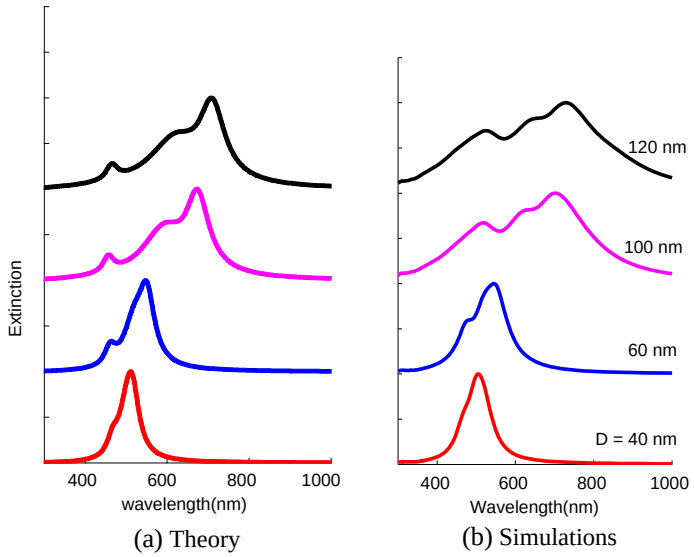

Figure 3: ((a) Theoretical calculations of the extinction spectrum of the asymmetric trimer. As the size of the nanodisks increased from $D = 40\,\text{nm}$ to $120\,\text{nm}$ the interaction of the particles become stronger and therefore the resonance of the two modes of the structure shifts to longer wavelength. (b) The numerical simulation results.

4. SUMMARY

This paper investigates the effects of the size and configuration on optical properties of nanodisk Ag trimer based on coupled dipole approximation (CDA). It analyses the interaction between the nanoparticles arranged in a symmetric and asymmetric trimer. The size effects of the asymmetric trimer on the interactions between the hybridized modes investigated both by numerical simulations and CDA method. The results obtained from CDA method is compatible with the numerical simulations due to the consideration of MLWA modifications.

REFERENCES

1. Fan, J. A., K. Bao, C. Wu, J. Bao, R. Bardhan, N. J. Halas, V. N. Manoharan, G. Shevets, P. Nordlander, and F. Capasso, "Fano-like interference in self-assembled plasmonic quadrumer clusters," *Nano Lett.*, Vol. 10, 4680–4685, 2010.
2. Bakker, R. M., H. Yuan, Z. Liu, V. P. Drache, A. V. Kildishev, and V. M. Shalaev, "Enhanced localized fluorescence in plasmonic nanoantenna," *App. Phys. Lett.*, Vol. 92, 043101, 2008.

3. Hao, F., Y. Sonnefraud, P. V. Dorpe, S. A. Maier, N. J. Halas, and P. Nordlander, "Symmetry breaking in plasmonic nanocavities: Subradiant LSPR sensing and tunable fano resonance," *Nano Lett.*, Vol. 8, 3983–3988, 2008.
4. Mukherjee, S., H. Sobhani, J. B. Lassiter, R. Bardhan, P. Nordlander, and N. J. Halas, "Fanoshells: Nanoparticles with built-in fano resonances," *Nano Lett.*, Vol. 10, 2694–2701, 2010.
5. Liu, N., T. Wiess, M. Mesch, L. Languth, U. Eigenthaler, M. Hirscher, C. Sönnichsen, and H. Giessen, "Planar metamaterial analogue of electromagnetically induced transparency for plasmonic sensing," *Nano Lett.*, Vol. 10, 1103–1107, 2010.
6. Kelley, L. K., E. Coronado, L. L. Zhao, and C. G. Schatz, "The optical properties of metal nanoparticles: The influence of size, shape and dielectric environment," *J. Phys. Chem. B*, Vol. 107, 668–677, 2003.
7. Palik, E., *Handbook of Optical Constants of Solids*, Academic Press, San Diego, CA, 1998.
8. Alegret, J., T. Rindzevicius, T. Pakizeh, Y. Alaverdyan, L. Gunnarsson, and M. Käll, "Plasmonic properties of silver trimers with trigonal symmetry fabricated by electron-beam litography," *J. Phys. Chem. C*, Vol. 112, 14313–14317, 2008.
9. Brandl, D. W., N. A. Mirin, and P. Nordlander, "Plasmon modes of nanosphere trimers and quadrumers," *J. Phys. Chem. C*, Vol. 110, 12302–12310, 2006.
10. Chaumet, P. C., K. Belkebir, and A. Rahmani, "Coupled-dipole method in time domain," *Optics Express*, Vol. 16, 20157–20165, 2008.
11. Bohrn, C. F. and D. R. Huffman, *Absorbtion and Scattering of Light by Small Particles*, Wiley, New York, 1983.
12. Novotny, L. and B. Hecht, *Principles of Nano-optics*, Cambridge University Press, UK, 2006.

Grounding Grid Safety Evaluation under Lightning Current

Farhan Hanaffi[1,2], **Wah Hoon Siew**[1], **and Igor Timoshkin**[1]

[1]University of Strathclyde, UK
[2]Universiti Teknikal Malaysia Melaka, Malaysia

Abstract— This paper presents a study about hazards that could occur when lightning currents flow through a ground-grid. Behaviour of a ground-grid when subjected to power-frequency fault currents is well studied and probably well understood. However, the behaviour of the ground-grid when subjected to transient currents is less well understood. The objective, therefore, is to provide better understanding of the behaviour of a ground-grid when excited by transient voltages and currents. The study is based on the energy transfer to a human body arising from step voltages on the surface of soil. Four different scenarios are considered to simulate different coordination of human feet. Finite Element Method (FEM) is used to solve exact Maxwell equation for modelling the grounding behaviour under lightning current. The grounding system was modelled in 3D.

1. INTRODUCTION

Grounding systems play an important role in protecting life or facilities from any fault or transients in a power system. The main purpose of a grounding system is to provide the lowest impedance path for transient currents especially lightning current of high magnitude and which has high frequency components. Behaviour of grounding under 50Hz/60Hz application is well understood [1]. However, under transient lightning currents, the ground reactance and the high frequency components of the lightning current may increase the value of step and touch voltage of the grounding grid. No Standards give detailed guidelines to design a grounding grid to consider transient and lightning current [2]. Therefore it is important to evaluate the safe threshold required under lightning current flow.

Electrical current flow through a human body is an important element to consider when considering safety of an electrical system. Duration, magnitude, and frequency components of current; and body weight influence the amount of current that can safely flow through a human body. The current flow through a human body may cause respiratory problem, ventricular fibrillation, cardiac fibrillation, muscular contraction and burn [3, 4]. Currently, there is very limited knowledge on safety limit for impulse current on human body.

In order to simulate and analyse the response of a ground-grid under lightning current, many researchers have developed their own models. Those models were based on circuit approach [5, 6], transmission line approach [7, 8] or electromagnetic theory approach [9, 10]. Circuit analysis is the most simple and easily observable method, but it cannot predict surge propagation delay On the other hand, the disadvantage of the transmission line method is that it is limited to a certain frequency thus making it less accurate to evaluate injected current with fast rise-times [11]. The electromagnetic theory approach makes less assumptions by solving Maxwell's equations but requires more computational time for a complex structure.

In this paper, the finite element method (FEM) is proposed to model and analyse the ground-grid's behavior under lightning current. FEM was chosen because it is necessary to model in 3D and to run time-domain simulations. COMSOL Multiphysics is an application package that is proven and tested by many researchers and it was also used by the authors. Results of this paper are compared with previous modeling method for validity. The method is applied to calculate ground potential rise due to lightning current and to evaluate safety limit on human based on energy flow through a human body. Four scenarios are considered in this study with different coordination of step voltages.

2. SAFETY THRESDHOLD

Base on electrocution experiment on animal using power frequency current, Dalziel [12] concluded that an impulse current with energy of 50 J is a safe limit. Bio-electromagnetic groups suggest that the absorbtion of 10 to 50 joules by a human body is the range of values that can cause ventricular fibrillation [13]. Energy that flows through a body is calculated using Equation (1) with an assumed

voltage applied directly from foot to foot with no other insulation.

$$Energy(J) = \frac{1}{R_b}\sum_{1}^{n}[V_n(t)]^2\Delta t \tag{1}$$

where R_b is body resistance which is assumed to be $1000\,\Omega$, n is the total number of voltage transients, V_n is voltage between the two feet and Δt is sample period.

3. FINITE ELEMENT METHOD (FEM) MODELING

The Finite Element Method (FEM) solves differential or integral equations by discretising the volume-space (usually with triangular vertices) and applying the governing equations to the surfaces defined by these points before solving the resultant matrices. The analysis using FEM generally involves four steps:

i. Discretization of the geometry to sub-region or element (meshing) typically triangular or tetrahedron.
ii. Attainment of the field equation as Governing equation in surface of element.
iii. Assembly of all the elements in the solution region by matrices.
iv. Solve the matrices obtained.

Nekhoul et al. [14] divides the grounding system into three domains, namely low conducting medium (soil), conducting media (conductors) and non-conducting media. Each domain is formulated using the magnetic vector potential (A) and scalar potential (V). M. Trlep et al. [15] solves Poisson equation by applying Galerkin's formulation of FEM and models the grounding conductors in 1D coupled with 3D soil model to improve simulation time. Q. Lei [16] uses the complex conductivity ($\sigma + j\omega\epsilon$) to consider frequency effect on ground-grid modelling. All previous FEM solutions assumed quasi static conditions in their simulations. As reported in [17, 18] the quasi static assumption resulted in the under-estimation of the step voltageat high frequency. Therefore, in the attempt to overcome this limitation, the wave Equation (2) is used as the governing equation to solve Maxwell's equations in this paper.

$$\nabla \times \mu_r^{-1}(\nabla \times A) + \sigma\mu_0\frac{\partial A}{\partial t} + \mu_0\frac{\partial}{\partial t}\left(\varepsilon_0\varepsilon_r\frac{\partial A}{\partial t}\right) = 0 \tag{2}$$

4. VALIDATION OF MODEL

Single horizontal grounding conductor and $10\,\text{m} \times 10\,\text{m}$ grounding grid are simulated to verify the numerical modelling used in this research. Single horizontal grounding with the radius of the copper conductor at 7.5 mm and the length at 20 m is used in this model. The conductor is buried 0.5 m in the soil with permittivity $\varepsilon_r = 50$ and soil resistivity $\rho = 100\,\Omega\cdot\text{m}$. Illustration of the configuration is shown in Figure 1.

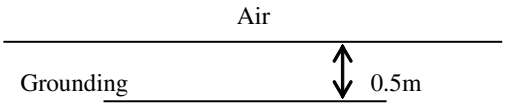

Figure 1: Illustration of horizontal grounding system.

Two different current impulses are injected into the conductor with 10 KA 1/5 µs as fast rise impulse and 100 KA 10/100 µs as slow rise impulse. As shown in Figures 2 and 3 the results are comparable with published results in [8, 10].

Another simulation was done with $10\,\text{m} \times 10\,\text{m}$ grounding grid with radius of conductor at 7 mm, the grid is buried 0.5 m in the soil with permittivity $\varepsilon_r = 9$ and soil resistivity $\rho = 1000\,\Omega\cdot\text{m}$. In this simulation, an impulse current with waveshape 0.36/26.8 µs was injected through a corner of the grid. All these parameters are identical to those in [8, 10], to allow comparisons. Figure 4 shows the transient voltage at the injected point. The result shows the injected voltage value is comparable with results from other simulations that use Method of Moment (MOM) and Transmission line method (TLM) [8, 9].

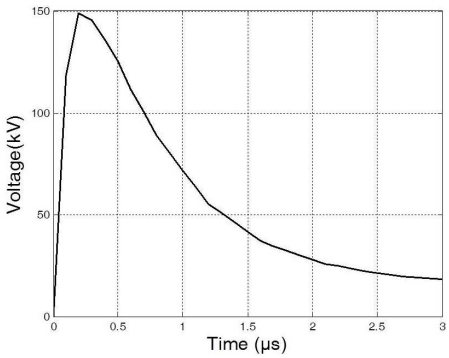

Figure 2: Transient voltage at injected point of 1/5 μs impulse current.

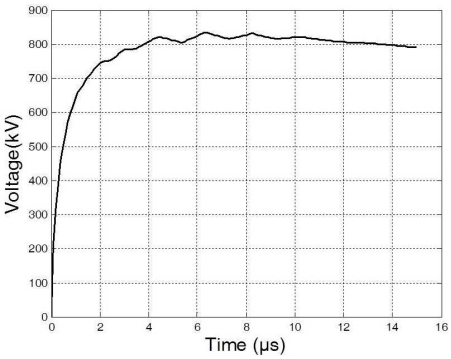

Figure 3: Transient voltage at injected point of 10/100 μs impulse current

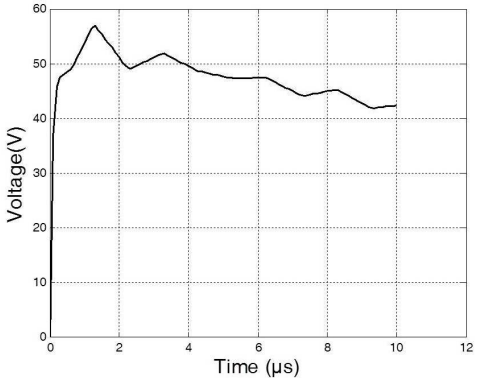

Figure 4: Transient voltage at injected point.

5. RESULTS AND DISCUSSIONS

In order to evaluate the safety level of grounding grid under lightning current, four different scenarios A, B, C and D are considered in this study as shown in Figure 5. Every scenario presents the step voltage as the voltage between two points that are 1 m apart.

These studies considered 200 KA 1.2/50 μs as the lightning current injected at the corner of the gid. Soil resistivity was $1000\,\Omega\cdot\mathrm{m}$, $\varepsilon_r = 9$ and $\mu_r = 1$. The grid consisted of $5\,\mathrm{m}\times 5\,\mathrm{m}\times 4$ of $50\,\mathrm{mm}^2$ coper conductors and buried 0.5 m below the soil. Step voltages were computed at the surface of the soil.

Step voltages for every scenario are presented in Figure 6. It shows the step voltage have different maximum value depending on the coordination of a human's feet. The scenarios for foot coordination that is parallel with the grounding conductor give lower step voltages. The step voltages are in general agreement with values published in [19].

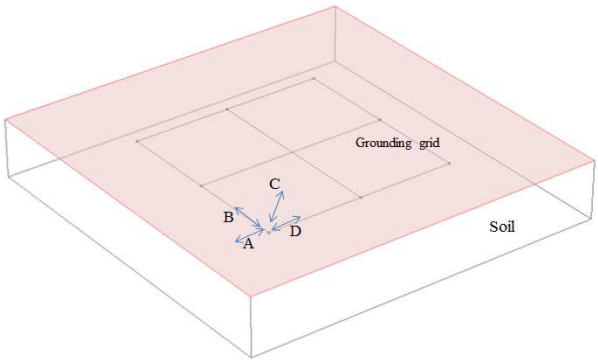

Figure 5: Grounding system considered in the simulation.

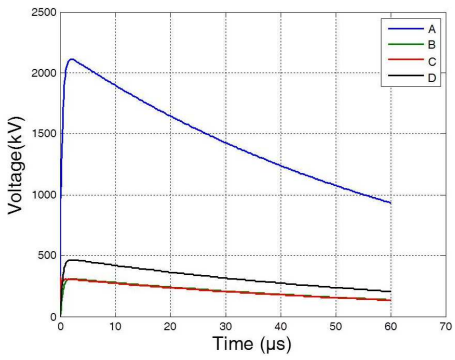

Figure 6: Step voltage for different case.

In order to evaluate the safety or otherwise of these voltages, the energy of these step voltage were calculated. Equation (1) was used with an assumed body resistance of 1000 Ω. Table 1 shows the energy that would flow through a human body for different scenarios and without scaling down the magnitude of the step voltage, which was obtained using a current of 200 kA peak. Based on the safety threshold, the entire scenario A is not safe because it exceeded 50 J as proposed by Dalziel. The results presented are preliminary results and further investigations are needed to improve the accuracy of the model in order to evaluate step voltages.

Table 1: Energy for different location of step voltage.

Scenario	Energy (kJ)
A	135.33
B	2.903
C	2.835
D	6.5923

6. CONCLUSION

This paper presented the simulation results based on the solution of Maxwell's equations using the Finite Element Method. Validation of the method showed good agreement with published results.

There is very limited study on safety threshold for human on impulse current. This preliminary study analysed four scenarios to simulate different coordinations between two feet. Simulation results show the feet coordination during a lightning discharge to ground can be a safety risk to human.

These preliminary results would be checked with experimental-model results and future study will consider the influence of soil properties and lightning parameters.

ACKNOWLEDGMENT

The authors gratefully acknowledge Ministry of Higher Education, Malaysia and Universiti Teknikal Malaysia Melaka for the postgraduate scholarship awarded during the development of this research.

REFERENCES

1. "IEEE guide for safety in AC substation grounding," IEEE Std 80-2000, i-192, 2000.
2. Griffiths, H., A. Haddad, and N. Harid, "Characterisation of earthing systems under high frequency and transient conditions," *39th International Universities Power Engineering Conference, UPEC*, Vol. 1, 188–192, 2004,
3. Cooray, V., C. Cooray, and C. J. Andrews, "Lightning caused injuries in humans," *Journal of Electrostatics*, Vol. 65, 386–394, 2007.
4. Golde, R. H. and W. R. Lee, "Death by lightning," *Proceedings of the Institution of Electrical Engineers*, Vol. 123, 1163–1180, 1976.
5. Ramamoorty, M., M. M. B. Narayanan, S. Parameswaran, and D. Mukhedkar, "Transient performance of grounding grids," *IEEE Transactions on Power Delivery*, Vol. 4, 2053–2059, 1989.
6. Mattos, M. A. F., "Grounding grids transient simulation," *IEEE Transactions on Power Delivery*, Vol. 20, 1370–1378, 2005.
7. Lorentzou, M. I., N. D. Hatziargyriou, and B. C. Papadias, "Time domain analysis of grounding electrodes impulse response," *IEEE Transactions on Power Delivery*, Vol. 18, 517–524, 2003.
8. Yaqing, L., N. Theethayi, and R. Thottappillil, "An engineering model for transient analysis of grounding system under lightning strikes: Nonuniform transmission-line approach," *IEEE Transactions on Power Delivery*, Vol. 20, 722–730, 2005.
9. Xiong, W. and F. P. Dawalibi, "Transient performance of substation grounding systems subjected to lightning and similar surge currents," *IEEE Transactions on Power Delivery*, Vol. 9, 1412–1420, 1994.
10. Grcev, L. D. and M. Heimbach, "Frequency dependent and transient characteristics of substation grounding systems," *IEEE Transactions on Power Delivery*, Vol. 12, 172–178, 1997.
11. Grcev, L., "Time- and frequency-dependent lightning surge characteristics of grounding electrodes," *IEEE Transactions on Power Delivery*, Vol. 24, 2186–2196, 2009.

12. Dalziel, C. F., "A study of the hazards of impulse currents," *Power Apparatus and Systems, Part III. Transactions of the American Institute of Electrical Engineers*, Vol. 72, 1032–1043, 1953.
13. Bernstein, T., "Effects of electricity and lightning on man and animals," *Journal of Forensic Science*, Vol. 18, Jan. 1973.
14. Nekhoul, B., C. Guerin, P. Labie, G. Meunier, R. Feuillet, and X. Brunotte, "A finite element method for calculating the electromagnetic fields generated by substation grounding systems," *IEEE Transactions on Magnetics*, Vol. 31, 2150–2153, 1995.
15. Trlep, M., A. Hamler, and B. Hribernik, "The analysis of complex grounding systems by FEM," *IEEE Transactions on Magnetics*, Vol. 34, 2521–2524, 1998.
16. Lei, Q., C. Xiang, Z. Zhibin, and L. Huiqi, "Grounding performance analysis of the substation grounding grids by finite element method in frequency domain," *IEEE Transactions on Magnetics*, Vol. 43, 1181–1184, 2007.
17. Olsen, R. G. and M. C. Willis, "A comparison of exact and quasi-static methods for evaluating grounding systems at high frequencies," *IEEE Transactions on Power Delivery*, Vol. 11, 1071–1081, 1996.
18. Grcev, L. and S. Grceva, "Comparison between exact and quasi-static methods for HF analysis of horizontal buried wires," *IEEE Transactions on Electromagnetic Compatibility*, Vol. 51, 1051–1054, 2009.
19. Gazzana, D. S., A. S. Bretas, M. Telló, D. W. P. Thomas, and C. Christopoulos, "Contribution to the study of human safety against lightning considering the grounding system influence and the variations of the associated parameters," *International Conference of Lightning Protection*, 1–5, Vienna, 2012.

Spontaneous Emission Enhancement at Finite-length Metal Nanowires

K. Filonenko[1], **M. Willatzen**[2], **and V. Bordo**[1]

[1]NanoSyd, Mads Clausen Institute, Syddansk Universitet, Alsion 2, DK-6400 Sønderborg, Denmark
[2]Department of Photonics Engineering, Technical University of Denmark
DTU Fotonik, Building 345 West, DK-2800 Kongens Lyngby, Denmark

Abstract— We study spontaneous emission enhancement of a two-level atomic emitter placed in a dielectric medium near a finite-length cylindrical metal nanowire. We calculate the dependence of the Purcell factor and the normalized decay rate to a continuous spectrum on the nanowire radius for several emitter transition wavelengths and different orientations of the transition dipole moment. For a particular transition wavelength we calculate the dependence of these quantities as well as the β-factor on the emitter distance from the nanowire and the nanowire radius. The obtained results demonstrate that the spontaneous emission characteristics exhibit significant differences as compared to the case of an infinite wire.

1. INTRODUCTION

Recently, growing attention has been focused on control over spontaneous emission of quantum emitters coupled to metal nanowires [1–10]. Such a system is not only of fundamental importance but also promises various applications, including single-plasmon sources [3], single-photon transistors [11], plasmonic amplifiers [12] and resonators [10], and nanowire-based spasers [13].

The conventional theoretical model which is used to calculate the emitter decay rate assumes that a metal nanowire has a cylindrical shape and is infinite in its axial dimension. Such an approach does not allow to describe the reflections from the nanowire end facets and hence the modes of the plasmonic nanocavity. In this paper, we overcome this drawback by applying a rigorous approach developed in Refs. [15, 16] which gives the dyadic Green's function for a cylindrical nanocavity. We demonstrate that taking into account finiteness of the nanowire length leads to considerably different results for the Purcell and β-factors as compared to the infinite-length approximation.

2. DEFINITIONS

The total spontaneous emission rate of an emitter in the presence of a cavity can be represented as a sum of different contributions:

$$\gamma^{\mathrm{tot}} = \sum_k \gamma^k + \gamma^{\mathrm{cs}}, \tag{1}$$

where γ^k is the decay rate to k-th discrete mode of the cavity and γ^{cs} is the decay rate to a continuous spectrum of modes. The corresponding normalized decay rates are then connected through

$$\frac{\gamma^{\mathrm{tot}}}{\gamma^0} = \sum_k F_p^k + \frac{\gamma^{\mathrm{cs}}}{\gamma^0}, \tag{2}$$

where γ^0 denotes the decay rate in an unbounded medium and

$$F_p^k = \frac{\gamma^k}{\gamma^0} \tag{3}$$

is the Purcell factor for the k-th discrete mode. The ratio

$$F_\beta^k = \frac{\gamma^k}{\gamma^{\mathrm{tot}}} = \frac{F_p^k}{\gamma^{\mathrm{tot}}/\gamma^0} \tag{4}$$

is called the β-factor and is extensively used in cavity quantum electrodynamics.

In this paper, we calculate the Purcell and β-factors for a dipole emitter located in the vicinity of a silver nanowire associated with the nanowire fundamental mode TM0. We compare the contributions of both discrete and continuous spectrum modes to the total normalized rate (2) for different orientations of the emitter dipole moment.

3. THEORETICAL MODEL

The nanowire is modeled by a silver cylinder of radius a, length L, and a wavelength-dependent dielectric permittivity $\epsilon_2(\lambda)$, which is found as an interpolation of the data for complex refractive index given in [17]. We use the approximation of an elongated nanowire [15], assuming that the length of the wire is much greater than its radius: $L \gg a$. A two-level quantum emitter with transition frequency ω, the corresponding wavelength $\lambda = (2\pi c)/\omega$ and the dipole momentum $\vec{\mu}$ is placed in the outer medium with constant permittivity $\epsilon_1 = 2$ at a distance d from the wire as is shown in Figure 1(a). We consider the radii in the range 10–50 nm and the emitter transition wavelengths in the range 500–1250 nm. In these ranges a silver nanowire supports two surface plasmon polariton modes: a transverse magnetic mode TM0 and a hybrid mode HE1. All other modes are cut off at higher radius values and therefore do not contribute to the total spontaneous emission rate in the considered range. Although the HE1 mode does not have a cutoff radius as all other higher order modes, it was shown in [2] that its mode volume grows exponentially as the wire radius gets smaller and therefore the mode is effectively cut off at very small radius values considered here. We therefore limit ourselves to a single-mode regime and calculate the dependence of the longitudinal wavenumber β on the radius a (Figure 1(b)) for several transition wavelengths ($\lambda = 500$ nm, 750 nm, 1000 nm and 1250 nm).

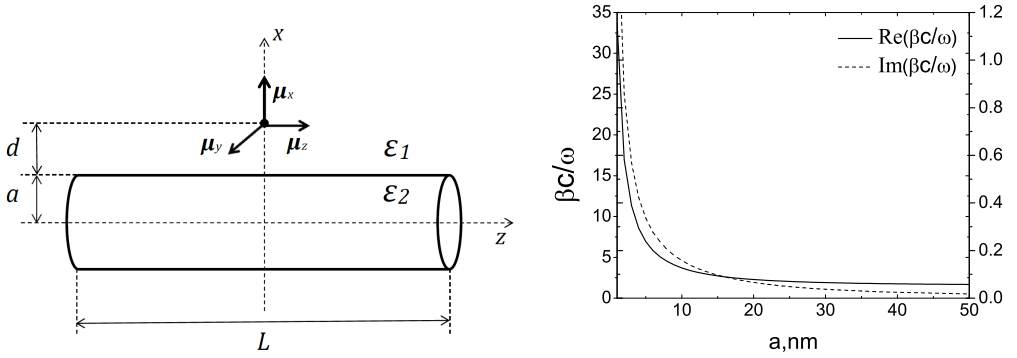

Figure 1: The model of the system: (a) Scheme showing the metallic wire and the orientations of the emitter along the axes of the rectangular coordinate system μ_x, μ_y, μ_z, (b) TM0 mode dispersion: real part of the normalized longitudinal wavenumber (left axis) and its imaginary part (right axis) as a function of the nanowire radius.

The electromagnetic field is described in terms of the electric and magnetic Hertz potentials, $\mathbf{\Pi}^e$ and $\mathbf{\Pi}^m$, satisfying the Helmholtz equations inside ($j = 2$) and outside ($j = 1$) the cylinder:

$$\nabla^2\mathbf{\Pi}^e(\mathbf{R}) + k_j^2\mathbf{\Pi}^e(\mathbf{R}) = -\frac{4\pi}{\epsilon_j}\mathbf{P}_j(\mathbf{R}), \tag{5}$$

$$\nabla^2\mathbf{\Pi}^m(\mathbf{R}) + k_j^2\mathbf{\Pi}^m(\mathbf{R}) = 0, \tag{6}$$

where $\mathbf{P}_j = \vec{\mu}\delta_{1j}\delta(\mathbf{R} - \mathbf{R}_0)$ is the electric polarization density of the external source, δ_{ij} is a Kronecker delta, $\delta(\mathbf{R} - \mathbf{R}_0)$ is Dirac's delta function centered at the position of the emitter, $\mathbf{R}_0$, and $k_j = (2\pi/\lambda)\sqrt{\epsilon_j(\lambda)}$ is the modulus of the wave vector in the medium with index $j \in \{1, 2\}$. The solutions to these equations dictate the electric and magnetic fields in both media [18]. In the next section, we calculate and plot different contributions to the normalized decay rate (2) and the β-factor using the relation [19]

$$\gamma^{\text{tot}} = \frac{2}{\hbar}\sum_{\alpha\beta}\mu_\alpha\mu_\beta \text{Im}\bar{\mathbf{G}}_{\alpha\beta}(\mathbf{R}, \mathbf{R}_0; \beta(a)), \tag{7}$$

where $\bar{\mathbf{G}}_{\alpha\beta}(\mathbf{R}, \mathbf{R}_0; \beta(a))$ are the rectangular components of the dyadic Green function of the system which was derived in [16] to describe the finite-length cylinder geometry.

4. RESULTS AND DISCUSSION

The rigorous analysis based on the theory developed in [16] allows one to make the following conclusions about the spontaneous emission to the TM0 mode in the limit $L \gg a$: (1) the Purcell

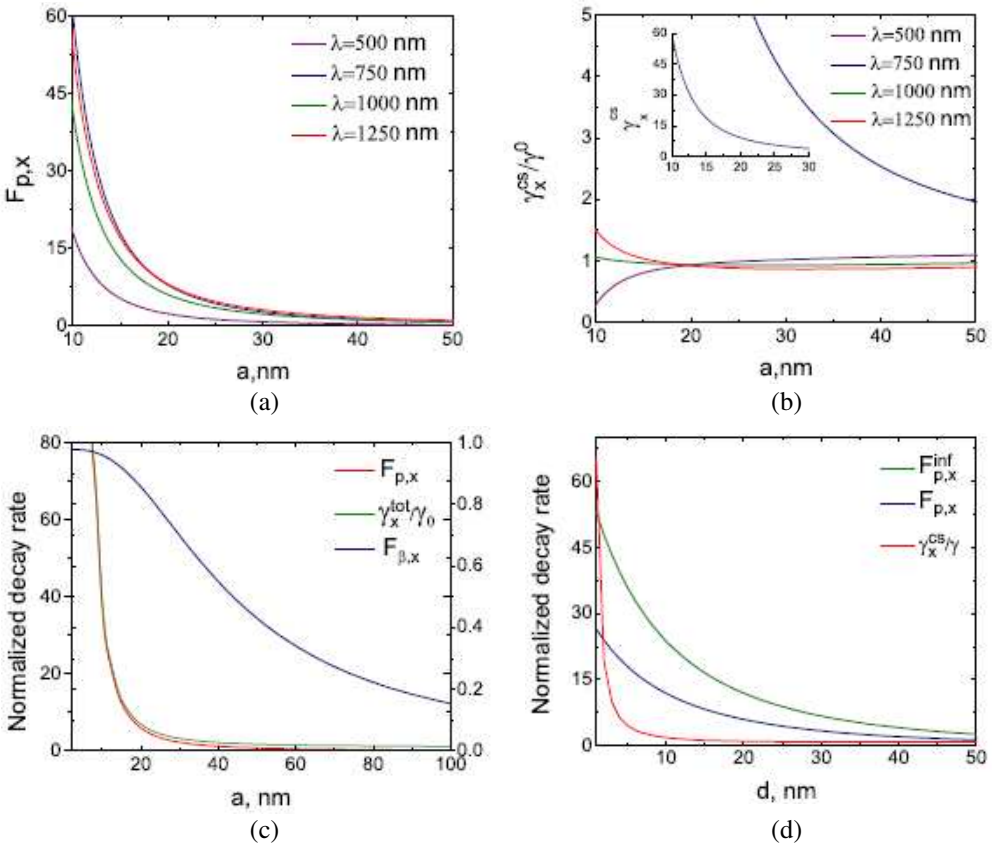

Figure 2: Normalized decay rates for a x-oriented dipole emitter: (a) the Purcell factor and (b) the normalized decay rate to a continuous spectrum plotted as a function of the nanowire radius for several emitter wavelengths λ with the emitter-wire distance taken as $d = a$, (c) the Purcell factor (red curve, left axis), the decay rate to a continuous spectrum (green curve, left axis), and the β-factor (blue curve, right axis) as a function of the radius a with $d = a$, $\lambda = 1\,\mu\text{m}$ and $\epsilon_2 = -50 + 8.5i$, (d) the Purcell factor in the limit of an infinite nanowire (green curve), the Purcell factor in the limit of an elongated nanowire (blue curve) and the decay rate to a continuous spectrum (red curve) as a function of the emitter-wire distance d with $a = 25\,\text{nm}$, $\lambda = 1\,\mu\text{m}$, $\epsilon_2 = -50 + 8.5i$.

factor for this mode does not depend on the length of the wire and the position of the emitter along the z-axis; (2) the mode is not excited if the dipole moment of the emitter is oriented along the y-axis. The first of these facts is in agreement with the statement, proved in [20, 21] for a semi-infinite wire, that the far-field reflection coefficient from the end facets for such a mode is equal to zero. As a consequence the mode does not have a Fabry-Perot-like structure.

We plot the normalized decay rates for the x-orientation of the emitter transition dipole moment $\vec{\mu}$ in Figure 2 as a function of the wire radius and the wire-emitter distance. Analogous results for z-orientation are similar and are not shown here. These plots give rather high Purcell factor values signifying effective excitation of the surface plasmon polariton mode. The dependence of the Purcell factor on the nanowire radius is calculated for several transition wavelengths and is represented in Figures 2(a) and 2(b). The distance changes along with radius as $d = a$. These figures show that in some range of parameters the decay to the TM0 mode dominates over the other decay channels. This takes place for all radii below a certain value which for $\lambda = 500\,\text{nm}$, 750 nm, 1000 nm, and 1250 nm is equal to 27 nm, 11 nm, 45 nm, and 53 nm, respectively, for the x-orientation of the transition dipole moment and to 37 nm, 50 nm, 33 nm, and 31 nm for the z-orientation. For larger radii the other decay channels start to dominate. For example, in the case of the x-orientation and for $\lambda = 750\,\text{nm}$ the normalized decay rate to the continuous spectrum is greater than the Purcell factor over the whole relevant range starting from 11 nm (blue curve in Figures 2(a) and 2(b)). This can be changed, however, by placing an emitter closer to the wire because, as is seen from Figure 2(d), the Purcell factor increases with decreasing distance.

In Figure 2(c) the Purcell factor (red curve) is compared with the total decay rate (2) (green

curve) for $\lambda = 1\,\mu$m depending on the nanowire radius. These quantities appear to be very close to each other for small radius values. Correspondingly, the β-factor plotted in the same figures (blue curve) approaches unity as the wire radius gets smaller. This makes the TM0 mode suitable for utilizing in a nanowire-based spaser. In Figure 2(d) we compare the Purcell factor calculated in the approximation of elongated nanowire (blue curve) with the one calculated in Ref. [7] in the limit of an infinite nanowire (green curve). It is found that these quantities differ by a factor of two in the whole range of the wire-emitter distance, d. This means that the infinite wire approximation largely overestimates the Purcell factor and is not at all accurate, at least for the problem under consideration.

5. CONCLUSION

The rigorous approach developed in Ref. [16] has enabled us to describe the spontaneous emission enhancement for a two-level quantum emitter in the vicinity of a finite-length cylindrical metal nanowire. We have calculated the Purcell and β-factors as well as the decay rate to the continuous spectrum of modes and plotted them as functions of the nanowire radius and the emitter-nanowire distance in the regime where a decay to a single surface plasmon polariton mode is essential. The Purcell and β-factors were found to be simultaneously maximal at extremely small radii and emitter-nanowire distances (below 30 nm which is much smaller than the half of the emission wavelength 500–1250 nm). This makes metal nanowires interesting for nanoscale spaser applications. The obtained results have been compared with the calculations in the approximation of an infinite nanowire. It is found that the infinite nanowire model largely overestimates the Purcell factor magnitude.

ACKNOWLEDGMENT

We are grateful to the Danish Council for Independent Research, Natural Sciences (FNU) for financial support ("Theory of Nanowire Plasmonic Lasers").

REFERENCES

1. Chang, D. E., A. S. Sørensen, P. R. Hemmer, and M. D. Lukin, "Quantum optics with surface plasmons," *Phys. Rev. Lett.*, Vol. 97, No. 5, 053002, 2006.
2. Chang, D. E., A. S. Sørensen, P. R. Hemmer, and M. D. Lukin, "Strong coupling of single emitters to surface plasmons," *Phys. Rev. B*, Vol. 76, No. 3, 035420, 2007.
3. Akimov, A. V., A. Mukherjee, C. L. Yu, D. E. Chang, A. S. Zibrov, P. R. Hemmer, H. Park, and M. D. Lukin, "Generation of single optical plasmons in metallic nanowires coupled to quantum dots," *Nature*, Vol. 450, No. 7168, 402, 2007.
4. Chen, G.-Y., Y.-N. Chen, and D.-S. Chuu, "Spontaneous emission of quantum dot excitons into surface plasmons in a nanowire," *Opt. Lett.*, Vol. 33, No. 19, 2212, 2008.
5. Chen, Y. N., G. Y. Chen, D. S. Chuu, and T. Brandes, "Quantum-dot exciton dynamics with a surface plasmon: Band-edge quantum optics," *Phys. Rev. A*, Vol. 79, No. 3, 033815, 2009.
6. Rukhlenko, I. D., D. Handapangoda, M. Premarante, A. F. Fedorov, A. V. Baranov, and C. Jagadish, "Spontaneous emission of guided polaritons by quantum dot coupled to metallic nanowire: Beyond the dipole approximation," *Opt. Express*, Vol. 17, No. 20, 17570, 2009.
7. Barthes, J., G. Colas des Francs, A. Bouhelier, J.-C. Weeber, and A. Dereux, "Purcell factor for a point-like dipolar emitter coupled to a two-dimensional plasmonic waveguide," *Phys. Rev. B*, Vol. 84, No. 7, 073403, 2011.
8. De Leon, N. P., B. J. Shields, C. L. Yu, D. E. Englund, A. V. Akimov, M. D. Lukin, and H. Park, "Tailoring light-matter interaction with a nanoscale plasmon resonator," *Phys. Rev. Lett.*, Vol. 108, No. 22, 226803, 2012.
9. Russell, K. J., T.-L. Liu, S. Cui, and E. L. Hu, "Large spontaneous emission enhancement in plasmonic nanocavities," *Nat. Photonics*, Vol. 6, No. 7, 2012.
10. Hümmer, T., F. J. García-Vidal, L. Martín-Moreno, and D. Zueco, "Weak and strong coupling regimes in plasmonic QED," *Phys. Rev. B*, Vol. 87, No. 11, 115419, 2013.
11. Chang, D. E., A. S. Sørensen, E. A. Demler, and M. D. Lukin, "A single-photon transistor using nanoscale surface plasmons," *Nat. Phys.*, Vol. 3, No. 11, 807, 2007.
12. Saleh, A. A. E., and J. A. Dionne, "Waveguides with a silver lining: Low threshold gain and giant modal gain in active cylindrical and coaxial plasmonic devices," *Phys. Rev. B*, Vol. 85, No. 4, 045407, 2012.

13. Liu, S.-Y., J. Li, F. Zhou, L. Gan, and Z.-Y. Li, "Efficient surface plasmon amplification from gain-assisted gold nanorods," *Opt. Lett.*, Vol. 36, No. 7, 1296, 2011.
14. Bordo, V. G., "*Ab initio* analytical model of light transmission through a cylindrical subwavelength hole in an optically thick film," *Phys. Rev. B*, Vol. 84, No. 7, 075465, 2011.
15. Bordo, V. G., "Model of Fabry-Pérot-type electromagnetic modes of a cylindrical nanowire," *Phys. Rev. B*, Vol. 81, No. 3, 035420, 2010.
16. Bordo, V., "Purcell factor for a cylindrical nanocavity: *Ab initio* analytical approach," *J. Opt. Soc. Am. B*, Vol. 29, No. 7, 1799–1809, 2012.
17. Johnson, P. B. and R. W. Christy, "Optical constants of the noble metals," *Phys. Rev. B*, Vol. 6, No. 12, 4370–4379, 1972.
18. Stratton, J. A., *Electromagnetic Theory*, McGraw-Hill, New York, 1941.
19. Wylie, J. M. and J. E. Sipe, "Quantum electrodynamics near an interface," *Phys. Rev. A*, Vol. 30, No. 3, 1185–1193, 1984.
20. Bordo, V. G., "Reflection and diffraction at the end of a cylindrical dielectric nanowire: Exact analytical solution," *Phys. Rev. B*, Vol. 78, No. 8, 085318, 2008.
21. Bordo, V. G., "Erratum: Reflection and diffraction at the end of a cylindrical dielectric nanowire: Exact analytical solution [*Phys. Rev. B*, Vol. 78, 085318, 2008]," *Phys. Rev. B*, Vol. 79, No. 3, 039901(E), 2009.

Carrier Phase and Amplitude Manipulation for Linearization and Dispersion Compensation in Radio-over-fiber Systems Using Mach-Zehnder Modulator

Shangyuan Li, Xiaoping Zheng, Fan Wei, Hanyi Zhang, and Bingkun Zhou
Tsinghua National Laboratory for Information Science and Technology
Department of Electronic Engineering, Tsinghua University, Beijing 100084, China

Abstract— Carrier phase and amplitude manipulation is an important signal processing method in microwave photonics. The authors proposed a series of work by realizing such manipulation with a single drive dual-parallel Mach-Zehnder modulator (DPMZM). By controlling the phase of the optical carrier, dispersion compensation can be achieved, while the amplitude tuning of the optical carrier can decrease the nonlinear distortions and improve the linearity. This manipulation method can also help establishing a millimeter-wave photonic up-converter, a frequency doubled opto-electronic oscillator, or a low-interference dual-direction radio-over-fiber (RoF) links.

1. INTRODUCTION

In radio-over-fiber (RoF) systems, electrical signal modulates the optical carrier, converting the electrical signal into optical domain and generating the up-converted signal bands. Comparing to the ideal modulation process, an actual modulation process would deteriorate the modulated signal and generate distorted sidebands, leading to a reduction of the dynamic range [1]. Meanwhile, the chromatic dispersion, originated from the transmission fiber or other devices, can also change the phase relationship between the carrier and the modulated sidebands, introducing power fading to the modulated signal and causing significant signal degradation [2]. Most traditional compensation methods have only focused on one of these two issues. However, for such an ROF system, they should better be treated simultaneously.

Mach-Zehnder modulators (MZM) is generally treated as an electrical-to-optical (EO) converter. However, recent progresses show that the MZM (or an MZM with complex structures) can play far more than an EO converter [3]. Special utilizations of the MZM can achieve linearization or dispersion compensation, and even resolve both the issues simultaneously. In this paper, we summarized the fundamental principles, techniques and applications that using MZMs to control the phase and amplitude of the optical carrier, to achieve multi-functions, including EO conversion, linearization and dispersion compensation, simultaneously.

By controlling the phase and amplitude of the optical carrier, the phase and amplitude relationship between the carrier and the sidebands can be altered accordingly. Analysis shows that the nonlinear distortion and fiber dispersion can be suppressed and compensated simultaneously, if a specific phase and amplitude condition between the carrier and the sidebands is settled. Such a condition can be achieved using a dual-parallel MZM (DPMZM), which has two sub-modulators that lie on a parent modulator. By tuning the three biases of the DPMZM, dispersion and nonlinear distortion can be compensated at the same time. Further studies show that such a technique can help establishing a millimeter-wave photonic up-converter, a frequency doubled opto-electronic oscillator (OEO), or a low-interference dual-direction RoF links.

2. ANALYTICAL MODEL

A simple microwave photonic system model that can transmit RF signal using SD-DPMZM is shown in Fig. 1. The RF signal is generated by a RF generator, modulate the continuous wave laser via the SD-DPMZM. The modulated signal is then detected in a photo-detector (PD). The photo-current generated from the PD is analyzed by a signal analyzer (SA).

2.1. General Model of SD-DPMZM

The structure of an SD-DPMZM is shown in Fig. 2. There are three MZMs in the modulator: MZM-1 and MZM-2 are the sub-modulators, where MZM-1 is driven by radio frequency (RF) signal $V_m(t)$ and dc-bias V_1, MZM-2 is driven by dc-bias V_2. These two sub-modulators acts as the two arms of the parent modulator, MZM-3. A dc-bias V_3 controls the phase relationship of these two sub-MZMs.

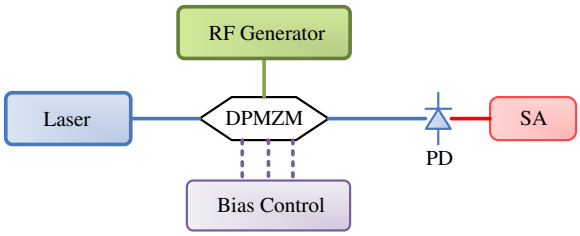

Figure 1: System model to modulate and regenerate RF signal.

The total output of the SD-DPMZM can be written as

$$E_O = \frac{E_I}{2}\left[\cos\frac{\phi_1(t)}{2} + \cos\left(\phi_2/2\right)e^{j\phi_3}\right] \tag{1}$$

where $\phi_i = \pi V_i/V_\pi$ is the dc-bias induced phase change of the i-th modulator, MZM-i ($i = 1, 2, 3$). $V_{\pi i}$ is the half wave voltage of MZM-i. $\phi_1(t)$ is the total phase change of MZM-1, where $\phi_1(t) = \phi_1 + \phi_m(t)$, and $\phi_m(t)$ is the RF signal introduced phase change to MZM-1, satisfies $\phi_m(t) = \pi V_m(t)/V_{\pi RF}$. In the later part of the paper, $\phi_m(t)$ is written as ϕ_m for short.

The photo-current generated from the PD originates from beating between all electronic field components in (1). Before fiber transmission, the photo-current is proportional to the optical intensity, which is given by

$$i = \Re \cdot E_O \cdot E_O^* = \frac{\Re E_I^2}{4}\left[\cos^2\frac{\phi_2}{2} + 2\cos\frac{\phi_1(t)}{2}\cos\frac{\phi_2}{2}\cos\phi_3 + \cos^2\frac{\phi_1(t)}{2}\right] \tag{2}$$

where $\Re$ is the responsivity of the PD. Equation (2) shows that the photo-current contains three terms. The first term is the self beating of the optical, generating a dc current. The cross beating between the optical and the modulated sidebands generates the second term, which is controlled by all the biases in the modulator. The third term, originated from the self beating of the sidebands, is only controlled by ϕ_1, and is proportional to the square of the second term.

Assuming an RF signal with an angular frequency of ω_m and an amplitude of V_s drives the SD-DPMZM. The RF signal causes a phase change of $\phi_m = m\cos(\omega_m t)$, and m, the modulation index, is defined as $m = \pi(V_s/V_{\pi RF})$. The modulated signal is then detected by a PD. The photo current can be derived for single tone modulation and given as

$$i_s'(t) = \frac{\Re E_I^2}{4}\sum_{k=0}^{3}\left[\Gamma'_k\cos(k\omega_m t)\right] \tag{3}$$

where

$$\Gamma'_0 = \left(2 + \cos\phi_2 + c + 4d\right)/2 - (c+d)m^2/8 \qquad \Gamma'_2 = -\left(c+d\right)m^2/8$$
$$\Gamma'_1 = -(b + a/2)m + (b + 2a)m^3/32 \qquad \Gamma'_3 = (b + 2a)m^3/96$$

where the four phase-related parameters, a, b, c, d, are defined as

$$a = \sin\phi_1,\ b = \sin(\phi_1/2)\cos(\phi_2/2)\cos(\phi_3);\ c = \cos\phi_1,\ d = \cos(\phi_1/2)\cos(\phi_2/2)\cos(\phi_3);$$

2.2. Carrier Phase Control for Dispersion Compensation

In [4], we have introduced a carrier phase shifting (CPS) modulation technique to control only the phase of the optical carrier to achieve dispersion compensation using an SD-DPMZM. The biasing conditions of a CPS system are: MZM-1 is biased at null point ($\phi_1 = \pi$), which nulls the optical carrier, allowing only the modulated sidebands to pass. MZM-2 is biased at maximum ($\phi_2 = 0$), which allows a maximum power transmission. The bias of MZM-3 controls the phase difference between the optical carrier from MZM-2 and the modulated sidebands from MZM-1. Thus Equation (1) can be rewritten for CPS modulation as

$$E_O = E_I\left\{\sin\left[\phi_m(t)/2\right] + e^{j\phi_3}\right\}/2 \tag{4}$$

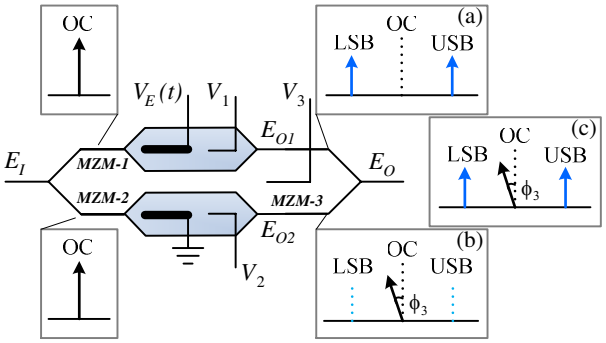

Figure 2: Operation principle of dispersion compensation.

There are two parts shown in Equation (4): The first part, $\sin[\phi_m/2]$ indicates a carrier-suppressed DSB (CSDSB) modulation of the laser. Such a part is generated in MZM-1 containing all the modulated signal sidebands, of which the optical spectrum is illustrated in Fig. 2(a). The second part $e^{j\phi_3}$ indicates a phase modulation in MZM-3 of the optical that come from MZM-2. There is no modulated sidebands in this part. Only the optical carrier appears here, as illustrated in Fig. 2(b). The spectrum of the total output from the modulator, E_O, is illustrated in Fig. 2(c). By controlling ϕ_3, we can generate a phase difference between the optical carrier and the modulated sidebands.

The photo-current can be derived using (2) and given by

$$i(t) = \frac{\Re E_I^2}{4}\left[1 + 2\cos\phi_3 \sin\frac{\phi_m(t)}{2} + \sin^2\frac{\phi_m(t)}{2}\right] \tag{5}$$

where the second term contains the baseband signal, of which the intensity is controlled by $\cos\phi_3$. Compared to (4), we can see that the phase change of the optical carrier is transformed to the intensity of the photo-current.

The transfer function of a piece of fiber with a length of L, neglecting the fiber loss, is given as $H(j\omega) = \exp(j\frac{1}{2}\beta_2 L\omega^2)$, where β_2 is the dispersion coefficient of the fiber. Detected by a photo-detector (PD), the optical signal after transmitted in the fiber can generate a series of photo-current, consisted of all harmonics of ω_m, among which the first-order harmonic (FOH) signal, $i_1(t)$, if $m \ll 1$ is satisfied, can be derived under the small signal approximation as,

$$i_1(t) \approx \tfrac{1}{16} m E_I^2 \cdot \exp(j\Omega t) \cdot \cos\left(\beta_2 L\Omega^2/2 - \phi_3\right) \tag{6}$$

From Equation (6) we can see that the intensity of the FOH is controlled by the dispersion and ϕ_3. The increase of dispersion, which increases the dispersion induced phase shift, $\beta_2 L\Omega^2/2$, will cause the power fading of an RoF link. However, by changing the bias of MZM-3, ϕ_3 can be tuned and satisfies $\phi_3 = \beta_2 L\Omega^2/2$. Under this condition, the power fading can be compensated and $i_1(t)$ is maximized. It is a pre-compensation method, where the phase shift is pre-set at the transmitter in an RoF link, given the knowledge of the link dispersion.

2.3. Carrier Amplitude Control for Modulator Linearization

To solely control the amplitude of the optical carrier, the SD-DPMZM is also a good candidate. Li proposed a MZM linearization method to eliminate the nonlinear distortion terms by solely control the amplitude of the optical carrier [5]. The SD-DPMZM is biased as followed: Bias MZM-1 and MZM-2 to control the amplitude of the optical carrier, and bias MZM-3 to satisfy $\phi_3 = 0$. Thus (1) can be rewritten as

$$E_O = E_I\left\{\cos\left[\phi_m(t)/2 + \phi_1/2\right] + \cos(\phi_2/2)\right\}/2 \tag{7}$$

Detected by a PD, the photo-current in 2) also have three terms. Both the second and the third term contain the modulated signal. However, ϕ_2 controls the contribution ratio from these two terms, by controlling the amplitude of the optical carrier from MZM-2.

Assuming two RF signals with angular frequencies of ω_1 and ω_2 and the amplitude of V_s drives the SD-DPMZM. The frequencies of these two tones are close, so that $|\omega_1 - \omega_2| \ll (\omega_1 + \omega_2)$. The

RF signal causes a phase change of $\phi_m(t) = m\cos(\omega_1 t) + m\cos(\omega_2 t)$. After detected by a PD, the photocurrent can be written as

$$i_{PD} \propto \{\Gamma_0 + \Gamma_1[\cos(\omega_1 t) + \cos(\omega_2 t)] + \Gamma_3[\cos(2\omega_1 t \pm \omega_2 t) + \cos(2\omega_2 t \pm \omega_1 t)] + \ldots\}$$

where

$$\Gamma_1 = \frac{a/2+b}{4}m - \frac{3(2a+b)}{128}m^3 + O(m^3) \qquad \Gamma_3 = \frac{2a+b}{128}m^3 - \frac{5(8a+b)}{12288}m^5 + O(m^5) \tag{8}$$

When $2a + b = 0$, the first term of Γ_3 is 0, which decreases the IMD3. Such condition can also be written as

$$4\cos(\phi_1/2) = -\cos(\phi_2/2) \tag{9}$$

Thus Equation (8) can be rewritten as $\Gamma_1 = -3am/8 + O(m^3)$, $\Gamma_3 = -5am^5/2048 + O(m^5)$.

From Equation (9) we can see that ϕ_1 should satisfy $\cos(\phi_1/2) \leq 0.25$, which means when $\cos(\phi_1/2) = 0.25$, Γ_1 can have a maximum value. This is the condition to satisfy both the linearization condition and maximize the FOH signal. It can be calculated that $\phi_1 = \arcsin(0.484)$.

Actually, there are two contributions of nonlinear inter-modulations in Equation (8), one is only related to a, corresponding to the bias condition of MZM-1, while the other is related to b, corresponding to all the biases of the modulator. Tuning MZM-1 and MZM-2 is actually tuning the power ratio of the signal from these two contributions. When $2a + b = 0$, the best condition meets and the best linearization is done.

2.4. Principle of Joint Phase and Amplitude Control

According to the two subsections above, we can see that independent control of the phase and amplitude of the optical carrier can achieve dispersion compensation and modulator linearization separately, which means that it is promisingly to combine these two methods to achieve a bi-function system [6].

Using similar calculation procedures in [4, 5], we can derive Γ_1 and Γ_3 accordingly when dispersion is considered as well as linearization. The expressions for Γ_1 and Γ_3 are:

$$\Gamma_1 = \frac{a/2+b'}{4}m - \frac{3(2a+b')}{128}m^3 + O(m^3) \qquad \Gamma_3 = \frac{2a+b'}{128}m^3 - \frac{5(8a+b')}{12288}m^5 + O(m^5) \tag{10}$$

where b' is determined by,

$$b' \approx \sin(\phi_1/2)\cos(\phi_2/2)\cos(\theta_n - \phi_3)$$

where $\theta_n = \beta_2 L\omega^2/2$, when the two tones are very close. Equation (10) is almost the same as Equation (8), however the parameters are different.

3. APPLICATIONS

Such kind of carrier phase and amplitude manipulation can be utilized in many different microwave photonic systems to achieve many functions, include including millimeter-wave RoF link with photonic up-conversion, a frequency doubled opto-electronic oscillator (OEO), or a low-interference dual-direction RoF links.

3.1. Millimeter-wave RoF Transmitter

By combining linearization technique with photonic up-conversion technique, a highly linear radio-over-fiber transmitter is proposed using an SD-DPMZM [7]. By optimizing the three biases in the modulator, the IMD3 from two origins cancel each other out, resulting in a large dynamic range. The phase and amplitude of the optical local oscillator (also called a heterodyne subcarrier source) are controlled in the DPMZM. An up-converted highly linear MMoF transmitter with an SFDR of 122.7 dBHz2/3 is experimentally obtained in the 40 GHz band. It is improved by 27-dB compared to traditional up-conversion methods.

3.2. Frequency Doubling Optoelectronic Oscillator

Wang proposed a frequency doubling OEO in [8], where a DPMZM is used as the electro-optical converter. The DPMZM is driven by an RF signal of about 10 GHz. By tuning the bias of MZM-3, the optical carrier has an initial phase shift of 90 degree compared to the sidebands, which is a phase-modulate-like spectrum. The beating of this optical signal can only generates 20 GHz photo-current, which is doubled in frequency compared to the driven signal. However, after transmitted through

a piece of fiber and a chirped fiber Bragg grating, which have a total dispersion of −416 ps/nm, the phase of the optical carrier is thus changed by 90 degree compared to the sidebands. Beating of such an optical signal at PD can generate 10 GHz electrical current, which drives the DPMZM and is also the output of the OEO.

3.3. Low-interference Dual-direction RoF Links

In a dual-direction RoF link with downlink carrier wavelength reuse, the re-modulation of uplink signal will generate adjacent channel interference optically (O-ACI). The strength of such an interference is determined by the modulation types in both uplink and downlink and varies as the dispersion changes. It is very severe for a subcarrier multiplexed dual-direction RoF system.

Wei proposed an O-ACI cancellation method using DPMZM at the central station (CS) for such a system. In downlink, the RF signal drives the DPMZM at the CS. Part of the downlink light is detected in the base station (BS), and the other part of the light is modulated by uplink signal and transmit back to the CS. MZM-3 is biased according to the RF frequency and the round-trip dispersion value, and have the effect as this: The downlink RF signal is canceled due to fiber dispersion when transmitted round-trip in the fiber that connected the CS and the BS. This means that the optical carrier has a phase difference of 90 degree compared the modulated sidebands. This bias condition allows the recovery of downlink signal at the BS, but eliminate the influence of the downlink signal to the uplink signal at the CS. The O-ACI is thus improved accordingly [9].

4. CONCLUSION

Carrier phase and amplitude manipulation is an interesting processing method in microwave photonics. It can be realized by a single drive DPMZM, which is simple in the system structure. This method can help establishing a millimeter-wave photonic up-converter, a frequency doubled OEO, or a low-interference dual-direction RoF links. There may be more potential applications using such kind of manipulation.

ACKNOWLEDGMENT

This work is supported in part by National 973 Project No. 2012CB315603 and 2012CB315604, National Nature Science Foundation of China (NSFC) under grant No. 61025004 and 61032005.

REFERENCES

1. Ackerman, E. I., "Broad-band linearization of a mach-zehnder electrooptic modulator," *IEEE Transactions on Microwave Theory*, Vol. 47, No. 12, 2271–2279, 1999.
2. Smith, G. H., D. Novak, and Z. Ahmed, "Overcoming chromatic-dispersion effects in fiberwireless systems incorporating external modulators," *IEEE Transactions on Microwave Theory*, Vol. 45, No. 8, 1410–1415, 1997.
3. Ferreira, A., T. Silveira, D. Fonseca, R. Ribeiro, and P. Monteiro, "Highly linear integrated optical transmitter for subcarrier multiplexed systems," *IEEE Photonics Technology Letters*, Vol. 21, No. 7, 438–440, 2009.
4. Li, S., X. Zheng, H. Zhang, and B. Zhou, "Compensation of dispersion-induced power fading for highly linear radio-over-fiber link using carrier phase-shifted double sideband modulation," *Optics Letters*, Vol. 36, No. 4, 546–548, 2011.
5. Li, S., X. Zheng, H. Zhang, and B. Zhou, "Highly linear radio-over-fiber system incorporating a single-drive dual-parallel machzehnder modulator," *IEEE Photonics Technology Letters*, Vol. 22, No. 24, 1775–1777, 2010.
6. Li, S., Jiaoyan Yu, X. Zheng, H. Zhang, and B. Zhou, "Simultaneous pre-compensation of modulation nonlinear and fiber dispersion for radio-over-fiber link," submitted to *IEEE Photonics Technology Letters*, 2013.
7. Li, S., X. Zheng, H. Zhang, and B. Zhou, "Highly linear millimeter-wave over fiber transmitter with subcarrier upconversion," *Conference on Lasers and Electro-Optics (CLEO)*, JWA4, Baltimore, USA, May 2011.
8. Wang, L., N. Zhu, W. Li, and J. Liu, "A frequency-doubling optoelectronic oscillator based on a dual-parallel machzehnder modulator and a chirped fiber bragg grating," *IEEE Photonics Technology Letters*, Vol. 23, No. 22, 1688–1690, 2011.
9. Wei, F., S. Li, X. Zheng, H. Zhang, and B. Zhou, "Improvement of optically generated adjacent channel interference in rof systems," *IEEE Photonics Technology Letters*, Vol. 25, No. 12, 1137–1140, 2013.

Linearization Techniques for Broadband Radio over Fiber Transmission

Xiupu Zhang[1, 2], **Bouchaib Hraimel**[2], **Ran Zhu**[2], **Dongya Shen**[1], **and Taijun Liu**[3]

[1]School of Information Science & Engineering, Yunnan University, Kunming, China
[2]Department of Electrical & Computer Engineering, Concordia University, Montreal, Canada
[3]College of Information Science & Engineering, Ningbo University, Ningbo, Zhejiang, China

Abstract— Linearization techniques are reviewed for broadband radio over fiber transmission. Four broadband linearization techniques, i.e., optical mixed polarization, analog pre-distortion, digital pre-distortion, and digital post-processing, are summarized.

1. INTRODUCTION

For the current wireless signal distribution from central stations to remote antenna sites, the technologies that are used for the distribution are optical digital transmission, microwave point to point transmission, digitized radio over fiber (RoF) transmission and analog RoF (ARoF) transmission. However, among these technologies, ARoF has been considered a key enabling technology for BWAN because of its broadband and cost effective seamless integration to wireless technologies and transparent to radio frequency carriers and data protocols. Because of its analog optical modulation nature, ARoF transmission is unfortunately very susceptible to intrinsic nonlinearities from electro-optic modulation (EOM) and any other optical and electronic components that are used for transmission. Therefore, the deployment of ARoF in BWAN requires cost effective broadband linearization.

Linearization is not a new research topic and two types of linearization had been proposed for wireless/microwave transmission: analog and digital pre-distortion circuits. Digital linearization is popular currently for wireless/microwave communications [1], leading to more than 20 dB improvement of spur free dynamic range (SFDR). However, based on current signal processing capability, digital linearization is limited to 100 MHz in bandwidth, and typically 20 MHz. On the other hand, analog linearization can be simple and low-cost, and more importantly broadband, but it offers less efficiency than digital linearization. Because of simplicity and low power consumption, tens of patents in analog linearization circuits have been awarded in US patent database, but no one is broadband. The future distribution must support multi-bands, broadband, and any frequency carriers from 400 MHz to 100 GHz. Therefore broadband linearization must be required.

When RF carriers are more than 20 GHz, where direct modulation of lasers may not be appropriate, external modulation has to be used such as using Mach-Zehnder modulator (MZM) and electro-absorption modulator (EAM). Unfortunately, these modulators introduce severe nonlinear distortion, and they are required to be linearized.

Due to the above, broadband linearization techniques have been intensively developed in recent years. In this presentation, we will review broadband linearization techniques based on optical mixed polarization (OMP), analog predistortion circuit (APDC), digital predistortion, and digital post-processing.

2. OPTICAL MIXED POLARIZATION (OMP)

Figure 1 shows the schematic of OMP linearized electro-optic modulator (EOM), which consists of a linear polarizer adjusted to an angle of α, an EOM and a second linear polarizer adjusted to an angle of β. The EOM considered is assumed an MZM or polarization dependent EAM, with transfer function T_{TE} and T_{TM} in x- and z-axis, respectively. The polarization dependence will allow for different amounts of modulation depth for the two orthogonal polarized states of light. The light entering the modulator passes through a linear polarizer set to an angle of α with respect to the z-axis, which will excite a superposition of TE and TM modes that will be modulated with different modulation depths. In other words, the z-(TM) and x-(TE) axis will carry different amounts of inter-modulation distortion (IMD) that is generated by EOM. The light then passes through a second linear polarizer (LP) that is angled to β with respect to the z-axis. By carefully selecting α and β of the two linear polarizers, the combined third-order nonlinear distortion carried by the orthogonal polarized lights exiting the EOM can be cancelled and the RF carrier power

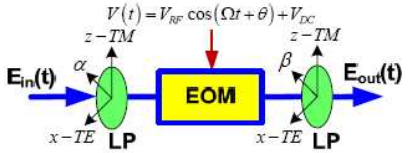

Figure 1: Schematic of optical mixed polarization linearized EOM. EOM: electro-optical modulator, LP: linear polarizer.

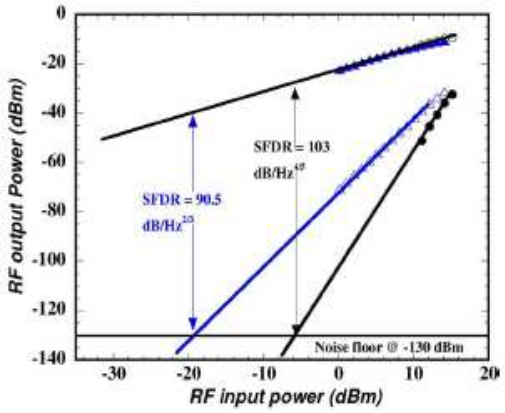

Figure 2: Measured SFDR in a normalized 1 Hz noise bandwidth for 20-km RoF system using the conventional and OMP MZM.

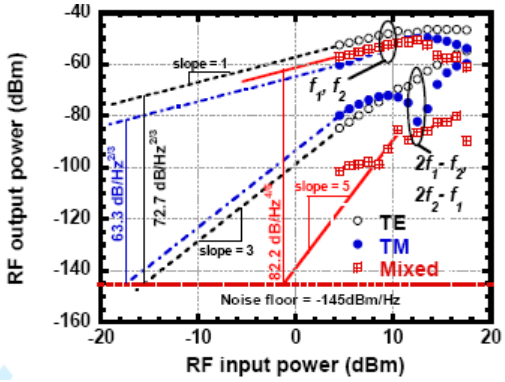

Figure 3: Measured SFDR in a normalized 1 Hz noise bandwidth for 20-km RoF system using TE, TM and OMP EAM.

is maximized at the output of the second linear polarizer. Because of its application in optical domain, OMP linearization technique is broadband and limited only by bandwidth of the EOM.

To linearize a $LiNbO_3$ z-cut MZM, the optimum angles of α and β are $\pm 79°$, leading 13-dB theoretically and 12.5 dB experimentally improvement of SFDR as shown in Fig. 2 [2]. To linearize a $LiNbO_3$ x-cut MZM, the optimum angles of α and β are dependent on bias voltage and change from $\pm 79°$ to $+79°$ roughly [3]. To linearize an polarization-dependent EAM, the optimum angles of α and β are dependent on bias voltage and changed within $\pm 80°$, and theoretically 14-dB SFDR was predicted with less sensitivity to α and β for our considered EAM, and experimentally 9.5 dB improvement was obtained as shown in Fig. 3 [4, 5]. After the linearization, 3rd order IMD (IMD3) is almost suppressed fully and the SFDR is mainly limited by the 5th order IMD. Applying this technique for a multi-band OFDM ultra-wideband signal over 20-km fiber at 200 Mb/s, the error vector magnitude (EVM) was improved by more than 9 dB and 3 dB for using single drive x-cut MZM (sd-xMZM) [3] and a polarization dependent EAM [5], respectively.

However, the drawback is that the OMP linearization introduces high optical insertion loss [3–5] except the fact that TE and TM mode transfer function have opposite slopes. Recently, this technique was improved by using a semiconductor optical amplifier (SOA) that is used to substitute the second LP in Fig. 1. Using this technique, both linearity and receiver sensitivity are improved compared to both TE-only MZM and OMP-MZM, as depicted from the linear characteristics shown in Fig. 4. It is shown that the technique of OMP-MZM+SOA leads to much better linearity and higher modulation efficiency. For this technique, the implementation is very simple: The first LP can be obtained by aligning two polarization states of laser output and MZM input with certain angles.

Applying this technique to an sd-xMZM [6], an SFDR of 130 dB/Hz$^{4/5}$ and more than 10 dB of improvement in EVM have been achieved for multiband-OFDM ultra-wideband signal over 20 km fiber at 480 Mb/s.

3. ANALOG PREDISTORTION CIRCUIT (APDC)

A broadband analog pre-distortion circuit (APDC) with a simple architecture was proposed [7], which uses anti-parallel diodes in two symmetrical paths with a push–pull configuration as shown in Fig. 5. The RF signal goes through the diodes, and the predistorted signal is generated simultaneously in the two paths without delay. This suggests that the predistortion circuit will not

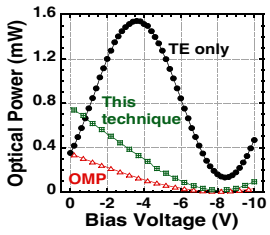

Figure 4: Optical power of the OFDM UWB signal using TE-only MZM, OMP-MZM and OMP-MZM+SOA (this technique) versus the bias voltage of MZM.

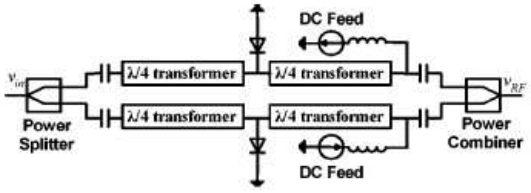

Figure 5: Schematic of the broadband analog predistortion circuit.

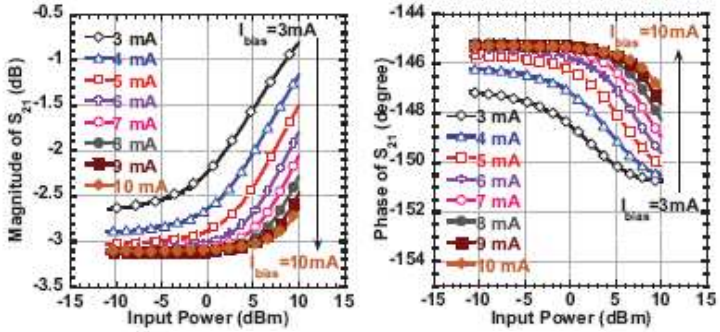

Figure 6: Measured (a) magnitude and (b) phase of S_{21} of the analog pre-distortion circuit versus input RF power at different bias currents.

generate even-order nonlinear distortion products. However, third-order nonlinear distortion products generated from the two paths will be added together, which is used to suppress the third-order nonlinear products of the RoF links.

The magnitude and phase of S_{21} of the APDC versus RF input power at different bias currents of the Schottky diodes are measured using a vector network analyzer and shown in Figs. 6(a) and (b), respectively. By tuning the bias current of the APDC, different levels of nonlinearity are generated to linearize different types of nonlinear components in broadband analog RoF links.

The use of this broadband APDC to linearize an EAM [7] and sd-xMZM [8] leads to 11 dB and 14 dB improvement of SFDR at 4 GHz, and suppression of the IMD3 by more than 7 dB and 6 dB over 3–5 GHz, as illustrated in Figs. 7 and 8, respectively. Moreover, the EVM of a multiband OFDM ultra wide band signal over 20 km fiber is improved by more than 1 dB and 2.5 dB for RoF links using EAM and sd-xMZM, respectively. Recently, an APDC covering the range of $7 \sim 18$ GHz and achieving ~ 10 dB improvement of SFDR was designed for an RoF link using MZM, which will be fully reported later. The APDC bandwidth is mainly limited by broadband lossless matching of the impedance of the used Schottky diodes to 50 Ohm. A lossy matching can extend this bandwidth to the intrinsic bandwidth of the Schottky diodes. Therefore, such a pre-distortion circuit can be designed for broadband operation and thus can be used for linearizing millimeter-wave over fiber systems.

4. DIGITAL PRE-DISTORTION (DPD)

Recently, a multi-band digital predistortion (DPD) technique was proposed [9] to linearize the subcarrier multiplexed (SCM) RoF system transmitting sparse multi-band RF signals with large blank spectra between the consecutive RF bands. DPD performs on the baseband signal of each individual RF signal before up-conversion and RF combination. By disregarding the blank spectra, the processing bandwidth of the proposed DPD technique is greatly reduced, which is only determined by the baseband signal bandwidth of each individual RF signal, rather than the entire bandwidth of the combined multi-band RF signals. Therefore, this technique can significantly reduce the digital processing bandwidth and allows the employment of low-cost narrow-band digital signal processing devices and digital to analog converters to linearize the RoF system with multiplexed subcarriers spanning over a wide frequency range. Moreover, this multi-band DPD technique is not sensitive

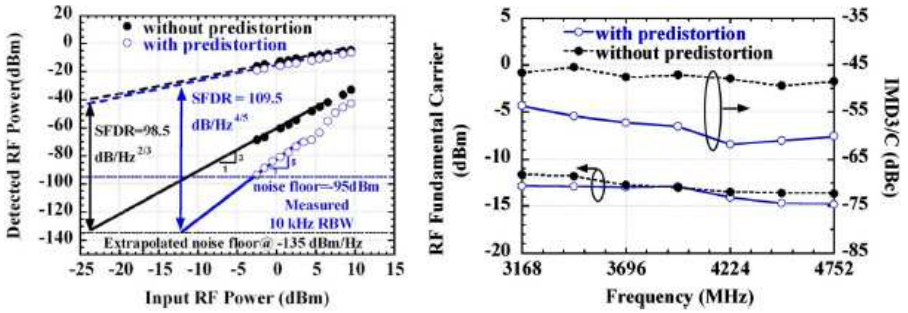

(a) (b)

Figure 7: Measured (a) SFDR and (b) frequency response of an RoF system using the EAM with and without using the analog pe-distortion circuit.

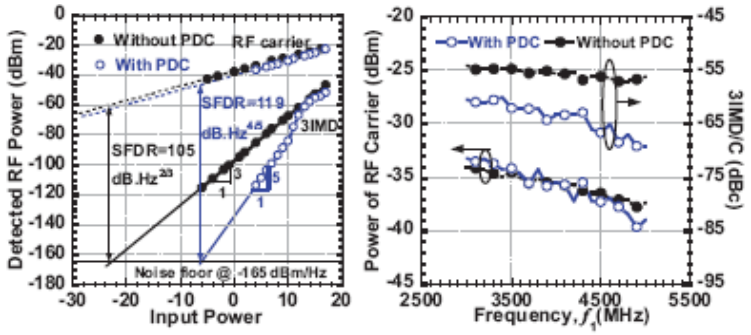

(a) (b)

Figure 8: Measured (a) SFDR and (b) frequency response of an RoF system using sd-xMZM with and without the analog pre-distortion circuit.

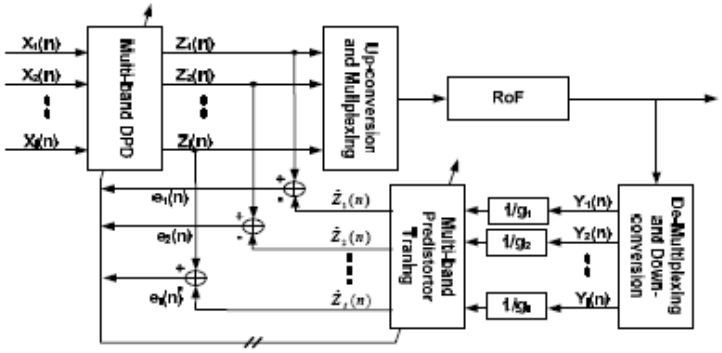

Figure 9: Schematic of DPD technique for linearing SCM-RoF.

to the signal modulation format and can be applied to any kinds of signals.

Figure 9 depicts the schematic of this technique. The inversed baseband signal of the RoF system for the i-th channel $Z_i(n)$ can be expressed as function of the input signal $X_i(n)$ and the nonlinear coefficients with memory of the predistortor training block, estimated using a simple least mean squares algorithm to minimize the signal error $e_i(n)$. Experimental demonstration was performed in a directly modulated SCM-RoF system transmitting two 64QAM modulated OFDM signals on 2.4 and 3.6 GHz band. It was shown that the adjacent channel power ratio (ACPR) is suppressed by 15 dB leading to significant improvement of the EVM performances of the signals on both of the two bands as shown in Fig. 10.

5. DIGITAL POST-PROCESSING (DPP)

After RoF transmission, the RF signal is first digitized and then post-processing is made to suppress the RoF transmission induced nonlinear distortion products. Fig. 11 shows a multi-stage signal processing technique that can be used to suppress multi-order nonlinear distortion products, leading to 5–9 dB improvement of SFDR over 0–6 GHz [10]. The main drawback is with using a high speed

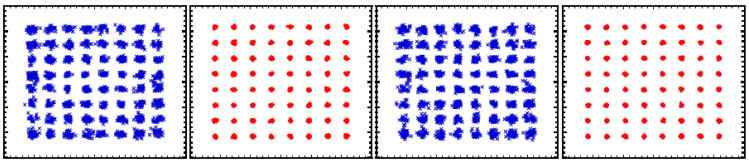

Figure 10: Constellations of the received signal: on 2.412/3.6 GHz (a), (c) without and (b), (d) with using multiband DPD technique.

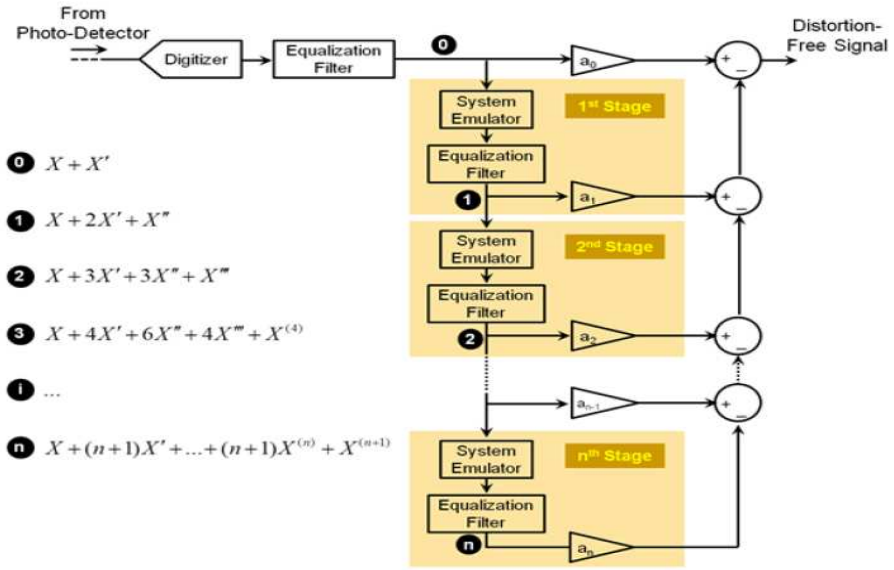

Figure 11: Digital post-processing technique for linearizing a RoF link.

digitizer.

6. CONCLUSION

We have reviewed broadband linearization techniques for analog radio over fiber using optical mixed polarization, analog pre-distortion, digital pre-distortion and digital post-processing. optical mixed polarization technique is simple and there is no bandwidth limitation. Particularly, optical mixed polarization combined with SOA makes linearization more efficient and less optical loss. Analog pre-distortion circuit can be ultra broadband and leads to moderate linearization efficiency. Digital pre-distortion linearization is only suitable for sparse RF signals, and not for multiband OFDM ultra wideband wireless signals. The application of digital post-processing is limited by high speed digitizer.

ACKNOWLEDGMENT

This work was supported in part by the Yunnan High-Tech Talents Recruitment Project 2012HA005, and also Ningbo University Sir Yue-Kong Pao's Chaired professorship and China "111" plan for Ningbo University.

REFERENCES

1. Katz, A., et al., "Truly wideband linearization," *IEEE Microwave Mag.*, S20–S27, Dec. 2009.
2. Masella, B., B. Hraimel, and X. Zhang, "Enhanced spurious-free dynamic range using mixed polarization in optical single sideband Mach–Zehnder modulator," *Journal of Lightwave Technology*, Vol. 27, No. 15, 3034–3041, 2009.
3. Hraimel, B., X. Zhang, T. Liu, T. Xu, Q. Nie, and D. Shen, "Performance enhancement of an OFDM ultra-wideband transmission over fiber link using a linearized mixed-polarization single-drive x-cut Mach-Zehnder modulator," *IEEE Transaction on Microwave Theory and Technique*, Vol. 60, No. 10, 3328–3338, 2012.

4. Hraimel, B., X. Zhang, W. Jiang, K. Wu, T. Liu, T. Xu, Q. Nie, and K. Xu, "Experimental demonstration of mixed polarization to linearize electro-absorption modulators in radio-over-fiber links," *IEEE Photonic Technology Letters*, Vol. 23, No. 4, 230–232, 2011.
5. Hraimel, B. and X. Zhang, "Performance improvement of radio-over fiber links using mixed polarization electro-absorption modulators," *IEEE Transaction on Microwave Theory and Technique*, Vol. 59, No. 12, 3239–3248, 2011.
6. Hraimel, B. and X. Zhang, "Suppression of radio over fiber system nonlinearity using a semiconductor optical amplifier and mixed polarization," *Conference on Optical Fiber Communication — OFC*, Paper JTh2A.59, CA, 2013.
7. Shen, Y., B. Hraimel, X. Zhang, G. E. R. Cowan, K. Wu, and T. Liu, "A novel analog broadband RF predistortion circuit to linearize electroabsorption modulator in multiband OFDM ultra-wideband radio over fiber system," *IEEE Transaction on Microwave Theory and Technique, Special Issue on Microwave Photonics*, Vol. 58, No. 11, 3327–3335, 2010.
8. Hraimel, B. and X. Zhang, "A low cost broadband predistortion linearized single drive x-cut Mach-Zehnder Modulator for radio-over-fiber systems," *IEEE Photonics Technology Letters*, Vol. 24, No. 18, 1571–1573, 2012.
9. Pei, Y., K. Xu, A. Zhang, Y. Dai, Y. Ji, and J. Lin, "Complexity-reduced digital predistortion for subcarrier multiplexed radio over fiber systems transmitting sparse multi-band RF signals," *Optics Express*, Vol. 21, No. 3, 3708–3714, 2013.
10. Lam, D., et al., "Digital broadband linearization of optical links," *Optics Letters*, Vol. 38, No. 4, 446–448, 2013.

A Study on OFDM Millimeter-wave Radio over Fiber System

Tam Hoang Thi and Mitsuji Matsumoto
Graduate School of Global Information and Telecommunication Studies, Waseda University, Tokyo, Japan

Abstract— Radio over Fiber (RoF) technology is considered as a promising technique for transmitting high data rate at effective cost in the next generation network because of combination of Optical Fiber transmission that provides huge band width and mobility of radio network. However, to take the advantageous of the technology, the kind of carry frequency used is very important. At this paper, a novel configuration with usage of Millimeter-Wave to transmit OFDM signal for utilizing broadband of optical fiber is proposed. The performance of the system is assessed in term of Signal to Distortion ratio (SDR) and symbol error rate (SER).

1. INTRODUCTION

Next generation ubiquitous network that assures to connect: anything, anytime and anywhere. It is novel network for the user but brings many challenging for network providers. Especially, more and more applications called band width consumer are deployed and under development. Band width consumer is the kind of services and applications that require huge band width and high speed transmission for example video on demand, video call or game online. Unfortunately, many services now are free on the Internet. Therefore, the problem the network provider facing now is to find out the technology having the ability to transmit high data rate at effective cost.

Moreover, Radio over Fiber (RoF) technology is considered as a promising technique for transmitting high data rate costly in the next generation network because of combination of Optical Fiber transmission that provides huge band width and mobility of radio network. Some advantages of RoF are high capacity, low cost, low power and easy to install [1]. RoF technology can be used for many applications such as office, train station or stadium. However, to take the advantages of the technology, the kind of carry frequency used is very important. Here, 60 GHz millimeter-wave (mm-Wave) is applied for the network for the reason that such high frequency can transmit high data bit rate. Besides, OFDM signal is becoming very popular. Most of advanced systems are using OFDM based signal such as LTE 4G or WiMAX network. So, the proposed system that uses RoF technology to transmit OFDM signal by mm-Wave seems to be potential for big bandwidth consumer applications.

In the second section, the basic RoF system and our proposed system are shown. In addition, components in the system will be briefly explained. Next, the system is theoretically analyzed and illustrated step by step following the system model with some assessments of system performance. The final section is the conclusion.

2. PROPOSED SYSTEM

The conventional RoF system is shown as Fig. 1. Basic RoF consists of two main parts: Base Station (BS) and Central Office (CO). CO will take care of complex functions such as signal processing, modulation, routing while BS is simple, small and cheap. Optical fiber transmits signals from CO to BSs. There, BS will use its antenna to transmit signal to users.

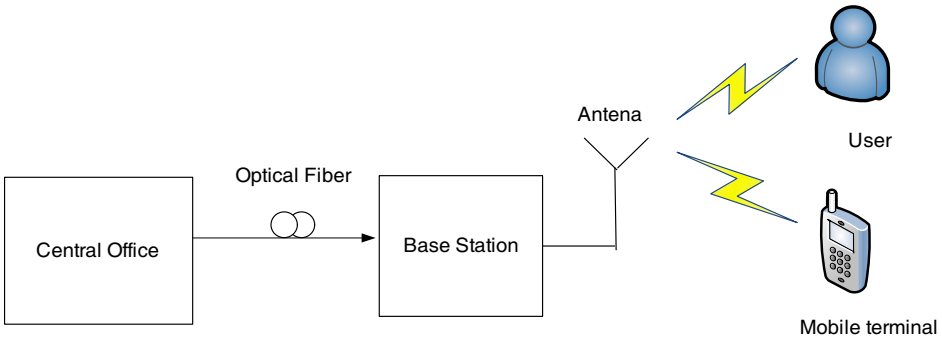

Figure 1: Basic RoF system.

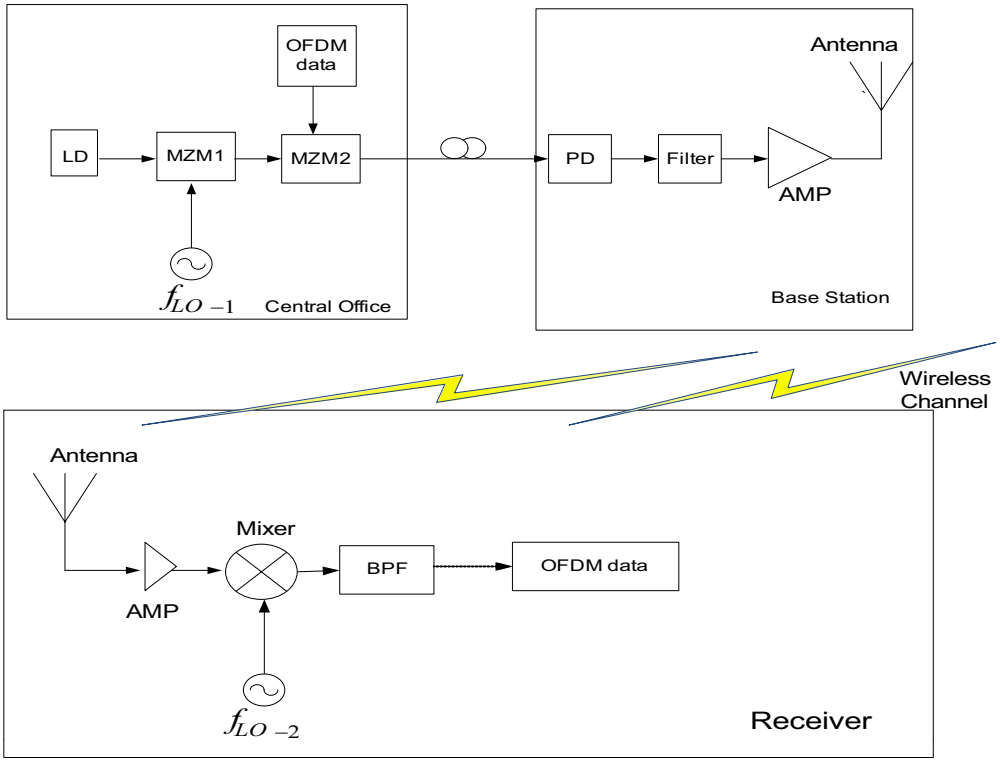

Figure 2: Downlink architecture of OFDM millimeter-wave radio over fiber system.

At the present, direct modulation is used widely in RoF system because of its simplicity. However, the significant problem of direct modulation at high frequency is chirping [1]. Hence, to overcome chirping, external modulation is used in our proposed system in Fig. 2. As can be seen, this model uses Mach Zehnder modulator as the external modulator. The purpose of elements in our system can be seen as follows. The first Mach Zehnder modulator (MZM1) produces the millimeter wave. Hence, It needs the light wave from LD and RF signal from the first local oscillator ($f_{LO\text{-}1}$). The second MZM (MZM2) works as an intensity modulator to modulate the OFDM data in to millimeter wave signal. At the base station, the PD converts the received optical signal to electronic signal. The electronic signal passes the filter and is amplified by before is fed to the antenna to transmit in the air. At the receiver, the received signal will be amplified by Amplifier (AMP) before multiplied with signal from the second oscillator ($f_{LO\text{-}2}$) at the mixer. The signal after the Mixer is filter by band pass filter (BPF) to get the signal at OFDM band.

3. SYSTEM ANALYSIS AND PERFORMANCE EVALUATION

3.1. System Analysis

In the architecture in Fig. 2, Antenna in the BS is charge of transmitting the mm-Wave OFDM signal in the wireless channel. From here, the system operates like normal wireless systems. For the sake of simplicity, only the signal after PD will be analyzed. The actual model used for our analysis is indicated in Fig. 3.

At first, the optical signals from the laser can be modeled as follows [2]:

$$x_{LD}(t) = A_{LD} \exp j(w_{LD}t + \Phi_{LD}(t)) \tag{1}$$

where A_{LD}, w_{LD}, and Φ_{LD} are amplitude, angular frequency and phase-noise of the signal from the LD, respectively.

The OFDM signal for N subcarriers can be written as [3]:

$$S_{\text{OFDM}}(t) = \sum_{n=0}^{N-1} X_n \exp\left[j\left(w_n + 2\pi f_0\right)t\right], \quad 0 \le t < T_s \tag{2}$$

where T_s is the symbol duration, w_n are the set of subcarriers' frequency and $(X_n = a_n + jb_n)$ is

the complex data symbol in the nth subcarrier, with a_n and b_n are the in-phase and quadrature modulation symbol, respectively.

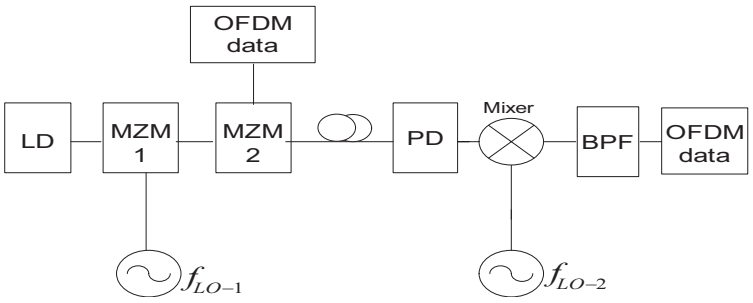

Figure 3: Downlink architect of OFDM mm-wave RoF for investigation.

Suppose that MZM1 produces double side band signal with the same amplitudes A as follows [4]:

$$E_{mmw}(t) = A\cos(w_{LD} + w_{RF})t + A\cos(w_{LD} - w_{RF})t \tag{3}$$

where w_{RF} is the angular frequency of the first local oscillator.

If MZM2 works as an intensity modulator (IM) with the optical modulation index (OMI): γ in the linear range of the IM, the signal after the second MZM can be expressed as follows [4]:

$$E(t) = [A\cos(w_{LD} + w_{RF})t + A\cos(w_{LD} - w_{RF})t] \times [1 + \gamma S(t)] \tag{4}$$

When the distance between central office and BS is not so far, the effects of optical fiber can be neglected. Using square law to find the photocurrent $I(t)$ after the PD, the current is achieved as follows:

$$\begin{aligned} I(t)_{PD} &= \Re|E(t)|^2 = \Re A^2\left[1 + 2\gamma S(t) + \gamma^2 S(t)^2\right] \quad \langle p1\rangle \\ &\quad + \Re A^2\cos(2w_{RF}(t))\left[1 + 2\gamma S(t) + \gamma^2 S(t)^2\right] \quad \langle p2\rangle \end{aligned} \tag{5}$$

where $\Re$ denotes the responsivity of the PD; $\langle p1\rangle$ denotes part 1 — the baseband OFDM signal; $\langle p2\rangle$ denotes part 2 — the mm-Waveave OFDM signal.

Suppose that only mm-Wave OFDM signal can be transmitted over PD. Therefore, the current of mm-Wave after the PD can be expressed as follows:

$$I_{mmw}(t) = \Re A^2\cos[2w_{RF}(t)]\left[1 + 2\gamma S(t) + \gamma^2 S(t)^2\right] \tag{6}$$

At the mixer, the mm-Wave current $I_{mmw}(t)$ will be multiplied with the signal from local oscillator. Assume that the signal from $f_{LO\text{-}2}$ is at the frequency $2w_{RF}$. The signal after the mixer can be shown as follows:

$$\begin{aligned} I(t)_{\text{Mixer}} &= I_{mmw}(t)\cos(2w_{RF}t) \\ &= \frac{1}{2}\left\{\Re A^2\left[1 + 2\gamma S(t) + \gamma^2 S(t)^2\right] + \cos(4w_{RF}(t)\,\Re A^2\left[1 + 2\gamma S(t) + \gamma^2 S(t)^2\right]\right\} \end{aligned} \tag{7}$$

After the BPF, the part that consists of $4w_{RF}$ frequency and DC component will be eliminated. Hence, the received current can be obtained as follows:

$$I(t) = \frac{1}{2}\Re A^2\left[2\gamma S(t) + \gamma^2 S(t)^2\right] = \Re A^2\gamma S(t) + \frac{1}{2}\Re A^2\gamma^2 S(t)^2 \tag{8}$$

In order to evaluate SDR, it is necessary to find power of the signal and distortion. Distortion power is calculated by the autocorrelation function and power spectral density (PSD) of the photocurrent. With the assuming that both OFDM signal and distortion are nearly Gaussian distribution in amplitude [5, 6], the spectrum of OFDM signal and distortion can be approximately rectangular.

Considering the second order distortion $S(t)^2$the autocorrelation function $R_{s^2}(\tau)$ can be defined as follows [5]:

$$R_{s^2}(\tau) = \sigma_s^4 + 2R_s^2(\tau) \tag{9}$$

where $R_s(\tau)$ represents the autocorrelation function of the signal $S(t)$, σ_s^2 represents the power of the original OFDM spectrum for $f_0 - B < |f| < f_0 + B$.

The PSD is the Fourier transform of autocorrelation function and can be expressed:

$$\begin{aligned} S_{S^2}(f) &= F\langle R_{S^2}(\tau)\rangle = F\langle\sigma_S^4\rangle + 2F\langle E_S^2(\tau)\rangle \\ &= \sigma_s^4 a_2^2\delta(f) + \frac{\sigma_s^4}{8B^2}a_2^2 \begin{cases} 2B - |f \pm f_0| & |f \pm f_0| < 2B \\ 0 & |f \pm f_0| \geq 2B \end{cases} \end{aligned} \tag{10}$$

where $\delta(f)$ is Dirac Delta Function, $F\langle\cdot\rangle$ denotes Fourier transform.

Thanks to the distortion power spectrum in equation (10), the distortion power is achieved as follows:

$$P_y = 2\int_0^B \left[\sigma_S^4 a_2^2\delta(z) + \frac{\sigma_S^4}{4B}a_2^2 - \frac{\sigma_S^4}{8B^2}a_2^2 z\right]dz = \frac{19}{4}\sigma_S^4 a_2^2 \tag{11}$$

where $z = |f \pm f_0|$ and $dz = df$, B is the OFDM signal bandwidth.

3.2. Performance Evaluation

Firstly, the SDR of the system will be considered. With the OFDM signal power after BPF [6] is $a_1^2\sigma_s^2$ and distortion power in (11), the SDR is given by:

$$SDR = \frac{\text{Signal Power}}{\text{Distortion Power}} = \frac{a_1^2\sigma_s^2}{\frac{19}{4}\sigma_s^4 a_2^2} = \frac{4}{19}\left(\frac{a_1}{a_2}\right)^2\frac{1}{\sigma_s^2} \tag{12}$$

Assume that the investigated signal $y(t) = f[s(t)]$ depending on the original OFDM signal $S(t)$ can be accurately represented as follows:

$$y = a_1 S(t) + a_2 S^2(t) \tag{13}$$

Compare (13) and (8), we have:

$$a_1 = \Re A^2\gamma \quad \text{and} \quad a_2 = \frac{1}{2}\Re A^2\gamma^2 \tag{14}$$

Therefore, (12) can be rewritten as follows:

$$SDR = \frac{16}{19\gamma^2\sigma_s^2} \tag{15}$$

For $\sigma_s^2 = 1$, the SDR depending on OMI is shown in Fig. 4. When OMI increases, SNR decreases.

For the fixed OMI of the MZM2 $\gamma = 20\%$, the SDR depending on variance σ_s^2 of original OFDM signal can be seen in Fig. 5. It can be seen that SDR drops sharply when the variance rises from 0 to 1.

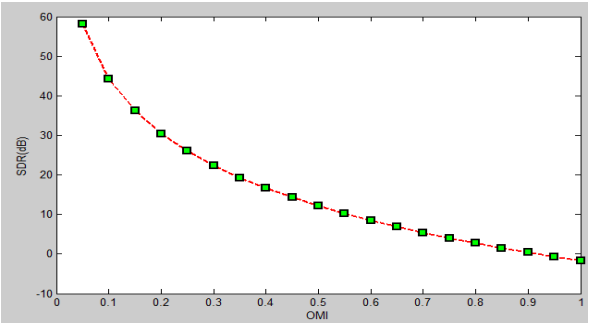

Figure 4: SDR as a function of optical modulation index.

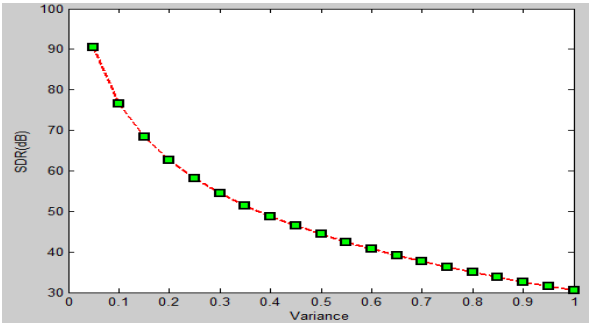

Figure 5: SDR as a function of power of OFDM signal.

The symbol error rate (SER) of QPSK and 16-QAM related to SDR can be shown in [6] as follows:

$$SER_{QPSK} = erfc\left(\sqrt[2]{\frac{SDR}{2}}\right) \quad \text{and} \quad SER_{16-QAM} = \frac{3}{2}erfc\left(\sqrt[2]{\frac{SDR}{10}}\right) \tag{16}$$

4. CONCLUSION

In this paper, a novel model that can transmit high bit rate date with a reasonable price is proposed and analyzed. The effect of OMI and signal power to SDR has been taken into account. In other word, the relationship between OMI and SDR as well as the relationship between OFDM signal power and SDR are clarified. As can be seen, when OMI or Variance increase, SDR will be decreased. Moreover, SER of QPSK and 16-QAM is also taken into account. Now, distortion in the PD and MZM is counted. For the future work, we would like to research other factors that can affect performance of the systems in terms of SNR, SDR and BER such as nonlinearity of LD and chromatic dispersion of optical fiber.

REFERENCES

1. Al-Raweshidy, H. and S. Komaki, *Radio over Fiber Technologies for Mobile Communications Nerworks*, 1st Edition, Artech House, 2002.
2. Cho, T.-S., C. Yun, J.-I. Song, and K. Kim, "Analysis of CNR penalty of radio-over-fiber systems including the effect of phase noise from laser and RF oscillator," *Journal of Lighwave Technology*, Vol. 23, No. 12, 4093–4099, December 2005.
3. Bekkali, A., C. B. Naila, K. Kazaura, K. Wakamori, and M. Matsumoto, "Transmission analysis of OFDM-based wireless services over turbulent radio-on-fso links modeled by Gamma-Gamma distribution," *IEEE Photonics Journal*, Vol. 2, No. 3, 510–520, June 2010.
4. Cao, Z., J. Yu, M. Xia, Q. Tang, Y. Cao, W. Wang, and L. Chen, "Reduction of intersubcarrier interference and frequency-selective fading in OFDM-ROF systems," *Journal of Lighwave Technology*, Vol. 28, No. 16, 2423–2429, August 2010.
5. Van den Bos, C., M. H. L. Kouwenhoven, and W. A. Serdijn, "The influence of non-linear distortion on OFDM bit error rate," *IEEE International Conference on Communications*, Vol. 2, 1125–1129, 2000.
6. Van den Bos, C., M. H. L. Kouwenhoven, and W. A. Serdijn, "Effecr of Smooth Nonlinear Distortion on OFDM symbol error rate," *IEEE Transactions on Communications*, Vol. 49, No. 9, 1510–1514, September 2001.

Retrieving Electromagnetic Properties of Anisotropic Magnetic Metamaterials: An Effective-medium Theory

Shiyang Liu[1, 2], **Zhifang Lin**[2], **and S. T. Chui**[3]

[1]Institute of Information Optics, Zhejiang Normal University, Jinhua, Zhejiang 321004, China
[2]State Key Laboratory of Surface Physics (SKLSP), Key Laboratory of Micro and Nano Photonic Structures (Ministry of Education), Department of Physics, Fudan University, Shanghai 200433, China
[3]Bartol Research Institute, University of Delaware, Newark, DE 19716, USA

Abstract— By arranging an array of single-crystal yttrium-iron-garnet (YIG) ferrite rods periodically in the air, we construct a kind of metamaterials with intrinsic magnetic response. It is accordingly called magnetic metamaterials (MMs). To investigate the electromagnetic (EM) properties of MMs, we develop an effective-medium theory (EMT) based on coherent potential approximation. It is demonstrated that a negative index metamaterial (NIM) is realized by use of MM, which can be magnetically tuned by an external magnetic field (EMF) from a negative index to a positive index. This can be corroborated by the calculation of the photonic band diagrams and the effective constitutive parameters. In addition, a nonreciprocal magnetic surface plasmon (MSP) resonance can be excited at the surface of an MM slab.

1. INTRODUCTION

Metamaterials are composite structured materials consisting of subwavelength resonant building blocks, which exhibit novel and unique electromagnetic (EM) properties, not occurring in nature. A typical class of such materials is the negative index metamaterials (NIM) [1, 2]. Various configurations are proposed and demonstrated to possess either negative refractive index or other particular properties. To investigate and characterize the optical properties of metamaterials, it is crucial to retrieve the effective permittivity ε_{eff} and the effective magnetic permeability μ_{eff}. Many approaches have been developed to deal with the issue and great progress has been achieved [3–7]. However, since most metamaterials designed base on the Pendry's scheme, most theories developed are particularly applied to such systems [3–5]. Recent researches have investigated a class of novel metamaterials consisting of ferrite rods, which exhibit an excellent controllable negative refractive behavior [8] and a tunable nonreciprocal magnetic surface plasmon (MSP) resonance [9] controllable by an external magnetic field (EMF). It is accordingly called magnetic metamaterial (MM). Due to the gyromagnetic property of the ferrite material, its magnetic permeability is a tensor with nonzero off-diagonal components, which is the origin of the nonreciprocity. Therefore, to depict the EM properties of the MM precisely, the anisotropy must be considered from the beginning of the effective-medium theory (EMT).

In the present paper, we present this EMT based on the coherent-potential approximation [7], which is developed particularly for the retrieval of the effective constitutive parameters of the anisotropic MMs. To confirm the validity of the technique, the corresponding photonic band structures of the MM are calculated, which are in good agreement with the EMT in the long wavelength limit. Our results also suggest that the consideration of anisotropy is of great importance in order to retrieve the effective constitutive parameters accurately and therefore illustrate the EM properties of MMs exactly. Besides, we are going to show that the MM can be used to realize controllable negative refraction. The MSP resonance and its time reversal symmetry (TRS) breaking nature can be illustrated by by EMT as well.

2. EFFECTIVE-MEDIUM THEORY

We present in this section the formulation of the EMT for two dimensional (2D) anisotropic MM and consider the transverse magnetic (TM) polarization. For convenience, we consider a system made of ferrite rods with permittivity ε_s and magnetic permeability $\widehat{\mu}$ of the second rank tensor for the fully magnetized ferrite [10]

$$\widehat{\mu} = \begin{pmatrix} \mu_r & -i\mu_\kappa & 0 \\ i\mu_\kappa & \mu_r & 0 \\ 0 & 0 & 1 \end{pmatrix}, \qquad \widehat{\mu}^{-1} = \begin{pmatrix} \mu_r' & -i\mu_\kappa' & 0 \\ i\mu_\kappa' & \mu_r' & 0 \\ 0 & 0 & 1 \end{pmatrix}, \quad \text{with} \tag{1}$$

$$\mu_r = 1 + \frac{\omega_m(\omega_0 - i\alpha\omega)}{(\omega_0 - i\alpha\omega)^2 - \omega^2}, \quad \mu_\kappa = \frac{\omega_m\omega}{(\omega_0 - i\alpha\omega)^2 - \omega^2}, \quad \mu_r' = \frac{\mu_r}{\mu_r^2 - \mu_\kappa^2}, \quad \mu_r' = \frac{-\mu_\kappa}{\mu_r^2 - \mu_\kappa^2},$$

where $\omega_0 = \gamma H_0$ is the resonance frequency with $\gamma = 2.8\,\mathrm{MHz/Oe}$ the gyromagnetic ratio; H_0 is the sum of the EMF applied in z direction and the demagnetization field, $\omega_m = 4\pi\gamma M_s$ is the characteristic frequency with $4\pi M_s$ the saturation magnetization, and α is the damping coefficient of the ferrite. The MM consists of an array of periodic ferrite rods of square lattice in an isotropic homogeneous medium with permittivity ε_0 and permeability μ_0. The geometry of the system is shown in Fig. 1, where the rod axes are along z direction and the radii of the ferrite rods are r_s.

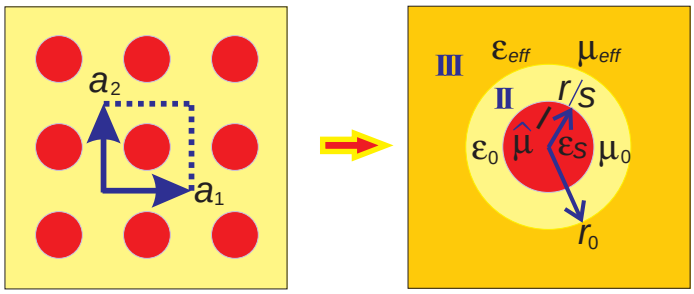

(a) (b)

Figure 1: (a) A 2D anisotropic MM consisting of the ferrite rods arranged as square lattice in the air background, and (b) its corresponding geometry in the effective-medium theory.

The scheme of the EMT is as follows: [11] (i) Transform the discrete periodic system in Fig. 1(a) into the effective medium with effective constitutive parameters ε_{eff} and μ_{eff} in Fig. 1(b); (ii) Take the unit cell of the MM as an equal-area coated rod with ferrite rod as its inner core and the background medium as the coated layer with radius $r_0 = a/\sqrt{\pi}$; (iii) The effective parameters ε_{eff} and μ_{eff} are determined by the condition that the scattering cross section of the coated rod in the effective medium vanishes in the long wave limit $k_{eff} r_0 \ll 1$ where $k_{eff} = k_0\sqrt{\varepsilon_{eff}}\sqrt{\mu_{eff}}$ with k_0 the wave-number in the vacuum, and $\mu_{eff} = (\mu_{re}^2 - \mu_{\kappa e})^2/\mu_{re}$ with μ_{re} and $\mu_{\kappa e}$ the components of the effective magnetic permeability tensor.

Firstly, we expand the EM waves in regions I, II, and III of Fig. 1(b) into the summation of the vector cylindrical wave functions (VCWFs) [12]

$$\mathbf{L}_n^{(J)}(k,\mathbf{r}) = \left[\frac{dz_n^{(J)}(\rho)}{d\rho}\mathbf{e}_r + \frac{in}{\rho}z_n^{(J)}(\rho)\mathbf{e}_\phi\right]e^{in\phi}, \tag{2a}$$

$$\mathbf{M}_n^{(J)}(k,\mathbf{r}) = \left[\frac{in}{\rho}z_n^{(J)}(\rho)\mathbf{e}_r - \frac{dz_n^{(J)}(\rho)}{d\rho}\mathbf{e}_\phi\right]e^{in\phi}, \tag{2b}$$

$$\mathbf{N}_n^{(J)}(k,\mathbf{r}) = z_n^{(J)}(\rho)e^{in\phi}\mathbf{e}_z, \tag{2c}$$

with k the wave vector, $\mathbf{r}$ the position vector, $\rho = kr$, $z_n^{(J)}(\rho)$ the Bessel function $J_n(\rho)$ and the first kind Hankel function $H_n^{(1)}(\rho)$ for $J = 1$ and 3, respectively. For the EM field in the region I

$$\mathbf{E}_s(k_s,\mathbf{r}) = \sum_n q_n^s\mathbf{N}_n^{s(1)}, \qquad \mathbf{H}_s(k_s,\mathbf{r}) = \sum_n \frac{k_s}{i\omega}q_n^s\left[i\mu_{\kappa s}'\mathbf{L}_n^{s(1)} + \mu_{rs}'\mathbf{M}_n^{s(1)}\right], \tag{3}$$

where $k_s = k_0\sqrt{\varepsilon_s}\sqrt{\mu_s}$ with $\mu_s = (\mu_{rs}^2 - \mu_{\kappa s}^2)/\mu_{rs} = 1/\mu_{rs}'$, μ_{rs}, and $\mu_{\kappa s}$ are given in Equation (1). In the coated layer area, i.e., in region II the corresponding EM field components are

$$\mathbf{E}_b(k_0,\mathbf{r}) = \sum_n \left[q_n^0\mathbf{N}_n^{0(1)} - b_n^0\mathbf{N}_n^{0(3)}\right], \qquad \mathbf{H}_b(k_0,\mathbf{r}) = \sum_n \frac{k_0}{i\omega\mu_0}\left[q_n^0\mathbf{M}_n^{0(1)} - b_n^0\mathbf{M}_n^{0(3)}\right], \tag{4}$$

where the superscript 0 implies k_0 is involved in VCWFs. Finally, in region III, we have

$$\begin{aligned}\mathbf{E}_e(k_{eff},\mathbf{r}) &= \sum_n \left[q_n^e\mathbf{N}_n^{e(1)} - b_n^e\mathbf{N}_n^{e(3)}\right],\\ \mathbf{H}_e(k_{eff},\mathbf{r}) &= \sum_n \frac{k_{eff}}{i\omega}\left\{q_n^e\left[i\mu_{\kappa e}'\mathbf{L}_n^{e(1)} + \mu_{re}'\mathbf{M}_n^{e(1)}\right] - b_n^e\left[i\mu_{\kappa e}'\mathbf{L}_n^{e(3)} + \mu_{re}'\mathbf{M}_n^{e(3)}\right]\right\},\end{aligned} \tag{5}$$

where the superscript e implies k_{eff} is involved in VCWFs, μ'_{re} and $\mu'_{\kappa e}$ are defined in Equation (1).

By matching the standard boundary conditions at $r = r_0$, it can be obtained that

$$\begin{pmatrix} q_n^e \\ b_n^e \end{pmatrix} = \frac{\pi}{2i\mu_0\mu'_{re}} \begin{pmatrix} \mathcal{A}_{11} & \mathcal{A}_{12} \\ \mathcal{A}_{21} & \mathcal{A}_{22} \end{pmatrix} \begin{pmatrix} q_n^0 \\ b_n^0 \end{pmatrix}. \tag{6}$$

According to rule (iii) of the EMT, the coated rod located in the effective medium subjects to null scattering. According to the Mie theory, the total scattering cross section is $C_{sca} = 4\sum_n |D_n^e|^2 / k_{eff}$ with $D_n^e = b_n^e/q_n^e$ the Mie scattering coefficients of the coated rod in the effective medium. In the limit $k_{eff} r_0 \ll 1$, only the dominated terms of $n = 0, \pm 1$ need to be considered. Taking account of $D_n^e = b_n^e = 0$, it is straightforward from Equation (6) to get

$$\frac{\mathcal{A}_{21}}{\mathcal{A}_{22}} = -\frac{b_n^0}{q_n^0} = -D_n^s, \quad n = 0, \pm 1, \tag{7}$$

where D_n^s are the Mie coefficients of the inner core ferrite rod. Then we can obtain the simplified equations determining ε_{eff} and μ_{eff}.

$$\varepsilon_{eff} = (1-f)\varepsilon_0 + f\widetilde{\varepsilon}_s, \qquad \frac{\mu_{eff} - \mu_0}{\mu_{eff} + \mu_0} = f\frac{\tilde{\mu}_s - \mu_0 - \xi}{\tilde{\mu}_s + \mu_0 + \xi}, \tag{8}$$

where f is the filling fraction with $f = r_s^2/r_0^2$, and

$$\begin{aligned} &\widetilde{\varepsilon}_s = 2\varepsilon_s F_2(x_s), \qquad \tilde{\mu}_s = \mu_s G_2(x_s), \qquad \xi = -\frac{(1-f)\mu_0^2(\mu_\kappa/\mu_r)^2(\tilde{\mu}_s/\mu_s)^2}{(1-f)\mu_0 + (1+f)\tilde{\mu}_s}, \\ &F_2(x_s) = J_1(x_s)/[x_s J_0(x_s)], \qquad G_2(x_s) = J_1(x_s)/\left[x_s J_1'(x_s)\right], \end{aligned} \tag{9}$$

with $x_s = k_s r_s$.

3. CONTROLLABLE NEGATIVE REFRACTION

As a candidate of the ferrite materials, single-crystal yttrium-iron-garnet (YIG) can be the first choice for its negligible low damping $\alpha = 3 \times 10^{-4}$. The saturation magnetization is $4\pi M_s = 1750\,\text{Oe}$ and the permittivity is $\varepsilon_s = 25$. In our proof-of-principle demonstration we set $\alpha = 0$ for convenience. In Figs. 2(b) and (d), we present ε_{eff} and μ_{eff} as the functions of the angular frequency ω for an MM composed of ferrite rods arranged as a square lattice in the air. The exerted EMFs satisfy $H_0 = 500\,\text{Oe}$ and $H_0 = 475\,\text{Oe}$, for the results shown in Figs. 2(b) and (d), respectively. It can be seen that within the frequency range from 15.5 GHz to 16.2 GHz, the system exhibits simultaneous negative ε_{eff} and μ_{eff} for $H_0 = 500\,\text{Oe}$, implying a working frequency range for the NIM. To confirm the result, the corresponding photonic band diagrams are calculated as shown in Figs. 2(a) and (c). Excellent agreement between two independent results is obtained. In particular, the working frequency of NIM corresponds to the second photonic band denoted by the blue line in Fig. 2(a). At about 16.2 GHz, one gets a so-called epsilon-near-zero (ENZ) medium, which can induce a longitudinal EM mode in the system, corresponding to the nearly flat third band labeled by the black line in Fig. 2(a). The comparison between the band diagram and ε_{eff} and μ_{eff} confirms the validity of the EMT. A particularly important results obtained with the EMT is that at $\omega = 16\,\text{GHz}$, the effective constitutive parameters $\varepsilon_{eff} = \mu_{eff} = -1$ is realized as marked by the horizontal solid green line in Figs. 2(a) and (b).

To demonstrate the manipulability of the negative refractive index by the EMF, we present in Fig. 2(d) ε_{eff} and μ_{eff} for a smaller EMF such that $H_0 = 475\,\text{Oe}$. The corresponding photonic band diagram is also given in Fig. 2(c). Good agreement can still be found for Figs. 2(c) and (d), which confirms once again the validity of the EMT. Compared to Figs. 2(a) with (b), it can be found that the photonic band diagram is shifted to a lower frequency range, so does the working frequency bandwidth of the NIM. At $\omega = 16\,\text{GHz}$, the refractive index is $n_{eff} = 1.13$ with $\varepsilon_{eff} = 0.92$ and $\mu_{eff} = 1.4$, no longer a negative one. The working frequency for the NIM is shifted downwards and located at about 15.5 GHz. Therefore, by appropriately adjusting the EMF, we can manipulate the working frequency for the NIM, which adds considerably to the flexibility in practical applications.

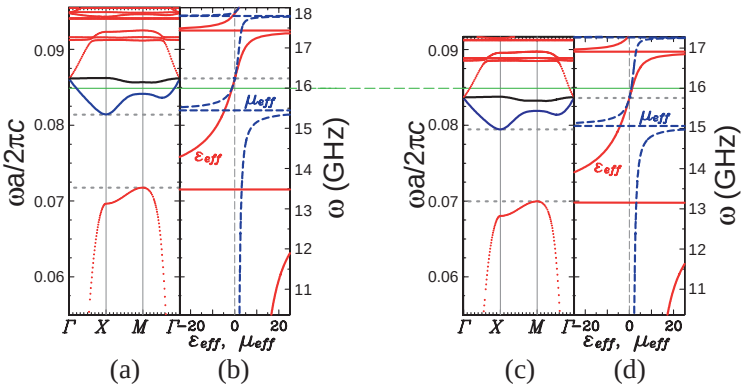

Figure 2: (a) Photonic band diagram for a 2D MM of square lattice with lattice constant $a = 10\,\text{mm}$, rod radius $r_s = 3.5\,\text{mm}$, and $H_0 = 500\,\text{Oe}$. (b) Effective permittivity ε_{eff} and effective permeability μ_{eff} as the functions of circular frequency ω for the system with the same parameters as in (a). (c) and (d) are the same as (a) and (b) except $H_0 = 475\,\text{Oe}$.

4. MSP RESONANCE IN MM

By adjusting the geometry of the MM into a square lattice with the lattice constant $a = 8\,\text{mm}$ and the rod radius $r = \frac{1}{4}a = 2\,\text{mm}$. The permittivity is taken as $\varepsilon_s = 15$ and the EMF is $H_0 = 900\,\text{Oe}$. We calculate the corresponding photonic band diagram and effective constitutive parameters. The results are shown in Fig. 3, where we can find flat bands in panel (a), around which two separate photonic band gaps come into appearance. The resonant frequency is $f_s = \frac{1}{2\pi}(\omega_0 + \frac{1}{2}\omega_m)$, at which we can find $\mu_r + \mu_\kappa = -1$, corresponding to resonance of a single ferrite rod [9]. The coupling of the neighboring MSP resonant states of each single ferrite rod results in the resonance of the whole system. In Fig. 3(b), we present the effective constitutive parameters calculated based on the EMT. It can be found that at the MSP resonant frequency $f = 4.97\,\text{GHz}$ the effective magnetic permeability $\mu_{eff} = -1$ as marked by the black dashed line, it is therefore a magnetic analogue of electric surface plasmon resonance, accordingly, called MSP resonance. A close examination of the results also suggests that double positive effective parameters correspond to the photonic bands, single negative effective parameter corresponds to the photonic gap, while the resonances correspond to the flat bands. It should be pointed out that the MSP resonance is different from the electric surface plasmon resonance in that the TRS is broken under an EMF. Accordingly, based on the MSP resonance we can realize some typical EM nonreciprocal properties. The unidirectional reflecting effect [13], unidirectional absorbing effect [14], and unidirectional waveguiding effect [15–18].

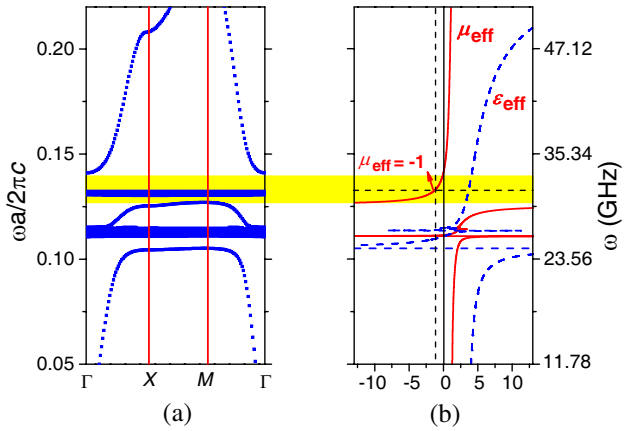

Figure 3: (a) The photonic band diagram for an MM of square lattice. (b) The retrieved effective constitutive parameters where the blue dashed line and red solid line correspond to the effective permittivity ε_{eff} and the effective magnetic permeability μ_{eff}, respectively.

5. CONCLUSION

In conclusion, we develop an EMT based on coherent potential approximation, which is particularly suitable for a 2D anisotropic MM consisting of an array of single-crystal YIG ferrite rods. By optimizing the parameters of the system, we demonstrate that a matched NIM with $\varepsilon_{eff} = \mu_{eff} = -1$ can be realizable by an MM and controllable by an EMF. Further investigation suggests that nonreciprocal MSP resonance can also be created. A lot of interesting unidirectional EM effects can be expected based on the MSP resonance.

ACKNOWLEDGMENT

This work was supported by National Natural Science Foundation of China (Nos. 10904020, 11174059, and 11274277), and the open project of SKLSP in Fudan University (No. KL2011_8). Liu is also supported the program for innovative research team in Zhejiang Normal University.

REFERENCES

1. Pendry, J. B., "Negative refraction makes a perfect lens," *Phys. Rev. Lett.*, Vol. 85, No. 18, 3966–3969, 2000.
2. Shelby, R. A., D. R. Smith, and S. Schultz, "Experimental verification of a negative index of reflection," *Science*, Vol. 292, No. 5514, 77–79, 2001.
3. Sarychev, A. K., R. C. McPhedran, and V. M. Shalaev, "Electrodynamics of metal-dielectric composites and electromagnetic crystals," *Phys. Rev. B*, Vol. 62, No. 12, 8531, 2000.
4. Smith, D. R., S. Schultz, P. Markos, and C. M. Soukoulis, "Determination of effective permittivity and permeability of metamaterials from reflection and transmission coefficients," *Phys. Rev. B*, Vol. 65, No. 19, 195104, 2002.
5. Smith, D. R., D. C. Vier, T. Koschny, and C. M. Soukoulis, "Electromagnetic parameter retrieval from inhomogeneous metamaterials," *Phys. Rev. E*, Vol. 71, No. 3, 036617, 2005.
6. Bregar, V. B., "Effective-medium approach to the magnetic susceptibility of composites with ferromagnetic inclusions," *Phys. Rev. B*, Vol. 71, No. 17, 174418, 2005.
7. Wu, Y., J. Li, Z. Q. Zhang, and C. T. Chan, "Effective medium theory for magnetodielectric composites: Beyond the long-wavelength limit," *Phys. Rev. B*, Vol. 74, No. 8, 085111, 2006.
8. Liu, S. Y., W. K. Chen, J. J. Du, Z. F. Lin, S. T. Chui, and C. T. Chan, "Manipulating negative refractive behavior with a magnetic field," *Phys. Rev. Lett.*, Vol. 101, No. 15, 157407, 2008.
9. Liu, S. Y., J. J. Du, Z. F. Lin, R. X. Wu, and S. T. Chui, "Formation of robust and completely tunable resonant photonic band gaps," *Phys. Rev. B*, Vol. 78, No. 15, 155101, 2008.
10. Pozar, D. M., *Microwave Engineering*, 3rd Edition, Wiley, New York, 2005.
11. Jin, J. F., S. Y. Liu, Z. F. Lin, and S. T. Chui, "Effective-medium theory for anisotropic magnetic metamaterials," *Phys. Rev. B*, Vol. 80, No. 11, 115101, 2009.
12. Bohren, C. F. and D. R. Huffman, *Absorption and Scattering of Light by Small Particles*, Wiley, New York, 1983.
13. Chui, S. T., S. Y. Liu, and Z. F. Lin, "Reflected wave of finite circulation from magnetic photonic crystals," *J. Phys.: Condens. Matter*, Vol. 22, 182201, 2010.
14. Yu, J. J., H. J. Chen, Y. B. Wu, and S. Y. Liu, "Magnetically manipulable perfect unidirectional absorber based on nonreciprocal magnetic surface plasmon," *EPL*, Vol. 100, 47007, 2012.
15. Liu, S. Y., W. L. Lu, Z. F. Lin, and S. T. Chui, "Magnetically controllable unidirectional electromagnetic waveguiding devices designed with metamaterials," *Appl. Phys. Lett.*, Vol. 97, No. 20, 201113, 2010.
16. Liu, S. Y., W. L. Lu, Z. F. Lin, and S. T. Chui, "Molding reflection from metamaterials based on magnetic surface plasmons," *Phys. Rev. B*, Vol. 84, No. 4, 045425, 2011.
17. Poo, Y., R. X. Wu, S. Y. Liu, Y. Yang, Z. F. Lin, and S. T. Chui, "Experimental demonstration of surface morphology independent electromagnetic chiral edge states originated from magnetic plasmon resonance," *Appl. Phys. Lett.*, Vol. 101, No. 8, 081912, 2012.
18. Shen, J., S. Y. Liu, H. W. Zhang, S. T. Chui, Z. F. Lin, X. Fan, X. M. Kou, Q. Lu, and J. Q. Xiao, "Robust and tunable one-way magnetic surface plasmon waveguide: An experimental demonstration," *Plasmonics*, Vol. 7, 287–291, 2012.

Theoretical Design of a Two-dimensional Acoustic Metafluid with Anisotropic Effective Mass Density

J. Arriaga[1], **L. Gumen**[2], **and A. A. Krokhin**[3]

[1]Instituto de Física, Benemérita Universidad Autónoma de Puebla
18 Sur y San Claudio, Edif. 110 B, Ciudad Universitaria, Puebla 72570, México
[2]Universidad Popular Autónoma del Estado de Puebla, 21 Sur 11, Puebla 72160, México
[3]Department of Physics, University of North Texas
1155 Union Circle 311427, Denton, TX 76203, USA

Abstract— The effective mass density is one of the most basic and important parameters in the study of elastic wave interactions with materials. In this work, we report an effective dynamic mass density for a two-component, two-dimensional (2D) periodic fluid-solid composite in which the fluid constitutes the host medium. Fluids and glasses are naturally isotropic in the absence of external fields, and anisotropy is a property which is usually associated with crystal solids. Anisotropy may, however, be artificially stimulated by embedding periodic structures in naturally isotropic fluids. Then these artificial structures — so called phononic crystals — may have very unusual properties. Within a narrow band of frequencies of sound the effective mass or the effective elastic modulus of specially designed phononic crystals may become anisotropic, take negative values, or acquire abnormally large imaginary part. Due to such "strange" properties that do not exist for natural materials these artificial structures are usually called metamaterials or metafluids. Using the plane-waves expansion method we derive (in the long wavelength limit) a formula for the effective mass tensor of the metafluid. The proposed formula is very general and it is valid for arbitrary Bravais lattices and arbitrary filling fractions of the cylinders. In particular, we calculate the effective mass tensor for sound waves in air with embedded lattice of aluminum cylinders having different cross sections. We consider cylinders with circular and triangular cross sections arranged in both rectangular and hexagonal lattice. The proposed method of calculation may find numerous applications for tailoring of metafluids with prescribed anisotropy which is necessary for design of acoustic cloaks.

1. INTRODUCTION

The field of so-called metamaterials started with a theoretical proposal of Veselago in 1968 [1], when he showed that if a material have both, the electric permittivity ϵ and magnetic permeability μ, negative, then its refractive index ($n = \sqrt{\epsilon\mu}$) must be calculated by taking the negative branch of square root. This pioneer proposal opens a new field in physics with novel properties not showed by natural materials. Negative refraction, superlens, and optical invisibility are some examples of the fascinating applications of these man-made materials. Recently, the technique of transformation optics [2, 3] was introduced to establish a correspondence between material constitutive parameters and coordinate transformations. Such correspondence is a basis for design of conceptual optical components that can control electromagnetic (EM) waves with unprecedented degrees of freedom, resulting in many interesting possibilities. Among all kinds of interesting devices based on the method of transformation optics, the invisibility cloaking is perhaps the most famous and intriguing [4, 5]. After Pendry's discovery of the mechanism for electromagnetic cloaking, which follows from the properties of the Maxwell equations under coordinates transformations [3], the concept of cloaking has been extended from EM fields to acoustics [6] and elasticity [7, 8].

However, invisible cloak requires acoustic materials which are anisotropic and inhomogeneous. Such materials are difficult to find in nature. Fortunately, artificial composite materials, can in principle be fabricated, and such "acoustic metamaterials" can exhibit exotic properties for effective mass density and bulk modulus. Cummer and Scuring [6] have predicted that acoustic cloaking similar to that previously proposed for electromagnetic waves, should be possible by means of acoustic materials having anisotropic and inhomogeneous mass density.

The Maxwell equations possess a special kind of symmetry (invariance) with respect to coordinate transformations. The wave equations that describe acoustic waves in fluids do not possess the same symmetry. Milton et al. [7] analysed the full equations of motion for a general elastic medium under coordinate transformations and found that, in general, the dynamical equations of elasticity are not invariant with respect to coordinate transformations. There is, at least one special

case, however, when the equivalence between electrodynamics and elastodynamics is complete. It has been known that in two dimensions (2D) acoustics and electrodynamics in isotropic media are exactly equivalent, see Ref. [9]. Moreover, this case is practically useful and can be experimentally realized.

Anisotropy is a property which is usually associated with crystalline solids. Fluids and glasses are naturally isotropic in the absence of external fields. Anisotropy may be artificially stimulated by embedding periodic structures in naturally isotropic fluids. Then these artificial structures — so called phononic crystals — may have very unusual properties. Within a narrow band of frequencies of sound the effective mass or the effective elastic modulus of specially designed phononic crystals may become anisotropic, take negative values, or acquire abnormally large imaginary part. In this work we demonstrate that a fluid filling the space between solid cylinders arranged in a two-dimensional lattice exhibits anisotropic dynamic mass for sound waves propagating through the lattice. Using the plane-waves expansion method proposed in Ref. [10] we derive (in the long wavelength limit) a formula for the effective mass tensor of the metafluid, and we show that it is possible to control the degree of anisotropy of the system. We calculate the effective mass tensor for sound waves in air with embedded lattice of aluminum cylinders with different cross sections. In particular, we consider cylinders with circular and triangular cross sections arranged in hexagonal (isotropic) and rectangular (anisotropic) lattices.

2. EFFECTIVE MEDIUM PARAMETERS

We consider a two-dimensional (2D) periodic arrangement of solid cylinders with arbitrary cross-section embedded in a non-viscous fluid. The axes of the cylinders are supposed to be along the z axis. In Figure 1, we show schematically a top view of this 2D periodic arrays of cylinders. We consider that the cylinders do not touch each other, so that the transverse modes are suppressed. Since a fluid supports propagation of longitudinal modes only, the propagation mode in a lattice is also a longitudinal one. Its phase velocity is given by the following relation,

$$c(\mathbf{n}) = \sqrt{\frac{B_{\mathit{eff}}}{\rho_{\mathit{eff}}}}, \tag{1}$$

where B_{eff} and ρ_{eff} is the effective bulk modulus and the effective mass density of the periodic system, respectively. In general, the speed of sound is dispersive, i.e., it depends on the Bloch vector $\mathbf{k}$. In the long-wavelength limit, however, only the dependence on the direction of propagation in the plane of periodicity $\mathbf{n} = \mathbf{k}/k$ survives. This dependence is the source of anisotropy in the mass density. In the low-frequency limit, the dispersion relation for a phononic crystal is always linear, $\omega = c(\mathbf{n})k$, and the speed of sound is found from the following equation,

$$c(\mathbf{n}) = \lim_{k\to 0}\left(\frac{\omega}{k}\right) \tag{2}$$

It turns out to be dependent not only on the direction of propagation $\mathbf{n}$ and the average characteristics of the periodic structure, but also on the details and geometry of the unit cell. Since the bulk modulus is known to depend on the average characteristics only,

$$\frac{1}{B_{\mathit{eff}}} = \frac{f}{B_c} + \frac{1-f}{B_f}, \tag{3}$$

it is the effective mass density which acquires all the details of the lattice structure and the dependence on the direction $\mathbf{n}$. Here B_c and B_f are the elastic modulii of the cylinders and fluid, respectively, and f is the fraction of the unit cell occupied by the cylinders. There have been several derivations of the effective mass density using different approximations. For example, Berryman using an approach similar to Maxwell-Garnet approximation, obtained the effective mass of a fluid with embedded circular cylinders arranged in a square lattice [11]. J. Mei et al. using multiple-scattering theory justified the validity of Berryman's result obtaining a good agreement with experimental results by Cervera et al. [12, 13]. However, all of them consider isotropic lattices which lead to isotropic effective mass density, i.e., ρ_{eff} is represented by a scalar. Recently, two different approaches to the problem of homogenization of phononic crystals have been proposed [14–16]. Both are based on multiple-scattering theory. They lead to analytical formulas for the effective

acoustic characteristics if finite number of terms (dipole, quadrupole, etc.) are kept in the expansion of scattering amplitude. These approaches are valid, however, for cylinders with circular cross-sections only. Thus, the acoustic anisotropy considered in Refs. [14–16] is due to asymmetry of the Bravais lattices.

We have used the plane wave expansion method to obtain the effective sound velocity in the long wavelength limit, valid for any Bravais lattice and any contrast between the acoustic impedances of the constituents. In this limit, the speed of sound in a 3D periodic fluid-fluid system was reported in Ref. [10]. This result is equally valid for a 2D system of solid cylinders embedded in a fluid. We explore Eqs. (1) and (2) and the result of Ref. [10] to introduce here the effective mass density

$$\frac{1}{\rho_{eff}(\mathbf{n})} = \frac{f}{\rho_c} + \frac{1-f}{\rho_f} - \sum_{\mathbf{G},\mathbf{G}'\neq 0} (\mathbf{n}\cdot\mathbf{G})(\mathbf{n}\cdot\mathbf{G}')\nu(\mathbf{G})\nu(-\mathbf{G}')[(\mathbf{G}\cdot\mathbf{G}')\nu(\mathbf{G}-\mathbf{G}')]^{-1}. \tag{4}$$

$\mathbf{G}$ and $\mathbf{G}'$ are the reciprocal lattice vectors of 2D periodic structure, $[\ldots]^{-1}$ means inversion of the matrix in brackets, and $\nu(\mathbf{G})$ are the Fourier coefficients of the periodic function,

$$\frac{1}{\rho(\mathbf{r})} = \sum_{\mathbf{G}} \nu(\mathbf{G}) \exp(i\mathbf{G}\cdot\mathbf{r}). \tag{5}$$

Equation (4) is exact in the quasi-static limit $\omega \to 0$. It takes into account all the dynamical and geometrical details of the periodic structure which affect the propagation of the sound at low frequencies. From Eq. (4) we observe that in general, the effective mass density is anisotropic, i.e., it depends on the direction of propagation $\mathbf{n}$. However, if the unit cell possesses third (or higher) rotational axis of symmetry, the dependence on $\mathbf{n}$ disappears. For these cases, in the long wavelength limit, the periodic structures are isotropic [17]. In the anisotropic case, the effective mass $\rho(\mathbf{n})$ given by Eq. (4) sweeps an ellipse in the x-y plane. For example, for a 2D lattice with rectangular symmetry the inverse mass density along the x- and y-directions can be written as,

$$\frac{1}{\rho_x} = \frac{f}{\rho_c} + \frac{1-f}{\rho_f} - \sum_{\mathbf{G},\mathbf{G}'\neq 0} G_x G'_x \nu(\mathbf{G})\nu(-\mathbf{G}')[(\mathbf{G}\cdot\mathbf{G}')\nu(\mathbf{G}-\mathbf{G}')]^{-1}. \tag{6}$$

$$\frac{1}{\rho_y} = \frac{f}{\rho_c} + \frac{1-f}{\rho_f} - \sum_{\mathbf{G},\mathbf{G}'\neq 0} G_y G'_y \nu(\mathbf{G})\nu(-\mathbf{G}')[(\mathbf{G}\cdot\mathbf{G}')\nu(\mathbf{G}-\mathbf{G}')]^{-1}. \tag{7}$$

3. NUMERICAL RESULTS

We calculate the dynamic mass density for a 2D crystal of solid cylinders in air background. Air has static mass density $\rho_f = 1.29\,\mathrm{kg/m^3}$ and bulk modulus $B_f = 141\,\mathrm{kPa}$. The cylinders are from aluminum with static mass density $\rho_c = 2712.63\,\mathrm{kg/m^3}$ and bulk modulus $B_f = 68.9\,\mathrm{GPa}$. Using these parameters, in a previous work, we have reported the effective mass tensor for sound waves in air with embedded lattice of aluminum cylinders having rectangular cross sections and arranged in a square lattice [18]. In this work, we consider cylinders with circular and triangular cross sections arranged in both, rectangular and hexagonal lattice. The considered systems are shown

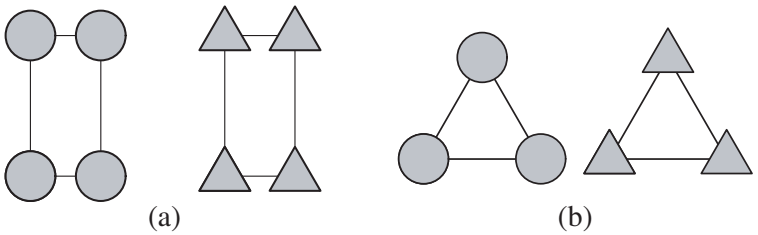

Figure 1: Schematic representation of the systems under study: (a) rectangular lattice with circular and triangular cylinders' (b) triangular lattice with circular and triangular cylinders.

schematically in Fig. 1. The Fourier coefficients $\nu(\mathbf{G})$ are given by,

$$\nu(\mathbf{G}) = \left(\frac{1}{\rho_c} - \frac{1}{\rho_f}\right)\frac{2i}{A_c G_y}\left\{e^{-i\frac{\sqrt{3}a}{4}G_y}\left[\frac{e^{i\frac{a}{4}G_x}\sin[(G_x+\sqrt{3}G_y)\frac{a}{4}]}{G_x+\sqrt{3}G_y} + \frac{e^{-i\frac{a}{4}G_x}\sin[(G_x-\sqrt{3}G_y)\frac{a}{4}]}{G_x-\sqrt{3}G_y}\right] - \frac{\sin(\frac{a}{2}G_x)}{G_x}\right\} \quad (8)$$

for the triangular cross-section of the cylinders and

$$\nu(\mathbf{G}) = (\frac{1}{\rho_c} - \frac{1}{\rho_f})2f\frac{J_0(|\mathbf{G}|r_0)}{|\mathbf{G}|r_0} \quad (9)$$

for the circular cross-section. In Eq. (8) A_c is the area of the unit cell, and a is the side of the triangle in Fig. 1. In Eq. (9) J_0 is the Bessel function of order zero, r_0 is the radius of the cylinders, and f the filling fraction of circular cylinders $f = \pi r_0^2/A_c$. All our calculation were done using $N = 4726$ plane waves in order to guarantee less than 1% numerical error. In Fig. 2, we show the effective mass density (normalized to the air density) as a function of the filling fraction for the case of the circular cylinders arranged in a rectangular lattice with aspect ratio 1 : 2. In this case, the system is anisotropic and in Fig. 2, we show the values of the ρ_x, ρ_y and ρ_x/ρ_y vs filling fraction in order to demonstrate the degree of acoustic anisotropy of the system. The results in Fig. 2 are shown for the interval of the filling fraction from zero to the maximum value ($\pi/8$) corresponding to close packing structure. Both components of the tensor mass density increase with the filling fraction, but this increase is greater for the y component due to narrower spacing along the y-axis. Strong spacing reduction along the y-axis forces the acoustic wave to propagates through the cylinders. To observe the anisotropy clearly, in Fig. 3 we plot ρ as a function of the direction of propagation $\mathbf{n}$ for three different values of the filling fraction. Figs. 3(a), (b), and (c) correspond to $f = 0.05$, 0.25, and 0.35 respectively. In this figure we clearly observe large anisotropy which appears at higher filling fractions.

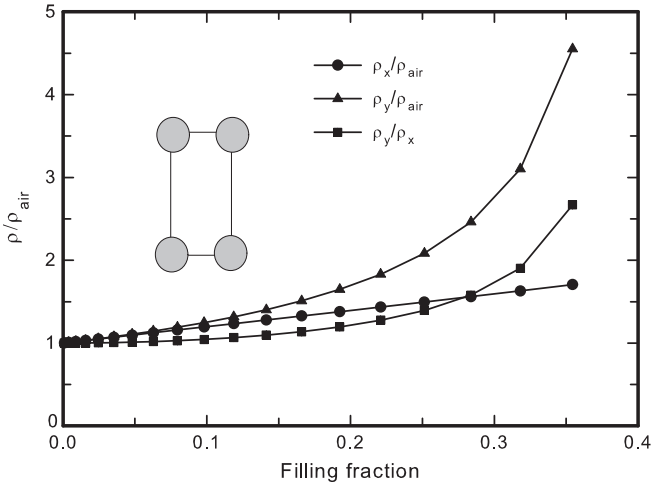

Figure 2: Dynamic mass density (normalized to the density of air) vs filling fraction. Insert shows the unit cell of the phononic crystal.

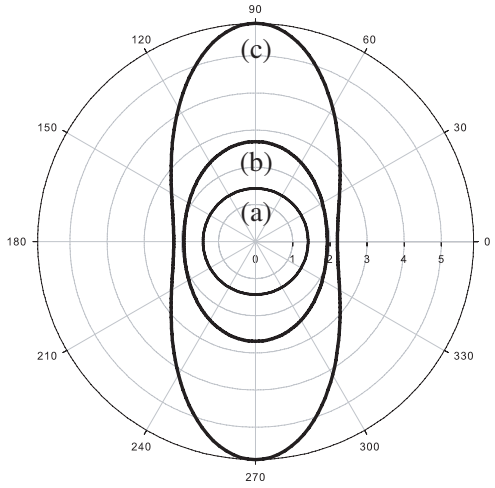

Figure 3: Mass density as a function of the direction of propagation $\mathbf{n}$ for the rectangular lattice shown in the insert in Fig. 2 for three different filling fractions: (a) $f = 0.05$, (b) $f = 0.25$, and (c) $f = 0.35$.

Because our formula, Eq. (4), is very general, we can consider arbitrary shape of the metallic inclusions. As an example of this, in Fig. 4, we plot the effective mass density for rectangular array of cylinders with triangular cross section. In Fig. 4(a), corresponding to the a-orientaion, we show the effective mass density for $f = 0.05$, 0.10, and 0.20. Fig. 4(b), corresponding to the b-orientation, shows $\rho(\mathbf{n})$ for $f = 0.05$, 0.16, and 0.26 respectively. From Fig. 4, we observe that larger anisotropy is obtained for the b-orientation, due to larger values of the filling fraction allowed

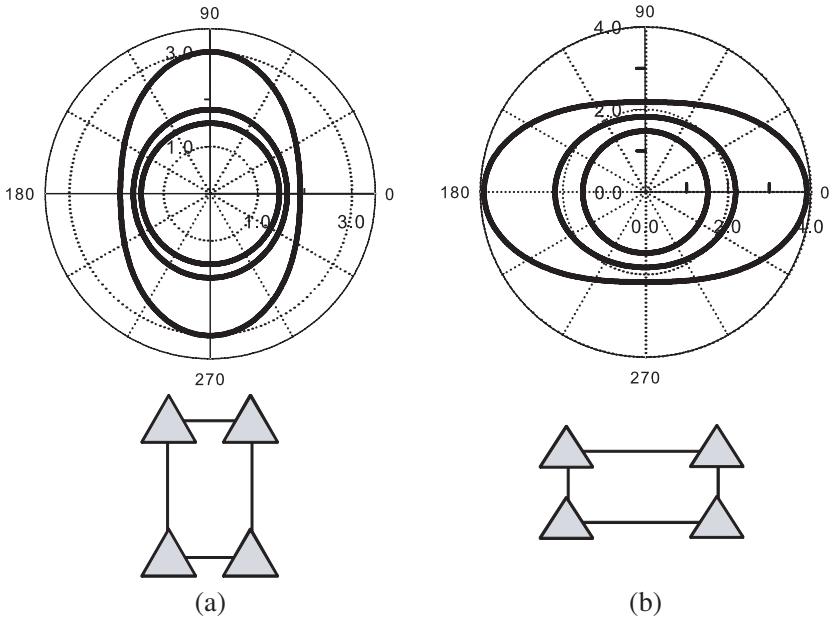

Figure 4: Effective mass density for the rectangular array of triangular cylinders for three different values of the filling fraction as a function of the direction of propagation **n**. From inner to outer curves: (a) $f = 0.05$, 0.10, and 0.20 for the so-called $a-$orientation showed in the low part of the figure, (b) $f = 0.05$, 0.16, and 0.26 for the b-orientation.

for this configuration. The maximum filling fraction for the orientations a and b are $\sqrt{3}/8 = 0.216$, and $1/(2\sqrt{3}) = 0.288$, respectively. Finally, in Fig. 5 we show mass density vs filling fraction for the hexagonal lattice of circular and triangular cylinders. This array is isotropic due to presence of a third order axis of symmetry. The maximum values of the filling fraction for this case is, $\pi/(2\sqrt{3}) = 0.906$, and 0.50 for the circular- and triangular-shaped cylinders, respectively. If we compare the values of the mass density corresponding to equal filling fractions, we observe practically the same values for circular and triangular cylinders. The hexagonal array with triangular cylinders, reaches its maximum value for the filling fractions near the close packing structure. The maximum value of the filling fraction for this case is 0.5, which is relatively low fraction for cylinders occupying empty space. This explains relatively low values obtained for the mass density. On the other hand, for the circular cylinders (see Fig. 5(a)), the mass density exhibits strong increment at high values of the filling fractions. For the values of f near the close-packing structure sound propagates mostly through metal which has practically an infinite mass density as compared to air.

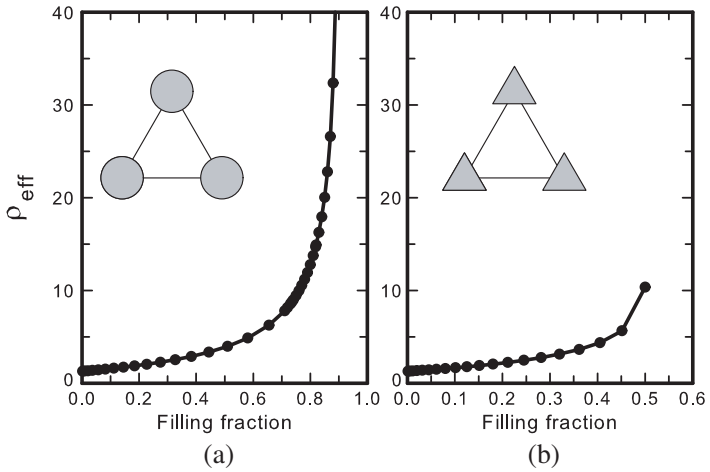

Figure 5: Isotropic effective mass density for the triangular array of (a) circular and (b) triangular cylinders, as a function of the filling fraction.

4. CONCLUSION

In summary, we propose a new exact formula to calculate the effective mass density of periodic two-dimensional metafluids. This formula is valid in the long wavelength limit, and it is free from any limitations over the geometry of the array and the cross-sectional shape of the cylinders. The results obtained in this work could be useful for practical realization of artificial metamaterials possessing very high anisotropy, which is necessary for design of acoustic cloaks.

ACKNOWLEDGMENT

This work has been partially supported by Conacyt-México under grant number 167939.

REFERENCES

1. Veselago, V. G., "The electrodynamics of substances with simultaneously negative values of ϵ and μ," *Sov. Phys. Usp.*, Vol. 10, 509–514, 1969.
2. Leonhardt, U., "Optical conformal mapping," *Science*, Vol. 312, 1777–1780, 2006.
3. Pendry, J. B., D. Schurig, and D. R. Smith, "Controlling electromagnetic fields," *Science*, Vol. 312, 1780–1782, 2006.
4. Schurig, D., J. J. Mock, B. J. Justice, S. A. Cummer, J. B. Pendry, A. F. Starr, and D. R. Smith, "Metamaterial electromagnetic cloak at microwave frequencies", *Science*, Vol. 314, 977–980, 2006.
5. Leonhardt, U. and T. Tomas, "Broadband invisibility by non-euclidean cloaking," *Science*, Vol. 323, 110–112, 2006.
6. Cummer, S. A. and D. Schurig, "One path to acoustic cloaking," *New J. of Physics*, Vol. 9, 1–9, 2007.
7. Milton, G. W., M. Briane, and J. R. Willis, "On cloaking for elasticity and physical equations with a transformation invariant form," *New J. of Physics*, Vol. 8, 1–20, 2006.
8. Norris, A. N. and A. L. Shuvalov, "Elastic cloaking theory," *Wave Motion*, Vol. 48, 525–538, 2011.
9. Kelders, L., J. B. Allard, and W. Laurkis, "Ultrasonic surface waves above rectangular-groove gratings," *J. Acoust. Soc. Am.*, Vol. 103, 2730–2733, 1998.
10. Krokhin, A. A., J. Arriaga, and L. N. Gumen, "Speed of sound in periodic elastic composites," *Phys. Rev. Lett.*, Vol. 91, 264302-1–264302-4, 2003.
11. Berryman, J. G., "Long-wavelength propagation in composite elastic media. 1. Spherical inclusions," *J. Acoust. Soc. Am.*, Vol. 68, 1809–1819, 1980.
12. Mei, J., Z. Liu, W. Wen, and P. Sheng, "Effective mass density of fluid-solid composites," *Phys. Rev. Lett.*, Vol. 96, 024301-1–024301-4, 2006.
13. Cervera, F., L. Sanchis, J. V. Sánchez-Pérez, R. Martínez-Sala, C. Rubio, and F. Meseguer, "Refractive acoustic devices for airborne sound," *Phys. Rev. Lett.*, Vol. 82, 023902-1–0923902-4, 2002.
14. Wu, Y., J. Mei, and P. Sheng, "Anisotropic dynamic mass density for fluid-solid composites," *Physica B*, Vol. 407, 4093–4096, 2012.
15. Mei, J., Y. Wu, and Z. Liu, "Effective medium of periodic fluid-solid composites," *EPL*, Vol. 98, 54001-p1–54001-p6, 2012.
16. Torrent, D. and J. Sánchez-Dehesa, "Multiple scattering formulation of two-dimensional acoustic and electromagnetic metamaterials," *New Journal of Physics*, Vol. 13, 09318-p1–093018-p25, 2011.
17. Krokhin, A. A., P. Halevi, and J. Arriaga, "Long-wavelength limit (homogenization) for two-dimensional photonic crystals," *Phys. Rev. B*, Vol. 65, 115208-1–115208-17, 2002.
18. Gumen, L., J. Arriaga, and A. A. Krokhin, "Metafluid with anisotropic dynamic mass," *Low Temp. Phys.*, Vol. 37, 975–978, 2011.

3D Numerical Simulations and Measurements of Effective Dielectric Properties of Oil-in-Water Emulsions

J. Vrba
Faculty of Biomedical Engineering, Czech Technical University in Prague, Czech Republic

Abstract— An existing 2D concept for the numerical estimation of effective dielectric properties of mixtures with random droplets' distribution was adapted here and expanded into 3D. The expansion of the concept to 3D introduces a new possibility for direct comparison of simulation results with measured values. Simulated effective permittivity of Water-in-Oil as well as of Oil-in-Water emulsions were compared to data estimated using two mixing formulas: Maxwell Garnett and Bruggeman. Dielectric properties estimated with the Maxwell Garnett mixing formula fits better dielectric properties of both Oil-in-Water and Water-in-Oil emulsions. Furthermore, dielectric properties of Oil-in-Water emulsions were measured using a commercial system Dielectric Probe Kit from Agilent Technologies. The measured data were compared with the dielectric properties estimated using both the Maxwell Garnett mixing formula and the numerical concept. All compared data fit well each other.

1. INTRODUCTION

Results of laboratory and field tests have shown that the high-power MW-field-induced separation of Oil and Water (O-W) emulsions has a potential to become a chemical-free alternative to conventional separation processes [1]. The separation mechanism of this process has not been fully understood yet and there is a need for further research. An important area of this research is development of an accurate method for estimation of the effective dielectric properties of treated emulsions.

An existing 2D concept for the numerical estimation of effective dielectric properties of mixtures with random droplets' distribution [2–6] was adapted here and expanded into 3D.

2. NUMERICAL APPROACH AND MEASUREMENTS

As in the original concept [2–6], the electric field distribution is computed here with the commercial and well-proven FEM simulation tool COMSOL Multiphysics. A MATLAB script was written which automatically generates a random mixture (impenetrable spherical inclusions randomly placed in the cubic computational domain) and assigns a proper (periodical/constant potential) boundary condition to every face located on the outer walls of the computational domain as well as the corresponding dielectric parameters to each subdomain. The script also controls other simulation parameters, e.g., temperature (temperature and frequency dependent models of dielectric properties of water were used [8]) and frequency, and it also starts the quasi-static electric COMSOL Multiphysics simulation and evaluation of volume integrals (in COMSOL Multiphysics) and

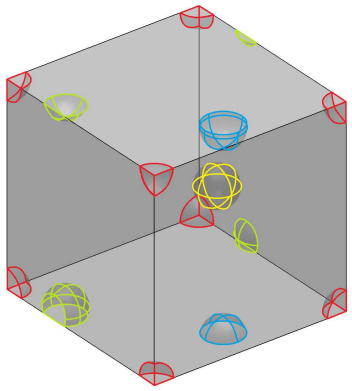

Figure 1: 3D view of a unit cell with 4 droplets in total. To make the geometry periodical with a spatial period in all three dimensions equal to the unit cell edge length a, the droplets exceeding unit cell side wall(s) have to have their counterpart on the opposite wall(s). Yellow, blue, green and red marked droplets exceed none, one, two and three unit cell walls, respectively.

subsequently evaluates the effective dielectric properties. The duration of one simulation is several minutes (approx. 2–4 min. depending on the complexity of the problem — oil/water volume fraction), therefore for each frequency and temperature even tens of simulations are manageable and statistical quantities, e.g., mean values and standard deviations, can be computed.

The expansion of the concept to 3D introduces a new possibility for direct comparison of simulation results with measured values. Here Water-in-Oil (W/O) as well as O/W emulsions were considered.

First simulated effective permittivity of the both emulsion kinds were compared to data estimated using two mixing formulas: Maxwell Garnett and Bruggeman [7].

The effective relative permittivity values were computed for both W/O and O/W emulsions for temperature $T = 23°\mathrm{C}$ and water/oil volume fractions from 1 to 15%. For each volume fraction, 10 statistically independent geometries (with randomly distributed droplets) were generated and simulated for the total of 11 frequencies in the frequency range from 1 to 10 GHz. The mean values and standard deviations were computed as well.

Second dielectric properties of the 5 and 10% commercial O/W emulsion in the frequency range 0.5–10 GHz were measured using a commercial system Dielectric Probe Kit from Agilent Technologies.

3. RESULTS

In Figure 2, the computed relative effective dielectric permittivity is compared with Bruggeman and Maxwell Garnett mixing formulas. The computed mean values usually lie between the two mixing formulas, which is also observed by other authors [3, 4, 9].

The Maxwell Garnett mixing formula fits better than the Bruggeman mixing formula. Especially for the O/W emulsion, the Maxwell Garnett mixing formula fits very well, see Figure 2.

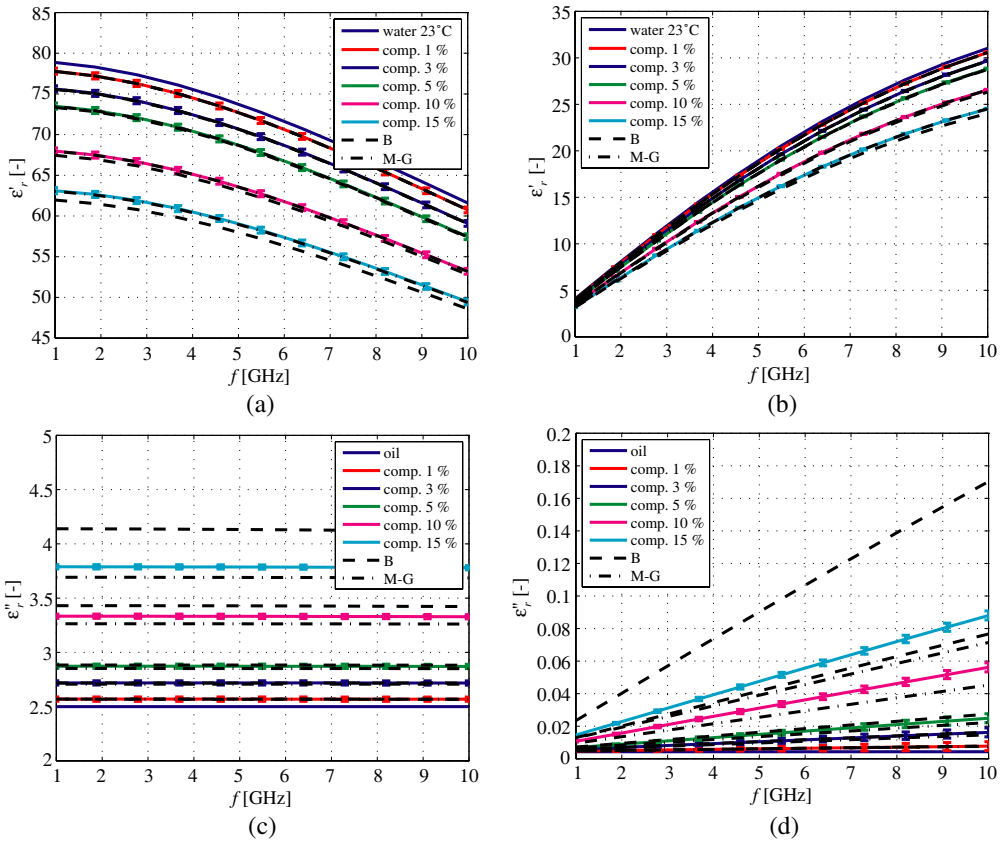

Figure 2: Computed mean values and standard deviations of the (a) real and (b) imaginary part of the complex effective relative permittivities of 1, 3, 5, 10 and 15% **O/W** and of the (c) real and (d) imaginary part of the complex effective relative permittivities of 1, 3, 5, 10 and 15% **W/O** emulsions at the temperature $T = 23°\mathrm{C}$. For comparison, the often used Maxwell Garnett and Bruggeman mixing formulas corresponding to each volume fraction are plotted as well.

The measured data are compared with the M-G models of dielectric mixtures with fixed volumetric oil fractions 0, 5 and 10% of oil. Emulsion temperature was $T = 20.5°\mathrm{C}$. The measured imaginary part of the complex permittivity shows the values for the lowest measured frequencies which differ from the values estimated with the M-G mixing formula. This difference can be attributed to the in the M-G model missing term for static electric conductivity. Static electric conductivity σ_s for several emulsion samples was measured during the research project [1]. Typically, the emulsions were prepared by mixing deionized water with an emulsion concentrate. Therefore, the conductivity was rather low, about $\sigma_s = 15\,\mathrm{mS/m}$.

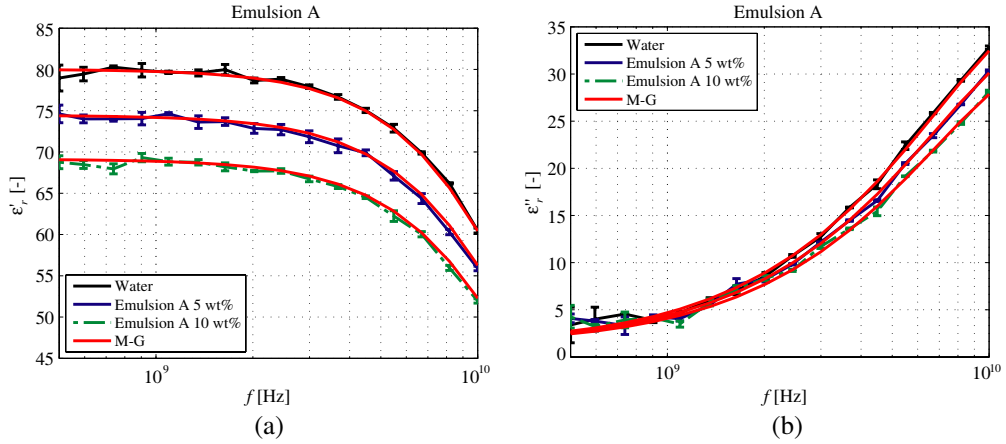

Figure 3: Dielectric properties (a) ε_r' and (b) ε_r'' of distilled water and 5 and 10% O/W emulsions A in the frequency range 0.5–10 GHz. Each curve represents an average value computed from three independent measurements and standard deviations are included in the form of error bars as indicators of the measurement accuracy. Red curves represent the M-G models of dielectric mixtures with fixed oil fractions: 0, 5 and 10% of oil. Measured dielectric properties of the corresponding emulsion concentrate and water dielectric properties [8] were used as input data for the evaluation of the M-G model. The temperature was $T = 20.5°\mathrm{C}$. Static conductivity of emulsion samples was measured and was equal to $\sigma_s = 14.9 \cdot 10^{-3}\,[\mathrm{S/m}]$.

4. CONCLUSIONS

The effective dielectric properties of emulsions were estimated numerically using an existing numerical concept, expanded here from 2D to 3D. The expansion of the concept to 3D introduced a new possibility for a direct comparison of simulation results with measured values. The effective dielectric properties of emulsions were also estimated using the Maxwell Garnett and Bruggeman mixing formulas. Furthermore, dielectric properties of commercial O/W emulsions were measured using a commercial system Dielectric Probe Kit from Agilent Technologies.

The mean values of the computed effective dielectric constants lie mainly between the Brugeman and Maxwell Garnett mixing formulas, which has been already observed in, e.g., [9–11]. For both W/O and O/W emulsions, the Maxwell Garnett mixing formula fitted the numerically estimated data better than the Bruggeman mixing formula. The standard deviations for the numerically estimated data were significantly smaller than those for the measured data (see Figure 3).

The measured data were compared with the dielectric properties estimated using the Maxwell Garnett mixing formula and with the numerical concept. All compared data fit well each other.

REFERENCES

1. Hubrich, M., B. Schmidt, M. Kozariszczuk, A. John, R. H. Jansen, J. Vrba, and J. Wellenbuescher, "Ecologically friendly microwave treatment of oil emulsions as contribution to conserving resources by effluent free manufacture in industry," Project No. 01RI0616B, Tech. Rep. No. 4.61.163, VDEh-Betriebsforschungsinstitut GmbH (BFI), VDEh-Betriebsforschungsinstitut, Sohnstr. 65, 40237 Duesseldorf, June 2010.
2. Krakovsky, I. and V. Myroshnychenko, "Modeling dielectric properties of composites by finite-element method," *Journal of Applied Physics*, Vol. 92, No. 11, 6743, 2002.
3. Brosseau, C., "A finite-element simulation study of the complex effective permittivity of two-phase random composite materials," *COMSOL Multiphysics Users Conference 2005*, November 2005.

4. Myroshnychenko, V. and C. Brosseau, "Finite-element method for calculation of the effective permittivity of random inhomogeneous media," *Physical Review E*, Vol. 71, 016701, January 2005.
5. Myroshnychenko, V. and C. Brosseau, "Finite-element modeling method for the prediction of the complex effective permittivity of two-phase random statistically isotropic heterostructures," *Journal of Applied Physics*, Vol. 97, No. 4, 044101, 2005.
6. Myroshnychenko, V. and C. Brosseau, "Effective complex permittivity of twophase random composite media: A test of the two exponent phenomenological percolation equation," *Journal of Applied Physics*, Vol. 103, No. 8, 084112, 2008.
7. Sihvola, A., *Electromagnetic Mixing Formulae and Applications*, The Institution of Engineering and Technology, May 2000.
8. Ellison, W. J., "Permittivity of pure water, at standard atmospheric pressure, over the frequency range 0–25 THz and the temperature range 0–100 C," *Journal of Physical and Chemical Reference Data*, Vol. 36, No. 1, 1–18, 2007.
9. Karkkainen, K., A. Sihvola, and K. Nikoskinen, "Effective permittivity of mixtures: Numerical validation by the FDTD method," *IEEE Transactions on Geoscience and Remote Sensing*, Vol. 38, No. 3, 1303–1308, 2000.
10. Pekonen, O., K. Karkkainen, A. Sihvola, and K. Nikoskinen, "Numerical testing of dielectric mixing rules by FDTD method," *Journal of Electromagnetic Waves and Applications*, Vol. 13, No. 1, 67–87, 1999.
11. Karkkainen, K., A. Sihvola, K. Nikoskinen, and O. Pekonen, "Limits for the effective permittivity of mixtures: numerical validation by the FDTD method," *IEEE 1999 International Geoscience and Remote Sensing Symposium, IGARSS'99 Proceedings*, Vol. 5, 2640–2642, 1999.

Flexible 3-D Printed Substrates for Antenna Applications

S. S. Bukhari and W. G. Whittow
School of Electronic, Electrical and Systems Engineering
Loughborough University, Loughborough, LE11 3TU, UK

Abstract— Consumer demand for small devices with wireless connectivity has put increasing pressure on antenna engineers to improve electromagnetic performance in smaller packages. These design constraints are further exacerbated by increasing demand for improved bandwidth, efficiency and frequency coverage. Including an additional degree of design freedom by manipulating the substrate shape and properties can help address these challenges.

This paper critically reviews the electromagnetic advantages of altering the dielectric substrate section of the antenna as opposed to the conducting elements. Changing the dielectric has been used to improve the bandwidth, efficiency and gain of antennas. Heterogeneous substrates have also been employed to lower the effective permittivity, suppress surface waves for high indexed substrate materials and reduce mutual coupling. These synthetic substrates are very difficult to manufacture using conventional technologies. Complex 3-D printed geometries can easily be manufactured from computer aided design models that can be exported directly from electromagnetic simulation software. 3-D printing allows the geometry to be varied in all three dimensions, therefore printed cavities of various shapes and sizes can lead to a smooth or discrete change in the effective permittivity. With the latest advances in additive manufacturing and 3-D printing, the antenna and radiofrequency designer will be able to control the local effective permittivity and the substrate shape to gain electromagnetic advantages.

1. CONTROL OF SURFACE WAVES AND CURRENT MODES

Microstrip antennas are light, low profile, conformal, compact structures which are normally fabricated on a homogeneous substrate. They can be regarded as a dielectric filled parallel plate waveguide radiating at discontinuities [1, 2]. The size of an antenna can be easily reduced by using a dielectric with a high-valued permittivity but this also increases the energy in the surface wave modes [3]. These surface waves decrease the efficiency of the antenna and also cause interference with the radiation pattern by getting diffracted from the edges of the finite sized ground plane [4]. These detrimental effects can therefore be reduced by suppression of surface wave modes. Heterogeneous substrates have been utilised, for a circular microstrip antenna, to completely suppress the surface waves caused by TM_0 mode, which is the main cause of surface wave radiation for thin substrate microstrip antennas [4]. The equivalence principle and cavity model allow the radiation patterns of a circular patch to be computed by considering it as a magnetic current ring. When the radius of this magnetic current ring is the same as the radius of the circular patch surface waves caused by the TM_0 mode are completely suppressed [5]. The radius of this ring was however larger than that for a typical patch, so an air cavity as shown in Figure 1 was introduced at the centre of the patch. This cavity decreased the effective dielectric index of the substrate, as the cavity was air-filled ($\varepsilon_r = 1$), leading to an increase in the size of the patch. The size of the patch is now equal to the magnetic current ring thus fulfilling the above condition for surface wave suppression and improving the radiation pattern of the antenna as a result [4]. This technique was also applied to a rectangular patch for surface wave suppression [6].

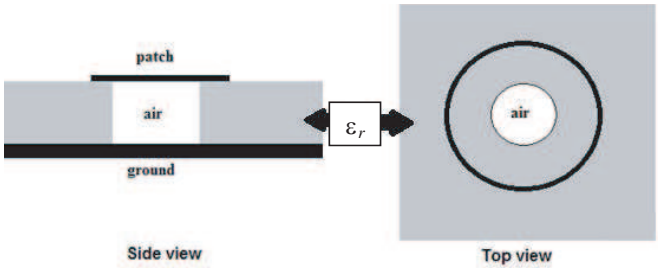

Figure 1: An air filled cored patch. The dark circle shows the boundary of the patch in the top view (redrawn from [4]).

The cored patch design was also applied to a microstrip antenna array in order to reduce the side lobe level, a characteristic coveted for radar applications and achieved by reduction of mutual coupling and surface waves [7]. A further reduction in side lobe level was obtained by introducing narrow metallic strips between the air-cored array elements [7]. Previously the author of this paper has been able to control the multi-band performance of the antenna by introducing air cavities at the radiating edges of the patch [8]. Heterogeneous substrates, prepared by removing the substrate surrounding the patch, partially and completely, have been used to increase the gain of a microstrip antenna by supressing the surface waves [9]. Substrate removal has also been applied to a cavity backed slot antenna and improvement in its bandwidth and efficiency [10].

2. ETCHED SUBSTRATES TO CONTROL LOCAL PERMITTIVTY

Another example of the benefits of varying the substrate geometry can be found in Monolithic microwave integrated circuits (MMIC) technology which allows the antennas to be integrated with other components of millimetre and microwave circuits [11]. High dielectric index increases the energy in the surface waves and also decreases the bandwidth of the antenna [3]. The use of thick substrates alleviates the bandwidth problem but increases the surface wave energy [3, 12]. A solution to the problem lays in hybrid integration schemes, where the antenna is on a material of low permittivity in contrast to the other components of the circuits but this approach increased the cost [13]. So a micromachined antenna, in which chemical etching was used to remove a large portion of silicon from beneath the antenna (as shown in Figure 2), was proposed [13]. The dielectric index of this newly formed structure of air-silicon substrate can be computed by utilising the cavity model [13]. An effective permittivity of 2.8 was obtained by removing half of silicon below the antenna in [12] and 2.2 was obtained for an air-silicon mixture having a ratio of 3 to 1, which led to an improvement in the antenna efficiency and bandwidth [13]. Mutual coupling among various antenna array elements was also improved by changing the dielectric index using micromachining [11]. Another design employed backside etching for removal of silicon below the radiating edges of the patch and caused a decrease in the value of the effective permittivity of the substrate [14]. Micromachining was also applied to increase the gain of an antenna where the patch was placed at the interface of the superstrate and micromachined air cavity [15].

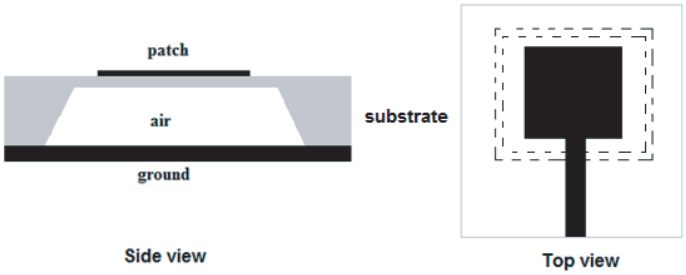

Figure 2: A micromachined patch antenna. The dotted boundary in the top marks the start and the end of the slanted edges. The edges are slanted due to anisotropic chemical etching (redrawn from [13]).

The conductive properties of silicon decrease the antenna efficiency, so a thin film of SiO_2 was deposited on the top of the micromachined substrate to reduce the substrate losses [16, 17]. Micromachined substrates with a SiO_2 layer have been used for both, a patch and a meandered dipole to improve the efficiency and bandwidth of the antenna, and reduce the effective permittivity [16, 17]. The efficiency of a differential fed dipole on a low resistive silicon substrate was improved by micromachining in such a way that the middle portion of the silicon was etched away and the newly formed cavity was then filled with SU8 photoresist, which isolated both silicon sections and also provided support to the SiN (Silicon Nitride) layer placed at the top of the substrate [18]. Another antenna where the shallow etched cavity, directly below the patch, was filled with SiO_2 and polyimide was presented in [19].

3. HETEROGENEOUS SUBSTRATES PREPARED VIA DRILLING HOLES

The effective permittivity of a high indexed dielectric (Duroid 6010) was reduced from 10.8 to 2.3 by drilling small periodic holes in the slab [20]. This synthesized material was then used to improve the bandwidth and efficiency of an antenna [20]. Similarly holes were drilled in the middle layer of a three layered stacked patch to reduce this layer's permittivity [21, 22]. This provided

sturdiness to the structure of the antenna without compromising the performance [21]. It was also observed that the synthesized heterogeneous dielectric behaved similarly to a low permittivity homogenous substrate [20, 22]. The permittivity of the substrate surrounding an antenna on a thick, high dielectric indexed was lowered via drilling holes in the structure, which suppressed the surface waves and thus caused an improvement in the radiation pattern without causing any reduction in the bandwidth [3]. The process of drilling holes for lowering the permittivity was also applied to tapered slot antenna with the purpose of increasing the effective thickness of the substrate, hence adding sturdiness to the antenna [23]. Synthesized dielectrics with both small and large sized holes produced identical radiation patterns [23]. Rotman lenses [24] are an important component of many beam forming networks and has been utilised in various applications including multi-beam receivers, beam steering antenna systems and automotive radar systems [25, 26]. Heterogeneous dielectrics have been employed to reduce the insertion loss in comparison Rotman lens with a homogeneous substrate. A gradient of permittivities, as indicated in Figure 3(a), was synthesized by varying the density of drilled holes in the substrate and used to bend the rays with in the lens for improved focussing. This also decreased the power loss due to spill-over to the side ports [26].

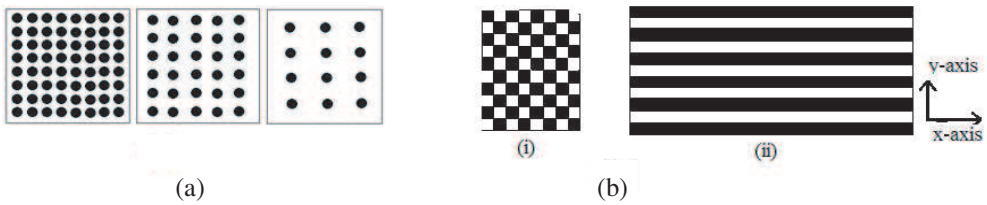

Figure 3: (a) A perforated dielectric slab where the density of air-filled holes varies the effective permittivity (redrawn from [26]). (b) The darker part indicates the section from which the substrate has been removed. The direction of electric field is along z-axis for (i) and y-axis for (ii) (redrawn from [27]).

4. COMPOSITE STRUCTURES

Composite structures are formed when materials with two different permittivities are combined yielding a bespoke effective dielectric index not readily available [28, 29]. In [28], such structures are synthesized by drilling holes in a slab of barium nitrate ($\varepsilon_r = 30$) and then filling these with Bi-Ba- Nd-Titanate (BBNT; $\varepsilon_r = 100$), to attain an effective permittivity of 46.

The effective permittivity of a material can also be tailored by introducing dielectric and metallic micro-scale inclusions inside a homogeneous material [30, 31]. By varying the density of the inclusions, the local effective permittivity can be controlled.

5. 3-D ANTENNAS AND SUBSTRATES: ADVANTAGES AND FABRICATION

Layered heterogeneous substrates, as in Figure 3(b), were synthesized using low temperature co-fired ceramics (LTCC) processing. Materials with a reduced loss tangent compared to the parent material were obtained and then utilised to realise filters with comparatively lower insertion losses [27]. The author has previously shown that 3-D substrates can be used to decrease the antenna size by exploiting the non-uniform electric fields of a patch antenna [32].

The advent of additive manufacturing (AM) techniques such as 3-D printing now enables any shape with intricate internal/external geometry to be created directly from a computer aided design (CAD) file. Currently, there are a wide range of polymers suitable for 3-D printing and these have a range of physical properties and flexible substrates can also be created. Furthermore, holes can be included to allow the antenna to be breathable for wearable applications. By leaving gaps in the CAD model — heterogeneous structures with air as the 2nd material can be considered. This has direct relevance for various antenna systems. Emerging AM techniques allow multiple materials to be printed and in the near future, dielectric and metallic structures will be created by the same AM machine. Therefore, elaborate miniaturised 3-D antenna geometries can be considered. 3-D printing can potentially reduce costs by only using material additively and by reducing the number of fabrication processes.

6. SUMMARY

Heterogeneous substrates have been used to use lower the dielectric index of the structure locally and improve the bandwidth and efficiency of different antenna structures. They are also used for

elimination and reduction of surface waves and increasing the gain of an antenna. They are usually prepared by the removal of a section of dielectric from the homogenous slab through etching and drilling holes. Therefore, 3-D printing offers a simple fabrication method for creating complex geometries that can facilitate electromagnetic advantages.

REFERENCES

1. Carver, K. and J. Mink, "Microstrip antenna technology," *IEEE Transactions on Antennas and Propagation*, Vol. 29, No. 1, 2–24, Jan. 1981.
2. Vaughan, M. J., K. Y. Hur, and R. C. Compton, "Improvement of microstrip patch antenna radiation patterns," *IEEE Transactions on Antennas and Propagation*, Vol. 42, No. 6, 1980–1983, 1994.
3. Colburn, J. S. and Y. Rahmat-Samii, "Patch antennas on externally perforated high dielectric constant substrates," *IEEE Transactions on Antennas and Propagation*, Vol. 47, No. 12, 1785–1794, 1999.
4. Jackson, D. R., J. T. Williams, A. K. Bhattacharyya, R. L. Smith, S. J. Buchheit, and S. A. Long, "Microstrip patch designs that do not excite surface waves," *IEEE Transactions on Antennas and Propagation*, Vol. 41, No. 8, 1026–1037, 1993.
5. Bhattacharyya, A. K., "Characteristics of space and surface waves in a multilayered structure," *IEEE Transactions on Antennas and Propagation*, Vol. 38, No. 8, 1231–1238, 1990.
6. Papapolymerou, I., R. F. Drayton, and L. P. B. Katehi, "Surface wave mode reduction for rectangular microstrip antennas," *IEEE Antennas and Propagation Society International Symposium, 1995 Digest*, Vol. 3, 1494–1497, 1995.
7. Bayat, N., H. R. Hassani, and S. Mohammad, "Sidelobe level reduction in microstrip patch antenna array," *Loughborough Antennas and Propagation Conference (LAPC)*, Loughborough, UK, 2011.
8. Whittow, W. G., C. C. Njoku, J. C. Vardaxoglou, and J. Joubert, "Designing multi-band and high bandwidth antennas with heterogeneous substrates," *2012 IEEE-APS Topical Conference on Antennas and Propagation in Wireless Communications (APWC)*, 748–751, 2012.
9. Yeap, S. B. and Z. N. Chen, "Microstrip patch antennas with enhanced gain by partial substrate removal," *IEEE Transactions on Antennas and Propagation*, Vol. 58, No. 9, 2811–2816, Sep. 2010.
10. Yun, S., D. Kim, S. Nam, and S. Member, "Bandwidth and efficiency enhancement of cavity-backed slot antenna using a substrate removal," *IEEE Antennas and Wireless Propagation Letters*, Vol. 11, 1458–1461, 2012.
11. Katehi, L. P. B., "Micromachined microstrip patch antenna with controlled mutual coupling and surface waves," *IEEE Transactions on Antennas and Propagation*, Vol. 49, No. 9, 1282–1289, 2001.
12. Zhang, M., Q. Chen, P. S. Hall, and V. F. Fusco, "Broadband microstrip patch antenna on micromachined silicon substrates," *Electronics Letters*, Vol. 34, No. 1, 8–9, 1998.
13. Papapolymerou, I., R. F. Drayton, and L. P. B. Katehi, "Micromachined patch antennas," *IEEE Transactions on Antennas and Propagation*, Vol. 46, No. 2, 275–283, 1998.
14. Chen, Q., V. F. Fusco, M. Zheng, and P. S. Hall, "Micromachined silicon antennas," *International Conference on Microwave and Millimeter Wave Technology Proceedings*, 289–292, 1998.
15. Aditya, S., C. K. Sim, D. Wu, W. T. Chua, Z. X. Shen, and C. L. Law, "High-gain 24-GHz CPW-Fed microstrip patch antennas on high-permittivity substrates," *IEEE Antennas and Wireless Propagation Letters*, Vol. 3, 30–33, 2004.
16. Ibrahim, A. and D. R. S. Cumming, "A micromachined 10 GHz meander dipole antenna on high resistivity silicon substrate for remote sensing applications," *Loughborough Antennas and Propagation Conference (LAPC)*, 345–347, Loughborough, UK, 2009.
17. Singh, V. K., "Ka-band micromachined microstrip patch antenna," *IET Microwaves, Antennas & Propagation*, Vol. 4, No. 3, 316–323, 2010.
18. Yan, J.-B. and R. D. Murch, "Fabrication of a wideband antenna on a low-resistivity silicon substrate using a novel micromachining technique," *Antennas and Wireless Propagation Letters*, Vol. 6, No. 11, 476–479, 2007.
19. Pan, W., S. Wu, and Y. Chen, "Micromachined patch antennas on synthesized substrates," *International Conference on Mirowave and Milimeter Wave Technology Proceedings*, 58–61, 2004.

20. Gauthier, G. P., A. Courtay, and G. M. Rebeiz, "Microstrip antennas on synthesized low dielectric-constant substrates," *IEEE Transactions on Antennas and Propagation*, Vol. 45, No. 8, 1310–1314, 1997.
21. Navarro, E. A., A. Luximon, I. J. Craddock, D. L. Paul, and M. Dean, "Multilayer and conformal antennas using synthetic dielectric substrates," *IEEE Transactions on Antennas and Propagation*, Vol. 51, No. 4, 905–908, Apr. 2003.
22. Navarro, E. A., I. J. Craddock, and D. L. Paul, "Synthetic dielectrics for planar antenna design," *Electronics Letters*, Vol. 36, No. 6, 491–493, 2000.
23. Muldavin, J. B. and G. M. Rebeiz, "Millimeter-wave tapered-slot antennas on synthesized low permittivity substrates," *IEEE Transactions on Antennas and Propagation*, Vol. 47, No. 8, 1276–1280, 1999.
24. Rotman, W. and R. Turner, "Wide-angle microwave lens for line source applications," *IEEE Transactions on Antennas and Propagation*, Vol. 11, No. 6, 623–632, Nov. 1963.
25. Archer, D. H. and M. J. Maybell, "Rotman lens development history at raytheon electronic warfare systems 1967–1995," *Antennas and Propagation Society International Symposium*, 31–34, 1995.
26. Schulwitz, L. and A. Mortazawi, "A new low loss rotman lens design using a graded dielectric substrate," *IEEE Transactions on Microwave Theory and Techniques*, Vol. 56, No. 12, 2734–2741, Dec. 2008.
27. Gong, X., T. Smyth, E. Ghaneie, and W. J. Chappell, "High-Q resonators and filters inside advanced low-temperature co-fired ceramic substrates using fine-scale periodicity," *IEEE Transactions on Microwave Theory and Techniques*, Vol. 56, No. 4, 922–930, 2008.
28. Psychoudakis, D., Y.-H. Koh, J. L. Volakis, and J. H. Halloran, "Design method for aperture-coupled microstrip patch antennas on textured dielectric substrates," *IEEE Transactions on Antennas and Propagation*, Vol. 52, No. 10, 2763–2765, Oct. 2004.
29. Psychoudakis, D., J. L. Volakis, Z. Wing, and J. W. Halloran, "Cavity-backed miniature wideband uhf circular polarized antenna with textured dielectrics," *IEEE Transactions on Antennas and Propagation*, Vol. 54, No. 12, 3586–3592, Dec. 2006.
30. Njoku, C. C., W. G. Whittow, and J. C. Vardaxoglou, "Simulation methodology for synthesis of antenna substrates with microscale inclusions," *IEEE Transactions on Antennas and Propagation*, Vol. 60, No. 5, 2194–2202, May 2012.
31. Njoku, C. C., W. G. Whittow, and J. C. Vardaxoglou, "Effective permittivity of heterogeneous substrates with cubes in a 3-D lattice," *IEEE Antennas and Wireless Propagation Letters*, Vol. 10, 1480–1483, 2011.
32. Whittow, W. G., "Microstrip patch antennas with 3-dimensional substrates," *Loughborough Antennas and Propagation Conference (LAPC)*, Loughborough, UK, 2012.

Estimation of Direction of Arrival Algorithms

T. Orul[1] and E. Afacan[2]

[1]Ministry of Labour and Social Security, Turkey
[2]Electrical and Electronics Engineering Department, Gazi University, Turkey

Abstract— MUSIC and ESPRIT algorithms are two of the most widely known and used signal source estimation techniques. This study aims at the comparison of the performances of these two techniques. In this study, the signals coming toward uniform linear antenna arrays are estimated using MUSIC and ESPRIT algorithms. Estimation performances of the same related to signal arrival angle are compared with each other. The obtained results show that MUSIC algorithm gives more accurate and definite results for moderately low SNR, whereas ESPRIT algorithm gives accurate results for moderately high SNR. On the other hand, ESPRIT algorithm provides ease of calculation, decrease in capacity and cost.

1. INTRODUCTION

Determination of signal sources has been used for both military applications such as radar systems, location finding systems, electronic warfare systems and daily life applications such as mobile communication systems, the determination of mine reservations, the detection of illegal radio broadcasting and finding the lost mountaineers. Studies about this topic had begun during 1960s [1]. Firstly, ML (Maximum Likelihood Estimation) was reorganized in such a way so as to estimate more than one signal [2]. Until the mid-1970s, the subarray based estimation methods were used after Pisarenko's method. Pisarenko originated this method in 1973 while examining the problem of estimating the frequencies of complex signals in white noise [3]. Then, Multiple Signal Classification (MUSIC) method was developed by Schmidt [4]. To avoid the disadvantages of MUSIC, Estimation of Signal Parameters via Rotational Invariance Techniques (ESPRIT) was developed by Roy and Kailath [5]. In this study, estimation performances of two of the mostly used subspace based estimation methods, MUSIC and ESPRIT, are compared. In the study uniform linear antenna arrays are used for both methods.

2. MUSIC (MULTIPLE SIGNAL CLASSIFICATION) ALGORITHM

MUSIC algorithm is a method of multiple signal classification with a high resolution which uses eigenvalues of covariance matrix of incident signals [4]. Using MUSIC algorithm, number of signals, direction of arrival (DOA), the strengths and cross correlations of incident signals and strength of noise can be estimated [4].

2.1. The Data Model

For the estimation of direction of arrival, firstly,the signal model is formulated. When D incident signals of which sources are in the far-field region are received by the linear antenna array which has M identical isotropic array elements, the total received signal can be characterized as follows [4]:

$$u\left(t\right)=\sum_{i=0}^{D-1}a\left(\phi_i\right)S_i\left(t\right)+n\left(t\right) \tag{1}$$

The total signal received from the array which is symbolized by $\mathbf{u(t)}$ is given as:

$$\mathbf{u}\left(t\right)=[\mathbf{a}(\phi_1)\mathbf{a}(\phi_2)\ldots\mathbf{a}(\phi_{D-1})]\begin{bmatrix}s_0(t)\\ \vdots \\ s_{D-1}(t)\end{bmatrix}+\mathbf{n}(t)=\mathbf{A}s(t)+\mathbf{n}(t) \tag{2}$$

where $\mathbf{s(t)}$ is the incident signal vector, $\mathbf{n(t)}$ is the noise vector and $\mathbf{a(Ø}_1)$ is the directional mode vector which is are sponse to a signal incident from the direction of the first signal.

Using this total signal received from the antenna array, covariance matrix is obtained as [4]:

$$\mathbf{R_{uu}}=E[\mathbf{u}\left(t\right)\mathbf{u}\left(t+\tau\right)]^*=\mathbf{AR_{ss}A}^*+\sigma_n^2\mathbf{I} \tag{3}$$

Eigenvalues and eigenvectors of $\mathbf{R}_{uu}$ covariance matrix are calculated. $\{\lambda_0, \ldots, \lambda_{M-1}\}$ refers to eigenvalues of $\mathbf{R}_{uu}$ while $\{q_i, \ldots, q_{M-1}\}$ refers to eigenvectors of $\mathbf{R}_{uu}$.

Number of incident signals is estimated using eigenvalues. K of eigenvalues of $\mathbf{R}_{uu}$ matrix equals 0. The number of incident signals, D, is estimated as $D = M - K$ [4].

To estimate the direction of arrival of incident signals, eigenvectors of $\mathbf{R}_{uu}$ matrix are used. Eigenvectors and the directional vectors which are the responses to incident signals are orthogonal:

$$\{a(\phi_0), \ldots, a(\phi_{D-1})\} \perp \{q_D, \ldots, q_{M-1}\} \tag{4}$$

Being calculated the directional vectors which are orthogonal against eigenvectors of $\mathbf{R}_{uu}$, MUSIC spectrum is calculated with the following formula and direction of arrival is estimated by finding D peak points:

$$P_{MUSIC}(\phi) = \frac{a^*(\phi)a(\phi)}{a^*(\phi)v_n v_n^* a(\phi)}, \quad v_n = [\ q_D \quad q_{D+1} \quad \ldots \quad q_{M-1}\ ] \tag{5}$$

3. ESPRIT (ESTIMATION OF SIGNAL PARAMETERS VIA ROTATIONAL INVARIANCE TECHNIQUES) ALGORITHM

ESPRIT algorithm, like MUSIC, is a subspace based estimation of direction of arrival method.

3.1. Array Geometry

ESPRIT algorithm requires an antenna array having a structure which can be separated into two identical subarrays with equal dimensions. The distance between the elements of these subarrays are constant and irrotational. Thus, the distance does not change and elements have the equal displacement when the array is displaced [5].

ESPRIT is based on the estimation of direction of arrival by using the constant displacement vector (Δ) as a reference direction. For this reason, ESPRIT does not require array spectrum and scanning of whole space area.

3.2. Data Mode

Antenna array consists of two subarrays indicated as ZX and ZY. The distance between these subarrays is Δ. The signals received by the ith doublet

$$x_i(t) = \sum_{k=1}^{d} s_k(t)a_i(\theta_k) + n_{xi}(t) \tag{6}$$

$$y_i(t) = \sum_{k=1}^{d} s_k(t)e^{j\beta\Delta\cos\theta_k}a_i(\theta_k) + n_{yi}(t) \tag{7}$$

Using this incident signal vector, covariance matrix $\mathbf{R_{zz}}$ is obtained and eigenvalues and eigenvectors are calculated [5]

$$\mathbf{R_{zz}E} = \sum\nolimits_n \bar{\mathbf{E}}\mathbf{\Lambda} \tag{8}$$

$$\mathbf{\Lambda} = \mathrm{diag}\{\lambda_1, \ldots, \lambda_{2m}\}, \quad \lambda_1 \geq \ldots \geq \lambda_{2m} \tag{9}$$

$$\bar{\mathbf{E}} = [e_1|\cdots|e_{2m}] \tag{10}$$

As in the MUSIC algorithm, using a minimum number of eigenvalues, the number of incident signals are estimated as $D = M - K$.

D eigenvectors which are related to the biggest D eigenvalues are used to obtain the signal subspace which is given in Eq. (11) and lower matrices are calculated [5].

$$\mathbf{E_s} \stackrel{def}{=} \sum\nolimits_n [e_1|\cdots|e_d] \Rightarrow \begin{bmatrix} \mathbf{E_x} \\ \mathbf{E_y} \end{bmatrix} \tag{11}$$

Since $\lambda 1 \geq \ldots \geq \lambda 2d$, eigenvalue decomposition is given as below:

$$\mathbf{E}_{XY}^*\mathbf{E}_{XY} \stackrel{def}{=} \begin{bmatrix} \mathbf{E}_X^* \\ \mathbf{E}_Y^* \end{bmatrix} [\mathbf{E}_X|\mathbf{E}_Y] = \mathbf{E\Lambda E}^* \tag{12}$$

This matrix $\mathbf{E}$ is divided into lower matrices whose dimensions are $D \times D$:

$$\mathbf{E} \stackrel{def}{=} \begin{bmatrix} \mathbf{E_{11}} & \mathbf{E_{12}} \\ \mathbf{E_{21}} & \mathbf{E_{22}} \end{bmatrix} \tag{13}$$

The eigenvalues of $\mathbf{\Psi} = -\mathbf{E}_{12}\mathbf{E}_{22}^{-1}$ are calculated with Eq. (14).

$$\hat{\varphi}_k = eigenvalue\left(-\mathbf{E}_{12}\mathbf{E}_{22}^{-1}\right), \quad \forall k = 0, \ldots \hat{D} - 1 \tag{14}$$

By using the eigenvalues and the equation given below, directions of arrival are estimated:

$$\hat{\theta}_k = \sin^{-1}\left\{ c\frac{\arg\left(\hat{\phi}_k\right)}{w_0\Delta} \right\} \tag{15}$$

4. STUDIES

In this section, estimation results of MUSIC and ESPRIT algorithms are given.

4.1. Simulation Results for MUSIC

The effects of number of elements (M), incident signal number (D) and signal to noise ratio (SNR) on the estimation performance of MUSIC algorithm are examined [6]. Simulation results are shown in Figures below.

Firstly, effects of the number of elements on the estimation performance are simulated and results are given in Fig. 1 and Fig. 2. When these are compared, it is clearly seen that the number of elements effect estimation performances and as the number of array elements increases, estimation performance increases.

Secondly, effects of the number of incident signals on the estimation are simulated and results are given in Fig. 3 and Fig. 4. To analyse the effect, two simulations were performed respectively for 2 incident signals and 4 incident signal by using the same antenna array and SNR. Decreased

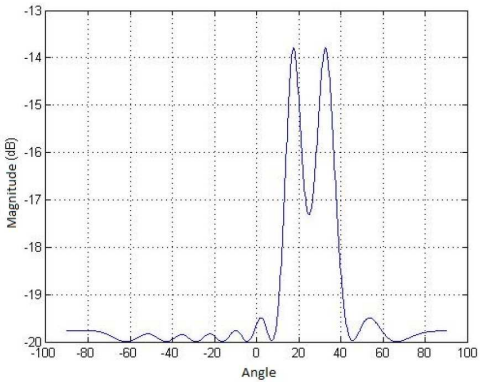

Figure 1: Estimation spectrum for $SNR = 40$, $M = 10$, $D = 2$, $(\theta) = 20, 30$ [6].

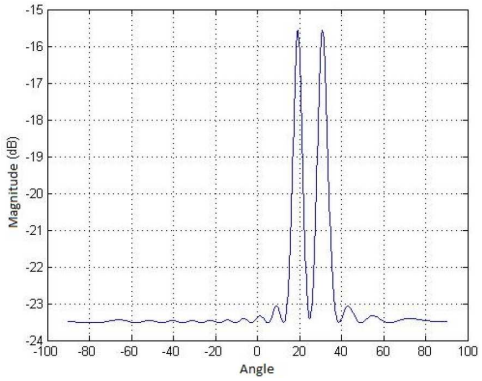

Figure 2: Estimation spectrum for $SNR = 40$, $M = 15$, $D = 2$, $(\theta) = 20, 30$ [6].

Table 1: ESPRIT — effect of SNR [6].

	DOA and Error Rate						Avg. Error Rate (%)
SNR	20°	Error (%)	50°	Error (%)	70°	Error (%)	
0	6.71	66.40	18.05	63.89	62.63	10.51	46.93
10	19.69	1.54	30.86	38.27	60.48	13.59	17.80
20	5.45	72.70	22.23	55.52	64.09	8.42	45.55
30	20.70	3.53	55.99	11.99	62.79	10.28	8.604
40	19.95	0.24	49.34	1.30	69.35	0.91	0.821
60	20.01	0.07	50.45	0.90	69.95	0.06	0.346
80	19.99	0.00	50.01	0.03	70.02	0.03	0.024
100	20.00	0.00	50.00	0.00	69.99	0.00	0.00

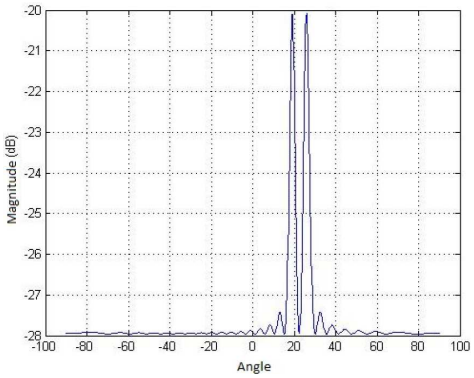

Figure 3: Estimation spectrum for $SNR = 40$, $M = 25$, $D = 2$, $(\theta) = 20, 25$ [6].

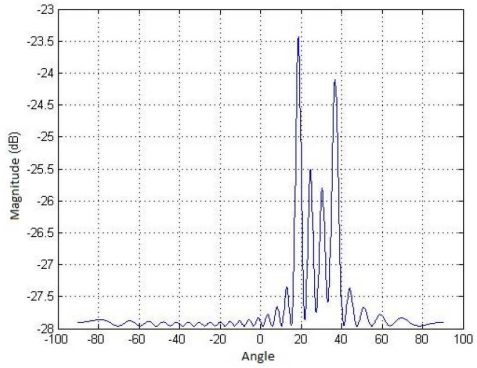

Figure 4: Estimation spectrum for $SNR = 40$, $M = 25$, $D = 4$, $(\theta) = 20, 25, 30, 35$ [6].

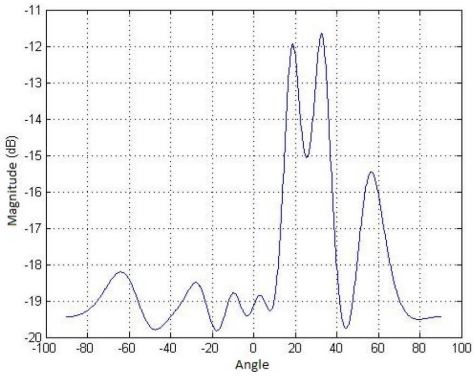

Figure 5: Estimation spectrum for $SNR = 0$, $M = 10$, $D = 2$, $(\theta) = 20, 30$ [6].

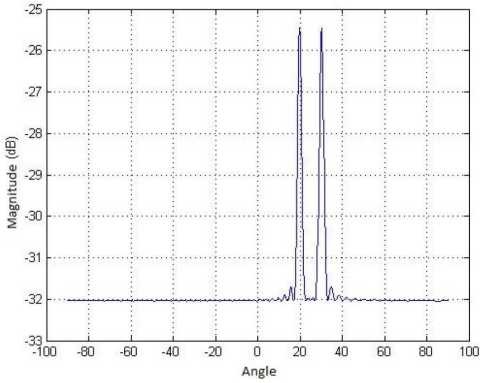

Figure 6: Estimation spectrum for $SNR = 100$, $M = 10$, $D = 2$, $(\theta) = 20, 30$ [6].

values of peak points in Fig. 4 show that estimation performances are affected negatively. As the number of incident signals increases, estimation performance decreases.

Lastly, the effects of the signal to noise ratio on the estimation are simulated and results are given in Fig. 5 and Fig. 6. By using the same incident signals and the same antenna array, which has 10 array elements, two simulations were performed respectively for the lowest SNR and the highest SNR. When these two spectrum analysed, it is seen that signal to noise ratio affects the estimation performance. As the value of SNR increases, estimation performance increases.

4.2. Simulation Results for ESPRIT

The estimation performances of ESPRIT algorithm are simulated and the results obtained are given in Tables 1 to 4. In simulation, effects of the number of array elements (M), the number of incident signals (D) and signal to noise ratio (SNR) are analysed [6].

Firstly, the directions of arrival of three incident signals which are received by the antenna array which has 15 array elements are chosen respectively as 20°, 50° and 70°. Then, the effects of signal to noise ratio (SNR) on estimation performance are simulated and results are given in Table 1. When the results given in Table 1 are analysed, it is clearly seen that changing SNR value affects the estimation performance.

Secondly,the effect of the number of array elements on the estimation performance is simulated for 3 incident signals. For this simulation signal to noise ratio is determined as 40 and the results are given in Table 2. When the results are analysed, it is seen that as the number of array elements increases, the estimation performance increases. For example, while the antenna array which has 3 array elements estimates three incident signals with 52% error, the antenna array which has 100 array elements estimates the same signals with 0% error. In this case, as the number of array elements increases, estimation performance of the array increases but at the same time complication of the process increases as well.

Finally, the effect of the number of incident signals on the estimation performance is simulated

Table 2: ESPRIT — Effect of number of elements [6].

	DOA and Error Rate						Avg. Error Rate (%)
M	20°	Error (%)	50°	Error (%)	70°	Error (%)	
3	8.78	56.05	67.36	34.7	23.89	65.87	52.21
5	10.07	49.63	60.93	21.87	37.83	45.94	39.15
7	15.96	20.19	32.71	34.5	48.32	30.96	28.57
10	21.53	7.67	64.00	28.01	43.49	37.86	24.51
15	20.14	0.72	69.79	39.59	50.75	27.49	22.60
20	19.80	0.99	49.67	0.64	69.45	0.78	0.806
50	19.99	0.00	49.97	0.04	69.92	0.10	0.051
100	20.0	0.00	50.00	0.01	70.00	0.01	0.008

Table 3: ESPRIT — Effect of the number of signals-1 [6].

No. of signal (D)	DOA	ESPRIT	Diff.	% Error	Avg. Error Rate (%)
1	20	19.995	0.004	0.022	0.022
2	−15	−14.998	−0.01	0.010	0.06
	20	20.022	−0.02	0.110	
3	−15	−15.287	0.287	1.914	5.380
	10	11.214	−1.214	12.147	
	30	29.375	0.624	2.081	
4	−25	−20.927	−4.072	16.290	21.303
	−15	−23.925	8.925	59.500	
	20	18.469	1.530	7.653	
	70	68.762	1.237	1.768	
5	−25	−21.768	−3.232	12.928	29.871
	−15	−6.240	−8.759	58.394	
	20	32.718	12.71	63.592	
	50	55.925	−5.925	11.85	
	70	68.184	1.815	2.5931	
8	−60	−59.991	−0.008	0.0135	0.1081
	−40	−39.962	−0.037	0.0940	
	−20	−20.075	0.075	0.374	
	10	9.964	0.035	0.3522	
	30	30.081	−0.081	0.2159	
	50	50.093	−0.093	0.1870	
	70	70.076	−0.076	0.1097	
	80	80.307	−0.307	0.3826	

Table 4: ESPRIT — Effect of the number of signals-1 [6].

No. of signal (D)	DOA	ESPRIT	Diff.	% Error	Avg. Error Rate (%)
10	−70	−70.204	0.204	0.2921	15.144
	−60	−59.676	0.323	0.5396	
	−50	−46.320	3.679	7.3588	
	−40	−37.288	2.711	6.7777	
	−30	−25.492	4.507	15.024	
	10	14.425	4.425	44.258	
	20	26.422	6.422	32.112	
	30	38.600	8.600	28.668	
	40	46.529	6.529	16.323	
	50	49.956	0.043	0.0866	
12	−80	−79.448	0.5512	0.689	20.765
	−70	−66.210	3.79	5.4142	
	−60	−52.220	7.7797	12.966	
	−50	−31.120	18.879	37.759	
	−40	−29.903	10.096	25.241	
	−30	−27.465	2.5346	8.4486	
	10	−0.246	10.246	102.46	
	20	13.594	6.4056	32.028	
	30	31.479	1.4791	4.9303	
	40	44.540	4.5406	11.351	
	50	46.238	3.7619	7.5238	
	60	60.217	0.2177	0.3628	

and the results are given in Table 3 and Table 4. For this simulation, SNR is determined as 40 and for up to 5 incident signals, 15 array elements are used but for 8, 10 and 12 incidents signals, 70 array elements are used. When the results are analysed, it is seen that as the number of incident signal increases, the error rate increases and the estimation performance of ESPRIT decreases.

5. CONCLUSION

Subspace based direction of arrival estimation algorithms such as MUSIC and ESPRIT have much higher resolution than other traditional beamformer methods. Therefore, these algorithms provide much higher resolution and accurate results for the cases in which there are more than one signal.

According to the obtained data, it is observed that depending on the number of incident signals, noise ratio and the number of array elements, the performances of both MUSIC and ESPRIT algorithms change.

For the low signal to noise ratio, that is to say, in the high noise environment, MUSIC has far lower diversion than that of ESPRIT; yet, it is seen that there are some deceptive peak values when

the spectrums are checked (Fig. 5).

Calculation complexity and the need for capacity, coming with the MUSIC algorithm which needs to examine the whole space, create a big cost disadvantage [6].

REFERENCES

1. Haykin, S., *Advances in Spectrum Analysis and Array Processing*, Prentice Hall Publication, 1991.
2. Capon, J., "High resolution frequency-wavenumber spectrum analysis," *Proc. IEEE*, Vol. 57, No. 8, 1408–1418, 1969.
3. Pisarenko, V. F., "The retrieval of harmonics from a covariance functio," *Geophys. J. Royal Astron. Soc.*, Vol. 33, No. 3, 347–366, 1973.
4. Schmidt, R. O., "Multiple emitter location and signal parameter estimatio," *IEEE Trans. on Antennas and Propagation*, Vol. 34, No. 3, 276–281, 1986.
5. Roy, R. H., "ESPRIT — Estimation of signal parameters via rotational invariance technique," Ph. D. Dissertation, Stanford University, Stanford, CA, 1987.
6. Orul, T., "Direction of arrival methods for smart antenna systems," M. Sc. Dissertation, Gazi University, Institute of Science, Ankara, 2012 (in Turkish).

A Study of SNR Degradation due to Impedance Mismatch in ESPAR Antennas

P. Daskalaki, K. Maliatsos, and A. G. Kanatas
Department of Digital Systems, University of Piraeus, Greece

Abstract— The recently proposed Beamspace MIMO (BS-MIMO) technique offer high multiplexing and beamforming capabilities using one RF chain. Electrically-Steerable Parasitic Array Radiator (ESPAR) antennas with a single active and multiple parasitic antenna elements are able to support the beamspace concept with reconfiguration of the antenna pattern with the dynamic variation of the reactance values of the parasitic elements. However, the impedance mismatch of the active element of the ESPAR antenna may deteriorate the performance due to SNR degradation. This paper provides simulation results for the input impedance and the reflection coefficient for a 3-element ESPAR antenna and it studies the return losses and the beam and null forming capability vs. the reactances of the two parasitic elements.

1. INTRODUCTION

The deployment of conventional MIMO systems at mobile terminals has been delayed due to implementation difficulties regarding the required array size and the need for multiple RF chains. The recently introduced Beamspace MIMO (BS-MIMO) can offer high multiplexing and beamforming capabilities using a single active and a number of parasitic elements [1].

In 1978, Harrington [2] proposed a dipole array type antenna with only one active dipole used as a feed element and multiple passive elements loaded with variable reactors. The parasitic dipoles are excited by the strong mutual coupling with the central element and with the selection of suitable reactors the desired beams can be formed. Since 1978, different antenna configurations for low-cost and compact beamforming terminals have been proposed. The switched parasitic antenna proposed in [3] using two parasitic reactance-loading dipoles provides a compact configuration that it is suitable for compactness-constrained mobile units compared to the majority of the already proposed wire parasitic antennas. However, it cannot produce continuous and autonomous beam and/or null, since its beam pattern is switched in a discrete way.

A smart antenna that has been proposed for mobile terminals is the Electrically-Steerable Parasitic Array Radiator (ESPAR) antenna [4–8]. The ESPAR antenna is suitable for low-cost, compact and low-power consumption configurations. The radiation patterns can be controlled electronically by an external DC voltage with the use of a varactor diode loaded in each of the passive elements [4]. It is important to mention that ESPAR antennas have the ability to achieve high-resolution beam and null steering with only one active RF port and several passive elements [8]. The fact that the antenna is fed by a single port is a substantial advantage for the deployment of MIMO in wireless communication terminals and it is also followed by a significant size reduction and lower power consumption.

This paper studies a structure of 3-element ESPAR antenna dipoles. The effect of the dynamic variation of the reactances on the impedance value of the active element is examined thoroughly. The relationship between the maximum directivity and the variable range of the two reactances is also discussed. Moreover, the way the reactance range affects the peak of the beam and the minimum value of the null of the radiation pattern is analyzed through simulation. Finally, the return losses due to the impedance mismatch of the active element resulting in SNR degradation is presented.

2. ANALYSIS OF ESPAR ANTENNA DESIGN

The ESPAR antenna configuration of this paper is depicted in Fig. 1. The radiated elements consist of 3 printed dipoles. The planar array is preferred compared to the dipole array in free space due to the size restrictions of the mobile units [3]. As Fig. 1 shows the single active element is placed between the two parasitic elements. Each passive element is loaded with variable reactors. The antenna is designed to have a resonant frequency at 2.5 GHz. The dipole element length is chosen to be 0.402λ and the inter-element spacing is 0.10λ. The reactance value jX applied to each parasitic element takes both negative and positive values and can be adjusted independently. The range is set from $-100\,\Omega$ up to $+100\,\Omega$. By altering the reactance values, the electrical length of the dipole

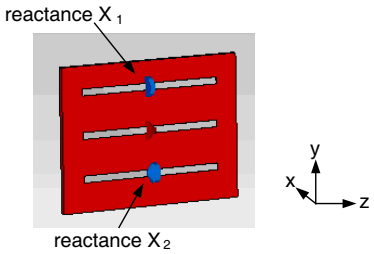

Figure 1: ESPAR antenna configuration.

also changes, so it can act as a director or a reflector [8]. The effect of the mutual coupling between the active and the parasitic elements and the impedance mismatch of the active element provide important information about the SNR degradation of our system. The simulations were performed in CST Microwave Studio and 4096 loading scenarios were evaluated over the range $-100\,\Omega$ to $+100\,\Omega$.

3. SIMULATIONS OF ESPAR ANTENNA DESIGN

Figure 2(a) shows the input impedances of the ESPAR antenna plotted on Smith Chart for 4096 samples. The average impedance was found to be 19.55-20.98i. In Fig. 2(b), the distribution of the Reflection Coefficient is plotted also on a Smith Chart and it can be seen that the spread is quite large due to the impedance mismatch of the active element.

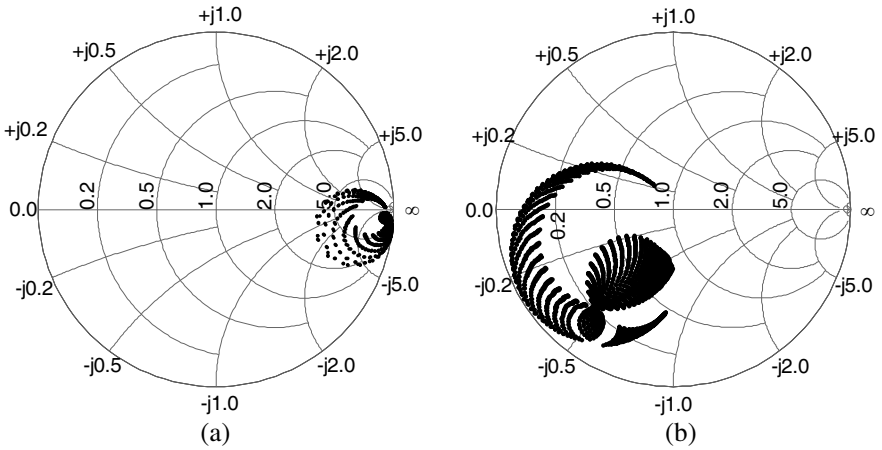

Figure 2: (a) Input impedance in Smith chart. (b) Reflection coefficient in Smith chart.

Figures 3 and 4 present the maximum of the beams and the minimum of the nulls over the reactance variation range respectively. It is noticed that for the 3-element ESPAR configuration, maximum directivity is achieved along axis y (at $\pm 90°$) due to the linear and uniform placement of the elements and the antenna behaves either as a director or a reflector while nulls appear on axis z (at $\pm 180°$).

In Fig. 5 the relationship of the variable reactance values X_1 and X_2 of the parasitic antennas to the maximum directivity (in dBi) is presented. While for most combinations of X_1 and X_2 the directivity value is near 1 (with maximum value 3.21 dBi), there are specific cases where directivity is significantly reduced down to -29 dBi.

Finally, the standard return loss and the VSWR at the active element are calculated for the specific range $-100\,\Omega$ to $+100\,\Omega$ based on [4]. The average return loss is equal to 9.25 dB and the VSWR is 2.05 ($\sigma = 0.34$). Fig. 6 presents the variation of the Return Loss versus X_1 and X_2. The return loss of the active element directly affects the effective transmitted power by the antenna configuration and thus it is connected to an SNR degradation at the receiver. This means that during the operation of a BS-MIMO system [9] with 3-element ESPAR antenna, the achieved SNR depends on the selected combination of reactances that can produce the desired radiation pattern. Thus, since pattern reconfiguration is performed in a symbol-by-symbol basis, the SNR value will continuously change. It must be noted that for small reactance values (which is usually

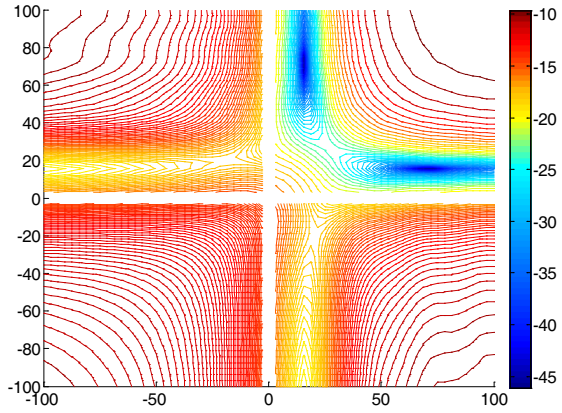

Figure 3: Maximum of beams versus X_1 and X_2 in dBi.

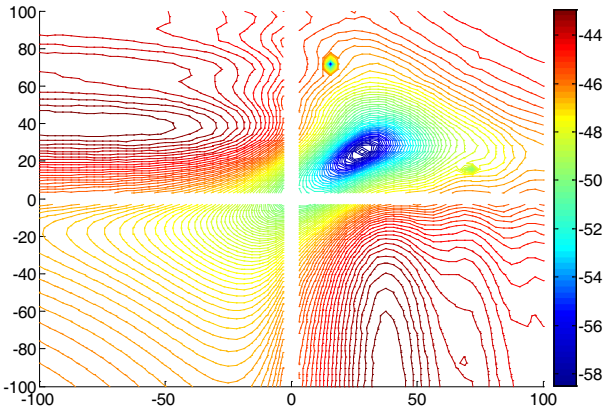

Figure 4: Minimum of nulls versus X_1 and X_2 in dBi.

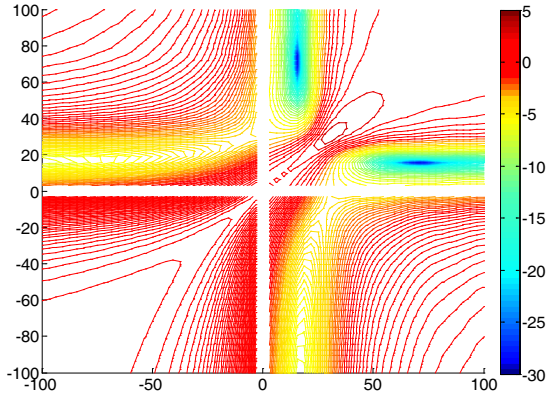

Figure 5: Maximum Directivity versus X_1 and X_2 in dBi.

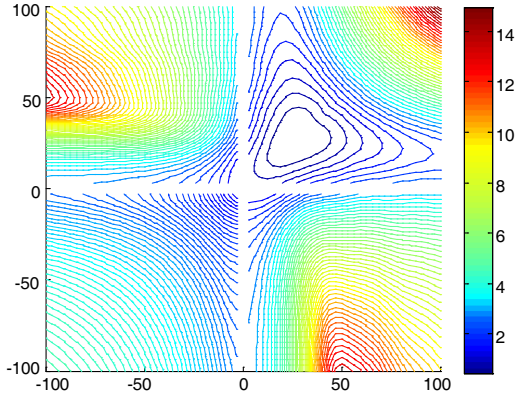

Figure 6: Return Loss versus X_1 and X_2 in dB.

the case in BS-MIMO), the losses and subsequently the SNR degradation remain low and approximately constant. However, in the cases where X_1 and X_2 have opposite sign, one of them should have a near-zero value. Otherwise the return loss increases abruptly and the BS-MIMO system performance will deteriorate.

4. CONCLUSIONS

The objective of this paper was to study the behavior of the 3-element ESPAR antenna concerning its directivity properties as well as the return losses at the active element due to the impedance mismatch caused by the mutual coupling of the elements. It was shown that for the specific configuration the variance of the reflection coefficient distribution over the combinations of reactances is significantly high. The most important result regarding the return losses was the fact that depending on the selection of X_1 and X_2 and the desired radiated pattern, the transmitted power and the effective SNR may significantly vary from 0.4 to 14.9 dB.

ACKNOWLEDGMENT

The research has been co-financed by the European Union (European Social Fund — ESF) and Greek national funds trough the Operational Program Education and Lifelong Learning of the National Strategic Reference (NSRF) — Research Funding Program: THALES, (INTENTION:MIS 379489) "Investing in knowledge society through the European Social Fund".

REFERENCES

1. Kalis, A., A. G. Kanatas, and C. B. Papadias, "A novel approach to MIMO transmission using a single RF front end," *IEEE Journal on Selected Areas in Communications*, Vol. 26, No. 6, 972–980, Aug. 2008.

2. Harrington, R. F., "Reactively controlled directive arrays," *IEEE Transactions on Antennas and Propagation*, Vol. 26, No. 3, 390–395, 1978.
3. Perruisseau-Carrier, J., O. N. Alrabadi, and A. Kalis, "Implementation of a reconfigurable parasitic antenna for beam-space BPSK transmissions," *Proceedings of 2010 European Microwave Conference (EuMA)*, 644–647, Paris, France, Sep. 2010.
4. Akiyama, A., K. Gyoda, T. Ohira, and M. Ando, "Numerical simulations on beam and/or null forming performance of ESPAR antennas," *Electronics and Communications in Japan,* Vol. 86, No. 1, 1–11, 2003.
5. Ohira, T., K. Gyoda, and S. Denno, "Microwave signal processing adaptive beamforming and electronically steerable passive array radiator antenna," *IEICE Technical Report,* Vol. 99, No. 213, 9–14 ,1999.
6. Gyoda, K. and T. Ohira, "Design of electronically steerable passive array radiator (ESPAR) antennas," *IEEE Antennas and Propagation Society International Symposium*, Vol. 2, 922–925, 2000.
7. Komatsuzaki, A., S. Saito, K. Gyoda, and T. Ohira, "Reactance optimization in ESPAR antenna by Hamiltonian algorithm," *IEICE Technical Report,* Vol. 85, No. 3, 381–390, 2002.
8. Carras, M., A. Kalis, and A. G. Constantinides, "Improving the frequency characteristics of the electronically steerable passive array radiator antenna," *1st International Symposium on Wireless Communication Systems*, Mauritius, 130–134, 2004.
9. Vasileiou, P., K. Maliatsos, E. Thomatos, and A. Kanatas, "Reconfigurable orthonormal basis patterns using ESPAR antennas," *IEEE Antennas and Wireless Propagation Letters*, Vol. 12, 448–451, 2013.

Antenna Array with Meshed Elements for Beamforming Applications

E. R. Escobar[1], **N. J. Kirsch**[1], **and R. B. Turner**[2]

[1]University of New Hampshire, USA
[2]NetBlazr, Inc., USA

Abstract— Next generation wireless systems will leverage multiple antennas to increase capacity and connectivity. However, antenna arrays tend to be obtrusive, which limits the locations in which they can be deployed. The purpose of this work is to present an optically transparent antenna array for beamforming applications as transparent arrays would be useful for a wider range of applications. We present a 1×8 array of dual polarized mesh antennas suitable for inter-building connectivity. This design includes details regarding patch modifications and inter-element spacing to address mutual coupling, fit overall physical design goals, and achieve high enough spatial diversity for beamforming applications. The performance of the antenna array is modeled in HFSS and compared to similarly designed arrays made from non-transparent materials (FR-4 and copper). Additionally we include an analysis of the resulting beamwidth and scan angles of the array using beamforming techniques.

1. INTRODUCTION

As demand for wireless communications increases, there is a growing need for reconfigurable networking systems that accommodate network topology changes, varying demand, and increased throughput. Mesh and heterogeneous networks (HetNets) address these needs [1]. However easily deployed systems use omni-directional antennas that limit performance and indoor units that restrict most such networks to a single building. Greater connectivity and throughput performance are possible using directional antennas to minimize interference and outdoor mounting allows inter-building links to form neighborhood networks. But such systems can be difficult or expensive to deploy. Easily installed high performance networks are possible with antennas installed indoors in windows, but the appearance and size of such traditional antennas are unacceptable. The solution is an optically transparent multi-element antenna with electronic beamforming and beamsteering. This eliminates manual aiming, supports automatic reconfiguration, and is unobtrusive.

There is a significant amount of prior work on optically transparent antennas made from materials such as Indium Tin Oxide (ITO) [2–7], AgGL [8, 9], and silver nanowires [10, 11]. This work shows that there is a trade-off in conductivity and transparency, yet reasonable efficiency can be achieved [2, 8]. While suitable for some applications, these materials can be difficult and costly to fabricate. As a trade-off, work has been done that shows thin copper wires (or other conductors) can be laid out in a mesh. The meshed wire structure has nearly the same conductivity as a solid piece of metal, but also some level of transparency [2, 12]. For our array, we consider microstrip antennas made with thin conductive wires in an open mesh (or grid) configuration that provides 80%–90% optical transmittance.

In our work, we present an eight element array of mesh antennas suitable for inter-building connectivity. Our contribution includes details of the design of the patch antenna's elements, taking into consideration the transparency due to wire thickness and grid density. We also consider the impact of ground planes and conductors made from meshed metal. The design includes details regarding patch modifications and inter-element spacing to address mutual coupling, fit overall physical design goals, and achieve high enough spatial diversity for beamforming applications. The performance of the antenna array is modeled in HFSS. Finally, we include details on the achieved phased array beam patterns and scan angles using beam forming techniques.

2. MESH ANTENNA DESIGN

To meet the objectives of a planar transparent antenna array, we began by designing a single dual-polarized microstrip patch antenna. The conductive and ground plane layers of the antenna were made from a fine-pitched open-mesh of copper wires. Previous work by Hautcoeur et al investigated mesh antennas with pitches of 100, 200, and 300 µm [9]. The transparency increases as the pitch, or distance between wires, increases. However, larger pitches limit the actual realizable L and W of the patch elements. For our patch as shown in Fig. 1, we chose 200 µm as a balance between

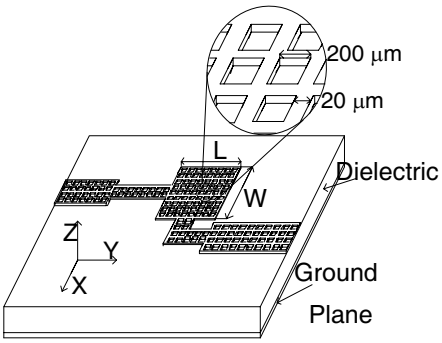

Figure 1: Design of a single meshed patch antenna.

transparency, conductivity, and manufacturability. This pitch, along with a copper wire line width of 20 μm and thickness of 35 μm produces an optical transparency of 82.6% and a conductivity of 1.205×10^7 S/m.

The radiating element is composed of the patch antenna and the feed line. The feed line includes a transmission line and a quarter-wave impedance transformer to match the 50 Ω feed input impedance. For structural rigidity and optical transparency, we chose polyethylene terephalate, PET, as the dielectric with a relative permittivity of $\epsilon_r = 2.6$, and a thickness of 3.3 mm.

The dimensions for the dual-polarized patch were calculated based on the classic patch antenna equations which take into consideration the resonant frequency of $f_c = 5.5$ GHz and the relative permittivity and thickness of the dielectric [13]. The dual-polarized single element shown in Fig. 1 has dimension of $L = W = 14.76$ mm. Given the dimensions of the L and W, the number of actual meshed lines must be determined. The number of mesh lines, N, that are required can be calculated with the dimension (K, where K is the length, L or width, W of the patch) by $N = (K + p)/(p + q))$, where p is the pitch and q is the line width.

3. ANTENNA PERFORMANCE

In this section, we present the HFSS simulation results of the single dual-polarized element and the eight-element array. There are an excessive number of objects in the simulation due to the mesh design. Therefore, we simplified the simulations by determining the parameters of the copper mesh wires and then simulated the antennas [9].

3.1. Single Element

First, we present the S-parameters of the single element. Fig. 2(a) shows the reflection coefficient for the input port for both polarization feeds. Both polarizations perform similarly, though the center frequencies are slightly different. When the patch antenna is excited by the vertically polarized feed, the center frequency is 5.48 GHz and the bandwidth is 4.1% whereas the horizontally polarized feed has a center frequency of 5.515 GHz and the bandwidth is 4.9%. These results are very comparable to those of a patch antenna composed from solid copper. Exciting a solid copper patch antenna to be vertically polarized, results in a center frequency of 5.495 GHz and the bandwidth is 4%, whereas when it is excited by a horizontally polarized feed, the center frequency is 5.525 GHz and the bandwidth is 4.8%.

We also present the radiation pattern for the mesh antenna and solid copper antenna each excited by the vertical and horizontally polarized feeds in Figs. 2(b) and 2(c). When the patch antenna is excited for a vertical polarization, the elevation plane beamwidth and azimuthal plane beamwidth is 74° and 140° respectively for the mesh antenna, whereas the elevation plane beamwidth is 64° and 120° respectively for the solid copper antenna. Likewise, when the patch antenna is excited for a horizontal polarization, the elevation plane beamwidth and azimuthal plane beamwidth is 62° and 130° respectively for the mesh antenna, whereas the elevation plane beamwidth is 66° and 128° respectively for the solid copper antenna. The mesh antenna has similar performance to the solid copper patch.

These results suggest that mutual coupling occurs between the patch and the different feed lines. Being a dual polarized patch antenna, two different feed lines were required allowing the patch to be excited for both vertical and horizontal polarizations. The mutual coupling can be reduced by a number of methods however, the beam width achieved is acceptable when considering the design

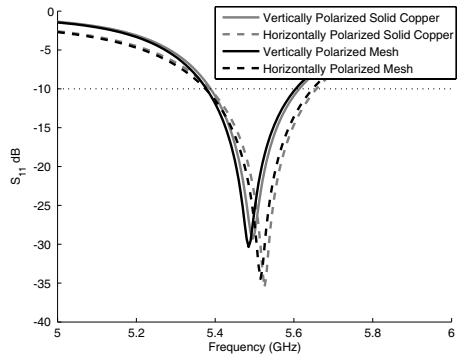

(a) Reflection coefficient

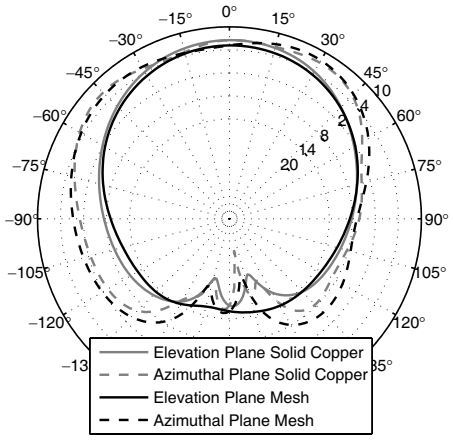

(b) Vertical radiation pattern (dB)

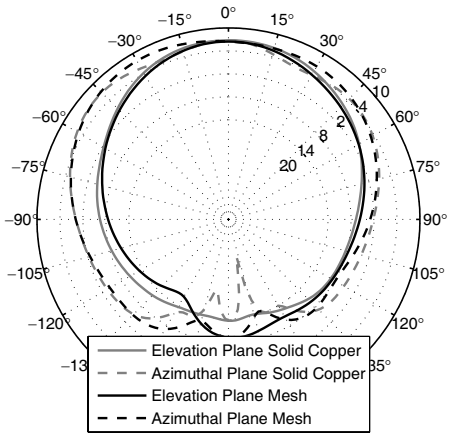

(c) Horizontal radiation pattern (dB)

Figure 2: Simulation results of the single dual-polarized copper mesh and solid copper patch antennas.

of a planar and compact array.

3.2. Antenna Array

In an effort to create a steerable antenna pattern over 120° with a beamwidth of 15°, we chose an eight element array [14]. The uniform linear array of mesh patches shown in Fig. 3 with an inter-element spacing of $d = 2.75\,\text{cm}$, which is $\lambda/2$ at 5.5 GHz. The performance of the ULA was validated through simulations by shifting the phase of each port in order to steer the main lobe in different directions. For a beamsteering direction, α, the weights for each element within the array geometry were determined by phased array theory [14]. Similarly, this array could be used for beamforming applications with different electronics [15].

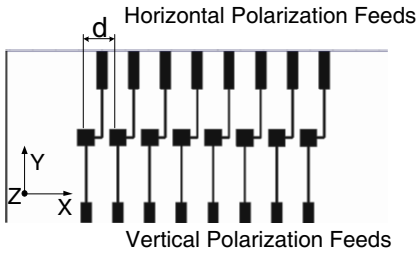

Figure 3: Design of a eight meshed patch antenna.

While radiation patterns were determined for many angles, we present the vertically and horizontally polarized radiation patterns in Fig. 4 for specific values of $\alpha = \{-60, -30, 0, 30, 60\}$. When excited using the vertically polarized feeds, the gains varied between 11.14 to 14.6 dB with a beamwidth varying between 14 to 16°; these results meet our goal. Exciting the the horizontally

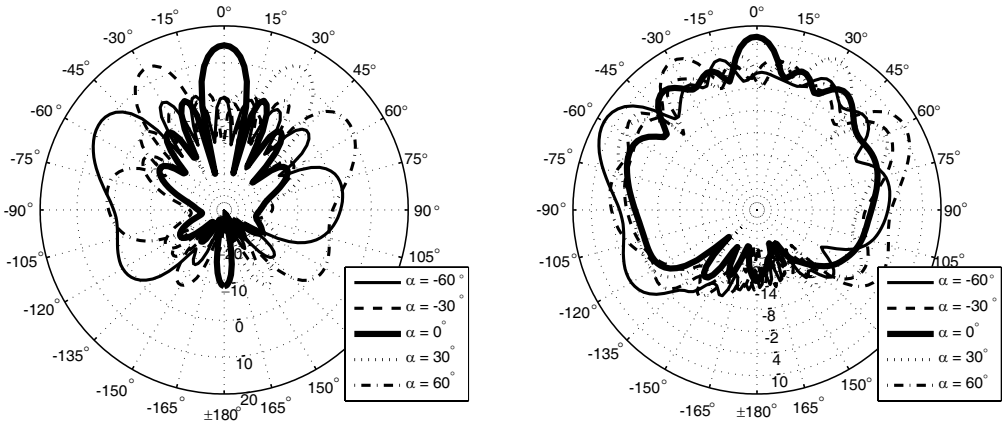

(a) Vertical polarization (b) Horizontal polarization

Figure 4: Simulated radiation patterns of the eight dual-polarized copper mesh patch antennas.

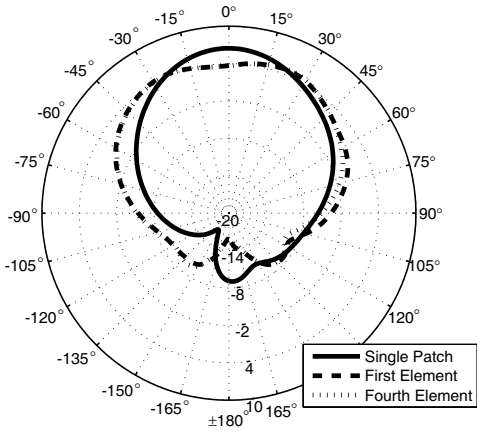

Figure 5: Radiation patterns of the elevation plane showing mutual coupling effects for a single antenna and the end and middle elements of the array.

polarized feeds results in gains between 9.5 and 12.2 dB with a beamwidth between 14 to 20°. The main lobe was at least 7.1 and 2.65 dB greater than the nearest side lobe for the vertical and horizontal polarizations respectively. The lower gain and higher side lobe energy is due to mutual coupling of the feed lines. The mutual coupling could be reduced by larger inter-element spacing, however our design is to have a compact planar dual-polarized antenna array.

To investigate the mutual coupling between the different patches and feed lines for the antenna array, we excited the horizontal feed of one element and terminated the others with a matched load. These simulations (shown in Fig. 5) show the mutual coupling effects by comparing end and middle elements and to a single non-array antenna. It is clear from Fig. 5 that the mutual coupling distorts the radiation pattern of each element in the antenna array, and can be used to explain why some side lobes were within 3 dB of the main lobe. In addition to the inter-element mutual coupling, there is mutual coupling due to the feeds between elements as observed in the radiation pattern for the single element.

4. CONCLUSION

Our goal was to investigate the feasibility of creating an optically transparent multi-element antenna capable of beamforming and beamsteering. First, we simulated a single dual polarized patch antenna with a meshed copper conductor and ground plane. With these results, we constructed an eight element ULA. The results from the radiation pattern show the antenna array is capable of forming beams through the 120° with a beamwidth of 15°. With the convenience of the physical size and transparency of the array, this antenna system will enable mesh networks without the need for a professional outdoor mounting. Future work in this area will include investigating a method

to reduce the mutual coupling between the patch antennas and feed lines, reduce the side lobe energy, as well as increasing the bandwidth and scan angle of the array.

ACKNOWLEDGMENT

This material is based upon work supported by the National Science Foundation under Grant No. (1248657).

REFERENCES

1. Akyildiz, I. F. and W. Xudong, "A survey on wireless mesh networks," *IEEE Communications Magazine*, Vol. 43, No. 9, S23–S30, 2005.
2. Yasin, T., R. Baktur, and C. Furse, "A comparative study on two types of transparent patch antennas," *General Assembly and Scientific Symposium*, 1–4, 2011.
3. Saberin, J. R. and C. Furse, "Challenges with optically transparent patch antennas," *IEEE Antennas and Propagation Magazine*, Vol. 54, No. 3, 10–16, 2012.
4. Guan, N., H. Furuya, K. Himeno, K. Goto, and K. Ito, "A monopole antenna made of a transparent conductive film," *International Workshop on Antenna Technology: Small and Smart Antennas Metamaterials and Applications*, 263–266, 2007.
5. Mias, C., C. Tsakonas, N. Prountzos, D. C. Koutsogeorgis, S. C. Liew, C. Oswald, R. Ranson, W. M. Cranton, and C. B. Thomas, "Optically transparent microstrip antennas," *IEE Colloquium on Antennas for Automotives*, 2000.
6. Kirsch, N. J., N. Vacirca, T. Kurzweg, A. Fontecchio, and K. Dandekar, "Performance of transparent conductive polymer antennas in a MIMO ad-hoc network," *Proc. of IEEE International Conference on Wireless Mobility*, Oct. 2010.
7. Kirsch, N. J., N. Vacirca, E. Plowman, K. Dandekar, A. Fontecchio, and T. Kurzweg, "Optically transparent conductive polymer RFID meandering dipole antenna," *Proc. of IEEE International Conference on RFID*, Apr. 2009.
8. Hautcoeur, J., F. Colombel, X. Castel, M. Himdi, and E. M. Cruz, "Optically transparent monopole antenna with high radiation efficiency manufactured with silver grid layer (AgGL)," *Electronics Letters*, Vol. 45, No. 20, 1014–1016, 2009.
9. Hautcoeur, J., F. Colombel, X. Castel, M. Himdi, and E. Motta-Cruz, "Radio frequency performances of transparent ultra-wideband antennas," *Progress In Electromagnetics Research C*, Vol. 22, 259–271, 2011.
10. Ito, K. and M. Wu, "See-through microstrip antennas constructed on a transparent substrate," *Seventh International Conference on (IEE) Antennas and Propagation*, Vol. 1, 133–136, 1991.
11. Clasen, G. and R. Langley, "Mesh patch antennas," *IEEE Transactions on Antennas and Propagation*, Vol. 52, No. 6, 1412–1416, 2004.
12. Turpin, T. W. and R. Baktur, "Meshed patch antennas integrated on solar cells," *IEEE Transactions on Antennas and Wireless Propagation Letters*, Vol. 8, 693–696, 2009.
13. Balanis, C. A., *Antenna Theory Analysis and Design*, 3rd Edition, Wiley-Interscience, New Jersey, 2005.
14. Hansen, R. C., *Phased Array Antennas*, John Wiley & Sons, 2009.
15. Krim, H. and M. Viberg, "Two decades of array signal processing research: The parametric approach," *IEEE Signal Processing Magazine*, Vol. 13, No. 4, 67–94, 1996.

Performance of Capacity Optimized Line-of-sight MIMO HAP-to-train Architectures

Emmanouel T. Michailidis,
Paraskevi N. Daskalaki, **and Athanasios G. Kanatas**
Department of Digital Systems, University of Piraeus
80 Karaoli & Dimitriou St., Piraeus 18534, Greece

Abstract— In this paper, the provision of high-speed broadband wireless railway services via high altitude platforms (HAPs) is studied and line-of-sight (LoS) propagation in the Ka frequency band is considered. A geometrical design method to construct full-rank capacity optimized HAP-to-train multiple-input multiple-output (MIMO) channels is applied. Then, an analysis of the sensitivity to imperfect positioning and orientation of the antenna arrays is performed with regard to the channel capacity. The results reveal relatively low sensitivity of the underlying system to displacements of antenna arrays from the optimal point. These results also depict that the orientation of the antenna arrays and the elevation angle of the platform significantly affect the channel capacity.

1. INTRODUCTION

The growing exigencies for efficient high-speed Internet access and audio, video and file transfer services in commercial train routes have prompted the development of satellite and wireless terrestrial networks [1]. Geostationary earth orbit (GEO) satellites intend to exploit line-of-sight (LoS) connections, whereas the terrestrial cellular infrastructure preserves link availability in propagation environments, where the direct communication to the satellite might not be feasible, i.e., tunnels and train stations. In recent years, the high-altitude platforms (HAPs) have also emerged [2, 3]. HAPs are quasi-stationary aerial platforms flying at a height approximately 20 km above the Earth's surface, in the stratosphere and capable of providing ubiquitous wireless access over large coverage areas at low cost. Several frequency bands have been licensed for communications through HAPs. Among them, the Ka (28/31 GHz) [4] and V (47/48 GHz) [5] bands were licensed for broadband fixed wireless access (BFWA) services and ensure adequate bandwidth. However, their application could be extended to mobile scenarios, such as vehicular, maritime, aeronautical and railway scenarios [6].

To meet the long-term evolution for railway (LTE-R) requirements [7] imposed by the International Union of Railways (UIC) and enhance the achievable data throughput, the application of the multiple-input multiple-output (MIMO) technology seems inevitable [8]. The MIMO gain strongly depends on the channel characteristics, which are mainly determined by the antenna configuration and the richness of scattering [9]. Although the propagation at mm-wave frequencies requires a strong, dominant LoS signal for sufficient coverage, mobility effects, such as multipath, shadowing, and blockage, which are also encountered at lower frequency bands, may exist due to the local environment in the vicinity of the trains, e.g., the presence of various metallic obstacles along the train trajectory for electrical power supply. Nevertheless, the railway environment is generally characterized by sparse (insignificant) multipath [10] and the elevation angles of the HAPs with respect to the trains are high [11] which in turns imply nearly LoS (open) propagation. Conceptually, LoS propagation correspond to a rank-deficient MIMO channel matrix and low spectral efficiency due to the increased spatial correlation introduced by the linear relationship of the phases of the received signals. However, using specifically designed antenna arrays at optimal positions, a full-rank MIMO channel may be achieved [12].

In [13], geometrical design recommendations were introduced for uniform linear arrays (ULAs) and the applicability of MIMO techniques to LoS-HAP channels for BFWA along with propagation models for the Ka and V frequency bands was studied. Nevertheless, there are some technical challenges for LTE-R due to the mobility of the trains up to 500 km/h, which leads to a time-varying and non-stationary radio channel. In addition, the stratospheric winds may vary the position of the HAP, which in turns influences the stabilization of beam pointing angles to HAP motion and requires heavy and slow mechanical steering. This paper examines the viability of reliable high-data rate communications for trains through HAPs at mm-wave frequencies and assesses the capacity

performance of capacity optimized LoS-MIMO channels using the geometrical design recommendations and the maximum capacity criterion introduced in [13]. Clear sky conditions are taken into account without incorporating atmospheric fading, which leads to different channel characteristics [14]. The parameters of interest are the height and the elevation angle of the platform with respect to the train, the carrier frequency, and the antenna array configuration. The results demonstrate and discuss the sensitivity of the capacity performance to the variation of the positioning and orientation of the antenna arrays.

The remainder of the paper is organized as follows. Section 2 describes the HAP-to-train LoS-MIMO system scenario, while Section 3 defines the channel capacity and the maximum capacity criterion. Section 4 provides results. Finally, conclusions are drawn in Section 5.

2. CHANNEL MODEL SCENARIO

The system model employed throughout this paper considers n_T transmit and n_R receive antenna elements installed on a HAP and the top of a train, respectively. All antennas are omni-directional and are numbered as $1 \leq p \leq q \leq n_T$ and $1 \leq l \leq m \leq n_R$, respectively. The spacing between HAP and train antenna elements is denoted δ_T and δ_R, respectively and angles θ_T and θ_R represent the orientation of the HAP and train antenna arrays, respectively. The heights of HAP and train antenna arrays are $h_T \approx 20$ km and $h_R \approx 3\,\mathrm{m} \ll h_T$, respectively. In addition, the elevation angle of the HAP with respect to the train is denoted β_T and dynamically changes with the movement of the train and/or the HAP. A minimum elevation angle of $\beta_{T,\min} = 30°$ and a maximum elevation angle of $\beta_{T,\max} = 60°$ are considered, which correspond to a $R_{\max} = h_T/\tan\beta_{T,\min} \approx 34.6\,\mathrm{km}$ and $R_{\min} = h_T/\tan\beta_{T,\max} \approx 11.5\,\mathrm{km}$ radius, respectively, and $d_{\max} = h_T/\sin\beta_{T,\min} \approx 40\,\mathrm{km}$ and $d_{\min} = h_T/\sin\beta_{T,\max} \approx 23.1\,\mathrm{km}$ LoS distance, respectively. Moreover, the carrier frequency and signal bandwidth are 28 GHz (downlink) and 25 MHz, respectively. It is assumed that there are N trains within the coverage area at a given time, which may be on the directly adjacent track and may travel toward or away from each other. These trains simultaneously transmit uncorrelated signals within the same frequency band. The maximum speed of the trains is considered to be 300 km/h. Therefore, a multiple HAP constellation should be used for sufficient coverage. Single-carrier quaternary phase-shift keying (QPSK) transmission is assumed based on the IEEE 802.16 standard for broadband fixed wireless access [15]. Fig. 1 depicts the geometrical characteristics of a HAP-to-train LoS-MIMO communication system with $n_T = n_R = 2$ antenna elements and defines the Cartesian coordinate system.

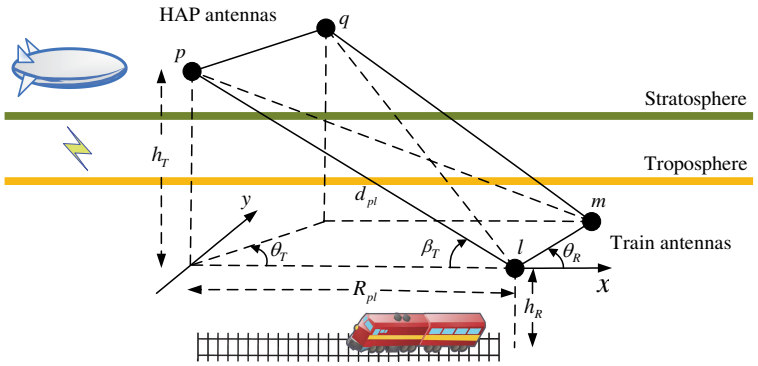

Figure 1: A geometrical model for HAP-to-train LoS-MIMO channels.

3. THE MAXIMUM CHANNEL CAPACITY CRITERION

Assuming that the channel is known to the receiver (train) and unknown to the transmitter (HAP), the available MIMO capacity can be obtained from [16]

$$C(t) = \log_2 \det\left(\mathbf{I}_{n_R} + \left(\frac{SNR}{n_T}\right)\mathbf{H}(t)\,\mathbf{H}^H(t)\right) \text{ bps/Hz}, \tag{1}$$

where $\mathbf{H}(t) = [h_{ij}(t)]_{n_R \times n_T}$ is the $n_R \times n_T$ channel matrix containing the free-space LoS responses between all array elements, $h_{ij} = e^{-j2\pi d(i,j)/\lambda}$ is the complex response between a transmit element i, and a receive element j, $d(i,j)$ is the LoS distance between the two elements, λ is the carrier

wavelength, $\mathbf{I}_{n_R}$ is the identity matrix of size n_R, *SNR* corresponds to the average signal-to-noise ratio at the input of the receiver, $(\cdot)^H$ denotes the complex conjugate transpose operator, and $\det(\cdot)$ denotes the matrix determinant. Note that the LoS distances between the antenna elements can be obtained using the geometrical model in Fig. 1 [13]. Besides, the maximum capacity of a 2×2 HAP-to-train LoS-MIMO channel can be reached, providing that antenna inter-element distance at both ends, the carrier wavelength, the height and elevation angle of the HAP, and the antenna array orientation fulfill the following criterion [13]:

$$\delta_T \delta_R = (2v+1)\,\frac{\lambda h_T}{2\sin\beta_T \sin\theta_T \sin\theta_R}, \tag{2}$$

where $v \in \mathbb{Z}$.

4. RESULTS

Although the route of the trains is definite and fixed and the path predictable, there is usually a need for high capacity over an area, rather than to a fixed point. Moreover, in practical situations, the parameters β_T, θ_T, and θ_R in (2) may be difficult to be determined with sufficient accuracy. Hence, a compromise is required, under more realistic deployment and propagation conditions or imperfectly positioned arrays. In this section, the sensitivity of the performance to the orientation and positioning of the arrays in practical high-speed railway scenarios is discussed and evaluated. Using (2) and considering that $v = 0$, $h_T = 20\,\text{km}$, $\beta_T = 45°$, and $\theta_T = \theta_R = 90°$, the required product between δ_T and δ_R for the 28 GHz frequency band is approximately $151.5\,\text{m}^2$. By assuming that the HAP antenna inter-element spacing is equal to $\delta_T = 30\,\text{m}$, the corresponding train spacing is set $\delta_R = 5.05\,\text{m}$.

Figure 2 examines the sensitivity of the performance to train antenna array shifting from the optimal point. Since multiple HAP constellations are required for sufficient coverage, the evaluation takes place in a location range (displacement range referring to the optimal initial point) from 0 to 20,000 m. This is assumed to be equivalent to the whole trajectory, i.e., the distance from the mid sub-platform-point (SPP) between two HAPs, i.e., the midpoint directly below the two HAPs, to the closest SPP of another HAP. In particular, Fig. 2 demonstrates the variation of the capacity with different antenna array displacements and shows the influence of up to 20,000 m shifting along x- and y-axis for SNR = 20 dB. One observes that the capacity is relatively insensitive to these displacements from the optimum point. For a maximum shifting of 20,000 m, the capacity is only 3.3% and 2.2% lower than the maximum capacity, respectively.

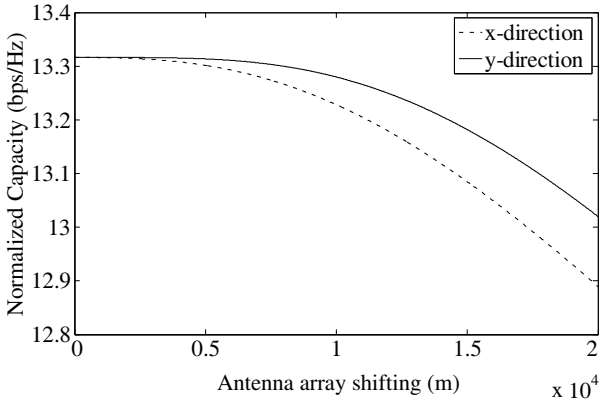

Figure 2: The normalized capacity obtained using the optimized HAP-to-train LoS-MIMO architecture as a function of the train antenna array shifting from the optimal point.

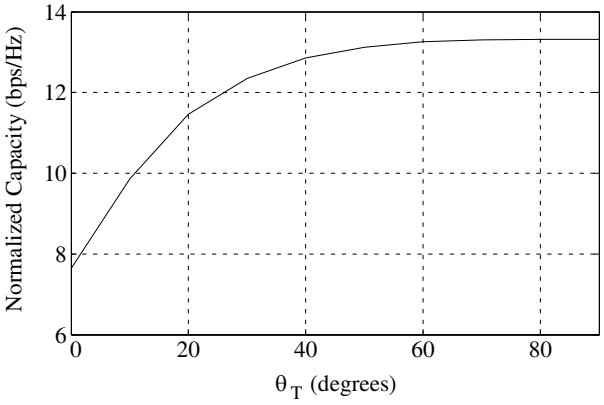

Figure 3: The normalized capacity obtained using the optimized HAP-to-train LoS-MIMO architecture for different orientation of the HAP antenna array.

Figure 3 demonstrates the channel capacity for different orientation of the HAP antenna array. The capacity is evaluated for SNR = 20 dB and $0 < \theta_T \leq 90°$. According to Fig. 3, decreasing θ_T from 90° to 45° has an insignificant effect on the capacity, while a further decrease in θ_T drastically decreases the capacity. Hence, the results show a large sensitivity (in terms of capacity) to the orientation of the arrays. From (2), it is clear that the same results apply for $0 < \theta_R \leq 90°$ and $0 < \beta_T \leq 90°$.

5. CONCLUSION

As the demand for uninterrupted quality broadband wireless services in the area of passenger transport in railways and high-data rate communications to multiple moving trains grow, the railroad scenario seems a promising and commercially attractive field for HAP-based systems. In this paper, a method to achieve orthogonality between spatially multiplexed signals has been employed to construct a full-rank HAP-to-train LoS-MIMO channel matrix at Ka frequency bands. Providing that the system parameters are carefully selected, the results have demonstrated the sensitivity of the capacity performance to the positioning and orientation of the arrays. These results imply that a thorough investigation of the design of any practical HAP-to-train LoS-MIMO system is required mainly in terms of the orientation of the antenna arrays and the elevation angle of the platform.

ACKNOWLEDGMENT

This work has been co-financed by the European Union (European Social Fund — ESF) and Greek national funds through the Operational Program "Education and Lifelong Learning" of the National Strategic Reference Framework (NSRF) — Research Funding Program THALES MIMOSA (MIS: 380041). Investing in knowledge society through the European Social Fund.

REFERENCES

1. Karimi, O. B., L. Jiangchuan, and W. Chonggang, "Seamless wireless connectivity for multimedia services in high speed trains," *IEEE J. on Selec. Areas in Commun.*, Vol. 30, No. 4, 729–739, May 2012.
2. Mohammed, A., A. Mehmood, F. Pavlidou, and M. Mohorcic, "The role of high-altitude platforms (HAPs) in the global wireless connectivity," *Proceedings of the IEEE*, Vol. 99, No. 11, 1939–1953, Nov. 2011.
3. White, G. P. and Y. V. Zakharov, "Data communications to trains from high-altitude platforms," *IEEE Trans. on Vehic. Technol.*, Vol. 56, No. 4, 2253–2266, Jul. 2007.
4. RESOLUTION 145 (Rev.WRC-07), "Use of the bands 27.9–28.2 GHz and 31–31.3 GHz by high-altitude platform stations in the fixed service," International Telecommunication Union, Geneva, Switzerland, 2007.
5. RESOLUTION 122 (Rev.WRC-07), "Use of the bands 47.2–47.5 GHz and 47.9–48.2 GHz by high-altitude platform stations in the fixed service and by other services," International Telecommunication Union, Geneva, Switzerland, 2007.
6. Morlet, C., A. B. Alamañac, G. Gallinaro, L. Erup, P. Takats, and A. Ginesi, "Introduction of mobility aspects for DVB-S2/RCS broadband systems," *Int. J. on Space Commun.*, Vol. 21, Nos. 1–2, 5–17, 2007.
7. Guan, K., Z. Zhong, and B. Ai, "Assessment of LTE-R using high speed railway channel model," *Proc. Int. Conf. Communications and Mobile Computing (CMC)*, 461–464, Apr. 2011.
8. Paulraj, A. J., D. A. Gore, R. U. Nabar, and H. Bolcskei, "An overview of MIMO communications — A key to gigabit wireless," *Proc. IEEE*, Vol. 92, No. 2, 198–218, 2004.
9. Jin, S., X. Gao, and X. You, "On the ergodic capacity of rank-1 Ricean-fading MIMO channels," *IEEE Trans. on Inform. Theory*, Vol. 53, No. 2, 502–517, 2007.
10. Gao, L., Z. Zhong, B. Ai, and L. Xiong, "Estimation of the Ricean K-factor in the high speed railway scenarios," *Proc. of the IEEE Wireless Communications and Networking Confenrence (WCNC'08)*, 775–779, 2008.
11. Spillard, C., E. Falletti, F. Sellone, J. D. Penin, J. L. Ruíz-Cuevas, and M. Mondin, "Report for EU Capanina project, deliverable D14," Mobile Link Propagation Aspects, Channel Model and Impairment Mitigation Techniques, Sep. 2004, Website of Capanina Project, [Online] Available: http://www.capanina.org.
12. Bohagen, F., P. Orten, and G. E. Oien, "Construction and capacity analysis of high-rank line-of-sight MIMO channels," *Proc. IEEE Wirel. Commun. and Netw. Conf.*, 432–437, Mar. 2005.
13. Michailidis, E. T. and A. G. Kanatas, "Capacity optimized line-of-sight HAP-MIMO channels for fixed wireless access," *Proc. International Workshop on Satellite and Space Communications (IWSSC) 2009*, 73–77, Siena, Tuscany, Italy, Sep. 10–11, 2009.
14. Arapoglou, P.-D., K. P. Liolis, and A. D. Panagopoulos, "Railway satellite channel at Ku band and above: Composite dynamic modeling for the design of fade mitigation techniques," *Int. J. Satell. Commun. Network.*, Vol. 30, No. 1, 1–17, 2012, DOI: 10.1002/sat.991.

15. "IEEE standard for local and metropolitan area networks, Part 16: Air interface for fixed broadband wireless access systems," IEEE Std 802.16-2001, Dec. 6, 2001.
16. Telatar, E., "Capacity of multiantenna gaussian channels," Tech. Memo., AT & T Bell Laboratories, Jun. 1995.

IEMI and EMC Considerations for Large Systems — Smart Grid Aspects

D. Månsson
Division of Electromagnetic Engineering, Royal Institute of Technology (KTH)
Teknikringen 33, Stockholm 100 44, Sweden

Abstract— The smart grid concept is the grid design philosophy that diversifies the power grids and the electricity markets. However a deep penetration of "prosumers" and distributed generation in urban environments could lead to significant problems from an electromagnetic compatibility (EMC) viewpoint. Traditional classification methods, used for small isolated systems, are inadequate tools to investigate, improve and evaluate mitigation measures for large distributed infrastructures such as a smart grid. Therefore, an alternative classification method, originally developed to investigate the vulnerability of large distributed systems from intentional electromagnetic interference (IEMI), is used here. The method is used to analyse the smart grid concept to investigate if the smart grid is, from an EMC and IEMI viewpoint for a large distributed system, an improvement or deterioration compared to traditional power grids (and the aspects that is attached to them).

1. INTRODUCTION

With the threat of global warming and diminished resources, the effective use of energy, on all levels of society, coupled with a low environmental impact of power generation, are vital points. Thus, to increase the effectiveness of our energy utilization, the idea of the "smart electricity grid" is internationally recognized and investigated. The key concepts of the smart grids are based around ICT[1], distributed generation of power and energy storage. Traditional concentrated large power generation will be supplemented or replaced with renewable energy sources whose production is geographically distributed. However these renewable energy sources are stochastic and, thus, the exact peak energy availability through, e.g., solar intensity or wind distribution, may not coincide with the peak energy demand. Therefore, the energy produced must be stored in an intermediary state in wait for the energy demand to increase. The stored energy can be in the form of chemical energy in batteries, potential energy of elevated water in a dam, kinetic energy in the momentum of a flywheel etc..

From this comes the concept of the "prosumer" (i.e., producer-consumer), e.g., a residential home with power generation through wind or solar power that can also store, and return to the grid, surplus energy not in demand locally. The local energy demand is obtained through so called "smart meters" and other measurements of the power consumed locally by devices and equipment. Thus, it is very important to obtain reliable measurements of voltages and currents. This information is the basis for determining the surplus or deficit of power available locally. For surplus energy that is returned to the grid, several financial procedures is discussed and tested around the globe.

All in all, this will require:

I. Complex electro-technical subsystems and power electronics for energy conversion, storage, and regulation.

II. Sophisticated ICT solutions for collecting, distributing and processing the vast amounts of information that is vital for the prosumer activities.

Therefore from this we here define and consider a smart grid to be:

"*An interconnected and interdependent non-linear system, wherein money, information and energy are flowing multidirectionally over domain boundaries wherein different limitations and demands may exist.*".

This gives the key concepts, but more importantly, that the mentioned transactions may be between different domains[2]. This is a vital observation that underlies the discussion in this paper.

[1] Information and Communications Technology.

[2] A "domain" is here considered to be a distinct part of a large distributed system; e.g., a subsection of a power grid.

2. INTRODUCTION TO ELECTROMAGNETIC COMPATIBILITY

All systems utilizing electromagnetic energy will, to some extent, emit energy in the form of electromagnetic fields and/or voltages and currents along connected cables and other conductors (if TEM mode is present as a mode of propagation). In addition, all systems utilizing electromagnetic energy can inherently, to some extent, be affected by such. It is important to remember that EMC is a desirable "state of being" that the considered systems can be in (in relation to its surroundings.

The definition of EMC is (according to the IEC [1]):

"The ability of an equipment or system to function satisfactorily in its electromagnetic environment without introducing intolerable electromagnetic disturbances to anything in that environment", wherein "electromagnetic environment is defined as *"the totality of EM phenomena existing at a given location."*.

Here, the definition of a system should not be limited to smaller equipment (e.g., computers) but can also be large distributed systems and fixed installations such as buildings, boats or even power grids. (The definition of "system" used is [2] "*system: multiple equipment or electrical units connected by cables, data links, etc.".*) All EMC problems can essentially be subdivided into five components (see Figure 1) and to increase the compatibility between two, or more, systems any of these five points can be addressed. These five components are:

1. The source of the physical disturbance (creating the electromagnetic interference (EMI)).
2. The suitability of the propagation path for the disturbance.
3. Interaction between the disturbance and system exterior (i.e., coupling to the system interior).
4. Internal coupling of the disturbance (i.e., spread of the disturbance inside the system)
5. At last, a component of the system is subjected to the disturbance, creating the EMI.

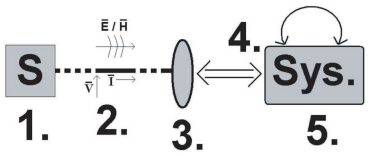

Figure 1: Decomposition of EMC problem in five components.

For many large complicated distributed systems, e.g., boats, buildings, etc. there often does not exist a particular individual responsible for the successful integration, with respect to EMC, of all subsystems and equipment during construction and overhauls. (Airplanes, however, is one exception.) Thus, different systems can be installed that may unintentionally disturb other electronic systems and, thus, decrease the overall performance of the system. In other word, there exists a severe lack of knowledge of the total system integration and behaviour (the interconnections and interdependencies between the different subsystems). (This is believed to be correlated to the relative obscurity of EMC as a discipline, even amongst most electrotechnical engineers. Fortunately, this is fundamentally a matter of information, awareness of the problem and education of the personal, which is, in part, solvable.) However, it is very important to remember that many severe, and some catastrophic, incidents due to EMI has occurred in the past [3] where the events leading up to the explosion on the USS Forestall in 1967 [4] and the sinking of the HMS Sheffield in 1982 are two of the more noticeable. A more recent incident in Sweden [5] involved problems with the radio communication at an airport. (The pilots were sometimes not able to communicate with the air traffic control and the reason was found to be two new LED advertising signs, with faulty EMC design, emitting radio frequency EMI in the communication bands of the air traffic.).

From the above, it should be clear that a large distributed system, as a whole, is inherently more prone to suffering from EMI problems than an isolated system.

3. CLASSIFICATION METHOD FOR INTENTIONAL EMI

Due to different reasons, it is not suitable to use traditional EMC classification methods (see [6]) when investigating the vulnerability of large distributed systems from intentional EMI (IEMI). The method developed (see [7]) to manage such situations is based on three main variables;

- Accessibility, the ability of gaining access to the different parts of the facility or critical components belonging to it.

- Consequence of a disturbance.
- Susceptibility of the system, which is further subdivided into.
  - Receptivity, the degree of the facility's ability to mitigate disturbances between and within electromagnetic topological zones.
  - Sensitivity, the different upset threshold levels of the equipment and subsystems inside the facility.
  - Redundancy, the availability of backup systems and ability to "degrade gracefully".

The method has successfully been used in cases with critical infrastructure installations.

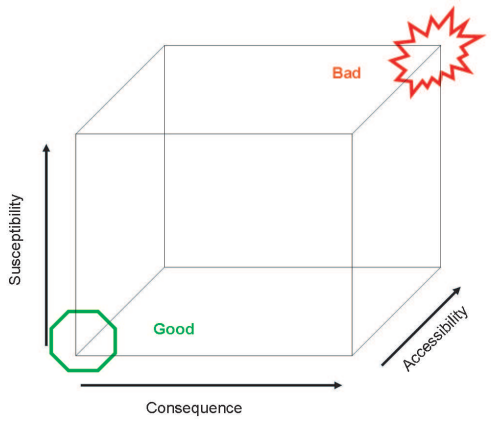

Figure 2: The IEMI cube centres on accessibility, susceptibility and the consequence of the attack to determine the vulnerability of a large distributed system against IEMI.

The advantage of this method is that it is inherently suitable to handle large distributed systems, such as a prosumer installation in a smart grid.

4. CONFORMITY TO ENVIRONMENT

To investigate the smart grid concept with this method we need first to discuss the main components of the smart grid concept. Power generated by renewable energy sources is, before eventual correction by power electronics, by nature often of highly varying power quality. Not only is the power quality inherently bad, but the power electronics (e.g., AC/AC converters) needed to acquire the 50 or 60 Hz signal can themselves, in the conversion process, be the cause of both conducted and radiated disturbances. For example, a power inverter on the market, advertised for use with photovoltaic cells, was found to have conducted disturbances of 17.6 dB over allowed limits and radiated emission of 10.3 dB over the limits [8]. In addition, a relative recent incident was reported in [9], wherein it was described how the fire department in Stockholm had communication problems at a certain location. The cause was traced to a church, where the newly installed LED lamps inside erroneously utilized pulse width modulation (PWM) that created radio frequency disturbances in the vicinity of the church. An investigation of the lamps showed that they did not comply with the EMC requirements necessary to be sold in Europe.

Such situations, might not pose a problem when power electronics are used where, and how, they were intended. However in a smart grid, the, e.g., AC/AC converters, might be situated in an electromagnetic environment for which they were originally not planned, and more importantly, designed for. Using the definition of a smart grid set forth above, we see that the quantities mentioned (e.g., power) can flow "over domain boundaries wherein different limitations and demands may exist." Using the example of a wind power plant at a prosumer's residential home, the above mentioned power electronics sits between the zone with high voltages (with large varying power quality) and the zone with low voltages and an approximate 50 or 60 Hz signal.

The issue is that these converters are usually, from an EMC point of view, designed and tested for an electromagnetic environment harsher than the residential home. It is difficult to translate the emission limits given in standards (e.g., [10]) to any general distance between transmitter and receiver so we can't say if the permissible emitted electromagnetic fields for industrial equipment are above the limits for immunity for normal residential COTS equipment. However, it is a well

established fact that residential COTS equipment can be interfered with [11] and especially an industrial environment is a challenge [12]. In [11] it was seen that COTS equipment bearing CE-mark and, thus, should comply with EMC requirements, could be interfered with at electric fields levels much lower than the EMC immunity requirement limits in the particular frequency band (few tenths of V/m compared to 3 V/m). The differences in required immunity limits for radiated fields, between an industrial and residential electromagnetic environment are significant (e.g., 10 V/m compared to 3 V/m (80–1000 MHz)). Clearly the industrial environment is a harsher electromagnetic environment, as the equipment is expected to withstand higher field values. Thus, the problem is that, in a prosumer installation, it can be expected that at the interface boundaries between different electromagnetic environments (different domains) equipment will be placed where they are not commonly found and expected (by the equipment designers). If the emissions from such equipment exceed the limits for the "low level" zone they will not exist in a harmonious state with that equipment and EMC is not achieved. In other words, the integration of future power components, in a prosumer installation, can be problematic.

5. SMART GRID EVALUATION

For the smart grid the unit of evaluation is here taken to be the prosumer installation, i.e., the stability and performance of the smart grid as a whole is dependent on the behaviour of this. Using the classification method described above the smart grid concept is analysed.

The consequence of an electromagnetic interference in a smart grid is believed to be significantly less than a traditional power grid. This is due to the inherent flexibility of distributed generation and energy storage, as well as factors discussed below.

Remembering the definition of the susceptibility of the system given above, the situation changes as follows.

The receptivity[3] of the system is unchanged as a smart grid installation has not, inherently, more mitigation against electromagnetic disturbances, than a traditional power grid installation. The sensitivity[4] of the system is also unchanged as we do not expect the subsystems and equipment of a smart grid installation to be significantly different than a traditional power grid installation. (As argued above it is the placement (point of installation) of the subsystems in a prosumer installation that is dominantly different, not the actual subsystems or equipment.).

The redundancy[5] of the systems is believed to be substantially improved as, per default, the smart grid as a whole has many backup units and alternative subsystems of operations (i.e., energy storage and distributed generation) that can continue operating if the normal operation of one particular installation is interfered with.

The accessibility term, as defined above, cannot directly be used here. The accessibility term is a measurement of how easy it is to gain access to the system and deliver an electromagnetic disturbance to a particular point in the system. I.e., how easy it is to introduce a large disturbance in the system where it, in a traditional EMC situation (normal unintentional EMI), would not be expected (due to mitigating measures installed) and pose a significant problem. Thus, the key point is that a significant disturbance is introduced in the system where it would not be expected, i.e., disturbance sources exist where they are not expected. This situation is similar to the discussion above, wherein, e.g., power electronics (producing noise/disturbances of detrimental levels) are introduced alongside relatively unprotected systems. Thus, we recognize the fact that "accessibility" can, in this non-IEMI scenario, be translated to how well subsystems and equipment conforms to their environment (as discussed above) and a "conform to environment factor" is formed. This is then related to how well the different systems of the prosumer installation adhere to regulation and standards (EMC and power quality) so that all subsystems and equipment are electromagnetically compatible with each other.

Thus, it is believed that the smart grid, as a concept with prosumers having local power generation and storage, leads to a power grid, as a whole, that is a substantial improvement over a traditional power grid structure with, more or less, centralized power generation.

ACKNOWLEDGMENT

This work was made possible through funding from the "STandUP for Energy" collaboration.

[3] Receptivity, the degree of the facility's ability to mitigate disturbances between and within electromagnetic topological zones.

[4] Sensitivity, the different upset threshold levels of the equipment and subsystems inside the facility.

[5] Redundancy, the availability of backup systems and ability to "degrade gracefully".

REFERENCES

1. http://www.iec.ch/emc/explained/environment.htm.
2. IEC Standard, 61000-6-6, "Electromagnetic compatibility (EMC) — Part 6-6: Generic standards — HEMP immunity for indoor equipment," 2003.
3. IEC Standard, 61000-1-5, "Electromagnetic compatibility (EMC) — Part 1-5: General — High power electromagnetic (HPEM) effects on civil systems," 2004.
4. Leach, R. and M. Alexander, "Electronic systems failures and anomalies attributed to electromagnetic interference," NASA Report 1374, National Aeronautics and Space Administration, Washington, CC 20546-0001, July 1995.
5. http://www.elsakerhetsverket.se/Global/PDF/Rapporter/EMC/Resultat%20fr%C3%A5n%20EMC-tillsyn%20av%20reklamskyltar.pdf.
6. Månsson, D., R. Thottappillil, and M. Bäckström, "Intentional EMI against critical infrastructures, a discussion on mitigation philosophy," *Proc. American Electro-Magnetics Conference*, 2010.
7. Månsson, D., R. Thottappillil, and M. Bäckström, "Methodology for classifying facilities with respect to intentional EMI," *IEEE Transactions on Electromagnetic Compatibility*, Vol. 51, No. 1, 46–52, February 2009.
8. http://www.elsakerhetsverket.se/sv/Produktsakerhet/Forsaljningsforbud/Vaxelriktare-for-solpanel-avger-storningar/.
9. http://www.elsakerhetsverket.se/Global/PDF/Aktuellt/2012/Aktuellt_2_12.pdf.
10. IEC Standard, 61000-6-4, "Electromagnetic compatibility (EMC) — Part 6-4: Generic standards — Emission standard for industrial environments," 2006.
11. Månsson, D., R. Thottappillil, T. Nilsson, O. Lundén, and M. Bäckström, "Susceptibility of civilian GPS receivers to electromagnetic radiation," *IEEE Transactions on Electromagnetic Compatibility*, Vol. 50, No. 2, 434–437, May 2008.
12. Chilo, J., C. Karlsson, P. Ängskog, and P. Stenumgaard, "EMI disruptive effect on wireless industrial communication systems in a paper plant," *Proc. of IEEE International Symposium on Electromagnetic Compatibility*, 2009.

An Experimental Characterization of Substation Impulsive Noise for a RF Channel Model

M. Au[1], **F. Gagnon**[1], **and B. L. Agba**[2]

[1]Electrical Engineering Department, École de Technologie Supérieure, Montréal, Canada
[2]IREQ (Hydro-Québec), Varennes, Canada

Abstract— Deploying wireless communication system, wireless sensors networks, for example, in a substation is problematic due to electromagnetic (EM) noise. The latter is partial discharges from high voltage (HV) equipments, electrical arcs from circuit breakers, etc. This paper deals with EM noise emitted by partial discharges (PD). PD pulses are highly impulsive and occur when the applied voltage is sufficient high. Our research work is to define metrics and methodology for electromagnetic noise characterization. This approach gives substantial information about RF channel in substations environments in which impulsive noise are omnipresent. This information will be useful for accurate channel modelling to ensure high quality in the transmitted signal.

1. INTRODUCTION

Substations are particular electromagnetic environment in which impulsive noise are omnipresent. These interferences can affect wireless communication performances [1, 2]. This specific noise radiates from high voltage equipments that containing imperfections and are well known as partial discharge (PD). Physically, when a high voltage stress is sufficiently high, a ionization process can occur within defects of a HV equipment [3, 4]. In this condition, partial discharge takes place and radiates in the HV environment. In substation, impulsive noise sources are multiple and are located randomly in space. Furthermore, PD pulse are inherently random in terms of magnitude, time occurrence and inter-arrival time [5, 6]. However, PD events are strongly dependent on the AC voltage of substation. For an accurate modelling of EM noise in substation, it is useful to characterize this particular electromagnetic environment. Portugués et al. [7] define metrics to characterize RF interference from partial discharge at 0 to 1 GHz. These metrics are not sufficient to characterize PD in terms of magnitude, inter-arrival time distributions. In this paper, our goal is to define metrics that can give sufficient information to characterize impulsive noise from PD for a RF channel model. We propose a methodology of measurement in RF range (780 MHz to 5 GHz). Measurements are made in a 735 kV substation. Results will be discussed in this paper.

2. MEASUREMENT SETUP AND METHODOLOGY

The measurement setup includes: antenna, filters and amplifier. Signals are captured with a real time oscilloscope. Measurement setup is presented on Figure 1:

- The antenna is a wideband (0.8–26 GHz) log periodic antenna from Rhode and Schwartz HL050, 8.5 dBi.
- A high pass filter from 780–3200 MHz, 50 Ω is integrated in our measurement system to cancel AM and FM communications, and other external interferences.
- A RF amplifier is employed from 30–3000 MHz with output power up to 12.8 dBm to ensure a better signal to noise ratio level.
- Protection equipment is a broadband limiter from 30–6000 MHz, 50 Ω. This component protect against unwanted signals up to 2.5 W.
- For data acquisition, the oscilloscope used is a serial data analyser LeCroy 13 GHz with 256 M samples max with 40 Gs/s max sample rate, 50 Ω input.

The measurement environment is a 735 kV substation where PD sources are randomly located in space. Although many measurements were made in different locations within the substation, only measurements of 2 locations are presented. The first location point is surrendered by HV pylons and power lines at 735 kV, circuit breakers, a current transformer and bush bar. The second location point includes HV pylons and power lines at 735 kV and bush bar. The atmospheric condition during the measurement campaign are: atmospheric pressure $P = 102$ khPa, temperature $T_c = 20°$C and humidity rate $H_r = 70\%$. A typical environment of the substation is shown on Figure 2.

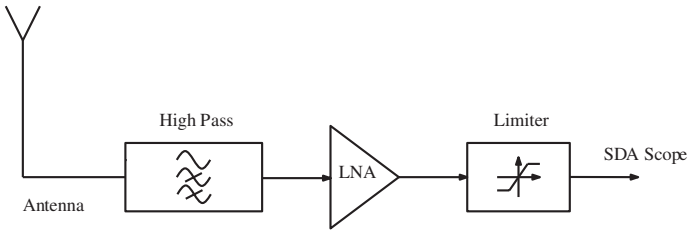

Figure 1: Measurement set up.

Figure 2: Typical HV equipments in the 735 kV substation.

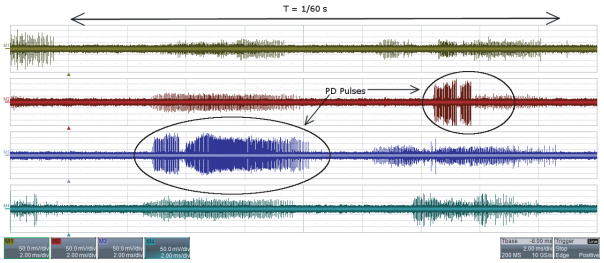

Figure 3: Typical captured waveforms at location point 2.

Our measurement methodology is synchronized to the voltage of the substation at 60 Hz. Waveforms are captured periodically at the beginning of each cycle of $T = \frac{1}{60}$ s. A sample rate of 10 Gs/s with 20 ms observation time is defined. AC power line of the substation are used to synchronize the scope to the voltage in substation. The scope can be synchronized to one of the three phases. Thus, PD pulses behaviour can have phase offset. For one location point, we capture 30 waveforms. Figure 3 gives an example of captured waveforms. The recorded measurements contains PD pulses and ambient noise from substation. Pulses are highly impulsive and have a magnitude above 50 mV/m.

3. CHARACTERIZATION METHODOLOGY

PD pulses are assumed to be a random process. The characterization of impulsive noise in substation is defined by distributions in terms of power density and occurrence. These distributions are

- Power density of PD pulse E_{s_τ} distribution (W/m$^2 \cdot$ s).
- PD occurrence φ distribution (s).
- Inter-arrival time $\Delta\varphi$ distribution (s).

They are expressed as $p(x)dx$, the probability that a PD pulse has a value between x and $x + dx$, independent of previous events. The phase resolved partial discharge (PRPD) is used in many publications to characterize PD pulse that degrade electrical insulations [5, 6, 8, 9]. It represents power density of PD pulse distribution for a measure in which observations are restricted to time interval Δt between t_{j-1} and t_j. PRPD can be written as

$$p(E_{s_\tau}|\Delta t) = \int_{t_{j-1}}^{t_j} p(t_n)p(E_{s_\tau}|t_n)dt_n \tag{1}$$

where $p(t_n)$ is the probability per unit time that a pulse will appear at t_n between t_{j-1} and t_j. $p(E_{s_\tau}|t_n)$ determines the probability that the pulse will have a power density E_{s_τ} if its occurrence is t_n.

The captured signal contains PD pulses waveform, ambient noise from substation and internal noise from oscilloscope. In order to isolate PD pulses, a methodology to extract them from overall noise is proposed as illustrated on Figure 4.

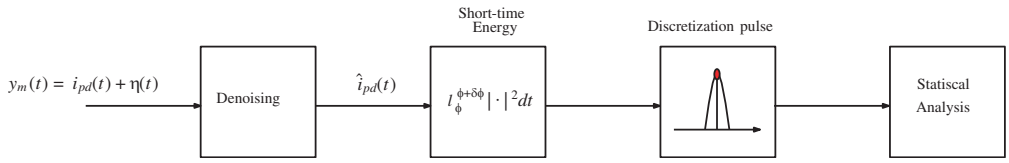

Figure 4: Overview of the methodology for measuring distributions.

- In order to extract PD pulses from these noise, we present a denoising methodology using discrete wavelets transform by using filter banks to wavelet analysis. The signal can be decomposed into wavelet coefficients and can be perfectly reconstructed. These wavelet coefficients are approximation and detail components of a signal in different frequency bands [10].

  The denoising procedure is to decompose the signal into wavelet coefficients for a given decomposition level. Then, a threshold is putted on these wavelets coefficients. Finally, signal is reconstructed using the inverse wavelet transform of the resulting wavelet coefficients after the threshold operation [10]. We assume that measured signals are PD pulse and additive ambient noise of the substation:

$$y_m(t) = i_{pd}(t) + \sigma\eta(t) \tag{2}$$

  The denoising operation is to estimate PD pulse $\hat{i}_{pd}(t)$ from the overall noise $\eta(t)$ with noise level σ. For our application, we use Daubechies wavelet with 8 vanishing moments for 30 decomposition levels. A hard threshold is applied to wavelet coefficients [10]. This threshold value is given by $T_h = \hat{\sigma}_i\sqrt{2\log(N_i)}$. Where $\hat{\sigma}_i$ is the estimate noise level of ambient noise and N_i is the length of signal at the i^{th} level of decomposition [11, 12]. A good estimation of σ is defined by

$$\hat{\sigma}_i = \frac{m_i}{0.6745} \tag{3}$$

  where m_i is the level-dependant median value of the decomposed signal. Threshold are rescaled by a level-dependent estimation of noise level.
- Power density of PD pulse E_{s_τ} is defined by windowing PD pulse waveform

$$E_{s_\tau} = \frac{1}{Z_0}\int_{-\infty}^{+\infty} |i_{pd}(t)w(t-\delta\phi)|^2 dt \tag{4}$$

  where $w(t)$ is the window waveform with a length $\delta\phi$. In our case, $w(t)$ is the hamming window and $\delta\phi = 164.1$ ns. The last parameter $\delta\phi$ is the maximum of the measured PD pulse duration.
- A pulse is sampled at the maximum value of the power density of pulse.

4. RESULTS AND DISCUSSIONS

4.1. PD Pulse Shape Analysis

Measured signals contain impulsive noise from partial discharge and other signals such as RF communication around 850 MHz, 1950 MHz and 2.1 GHz. Harmonics caused by interleaving artefacts, clock feed through, etc. from scope. They can be seen at 1.25, 2.5 and 3.75 GHz (Figure 6(a)). The measured signal can be described as a regular function where PD pulses are seen as singularities due to fast transient character of pulse shape.

Applying the wavelet decomposition, wavelet coefficients containing details of the signal (fine scales) have high coefficients values when signal have impulsive components [10]. Therefore, PD pulses can be extracted by applying the hard threshold. For small values of wavelet coefficients, the signal is probably regular locally. All coefficients $|\langle y_m, \psi_{i,n}\rangle| \leq T_h$ are set to zero. As the results, the denoising process is an adaptive smoothing filter that depends on the regularity of the signal. Figures 5 and 6(b) show results from denoising process. Harmonics and RF communications signals are suppressed properly. Impulsive noise in substation is wide band interference where its major energy are located at about 800 MHz. The measured PD pulse waveform can be described as

$$i_{pd}(t) = I_0 e^{-\alpha t}\left[A\cos\omega_c t + B\sin\omega_c t\right] \tag{5}$$

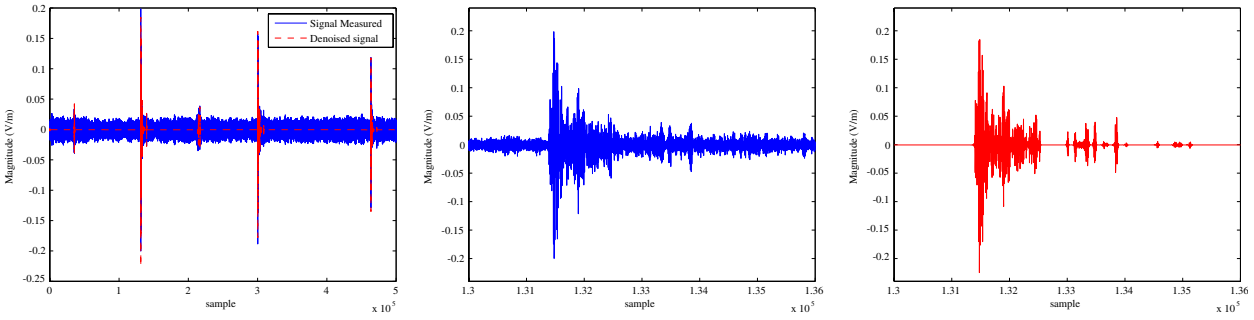

Figure 5: Pulse shape of PD pulse (location point 2). (a) PD pulses waveform. (b) Zoom into a PD pulse. (c) Zoom into a denoised PD pulse.

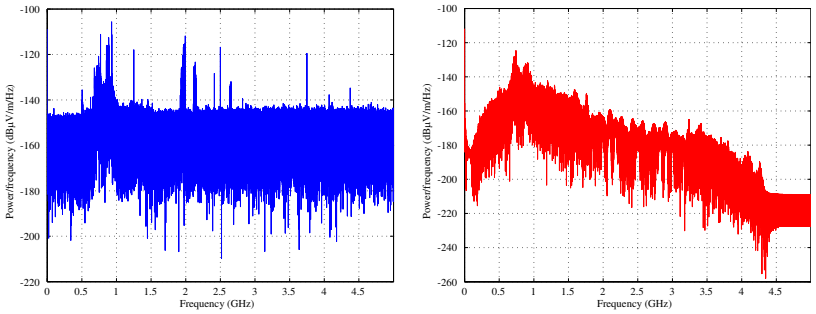

Figure 6: Power spectrum density of PD pulses (location point 2). (a) PSD of PD pulses. (b) Estimate PSD of PD pulses.

where I_0 is pulse magnitude, α is the damped effect parameter, and ω_c is the resonant frequency. A and B are constants. In the substation environment, the pulse shape can be spread and distorted due to multi-path effect.

4.2. Statistical Results of PD Events

Statistical results from measurements are presented and discussed. PRPD on Figure 7 shows the power density distribution with a fixed interval time $\Delta t = 50\,\mu$s. In both results, the reference voltage in which scope is synchronized is plotted. Results show PD pulses in substation are time dependent to the AC voltage. Two clusters of PD can be seen due to periodic variation of substation voltage at 60 Hz. This observation shows that it exists regions where the applied field is sufficiently high to lead discharge event. The random character of PD pulses are interpreted as ionization process that lead discharge conditions are a random process dependent to the 60 Hz of the substation. We also observed that PD pulses behaviour have a phase offset.

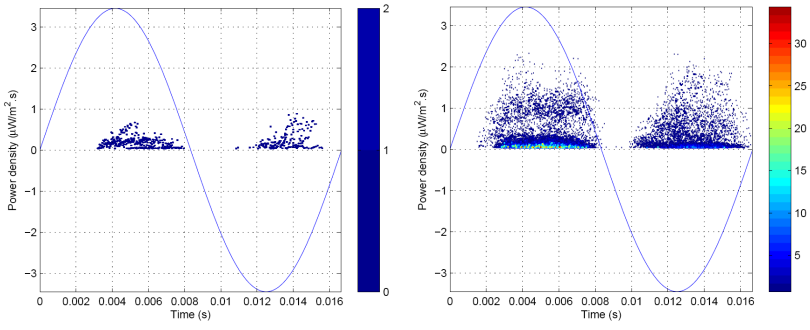

Figure 7: Phase resolved partial discharge of measurements. (a) Location point 1. (b) Location point 2.

PDF and CDF of energy, PD occurrence and the inter-arrival time from the measurement campaign are presented on Figures 8 and 9. In location point 1, discharges have mean power density value, $E_{s_{\tau,1}} \simeq 0.19\,\mu\text{W/m}^2\cdot$ s and $E_{s_{\tau,2}} \simeq 0.28\,\mu\text{W/m}^2\cdot$ s, and low occurrence compared to

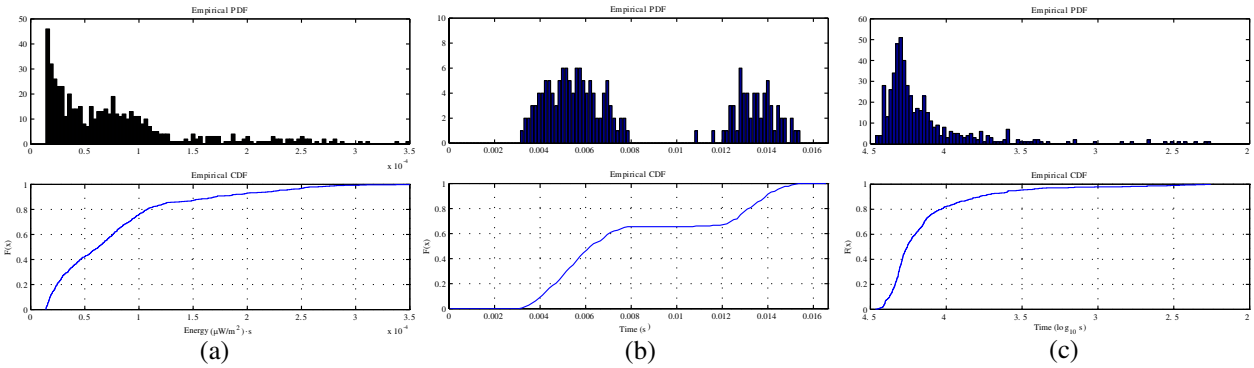

Figure 8: Statistical results of PD pulses in location point 1. (a) Power density distribution $E_{s\tau}$. (b) PD occurrence distribution φ. (c) Inter-arrival time distribution $\Delta\varphi$.

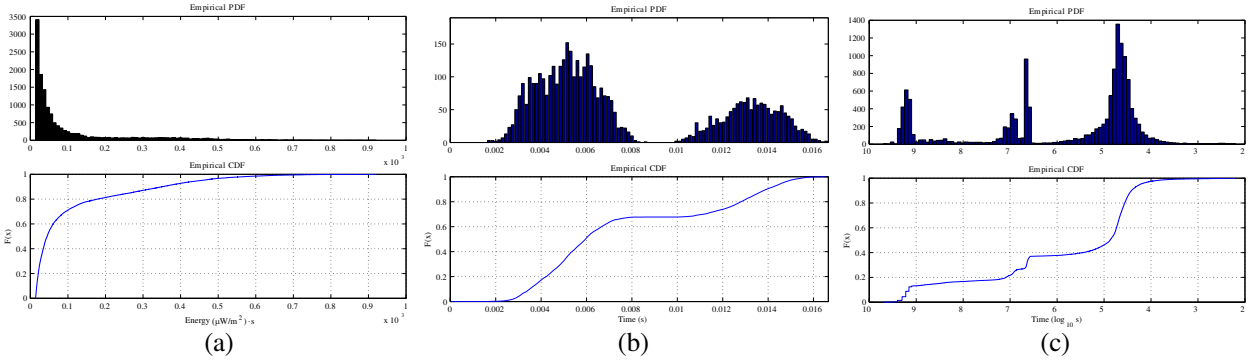

Figure 9: Statistical results of PD pulses in location point 2. (a) Power density distribution $E_{s\tau}$. (b) PD occurrence distribution φ. (c) Inter-arrival time distribution $\Delta\varphi$.

results of location point 2. The inter-arrival time are longer than the latter, mean value are 71.9 µs and 1.38 µs respectively. Figures 8(a) and 9(a) show that power density of PD distributions can be seen as exponential random variable, we can observe that the probability that pulse have higher power density value decreases exponentially.

For PD occurrence on Figures 8(b) and 9(b), we introduce $_+$ and $_-$ notation that denotes the first cluster of discharge when the reference voltage is positive and the negative respectively. Results show that a PD pulse has high probability occurrence at $\varphi_+ \simeq 5$ ms and $\varphi_- \simeq 13.5$ ms. Occurrences are higher in positive region than the negative. These random variables can be seen as two Gaussian distributions where means are μ_+ and μ_- and their variances are $\sigma_+^2 < \sigma_-^2$.

On Figures 8(c) and 9(c) inter-arrival time distributions are plotted in logarithmic scale due to large value but low occurrence (time inter-cluster) and small value but high occurrence (time inter-pulse). We see the difference between location point 1 and 2. For the first one, $\Delta\varphi$ seems to be a Poisson random variable. The last one, $\Delta\varphi$ seems to be a mixture of random variables. This observation can be interpreted by many PD sources are captured in this location point.

5. CONCLUSION

Impulsive noise in substation are related to electrical breakdown. When HV equipments contain imperfections, a high electric field can lead to discharge by ionization process. These conditions are not a sufficient to lead discharge phenomena. Other factors can affect discharge apparition such as atmospheric conditions, geometry of defects and surface condition on insulations. Thus, it gives stochastic behaviour of pulse events. In a 735 kV substation, we characterize these fast transient phenomena in terms of power density, time occurrence and inter-arrival time distributions in RF range. Results show that PD are highly impulsive noise with very wide band frequency. High values of power density of PD pulses show that they can interfere with RF communications system. Statistical results of our measurements show that PD are a random process dependent of the AC voltage in terms of pulse magnitude, inter-arrival time occurrence and its time occurrence. Impulsive noise in the substation can be seen as shot noise with wideband frequency at 0.8 to 5 GHz. It can be modelled for RF channel as the succession of impulsions where magnitudes and

the inter-arrival time are mixture of random variables according to statistical results. Discharge events occur periodically at 60 Hz with two clusters of discharges where distributions of these events can be Gaussian random variable. The ongoing work is to discuss the impact of atmospheric conditions on these results.

ACKNOWLEDGMENT

Authors would like to thanks Jean Béland, Marthe Kassouf and Sylvain Morin from IREQ for their support.

REFERENCES

1. Madi, G., F. Sacuto, B. Vrigneau, B. L. Agba, Y. Pousset, R. Vauzelle, and F. Gagnon, "Impacts of impulsive noise from partial discharges on wireless systems performance: Application to mimo precoders," *EURASIP Journal on Wireless Communications and Networking*, Vol. 186, 1–12, 2011.
2. Bhatti, S. A., Q. Shan, I. A. Glover, R. Atkinson, I. E. Portugues, P. J. Moore, and R. Rutherford, "Impulsive noise modelling and prediction of its impact on the performance of wlan receiver," *17th European Signal Processing Conference*, 1680–1684, 2009.
3. Bartnikas, R., "Some observations on the character of corona discharges in short gaps," *IEEE Transactions on Electrical Insulation*, Vol. 6, 63–75, 1971.
4. Bartnikas, R. and E. J. McMahon, "Engineering dielectrics volume 1 corona measurement and interpretation," American Society for Testing and Meterials, 1979.
5. Brunt, R. J. V. and S. V. Kulkarni, "Stochastic properties of trichel-pulse corona: A non-markovian random point process," *Physical Review A, General Physics*, Vol. 42, No 8, 4908–4932, 1990.
6. Brunt, R. J. V., "Stochastic properties of partial-discharge phenomena," *IEEE Transactions on Electrical Insulation*, Vol. 26, No. 5, 902–947, 1991.
7. Portugués, I., P. I. Moore, and I. A. Glover, "Characterisation of radio frequency interference from high voltage electricity supply equipment," *ICAP. Twelfth International Conference on Antennas and Propagation (Conf. Publ. No. 491)*, Vol. 2, 820–823, 2003.
8. Fruth, B. and L. Niemeyer, "The importance of statistical characteristics of partial discharge data," *IEEE Transactions on Electrical Insulation*, Vol. 27 No. 1, 60–69, 1992.
9. Hudon, C. and M. B'elec, "Partial discharge signal interpretation for generator diagnostics," *IEEE Transactions on Dielectrics and Electrical Insulation*, Vol. 12, No. 2, 297–319, 2005.
10. Mallat, S., *A Wavelet Tour of Signal Processing*, Academic Press, 1998.
11. Krim, H., D. Tucker, S. Mallat, and D. Donoho, "On denoising and the best signal representation," *IEEE Transactions on Information Theory*, Vol. 45, No. 7, 2225–2238, 1999.
12. Donoho, D., "De-noising by soft thresholding," *IEEE Transactions on Information Theory,* Vol. 41 No. 3, 613–627, 1995.

Wavelet Analysis of the First Pulse of Initial Breakdown Process in Lightning Discharges

Mona Riza Mohd Esa[1, 3], **Mohd Riduan Ahmad**[2, 3], **and Vernon Cooray**[3]

[1]Universiti Teknologi Malaysia, UTM Skudai, Johor, Malaysia
[2]Universiti Teknikal Malaysia Melaka, Malaysia
[3]Division of Electricity, Department of Engineering Sciences
Uppsala University, Uppsala, Sweden

Abstract— Wavelet transformation is used in order to seek for differences in the initial breakdown process between negative cloud-to-ground flash (CG−), positive CG (CG+), cloud flash (IC), and isolated breakdown (IB) processes. 72 waveforms were selected from 885 waveforms recorded between May and August 2010 at the premise of Uppsala University, Uppsala, Sweden. The analysis was conducted only on the first electric field pulse for each lightning process and the output from the wavelet transformation is plotted as normalized power spectrum. The first pulses in CG− are found to radiate intensely in average frequency between 186 and 1637 kHz. The energy radiated by the first pulses of CG+ mainly concentrated in the average frequency between 57 and 599 kHz. As for the IC, the first pulses found to be spread out in the average frequency between 461 and 3570 kHz and for IB, the energy spread out between 44 and 279 kHz. The CG+ and IB flashes tend to radiate at lower frequency region within smaller range compared to CG− and IC. IB has the smallest frequency range around 235 kHz while the frequency range of IC and CG− are more than 10 times and 6 times larger than IB, respectively. Furthermore, IC and CG− have comparable initial-to-overshoot peak ratio with 1.7 and 1.6, respectively, which higher than CG+ and IB at least with a factor of 1.4. It can be speculated that the initial breakdown processes of IC and CG− flashes are most likely initiated from the same discharge process in the thundercloud and differ from the discharge process of CG+ and IB.

1. INTRODUCTION

The most well known breakdown studied in lightning research is known as cloud-to-ground (CG) flashes where such breakdown process is usually started with initial or preliminary breakdown process (PBP) and normally followed by stepped leaders and return strokes. Another breakdown process which is not resulting to return stroke are breakdown process associated with cloud flash (IC) and isolated breakdown (IB). Previously, Ahmad et al. [4] have studied the temporal characteristics of the first electric field pulse for IC and CG− in time domain. In this paper, we are motivated to extend the study by analyzing the first pulse through the wavelet perspective or in the time-frequency domain. Also we extend the analysis further to include CG+ and IB flashes.

2. MEASUREMENT SETUP

The measurements were done in the premise of Ångström Laboratory, Uppsala University, Sweden (59.8°N and 17.6°E) during summer thunderstorm between May and August 2010. The measuring system consists three main parts as shown in Figure 1 namely the parallel plate flat antenna unit, the buffer circuit unit and the recording unit (digital transient recorder) which was the same setup used by Mohd. Esa et al. [3] in their works and explained by Cooray [1]. A broadband antenna system equipped with parallel flat-plate was used to capture fast vertical electric field changes and the decay time constant was fixed at 15 ms that been determined by the impedance values in the buffer circuit unit. The output of the buffer was driven to a 4-channel 12-bit Yokogawa SL1000 Digital Storage Oscilloscope capturing unit. A coaxial cable was used to connect the antenna and buffer circuit and 50 Ω-terminated coaxial cable was used to connect the buffer circuit and the recording unit. The data presented in this paper were recorded at 20 MS/s (50 ns time resolution) with 30 ms delay.

3. RESULTS, ANALYSIS AND DISCUSSIONS

From the total of 885 waveforms, 72 waveforms have been selected to be analyzed and such waveforms are divided into different type of lightning event namely negative ground flash (CG−), positive ground flash (CG+), cloud discharge (IC) and isolated breakdown discharge (IB). The first pulse of each lightning event is then analyzed using wavelet transformation and then plotted in time and

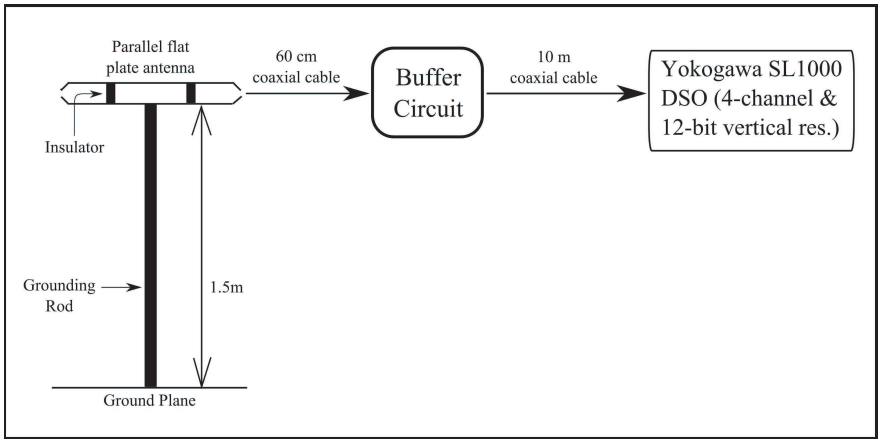

Figure 1: Parallel flat antenna used in the measurements. (Partially adapted from Cooray [1]).

frequency domain as illustrated in Figure 2 below. As have been described by Miranda [2] and Sharma et al. [5], each pulse will have 2 parts or stages; initial and overshoot. To understand the colour distribution in wavelet power spectrum energy radiation, two main regions are utilized in this work; spectral region and spread region. Since power spectrum magnitude has been normalized, spectral region is defined as the energy of power spectrum that radiate above 30% or 0.3 of the maximum magnitude. For the spread region, the power spectrum that radiate more than 90% (or 0.9) of maximum magnitude will be selected. The value which is less than 0.3 will be noted as noise.

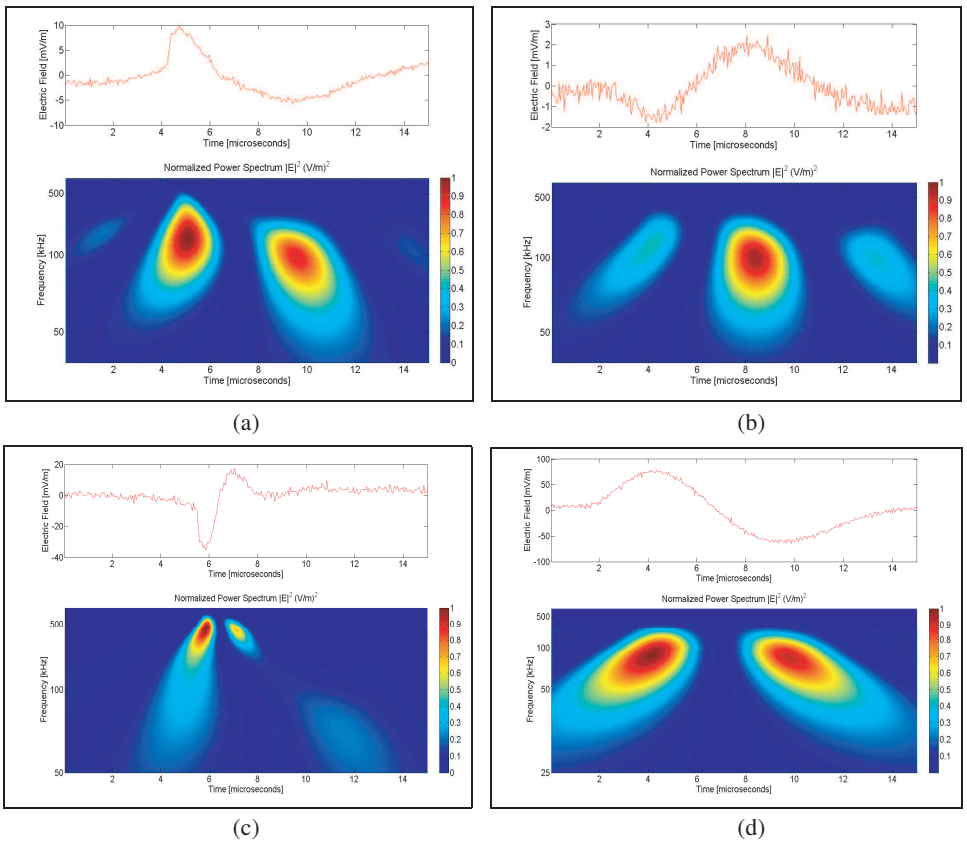

Figure 2: Wavelet power spectrum of the first pulse with single peak pulse and single spread wavelet transformation pertinent to (a) negative CG (CG−), (b) positive CG (CG+), (c) cloud Flash (IC) and (d) isolated Breakdown discharge (IB).

It is discovered that about 23 are from CG−, 12 are contributed by CG+, 28 IC and 11 IB. For

example, Figure 1(a) shows that the spectral region for both initial and overshoot stages are lying from 50 to 500 kHz. Whereas, the spread region are approximately between 100 kHz to 200 kHz and 80 kHz to 120 kHz for initial and overshoot stages, respectively. The example for CG+, IC and IB single peak pulse and single spread power spectrum can be seen in Figures 1(b), 1(c) and 1(d), respectively.

In Table 1, it can be observed that the order from the highest to the lowest average values (both maximum and minimum) starts with IC followed by CG−, CG+ and IB in both spectral and spread regions which is also covers during both initial and overshoot stages. It seems that, both the average maximum and minimum frequencies for IC are at least double than CG− average values and about 10 and 6 times higher than IB and CG+, respectively. It shows that IC seems to start the process of initiation at higher frequency which in average it starts to radiate intensely at more than 450 kHz and possible to radiate up to higher microwave region. On the other hand, IB's first pulse shows that it only requires in average about 40 kHz in order to start the initiation process.

Table 1: Statistic for first pulse of different type of lightning events.

Statistics		Initial Stage		Overshoot Stage		Ratio of power peak of initial stage and overshoot stage
		Spectral range (kHz)	Spread region (kHz)	Spectral range (kHz)	Spread region (kHz)	
CG−	Minimum	23	42	22	35	0.67
	Maximum	7645	3987	5714	4198	3.12
	Average	186–1637	475–821	391–1020	572–730	1.6
CG+	Minimum	26	51	23	37	0.44
	Maximum	2174	758	893	649	1.84
	Average	62–599	148–243	57–278	107–166	1.06
IC	Minimum	20	41	21	42	0.6
	Maximum	12195	7418	9141	6329	2.93
	Average	461–3570	1007–1744	663–2067	919–1439	1.7
IB	Minimum	22	46	13	30	0.73
	Maximum	1064	595	926	495	2.29
	Average	45–279	97–146	44–218	92–122	1.17

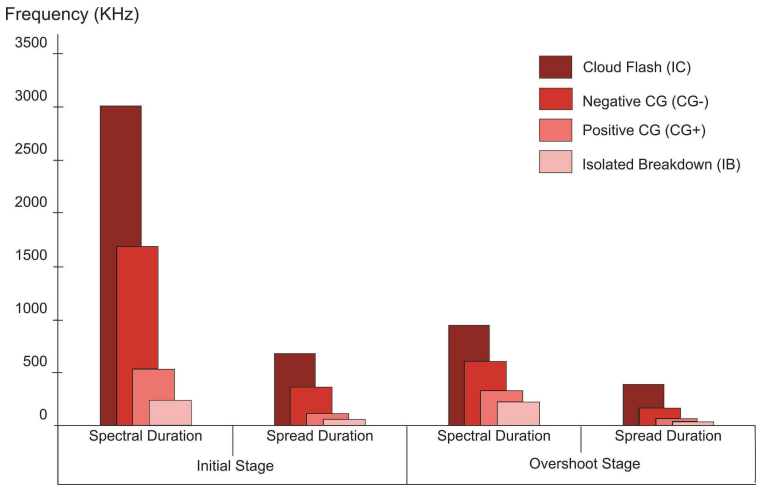

Figure 3: Frequency differences pertinent to lightning events.

Figure 3 illustrates the frequency differences or bandwidth, where frequency difference implies the difference between mean maximum frequency and mean minimum frequency. It is discovered that the highest bandwidth to the lowest bandwidth are following the same trend as observed in previous parameters. In comparison, the frequency difference of IC is found to be more than twice

compared to CG− and more than CG+ at least with the factor of 6. It is speculated that the energy radiated by the first pulse of IC is overwhelmingly high.

The highest mean ratio of initial peak to overshoot peak is gained by IC which is a slightly higher than CG− with 1.7 and 1.6, respectively. The average ratio gained by first CG− pulse in this paper is found to be slightly lower than the average ratio reported by Sharma et al. [5] where the average ratio of initial to overshoot power peak for the first 200 µs of preliminary breakdown pulses was 1.8. As for IB, it is found to be lower than the first two lightning events' mean ratio but almost comparable with CG+; 1.17 and 1.06, respectively. It shows that in all type of lightning events the energy radiated by initial is stronger than overshoot energy. This is maybe due to the effect of propagation which is prone to overshoot stage as speculated by Miranda [2]. However, due to the ratio gained by IC and CG− is at least 1.4 higher than CG+ and IB, it can be speculated that the intensity of energy radiated from IC is similar to CG− but differ from CG+ and IB.

4. CONCLUSION

Wavelet transformation has been done to 72 first pulses' concerning to CG−, CG+, IC and IB in order to understand and identify any distinctive features between these lightning events. It is found that IC dominates in all four selected parameters such as mean maximum and minimum frequencies, frequency difference and initial-to-overshoot ratio with at least twice higher than CG− and higher than CG+ with the factor of 6. It is also observed that IB gained the lowest in all parameters except in the initial-to-overshoot peak ratio. It is found that in average the energy radiated during initial stage is always higher than during the overshoot stage with at least the factor of 1.06 which is gained by CG+.

ACKNOWLEDGMENT

We would like to express our appreciation to Mr. Zikri Abadi Baharudin and Mr. Pasan Hettiarachchi for providing the data from their measurement to be used in this paper.

REFERENCES

1. Cooray, V., "The mechanism of lightning flash," *The Lightning Flash*, V. Cooray, ed., 214–215, The Institutions of Electrical Engineers (IEE), London, 2003.
2. Miranda, F. J., "Wavelet analysis of lightning return stroke," *Journal of Atmospheric and Solar-Terrestrial Physics*, Vol. 70, 1401–1407, 2008.
3. Mohd. Esa, M. R., M. R. Ahmad, V. Cooray, and M. Rahman, "Distinctive features of initial breakdown process between ground and cloud discharges," *16th Asean Conference on Electrical Discharges (ACED)*, Johor Bahru, Malaysia, December 10–12, 2012.
4. Ahmad, N. A., M. Fernando, Z. A. Baharudin, M. Rahman, V. Cooray, Z. Saleh, J. R. Dwyer, and H. K. Rassoul, "The first electric field pulse of cloud and cloud-to-ground lightning discharges," *Journal of Atmospheric and Solar-Terrestrial Physics*, Vol. 72, 143–150, 2010.
5. Sharma, S. R., V. Cooray, M. Fernando, and F. J. Miranda, "Temporal features of different lightning events revealed from wavelet transform," *Journal of Atmospheric and Solar-Terrestrial Physics*, Vol. 73, 507–515, 2011.

Amorphous/Silicone Composites and Their Applications in Microwave Attenuation

Z. W. Li, Z. H. Yang, and M. J. Chua
Temasek Laboratories, National University of Singapore
5A, Engineering Drive 1, Singapore 117411, Singapore

Abstract— Amorphous membrane, consisting of amorphous flakes and ferrite nanoparticles, has been prepared using the infiltration method. The composites with the membrane fillers show greatly increased complex permeability due to the in-plane arrangement of fillers and relatively small complex permittivity, as compared to general amorphous-filler composites. Therefore, the impedance matching between the composites and free space is improved and the attenuation effect is enhanced. The composites has better attenuation properties with low reflectivity and broad bandwidth, as compared to other amorphous composites.

1. INTRODUCTION

Electromagnetic (EM) composites can strongly attenuate EM energy that propagates into the materials, thus achieving reflection reduction at the boundary between the materials and free space. In recent years, EM composites have attracted much attention, due to their extensive applications in industry, commerce and defence. EM composite is a mixture of magnetic fillers and polymer. Usually used magnetic fillers are spinel and barium ferrites [1–3] and metallic including amorphous [4–6] materials.

In this work, to decrease the large permittivity, amorphous flakes covered by ferrite nanoparticles with a core-shell-like structure is prepared by mechanical ball-milling. Then, to increase permeability, the membranes with an in-plane arrangement of the amorphous flakes are fabricated using an infiltration method. The results show that the amorphous-membrane-filler composites can significantly enhance permeability and improve attenuation properties, as compared to general amorphous-filler composites.

2. EXPERIMENT

Co-based amorphous ribbon with thickness of 25 μm was purchased from MetGlas Company, Model number 2714A. Three fillers for composites were prepared. (1) The ribbon was cut into small pieces with dimension of about 5 mm and followed by ball-milling for 270 min to form flakes, whose size is about 75 μm (sample #1). (2) The amorphous flakes were mixed with spinel ferrite $Ni_{0.23}Cu_{0.1}Zn_{0.67}Fe_2O_4$ (NiZnCu) nanoparticles and followed by ball-milling for another 60 min. The weight ratio of the amorphous and ferrite is 80 : 20, which is known as samples #2. (3) Sample #2 was fabricated into membranes using an improved infiltration method [7].

The three amorphous fillers were mixed, respectively, with silicone to be prepared into composites #1–#3. The composites were annular disks in shape with an outer diameter of 6.9 mm, inner diameter of 3 mm and thickness of about 2 mm for microwave measurement. Volume concentration p is 21, 36 and 40%, respectively, for the three composites, #1, #2 and #3. The complex permittivity and permeability were measured over 0.1 to 10 GHz using an HP5230A Vector Network Analyzer with Transmission-Reflection-Line calibration. The measurement fixture is a segment of 7 mm coaxial air-line with length of 49.96 mm. Also, complex permeability was measured from 0.005 to 1 GHz using Agilent E4991A RF impedance/materials analyzer with open-short-load calibration. The measured fixture is 16454A.

3. RESULTS AND DISCUSSION

3.1. High-frequency Permeability and Permittivity

Figure 1 shows the complex permeability and permittivity for composites with three types of amorphous fillers, namely the amorphous-flake-filler (#1), mixing-fillers of amorphous flakes and ferrite nanoparticles (#2) and membrane-fillers with in-plane arrangement (#3).

Composite #1 has complex permeability with $\mu'_0 = 13$ and $\mu''_{\max} = 3.8$. However, the giant permittivity is observed for the amorphous composite due to conductive material. ϵ' is 180 at 0.1 GHz and ϵ'' is 82. Further, both ϵ' and ϵ'' are strongly dependent on frequency.

For composite #2, the conductive amorphous flakes are separated by the insulating ferrite nanoparticles, and thus increasing the electric resistivity ρ. The measured ρ is 100 Ω-cm for #1 and increases to 236 Ω-cm for #2. Based on the Maxwell-Wagner-Sillars interfacial polarization theory [8], the larger resistivity leads to smaller permittivity and weakened frequency dependence of permittivity. From Fig. 1, both ϵ' and ϵ'' of composite #2 is greatly decreased, as compared to composite #1; ϵ' decreases from 180 and 40 at 0.1 GHz and ϵ'' from 82 and 2. On the other hand, the permeability is also reduced. μ_0' and $\mu''_{\max}$ reduces from 13 to 7 and from 3.8 to 2.3, respectively. The decrease in permeability may be attributed to two factors. First, the permeability of $Ni_{0.23}Cu_{0.1}Zn_{0.67}Fe_2O_4$ nanoparticles with $p = 50\%$ was measured. μ_0' and $\mu''_{\max}$ are only 6 and 1.8, respectively, which are much smaller than the values of amorphous-flake-filler composites. Second, when the domain wall is dominant, a weakened permeability from reversible wall movement is obtained from increased coercivity H_c by $(\mu_0' - 1) \propto M_s/H_c$ [9]. As compared to sample #1, M_s of sample #2 does not appreciably change, while H_c significantly increases from 1.4 to 10.7 Oe. Consequently, μ_0' is much smaller for composite #2 than for #1. However, the resonance is shifted to higher frequency, from 0.4 to 1.2 GHz.

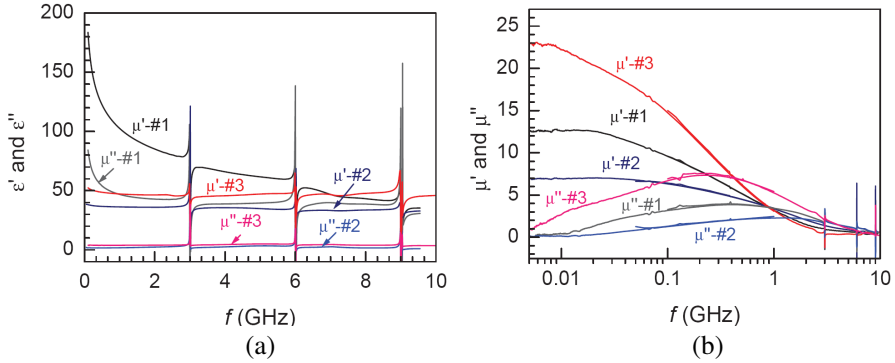

Figure 1: Complex (a) permittivity and (b) permeability for amorphous-flake-filler (#1), mixing-filler with amorphous flakes and ferrite nanoparticles (#2) and membrane-filler with in-plane arrangement (#3) composites.

To overcome the drawback of low μ_0' and $\mu''_{\max}$, the membrane-filler composite #3 were fabricated using infiltration method. Fig. 1(b) shows that μ_0' and $\mu''_{\max}$ significantly increases by more than threefold for the membrane-filler composite #3, as compared to #2; μ_0' increases from 7 to 22 and $\mu''_{\max}$ from 2.3 to 7.5. According to Maxwell-Garnett mixing law,

$$\mu_0' = \frac{p\left(\mu_{b0}' - 1\right)}{(1-p)\left(\mu_{b0}' - 1\right) N_d + 1} + 1 \tag{1}$$

where μ_0' and μ_{b0}' is the static permeability of composites and the corresponding bulk materials, respectively, and N_d is the effective demagnetizing factor of fillers, which is related to the shape and direction of fillers along ac magnetic field. Therefore, the permeability of composites is closely associated to effective N_d. In general, the fillers are randomly distributed in composites. However, in the amorphous membranes, the fillers are in-plane arrangement and effective N_d is much smaller than that in general amorphous composites (#1 and #2), and thus significantly enhancing the permeability μ_0'.

On the other hand, it is observed that the values of ϵ' and ϵ'' are about 40 and 2, respectively, for the composite #2 with random arrangement fillers, while ϵ' and ϵ'' increase to 52 and 4 for the composite #3 with in-plane arrangement fillers. The increase is attributed to the relatively smaller demagnetization factors perpendicular to the electric field direction for in-plane arrangement fillers than for random arrangement fillers [7]. Nevertheless, these values are still far below 180 and 82 for composite #3 with pure amorphous flake fillers.

3.2. Attenuation Characteristics

The EM reflection property of material is typically characterized in terms of the power reflection of a plane wave reflected from an infinite slab of the material that is backed by a metallic surface. The reflectivity or reflection loss of composites, generally produced for normal incidence, is expressed

in decibels RL (dB) [10]

$$RL\ (\text{dB}) = 20\log_{10}\left|\frac{Z_{in}-Z_0}{Z_{in}+Z_0}\right| \tag{2}$$

and

$$Z_{in}/Z_0 = \sqrt{\frac{\mu}{\epsilon}}\tanh\left[j\frac{2\pi ft}{c}\sqrt{\mu\epsilon}\right] \tag{3}$$

where Z_{in} is the impedance of the composites backed by the ground plane, Z_0 is the intrinsic impedance of free space, c is the velocity of light in free space, t is the thickness of composites, f is the frequency of the incident EM wave, $\mu = \mu' - j\mu''$ is the complex permeability and $\epsilon = \epsilon' - j\epsilon''$ is the complex permittivity. The reflectivity R, as a function of frequency f, is calculated at different thickness (t = 0.25–0.8 cm) of composites, based on Eqs. (2) and (3). The results are shown in Figs. 2(a), (b) and (c) for composites #1, #2 and #3, respectively, which are composites with the pure amorphous flake fillers, mixing fillers of amorphous flakes and ferrite nanoparticles, and in-plane arrangement membrane fillers. From Fig. 2, two of important properties, the reflectively RL and the percentage bandwidth W_P for $RL \leq -10$ dB, are be obtained.

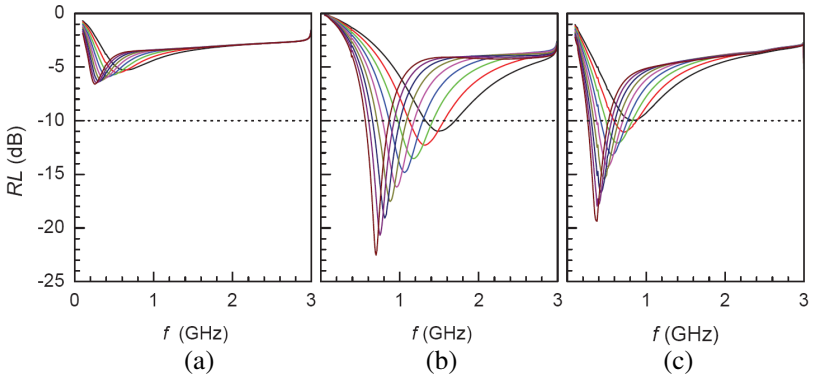

Figure 2: The dependence of reflectivity RL on frequency f with various thickness t = 0.4 to 0.8 cm (each step interval of 0.05 cm from right to left) for composites, (a) #1, (b) #2 and (c) #3.

From the viewpoint magnitude of reflectivity, the maximum $|RL|$ cannot reach 10 dB at thickness t = 0.25–0.8 cm for composite #1, while $|RL| \geq 10$ dB can be achieved for composites #2 and #3. Therefore, the two composites have superior attenuation properties, as compared to composite #1. From the viewpoint of bandwidth, the frequency bands cover over 0.65–1.0 GHz and achievable maximum percentage bandwidth $W_{P,\max}$ with $RL \leq -10$ dB is 43% at t = 0.70 cm for composite #2, while the frequency bands cover over 0.37–0.57 GHz and $W_{P,\max}$ is 71% at t = 0.75 cm for composite #3, as shown in Fig. 3(a). $W_{P,\max}$ increases by 65 % for composite #3, as compared to #2. At t = 0.5 cm, the frequency bands covers from 0.97 to 1.42 GHz and the percentage bandwidth W_P is 37 % for composite #2, while bandwidth covers from 0.48 to 0.83 GHz and W_P is 53 % for composite #3, as shown in Fig. 3(b). W_P at t = 0.5 cm increases by 54%, as compared to #2. It concludes that the attenuation performance is better for composite #3 than for #2.

To achieve broad bandwidth with low reflectivity, $\sqrt{\mu/\epsilon}$ should be close to unity for the impedance matching between materials and free space, and $\mu''_{\max}$ should be large enough to attenuate the incident EM wave inside the materials. Although μ'_0 and $\mu''_{\max}$ are larger for the pure amorphous-flake-filler composite #1 than for the mixing-filler composites (#2), ϵ' and ϵ'' is much larger for the former than for the latter. Consequently, the impedance matching between materials and free space is worsened for composite #1, as compared to #2. Fig. 4(a) shows the calculated values of $\text{Re}\sqrt{\mu/\epsilon}$ for the three composites. It is obvious that the matching values of composites #2 and #3 are close and are considerably larger than 0.2 of composite #1. It is the mismatching that incident EM waves are difficultly coupled to the composites and a large amount of the waves is reflected to free space for composite #1. Therefore, $RL \leq -10$ dB cannot be obtained at all in the whole frequency range. On the other hand, Fig. 4(b) shows that, as compared to #2, μ'' of composite #3 is significantly enhanced at a frequency range of 0–2 GHz, especially at $f < 1$ GHz. The incident EM energy in composites is more attenuated for #3 than for #2. As a result, the attenuation properties of #3, such as W_P are improved, as compared to #2.

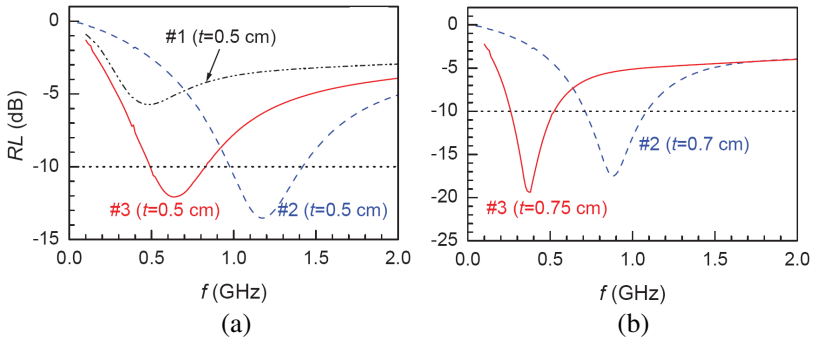

Figure 3: The comparison of reflective properties for #3, #2 and #1, (a) maximum percentage bandwidth $W_{P,\max}$ and (b) bandwidth W_P at the thickness of 0.5 cm.

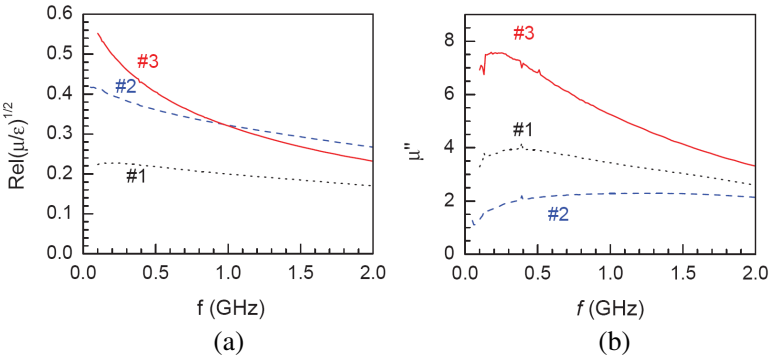

Figure 4: The comparison of (a) matching values $\mathrm{Re}\sqrt{\mu/\epsilon}$ and (b) μ'' for composites #3, #2 and #1.

4. CONCLUSION

(1) Composites with the three amorphous fillers are prepared, which are pure amorphous flake fillers, the mixture fillers of amorphous flakes and ferrite nanoparticles with core-shell-like structure using mechanical ball-milling, and membrane fillers based on the mixture using an improved infiltration method.

(2) Their high-frequency magnetic and dielectric properties are studied. The mixing-filler composites (amorphous flakes and ferrite nanoparticles) can greatly decrease both ϵ' and ϵ''. Due to an in-plane arrangements, the amorphous-membrane-filler composite is able to significantly enhance μ_0' and $\mu''_{\max}$.

(3) For the membrane-filler composite, the impedance matching between the composite and free space is significantly improved due to enhanced μ and decreased ϵ, and the attenuation effect is increased due to larger $\mu''_{\max}$. As a result, the amorphous composites with membrane fillers has better attenuation properties with low reflectivity and broad bandwidth at low microwave band of 0.5–1 GHz, as compared to other two amorphous-filler composites.

ACKNOWLEDGMENT

The authors would like to acknowledge the Defence Research and Technology Office (DRTech), Singapore for its financial support to this work.

REFERENCES

1. Kim, S.-S., D.-H. Han, and S.-B. Cho, "Microwave absorbing properties of sintered Ni-Zn ferrite," *IEEE Trans. Magn.*, Vol. 30, No. 6, 4554–4556, 1994.
2. Cho, H. S. and S. S. Kim, "M-hexaferrites with plannar magnetic anisotropy and their application to high-frequency microwave absorbers," *IEEE Trans. Magn.*, Vol. 35, No. 5, 3151–3153, 1999.
3. Li, Z. W., L. F. Chen, Y. P. Wu, and C. K. Ong, "Microwave attenuation properties magnetic properties of W-type barium ferrite composites," *J. Appl. Phys.*, Vol. 96, 534–539, 2004.

4. Deng, L. W., J. J. Jiang, S. C. Fan, Z. K. Feng, W. Y. Xie, X. C. Zhang, and H. H. He, "GHz microwave permeability of FeCoZr amorphous materials synthesized by two-step mechanical alloying," *J. Magn. Magn. Mater.*, Vol. 264, 50–54, 2003.
5. Wu, L. Z., J. Ding, H. B. Jiang, C. P. Neo, L. F. Chen, and C. K. Ong, "High frequency complex permeability of iron particles in a nonmagnetic matrix," *J. Appl. Phys.*, Vol. 99, 083905, 2006.
6. Zhou, P. H., J. L. Xie, Y. Q. Liu, and L. J. Deng, "Composition dependence of microstructure, magnetic and microwave properties in ball-milled FeSiB nanocrystalline flakes," *J. Magn. Magn. Mater.*, Vol. 320, 3390–3393, 2008.
7. Liu, L., Z. H. Yang, C. R. Deng, Z. W. Li, M. A. Abshinova, and L. B. Kong, "High frequency properties of composite membrane with in-plane aligned Sendust flake prepared by infiltration method," *J. Magn. Magn. Mater.*, Vol. 324, 1786–1790, 2012.
8. Hanai, T. and K. Sekine, "Theory of dielectric relaxations due to the interfacial polarization for two-component suspensions of spheres," *Colloid & Polymer Sci.*, Vol. 264, 888–895, 1996.
9. Dionne, G. F., "Magnetic relaxation and anisotropy effects on high-frequency permeability," *IEEE Trans. Magn.*, Vol. 39, No. 5, 3121–3126, 2003.
10. Knott, E. F., J. F. Shaeffer, and M. T. Tuley, *Radar Cross Section*, 2nd Edition, Artech House, Boston, 1993.

Impact of Technology on the Shielding Effectiveness of Barrier Materials Damping Frequency Selected Electromagnetic Fields

Jan Ziaja, **Grzegorz Szafran**, **and Maciej Jaroszewski**
Faculty of Electrical Engineering, Wrocław University of Technology, Poland

Abstract— In the present study compared the effects of methods of preparation and the type of material used for shielding effectiveness (SE) selectively chosen frequency electromagnetic field (EMF). Composite materials were obtained by metallization surface of non-woven and polypropylene film. Metallization process was performed by magnetron sputtering and vacuum evaporation (vaccum deposition). Deposited materials are copper (Cu), silver (Ag) and Zn - In a composition by weight of 80/20. The results of this study indicate that this type of shielding composite materials can be a significant competitive with currently used conventional materials.

1. INTRODUCTION

The subject matter of electromagnetic field shielding is of current interest for various reasons, the most important of which are:

- environmental protection (the impact on the environment of constantly emerging new devices that emit electromagnetic field — especially those that emit gigahertz-range frequencies),
- protection of human health. It is worth noting that a number of regulations on protection of human health and environment against electromagnetic fields were created and continue to be created today.

The harmful effects of electromagnetic fields (EMF) occur during the use of sources of electromagnetic radiation, which are:

- radio and television broadcast antennas,
- radio-location and navigation devices,
- mobile telephony,
- heating devices,
- medical diagnostic and physiotherapy equipment.

Therefore, new EMF shielding materials and composites, as well as methods for their manufacture, are sought.

These new materials, used in the electromagnetic shielding technologyusually must be characterized by both flexibility and selectivity shielding electromagnetic field. These properties result from the use of a suitable material on the substrate and the application of on its surface, the conductive coating [1–4], usually with the specified geometry [5–7].

The application of conductive layers is achieved by screen printing, vacuum evaporation or magnetron sputtering. The use of screen printing method to produce EMI (Electromagnetic Interference) shielding materials is a profitable and cost-effective solution. Magnetron sputtering method, on the other hand, provides thorough cleaning and activation of the surface. As a result, deposited metallic layers exhibit very high adhesion strength.

The present study compares the shielding effectiveness (SE) ratio of shielding materials prepared by vacuum evaporation and magnetron sputtering with the materials produced with screen printing

2. PRODUCTION TECHNOLOGY OF SHIELDING MATERIALS

The shielding materials were made in the form of metallized polyethylene terephthalate (PET) film of a thickness of 0.1 mm and polypropylene based non-woven fabrics of a basis weight of $150\,\mathrm{g/cm^2}$. The metallization process of non-woven PP fabrics was performed by sputtering metallic targets with the following composition by weight: 80% Zn — 20% In and 99.99% Zn or 99.99% Cu. A WMK-100 type magnetron gun was used for the research, powered with the DPS (Dora Power System) pulsed power supply unit of the following operating parameters: max power — 12 kW, group frequency — $f_g = 100\,\mathrm{Hz}$–$5\,\mathrm{kHz}$, frequency of magnetron gun unipolar DC-M power supply — $f = 80\,\mathrm{kHz}$. Samples were prepared utilizing magnetron sputtering method on non-woven PP fabric and PET film with the following parameters:

- power (P) supplied to the WMK-100-type magnetron: 300 W [Watt],
- apparent power (Pc): 10 W,
- pressure (p) in a vacuum chamber: 0.5×10^{-3}–2.5×10^{-3} Torr,
- target supply current (I): 0.5–2.75 A,
- reactive gas (neutral gas): argon [Ar],
- distance between mask and target: 100 mm,
- group frequency [f_g]: 1.2–4.5 kHz,
- sputtering time (t): 1–30 min.,
- targets: 99.99% Zn, 80% Zn — 20% In, Cu.

The second method of manufacturing shielding materials involved vacuum evaporation of Ag, Zn and Cu. The process was performed at a pressure of 2.5×10^{-5} Torr after a thorough cleaning of non-woven PP fabrics and PET film.

In order to compare the methods of fabrication of shielding materials, it has been decided to use Jerusalem crosses, as described in [5–7] (Fig. 1). Also a similar geometrical dimensions were used:

- period of unit cell $p = 33.5$ mm,
- length of load $l = 27$ mm,
- conductor width $w = 2$ mm,
- cell separation distance $s = 1.5$ mm.

The only difference compared to [5] is the thickness of prepared layers, contained within a range of $t = 0.5$–2 m.

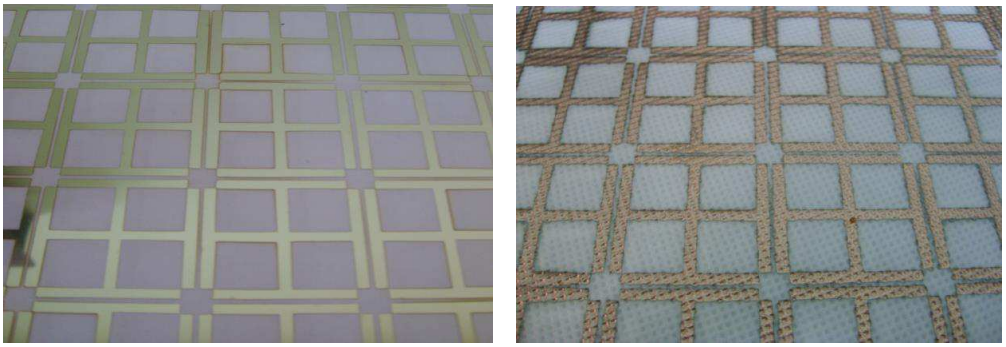

(a) (b)

Figure 1: Metallic Jerusalem crosses deposited on: (a) PET film, (b) non-woven PP fabric.

Figure 2: Non-woven polypropylene fabric with a layer of copper, deposited using magnetron sputtering method.

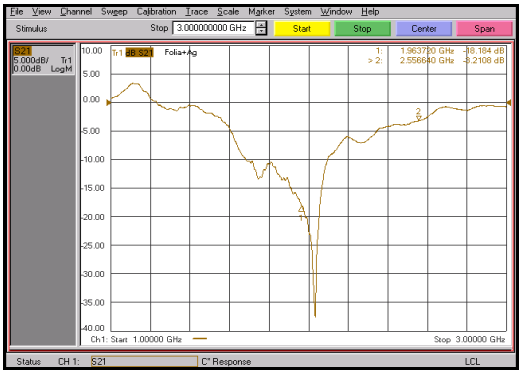

Figure 3: PET film with a layer of silver, deposited using vacuum evaporation method.

3. SHIELDING EFFECTIVENESS (SE) TESTING

Shielding effectiveness measurements were performed at the Institute of Telecommunications, Data Communications and Acoustics of Wroclaw University of Technology. SE testing took place in an anechoic chamber. The measuring system consisted of HF 906 transmitting and HF 907 receiving antennas, as well as Agilent Technologies N5230A analyzer, with a measuring range of 300 Hz–20 GHz. The distance between the transmitting and receiving antennas was 600 mm. The best results regarding shielding attenuation SE $\sim$ 40 dB were obtained for copper layers deposited by magnetron sputtering (Fig. 2) and for layers of silver, prepared by vacuum evaporation (Fig. 3). Comparable SE values were obtained for the metallic layers deposited on PET film utilizing both the sputtering and vacuum evaporation methods. An interesting fact is that similar SE values were obtained for substrates of non-woven polypropylene fabrics, despite the fact that the metallic layers are characterized by high porosity and heterogeneity. However, conductive connections that are being formed provide good electrical conductivity, which is a prerequisite for high values of SE.

4. CONCLUSIONS

The designed and prepared (Jerusalem cross-shaped) metallic shields in the form of a polymer-metal composite were characterized by shielding effectiveness (SE) values from 15 to 40 dB.

The best shielding efficiency for the selected frequency of 1.8 GHz was obtained on the samples of Ag+PET and Cu+PP (approx. 35–40 dB), which was higher than the value described in the article [5], despite much smaller thickness of deposited metallic layers.

In view of the technology of preparation of the layers and the advantages and disadvantages of methods used to deposit the selective shielding materials onto the substrate, it can be concluded that the method of screen printing or vacuum evaporation can be successfully replaced by magnetron sputtering.

ACKNOWLEDGMENT

This paper was funded as a part of the statutory research conducted at the Institute of Electrical Engineering Fundamentals.

REFERENCES

1. Koprowska, J., M. Pietranik, and W. Stawski, "New type textiles with shielding properties," *FIBRES & TEXTILES in Eastern Europe*, Vol. 12, No. 3(47), July–October 2004.
2. Brzezinski, S., T. Rybicki, I. Karbownik, K. Śleedzińska, and I. Krawczyńska, "Usability of a modified method for testing emissivity to assess the real shielding properties of textiles, *FIBRES & TEXTILES in Eastern Europe*, Vol. 18, No. 5(82), 76–80, 2010.
3. Maciej, J., P. Janina, Z. Jan, and O. Mariusz, "Composites made of polypropylene nonwoven fabric with plasmas layers," *Polypropylene*, Ed. by Fatih Dogan, 317–328, Rijeka, InTech, 2012,
4. Jan, Z., K. Joanna, and J. Jaroslaw, "Using plasma metallisation for manufacture of textile screens against electromagnetic fields," *FIBRES & TEXTILES in Eastern Europe*, Vol. 16, No. 5, 64–66, 2008.
5. Wang, L. B., K. Y. See, J. W. Zhang, B. S. I. Albert, and C. W. Lu, "Ultrathin and flexible screen-printed metasurfaces for EMI shielding applications," *IEEE Transactions on Electromagnetic Compatibility*, Vol. 53, No. 3, 700–705, 2011.
6. Salam, B., W. L. Lai, L. C. W. Albert, and L. B. Keng, "Low temperature processing of copper conductive ink for printed electronics applications," *13th Electronics Packaging Technology Conference*, 251–255, 2011.
7. Masud, M. M., B. Ijaz, I. Ullah, and B. Braaten, "A compact dual-band EMI metasurface shield with an actively tunable, polarized lower band," *IEEE Transactions on Electromagnetic Compatibility*, Vol. 54, No. 5, 1182–1185, 2012.

EM-safety: Low Frequency Magnetic Field Exposure in Vehicles with Electrical Powertrains

A. R. Ruddle[1], **L. Low**[1], **and A. Vassilev**[2]

[1]MIRA Limited, Watling Street, Nuneaton, Warwickshire, CV10 0TU, UK
[2]CEA-Leti, MINATEC Campus, 17 rue des Martyrs, 38054 GRENOBLE Cedex 9, France

Abstract— Although there are not currently any specific product standards relating to in-vehicle electromagnetic field exposure, there are general recommendations for field exposure limits from various national and international bodies, such as ICNIRP. Thus, there is a need to develop an understanding of the electromagnetic environment that may result in vehicles equipped with electrical powertrains, and to take account of occupant magnetic field exposure in the design and integration of such vehicles. The FP7 project "EM-Safety" has therefore undertaken measurements and numerical simulations of these issues. This paper provides an overview of some of this work.

1. INTRODUCTION

Vehicle electrification is currently being widely promoted in order to help improve urban air quality, to support efforts to reduce carbon emissions, and to limit reliance on fossil fuels. However, a new feature of hybrid and electric vehicles is that they require significant electrical power (perhaps as high as 200 kW, depending on the vehicle type [1]) to be routed around the vehicle between the on-board power sources (stored and/or generated) and electrical machines that act as traction motors in drive mode or generators under braking conditions. Given the size and space constraints of vehicles, the electrical powertrain components may be located in relatively close proximity to the occupants. Consequently, the occupants of such vehicles will be exposed to low frequency magnetic fields arising from currents flowing in the high voltage power network, traction batteries, and associated devices including inverters and electrical machines. Thus, establishing the electromagnetic safety of the in-vehicle environment will be important to ensure the acceptability of such vehicles to consumers.

Low frequency magnetic fields due to currents on the high voltage power distribution system are likely to be significant contributors to the in-vehicle electromagnetic environment associated with electric powertrain. The complexity of vehicle geometry is such that 3D magnetic field simulation is needed in order to predict the relationship between power cable current paths and the magnetic fields that can be expected to result in regions of interest. This paper outlines results from measurements and simulations of occupant magnetic field exposure based on a small electric vehicle. The results are compared with recommendations for limiting general public exposure to electromagnetic fields identified by the EU [2], which are based on recommendations from the International Commission for Non-Ionizing Radiation Protection (ICNIRP [3]). The fields are also compared with the recently revised ICNIRP recommendations [4], which relate specifically to electro-stimulation effects on nerves and muscles due to low frequency magnetic field exposure.

2. MAGNETIC FIELD MEASUREMENTS

Magnetic field measurements have been carried out on a number of representative electric vehicles of various types in the course of the EM-Safety project [5]. The magnetic fields were measured using a three-axis Bartington fluxgate magnetic field sensor with low noise ($< 10\,\mathrm{pT}/\sqrt{\mathrm{Hz}}$) and high sensitivity (i.e., 10 V output at 100 μT) characteristics. Previous off-board radiated emissions measurements on electric vehicles [6] (above 30 MHz) indicated some enhanced levels during acceleration and deceleration. The magnetic field measurements were therefore carried out over periods of around 45 s to allow acceleration and deceleration cycles to be evaluated. A total of five field sensors and one current sensor were monitored using a 16-channel analyser to filter, sample and record the associated waveforms. The signal sampling frequency was 5.12 kHz, and the cut-off frequency for the low pass filter was 2 kHz. The field probes were placed at points representing the head, seat and foot using a "mannequin" structure to ensure reproducible positioning.

A common feature of these measurements [5], and of other reported experiments [7], is that the highest fields tend to be found where the body is close to high power cables (often near the feet of the driver or front passenger) or traction batteries (e.g., around the lower back for rear

passengers in vehicles with batteries located in the rear [7]). Batteries may also be mounted below the occupants in some vehicle architectures, while the electric motor is often located at the front axle. The power cables may carry current in single-phase or three-phase form, depending on the design of the system. Although the recommended exposure limits for DC magnetic fields are very high, single-phase high voltage cables also carry significant current transients. It can be seen that the magnetic field waveform observed in the vicinity of the floor of the vehicle developed in the EC project "PMOB"correlates with the current waveforms measured on the high voltage power cables to the inverters (see Figure 1). These waveforms contain finite frequency components that could present potential human health concerns if the rate of change of magnetic field is sufficiently high.

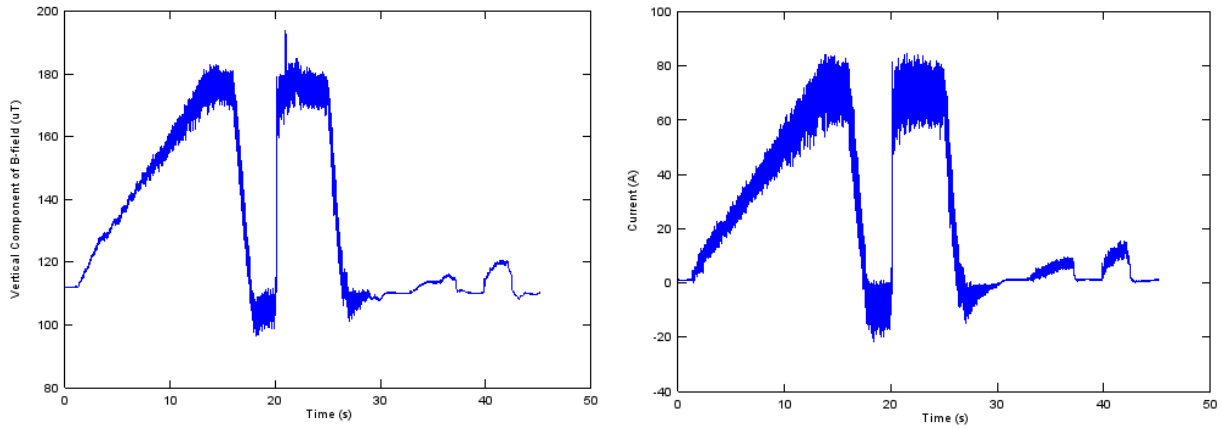

(a) Vertical component of magnetic flux density (b) Single-phase current to inverter

Figure 1: Magnetic flux density and inverter current waveforms measured in PMOB vehicle.

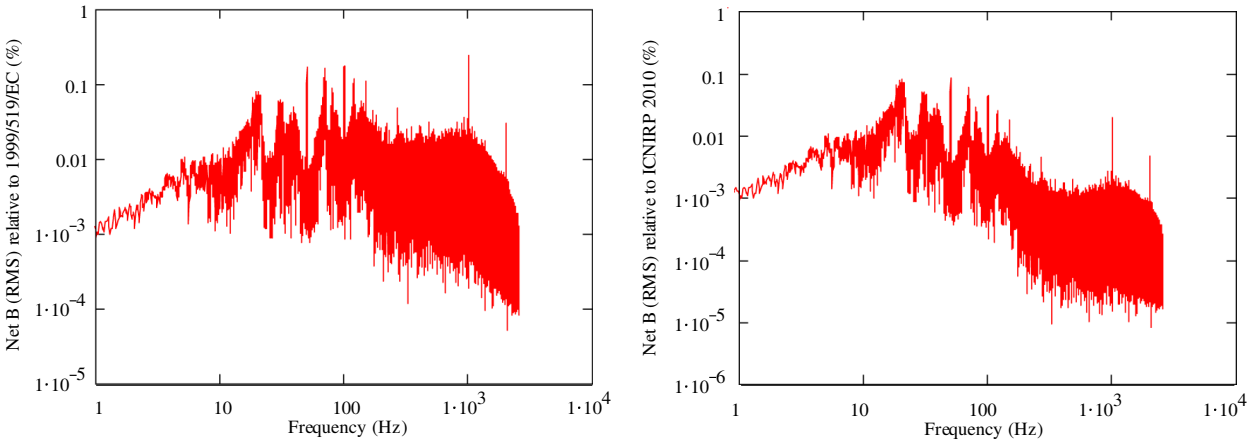

(a) 1999/519/EC [2] (b) ICNIRP 2010 [4]

Figure 2: Net RMS magnetic flux density relative to magnetic flux density reference levels of [2, 4].

3. MAGNETIC FIELD EXPOSURE ASSESSMENT

In measured field spectra the individual frequency components are relatively small compared to the field reference levels (see Figure 2). However, ICNIRP requires additive effects to be taken into account for multiple frequency exposures, so the levels that can be tolerated for any particular frequency are not fixed, but decrease with the number and intensity of other frequencies that are present. Thus, simply comparing field spectra with the reference levels is overly optimistic.

For non-sinusoidal exposures, combining the frequency components using a simple summation of relative amplitudes can lead to excessively conservative threat assessments as all components are treated as in-phase. However, a more realistic time-varying field exposure measure can be derived (based on an inverse Fourier transform) that not only takes account of the additive effects

of multiple frequency exposures, but also reflects the relative phase of the spectral components [4]. There is no time-averaging in this as electro-stimulation effects are effectively instantaneous [2].

For non-sinusoidal and spatially non-uniform magnetic fields, a set of time-varying magnetic field exposure measures can be determined at points $\mathbf{r}_j$ for field components k using [4]:

$$me_k\left(t_i, \mathbf{r}_j\right) = \left| \sum_{n=N}^{P} \frac{|B_{jkn}|}{\sqrt{2} B_{RL}\left(n\Delta\right)} \cos\left\{2\pi n \Delta t_i + \arg(B_{jkn}) + \phi\left(n\Delta\right)\right\} \right| \tag{1}$$

where the terms B_{jkn} represent the nth of M complex Fourier components for frequencies $n\Delta$ (where n is an integer $0 \leq n \leq M/2$ and Δ is the corresponding frequency increment) derived from $M+1$ time samples obtained from the magnetic flux density waveform $B_{jk}(t_i,\mathbf{r}_j)$ for field component k at point $\mathbf{r}_j$ and time t_i (where $0 \leq i \leq M$), while $N\Delta \geq 1$ and $P\Delta \leq 10^7$ such that the summation is limited to the band 1 Hz to 10 MHz [2–4]. The parameters $\phi(n\Delta)$ are the phase angles of the filter function, which vary according to the frequency dependence of the particular reference level. The filter phase angles are specified as π, $\pi/2$, 0 and $-\pi/2$ radians where the frequency dependence of the reference level varies as f^{-2}, f^{-1}, f^0 and f, respectively(see Appendix to [4]). The magnetic field reference levels $B_{RL}(n\Delta)$, which are specified as RMS values in [2–4], are multiplied by $\sqrt{2}$ in (1) in order to obtain the corresponding peak values for comparison with the magnitude of the spectral components.

If $me_k(t_i,\ \mathbf{r}_j) \leq 1$ then the field component k at point $\mathbf{r}_j$ complies with the reference levels. However, the treatment of general fields with three orthogonal components is not specified in [4]. It has therefore been assumed that a total magnetic field exposure measure $ME(t_i, \mathbf{r}_j)$ for point $\mathbf{r}_j$ at time t_i should be determined using vector addition of the measures derived for each of the three field components, and that this should meet the criterion:

$$ME\left(t_i, \mathbf{r}_j\right) = \sqrt{\sum_{k=1}^{3} \left[me_k\left(t_i, \mathbf{r}_j\right)\right]^{\,2}} \leq 1 \tag{2}$$

Time-varying exposure measures derived from the sample field data using this approach are shown in Figure 3, based on the EU and ICNIRP 2010 limits (respectively). These results indicate that the worst-case instantaneous exposure is less than 20% of the EU reference levels [2], and less than 5% of the ICNIRP 2010 reference levels for general public exposure [4]. The slightly different shapes of these two plots reflect the differences in the reference levels.

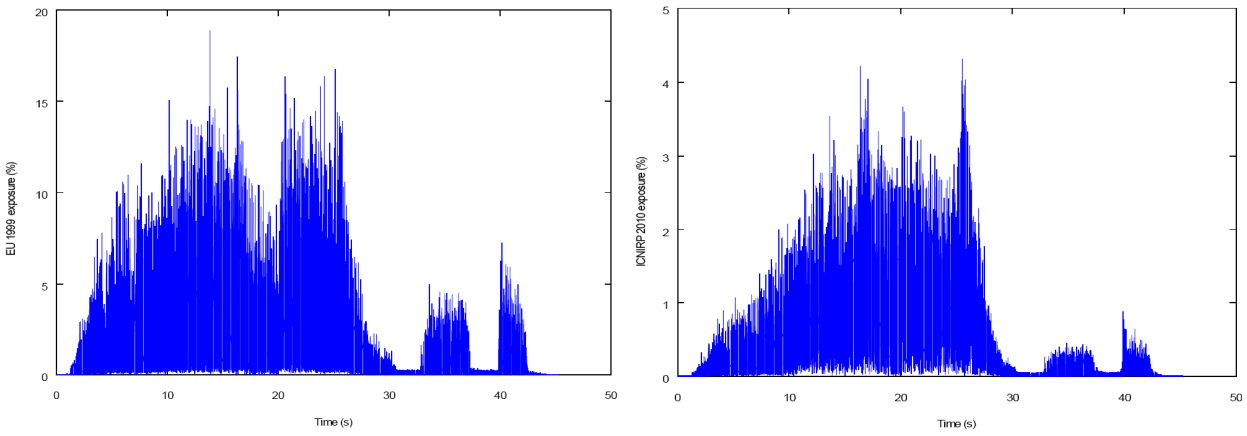

(a) 1999/519/EC [2] (b) ICNIRP 2010 [4]

Figure 3: Time-varying exposure measures derived from measured magnetic fields based on [2, 4].

4. SIMULATION OF IN-VEHICLE MAGNETIC FIELD AND EXPOSURE

The measurements shown in Figure 1 suggest that the in-vehicle magnetic field exposure could be predicted from measured cable currents using 3D field models. Numerical simulations based on a finite element model of a small electric vehicle with a steel chassis and dielectric body panels

(see Figure 4) have been used to derive time-varying field exposure measures from measured cable current transients. The magnetic field calculations were carried out using Flux3D [8]. A sample exposure measure derived from the model is illustrated in Figure 5, for a case with a simple steel plate included as a shield between the battery loop and the passenger compartment.

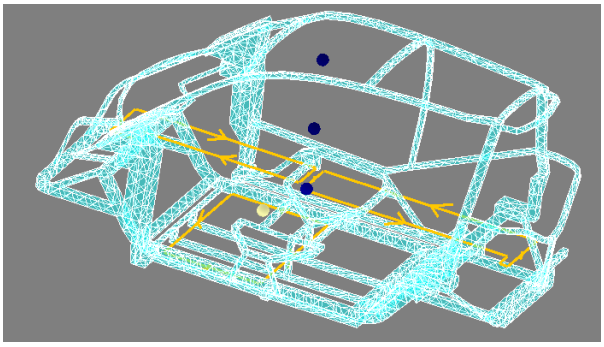

Figure 4: Finite element model for the steel chassis of a small electric vehicle, showing assumed current loops (arrows) and field output points (circles).

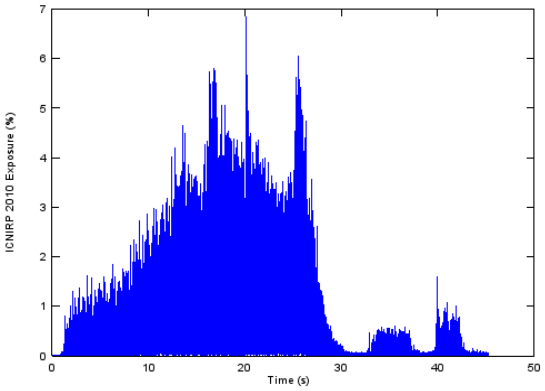

Figure 5: Exposure measure derived from simulation of vehicle with large battery loop and shield, for ICNIRP 2010 general public reference levels.

For this model the simulation output file size was around 1.1 Gbytes per time or frequency step. Consequently, a direct time-domain simulation of the magnetic field waveform associated with the measured current waveform was impracticable, as more than 220,000 time-steps were recorded in the current measurement. However, the frequency response of the magnetic field components computed at the observation points was found to be smoothly varying in the frequency domain. Consequently, data from a more manageable small number of frequencies could be used to interpolate relatively sparse spectral data to match the much larger number of frequencies that were extracted from the measured time series for the inverter current.

Assuming the (complex) current spectrum I_n for frequencies $n\Delta$ (where n is an integer $0 \leq n \leq M/2$) to be derived from $M+1$ time samples with a corresponding frequency increment Δ, the magnetic flux density waveform $B_k(t_i, \mathbf{r}_j)$ for field component k at observation point $\mathbf{r}_j$ and time t_i (where i is an integer $0 \leq i \leq M$) is estimated from the inverse Fourier transform as:

$$B_k\left(t_i, \mathbf{r}_j\right) = \frac{1}{2} k_0\left(\mathbf{r}_j\right) \ |I_0| + \sum_{n=1}^{M/2} k_n\left(\mathbf{r}_j\right) \ |I_n| \cos\left\{2\pi n \Delta t_i + \arg\left(I_n\right)\right\} \tag{3}$$

where $k_n(\mathbf{r}_j)$ is the computed transfer function relating a 1 A current at frequency $n\Delta$ to component k of the resulting magnetic flux density at point $\mathbf{r}_j$. The corresponding field exposure measure is:

$$ce_k\left(t_i, \mathbf{r}_j\right) = \left| \sum_{n=N}^{P} \frac{k_n\left(\mathbf{r}_j\right) \ |I_n|}{\sqrt{2} B_{RL}\left(n\Delta\right)} \cos\left\{2\pi n \Delta t_i + \arg\left(I_n\right) + \phi\left(n\Delta\right)\right\} \right| \tag{4}$$

where $N\Delta \geq 1$ and $P\Delta \leq 10^7$, such that the summation is limited to the band 1 Hz to 10 MHz [2–4], as in Equations (1) and (2). These component results are also combined by vector addition, as in (2).

A lack of detailed current path geometry prevented direct validation of the simulations against the measurements. Nonetheless, the predicted levels for representative configurations encompass the measured fields and are thus considered to be credible. Furthermore, the simulation results obtained from a range of model variants indicate that, for the specific configurations studied in this work, the field from battery currents could be reduced by a factor of ~ 20 by minimizing the battery loop area and by a factor of ~ 7 by including a simple steel plate as a battery shield.

5. CONCLUSIONS

The exposure results obtained from magnetic field measurements evaluated relative to 1999/519/EC [1] are broadly in line with those reported in [6], although the latter (which range up to $\sim 15\%$ of

the 1998 ICNIRP [2] general public reference levels) were obtained over shorter (2 s) periods under constant drive conditions for a wider frequency band (up to 100 kHz).

The model results indicate that the in-vehicle magnetic field can be predicted from measured current transients by using 3D numerical models of the traction current paths and vehicle structure to estimate frequency domain current-field transfer functions. The simulations have also been used to demonstrate that the magnetic field in the passenger compartment could perhaps be reduced by simple installation measures, such as minimising the area of current loops and adding shielding structures near significant sources. Other possible field mitigation approaches investigated include the twisting of high-voltage power cables in order to obtain enhanced spatial field decay rates.

ACKNOWLEDGMENT

The research leading to these results has received funding from the European Community's Framework Programme (FP7/2007-2013) under grant agreement No. 265772. The authors are grateful for the support and contributions of other members of the EM-Safety project consortium, from CEA-LETI (France), Centro Ricerche Fiat (Italy), Leibniz Universität Hanover (Germany), IPM (Italy), MIRA (UK), Prysmian (Italy), SINTEF (Norway), TAMAG Iberica (Spain), the Technical University of Braunschweig (Germany) and the University of Torino (Italy). Further information can be found on the project website (www.sintef.no/Projectweb/EM-Safety). The electric vehicle investigated in this work was developed by IFEVS and Polimodel in the course of the collaborative research projects P-MOB (FP7-ICT-260087, http://eeepro.shef.ac.uk/p-mob/) and WIDE-MOB (FP7-SST-266129, http://eeepro.shef.ac.uk/wide-mob/), which are also supported by the European Community's FP7 Research Framework Programme.

REFERENCES

1. De Santiago, J., et al., "Electrical motor drivelines in commercial all-electric vehicles: A review," *IEEE Trans. Vehicular Technology*, Vol. 61, No. 2, 475–484, February 2012.
2. 1999/519/EC, "Council Recommendation of 12th July 1999 on the limitation of exposure of the general public to electromagnetic fields (0 Hz to 300 GHz)," *Official J. EC*, No. L 199, 59–70, Jul. 30, 1999.
3. ICNIRP, "Guidelines for limiting exposure to time-varying electric and magnetic fields (up to 300 GHz)," *Health Physics*, Vol. 74, No. 4, 494–522, April 1998.
4. ICNIRP, "Guidelines for limiting exposure to time-varying electric and magnetic fields (1 Hz to 100 kHz)," *Health Physics*, Vol. 99, No. 6, 818–836, December 2010.
5. Vassilev, A., "Representative vehicle exposure measurements," EM-Safety Project Deliverable D2.3, June 2012.
6. Ruddle, A. R., D. A. Topham, and D. D. Ward, "Investigation of electromagnetic emissions measurements practices for alternative powertrain road vehicles," *Proc. 2003 IEEE Int. EMC Symp.*, 543–547, Boston, USA, August 2003.
7. Schmid, G., R. Überbacher, and P. Göth, "ELF and LF magnetic field exposure in hybrid- and electric cars," *Proc. Bio-electromagnetics Conf. 2009*, Paper 9-3, Davos, Switzerland, June 2009.
8. Flux page of CEDRAT Group website, 2013, [Online] Available at: http://www.cedrat.com/en/software/flux.html.

Magneto-optical Investigations of Co- and Fe-rich Composite Glass Covered Microwires

A. Chizhik[1], **A. Zhukov**[1, 2], **and J. Gonzalez**[1]

[1]Universidad del País Vasco, UPV/EHU, San Sebastián, Spain
[2]IKERBASQUE, Basque Foundation for Science, Bilbao 48011, Spain

Abstract— Here we present the last results of magneto-optical Kerr effect (MOKE) study of the formation and transformation of surface domain structure in the series of Co and Fe rich microwires. The microwires of the metallic nucleus diameter of 100 µm and glass coating thickness of 20 µm have been studied by MOKE microscopy. The great variety of the types of surface domain structures has been found in two studied classes of microwires.

1. INTRODUCTION

The elucidation of the basic mechanisms of the magnetization reversal in magnetic amorphous wires is the subject of wide experimental and theoretical investigation [1–8]. Nevertheless, the direct observation of these mechanisms was not performed up to now. During last years studying intensively the magnetic and magneto-optical properties of the Co-rich and Fe-rich glass covered amorphous microwires we approached close to the understanding of ways to manage and select these mechanisms [9]. Recently, we have performed investigation of large series of the glass covered microwires of different compositions, metallic nucleus diameters (0.8 µm–100 µm) and the glass covering thickness (2 µm–50 µm). As a result of the analysis of these investigations we have chosen two types of microwires: of nominal compositions $Fe_{5.71}Co_{64.04}B_{15.88}Si_{10.94}Cr_{3.40}Ni_{0.03}$ and $Fe_{71.7}B_{13.4}Si_{11}Nb_3Ni_{0.9}$ with metallic nucleus radius of 50 µm, glass coating thickness of 20 µm. These microwires with negative and positive magnetostriction demonstrate perfect magnetic domain structures. We have selected these microwires for the detailed investigation of the mechanisms of the magnetization reversal.

2. EXPERIMENTAL DETAILS

The observation of the magnetic domains in the surface of Co and Fe rich glass covered microwires has been performed by means of optical polarizing microscopy working in reflective mode using the longitudinal magneto-optical Kerr effect (MOKE) configuration [9]. The surface magnetic domains were visualized due to the different in-plane components of the surface magnetization that transforms to black-white contrast when the polarized light reflects from the surface of the microwire. The surface is cylindrically shaped. The obtained MOKE images of the domain structures show the difference of in-plane magnetization components. As a result of the MOKE images processing the hysteresis loops were obtained from the magneto-optic intensity for different values of the external magnetic field.

In this investigation, we are paying attention mainly on the transformation of surface domain structure. The experiments have been performed using crossed magnetic field which was the vector sum (H_Σ) of axial (H_{AX}) and circular (H_{CIRC}) magnetic fields. In order to produce the circular magnetic field H_{CIRC}, an electric current flowing I through the wire has been used. A pair of Helmholtz coils provided an axial magnetic field.

3. RESULTS AND DISCUSSION

First, we have studied the Co-rich microwires. As a dependence of the external magnetic field configuration it was observed four different mechanisms of the surface magnetization reversal. The increase of the DC circular magnetic field ($H_{CIRC\ DC}$) causes the change of the type of mechanisms.

Initially, the magnetization reversal has been studied in the case of $H_{CIRC} = 0$ (Fig. 1(a)). The image of domain structures has been obtained for the magnetic field applied parallel. The dark magnetic domain appears at the surface of the sample when the amplitude of H_{AX} was -0.22 Oe. When the magnetic field sweep continues, the dark domains increase with simultaneously decrease of the bright ones. This experiment corresponds well to the found earlier long distance quick motion of the solitary circular domain walls [9].

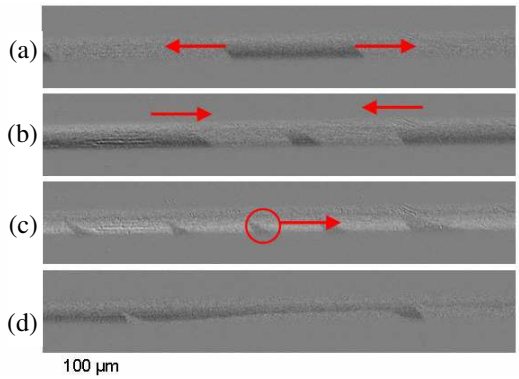

Figure 1: Images of surface magnetic domain structure for: (a) $H_{CIRC\ DC} = 0$, (b) $H_{CIRC\ DC} = 0.48$ Oe, (c) $H_{CIRC\ DC} = 0.8$, (d) $H_{CIRC\ DC} = 1.12$.

Then we have passed to the experiments with the presence of DC circular magnetic field. It was found that the increase of circular magnetic field causes the successive changes of the mechanism of the magnetization reversal. Here we present three different types of this mechanism as a dependence of $H_{CIRC\ DC}$ amplitude.

Figure 1(b) presents the image of domain structures which corresponds to the transformation of the surface domain structure induced by the axial magnetic field for $H_{CIRC\ DC} = 0.48$ Oe. At the initial stage, the magnetization reversal occurs in the same way as in the previous case: the domain nucleation is followed by the DW motion across the sample but the size of the nucleated domains is relatively smaller. However at the next step the mechanism of magnetization reversal changes. In this case the effect of domain suppression is observed — the advantageous dark domain placed in the centre of the frame, disappears under the pressure of two moved domain walls (marked by the red arrows). The specific feature which we consider as a key one is the difference in the angle of the inclination of the domain walls: the left DW of the bright domains is more inclined toward the axial direction than the right DW.

The next observed mechanism of the magnetization reversal — the effect of drift of the surface domains is the consequence of the subsequent increasing of the $H_{CIRC\ DC}$ (see Fig. 1(c))). Under the DC circular magnetic field of 0.8 Oe the magnetization reversal occurs basically as the nucleation of multiple domains followed by the directed motion of the wedged domains as whole objects along the microwire. The size of the moved domains decreases during the drift process up to the complete disappearance of wedged domains.

The formation and transformation of the vortex-like domain structure (Fig. 1(d)) is the last type of the mechanisms of the magnetization reversal observed in Co-rich microwires. The DC circular magnetic field increase causes the formation of the compact structure which could be qualified as a non-planar vortex-type structure. The domain structure observed here under the present configuration of two crossed magnetic fields is very unusual and unexpected in magnetic microwires. At the first stage this surface structure is characterized by the extended part with the domain wall parallel to the wire axis. As we can see, the rotation of the magnetization by 360° appears in this vortex. Under the action of an axial magnetic field, fluent DW motion and jump-like rearrangement of the whole domain structure takes place. As a result of this rearrangement, at a special moment, the vortex-type domain transforms to a quasi periodical multi-domains structure with wedged-shape domains.

For all the presented experiments the external magnetic being the sum of AC axial magnetic field and DC circular magnetic field, rotates on the imaginable cylindrical shape. In this way H_{Σ} follows to the non-plane inclined trajectory. The shape of this non-plane line depends on the value of the $H_{CIRC\ DC}$. We consider that when the value of the $H_{CIRC\ DC}$ is high enough this rotation of the sum magnetic field induces the formation of vortex-type domain structure.

Figure 2 presents the experimental results obtained in Fe-rich microwires. The character of the obtained results is determined basically by positive magnetostriction which characterizes this type the microwire. The positive magnetostriction causes the surface magnetic domain structure with radial magnetization and closure domains. The magnetization in the mono-domain or multi-domains closure structure has a direction inclined from the axial direction that results in surface helical magnetic structure [10].

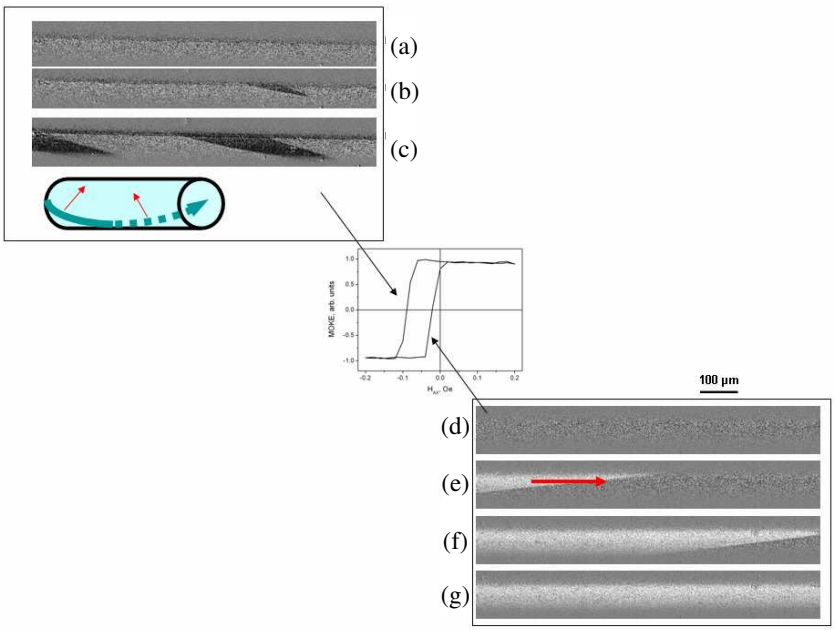

Figure 2: (a)–(g) MOKE hysteresis loop and images of surface magnetic domain structure transformation.

MOKE hystersis loop presented in the Fig. 2 is characterized by the asymmetrical shape and a shift along the axial magnetic field axis. It was found that the magnetization reversal occurs in different ways for two different half-curves of the hystersis loop. When the axial magnetic field changes from H_{AX}^{-} to H_{AX}^{+} the sharp jump of the magnetization reversal takes a place. This jump is related to the long distance motion of the solitary inclined domain wall [9]. The series of the Images of surface magnetic domain structure presented in the low-right part of the Fig. 2, demonstrate this motion of solitary DW. When the axial magnetic field changes from H_{AX}^{+} to H_{AX}^{-} another mechanism of the magnetization reversal is observed. For this case the formation and the transformation of "serpentine-type" DW happen (see upper-left part of the Fig. 2). This unusual mechanism has not been reported never before. Magnetization reversal stars from the mono-domain state. At the first stage the small, narrow wedge-shaped domain appears. With the axial field decrease this domain increases in length and width simultaneously performing the serpentine-type motion in the surface of the wire. Two steps of this serpentine domain structure are presented in the Fig. 2(c).

Analyzing the results obtained for the Co-rich microwire we use our theoretical model presented in [3]. Following this model we consider that the crossed axial-circular magnetic field induces different types of helical magnetic structure in the surface of the microwire. According to our previous calculation we created the phase diagram (Fig. 3) which demonstrates the possible helical magnetic phases depending on the values of axial and circular magnetic fields (the phases are marked in the figure as (1), (2), (3) and (4)). This phase diagram shows the dependencies of the

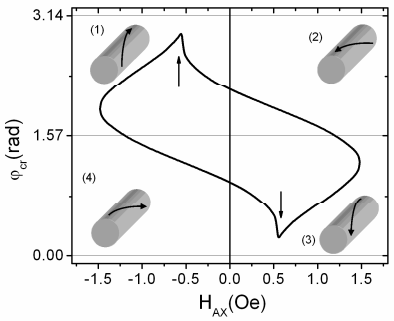

Figure 3: Phase diagram. The critical angle as functions of the axial applied magnetic field.

critical angle of the magnetization φ_{cr} on the axial magnetic field. There is a curve for the the angle of helical anisotropy $\alpha \neq 0$. We consider that namely this case is realized in our experiments taking into account that the domain walls have the inclined shape when $H_{CIRC\ DC} = 0$ that confirms the helical (non-circular) character of the surface domain structure.

It is clear from the phase diagram that the specific area exists (between two arrows in the phase diagram) where four helical magnetic states could co-exist in stable or meta-stable conditions. Different angles of the inclination of domain walls which is observed in the Fig. 1 clear confirms the co-existence of as minimum three helical states. The helical states are very sensitive to circular magnetic field. Successive increase of $H_{CIRC\ DC}$ causes the competition between different helical structures and also between the domain nucleation and DW propagation process. Therefore, the main reason of the observed effects of domain suppress and domain drift is determined by the coexistence of different helical states in the microwire. The co-existence realizes in the specific multi-domain structure when the angle of the domain wall alternates along the wire. The domain walls which separates different helical states have different angle of inclination and accordingly, different velocity. Finally, when the $H_{CIRC\ DC}$ is high enough, the helical structure of the different types is captured into the magnetization reversal initiating simultaneous coexistence of four magnetic structures in the form of the surface un-plane vortex.

The experimental results obtained in Fe-rich microwires also have been analyzed in the frame of the mentioned model of the coexistence of the helical magnetic states. The asymmetrical shape found the realization in two different mechanisms: long distance motion of the solitary inclined domain wall and serpentine DW motion. The strong competition between surface helical structures leads to the nucleation of the advantageous domain in very narrow angle diapason of the direction of magnetization that realized in the formation of the serpentine DW. The motion of the solitary DW is the demonstration of another effect — helical magnetic bistability [11]. During the magnetization reversal which starts in the negative field, the domain nucleation process is suppressed placing in the forefront the DW motion.

In summary, we demonstrate the great variety of the mechanisms of magnetization reversal in magnetic microwires. The combination of the crossed magnetic fields with helical anisotropy causes the different types of surface magnetic structures and their transformation. The main mechanism — long distance motion of the solitary domain wall was observed in Co-rich wires with negative magnetostriction and in Fe-rich wires with positive magnetostriction. Taking into account that we have observed this mechanism in microwires of scale of about 10 µm [9] and in microwires of sub-micron scale we could conclude that it a basic mechanism of the magnetization reversal in glass covered magnetic microwires. Another important point is the coexistence of stable and meta-stable magnetic phases with different chirality. Varying the magnetic field configuration we can manage also the competition between the domain nucleation and domain wall motion that induces such effects as drift and suppression of magnetic domains and formation of serpentine-type domain wall.

ACKNOWLEDGMENT

This work was supported by EU ERA-NET programme under project "SoMaMicSens" (MANUNET-2010-Basque-3), by EU under FP7 "EM-safety" project, by Spanish Ministry of Science and Innovation, MICINN under Project MAT2010-18914, by the Basque Government under Saiotek 11 MICMAGN project (S-PE11UN087) and by federal target program "Scientific and scientific-pedagogical personnel of innovative Russia", state contract No. 14.A8.21.0762 .

REFERENCES

1. Vázquez, M., H. Chiriac, A. Zhukov, L. Panina, and T. Uchiyama, *Phys. Stat. Sol. (a)*, Vol. 208, 493, 2011.
2. Parkin, S. S. P., M. Hayashi, and L. Thomas, *Science*, Vol. 320, 190, 2008.
3. Chizhik, A., V. Zablotskii, A. Stupakiewicz, C. Gómez-Polo, A. Maziewski, A. Zhukov, J. Gonzalez, and J. M. Blanco, *Phys. Rev. B*, Vol. 82, 212401, 2010.
4. Chizhik, A., A. Stupakiewicz, A. Maziewski, A. Zhukov, and J. Gonzalez, *IEEE Trans. Magn.*, Vol. 48, 3800, 2012.
5. Panina, L. V. and D. P. Makhnovskiy, *Encyclopedia of Materials: Science and Technology Pages*, Elsevier, Amsterdam, Netherlands, 2008.
6. Pal, S. K., A. K. Panda, M. Vazquez, and A. Mitra, *J. Mater. Process. Technol.*, Vol. 172, 182, 2006.
7. Ausanio, G., V. Iannotti, and L. Lanotte, *Sens. Actuators A*, Vol. 153, 162, 2009.

8. Chiriac, H., S. Corodeanu, M. Lostun, G. Ababei, and T.-A. Óvári, *J. Appl. Phys.*, Vol. 107, 09A301, 2010.
9. Chizhik, A., A. Stupakiewicz, A. Maziewski, A. Zhukov, J. Gonzalez, and J. M. Blanco, *Appl. Phys. Lett.*, Vol. 97, 012502, 2010.
10. Hernando, B., M. L. Sánchez, V. M. Prida, J. D. Santos, J. Olivera, F. J. Belzunce, G. Badini, and M. Vázquez, *J. Appl. Phys.*, Vol. 103, 07E716, 2008.
11. Chizhik, A., A. Zhukov, J. M. Blanco, and J. Gonzalez, *J. Magn. Magn. Mater.*, Vol. 324, 3563, 2012.

Designed Surface Waves at an Interface of Plasmonic Nanolayered Metamaterial and Isotropic Dielectric

S. M. Vuković[1, 2], C. J. Zapata-Rodríguez[3], J. J. Miret[4], and Z. Jakšić[1]

[1]Center of Microelectronic Technologies and Single Crystals, Institute of Chemistry Technology and Metallurgy, University of Belgrade, Njegoseva 12, Belgrade 11000, Serbia
[2]Texas A & M University at Qatar, P. O. Box 23874, Doha, Qatar
[3]Department of Optics, University of Valencia, Dr. Moliner 50, Burjassot 46100, Spain
[4]Department of Optics, Pharmacology and Anatomy, University of Alicante P. O. Box 99, Alicante, Spain

Abstract— We analyzed surface wave propagation along the interface between a semi-infinite dielectric and a metal-dielectric nanostructured multilayer with indefinite permittivity, cut normally to the layers. Hyperbolization of the space dispersion (diffraction) is discussed within distinct spectral regimes. Surface waves are of hybrid TE-TM polarization, propagate obliquely or normally to the optical axes, and are more tightly confined to the surface compared to the convenient surface-plasmon-polaritons. It is demonstrated that the effective-medium approximation may reveal results that severely deviate from exact solutions. Our numerical simulations using the finite-element method predict the existence of long range oblique surface waves.

1. INTRODUCTION

Nanostructured metal-dielectric (MD) multilayers can be considered the simplest plasmonic metamaterials, but they are also highly versatile. They are able to sustain bulk high-frequency plasmonic modes. If such metamaterial is cut perpendicularly to the layers, it can also sustain electromagnetic surface waves [1, 2]. For infrared and visible wavelengths, the MD multilayers may behave as uniaxial plasmonic crystals. This enables a simplified description of the medium by using the effective medium approximation (EMA), which explicitly involves a homogenization of the nanostructured metamaterial. Under certain conditions, the permittivity that is given as a second-rank uniaxial tensor may satisfy Dyakonov dispersion equation [3], and may contain elements of opposite sign, leading to hyperbolic metamaterials [4]. The dispersion of Dyakonov-like surface waves (DLSW) in non-hyperbolic MD metamaterials was studied in Refs. [2, 5]. Although the existence of DLSW in anisotropic plasmonic crystal with indefinite permittivity was shown in [1], the authors provided only a qualitative study of hyperbolic DLSW.

Here we present an investigation of DLSW dispersion, diffraction and propagation along the interface between a plasmonic crystal and an isotropic dielectric. In that case, within the framework of the effective-medium approximation (EMA), nanostructured plasmonic multilayer behaves like a uniaxial crystal whose optical axes lies in the interface plane with isotropic dielectric. When the frequency is fixed and losses in metal are neglected, bulk electromagnetic wave diffraction can be described by isofrequency surfaces in the k-space. Such surfaces can be closed (sphere, ellipsoid) resembling isotropic or anisotropic dielectric, or open (hyperboloid with one or two sheets) depending on the metal filling factor in the binary unit cell of plasmonic multilayer [4]. Open surfaces show metallic properties in one direction and dielectric in the other (perpendicular). In addition, there are frequencies and the filling factors for which only evanescent solutions are possible. Then the plasmonic multilayer resembles anisotropic metal without propagating bulk waves. However, favorable conditions may appear in that case for propagation of surface modes along and localized near the interface with isotropic dielectric.

2. DLSW AT THE INTERFACE OF HYPERBOLIC PLASMONIC CRYSTAL

Here we put emphasis on EMA. The periodic binary structure is made of two materials alternatively stacked along the z axis. This metamaterial fills the semi-space: $x < 0$. Specifically, a transparent material of dielectric constant ε_d and slab width w_d is followed by a metallic layer with its corresponding parameters ε_m and w_m. In our numerical simulations we set $\varepsilon_m = 1 - \omega^{-2}$, associated with the Drude model (frequencies are given in units of the plasma frequency ω_p). For the purpose of this consideration we neglect losses. Finally we set an isotropic material of dielectric constant ε filling the space $x > 0$. Validity of EMA is usually related to the assumption that the period

$\Lambda = w_m + w_d$ is much shorter than the wavelength. However, the inclusion of nanostructured metallic elements dictates a refinement in the EMA because of the fact that the width of metallic layers can be larger than the skin depth of noble metals which is deeply subwavelength. Material homogenization requires the metallic layers be of the sizes of a few nanometers [8, 9]. In this case, the plasmonic lattice behaves like a uniaxial crystal whose optical axis is normal to the layers (the z axis in Figure 1). The dyadic relative permittivity is set as $\bar{\bar{\varepsilon}} = \varepsilon_\perp(\mathbf{xx} + \mathbf{yy}) + \varepsilon_{||}\mathbf{zz}$, where $\varepsilon_{||}$ and $\varepsilon_\perp$ are evaluated analytically using

$$\left[\varepsilon_\perp, \varepsilon_{||}^{-1}\right] = (1-f)\left[\varepsilon_d, \varepsilon_d^{-1}\right] + f\left[\varepsilon_m, \varepsilon_m^{-1}\right] \tag{1}$$

where $f = w_m/(w_d + w_m)$ stands for the metallic filling factor in the unit cell. Therefore, the engineered anisotropy of the 1D lattice is modulated by the filling factor of the metal, but also by its strong dispersive character. Dispersion in metals determines the characteristics of the plasmonic-crystal anisotropy.

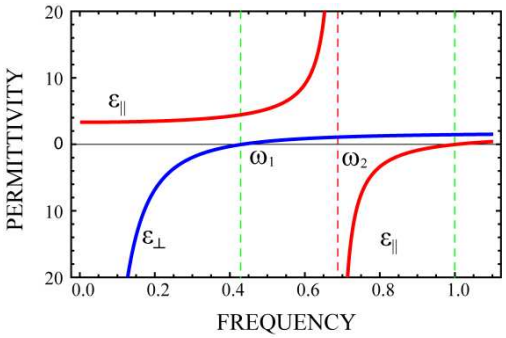

Figure 1: Permittivity components $\varepsilon_{||}$ and $\varepsilon_\perp$ as a function of normalized frequency ω for the MD lattice of Figure 1 assuming $f = 0.33$ and $\varepsilon_d = 2.25$.

In Figure 1 we represent permittivities $\varepsilon_{||}$ and $\varepsilon_\perp$ for a wide range of frequencies, when $f = 0.33$ and $\varepsilon_d = 2.25$. In the low-frequency range, $\omega \ll 1$, we obtain that $\varepsilon_\perp \approx f\varepsilon_m < 0$ and $0 < \varepsilon_{||} \approx \varepsilon_d/(1-f)$. The plasmonic structure behaves essentially as a metal and, therefore, only evanescent TE^z waves ($E_z = 0$) can exist. On the other hand, the dispersion of bulk TM^z waves ($B_z = 0$) follows a one-sheet hyperboloid,

$$\frac{k_x^2 + k_y^2}{\varepsilon_{||}} + \frac{k_z^2}{\varepsilon_\perp} = \omega^2, \tag{2}$$

where spatial frequencies are normalized to $k_p = \omega_p/c$. The hyperbolic dispersion exists up to a frequency $\omega_1 = \tilde{\omega}(0, \varepsilon_d, f)$ for which $\varepsilon_\perp = 0$. In that case

$$\tilde{\omega}\left(\varepsilon, \varepsilon_d, f\right) = \left[1 + \varepsilon/f + \varepsilon_d\left(1-f\right)/f\right]^{-1/2}. \tag{3}$$

In our numerical example that frequency is $\omega_1 = 0.426$. For slightly higher frequencies, Equation (2) represents an ellipsoid with a major semi-axis $\omega\sqrt{\varepsilon_{||}}$. However, such a value diverges at a frequency $\omega_2 = \tilde{\omega}(0, \varepsilon_d, 1-f)$. Here $\omega_2 = 0.686$. Note that $\omega_1 < \omega_2$ only if $f < 1/2$. Finally, Equation (2) represents a hyperboloid of two sheets in the range $\omega_2 < \omega < 1$. The frequency in the upper limit is established by the condition $\varepsilon_{||} = 0$, or equivalently $\varepsilon_m = 0$, occurring at the plasma frequency. We expect to find localized solutions near the interface $x = 0$ with the amplitudes decaying as $|x| \to \infty$. Since we treat the plasmonic lattice as a uniaxial crystal, we may establish analytically the diffraction equation that gives the in-plane wave vector $\mathbf{k}_D = [0, k_y, k_z]$ of the surface wave. For that purpose we follow Dyakonov [3] by considering a modal treatment of the problem. DLSW may be found in different regimes, which depend not only on the values characterizing the permittivity of the medium, but also that of the surrounding isotropic material ε.

We can find stationary solutions of Dyakonov's equation only if $\varepsilon < -\varepsilon_\perp$. This occurs when $0 < \omega < \omega_0$. In our numerical example $\omega_0 = 0.343$. Figures 2(a)–(b) illustrate DLSW dispersion curve for some frequencies in the range $0 < \omega < \omega_0$. In these two cases, the DLSW curve approaches a hyperbola. In contrast to what is shown in Figure 2(b), we find a band-gap around $k_z = 0$ in (a); generally, it occurs if $\omega < 0.324$. In this sense we point out that Dyakonov's solution at $k_z = 0$ is

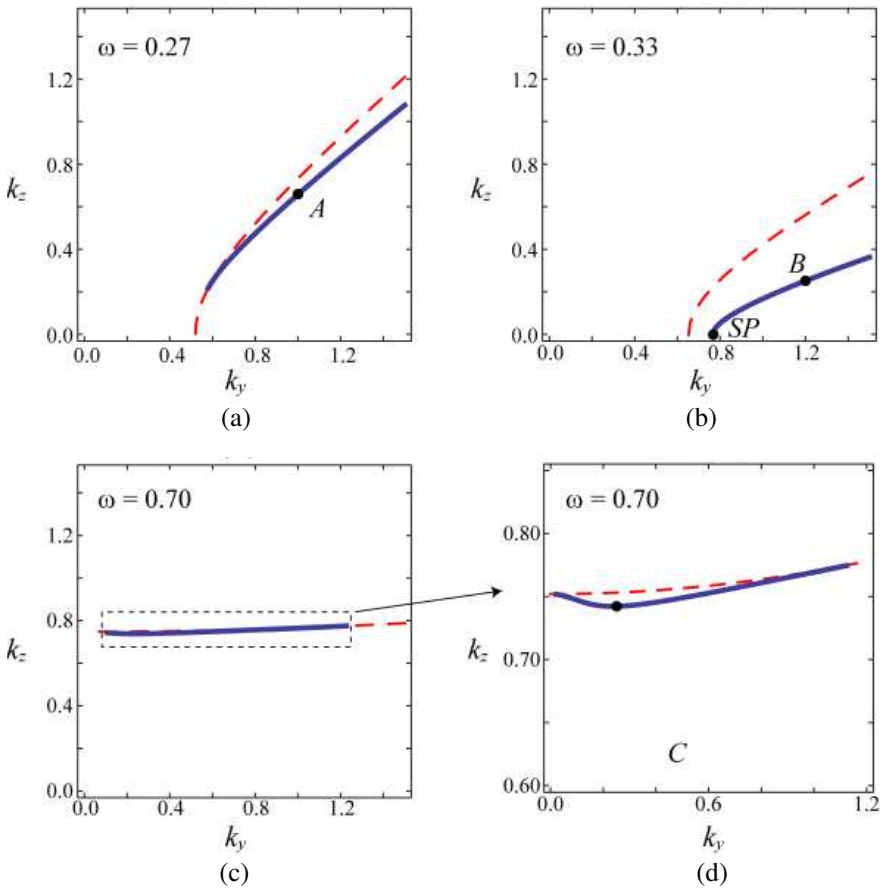

Figure 2: Solutions of Dyakonov's equation (solid lines), for our hyperbolic metamaterial at an interface with air ($\varepsilon = 1$), at different frequencies: (a) $\omega = 0.27$, (b) $\omega = 0.33$, (c) $\omega = 0.70$. As a reference we also include bulk extraordinary wave space dispersion (dashed red lines). (d) Dispersion curve as in (c) but magnified for the range of interest. Points A, B, C, and SP are used in Figure 3.

constrained to the condition $k_y \geq \omega\sqrt{\varepsilon_{||}}$. Next we consider the high-frequency band $\omega_2 < \omega < 1$ where $\varepsilon_{||} < 0 < \varepsilon_{\perp}$. The plot shown in Figure 2(c) corresponds to this case. The DLSW curve approaches the dispersion curve of the bulk extraordinary (e) wave, as is the case in Figures 2(a) and (b). In contrast, it crosses the dispersion curve of the e-wave at two different points, where the curve begins and ends. In comparison, the angular range of DLSW becomes significantly low.

Figure 3 shows the profiles of the magnetic field components B_x and B_z for the points A, B, and C, all highlighted in Figure 2. Also we include the field at the point SP shown in Figure 2(b), which corresponds to a conventional surface plasmon ($B_x = 0$).

For the cases A and B, the field caused by the large in-plane wavenumber of DLSW pattern remains tightly confined near the surface $x = 0$ within a few units of $1/k_p$; note that $k_z = 0.660$ for the point A and $k_z = 0.254$ for the point B. In contrast, the lowest confinement is produced at point C: $\mathbf{k}_D = [0,\ 0.25,\ 0.74]$ at $\omega = 0.70$. In this case, the dominant contribution of the extraordinary wave acts against localization near the surface.

3. ON VALIDITY OF EMA

In the previous section we have utilized EMA to represent MD multilayered metamaterial as a uniaxial plasmonic crystal. However, it was shown recently that EMA does not describe properly neither nonlocalities (even in the case of negligible losses) [6], nor it takes into account correctly metallic losses [7]. In fact, the MD layered nanostructure demonstrates strong optical nonlocality due to excitation of surface plasmon polaritons, depending on the thicknesses of the layers. The dispersion and diffraction properties of the periodic nanolayered metamaterial can be dramatically affected by strong coupling among surface plasmon polaritons excited at metal-dielectric interfaces.

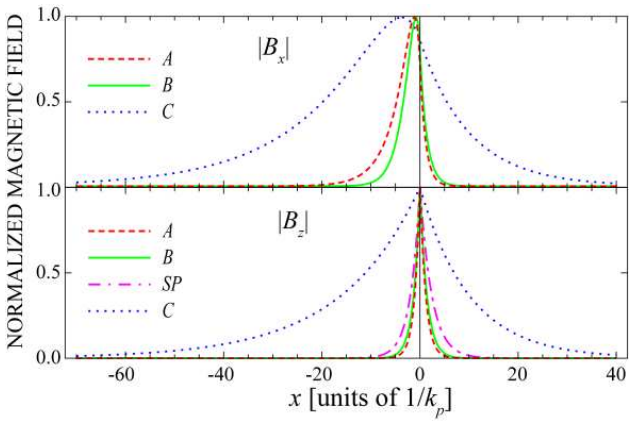

Figure 3: Variation of magnetic field components along the x-axis for the points A, B, and C highlighted in Figure 2. We include the point SP associated with pure TM^x surface waves.

In many cases, EMA produces results that are so different from the exact transfer-matrix method that they cannot be taken into account as small corrections [8]. In particular, the existence of an additional extraordinary wave has been revealed [7] which enables double refraction of TMz-polarized beam into negatively and positively refracted parts within the favourable frequency range. However, hyperbolic metamaterials require frequency ranges outside of the double refraction range.

The Bloch waves involved in the formation of the DLSW and caused by nonlocality in the nanostructured medium have an impact on the wave vector $\mathbf{k}_D$ at the interface $x = 0$, but also put additional constrains on this boundary. Since the introduction of an effective permittivity requires some kind of field averaging normally to the metal-dielectric layers, the excitation of evanescent fields in the isotropic medium would be fundamentally governed by the value of $\mathbf{k}_D$ which determines the attenuation constants. However, spatial dispersion also leads to strong field oscillations across the system [6–8]. This means that the conventional boundary conditions imposed by the Dyakonov dispersion equation are not valid anymore. Such a strong variation of the field is set on the scale of a single layer. Consequently, evanescent fields with spatial frequencies much higher than $\mathbf{k}_D$ will participate vigorously in the isotropic medium in the close vicinity of the boundary. Our FEM simulations using COMSOL Multiphysics software show that these high-frequency components of the field are concentrated near the edge of the metallic layers adjoining the isotropic medium.

4. CONCLUSION

Our theoretical and numerical analysis shows that various conditions can be designed to enable distinct regimes of DLSW propagation for various cases of isofrequency surfaces. In general, surface waves are hybrid TE-TM polarized, propagate obliquely to the optical axes within the certain range of angles, and are more tightly confined at the interface than the standard surface plasmon polaritons.

Dissipation due to losses in metallic layers and nonlocal effects due to finite layer width have been studied using the finite-element method by means of the COMSOL Multiphysics software. We would like to emphasize that a "red shift" appears in the propagation constant due to nonlocal effects. Furthermore, the fields are enhanced on the edges of the metallic films, as well as inside the dielectric nanolayers, lowering dissipation in lossy metamaterial. The imaginary part of the wavevector decreases sharply compared to EMA estimates, enabling much longer propagation lengths. Finally, it is worth noting that the properties of the surface states rapidly change with the refractive index of isotropic dielectric cladding, suggesting potential applications in imaging and chemical and biological sensing.

ACKNOWLEDGMENT

This research was funded by the Qatar National Research Fund under the project NPRP 09-462-1-074, by the Spanish Ministry of Economy and Competitiveness under the project TEC2009-11635, and by the Serbian Ministry of Education and Science under the projects III 45016 and TR 32008.

REFERENCES

1. Jacob, Z. and E. E. Narimanov, "Optical hyperspace for plasmons: Dyakonov states in metamaterials," *Appl. Phys. Lett.*, Vol. 93, No. 22, 221109–221111, 2008.
2. Vuković, S. M., I. V. Shadrivov, and Yu. S. Kivshar, "Surface bloch waves in metamaterial and metal-dielectric superlattices," *Appl. Phys. Lett.*, Vol. 95, No. 4, 041902–041904, 2009.
3. Dyakonov, M. I., "New type of surface waves propagating at an interface," *Sov. Phys. JETP*, Vol. 67, No. 4, 119–123, 1988.
4. Krishnamoorty, H. N. S., Z. Jacob, E. E. Narimanov, I. Kretzschmar, and V. M. Menon, "Topological transitions in metamaterials," *Science*, Vol. 336, 205–208, 2012.
5. Miret, J. J., C. J. Zapata-Rodriguez, Z. Jakšić, S. M. Vuković, and M. R. Belić, "Substantial enlargement of angular existence range for Dyakonov-like surface waves at semi-infinite metal-dielectric superlattice," *J. Nanophoton.*, Vol. 6, 063525-1–10, 2012.
6. Orlov, A. A., P. M. Voroshilov, P. A. Belov, and Yu. S. Kivshar, "Engineered optical nonlocality in nanostructured metamaterials," *Phys. Rev. B*, Vol. 84, No. 4, 045424-045424-4, 2011.
7. Orlov, A., I. Iorsh, P. Belov, and Yu. Kivshar, "Complex band structure of nanostructured metal-dielectric metamaterials," *Opt. Express*, Vol. 21, No. 2, 1593–1598, 2013.
8. Elser, J., V. A. Podolskiy, I. Salakhutdinov, and I. Avrutsky, "Nonlocal effects in effective-medium response of nanolayered metamaterials," *Appl. Phys. Lett.*, Vol. 90, No. 19, 191109.1–3, 2007.

High Quality Porous Silicon Multilayer Structures for Infra-red Applications

Z. Lazcano and J. Arriaga
Instituto de Física, Benemérita Universidad Autónoma de Puebla
18 Sur y San Claudio, Edif. 110 B, Ciudad Universitaria, Puebla 72570, México

Abstract— We present a systematic method to obtain homogeneous thick porous silicon (PSi) layers as well as multilayer structures by introducing etching breaks. During these breaks no current is applied and the electrochemical etching of the Silicon wafer stops several times during the whole process. The time length of the etch break, the number of repetitions of these breaks, and the total etching time are the parameters that we control to obtain mechanically stable structures with minimum chirp. Since periodic systems present well defined stop-bands in the optical reflectance, we determine the porosity of the constituent layers, by fitting them to the measured spectrum. By comparing the experimental spectrum with the obtained theoretically allow us to evaluate the quality of the samples. The sample thicknesses were measured by profilometry for thin layers (1–10 µm), meanwhile we used an optical microscope for thick layers (more than 20 µm). The theoretical simulations of the reflectivity spectrum in the PSi structures were performed using the transfer matrix method. Bruggeman's effective medium approximation was used to estimate the refractive index for layers with different porosities. The reflectance spectrum was measured by Fourier Transform Infrared (FTIR) spectrometry as a function of the wavelength in the near and mid infrared (MIR) range. We successfully grew thick porous silicon single layers with porosities from 43% to 73%, and a multilayer periodic structure with large refractive index mismatch for optical application in IR range or acoustic investigations in GHz frequencies.

1. INTRODUCTION

Porous silicon (PSi) based structures for optical applications in the visible and near infrared wavelength ranges (400–1600 nm) are constructed with layers with thicknesses of the order of nanometers, and they are widely studied and successfully fabricated. Examples of these structures include: Bragg reflectors, omnidirectional mirrors, Fabry-Perot microcavities, and rugate filters [1–3]. However, PSi structures for mid-infrared (MIR) applications require thicker samples, of the order of microns, and they are not easily obtained. However, it is well known that PSi layers prepared by electrochemical etching are not perfectly homogeneous throughout their depth, because during the PSi formation on p-doped substrates the microstructure and the porosity of the layers change with depth [4, 5]. This effect becomes significant for layer thicknesses of the order of microns.

Porous silicon layers with high homogeneity are very important for different applications such as biosensors in the IR range, or ultrasonic devices in the GHz interval of frequencies [6, 7]. With this in mind, in this work we present a systematic method to obtain thick homogeneous PSi layers, as well as multilayer structures. The homogeneity of the porous silicon layers depends mainly on two aspects: a chemical dissolution of silicon in the electrolyte [8], and changes in HF concentration during the anodization process [9–11].

According to the most accepted models for the formation of PSi, the dissolution of the Silicon takes place at the bottom of the pores and as a result of the chemical reaction, an excess of hydrogen H_2 escapes in form of bubbles through the electrolyte solution [8, 12, 13]. This hydrogen bubbles leads to a limitation in the diffusion of the electrolyte producing changes in the HF concentration, increasing the porosity and reducing the etch rate. Therefore, the depletion of HF at the tips of the pore leads to thinner layers with higher porosities.

2. EXPERIMENTAL DETAILS

The effect of the HF depletion at the tips of the pores can be observed in the Bragg mirror of Figure 1. This mirror was fabricated according to the standard procedure of applying periodically two different constant current densities. We observe thinner layers when we move to the substrate side, the right side in this figure, because the etch rate changes when the HF drops. The thicknesses of the layers get smaller than expected and the drop in the HF concentration produces higher porosities. For the Bragg mirror of Figure 1, the thickness of the layer with low porosity (light

region) changes in 4% throughout the whole mirror, from 1.72 µm at the top to 1.65 µm at the bottom. On the other hand, the layers with high porosity (dark regions in Figure 1) change dramatically, from 4.6 µm at the top, to 3.08 µm at the bottom, i.e., a 34% throughout the whole mirror. These high porous layers are marked by arrows in the figure to guide the eye. In order to obtain homogeneous thick samples, it is necessary to maintain the etch rate constant. This can be done by introducing etching breaks where no current is applied, stoping the electrochemical etching, and allowing the excess of hydrogen to escape in order to recover the original HF concentration. In this work, we analyze the time length of these etch breaks, the number of repetition of the breaks, and the total etching time, in order to obtain thick homogenous structures.

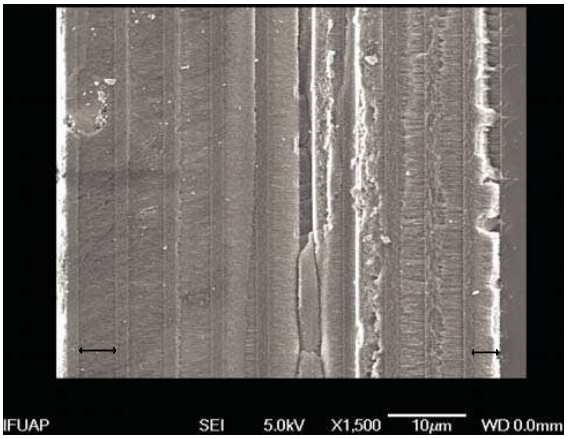

Figure 1: SEM micrography of the Bragg mirror fabricated without etch breaks. The structure consists of 10 periods of two layers (low and high porosity). We can observe thinner layers towards the substrate (at the right in the image) due to the etch rate reduction.

3. RESULTS

The samples analyzed in this work were fabricated by electrochemical etching of boron doped silicon wafers with 0.007–0.013 Ω· cm resistivity and (100) orientation. The wafers were etched with an electrolyte consisting of HF (40%) and ethanol (99.98%) in the volumetric ratio 1 : 1. The thicknesses of the samples were determined by profilometry for thin layers (1–10 µm), and using an optical microscope for layers with thicknesses larger than 20 µm. We used scanning electron microscope (SEM) to corroborate some measurements. The theoretical simulations of the reflectivity were performed using the transfer matrix method (TMM) [14]. To estimate the refractive index corresponding to layers with different porosities, we used the Bruggeman's effective medium approximation [15]. The reflectance spectrum was measured by a Bruker Equinox 55 Fourier Transform Infrared (FTIR) spectrometer as a function of the wavelength in the MIR range (1–12 µm) using unpolarized light and an angle of incidence of 20°. The porosities of the layers were obtained by fitting the theoretical reflectance curves with those measured.

In Figure 2 we show the etch rate and the average porosity as a function of the etching time for different current densities for layers with thicknesses from 2 µm to 100 µm. These results show the general accepted trends for the PSi formation from p-type Si wafers, i.e., higher current densities lead to higher porosities as well as a dramatically reduction of the etch rate [16]. From the figure, we observe that without any etch break, the etch rate decreases in time, and this reduction is more important for higher current densities. This reduction of the etch rate is due to the excess of hydrogen bubbles in the porous, as it was mentioned above. Before fabricate periodic homogeneous structures, we growth different single layers changing the etching conditions and keeping constant both, the current density and the etching time. The etching conditions were changed by introducing a number of breaks, were no density current was applied for a certain time (break time), in the electrochemical etching. This was done to measure the effect of the number and length of the applied breaks. In Table 1 we present the measured thickness and the determined porosity for different etching conditions. The samples were obtained by applying a current density (183 mA/cm^2) during a certain time, denoted here as step length, and then the density current is interrupted during certain time, denoted here as break time. This procedure is repeated until the total electrochemical time is reached, 5 minutes for all the samples considered here.

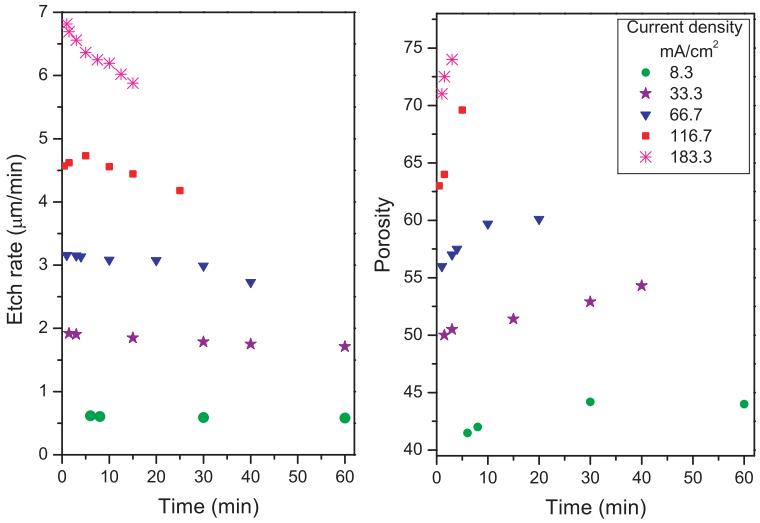

Figure 2: Etch rate and porosity as a function of time for different current densities. We can observe that for high current densities the etch rate get smaller at longer times. In the right figure we observe that the porosity increases with time for high current densities.

For all the samples, we compare the measured reflectance spectrum with the obtained theoretically considering a layer with an homogeneous porosity. The value of the porosity that reproduces better the spectrum appears in the fourth column of Table 1. For the first sample, obtained without any etch break, the reflectance spectrum is very irregular,corresponding to a non-homogeneous layer, and it cannot be adjusted theoretically. The same occurs for the sample denoted as A, obtained by applying the density current during 300 steps of one second followed by a break time of 10 seconds. For this sample, the applied etch breaks has not been enough to correct the gradient in the porosity, and it is not possible to adjust the reflectance spectrum. Samples denoted as B, C, D, and E, were obtained by applying the current density during 0.5, 0.4, 0.2, and 0.1 seconds, and interrupting the current during break times of 5 seconds for sample B, and 2 seconds for the others, as observed in Table 1. In the last column of Table 1, we present the measured thickness obtained using an optical microscope. From Table 1, we observe that the average porosity get smaller when we reduce the time during which the current is applied, except for sample E. For this sample, we obtained the highest porosity and the lowest thickness, due to the reduction of the etching rate and to the etching far away from the etch front [8]. From the results of Table 1, we consider as optimal growing conditions for thick samples with high porosity, the associated to sample D. As we can observe from Figure 2, if we applied a low current density, we obtain layers with low porosity for which its etching rate is almost constant.

Using the previous information about the number and duration of the etch breaks, we fabricate a periodic structure appropriate for acoustic applications or optical devices in the infrared part of the electromagnetic spectrum. As we mentioned before, this kind of periodic structures must include thick layers. Using the fact that periodic systems present well defined band gaps in the optical reflectance spectrum, we can compare the experimental results with those obtained from our simulations considering perfect homogeneous layers. In Figure 3, we present the reflectance

Table 1: Step length and break time used to fabricate homogeneous single layers. The average porosity and thicknesses correspond to those used in the simulations to reproduce the measured spectra.

sample	Step length (s)	Break time (s)	Average Porosity (%)	Measured thickness (μm)
Normal	300	-	-	31.8
A	1.0	10.0	-	33.6
B	0.5	5.0	78.0	33.4
C	0.4	2.0	73.1	33.5
D	0.2	2.0	72.1	37.8
E	0.1	2.0	76.8	35.7

spectrum for a Bragg mirror obtained by the periodic sequence of two layers with high and low porosity, repeated 10 times. Our periodic structure consists of two layers denoted as A and B, repeated periodically. For the low porosity layers (A) we introduced etch breaks to avoid the buildup of hydrogen bubbles, although the effect of the etch breaks is not very important in this case. The layer A has a thickness of 0.95 µm and a porosity of 47%, and was obtained by applying the current density (11.6 mA/cm^2) during 30 steps of 2.3s and interrupting the current during 2 s (break time). The layer B was obtained by 90 steps of 0.2 s using a current density of 185.4 mA/cm^2, each step followed by a etch break of 2 s. The thickness of B layer is 1.88 µm and its porosity is 77.8%. The total thickness of the structure is 28.6 µm, corresponding to the measured value. In the figure we show the reflectance as a function of the wavelength from 1.0 µm to 12.0 µm (i.e., in the near and mid infrared). The solid line corresponds to the theoretical simulation for a periodic homogeneous structure using the transfer matrix method with the parameters mentioned before. The doted line is the measured spectrum for the periodic structure fabricated without any breaks, i.e., applying a constant current density during the whole etching time. The dashed line corresponds to the structure fabricated by applying etching breaks in order to maintain the etch rate constant to ensure homogeneous porosity in both layers along the whole structure. As we can observe, there is an excellent agreement between the theoretical results and the measured spectrum. We observe a very well defined gap extending from 8000 to 11000 nm. This gap corresponds to the first photonic gap of the structure according to the parameters used in the fabrication, thicknesses and refractive indexes, and is located in the mid infrared part of the electromagnetic spectrum.

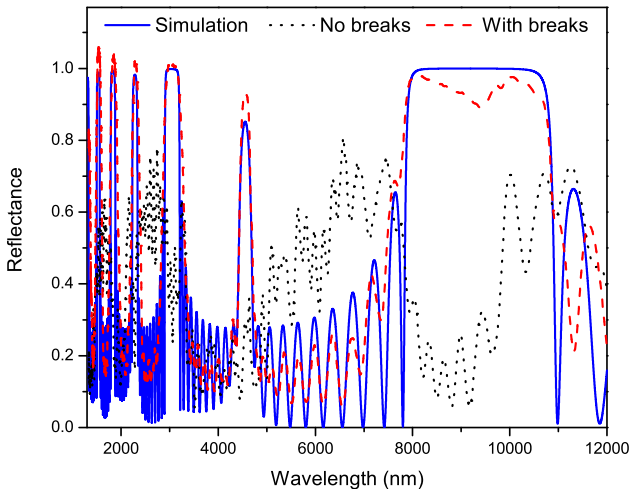

Figure 3: Reflectance spectrum of the periodic system studied in this work. Dotted line corresponds to the system fabricated using the "standard" electrochemical etching (no etch breaks), dashed line corresponds to the structure obtained by applying a constant current density during a certain number of time steps, and applying an etch break after each time step. Solid line is the theoretical spectrum obtained considering homogeneous porous layers. Observe the excellent agreement in the spectra between the theoretical and the "etched" structure.

4. CONCLUSION

We successfully fabricated thick porous silicon multilayer structures with large refractive index mismatch for optical applications in IR range and with possible acoustic applications in GHz frequencies. By introducing etch breaks we achieve samples in good agreement with theoretical simulations. We found optimal etching conditions: number and length of etch breaks for different porosities.

ACKNOWLEDGMENT

This work has been partially supported by Conacyt-México under grant number 167939.

REFERENCES

1. Estevez, J. O., J. Arriaga, A. Méndez-Blas, and V. Agarwal, "Omnidirectional photonic bandgaps in porous silicon based mirrors with a Gaussian profile refractive index," *Appl. Phys.*

Lett., Vol. 93, 191915, 2008.
2. Reece, P. J., G. Lérondel, W. H. Zheng, and M. Gal, "Optical microcavities with subnanometer linewidths based on porous silicon," *Appl. Phys. Lett.*, Vol. 81, 4895–4897, 2002.
3. Ishikura, N., M. Fujii, K. Nishida, S. Hayashi, J. Diener, "Dichroic rugate filters based on birefringent porous silicon," *Opt. Express*, Vol. 16, 15531–15539, 2008.
4. Foss, S. E., P. Y. Y. Kann, and T. G. Finstad, "Single beam determination of porosity and etch rate in situ during etching of porous silicon," *J. Appl. Phys.*, Vol. 97, 114909-1–114909-11, 2005.
5. Thönissen, M., M. G. Berger, S. Billat, R. Arens-Fischer, M. Krüger, H. Lüth, W. Theis, S. Hillbrich, P. Grosse, G. Lerondel, and U. Frotscher, "Analysis of the depth homogeneity of p-PS by reflectance measurements," *Thin Solid Films*, Vol. 297, 92–97, 1997.
6. Aliev, G. N., B. Goller, D. Kovalev, and P. A. Snow, "Hypersonic acoustic mirrors and microcavities in porous silicon," *Appl. Phys. Lett.*, Vol. 96, 124101, 2010.
7. Thomas, L., G. N. Aliev, and P. A. Snow, "Hypersonic rugate filters based on porous silicon," *Appl. Phys. Lett.*, Vol. 97, 173503, 2010.
8. Smith, R. L. and S. D. Collins, "Porous silicon formation mechanisms," *J. Appl. Phys.*, Vol. 71, R1–R22, 1992.
9. Lehmann, V., "The physics of macropore formation in low doped n-type silicon," *J. Electrochem. Soc.*, Vol. 140, 2836–2843, 1993.
10. Billat, S., M. Thönissen, R. Arens-Fischer, M. G. Berger, M. Krüger, and H. Lüth, "Influence of etch stops on the microstructure of porous silicon layers," *Thin Solid Films*, Vol. 297, 22–25, 1997.
11. Thönissen, M., S. Billat, M. Kürger, H. Lüth, M. G. Berger, U. Frotscher, and U. Rossow, "Depth inhomogeneity of porous silicon layers," *J. Appl. Phys.*, Vol. 80, 2990–2993, 1996.
12. Canham, L. T., "Silicon quantum wire array fabrication by electrochemical and chemical dissolution of wafers," *Appl. Phys. Lett.*, Vol. 57, 1046–1048, 1990.
13. Lehmann, V. and U. Gosele, "Porous silicon formation — A quantum wire effect," *Appl. Phys. Lett.*, Vol. 58, 856–858, 1991.
14. Pochi, Y., *Optical Waves in Layered Media*, Jhon Wiley and Sons, New York, 1988.
15. Khardani, M., M. Bouaïcha, and B. Bessaïs, "Bruggeman effective medium approach for modelling optical properties of porous silicon: Comparison with experiment," *Phys. Status Solidi C*, Vol. 4, 1986–1990, 2007.
16. Gaburro, Z., "Interferometric method for monitoring electrochemical etching of thin films," *J. Electrochem. Soc.*, Vol. 150, C381–C384, 2003.

A Metal-dielectric Composited Film Applied to Enhance the Fluorescence Imaging

Taikei Suyama[1], **Xiaowei Ji**[2], **and Yaoju Zhang**[3]

[1]Department of Electrical and Computer Engineering, Akashi National College of Technology Akashi, Japan
[2]Graduate School of Science and Technology, Kumamoto University, Kumamoto, Japan
[3]Department of Physics and Electronic Information, Wenzhou University, Wenzhou, China

Abstract— Fluorescence labeling is the prevailing imaging technique in cell biology research. When they involve statistical investigations on a large number of cells, experimental studies require both low magnification to get a reliable statistical population and high contrast to achieve accurate diagnosis on the nature of the cells' perturbation. Because microscope objectives of low magnification generally yield low collection efficiency, such studies are limited by the fluorescence signal weakness. To overcome this technological bottleneck, E. Le Moal and E. Fort, et al. proposed a method based on metal-coated substrates that enhanced the fluorescence process and improved collection efficiency in fluorescence microscope observation and that could be directly used with a common microscope setup. In this paper, we use an Ag-Si_3N_4-Ag multilayer film coated on the substrate and numerically analysis the optical behavior of a fluorophore which was placed above the composited film coated on the substrate. The results shows, using an Ag-Si_3N_4-Ag composited film, the fluorescence imaging can be enhanced markedly.

1. INTRODUCTION

Many biological studies and applications involve biomolecule detection by means of fluorescence. The use of fluorescent markers is notably the most widespread labeling technique for cell imaging. A large range of fluorophores with distinctive spectral characteristics are available, providing many possibilities for multi-color biological labeling. Using a multicolor set of functionalized dyes (biomarkers) and appropriate optical filters, one can selectively image parts of the cell or track several active biomolecules inside the cell. However, the extinction coefficient of these fluorescent molecules is relatively weak compared with those of fluorescent nanoparticles. Consequently, the detection of low concentrations of fluorophores is limited by the weakness of the fluorescence signal. Another drawback of molecular fluorophores is their low photostability. When an assembly of fluorophores is continuously excited, their emitted light progressively fades as light induces their destruction. Signal intensities can then hardly be standardized.

Signal weakness and photoreactivity have been partly overcome as a result of recent progress in the use of semiconductor nanocrystals, commonly called quantum dots, in biology. However, they introduce new problems such as blinking of the emission signal and low biocompatibility that restrict the scope of in vivo applications.

Despite the increasing interest raised by fluorescent nanoparticles, the use of fluorescent molecules as markers for biomedical applications still has relevance and attractiveness. In addition to the development of new fluorescent markers, the renewed interest in standard molecular fluorophores had been motivated by the development of innovative optical techniques for fluorescence enhancement.

During the recently years, metal surfaces play a unique role in many biomolecular techniques such as the self-assembly and self-organization of proteins and lipids [1, 2]. A thin metal film can produce the surface plasmon-coupled emission (SPCE). The surface plasmon-coupled emission method was proposed as a high sensitivity and efficient fluorescence detection method by Lakowicz, et al. [3, 4]. They showed, through imaging fluorophores near to a silver-coated glass substrate, that the fluorescence emission was highly directional and this increased the collection efficiency to nearly 50%, as well as contributed to low background noise. SPCE has found a number of applications in areas such as biotechnology and biological measurements [5, 6].

In this work, we consider fluorophores placed above an Ag-Si_3N_4-Ag multilayer film surface and describe the physical mechanisms of fluorescence enhancement. To do so, the optical behavior of the fluorophores was simulated implementing a simple electric-dipole model.

2. THEORY

As shown in Fig. 1, we assume that the oil filled in between the objective lens and the cover glass has the same refractive index with the cover glass, a metal-dielectric multilayer film is coated on the cover glass. Fluorescent molecule is located near the focal point of the objective lens at a distance d from the metal-dielectric multilayer film surface. In order to efficiently excite the fluorescence, in this paper, we consider a radially polarized beam incident on the objective lens.

2.1. Excitation of Dipole in the Object Space

Using the method proposed by P. Török [7, 8], the excitation field E_w in the object space is simply given by

$$E_w = \begin{bmatrix} E_{w,r} \\ E_{w,\varphi} \\ E_{w,z} \end{bmatrix} = \begin{bmatrix} i\int_0^{\theta_{g,\max}} t_p \cos\theta_w \sqrt{\cos\theta_g} \sin\theta_g J_1\left(k_g r \sin\theta_g\right) \exp\left(i\Phi\right) \exp\left[ik_w z \cos\theta_w\right] d\theta_g \\ 0 \\ -i\int_0^{\theta_{g,\max}} t_p \sin\theta_w \sqrt{\cos\theta_g} \sin\theta_g J_0\left(k_g r \sin\theta_g\right) \exp\left(i\Phi\right) \exp\left[ik_w z \cos\theta_w\right] d\theta_g \end{bmatrix} \tag{1}$$

where $\theta_{g,\max}$ is the focusing angle of objective lens. Obviously, as the dipole is excited by a p-polarized incident plane wave, the electric field component in the direction of the polar angle is zero.

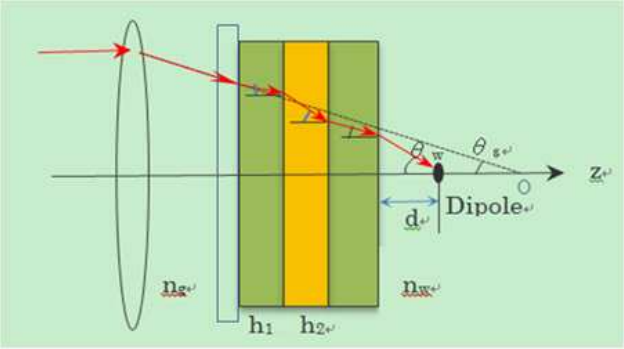

Figure 1: Focusing of excitation light passing through the multilayer films.

2.2. Electric Field in the Image Space

With the vector diffraction theory and some methods that proposed by Wolf, Arnoldus and Foley, et al. [9–13], we can obtain the expression of the electric field E_a in the image space. It is simply given by

$$E_a(r,\varphi,z) = \begin{bmatrix} E_{a,r} \\ E_{a,\varphi} \\ E_{a,z} \end{bmatrix} = \begin{bmatrix} -\frac{ik_a}{2}\left\{\mu \sin\theta_d \cos\left(\phi_d-\varphi\right)\left[K_0^I + K_2^I\right] - \mu\cos\theta_d\left[2iK_1^I\right]\right\} \\ -\frac{ik_a}{2}\left\{\mu \sin\theta_d \sin\left(\phi_d-\varphi\right)\left[K_0^I - K_2^I\right]\right\} \\ -\frac{ik_a}{2}\left\{\mu \sin\theta_d \sin\left(\phi_d-\varphi\right)\left[K_0^I - K_2^I\right] - \mu\cos\theta_d\left[2iK_0^\Pi\right]\right\} \end{bmatrix} \tag{2}$$

where

$$\begin{aligned}
K_0^I &= \int_0^\sigma \sqrt{\frac{\cos\theta_a}{\cos\theta_g}} \sin\theta_a \left(\tau_s + \tau_p \cos\theta_w \cos\theta_a\right) J_0\left(k_a r \sin\theta_a\right) \exp\left(ik_a z\cos\theta_a\right) \exp\left(i\Phi\right) d\theta_a \\
K_1^I &= \int_0^\sigma \sqrt{\frac{\cos\theta_a}{\cos\theta_g}} \sin\theta_a \times \tau_p \sin\theta_w \cos\theta_a J_1\left(k_a r \sin\theta_a\right) \exp\left(ik_a z\cos\theta_a\right) \exp\left(i\Phi\right) d\theta_a \\
K_2^I &= \int_0^\sigma \sqrt{\frac{\cos\theta_a}{\cos\theta_g}} \sin\theta_a \left(\tau_s - \tau_p \cos\theta_w \cos\theta_a\right) J_2\left(k_a r \sin\theta_a\right) \exp\left(ik_a z\cos\theta_a\right) \exp\left(i\Phi\right) d\theta_a \\
K_0^\Pi &= \int_0^\sigma \sqrt{\frac{\cos\theta_a}{\cos\theta_g}} \sin\theta_a \times \tau_p \sin\theta_w \sin\theta_a J_0\left(k_a r \sin\theta_a\right) \exp\left(ik_a z\cos\theta_a\right) \exp\left(i\Phi\right) d\theta_a \\
K_1^\Pi &= \int_0^\sigma \sqrt{\frac{\cos\theta_a}{\cos\theta_g}} \sin\theta_a \times \tau_p \cos\theta_w \sin\theta_a J_1\left(k_a r \sin\theta_a\right) \exp\left(ik_a z\cos\theta_a\right) \exp\left(i\Phi\right) d\theta_a
\end{aligned} \tag{3}$$

where $J_n(\cdot)$ is the Bessel function of the first kind of n order, Φ is the wavefront aberration function, the subscript w, a, g denote that the variable quantity locate in the objective space, the imaging space and the space between the objective lens and the cover glass respectively.

2.3. Intensity in Image Space

The intensity that is detected in the image space is

$$I \propto \left(|E_{a,r}|^2 + |E_{a,\varphi}|^2 + |E_{a,z}|^2\right) \Big/ P_T \tag{4}$$

where the normalization factor P_T is the total power emitted by the dipole in the presence of a metal interface [14, 15]. For a dipole which is perpendicularly oriented to the metal interface, $\theta_d = 0°$, the intensity is rotationally symmetric

$$I_\perp \propto 4\left(\left|K_1^I\right|^2 + \left|K_0^\Pi\right|^2\right) \Big/ P_T \tag{5}$$

On the other hand, the image of a dipole which has an orientation parallel to the metal interface along the x direction is not rotationally symmetric, that is, it has a dependence on ϕ

$$I_{||} \propto \left(\left|K_0^I\right|^2 + \left|K_2^I\right|^2 + 4\cos^2\varphi\left|K_1^\Pi\right|^2 + 2\cos 2\varphi \mathrm{Re}\left[K_0^I K_2^{I*}\right]\right)/P_T \tag{6}$$

3. NUMERICAL RESULTS

We assume that the thickness of the metal film and the dielectric film are h_1 and h_2, respectively. h is the distance between the interface and the geometric focus of the objective lens, and $\theta_{g,\max} = 60°$, $d = 20\,\mathrm{nm}$. In this paper, we assume the metallic material is silver (Ag), which have different refractive indexes of exciting light and emitted light. As our numerical results showed that, the larger the refractive index of the dielectric film between the metal films was, the more beneficial to strengthen the two-way transmissions of light. To this end, we take a high refractive index material of amorphous silicon (Si_3N_4). At first, we make a comparison of the maximal intensity of the focused light spot in two cases: one is using an Ag-Si_3N_4-Ag multilayer film coated on the cover glass, another is using a single-layer metal film. As shown as in Fig. 2, we can see that, in the first case of using the Ag-Si_3N_4-Ag multilayer film, when $h = -2h_1 - h_2 = 47.5\,\mathrm{nm}$, the intensity of focused light spot obtains the maximum value $|E_w|^2_{\max} = 0.616$. And in the case of using a single metal film, when $h_1 = 44\,\mathrm{nm}$, $h = -21\,\mathrm{nm}$, the intensity of the focused light spot obtains the maximum value, $|E_w|^2_{\max} = 2.446 \times 10^{-3}$. Here the negative h means that the right surface of the Ag-Si_3N_4-Ag multilayer film should be in the right side of the geometric focus of the objective lens, as shown as in Fig. 1. It is obvious that the intensity of the spot center can be enhanced by about 251 times using an Ag-Si_3N_4-Ag multilayer film coated on the cover glass than the single-layer metal film.

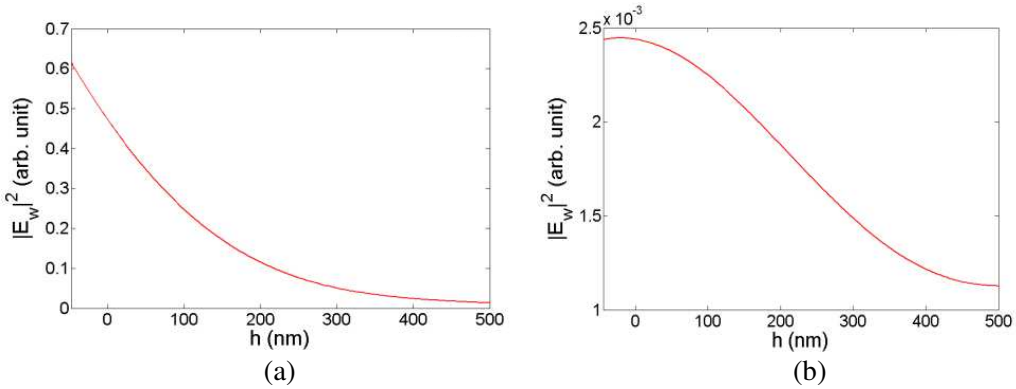

Figure 2: Intensity at the electric dipole versus the distance h between the interface and geometric focus. (a) The case of the Ag-Si_3N_4-Ag multilayer film, (b) the case of the single-layer metal film.

As shown as in Fig. 3, we compared the normalized imaging intensity of emission by the dipole along the x direction in the focal plane in the case of using two different films: an Ag-Si_3N_4-Ag multilayer film and a single-layer metal film. Orientation angles of the dipole are $\theta_d = \varphi_d = 0°$.

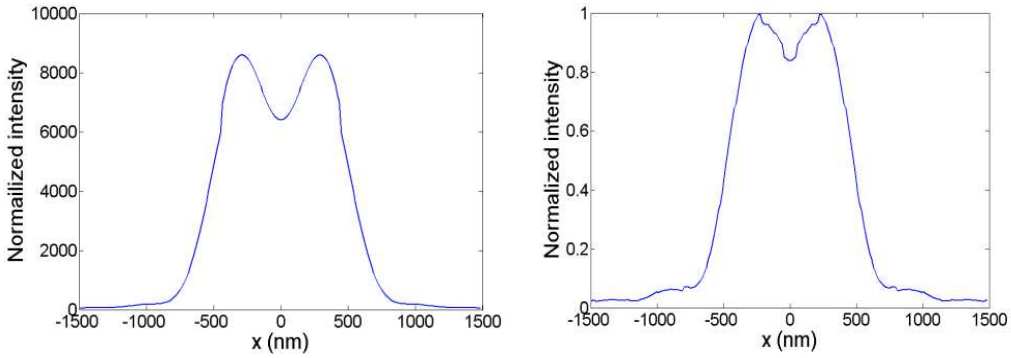

Figure 3: Normalized intensity of emission by a dipole along the x direction in the focal plane of $z = 0$. (a) The multilayer film with $h_1 = 5.25\,\text{nm}$ and $h_2 = 37\,\text{nm}$, (b) the single-layer metal film with $h_1 = 44\,\text{nm}$.

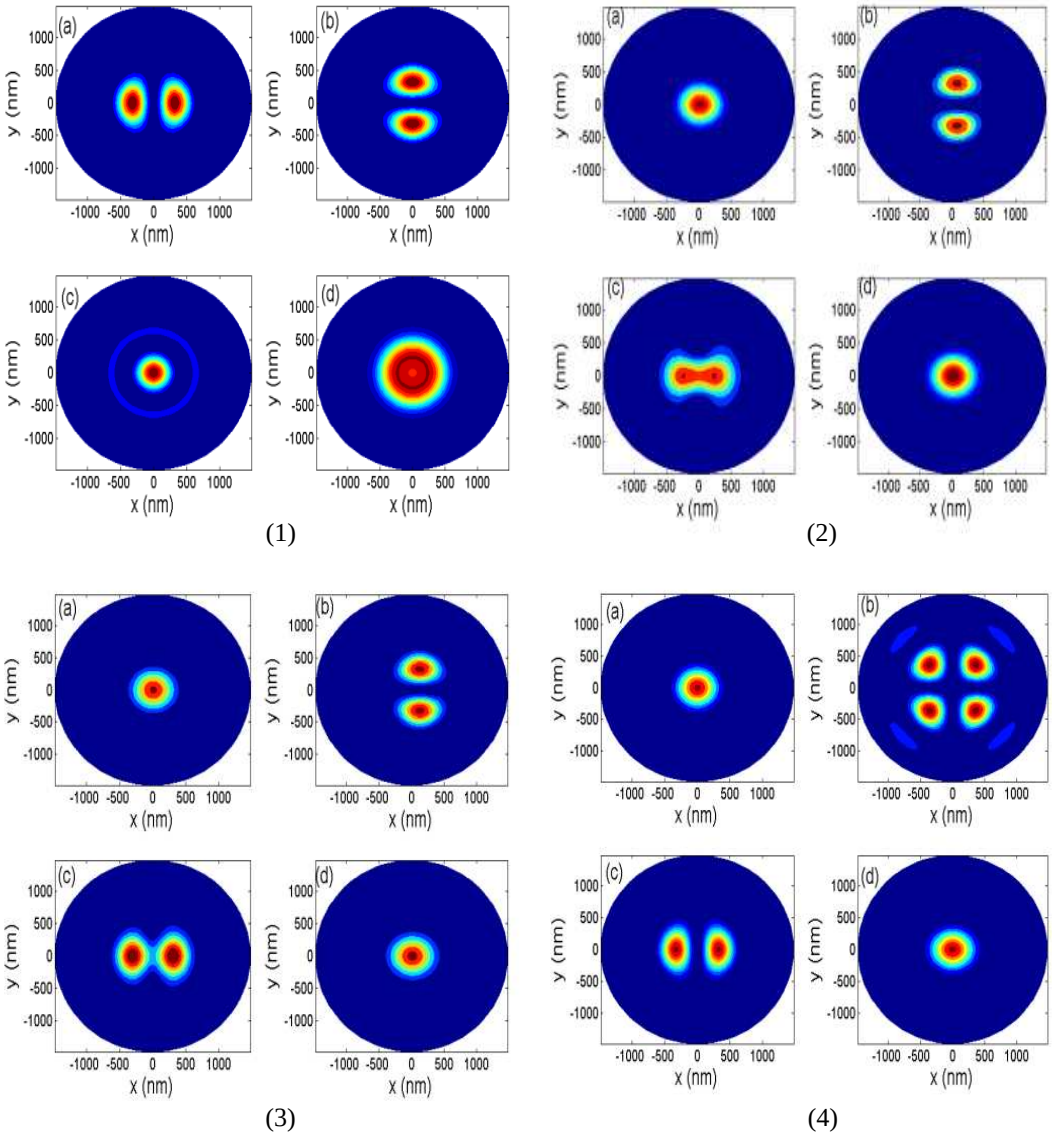

Figure 4: Intensity distribution of emission by a dipole with different orientation angles in the focal plane in image space. (1) $\theta_d = \varphi_d = 0°$; (2) $\theta_d = \frac{\pi}{4}, \varphi = 0°$; (3) $\theta_d = \frac{\pi}{3}, \varphi_d = 0°$; (4) $\theta_d = \frac{\pi}{2}, \varphi_d = 0°$. (a), (b) and (c) are the component intensities of $|E_{ax}|^2, |E_{ay}|^2$ and $|E_{az}|^2$, respectively, (d) is the total intensity of $|E_{ax}|^2 + |E_{ay}|^2 + |E_{az}|^2$.

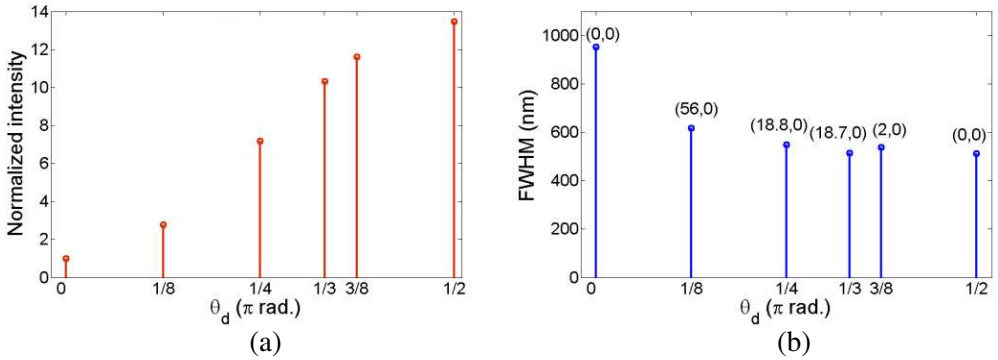

Figure 5: Central intensity (a) of spot and its FWHM, (b) for the total intensity versus the pole angle of the dipole, where numbers atop each lines denote the (x, y) coordinates of the spot center.

Intensities are normalized to the maximum imaging intensity in case of using the single-layer metal film. The figure shows, using the Ag-Si_3N_4-Ag multilayer film coated on the cover glass, the imaging intensity of the fluorescence can be enhanced by thousands of times than using a single-layer metal film. This may overcome the drawback of molecular fluorophores such as signal weakness and photoreactivity.

Then we study the correlation between imaging facula and orientation of a single dipole. The intensity distributions of emitted light by a dipole with different orientation angles on the focal plane in imaging space are shown in Fig. 4. In these figures, we represented the intensity distributions of components $|E_{ax}|^2, |E_{ay}|^2$, $|E_{az}|^2$ and the total intensity of $|E_{ax}|^2 + |E_{ay}|^2 + |E_{az}|^2$ with different orientation angles. Comparing these charts of the intensity distribution, despite the imaging intensity distributions of the dipole with different orientations have a same looks, the strength and the size of the light spot are different.

Finally, we study the light intensity of the total light intensity imaging facula center and the full width at half maximum versus the pole angle of dipole. As shown as in Fig. 5, with the increase of dipole azimuth (electric dipole moment by parallel optical axis to the vertical axis), the intensity of the light spot is increased gradually. When the dipole moment is parallel to the optical axis, the size of the imaging facula is larger. When the dipole moment is perpendicular to the optical axis, the size of the imaging facula is smaller. If a polarizer is placed in front of the detector, the imaging of x or y polarization component can be obtained. The intensity patterns $(|E_{ax}|^2, |E_{ay}|^2)$ of x and y polarization component or the positions change with the azimuth θ_d. These results indicate that, using a metal-dielectric multilayer film, a single dipole can be detected. And this can be used in many optical devices.

4. CONCLUSION

In this paper, we consider fluorophores placed above an Ag-Si_3N_4-Ag multilayer film surface and describe the physical mechanisms of fluorescence enhancement. The optical behavior of the fluorophores was simulated implementing a simple electric-dipole model and compared the results with a single-layer metal film. The results shows, using a metal-dielectric multilayer film, the intensity of the spot center can be enhanced by 251 times than using a single-layer metal thin film. And the intensity of the fluorescence imaging can be increased by thousands of times. With the increase of dipole azimuth (electric dipole moment by parallel optical axis to the vertical axis), the intensity of the light spot is increased gradually. This may overcome the shortcomings of traditional fluorescence such as low imaging intensity and difficulty to detect.

REFERENCES

1. Moal, E. L., E. Fort, and S. Leveque-Fort, et al., "Enhanced fluorescence cell imaging with metal-coated slides," *Biophysical Journal*, 2150–2161, March 2007.
2. Suyama, T. and Y. Okuno, "Enhancement of TM-TE mode conversion caused by excitation of surface plasmons on a metal grating and its application for refractive index measuremen," *Progress In Electromagnetics Research*, Vol. 72, 91–103, 2007.
3. Lakowicz, J. R., "Directional surface plasmon-coupled emission: A new method for high sensitivity detection," *Biochem. and Biophys. Res. Comm.*, Vol. 307, No. 3, 435–439, 2003.

4. Lakowicz, J. R., "Radiative decay engineering. 3. Surface plasmon-coupled directional emission," *Anal. Biochem*, Vol. 324, No. 2, 153–169, 2004.
5. Stefani, F. D., K. Vasilev, N. Bocchio, N. Stoyanova, and M. Kreiter, "Surface-plasmonmediated single-molecule fluorescence through a thin metallic film," *Phys. Rev. Lett.*, Vol. 94, No. 2, 023005-4, 2005.
6. Tang, W. T., E. Chung, Y. H. Kim, P. T. C. So, and C. J. R. Sheppard, "Investigation of the point spread function of surface plasmon-coupled emission microscopy," *Opt. Express*, Vol. 15, No. 8, 4634–4646, 2007.
7. Török, P., P. Varga, Z. Laczik, and G. R. Booker, "Electromagnetic diffraction of light focused through a planar interface between materials of mismatched refractive indices: Structure of the electromagnetic field," *J. Opt. Soc. Am. A*, Vol. 12, No. 2, 325–332, 1995.
8. Van de Nes, A., L. Billy, S. Pereira, et al., "Calculation of the vectorial field distribution in a stratified focal region of a high numerical aperture imaging system," *J. Opt. Express*, Vol. 12, No. 7, 1281–1293, 2004.
9. Richards, B. and E. Wolf, "Electromagnetic diffraction in optical systems. II. Structure of the image field in an aplanatic system," *Proc. Roy. Soc. (London) A*, Vol. 253, 358–379, 1959.
10. Török, P., P. D. Higdon, and T. Wilson, "Theory for confocal and conventional microscopes imaging small dielectric scatterers," *J. Mod. Opt.*, Vol. 45, 1681–1698, 1998.
11. Török, P., P. Varga, Z. Laczik, and G. R. Booker, "Electromagnetic diffraction of light focused through a planar interface between materials of mismatched refractive indices: An integral representation," *J. Opt. Soc. Am. A*, Vol. 12, 325–332, 1995.
12. Higdon, P. D., P. Török, T. Wilson, and J. Microsc, "Imaging properties of high aperture multiphoton fluorescence scanning optical microscopes," *Journal of Microscopy*, Vol. 193, No. 2, 127–141, February 1999.
13. Arnoldus, H. F. and J. T. Foley, "Transmission of dipole radiation through interfaces and the phenomenon of anti-critical angles," *J. Opt. Soc. Am. A*, Vol. 21, 1109–1117, 2004.
14. Enderlein, J. and M. Böhmer, "Influence of interface-dipole interactions on the efficiency of fluorescence light collection near surfaces," *Opt. Lett.*, Vol. 28, 941–943, 2003.
15. Hellen, E. H. and D. Axelrod, "Fluorescence emission at dielectric and metal-film interfaces," *J. Opt. Soc. Am. B*, Vol. 4, 337–349, 1987.

Generation of Difference-frequency Radiation by Spatially Limited Few-cycle Laser Pulse in Thin Crystal of GaAs

A. A. Hakhoumian[1], **R. M. Martirosyan**[2, 3, 4], **and G. D. Hovhannisyan**[2, 3]

[1]Ashtarak Institute of Radiophysics & Electronics
Alikhanian Bros., 1, IRPhE, Ashtarak 378410, Armenia
[2]Department of Radiophysics, Yerevan State University
A. Manoogian St., Yerevan 375049, Armenia
[3]Department of Microwave Engineering and Communication
Yerevan State University, A. Manoogian St., Yerevan 375049, Armenia
[4]National Academy of Sciences of Armenia
24 Marshal Baghramian Ave., Yerevan 0019, Armenia

Abstract— For theoretical description of difference frequency radiation (DFR) generation due to the interaction of a spatially limited linearly-polarized few-cycle laser pulse with a nonlinear crystal, the diffractive spatial and dispersive temporal spreadings of a broadband laser pulse should be taken into account, which in its turn leads to imposing a limit on the crystal length. At the same time it's evident that decreasing the thickness of nonlinear crystal will allow decreasing the temporal dispersive spreading. At nonlinear interaction of a few-cycle laser pulse with a nonlinear crystal, some pairs of frequency components may be extracted the mixing of which results in DFR generation. For efficient generation of DFR pulses in the process of nonlinear interaction of the spatially limited few-cycle duration pulse, the beam waist variation should be negligible during propagation in nonlinear crystal. In this work we present the results of theoretical study and computational modelling of the DFR generation by interaction of spatially limited few cycle laser pulses with a GaAs thin crystal. We have performed numerical time-integration of the system of nonlinear Maxwell equations by the finite-difference method. We considered the laser pulse with central wavelength 1.98 μm, duration 17 fs, beam waist 10 μm, electric field amplitude 100 MV/m and intensity 3.93 GW/cm^2, propagating along the normal to the ⟨110⟩ plane in 14.7 μm thick GaAs crystal. In the nonlinear part of the medium polarization we take into account the second-order instantaneous nonlinear susceptibility. The action of the beam waist variation on the DFR efficiency generation is studied.

1. INTRODUCTION

At nonlinear interaction of a few-cycle laser pulse with a nonlinear crystal, some pairs of frequency components may be extracted the mixing of which results in difference frequency radiation (DFR) generation. For generation of DFR radiation an isotropic GaAs crystal having a transparency band 0.9–17 μm and the absorption coefficient less than 5 cm^{-1} in the range lower than 3 THz is widely used [1]. The coefficient of nonlinear susceptibility of GaAs is sufficiently large and comparable with that of such crystals as ZnTe, GaP, GaSe, which are also widely used for generation of DFR. It should be noted that the wavelength of the pumping fs pulse should be longer than 1.75 μm, since at this wavelength two-photon absorption takes place in the GaAs crystal. So, for generation of DFR using parametric interaction of fs few-cycle laser pulses propagating in a GaAs crystal, it is very prospective to use fiber-optical lasers which generate fs pulses in infrared wavelength range of 2 μm. An interest observed recently to finite-difference time-domain (FDTD) methods of direct numerical time integration in femtosecond processes is explained by the fact that this approach allows sufficiently simple modelling of a variety of nonlinear optical phenomena of few-cycle laser pulses using only information on the optical properties of the medium. This model is rather universal and allows modelling both the simplest case of the free space and various combinations of nonlinear and dispersive media [2]. In the present work we present the results of theoretical study and 2D computational modeling of the DFR generation by interaction of few cycle laser pulses with a GaAs thin crystal.

2. 2D MATHEMATICAL MODEL FOR DESCRIPTION OF NONLINEAR INTERACTION OF SPATIALLY-LIMITED LINEARLY-POLARIZED FEMTOSECOND LASER PULSE WITH A GAAS CRYSTAL

Let us assume that neither the electromagnetic field excitation nor the model geometry has any variation in the y-direction, which coincides with the normal to the ⟨110⟩-plane of a GaAs crystal.

That is, we assume that all partial derivatives of the fields with respect to y equal zero, and that the structure being modeled extends to infinity in the y-direction with no change in the shape or position of its transverse cross section. We now proceed with Maxwell equations for the TE_y mode. Neglecting magnetic and electric losses, the following system of Maxwell equations for the electric (E_z, E_x) and magnetic (H_y) fields can be written:

$$\begin{aligned} \frac{\partial D_z}{\partial t} &= \frac{\partial H_y}{\partial x}, \\ \frac{\partial D_x}{\partial t} &= -\frac{\partial H_y}{\partial z} \\ \frac{\partial H_y}{\partial t} &= \frac{1}{\mu_0}\left(\frac{\partial E_z}{\partial x} - \frac{\partial E_x}{\partial z}\right) \end{aligned} \tag{1}$$

$$\begin{aligned} E_x &= \frac{D_x - (P_{xL} + P_{xNL})}{\varepsilon_0} \\ E_z &= \frac{D_z - (P_{zL} + P_{zNL})}{\varepsilon_0} \end{aligned} \tag{2}$$

where ε_0 is the permittivity of free space, μ_0 is magnetic permeability of free space, D_x, D_z are the Cartesian components of the electric induction, P_{xL}, P_{zL} are the components of the linear part of the medium polarization, and P_{xNL} and P_{zNL} are those of nonlinear parts. The components D_z, D_x of the electric induction are determined from constitutive equations, where linear dispersion as well as nonlinear polarization of the medium are successively taken into account,

$$D_z = \varepsilon_0 E_z + P_{zL} + P_{zNL} \tag{3}$$

$$D_x = \varepsilon_0 E_x + P_{xL} + P_{xNL} \tag{4}$$

For the chosen geometry the nonlinear polarization of the medium caused by the quadratic susceptibility may in the quasistatic approximation be represented as

$$P_{zNL}(t) = \varepsilon_0 d_{14} E_x^2(t), \quad P_{xNL}(t) = \varepsilon_0 d_{14} E_z(t) E_x(t) \sqrt{2} \tag{5}$$

where $d_{14} = \chi^{(2)}_{xyz}/2 = 150 \cdot 10^{-12}\,\mathrm{m/V}$ is the coefficient of nonlinear susceptibility of the GaAs crystal. We consider as an isotropic nonlinear dispersive medium a GaAs crystal, which is transparent in the spectral range (0.97–17) μm and the linear susceptibility of which may be, according to [1], represented as

$$\chi^{(1)}(\omega) = n^2(\omega) - 1 = b_0 + \sum_{i=1}^{3} b_i (2\pi c)^2 / \left(\omega_i^2 - \omega^2\right) \tag{6}$$

where $b_0 = 4.372514$, $b_1 = 27.83972$, $b_2 = 0.031764 + 4.35 \cdot 10^{-5} \cdot \Delta T + 4.664 \cdot 10^{-7} \cdot \Delta T^2$, $b_3 = 0.00143636$, $\lambda_1 = (0.4431307 + 0.50564 \cdot 10^{-4} \cdot \Delta T)\,\mu\mathrm{m}$, $\lambda_2 = (0.8746453 + 0.1913 \cdot 10^{-3} \cdot \Delta T - 4.88210^{-7} \cdot \Delta T2)\,\mu\mathrm{m}$, $\lambda_3 = (36.9166 - 0.011622 \cdot \Delta)\,\mu\mathrm{m}$ ($\lambda_i = 2\pi c/\omega_i$), and ΔT is the deviation of the temperature from room temperature $t = 22^{\circ}\mathrm{C}$ ($T = 293\,\mathrm{K}$). As shown in [2], in infrared range of wavelengths, $3 \div 18\,\mu\mathrm{m}$, we can use the quasistatic approximation, which corresponds to instantaneous nonlinear response of the medium. In accordance with (6), the linear response of the medium is determined by the following expression:

$$P_{xL,zL}(\omega) = \varepsilon_0 \left(b_0 + \sum_{i=1}^{3} b_i (2\pi c)^2 \Big/ \left(\omega_i^2 - \omega^2\right)\right) E_{x,z}(\omega) == \varepsilon_0 b_0 E_{x,z}(\omega) + \sum_{i=1}^{3} P_{ixL,izL}(\omega). \tag{7}$$

The system of Equation (7) may be written in the form of a system of differential equations in the following way:

$$\frac{1}{\omega_i^2}\frac{\partial^2 P_{izL,ixL}}{\partial t^2} + P_{izL,ixL} = \varepsilon_0 \frac{b_i (2\pi c)^2}{\omega_i^2} E_{z,x}(t), \tag{8}$$

where $i = 1, 2, 3$. Equation (8) describes linear dispersive properties of the medium in the transparency band in accordance with the classical Lorentz model. By taking into account (5) and (7),

the components D_z and D_x of the electric induction may be written as

$$D_z = \varepsilon_0 E_z + \varepsilon_0 b_0 E_z + \sum_{i=1}^{3} P_{izL} + \varepsilon_0 d_{14} E_x^2, \quad D_x = \varepsilon_0 E_x + \varepsilon_0 b_0 E_x + \sum_{i=1}^{3} P_{ixL} + \sqrt{2}\varepsilon_0 d_{14} E_z E_x \quad (9)$$

We applied the above-described classical model for theoretical investigation and computational modelling of the difference frequency generation by interaction of few cycle laser pulses in a GaAs crystal in plane wave approximation [2]. In the present work we use the finite-difference scheme of solution of nonlinear Maxwell equations realised in [2].

3. SIMULATION RESULTS

The numerical estimation shows that relative error of phase velocity is less than 0.18% and the relative error of group velocity is less than 0.63%. Numerical simulation was performed for the following initial conditions:

$$E_x(t, x, z = 0) = E_{x0} \exp\left(-\frac{t^2}{\tau_0^2}\right) \exp\left(-\frac{x^2}{\sigma_0^2}\right) \cos\left(\frac{2 \cdot \pi \cdot c}{\lambda_0} t\right), \quad E_z(t, x, z = 0) = 0 \quad (10)$$

where $\lambda_0 = 1.98\,\mu\text{m}$ is the central wavelength, $2\tau_0 = 17.16\,\text{fs}$ the duration of the pulse, and $E_{x0} = 100\,\text{MV/m}$ the initial pulse amplitude. In simulations the value of beam waist $2\sigma_0$ was swept from $3\lambda_0 = 5.94\,\mu\text{m}$ to $5\lambda_0 = 9.9\,\mu\text{m}$. The medium length was chosen to be $L = 14.74\,\mu\text{m}$. Let's estimate the characteristic lengths, which describe the pulse interaction with nonlinear medium. According to [3], for increasing the DFR generation efficiency the choice of pumping beam waist is determined by the condition

$$\sigma_0 \leq \sigma_{eff} = \lambda_{DF} / \pi n_{DF}(\lambda_{DF}) \sin(\alpha) \quad (11)$$

where, α is the angle between the DFR wave vector and the z-axis. Therefore, to increase the DFR generation efficiency in the finite spectral range, the beam radius should be shorter than the DFR wavelength in the crystal. The angular divergence of the generated DFR is, according to (11),

$$\alpha_0 = \arcsin\{\lambda_{DF} / \pi n_{DF}(\lambda_{DF}) \sigma_0\} \quad (12)$$

Figure 1 shows the dependence of pumping beam effective radius $\sigma_{eff}(\lambda_{DF}, \alpha)$ (12) on the DFR wavelength and the angle α as a contour plot with levels and values of α indicated.

As seen in Fig. 1 and follows from Equation (11), for $\lambda_{DF} = 5\,\mu\text{m}$ and at $\sigma_{eff}(\lambda_{DF}, \alpha)$ we observe $\alpha_0 = 9.32°$, but at $\sigma_0 = 4.95\,\mu\text{m}$ the value $\alpha_0 = 5.57°$ is observed; for $\lambda_{DF} = 15\,\mu\text{m}$ and at $\sigma_0 = 2.97\,\mu\text{m}$ $\alpha_0 = 29.12°$, but at $\sigma_0 = 4.95\,\mu\text{m}$ $\alpha_0 = 16.97°$. Fig. 2 demonstrates the 3D representation of the propagation of the x- and z-polarized pulses at the time 33 fs, 66 fs, 99 fs

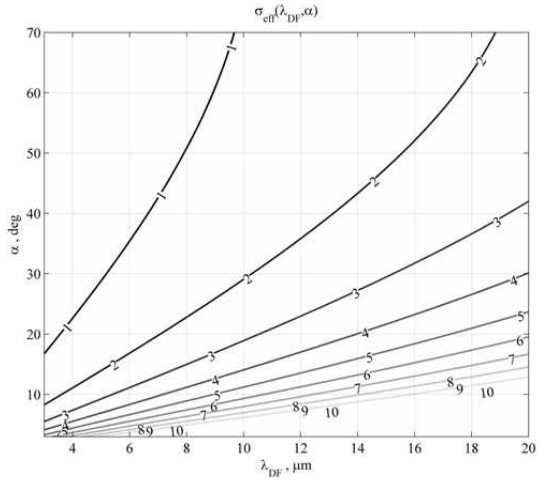

Figure 1: The effective radius of pumping beam versus DFR wavelength and divergence angle.

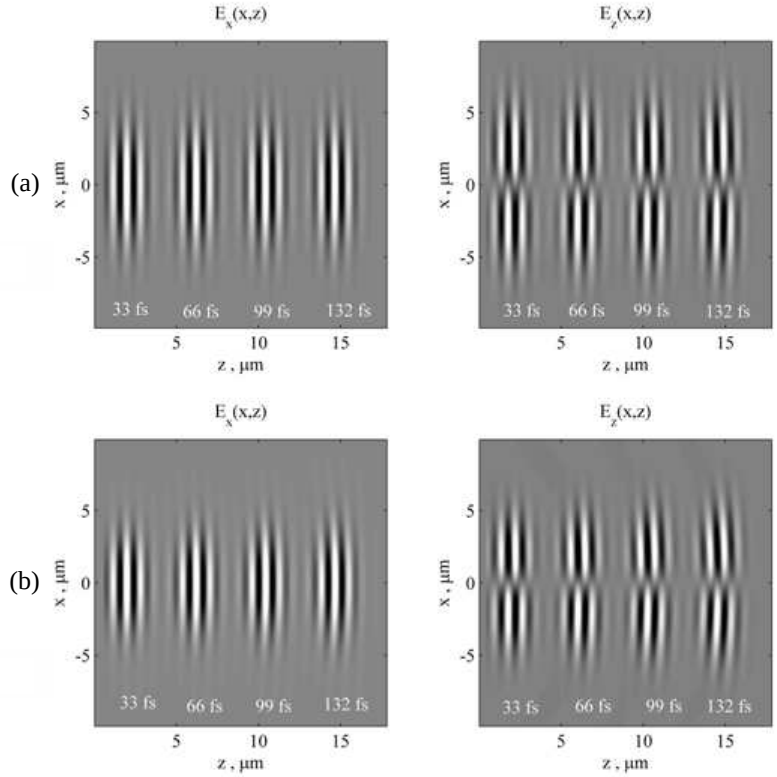

Figure 2: The three dimensional representation of the propagation of the x- and z-polarized pulses at the times 33 fs, 66 fs, 99 fs, and 132 fs for the initial x-polarized Gaussian pump beam diameter (a) 9.9 μm and (b) 5.94 μm.

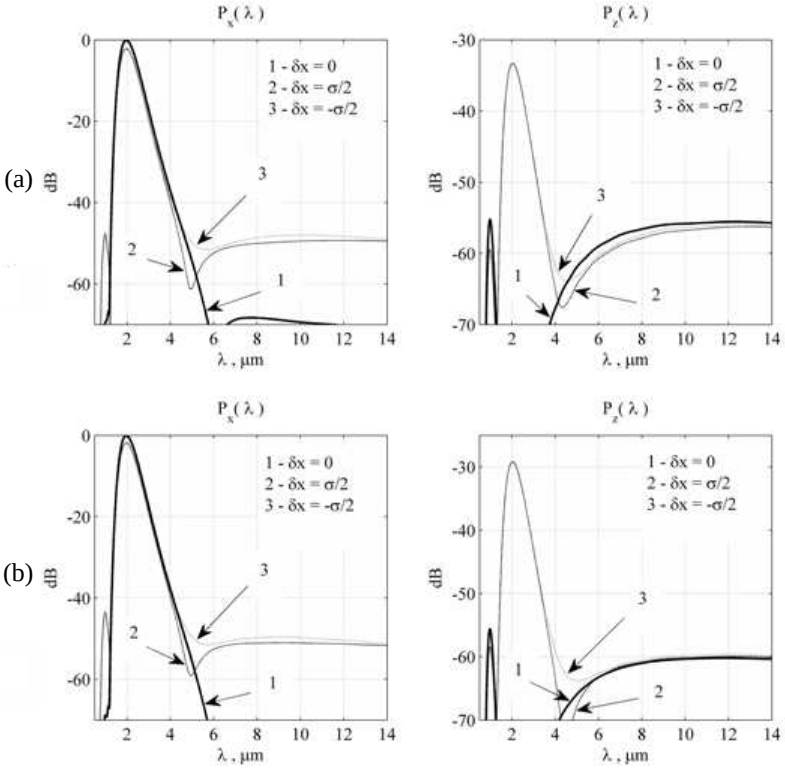

Figure 3: The wavelength dependences of the power density of x- and z-polarized pulses at crystal output at lateral coordinates $\delta x = 0$; $\pm\sigma_0/2$ and beam diameters (a) 9.9 μm and (b) 5.94 μm.

and 132 fs for the initial x-polarized Gaussian pump beam diameter of 9.9 μm (a) and 5.94 μm (b), respectively.

Figure 3 shows the wavelength dependence of the power density for x- and z-polarized pulses at crystal output at lateral coordinates $\delta x = 0; \pm\sigma_0/2$ and beam diameters 9.9 μm (a) and 5.94 μm (b); the values of the power density are scaled to the power density of the initial x-polarized pulse at $\delta x = 0$. The spectral distributions at the crystal output, shown in Figs. 3(a) and 3(b), are obtained with taking into account the reflection coefficients for normal incidence at the air-GaAs interface, which equals −5.367 dB at 1.98 μm. Formation of spectral supercontinuum in the range of difference frequencies is well seen in these figures. Fig. 3 also shows that the spectral distribution of power density at the beam axis ($\delta x = 0$) of z-polarized pulse contains spectral components only in the range of sum ($\lambda_{DF}/2$) and difference frequencies and none around λ_0. Spectral components around λ_0 arise at the distance $\delta x = \pm\sigma_0/2$ from the axis. The power density of the z-polarized pulse in the range from 10 μm to 14 μm is about −64.5 dB for beam radius $\sigma_0 = 9.9$ μm and −60 dB for beam radius $\sigma_0 = 5.94$ μm. The pattern of spectral distribution of the x-polarized pulse is seen in Fig. 3 to be opposite. Spectral components at $\delta x = 0$ are observed only around λ_0, whereas at $\delta x = \pm\sigma_0/2$ components arise in the range of sum and difference frequencies. Power density for x-polarized pulse in the range from 10 μm to 14 μm is about −50 dB for both values of beam radius $\sigma_0 = 9.9$ μm and 5.94 μm. For numerical simulations of filtration of DFR from spectral supercontinuum formed at the crystal output, we used a low pass filter with the following transfer function $-h(\nu) = 1/\left(1 + \nu^2/\nu_c^2\right)$, where $\nu_c = 81.71$ THz ($c/\nu_c = 3.67$ μm). It is, obvious that if the realistic filters are employed, phase relations are determined by the phase-frequency characteristic of the filter also. Fig. 4 gives the three dimensional representation of propagation of the x- and z-polarized filtered DFR pulses at the time 132 fs for initial x-polarized Gaussian pump beam with diameter (a) 9.9 μm and (b) 5.94 μm.

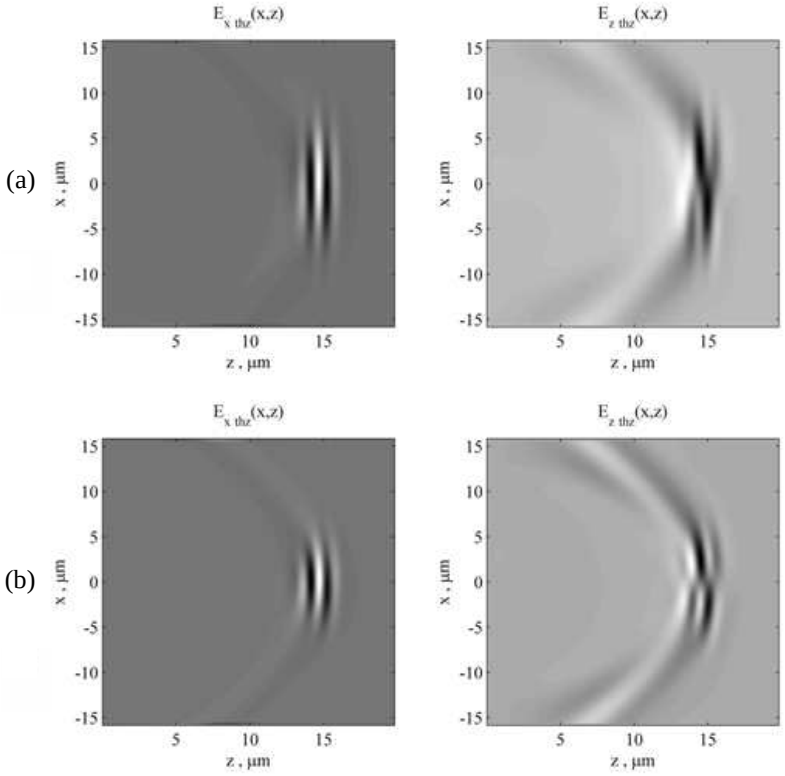

Figure 4: The 3D representation of the propagation of the x- and z-polarized filtered DFR pulses at the time 132 fs for the initial x-polarized Gaussian pump beam diameter (a) 9.9 μm and (b) 5.94 μm.

Figure 5 shows the temporal profiles of x- and z-polarized filtered DFR pulses at crystal output at $\delta x = 0; \pm\sigma_0/2$ and initial x-polarized beam diameters (a) 9.9 μm and (b) 5.94 μm. It is seen that the temporal profiles of DFR pulses at $\delta x = 0$ are practically the same for both values of diameter

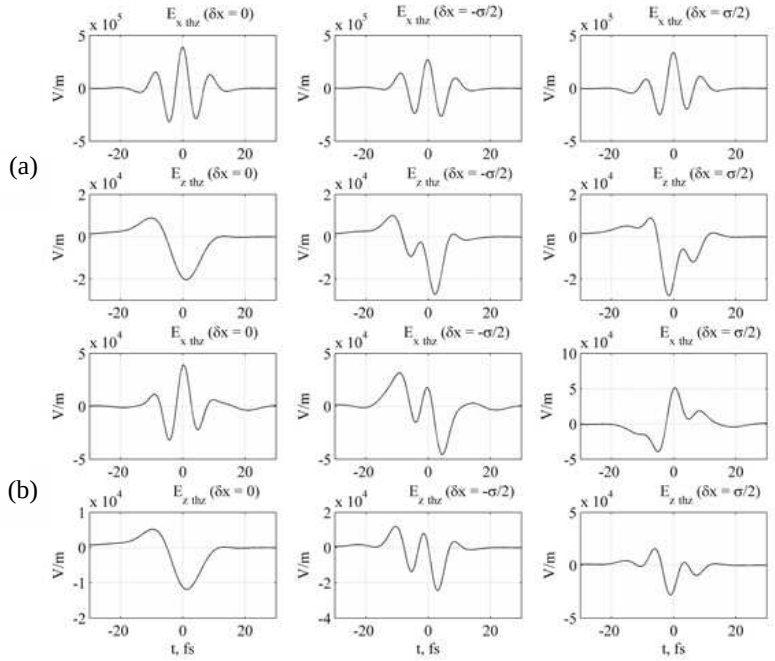

Figure 5: The temporal profiles of x- and z-polarized filtered DFR pulses at crystal output at $\delta x = 0; \pm\sigma_0/2$; the initial x-polarized beam has the diameter (a) 9.9 μm and (b) 5.94 μm.

of the initial x-polarized beam, while at $\delta x = \sigma_0/2$ and $\delta x = -\sigma_0/2$ and beam diameter 9.9 μm the temporal profiles of x- and z-polarized DFR pulses are mutually inverted in time (Fig. 5(a)), but for diameter 5.94 μm they are not (Fig. 5(b)).

4. CONCLUSION

According to obtained results by increasing of initial x-polarized beam waist $2\sigma_0$ from 6 μm up to 10 μm the efficiency of DFR for z and x-polarized pulses decrease from $3.1 \cdot 10^{-6}$ down to $2.56 \cdot 10^{-6}$ and from $2.018 \cdot 10^{-6}$ to $1.921 \cdot 10^{-6}$ respectively. DFR generation efficiency for z-polarized DFR decreases by 17.42% and by 4.81% for x-polarized pulse. It's shown that in considered geometry, the DFR generation efficiency for the x-polarized pulse is less sensitive to the decreasing of initial beam waist. At generating the DFR by interaction of spatially-limited few cycle duration laser beams with a GaAs thin crystal in cross-section distribution of near field DFR the certain coordinate corresponds to appropriate spectral component. Obtained results can be used for realization of space-time filtration of DFR pulse.

REFERENCES

1. Skauli T., et al., "Improved dispersion relations for GaAs and applications to nonlinear optics," *J. Appl. Phys.*, Vol. 94, No. 10, 6447–6455, 2003.
2. Hovhannisyan, D. L., et al., "Theoretical investigation and computational modeling of the difference frequency generation by interaction of few cycle laser pulses in a GaAs crystal," *Journal of Modern Optics*, Vol. 57, No. 14–15, 1228–1242, 2010.
3. Martirosyan, A. S., et al, "Radiation of difference frequencies at optical rectification of spatially limited femtosecond laser pulse in the periodically poled GaAs crystal," *SPIE Photonics Europe, Conferences*, April 12–16, 2010, DOI: 10.1117/12.852578, Exhibition: April 13–15, 2010, Belgium Photonics Europe 2010.

Triple Band Planar Monopole Antenna for MIMO Application

Hashimu Uledi Iddi[1, 2], **M. R. Kamarudin**[1], **T. A. Rahman**[1], **A. Y. Abdurahman**[1], **R. Dewan**[1], **and A. S. Azini**[1]

[1]Wireless Communication Centre (WCC), Faculty of Electrical Engineering
Universiti Teknologi Malaysia, Malaysia
[2]College of Information and Communication Technologies
University of Dar es Salaam, P. O. Box 35131, Dar es Salaam, Tanzania

Abstract— A triple band planar monopole antenna for MIMO application is presented in this paper. The antenna array consists of two triple band monopole antennas with three copper strips, which operate at three frequency bands (2.4, 3.5 and 5.8 GHz). The antenna has been simulated using CST software and the prototype has been fabricated using FR4 substrate. The antenna provides the −10 dB bandwidths (BWs) of 308 MHz (from 2.2275 to 2.5354 GHz), 472 MHz (from 3.337 to 3.809 GHz) and 1.688 GHz (from 5.488 to 7.176 GHz) for 2.4, 3.5 and 5.8 GHz respectively. The antenna array achieve low mutual coupling of −22 dB at separation distance of 10 mm, which is approximately $\lambda/12$. There is good agreement between the measurement and simulation results in terms of return loss and radiation pattern.

1. INTRODUCTION

The high data rate transmission and reduced transmit power demand have attracted a lot of research interests to investigate the use of Multiple Input Multiple output (MIMO) in wireless applications. The MIMO systems demonstrate the increased efficiency in rich multipath environment [1]. Small size, low profile and simple structure are required in some of the antenna arrays for MIMO application, so that more than one antenna can be placed as close as possible without increasing the mutual coupling between the antenna elements. Achieving high data rate and low mutual coupling is a challenging task in small device, as more than one antennas have to be placed together. A lot of studies have been conducted on the investigation of how to reduce mutual coupling between antenna elements [2, 3] while still keeping them as close as possible. However, most of the studies that have been reported have the demerits of complex antenna structures and large separation distances.

A triple band monopole antenna array for MIMO application has been presented in this paper. The antenna array achieved low mutual coupling of −22 dB at a separation distance of 10 mm, which is approximately $\lambda/12$. There is good agreement between the measurement and simulation results in terms of return loss and radiation pattern.

2. ANTENNA DESIGN

The geometry and dimension of the proposed triple band monopole antenna and the antenna array are shown in Figures 1(a) and 2 respectively; while the prototype of the triple-band antenna array is shown in Figure 1(b). The antenna consists of three copper strips which contribute to the three resonance frequencies of the proposed antenna. The antenna has been designed using CST Microwave studio software. The substrate used is FR4 with permittivity of 4.5, loss tangent of 0.019 and thickness of 1.6 mm. It has been observed that the resonance frequency is influenced by the antenna's copper strip length which is approximately one-quarter of wavelength of the operating frequency. The two triple band monopole antennas are placed orthogonal to each other separated by distance, d. The antenna has overall dimensions of $20 \times 40 \times 1.6\,\text{mm}^3$ and $40 \times 75 \times 1.6\,\text{mm}^3$ for single triple band monopole antenna and the antenna array as shown on Figure 1(a) and Figure 2 respectively. The prototype of the triple-band antenna is shown in Figure 1(b).

3. RESULTS AND DISCUSSION

The triple band monopole antenna and antenna array have been analyzed for MIMO application. The antennas are placed firstly in parallel and then orthogonal to each other, separated by distance, d. It has been observed that the orthogonal configuration gives lower values of mutual coupling, and has therefore been used in this investigation.

The comparison between the simulated and measured return losses of the proposed monopole antenna are shown in Figure 3(a). The return loss results are based on port 1. As it can be observed

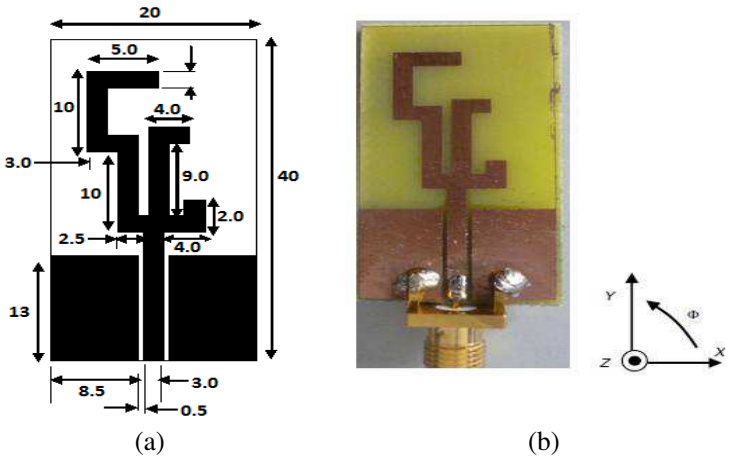

Figure 1: Triple band monopole antenna (a) geometry and (b) prototype [4].

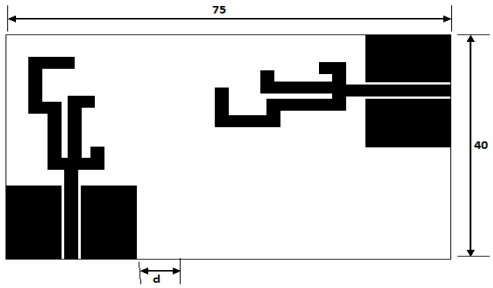

Figure 2: Geometry of triple band monopole antenna array.

from Figure 3(a), the antenna provides the −10 dB BWs of 308 MHz (from 2.2275 to 2.5354 GHz), 472 MHz (from 3.337 to 3.809 GHz) and 1.688 GHz (from 5.488 to 7.176 GHz) for 2.4, 3.5 and 5.8 GHz respectively. It can be seen that the measured and simulated return loss characteristics of the optimized antenna are in good agreement, with small deviation in the measurement results at 3.5 GHz. The antenna also satisfies the requirements of the 2.4/5.8 GHz WLAN and 3.5 GHz WiMAX antenna applications. The simulated S-parameters of the proposed monopole antenna array are shown in Figure 3(b). It can be seen that the antenna array achieved low mutual coupling of −22 dB at separation distance of 10 mm, which is approximately $\lambda/12$ of the first resonant frequency.

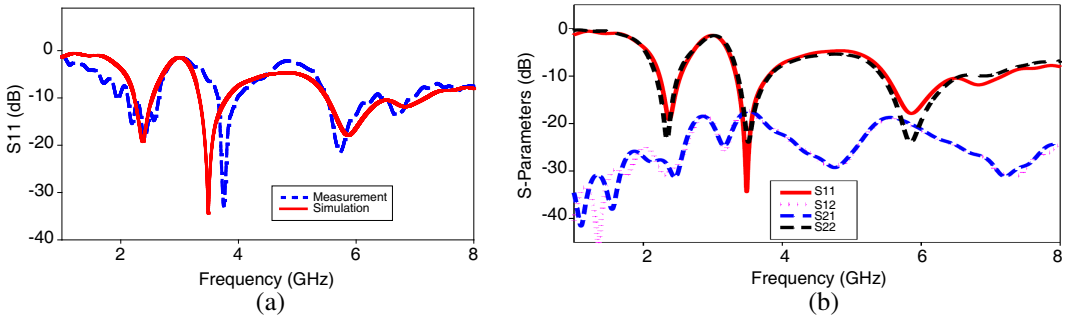

Figure 3: (a) Measured and simulated return losses of triple band monopole antenna and (b) simulated S-parameters results of antenna array.

The simulated radiation pattern of the proposed antenna array has been analyzed. The E-plane and H-plane radiation patterns at 2.45 GHz, 3.5 GHz and 5.8 GHz were investigated. Figure 4 shows The E-plane radiation patterns are shown in Figure 4 at the afore-mentioned frequency bands. It can be seen that the E-plane radiation pattern are bi-directional Figure 5. The corresponding H-plane radiation patterns are shown in Figure 5. It was observed that H-plane radiation patterns

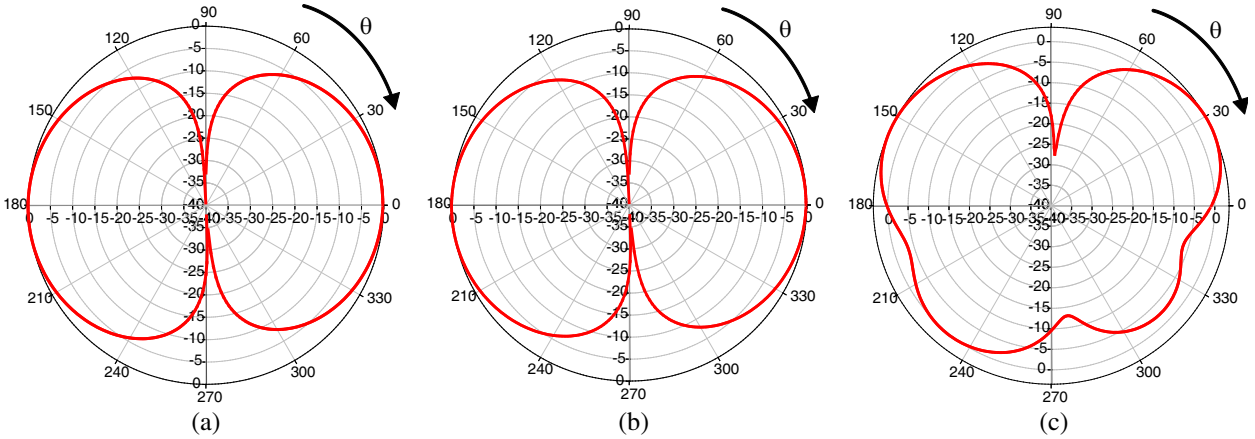

Figure 4: Simulated E-plane radiation pattern of the proposed triple-band antenna array at (a) 2.45 GHz, (b) 3.5 GHz, (c) 5.8 GHz.

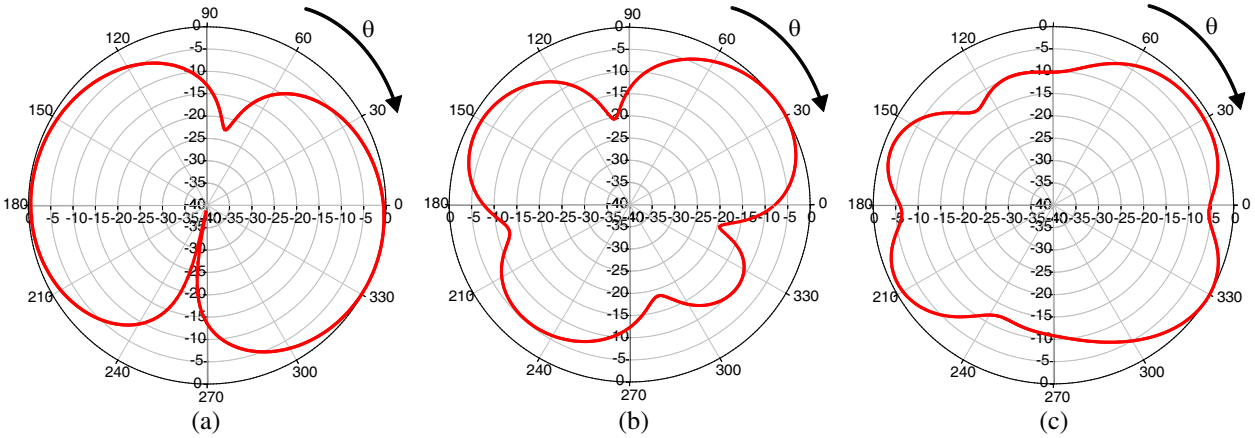

Figure 5: Simulated H-plane radiation pattern of the proposed triple-band antenna array at (a) 2.45 GHz (b) 3.5 GHz (c) 5.8 GHz.

are close to omnidirectional at 3.5 GHz and 5.8 GHz, while it is bi-directional at 2.45 GHz.

4. CONCLUSIONS

A monopole antenna array for MIMO application has been presented in this paper. The proposed antenna provides the −10 dB BWs of 308 MHz (from 2.2275 to 2.5354 GHz), 472 MHz (from 3.337 to 3.809 GHz) and 1.688 GHz (from 5.488 to 7.176 GHz) for 2.4, 3.5 and 5.8 GHz respectively. The antenna array achieved low mutual coupling of −22 dB at a separation distance of 10 mm, which is approximately $\lambda/12$. There is good agreement between the measurement and simulation results in terms of return loss and radiation pattern.

ACKNOWLEDGMENT

The authors would like to thank to Ministry of Higher Education (MOHE) and UTM GUP (vote 01H00) and vote 00G36 for sponsoring this work. Besides, thanks to the members of Wireless Communication Center (WCC), UTM for helping and providing resources to enable this work to be completed. Finally, a special thanks goes to University of Dar es Salaam (UDSM) for the scholarship.

REFERENCES

1. Foschini, G. J. and M. J. Gans, "On limits of wireless communications in a fading environment when using multiple antennas," *Wireless Personal Communications*, Vol. 6, 311–335, 1998.
2. Iddi, H. U., M. R. Kamarudin, T. A. Rahman, and R. Dewan, "Design of dual-band B-shaped

monopole antenna for MIMO application," *2012 IEEE Antennas and Propagation Society International Symposium (APSURSI)*, 1–2, 2012.

3. Mohsen, S., M. Alireza, T. Ahad, and H. Teimur, "Mutual coupling reduction of microstrip antennas using defected ground structure," *10th IEEE Singapore International Conference on Communication Systems, ICCS 2006*, 1–5, 2006.
4. Iddi, H. U., M. R. Kamarudin, T. A. Rahman, A. Y. Abdurahman, M. Khalily, and M. Jamlos, "Triple-band CPW-fed planar monopole antenna for WLAN/WiMAX application," *Microwave and Optical Technology Letters*, Vol. 55, 2209–2214, 2013.

A Novel Wideband and Dual-polarized Cross-antenna for Satellite Communications

Haiyang Zhang, **Yann Mahe**, **and Tchanguiz Razban**
IETR UMR 6164, Polytech Nantes, LUNAM Université, Université de Nantes
La Chantrerie, rue C. Pauc, 44306 Nantes cedex 03, France

Abstract— In this paper, a novel broadband and dual-polarized antenna is presented. This antenna is based on the use of two rectangular patch resonators positioned perpendicularly with respect to each other, 5 other parasitic elements are used to increase the bandwidth. Very thin gaps between the elements are carried out to enhance the coupling and maximize the isolation. The results obtained by simulation and measurement show that this solution achieves about 2.2 GHz bandwidth from 9.0 GHz to 11.2 GHz while the isolation between the two ports are around 20 dB. This antenna has a very small profile, it is suitable to compose a big antenna array for satellite communications.

1. INTRODUCTION

Satellite communication antennas need to have performances like broadband, highly directional, dual polarization and be easy to install. The parabolic reflector antenna covers most of these criteria as a high gain and directivity due to the focusing effect of the reflector. However, the main drawback of parabolic antenna is related to its structure which it requires a mechanical device to steer itself to receive signals from more than two satellites and its integration into the urban space can cause significant visual pollution. The search for alternative solutions has never stopped.

B. Li et al. propose a wide band and dual-polarization patch antenna [1]. Two bow-tie shaped patches are arranged and fed orthogonally to obtain the horizontal and vertical polarizations. The insertion of the H-shaped slots on each element increases the bandwidth. The results show a relatively low level of cross-polarization in the characteristic planes E and H. In [2], the cross-shaped slots excited by coplanar lines enable a dual linearly polarized antenna. The bandwidth of 19% is then obtained. The major drawback of the two solutions is the use of relatively complex multilayer structures which does not consider industrialization at high volume. In [3], P. Kumar et al. propose a new cross-shaped antenna with a ground plane completely demetallized. They were able to get a bandwidth of 28% with reasonable directivity. Although the conception of antenna is attractive, there is only one linear polarization obtained with this solution.

In this paper, we present a new broadband and dual-polarized antenna. The antenna operates in the band of 9–11.2 GHz. It has two arms which are orthogonal to each other, the whole structure looks like a small cross. For each arm we use a corner truncated microstrip patch as the driven element and three other patches with the same dimensions as parasitic elements to expand the bandwidth. A study of the distance between elements has been carried out to enhance resonating and maximize the isolation between two feeding ports. This structure of antenna is optimized, fabricated and tested, very good agreement is observed between simulation and measurement which show that this solution has a relative bandwidth greater than 20% with respect to the central frequency at 10 GHz and isolation about 20 dB.

In the second section, we present the design parameters of the antenna. Then in Section 3, two parameters which effect on the bandwidth and resonating depth are studied, optimal values and their analysis are given. In the last section we give some conclusions of this work.

2. ANTENNA CONCEPTION

It is well known that rectangular patch antenna has a narrow bandwidth of a few percent depending on the relative permittivity and the thickness of substrate and the geometry of the antenna. Parasitic patches are introduced to locate close to the main radiating patch to expand the band [4]. With this idea, the proposed cross patch antenna is designed, its geometry is presented in Figure 1.

The substrate used is Teflon, it has a thickness of 1.52 mm with a relative permittivity 2.55, $\tan\delta = 0.007$. All the patches of the antenna are 6.55 mm wide, they are arranged in a cross to achieve dual orthogonal linear polarization. The two elements which are etched with U-shaped slots are excited by directly coupling to microstrip feeding line via probes with the diameter of 0.6 mm. In the rest part of this paper, these elements are called "driven patches." The other

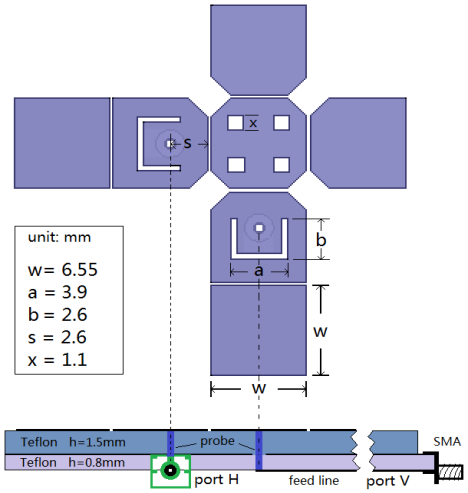

Figure 1: Geometry of the proposed cross patch antenna with the detailed dimensions.

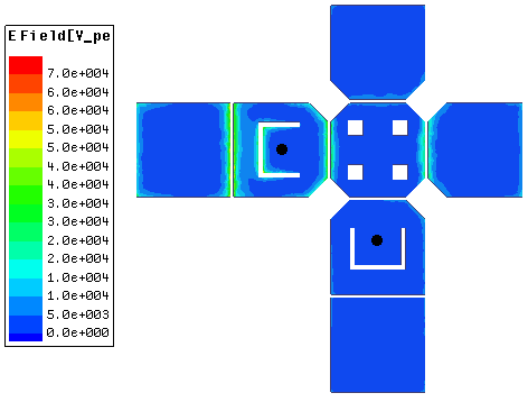

Figure 2: Electric field of cross antenna at 10.25 GHz.

parasitic elements are excited by the power which is coupled from driven patches. The optimal width between each patch is found to be 250 µm which makes it possible for relatively strong electromagnetic coupling. To reduce the coupling energy between the two driven patches so as to improve the polarization isolation, several angles of driven and parasitic patches are cut. Similarly, four demetallization squares are introduced into the central patch to improve isolation by forcing RF current flowing along a specified direction. The combination of the two techniques significantly improves the isolation between two ports. To limit the inductive effect which is introduced by probes and enhance the resonating, U-shaped slot is introduced in each driven patches [5]. These slots are therefore the main objective of improving the performance.

In Figure 2, we give the distribution of the electric field when the antenna is fed along its horizontal axis. The result, obtained by HFSS software, shows that in this configuration, the power is mainly localized around the slot and gaps on the horizontal axis. It can also be seen that the level of electric field on the vertical arm of the antenna is very low which indicates a very good isolation. A prototype is thus manufactured, as shown in Figure 3.

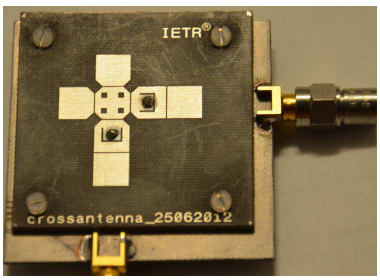

Figure 3: Realized prototype of cross antenna.

3. RESULTS AND DISCUSSION

Several parameters are studied to optimize the frequency response of the antenna such as the lengths and widths of the slots, the position of the feeding point and the width of the gaps providing coupling between patches. Some results are given in Figure 4.

Figure 4(a) shows the bandwidth of the antenna is very sensitive to the length of the U-shaped slot, and Figure 4(b) indicates that the input impedance is maintained dependent on the offset of the feed point in the band. According to the simulation, for an input impedance of 50 Ω, the selected parameters are the length of slot 3.9 mm and the offset of feed point 2.6 mm.

The proposed antenna has been fabricated and measured with the vector network analyzer Agilent E8364B. The reflection coefficients obtained by simulation and measurement are given in Figure 5.

It can be seen that the −10 dB bandwidth obtained on the horizontal polarization port is 1.9 GHz, about 19% in simulation. Measurements on the prototype show good agreement with

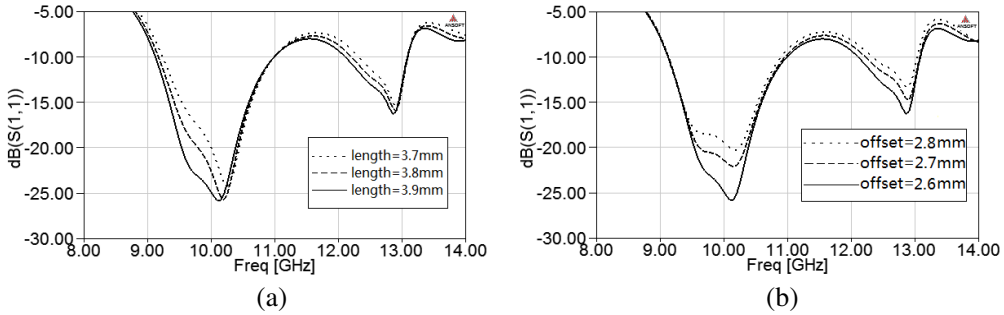

Figure 4: Simulated S_{11} when tuning the length of (a) U-slot and (b) the offset of feeding point.

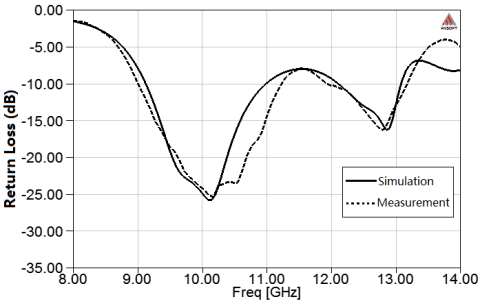

Figure 5: Simulated and measured return loss.

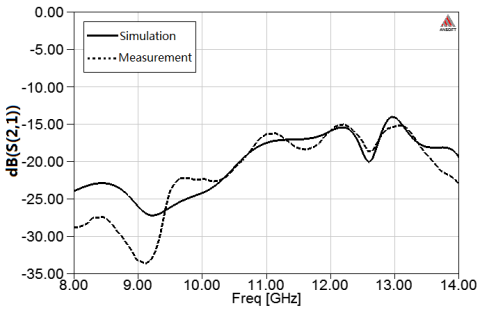

Figure 6: Simulated and measured S_{21}.

simulations. Bandwidth obtained is even slightly larger and reaches up to 2.2 GHz and about 22% for relative bandwidth with respect to the central frequency. The same properties are found on the vertical port both in simulation and measurement due to the symmetric characteristic of the structure.

In Figure 6, we give the results of simulated and measured isolation between the two ports. The isolation remains above 20 dB up to 10.5 GHz, and it increases slightly while frequency increases but remains lower than 15 dB in the band. This incensement can be attributed to the effects of capacitive coupling at the gaps between elements. Indeed, as the frequency increases, the electric field in these areas is more intense and the coupling between orthogonal elements increases, which leads to a decrease in the isolation between ports.

The simulated radiation pattern are presented in Figures 7(a) and 7(b) at 10.25 GHz. These results are given when only the horizontal port is excited. We can see that the gain of this antenna is about 10 dBi and that, in these two planes, the cross-polarization level is better than 20 dB in normal axis. A deterioration in the level of cross-polarization is observed in H-plane when it deviates from the normal axis.

The radiation performance of the antenna on its bandwidth is shown in Figure 8. In this figure, we represent the evolution of the gain and radiation efficiency as a function of frequency. These results of the simulation show that the gain is greater than 7 dBi during the band 8.5–12 GHz to

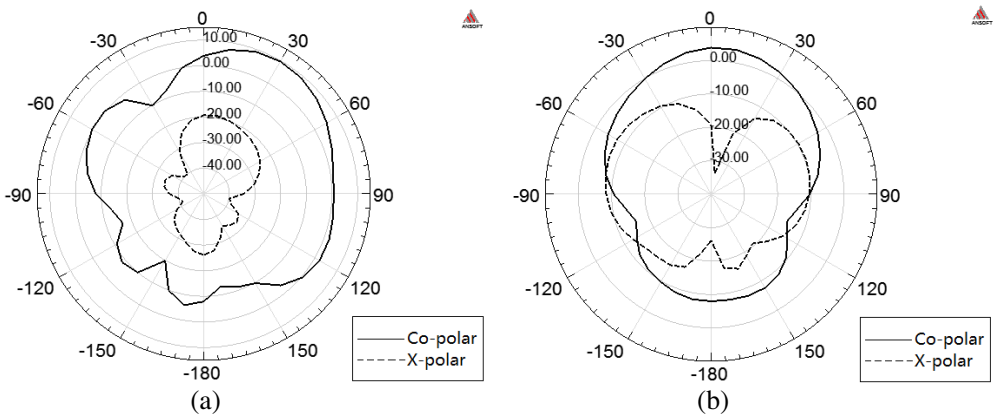

Figure 7: Simulated radiation patterns for (a) E plans and (b) H plan at 10.25 GHz.

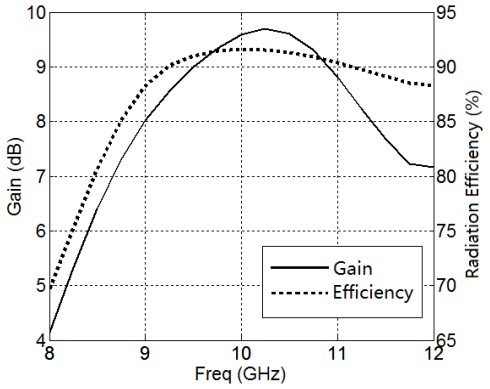

Figure 8: Simulated gain and efficiency of cross patch antenna.

a maximum of 9.6 dBi. The radiation efficiency is greater than 70% over the analysis band with a maximum of 92%.

4. CONCLUSION

A new broadband and dual-polarization patch antenna was presented. The antenna is composed of two driven patches fed by coaxial cable and five parasitic patches to expand bandwidth. This antenna resonates well in the band 9.0 GHz to 11.2 GHz, while the isolation is lower than −16 dB along the whole band. The simulated results also indicate that the antenna has a big gain and high radiation efficiency. Using PCB technology, the antenna can be printed on a 1.5 mm thickness TEFLON substrate and the feeding line on the same material but the thickness is 0.8 mm. The structure of the antenna makes it possible to have two orthogonal polarizations of good quality since the cross-polarization is lower than 20 dB compared to the main polarization. The simulation results also indicate that the antenna has a big gain and very high radiation efficiency. It is important to note that the dimensions of this antenna are compatible with networking to increase directivity for satellite communication applications.

REFERENCES

1. Li, B., Y.-Z. Yin, W. Hu, Y. Ding, and Y. Zhao, "Wideband dual-polarized patch antenna with low cross polarization and high isolation," *IEEE Antenna and Wireless Propagation Letters*, Vol. 11, 2012.
2. Rowe, W. S. T. and R. B. Waterhouse, "Integratable wide-band dual polarized antennas with rear field cancellation," *IEEE Trans. on Antennas and Propag.*, Vol. 51, No. 3, Mar. 2003.
3. Kumar, P., A. K. Singh, T. Chakravarty, G. Singh, and S. Bhooshan, "A novel printed cross antenna for wideband application," *International Workshop on Antenna Technology: Small and Smart Antennas Metamaterials and Applications, IWAT'07*, 255–258, 2007, 1-4244-1088-6/07.
4. Wong, K.-L., *Planar Antennas for Wireless Communications — Wireless Series in Microwave and Optical Engineering*, John Wiley & Sons, Inc., Hoboken, New Jersey, 2003.
5. Lee, K. F., S. L. S. Yang, et al., "The versatile U-slot patch antenna," *IEEE Antennas and Propagation Magazine*, Vol. 52, No. 1, 71–88, Feb. 2010.
6. Laheurte, J.-M., "Petites antennes communic-ations sans fil et terminaux," Institue Télécom et La Voisier, Paris, 2011.
7. Di Bari, R., T. Brown, S. Gao, et al., "Dual-polarized printed S-band radar array antenna for spacecraft applications," *IEEE Antenna and Wireless Propagation Letters*, Vol. 10, 987–990, 2011.
8. Sharma, P. and R. A. Rodrìgue-Solìs, "Dual-polarized X-band microstrip patch sub-array for off-the-grid radar array antenna," *2011 IEEE International Symposium on Antennas and Propagation (APSURSI)*, 577–579, 2011.
9. Xu, J., X. Jiang, and S. Li, "Design of Ku band broad bandwidth microstrip antenna," *Journal of Guilin University of Electrionic Technology*, Vol. 26, No. 4, 264–267, Aug. 2006.

Novel Design of Miniaturized Triple Band Square Microstrip Patch Antenna with F Slot for Fixed Service Satellite and Microwave C Band Applications

Faria Jaheen[1] and Abdullah Al Noman Ovi[2]

[1]American International University, Bangladesh
[2]Bangladesh University of Engineering and Technology, Bangladesh

Abstract— In this paper, a novel design of miniaturized triple band square microstrip patch antenna has been proposed for C-band applications. To reduce resonant frequency of TM_{030} mode to act like TM_{010} mode and obtain tri-band operation, an F shaped slot is etched on diminutive square patch (23 mm × 23 mm patch) of the probe feed antenna. The simulated results show that the antenna can cover Fixed Service Satellite (FSS) at 3.907 GHz, mobile communication at 4.573 GHz and aeronautic radio navigation at 5.311 GHz. The proposed antenna has accomplished directivity and gain above 7 dB at each band. The design and performance of the proposed antenna is carried out using CST Microwave Studio' based realistic simulation.

1. INTRODUCTION

Rapid progress in modern satellite communication has encouraged exhaustive research concerning multi-band, compact, high directive and single feed planar antennas. Again it is often required to integrate reasonably a few RF modules for different frequencies into a segment of equipment for various applications. For such applications multi-band microstrip patch antennas are considered as an evident preference due to their low cost, low weight, low profile, good integration with RF devices, conformability, ease of fabrication and good performance.

Several methods are built up for obtaining multi-band antenna characteristics. Generally they are divided into two type, i.e., multi-resonator antennas and reactive loading antennas depending upon the number of radiating elements. Multi-resonator antennas achieves multi resonant behavior by means of multiple radiating elements each supporting sturdy currents and radiation at its resonance. Aperture-coupled parallel microstrip dipoles [1] as well as the multi-layer stacked-patch antennas using circular [2], annular [3], rectangular [4], and triangular [5] patches are included in this category. Due to having multiple substrate layers in structure multi-resonator antennas are large size and costly.

In comparison with multi-resonator antennas, reactive loading antennas with slot configurations exhibit superior characteristics including wider bandwidth, less conductor loss and better isolation. Particularly, the slot-loaded structure is a handy approach for accomplishing multi-band and broadband operation. Moreover, feeding these structures can be simpler by using suitable points to slot techniques for different slots and the simultaneous use of slots with short-circuit vias, allows obtaining an FR from 1.3 to 3 depending on the number of vias as explained in [6]. More than a few reactive loading antennas have been developed for multi-band operation [7–10]. Single layer simple structures for linear polarization have been proposed in [11] by introducing slots parallel to radiating edges of patch. Some dual-band patch antennas with simple structure have been proposed in [12, 13]. Mode modification in rectangular microstrip patch antenna was performed using symmetrical rectangular slots closed to radiating edges [14], J slot [15], fractural shaped slot [16], dual T shaped slit [17] and a center rectangular slot and an additional triangular slot [18] etc. Symmetrical slot loading in elliptical patch antenna also lead to the same result [19].

This paper presents a multi-band antenna-design approach based on inserting F slot into the patch. The whole system is fed by a coaxial probe into the substrate, with an input impedance of 50 Ω. The main objective of our work is to reduce the size of the antenna very effectively without affecting its radiation pattern and directivity. Our work attains additional size reduction in comparison to conventional structure with high directivity and satisfactory radiation pattern.

2. ANTENNA DESIGN

Figure 1 shows the basic design of our proposed compact single-fed (probe fed) microstrip antenna. The square patch has equal side length $L = 23$ mm. Permittivity of the substrate is 2. The thickness of the substrate is $t = 1.5$ mm. Other dimensions are given in Figure 1.

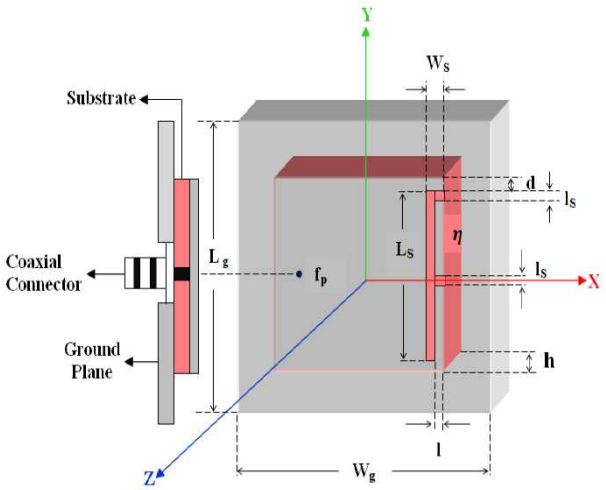

Figure 1: Geometry of proposed square microstrip patch antenna with F slot. Detailed information and constitutive parameters are: $L_g = 32\,\text{mm}$, $W_g = 32\,\text{mm}$, $L_s = 20\,\text{mm}$, $W_s = 2\,\text{mm}$, $l_S = 1\,\text{mm}$, $d = 1\,\text{mm}$, $l = 1\,\text{mm}$, $h = 1.5\,\text{mm}$, $\eta = 2$ and feed position f_p: $(x, y) = (0, -5.5\,\text{mm})$ considering origin at the centre of the patch.

To obtain tri-band operation an F slot is loaded next to one of the radiating edges of the antenna. Figure 2 shows S-parameter performance of the proposed square microstrip patch antenna. It demonstrates the designed antenna return loss. Other antenna parameters are given in Table 1.

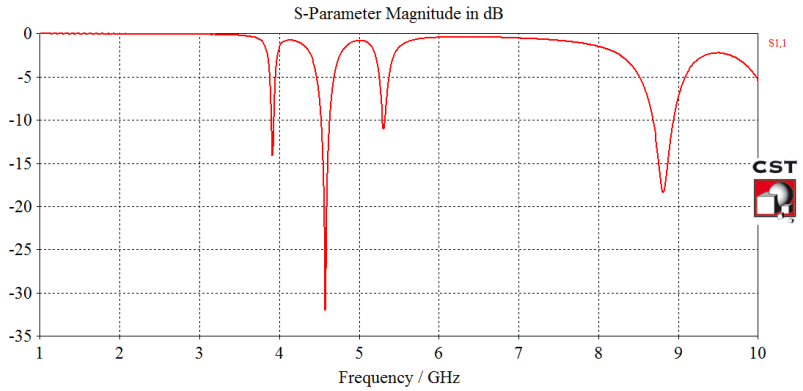

Figure 2: S-parameter performance of the proposed square microstrip patch antenna, TM_{010} mode at 3.907 GHz, modified $\text{TM}_{0\delta0}$ $(1 < \delta < 3)$ mode at 4.573 GHz and TM_{030} mode at 5.311 GHz.

Table 1: Antenna parameters.

Mode	Resonant Frequency (GHz)	S_{11} (dB)	Directivity (dB)	Gain (dB)
TM_{010}	3.907	-14.107	7.383	7.272
$\text{TM}_{0\delta0}(1 < \delta < 3)$	4.573	-31.996	7.685	7.682
TM_{030}	5.311	-10.981	7.580	7.576

3. TRIPLE BAND OPERATION

Corresponding to cavity perturbation theory, when a resonant cavity is perturbed, i.e., when a foreign object with distinct material properties is introduced into the cavity or when a general shape of the cavity is changed, electromagnetic fields inside the cavity change consequently. The underlying assumption of cavity perturbation theory is that electromagnetic fields inside the cavity after the change differ by a very small amount from the fields before the change. But the change in

cavity causes significant change in resonant frequency. The concept of cavity perturbation theory has been used in proposed antenna to introduce the novel concept of additional modified $TM_{0\delta0}$ mode and to derive the antenna for triple band operation.

Again, according to cavity model, the first three modes that can be excited in the cavity are usually denoted by TM_{010}, TM_{020} and TM_{030}. These modes correspond to longitudinal currents distributed on the patch which have nulls at the radiating edges. The TM_{010} is the most used in realistic purposes since the TM_{020} mode has a broadside-null radiation pattern and the TM_{030} produces grating lobes. Modes higher than TM_{030} mode are quite unusual and show substandard radiation performance as TM_{020} mode (broadside null).

Due to etching slots adjacent to radiating edges of antenna, the currents of TM_{030} resonant frequency circulate around the slot and become similar to the TM_{010} mode; thus the slot also modify three lobe shape of TM_{030} mode to regular behavior, but they do not perturb TM_{010} mode significantly [11]. In this paper, loaded F slot near one of the radiating edges introduces modified $TM_{0\delta0}$ $(1 < \delta < 3)$ mode. Figures 5 & 6 show the 3D and polar plot of modified $TM_{0\delta0}$ $(1 < \delta < 3)$ mode for the proposed antenna. In addition, the slot modifies the grating lobe shape of TM_{030} mode to regular behavior (as Figures 7 & 8) and derives the antenna for triple band operation.

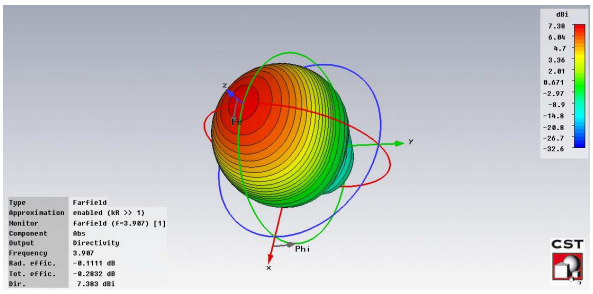

Figure 3: 3D radiation pattern of TM_{010} mode at 3.907 GHz.

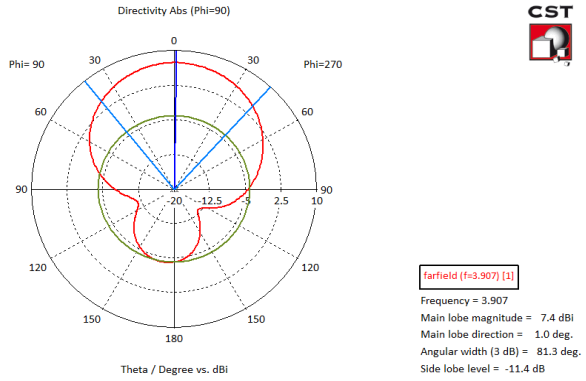

Figure 4: Polar plot of TM_{010} mode at 3.907 GHz.

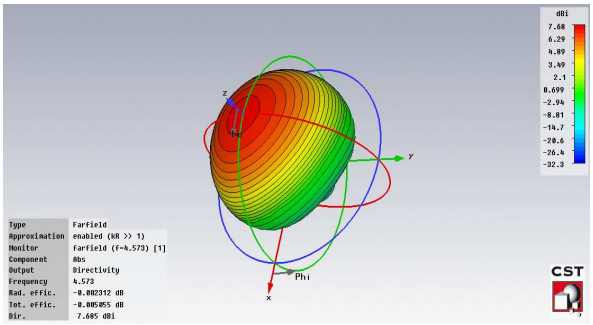

Figure 5: 3D radiation pattern of modified $TM_{0\delta0}$ $(1 < \delta < 3)$ mode at 4.573 GHz.

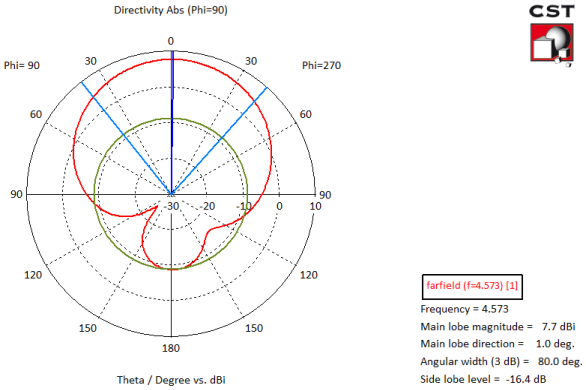

Figure 6: Polar plot of modified $TM_{0\delta0}$ $(1 < \delta < 3)$ mode at 4.573 GHz.

4. ANTENNA APPLICATIONS

Diverse applications can be the focus for this novel designed antenna, since it is a multi-resonant antenna along with high directivity according to simulation results. Each resonant frequency can be the subject of various applications in the planet of advanced satellite communication and microwave C band applications. Figure 2 specifies the presence of three resonant frequencies and S_{11} parameter going under -10 dB. The applications of these three resonant frequencies are listed below:

1. 3.907 GHz: Fixed Service Satellite (FSS), communication satellite downlinks applications;

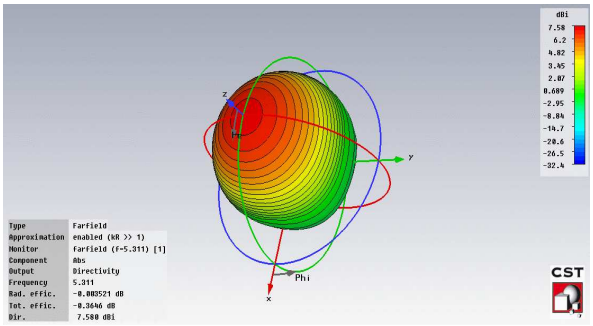

Figure 7: 3D radiation pattern of TM_{030} mode at 5.311 GHz.

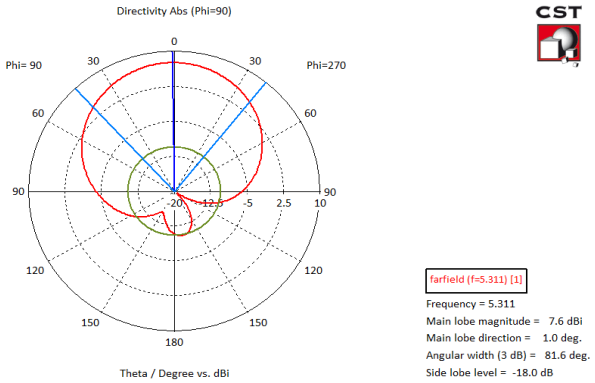

Figure 8: Polar plot of TM_{030} mode at 5.311 GHz.

2. 4.573 GHz: Mobile communication applications;
3. 5.311 GHz: Aeronautic radio navigation, IEEE 802.11a Wi-Fi and cordless telephone applications.

5. CONCLUSION

A novel triple-band compact patch antenna is proposed in this paper. Detailed simulation studies of the antenna have been carried out by Perfect Boundary Approximation (PBA) and unbeatable efficient Finite Integration Technique (FIT) based "CST Microwave Studio" realistic simulator. Parametric study is also obtained to demonstrate the performance of proposed antenna. The small size, high directivity and high gain of this antenna generate it be compatible for many applications such as Fixed Service Satellite, mobile communication, aeronautic radio navigation and microwave C band applications.

REFERENCES

1. Croq, F. and D. M. Pozar, "Multifrequency operation of microstrip antennas using aperture coupled parallel resonators," *IEEE Transactions on Antennas and Propagation*, Vol. 40, No. 11, 1367–1374, 1992.
2. Long, S. A., and M. D. Walton, "A dual-frequency stacked circular-disc antenna," *IEEE Transactions on Antennas and Propagation*, Vol. 27, No. 3, 1281–1285, 1979.
3. Dahele, J. S., K. F. Lee, and D. P. Wong, "Dual frequency stacked annular-ring microstrip antenna," *IEEE Transactions on Antennas and Propagation*, Vol. 35, No. 11, 1281–1285, 1987.
4. Wang, J., R. Fralich, C. Wu, and J. Litva, "Multifunctional aperture coupled stack antenna," *Electron. Lett.*, Vol. 26, No. 25, 2067–2068, 1990.
5. Mirschekar-Syankal, D. and H. R. Hassani, "Characteristics of stacked rectangular and triangular patch antennas for dual band application," *IEEE 8th ICAP*, Edinburgh, Mar. 1993.
6. Wang, B. F. and Y. T. Lo, "Microstrip antenna for dual-frequency operation," *IEEE Transactions on Antennas and Propagation*, Vol. 32, No. 9, 938–943, 1984.
7. Zhong, S. S. and Y. T. Lo, "Single element rectangular microstrip antenna for dual-frequency operation," *Electronics Letters*, Vol. 19, No. 8, 298–300, 1983.
8. Schaubert, D. H., F. G. Ferrar, A. Sindoris, and S. T. Hayes, "Microstrip antennas with frequency agility and polarization diversity," *IEEE Transactions on Antennas and Propagation*, Vol. 29, 118–123, 1981.
9. Wang, B. and Y. Lo, "Microstrip antenna for dual-frequency operation," *IEEE Transactions on Antennas and Propagation*, Vol. 32, 938–943, 1984.
10. Maci, S. and G. B. Gentili, "Dual-frequency patch antennas," *IEEE Antennas and Propagation Magazine*, Vol. 39, 13–20, 1997.
11. Maci, S., G. B. Gentili, P. Piazzesi, and C. Salvador, "Dual-band slot-loaded patch antenna," *IEEE Proc.-Microw. Antennas Propag.*, Vol. 142, No. 3, Jun. 1995.
12. Chen, J. S. and K. L. Wong, "A single-layer dual-frequency rectangular microstrip patch antenna using a single probe feed," *Microwave and Optical Technology Letters*, Vol. 11, 38–84, 1996.

13. Antar, Y. M. M., A. I. Ittipiboon, and A. K. Bhattachatyya, "A dual-frequency antenna using a single patch and an inclined slot," *Microwave and Optical Technology Letters*, Vol. 8, 309–311, 1995.
14. Chowdhury, M. R., M. R. A. Zuboraj, A. A. N. Ovi, and M. A. Matin, "Novel design of triple band rectangular patch antenna loaded with metamaterial," *Progress In Electromagnetics Research Letters*, Vol. 21, 99–107, 2011.
15. Ovi, A. A. N., M. R. Chowdhury, R. A. Zuboraj, and M. A. Matin, "Design of miniaturized dual band microstrip antenna loaded with asymetric J slot," *J. Electr. Eng. Electron. Technol.*, 2013.
16. Ali, S. A., U. Rafique, U. Ahmad, and M. A. Khan, "Multiband microstrip patch antenna for microwave applications," *IOSR Journal of Electronics and Communication Engineering (IOSR-JECE)*, Vol. 3, No. 5, 43–48, Sep.–Oct. 2012, ISSN: 2278-2834, ISBN: 2278-8735.
17. Maidurrahaman, S. M., S. Das, V. K. Yadaw, A. P. Ramkanu, and A. Karmkar, "New compact tri-band microstrip patch antenna using dual T-shaped slit for Wi-Max and microwave C band application," *International Journal of Engineering Sciences Research-IJESR*, Vol. 3, No. 5, Sept.–Oct. 2012, ISSN: 2230-8504; e-ISSN-2230-8512.
18. Costantine, J., K. Y. Kabalan, A. EI-Hajj, and M. Rammal, "New multi-band microstrip antenna design for wireless communications," *IEEE Antennas and Propagation Magazine*, Vol. 49, No. 6, Dec. 2007.
19. Ovi, A. A. N., N. Saha, S. Dey, and N. N. Alam "Symmetrical slot loaded dual band elliptical microstrip patch antenna," *PIERS Procedings*, 538–541, Moscow, Russia, Aug. 19–23, 2012.

Invariant Embedding Method Modification for Calculation "Woodpile" Photonic Crystal

V. L. Kuznetsov and A. S. Rudkovskiy
Moscow State Technical University of Civil Aviation, Russia

Abstract— Modification of the invariant imbedding method to describe the interaction of 3D electromagnetic field with "woodpile" photonic crystal of finite thickness is considered in this paper. This modification allows solving a problem of evanescent modes resonant amplification during numerical calculations for the first layer of photonic crystal. The mathematical model created in this work gives good agreement with physical experiment results.

1. INTRODUCTION

Invariant embedding method should be marked as perspective among the existing methods for the description of PC. Like in transfer matrix methodology [1], it considers scattering medium as a set of elementary layers separated by gaps, but, in contrast to [1], is reduced to embedded equations directly for electromagnetic waves reflection and transmission matrix coefficients [2, 3].

Integration of the embedded equations allows getting these characteristics of the PC for all thicknesses less than specified. However, this advantage, at first glance, of the method leads to necessity of its modification for the analysis of 3D PC Woodpile type. The problem lies in the fact that under certain conditions, evanescent waves can resonate and increase in PC of final thickness. This effect Pendry et al. [4] proposed to use for the possible replacement of metamaterial superlens by 2D PC. The essence of evanescent wave's amplification is explained by unlimited energy supply from the incident wave in the PC. Under such conditions the amplitudes of the diffracted field increases (in time) indefinitely.

We are interested in this issue, because similar resonance effects arise in results of embedded method: for a lossless medium there are thicknesses of PC where some (not all) elements of reflection and transmission matrices corresponding to evanescent modes tend to infinity.

In the paper, a modification of the invariant embedding method is proposed which allows to "activate" interaction between all possible modes at the initial stage of equations integration. This approach allows to organize the "outflow channel" of energy from the evanescent modes, which were isolated and had resonances under standard method.

2. EVANESCENT MODES AMPLIFICATION PRINCIPLE

Consider monochromatic evanescent wave with frequency $\omega = ck$ incidence on a flat layer of thickness d which consists of medium with real permittivity $\varepsilon > 1$ (lossless medium). Let's choose the parameters in a way that wave vector was complex outside the layer and real inside. This will take place if $\vec{q}$ — the transverse component of the wave vector $\vec{k}$ satisfies the conditions $\varepsilon k_0^2 > q^2 > k_0^2$, i.e., incident evanescent wave becomes propagating inside the layer. Layer borders for this propagating wave are perfect mirrors and in this case electromagnetic field is "blocked" in resonator. According to entrenched notions [5] field amplitude inside the layer can be calculated using following formula:

$$E = E_0 \left\{ 1 + r^2 \exp\left(2ik_{\varepsilon z} d\right) + \left[r^2 \exp\left(2ik_{\varepsilon z} d\right) \right]^2 + \ldots \right\} = E_0 / \left[1 - r^2 \exp\left(2ik_{\varepsilon z} d\right) \right] \qquad (1)$$

Here E_0 — complex amplitude of a field which penetrate into a layer through its top border (incident field interact with a layer from above), $r = \exp(-i\,\delta)$ — reflection coefficient from layer border for propagating wave (δ in our case has real value).

It can be seen from (1) that if $(\delta + k_{\varepsilon z} d) \to \pi n$, n — integer, than field amplitude $E \to \infty$. Calculating formally reflection coefficient as ratio between reflected and incidence field we can conclude that in this case it should tend to infinity. The same result follows both from equations

presented in [5] and from embedded equations analytical solution for homogeneous layer:

$$\frac{dR}{dz} = R\cdot\rho\cdot R + R\cdot\tau + \tau\cdot R + \rho$$

$$R(z) = \frac{\rho\cdot\sin\left(z\cdot\sqrt{\rho^2-\tau^2}\right)}{\sqrt{\rho^2-\tau^2}\cdot\cos\left(z\cdot\sqrt{\rho^2-\tau^2}\right) - \tau\cdot\sin\left(z\cdot\sqrt{\rho^2-\tau^2}\right)}$$

where $\tau = i\cdot k_z + \frac{i\cdot(\varepsilon-1)}{2\cdot k_z}$; $\rho = \frac{i\cdot(\varepsilon-1)}{2\cdot k_z}$.

Reflection coefficient dependence as function of layer thickness and transverse component of the wave vector module — $|\vec{q}|$ presented in (Fig. 1). Notice that due to fact that evanescent mode do not transfer energy in the direction perpendicular layer borders its flux equal to 0, i.e., observed singularities do not lead to any inconsistencies of the law of conservation of energy.

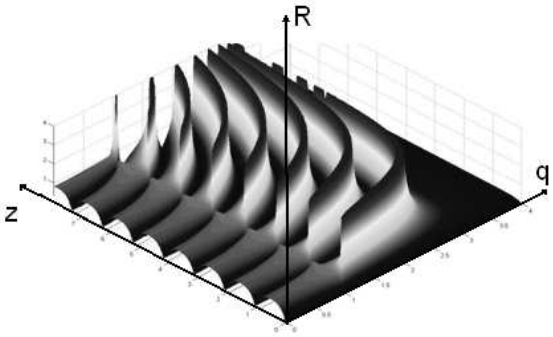

Figure 1: Reflection coefficient dependence as function of layer thickness and transverse component of the wave vector module.

Let's now discuss resonance effects in two dimensional photonic crystal (2D PC). Consider transverse components of the wave vectors which interact inside 2D PC (Fig. 2). They differ by an integer number of reciprocal lattice vectors — $\vec{\kappa}$. Usually propagated waves considered as initial and in this case inside 2D PC modes which represented in (Fig. 2(a)) generated. Among these modes there are evanescent modes, however resonance effects for them smoothed because in case of modes interactions part of the energy which is accumulated in evanescent modes region transferred to propagated modes region and leaves PC. Thus, propagated modes play a role of dissipative processes fore evanescent modes.

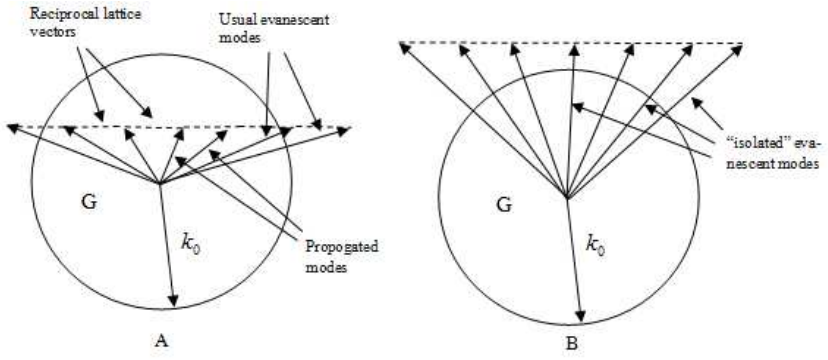

Figure 2: Different type of modes inside PC.

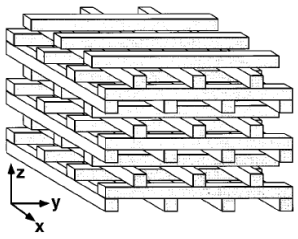

Figure 3: Woodpile PC which is investigated.

Situation changes when we start to investigate woodpile photonic crystal which is presented in (Fig. 3). In the beginning of embedded equation integration (bottom layer of bars) it would seem that we again deal with 2D PC which was discussed earlier but this is not the case because incidence field consist of full set of modes which take place in 3D PC. Particularly part of incident field consists of modes which presented in (Fig. 2(b)). For these modes process of energy outflow

which was discussed above do not work. Energy swap exists only among these evanescent modes and in this case energy does not leave PC. As a result the same effect of energy accumulation occurs as have already been observed in case of isotropic layer and resonance effects became inevitable inside the first layer of PC.

3. INVARIANT EMBEDDING METHOD MODIFICATION FOR CALCULATION OF WOODPILE PC

Resonances can be smoothed if we organize interaction between "isolated" evanescent modes and propagating modes, i.e., create energy "outflow channel". It should be mentioned that resonances also disappear if medium with complex permittivity assumed in the mathematical model, but in this case it's impossible to check the results of calculation using Pointing theorem. Hence taking into account dissipation inside the medium significantly decrease reliability of results.

In this work, we suggest alternative approach of organizing energy outflow for evanescent modes which allows from the first steps of embedded equations integration model Woodpile PC as three dimensional structure which do not have "isolated" evanescent modes. This is achieved by increasing PC thickness adding elementary layers both from upper and lower borders and by taking boundary between layers with different orientation of bars as initial point for calculations (Fig. 4). In this case there are interactions between modes which transverse components of the wave vector $\vec{q}$ satisfy the condition $\vec{q}' = \vec{q}'' + \vec{\kappa}_1 \cdot n + \vec{\kappa}_2 \cdot m$, $n,\ m \in Z$. Here $\vec{\kappa}_1$ and $\vec{\kappa}_2$ — orthogonal vectors which correspond to adjacent layers with different orientation of dielectric bars. Thus all evanescent waves interacts with propagating waves which provide outflow of energy from the crystal. Particularly new approach organizes interaction between modes which were presented in (Fig. 2(a)) and (Fig. 2(b)).

For technical realization of new approach we following work [3] will seek exploded solution of the matrix equation for full scattering matrix S which has following view:

$$\frac{dS}{dz} = \chi^+ + \xi^+ \cdot S + S \cdot \xi^- + S \cdot \chi^- \cdot S, \tag{2}$$

here $\mathbf{S} = \begin{pmatrix} R^+ & T^+ \\ T^- & R^- \end{pmatrix}$; $\chi^\pm = \begin{pmatrix} \rho^\pm & 0 \\ 0 & 0 \end{pmatrix}$ and $\xi^\pm = \begin{pmatrix} \tau^\pm & 0 \\ 0 & 0 \end{pmatrix}$, $\rho^\pm$ and $\tau^\pm$ — matrix characteristics of reflection and transition for elementary layer explicit form of which is determined by the geometry and the structure of Woodpile PC.

It also can be shown that embedded equation general view for S-matrix if thickness of crystal is increasing by adding elementary layers from below similar to (2) and difference between them is only in details:

$$\frac{dS}{dz} = \tilde{\chi}^- + \tilde{\xi}^- \cdot S + S \cdot \tilde{\xi}^+ + S \cdot \tilde{\chi}^+ \cdot S. \tag{3}$$

here $\tilde{\chi}^\pm = \begin{pmatrix} 0 & 0 \\ 0 & \rho^\pm \end{pmatrix}$ and $\tilde{\xi}^\pm = \begin{pmatrix} 0 & 0 \\ 0 & \tau^\pm \end{pmatrix}$, and matrices $\rho^\pm$ and $\tau^\pm$ are the same as in (2). Integration of (3) goes to the direction $z < 0$.

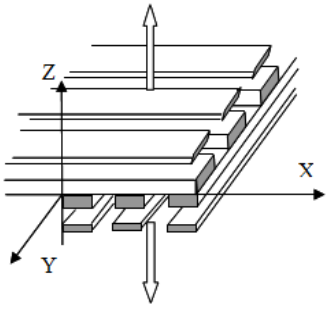

Figure 4: Increasing PC thickness in two directions in case of invariant embedding method modification.

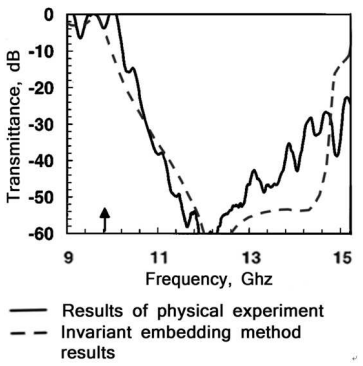

Figure 5: Comparison of physical experiment with numerical results for Woodpile PC.

Systems of Equations (2), (3) should be supplemented with apparent initial conditions $\mathbf{S}(0) = \begin{pmatrix} 0 & I \\ I & 0 \end{pmatrix}$, where I — the identity matrix.

Procedure of integration Equations (2), (3) can be described in a following way: in the beginning we integrate (2) in the interval $(0, z_1)$ with initial condition $\mathbf{S}(0)$ to find $\mathbf{S}(z_1)$, then we integrate (3) in the interval $(0, -z_1)$ with initial condition $\mathbf{S}(z_1)$ to find $\mathbf{S}(-z_1)$. On the next step we again integrate (2) but in the interval (z_1, z_2) with initial condition $\mathbf{S}(-z_1)$ and so on.

4. NUMERICAL RESULTS

To check efficiency of embedded method modification we matched results of physical experiment [6] with results of our calculations using Equations (2) and (3). For investigation we choose Woodpile PC (Fig. 3) which consists of 12 layers formed by industrial aluminum bars with square cross-section 3.1×3.1 mm and structure period 11.2 mm. In our case we assume normal incidence of electromagnetic wave on top layer of PC.

Comparison of experimental frequency dependencies for transition coefficient and numerical results of calculations for such a PC presented in (Fig. 5).

We check energy balance using Pointing theorem on every step of integration and it was shown that error does not exceed $3 \cdot 10^{-11}$.

To check stability of stop band additional calculations were made when field incident on a crystal with different angles. We made calculations when wave vector has following angles in spherical coordinate system connected with PC: $\theta = \pi/7$ and $\varphi = \pi/7$. From results presented it can be seen that stop band is stable in frequency region 10–14 GHz (Fig. 6).

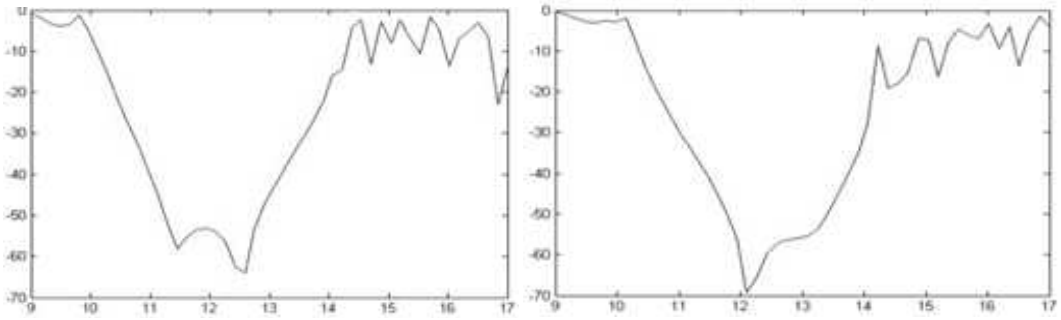

Figure 6: Initial field oblique incidence case. (a) Correspond to vertical polarization case, (b) to horizontal polarization case.

REFERENCES

1. Barnes, C. and J. B. Pendry, "Multiple scattering of waves in random media: A transfer-matrix approach," *Proc. R. Soc. Lond. A*, Vol. 435, No. 1893, 1991.
2. Barabanenkov, Y. N., V. L. Kouznetsov, and M. Y. Barabanenkov, "Transfer relations for electro-magnetic wave scattering from periodic dielectric one-dimension interface: TE polarization," *Progress In Electromagnetic Research*, Vol. 24, 39–75, 1999.
3. Barabanenkov, Y. N. and M. Y. Barabanenkov, "Energy invariants to composition rules for scattering and transfer matrices of propagating and evanescent waves in dielectric structures," *PIERS Proceedings*, 10–12, Cambridge, USA, Mar. 26–29, 2006.
4. Luo, C., S. G. Jonson, J. D. Joanopoulos, and J. B. Pendry, "Subwavelength imaging in photonic crystals," *Phys. Rev. B*, Vol. 68, 2003.
5. Born, M. and E. Wolf, *Principles of Optics*, Pergamon Press, Oxford, 1965.
6. Ozbay, E., "Layer-by-layer photonic crystals from microwave to far-infrared frequencies," *J. Opt. Soc. Am. B*, Vol. 13, 1996.

A Homogeneous Magnetostatic Field Exposure System for Presowing Magnetic Treatment of Seeds

M. A. Azpúrua, Y. Sánchez, and E. J. Páez
Instituto de Ingeniería, Venezuela

Abstract— This paper presents a system for the generation of spatially homogeneous magnetic field, which is intended for the application of magnetic treatments on seeds. The system consists of an array of six coils, which have been sized and located in the space in order to optimize both the spatial homogeneity of the magnitude of magnetic flux density and the average magnitude of it within the volume of interest. The optimization process is implemented using a semi-analytical method that uses the generic equations that model the static magnetic flux density generated by thin wire rectangular coils fed with direct current, within an iterative TABU search algorithm under multiple constraints: the maximum and minimum dimensions of the coils, the maximum number of turns of the windings, the maximum allowable power consumption for each winding and the enameled wire gauge to be used in the windings. The designed system nominal characteristics allow the generation of a magnetic induction up to 10 mT for a current of approximately 14.5 A achieving a spatial homogeneity of 99% in the magnitude of the magnetic flux density over a rectangular volume of $0.5\,\mathrm{m} \times 0.5\,\mathrm{m} \times 1\,\mathrm{m}$ (250 lt). The experimental validation was performed following the test protocol that includes measuring the magnetic flux density and power consumption of the coils. The designed device presents a satisfactory performance considering the system constructive tolerances and made possible the implementation of the aforementioned magnetic treatment on large seed samples simultaneously, ensuring control of the exposure dose for further experimental studies on the influence of static magnetic fields in the process of seed germination, water uptake relations and subsequent developments.

1. INTRODUCTION

Some applications require a highly homogeneous and controlled magnetic field generation such as in bioelectromagnetism research [1]. Many of the experiments conducted to study the effect of magnetic treatment on biological systems require devices that can generate magnetic fields which ensures repeatable and controlled exposure to the samples involved in these experiments also allowing to the experimenter to observe, handle and easily place the samples. Therefore, the working volume must be easily accessible and, the electrical design and construction should be as simple as possible. In this regard, arrangements of air core coils have traditionally been used to ensure a certain spatial distribution of electromagnetic fields when fed by an electric current [2–7].

One of the applications where controlled exposure to magnetic fields may be used in the improvement of production processes is the magnetic stimulation of seeds. In the last decade there have been numerous studies that have shown both experimentally [8] and theoretically [9] that the influence of magnetic field on the seeds can regulate water relations prior to germination, enhancing the rate of absorption of fluids and therefore increasing the germination rate and the yield of the crops.

However, the underlying technological challenge for harnessing the phenomenon of seeds stimulation through magnetic treatment falls in the design of a system to generate spatially homogeneous magnetic fields over a large enough volume to simultaneously treat a seed lot in order to make this technology viable. In this regard, it was required to design a coils arrangement that generates on average up to 10 mT in a volume of $0.5\,\mathrm{m} \times 0.5\,\mathrm{m} \times 1\,\mathrm{m}$ (250 lt) and with 99% spatial homogeneity for the magnetic flux density.

For this purpose, a semi-analytical method for the design of coil systems was developed to synthesize highly homogeneous magnetostatic field distributions based on an optimization process that employs generic equations to model the magnetostatic flux density generated by rectangular wire coils fed by a continuous current, within an iterative TABU search algorithm under multiple restriction, such as, maximum and minimum dimension of coils, maximum number of turns in the windings, the maximum allowed power consumption for each winding and the wire gauge used for the windings [10].

Once the nominal specifications of the designed system are satisfied, another aspects that affect the manufacturing process and the measurement of the field homogeneity must be considered. In this regard, these research present the designed system implementation and validation of the fundamental electric and magnetic parameters that guarantee the system aptitude.

2. DESCRIPTION OF THE MAGNETOSTATIC FIELD GENERATION SYSTEM

The magnetostatic field generation system has a set of six square coils ($N = 6$) of 1 m average side length ($a_i = b_i = 0.5\,\mathrm{m}$), coaxial about the longitudinal axis ($h_1 = -72.9\,\mathrm{cm}$, $h_2 = -36.7\,\mathrm{cm}$, $h_3 = -11.6\,\mathrm{cm}$, $h_4 = 11.6\,\mathrm{cm}$, $h_5 = 36.7\,\mathrm{cm}$, $h_6 = 72.9\,\mathrm{cm}$), electrically connected in series, built with enameled copper wire AWG 10, fed by a maximum dc electrical current ($I_{\max}$) of 14.49 A, and whose windings, end to end, have the following number of turns, $n_1 = 368$, $n_2 = 160$, $n_3 = 140$, $n_4 = 140$, $n_5 = 160$ and $n_6 = 368$, respectively.

The mathematical model used to theoretically calculate the spatial distribution of the magnetic flux density is based on the superposition of the magnetic induction analytically obtained for each winding, using the Bio-Savart law considering the spirals as current filaments (thin wire coils). Figure 1 shows the magnetic flux density distribution calculated with the aforementioned model. This model used was computationally validated by simulation using the Finite Element Method (FEM) through of the program *COMSOL Multiphysics*^{TM} *4.2* [7].

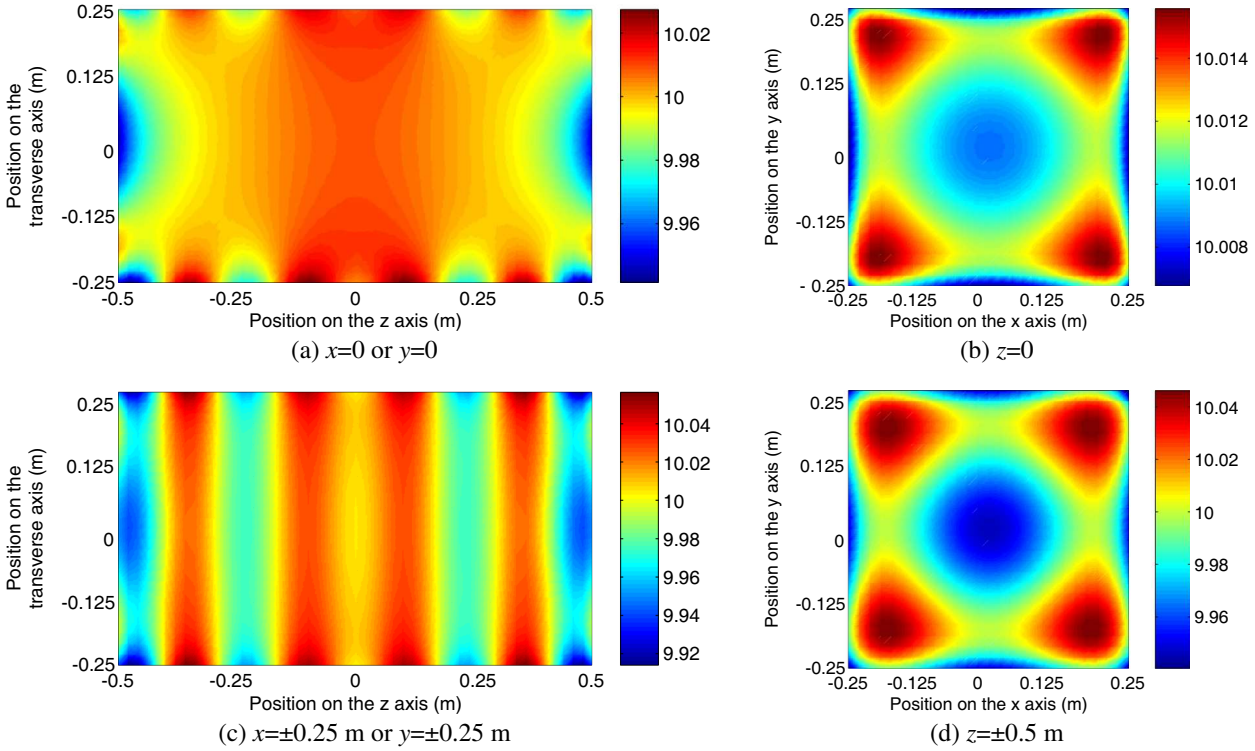

(a) x=0 or y=0 (b) z=0

(c) x=±0.25 m or y=±0.25 m (d) z=±0.5 m

Figure 1: Magnitude of the magnetic flux density of the designed coil system in the external faces of V. Note: The colorbar scale indicates the magnitude of the magnetic flux density in units of militesla.

The theoretical results obtained for this coil system were a spatial homogeneity of magnetic flux density within the volume of interest, $H = 98.7\%$, with an average magnitude of the magnetic flux density within the volume of interest, $\bar{B} = 10.00\,\mathrm{mT}$, a maximum value for the magnitude of the magnetic flux density within the volume of interest, $B_{\max} = 10.05\,\mathrm{mT}$, and a minimum value for the magnitude of the magnetic flux density within the volume of interest, $B_{\min} = 9.92\,\mathrm{mT}$.

On the other hand, FEM simulation results were $B_{\max\ FEM} = 10.14\,\mathrm{mT}$, $B_{\min\ FEM} = 9.84\,\mathrm{mT}$, $\bar{B}_{FEM} = 10.00\,\mathrm{mT}$ and $H_{FEM} = 97.23\%$.

Regarding power consumption and considering that the system is fed by dc current, it can be modelled, in steady-state, as a fully resistive system, wherein each of the coils dissipates by Joule effect a power given by (1),

$$P_i = {I_i}^2 R_i \approx {I_i}^2 \rho_{\mathrm{Cu}} n_i \frac{4 l_{turn}}{\pi d^2}, \tag{1}$$

where R_i is the dc resistance of the i-th coil, which is approximated from the electrical resistivity of copper wire, ρ_{Cu} (at 25°C of room temperature), the wire length, l, and its transversal cross-sectional area, A. The cable length is estimated from the average length of a single turn, l_{turn},

multiplied by the number of turns of the winding, n_i. A is calculated by assuming a circular cross section of diameter d.

Considering the above, is estimated that power consumption is 996 W for windings 1 and 6, 433 W for windings 2 and 5, and 379 W for windings 3 and 4.

In relation to the mechanical characteristics of the device, it is important to emphasize that structure on which is held every winding was built by bending an aluminum profile of $2'' \times 2'' \times 3$ mm to form a square geometry with an average length of 1 m for each side. The aluminum frames were strengthened in the corners using welding. The support structure was made of plywood and it also has a wheel at each of the 12 support points in order to transfer all the weight to the floor. The windings mass is approximately 70 kg, 30 kg and 26.5 kg for windings 1 & 6, 2 &5 and 3 & 4, respectively. The total mass to the system is about 300 kg (See Figure 2).

Figure 2: Coil-systems for homogeneous magnetostatic field generation.

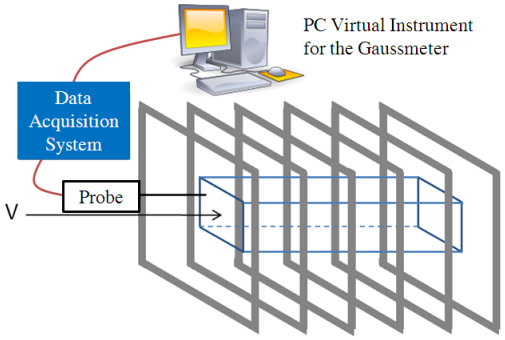

Figure 3: Experimental validation process for the highly homogeneous magnetic field generation system.

3. VALIDATION OF THE HOMOGENEITY MAGNETIC FLUX DENSITY

The spatial homogeneity of the magnetic field, H, is a measure of the variability of the magnetic field within a defined region of space. Different approaches have been taken to quantify H. Consequently, for the scope of this work the most suitable definition of H is given by (2) [11], as it provides a single global index that summarizes the maximum variation of the magnitude of the magnetic flux density, B, within the volume of interest, V, with respect to its average value of B, $\bar{B}$. This is important in biomagnetic experimentation in order to control the doses and the treatments applied to the samples being evaluated.

$$H = 1 - \frac{\max(B) - \min(B)}{\bar{B}} \tag{2}$$

Since the magnetic flux density is a vector variable that is distributed continuously in space, following a experimentally unknown pattern, an exact quantification of the homogeneity of the magnetic field within the volume of interest would require the experimental determination of these changes using an infinite number of measurements of B at all points within V. Since this is not feasible, the volume of interest must be regularly sampled to define a three-dimensional square grid, in which each point represents a measurement point that marks the location of the gaussmeter triaxial probe that measures the orthogonal components of the magnetic flux density vector in relation to the cartesian coordinate system used as reference.

The magnetic field measurements is performed with a calibrated triaxial gaussmeter (See Figure 3) specifically designed for requirements of these project and whose characteristics are described in [12].

For each of the measuring points, the gaussmeter calculates the magnitude of the magnetic flux density and their average, maximum and minimum values. The different values obtained for B, are recorded for the computation of H using (2), after the completion of the measurement process.

Finally, the electrical parameters of the coil system were validated measuring the voltage, the current and the resistance of each winding, in order to calculate indirectly the power consumption through their relations.

4. RESULTS

Based on the measurements results, spatial homogeneity of magnetic flux density was estimated at 97.29% within the volume of interest, taking $\bar{B} = 9.98\,\mathrm{mT}$, $B_{\max} = 10.10\,\mathrm{mT}$ and $B_{\min} = 9.83\,\mathrm{mT}$.

Regarding the distribution of magnetic flux density, Figure 4 shows that the magnetic field has a response approximately constant over the longitudinal extension of the volume of interest $[-0.5,\ 0.5]$ m both for the central axis ($x = 0,\ y = 0$) and for one of the edges of V. It also shows that the results are consistent with the estimates obtained using the model described in [7, 10] and comply with the requirements and design constraints, particularly established for this application, within the uncertainty of measurements [10, 12] and tolerances to manufacturing errors. Consequently, the results also validates experimentally the design method and the model used to estimate the distribution of the magnetic field.

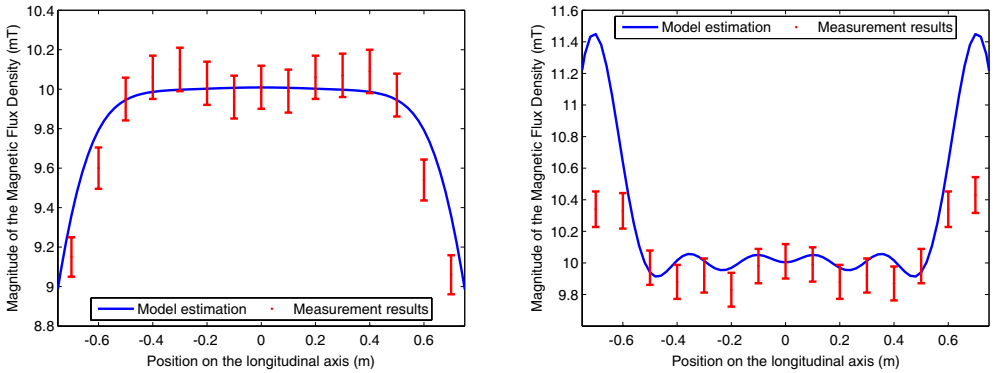

(a) $(x; y) = (0; 0)$ (b) $(x; y) = (0.25; 0.25)$ m

Figure 4: Magnitude of the magnetic flux density of the designed coil system.

Table 1 shows the results of the validation of the electrical parameters for each winding. The results are satisfactory considering the uncertainty in the measurement ($\pm 5\%$) and the increment in the power consumption caused by the rise of the temperature, and therefore of the resistance, associated to the continuous operation of the coil system fed by the maximum input current.

Table 1: Electrical parameters validated for the designed coil system.

Parameter	Coil 1	Coil 2	Coil 3	Coil 4	Coil 5	Coil 6
R_i (Ω)	4.83	2.26	1.85	1.91	2.16	4.79
P_i (W)	1016.21	475.49	389.26	401.85	454.45	1077.92

5. CONCLUSION

A laboratory prototype of a system for magnetic stimulation of seed with application in improving crop yield has been implemented. This was designed and validated using techniques, models, algorithms and tools developed specifically for the design requirements. The results show that this coil configuration allows to globally synthesize highly homogeneous magnetostatic fields over a large working volume, when compared with other coil configurations previously reported. Also, since the definition used in the spatial homogeneity of the magnetic flux density is a global parameter, the results achieved show superior performance to those presented in similar designs. Consequently, designed device presents a satisfactory performance and is potentially scalable.

REFERENCES

1. Kirschvink, J. L., "Uniform magnetic fields and double-wrapped coil systems: Improved techniques for the design of bioelectromagnetic experiments," *Bioelectromagnetics*, Vol. 13, No. 5, 401–411, 1992.
2. Cvetkovic, D. and I. Cosic, "Modelling and design of extremely low frequency uniform magnetic field exposure apparatus for in vivo bioelectromagnetic studies," *29th Annual International Conference of the IEEE on Engineering in Medicine and Biology Society*, 1675–1678, Lyon, France, Aug. 2007.

3. Pulyer, Y. and M. Hrovat, "Methodology for universal synthesis of magnetic designs based on field specifications," *IEEE Transactions on Magnetics*, Vol. 38, No. 3, 1553–1563, 2002.
4. Brooks, N. and T. Baldwin, "Modelling and design of extremely low frequency uniform magnetic field exposure apparatus for in vivo bioelectromagnetic studies," *Proceedings of the Thirty-fourth Southeastern Symposium on Systems Theory*, 1675–1678, Huntsville, Alabama, Mar. 2002.
5. Bongiraud, J. P., G. Cauffet, C. Jeandey, and P. Le Thiec, "An optimization method for magnetic field generator," *2nd International Conference on Marine Electromagnetic*, 161–168, Brest, France, Jul. 1999.
6. McClung, A., "Characterization of the magnetic field of a cosine coil distribution," *University of Washington Report*, Vol. 2, No. 3, 1–6, 2009.
7. Azprua, M. A., "A semi-analytical method for the design of coil-systems for homogeneous magnetostatic field generation," *Progress In Electromagnetics Research B*, Vol. 37, 171–189, 2012.
8. García, F., L. Arza, and I. Almanza, "Influence of a stationary magnetic field on water relations in lettuce seeds," *Part II: Experimental Results. Bioelectromagnetics*, Vol. 22, No. 8, 596–602, 2001.
9. García, F. and L. Arza, "Influence of a stationary magnetic field on water relations in lettuce seeds," *Part I: Theoretical Considerations. Bioelectromagnetics*, Vol. 22, No. 8, 589–595, 2001.
10. Azpúrua, M. A., "Estimación de la incertidumbre en la medición de la homogeneidad espacial del campo magnético en sistemas de generación de campo Magnetostático utilizando el Método de Monte Carlo," *5to Congreso Iberoamericano de Estudiantes de Ingeniería Eléctrica (V CIBELEC 2012)*, TEL1–TEL8, Mérida, Venezuela, May 2012.
11. Di Barba, P., F. Dughiero, and E. Sieni, "Magnetic field synthesis in the design of inductors for magnetic fluid hyperthermia," *IEEE Transactions on Magnetics*, Vol 46, No. 8, 2931–2934, 2010.
12. Sánchez, Y., C. Rosi, M. A. Azpúrua, and J. Marañón, "Caracterización y estimación de la incertidumbre en la medición de inducción magnética utilizando un gaussímetro basado en sensores de efecto hall," *10^{mo} Congreso Internacional de Metrología Eléctrica, X SEMETRO*, Buenos Aires, Argentina, Sep. 2013.

Fractal Zone Plates for Terahertz Focusing and Imaging

W. D. Furlan[1], **V. Ferrando**[1, 2], **A. Calatayud**[2], **and J. A. Monsoriu**[2]

[1]Departamento de Óptica, Universitat de València, Burjassot 46100, Spain
[2]Centro de Tecnologías Físicas
Universitat Politècnica de València, Valencia 46022, Spain

Abstract— We present novel designs for diffractive lenses with low chromatic aberration to be used in terahertz focusing and imaging. Conventional diffractive lenses (Fresnel zone plates) have been successfully applied in this area due to their low, attenuation, thickness, and weigth. However, the strong chromatic aberration of these diffractive lenses limit their application only to systems with narrowband sources. We propose Fractal zone plates (FrZP) as a special type of zone plate where the pattern of the zones is fractal along the square of the radial coordinate. As a result, these lenses produce multiple foci with a self-similar structure. The main lobes of the different foci provided by a FrZP coincide in the axial position with those obtained with a conventional Fresnel zone plate, but the subsidiary foci of the FrZP provide an extended depth of focus for each wavelength that partially overlap with the other one, creating an overall extended depth of focus which is less sensitive to the chromatic aberration. We have tested the THz imaging capabilities of FrZPs with broadband sources and compared their performance against a conventional Fresnel zone plate of the same main focal distance.

1. INTRODUCTION

A growing interest in Zone Plates [1] has been experienced during the last years because they are becoming key elements in obtaining images in several scientific and technological areas such as THz tomography [2] and soft X-ray microscopy [3, 4]. Fresnel Zone Plates (FZP) have currently found a large number of new applications in the terahertz wavelength range given that they satisfy the increasing demand for more compact, light-weight, and cost-effective systems and components [5–11]. However, mainly to their high chromatic aberrarion conventional FZPs have inherent limitations. With this motivation, our group proposed Fractal Zone Plates (FrZPs) as new promising 2D photonic structures [12, 13]. A FZP can be thought as a conventional zone plate with certain missing zones. A FrZP is characterized by its fractal profile along the square of the radial coordinate.

The axial irradiance provided by a FrZP when it is illuminated with a monochromatic plane wavefront presents multiple foci. The internal structure of each focus exhibits a characteristic fractal structure, reproducing the self-similarity of the originating FrZP. It has been shown that this property can be profited in image forming systems to obtain an extension of the depth of field [14, 15].

In this contribution the axial irradiance provided by FrZPs is numerically evaluated for the terahertz range.

2. LENS DESIGN

As is well known, conventional FZPs consist of alternate transparent and opaque concentric rings, the radii of which are proportional to the square root of natural numbers. The transmitance of FZPs can be obtained as a periodic binary function, $q_{FZP}(\zeta)$, which is represented using a new variable, $\zeta = r_0^2$ and it is rotated around the origin, being $r_0 = r/a$ the normalized radial coordinate where a is the radi of the lens. The generating function can be written mathematically as a Ronchi-type binary periodic function with period p:

$$q_{FZP}(\zeta, p) = \mathrm{rect}\,(\zeta - 0.5)\,\mathrm{rect}\left[\frac{\mathrm{mod}\left(\zeta + \frac{p}{2} - 1, p\right)}{p}\right], \tag{1}$$

being the function $\mathrm{mod}(x, y)$ gives the remainder of the division of x by y, and the function $\mathrm{rect}(x)$ takes the value 1 for $|x| \leq 1$ and 0 elsewhere.

In a similar way, one constructs FrZPs by replacing the binary generating periodic function described above with a binary function with a fractal profile. Consider, for example, the regular Cantor fractal, which is constructed iteratively. In the first stage ($S = 0$) the initial segment is divided into an odd number of segments, $(2N - 1)$, and the segments in the even positions are

removed (In this work we study a FrZP based on the triadic Cantor set ($2N-1=3$)). For the remaining N segments at the first stage this slicing-and-removing process is repeated in the second stage, and so on. The pupil function can be written mathematically as

$$q_{FrZP}(\zeta, N, S) = \prod_{i=0}^{S} q_{ZP}\left[\zeta, \frac{2}{(2N-1)^i}\right], \tag{2}$$

and the equivalent FZP pupil function is obtained using Eq. (1) with

$$p(N, S) = \frac{2}{(2N-1)^S}. \tag{3}$$

The obtained pupiles for the FrZP and its equivalent FZP with $N=2$ and $S=3$ can be seen in Fig. 1.

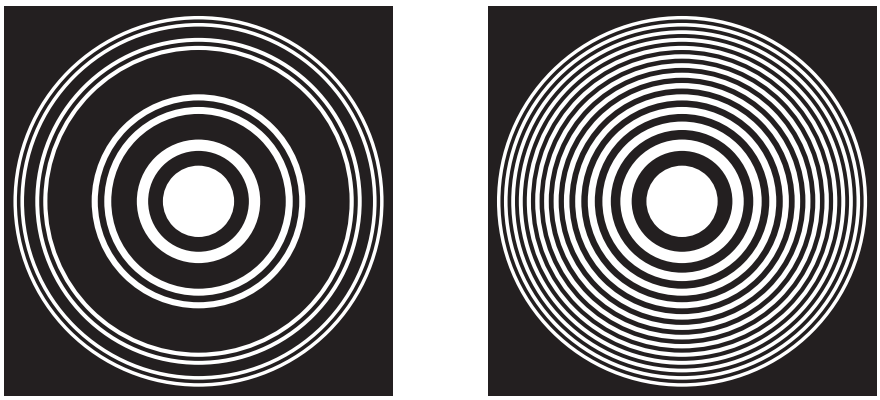

(a) (b)

Figure 1: (a) Pupil for the FrZP based on the order $S=3$ triadic Cantor set and (b) its equivalent FZP.

Figure 1(a) shows the pupil for the FrZP based on the order $S=3$ triadic Cantor set, which can be compared to its equivalent FZP shown in Fig. 1(b). Note that the FrZP pupil is the FZP pupil with some missing rings.

3. FOCUSING PROPERTIES

Under a monochromatic plane wave illumination of wavelength λ, the diffracted axial irradiance provided by an optical system with a rotationally invariant normalized pupil function is obtained from the Fresnel-Kirchhoffs scalar diffraction theory and it can be written as

$$I(z) = \left(\frac{\pi a}{\lambda z}\right)^2 \left| \int_0^1 q(\zeta) \exp\left(-i\frac{\pi a^2 \zeta}{\lambda z}\right) d\zeta \right|^2, \tag{4}$$

where z is the propagation length.

To compare the axial behavior of a FrZP with its equivalent FZP (A FZP with the same focal length), we will obtain analytically the axial irradiance distributions in both cases. The axial irradiance provided by a FZP obtained with Eq. (4) leads to the well known result [16]

$$I_{FZP}(z, N, S) = \frac{\sin^2\left[\frac{M\pi a^2}{\lambda z(2N-1)^S}\right]}{\cos^2\left[\frac{\pi a^2}{2\lambda z(2N-1)^S}\right]}, \tag{5}$$

being M the number of transparent zones given by the smallest integer greater, or equal to, $(2N-1)^S/2$. The axial irradiance provided by the FrZP

$$I_{FrZP}(z, N, S) = 4\sin^2\left[\frac{\pi a^2}{2\lambda z(2N-1)^S}\right] \prod_{i=1}^{S} \frac{\sin^2\left[\frac{N\pi a^2}{\lambda z(2N-1)^i}\right]}{\sin^2\left[\frac{\pi a^2}{\lambda z(2N-1)^i}\right]}, \tag{6}$$

For both, the FrZP and the corresponding FZP, the main focus occurs at

$$f(N,S) = \frac{a^2}{\lambda(2N-1)^S}. \tag{7}$$

We have computed the axial irradiance provided by the pupils shown in Fig. 1 for different wavelengths in the THz range. The radii of the simulated lens has been choosen $a = 28.44\,\text{mm}$ in order to have a $f = 100\,\text{mm}$ focal length for $\nu = 1\,\text{THz}$. In Fig. 2 we represented the normalized axial irradiance provided by these lenses.

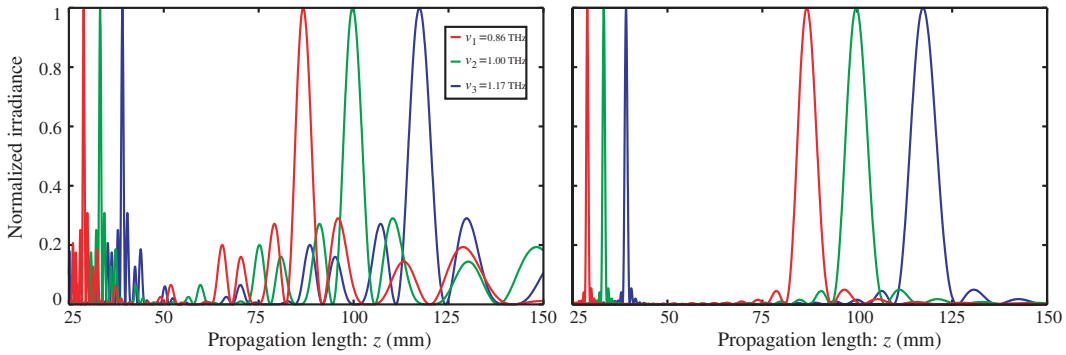

Figure 2: Point spread functions for different wavelengths. The axial irradiances were computed by using Eq. (4) for $a = 28.44\,\text{mm}$ and $\lambda = 345\,\mu\text{m}$ ($\nu = 0.85\,\text{THz}$) [red], $\lambda = 300\,\mu\text{m}$ ($\nu = 1\,\text{THz}$) [green], and $\lambda = 255\,\mu\text{m}$ ($\nu = 1.17\,\text{THz}$) [blue] for the (a) FrZP based on the $S = 3$ order triadic Cantor set, and (b) its equivalent FZP.

As can be seen, the principal lobes of the different foci provided by a FrZP coincide in the axial position with those obtained with a conventional Fresnel zone plate, but the FrZP produces a sequence of subsidiary foci around each major focus following the fractal structure of the FrZP itself. In general, the position, the intensity and the 3D shape of the focal spot depend on the fractal level of the encoded fractal function $q(\zeta)$. In all cases these subsidiary foci of the FrZP provide an extended depth of focus for each wavelength that partially overlaps with the other ones, creating an overall extended depth of focus that is less sensitive to chromatic aberration.

We have tested experimentally the imaging capabilities of FrZP in the visible range. Fig. 3 shows the image of a test object provided by a FrZP, and for comparison purposes, the image obtained with a FZP of the focal distance. As the light throughput of the FrZP is lower, the corresponding image is faint but, as can be seen, it is less chromatically aberrated.

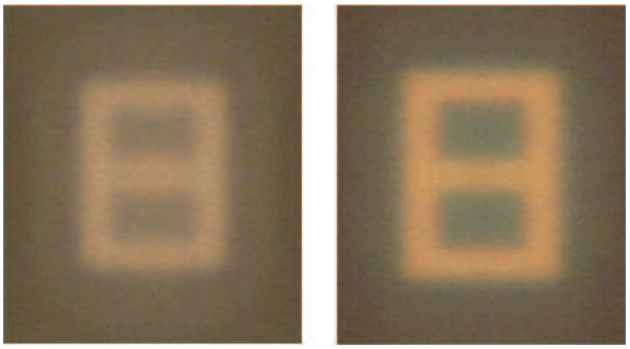

Figure 3: Images of a test object provided by (a) a FrZP and by (b) a FZP, for the focal distance (at 633 nm) is 124 mm and $a = 2.52\,\text{mm}$. The images were obtained using visible light (150 W EKE 3220 K halogen lamp).

4. CONCLUSION

We believe that the improved imaging capabilities, due to the increased focal depth and the reduced chromatic aberration, that FrZPs offer in polichromatic imaging could be profitable in the terahertz range. Thus, our proposal overcome the inherent limitations of Fresnel zone plates maintaining the desired large numerical aperture. While our lens designs are tested with THz radiation, the design considerations are applicable also to other regions of the electromagnetic spectrum.

ACKNOWLEDGMENT

We acknowledge the financial support from Ministerio de economía y competitividad (grant FIS2011-23175) and Generalitat Valenciana (grant PROMETEO2009-077), Spain.

REFERENCES

1. Ojeda-Castañeda, J. and C. Gómez-Reino, *Selected Papers on Zone Plates*, SPIE Optical Engineering Press, Washington, 1996.
2. Wang, S., X. Zhang, M. Maley, M. Hundley, L. Bulaevskii, A. Koshelev, and A. Taylor, "Terahertz tomographic imaging with a fresnel lens," *Opt. Photonics News*, Vol. 13, No. 12, 58–58, 2002.
3. Wang, Y., W. Yun, and C. Jacobsen, "Achromatic Fresnel optics for wideband extreme-ultraviolet and X-ray imaging," *Nat.*, Vol. 424, No. 6944, 50–53, 2003.
4. Kipp, L., M. Skibowski, R. L. Johnson, R. Berndt, R. Adelung, S. Harm, and R. Seemann, "Sharper images by focusing soft X-rays with photon sieves," *Nat.*, Vol. 414, No. 6860, 184–188, 2001.
5. Siemion, A., A. Siemion, M. Makowski, J. Suszek, J. Bomba, A. Czerwinski, F. Garet, J.-L. Coutaz, and M. Sypek, "Diffractive paper lens for terahertz optics," *Opt. Lett.*, Vol. 37, No. 20, 4320–4322, 2012.
6. Walsby, E. D., S. M. Durbin, D. R. S. Cumming, and R. J. Blaikie, "Analysis of silicon terahertz diffractive optics," *Curr. Appl. Phys.*, Vol. 4, Nos. 2–4, 102–105, 2004.
7. Wang, S., T. Yuan, E. D. Walsby, R. J. Blaikie, S. M. Durbin, D. R. S. Cumming, J. Xu, and X.-C. Zhang, "Characterization of T-ray binary lenses," *Opt. Lett.*, Vol. 27, No. 13, 1183–1185, 2002.
8. Wiltse. C., "Diffractional optics for terahertz frequencies," *Proceeding of SPIE Symposium*, 127–135, September 2004.
9. Walsby, E. D., S. Wang, J. Xu, T. Yuan, R. Blaikie, S. M. Durbin, X.-C. Zhang, and D. R. S. Cumming, "Multilevel silicon diffractive optics for terahertz waves," *J. Vac. Sci. Technol. B*, Vol. 20, No. 6, 2780–2784, 2002.
10. Walsby, E. D., J. Alton, C. Worrall, H. E. Beere, D. A. Ritchie, and D. R. S. Cumming, "Imprinted diffractive optics for terahertz radiation," *Opt. Lett.*, Vol. 32, No. 9, 1141–1143, 2007.
11. Wiltse. J, "Zone plate designs for terahertz waves," *Proceeding of SPIE Symposium*, 167–179, May 2005.
12. Saavedra, G., W. D. Furlan, and J. A. Monsoriu, "Fractal zone plates," *Opt. Lett.*, Vol. 28, No. 12, 971–973, 2003.
13. Furlan, W. D., G. Saavedra, and J. A. Monsoriu, "Fractal zone plates produce axial irradiance with fractal profile," *Opt. Photonics News*, Vol. 14, No. 12, 31–31, 2003.
14. Furlan, W. D., G. Saavedra, and J. A. Monsoriu, "White-light imaging with fractal zone plates," *Opt. Lett.*, Vol. 32, No. 15, 2109–2111, 2007.
15. Ge, X., Z. Wang, K. Gao, D. Wang, Z. Wu, J. Chen, Z. Pan, K. Zhang, Y. Hong, P. Zhu, and Z. Wu, "Use of fractal zone plates for transmission X-ray microscopy," *Anal. Bioanal. Chem.*, Vol. 404, No. 5, 1303–1309, 2012.
16. Boivin, A., "On the theory of diffraction by concentric arrays of ring-shaped apertures," *J. Opt. Soc. Am.*, Vol. 42, No. 1, 60–64, 1952.

A Terahertz Source with High Frequency Accuracy Using a Mach-Zehnder-modulator-based Flat Comb Generator for High Resolution Spectroscopy

Isao Morohashi, **Yoshihisa Irimajiri**, **Takahide Sakamoto**, **Norihiko Sekine**, **Tetsuya Kawanishi**, **Motoaki Yasui**, **and Iwao Hosako**
National Institute of Information and Communications Technology, Japan

Abstract— In this paper, we repot on generation of THz waves with high accuracy and precise controllability of the frequency using a photonic down-conversion technique. A 2.5 THz-spanned optical comb signal was generated by a combination of a Mach-Zehnder-modulator-based flat comb generator and a dispersion-flattened dispersion-decreasing fiber. By mixing a two-tone signal extracted from the comb signal, THz signals have generated, in which the C/N ratio of them was greater than 30 dB.

Terahertz (THz) waves attract great deal of attention in material research, gas sensing and so forth [1]. For these applications, time-domain spectroscopy (TDS) is widely used. Although the THz-TDS can simultaneously acquire amplitude and phase spectra, the frequency resolution is limited by the temporal window of signal waveforms. Photonic down-conversion techniques are a good candidate for THz sources with precise frequency tuning, because the frequency of THz signals can be precisely controlled by the frequency separation of two-tone signals. Optical combs generated by a modulator-based source are suitable for creating the two-tone signals, because of high frequency accuracy and controllability [2]. Recently, a Mach-Zehnder-modulator (MZM)-based flat comb generator (MZ-FCG) has proposed and demonstrated [3, 4]. The MZ-FCG can generate ultraflat comb signals using single MZM. In addition, the MZ-FCG can operate with alignment-free and turn-key starting. In our previous work, we have demonstrated generation of millimeter waves with narrow linewidth and low phase noise by using the MZ-FCG [5]. In this paper, we repot on generation of THz waves with high frequency accuracy using the MZ-FCG.

Figure 1(a) shows the mechanism of comb generation using the MZ-FCG. A dual-drive-type MZM fabricated on a $LiNbO_3$ crystal was used. The MZM is driven by two large-amplitude rf sinusoidal signals with slightly different amplitudes. A continuous-wave (cw) light led to the MZM is converted to a comb signal. The spectral spacing is directly related to the rf frequency, and the number of sidebands depends on the rf power. Thus, the bandwidth of the comb signal is decided by the frequency and the power of the rf signal. When the condition of $\Delta A \pm \Delta\theta = \pi/2$ is satisfied (comb flattening condition), the amplitudes of the comb modes are flattened out, where ΔA is the amplitude difference between the rf signals, and $\Delta\theta$ is the optical phase difference between the two arms of the MZM [4, 6]. In the comb flattening condition, the generated comb signal has linear chirp, so that it can be formed to a picosecond pulse train in the time domain by compensating the chirp using a standard single-mode fiber (SMF). Figure 1(b) shows the configuration of the MZ-FCG. The MZ-FCG was driven by a 10 GHz rf signal. A cw light incident into the MZ-FCG is converted to an ultraflat comb signal. The comb signal was launched into a 1.2 km-long single-mode fiber to form picosecond pulse trains. The picosecond pulse train was conducted to a dispersion-flattened dispersion-decreasing fiber (DF-DDF) to generate broadband comb signal by an adiabatic soliton

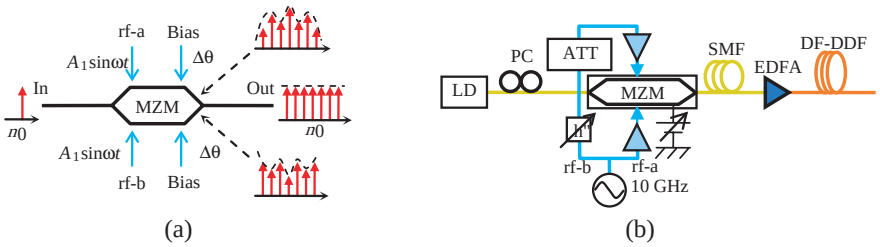

Figure 1: (a) The mechanism of comb generation by the MZ-FCG. (b) The experimental configuration of broadband comb generation. ϕ, rf phase shifter; ATT, rf attenuator; PC, polarization controller; DF-DDF, dispersion-flattened dispersion-decreasing fiber.

compression process. Figure 2 shows a spectrum of a generated comb signal. In Figure 2(a), 40 modes were clearly observed, and the 10 dB-reduction bandwidth was 340 GHz. By compensating the chirp of the comb signal using the single-mode fiber, a 2.8 ps-width pulse was generated. The picosecond pulse was amplified by the EDFA, and launched into the DF-DDF. Figure 2(b) shows a spectrum of a broadband comb signal. The comb signal spanned over 20 nm, which corresponds to a bandwidth of 2.5 THz.

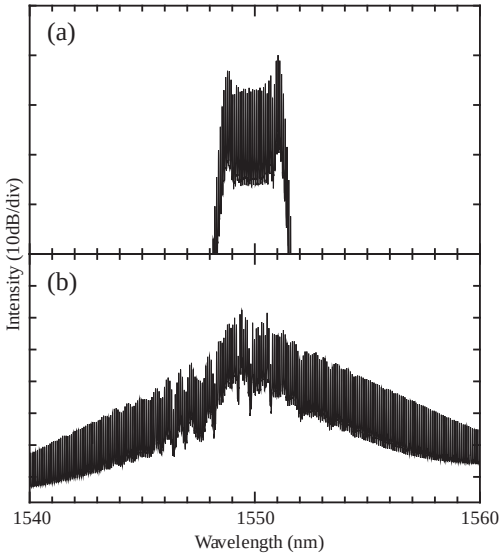

Figure 2: The optical spectrum of a 10 GHz-spaced comb signal generated by the MZ-FCG.

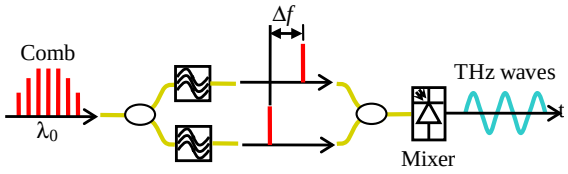

Figure 3: The basic concept of MMW generation using comb signals generated by the MZ-FCG.

Figure 4 shows the basic concept of THz wave generation. Two optical modes are extracted from the broadband comb signal by using a pair of optical filters. The extracted modes are launched into a photomixer such as uni-traveling carrier photodiodes (UTC-PDs). In this scheme, there are two methods for the frequency tuning of THz signals; one is a coarse adjustment by tuning the frequency of the filters which changes the selection of the comb modes. The other is fine tuning by changing the frequency of rf signal driving the MZ-FCG, f_m, which can precisely tune the THz frequency. The frequency stability of the THz signal is depends on that of the rf signal.

Figure 4 shows experimental setup for THz wave generation. The comb signal generated by the MZ-FCG was halved by a 3 dB optical coupler. An optical two-mode signal for photomixing was extracted from the comb signal by using a pair of optical tunable bandpass filters (TBFs) with the minimum pass-bandwidth of 6 GHz. The extracted two modes are combined by another 3 dB

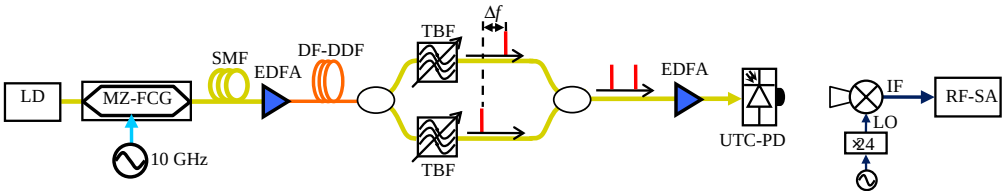

Figure 4: Schematic illustration of the experimental setup for MMW signal generation. TBF, optical tunable bandpass filter; RF-SA, rf spectrum analyzer.

coupler. Figures 5(a)–(c) show optical spectra of the two-tone signals. A two-tone signal with the high extinction ratio was successfully extracted, in which the frequency separations were 600, 700, and 750 GHz, respectively. The two-tone signals were launched into an antenna-integrated-type UTC-PD with a nominal bandwidth of greater than 1 THz. The UTC-PD radiated THz signals into air via silicon hemispherical lens. This generated THz signals were characterized by the down-conversion technique. The THz signals were coupled to a 24-multiplying harmonic mixer and down-converted to a RF signal. The intermediate frequency (IF) signal of the mixer was measured by a spectrum analyzer. Figures 5(d)–(f) show an rf spectra of generated THz signals. A THz signal centered at 600, 700, and 750 GHz, which correspond to the frequency separation of the two-tone signals, were successfully generated. The C/N ratios of THz signals were greater than 30 dB at the resolution bandwidth of 1 Hz.

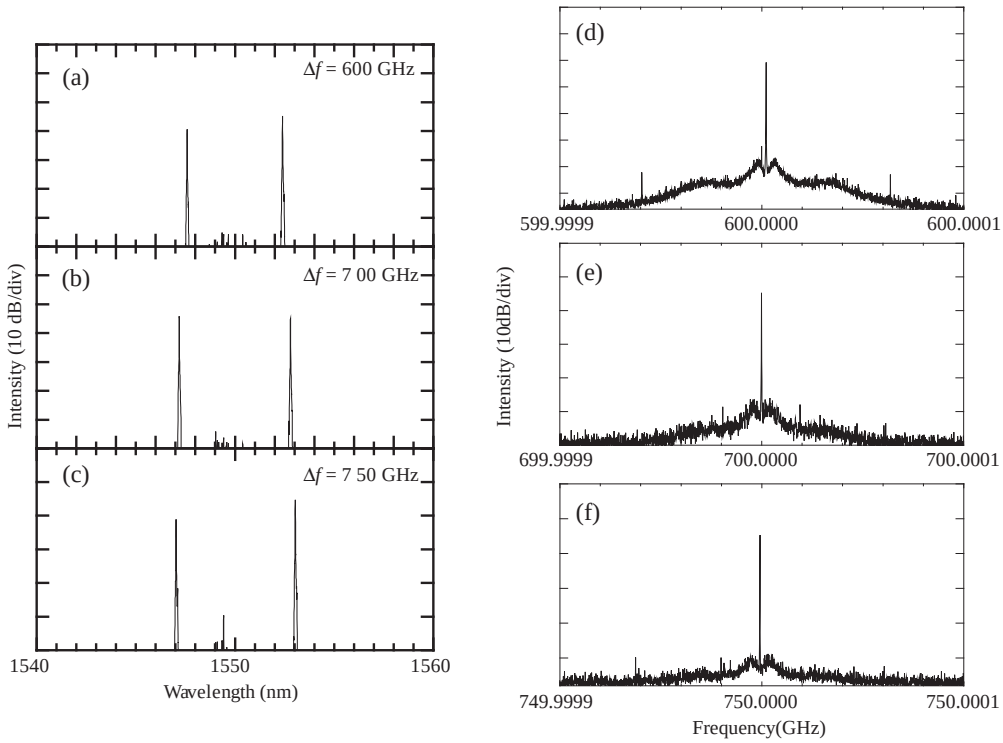

Figure 5: (a)–(c) The optical spectra of the two-tone signals, and (d)–(f) the spectra of the generated THz signals.

In conclusion, we have successfully generated THz signal by using the combination of the MZ-FCG and the DF-DDF. By extracting arbitrary two modes from the optical frequency comb broadening over 2.5 THz, high stable and accurate THz-cw was generated. In the generation of THz signals, we have confirmed that the signal has the C/N ratio of greater than 30 dB. Photonics down-conversion technique using optical two-tone signals of the optical comb is a good candidate for a THz source with high accuracy and precise frequency tuning.

REFERENCES

1. Tonouchi, M., "Cutting-edge terahertz technology," *Nat. Photon.*, Vol. 1, 97–105, Feb. 2007.
2. Kawanishi, T., S. Oikawa, K. Yoshiara, T. Sakamoto, S. Shinada, and M. Izutsu, "Low noise photonic millimeter-wave generation using an integrated reciprocating optical modulator," *IEEE Photon. Technol. Lett.*, Vol. 17, No. 3, 669–671, 2005.
3. Song, H., N. Shimizu, and T. Nagatsuma, "Broadband-frequency-tunable sub-terahertz wave generation using an optical comb, AWGs, optical switches, and a uni-traveling carrier photodiode for spectroscopic applications," *IEEE Lightw. Technol.*, Vol. 26, No. 15, 2521–2530, 2008.
4. Sakamoto, T., T. Kawanishi, and M. Izutsu, "Asymptotic formalism for ultraflat optical frequency comb generation using a Mach-Zehnder modulator," *Opt. Lett.*, Vol. 32, No. 11, 1515–1517, 2007.

5. Morohashi, I., T. Sakamoto, H. Sotobayashi, T. Kawanishi, and I. Hosako, "Phase noise characteristics of millimeter waves generated by Mach-Zehnder-modulator-based flat comb generator," *The International Conference on Infrared, Millimeter, and Terahertz Waves (IRMMW-THz 2010)*, 1–2, 2010.
6. Morohashi, I., T. Sakamoto, H. Sotobayashi, T. Kawanishi, and I. Hosako, "Broadband wavelength-tunable ultrashort pulse source using a Mach-Zehnder modulator and dispersion-flattened dispersion-decreasing fiber," *Opt. Lett.*, Vol. 34, No. 15, 2297–2299, 2008.

Harmonic and Intermodulation Performance of a Radio-frequency Plasma Capacitor

Muhammad Taher Abuelma'atti
King Fahd University of Petroleum and Minerals, Box 203, Dhahran 31261, Saudi Arabia

Abstract— In this paper, closed-form approximate expressions for the harmonic and intermodulation performance of a radio-frequency plasma capacitor are presented. These expressions are obtained by approximating the nonlinear capacitor-voltage characteristic using a Fourier-series. These expressions are valid over a wide range of the voltage applied across the capacitor and can be used for investigating the large signal performance of the capacitor.

1. INTRODUCTION

At present there is a growing interest in the use of the dielectric properties of gas discharge plasma to develop continuously variable radio-frequency capacitors [1]. This is attributed to their relatively high capacitance ratio, and high quality factor at relatively high frequencies in addition to their promising impedance characteristics [1]. However, only very little has been written about their nonlinear performance under relatively large signal conditions [2, 3]. It is very well known that under large signal conditions device and/or system nonlinearities will result in harmonic and intermodulation products that may propagate through the system and result in system performance degradation. Therefore, in order to assess the potential of the plasma capacitors it is essential to assess its nonlinear performance under large signal conditions.

Following the procedure described in [2] the dynamic sheath capacitance of a planar plasma capacitor can be described by Equation (1).

$$C_s(t) = \frac{\varepsilon_0 A_{RF}}{\sqrt{2\left(\frac{\varepsilon_0 V_s(t)}{en_s} + \frac{1}{6}(1-\alpha)^2 s_{DC}^2\right)}} \tag{1}$$

In Equation (1), $0 \leq \alpha \leq 1$ is a fraction that determines the ion distribution profile, s_{DC} is the DC electron sheath width, ε_0 is the permittivity of the free space, A_{RF} is the area of the capacitor plate, $V_s(t)$ is the total voltage across the sheath, n_s is the electron density at the sheath edge and e is the electron charge. Using Equation (1), the current through the capacitor can be described by

$$\begin{aligned} i_s(t) &= \frac{d(C_s(t)V_s(t))}{dt} = C_s(t)\frac{dV_s(t)}{dt} + V_s(t)\frac{dC_s(t)}{dt} \\ &= \left(\frac{\varepsilon_0 A_{RF}}{\sqrt{2\left(\frac{\varepsilon_0 V_s(t)}{en_s} + \frac{1}{6}(1-\alpha)s_{DC}^2\right)}} - \frac{\varepsilon_0 A_{RF}\left(\frac{\varepsilon_0}{en_s}\right)}{\sqrt[3]{2\left(\frac{\varepsilon_0 V_s(t)}{en_s} + \frac{1}{6}(1-\alpha)s_{DC}^2\right)}} \right) \frac{dV_s(t)}{dt} \end{aligned} \tag{2}$$

With $\varepsilon_0 \approx 9x10^{-12}\,\mathrm{F/m}$, $e \approx 1.6x10^{-9}\,\mathrm{Coulombs}$ and $n_s = 10^{16} - 10^{17}\,\mathrm{m}^{-3}$ the second term on the right hand side of Equation (1) can be ignored compared to the first term and Equation (2) reduces to

$$i_s(t) \approx \left(\frac{\varepsilon_0 A_{RF}}{\sqrt{2\left(\frac{\varepsilon_0 V_s(t)}{en_s} + \frac{1}{6}(1-\alpha)s_{DC}^2\right)}} \right) \frac{dV_s(t)}{dt} \tag{3}$$

Equation (3) is nonlinear. Thus, a multisinusoidal voltage, $V_s(t)$ applied across the capacitor would result in harmonics and intermodulation components in the capacitor current. However, in its present form Equation (3) cannot yield closed-form expressions for the amplitudes of these harmonic and intermodulation components. Recourse to numerical solutions is, therefore, inevitable or alternatively experimental measurements can be used to assess the performance of the planar

plasma capacitor excited by a two-sinusoids input voltage [2]. While this may be a useful approach to assess the harmonic and intermodulation performance of a plasma capacitor resulting from a two-sinusoids input voltage, it is extremely hard to predict the performance of the capacitor under the effect of a multisinusoidal input voltage. Moreover, this approach does not allow the insight into the effect of various parameters of the capacitor on its harmonic and intermodulation performance.

The major intention of this paper is, therefore, to present an approximate analysis that leads to closed-form approximate expressions that can be used to assess the harmonic and intermodulation performance of the plasma sheath capacitor under multisinusoidal input voltage. To the best of the author's knowledge no attempt has been reported in the open literature to obtain such closed-form approximate expressions.

2. ANALYSIS

Here we propose to rewrite Equation (3) as follows

$$y(t) = \frac{1}{\sqrt{1+x(t)}} \frac{dx(t)}{dt} \tag{4}$$

In Equation (4),

$$y(t) = \frac{i_s(t)}{en_s A_{RF} \sqrt{\frac{1}{12}(1-\alpha)s_{DC}^2}} \tag{5}$$

is the normalized capacitor current, and

$$x(t) = \frac{V_s(t)}{\frac{en_s(1-\alpha)s_{DC}^2}{6\varepsilon_0}} \tag{6}$$

is the normalized applied voltage. In its present form Equation (4) can not yield closed-form analytical expressions for the amplitudes of the harmonic and intermodulation components of the normalized current, $y(t)$, resulting from a normalized multisinusoidal input voltage, $x(t)$. Here we propose to approximate the term $1/\sqrt{1+z}$ using the Fourier-series expansion given by

$$\frac{1}{\sqrt{1+z}} \cong a_0 + \sum_{m=1}^{M} \left(a_m \cos\left(\frac{2m\pi}{D} z\right) + b_m \sin\left(\frac{2m\pi}{D} z\right) \right) \tag{7}$$

In Equation (7) the parameters $D,\ a_0,\ a_m,\ b_m,\ m = 1, 2, \ldots, M$ are fitting parameters that can be easily obtained using the procedure described in [4] using simple algebraic calculations and without recourse to sophisticated and/or dedicated software.

Using Equation (7) and assuming that the normalized input voltage is an equal-amplitude two-sinusoids of the form

$$x(t) = X(\sin\omega_1 t + \sin\omega_2 t) \tag{8}$$

then the normalized capacitive current can be expressed as

$$\begin{aligned} y(t) \ \cong \ & \left[a_0 + \sum_{m=1}^{M} \left(a_m \cos\left(\frac{2m\pi}{D} X(\sin\omega_1 t + \sin\omega_2 t\right) + b_m \sin\left(\frac{2m\pi}{D} X(\sin\omega_1 t + \omega_2 t\right)\right)\right] \\ & (X(\omega_1 \cos\omega_1 t + \omega_2 \cos\omega_2 t)) \end{aligned} \tag{9}$$

Using the trigonometric identities

$$\sin(\beta\sin\theta) \ = \ 2\sum_{l=0}^{\infty} J_{2l+1}(\beta)\sin(2l+1)\theta$$

$$\cos(\beta\sin\theta) \ = \ J_0(\beta) + 2\sum_{l=1}^{\infty} J_{2l}(\beta)\cos(2l)\theta$$

where $J_l(\beta)$ is the Bessel function of order l, and after simple mathematical manipulations, it is easy to show that

$$Y_{1(\omega_1)}/\omega_1 = Y_{1(\omega_2)}/\omega_2 = X\left(a_0 + \sum_{m=1}^{M} a_m J_2\left(\frac{2m\pi}{D}X\right) J_0\left(\frac{2m\pi}{D}X\right)\right) \tag{10}$$

for the normalized capacitive current component at frequencies ω_1 and ω_2,

$$Y_{3(\omega_1)}/\omega_1 = Y_{3(\omega_2)}/\omega_2 = X\left(\sum_{m=1}^{M}\left(a_m J_0\left(\frac{2m\pi}{D}X\right)\left(J_2\left(\frac{2m\pi}{D}X\right) + J_4\left(\frac{2m\pi}{D}X\right)\right)\right)\right) \tag{11}$$

for the normalized capacitive third-harmonic current components at frequencies $3\omega_1$ and $3\omega_2$,

$$Y_{2(\omega_1)}/\omega_1 = Y_{2(\omega_2)}/\omega_2 = X\left(\sum_{m=1}^{M}\left(b_m J_0\left(\frac{2m\pi}{D}X\right)\left(J_1\left(\frac{2m\pi}{D}X\right) + J_3\left(\frac{2m\pi}{D}X\right)\right)\right)\right) \tag{12}$$

for the normalized capacitive second-harmonic components at frequencies $2\omega_1$ and $2\omega_2$,

$$Y_{2,1}/\omega_1 = X\sum_{m=1}^{M}\left(a_m J_2\left(\frac{2m\pi}{D}X\right) J_0\left(\frac{2m\pi}{D}X\right)\right) \tag{13}$$

for the normalized capacitive third-order intermodulation current components at frequencies $2\omega_1 \pm \omega_2$, and

$$Y_{1,1}/(\omega_1 + \omega_2) = X\sum_{m=1}^{M}\left(b_m J_1\left(\frac{2m\pi}{D}X\right) J_0\left(\frac{2m\pi}{D}X\right)\right) \tag{14}$$

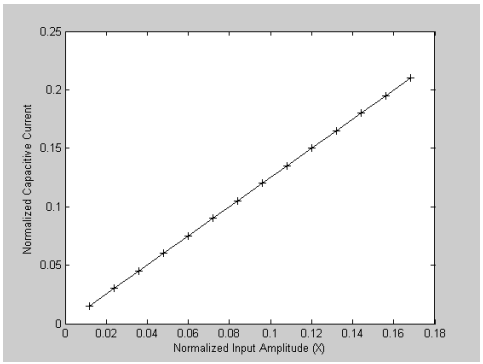

(a)

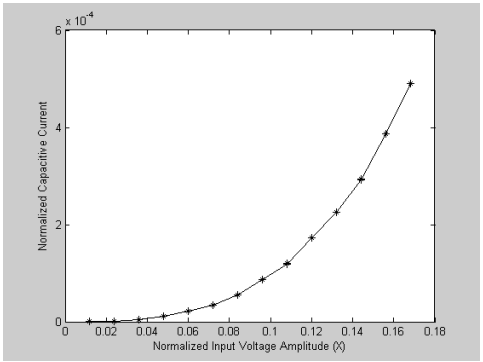

(b)

*:Third-harmonic
+: Third-order intermodulation

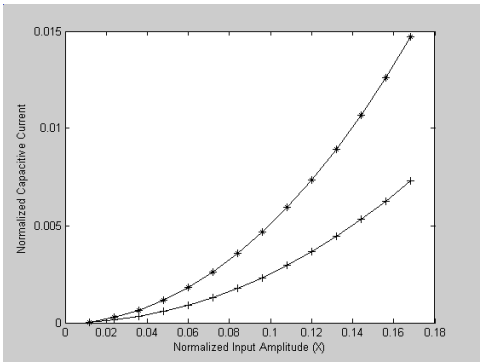

(c)

*: Second-order intermodulation
+: Second-harmonic

Figure 1: (a) Variation of the normalized fundamental capacitive current component. (b) Variation of the normalized third-harmonic and third-order intermodulation capacitive current components. (c) Variation of the normalized second-harmonic and second-order intermodulation capacitive current components.

for the normalized capacitive second-order intermodulation current components at frequencies $\omega_1 \pm \omega_2$. For the special case with $\omega_1 \cong \omega_2$, Equation (14) reduces to

$$Y_{1,1}/\omega_1 = 2X \sum_{m=1}^{M} \left(b_m J_1 \left(\frac{2m\pi}{D} X \right) J_0 \left(\frac{2m\pi}{D} X \right) \right) \tag{15}$$

Inspection of Equations (10)–(15) clearly shows that the amplitudes of the normalized capacitive current components at the fundamental, harmonic and intermodulations frequencies are frequency dependent.

Using Equations (10)–(13) and (15) the harmonic and intermodulation performance of a radio frequency plasma capacitor was calculated assuming two tone equal-amplitude exciting voltage. The results are shown in Fig. 1. Inspection of Fig. 1 clearly shows that the normalized amplitudes of the capacitive current components are monotonically increasing with the normalized amplitude of the input voltage tone. Moreover, the normalized capacitive current components at the third-harmonic and the third-order intermodulation frequency components are almost equal and are much smaller than the normalized amplitudes of the capacitive current components at the second-harmonic and the second-order intermodulation frequency components. Furthermore, it appears that the second-order intermodulation capacitive current component is higher than the second-harmonic capacitive current component. These trends are in excellent agreement with the experimental results reported in [2].

3. CONCLUSION

In this paper, closed-form approximate analytical expressions for the harmonic and intarmodulation performance of RF plasma capacitors excited by an arbitrary multisinusoidal voltage have been presented. To the best of the author's knowledge no such analytical expressions are available in the open literature. Using these expressions the harmonic and intermodulation performance of the RF plasma capacitor excited by a two-tone equal-amplitude input voltage has been studied and the calculated results, showing that the second-order intermodulation component is dominant, are in excellent agreement with the previously reported experimental results.

REFERENCES

1. Linardakis, P. and G. G. Borg, "Small-signal impedance of a radio frequency plasma capacitor," *IEEE Microwave and Wireless Components Letters*, Vol. 17, 763–765, 2007.
2. Linardakis, P. and G. G. Borg, "Harmonic and intermodulation distortion output of a radio-frequency plasma capacitor small-signal impedance of a radio frequency plasma capacitor," *IEEE Microwave and Wireless Components Letters*, Vol. 18, 164–166, 2008.
3. Hilbish, R. T., R. M. Montgomery, and R. A. Holmes, "Frequency conversion in the sheath capacitance of a glow discharge plasma," *Journal of Applied Physics*, Vol. 39, 5782–5791, 1968.
4. Abuelma'atti, M. T., "Simple method for calculating Fourier coefficients of experimentally obtained waveforms," *Proceedings IEE — Science Measurement, Technology*, Vol. 141, 177–178, 1994.

Study of the Dispersive Properties of Three-dimensional Magnetized Plasma Photonic Crystals with Diamond Lattices

Hai-Feng Zhang[1, 2], **Shao-Bin Liu**[1], **Hai-Ming Li**[1], **and Bing-Xiang Li**[1]

[1]College of Electronic and Information Engineering
Nanjing University of Aeronautics and Astronautics, Nanjing 210016, China
[2]Nanjing Artillery Academy, Nanjing 211132, China

Abstract— In this paper, the dispersive properties for two types of three-dimensional (3D) magnetized plasma photonic crystals (MPPCs) composed of homogeneous dielectric and magnetized plasma with diamond lattices (dielectric spheres immersed in magnetized plasma background or vice versa) are theoretically investigated based on a modified plane wave expansion method, as incidence electromagnetic wave vector is perpendicular to the external magnetic field. The influences of plasma collision frequency, filling factor, the external magnetic field and plasma frequency on the dispersive properties of both types of MPPCs are investigated in detail, respectively. From the numerical results, it has been shown that not only the locations but also relative bandwidths of the photonic band gaps (PBGs) for both types of 3D MPPCs can be manipulated by plasma frequency, filling factor and the external magnetic field, respectively. However, the plasma collision frequency has no effect on the PBGs for two types of 3D MPPCs. The locations of flatbands regions can not be tuned by any parameters except for plasma frequency and the external magnetic field.

1. INTRODUCTION

Since firstly proposed by Hojo and Mase [1], the photonic crystals (PPCs) have been attracted the great attentions of researchers. The dispersive properties of one- or two-dimensional (2D) PPCs have been studied in detailed. All of the interesting properties of PPCs are dependent on the dispersive characteristics of the plasma. However, if the external magnetic field is introduced in the plasma, the magnetized plasma becomes an anisotropic medium. Therefore, the magnetized plasma photonic crystals (MPPCs) have some superior properties compared to the unmagnetized PPCs. The MPPC also has triggered a flood of researches. Zhang et al. [2] and Qi et al. [3] analyzed the transmission characteristics of 1D MPPCs with dielectric and plasma defect layers by FDTD method and TMM, respectively. They demonstrated that defect mode can be modulated by the plasma or external magnetic field in a larger frequency region. Hamidi et al. [4] investigated the magneto-optical properties of 1D magnetized coupled resonator PPCs. He found the magneto-optical properties of such structure can be tuned by the parameters of such MPPCs. For the 2D case, the PBGs structure of 2D MPPCs for TE polarization is studied by Qi [5]. She found flatbands regions appeared in the dispersion curves due to the role of external magnetic field, and the PBGs can be tuned by the parameters of MPPCs. On the other hand, Zhang et al. [6] and Qi et al. [7] arranged plasma periodically by the external magnetic field to form a new kind of MPPCs, which are only composed of the plasma. They pointed out that the PBGs of such MPPCs also can be controlled by the external magnetic field. All the works mentioned above only focused on the dispersive properties of 1D or 2D MPPCs. To our knowledge, there are few reports about 3D MPPCs since the work of Zhang et al. [8] about the PBGs properties of 3D unmagnetized PPCs. In this paper, we intend to investigate the dispersive properties of 3D MPPCs with diamond lattices by a modified PWE method. Two types of the 3D MPPCs are proposed. The first type (type-1) is a 3D MPPCs which dielectric spheres are arranged in the magnetized plasma background periodically with diamond lattices, while the second one (type-2) is a complementary structure composed of magnetized plasma spheres in the dielectric background.

2. THEORETICAL MODEL AND NUMERICAL METHOD

The standard Brillouin zone and schematic structures of 3D MPPCs with diamond lattices can be found in many textbooks and reports. Thus, they are not shown here. Consider the radius of the spheres and lattice constant are R and a respectively; the relative dielectric function for dielectric and magnetized plasma are ε_a and ε_p, respectively. Assumed the external magnetic field is perpendicular to the incidence electromagnetic wave vector at any time. In this case, there are two different modes. One configuration is called ordinary mode, and the other is extraordinary

mode. The ordinary mode is unaffected by the external magnetic field. Thus, we shall limit our consideration to extraordinary mode case, and the ε_p is given by [9]:

$$\varepsilon_p = \frac{\left[\omega(\omega + j\nu_c) - \omega_p^2\right]^2 - \omega^2\omega_c^2}{\omega^2\left[\left((\omega + j\nu_c)^2 - \omega_c^2\right)\right] - \omega\omega_p^2(\omega + j\nu_c)} \tag{1}$$

In this expression, ω_p, ν_c, ω_c and ω are the plasma frequency, the electron collision frequency, plasma cyclotron frequency and the angular frequency, respectively. In order to obtain the band diagrams of 3D MPPCs, the PWE method is used as mentioned by Zhang et al. [10], which can calculate successfully the PBGs for the PCs composed of the frequency-dependence medium.

3. NUMERICAL RESULTS AND DISUSSION

As we know, a symmetric set of primitive vectors for the diamond lattice is $\mathbf{a}_1 = (0.5a, 0.5a, 0)$, $\mathbf{a}_2 = (0, 0.5a, 0.5a)$, $\mathbf{a}_3 = (0.5a, 0, 0.5a)$. The reciprocal lattice vector basis can be defined as $\mathbf{b}_1 = (2\pi/a, 2\pi/a, -2\pi/a)$, $\mathbf{b}_2 = (-2\pi/a, 2\pi/a, 2\pi/a)$, $\mathbf{b}_3 = (2\pi/a, -2\pi/a, 2\pi/a)$. The high symmetry points have the coordinate as $\Gamma = (0, 0, 0)$, $X = (2\pi/a, 0, 0)$, $W = (2\pi/a, \pi/a, 0)$, $K = (1.5\pi/a, 1.5\pi/a, 0)$, $L = (\pi/a, \pi/a, \pi/a)$, and $U = (2\pi/a, 0.5\pi/a, 0.5\pi/a)$. The convergence accuracy is better than 1% for the lower energy bands, when a total number of 729 plane waves can be used [11]. Without loss of generality, we plot $\omega a/2\pi c$ with the normalization convention $\omega_{p0}a/2\pi c = 1$. Thus, we can define the plasma frequency as $\omega_p = \omega_{p1} = 0.3\pi c/a = 0.15\omega_{p0}$ to make the problem scale-invariant, and we also choose the plasma collision frequency as $\nu_c = \nu_o = 0.02\omega_{pl}$, $\varepsilon_a = 13.9$, and $\mu_a = 1$, respectively. The plasma cyclotron frequency is $\omega_c = 0.8\omega_p$. Here, we only focus on the properties of first (1st) PBG and flatbands regions for such 3D MPPCs.

The dispersion curves for two types of MPPCs with different parameters of magnetized plasma are plotted in Figs. 1–2. The red shaded regions indicate PBGs. As shown in Fig. 1(a), if $\omega_p = 0$, $\omega_c = 0$ and $\nu_c = 0$, the type-1 MPPCs can be look as a conventional dielectric-air PCs. There are three PBGs presenting themselves at 0.4120–0.4847 ($2\pi c/a$), 0.6768–0.6796 ($2\pi c/a$) and 0.9018–0.9190 ($2\pi c/a$) in the frequency region, respectively. As the external magnetic field is introduced into the PCs, the PBGs are changed and two flatbands regions appear as shown in Fig. 1(b). The PBGs cover 0.4217–0.4963 ($2\pi c/a$), 0.6811–0.6835 ($2\pi c/a$) and 0.9046–0.9226 ($2\pi c/a$), and two flatbands regions are located 0–0.1015 ($2\pi c/a$) and 0.1923–0.2215 ($2\pi c/a$), respectively. The main reason for formed the flatbands is because the existence of surface plasmon modes [12]. If the external magnetic field is existing, the cutoff frequencies for the left and right circular polarization are $f_L = 0.1015(2\pi c/a)$ ($f_L = -\omega_c/2 + \sqrt{\omega_c^2/4 + \omega_p^2}$) and $f_R = 0.2215(2\pi c/a)$ ($f_R = \omega_c/2 + \sqrt{\omega_c^2/4 + \omega_p^2}$). The upper hybrid frequency $f_U = 0.1923(2\pi c/a)$ ($f_R = \sqrt{\omega_c^2 + \omega_p^2}$) [13]. Then, f_L, f_R and f_U are nearly corresponding to the upper edge frequencies of two flatbands regions and the lower edge of second flatbands region, respectively, which mean that the flatbands are caused by the magnetized plasma itself. Compared to Fig. 1(a), the 1st PBG is enlarged as shown in Fig. 3(c).

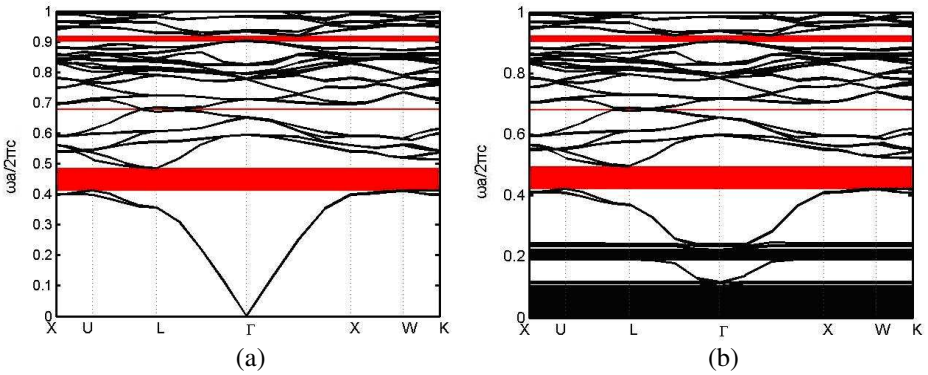

Figure 1: The band structure of type-1 MPPCs with $\varepsilon_a = 13.9$ and $f = 0.36$ but with different ω_p, ω_c and ν_c, respectively. (a) $\omega_p = 0$, $\nu_c = 0$, $\omega_c = 0$, and (b) $\omega_p = 0.15\omega_{p0}$, $\nu_c = 0.02\omega_{pl}$, $\omega_c = 0.8\omega_p$, respectively. The red shaded regions indicate PBGs.

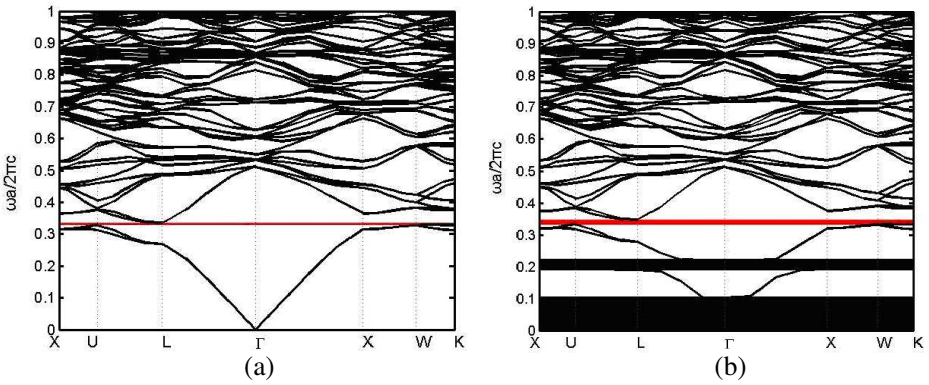

Figure 2: The band structure of type-2 MPPCs with $\varepsilon_a = 13.9$ and $f = 0.36$ but with different ω_p, ω_c and ν_c, respectively. (a) $\omega_p = 0$, $\nu_c = 0$, $\omega_c = 0$, and (b) $\omega_p = 0.15\omega_{p0}$, $\nu_c = 0.02\omega_{pl}$, $\omega_c = 0.8\omega_p$, respectively. The red shaded regions indicate PBGs.

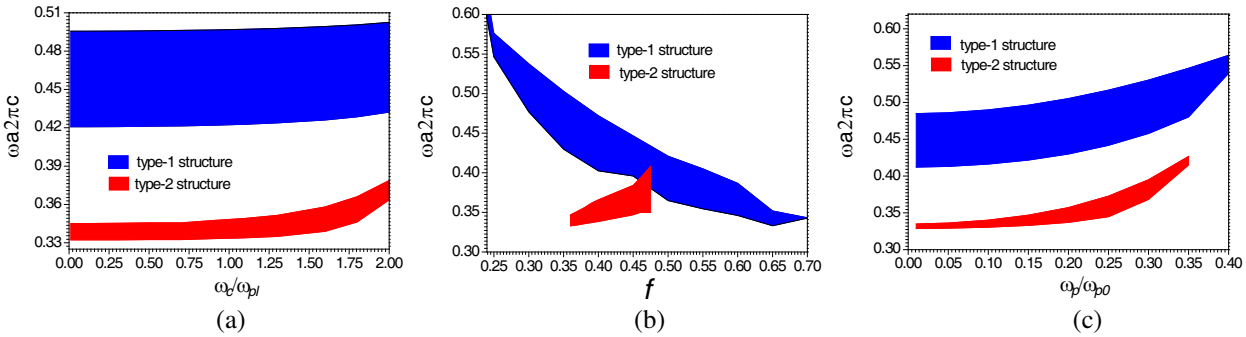

Figure 3: The effects of different parameters on the PBGs for two types of MPPCs. (a) ω_c, (b) f and (c) ω_p. The red shaded regions indicate PBGs.

Fig. 2(a) shows that there is only one PBG for type-2 MPPCs which runs from 0.3289 to 0.3348 ($2\pi c/a$). In Fig. 2(b), it can be seen that the edges of PBG are upward to higher frequencies, and such PBG is broaden as the external magnetic field is introduced. The PBG and flatbands regions cover 0–0.1015 ($2\pi c/a$), 0.1923–0.2215 ($2\pi c/a$) and 0.333–0.3468 ($2\pi c/a$), respectively. Compared to Fig. 2(a), the bandwidth is increased by 0.0079 ($2\pi c/a$). As mentioned above, the inclusion of magnetized plasma in 3D dielectric-air PCs can enlarge the frequency ranges of PBGs, and the central frequencies shift to higher frequencies.

We plot the effects of different parameters on the PBGs for two types of MPPCs in Fig. 3. The shaded regions indicate the PBGs. Figs. 3(a) and (c) show that the edges of PBGs are upward to higher frequencies with increasing ω_c and ω_p. The bandwidth for type-1 structure decreases but that for type-2 structure increases first then decreases as with increasing ω_c and ω_p. The maximum relative bandwidths of 1st PBGs for both structures are 0.1632 and 0.0553, which can be found at $\omega_c/\omega_{p1} = 0.01$ and 1.8, respectively. If $\omega_p/\omega_{p0} = 0.01$ and 0.4, the maximum relative bandwidths also can be obtained, which is 0.1625 and 0.0774, respectively. As we know, the bandwidths of the PBGs are governed by refractive contrast for 3D MPPCs and the positions of the PBGs are governed by the average refractive index of 3D MPPCs. Changing ω_c and ω_p mean the refractive contrast and the average refractive index of 3D MPPCs are changed. Therefore, the PBGs can be tuned by ω_c and ω_p. It is clear in Fig. 3(b) that, the edges of 1st PBG for type-1 MPPCs shift downward to lower frequencies, and the bandwidth increases first then decreases with increasing f. For type-2 structure, the edges of 1st PBG are upward to higher frequencies with increasing f. The maximum relative bandwidths of 1st PBGs for both structures are 0.1594 and 0.1538, which can be found at $f = 0.4$ and 0.475, respectively. However, for type-1 structure, it is noticed that if dielectric filling factor is small enough and close to null, the 3D MPPCs can be looked as a plasma magnetized block. The flatbands region will disappear. It is noticed that the ν_c has no effect on the PBGs [14].

Finally, we investigate the influences of the parameters of 3D MPPCs on the two flatbands regions. As mentioned above, The f_L, f_R and f_U are nearly corresponding to the edges frequencies

of the flatbands regions. Thus, the edges of two flatbands regions can not be tuned by the ε_a, ν_c and f, respectively. This is because the f_L, f_R and f_U don't depend on f, ε_a and ν_c, respectively. However, the f_L, f_R and f_U depend on the ω_p and ω_c, respectively. Consequently, the locations of two flatbands regions only can be tuned by the ω_p and ω_c.

4. CONCLUSIONS

In summary, the dispersive properties for two types of 3D MPPCs with diamond lattices composed of homogeneous magnetized plasma and dielectric have been theoretically studied by PWE method. The numerical results show the MPPCs have larger PBG and two flatbants regions appear compared to the same air-dielectric PCs. The flatbands caused by the existence of surface plasmon modes. The f_L, f_R and f_U are nearly corresponding to the edges frequencies of the flatbands regions. The location of flatbands region just only can be modulated by the plasma frequency and external magnetic field. The PBGs can be tuned in a larger frequency by changing plasma frequency, filling factor and the external magnetic field, respectively. However, the plasma collision frequency has no effects on the dispersive properties of 3D MPPCs.

ACKNOWLEDGMENT

This work was supported by the Fundamental Research Funds for the Central Universities and the Funding of Jiangsu Innovation Program for Graduate Education (Grant No. CXZZ11_0211).

REFERENCES

1. Hojo, H. and A. Mase, "Dispersion relation of electromagnetic waves in one dimensional plasma photonic crystals," *Plasma Fusion Res.*, Vol. 80, No. 2, 89–90, 2004.
2. Zhang, H. F., M. Li, and S. B. Liu, "Defect mode properties of magnetized plasma photonic crystals," *Acta Phys. Sin.*, Vol. 58, No. 2, 1071–1076, 2009.
3. Qi, L., Z. Yang, and T. Fu, "Defect modes in one-dimensional magnetized plasma photonic crystals with a dielectric defect layer," *Phys. Plasma*, Vol. 19, No. 1, 012509, 2012.
4. Hamidi, S. M., "Optcal and magneto-optical properties of one-dimensional magnetized coupled resoner plasma photonic crystals," *Phys. Plasma*, Vol. 19, No. 1, 012503, 2012.
5. Qi, L., "Photonic band structures of two-dimensional magnetized plasma photonic crystals," *J. Appl. Phys.*, Vol. 111, No. 7, 073301, 2012.
6. Zhang, H. F., S. B. Liu, X. K. Kong, B. R. Bian, and Y. N. Guo, "Dispersion properties of two-dimensioanl plasma photonic crystals with periodically external magnetic field," *Solid State Commun.*, Vol. 152, No. 7, 1221–1229, 2012.
7. Qi, L. and X. Zhang, "Band gap characteristics of plasma with periodically varying external magnetic field," *Solid State Commun.*, Vol. 151, 1838–1841, 2011.
8. Zhang, H. F., S. B. Liu, X. K. Kong, C. Chen, and B. R. Bian, "The characteristics of photonic band gaps for three-dimensional unmagnetized dielectric plasma photonic crystals with simple-cubic lattice," *Optic Commun.* Vol. 288, 82–90, 2013.
9. Zhang, H. F., S. B. Liu, and X. K. Kong, "Photonic band gaps in one-dimensional magnetized plasma photonic crystals with arbitrary magnetic declination," *Phys. Plasma*, Vol. 19, No. 12, 122103, 2012.
10. Zhang, H. F., S. B. Liu, H. Yang, and X. K. Kong, "Analysis of band gap in dispersive properties of tunable three-dimensional photonic crystals doped by magnetized plasma," *Phys. Plasma*, Vol. 20, No. 3, 032118, 2013.
11. Zhang H. F., S. B. Liu, and X. K. Kong, "Dispersion properties of three-dimensional plasma photonic crystals in Diamond lattice arrangement," *J. Lightwave Technol.*, Vol. 17, No. 11, 1694–1702, 2013.
12. Zhang, H. F., S. B. Liu, X. K. Kong, C. Chen, and B. R. Bian, "The properties of photonic band gaps for three-dimensional plasma photonic crystals in a diamond structure," *Phys. Plasma*, Vol. 20, No. 4, 042110, 2013.
13. Ginzburg, V. L., *The Propagation of Electromagnetic Wave in Plasma*, Pergamon, Oxford, UK, 1970.
14. Zhang, H. F., S. B. Liu, and B. X. Li, "The properties of photonic band gaps for three-dimensional tunable photonic crystals with simple-cubic lattices doped by magnetized plasma," *Optics & Laser Technol.*, Vol. 50, 93–102, 2013.